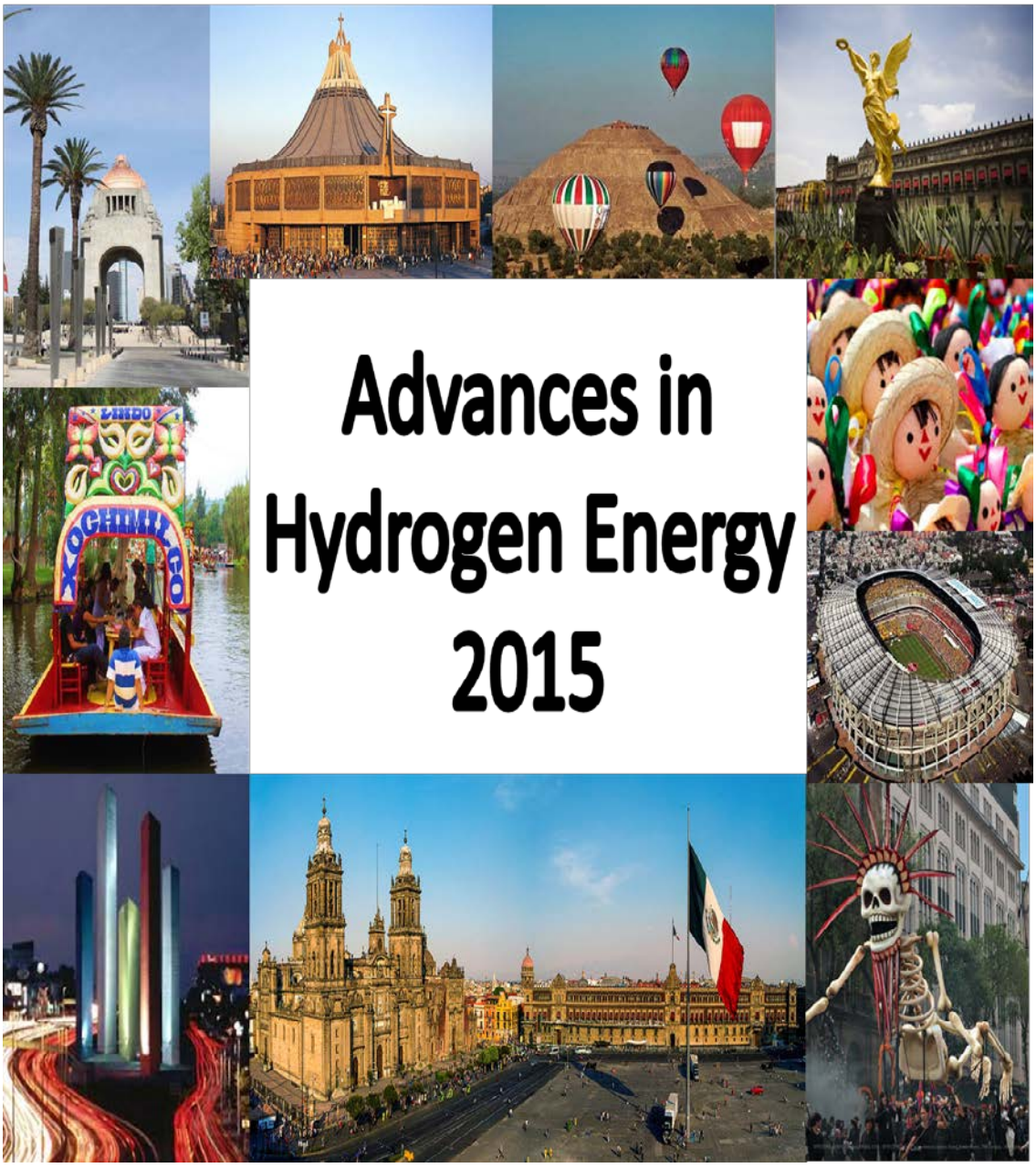

Héctor M. Poggi-Varaldo, GiovanniHernández-Flores, Omar Solorza-Feria

Advances in Hydrogen Energy-2015

Editors:
Héctor M. Poggi-Varaldo, Giovanni Hernández-Flores, Omar Solorza-Feria

Sociedad Mexicana de Hidrógeno AC
México D.F., México

1st edition

Preface

This book compiles and organizes as chapters selected full contributions of the *15th International Congress of the Mexican Hydrogen Society (15IC MHS)* held in September 22-25, 2015, in the installations of the Center for Advanced Studies and Research (CINVESTAV), Mexico City, Mexico.

This book aims at reaching a wide audience including researchers, practitioners, managers, and students who aspire to learn about or to create a deeper scientific foundation for Hydrogen-based energies, design and engineering of fuel cells and other systems based on Hydrogen, and its management and innovation.

The *15IC MHS* accepted a total of 144 abstracts and 76 articles were selected and edited to be part of this book (Table 1) after a strict peer-reviewing process. It is worth highlighting the increase of the contributions classified under the topics **Renewable energy systems** and **Nanostructured materials**, that constituted nearly 20% each of the total abstracts and were close to the most classic and mature subject **Hydrogen production, storage and applications**. Biological hydrogen production, biorefineries, microbial fuel cells, nanomaterials for electrodes, membrane/separator design and testing, coupling solar energy to hydrogen production, are examples of emerging topics covered. Together, they make nearly half of the abstracts of the Congress.

Table 1. Distribution of articles per technical subject of the Congress.

Subject	No. Articles	Proportion (%)
Hydrogen production, storage and applications	14	18.42
Direct oxidation fuel cells	5	6.58
Fuel cells components and stacks	8	10.53
Modeling and design	7	9.21
Renewable energy systems	15	19.74
Control and power conditioning	3	3.95
Policies, economy and market strategies	4	5.26
Nanostructured materials	16	21.05
Environmental aspects	3	3.95
Miscellaneous	1	1.32
TOTAL	76	100.00

The profile of the article distribution is consistent with the locomotive effect of Hydrogen on other renewable energies systems (via coupling, integration, preparation, etc.) as well as the use of Nanoscience-Nanotechnology approaches for desigining and optimizing materials related to Hydrogen energy. Moreover, it is a strong indicator of the high degree of innovation that characterizes Hydrogen energy R&D.

This book "*Advances in Hydrogen Energy-2015*" offers a unique set of cutting-edge approaches and knowledge in Hydrogen energy and it becomes, undoubtedly, a valuable tool in developing new strategies for fostering the Hydrogen Energy new era. It is the first of a series of books from the Mexican Hydrogen Society that we hope will continue in the future for the benefit of researchers, practitioners, students, and decision-makers.

Professor Dr. Héctor M. Poggi-Varaldo
Group Leader, Environmental Biotechnology and
Renewable Energies R&D Group
Dept. of Biotechnology and Bioengineering
CINVESTAV del IPN, Mexico City, Mexico.

Acknowledgements

The Mexican Hydrogen Society and the Editors of this Book acknowledege the contribution of the following persons:

Ms. Lilián Domínguez-Montero, B.S. Chem.Eng., with the GBAER, DCTS, CINVESTAV
Mr. Jaime Borbolla-Gaxiola with the GBAER, DBB, CINVESTAV
Ms. Miriam Tellez-Cruz with the FC&H2 Group, DQ, CINVESTAV
Ms. Luz de María Bretón-Deval, M.Sc., with the GBAER, DBB, CINVESTAV

Also, the effort and participation of the Reviewers in the peer-review process of the Abstracts and selected Articles is gratefully acknowledged:

Acuapan Hernández Javier – CINVESTAV-IPN
Arriaga Gerardo – CIDETEQ
Barbosa Pool Romeli – UQROO
Benavides Cantú Roberto – CIQA
Bretón Deval Luz de María – CINVESTAV-IPN
Cabañas Moreno Gerardo – CINVESTAV-IPN
Camacho Pérez Beni – UTTEC
Cano Ulises – IIE
Cañizares Villanueva Rosa Olivia – CINVESTAV-IPN
Cercado Quezada Bibiana – IPICYT
Collins Martínez Virginia H.– CIMAV
De Landa Castillo Fray – IPN
Domínguez Benetton Xochitl – VITO
Domínguez Montero Lilian E. – CINVESTAV-IPN
Durón Torres Sergio – UAZ
Escamilla-Alvarado Carlos – UANL
Escobar Morales Beatriz – CICY
Fernandez Madrigal Arturo – UNAM
Fernández Valverde Suilma Marisela – ININ
Fernández Villagómez Georgina – UNAM
González Becerra Aldo E. – CSIC-CBM SEVERO OCHOA
González García Gerardo – UACM
González Huerta Rosa de Guadalupe – ESIQIE-IPN
Hernández Melchor Dulce J. – UTTEC
Hernández-Flores Giovanni – CINVESTAV-IPN
Juárez López Katy – IBT-UNAM
López Chávez Ernesto – UACM
López Ortiz Alejandro – CIMAV
Martínez Casillas Diana – UNIVERSIDAD DE BUENOS AIRES
Matsumoto Kuwabara Yasuhiro – CINVESTAV-IPN

Morales Acevedo Arturo – CINVESTAV-IPN
Muñoz-Páez Karla M. – IPN
Ortega Clemente Alfredo – ITBOCA
Ortega-Martínez Areli del Carmen – UV
Pérez Robles Juan Francisco – CINVESTAV-QRO
Poggi-Varaldo Héctor M. – CINVESTAV-IPN
Ponce Noyola M. Teresa – CINVESTAV-IPN
Ramos Sánchez Guadalupe – UAM-I
Reguera Edilso – CICATA-IPN
Reyes-Rodríguez José Luis – CINVESTAV-IPN
Rodríguez Varela F. Javier – CINVESTAV- SALTILLO
Romero Castañón Tatiana – IIE
Romero Cedillo Leticia – CINVESTAV-IPN
Roquero Pedro – UNAM
Sathish Kumar Kamaraj – UPA
Solorza-Feria Omar – CINVESTAV-IPN
Suárez Alcántara Karina – UNAM-MORELIA
Valenzuela Zapata Miguel Ángel – IPN
Vazquez Huerta Gerardo – UAM
Vazquez-Larios Ana Line – ITS Tierra Blanca
Verde Gómez Ysmael – ITC
Zanella Rodolfo – UNAM

Content

Chapter 3.3. Polystyrene-co-acrylic acid proton exchange membranes: morphology and mechanical properties. L. Melo, R. Benavides, G. Martínez, M.L. López, MMS Paula and L. Da Silva

Chapter 3.4. Pneumatic-Thermic press for manufacturing fuel cell electrodes. L. Belin-Sandoval, B. Escobar, L.A. Soto-Ramirez, J.C. Cruz, Victor M. Sanchez and Romeli Barbosa

Chapter 3.5. An optimization study of the EPD parameters of Pt/C to fabricate PEM fuel cell electrodes using non-asymmetric AC electric field. W.J. Pech-Rodríguez, D. González-Quijano, G. Vargaz-Gutierrez, J.I. Escalante-Garcia and F.J. Rodríguez-Varela

Chapter 3.6. Electrocatalytic Oxygen Reduction Reaction (ORR) on nanostructured Pt-NiTiO3/C catalyst in alkaline media. A. Hernández-Ramírez, M. E. Sánchez-Castro, Kalasapurayil Kunhiraman Aruna, Palanisamy Karthikeyan Manoharan and F. J. Rodríguez-Varela

Chapter 3.7. Synthesis and characterization Pt/Wo3 supported on CNT for oxygen reduction reaction. E. Oseguera, C. Cortés-Escobedo and R. de G González-Huerta

Chapter 3.8. $CoTiO_3$ deposited by laser ablation on a commercial alkaline membrane: electrochemical performance for the ORR reaction in alkaline media. R. Basurto Sánchez, T. Romero Castañon, L.Escobar Alarcon, M. A. García Contreras, J. Bonifacio Martínez, E. Ordoñez-Regil, S. M. Fernández Valverde

4. Modeling and design

Chapter 4.1. Design of a microfluidic system in a PEMFC cell. L. M. Ponce-Herrera, G. Carbajal-De la Torre, S. A. Gamboa-Sánchez, K. Suarez-Alcantara, M. Villagómez-Galindo and M. A. Espinosa-Medina

Chapter 4.2. Design and analysis of photovoltaic-hydrogen system for illumination and fuel cell characterization. J. Olmedo-González, R. de G. González-Huerta, M. Tufiño-Velázquez and G. Contreras Puente

Chapter 4.3. Dissociative mechanism of oxygen reduction reaction (ORR) on Pd-Cu disordered binary alloy metal surfaces: A theoretical study. E. López-Chávez, A. García-Quiroz, G. González-García, Y. A. Peña-Castañeda, J. A. I. Díaz-Góngora and F. L. Castillo-Alvarado

Chapter 4.4. Numerical study of heat transfer in a PEM fuel cell with different flow- fields. J. Macedo-Valencia, J. M. Sierra, S. Figueroa-Ramírez, H. Mandujano and M. Meza

5. Renewable energy systems

Chapter 5.10. Biological production of CO2-free hydrogen by anaerobic microbial mixed microflora in an upflow anaerobic sludge blanket (UASB) reactor. I.M.M. Moreno-Dávila, E.B. Herrera-Ramírez, L.J. Ríos González and Y. Garza-García

Chapter 5.11. Effect of the phenolic compounds in the sugar cane bagasse saccharification for the lignocellulosic ethanol production. E. González-Bautista, J. C. Santana-Morales, A. C. Ramos-Valdivia, H. M. Poggi-Varaldo, and T. Ponce-Noyola

Chapter 5.12. Microbial fuel cells equipped with low cost membranes for the treatment of leachates from byohydrogen production. G. Hernández-Flores, H. M. Poggi-Varaldo and O. Solorza-Feria

Chapter 5.13. Microbial fuel cells fed with municipal wastewater and leachates. G. Hernández-Flores, H. M. Poggi-Varaldo

Chapter 5.14. Optimal slow pyrolysis of pomace reaction conditions for the generation of a feedstock gas for hydrogen production. M. R. Baray Guerrero, J. M. Salinas Gutiérrez, M. J. Meléndez Zaragoza, A. López Ortiz, and V. Collins-Martínez

Chapter 5.15. Potential of pretreated solids applied to an OFMSW biorefinery to improve the performance of hydrogen production: a review. L. Romero-Cedillo, H. M. Poggi-Varaldo, T. Ponce-Noyola, E. Ríos-Leal, A.C. Ramos-Valdivia, C.M. Cerda-García Rojas, J. Tapia-Ramírez

6. Control and power conditioning

Chapter 6.1. Energy management system for a hybrid hydrogen-solar. O. Aguado-Sánchez, R.G González-Huerta and D.J Cortés-Rodríguez

Chapter 6.2. Control implementation of a DC-DC energy router for renewable sources. D. Navarro Durán, E. Perez Hernandez, J. Resa Trejo and D. Cortes Rodriguez

Chapter 6.3. Cascaded multilevel inverter for fuel cell applications. V. Sanchez, J. Rosas-Caro, A. Valderrabano, F. Beltrán, R. Barbosa and B. Escobar

7. Policies, economy and market strategies

Chapter 7.1. Infraestructure analysis of the hydrogen refueling station in Mexico. N. Nuñez García, D. Morales Herrera, A. Zaragoza González, M. Sanchez Vazquez and R. González Huerta

8. Nanostructured materials

9. Environmental aspects

10. Miscellaneous

Chapter 10.1. Revising the molecular dynamics of hydrogen within the sulfur-ammonia fotothermochemical cycle through NMR spectroscopy. R. Orozco-Mena, R. Marquez-Montes, J. Mendoza-Chacón, E. Herrera-Peraza, H. Romero-Paredes, D. Chavez-Flores and V. H. Ramos-Sánchez

1
Hydrogen production, storage and applications

Chapter 1.1. Use of Hydrogen for sustainable urban transport in Cuenca, Ecuador: a theoretical study

F. Posso[a,*]; J. L. Espinoza[a]; J. Sánchez[a]; J. Zalamea[b]

[a] Prometeo Researcher, Universidad de Cuenca. Av. 12 de Abril s/n y Agustín Cueva. Cuenca, Ecuador
[b] Department of Sciences, Universidad de Los Andes, Av. La ULA. San Cristóbal, 5001. Venezuela
[c]Department of Electric and Electronics Engineering, Universidad de Cuenca. Av. 12 de Abril s/n y Agustín Cueva. Cuenca, 01010168. Ecuador,
[d]School of Chemical Engineering, Universidad de Cuenca. Av. 12 de Abril s/n y Agustín Cueva. Cuenca, 01010168. Ecuador,
[e]CELEC EP – Hidropaute Business Unit, Cuenca. Panamericana Norte km 7, Cuenca, Ecuador

ABSTRACT

The use of H_2 in urban public transport in the city of Cuenca, Ecuador is analyzed by modeling and simulating the H_2 production that would meet different levels of demand. This study proposes to use spilled turbinable energy, STE, to obtain H_2 via electrolysis due to the proximity of Cuenca to the Paute-Integral Hydroelectric Complex, which produces the largest amount of that available energy in Ecuador. STE is energy that could be generated from turbinable water that is spilled for diverse operational reasons. By combining the cost of excess electricity and the value billed to large consumers, it is possible to meet the energy demands of 100%, 50% and 10% of Cuenca's public bus fleet. This analysis determines the size of the electrolytic plant as well as the cost of hydrogen production, valued at 1.76 US$/kg in the best-case scenario, which is comparatively less than the value obtained in other Latin American and European cities for the same end use. The cost of H_2 production is 1.8 times the selling price of diesel in Ecuador but when compared to the price at which the State buys diesel on the international market, the results show that the cost of H_2 is 0.63 times the cost of diesel. The study proves that the best economic scenario is to cover 100% of the energy demand of the bus fleet, though this proposal could be implemented in stages. Despite the potential for full coverage of the energy required, aspects related to both infrastructure and costs should be studied in depth and are not included in this analysis. For example, the location of the electrolysis plant, the storage system, the scheme of distribution and supply of H_2, the optimal size of the fuel cell bus fleet and their associated costs, among others. We conclude that H_2 production from untapped hydropower and its use in Cuenca's urban transport is a niche opportunity for leading the country towards a H_2 economy. The results also provide valuable information for the Ecuadorian State in its efforts to diversify the country's energy matrix into a sustainable development path.

Keywords: Hydrogen production, H2-FC buses, Cost model, Sustainable transport

---

*Author for correspondence: Fausto Posso, Phone: (593) 990411328. Mail: fausto.posso@ucuenca.edu.ec

1. Introduction

Among the several options to obtain hydrogen – H_2, electrolysis is one of the most efficient and less pollutant ways, especially in the case of hydropower [1]. The H_2O electrolysis from hydroelectricity will be cost-effective where this energy source is abundant and cheap. The most used way of assessing the amount of H_2 obtainable from hydropower is based on the called "spilled turbinable energy", STE, understood as the power that could be generated from turbinable water that must be spilled due to various reasons: demand reduction, high values of inflow to the dam or operational reasons [2].

This form of renewable H_2 production has been studied in several countries. In the northeast of Brazil the production of electrolytic H_2 was analyzed by the combination of solar energy, wind power and STE [3]. Similarly, an inventory of the amount of the spilled turbinable water, STW, from the 100 largest hydroelectric plants in the country was done concluding that the electricity that could be produced is 106 TWh, and in turn would produce $3.22x10^9$ kg of H_2 [4]. A more specific study determines the STE from Iguaçu by considering the monthly average volume of STW, for a six year period. The analysis obtained a maximum STE value of 1,054,899 MWh and a minimum of 9,559 MWh. The most important result of this study indicates that the energy demand to produce enough electrolytic H_2 to move the entire fleet of public transport in the city of Foz de Iguacu, was between 1.5% and 8.5% of that energy in excess, which indicates the magnitude of the energy potential that is not used [2]. Similarly, in Paraguay it has been studied the H_2 production by using the STE from Iguacu dam (shared with Brazil). The study proposes to use H_2 in order to obtain hidro-methane as a fuel for vehicles instead of natural gas [5]. In Colombia, the production of electrolytic H_2 from STE has been analyzed at the Amoyá hydroelectric plant, located in the center of the country, with the aim of providing electricity and heat for meeting the needs of a hypothetical population of 16,000 inhabitants located near to the site of production [6].

In North America, the potential production of H_2 from hydropower was estimated assuming that 30% of the annual electricity production generated from 1,321 plants in the country can be considered as STE. This energy might be directed to hydrogen production obtaining a value of $1x10^6$ tons of H_2 for year 2006 [7]. In Canada it was proposed the production of H_2 by electrolysis from surplus hydropower in a plant located in the northwest of the country, with an average of 63% of idle capacity, resulting in a production between 4 and 7 tons of H_2/day [8]. Finally in Ecuador it was analyzed the production of H_2 by electrolysis from STE at the Paute-Molino power plant, located in the south of the country, establishing the use of H_2 as an energy carrier and chemical feedstock. The analysis considers two scenarios depending on the amount of STW for H_2 production, 30 % and 50 % of its annual total, reaching an annual H_2 production of 5,400 t/year and 10,802 t/year, respectively [9].

This review shows that the H_2 production from STE is an open topic and its potential use has attracted the interest of researchers, particularly in the Latin American region due to its enormous hydropower potential. However, from the analysis of the studies conducted so far it can be presumed that the percentage of usable spills included in the calculations are the product of rough estimates that do not show in detail both the historical behavior of such discharges and the actual percentage of availability for H_2 production, as the amount obtained in several cases might be largely overestimated. This paper aims to overcome

these methodological limitations by considering actual STE values for H_2 production. In this context, the main purpose of this paper is to estimate the potential production of H_2 in Ecuador from the available STE at the country's largest hydroelectric plant and its subsequent use in urban public transport in the Andean city of Cuenca. For the technical and economic analysis, three scenarios of H_2 penetration are raised depending on the level of demand coverage. This allows assessing the role of this energy carrier as contributor to characterize Cuenca as a sustainable city in Latin America and to incorporate Ecuador to the Hydrogen Economy. Finally, the study seeks to provide elements that can contribute to the transformation of the Ecuadorian energy matrix towards a structure dominated by renewables energies.

2. Materials and Methods

2.1 Available surplus hydropower

The electricity required for H_2 production by electrolysis would be provided by the "Paute- Integral" Hydroelectric Complex, located at the southern region, which consists of 2 plants in operation and 2 future plants. The first plant is Mazar, with a total installed capacity of 170 MW. The second plant is Molino with generation capacity of 1,100 MW. The following plant is Sopladora, which approaches Molino's turbined flow through a direct interconnection. This project is under construction and its design power reaches 487 MW. It is planned to start its operation during the first semester of year 2016, so it will be considered in the present study. Finally, Cardinally plant will have an installed capacity of 590 MW. Since the project has not started its construction yet, Cardenillo will not be considered in this study.

The underlying concept of STE is that if a hydroelectric dam is spilling water from its reservoir, its production is not always at 100% of its installed capacity. There are various causes for this condition related either to weather or operational aspects. Whatever the cause, the result is that more water than strictly necessary is spilled, and thus the energy difference between the maximum capacity and the actually produced is wasted. This STE is not a direct proportion of the spilled volume but rather is site-specific as depends on the operating conditions of each plant. In this study, Mazar and Molino power plants' operational regimes during the last four years have been analyzed. It has been found as a normal situation that, in spilling conditions, the plants work with less than the rated power during dawns, so there is a STE whose monthly average is presented in Table 1. This behavior is extensible to Sopladora, because it is a project without dam and its power depends on the flow rate from Molino.

2.2. The use of H_2 in Cuenca's urban bus fleet

For the analysis of this end-use of H_2 energy, three scenarios are proposed to replace diesel used in vehicles with internal combustion engines for H_2 vehicles to be powered by fuel cells. Such scenarios are defined by the percentage of replacing diesel buses in the urban fleet of the city of Cuenca, equal to 100%, 50% and 10%, and determining the level of satisfaction of each scenario. In all cases, the amount of H_2 produced comes from the unused energy in Mazar, Molino, and Sopladora power plants, which would effectively be available for that purpose. It is important to note that the average usable energy, while

roughly corresponds to 11% of the STE, represents only 1% of the total energy produced and dispatched by those plants to the Interconnected National System.

Table 1. Actual monthly averages of available STE in Mazar, Molino, and Sopladora power plants. Period 2011-2014

	Available STE (MWh)		
Month	**Mazar**	**Molino**	**Sopladora**
January	364	672	299
February	-	-	-
March	250	6	3
April	169	6,075	2,706
May	80	1,564	697
June	575	4,012	1,787
July	4,186	31,001	13,810
August	1,622	5,455	2,430
September	11	4,264	1,900
October	2,689	1,912	851
November	19	-	-
December	47	899	400
TOTAL	10,013	55,859	24,731
% of the Total Spilled Energy	**8.19%**	**11.91%**	--

The fleet of public transport buses operating in Cuenca´s urban area consists of 448 units, spread over 28 routes [10]. Considering a daily average of 5 tours per bus, the annual distance traveled by the urban fleet, R_{AB}, equals to 26,240,508 km, assuming its operation during 360 days/year. With this figure and knowing the performance of H_2 buses, R_{H2}, as 0.10 kg/km [4, 11, 12], the amount of 2.62 million kg H_2/year would be required for that operation. The quantity of H_2 to be obtained from the use of STE from Molino, Mazar and Sopladora, Table 2, is equal to 1.64×10^6 kg H_2/year. This amount of H_2 could meet 63% of the energy needs for the entire bus fleet of Cuenca. A more precise estimate that represents better the actual situation is taking as baseline the average monthly production of H_2 and comparing the three scenarios for the demand analysis, Table 2.

Table 2. Met Demand for the three substitution scenarios

		Scenario 1 100 % Demand		**Scenario 2 50 % Demand**		**Scenario 3 10 % Demand**	
	Monthly Production (kg)	Demand H_2 (kg)	Meeting (%)	Demand H_2 (kg)	Meeting (%)	Demand H_2 (kg)	Meeting (%)
January	2.41E+04	2.19E+05	11.04	1.09E+05	22.08	2.19E+04	110.42
February	0.00E+00	2.19E+05	0,00	1.09E+05	0.00	2.19E+04	0,00
March	4.68E+03	2.19E+05	2.14	1.09E+05	4.28	2.19E+04	21.40
April	1.62E+05	2.19E+05	74.02	1.09E+05	148.03	2.19E+04	740.16
May	4.23E+04	2.19E+05	19.36	1.09E+05	38.71	2.19E+04	193.57
June	1.15E+05	2.19E+05	52.71	1.09E+05	105.42	2.19E+04	527.11
July	8.86E+05	2.19E+05	405.19	1.09E+05	810.39	2.19E+04	4051.93
August	1.72E+05	2.19E+05	78.62	1.09E+05	157.24	2.19E+04	786.21
September	1.12E+05	2.19E+05	51.06	1.09E+05	102.12	2.19E+04	510.62
October	9.86E+04	2.19E+05	45.09	1.09E+05	90.18	2.19E+04	450.91
November	3.44E+02	2.19E+05	0.16	1.09E+05	0.31	2.19E+04	1.57
December	2.43E+04	2.19E+05	11.13	1.09E+05	22.27	2.19E+04	111.33

From the results of Table 2, it can be determined that the average satisfaction level for each scenario is 63%, 125%, and 625%, respectively. However this level is not homogeneous, but rather with large monthly changes as there are months with a production surplus and others with unmet demand, being February an extreme case with zero demand met. Furthermore, as expected, by decreasing the H_2 monthly demand it is possible to cover a greater number of months per year with such an energy carrier (Figure 1).

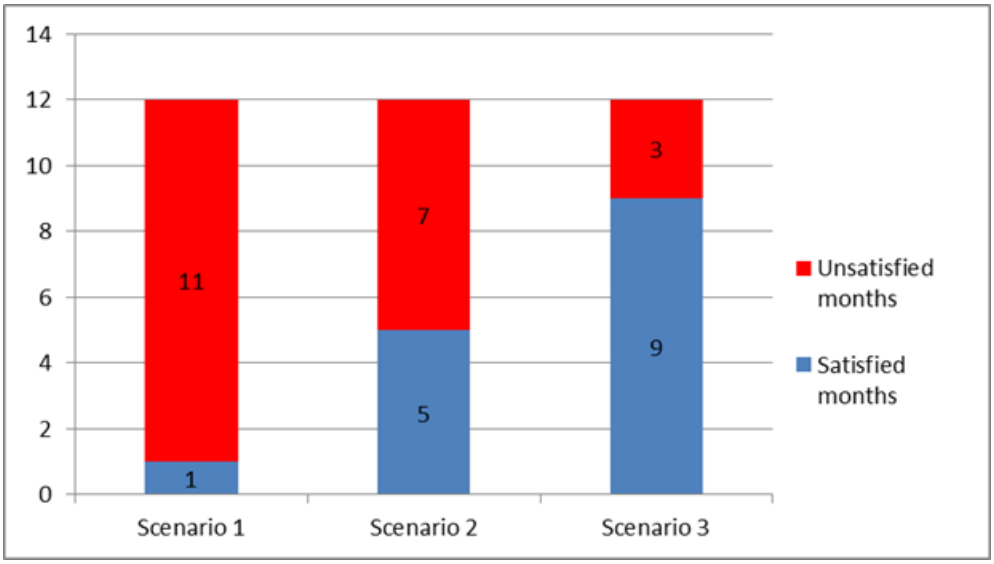

Fig. 1 Months with met and unmet demand for each scenario

It is appreciated that none of the three scenarios can meet the H_2 demand for every month, whereupon two alternatives are proposed: 1) to buy the electricity needed to produce the H_2 during the deficit months at the value billed to large consumers; and 2) to store H_2 surplus of the corresponding months in order to use it in the months with H_2 deficit. The second alternative, storing large volumes of H_2 for periods of several months, in addition to technological complexity, would increase significantly the costs. Furthermore, this alternative does not apply to the scenario one in which there is no full H_2 availability. Therefore, in order to have a preliminary estimate of the costs associated to H_2 production, the first alternative is proposed, taking into account the differential energy cost depending on the type of electricity used during the electrolysis process.

2.3 Cost model for using H_2 in the city of Cuenca's fleet

2.3.1 Overview

For each of the three scenarios, the model estimates the production cost for electrolysis H_2 from hydropower, based on the amount of H_2 required for the end use proposed. In that sense, this approach is conceptually a bottom up model. This type of method has been used in various technical and economic studies on H_2 production for different applications [2,13], and proceeds through the classification of annualized costs, input costs, investment costs, and operation and maintenance costs. Similar economic studies are considered

regarding the use of H_2 in urban transport in Asuncion in Paraguay [14]; Foz do Iguacu in Brazil [2]; London, England [15] and Madrid, Spain [16]. For H_2 production, a typical proton exchange membrane –PEM electrolyzer was selected, with an average life of 15 years and a production capacity of 0.1 to 30 Nm^3/ hr [17]. This is the range at which H_2 production is estimated for the case study.

2.3.2 Input cost

They involve the costs of electricity and water needed to produce H_2 by electrolysis, which are obtained from the following expressions.

$$P_{H2} = F_M R_{AB} R_{H2} \quad (1)$$

In equation (1), PH2 is the annual production hydrogen (kg/year) and F_M represents any losses in the operation of the electrolysis plant, with unit energy consumption, C_{UE}, equals to 52.53 kWh/kg of H_2 [13]. This includes energy consumption by auxiliary equipment required for the treatment and compression of gases, and is equivalent to an energy efficiency conversion of 75%, which is an average value of those reported in the literature for the electrolytic system [2, 13, 14]. The annual energy consumption in this system is obtained as:

$$C_{AE} = P_{H2} C_{UE} \quad (2)$$

And the cost of electricity:

$$C_E = C_{AE} C_{EG} \quad (3)$$

where C_{EG} represents the cost of electricity generation. This value is composed of both the cost of electricity in excess, estimated at US $ 0.011/kWh, and the cost established to large consumers, US$ 0.05/kWh. These two figures were supplied by the public company CELEC EP-Hidropaute, responsible for the operation of Molino and Mazar hydropower plants, and in charge of the construction of Sopladora. So the cost of electricity will be a variable value depending on both the scenario and the month concerned, and from which the annual average value will be obtained to be used in equation (3).

To calculate the cost of water, source of H_2, the industrial tariff of this input is used for the city of Cuenca, T_w, equals to 0.8 US$/$m^3$ [18] , considering that 1 liter of water is required to obtain 1 m^3 of H_2 [13, 14], such that:

$$C_{WATER} = C_w T_w \quad (4)$$

where:

$$C_w = P_{H2V} x\ (0.001\ m^3\ H_2O / 1\ m^3\ H_2) \quad (5)$$

The equation for the annual cost of inputs is:

$$C_{INS} = C_E + C_{WATER} \quad (6)$$

2.3.3 Cost of the electrolysis plant

It is represented mainly by the cost of the electrolyzer and ancillary equipment, and is calculated from the energy needed to produce the required amount of H_2. First, the power plant is given by:

$$P = C_{AE}/DI \quad (7)$$

To represent the unit cost of the electrolyzer, C_{EL}, the equation proposed in [13] is used, which was obtained from a mathematical nonlinear regression procedure that takes into account the cost reduction due to the economy of scale, and applicable for power values in plants between 5 MW and 30 MW. This expression is :

$$C_{EL} = 1{,}499.74\ P^{-0.2167} \qquad R^2 = 0.987 \quad (8)$$

From (7) and (8), the cost of installing the electrolyzer and other additional equipment is calculated as:

$$C_{IE} = P\ C_{EL} \quad (9)$$

To calculate the annualized cost of investment in the lifetime of the installation, the expression of Capital Recovery Factor, FRC, is used for an average interest rate for investments in the industrial sector of Ecuador for February 2015 [19]:

$$FRC = d(1+d)^n/((1+d)^n-1) \quad (10)$$

Such that:

$$C_{INV} = C_{IE}\ FRC \quad (11)$$

2.3.4 Cost of operation and maintenance

In this case, it is assumed that the cost is simply a percentage of annualized investment costs, assessing the percentage of 5%, [2, 13, 14], then:

$$C_{OM} = OM\ C_{INV} \quad (12)$$

2.3.5 Total cost of H_2 production

The general expression for estimating the cost of H_2 production from hydropower related to the amount of H_2 produced is:

$$C_{TP} = (C_{INS}+C_{INV}+C_{OM})/P_H \quad (13)$$

Table 3 summarizes the parameters considered in the cost model.

3. Results and Discussion

The main results of the cost model are presented in Table 4. It can be seen that the total cost of H_2 production reaches the value of $1.77/Kg in the best case scenario. In Figure 2 it can be noted that the input costs decrease when the rate of demand coverage falls, which can be explained by taking into account that such a reduction implies a greater contribution of low-cost electricity, from the STE, to the cost of inputs. Meanwhile, the cost of investment does not change because it is expected to produce the maximum amount of H_2 in all scenarios. The percentage distribution of costs according to their nature, for Scenario One, shows the preponderance of the inputs cost, Figure 3. This corroborates the importance of electricity in

Table 3. Parameters of the cost model

Parameter	Symbol	Unit	Value
Water density	ρ_{H2O}	Kg m^{-3}	1,000
Gravity	G	m s^{-2}	9.8
H_2High Heat Value	HHV	kWh kg^{-1}	39.4
Management Factor	F_M	dimensionless	1.1
Annual distance traveled by buses	R_{AB}	km	26,240,508
Performance of H_2 buses	R_{H2}	kg km^{-1}	0.1
Performance of diesel buses	R_D	l km^{-1}	0.7
Electrolyzer unit energy consumption	C_{UE}	kWh kg^{-1}	52.53
Water rate	T_a	US$ m^{-3}	0.8
Plant availability	DI	h	8,328
Life time period	N	year	15
Active interest rate	I	dimensionless	10 %
Capital Recovery Factor	FRC	dimensionless	0,1315
O&M Rate	OM	dimensionless	5 %

Table 4. Results from the cost model for sustainable urban transport in Cuenca

Variable	Symbol	Unit	Value		
			Scen. 1 (100%)	Scen. 2 (50%)	Scen. 3 (10%)
Annual H_2 production (mass)	P_H	kg $year^{-1}$	2,89E+06	2,89E+06	2,89E+06
Annual H_2 production (volume)	P_{H2V}	m^3 $year^{-1}$	3,21E+07	3,21E+07	3,21E+07
Annual electricity consumption	C_{AE}	kWh $year^{-1}$	1,38E+08	1,38E+08	1,38E+08
Annual electricity cost	C_E	US$ $year^{-1}$	4,90E+06	3,82E+06	2,76E+06
Annual water consumption	C_a	m^3 $year^{-1}$	2,92E+04	2,92E+04	2,92E+04
Annual water cost	C_{AGUA}	US$ $year^{-1}$	2,34E+04	2,34E+04	2,34E+04
Annual input cost	C_{INS}	US$ $year^{-1}$	4,92E+06	3,85E+06	2,78E+06
Power of electrolysis plant	P	MW	16,55	16,55	16,55
Electrolyzer unit cost	C_{EL}	$ kW^{-1}	816,37	816,37	816,37
Electrolyzer installation cost	C_{IE}	$	1,35E+07	1,35E+07	1,35E+07
Annual investment cost	C_{INV}	$ $year^{-1}$	1,78E+06	1,78E+06	1,78E+06
Annual O&M cost	C_{OM}	$ $year^{-1}$	8,88E+04	8,88E+04	8,88E+04
Total production cost	C_{TP}	$ kg^{-1} H_2	2,59E+00	2,18E+00	1,77E+00

the cost structure of H_2 production by electrolysis. In the scenarios 2 and 3, inputs contribute with 67 % and 60 % of total costs, respectively, keeping the inputs primacy.

Considering the energy equivalence between diesel and H_2, the resulting value of US$ 1.77/kg of H_2 is 1.83 times the current cost (subsidized) of diesel Premium used in public transport in Cuenca, equals to 0.29 US$/l [20]. But if the comparison is done with the price at which the Ecuadorian State buys diesel in the international market, 0.84 US$/l [21], it results that the cost of H_2 is 0.64 times the cost of diesel. This means that the use of H_2 in buses is, in principle, economically competitive when considering the actual cost of diesel.

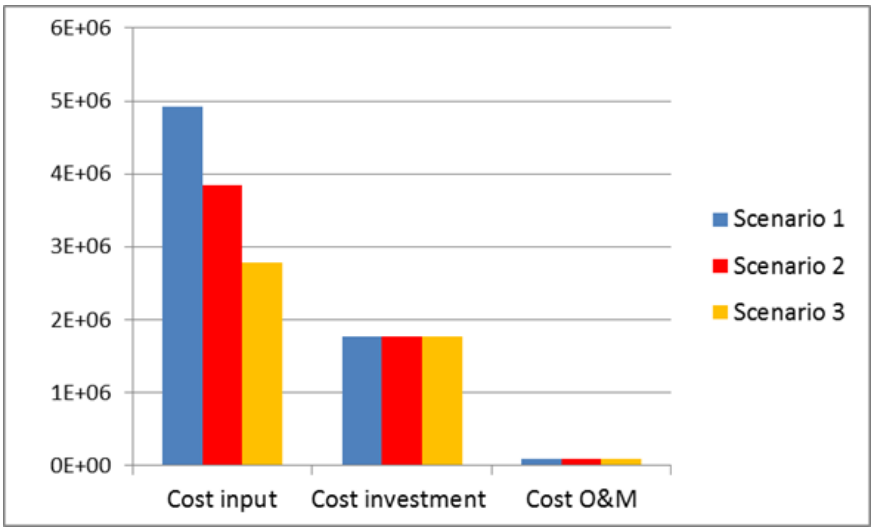

Fig. 2. Cost variations under the scenarios analyzed

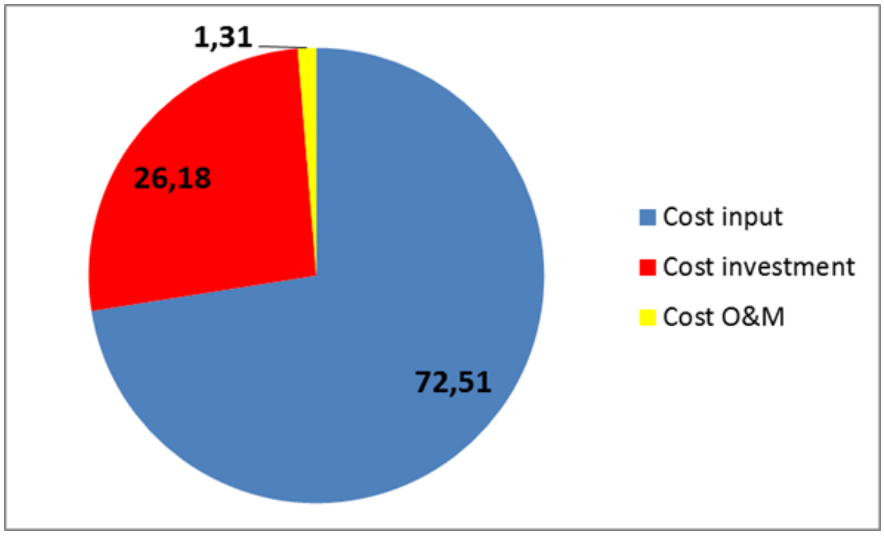

Fig. 3 Percentage distribution of H_2 production costs. Scenario 1

4. Conclusion

The potential production of H_2 from hydropower in Ecuador has been estimated, considering the existing STE in "Paute- Integral" Hydroelectric Complex and focusing on the use of this energy carrier in the urban public transport of Cuenca. Through the combination, in different proportions, of the excess electricity cost and the value billed to large consumers it is possible to meet the need of 100 %, 50% and 10% of the buses fleet in the city. Although the scenario of 100% coverage of the energy demand might be the best economically, the project proposed to Cuenca could be implemented in stages starting at 10% coverage. Despite the energy potential for full coverage of the demand and the cost competitiveness of H_2 production, aspects related to both infrastructure and fleet costs should be studied in depth.

Acknowledgements

Special thanks to the Secretariat of Higher Education, Science, Technology and Innovation of the Republic of Ecuador -SENESCYT's Prometheus Project for sponsoring this work. The authors also thank CELEC EP-Hidropaute for providing the information related to its hydropower plants.

References

[1] Richa K., Buddhi D., Sawhney R. L. Comparison of environmental and economic aspects of various hydrogen production methods. Renewable and Sustainable Energy Reviews 2008, 12:553-563

[2] Riveros-Godoy G., Cavaliero C., Silva E., Analysis of electrolytic hydrogen production models and distribution modes for public urban transport: study case in Foz do Iguacu, Brazil 2013; Int. J. Energy Res. 37: 1142–1150

[3] Da Silva E., Marin Neto A., Ferreira P., Camargo J., Apolinario F., Pinto C., Analysis of hydrogen production from combined photovoltaics, wind energy and secondary hydroelectricity supply in Brazil Solar Energy 2005; 78: 670–677

[4] Padilha J., da TrindadeL., de Souza R., Miguel M., An evaluation of the potential of the use of wasted hydroelectric capacity to produce hydrogen to be used in fuel cells in order to decrease CO_2 emissions in Brazil. Int. J. Hydrogen Energy 2009; 34: 7898-7902

[5] Rivarolo M., Bellotti D., Mendieta A., Massardo A., Hydro-methane and methanol combined production from hydroelectricity and biomass: Thermo-economic analysis in Paraguay. Energy Conversion and Management; 2014; 79: 74-84

[6] Carvajal-Osorio H., Babativa J., Alonso J., Estudio sobre producción de H_2 con hidroelectricidad para una economía de hidrógeno en Colombia. Ingeniería y Competitividad 2010; 12:31-42

[7] Milbrandt A., Mann M., Potential for Hydrogen Production from Key Renewable Resources in the United States. 2007 Technical Report NREL/TP-640-41134

[8] Oullette N., Rogner H., Scott D., Hydrogen form remote excess hydroelectricity. Part I: production plant and production costs, Int. J. Hydrogen Energy 1995; 20: 865-871

[9] Pelaez-Samaniego M., Riveros-Godoy G., Torres-Contreras S., Garcia-Perez T., Albornoz-Vintimilla E., (2014) Production and use of electrolytic hydrogen in Ecuador towards a low carbon economy Energy 2014; 64: 626-631

[10] http://www.cuenca.gov.ec/. Dirección Municipal de Transito, DMT-GAD Cuenca. Recorrido de buses urbanos Cuenca 2013. Last Access 06/04/2015

[11] Hua T., Ahluwalia R., Eudy L., Singer G., Jermer B., Asselin-Miller N., Wessel S., Patterson T., Marcinkoski J. Status of hydrogen fuel cell electric buses worldwide. Journal of Power Sources 2014; 269: 975-993

[12] http://www.ceem.unsw.edu.au/sites/default/files/uploads/Hydrogen Fuel Cell Buses: An Economic Assessment. Last Access 06/09/2015

[13] Contreras A., Posso F., Veziroglu T., Modeling and simulation of the production of hydrogen using hydroelectricity in Venezuela Int. J. Hydrogen Energy 2007; 32:1229-1234
[14] Galeano M., Peres da Silva E., Camargo J., Are HFC buses a feasible alternative for urban transportation in Paraguay? Int. J. Hydrogen Energy 2012; 37: 16177-16185
[15] Shayegan S., Pearson P., Hart D., Analysis of the cost of hydrogen infrastructure for buses in London. J. Power Sources 2006; 157: 862–874
[16] Vidueira J., Contreras A., PV autonomous installation to produce hydrogen via electrolysis, and its use in FC buses. Int. J. Hydrogen Energy 2003; 28: 927 – 937
[17] Bhandari, R., Trudewind C., Zapp, P. Life cycle assessment of hydrogen production via electrolysis- a review. J. Cleaner Production 2013; 85: 151-163
[18] http://www.etapa.net.ec/Productos-y-servicios/Agua-potable/Tarifas. Last Access: 06/ 08 / 2015
[19] http://contenido.bce.fin.ec/docs.php/documentos/Estadisticas/TasasInteres.html Banco Central de Ecuador 2015. Last Access 06/10/2015
[20] http://es.globalpetrolprices.com/diesel_prices/#Ecuador. Last Access 06/11/2015
[21] http://www.bce.fin.ec/index.php/informacion-estadistica. Banco Central de Ecuador Ingresos y egresos: comercialización interna de derivados importados 2014. Last Access 09/11/2015

Chapter 1.2. Photobiological Hydrogen production by *Chlamydomonas* sp. and *Chlorella* sp.

E.M. Hernández-Hernández[a]; C.A. Cortés-Escobedo[b*]; R. Olvera-Ramírez[a]

[a]Escuela Nacional de Ciencias Biológias-IPN, Prolongación de Carpio y Plan de Ayala, S/N, Casco de Santo Tomás, Miguel Hidalgo, México, D.F.
[b]Centro de Investigación e Innovación Tecnológica-IPN, Cda. CECATI S/N, Santa Catarina, Azcapotzalco, México D.F.

ABSTRACT

Energy generation currently has significant environmental impacts, an alternative to this problem are hydrogen technologies. It has been discovered that some green algae and cyanobacteria are able to generate molecular hydrogen (H_2) photosynthetically, this process is called biophotolisis. The aim of this research was to evaluate the production of H_2 in mineral medium whitout sulfur in *Chlamydomonas* sp and *Chlorella* sp. cultures in suspension and immobilized in alginate. Growth kinetics during cultivation in mineral medium BG-11, and the effect of immobilization on the cell growth are reported and discussed. Hydrogen production induction was tested in sulfur deprivation, anaerobic conditions and continuous light for 19 days by using a Differential Electrochemical Mass Spectrometer (DEMS) to identify hydrogen presence. The gas samples analysis showed positive results for H_2 production in all the cultures, neverthless the immobilization technique improved hydrogen production specially in *Chlamydomonas* sp. On the other hand, *Chlamydomonas* sp. immobilization influences on its growth rate but it does not affect the survival. Additionally *Chlamydomonas* sp. was more resistant to stress conditions than *Chlorella* sp. The use of immobilization technique facilitates organisms handling without affecting the production of hydrogen, so making necessary adjustments, the procedure for obtaining hydrogen on a photobioreactor can be scaled and coupled to fuel cells.

Keywords: Biohydrogen, Biophotolisis, Sulfur deprivation, *Chlamydomonas* sp, *Chlorella* sp.

1. Introduction

Since XVIII century mankind have used fossil sources to cover its energy needs using combustion to obtain electricity and heat. The use of these natural resources implies, besides the close and progressive shortage, a constant environmental diminishing, that is manifested in CO_2, NO_x, and SO_x emissions, favoring the hardening of the greenhouse

---

* Author for correspondence:
Claudia Alicia Cortés Escobedo, 57296000 ext. 62311, Cerrada de Cecati S/N. Col. Santa Catarina Azcapotzalco México D. F. CP:02250, claudia.alicia.cortes@gmail.com

effect, a progressive augmentation of desertification and erosion, so the modification of higher biomes with the consequent diminishing of biodiversity [1, 2].

The challenge today is to diminish the fossil fuel demand to make equal and at best, diminishing to lower rate with respect to the use of these, administering the resources that remain as much as possible to make the energy transition easy. So, it is important to have a realistic vision about the possibilities and the problems related to the use of renewable energies [3].

The biological production of hydrogen is performed by four main processes: direct and indirect biophotolysis, photofermentation and dark fermentation, as well as the combination between such processes. These hydrogen generation methods do not generate a big environmental impact, and the energetic expenditure is less, compared to thermochemical and electrochemical processes, because these production methods are reduced to four main biological processes: photosynthesis, glycolysis, nitrogen fixation and fermentation. The cyanobacteria and the microalgae break water molecule directly in hydrogen and oxygen in the presence of light with photosynthetic activity [4], process called biophotolysis.

The studies with respect to this subject have revealed that the absence of sulfur in the *Chlamydomonas reinhardtii* culture medium produces a specific but reversible decay of the oxygen photosynthesis, without affecting the mitochondrial respiration rate. So, in tightly-sealed culture, this photosynthesis-respiration instability originated by the lack of sulfur, results in an overall oxygen consumption produced by cells, causing anaerobiosis in the culture medium. Such a condition induces the production of H_2 [5].

In this same way, it has been found that the enzymatic mechanism that favors the production process of hydrogen, particularly the Fe-hydrogenase is highly sensitive to O_2, so it makes necessary the temporal separation of the O_2 and H_2 photoproduction reactions [6, 7].

Additionally it was shown that *Chlamydomonas reinhardtii* in absence of sulfur and immobilized in fiberglass matrices is able to produce hydrogen. It is concluded that such immobilization favors the quantity of H_2 produced with respect to suspension cultures [8].

In this work the biological production of hydrogen from *Chlorella* sp. and *Chlamydomonas* sp. was explored using suspension systems in sodium alginate. The latter intended to make the hydrogen production with such organisms more efficient.

2. Materials and Methods

2.1. Strains and culture media

Chlorella sp. and *Chlamydomonas* sp. strains (Vegetal Physiology Lab. ENCB) was grown on BG-11 medium, in air, under photoperiod illumination (cool white fluorescence lamps) at ~30 C.

2.2. Immobilized cultures

2.8 g half-viscosity alginate sodic (SIGMA, 9005-383) was dissolved in 156 mL phosphate-free BG-11 medium. Additionally 25 mL propagation culture was centrifuged to 3500 rpm with a centrifuge Damon/IEC División PR-6000 during 30 minutes; the biomass concentrate obtained; 0.43g *Chlorella* sp. and 0.79g *Chlamydomonas* sp.; it was

resuspended in 25 mL phosphate-free BG-11 medium. This cell concentrate was incorporated with the alginate solution and BG-11 medium, phosphate-free, prepared previously [9].

2.3. Growth kinetics

In suspended cultures, 10 mL samples were taken every three days, during 35 days. In each sample chlorophyll was evaluated by the SCOR-UNESCO technique [10] for each one of the strains. For the immobilized cultures it was taken a culture sphere every three days, during 35 days. In such samples chlorophyll was evaluated with the same technique.

2.4. Stress induction by sulfur-deprived

Once passing the time of the growth kinetics, 200 mL from the suspended cultures were harvested, which were centrifuged to 3500 rpm during 30 minutes to eliminate the culture medium. The biomass was resuspended in 250 mL from the sulfur-free BG-11 medium, and it was kept in ventilation and photoperiod 12:12 during 7 days to eliminate any sulfur remaining. In immobilized cultures, the culture medium was eliminated by decantation and 250 ml sulfur-free and phosphate-free medium, keeping the ventilation and the same photoperiod during 7 days.

Passing this time, the cultures were moved to 125 mL Erlenmeyer flasks, placing 125mL suspension culture or 125mL immobilization spheres in every flask, remaining a 4 flask total, 2 suspended cultures, and 2 immobilized cultures, for each one of the strains.

Septum Suba-Seal® (24/40) caps were placed to each of the flasks to keep the system closed, and by means of a 21G-caliber catheter and a vacuum pump the highest quantity of air possible was eliminated. Finally the flasks were placed in continuous lighting.

2.5. H_2 Production Qualitative Proof

After 19 days that the stress induction process by sulfur-deprivation has begun, many gas samples from the flasks were taken with a Microliter 701 series syringe-Hamilton, immediately the gas sample was injected in a Differential Electrochemical Mass Spectrometer (DEMS), quadrupole with a Faraday-SEM detector (Prisma SGC 300, Pfeiffer).

For this, a teflon adaptor was built and fitted to the equipment with an air valve, this valve was connected with a 1/16 in internal diameter polyurethane hose to a 21G-caliber catheter. This latter was connected to a 5mL glass flask with a septum cap. The vacuum pressure was approximately 2.6×10^{-4} mbar during the admittance of the gas samples. The results were processed with the Origin 8.0 program [11].

3. Results and Discussion

The growth of both strains in suspended cultures (Fig. 1) shows an exponential trend that belong to a common population growth in extremely good conditions, what coincides with previously study of the *Chlorella sorokiniana* growth in different culture conditions, finding always an exponential growth in autotrophic conditions [12].

Thru the obtained model, the exponential growth of the strains was tested, *Chlamydomonas* sp. $Y = 0.198\ e\ 0.0856x$, $R^2 = 0.80$ for *Chlorella* sp. $Y = 0.34e0.0608x$, R^2

= 0.85 (Fig. 1a). In this way, these results show that the culture medium used permits the adequate development of both organisms, given that the BG-11 medium [13] contains macronutrients and micronutrients, necessary for the microalgae growth, in accordance with the requirements established [14]. It is important to point out that the maximum growth for both was reached after 25 days, results that are similar to studies reported when

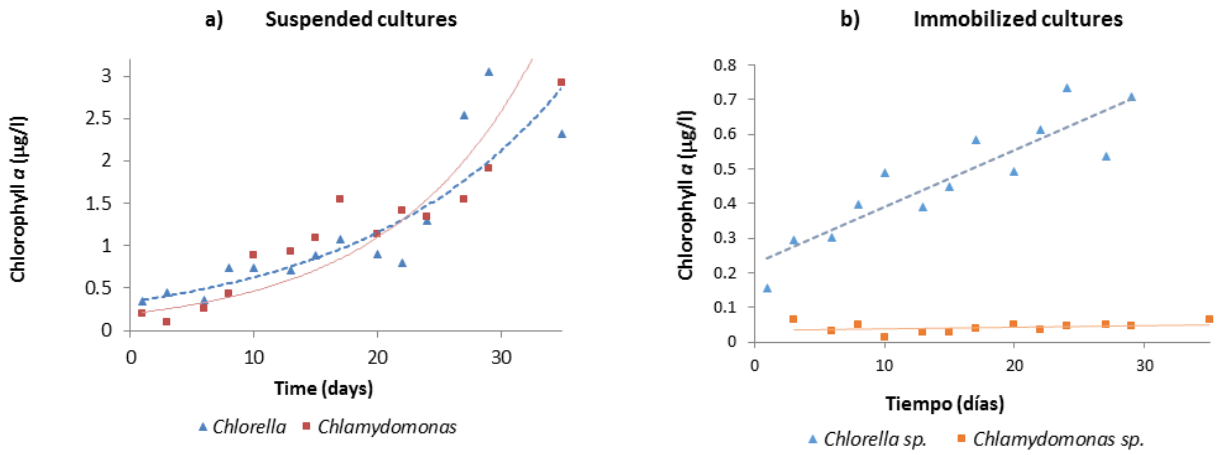

Fig.1. *Chlorella* sp. and *Chlamydomonas* sp. growth kinetics:
(a) suspended culture; (b) immobilized cultures.

evaluated the effect on the *Chlorella vulgaris* growth, in different culture media, and found that with a medium based on minerals similar to those of the BG-11 medium reach the maximum growth of 22 days [15].

The growth kinetics in immobilization conditions for both strains changed from an exponential trend to a lineal trend (Fig. 1b). It can be inferred that for *Chlorella* sp. $y = 0.017x + 0.22$; $R^2 = 0.81$ the growth velocity diminishes drastically in immobilization conditions, but without stopping the growth. This, in comparison with the obtained value in suspended cultures (Fig.1a). On the contrary, the *Chlamydomonas* sp. $y=0.002x + 0.013$; $R^2 = 0.81$ growth during the evaluated time (35 days) is affected, having a growth velocity very close to zero, what indicates that there was not any growth (Fig.1b).Given the morphological characteristics of the strain, the observed phenomenon is attributed to immobilization. This turns out to be a condition that alters the cell mobility. Also during the preparation of spheres these are placed in a $CaCl_2$ high concentration solution, what could provoke loss of flagella and cell aggregation by mucilage secretion, as it is pointed studies on halotolerance on *Chlamydomonas reinhardtii* [16]. It is extremely important to mention that after 45 days the strain began to accelerate its growth, which was abundant.

Nonetheless these results could be contrasted with the viability studies of *Chlamydomonas reinhardtii* in different immobilization brackets (carrageenan, Ba-alginate, Calcium Alginate, polyurethane and agar), showing that the Calcium Alginate is the most adequate bracket because of its stability, compatibility with viability, and high cell retention

[16]. Then, the growth observed in the strain that was studied in this work is due to a lengthening in the lag phase, by effect of immobilization, while cell viability is kept.

The *Chlorella* sp. gas samples in suspended and immobilized cultures gave practically null during the H_2 detection by means of DEMS (Fig. 2). Due to the interference in such signals, the results softened with the help of the Origin 8.0 program (Origin Lab, [version 8]), what allowed to see a little H_2 signal for the immobilized culture differently from the suspended culture that did not offer any signal. These results indicate the possibility of H_2 production by *Chlorella* sp., just if the conditions for this process are completed, and the potentiality of this strain as an H_2 producer is not discarded due to the results reported [17,18] in a qualitative way show the capability of *Chlorella vulgaris* and *Chlorella* sp. for generating hydrogen by the absence of sulfur in the culture medium and anaerobiosis. This latter requirement is essential, due the O_2 presence in the medium inhibits the hydrogenase activity, so the H_2 production would not occur during a long period [7].

It is important to mention that in immobilization conditions the gas formation was favored, what indicates that this favors the hydrogen production. Such an assertion coincides with the recently published evaluate the hydrogen quantity produced by *Chlamydomonas reinhardtii* in different immobilization matrices [8].

In figure 3 the signal detected by DEMS can be observed when entering. It is clearly noticed a considerable increase in the detected ionic current, what indicates the presence of the gas. Additionally it is observed a difference between the signal of suspended culture gas with respect to the signal of the immobilized culture; clearly this latter is higher in terms of ionic current. This is because in immobilization conditions the hydrogen production is favored significantly [8] and the immobilization systems present an increment in the free systems productivity facing the free systems because there are changes in the membrane permeability induced by cell-matrix interactions. Also the immobilization is more similar to the physicochemical conditions of the natural environment [16].

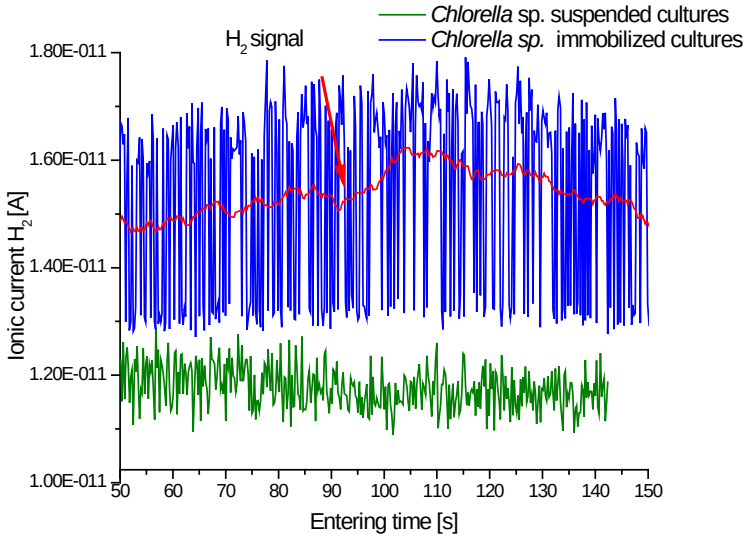

Fig. 2. H_2 signal in *Chlorella* sp. gas sample of suspended and immobilized cultures.

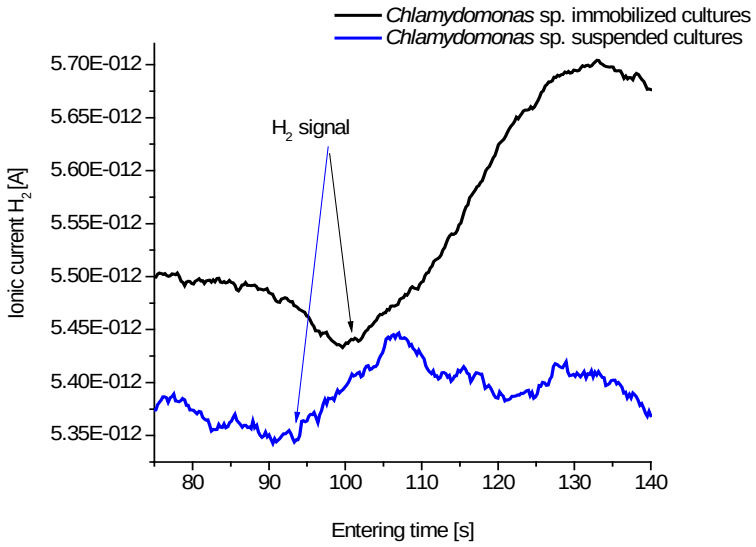

Fig. 3. H_2 signal in *Chlamydomonas* sp. gas sample of suspended and immobilized cultures

In the same way, the created system -in this case spheres-, becomes a microenvironment or micro system, what favors the stability within the system [19], and so, it lets putting all the requirements together to make the hydrogen production possible, as anaerobiosis and the activation of enzymatic complexes [20].

It is important to mention that when these tests are finished, the suspended *Chlorella* sp. cultures showed a dark yellow color, indicating cell death. The *Chlamydomonas* sp. cultures did not show a color change. So it can be inferred that *Chlamydomonas* sp. is more resistant to the stress conditions originated by the absence of sulfur in the culture medium.

4. Conclusion

The *Chlorella* sp. y *Chlamydonas* sp. growth is not affected by immobilizing them in alginate. Additionally, *Chlamydomonas* sp. showed a better performance in the hydrogen production capability in suspended and also immobilized systems. In the same way, the alginate immobilization favors the hydrogen production and the feasibility of both strains to get H_2 as a source of sustainable energy.

Acknowledgements

This work was supported in part by the Laboratory of Plant Physiology at the National School of Biological Sciences and the Laboratory of Clean Energy at Research Center and Technological Innovation, at IPN. This study was financially supported by the projects: CONACYT CB-157925 and 160 333 MULTI SIP 1540. The authors thank Dr. Arturo Manzo Robledo for his support.

References

[1] Díaz C.R., Escárcega C. S. Desarrollo sustentable. Una oportunidad para la vida. México: McGraw-Hill Interamericana Editores. 2009.

[2] Laborde M. A., Rubiera G.F. La economía del hidrógeno. En: Laborde, Rubiera. La energía del hidrógeno. Madrid. CYTED 2010; 7-10.

[3] Al-Hallaj S., Kisynski K. Hybrid Hydrogen Systems. Stationary and Transportation Applications. New York, Springer-Verlag. 2001; 1-7.

[4] Melis A. Photosynthetic H_2 metabolism in *Chlamydomonas reinhardtii* (unicellular green algae). Planta 2007; 226: 1075-1086.

[5] Melis A., Zhang L., Forestier M., Ghirardi M. L., Seibert M. Sustained Photobiological Hydrogen Gas Production upon Reversible Inactivation of Oxygen Evolution in the Green Alga *Chlamydomonas reinhardtii*. Plant Physiology 2002; 122: 127-136.

[6] Fedorov A. S., Sergey K., Ghirardi M., Seibert M. Continuous Hydrogen Photoproduction by *Chlamydomonas reinhardtii* using a novel Two-Stage, Sulfate-Limited Chemostat System. Applied Biochemistry and Biotechnology. Humana Press Inc. 2005; 121-124: 403-413.

[7] Ghirardi M. L., Togasaki R. K., Seibert M. Oxygen sensitivity of algal H_2-Production. Applied Biochemistry and Biotechnology 1997; 63-65:142-151.

[8] Laurinavichene T. V., Fedorov A. S., Ghirardi M. L., Seibert M., Tsygankov. A. A. Demonstration of sustained hydrogen photoproduction by immobilized, sulfur deprived *Chlamydomonas reinhardtii* cells. International Journal of Hydrogen Energy 2006; 31: 659-667.

[9] Brouers M., Shi D. J., Hall D. O. Immobilization methods for cyanobacteria in solid matrices. En: Packer, L. Packer, G. y Glazer A. Methods in enzymology. New York: Academic Press 1988; 629-636. SCOR-UNESCO. Determination of chlorophyll in seawater. UNESCO Technical Papers in Marine Science. 1980; 35p.

[10] Origin Pro (Versión 8) [Software]. 2007. Origin Lab Corporation.

[11] Ortiz-Moreno M. L., Cortés C. E., Sánchez-Villarraga J., Padilla J., Otero-Paternina A. M. Evaluación del crecimiento de la microalga *Chlorella sorokiniana* en diferentes medios de cultivo en condiciones autotróficas y mixotróficas. ORINOQUIA 2012; 16-1:12-20.

[12] Rippka R., Deruelles J., Waterbury J. B., Herdman M., Stainer R. Y. Generic assignments, strain histories and properties of pure cultures of cyanobacteria. Gen Microbiol 1979; 111: 1-61.

[13] Watanabe M. Freshwater Culture Media. En: Algal Culturing Techniques. Andersen R. El Sevier Academic Press 2013; 16-17.

[14] Muñoz-Peñuela M., Ramírez-Merlano J. A., Otero A., Medina-Robles V. M., Cruz-Casallas P., Velasco-Santamaría Y. M. Efecto del medio de cultivo sobre el crecimiento y el contenido proteico de *Chlorella vulgaris*. Revista Colombiana de Ciencias Pecuarias 2012; 438-449.

[15] León B. R. Estudios de halotolerancia en el alga verde unicellular *Chlamydomonas reinhardtii*. Fotoproducción de glicerol por células libres e inmovilizadas. Tesis doctoral. Universidad de Sevilla. España 1997.

[16] Contreras J. B., Scott J. A., Mendoza C. L., Espinal G., Zapata, Z. Potencial de algas verdes para la producción fotobiológica de hidrógeno. CIENCIA Y SOCIEDAD 2008; XXXIII-3: 307-327.

[17] García S. L. Producción fotobiológica de biohidrógeno en la cianophyta (*Arthrospira* sp.) Y la Chlorophyta (*Chlorella* sp.) En condiciones de estrés metabólico. Tesis de licenciatura. Universidad de Guayaquil, Ecuador 2012.

[18] Mallick N. Immobilization of microalgae. En: Guisán J. M. Methods in Biotechnology: Immobilization of Enzymes and Cells. 2°Ed.Totowa. Humana Press Inc. 2006; 22: 373-383.

[19] Shi D.J, Brouers M., Hall D.O., R.J. Robins. The effects of immobilization on the biochemical, physiological and morphological features of Anabaena azollae. Planta 1987; 172: 298-308.

Chapter 1.3. Photocatalytic hydrogen production on Au-TiO_2 surface modified with Pd, Co and Ni

E. Albiter[a]; C. E. Barrios[a]; J. M. Gracia-Jiménez[b]; R. Zanella[a,*]

[a] Centro de Ciencias Aplicadas y Desarrollo Tecnológico - Universidad Nacional Autónoma de México, Ciudad Universitaria, Circuito Exterior s/n., Apdo. Postal 04510, Del.Coyoacán, Distrito Federal, México.
[b] Instituto de Física - Benemérita Universidad Autónoma de Puebla, Apdo. Postal J48, Col. San Manuel 72570- Puebla, México.

ABSTRACT

The photocatalytic production of hydrogen over Au/TiO_2 based photocatalysts was studied, using methanol as sacrificial agent (vol. ratio 20:180 CH_3OH:H_2O). Also, the effect of surface modification with Pd, Co and Ni oxides on the production of H_2 under UV light irradiation (~ 254 nm) was assessed. The metal oxides were first deposited on TiO_2 (Degussa P25) by incipient wetness impregnation followed by thermal treatment under H_2 (Pd and Co) or air (Ni). After that, Au was deposited by deposition-precipitation with urea (DPU) and then the catalysts were thermally activated at 300 °C under air atmosphere (Spatial Velocity = 2 g/ml.min). The prepared photocatalysts were characterized by UV-Vis spectroscopy, photoluminescence (PL), EDS and HRTEM. The nominal metal content was ~ 0.5 wt. % and the Au:M_xO_y molar ratio was 1:1. The samples presented the characteristic UV absorption of TiO_2 and the absorption peak in the visible region associated with the surface plasmon absorption of Au nanoparticles (NP) (~ 550 nm). The (HR)TEM experiments showed that the metallic particles size was < 3 nm.
The Au-Pd oxide photocatalyst exhibited the highest H_2 production (5 mmol $H_2.g_{cat.}^{-1}h^{-1}$) because of palladium was able to maintain its metallic state and its ability to act as electron sink. The Au-Ni oxide and Au-Co oxide photocatalyst showed a similar performance (3.5 and 3mmol $H_2.g_{cat.}^{-1}h^{-1}$) compared to the Au/TiO_2 material (3.3 mmol $H_2.g_{cat.}^{-1}h^{-1}$) despite the fact that they had a smaller amount of Au. The PL experiments showed that the presence of Au metal NP reduce the electron-hole recombination but also the presence of oxides in the Au-M_xO_y materials further enhance the charge separation, compared with Au/TiO_2 reference photocatalyst. The improved activity can be explained in terms of the enhanced charge separation observed in PL results, compared to the other materials the Au-Pd oxide photocatalyst showed the highest reduction in PL intensity signal..

Keywords: Hydrogen production, Water splitting, Au nanoparticles, TiO_2

1. Introduction

The energy consumption in the world will steadily increase due to the global rise in world's population. The use of solar energy represents a sustainable alternative to cover the global

---

* Author for correspondence: R. Zanella Specia, tel.+52 55 56228635; rodolfo.zanella@ccadet.unam.mx

energy demand, but due to the intermittent and fluctuating nature of this energy, it should be converted to other forms that can be stored. Hydrogen (H_2) is a suitable energy carrier that can be a potential candidate to address this problem because it can be directly produced using solar energy by means of photocatalytic water splitting [1–5]. Most of the photocatalytic systems may need the addition of organic or inorganic sacrificial agents in order to improve the produced quantity of H_2 [3,6,7], and methanol is one of the most frequently used [8–11]. The function of these sacrificial agents is to capture the photogenerated holes, reducing the probability of electron-hole recombination and, in the case of organic agents, an additional source of protons [12].

Although TiO_2 is one of the most studied photocatalyst owing to its high stability, non-toxicity, wide availability and low cost, it presents several disadvantages in photocatalytic water splitting: (a) it can only absorb UV light due to its large band gap (~3.2 eV), (b) fast recombination of the photogenerated electrons and (c) large overpotencial for H_2 and CO_2 reduction. Another way of enhance the photocatalytic efficiency of TiO_2, besides the use of sacrificial agents, is the deposition of metal or metal oxides that act as co-catalyst on the surface of the semiconductor. These co-catalysts should be stable, inexpensive and environmental-friendly. It has been reported that the deposition of noble metals, such as Au and Pd, on the surface of TiO_2 enhances the H_2 production through the formation of a Schottky barrier on the metal/TiO_2 interface. Among metal oxides, Ni and Co based co-catalysts have been studied and showed good photocatalytic performance [13] and one of their advantage is their lower cost, compared with noble metals. The aim of the present work is to study the use of Pd, Ni and Co based co-catalysts to partially replace Au as the main co-catalyst.

2. Materials and Methods

2.1. Materials and reagents

TiO_2 P25 (Evonik) was used as support, $HAuCl_4$ trihydrate (99.9 %), $Pd(NO_3)_2$ hydrated (99.9 %), $Ni(NO_3)_2$ hexahydrate (99.999 %), $Co(NO_3)_2$ hexahydrate (98 %) were provided from Aldrich and were used for the surface modification of TiO_2 with nanoparticles of Au, Pd, Co and Ni. All gases were used (H_2 99.999% and air 99.999%) without prior purification. Tri-distilled water was used in all experiments.

2.2. Synthesis of titanium dioxide modified with Pd, Co and Ni

Monometallic catalysts were prepared by incipient wetness impregnation using aqueous solutions of the precursors with further drying (80 °C, 2 h). The impregnated materials were thermally activated at 300 °C for 2 h using H_2 flow of 0.5 $ml \cdot min^{-1}$ per gram of photocatalyst and a heating rate of 2 °C min^{-1}. The nickel-based catalyst was activated under air flow using the same conditions. The materials were stored under vacuum.

2.3. Synthesis of titanium dioxide modified with Au-Pd, Au-Co and Au-Ni

Bimetallic catalysts were prepared following the same procedure used for monometallic catalysts. Pd, Co or Ni was first deposited and then Au was added by deposition-precipitation with urea (DPU) following the previously reported procedure [14,15]. The nominal loading was fixed in 0.5 wt. % and the molar ratio Au/M =1 (M= Pd,

Co and Ni). Briefly, the gold precursor $HAuCl_4.3H_2O$ was added to a container under vigorous stirring to obtain the desired gold loadings (0.25 wt.%) with a final concentration of $4.2.10^{-3}$ M. Afterward, urea was added to the solution (0.42 M, Aldrich, 98%) and then the previously impregnated P25 was added to this solution. This reaction mixture was kept in a sealed vessel under vigorous stirring at 80 °C for 16 h. After the deposition time, the support was recovered by centrifugation and washed 4 times with water (100 ml/g). Next, the recovered catalysts were dried for 2 h at 80 °C under vacuum. All the bimetallic catalysts were thermally activated for 2 h at 300 °C, using a heating rate of 2 °C min^{-1} and an air flow of 1 $ml \cdot min^{-1}$ per gram of photocatalyst. Finally, the treated photocatalysts were stored under vacuum.

2.4. Characterization

Diffuse reflectance (DR) UV-Visible spectra of the catalysts were obtained using a Cary 5000 spectrophotometer equipped with a Praying Mantis DR accessory and Teflon as reference material. Photoluminescence (PL) measurements were conducted at room temperature using a homemade spectrophotometer with UV laser (378 nm, 12 mW) as excitation source, a SPEX 1000M monochromator, a GaAs photomultiplier (RCA-C31034) and a DATA SCAN amplifier. The elemental analysis was determined by electron dispersion scattering (EDS) using a Scanning Electron Microscope JEOL 5900-LV though microanalysis on an EDS Oxford ISIS.

2.5. Photocatalytic activity

The photocatalytic activity was studied in a homemade photo-reactor containing a volume of 200 ml of a water/methanol solution (variable molar ratio) and 100 mg of photocatalyst. This reactor was sealed and connected to a peristaltic pump to inject the sample into a gas chromatograph (GC Agilent 7820) to measure the H_2 concentration in the reaction atmosphere. The GC was equipped with a thermal conductivity detector (column Agilent CP7920) and argon was used as carrier gas. The total volume of the reaction system was 504 ml. The irradiation source was a UVP mercury lamp with primary emission at 254 nm with intensity of 2.2 mW cm^{-2}. To assure the adsorption/desorption equilibrium, the system was put in an ultrasonic bath for 5 min, stirred in the dark for 30 min and degassed by bubbling nitrogen prior to the photochemical reaction. After the irradiation time, the used photocatalysts were collected by centrifugation.

3. Results and Discussion

3.1. Synthesis and characterization of catalysts

Previously, we had studied and optimized the effect of parameters such as gold loading, mass of catalyst, thermal and atmosphere of the pre- treatment to H_2 production by photocatalysts based on Au nanoparticles supported on TiO_2 (P25, Evonik) under UV light (254 nm) [16]. In order to extend our study to control the global process of H_2 photoproduction, we performed studies to clarify the influence of methanol concentration in the photocatalytic production of H_2. Many organic compounds have been used as sacrificial donors, however methanol is the most used due to its splitting energy demand (16.1 $kJ.mol^{-1}$) compared to water and the high C:H ratio (1:4).

In order to study the influence of the methanol concentration in the photocatalytic production of H_2, it was varied from 0.01 to 1 mol fraction. In this set of experiments Au/TiO_2, with a nominal loading of 0.5 wt.% of Au, was used as photocatalyst [14,16]. Figure 1 shows the production rate and yield of H_2 over the evolution of methanol concentration. The production rate was calculated using the slope of the plot of evolved H_2 moles *versus* the reaction time. These reaction profiles were fitted to a lineal model and the slope of this model corresponds to the production rate of H_2 (units: mmol H_2 h^{-1} g_{cat}^{-1}). The H_2 yield was calculated according to Eq. 1:

$$Y_{H2} = \frac{n_{H_2}}{2n_{MeOH}} \quad (1)$$

Where n_{H2} are the moles of H_2 produced per gram of catalyst after 6.5 h under reaction conditions and n_{MeOH} are the initial moles of methanol.

As shown in Figure 1, the production rate improved as the quantity of methanol increased, reaching a maximum of 9.6 mmol H_2 h^{-1} g_{cat}^{-1} when the mole fraction of methanol was ~ 0.6, and after this point a decrease in the production rate was observed for our system. Generally, the photocatalytic oxidation of organic compounds follows a Langmuir-Hinshelwood (L-H) model, which states that at low concentrations of substrate a pseudo-first order kinetics is observed, and at high concentrations, a pseudo-zero order kinetics is observed [17,18]. The L-H model can be used to partially explain the behavior observed in Figure 1, where the production rate increased almost linearly until the mole fraction of methanol was ~0.6 (first order kinetics). After this value, the production rate should be independent of the methanol concentration (zero order kinetics).

However, in our experiments the production rate decreased, which could be explained in terms of the absorption of methanol on the surface of the photocatalyst and also in terms of UV light absorption of methanol. According to the UV-Vis spectrum of methanol, it can absorb UV light below ~260 nm and at higher methanol concentrations, the formation of several layers of methanol over the surface of the catalyst is possible [18]. Therefore, when the methanol concentration was increased, the amount of light (λ = 254 nm) absorbed by the photocatalyst was reduced, due to the formation of additional layers of methanol, causing the decrease in the production rate.

Moreover, the plot of yield of H_2 as a function of methanol concentration (red trace in Figure 1), shows that the yield decreased exponentially as the methanol concentration increased; at a mole fraction of ~0.02, the yield of H_2 remained almost constant. Finally, the optimal value of the methanol concentration was set as the minimum quantity of methanol that maximizes both the production rate and H_2 yield. This value, that corresponds to the point where both graphics intersect, was ~0.05 mole fraction of methanol, which corresponds to 20 mL in the case of our reaction system.

Once the optimal concentration of methanol was found, the photocatalytic activity of the mono and bimetallic catalysts was evaluated, and the corresponding results are shown in the Figure 2a and Figure 2b, respectively. All the monometallic photocatalysts were more active than unmodified TiO_2 P25, which showed a H_2 production rate of 0.24 mmol h^{-1} g_{cat} (see Table 1). These results indicated that the presence of the metal species on the surface of TiO_2 was outstanding to enhance the photocatalytic production of H_2;

therefore, in order to properly compare the obtained results, they were normalized respect to the actual metal content measured by EDS.

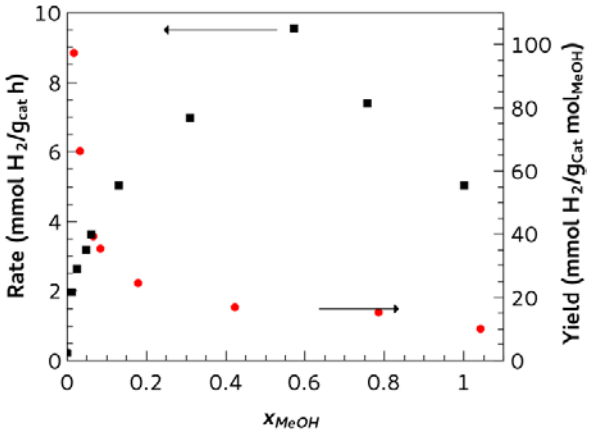

Fig. 1. H_2 production rate and yield as a function of methanol concentration.

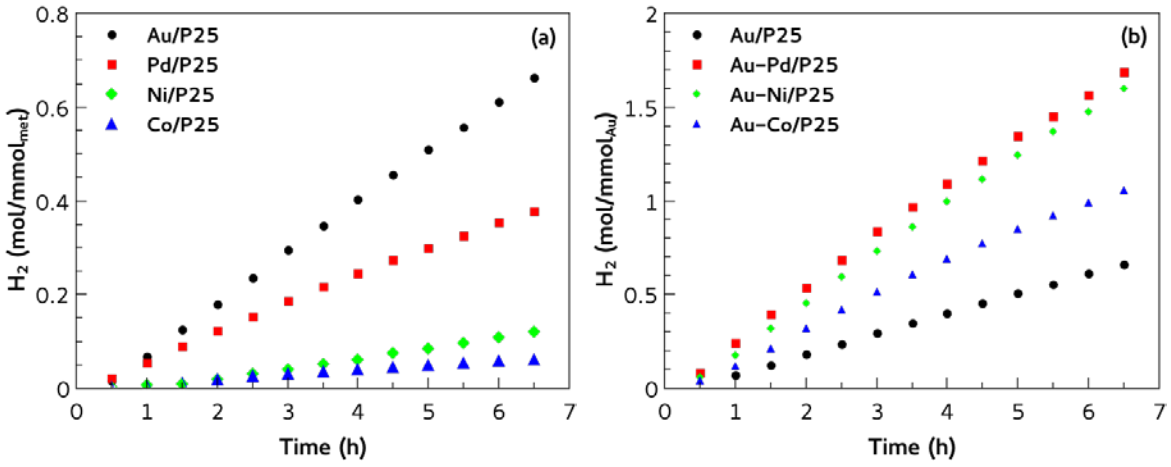

Fig. 2. H_2 production over: (a) monometallic. and (b) bimetallic photocatalysts.

As it can be observed in Figure 2a and Table 1, Au/P25 and Pd/P25 showed the highest production rate per mmol of metal, followed by the Ni/P25 and Co/P25 photocatalysts. It has been reported that these metals can enhance the photocatalytic production of H_2 due to the formation of p-n heterojunction in the case of Ni and Co oxides species [14,19–21] or through the formation of a Schottky barrier in the case of Au^0 and Pd^0 [14,22–24]. The presence of these two phenomena can minimize the probability of the electron-hole recombination, resulting in a better photocatalytic performance. In our materials, this reduction in the electron-hole recombination was corroborated by PL

experiments, where the emission intensity was lower than the intensity presented by the unmodified P25 (vide infra).

In case of bimetallic photocatalysts a portion of Pd, Ni or Co was replaced by Au, and the H_2 production was normalized respect to the Au content. According to the results shown in Figure 2b, all the bimetallic materials produced a higher quantity of H_2 per mmol of Au than the Au/P25 photocatalyst, showing the greatest H_2 production the Au-Pd/P25 and Au-Ni/P25 catalysts. It is interesting to note that TiO_2 P25 promoted by two metal species showed a higher production rate than monometallic Au/P25. Regarding Au-Pd/P25, this enhancement could be explained by the formation of Au/Pd alloys [23,25,26]. The presence of these alloys can further increase the interfacial charge transfer and reduce the electron-hole recombination than the Au or Pd alone. To the best of our knowledge, the preparation of Au photocatalyst modified with Ni or Co has been scarcely studied. As mentioned earlier, the deposition of Ni or Co oxide species on the surface of TiO_2 can lead to the formation of a composite material and the deposition of Au over the surface of this composite could create an additional Schottky barrier. In the PL results, it was observed that the signal intensity presented by the bimetallic photocatalysts was lower than the one showed by the monometallic materials, indicating that the formation of this additional barrier was accomplished.

Table 1. Parameters of the evaluated photocatalyst.

Photocatalyst	Eg (eV)	Au Content (wt.%)	Total Metal Content (wt.%)	H_2 production rate r_{Au} (mol H_2 h^{-1} $mmol_{Au}^{-1}$)
Au-Pd/P25	2.98	0.37	0.65	0.27
Au-Ni/P25	3.16	0.27	0.46	0.26
Au-Co/P25	3.16	0.35	0.58	0.17
Au/P25	3.21	0.62	0.62	0.11
Pd/P25	3.16	-	0.37	0.06[a]
Ni/P25	3.11	-	0.26	0.02[a]
Co/P25	3.15	-	0.31	0.01[a]

Notes: [a]In the case of the monometallic photocatalysts, H_2 production rate is normalized respect to the corresponding metal content, instead the Au content.

3.2. Optical and photoluminescence properties

Figure 3 shows the absorption spectra of UV-Vis diffuse reflectance spectroscopy (DRS) of the three bimetallic calcined samples and bare TiO_2 (P25) as a reference. TiO_2 showed zero absorption in the visible region as indicated in the spectrum. All samples

showed a broad absorption band at 380 nm assigned to TiO_2 bulk anatase phase [27], which is attributed to-ligand-to metal charge transfer (LMCT) from O^{2-} to Ti^{4+} indicating the presence of tetrahedrally coordinated Ti^{4+} ions. All the Au loaded samples, except Au-Pd/P25, showed a broad absorption band at ~ 550 nm assigned to the surface plasmon resonance (SPR) of metallic Au nanoparticles, produced from the collective oscillations of the free conduction band electrons induced by the incident electromagnetic radiation on Au nanoparticles [28].

The intensity and position of plasmon band depends on the gold content, particle size and the surrounding environment [29–31]. As can be observed, the SPR intensity followed the order: Au/P25 > Au-Co/P25 > Au-Ni/P25, which can be explained by the Au content in the photocatalyst (see Table 1).

It is worth highlighting the lower intensity of the SPR band in the sample Au-Pd/P25. It has been reported that if the size of Pd particles is smaller than 10 nm, they absorb only in the UV region [32]. Clusters and larger particles will exhibit a red shift and an enhanced ability to absorb visible light [33]. So, in the Au-Pd/P25 bimetallic sample, the Pd particles were smaller than 10 nm, probably in an intimate interaction with Au particles. This ill-defined SPR band could be caused by formation of an Au-Pd alloy.

It is well know that Au-Pd alloy formation is possible because both metals are miscible in the whole range of compositions [34]. Presumably, in this sample could exist small Pd ensembles enriched by Au enriched surfaces of Au-Pd alloys [35–37] or also a surface enriched by Pd with Au in the core of the particles.

The study of band gaps (E_g) is important to determine the energy of the light absorbed to generate electron-hole pairs. The band gaps of all calcined samples were calculated according to the modified Kubelka- Munk function $[F(R)\,E]^{½}$ vs. the energy of absorbed light, E [38]. The band gaps values are listed in Table 1. These results show that the introduction of metallic nanoparticles (such as Au or Pd, Ni and Co), with similar work functions, has no influence on the band gap energy of the TiO_2 matrix (3.25 eV), the same behavior is observed for bimetallic samples.

Photoluminescence spectroscopy (PL) is widely used to understand the recombination of electron holes pairs. In general, a strong PL signal at 440 nm was observed in TiO_2 catalysts, with the exited wavelength of 325 nm. The spectral emission in the range 370-800 nm is shown in Figure 4.The intensity of PL emission spectrum of all monometallic catalyst (not shown) were decreased compared to TiO_2 bare spectra. This is attributed to the surface metal modification of Ni, Co and Pd that capture the excited electrons and reduce the electron-hole recombination process.

In case of monometallic Au/P25 sample the intensity of signal at 440 nm decreased respect to TiO_2 bare indicating the loose of ability of the recombination centers. Instead, the intensity of the peak at 440 nm of bimetallic samples was reduced to completely disappear in Au-Pd/P25 and Au-Ni/P25 calcinated samples. This observation suggested a low recombination frequency and a high mean life of charge carriers of theses bimetallic samples that could explain the to increase in the activity of H_2 production by photocatalysis.

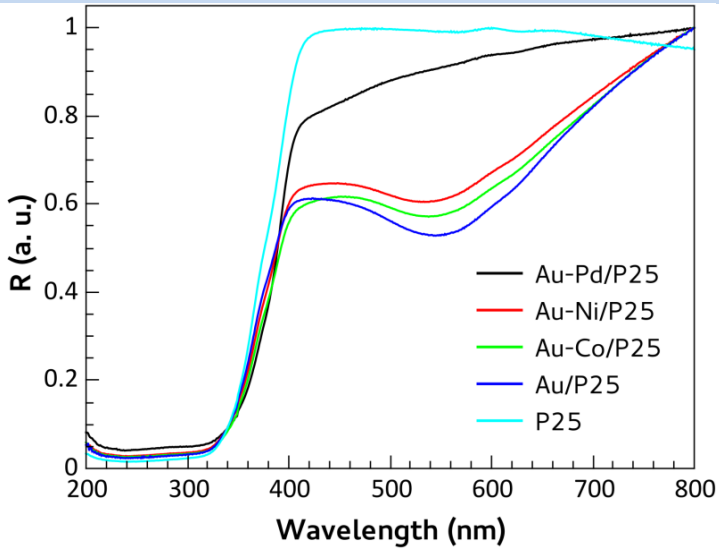

Fig. 3. UV-Vis DR spectra of the bimetallic photocatalysts.

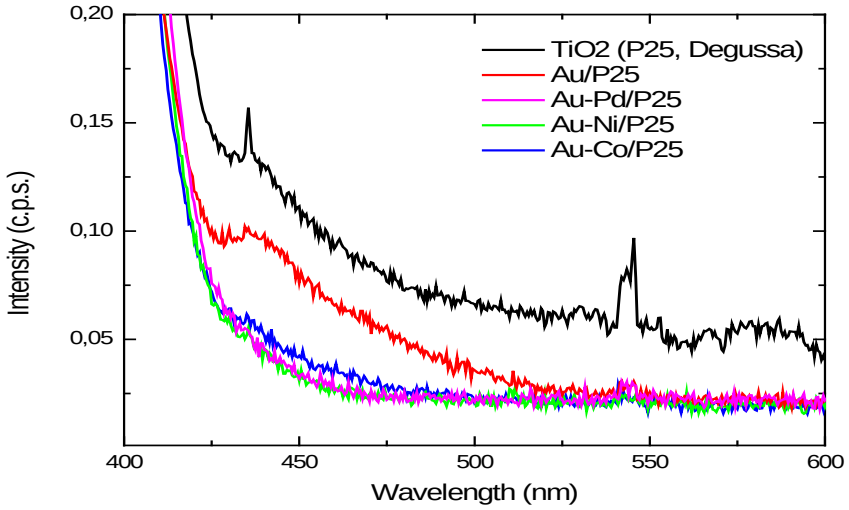

Fig. 4. Photoluminescence emission spectra of a)P25 (black line),b) Au/P25 (red line), Au-Pd/P25 (magenta line), Au-Ni/P25 (green line), Au-Co/P25 (blue line).

4. Conclusion

A series of Au-M/P25 (M = Pd, Ni and Co) bimetallic photocatalysts were prepared by sequential wetness impregnation (M) and DPU (Au). Au/P25 showed the better H_2 production rate per mol of deposited metal in monometallic catalysts, while Au-Pd/P25 and Au-Ni/P25 photocatalysts showed the highest H_2 production rate per mol of deposited Au, closely followed by the Au-Co/P25 catalyst. This increased H_2 production can be explained by the suppression of electron-hole recombination, as evidenced by PL results. The obtained results showed that Au can be replaced with Pd, Ni and Co, acting as promoters co-catalysts to increase the H_2 production (for example, Pd), or reduce the final cost of the photocatalyst if Au was replaced with less expensive metals as Co or Ni.

Acknowledgements

The authors wish to acknowledge the financial support granted by project DGAPA-UNAM IN103513, México. CEB and E. Albiter would like to acknowledge UNAM-DGAPA and CONACYT for the respective postdoctoral grants.

References

[1] D.Y.C. Leung, X. Fu, C. Wang, M. Ni, M.K.H. Leung, X. Wang, X. Fu, Hydrogen Production over Titania-Based Photocatalysts, ChemSusChem. 3 (2010) 681–694.
[2] X. Chen, S. Shen, L. Guo, S.S. Mao, Semiconductor-based Photocatalytic Hydrogen Generation, Chem. Rev. 110 (2010) 6503–6570.
[3] P. Lianos, N. Strataki, M. Antoniadou, Photocatalytic and photoelectrochemical hydrogen production by photodegradation of organic substances, Pure Appl. Chem. 81 (2009) 1441–1448.
[4] A.J. Esswein, D.G. Nocera, Hydrogen Production by Molecular Photocatalysis, Chem. Rev. 107 (2007) 4022–4047.
[5] S.-C. Moon, Y. Matsumura, M. Kitano, M. Matsuoka, M. Anpo, Hydrogen production using semiconducting oxide photocatalysts, Res. Chem. Intermed. 29 (2003) 233–256.
[6] M. Bowker, Sustainable hydrogen production by the application of ambient temperature photocatalysis, Green Chem. 13 (2011) 2235–2246.
[7] W. Fan, Q. Zhang, Y. Wang, Semiconductor-based nanocomposites for photocatalytic H2 production and CO2 conversion, Phys. Chem. Chem. Phys. 15 (2013) 2632–2649.
[8] F. Guzman, S.S.C. Chuang, C. Yang, Role of Methanol Sacrificing Reagent in the Photocatalytic Evolution of Hydrogen, Ind. Eng. Chem. Res. 52 (2013) 61–65.
[9] A. Naldoni, M. D'Arienzo, M. Altomare, M. Marelli, R. Scotti, F. Morazzoni, E. Selli, V. Dal Santo, Pt and Au/TiO2 photocatalysts for methanol reforming: Role of metal nanoparticles in tuning charge trapping properties and photoefficiency, Appl. Catal. B Environ. 130–131 (2013) 239–248.
[10] S. Pany, B. Naik, S. Martha, K. Parida, Plasmon Induced Nano Au Particle Decorated over S,N-Modified TiO2 for Exceptional Photocatalytic Hydrogen Evolution under Visible Light, ACS Appl. Mater. Interfaces. 6 (2014) 839–846.
[11] F. Gärtner, S. Losse, A. Boddien, M.-M. Pohl, S. Denurra, H. Junge, M. Beller, Hydrogen Evolution from Water/Alcohol Mixtures: Effective In Situ Generation of an Active Au/TiO2 catalyst, ChemSusChem. 5 (2012) 530–533.
[12] H. Bahruji, M. Bowker, P.R. Davies, F. Pedrono, New insights into the mechanism of photocatalytic reforming on Pd/TiO2, Appl. Catal. B Environ. 107 (2011) 205–209.

[13] Z. Yan, H. Wu, A. Han, X. Yu, P. Du, Noble metal-free cobalt oxide (CoOx) nanoparticles loaded on titanium dioxide/cadmium sulfide composite for enhanced photocatalytic hydrogen production from water, Int. J. Hydrog. Energy. 39 (2014) 13353–13360.
[14] S. Oros-Ruiz, R. Zanella, S.E. Collins, A. Hernández-Gordillo, R. Gómez, Photocatalytic hydrogen production by Au–MxOy (M=Ag, Cu, Ni) catalysts supported on TiO2, Catal. Commun. 47 (2014) 1–6.
[15] R. Zanella, S. Giorgio, C.R. Henry, C. Louis, Alternative Methods for the Preparation of Gold Nanoparticles Supported on TiO2, J. Phys. Chem. B. 106 (2002) 7634–7642.
[16] S. Oros-Ruiz, R. Zanella, R. López, A. Hernández-Gordillo, R. Gómez, Photocatalytic hydrogen production by water/methanol decomposition using Au/TiO2 prepared by deposition–precipitation with urea, J. Hazard. Mater. 263, Part 1 (2013) 2–10.
[17] J.-M. Herrmann, Heterogeneous photocatalysis: fundamentals and applications to the removal of various types of aqueous pollutants, Catal. Today. 53 (1999) 115–129.
[18] L.S. Al-Mazroai, M. Bowker, P. Davies, A. Dickinson, J. Greaves, D. James, L. Millard, The photocatalytic reforming of methanol, Catal. Today. 122 (2007) 46–50.
[19] J.-D. Lin, S. Yan, Q.-D. Huang, M.-T. Fan, Y.-Z. Yuan, T.T.-Y. Tan, D.-W. Liao, TiO2 promoted by two different non-noble metal cocatalysts for enhanced photocatalytic H2 evolution, Appl. Surf. Sci. 309 (2014) 188–193.
[20] T. Sreethawong, Y. Suzuki, S. Yoshikawa, Photocatalytic evolution of hydrogen over mesoporous supported NiO photocatalyst prepared by single-step sol–gel process with surfactant template, Int. J. Hydrog. Energy. 30 (2005) 1053–1062.
[21] B.A. Nail, J.M. Fields, J. Zhao, J. Wang, M.J. Greaney, R.L. Brutchey, F.E. Osterloh, Nickel Oxide Particles Catalyze Photochemical Hydrogen Evolution from Water—Nanoscaling Promotes P-Type Character and Minority Carrier Extraction, ACS Nano. 9 (2015) 5135–5142.
[22] J. Cihlar Jr., E. Bartonickova, J. Cihlar, Low-temperature sol–gel synthesis of anatase nanoparticles modified by Au, Pd and Pt and activity of TiO2/Au, Pd, Pt photocatalysts in water splitting, J. Sol-Gel Sci. Technol. 65 (2013) 430–442.
[23] M. Bowker, C. Morton, J. Kennedy, H. Bahruji, J. Greves, W. Jones, P.R. Davies, C. Brookes, P.P. Wells, N. Dimitratos, Hydrogen production by photoreforming of biofuels using Au, Pd and Au–Pd/TiO2 photocatalysts, J. Catal. 310 (2014) 10–15.
[24] J. Yang, H. Yan, X. Zong, F. Wen, M. Liu, C. Li, Roles of cocatalysts in semiconductor-based photocatalytic hydrogen production, Philos. Trans. R. Soc. Lond. Math. Phys. Eng. Sci. 371 (2013) 20110430.
[25] Y. Xin, L. Wu, L. Ge, C. Han, Y. Li, S. Fang, Gold–palladium bimetallic nanoalloy decorated ultrathin 2D TiO2 nanosheets as efficient photocatalysts with high hydrogen evolution activity, J. Mater. Chem. A. 3 (2015) 8659–8666.
[26] R. Su, R. Tiruvalam, A.J. Logsdail, Q. He, C.A. Downing, M.T. Jensen, N. Dimitratos, L. Kesavan, P.P. Wells, R. Bechstein, H.H. Jensen, S. Wendt, C.R.A. Catlow, C.J. Kiely, G.J. Hutchings, F. Besenbacher, Designer Titania-Supported Au–Pd Nanoparticles for Efficient Photocatalytic Hydrogen Production, ACS Nano. 8 (2014) 3490–3497.
[27] S.K. Parayil, H.S. Kibombo, L. Mahoney, C.-M. Wu, M. Yoon, R.T. Koodali, Synthesis of mixed phase anatase-TiO2(B) by a simple wet chemical method, Mater. Lett. 95 (2013) 175–177.
[28] T. Yonezawa, H. Matsune, T. Kunitake, Layered Nanocomposite of Close-Packed Gold Nanoparticles and TiO2 Gel Layers, Chem. Mater. 11 (1999) 33–35.
[29] K.M. Parida, N. Sahu, A.K. Tripathi, V.S. Kamble, Gold Promoted S,N−Doped TiO2: An Efficient Catalyst for CO Adsorption and Oxidation, Environ. Sci. Technol. 44 (2010) 4155–4160.
[30] Y. Wu, H. Liu, J. Zhang, F. Chen, Enhanced Photocatalytic Activity of Nitrogen-Doped Titania by Deposited with Gold, J. Phys. Chem. C. 113 (2009) 14689–14695.
[31] S. Linic, P. Christopher, D.B. Ingram, Plasmonic-metal nanostructures for efficient conversion of solar to chemical energy, Nat. Mater. 10 (2011) 911–921.
[32] S.K. Mohapatra, N. Kondamudi, S. Banerjee, M. Misra, Functionalization of Self-Organized TiO2 Nanotubes with Pd Nanoparticles for Photocatalytic Decomposition of Dyes under Solar Light Illumination, Langmuir. 24 (2008) 11276–11281.
[33] Y. Xiong, J. Chen, B. Wiley, Y. Xia, Y. Yin, Z.-Y. Li, Size-Dependence of Surface Plasmon Resonance and Oxidation for Pd Nanocubes Synthesized via a Seed Etching Process, Nano Lett. 5 (2005) 1237–1242.

[34] H. Okamoto, T.B. Massalski, The Au−Pd (Gold-Palladium) system, Bull. Alloy Phase Diagr. 6 (1985) 229–235.
[35] B. Pawelec, A.M. Venezia, V. La Parola, E. Cano-Serrano, J.M. Campos-Martin, J.L.G. Fierro, AuPd alloy formation in Au-Pd/Al2O3 catalysts and its role on aromatics hydrogenation, Appl. Surf. Sci. 242 (2005) 380–391.
[36] A. Corma, P. Serna, Chemoselective Hydrogenation of Nitro Compounds with Supported Gold Catalysts, Science. 313 (2006) 332–334.
[37] Y. Pluntke, L.A. Kibler, D.M. Kolb, Unique activity of Pd monomers: hydrogen evolution at AuPd(111) surface alloys, Phys. Chem. Chem. Phys. 10 (2008) 3684–3688.
[38] R. López, R. Gómez, Band-gap energy estimation from diffuse reflectance measurements on sol–gel and commercial TiO2: a comparative study, J. Sol-Gel Sci. Technol. 61 (2012) 1–7.

Chapter 1.4. Co-culture specific bacteria for hydrogen production in organic waste in different culture media

E. Avila-Vera[*a,b]; D. Alcantara-Díaz[c]; G. Roa-Morales[b]; S.M. Fernandez-Valverde[a*]

[a]Depto. de Química, [c]Depto de Biología ININ, Apartado Postal 18-1027, México DF 11801, México, D.F.
[b]Depto de Posgrado, Facultad de Química, UAEMéx. Paseo Tollocan esq. Paseo Colón, Toluca, México.

ABSTRACT

Fruit and vegetable waste (FVW) deposited in landfills contaminates air, land and underground water. Those wastes could be raw material for H_2 production. In order to utilize FVW it is necessary to determine its seasonal composition. Samples of FVW were obtained from Toluca's city market from November to December 2014. The samples were analyzed to determine proteins, fiber, fat and carbohydrates content. The carbohydrate percentage was 6.7 ± 0.3, equivalent to the 6.4 ± 0.5 observed in samples collected between May to October, regardless of the season or kind of FVW in the mixture. An *Enterobacter cloacae* and *Clostridium butyricum* co-culture was used for H_2 production. The co-culture was grown in 1 g of FVW (wet mass basis); 10 mL of growth medium (pH of 5.5) were mixed in 20 mL hermetically sealed glass bottles. L-cysteine or iron sulfate solutions were added and oxygen was displaced by a nitrogen gas current. Once the anaerobic conditions were established the bottles were heated for 20 minutes at 120 ^oC and allowed to reach room temperature, 2 drops of solution was taken and used for microorganism quantification, on a Petroff-Hausser chamber, and counted directly by microscopy. In the first place, the effect of L-cysteine or iron sulphate in phosphate solution on the growth *Clostridium butyricum* in the presence of FVW was assessed. L-cysteine alone inhibits bacterium growth until 80 h. In the case of iron sulfate, we observed rapid bacterial growth followed by a marked decreased in growth after 25 h. Finally the bacterial number increases by 113% in 8 h when the media contains a mixture of iron sulfate and L-cysteine. Results indicate that trace compounds added to the culture medium do not affect H_2 production, as FVW provides sufficient C and N sources as well as micronutrients necessary for the bacterial metabolism. There was no significant difference in bacterial growth rate with or without added compounds. Thus, FVW with no additional substances is sufficient as growth medium for co-cultures of the H_2-producing bacteria used in this study.

Keywords: Hydrogen production, Biohydrogen , Organic waste

1. Introduction

The world population growth has caused progressive energy consumption, which greatly depends on fossil fuel sources. Therefore, the increasing generation of carbon

---

* Authors for correspondence: Dr. S.M. Fernández-Valverde, E. Avila-Vera, evaristovae@yahoo.com.mx

greenhouse gasses has resulted to air pollution, global warming and the sever depletion of fossil fuel sources.

Hydrogen is a promising clean and environmental friendly energy carrier since its combustion releases H2O without greenhouse gases [1]. Hydrogen production through biological route using waste biomass is an important area for bioenergy production. Biological hydrogen production is classified into four categories, (1) biophotolysis of water, (2) photodecomposition of organic compounds (3) fermentative hydrogen to breakdown carbohydrate-rich substrates to hydrogen and other products such as acids and alcohols using anaerobic bacteria and (4) hybrid systems combining dark and photofermentation. Among all these processes, the dark fermentation route is the most feasible technology because not require any external source and can be run at low cost [2]. Pure carbohydrate sources are expensive raw materials for real scale hydrogen production. Nevertheless, the majority of the studies use pure carbohydrates as substrate, like monosaccharides, disaccharides or polysaccharides. Simple sugars such as glucose, sucrose, and lactose are the most common used substrates due to their ease biodegradability and simple structure [3,4]. However, real life applications involve complex sugars, and thus it is indispensable to employ these substrates in the dark fermentation process in order to provide relevant insight into system performance [5-7]. The majority of the research on biohydrogen production from food waste has been conducted under dark fermentation [2, 8-14].

On the other hand, is important to know the composition of residues for an adequate handling and disposition of solid waste (SW), because it generates diverse problems to the environment qein air, water and ground. Food waste, the mayor component in municipal solid waste accounted for 52 ± 2% of the total waste in México. This waste is composed of raw and cooked food discarded before or during food preparation. It has high volatile solids content, moisture and salinity, thus the organic waste decomposition is the main source of unpleasant odor, leachates produces, groundwater contamination, greenhouse gas emission [2] and vermin attraction. Nowadays food waste has gained interest as a potential feedstock for bioenergy. The anaerobic digestion process provides a very efficient way to transform organic waste into an innocuous gas, which is capable of providing clean energy. In general, biohydrogen production results from carbohydrate degradation through acidogenesis and acetogenesis routes and it is highly sensitive to certain environmental conditions such as pH, volatile fatty acids, temperature, hydrogen partial pressure, inoculum sources and food waste concentrations [2,15]. Utilizing renewable energy resources such fruit and organic waste for biohydrogen production can be a promising approach for replacing fossil fuels and at the same time to solve the waste disposal problem [2].

Hydrogen production yield is significantly influenced by the bacterial metabolism. The inoculum used for fermentative hydrogen production include mixed communities of anaerobic bacteria, compost piles, and pure cultures of known species of hydrogen-producing bacteria [7]. The use of co-cultures help to maintain anaerobic conditions for strict high hydrogen producers and eliminate the need for an expensive reducing agent and either can improve the hydrolysis of complex sugars and plant biomass. Therefore, a strict anaerobe such as *Clostridium sp*., and a facultative anaerobe such as *Enterobacter sp*., are co-cultured in the same reactor under optimum culture conditions for H_2 production, to achieve stable and high-yield H_2 production [7,16,17]. Yokoi et al. examined H_2 production

with a consortium of *Clostryydium. butyricum-Enterobacter aereogenes* with 0.1% L-cysteine as reducing agent, (16,17). To test the influence of the metal cofactors of hydrogenases on H_2 production, Martins et al. studied the medium supplemented with Fe, with Fe and Ni or with Fe, Ni and Se for different hydrogenases [18] only Se increases the hydrogen production yield.

In the present work we studied for the first time the composition of the solid waste generated in the Toluca city market in winter and in second time the influence of L-cysteine to reduce oxygen in the medium and the influence of Fe in grown hydrogen producer bacteria in the *Clostridium butyricun* and *Enterobacter cloacae* co-culture as inoculum for FVW for hydrogen production.

2. Materials and Methods

2.1. Fruits and Vegetables samples and analytical methods

For the present study, we gathered the residues generated daily during the months of November and December from 20 grocery stores from central market of Toluca city that is conformed for more than 200 grocery stores. The residues produced every day for two weeks were collected and refrigerated and subsequently characterized by quarter method with Mexican norms NMX-AA-015-1985 and NMX-AA-022-1985 in order to know the composition of fruits, vegetables and not degradable materials [20,21]. Carbohydrate, protein and lipid composition of organic waste analyses with the AOAC food techniques LEER [22].

2.2. Microorganism and culture growth conditions.

Culture media for the *Enterobacter cloacae* and *Clostridium butyricum* co-culture contained 0.75 g/L agar, 15 g/L caseron enzymatic hydrolysate, 0.5 g/L L-cysteine, 5.5 g/L dextrose, 0.001 g/L resazurine, 2.5 g/L sodium chloride 0.5 g/L sodium thioglicolate and 5 g/L yeast extract. The microorganisms was cultivated every month using 1% (v/v) inoculum.

For hydrogen production with the organic waste a modified medium containing 10.5 g/L K_2HPO_4, 4.5 g/L KH_2PO_4 y 1.0 g/L $(NH_4)_2SO_4$, and 0.001 g/L rezasurine, For this study addition of L-cysteine or $FeSO_4$ or both after the bottles were sealed with butyl rubber stoppers and aluminum crimp seals. Nitrogen avoided aerobic conditions inside the bottles, a nitrogen flux displace oxygen. The bacterial growth done in Batch experiments at 37°C, without pH control using 25 mL serum bottles with a working volume of 10 mL and N_2 as gas headspace.

2.3. Microorganism quantification

For biohydrogen production bacteria studies, 0.1 mL of the co-culture, 10 mL of growth medium (pH of 5.5) described above and 1g of FVW (wet mass basis) introduced in 20 mL glass bottles hermetically sealed with butyl rubber stoppers and aluminum crimp seals. L-cysteine or iron sulfate solutions added and anaerobic conditions establish. Once the anaerobic conditions established the bottles heated for 20 minutes at 120 °C and then allowed to reach room temperature. Afterwards a 0.1 ml of of co-culture inoculum was add to 16 samples of tested reducing agent or iron as hydrogenase cofactor or the mixture of both. Introduced in the shaking bath at 37 ^{O}C samples were taken every two hours and

bacteria counted. drops of solution was taken and used for microorganism quantification, on a Petroff-Hausser chamber, and counted directly in a CARL ZEISS microscope, then we counted 5 square that had 16 little square and calculated the bacteria with equation 1 [23].

Bacteria/mL = (A/B)(20*20*50*1000)/16 (1)

where:
A = total bacteria counted in all squares
B = counted squares
16 = number of little squares inside big square
20 = side square (1/20 mm)
50 = square depth (1/50 mm)
1000 = volume in every square (1/1000mL)
Each experiment was by duplicate.

3. Results and Discussion

The composition of FVW samples collected from 20 grocery stores in randomized form of the total 200 grocery stores of Toluca Market City Center, homogenized with quarter method are presented in Fig. 1.

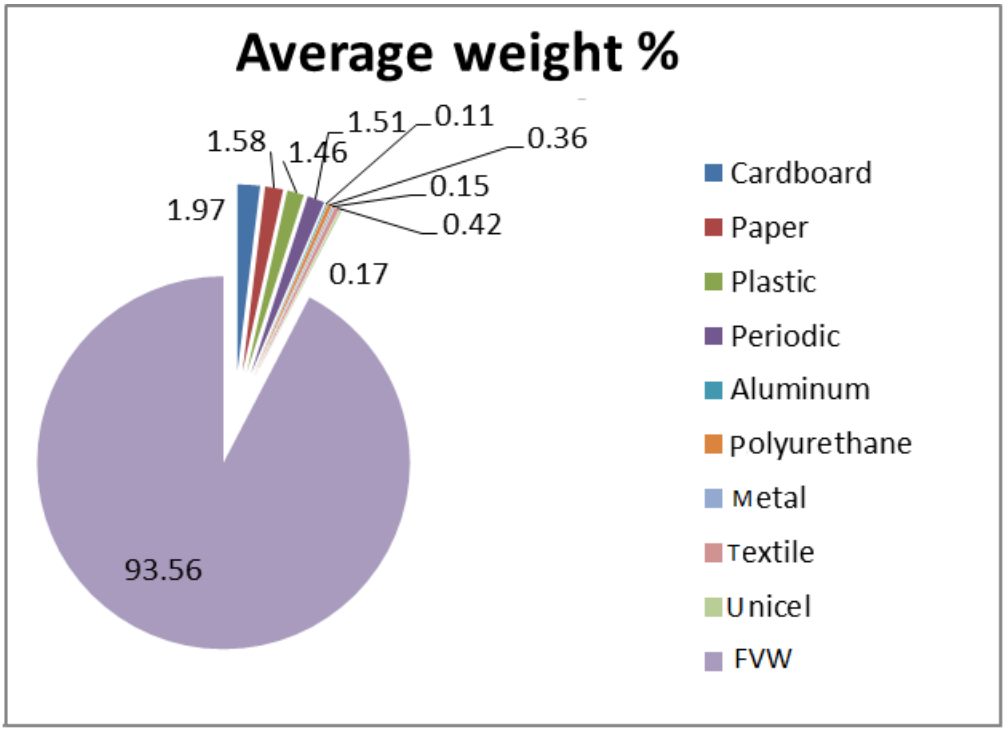

Fig.1. Composition in weight (%) of FVW from Toluca Market City Center

The residues FVW generated in the Toluca Market City Center (TMCC) were mainly organic residues of FV with 93.53 % in weight. Those residues are peels of FV, food in decomposition or leaves. The not degradable materials coming from handle or packages of FV and represents only 6.44 % in weight. Only organic material was analyzed, Table 1 reports The FV composition of residues.

The most representative components of FV generated in November and December were lettuce, pineapple, watermelon, lima vean, orange, nopal, corn and leaves, see Table 1, nevertheless, the composition of FV residues depends of season, customs of people, city or climate. The weight percentage of carbohydrates, fiber, proteins and lipids in wet base for FVW are reported in Table 2, almost the same average for protein carbohydrates and lipids, no matter of FVW composition was found. The average quantity of protein, fiber, carbohydrates and lipids are similar in every sample with 6.63±0.3 of protein, 9.86±1.6 of fiber, 6.34±0.3 of carbohydrates, 1.33±0.1 of lipids and 77.34±1.6 of humidity. The 6.34 % of carbohydrates is the same value obtained for the samples of FVW collected between May to August in the same place [23]. These results indicated that FVW could provide the quantities of carbon, nitrogen and metals necessary for bacterial metabolism of *Enterobacter cloacae and Clostridium butyricum* utilized in these experiments.

The influence of L-cysteine in bacterial growth, Fig. 2, shows that during oxygen consumption the bacterial growth decreases. L-cysteine alone inhibits bacterium growth until 80 h and we infer that exist interference between L-cysteine and *E. cloacae* because both are redactor agents in the co-culture. Nevertheless the co-culture without L-cysteine grown better because the *E. cloacae* is a facultative bacteria that consume naturally the oxygen in the medium and works in collaboration with the *C. butyricum* establishing an anaerobic conditions by of. Yokoi *et al.* [16] reported the enhancement of hydrogen production with L-cysteine for *Clostridium butyriucum,* the lag time changed from 12 h. to 5h. And with the co-culture of *Clostridium butyriucum and enterobacter aerogenes* the lag time was reduced. From 5 h to 2 h. Comparing the performance of both co-cultures, in our case the crystal growth decreases in the presence of L-Cysteine.

The influence of $FeSO_4$ as metal cofactor of hydrogenases in bacterial growth then on hydrogen production as seen in Fig3. In this case, a rapid bacterial growth followed is observed with a marked decreasing after 25 h. From the results it could be infer that $FeSO_4$ benefit the bacterial growth in approximatively 10 % that means the FVW must give the metals cofactor for the enzyme performance, although for minimize the costs of process of hydrogen production.

Finally, the medium with a mixture of L-Cysteine and iron and sulfate, has a bacterial growth of 113% at 8 h, as shows in Fig. 4. That means that: the increasing yield is equivalent to that obtained only with iron sulfate.

Table 1. Composition of fruit or Vegetable from samples of Toluca central market

Fruit or Vegetable	% in weight				Average (%)
	Nov 5	Nov 19	Dec 2	Dec 17	
Lettuce	7.00	3.40	2.00	9.33	5.43
Pea	1.20	1.30	3.70	4.50	2.67
Pineapple	8.00	2.90	16.00	10.40	9.33
Apple	1.40	Nd	0.79	0.88	1.02
Jicama	5.80	2.00	Nd	1.78	3.19
Coriander	0.40	5.00	1.22	1.00	1.91
Watermelon	11.00	7.10	1.60	2.55	5.56
Lima vean	8.67	Nd	3.90	13.80	8.79
Pomegranate	5.40	Nd	0.52	0.33	2.08
Melon	1.00	3.40	2.00	8.20	3.65
Orange	11.00	14.20	8.30	4.67	9.54
Nopal	8.50	14.30	2.00	1.55	6.59
Tomato	0.60	8.20	5.85	12.70	6.84
Grape	1.40	0.50	0.52	Nd	0.81
Potato	2.80	Nd	2.00	1.00	1.90
Cauliflower	7.45	Nd	3.90	Nd	5.68
Corn	2.60	3.50	24.00	8.20	9.58
Onion	3.80	Nd	2.30	0.22	2.11
Pumpkin	3.60	3.00	3.14	Nd	3.01
Lemon	3.40	Nd	1.40	2.44	2.41
Banana	2.60	Nd	Nd	Nd	2.60
Chili	1.80	3.40	0.44	Nd	1.88
Strawberry	Nd	1.00	1.75	2.44	1.73
Fig	Nd	0.70	Nd	Nd	0.70
Guava	Nd	2.20	Nd	0.33	1.27
Papaya	Nd	0.80	0.44	4.00	1.75
Pear	Nd	2.30	Nd	0.11	1.21
Carrot	Nd	4.80	Nd	Nd	4.80
Avocado	Nd	3.10	Nd	Nd	3.10
Leaves	Nd	13.00	Nd	Nd	13.00
Cabbage	Nd	Nd	2.00	Nd	2.00
Celery	Nd	1.13	3.23	Nd	2.18
Peach	Nd	Nd	1.00	Nd	1.00
Broccoli	Nd	Nd	2.89	Nd	2.89
Mango	Nd	Nd	1.30	6.67	3.99
Cucumber	Nd	Nd	Nd	2.30	2.30
Mamey	Nd	Nd	Nd	2.10	2.10
Total	**100**	**100**	**100**	**100**	

Table 2. Concentration of macromolecules from sample of FV

Parameter	% in weight				Average
	M1	M2	M3	M4	% in weight
Protein	6.41	6.40	7.10	6.60	6.63 ± 0.3
Fiber	8.29	10.52	10.81	9.80	9.86 ± 1.6
Carbohydrates	6.70	6.14	6.22	6.30	6.34 ± 0.3
Lipids	1.31	1.22	1.43	1.34	1.33 ± 0.1
Humidity	77.29	75.72	78.44	77.90	77.34 ± 1.6

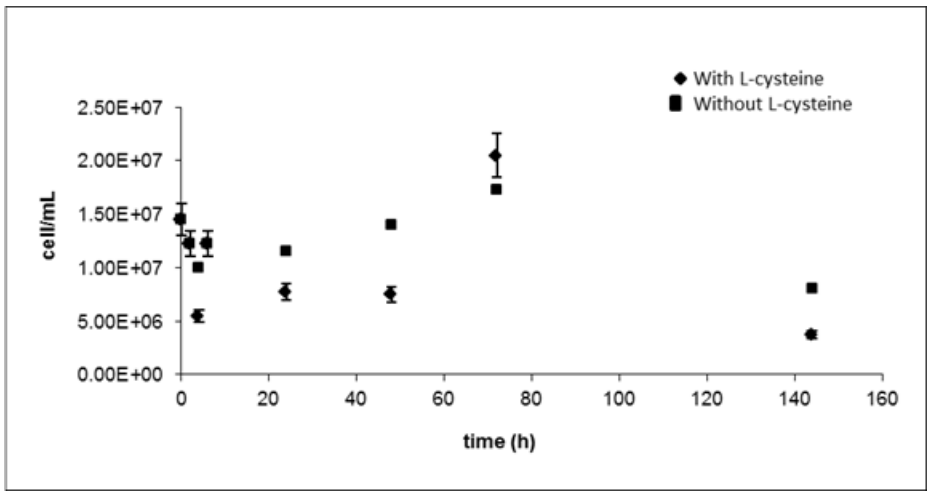

Fig.2. Influence of L-cysteine in grown co-culture

.

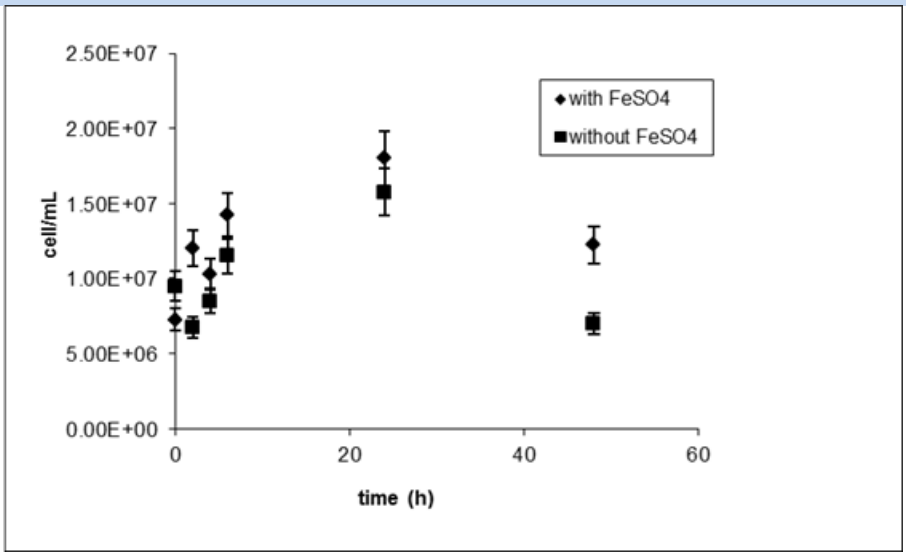

Fig.3. Influence of $FeSO_4$ in grown co-culture

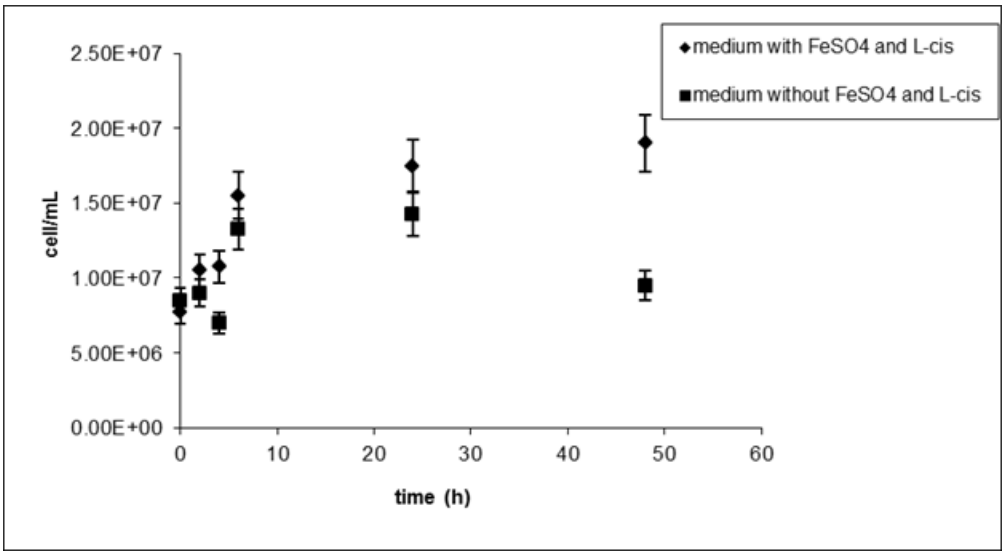

Fig.4. Influence of L-cysteine and $FeSO_4$ in grown co-culture

From these results and to have a convenient cost for hydrogen produced from FVW the decision is to work with no extra compounds additions to the FVW in the pilot state of hydrogen production.

4. Conclusion

The composition of FVW is different in every sample for fruit or vegetable and depends of season, customs of people, climate, and city. Although the quantities of carbohydrates, proteins, fats and fiber analyzed are quite similar. The results indicate that trace compounds added to the culture medium do not affect hydrogen production because FVW provides sufficient carbon and nitrogen sources as well as micronutrients (i.e. iron) necessary for the bacterial metabolism. Additionally, there was no significant difference in bacterial growth rate with or without added L-cisteine or iron sulfate compounds. Thus, FVW is sufficient as growth medium for co-cultures of *Enterobacter Cloacae* and *Clostridium butyricum* hydrogen-producing bacteria.

Acknowledgements

UAEMex and ININ sponsored this work. Evaristo Avila Vera thanks CONACYT for his Post-Doctoral Scholarship. The authors thank also the technicians of the chemistry laboratory of ININ and technicians of the Chemistry department of the CCIQS de la UAEMex for their technical help.

References

[1] Abdeshahian P., Al-Shorgani N.K.Nasser, Salih N.K.M., Shukor H., Kadier A., Hamid A.A, Kalil M.S. The production of biohydrogen by a novel strain Clostridium sp. YM1 in dark fermentation process. Int J. Hydrogen Energy 2014; 39: 12524-12531.

[2] Yasin N.H.M., Mumtaz T., Hassan M.A., Rahman N.A, Food waste and food processing waste for biohydrogen production: A review. J. of Environmental Management 2013; 130: 375-385.

[3] Hu B., Chen S. Pretreatment of methanogenic granules for immobilized hydrogen fermentation. Int J. Hydrog Energy 2007; 32: 3266-3273.

[4] Hafez H., Nakhla G. El. Naggar MH, Elbeshbishy E, Baghchehsaraee B. Effect of organic loading on a novel hydrogen bioreactor. Int J Hydrog Energy 2010; 35: 81-92.

[5] Cheng X., Liu C. Hydrogen production via thermophilic fermentation of cornstalk by Clostridium thermocellum. Energy Fuels 2011; 25: 1714-1720.

[6] Lo Y., Lu W., Chen C., Chang J. Dark fermentative hydrogen production from enzymatic hydrolysate of xylan and pretreated rice straw by Clostridium butyricum CGS5. Bioresour Technol 2010; 101: 5885-5891.

[7] Elsharnouby O., Hafez H., Nakhla G., El Naggar H. A critical literature review on biohydrogen production by pure cultures. Int J. Hydrog Energy 2013; 38: 4945-4966.

[8] Yasin, H.M.N., Nor'aini, A.R., Hasfalina, C.M., Yusoff, M.Z.M., Hassan, M.A. Microbial characterization of hydrogen-producing bacteria in fermented food waste at different pH values. Int. J. Hydrogen. Energy 2011; 36: 9571-9580.

[9] Yasin, H.M.N., Nor'Aini, A.R., Ismail, F., Yusof, M.Z.M., Hassan, M.A. Effect of different temperature, initial pH and substrate composition on biohydrogen production from food waste in batch fermentation. Asian J. Biotechnol 2009; 1: 42-50.

[10] Kim, D.H., Kim, S.H., Shin, H.S. Hydrogen fermentation of food waste without inoculums addition. Enzyme. Microb. Technol 2009; 45: 181-187.

[11] Kim, D.H., Kim, S.H., Ko, I.B., Lee, C.Y., Shin, H.S. Start-up strategy for continuous fermentative hydrogen production: early switchover from batch to continuous operation. Int. J. Hydrogen. Energy 2008; 33: 1532-1541.

[12] Kim, S.H., Han, S.K., Shin, H.S. Feasibility of biohydrogen production by anaerobic co-digestion of food waste and sewage sludge. Int. J. Hydrogen. Energy 2004; 29: 1607-1616.
[13] Han, S.K., Shin, H.S. Biohydrogen production by anaerobic fermentation of food waste. Int. J. Hydrogen. Energy 2004; 29: 569-577.
[14] Pan, J., Zhang, R., El-Mashad, H.M., Sun, H., Ying, Y. Effect of food to microorganism ratio on biohydrogen production from food waste via anaerobic fermentation. Int. J. Hydrogen. Energy 2008; 33: 6968-6975.
[15] Ren, N., Li, J., Li, B.,Wang, Y., Liu, S. Biohydrogen production from molasses by anaerobic fermentation with a pilot-scale bioreactor system. Int. J. Hydrogen. Energy 2006; 31: 2147-2157.
[16] Yokoi H., Tokushige T., Hirose J., Hayashi S., Takasaki Y. H_2 production from starch by a mixed culture of Clostridium butyricum and Enterobacter aerogenes. Biotechnol Lett 1998; 20: 143-147.
[17] Yokoi H., Maki R., Hirose J., Hayashi S. Microbial production of hydrogen from starch-manufacturing wastes. Biomass Bioenerg 2002; 22: 389-95.
[18] Valente F.A.A., Almeida C.C., Pacheco I., Carita J., Saraiva L.M., Pereira I.A.C. Selenium is involved in regulation of periplasmic hydrogenase gene expression in Desulfovibrio vulgaris Hildenborough. J Bacteriol 2006; 188: 3228-35.
[19] Martins M., Pereira J,A,C. Sulfate-reducing bacteria as new microorganisms for biological hydrogen production. Int. J. Hydrogen. Energy 2013; 38: 12294-12301.
[20] NMX-AA-022-1985. PROTECCION AL AMBIENTE-CONTAMINACION DEL SUELO-RESIDUOS SOLIDOS MUNICIPALES-SELECCION Y CUANTIFICACION DE SUBPRODUCTOS. SECOFI 1985.
[21] NMX-AA-015-1985. PROTECCION AL AMBIENTE - CONTAMINACION DEL SUELO - RESIDUOS SOLIDOS MUNICIPALES - MUESTREO – METODO DE CUARTEO. SECOFI 1985. http://www.semarnat.gob.mx/leyesynormas/Normas%20Mexicanas%20vigentes/NMX-AA-015-1985.pdf
[22] Lees R. Food analysis: Analytical and Quality Control Methods for the Food Manufacturer and Buyer. Leonard Hill Books. Blackie and Son Limited. Bishopbriggs. Glasgow 1982; Gran Bretaña.
[23] Madigan M.T. Martinko J.M. Parker J. Biología de los microorganismos Ed. Prince Hall. 2004.
[24] Avila-Vera E. , Alcántara D., Fernández-Valverde S:M, Molina-Ruvalcaba G., Borja-Salim MM., Hernández-Barriel M.C., Jover de la Prida J. Determinación de las condiciones experimentales para la obtención de hidrógeno a partir de desechos de frutas y verduras. 2008; Conference Proceedings, XXIV Congreso Técnico Científico ININ-SUTIN.

Chapter 1.5. Assembly and characterization of a PEM electrolyser for hydrogen generation from wave power

D. Moreno Antonio[a,b] *; R. Sánchez Dirzo[a]; R. de G. González Huerta[b]

[a]UNAM, FES-Zaragoza, Batalla de Mayo, Col. Ejército de Oriente C.P. 09230, México D.F
[b]ESIQIE IPN, Laboratorio de Electroquímica y Corrosión, UPALM, C.P. 07738, México D.F.

ABSTRACT

The world is now facing enormous challenges associated with pollution, emissions of greenhouse gases, climate change and the need for sustainable development. The production of H_2 from renewable energy sources has the potential to bring a local energy solution through the electrolysis of water. A PEM electrolyser can produce H_2 continuously by converting electrical energy into chemical energy without any purification process and is one of the most important electrochemical energy-related processes.
The "BlowJet" is a wave energy conversion (WEC) device, which is currently being tested in a wave flume. The purpose of this device is to concentrate the energy of a wave train and offer it in a form more readily available as a jet that is capable of powering a turbine generator. A current pulse is generated with a specific voltage and amperage (1.5-2 V and 0.05-0.3 A). A PEM electrolyser performance depends mainly on the structure and electrochemical characteristics of the membrane electrodes assembly (MEAs). In this work different MEAs were analyzed using as the cathode platinum catalyst in a concentration of 0.3 mg/cm^2 and the RuO_2 and IrO_2 in the anode with concentrations of 4.5 mg/cm^2 and 1.5 mg/cm^2 respectively. Before each preparation of MEA, the Nafion 115 membrane is chemically activated with hydrogen peroxide and sulfuric acid using standard methodology. Before spraying, the membranes were dried and flattened. The variables were: number of catalyst and hot pressing conditions 5 tons and 120 ° C. Performance curves were obtained and compared with commercial device, thereby reducing the ohmic resistance of the MEA, and equating the commercial device.

Keywords: Electrolysis, Hydrogen production, PEM electrolyzers, Blowjet

1. Introduction

The use of fossil fuels is causing major pollution problems worldwide and their impact on the environment and health of each being on the planet, with the present rate of extraction is estimated that less than 40 years of global reserves they are out almost

---

* Author for correspondence:
David Alberto Moreno Antonio, T.:01 55 16437636, E.: davidmorenoantonio@hotmail.com

entirely. It is necessary that renewable energy will be included in the current global energy model, energies that would have a low cost and much lower environmental impact than fossil fuels.

Around the world they are operating power plants that use renewable energy as a primary source of energy, but for the installation of one of these power plants must overcome great inconvenience being principally the locality of energy, intermittent power supply and / or large portions of the field for construction. [1, 2]

Although the electrical energy supplied by this type of plant represents a sector that has a very wide application, it leaves out many other main. The energy supplied by renewables should cover most demands of the current energy model, we propose to hydrogen as an energy vector of renewable energy, it is a clean fuel and can be used for generating heat from combustion, to generate electricity in fuel cells, or as a feedstock in different industries types, hydrogen is found to be the best options to energy storage in chemical form. [3]

Hydrogen can be obtained from water electrolysis, a process in which electrical energy is provided by renewable energy to obtain a sustainable and clean hydrogen. [4]

Mexico has more than 11 kilometers of coastline, which are only exploited for fishing and tourism, but we need to use this resource to our advantage, the energy from the waves is one of the easiest to convert. Around the world they have designed variety of devices for harnessing ocean energy (TAPCHAN, marine turbines, buoys, to mention a few), but these infrastructures represent a strong investment when being installed and maintenance.

In Mexico the investigations to find a system of easy construction, installation and low initial investment, it is named "Blowjet" system based on the Bufadora from Ensenada Baja California. This experimental device provides a current pulse to 0.3 A at 2 V. [5]

The PEM electrolyzers has low ohmic resistance, it allows the generation of hydrogen from the power granted by the "Blowjet", the performance of a PEM electrolyser depends mainly on: the types and amounts of catalysts applied to evolution reactions hydrogen and oxygen, the gas diffuser type and design of the collector plates.

In this work, different ways of performing membrane electrodes assemblies (MEAs) were analyzed, using Nafion 115 membrane transfer, platinum as cathodic catalyst, a mixture of iridium oxide and ruthenium oxide as anode catalysts, gases diffuser was constant carbon cloth, the current collectors made of stainless steel of 1 mm thick and with 0.5 mm circular holes throughout its range. All membrane electrode assemblies have a constant active area of 9 cm^2.

2. Materials and Methods

2.1 Activation of the membranes

The membranes were previously cut, were subjected to a cleaning process with 3% w H_2O_2 solution at 80 ° C for one hour, subsequently to this we proceeded to the activation of the membranes with H_2SO_4 solution for one hour at 80 °C. After cleaning processes and activation of the membranes, these were rinsed with deionized water at 80 °C for one hour each time, at the end of the last rinse the membranes were stored immersed in deionized water until the time of use. [6]

2.2 Preparation of the catalyst inks

We prepared two pairs of catalytic inks with different concentrations of catalyst each one, the catalyst concentration of the first pair was for the cathode: 0.02 mg/cm^2 of platinum whilst for the anode concentrations were 1.25 mg/cm^2 and 3.32 mg/cm^2 of iridium and ruthenium in oxide form respectively; for the second pair of inks the concentrations were 0.3 mg/cm^2 of platinum for the cathode while the anode concentrations were 1.5 mg/cm^2 and 4 mg/cm^2 of the oxides of iridium and ruthenium respectively.

Plus the use of diluents such as water and ethanol, for proper adhesion to the membrane it was used liquid Nafion, catalysts and diluents were mixed using an ultrasonic bath for 30 minutes to ensure perfect integration between components.

2.3 Membrane electrodes assemblies

The inks were applied directly to the Nafion membrane (previously dried), through a manual airbrush with an air pressure of 5 psi. After application of the ink to the membrane, it is allowed to dry over 24 hours.

To ensure proper contact assemblies these are hot pressed at a temperature of 120 °C at a pressure of 5 tons f/cm^2 for a period of 5 seconds, after this time the pressure is decreased to 200 kg to complete two minutes of pressing.

Tree different assemblies were prepared: A: in this assembly the first pair of catalytic inks are used and the gas diffusers were pressing with the membrane. B: In this second assembly was used the second pair of catalytic inks and the gas diffusers were pressed with the membrane. C: in this third and final assembly catalytic inks only against the membrane pressed, while the diffusers gas were put when fully arm the electrolyzer.

Table 1. Nomenclature of membrane electrodes assemblies

Membrane Electrodes Assemblies (MEAs)	**Characteristics**
A	Gas diffusers were pressing with the membrane Cathode: 0.2 mg/cm^2 of platinum Anode: 1.25 mg/cm^2 IrO_2 and 3.32 mg/cm^2 RuO_2
B	Gas diffusers were pressed with the membrane Cathode: 0.3 mg/cm^2 of platinum Anode: 1.5 mg/cm^2 IrO_2 and 4 mg/cm^2 RuO_2
C	Catalytic inks were pressed only against the membrane without gas diffusers Cathode: 0.3 mg/cm^2 of platinum Anode: 1.5 mg/cm^2 IrO_2 and 4 mg/cm^2 RuO_2

2.4 Characterization

2.4.1 Electrolysis system

The experiments were performed in a probe electrolysis cell, which is possible to change the different MEAs, hydrogen produced from water electrolysis was measured with

a digital flowmeter gas. Gas volumes were measured at atmospheric pressure (585 mm/Hg) and room temperature 20 °C.

2.4.2 Curve performance and system efficiency

A sweep of current was done using a power source Matrix model MPS-30031k-3 30 V-3 A to obtain the performance curve, using the following values of current in amps 0.01, 0.04, 0.08, 0.1, 0.2 , 0.3. In each current applied a generated voltage is register, so the curve I vs V of each of the manufactured assemblies was generated. Also the characterization of a commercial device was performed in order to compare the results of all cases.

3. Results and Discussion

The reactions that take place at the anode and cathode are described as electrolysis in an acidic medium. Taking this:

$$\text{Anode (+)} \quad 2\,H_2O \rightarrow O_2 + 4\,e^- + 4\,H^+ \quad (E_{ox}^\circ = -1.23\ V) \qquad (1)$$

$$\text{Cathode (-)} \quad 4\,H^+ + 4\,e^- \rightarrow 2\,H_2 \quad (E_{red}^\circ = 0\ V) \qquad (2)$$

$$\text{General} \quad 2\,H_2O \rightarrow 2\,H_2 + O_2 \quad (E_{cell}^\circ = -1.23\ V) \qquad (3)$$

In order to obtain the efficiencies of the electrolyzer the volume data obtained in the experiments they must be converted to a volume at standard conditions.

$$V_n = V_1 \frac{(P-P_V)}{760} \frac{273}{T+273} \qquad (4)$$

Where V1 is the volume obtained in liters (experimental conditions), P and Pv are respectively atmospheric and vapor pressures measured in mm Hg and T is room temperature in °C.

With the following equation theoretical volume (it was obtained using Faraday laes) that would be generated from the electrolysis to ideal conditions in liters of seconds is determined by equation 5.

$$V_T = 1.26619x10^{-4}\, I\, t \qquad (5)$$

Where I is the current at which we calculate the theoretical volume and t is time in seconds that we allow the current to flow in the cell.

To obtain efficiency percentage it was used the equation 6.

$$\eta = \frac{V_n}{V_T}(100) \qquad (6)$$

In Fig. 1. We can observe the electrolyzer's curves performance from each MEA, likewise the performance curve of a commercial electrolyzer is shown. The assembly "A"

shows the greatest potential of all tested whether the amount of current that is applied assemblies.

The assembly performance curve "B" even though its resistivity is lower is still above the performance of the commercial device.

It can be seen that the assembly "C" has the lowest potential even equaling the commercial device.

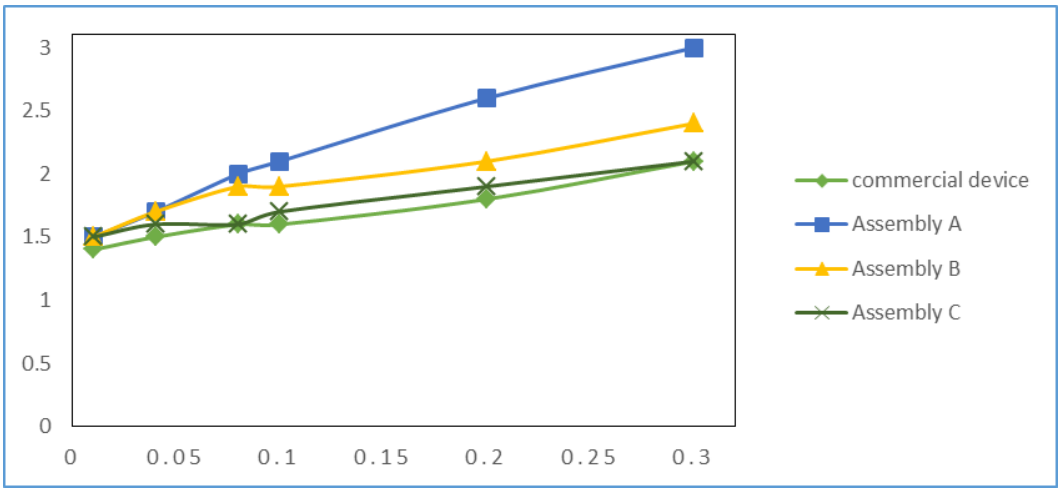

Fig. 1. Comparison of each electrolyzers with their respective assemblies.

Table 2 shows the current efficiencies obtained for each electrolyzer to the currents applied in each of the 3 different assemblies.

Table 2. Efficiencies of each assembly

Assembly		**A**		**B**		**C**	
Amp. App.	V_T	V_n	η	V_n	η	V_n	η
0.1	0.0007597	0.00059781	78.688	0.00066037	86.923	0.00066732	87.838
0.2	0.0015194	0.00122342	80.518	0.00137635	90.583	0.00140416	92.413
0.3	0.0022791	0.00166831	73.198	0.00208538	91.498	0.00210624	92.413

4. Conclusion

In this work, different ways of performing membrane-electrode assemblies were presented, so characterizations of each respective already assembled in electrolysers.

With the analysis of results, we conclude that the MEA "C" and its method of production are the best to use in joint testing with "Blowjet" device because of its low

ohmic resistance and current efficiencies of 92.41% for hydrogen generation are best obtained.

Acknowledgements

The authors express their gratitude to the FES Zaragoza UNAM, the project PAPIME PE104312, to Instituto Politécnico Nacional has been supported by multidisciplinary project IPN-SIP 1683 and Programa Redes Temáticas CONACYT/RTH2

References

[1] Madrid A. Energías Renovables (Fundamentos, Tecnologias y Aplicaciones). 1ra Ed., INO Reproducciones S.A. /AMV Ediciones. Madrid 2009; 220-222

[2] González Huerta R., Oliver Tolentino M. A., Rodríguez Varela F. J. Hidrógeno producción y almacenamiento: Retos hacia su uso como vector energético sustentable. CreateSpace, USA. 2013; 307

[3] Fernández Salgado J. M., Tecnología de las Energías Renovables. 1ra Ed Mundi-Prensa S.A. / AMV Ediciones. Madrid 2009; 9-12

[4] Mantell C. L. Ingeniería Electroquímica. 4ta Ed. Editorial Reverté S.A. España 2003; 304-307,

[5] Chávez Cárdenas X., Mendoza Baldwin E.G., Sánchez Dirzo R., Silva Casarín R. Diseño Hidrodinámico y Evaluación de un Dispositivo Marino Energético, “Blow-Jet”. XXI Congreso Nacional de Hidráulica, Guadalajara Jalisco. México. 2010.

[6] Carmo M., Fritz D. L., Mergel J., Stolten D. A comprehensive review on PEM wáter electrolysis. Int. J. Hydrogen Energy 2013; 38: 4919

Chapter 1.6. TiO_2 nanotubes array sensitized with CdS and Sb_2S_3, for photoelectrochemical hydrogen generation

J. E. Carrera-Crespo[a*]; G. Ramos-Sánchez[a]; V. De la Luz[a]; F. González[b]; E. Barrera[b]; I. González[a]

Universidad Autónoma Metropolitana-Iztapalapa. ([a])Departamento de Química. ([b])Departamento de IPH. Av. San Rafael Atlixco No. 186, C. P. 09340. Ciudad de México, Distrito Federal.

ABSTRACT

Photoelectrochemical H_2 production is currently being considered as a potential clean and renewable route for energy generation. TiO_2 nanotube arrays (TNAs) are interesting photoanodes with potential use in photoelectrochemical cells for H_2 production. Due to its 1D geometry, the recombination processes is diminished while the electron transport is accelerated toward the counter electrode, where they are subsequently scavenged by hydrogen ions on Pt cathode forming hydrogen gas. Moreover, the low fabrication cost, chemical stability, high specific surface area, photosensitivity, and catalytic potential, make TNA´s valuable as photocatalytic and photoelectrocatalytic supports. However, the optical absorption range of TiO_2 (<387 nm) limits its practical use. Sensitization with narrower band gap semiconductors has been attempted to improve the photoresponse of TNAs in the visible region. In this work, we propose TNAs sensitization with CdS and Sb_2S_3 nanoparticles, employing an electrochemical/thermal/chemical method, in order to improve the photoelectrochemical performance of TNAs and its use in photoelectrochemical cells for hydrogen production. TNAs sensitized with CdS and Sb_2S_3 (Sb_2S_3/CdS/TNAs) were characterized by scanning electron microscopy (SEM), X-ray diffraction (XRD), electrochemical impedance spectroscopy (EIS) and UV-Vis diffuse reflectance absorption spectra (DRS). We also investigated the photoelectrochemical behavior of the Sb_2S_3/CdS/TNAs photoelectrodes in a conventional three-electrode cell, and their H_2 production capacity in a H-type photoelectrochemical cell using a platinum plate as counter electrode. The Sb_2S_3/CdS/TNAs photoelectrodes showed a significant increase in H_2 production, compared with TNAs, Sb_2S_3/TNAs and CdS/TNAs photoelectrodes.

Keywords: Photoelectrochemical hydrogen production, Electrochemical/thermal/chemical method, Sb_2S_3/CdS/TNAs Bphotoanodes

1. Introduction

Photoelectrochemical hydrogen production is currently being considered as a potential clean and renewable route for energy generation [1]. TiO_2 nanotube arrays (TNAs) are

---

* Corresponding author:
J. E. Carrera-Crespo, (+52)5558044671 ext. 13, edgarcrespo@xanum.uam.mx

interesting photoanodes with potential use in photoelectrochemical cells for hydrogen production. Due to its 1D geometry, the recombination processes are diminished while the electron transport is accelerated toward the counter electrode, where they are subsequently scavenged by hydrogen ions on Pt cathode forming hydrogen gas [2].

Moreover, the low fabrication cost, chemical stability, high specific surface area, photosensitivity, and catalytic potential, make TNA´s valuable as photocatalytic and photoelectrocatalytic supports [2]. However, the optical absorption range of TiO_2 (<387 nm) limits its practical use [3]. Sensitization with narrower band gap semiconductors such as CdS [3, 4] and Sb_2S_3 [5, 6] has been attempted to improve the photoresponse of TNAs in the visible region, making them suitable for use in photoelectrochemical hydrogen production employing solar energy. However, CdS shows a band gap close to 2.4 eV [7], using only the wavelengths of the visible spectrum shorter than 510 nm. On the other hand, although the band gap of Sb_2S_3 is close to the maximum of the solar spectrum on the Earth surface [8], its low band gap (1.7 eV [8]) may cause an increase in the recombination of the photogenerated charge carriers. Despite this, a combination core-shell type of these semiconductors could improve the photoelectrochemical performance, due to higher light absorbance and a shorter recombination; since the Sb_2S_3 would increase the light absorption and the CdS could act as a buffer layer modifying the surface states and diminishing recombination in Sb_2S_3 [9].

For this reason, in this work a Sb_2S_3/CdS/TNAs photoelectrode is proposed. This material is obtained for first time using an electrochemical/thermal/chemical method [10], analyzing its optical properties, photoelectrochemical response, hydrogen production capacity and photo-stability at a bias potential applied of 0.5 V vs Ag/AgCl/3M KCl. Moreover, to identify the semiconductors, as well as their photo-stability, an excess of precursor particles were electrodeposited on the TNAs, clogging them. Because of this, only the results obtained with Sb_2S_3/CdS/TNAs, Sb_2S_3/TNAs and CdS/TNAs are showed.

2. Materials and Methods

TNAs were obtained by potentiostatic anodization of titanium foils (Alfa Aesar, 0.25 mm thickness, 99.5% purity), previously mechanically polished and degreased by sonication in acetone for 10 minutes. Anodic oxidation was carried out during 4 h at 55 V in a two-electrode cell using a Pt (Alfa Aesar, 99.99%) wire as counter electrode. An ethylene glycol solution containing 0.1 M NH_4F (Alfa Aesar, 96%) and 10% H_2O was used as the electrolyte, and kept under magnetic stirring. After anodic oxidation, the as-prepared samples were rinsed with water and ethanol, left to air-dry, and heat treated in air at 450 °C for 0.5 h (heating rate, 10 °Cmin^{-1}) [11]. The annealed samples were sonicated in water for 10 min previous to precursor particles electrodeposition. The pulsed electrodeposition of Cd and/or Sb on TNAs, was carried out in an AUTOLAB (model PGSTAT302N) potentiostat/galvanostat, using a conventional three-electrode cell with TNAs as working electrode, a Saturated Calomel Electrode (SCE) as reference electrode, and a platinum plate as counter electrode. Cadmium was electrodeposited using an electrolyte with pH=2, containing 0.002 M $CdSO_4$ and 0.1 M Na_2SO_4 in a solution of water:ethanol (70:30, %v) [10], for 8000 cycles. Antimony was electrodeposited employing a solution with pH=2, containing 0.002 M Sb_2Cl_3, 0.03 M $Na_3C_6H_5O_7 \cdot H_2O$ and 0.06 M $C_6H_8O_7 \cdot H_2O$ [12], dissolved

in water:ethanol (70:30, %v), for 8000 cycles. To obtain the Sb/Cd/TNAs sample, first cadmium was electrodeposited for 4000 cycles and subsequently antimony was electrodeposited using the same number of cycles. After that, the samples were annealed at 400 ºC for 1 hour, in a muffle furnace in the presence of air, to oxidize precursor particles. Finally, the samples were exposed to a 1 mL/s of a gas mixture containing 15% H_2S/H_2, in a glass reactor at 350 ºC for 30 minutes, in order to transform the oxides to sulfides. The absorption spectra were obtained by using the diffuse reflectance technique. The measurements were performed in a Varian Cary 5 UV-Vis-NIR spectrophotometer equipped with a Praying Mantis (Harrick Scientific Products, Inc.) accessory for diffuse reflection spectroscopy. The spectra were recorded in the wavelength range between 200 nm and 800 nm. Photoelectrochemical performance and hydrogen production was carried out in a H-type photoelectrochemical cell, without membrane between the compartments, equipped with a quartz window, using a solution containing 0.5 M Na_2SO_4 and 0.1 M citric acid, bubbled with N_2 gas for 5 minutes before each test. Sensitized TNAs with an exposed area of 3 cm^2 were used as working electrode, and Ag/AgCl/3M KCl and platinum plate were employed as reference and counter electrode, respectively. Measurements were recorded by a personal computer coupled to a Bas-Epsilon potentiostat. The illumination was provided by a 100 W Xe-arc lamp (100 mW/cm^2), enclosed in a Newport Q Housing model 60025. Hydrogen production in platinum counter electrode was measured employing a gas chromatograph (Shimadzu GC-8A), using nitrogen gas as the carrier gas for GC analysis.

3. Results and Discussion

3.1 Optical properties

The UV-visible absorption spectra of the Sb_2S_3/CdS/TNAs, Sb_2S_3/TNAs, CdS/TNAs and TNAs photoelectrodes, are shown in Fig. 1. TNAs spectrum shows an wide absorption peak in the visible region (Fig 1(iv)), attributed to the presence of carbon on the surface or TNAs due to the organic electrolytes used for films preparation [13]. This spectrum also exhibits a sharp increase in absorption close to 390 nm, characteristic of the anatase phase of TiO_2 [14]. Moreover, in the spectra obtained for CdS/TNAs (Fig. 1(i)), Sb_2S_3/CdS/TNAs (Fig. 1(ii)) and Sb_2S_3/TNAs (Fig. 1(iii)), the absorption peaks of TNAs are not observed because the nanotubes are being clogged for large particles of chalcogenides, for this reason only one transition is detected in each of these samples. Band gap values for the above samples were calculated from the diffuse reflectance spectra using the method proposed by Chakrabarti et al. [15]. The band gap values obtained by each sample are shown in Table 1, where the value calculated for TNAs is close to that reported for anatase titania (3.19 eV [16]). Otherwise, the values obtained for Sb_2S_3/TNAs and Sb_2S_3/CdS/TNAs confirm the presence of antimony (III) sulfide, which has reported a band gap of 1.7 eV [8]. Also, the fact that only Sb_2S_3 transition is observed in Sb_2S_3/CdS/TNAs sample (Fig. 1(ii)), suggests that CdS particles are fully covered for antimony sulfide.

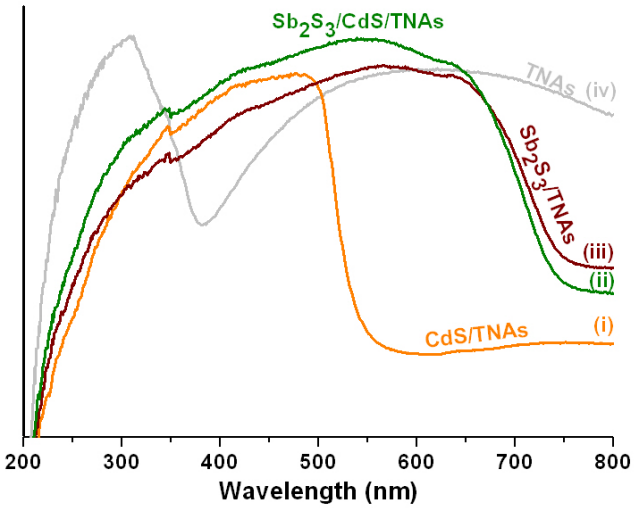

Fig. 1. Absorbance spectra obtained for the different TNAs films sensitized with the chalcogenide or chalcogenides indicated in the figure.

Table 1. Band gap values comparison between the values obtained using the method proposed by Chakrabarti et al. [15] and the reported in literature.

Sample	Band gap calculated from Chakrabarti method (eV)	Band gap reported in literature (eV)		
		TiO_2	CdS	Sb_2S_3
TNAs	**3.18**	**3.19 [16]**		
CdS/TNAs	**2.21**		**2.4 [7]**	
Sb_2S_3/TNAs	**1.65**			**1.7 [8]**
Sb_2S_3/CdS/TNAs	**1.66**			

3.2 Photoelectrochemical performance and hydrogen production capacity

The photoresponse measurement and hydrogen generation capacity of the samples, were evaluated using a three electrode configuration double-compartment (H-type) homemade cell (Fig 2.). When is applied a bias potential of 0.5 V vs Ag/AgCl (3 M KCl), the current is practically zero in the dark for all the samples (Fig. 3), but this increases considerably when the photoelectrodes are illuminated due to the generation of electron-hole pair, where the holes should oxidize to sacrificial donor electron present in the electrolyte and the electrons go to the counter electrode to carry out proton reduction producing hydrogen. However, current transients in Figure 3(i) suggest that CdS suffer a significantly oxidation when is illuminated because the current increases to values near to 7 mA and rapidly decreases to approximately 1.5 mA. On the other hand, the current transient of Sb_2S_3/TNAs sample (Fig. 3(iii)) does not show a fast oxidation, but the current tends to increase slowly, being this behavior attributed to the photodegradation of Sb_2S_3. Surprisingly, the current transient of Sb_2S_3/CdS/TNAs (Fig. 3(ii)) does not show the

increase of current detected with CdS/TNAs sample, indicating that CdS is being protected for a coat of Sb_2S_3, as suggested the results obtained by diffuse reflectance spectroscopy (Fig. 1(ii)). Also, after 35 minutes, the photocurrent reaches a stationary behaviour, associated to the presence of CdS that could be act as a buffer layer [9], favoring the charges separation and preventing the Sb_2S_3 photooxidation, thus, a greater current is generated, as shown in Fig. 3(ii), where the Sb_2S_3/CdS/TNAs photoelectrode achieved the highest photocurrent.

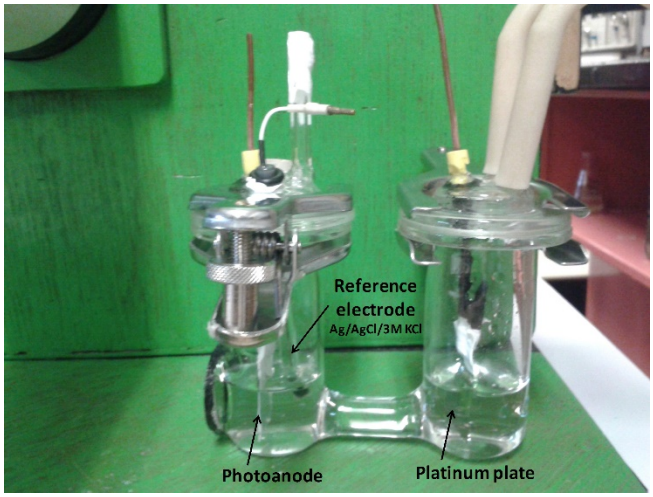

Fig. 2. Image of the double-compartment homemade cell employed in photoelectrochemical hydrogen production

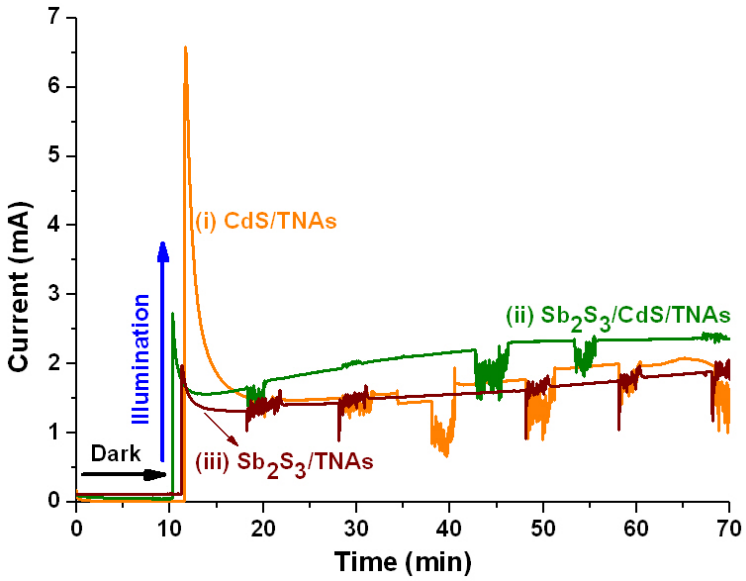

Fig. 3. I vs t curves measured during the photoelectrochemical hydrogen generation, carried out at 0.5 V vs Ag/AgCl/3 M KCl, in the dark (first 10 min) and with illumination for 60 min, in an aqueous electrolyte containing 0.5 M Na_2SO_4 and 0.1 M citric acid.

The amount of hydrogen generated was calculated from the current generated during the illumination (Fig. 3) and also of the analysis for GC (Table 2). Although differences exist between the hydrogen calculated using the I vs t curves and the analyzed by GC, in both the highest production of hydrogen was achieved for the Sb_2S_3/CdS/TNAs photoelectrode. This difference could be associated to the parasite electrochemical reactions or to low collection efficiency of hydrogen generated. Additional experiments are performing to confirm this proposal.

Table 2. Amount of hydrogen produced using a three electrode configuration double-compartment homemade cell, applying a bias potential of 0.5 V vs Ag/AgCl, in an electrolyte containing 0.5 M Na_2SO_4 and 0.1 M citric acid.

Sample	Time (min)	H_2 (µmol) [calc. curves I vs t]	H_2 (µmol) [GC]
Sb_2S_3/CdS/TNAs	60	38.34	10.23
CdS/TNAs	60	31.45	6.54
Sb_2S_3/TNAs	60	28.96	2.26

4. Conclusion

In this study, Sb_2S_3/TNAs, CdS/TNAs and Sb_2S_3/CdS/TNAs photoelectrodes were obtained employing an electrochemical/thermal/chemical route, where the precursor particles were electrodeposited, subsequently oxidized and finally sulfurized. UV-Vis diffuse reflectance spectroscopy characterization confirms that CdS and Sb_2S_3 were synthesized using TiO_2 nanotubes as substrate. Also, when Sb is electrodeposited on Cd/TNAs, all the cadmium is coated by antimony, since the absorption spectrum of Sb_2S_3/CdS/TNAs sample only reveals a transition associated to the Sb_2S_3. The above was confirmed with the photoelectrochemical response results, due to that CdS/TNAs sample suffered considerable photo-oxidation unlike Sb_2S_3/CdS/TNAs photoelectrode, which exhibited the best photo-stability and generated photocurrent. This behavior was associated with the different roles of each chalcogenide, where Sb_2S_3 is responsible of visible-light absorption and CdS act as buffer layer diminishing recombination of charge carriers photogenerated in Sb_2S_3. Moreover, the results obtained in this first attempt with TNAs clogged for a great amount of chalcogenide, demonstrate a promising way for obtaining efficient photoanodes for photoelectrochemical hydrogen production using solar energy.

Acknowledgements

The authors are indebted to the CONACyT (Mexico) for their financial support to carry out this work (Project INFR-2011-1-163250). J.E. Carrera-Crespo is grateful to CONACyT for the PhD fellowship granted and with MHS for the scholarship given to him to participate in the XV International Congress of the Mexican Hydrogen Society. The authors thank Laboratorio de Catálisis Ambiental UAM-I for the support to carry out the sulfurization process.

References

[1] D. H. Kim, H. S. Han, I. S. Cho, W. M. Seong, I. J. Park, J. H. Park, S. Shin, G. D. Park, S. Park, S. Lee, K. S. Hong, CdS-sensitized 1-D single-crystalline anatase TiO_2 nanowire arrays for photoelectrochemical hydrogen production, Int J Hydrogen Energ 2015; 40:863-869

[2] S. Chaguetmi, F. Mammeri, M. Pasut, S. Nowak, H. Lecoq, P. Decorse, C. Constentin, S. Achour, S. Ammar, Synergetic effect of CdS quantum dots and TiO_2 nanofibers for photoelectrochemical hydrogen generation, J Nanopart Res 2013; 15:article 2140

[3] Q. Zhang, L. Wang, J. Feng, H. Xu, W. Yan, Enhanced photoelectrochemical performance by synthesizing CdS decorated reduced TiO_2 nanotube arrays, Phys Chem Chem Phys 2014; 16:23431-23439

[4] L. Sang, H. Tan, X. Zhang, Y. Wu, C. Ma, C. Burda, Effect of quantum dot deposition on the interfacial flatband potential, depletion layer in TiO_2 nanotube electrodes, and resulting H_2 generation rates, J Phys Chem C 2012; 116:18633-18640

[5] H. Xie, W. Que, Z. He, P. Zhong, Y. Liao, G. Wang, Preparation and photocatalytic activities of Sb_2S_3/TiO_2 nanotube coaxial heterogeneous structure arrays via an ion exchange adsorption method, J Alloy Compd 2013; 550:314-319

[6] G. G. Bessegato, J. C. Cardoso, B. F. da Silva, M. V. B. Zanoni, Enhanced photoabsorption properties of composites of Ti/TiO_2 nanotubes decorated by Sb_2S_3 and improvement of degradation of hair dye, J Photoch Photobio A 2014; 276:96-103

[7] M. Qorbani, N. Naseri, O. Moradlou, R. Azimirad, A. Z. Moshfegh, How CdS nanoparticles can influence TiO_2 nanotube arrays in solar energy applications?, Appl Catal B-Environ 2015; 162:210-216

[8] A. V. Kozytskiy, O. L. Stroyuk, M. A. Skoryk, V. M. Dzhagan, S. Y. Kuchmiy, D. R. T. Zahn, Photochemical formation and photoelectrochemical properties of TiO_2/Sb_2S_3 heterostructures, J Photoch Photobio A 2015; 303:8-16

[9] J. Jiao, Z. Zheng-Ji, Z. Wen-Hui, W. Si-Xin, CdS and PbS quantum dots co-sensitized TiO_2 nanorod arrays with improved performance for solar cells application, Mat Sci Semicon Proc 2013; 16:435-440

[10] J. E. Carrera-Crespo, F. González, E. Barrera, I. González, 226th Meeting of The Electrochemical Society,https://ecs.confex.com/ecs/226/webprogram/Paper40896.html, Cancún, México, (2014).

[11] P. Acevedo-Peña, J. E. Carrera-Crespo, F. González, I. González, Effect of heat treatment on the crystal phase composition, semiconducting properties and photoelectrocatalytic color removal efficiency of TiO_2 nanotubes arrays, Electrochim Acta 2014; 140:564-571

[12] L. Li, Y. Xiao, Y. Yang, X. Huang, G. Li, L. Zhang, A facile route to fabricate single-crystalline antimony nanotube arrays, Chem lett 2005; 34(7):930-931

[13] S. Kurian, H. Seo, H. Jeon, Significant enhancement in visible light absorption of TiO_2 nanotube arrays by surface band gap tuning, J Phys Chem C 2013; 117:16811-16819

[14] E. Guo, L. Yin, L. Zhang, CdS quantum dot sensitized anatase TiO_2 hierarchical nanostructures for photovoltaic application, Cryst Eng Comm 2014; 16:3403-3413

[15] S. Chakrabarti, D. Das, D. Ganguli, S. Chaudhuri, Tailoring of room temperature excitonic luminescence in sol-gel zinc oxide-silica nanocomposite films, Thin Solid Films 2003; 441:228-237

[16] D. Regonini, C. R. Bowen, A. Jaroenworaluck, R. Stevens, A review of growth mechanism, structure and crystallinity of anodized TiO_2 nanotubes, Mat Sci Eng R 2013; 74:377-406

Chapter 1.7. Quantum yield for hydrogen production in photocatalytic water splitting using TiO_2-Pt prepared by different methodologies

A. Calzada Hernández[a]; F. Orozco[a]; F. Guayaquil[b]; S. Escobedo[b]; C. Guzman[a]; H. de Lasa[b]; B. Serrano Rosales[a*]

[a]Universidad Autonoma de Zacatecas, Maestria en Ciencias de la Ingeniería, Zacatecas, México.
[b]Western University, Faculty of Engineering, Chemical Reactor Engineering Centre (CREC), London, ON, Canada.

ABSTRACT

The present study reports quantum yield calculations for H_2 production using a Pt modified titanium dioxide in a slurry medium, under near-UV irradiation, during the photocatalytic water splitting. The photocatalyst was prepared using three different methods: incipient wetness, wet impregnation and sol-gel. The catalysts were characterized by BET, X-ray diffraction, diffuse reflectance to obtain surface area, crystalline phases and the energy of band gap respectively. The results show that the photocatalysts by sol-gel have a greater surface area and crystal size smaller unlike the other two catalysts, and the three types of catalysts have a dominant anatase crystalline phase and a decrease of the band gap. Experiments were performed in a Photo CREC Water II Reactor adapted with a hermetic tank without air and using argon instead as carrier, with a photocatalyst load of 0.15 g/L and acid medium (pH=4.0). Regarding H_2 formation via $H^{\bullet}$ free radicals, the addition of a 2 vol.% ethanol scavenger allowed to achieve significant amounts of H_2. It was observed that the same amount of hydrogen was obtained after six hours of experiment with the catalyst prepared with sol-gel, wet impregnation and eventually with incipient wetness. However, the most important point is that the calculated values of the quantum yields are different for the three photocatalysts, with the highest value for the experiment with sol-gel photocatalyst, showing good degree of photon utilization and confirming the utility of the Pt modified TiO_2 photocatalyst and Photo CREC Water II Unit set up for the H_2 production, via water splitting.

Keywords: Hydrogen production; photocatalysis; quantum yield; photo CREC reactor

1. Introduction

Humanity depends heavily on the use of fossil fuels for energy, creating pollution and contributing to the climate change. The alternative energies will be the solution and among.

---

* Author for correspondence:
B. Serrano Rosales, 52-492-9256690, ext 4668, beniser@prodigy.net.mx

them, the hydrogen is an attractive technological promise. Currently one of the main problems is that 95% of hydrogen is produced from fossil fuels and the remaining 5 % is through alternative energy source [1]Heterogeneous photocatalysis is a technic based on the excitation of a semiconductor when it is irradiated with light of enough energy to promote an electron from the valence band to the conduction band. In this way a couple of electrical charges is generated: the electron (e-) and the hole (h+). The pairs of charge can migrate to the surface of the material and in this place begin the redox reactions[2–4]. To avoid the recombination of these charges it is necessary to have available a reservoir (usually noble metal) for the electrons in the semiconductor which eventually will react with the protons (H+) present in the water to produce the hydrogen free radical (H•) and finally two free radicals will form a hydrogen molecule H_2.

By other side, the holes will react with the ions OH^- present in the water to produce OH• which is a powerful oxidant and will react with the scavenger compound. With this process, an equilibrium of charges consumption is performed, but, it will be necessary also to evacuee the air to avoid the presence of oxygen which could compete with the protons to react with the electrons, reducing the hydrogen production.

However, to increase the hydrogen production, it is still necessary to improve the semiconductor catalysts that contribute to water splitting. This occurs via the modification of both the energy band gap and the formation of Schottky barrier which retards the charge recombination at the semiconductor particle outer surface. This phenomenon appears to promote the efficient separation of holes and electrons charges under UV or visible light irradiation [5].

Theoretically, all types of semiconductors meet the above in order to be used as a photocatalysts for hydrogen production. However, several semiconductors such as CdS and SiC, cause photo corrosion, and are not suitable for water splitting. Currently TiO_2 is the most widely used photocatalyst due its high photocatalytic activity, high chemical stability and a long lifetime of pair electron /hole [5].

The development of novel semiconductors (photocatalysts) has increased in recent years. New materials such as TiO_2 combined with either tantalate compounds or noble metals under UV or visible light have gained importance for hydrogen production and display promising properties[2,6,7], and they have been studied in different conditions and two of them are the most important. The presence of sacrificial agent and a noble metal are conditions that help to slow down the recombination between the pair hole/electron, enhancing the efficiency of photocatalytic hydrogen production.

Organic compounds (hydrocarbons) are widely used as electron donor or called sacrificial agent for photocatalytic hydrogen production as they can be oxidized by holes. EDTA, methanol, ethanol, CN^-, lactic acid and formaldehyde have been tested and proved to be effective to enhance hydrogen production[8–10]. Nevertheless, to be able to use them in practice, electron donors must be cheap and easily accessible, and be a waste from renewable resource, such as ethanol. This will make hydrogen production a sustainable process.

A good candidate for a sacrificial agent is the ethanol, because it is cheap at low concentrations (1-2 vol%), which can be obtained from the natural fermentation process through of glucose, fructose, sucrose and even agricultural waste.

In the present study, experiments of hydrogen formation via water splitting were performed using a modified Photo CREC Water II Reactor with ethanol 2 vol.% as a h^+

scavenger, TiO_2 loaded with Pt. Furthermore, the work has been focused on the effects of the presents of metal ion on the photocatalyst and the different preparations methodologies such as incipient impregnation, wetness impregnation and sol-gel.

Experiments with near-UV light and Pt modified TiO_2 were performed under the special condition of having "all" irradiated photons with photon energies superseding the band gap of the semiconductor. This approach also allows establishing quantum yields (QY) for hydrogen production using the entire irradiation beam spectrum from the near UV lamp. The QY for hydrogen production is a number ratio resulting from equating the rate of H• molecules produced over the number of photons absorbed in the material photocatalyst Eqs. (1).

$$\varphi\ (\%)=[dN_i/dt]/P_a \times 100 \qquad (1)$$

Where the N_i is the number of moles of the produced H• free radical, dN_i/dt is the derivate of the moles profile, P_a is the Einsteins of photons emitted by the lamp with wavelengths less than 388 nm.

2. Materials and Methods

2.1. Preparation of Pt/TiO_2 photocatalyst

Incipient impregnation (**A**). DP25 Titanium dioxide from Evonik Degussa Co. and a 99.9 wt% $H_2PtCl_6 \cdot xH_2O$ reagent from Sigma-Aldrich Co, were used as a semiconductor "support" and Pt precursor respectively. DP25 was dried at 140 °C for 6 h before impregnation to desorb water and some other species potentially present on the TiO_2 particles. The precursor was dissolved in distillated water to produce Pt solution of 1 wt% concentration.

This material was already studied and presented a good performance for hydrogen production, and is taken as a reference for the two other material.

The first Pt impregnation step was carried out at vacuum conditions with continuous mixing of the TiO_2 support. A 4 ml of the precursor solutions was employed, and was added to 5 g of TiO_2 in a drop-by-drop manner. The wet photocatalyst was heated up to 140 °C during 30 min using a 4.6 °C/min temperature ramp. Furthermore, the material was left for another 3 h at 160 °C. This allowed water evaporation from the TiO_2, the resulting photocatalysts cake was crushed and later grinded in a mortar.

The resulting particles were heated up to 450 °C during 1 h using a 7.5 °C/min temperature ramp and were left in the oven at 450 °C for another 3 h. Finally, the photocatalyst was placed in flow reactor unit under a 1 cm^3/s of Ar/H_2 (90/10 %, Praxair) reducing mixture. This material was study previously and presented a good performance for hydrogen production, and is taken as a reference for the two other material.

Wetness impregnation (**B**). 2 grams of DP25 TiO_2, were placed in a solution of 10 ml deionized water, under continuous stirring. The dopant solution was prepared with $H_2Pt(NO_2)SO_4$ at different concentration to get a loading platinum of 0.4 wt.% in the TiO_2. This dopant solution is added to TiO_2, and allowed to mix for one hour. Unlike to the first methodology where a gas mixture Ar/H_2 was used for the reduction. Now, a reducing solution of $NaBH_4$ 0.03 M was added, and then was left in rest for 10 h. The resulting solution was filtered and finally dried at 110 °C for 18 h, and calcined at 450 °C for 3 h.

Sol-gel (**C**). The synthesis of the TiO_2 substrate was obtained by slowly dissolving the titanium precursor (titanium isopropoxide, 97 % Aldrich, TTIP) in an organic solvent (isopropanol, 99.9 %, J. T. Baker), under nitrogen atmosphere. The hydrolysis process was then performed by adding water with the dopant solution of Pt, which was prepared with $H_2Pt(NO_2)SO_4$ to get a load of platinum of 0.4 wt.% in the TiO_2. The volume of the organic solvent was 70 ml and 60 ml of water plus 10 ml of the dopant solution. To get the metallic state, a solution of $NaBH_4$ 0.03 M was added.

The obtained solution was continuously stirred. In the next step it was transferred to Teflon-lined vessels and placed into a microwave reaction system Milestone with the power of 1200 W and a temperature of 215 °C for 30 minutes. The resulting solution was allowed to rest for 1 h and then it was filtered, washed and dried at 110 °C and finally calcined at 450 °C for 3h, with the same temperature ramp used in the others preparations.

2.2. Photocatalysts characterization

The prepared catalysts were characterized by specific surface, diffuse reflectance and X-ray techniques. The specific surface area of all prepared photocatalysts were determined using a BET surface analyzer (Micrometrics, ASAP 2010) and using nitrogen adsorption. A photocatalysts sample was dried and degassed in a sample tube at 250 °C for at least 3 h before adsorption. The bandgap energy (E_{bg}) values were determined from diffuse reflectance measurements (Cary 500 UV-Vis-NIR Varian spectrophotometer) by applying the Kubelka-Munk function, F(R), and the E_{bg} corresponds to the point where the linear increase of the Kubelka-Munk function starts[11]. X-ray diffraction analysis (XRD) were obtained using a diffractometer RIGAKU Ultima IV a Multi-Purpose Diffractometer.

2.3 BLB irradiation lamp characterization

StellarNet EPP2000C-25 LT16 Spectrometer was used to determine the energy spectrum of the BLB lamp through the fused silica windows in the Photo CREC Water II Reactor, which was used to determine the Einsteins of photons emitted by the lamp after the integration of the spectrum.

2.4. Photocatalytic reactor

A novel Photo CREC Water II Reactor was used in the present study. This reactor includes two concentric tubes to provide a radial and axial symmetric irradiation field. The first tube is a transparent inner cylinder of Pyrex glass, that was used due to the fact it only absorbs 5% of the emitted near UV-Light (It has a good near UV-Light transmission properties) and has a low cost. A Black Light Blue Lamp of 15 W is placed inside this glass tube and has an emission range of 340-410 nm. The second and outer tube is made out of UV opaque polyethylene to minimize radiation reflection. The reactor has a mixed tank, which was designed and equipped to accomplish a good mixing of the slurry TiO_2 water/ethanol solution, to take the samples of gas and liquid, to store H_2 and to feed the inert gases N_2 or Ar. A centrifugal pump circulates the fluid throughout the system and is used to modify the flow rate.

Prior to the experiments, 0.15 g/L of the photocatalyst was sonicated for a 10 min period to ensure good particle distribution in the slurry solution before being added to the water/ethanol solution in the storage tank.

2.5. Analytical techniques

The GC, a unit manufactured by Shimadzu CG-2010 equipped with a Grace Hayesep D packed column 100/120 mesh(9.1 m x 2 mm x 2 mm nominal) was used to separate H_2 for the other gases presented in the mix/storing tank, using a TCD. The Ar carrier gas has high purity (Praxair 99.999%). The use of argon as carrier allows increasing the sensitivity of the detector toward H_2. The samples were taken manually (Hamilton CO. gastight valve-syringe of 1 ml) from the mix/storing H_2 tank at set times. The injection was made using several mixture of know gas concentrations.

3. Results and Discussion

3.1 Photocatalysts characterization

The results of the different characterizations are reported in the Table 1. It can be seen that the material prepared with method C has a superficial area bigger than that of the materials prepared by the methods A and B. Furthermore, between the method of reference A and the method C there is a clear diminution of the band gap energy, and consequently the material can be excited with light of bigger wavelengths , closer to visible light. Particularly with the method C there is a decrease in E_{gb} due the presence of platinum.

Table 1. Results of the different characterizations for the TiO_2 photocatalysts.

Method	Weight % of Pt loaded	Average superficial area (m^2/g)	E_{gb} (eV)
DP25	0	50	3.2
A	1	54	2.73
B	0.4	56	3.1
C	0	125	3.2
	0.4		3.1

Figure 1 reports the XRD diffractogram for DP25 and the materials modified with Pt. One can note that the characteristic 2θ diffraction anatase peaks at 25°, 37°, 48°, 54° and 55° were consistently observed. The smaller XRD peaks at 27° and 69° were also present, given the rutile content in each material. There were no other XRD peaks as one could expect for platinum at 40° and 46° of 2θ values[5].

3.2 Hydrogen production

Figure 2 presents the hydrogen profiles for the experiments carried out with the catalysts prepared by the two methods wetness impregnation and sol-gel with 0.42 wt. % Pt load and its comparison with DP25.

It can be appreciated in Fig. 2 that H_2 production increased with the presence of Pt. This is an evidence about the very import role of the platinum in this process, the Pt acts as a reservoir of electrons from the conduction band of TiO_2 [9]. In this way the recombination

of the couple of electrical charges is avoided and their usage is optimized. In this case the optimum load of Pt was not found.

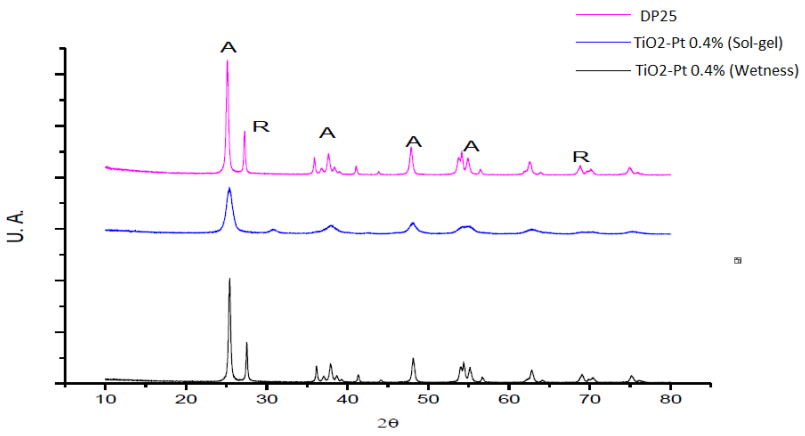

Fig. 1. XRD Diffractometer for DP25 and TiO_2 modified with Pt wt. 0.4% prepared by wetness impregnation and sol-gel, with the characteristic phase peaks anatase (A), and rutile (R)

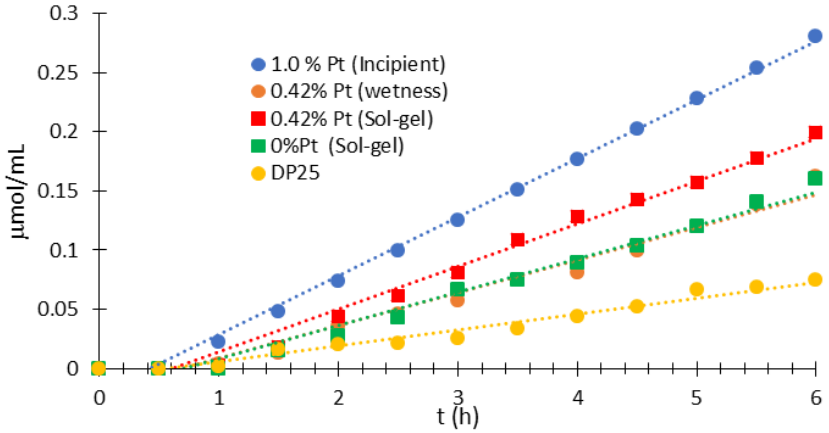

Fig. 2. Profiles of hydrogen concentration using TiO_2 catalysts prepared by a) incipient impregnation b) wetness impregnation and C) sol-gel.

In the time of the experiment, for all the cases with and without Pt, the behavior of the concentration profiles is linear with a constant slope for each catalyst, and this is associated with the pH value used to perform these experiments and there is concordance with the results of Escobedo et al. 2013, who found that working with neutral and basic pH values, the slopes were not constant, but using acid pH=4.0 the slopes of the profiles are constant. Besides, using TiO_2 produced by sol-gel without Pt, yielded more H_2 (0.16 µmol/L) that the

TiO_2 DP25 (0.075 μmol/L), probably because the first one has bigger surface area than the last one.

Figure 3 reports the values of quantum yields for each experiment performed with catalysts by incipient impregnation, wetness impregnation and sol-gel method. They were calculated with the procedure described in the section 2.3.

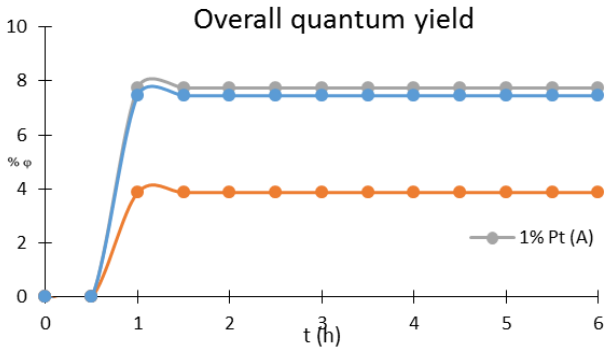

Fig. 3. Quantum yield profiles for experiments carried out with TiO_2 prepared by (A) incipient impregnation, (B) wetness impregnation and (C) sol-gel.

In can be observed that the values of the quantum yield are constant for each experiment, as a result of the linear behavior of the hydrogen concentration profiles. This constant values imply the effectiveness of the Photo CREC Water II for hydrogen production and the appropriate utilization of photons absorbed by the photocatalyst. The quantum yield profiles for this type of catalysts have similar behavior those of the sol-gel catalysts. The quantum yield profiles show a flat region for each experiment.

4. Conclusion

1.- All the catalysts reported linear hydrogen concentration profiles at pH=4.0, indicating that the method of preparation of the catalysts does not have influence in the tendency of the behavior of the profiles. However it affects the values of the concentration profiles due each catalyst has a different catalytic activity.

2. - For all catalysts, the hydrogen production increased with the presence of platinum indicating the very important role played by Pt as trapper of electrons generated during the irradiation of TiO_2.

3. - The maximum value of quantum yield (10%) corresponds to the experiment carried out with the sol-gel catalyst, probably because it reported the biggest superficial area and smaller band gap.

Acknowledgements

Alan R. Calzada thanks to CONACYT the scholarship awarded through the Master in Engineering Science Program of UAZ, to the ELAP-2014 Program sponsored by Canadian

Government to perform a six months research stay in CREC-UWO, and to the fellowship from the SMH and XV International Congress of the Mexican Hydrogen Society.

References

[1] Bahruji H, Bowker M, Davies PR, Pedrono F. New insights into the mechanism of photocatalytic reforming on Pd/TiO2. Appl Catal B Environ 2011;107:205–9. doi:10.1016/j.apcatb.2011.07.015.

[2] Bahruji H, Bowker M, Davies PR, Al-Mazroai LS, Dickinson A, Greaves J, et al. Sustainable H2 gas production by photocatalysis. J Photochem Photobiol Chem 2010;216:115–8. doi:10.1016/j.jphotochem.2010.06.022.

[3] Kudo A. Development of photocatalyst materials for water splitting. Int J Hydrog Energy 2006;31:197–202. doi:10.1016/j.ijhydene.2005.04.050.

[4] Kudo A. Recent progress in the development of visible light-driven powdered photocatalysts for water splitting. Int J Hydrog Energy 2007;32:2673–8. doi:10.1016/j.ijhydene.2006.09.010.

[5] Escobedo Salas S, Serrano Rosales B, de Lasa H. Quantum yield with platinum modified TiO2 photocatalyst for hydrogen production. Appl Catal B Environ 2013;140–141:523–36. doi:10.1016/j.apcatb.2013.04.016.

[6] Bahruji H, Bowker M, Brookes C, Davies PR, Wawata I. The adsorption and reaction of alcohols on TiO2 and Pd/TiO2 catalysts. Appl Catal Gen 2013;454:66–73. doi:10.1016/j.apcata.2013.01.005.

[7] Yoong LS, Chong FK, Dutta BK. Development of copper-doped TiO2 photocatalyst for hydrogen production under visible light. Energy 2009;34:1652–61. doi:10.1016/j.energy.2009.07.024.

[8] Zheng X-J, Wei L-F, Zhang Z-H, Jiang Q-J, Wei Y-J, Xie B, et al. Research on photocatalytic H2 production from acetic acid solution by Pt/TiO2 nanoparticles under UV irradiation. Int J Hydrog Energy 2009;34:9033–41. doi:10.1016/j.ijhydene.2009.09.019.

[9] Nada AA, Barakat MH, Hamed HA, Mohamed NR, Veziroglu TN. Studies on the photocatalytic hydrogen production using suspended modified photocatalysts. Int J Hydrog Energy 2005;30:687–91. doi:10.1016/j.ijhydene.2004.06.007.

[10] Bamwenda GR, Tsubota S, Nakamura T, Haruta M. Photoassisted hydrogen production from a water-ethanol solution: a comparison of activities of Au [illegible]TiO2 and Pt/TiO2. J Photochem Photobiol Chem 1995;89:177–89. doi:10.1016/1010-6030(95)04039-I.

[11] Esquivel K, Nava R, Zamudio-Méndez A, González MV, Jaime-Acuña OE, Escobar-Alarcón L, et al. Microwave-assisted synthesis of (S)Fe/TiO2 systems: Effects of synthesis conditions and dopant concentration on photoactivity. Appl Catal B Environ 2013;140–141:213–24. doi:10.1016/j.apcatb.2013.03.047.

Chapter 1.8. Effect of neodymium addition to Rh/Al_2O_3 catalysts in the activity and selectivity to hydrogen by CH_4 dehydrogenation

M. Caballero Diaz[a,*]; G. Del Angel Montes[a]; A. Bonilla Sánchez[a]; D. Monroy Hernández[a]; I. Rangel[a]

[a] Departamento de Química, Área de Catálisis, Universidad Autónoma Metropolitana-Unidad Iztapalapa, Av. San Rafael Atlixco No. 186, C.P. 09340, A.P 55-534. México D. F. México.

ABSTRACT

The methane dehydrogenation reaction was carried out on $Rh/\gamma\text{-}Al_2O_3$-Nd catalysts. They were synthesized by wet impregnation of the $\gamma\text{-}Al_2O_3$-Nd supports at 1 and 10 wt% of neodymium and 1wt% of rhodium using $Nd(NO_3)_36H_2O$ and $RhCl_3.3H_2O$ as precursors. Temperature ranged from 400 to 700 °C at intervals of 100 °C with a rate of 5 ºC min^{-1}. Experiments consisted of a previous thermal treatment to the catalysts with flowing nitrogen for 15 min at room temperature. Then, a pure CH_4 (high purity) feed steam (2 mL min^{-1}) was introduced into the reactor, the products were analyzed by gas chromatography. The activity determinations were carried out in a quartz glass microreactor system with a fixed bed at atmospheric pressure and catalyst load of 0.05 g.
The $Rh/\gamma\text{-}Al_2O_3$, Rh-Nd1% and $Rh/\gamma\text{-}Al_2O_3$-Nd10% catalysts showed CH_4 conversions of 74, 79 and 75% and selectivities to hydrogen of 89, 65 and 100% respectively at 700 °C. The metal particle size of Rh and the acidity influenced these results; since the catalyst with the largest particle size ($Rh/\gamma\text{-}Al_2O_3$-Nd10%) ~ 3.4 nm and the lowest acidity, 96 $\mu molg^{-1}$, was the most selective to hydrogen. The $Rh/\gamma\text{-}Al_2O_3$, $Rh/\gamma\text{-}Al_2O_3$-Nd1% catalysts presented also selectivities towards ethane and ethylene, which came from the mobility of the CHx species on Rh surface during the degradation of methane. The performance of the $Rh/\gamma\text{-}Al_2O_3$-Nd10% catalyst is explained by the high interaction of Rh and alumina-Nd. The carbon produced during the reaction was graphitic type which was deposited on the Rh surface and on the support. The $Rh/\gamma\text{-}Al_2O_3$ catalyst doped with 10% of neodymium and the particle size of Rh of around 3.4 nm resulted with the highest production of hydrogen in the methane the dehydrogenation. The graphitic carbon produced during the reaction does not affect significantly the H_2 production, since it is also deposited on the support.

Keywords: Hydrogen, Methane decomposition, Rh/Alumina-Nd, TEM

1. Introduction

At the present time there is a clear need to find an alternative energy source that will replace, at least partially and progressively, to fossil fuels in the near future and hydrogen

---

* Author for correspondence: Marina Caballero Diaz, Tel (55)5804-4668 Fax (55)5804-4666
E-Mail: marcabdi@yahoo.com.mx

seems to be one of the most promising energy sources, considered as environmentally benign, hydrogen gas may someday replace fossil fuels for various applications such as automobiles and power plants [1]. Currently, hydrogen finds application as a chemical rather than a fuel in commercial operations, but if hydrogen is used to replace existing fuel, suitable methods must be developed for large-scale production.

The amount of energy produced during the hydrogen combustion is higher than that obtained by any other fuel. The advantages of hydrogen as an energy source is that represent an abundant raw material and its combustion does not produce CO_2, but only water vapor, which makes it an ideal candidate for the reduction of the so-called "greenhouse effect" [2-4]. Since current commercial methods of hydrogen production, necessarily involve the use of fossil fuel, generating significant quantities of pollutants (primarily CO_2). Recent investigations have focused on improving the process of hydrogen production by decomposition of methane to form hydrogen and elemental carbon as an attractive alternative to the steam reforming [5], using metal or carbon catalysts for a higher conversion of methane and stability long-term catalyst [6-8]. For simultaneous production of hydrogen and nanocarbon particles, nickel-based catalysts have been used, the major drawback in the case of the decomposition on metal catalysts (Ni, Co or Fe), is that catalyst is quickly deactivated because of deposits of carbon [9, 10].

In general, the noble metals show better catalytic activity and resistance to the deactivation, but the use of the catalysts based Ni is due to its lower cost [11].
In recent years, has begun to investigate the behavior of the addition of lanthanides elements to noble metal catalyst [12]. It is assumed that the component of cerium has a crucial role in the maintenance of the catalytic activity of noble metal, at the same time, the oxide of cerium shows a good stability in precious metals, such as Ru, Rh, Pd, Pt.

In the present work, we investigated the catalytic behaviors of Rh/Al_2O_3, Rh/Al_2O_3-Nd catalysts at two concentrations of Nd, 1 and 10 wt% for the production of hydrogen from the dehidrogenation of methane. The characterization was done by N_2 adsorption-desorption, X ray diffraction, H_2-TPR temperature programmed reduction, FT-IR of pyridine adsorption, EDS-SEM and HRTEM. The reaction of dehydrogenation of methane catalytic tests were conducted from 400 to 700 ° C each 100 °C and the last at 750 °C.

2. Materials and Methods

2.1 Supports and catalysts preparation

The γ-Al_2O_3 support was prepared from Boehmite Catapal B. Firstly the Boehmite was dried to 120° C for 12 hours, after the solid was calcined in air flow of 60 mL/min for 24 h using a ramp of temperature of 25°C to 650°C. The supports containing neodymium, γ Al_2O_3-Nd were prepared by impregnation of the Boehmite with the necessary quantity of $Nd(NO_3)_3 \cdot 6H_2O$ (Strem Chemicals, 99.99%) aqueous solutions to obtain 1 and 10 wt% of Nd in the support. Then, the solids were dried in an oven to 120°C for 12 h, after that, the samples were calcined at 650°C in air flow of 60 mL/min for 24 h using a ramp of temperature with a speed of 2 °C/min.

The Rh/γ-Al_2O_3-Nd1% and Rh/γ-Al_2O_3-Nd10% catalysts were prepared by wet impregnation. The supports were impregnated with $RhCl_3 \cdot 3H_2O$ (Strem Chemicals, 99.99%) aqueous solution. The solids were left in stirring for 3 hours in a rotary evaporator at 30 rpm. After that, the water is evaporated using a water bath at 60 ° C and a vacuum of 72 millibars. Subsequently the solids were dried in an oven at 120 °C, for 12 hours. The catalysts were calcined in air at 500 °C under air flow of 60 mL/min for 5 hours and finally, the catalysts were reduced in H_2 flow of 60 mL/min at 500 °C for 5 hours, using a ramp heating with a speed of 2 °C/min for both processes.

2.2. Characterization

The specific surface areas of the catalysts were obtained from the nitrogen adsorption isotherms generated with a Quantachrome Multistation Autosorb 3B analyzer. Before adsorption, the calcined supports were out gassed at 300 ºC under vacuum (10^{-3} Torr) for 2 h. The specific surface areas were calculated with the BET equation and the mean pore size by the BJH method.

The X-ray diffraction patterns of the supports were obtained using a Bruker D-8 Advance X-ray powder diffractometer equipped with a Cu Kα radiation anode in Bragg-Brentano geometry. The detection was carried out using a Lynxeye detector, which is a linear-type. Intensity data was measured in continuous mode through the 2θ ranges between 10° to 70° with a 2θ step of 0.02°.

The TPR determinations were carried out in a CHEMBET-3000 (QUANTACHROME Co) apparatus using 0.2 g of catalyst by means of the following protocol: samples were heated at 300°C under nitrogen flow (10 mL min^{-1}) during 30 min. Then, the samples were cooled dawn to room temperature and a mixed gas flow (5%H_2/95%N_2) was passed through the cell. The TPR profiles were registered using a heating program of 10°C min^{-1} from room temperature up to 500 °C using a flow rate of the gas mixture of 10 mL min^{-1}.

This study was carried out using a Nicolet 170 SX equipment with Fourier transform. The sample pressed in thin wafers were placed in a glass Pyrex cell with CF_2 windows coupled to a vacuum line, in order to be evacuated (10^{-3} Torr) in situ at 400ºC for 30 min to remove impurities. Then, temperature was decreased to room temperature and the pyridine was introduced to the cell to attain the adsorption equilibrium. The excess of pyridine was evacuated at the same temperature. After, the adsorbed pyridine was desorbed from room temperature to 400 ºC at intervals of 100ºC. The quantities of the adsorbed pyridine were obtained from the integrated absorbance bands [13].

This study was performed on an electron microscope of field emission 2010FEG JEM that operates at 200 kV. The samples were powdered in an agate mortar and were suspended in ethanol at room temperature and dispersed in an ultrasonic bath for two minutes, then one drop of the solution was deposited on a carbon copper grid.
SEM images were taken in a JEOL HRSEM 7600F with an acceleration voltage of 15 kV with a point of resolution of 1 nm. This microscope has an unit of elemental analysis EDS (INCA Sight), with linear modes and cartography.

2.3. Catalytic activity

The activity determinations were carried out in a quartz glass microreactor system (figure 1) with a fixed bed at atmospheric pressure and catalyst load of 0.05 g. The reaction

temperatures varied from 400 to 700 °C, the increase of temperature was on steps of 100ºC and the last at 750 ºC with a rate of 5 ºC min^{-1}. Experiments consisted in a previous thermal treatment to the catalysts with flowing nitrogen for 15 min at room temperature. Then, a pure CH_4 (high purity) feed steam (2 mL min^{-1}) was introduced into the reactor.

The inlet and outlet effluents were monitored by an on line gas chromatograph Shimadzu GC-2014 equipped with 6 packed column and a thermal conductivity detector (TCD) which allows the measurement of hydrogen, and a flame ionization detector (FID), for detect organic compounds such as CH_4, CO_2 and CO. The main products detected were: H_2, C_2 compounds.

The methane conversion was calculated as the amount of methane converted throughout the experiment over the amount admitted during that step. The selectivity was the amount of each product H_2, C_2H_4, or C_2H_6 collected at reactor outlet over the methane converted.

3. Results and Discussion

The diffraction patterns of the Rh catalysts supported on Al_2O_3 and Al_2O_3-Nd are showed the characteristic peaks of Al_2O_3 gamma phase. The Rh/Al_2O_3-Nd1% catalyst does not show notable difference in the diffractogram respect to the Rh/Al_2O_3 catalyst. However the Rh/Al_2O_3-Nd10% catalyst shows lower intensity alumina peaks which indicate low crystallinity of the solid.

The BET specific surface area most affected was for Rh/Al_2O_3-Nd10% catalyst, where the decrease was around 20%, this result can be explained by a probable blockage of some porous of the alumina by neodymium oxide. The pore volume follows the same trend of decrease in those samples.

The mean Rh particle size of the fresh catalysts is showed in Table 1. The mean particle size was determined by $ds = \Sigma\, nd^3/nd^2$ equation, where ds, is the mean particle size of the Rh particles; n, the number of particles of diameter d, measured directly on the micrographics. The particle size of Rh was 1, 2.1 and 3.4 nm for Rh/γ-Al_2O_3, Rh/γ-Al_2O_3-Nd1% and Rh/γ-Al_2O_3-Nd10% catalysts respectively.

The acidity of the catalysts was determined by FT-IR of pyridine adsorption. Lewis acid sites were the only type of sites observed in all the samples, the values measured at 200ºC, where the adsorption corresponds to pyridine chemisorbed on the surface, are reported in Table 1. Rh/γ-Al_2O_3-Nd10% (96 μmolg^{-1}) catalyst presents the lowest acid sites respect to Rh/γ-Al_2O_3 (123 μmolg^{-1}) and Rh/γ-Al_2O_3-Nd1% (131 μmolg^{-1}) catalysts. The rare earth show basic properties [14], then, the higher amount of Nd in Rh/γ-Al_2O_3-Nd10% catalyst leads to decrease the acidity on the surface in this catalyst.

The reduction profiles (H_2-TPR) for Rh/Al_2O_3, Rh/Al_2O_3-Nd1% and Rh/Al_2O_3-Nd10% catalysts showed two reduction peaks in all Rh samples, the lower temperature reduction peak has been attributed to the reduction of three dimensional Rh_2O_3 crystallites [15-17]. The reduction peak at higher temperature was associated to reduction of rhodium oxidized specie that interacts with the support, although, other authors have proposed that this second peak is related to the reduction of two dimensional Rh_2O_3 particles [17].

Table 1. Characteristics of the Rh catalysts.

Supports	[1]mean Rh particle size (nm)	[2]Lewis acidity $\mu molg^{-1}$	Area BET m^2g^{-1}
$Rh/\gamma\text{-}Al_2O_3$	1.0	123	284
$Rh/\gamma\text{-}Al_2O_3$-Nd1%	2.1	131	237
$Rh/\gamma\text{-}Al_2O_3$-Nd10%	3.4	96	227

[1]Fresh catalysts.
[2]Determined at 200ºC

3.1 Catalytic activity and reactor

The activity of the Rh catalysts for the dehydrogenation of methane was conducted at temperatures of 400, 500, 600, 700 and 750ºC with undiluted methane flowing and a space velocity of 2 L $h^{-1}g^{-1}$, see Table 2.

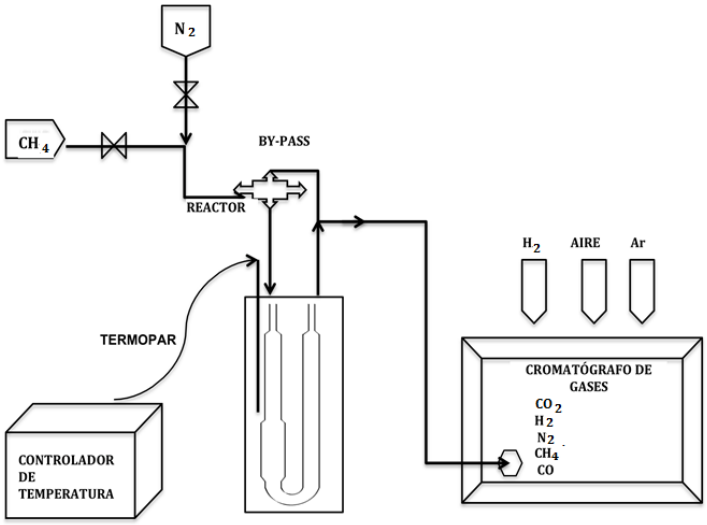

Fig. 1. The activity determinations were carried out in a quartz glass microreactor system

Table 2 shows the methane conversion as function of the temperature; it can be seen that the conversion of methane increases as the temperature increase from 400ºC to a maximum conversion at 700ºC, then it decrease at 750ºC.

The methane decomposition for the different catalysts at 400ºC shows good activity corresponding to the following catalysts sequence: $Rh/\gamma\text{-}Al_2O_3$-Nd1%, the most active, followed of $Rh/\gamma\text{-}Al_2O_3$ and $Rh/\gamma\text{-}Al_2O_3$-Nd10% respectively. However, at high

temperature (700°C). The Rh/γ-Al_2O_3-Nd1% catalyst showed the highest conversion, catalyst with a mean particle size of 2.1 nm.

Table 2. Conversion for the methane decomposition on Rh/Al_2O_3-Nd catalysts.

Catalyst	Temperature (ºC)	Conversion (%)
Rh/γ-Al_2O_3	400	45
	500	51
	600	58
	700	74
	750	71
Rh/γ-Al_2O_3-Nd1%	400	50
	500	55
	600	62
	700	79
	750	68
Rh/γ-Al_2O_3-Nd10%	400	39
	500	47
	600	53
	700	75
	750	66

The dehydrogenation of CH_4 is a reaction that is carried out on the metal in reduced state and also that the structure of the metal particle size can influence the activity [18]. The Rh/γ-Al_2O_3-Nd10% catalyst with the highest load of neodymium and the largest particle size was the most selective to hydrogen at 700 and 750 °C temperature, Table 3.

In the course of the methane decomposition over the Rh surface a deposit of the carbonaceous intermediates is produced. These carbon formed during the reaction was deposited mainly on the support. Which showed an optimal surface acidity, where the carbonaceous species were deposited keeping the Rh metal surface particles clean for the reaction. A graphitic type carbon was formed on the catalysts in according to the temperature of reaction and determined by HRTEM (Fig.2).

Table 3. Selectivities to H_2, C_2H_4 and C_2H_6 for all the catalysts at 700 and 750 ° C.

Catalyst	Temperature (ºC)	Selectivity (%)		
		H_2	C_2H_4	C_2H_6
Rh/γ-Al_2O_3	700	89	8	3
	750	85	8	7
Rh/γ-Al_2O_3-Nd1%	700	65	23	12
	750	63	12	25
Rh/γ-Al_2O_3-Nd10%	700	100	0	0
	750	100	0	0

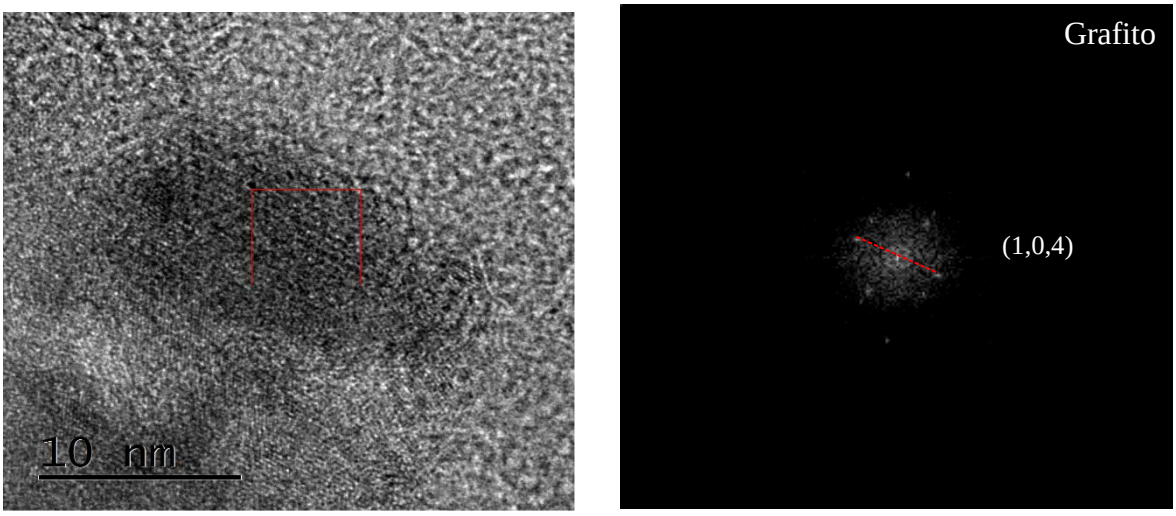

Fig. 2. HRTEM Image of carbon type formed during the reaction.

4. Conclusion

The methane dehydrogenation is a structure sensitivity reaction on Rh catalysts. The Rh/γ-Al_2O_3, Rh/γ-Al_2O_3-Nd1% and Rh/γ-Al_2O_3-Nd10% catalysts showed CH_4 conversions of 74, 79 and 75% and selectivities to hydrogen of 89, 65 and 100% respectively at 700 °C. The metal particle size of Rh and the acidity influenced these results; since the catalyst with the largest particle size (Rh/γ-Al_2O_3-Nd10%) ~ 3.4 nm and

the lowest acidity, 96 $\mu molg^{-1}$, was the most selective to hydrogen.

The difference in the degree of interaction of Rh with the support induces changes in the binding energy, which affect the activity and selectivity of methane decomposition. The CH_4 adsorbs dissociatively on Rh surface particles producing H_2 and CHx (x=3-0) species. The Rh/γ-Al_2O_3, Rh/γ-Al_2O_3-Nd1% catalysts presented also selectivities towards ethane and ethylene, which came from the mobility of the CHx species on Rh surface during the degradation of methane.

The performance of the Rh/γ-Al_2O_3-Nd10% catalyst is explained by the high interaction of Rh and alumina-Nd maintaining a limited mobility of the dehydrogenated species. The carbon produced during the reaction was graphitic type which was deposited mainly and on the support.

Acknowledgements

We acknowledge CONACYT for the support provided to the Project CB-105158 Fond SEP-CONACYT. Marina Caballero thanks to CONACYT for the grants awarded.

References

[1] Malaika A, Krzyzynska B, Kozlowski M. Catalytic decomposition of methane in the presence of in situ obtained ethylene as a method of hydrogen production. Int J. Hydrogen Energy 2010; 35:7470-7475.

[2] Shah N, Panjala D, Huffman JP. Hydrogen production by catalytic decomposition of methane. Energy & Fuels 2001; 15:1528-1534.

[3] Shah N, Wang Y, Panjala D, Huffman G. Production of Hydrogen and Carbon Nanostructures by Non-oxidative Catalytic Dehydrogenation of Ethane and Propane. Energy Fuels 2004; 18:727–735.

[4] Wang Y., Shah N., Huffman G. Simultaneous production of hydrogen and carbon nanostructures by decomposition of propane and cyclohexane over alumina supported binary catalysts. Catal Today 2005; 99:359–364.

[5] Muradov N. Hydrogen via methane decomposition: an application for decarbonization of fossil fuels. Int J Hydrogen Energy 2001; 26:1165-75.

[6] Makoa M, Coville N, Sokolovskii V. Characterisation of Co/Mg/Al_2O_3 high pressure partial oxidation catalysts. Catalysis Today 1999; 49:11–16.

[7] Avdeeva L, Reshetenko T, Ismagilov Z, Likholobov V. Iron-containing catalysts of methane decomposition: accumulation of filamentous carbon. Appl Catal A 2002; 228: 53-63.

[8] Lee K, Han G, Yoon K, Lee B. Thermocatalytic hydrogen production from the methane in a fluidized bed with activated carbon catalyst. Catal Today 2004; 93-95:81-86.

[9] Muradov N. CO_2-free production of hydrogen by catalytic pyrolysis of hydrogen fuel. Energy Fuels 1998; 12: 41-48.

[10] Moliner R, Suelves I, Lázaro MJ, Moreno O. Thermocatalytic decomposition of methane over activated carbons: influence of textural properties and surface chemistry. Int. J. Hydrogen Energy 2005; 30:293-300.

[11] Rostrup-Nielsen JR, Sehested J, Norskov JK. Hydrogen and synthesis gas by steam and CO_2 reforming. Adv Catal 2002; 47:65-139.

[12] Ferro S. Physicochemical and Electrical Properties of Praseodymium Oxides. Int J Electrochemistry 2011; 2011:1-17.

[13] Emeis CA. Determination of integrated molar extinction coefficients for infrared adsorption bands of pyridine adsorbed on solids acid catalysts. J Catal 1993; 141:347-354.

[14] Tanabe T, Morikawa A, Hatanaka M, Takahashi N, Nagai Y, Sato A, Kuno O, Suzuki, H, Shinjoh H. The interaction between supported Rh- and Nd_2O_3-enriched surface layer on ZrO_2 for Rh sintering suppression. Catal Today 2012; 184:219–226.
[15] Hwang CP, Yeh CT, Zhu Q. Rhodium-oxide species formed on progressive oxidation of rhodium clusters dispersed on alumina. Catal Today 1999; 51:93-101.
[16] Ferrandon M, Krause T. Role of the oxide support on the performance of Rh catalysts for the autothermal reforming of gasoline and gasoline surrogates to hydrogen. Appl Catalysis A: General 2006; 311:135–145.
[17] Taniguchi T, Lizuka W, Nagata Y, Uchida T, Samata H. Magnetic properties of RRhO3 (R=rare earth). J Alloys Compd 2003; 350: 24-29.
[18] Ma J, Reng S, Pan D, Li R, Xie K. PVP-Pt nanoclusters supported zeolite catalysts for converting methane to higher hydrocarbon at low temperature. Reactive & Functional Polymers 2005;62:31–39.

Chapter 1.9. Hydrogen adsorption process in Mg-Al compounds (Mg25Al, Mg50Al) almost standard conditions for pressure and temperature

J. L. Iturbe – García[a,*]; B. E. López – Muñoz[a]

[a]Departamento de Química, Instituto Nacional de Investigaciones Nucleares, Km 36.5 Carretera México-Toluca s/n, la Marquesa, C.P. 52045, Ocoyoacac, Estado de México, Tel: (01-55) 53297200 ext. 12274, fax: (01-55) 53297301

ABSTRACT

In this work the H_2 adsorption/desorption process in various Mg – Al compounds is presented. These Mg and Al compounds were subjected to hydrogenation process in both Thermogravimetric Analyzer and a micro reactor systems. In the last equipment, pressure, temperature and contact time were varied trying to perform hydrogenation experiments in the best environmental conditions. The Mg50Al, Mg25Al alloys were used in this investigation, for decreasing its particle size high energy mechanical milling was performed by placing 2 g of each sample (Mg50Al and Mg25Al) and milling media into a stainless steel vial for milling during only a period of 5 hr using white gasoline as process control agent and without control agent for Mg50Al and Mg25Al respectively. Magnesium oxide-aluminum (MgOAl) phase was also used for hydrogen adsorption, this material was prepared in an electric tube furnace under normal atmosphere from intermetallics described above. The hydrogenation process was carried out by placing the samples into the micro reactor under vacuum for one hour at 300° C, then the system was cooled to 50° C, immediately H_2 was put in contact with the materials at a pressure of 20 atm for 5 min. The samples were analyzed before and after hydrogenation process by TGA, SEM, XRD and gas chromatography. Results indicate that these materials adsorb H_2 at moderate pressure and temperature conditions. The H_2 concentration values of each compound are reported in weight percentages. The technique of gas chromatography was used to verify the presence of H_2 in the compounds studied according to the results obtained by the TGA system.

Keywords: Hydrogen adsorption, Magnesium-aluminum compounds, Thermogravimetric analysis, Gas chromatography

1. Introduction

Actually the development of hydrogen technology demands a solution to problems such as finding new methods and materials for use in the production and storage of hydrogen safely

---

* Author for correspondence: J. L. Iturbe – García, Tel: (01-55) 53297200 ext. 12274, fax: (01-55) 53297301, C.P. 52045; mail: joseluis.iturbe@inin.gob.mx

through solid materials such as metal hydrides among many others both for use in fuel cells [1, 2]. Although hydrogen has some important features to become an energy vector especially in some applications, needs to overcome two obstacles that could curb its use if not resolved satisfactorily. While it is the lightest existing atoms, it is also the most voluminous in its gaseous state at standard temperature and pressure. Moreover, its ability to release energy makes it a particularly flammable gas under certain conditions and in the presence of oxygen. Therefore, before use, will have to solve the complex problems of production, storage and distribution in the conditions of volume and safety, as well as operations cost [3].

Hydrogen is naturally found in form of chemical compounds, most commonly in water and hydrocarbons and can also be produced by some processes from fossil fuels which can be obtained using renewable energy sources. At present there are different ways to store hydrogen, the choice depends on various factors such as the final process in which it is to be used, some options are compressed gases, cryogenic liquids, metal hydrides, carbon nanostructures, alanates etc. In metal hydride systems, surface area and particle size of the material are very important parameters for increased storage capacity in hydrogen, lower temperature and pressure, improve the kinetics of material and in some cases reduce the activation time [4].

There have been studies on synthesis and characterization of intermetallics for further use in hydrogen storage. It has been reported that the magnesium hydride milled for three hours under argon atmosphere with some additive (Al_2O_3, SiC, V or graphite), a particle size of about 20 nm is obtained, with graphite greater absorption capacity is obtained (6 wt%) than the other compounds (about 4% by weight) [5,6]. Various metal-hydrogen systems for reversible hydriding-dehydriding of magnesium are considered as a possible storage option among them Mg-base alloys are attractive materials for hydrogen storage applications because of their high gravimetric hydrogen storage densities of up to 7.6 wt.% for some applications in the case of MgH_2 [7 – 10]. However, the major problem with magnesium as a reversible hydrogen storage material is the slow reaction kinetics of its adsorption/desorption process, the kinetics has been improved by adding an appropriate catalyst into the system as well as by ball milling that introduces defects with improved surface properties.

On the other hand, are also actually studying new hydrogen storage materials which have special structural features unlike other compounds, including nanopores can also be mentioned, mesopores, micropores, this classification depends on the pore diameter which can store different types of gases for example hydrogen. Resonant fluctuations in charge distributions, which are called dispersive or Van der Waals interactions, are the origin of the physisorption of gas molecules onto the surface of a solid. In this process, a gas molecule interacts with several atoms at the surface of a solid. These compounds have several advantages, one of which is that in the processes of absorption/desorption hydrogen require less energy to carry out this process unlike metal hydrides, because in these last require further energy to break the chemical bond between the hydrogen and metal, so in nanoporous compounds is more rapid their kinetics and therefore requires less energy cost (Hydrogen reacts at elevated temperatures with many transition metals and their alloys to form hydrides [11-15]). The hydrogen carries a partial negative charge, depending on the metal, but an exception is PdH0.7. Pt and Ru are able to adsorb considerable quantities of

hydrogen, which becomes activated. These two elements, together with Pd and Ni, are extremely good hydrogenation catalysts, although they do not form hydrides [16]. Tremendous efforts have been performed to the research and development of materials that can hold sufficient hydrogen in terms of gravimetric and volumetric densities, and, at the same time, possess suitable thermodynamic and kinetic properties. Over approximately a decade of exploration, the scope of candidate materials has expanded greatly, from traditional metal hydrides to complex hydrides and chemical hydrides, and from activated carbon to carbon nanotubes and metal organic frameworks [17,18]. The use of advanced synthetic routes also yields a range of physical states from bulk crystalline structures to amorphous states to nanostructures. Mg25Al, Mg50Al intermetallics were used in this work for hydrogen retention and to see which absorbs more hydrogen and know the most suitable for use in hydrogen storage.

2. Materials and Methods

The utilization of these compounds were derived from a Mg25Al and Mg50Al alloys which were identified as MgOAl25 and MgOAl50 and prepared as follows: The Mg25Al and Mg50Al intermetallics were synthesized by melting, using a thermal induction oven in an argon atmosphere. Elements of Mg and Al with purity of 99.8% were used to prepare the intermetallics before mentioned. The ingots obtained were submitted to a homogenization heat treatment at 300°C for 72 hours, these conditions of homogenization are used because the treatment thermal recommended must be greater to 0,5 MT where MT is the melting temperature for both alloys (Mg25Al and Mg50Al). The ingot was devastated using a flat to obtain particle sizes ranging from a few microns to several millimeters. Then the particle size was diminished under an inert atmosphere with a high energy mill type spex built at ININ. The milling time was 5 h at room temperature, in both intermetalics. These compounds were characterized before performing the reactions with hydrogen by X-ray diffraction (XRD), scanning electron microscopy (SEM), and thermogravimetric analysis (TGA) techniques, these analyses were performed in order to know different phases formed, their morphology, and the mass loss within its structure respectively. The micro – reactor for hydrogen adsorption process was also used in these compounds. This system was programmed to 300° C under vacuum for two hours to remove impurities before contact with hydrogen then it was cooled to 50° C and a hydrogen pressure of 20 atmospheres was introduced for 5 minutes. Hydrogen analysis was performed using TGA and gas chromatography system. After end of hydrogenation process, the vial was sealed with an aluminum O-ring to avoid that hydrogen can to escape, hydrogen samples were taken with a syringe and injected to the chromatograph, this process was carried out at room temperature.

3. Results and Discussion

Figure 1 shows a micrograph of particles which were roughed from MgAl ingot for both Mg25Al and Mg50Al. These materials were obtained by melting metals. The image show various particle shapes obtained from MgAl ingot and roughing with a flat, different

morphologies and sizes are observed. The forms is due to edges presented by lime, with irregular shape, heterogeneous that not have a defined morphology and its particle sizes varied from a few microns to several millimeters. The particles present in one side a smooth shape and opposite side folds around edges as well as toothed form due to mechanism performed of roughing, as demonstrated in images A, B, C and D figure 1. This morphology

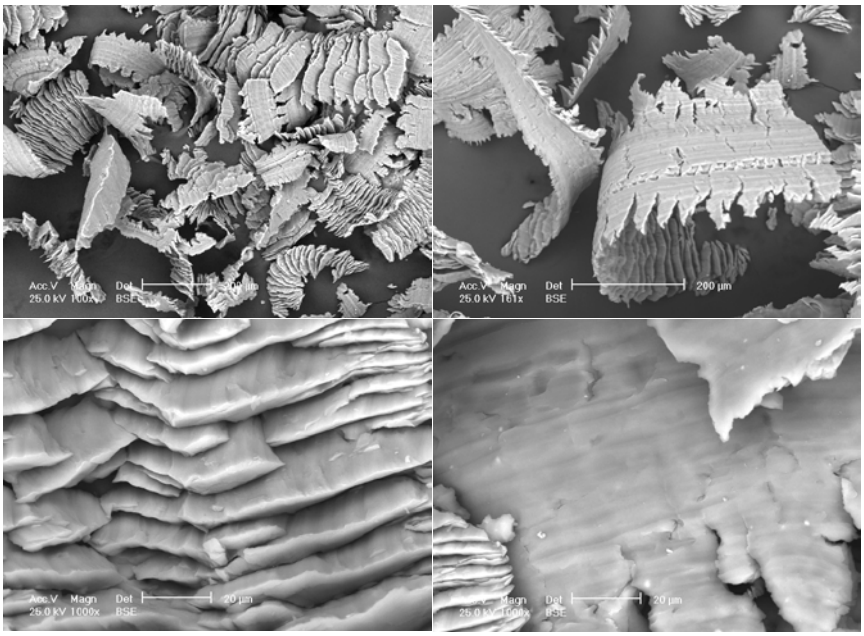

Fig. 1. Micrograph of MgAl particles with a composition of 25:75 at%, which were roughed with a flat.

is also due to effort carried to deal with the lime ingot and physical properties of material as different melting points of each metal as they are considered soft metals and alloy has some malleability, especially the larger ones observed in semicircular toothed on both sides of all particles. Elemental composition before hydrogen contact were 25, 50 and 75, 50at% for Mg and Al respectively. The results obtained by EDAX sonde which is coupled to the microscope shows the percentages in both weight and atomic materials we can know the elemental composition of Mg25Al and Mg50Al alloys. These results registered are not quantitative and can only be considered since point of view semi qualitative. However, these ones give us an idea of percentages being considered and according to theoretical values of 75, 50 and 25, 50 for Mg and Al, respectively, the atomic percent of both metals is very close to theoretical values obtained for this type of alloys. The results from X-ray diffraction analysis were able to identify two phases, the first phase was Mg17Al12 and second magnesium, which were identified by JCPDS cards 01 – 073-1148 and 4-770 respectively.

The presence of magnesium as metal is normal and that despite having made thermal homogenization process is not enough to have compound evenly appearing a little magnesium alone.

Fig. 2 shows a micrograph of Mg25Al intermetallic particles which was milled for 5 hours to obtain them in powder form. The image was obtained at 3000 magnification scale according to various particle sizes are heterogeneously with manometric values to several microns, and form aglomerates which in turn contain smaller particles, which have certain structural characteristics not well defined morphology giving impression that it is a spongy

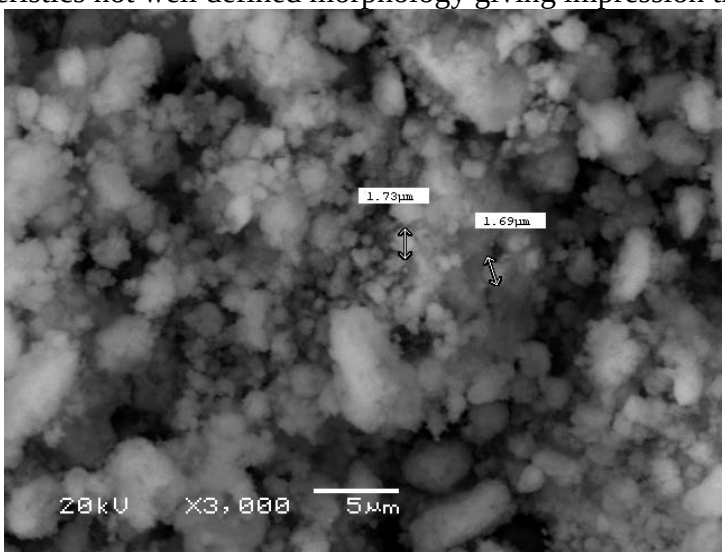

Fig. 2. Micrograph of Mg25Al particles obtained after 5 h of mechanical milling

material. The diminished particles procedure is considered as a reactive ball milling. It is important to emphasize that the system warm-up was controlled with an air current from a small fan that was placed near the container, to homogenize the temperature during milling times and to avoid their adhering to stainless steel container's surface with 50 microliters of gasoline white. This material was analyzed before being subjected to hydrogenation process by TGA technique which was programmed to 400 ° C to remove impurities that might have on its structure and to know the conditions which would be submitted to hydrogen absorption into microreactor.

Figure 3 shows a thermogram of Mg25Al particles milled for 5 h. The spectrum corresponds to material before hydrogenation process. The shape of this spectrum is a representation of results obtained by TGA technique for all samples after milling and hydrogenated. The spectrum indicates the mass loss as a function of temperature, these values are recorded at different intervals from 100 to 400 ° C. As shown in the figure, values are indicated in percent and in mass units. Temperature values discloses the experimental conditions to be taken into account for heat treatment to be applied within the microreactor to release impurities containing in its structure before performing hydrogenation process. In this particular case, the first interval was considered from ambient to 100 ° C reports a mass loss of 3.86% equivalent to 0.36 mg, the second range up to 200 ° C such loss was 6.26% or 0.59 mg and finally 400 ° C the value was 14.29% which equates to 1.34 mg. Moreover, the results obtained in hydrogenation processes within the microreactor for Mg50Al Mg25Al are reported in Table 1, which indicates the sample identification, mass loss in percent and mg of each temperature range at 100, 200 and 400° C. The experimental hydrogenation process carried out in both samples (Mg25Al and

Mg50Al) within the microreactor was at 300 ° C with vacuum for one hour, then the system was cooled to 50 ° C and under these conditions hydrogen was introduced at 20 bars, the hydrogen contact time was 5 minutes.

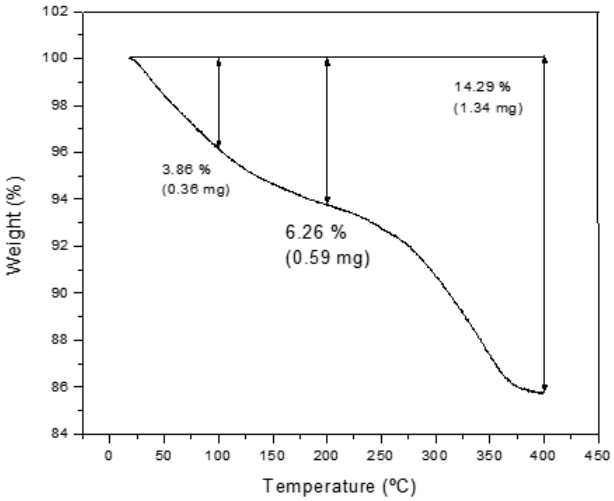

Fig. 3. Thermogram of Mg25Al after milling process, which is a representation of all analyzed samples.

The results indicated as MO samples were analyzed after milling process to Mg25Al and Mg50Al particles. In each material 5 cycles of absorption / desorption hydrogen process were performed and identified as M1 to M5 (second column). The minimal and maximal values obtained in the first temperature range (from ambient to 100 ° C) were 2.63% (0.08 mg) to 3.64% (0.12 mg) for Mg25Al and 1.24% (0.11 mg) to 2.92% (0.18 mg) for Mg50Al. The following results were obtained at 200 ° C, whose values were 3.96% (0.12 mg) to 4.46% (0.42 mg) and 1.79% (0.16 mg) to 3.98% (0.56 mg) and finally for 400 ° C were between 5.27% (0.17 mg) a a nd 7.50% (0.69 mg) and 2.72% (0.24 mg) to 4.88% (0.68 mg) for Mg25Al Mg50Al samples respectively. These values indicate the hydrogen concentration in each material that were retained within its structure. It should be mentioned that according to the results by microscopy, these materials presented a spongy morphology, which would indicate that hydrogen was physisorbed which were verified by gas chromatography.

To verify the presence of hydrogen in Mg25Al and Mg50Al compounds certain amount of material was placed in a vial and carried out the hydrogenation process according to the experimental procedure described above. The results are shown in Figure 4 corresponding to Mg25Al hydrogenated sample. This figure shows a series of hydrogen spectra, spectrum A corresponds to a hydrogen sample which was used as a standard and was taken directly from hydrogen tank to determine the retention time within column and compared to other samples from hydrogenated material. B1 to B5 spectra corresponding to

five samples taken from the vial and analyzed under the same conditions as the pattern of hydrogen.

Table 1. Results reported by thermogravimetric analysis of Mg25Al and Mg50Al compounds using the micro-reactor for hydrogenation process.

Samples	Identification	100°C % (mg)	200°C % (mg)	400°C % (mg)
Mg25Al	MO	5.03 (1.59)	9.29 (2.99)	16.13 (5.05)
	M1	3.3 (0.37)	4.34 (0.49)	6.82 (0.77)
	M2	3.41 (0.32)	4.46 (0.42)	7.50 (0.69)
	M3	3.07 (0.10)	4.35 (0.14)	6.01 (0.19)
	M4	2.63 (0.08)	3.96 (0.12)	5.27 (0.17)
	M5	3.64 (0.12)	5.15 (0.17)	6.69 (0.22)
Mg50Al	MO	2.59 (0.40)	3.67 (0.56)	10.63 (1.63)
	M1	2.92 (0.18)	3.92 (0.23)	4.77 (0.23)
	M2	2.18 (0.30)	3.12 (0.42)	4.85 (0.66)
	M3	2.89 (0.41)	3.98 (0.56)	4.88 (0.68)
	M4	2.04 (0.14)	2.76 (0.18)	4.11 (0.27)
	M5	1.24 (0.11)	1.79 (0.16)	2.72 (0.24)

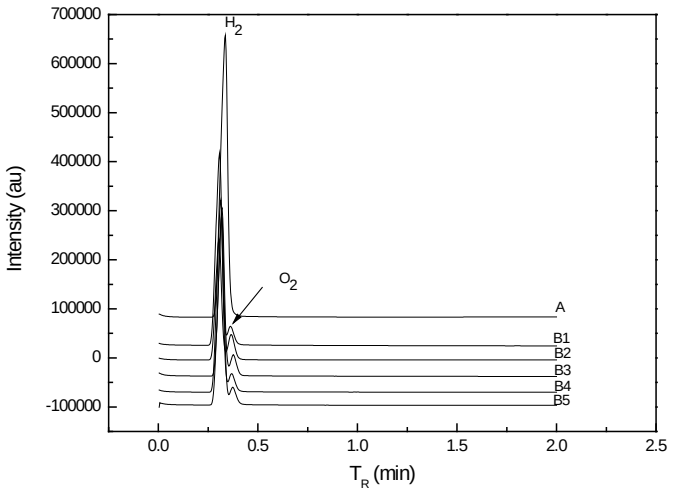

Fig. 4. Chromatogram of hydrogen from different analyzed samples

It can be seen that both spectra patterns as five events coincide well, this means that hydrogen retention time within column was the same. Not hydrogen desorption heat energy required for hydrogen to flow through the material which allowed the analysis to room temperature. With this analysis shows that MgAl materials were retained the hydrogen within their structure. In all spectra of the figure a small peak appears which was identified as oxygen, the presence of this gas is that when injecting the sample into the chromatograph, the syringe tip is exposed to ambient and carries small amount of air for this reason is the presence of this element. It was proved in this study with milling process that nanoparticles from Mg25Al and Mg50Al compounds were obtained with a spongy morphology which facilitated hydrogen retention in these materials, on the other hand, the experimental conditions carried out were not appropriate to form hydride phases possibly due to low temperature inside the microreactor applied in hydrogenation process, which was only 50° C.

4. Conclusion

The Mg25Al Mg50Al alloys were prepared by thermal fusion induced method in an oven with inert atmosphere. The particles were obtained by roughing MgAl ingot through a flat file. Powders of same material were also prepared by high energy mechanical milling. Certain experimental conditions for absorption/desorption hydrogen process in the micro-reactor were found. These particles absorb hydrogen in percentages ranging from 5.27 to 7.5 and 2.72 to 4.88wt% for both materials reported by TGA at 400°C. Hydrogen desorption process from Mg25Al and Mg50Al were carried out under normal conditions, ie, at room temperature and verified by gas chromatography. The contact time between the materials and hydrogen was very short to moderate pressure. It did not observe any hydride formation perhaps because the experimental conditions were not appropriate principally the temperature. MgAl powders possibly present in its crystal structure micropores where the hydrogen remain physisorbed.

Acknowledgements

Thanks to personnel of SEM, XRD, TGA and Chromatographic techniques for their valuable assistance in the analysis carried out in this work.

References

[1] Ball M., Weeda M. The hydrogen economye vision or reality? Internationa Journal of Hydrogen Energy 2015; 40: 7903-7919.
[2] Fichtner M. Nanotechnological aspects in materials for hydrogen storage, Adv Eng Mater 2005; 7: 443–455.
[3] Züttel, A. Hydrogen storage methods. Nature 2004: 91: 157-172.
[4] Sakintuna B., Lamari-Darkrim F. and Hirscher M. Metal hydride materials for solid hydrogen storage: a review, Int J Hydrogen Energy 2007; 32: 1121–1140.
[5] Güvendiren M., Baybörü E., Öztürk T. Effects of additives on mechanical milling and hydrogenation of magnesium powders. International Journal of Hydrogen Energy, 2004; 29: 491-496.

[6] Haluska, M. et al. Hydrogen Storage in Single Walled Carbon Nanotubes, Proceedings from 8th European Conference on Solid State Chemistry, Oslo, Norway 2001: July 2001.
[7] Jain. I.P., Lal C. and Jain A. Hydrogen storage in Mg: a most promising material, Int J Hydrogen Energy 2010; 35: 5133–5144.
[8] Gutfleisch O., Dal Toè S., Herrich M., Handstein A. and Pratt A. Hydrogen sorption properties of Mg–1 wt.% Ni–0.2 wt% Pd prepared by reactive milling, J Alloys Compd 2005; 404–406: 413–416.
[9] Liang G., Huot J., Boily S., Van Neste A. and Schulz R. Catalytic effect of transition metals on hydrogen sorption in nanocrystalline ball milled MgH_2–Tm (Tm = Ti, V, Mn, Fe and Ni) systems, J Alloys Compd 1999; 292: 247–252.
[10] Gross K.J., Chartouni D., Leroy E., Zuttel A., Schlapbach L. Mechanically milled Mg composites for hydrogen storage: the relationship between morphology and kinetics J. Alloys Comp. 1998**;** 259-270.
[11] Zaluski L., Zaluska A. and Strom-Olsen J.O. Nanocrystalline metal hydrides, J Alloys Compd 1997; 253-254: 70–79.
[12] Aguey-Zinsou K.F., Ares Fernandez J.R., Klassen T. and Bormann R. Effect of Nb_2O_5 on MgH_2 properties during mechanical milling, Int J Hydrogen Energy 2007; 32: 2400–2407.
[13] Kowalczyk P., Holyst R., Terrones M. and Terrones H. Hydrogen storage in nanoporous carbon materials: myth and facts. Physical Chemistry Chemical Physics 2007; 9: 1786-1792.
[14] Yang Y. Synthesis of ordered microporous carbons containing well dispersed platinum nanoparticles. Carbon Proceedings Seattle, Washington, USA, The American Carbon Society, 2007.
[15] Mueller, W. M., et al., (eds.), Metal Hydrides, Academic Press, New York, 1968.
[16] A. Züttel, Ch. Nutzenadel, G. Schmid, Ch. Emmenegger, P. Sudan, L. Schlapbach, Ž. Thermodynamic aspects of the interaction of hydrogen with Pd clusters Applied Surface Science 2000; 162–163: 5715-7517.
[17] Hirscher M., Becher M., Haluska M., Quintel A., Skakalova V., Choi Y.M., Dettlaffweglikowska U., Roth S., Stepanek I., Bernier P., Leonhardt A. And Fink J. Hydrogen storage in carbon nanostructures. Journal of Alloys and Compounds 2002; 330-332: 654-658.
[18] Thomas, K.M. Hydrogen adsorption and storage on porous materials. Catalysis Today, 2007; 120(34):389-398.

Chapter 1.10. Used disposable diapers as substrate for hydrogen production: effect of temperature and diaper conditioning

P. X. Sotelo-Navarro[a]; H. M. Poggi-Varaldo[b,*]; S. J. Turpin-Marion[a]; R. M. Espinosa-Valdemar[a]; A. Vázquez-Morillas[a]; M. Beltrán-Villavicencio[a]

[a] Department of Energy, Sustainable Technologies Laboratory, UAM-A, México, D. F.
[b] Departament of Biotechnology and Bioengineering, Environmental Biotechnology and Renewable Energy Group, Cinvestav-IPN, México, D.F., Av. Instituto Politécnico Nacional #2508 Col. San Pedro Zacatenco, México, D.F. C.P. 07360

ABSTRACT

The aim of this work was to evaluate the effect of temperatuRe (35 and 55 ºC) as well as diaper conditioning on bioH_2 production in bach fermentation of *used* disposable diapers. The cumulative bioH_2 production was evaluated in batch mini-reactors for whole diapers (*WD*), diapers without plastic components (*PSD*), manually separated diapers without feces and plastic (*MSD*), and reactors containing only inoculum as a control. All diaper samples were ground in a hammer mill. Substrate was set at 25% of total solids and inoculum was loaded at a ratio of 10% *TS*. When the bioH_2 production reached a plateau, the headspace of the reactors was flushed with N_2 and they were re-incubated without feeding substrate nor inoculum, following a procedure known as *SSAHF-IV* (solid substrate anaerobic hydrogenogenic fermentation with intermittent venting).

Results showed that bioH_2 cumulative production was higher at 55 ºC than at 35 ºC, which may be due to the limited growth of hydrogen consumers and faster metabolic activity of the bacteria reported for the thermophilic range. We expected higher cumulative bioH_2 productions for the diapers without the plastic components (*PSD*) because the latter are not biodegradable and could account for *ca.* 30% of the diaper weight. In contrast to our expectations, the average cumulative bioH_2 production followed the order *WD* > *MSD* > *PSD*. There was a slightly significant interaction temperature-diaper conditioning.

In general, our tests showed low yields in the production of H_2 at both temperatures compared to those obtained in the literature for organic waste. It is likely that sodium polyacrylate (*SAP* ; a polymer that is used as urine super absorbent in disposable diapers) could have played an inhibitory effect. Research is ongoing to overcome this effect and increase the suitability of used disposable diapers as substrate for bioH_2 generation.

1. Introduction

Disposable diapers are a symbol of the throwaway culture. In Mexico constitute 6.52% of the urban waste, i.e., about 7,000 tons per day, which are usually sent to landfills without

Keywords: Hydrogen production, disposable diaper, fermentation

---

* Author for correspondence:
Professor Dr. Héctor M. Poggi-Varaldo, T.: 5747-3800 x 4321, E: r4cepe@yahoo.com

treatment [1, 2]. There is a challenge in the handling this type of waste. However, disposable diapers are primarily composed of cellulose and synthetic fibers that can be treated by biological methods. The typical composition of a disposable baby diaper described by EDANA [3], is 36.6% cellulose pulp, 30.7% *SAP* , 16% polypropylene, 6.2% low-density polyethylene, and 10.5% made of elastic and adhesive tapes. A used infant diaper also contains residues such as feces and urine, which consists of approximately 30 g of carbon, 10-12 g of nitrogen, 2g of phosphorus and 3 g of potassium capable of being degraded. The bulk of this waste has been reported in several studies: Torrijos *et al.* [4] determined a content of 192 g of excreta, consisting on average of 18% feces and 82% urine; Colón *et al.* [5] reported an average droppings by diaper 171 g, but with a different distribution (6% stool and 94% and urine).

Dark fermentation of wastes seems to be an attractive technique for H_2 production [6, 7]. H_2 can be considered the best energy alternative because it can be produced by biological means: it has the highest energy density as fuel, it is versatile since can be used both as a primary or secondary energy source, and it is environmentally-friendly since water is the main combustion product on the one hand, while on the other hand no aggressive pollutants are generated in H_2 use or combustion [8, 9].

The important content of cellulose of disposable diaper indicates that this waste can be an attractive substrate for biofuel production. However, there are several factors to take into account for a significant production of H_2, such as: temperature, diaper composition, pH, substrate concentration, type of reactor, alkalinity, enrichment method of inoculum, inoculum type, method of inhibition of methanogenesis, among others [10-12].

Among the biological treatments that can be applied to used disposable diapers, composting process has been reported and its feasibility has been demonstrated [5, 13-16]. However, composting is a sink of energy associated to aeration. Anaerobic co-digestion of the biodegrable fraction (cellulose) of disposable diapers with waste activated sludge was tested, and a yield of 280 mL of CH_4/g was observed [4].

Yet, to the best of our knowledge, there are no studies on H_2 production of used disposable diapers. Therefore, this work aimed at evaluating the H_2 production in batch mini-reactors for whole diapers (*WD*), diapers without plastic components (*PSD*), manually separated diapers without feces and plastic (*MSD*), and reactors containing only inoculum as a control at two temperatures (35 and 55 ºC).

2. Materials and Methods

2.1. Experimental design and reactors

The experimental design was organized as a 2*4 factorial and examined the effect and interactions of two factors (incubation temperature, 35 or 55 ºC, and diaper conditioning) on H_2 production in batch fermentation of *used* disposable diapers as substrate. The process chosen was based on the solid substrate anaerobic hydrogen fermentation with intermittent venting and headspace flushing (*SSAHF-IV*) according to procedures reported elsewhere [9,17], with three types of substrate (diaper conditioning, i.e., whole diapers, *WD*; diapers without plastic components, *PSD*; and manually separated diapers without feces and plastic, *MSD*). Control bioreactors contained only inoculum.

2.1. Experimental minireactors and procedure

Glass bottles of 120 mL capacity were loaded according to the physicochemical characteristics of each substrate. Calculations were performed to establish a working volume in 50 ml mini-reactor a total solids content of 25 % and 10 % inoculum in each mini-reactor. All treatments were run by triplicate.

2.3. Analyses

The main monitoring parameter was hydrogen concentration in biogas. It was determined by gas chromatography in a Gow-Mac chromatograph model 350 fitted with a thermal conductivity detector and Molecular Sieve 5A packed column. The injector, detector and column temperatures were 25, 100 and 25 ºC, respectively. Argon was the carrier gas. Volatile organic acids (*VOA*), lactic acids and solvents were analyzed as reported elsewhere [7, 12].

2.4. Calculations

Acetate to butyrate ratio *A/B* (1) is an indirect indicator of hydrogenesis. Theoretically, acetic fermentation from hexose would yield four mol of hydrogen whereas butyric yields only two [6]. If we assume that 50% of hexose is fermented to H_2 plus acetic acid whereas the other 50% is fermented to H_2 plus butyric acid.

A/B (COD basis) = *HAc /HBu* (1)

where:
HAc = acetic acid concentration expressed in mg CODequivalent/Kg
HBu = butyric acid concentration expressed in mg CODequivalent/Kg

The ρ factor Eq. 2 was defined as the sum of the organic acids (as COD), divided by the sum of solvents (as COD). It indicates whether metabolism was leaned to acidogenesis or solventogenesis. Low ρ values would be associated to solventogenesis, and consequently, related to poor hydrogen generation [21].

$\rho = \Sigma VOA/\Sigma$solvents (2)

where:
ΣVOA= sum of volatile organic acids (acetic, butyric, propionic acids)
Σsolvents= sum of solvents (acetone, butanol, ethanol, metanol)

3. Results and Discussion

In the first *SSAHF-IV* of disposable diapers, intermittent venting coupled to convenient flushing of reactor headspace with N_2, allowed three cycles of hydrogen generation with no addition of new substrate or inoculum between cycles (Figure 1). A fourth cycle was attempted, but no noticeable hydrogen generation was found. Interestingly, on the average the cumulative bioH_2 production followed the order *WD* > *MSD* > *PSD*.

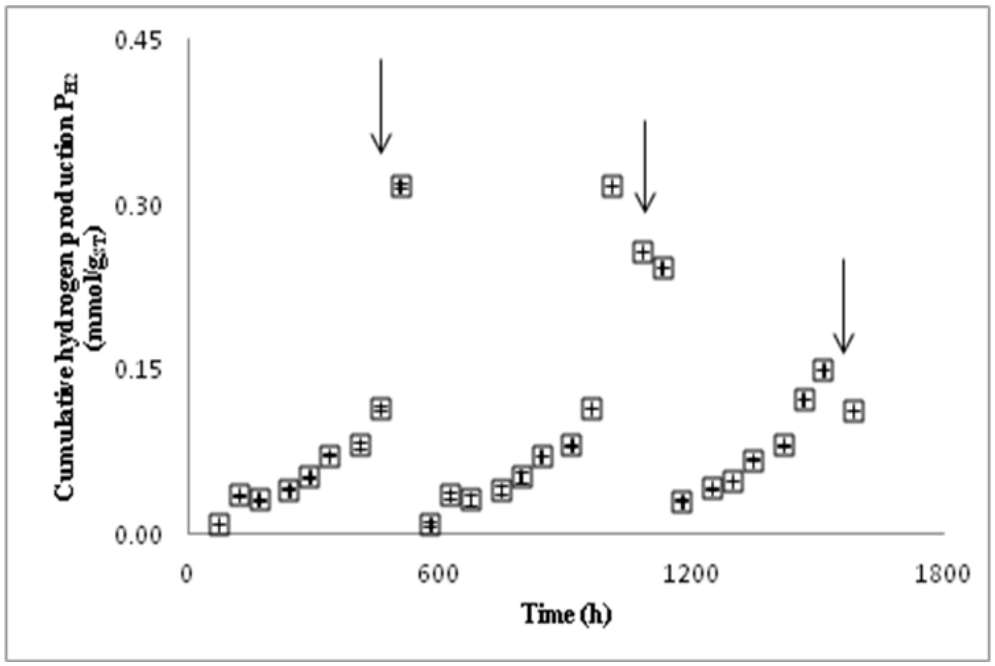

Fig. 1. Time course of H_2 production in batch mini-reactor of *WD*. Keys: vertical arrows indicate flushing of bioreactor headspace with N_2**.**

In general, operation at thermophilic regime was associated to better bioreactor performance than mesophilic regime. Results showed that bioH_2 cumulative production was higher at 55 ºC than at 35 ºC, which may be due to the higher growth of hydrogen consumers and faster metabolic activity of the bacteria reported for the thermophilic range. As Karadag [18] mentioned, comparisons have been made widely in the mesophilic range because less energy is required to take over. On the other hand, Zeidan and van Niel [19] found that thermophilic dark fermentation was more effective than mesophilic, finding yields close to the theoretical yield of 4 mol H_2/mol glucose.

Cumulative P_{H2} (production of H_2) in subsequent incubation cycles in our work were lower than those obtained in the first cycle (Table 1), as expected. The intermittent venting plus one time flushing with inert gas, seemed to avoid the inhibitory effect of high pH_2 (and, likely, it also decreased de CO_2 concentration in biogas, minimizing a possible loss of H_2 via acetogenesis).

The cumulative P_{H2} obtained in our work is low compared with that obtained from the organic fraction of municipal solid waste (*OFMSW*) that was in the range 0.25 to 4.8 mmol H_2/g_{TS} [17, 20-22]. There was preliminary evidence that sodium polyacrylate (*SAP* ; a polymer that is used as urine super absorbent in disposable diapers) could have inhibited to some extent the biohydrogen production. Research is ongoing to overcome this effect and increase the suitability of used disposable diapers as substrate for bioH_2 generation.

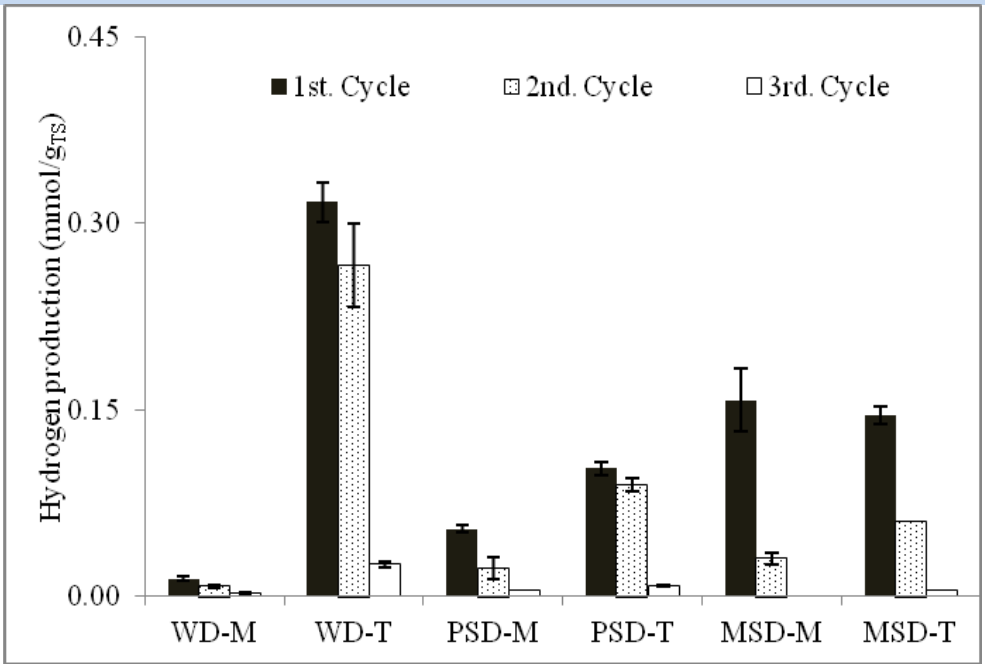

Fig. 2. BioH_2 production per cycle of incubation in batch *SSAFH-IV* of conditioned diapers

A higher cumulative H_2 production at 55 ºC compared with that at 35 ºC could be associated to a lower *ΔpH* (1.4, defined as pH initial-pH final) than *ΔpH* in 35 ºC (2.6, average). The high *ΔpH* (lower final pH) could affect the H_2 producers, since the microorganisms could not adjust to the fast change and possibly a (partial) shift to solventogenesis could have occurred [12, 23].

Acetic acid, propionic acid, butyric acid, lactic acid, acetone, methanol, ethanol and butane were the soluble microbial products detected in this work (Table 2). The ratio A/B is a parameter that may indicate the metabolic pathway favored in the fermentative process, the threshold value of ratio expressed in units of COD-equivalent is 0.79: if the A/B value is less than 0.79 the H_2 production via HBu is probably predominant, therefore if the value *A/B* is high as 0.79 the H_2 production via HAc is probably predominant [20]. In this experiment, the *A/B* ratios in all reactors were lower than the 0.79, and it can be said that the H_2 production via butyric acid was probably predominant.

The statistical analysis of the total production of bioH_2 in the dark fermentation, involving two factors (temperature and diaper conditioning) is presented in Table 3 [24]. The factor 'temperature' had a significant effect (p = 0.06). Indeed, in general, bioH_2 generation at 55ºC was superior to that at 35ºC. Interestingly, the factor 'diaper conditioning' was not significant (p > 0.10). The interaction (Temperature x Diaper conditioning) was mildly significant (p = 0.15).

Figure 3 shows the graph of interaction between the factors involved in the evaluation of hydrogen production indicating that there was an interaction between the two factors**.** The interaction translated in a different trend on P_{H2} with temperature for the *MSD* and *PSD* compared to that of *WD*. In effect, P_{H2} increase at 55ºC of *MSD* and *PSD* compared to

Table 1. BioH_2 from used disposable diapers in each incubation cycle and total biohydrogen production.

Factor		P_{H2} [a]			Total P_{H2} $(\Sigma P_{H2})^{b}_{i=1}^{3}$	Initial pH	Final pH	ΔpH
Conditioning	Temperature (ºC)	1	2	3				
WD	35	0.014±0.014	0.007±0.003	0.003±0.003	0.024±□.009	7.08	4.69	2.39
WD	55	0.32±0.019	0.27□0.01	0.026±0.014	0.609±0.304	7.11	5.76	1.35
PSM	35	0.054±0.055	0.022±0.022	0.004±0.004	0.081±0.002	8.75	5.05	3.70
PSM	55	0.102±0.032	0.089±0.011	0.008±0.005	0.200±0.035	7.08	5.66	1.42
MSD	35	0.16±0.144	0.030±0.03	0.000±0.000	0.188±0.133	7.11	5.40	1.71
MSD	55	0.145±0.004	0.060±0.004	0.005±0.000	0.21±0.046	8.75	7.24	1.51

[a]Net H_2 production average in each incubation cycle (mmoles H_2/g_{TS}), [b] Cumulative sum of H_2 produced in the three incubation cycles, (mmoles H_2/g_{TS}).

Table 2. Profile of cumulative metabolites of bio-hydrogen production with used disposable diapers.

Reactor	Metabolites (mg_{COD}/Kg_{wb})										*A/B*	*ρ*
	HAc	*HPr*	*HBu*	*ΣVOA*	*HLac*	*AcOH*	*MetOH*	*EtOH*	*BuOH*	*Σsolv*		
WD-M	3843	24352	12232	40427	6502	7.20	2182	4183	2580	8952	0.31	4.52
WD-T	201	3366	18502	22069	3305	5.18	1890	4010	3487	9392	0.01	2.35
PSM-M	930	3088	13573	17591	7821	2.45	ND	6540	ND	6542	0.07	2.69
PSM-M	131	2020	12583	14734	1965	1.61	ND	7140	ND	7142	0.01	2.06
MSD-M	2651	6902	37217	46770	872	1.00	800	650	ND	1451	0.07	32.23
MSD-T	135	3221	6703	10059	2469	0.61	893	773	ND	1666	0.02	6.04

HAc: acid acetic; HPr: acid propionic; HBu: acid butyric; HLac: acid lactic; ΣVOA: sum volatile organic acid; AcOH: acetone; MetOH: metanol;, EtOH:ethanol; BuOH: butanol; Σsolv: sum of solvents; A/B: Ratio acetic acid to butyric acid on COD basis; ρ;ΣVOA/Σsolvents factor

Table 3. Analysis of variance for P_{H2}.

Source	Sum of Squares	Degrees of freedom	Mean of the sum of squares	*F*	*p(F)*
MAIN EFFECTS					
A:Temperature	0.264	1	0.264	4.39	0.06
B:Diaper conditioning	0.096	2	0.048	0.80	0.47
INTERACTIONS					
AB	0.271	2	0.135	2.26	0.15
RESIDUAL	0.721	12	0.060		
TOTAL (CORRECTED)	1.353	17			

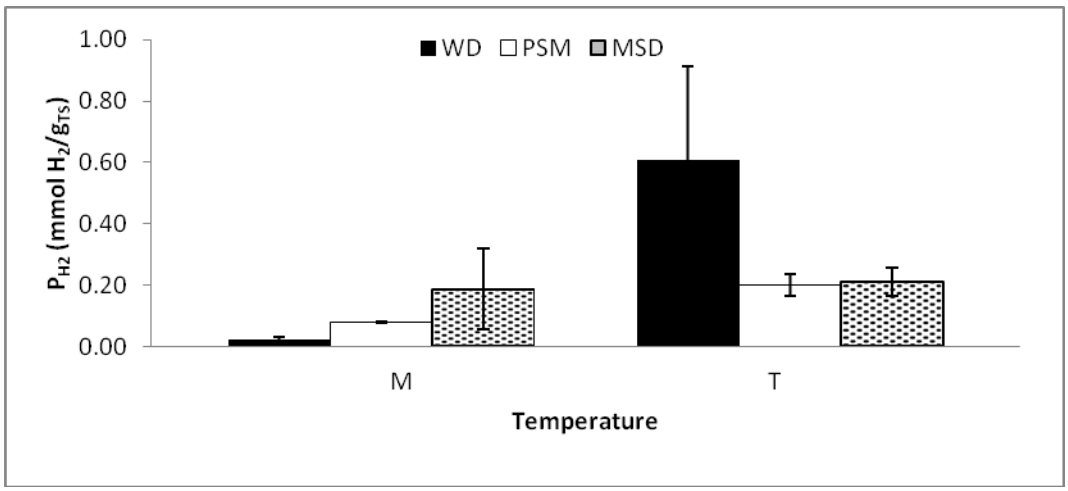

Fig. 3. Interaction between factors 'Temperature' and 'Diaper conditioning' for the response variable cumulative bioH_2 production.

35°C was very low-to-low, whereas the P_{H2} increase with process temperature at 55°C was very drastic (nearly 12-fold).

4. Conclusion

- On the average the cumulative bioH_2 production followed the order *WD* > *MSD* > *PSD*.
- In general, operation at thermophilic regime was associated to higher P_{H2} values than in mesophilic regime.
- There was a mildly significant interaction temperature-diaper conditioning.

Acknowledgements

The authors wish to thank the National Council of Science and Technology (CONACYT) for a graduate scholarship to PXS-N and support to CINVESTAV's infrastructure project 188221 of HMP-V.

References

[1] SEMARNAT, Secretaría de Medio Ambiente y Recursos Naturales. *Diagnóstico básico para la gestión integral de los residuos*, 2012, México, D. F., México.

[2] Espinosa-Valdemar R. M., Turpin-Marion S., Delfín-Alcalá I., Vázquez-Morillas A. Disposable diapers biodegradation by the fungus *Pleurotus ostreatus*. Waste Management, 2011; 31:1683–1688.

[3] Oh, T. K. y Shinogi, Y. Characterization of the pyrolitic solid derived from used disposable diapers. Enviromental Technlogy ,2013. 34:24, 3153-3160.

[4] Torrijos, M., Sousbie, P., Rouez, M., Lemunier, M., Lessard, Y., Galtier, L., Simao, A., Steyer, J. P. Treatment of the biodegradable fraction of used disposable diapers by co-digestion with waste activated sludge. Waste Managemen,t 2014, 34(3):669-675.

[5] Colón, J., Ruggieri, L., Sánchez, A., González, A., Puig, I. Possibilities of composting disposable diapers with municipal solid wastes. Waste Management Research, 2011, 29:249–259.

[6] Das D., Veziroglu T.N. Hydrogen production by biological processes: a survey of literature. Int J. Hydrogen Energy, 2001; 26:13-28.

[7] Valdez-Vázquez I., Poggi-Varaldo, H, M. Hydrogen production by fermentative consortia, Renew. Sustain. Energy. Rev. 2009, 13:1000-1013.

[8] Mizuno O., Dinsdale R., Hawkes F. R., Noike T. Enchancement of hydrogen production from glucose by nitrogen gas sparcing. Bioresour. Technol,. 2002; 73:59-65.

[9] Muñoz-Páez K. M., Ríos-Leal E., Valdez-Vazquez I., Rinderknecht-Seijas N., Poggi-Varaldo H. M. Re-fermentation of washed spent solids from batch hydrogenogenic fermentation for additional production of biohydrogen from the organic fraction of municipal solid waste J. Environ. Manage,. 2012; 95:S355-S359.

[10] Cavinato C., Bolzonella D., Fatone F., Cecchi F., Pavan P. Optimization of two-phase thermofilic anaerobic digestión of biowaste for hydrogen and methane production through reject water recirculaion. Bioresource Technology 2011; 102(8):8605-8611.

[11] Kothari R., Singh D. P., Tyagi V. V. Fermentative hydrogen production an alternative clean energy source. Renewable ans Sustainable Energy Reviews, 2012; 16: 2337-2346.

[12] Muñoz-Páez K. M., Poggi-Varaldo H. M., García-Mena J., Ponce-Noyola M. T., Ramos-Valdivia A . C., Barrera-Cortés J., Robles-González I. V., Ruiz-Ordaz N., Villa-Tanaca L., Rinderknecht-Seijas N. Cheese whey as substrate of batch hydrogen production: Effect of temperature and addition of buffer. Waste Management and Research 2014; 32(5):434-440.

[13] Colón, J., Mestre-Montserrat, M., Puig-Ventosa, I., Sánchez, A. Performance of compostable baby used diapers in the composting process with the organic fraction of municipal solid waste. Waste Management, 2013; 33(5):1097-1103.

[14] Espinosa, V. R. M., Sotelo, N. P. X., Quecholac, P. X., García, R. M. A., Beltrán, V. M., Ojeda, B. S. y Vázquez, M. A. Biological recycling of used baby diapers in a small-scale composting system. Resources, Conservation and Recycling, 2014; 87:153-157.

[15] Sotelo-Navarro, P.X. Composteo de pañales desechables usados mediante biorreactores aerobios y pilas aireadas. Tesis para obtener el título de Maestría. Universidad Autónoma Metropolitana. 2014; México, D. F.

[16] Espinosa, R.M., Delfin-Alcalá, I., Turpin, S., Contreras, J. L. Kinetic study of batch biodegradation of diapers. International Journal of Chemical Reactor Enginnering, 2003;1.

[7]Valdez-Vazquez, I., Sparling, R., Risbey, D., Rinderknecht-Seijas, N. Poggi-Varaldo, H. M. Hydrogen generation via anerobic fermentation of paper mill wastes. Bioresource Technology 2005; 96(17): 1907-1913.

[18] Karagad, D. Anaerobic H_2 production at elevated temperature (60 ºC) by enriched mixed consortia from mesophilic sources. International Journal of Hydrogen Energy 2011; 36: 458-465.
[19] Zeidan, A. A. y van Niel, W. J. A quantitative analysis of hydrogen production efficiency of the extreme thermophile Caldicellulosiruptor owensenses OLT. International Journal of Hydrogen Energy 2010 ; 35 :1128-1137.
[20] Robledo-Narvaez, P.N., Muñoz-Páez, K. M., Poggi-Varaldo, H. M., Ríos-Leal, E., Calva-Calva, G., Ortega-Clemente, L. A., Rinderknecht-Seijas, N., Estrada-Vázquez, C., Ponce-Noyola, M. T., Salazar-Montoya, J. A. The influence of total solids content and initial pH on batch biohydrogen production by solid substrate fermentation of agroindustrial wastes. Journal of Environmental Management, 2013; 128:126–137.
[21] Lee, D.Y., Ebie, Y., Xu, K.Q., Li, Y.Y., Inamori, Y. Continuous H_2 and CH_4 production from high-solid food waste in the two-stage thermophilic fermentation process with the recirculation of digester sludge. Bioresour. Technol. 2010 ;101(1), S42-S47.
[22] Muñoz-Páez, K. M., Ríos-Leal, E., Ponce-Noyola, M. T., Esparza-García, F., García-Mena, J., Poggi-Varaldo, H. M. Hydrogen from fermentation of municipal organic wastes mixed with fruit-juice industry. *Proceedings of the IWA 5th International Symposium on Anaerobic Digestion of Solid Waste and Energy Crops*, Hammament, Tunisia, 2008.
[23] Khanal, S. K., Chen, W. H., Lin, L. y Sung. Biological hydrogen production: effects of pH and intermediate products. International Journal of Hydrogen Energy, 2004 ; 29:1123-1131.
[24] Montgomery, D.. *Design and analysis of experiments*. 1991 3rd edn, John Wiley Inc. New York NY USA.

Notation

A/B	ratio of concentration of acetic acid to butyric acid, on COD basis
F	Fisher statistic
M	mesophilic regime
MSD	manually separated diapers without feces and plastic
OFMSW	organic fraction of municipal solid waste
p(F)	p-value, i.e., the probability of the Fisher statistic in the ANOVA
P_{H2}	production of H2
pH_2	hydrogen partial pressure
PSD	diapers without plastic components
SAP	sodium polyacrylate
SSAHF-IV	solid susbstrate anaerobic hydrogen with intermittent venting
T	thermophilic regime
VOA	volatile organic acids, i.e., low molecular weight organic acids
WD	whole diapers

Greek characters

ΔpH	difference between initial pH and final pH in batch bioreactors
ρ	$\Sigma VOA/\Sigma solvents$

Chapter 1.11. Hydrogenation and dehydrogenation reactions at air-exposed Mg-Fe mixtures

K. Suárez-Alcántara[a]*; J. A. Palacios[b]; T. Funatsu[c]; G. Cabañas-Moreno[d]

[a] Unidad Morelia del Instituto de Investigaciones en Materiales de la Universidad Nacional Autónoma de México, Antigua carretera a Pátzcuaro 8701, Col. Ex-hacienda de San José de la Huerta, Morelia, Michoacán, 58190, México.
[b] ESIME Zacatenco, Av. Luis Enrique Erro S/N, Unidad Profesional Adolfo López Mateos, Zacatenco, Delegación Gustavo A. Madero, Distrito Federal, 07738, México.
[c] Techno System CO., LTD, Karasakinaka 3-1-1, Takatsuki-City, Osaka, Japan.
[d] Centro de Investigación y de Estudios Avanzados, IPN, Av. Instituto Politécnico Nacional 2508, México, D. F., 07360, México.

ABSTRACT

The hydrogenation and dehydrogenation reactions at 12-hours air-exposed Mg-Fe(3wt.%) and Mg-Fe(6wt.%) mixtures were studied and compared to air-exposed Mg. Powder X-ray diffraction of the studied materials confirmed the formation by ball milling of fine mixtures. No evidence of formation of Mg-Fe alloys or Mg_2FeH_6 (after hydriding) was found. Evidence of a relationship between MgO formation and crystallization after air-exposure and hydrogen annealing respectively with Fe content was found. The hydrogen uptake was 5.4 wt. %, 5.6 wt. % and 6.2 wt. % for air-exposed Mg, Mg-Fe(3wt.%) and Mg-Fe(6wt.%) mixtures respectively. Fe addition had a beneficial influence on the kinetics and the hydrogen uptake/ release compared to air-exposed Mg. From Pressure- Composition Temperature curves (PCT) the enthalpy and entropy of hydrogenation of air exposed Mg-Fe mixtures did not differ from Mg-reported data. Thus Fe had not influence on hydrogenation/dehydrogenation thermodynamics.

Keywords: Hydrogen storage, Air exposed magnesium, Mg-Fe mixtures

1. Introduction

Hydrogen is a promising alternative to fossil fuels, however for a practical application it is necessary to develop large-scale production systems of materials for the H_2 production-use and storage chain. Among this three basic research topics of the “hydrogen economy”, the H_2 storage materials is not well-developed. Still the “perfect” H_2 storage material must be developed. On the road for that “perfect” H_2 storage material, Mg/MgH_2 and its alloys have been extensively studied [i-4].

---

* Author for correspondence:
Dr. Karina Suárez Alcántara, +52 56237300 ext 80548, karina_suarez@iim.unam.mx

However, it is agreed that Mg/MgH_2 is not suitable for mobile or demanding applications due to its high dehydriding temperature, relatively low hydriding/dehydriding kinetics and not enough energy storage density. Niche applications where neither the working temperature nor weight/volume restrictions arise, are still possible; for example heat storage or stationary applications [ii]. Fe have been reported as a suitable additive for improving hydriding/dehydriding kinetics, for example at the $2LiBH_4/ MgH_2$ system [iii]; also Fe is a common contamination of the ball milling process when Fe-milling vials or balls are used [iv, v, vi]. In the present work, the hydriding and dehydriding reactions at two Mg-Fe mixtures are presented.

The large-scale production systems of hydrogen storage materials must be efficient, cheap and environmentally friendly. An important weakness of any intended large-scale production will be the high cost of preparation, management and storage of hydrogen storage materials under high purity argon atmosphere. This weakness is common to all hydrogen storage materials based on metal hydrides that are sensible to oxygen and air-moisture. The formation of an oxide layer (i.e. MgO over Mg) have been recognized to decrease the diffusion of atomic hydrogen and to diminish the hydrogen storage capacity [vii]. In contrast, several oxides of transition metals, included MgO itself [viii], had been found beneficial in the hydrogenation kinetics of Mg [ix, x]. Recently, it was demonstrated the possibility of hydrogen storage in Mg-Li alloys that have been intentionally exposed to air [xi]. In the present work we propose the production of Mg-Fe mixtures, their intentional air-exposure and finally demonstrate the hydriding/dehydriding reactions.

2. Materials and Methods

2.1 Materials preparation

Mg-Fe mixtures were prepared by ball milling in two different proportions: 3 wt.% and 6 wt. % of Fe respectively. Hereafter they will be nicknamed Mg-Fe(3wt.%) and Mg-Fe(6wt.%). Raw metals Mg and Fe (99.8% purity, Alfa Aesar) were stored in an argon-filled glove box until mixture preparation. Each milling batch consisted of 30 grams of metals and 3 mL of methanol as milling control agent. The ball to powder ratio was 11:1. Milling vial and balls were made of hardened steel. Sample preparation was performed without air or moisture protection; then the (open) milling vial with metals, methanol and balls were introduced in an argon-filled glove box. The milling vial was then closed in Argon atmosphere. The ball milling was performed in a planetary mill (Fritsch Pulverisette 6) at 350 rpm. The total effective milling time was 60 hours in 40 cycles of 1.5 hours of milling and 0.5 hours pause. After milling, the vial was cooled down to room temperature; then the vial lid was opened and the as-milled powders were gradually exposed to the air for 12 hours. As-milled powders were collected and stored in argon atmosphere to avoid further oxidation during storage. Posterior handling and characterization of materials were performed at air.

A sample of Mg was prepared with the same procedure as Mg-Fe mixtures, i.e. exposed to air for 12 hours. The characterization of the air-exposed Mg is presented for comparison whenever necessary.

2.2 Hydrogenation/ dehydrogenation cycling and Pressure-Composition-Temperature (PCT) data collection

Hydrogen storage properties were tested on a carefully calibrated gravimetric equipment (PCTM-6000 Techno Systems CO., LTD). A sample of about 3 grams of each Mg-Fe mixture and Mg was used for hydrogenation/ dehydrogenation reactions characterization. The weighting of the samples and transfer to the PCTM-6000 equipment was performed without air protection devices, i.e. globe bags. Once the samples were in place at the PCTM-6000 sample-chamber and sealed; they were pre-treated by vacuum pumping for 30 minutes, then a temperature of 350°C was settled while continuing vacuum (30 minutes heating time). Only when reaching the isothermal condition the hydrogen gas pressure was increased.

Hydrogenations were performed at 30 bar hydrogen pressure. Dehydrogenations were performed by reducing the hydrogen pressure to 0.1 bar. The hydrogenation/ dehydrogenation cycles were performed in a time-programmed way. For the hydrogenation, the hydrogen pressure was increased from 0.1 bar to 30 bar during 5 minutes and then the pressure was held at 30 bar for 55 minutes. The dehydrogenation was carried out by decreasing the hydrogen pressure from 30 bar to 0.1 bar during 5 minutes, then the pressure was held at 0.1 bar for 55 minutes. Three hydrogenation/ dehydrogenation cycles were performed; at the Results section it is always reported the 3rd cycle. Then, a temperature of 300°C was settled and the hydrogenation/ dehydrogenation three-cycling was performed. After that, a temperature of 250°C was fixed and three hydrogenation/dehydrogenation cycles were done. In case that any dehydrogenation was not completed in the fixed time, particularly at 250°C, the dehydrogenation was forced by heating up to 350°C for 30 minutes, and then decreasing again the temperature. A sample of Mg was pre-treated in the same way as the Mg-Fe mixtures. However cycling time-window was opened to 2.5 hours of hydrogenation and 2.5 hour dehydrogenation.

Pressure-Composition-Isothermal (PCT) curves were measured at 350°C and 300°C after all cycling for the air-exposed Mg-Fe mixtures. Each PCT curve (complete hydrogenation and dehydrogenation reactions) data collection lasted 1 week. Pressure was gradually increased or reduced in a programmed way, provided a “stability” condition was achieved. This stability condition means no change in the registered weight in a selected number of measured-points, here 0.1 mg in 60 measured-points.

Finally to perform the physical characterization at the hydrogenated state, the samples were heated to 350°C and 30 bar hydrogen pressure for 1 hour.

2.*3 Physical characterization*

The morphology of as-prepared mixtures and the hydrogenated materials was analyzed in a scanning electron microscope (SEM, XL/SFEG/SIRION, FEI Company). Samples were dispersed on carbon tape and transferred to the SEM-chamber. Crystal structure identification was performed on a diffractometer model SIEMENS D-500, at monochromatic CuKα1 radiation (λ = 1.54056Å). The X-ray diffraction patterns (XRD) were taken at the range from 15° to 80° in 2θ, at a step of 0.03° and 5 seconds per step. XRD patterns were analyzed by help of the MAUD software and the crystal data available at the ICSD (Inorganic Crystal Structure Database- Karlsruhe) or at the COD (Crystallography Open Database). Rietveld analysis were performed with the MAUD Software in the whole range of 2θ, i.e from 15° to 80°.

3. Results and Discussion

3.1 SEM and DRX characterization of as-milled and air-exposed materials

Figure 1 presents the SEM image of as-milled Mg-Fe(3wt.%). Images of the as-milled Mg and Mg-Fe(6wt.%) materials are available at the supplementary material. The Ball-milling process produced Mg-Fe particles between 1 and 50 μm, with a large number of particles around 10 μm size. The irregular morphology was a common characteristic of Mg, Mg-Fe(3wt.%) and Mg-Fe(6wt.%) samples produced by ball milling. Particle surface shows stacked material in agreement with cold-wedding of materials during ball milling.

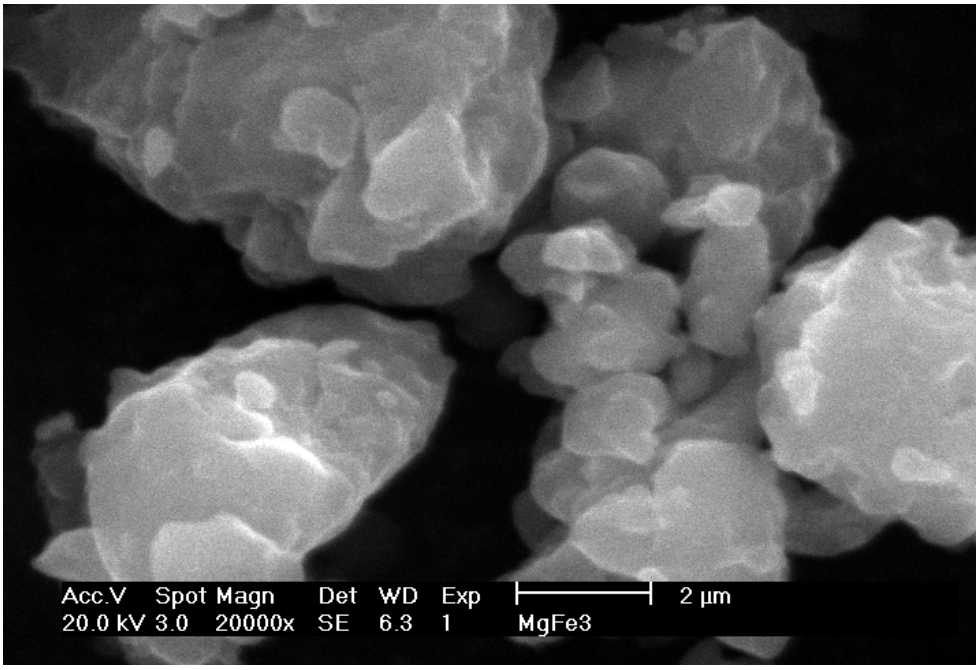

Fig. 1. Electron microscope micrographs of as prepared materials of Mg-Fe(3wt.%).

XRD of the as-milled and air-exposed materials are presented in Figure 2. The diffractograms present the characteristic Mg peaks in addition to Fe peaks. No Mg-Fe alloys were found. Thus the prepared materials are fine mixtures of Mg and Fe. Despite the expected oxide formation by the 12 hours of air-exposure, neither magnesium oxides nor iron oxides were evident at the diffractograms. This is re-taken at the Discussion section. Table 1 shows the cell lattice and the refined crystal size. The Mg cell lattice was essentially not modified by the ball milling or the Fe addition. The crystal size of Mg ranges approximately 300-400 Å. The crystal size of Fe appears to be dependent on the quantity of Fe in the sample.

Table 1. Refined cell lattice and crystal size of as-milled materials.

Material	Cell Lattice [Å]	Refined crystal size [Å]
	Mg: a=3.20944 Å (ICSD 642651), c= 5.21076 Å	
	Fe: a=2.869 Å (ICSD 180969)	
Mg	Mg: a= 3.212(4); c= 5.21535)	Mg: 355 ± 3
Mg-Fe(3wt.%)	Mg: a= 3.212(2); c= 5.216(4)	Mg: 299 ± 2
	Fe: a= 2.869(3)	Fe: 354 ± 16
Mg-Fe(6wt.%)	Mg: a=3.203(1); c= 5.200(4)	Mg: 407 ± 7
	Fe: a=2.862(2)	Fe: 1000 ± 59

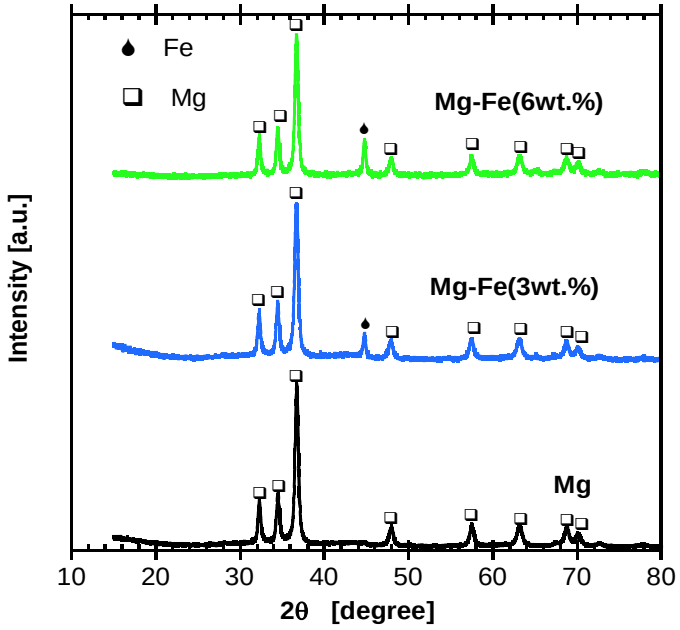

Fig. 2. Powder X-ray diffraction patterns of as prepared (milled and air-exposed) Mg, Mg-Fe(3wt.%) and Mg-Fe(6wt.%) mixtures.

3.2 Hydrogenation/ dehydrogenation cycling results

Figure 3 presents the hydrogenation/ dehydrogenation cycling of Mg-Fe(3wt.%) mixture at 350°C, 300°C and 250°C. The maximum hydrogen uptake of 5.6 wt.% was achieved at 350°C. Released hydrogen accounted for 5.4 wt. % at 350°C. Hydrogenation/ dehydrogenation reactions were completed in 10 minutes at this temperature. At 300°C the hydrogen uptake was finished in 30 minutes reaching 5.4 wt.% of hydrogen uptake; meanwhile dehydrogenation reaction was slower achieving only 4.8 wt.% of hydrogen releasing. The hydrogenation/ dehydrogenation reactions at 250°C were not completed in the programmed time. The hydrogen uptake was 4.8 wt.%, meanwhile only 1.1 wt. % hydrogen was desorbed both in one hour time. The hydrogen uptake/ release and the hydrogenation kinetics correspond well with the temperature, i.e. higher temperature, higher kinetics and hydrogen uptake.

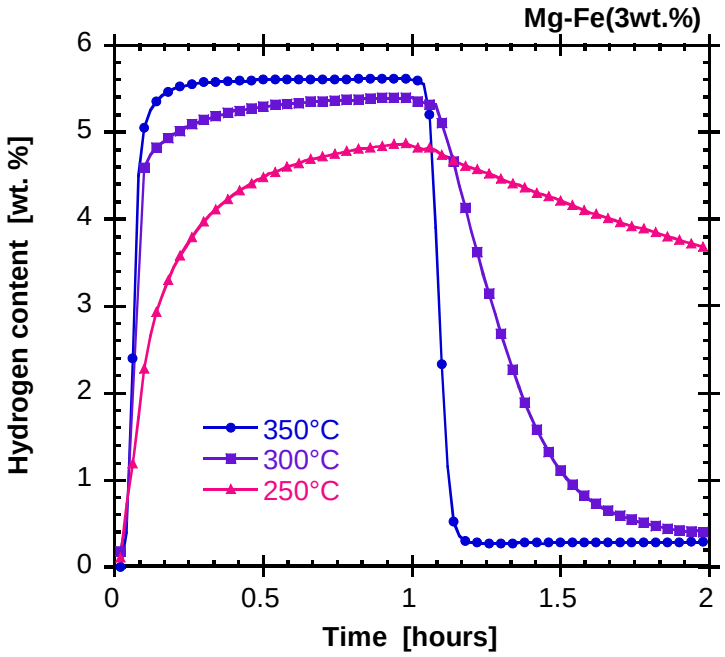

Fig. 3. Hydrogenation / dehydrogenation cycles of the Mg-Fe(3wt.%) mixture (ball milled and air-exposed). Hydrogenation 30 bar, dehydrogenation 0.1 bar.

Figure 4 presents the hydrogenation and dehydrogenation cycles for the mixture Mg-Fe(6wt.%). In this mixture the maximum hydrogen uptake was 6.2 wt. % at 350°C. This indicates an increase in the hydrogen uptake with an increase in the Fe content as compared with Mg-Fe(3wt.%). The maximum hydrogen uptake at 300°C was 5.8 wt.%. Hydrogenation reactions were mostly completed in 10 minutes at 350°C and 300°C. At 250°C, the hydrogen uptake was 5.0 wt.% and the kinetics was remarkable slower compared with the experiments at higher temperatures.

Other observed effects of Fe addition were the improvement of the dehydrogenation kinetics and of the total released hydrogen. At 350°C and 300°C the fast part of the hydrogenation reaction lasted about 10 minutes, at 200°C it was about 30 minutes. Dehydrogenation reaction was well completed at 350°C and 300°C. Within 1 hour dehydrogenation at 250°C, the mixture Mg-Fe(6wt.%) released 2.9 wt. %.

Figure 5 presents the hydrogenation/ dehydrogenation cycles of air-exposed Mg. Hydrogen uptake at 350°C was about 5.4 wt.% after 2.5 hours reaction. Dehydrogenation reaction was slow, it was completed after 1 hour reaction. Hydrogenation at 300°C followed practically the same kinetics that at 350°C, however dehydrogenation was not completed within 2.5 fixed reaction test-time; only about 1 wt.% hydrogen was released. No hydrogenation/ dehydrogenation reactions were obtained at the air-exposed Mg at 250°C. Thus a clear beneficial effect of Fe addition was found. Table 2 resumes the data of hydrogen uptake at Mg-Fe mixtures and Mg.

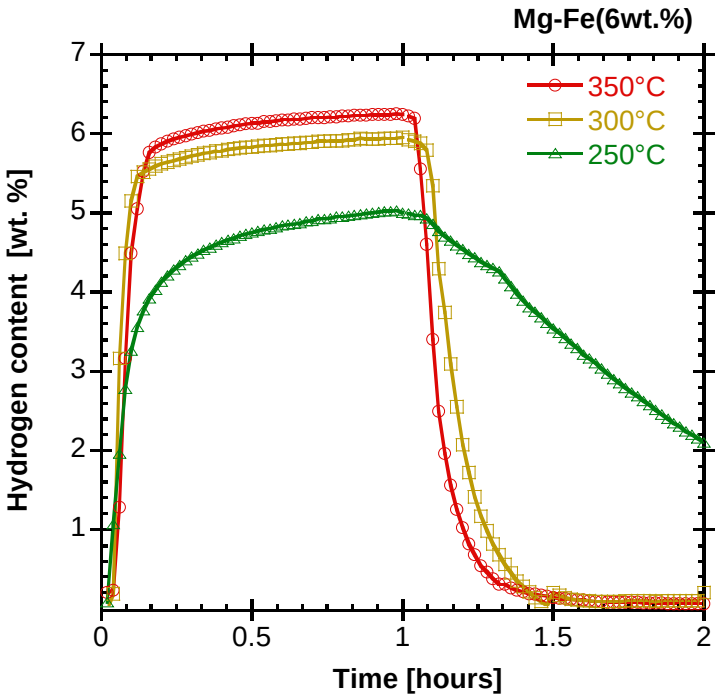

Fig. 4. Hydrogenation / dehydrogenation cycles of the Mg-Fe(6wt.%) mixture (ball milled and air-exposed). Hydrogenation 30 bar, dehydrogenation 0.1 bar.

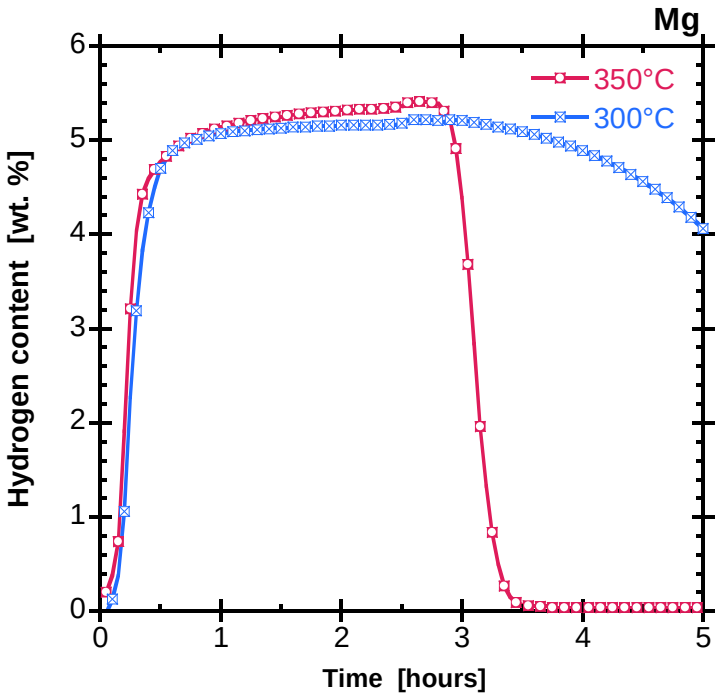

Fig. 5. Hydrogenation / dehydrogenation cycles of the Mg (ball milled and air-exposed). Hydrogenation 30 bar, dehydrogenation 0.1 bar.

Table 2. Hydrogen uptake/release data of air-exposed Mg, Mg-Fe(3wt.%) and Mg-Fe(6wt.%).

Material	Hydrogen uptake [wt.%]	Hydrogen release [wt.%]
Mg	250°C: No reaction	250°C: No reaction
	300°C: 5.0	300°C: 1.0
	350°C: 5.4	350°C: 5.4
Mg-Fe(3wt.%)	250°C: 4.8	250°C: 1.1
	300°C: 5.4	300°C: 5.0
	350°C: 5.6	350°C: 5.3
Mg-Fe(6wt.%)	250°C: 5.0	250°C: 2.9
	300°C: 5.8	300°C: 5.8
	350°C: 6.2	350°C: 6.2

3.3 Pressure-Composition-Temperature (PCT) data collection

Figure 6 and Figure 7 present the PCT curves of Mg-Fe(3wt.%) and Mg-Fe(6wt.%) mixtures at 350°C and 300°C. The hydrogen uptake and release were the same as obtained in the hydrogenation and dehydrogenation cycle reactions. Even more, the PCT curves at Figures 6 and 7 demonstrate that the hydrogen release can be possible at 1 bar, although in the present work 0.1 bar hydrogen pressure was used.

In a related study of air-exposed Mg-Li alloys [14]; PCT of Mg at 350°C showed a huge hysteresis (more than ten-fold H_2-pressure) between the hydrogenation and dehydrogenation reaction. At the Mg-Fe(3wt.%) and Mg-Fe(6wt.%) mixtures, there was an appreciable hysteresis between hydrogenation and dehydrogenation isotherms. However, PCT plots of Figures 6 and 7 reveal that the hysteresis was significantly reduced by the Fe incorporation to Mg. Despite only two PCT experiments at different temperatures (350°C and 300°C) were performed on Mg-Fe mixtures, the reaction enthalpy and entropy was obtained with the van´t Hoff relationship [xii]:

$$\ln(p_{H_2}) = \frac{\Delta H}{RT} - \frac{\Delta S}{R} \qquad (1)$$

The enthalpy and entropy values were basically the same for both Mg-Fe mixtures. For the hydrogenation reactions, the values: ΔH_{abs} = -62 kJ mol $^{-1}$ H_2 and ΔS_{abs} = -117 J K $^{-1}$ mol $^{-1}$ H_2 were obtained. For the dehydrogenation reactions the values were: ΔH_{des} = -74 kJ mol $^{-1}$ H_2 and ΔS_{des} = -130 J K $^{-1}$ mol $^{-1}$ H_2. The enthalpy and entropy values are consistent with values reported for Mg/ MgH_2 system [15]. These data indicate rather a kinetic effect than a thermodynamic effect by the addition of Fe to Mg.

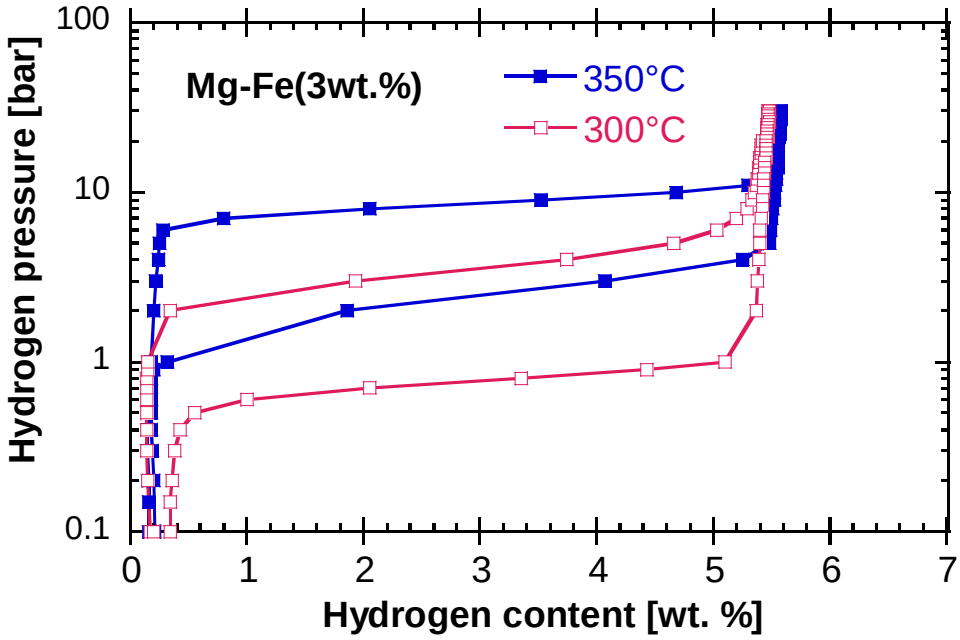

Fig. 6. PCT diagram of Mg-Fe(3wt.%) mixture.

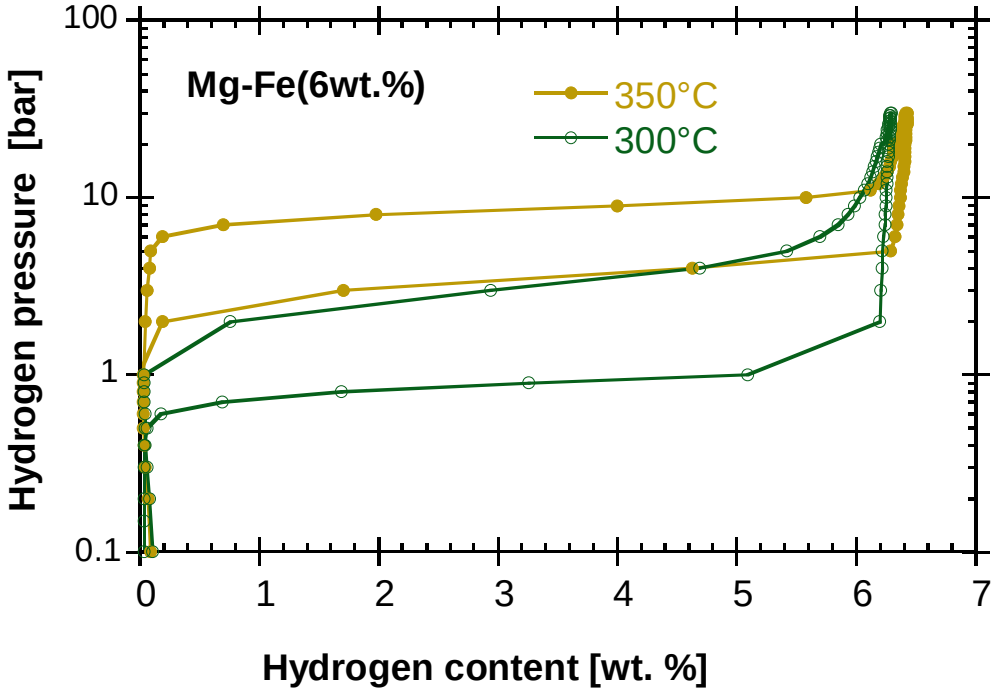

Fig. 7. PCT diagram of Mg-Fe(6wt.%) mixture.

3.4 SEM and DRX characterization of hydrogenated materials results

Figure 8 presents the SEM image of hydrogenated Mg-Fe(3wt.%). Interestingly, it was observed the formation of globular nodules all over the particle surface. After heat pre-treatment and hydrogenation/ dehydrogenation cycles, particle sizes do not experiment significant changes. The particle size ranged between 1 and 50 μm, with a large number of particles around 10 μm size. SEM images of hydrogenated Mg and Mg-Fe(6wt.%) are similar to Mg-Fe(3wt.%) SEM images and can be found in the supplementary material.

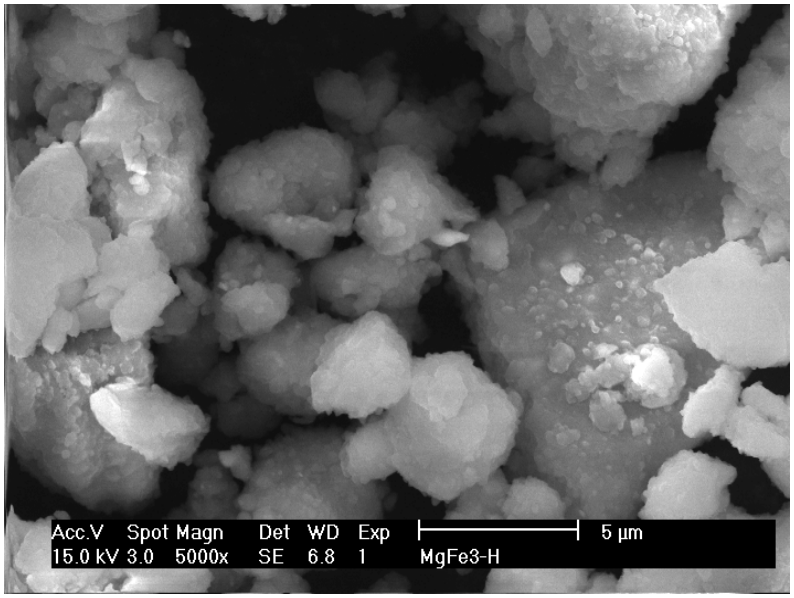

Fig. 8. Electron microscope micrographs of hydrogenated Mg-Fe(3wt.%).

Figure 9 presents the XRD patterns of hydrogenated materials; the main phases are MgH_2, unreacted Mg, Fe and MgO. The MgO was expected to form after the 12-hours of air exposure as an amorphous layer. Also as expected, only after heat treatment the MgO crystalized and become evident at RXD experiments. Table 3 presents the relevant-Rietveld refined data of hydrogenated materials. Cell lattices of MgH_2, MgO and Fe were not presented in Table 3; their values were in agreement with the reported data at ICSD or COD crystallographic databases. Thus no change in the crystallographic parameters were generated by heat pre-treatment and hydrogenation/ dehydrogenation reactions. On the other hand, MgO crystal size and content at the sample seems to have a direct relationship to the Fe addition level. MgO content was reduced from 31.8 wt.% to 5.5 wt.% by the addition of Fe. Additionally, the MgO crystal size was progressive increasing with the Fe content.

Table 3. Rietveld analysis of hydrogenated materials.

Material	MgO content [wt.%]	MgO crystal size [Å]	MgH_2 crystal size [Å]	Fe crystal size [Å]
Mg	31.8 ± 0.4	36.5 ± 0.6	251.3 ± 0.8	---
Mg-Fe(3wt.%)	23.5 ± 0.4	47.6 ± 0.9	252.6 ± 0.9	603.0 ± 17.1
Mg-Fe(6wt.%)	5.5 ± 0.6	114.3 ± 24.5	391.9 ± 5.3	754.0 ± 48.7

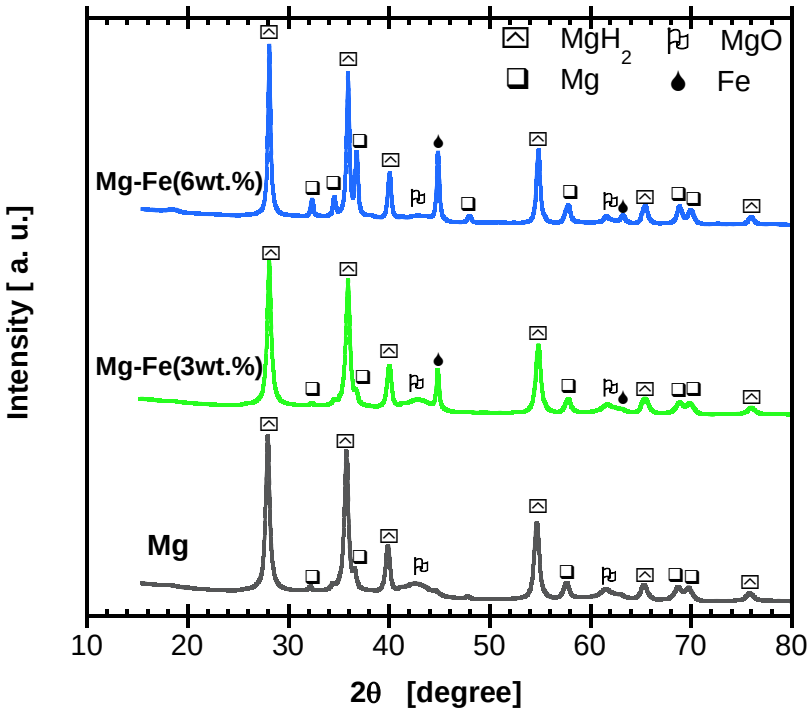

Fig. 9. Powder X-ray diffraction patterns of hydrogenated Mg, Mg-Fe(3wt.%) and Mg-Fe(6wt.%) mixtures.

3.5 Discussion

3.5.1 The Fe effect.

The observed effects of Fe addition were an increase of the hydrogen uptake, release, and in general, an improvement of hydrogenation/ dehydrogenation kinetics; even if the samples were exposed to the air. Similar results have been reported for Mg materials that were carefully protected against air-exposure. Amirkhiz et al [xiii] reported a beneficial effect of Fe and Fe-Ti addition to Mg (handled in high purity Argon) for dehydrogenation reaction at 250°C. Amirkhiz suggests that nucleation sites are formed at the interface of the catalyst Fe and MgH_2 particles [16]. Barkhordarian et al suggest that a metal-support interaction, i.e. metal catalyst and oxide support can influence the catalytic activity [xiv]. Both effects can be present in the studied materials, particularly at Mg-Fe(6wt.%) where the MgO was in less quantity and bigger nanocrystals interacting with Fe; producing

simultaneously an adequate nucleation site and leaving Mg/MgH_2 clear areas for the hydrogenation/dehydrogenation reactions. Fe/MgO interaction can be the responsible of the hydrogen uptake and release observed at Mg-Fe(6wt.%).

3.5.2 The air-exposure effect.

It was expected the formation of an oxide layer after air-exposure. The major negative effects of MgO layer are recognized as the reduction of the hydrogen uptake capacity and slow reaction kinetics [xv] by blocking active sites and reducing hydrogen diffusion. However, XRD of as-milled and air-exposed materials did not bring evidence of the presence of that layer. After heat pre-treatment, hydrogenation/ dehydrogenation cycles and PCT data collection, it was observed the crystallization of that layer. The kinetics of MgO growing over Mg is well-known [xvi, xvii]; a MgO film grows rapidly up to some critical thickness and then stops. The critical thickness is dependent on temperature [19, 20]. In the Mg and Mg-Fe mixtures the MgO amorphous layer was formed at room temperature and modified by the almost 3 weeks of heating and successive hydrogen exposure and vacuum. Friedrichs et al have proposed that that the MgO formed on top of MgH_2 is active by the formation of oxygen vacancies during hydrogen exposure and heating [xviii]. At our samples, the negative effects of MgO formation were surpassed by the changes at the MgO due to pre-treatment, successive cycling and proper interaction Fe/MgO.

4. Conclusion

Mg-Fe(3wt.%) and Mg-Fe(6wt.%) mixtures were prepared by ball milling, exposed to air for 12 hours and tested for hydrogen storage capabilities. It was observed a negative effect by the MgO formation surpassed by the addition of Fe; a proper Fe/MgO interaction can be responsible of the hydrogen uptake/ release characteristics. It was demonstrated that between 5.6 wt.% and 6.2 wt.% of hydrogen storage is feasible in an experimental range of 250°C-350°C at air-exposed Mg-Fe mixtures.

Acknowledgements

The present work was supported by the PAPIIT-UNAM project IA100415. KSA wants to thank to*"Red temática del hidrógeno CONACyT-252003, subprograma para el desarrollo del almacenamiento de hidrógeno"* for the mobility grant.

References

[1] Jia Y., Sun C., Shen S., Zou J., Mao S.S., Yao X. Combination of nanosizing and interfacial effect: Future perspective for designing Mg-based nanomaterials for hydrogen storage. Renewable and Sustainable Energy Reviews 2015; 44: 289–303.

[1] Felderhoff M., Bogdanović B. High Temperature Metal Hydrides as Heat Storage Materials for Solar and Related Applications. Int. J. Mol. Sci. 2009;10:325-344.

[1] Puszkiel J.A., Gennari F.C., Arneodo Larochette P., Ramallo-Lopez J.M., Vainio U., Karimi F., Pranzas P.K., Troiani H., Pistidda C., Jepsen J., Tolkiehn M., Welter E., Klassen T., Bellosta von Colbe J., Dornheim M. Effect of Fe additive on the hydrogenation-dehydrogenation properties of 2LiH + MgB_2/2$LiBH_4$ + MgH_2 system. J. of Power Sources 2015; 284: 606-616.

[1] Suryanarayana C. Mechanical alloying and milling. Progress in Materials Science. 2001; 46: 1-184.

[1] Baum L., Meyer M., Mendoza-Zélis L. Hydrogen storage properties of the Mg/Fe system. Physica B 2007; 389: 189-192.
[1] Zhou D.W., Li S.L., Varin R.A., Peng P., Liu J.S., Yang F. Mechanical alloying and electronic simulations of 2Mg–Fe mixture powders for hydrogen storage. Materials Science and Engineering A 2006; 427: 306-315.
[1] Ostenfeld C.W., Johansson M., Chorkendorff I. Hydrogenation properties of catalyzed and non-catalyzed magnesium films. Surface Science 2007; 601: 1862-1869.
[1] Borgschulte A., Bielmann M., Züttel A., Barkhordarian G., Dornheim M., Bormann R. Hydrogen dissociation on oxide covered MgH_2 by catalytically active vacancies. Applied Surface Science 2008; 254: 2377-2384.
[1] Barkhordarian G., Klassen T., Bormann R. Effect of Nb_2O_5 content on hydrogen reaction kinetics of Mg. Journal of Alloys and Compounds 2004; 364: 242- 246.
[1] Barkhordarian G., Klassen T., Bormann R. Fast hydrogen sorption kinetics of nanocrystalline Mg using Nb_2O_5 as catalyst. Scripta Materialia 2003; 49: 213-217.
[1] Suarez-Alcantara K., Palacios-Lazcano A.F., Funatsu T., Cabañas-Moreno J.G. Mg-M-LiH alloys prepared by mechanical milling and their hydrogen storage characteristics. Int. J. of Hydrogen Energy 2015; *in press*.
[1] Bogdanovic B., Bohmhammel K., Christ B., Reiser A., Schlichte K., Vehlen R., Wolf U. Thermodynamic investigation of the magnesium–hydrogen system. J. Alloys and Compounds 1999; 282: 84-92.
[1] Amirkhiz B.S., Zahiri B., Kalisvaart P., Mitlin D. Synergy of elemental Fe and Ti promoting low temperature hydrogen sorption cycling of magnesium. Int. J. of Hydrogen Energy 2011; 36: 6711 -6722.
[1] Barkhordarian G., Klassen T., Bormann R. Catalytic Mechanism of Transition-Metal Compounds on Mg Hydrogen Sorption Reaction. J. Phys. Chem. B 2006; 110: 11020-11024
[1] Jensen T.R., Andreasen A., Vegge T., Andreasen J.W., Stahl K., Pedersen A.S., Nielsen M.M., Molenbroek A.M., Besenbacherh F. Dehydrogenation kinetics of pure and nickel-doped magnesium hydride investigated by in situ time-resolved powder X-ray diffraction. Int. J. of Hydrogen Energy 2006; 31: 2052 – 2062.
[1] Do T., Splinter S.J., Chen C., McIntyre N.S. Measurement of oxide film growth on Mg and A1 surfaces over extended periods using XPS. Surface Science 1997; 387: 192-198.
[1] Chen C., Splinter S.J., Do T., Mclntyre N.S. The oxidation kinetics of Mg and A1 surfaces studied by AES and XPS. Surface Science 1997; 382: L652 L657.
[1] Friedrichs O., Sanchez-Lopez J.C., Lopez-Cartes C., Klassen T., Bormann R., Fernandez A. Nb_2O_5 "Pathway effect" on hydrogen sorption in Mg. J. Phys. Chem. B 2006;110:7845-7850.

Chapter 1.12. $W_{1-x}Mo_xO_3*0.33H_2O$ Compounds Synthetized by Hydrothermal and Microwave-radiation for H_2 Production

A. Arzola-Rubio; J. Camarillo-Cisneros; V. Collins-Martínez*

Centro de Investigación en Materiales Avanzados S. C., Miguel de Cervantes 120, C. P. 31136, Chihuahua, Chih. México

ABSTRACT

WO_3 has been thoroughly investigated and optimized to deliver high single wavelength quantum efficiencies. Unfortunately the stability of this oxide in aqueous environments, aided by an energetically low valence band which is defined largely by O 2p energy levels, also brings a large band gap which renders these materials transparent to most of the incident solar illumination. A series of hydrated Tungsten-Molybdenum oxides have been synthesized by hydrothermal and microwave radiation techniques. In both cases the $WO_3 \cdot 0.33H_2O$ crystal lattice can be substituted with up to 75% Mo without structural alterations of the orthorhombic host structure. These products have a band gap suited at the visible range (~2.00 eV). Experimental data were explained by means of first-principle calculations in the framework of DFT and DFT+U; indirect semiconductors were obtained. Both compounds were evaluated for H_2 production.

Keywords: H_2 generation; water splitting; photocatalysis; tungstates

1. Introduction

Hydrogen is considered as an ideal energetic vector for the future. Hydrogen fuel can be produced from clean and renewable energy sources and, thus, its life cycle is clean and renewable. Solar and wind are the two major sources of renewable energy and they are also the promising sources for renewable hydrogen production. However, presently, renewable energy contributes only about 5% of the commercial hydrogen production primarily via water electrolysis, while other 95% hydrogen is mainly derived from fossil fuels [1]. Renewable hydrogen production is not popular yet because the cost is still high.

Photovoltaic water electrolysis may become more competitive as the cost continues to decrease with the technology advancement; however, the considerable use of small band gap semiconducting materials may cause serious life cycle environmental impacts.

---

* Author for correspondence: V. Collins Martinez, T: +526144391129; E: virginia.collins@cimav.edu.mx

Alternatively, photocatalytic water-splitting using unary and binary WO_3 compounds for hydrogen production offers a promising way for clean, low-cost and environmentally friendly production of hydrogen by solar energy. WO_3 compounds can be used for photocatalytic water splitting to produce hydrogen gas using visible solar light, because of its narrow bandgap. Earlier studies of the photo electrochemical behavior of both polycrystalline and monocrystalline WO_3 provided instructive knowledge for the development of photocatalytic water-splitting systems [2, 3]. The difficulty in the overall water splitting (both reduction and oxidation of H_20 molecules are to be achieved) by WO_3 is that the lower edge of the CB lies below the redox potential of H_20/H_2. This means that the reduction of water molecules to generate hydrogen gas is thermodynamically unfavorable [4]. Applying a bias potential to the system can overcome the energy barrier for the photogenerated electrons to be ejected into the adsorbed water molecules [5]. Coupling with other semiconductor materials [6] and doping by metal ions [7] are other alternatives to make use of the oxidation power of WO_3 for water splitting. WO_3 also found interesting applications in electrochromic [8] and photochromic [9] devices such as large area displays and "smart windows" because WO_3 films can be switched between different optical states under different electro-chemical or optical conditions. The electrochromic effect is caused by the electrochemical reaction between the WO_3 electrode and protons in the electrolyte solution, under the influence of a bias potential to provide charge carriers (electrons in this case). The electrons can then create color centers by reducing the W^{6+} species to W^{5+} species. The photochromism effect of WO_3 is due to the formation of an identical absorption band upon light irradiation. This process is completely reversible by exposing the reduced sample to oxygen gas. DFT has been a handy tool to corroborate gap experimental data and also as a method itself to use in simulate tendencies. Recently, Zhou et al., [10] was capable of modulate the band gaps of the $W_{1-x}Mo_xO_3$ materials by changing the Mo/W ratio. They successfully prepared a series of $W_{1-x}Mo_xO_3*0.33H_2O$ micro/nanostructures with controlled stoichiometry (x = 0, 0.25, 0.50, 0.75). They stated that the increase of the Mo content, the band gap of $W_{1-x}Mo_xO_3*0.33H_2O$ narrowed from 3.25 to 2.77 eV.

In this work we synthetized a series of $W_{1-x}Mo_xO_3*0.33H_2O$ nano/microstructures similar to Zhou et al. [10] from other precursors such as ammonium heptamolybdate and ammonium metatungstate instead of metal powders. We used 2.2M HNO_3 to acidify the solutions instead of forming the peroxopolytungstic and molybdic acid solutions. Our primary objective was to study their enhanced band gaps as a function of the Mo content and its capability of photocatalytically hydrogen production.

2. Experimental

For a usual synthesis, y mmol (y = 0, 2.5, 5.0, 7.5, and 10.0) of Ammonium heptamolybdate tetrahydrate and (10 - y) mmol of Ammonium metatungstate hydrate were dissolved in a mixture of 21 mL of H_2O, 9 mL of 30 wt.% H_2O_2 , and 3 mL of 2.2M HNO_3. The solution was then transferred into a Teflon vial then placed in a stainless-steel autoclave and, sealed, and hydrothermally treated at 180°C for 24 h. The solid solutions were collected by centrifugation, washed with deionized water 3 times, and dried at room

temperature. For the microwave synthesis, the reactants are the same just the quantities vary. There were dissolved in a mixture of 9 mL of tridistilled H_2O, 4 mL of 30 wt. % H_2O_2, and 1.5 mL of 2.2 M HNO_3. Each solution was then transferred into a Teflon vial and placed in an EasyPrep vessel inside a CEM MARS 6 microwave, sealed and hydrothermally treated at 200 °C with a heat ramp of 15 min (13°C/min) and 5 min plateau with a 20 min total time heating. The resultant products with y = 0, 2.5, 5.0, 7.5, and 10.0 were designated as WH1 (WO_3*0.33H_2O) for hydrothermal and WH1m for MW synthesis; WM25 ($W_{0.75}Mo_{0.25}O_3$*0.33H_2O) for hydrothermal and WM25m for MW; WM50 ($W_{0.50}Mo_{0.50}O_3$*0.33H_2O) for hydrothermal and WM25m for MW; WM75 ($W_{0.25}Mo_{0.75}O_3$*0.33H_2O) for hydrothermal and WM75m for MW and MH1 (MoO_3*0.55H_2O) for hydrothermal and MH1m for MW, respectively.

X-ray diffraction (XRD) patterns were recorded on a Philips X'Pert MPD X-ray Diffractometer with Cu KR radiation (ƛ=1.54056 Å) at 40 kV and a current of 30 mA. Scanning electron microscopy (SEM) images were obtained on a cold field emission JEOL JSM-7401F microscope operated at 5 and 17 kV. An energy-dispersive X-ray spectroscopy (EDS) facility (Oxford INCA X-Sight) attached to the SEM was employed to analyze the chemical composition. UV-vis diffusive reflectance spectra (DRS) were obtained on a Lambda 9 UV-vis spectrometer. The Brunauer-Emmett-Teller (BET) surface areas were measured on a nitrogen adsorption apparatus (Quadrasorb SI, Quantachrome). The samples were degassed at 150-250°C for 12 h before the measurement. All ab-initio calculations were performed using the Quantum Espresso code in the framework of density functional theory (DFT). Due to the known band gap sub-estimation in DFT treatments (by the presence of "d" orbitals in W and Mo) DFT+U method was employed. The models for calculating WH1 and MH1 oxides were to reduce the unit cells from conventional to primitive, while the bimetallic solutions (WM25, WM50 and WM75) were calculated by means of 2x2x1 supercells. In all systems, the hydrated unit cell were employed (to XRD pattern fitting and to DFT calculations), however in both theoretical approach the H atoms are excluded. Hydrogen production was monitored using a gas chromatography Perkin Elmer, Clarus 500, a batch quartz photoreactor and a 250 W mercury lamp (Figure 1).

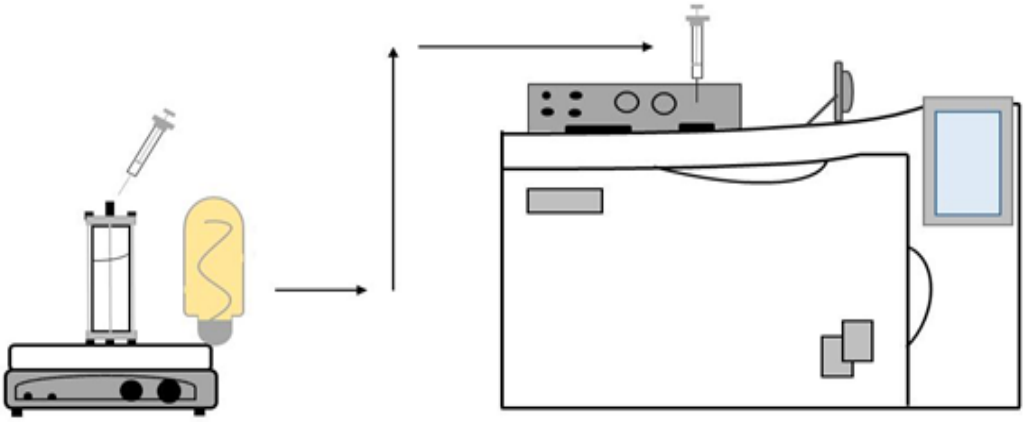

Fig. 1. Scheme of the photocatalytic evaluation system.

3. Results and discussion

All XRD patterns are included in Figure 2. For WH1 the indexing corresponds to orthorhombic crystal, space group Aba2 and lattice parameters a = 7.323Å, b=7.690Å, c=12.772Å (calculated from ICSD using POWD- 12++ 228, 695 (1997)). For Mo fraction x = 0:25; 0:50, and 0:75 the space group was maintained, indicating that W in WO_3*0.33H_2O can be substituted up to 75% by Mo. According to the references [11,12] the appearance of new diffraction peaks in this case is due to the reduced symmetry from an F-centered orthorhombic cell for WO_3*0.33H_2O to a C-centered orthorhombic cell for $W_{0.25}Mo_{0.75}O_3$*0.33H_2O caused by increased distortions induced by Mo substitution. For MH1 (x = 1.00), the XRD pattern can be assigned to hexagonal MoO_3*0.55H_2O (calculated from ICSD using POWD- 12++ 228, 695 (1997), space group P63/m, lattice parameters a= 1.0584 nm, b = 1.0584 nm, c = 0.3727 nm).

Figure 3 (I) represents the SEM images of the solid solutions of the hydrothermal synthesis. For WH1 (a), WM25 (b), WM50 (c) and WM75 (d), the products are mainly composed of nanometer sized flakes (200 nm in size). We can observe micro irregular particles for MH1 (e) with widths and lengths of approximately 29000±15000 nm. Measurements values can be found in Table 1. SEM micrographs in Figure (II) shows synthetized solid solutions by microwave radiation of WH1m (a) that has a particle size of 104 nm and regular and elongated hexagonal-like morphology, WM25m (b) and WM50m (c) have an average particle size of 195 nm with regular hexagonal-like morphology, WM75m (d) has irregular morphology and particle size of 1500 nm, and MH1m (e), the products are mainly composed of micro meter particles of 6600 ± 5100 nm.

It can be observed, between more Mo atoms enters to the crystalline lattice, the particle is bigger. Figure 3(III) shows bright field transmission electron micrographs for materiales synthetized hydrothermally. The first four images show ”hexagonal” flake-like morphologies with a length and width of around 600 nm and 150 nm, respectively. For sample MH1, we observe micrometric size particles with an irregular hexagonal rod shape. Micrographs obtained at low magnification correspond to TEM micrographs at Figure 3 (IV) for all chemical compositions (WH1m-WM75m) obtained with microwave radiation. Micrographs from Figure 3-IV(a,c,e,g) show hexagonal flakes morphology with average lengths of ~100nm and widths of ~150nm.

From the absorption spectra of the samples (hydrothermal and microwave), it is under study that substitution shifts the absorption edge of $W_{1-x}Mo_xO_3$*0.33H_2O from the UV to visible region (Figure 4 a-b). Now, we can determine the effective reduction in the band gap (BG) of these solid solutions due to the incorporation of Mo. The line drawn on the linear part of $[F(R)h\gamma]^{1/2}$ vs. hν curve at $[F(R)h\gamma]^{1/2} = 0$ gives the band gap.

In pure WO_3, the electronic transition occurs directly from VB to CB. For the W/Mo samples, the results are rather similar to that of WO_3 0.33H_2O except that they show more absorption in the visible range (~440 nm). With the introduction of 25% of Mo, a significant shift can be observed (compared against WO_3*0.33H_2O), indicating a narrowing of the band gap. With even more Mo fraction, shifts can be observed.

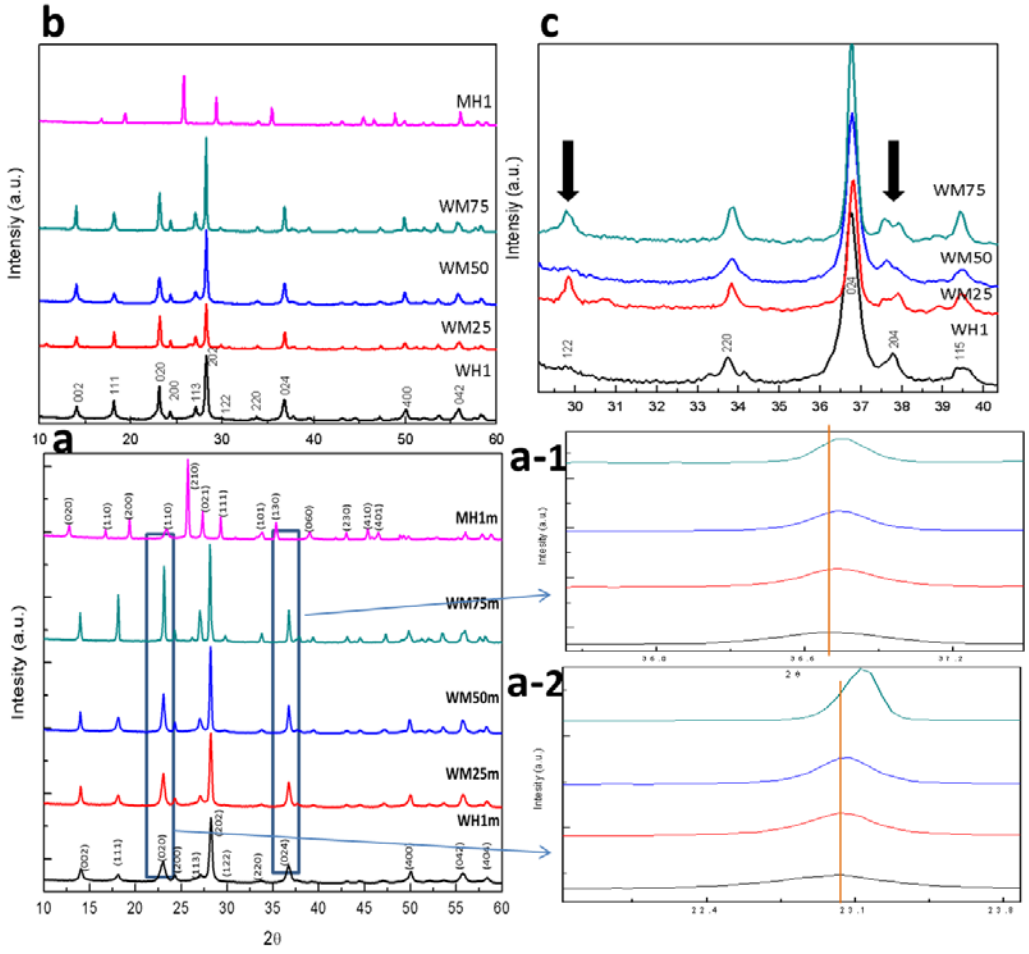

Fig. 2. (a) XRD patterns of compounds synthetized by microwave radiation; (a-1 and a-2) Zoom of peaks at 2θ = 23 and 2θ = 36. F; (b) XRD patterns of compounds synthetized by hydrothermal synthesis; (c) Appearing and splitting of peaks at 2θ = 30 and 2θ = 38

Table1. Theoretical and experimental Mo content, BET surface area and band gap.

		EDS MW	**EDS hydro**	**BG hydro**	**BG MW**	**BG hydro**	**SP MW**
Sample	$X_{theorical}$ [1]	X_{EDS} [2]	X_{EDS} [2]	Eg (eV) [5]	Eg (eV) [5]	Particle size (nm)	Particle size (nm)
WH1m	0	0	0	2.4	2.55	104±51	73±35
WM25m	25	6.3	21	1.95	2.37	192±52	337±223
WM50m	50	9.3	37	1.93	2.35	202±99	103±65
WM75m	75	57.0	55	1.90	2.15	1500±470	163±57
MH1m	100	100	100	2.3	2.25	6600±5100	4500±15000

[1]Theoretical Mo content, [2]Mo content of hydrothermal and microwave synthesis determined from EDS, [4]Band gap of compounds synthetized by microwave radiation, [5]Band Gap of compounds synthetized by hydrothermal synthesis.

For x = 0.25, 0.50, and 0.75, the band gaps of the solid solutions are 2.37, 2.35, and 2.15 eV for hydrothermal and for microwave radiation the values are 1.95, 1.93 and 1.90 eV. The band gap of MH1 and MH1m, which is 2.25 and 2.30 eV respectively, does not follow the trend of the $W_{1-x}Mo_xO_3$*0.33H_2O solid solutions due to its structural difference. We believe that the narrowing of the BG is because of the additional fraction of Mo as Zhou et al. [10] stated: "The increased M^{5+} fraction and thus enhanced intervalency-transition are responsible for the narrowing of the band gap".

DFT calculations resulted in decrease of the electronic gap in function of Mo addition, going from 0.491, 0.435, 0.433 and 0.418 eV to WH1, WM25, WM50 and WM75 respectively. However metallic character was obtained in MH1 compound; in disagree to experimental measured value. The gap trend was also investigated by incorporating the Hubbard correction, optimizing the on-site Coulomb value in WH1 to U = 6 eV. This U value was extended to all other compositions, to take an approach that is independent of the amount of added Mo, the potential was applied over "d" orbital of oxygen atoms. The band structure showed in Figure 5 correspond to the results of DFT+U, which had the same gap trend; i.e. the gap decrease function of the Mo amount, obtaining 2.63 eV for WH1, 2.26 eV for WM25, 2.04 eV for WM50 and 1.98 eV for WM75 and indirect gaps. The gap reduction (and the enhanced efficiency in photocatalysis) by adding Mo is because of the extra bands below the conduction bands.

Our model correctly captures the current trend WH1 to WM75. Regarding MH1 structure, equal to DFT result, it was not possible to obtain semiconductor character. The clear relationship between band structures of the hydrated compound MH1 and its anhydrate analogy Mo_2O_3, which presents electronic gap (not shown), suggest that the measured gap could result from the combined presence of molybdenum oxide created by O vacancies. Different MH1 models with O vacancies were tested, despite the metallic character was not modified. In our employed models, it was not possible to investigate the importance of taking into account H atoms (thus dispersive forces) and its effect on the electronic gap, however will be presented in a future work.

In the Raman spectra, Figure 6 (a) reveals that all compounds synthetized by hydrothermal techniques (sample patterns were normalized), except MH1, show two strong peaks at 720 and 813 cm^{-1}, one medium peak at 280 cm^{-1} and one weak peak located at 336 cm^{-1}. There are very weak signals at 450 and 1000 cm^{-1}, respectively. The two strong peaks located at 720 and 813 cm^{-1} are due to stretching vibrations ν(W-O-W) of the bridging oxygen atoms, the peak at 336 cm^{-1} is characteristic of ς(O-W-O) deformation mode, and the weak signal at 1025 cm^{-1} could be attributed to the stretching mode of the terminal W=O double bond [13]. Because the solid solutions containing X= 0.25, 0.50, and 0.75 (WM25, WM50 and WM75) are quite similar to the X=0 (WH1), the Raman spectra show structural similarity of these samples. When the Mo atoms are in the crystal cell, there is a shift in the position of some bands. The bands located at 720 and 813 cm^{-1} gradually shift to 750 and 845 cm^{-1}, respectively, for the WM75 sample. At the same time these peaks become broader, which may be due to either disorder or loss of long distance translational periodicity (of high atomic number atoms) [14]. For MH1, the representative Raman bands of MoO_3*0.55H_2O are the frequency range of 200 to 1000 cm^{-1}. At 900 and 1000 cm^{-1}, we observe two bands that correspond to ν(O=Mo=O) and ν(Mo=O) stretching, respectively.

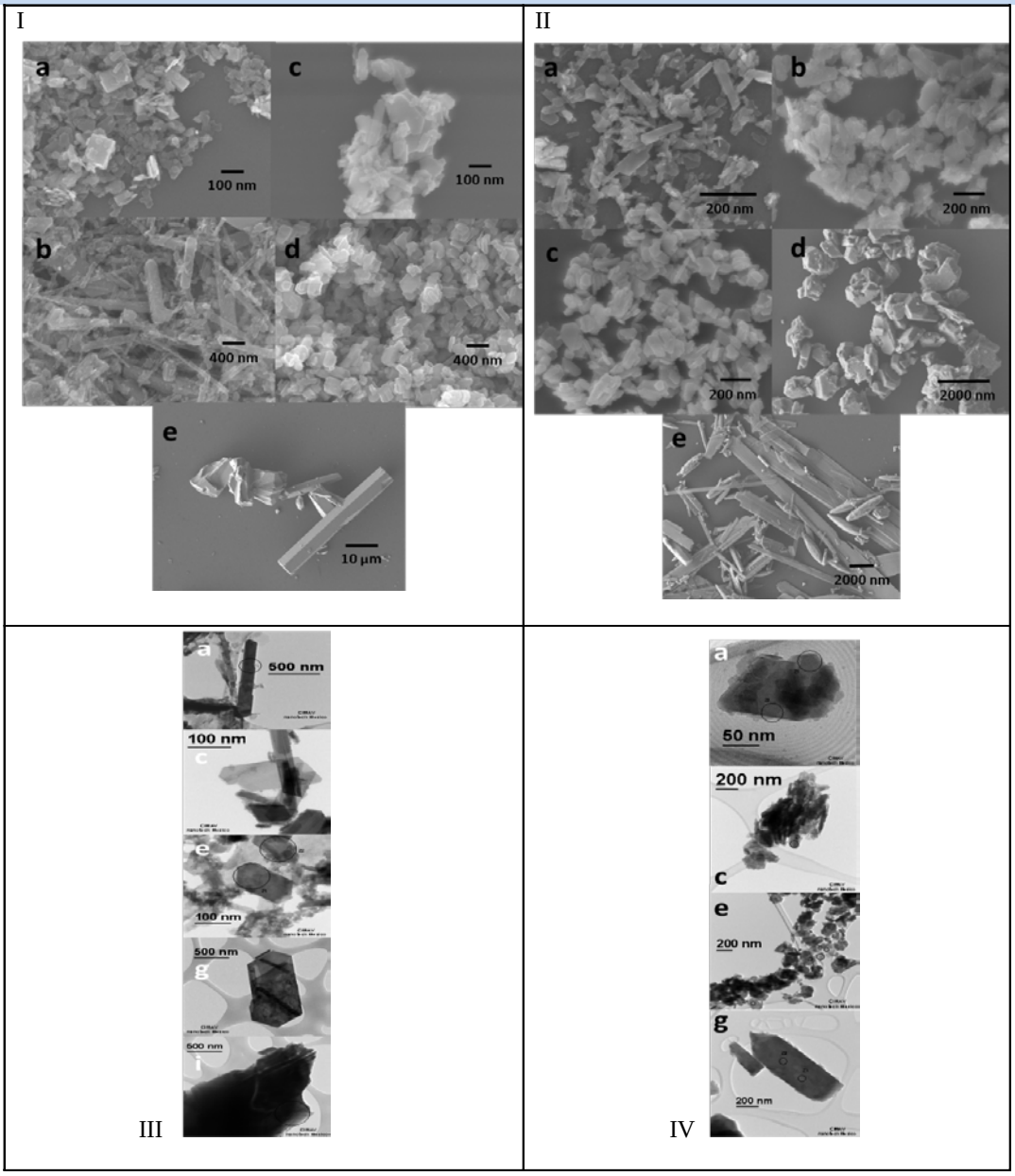

Fig. 3. (I) SEM images of (a) WH1, (b) WM25, (c) WM50, (d) WM75, and (e) MH1 compounds synthetized by hydrothermal technique. **(II)** SEM images of (a) WH1m, (b) WM25m, (c) WM50m, (d) WM75m, and (e) MH1m compounds synthetized by MW radiation. **(III)** TEM images of (a) WH1, (c) WM25, (e) WM50, (g) WM75 and (i) MH1 solid solutions synthetized by hydrothermal techniques. **(IV)** TEM images of (a) WH1m, (c) WM25m, (e) WM50m and (g) WM75m solid solutions synthetized by microwave radiation.

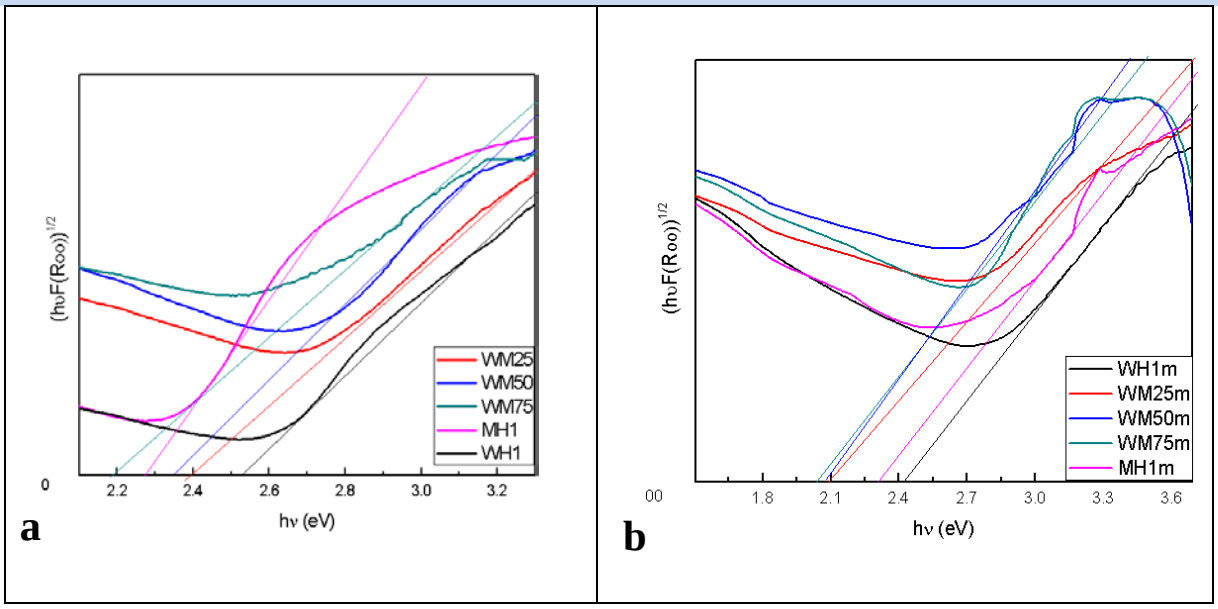

Fig. 4. Determination of band gap of each method: hydrothermal (a) and microwave (b) by drawing a line at $[F(R)h\gamma]^{1/2}=0$

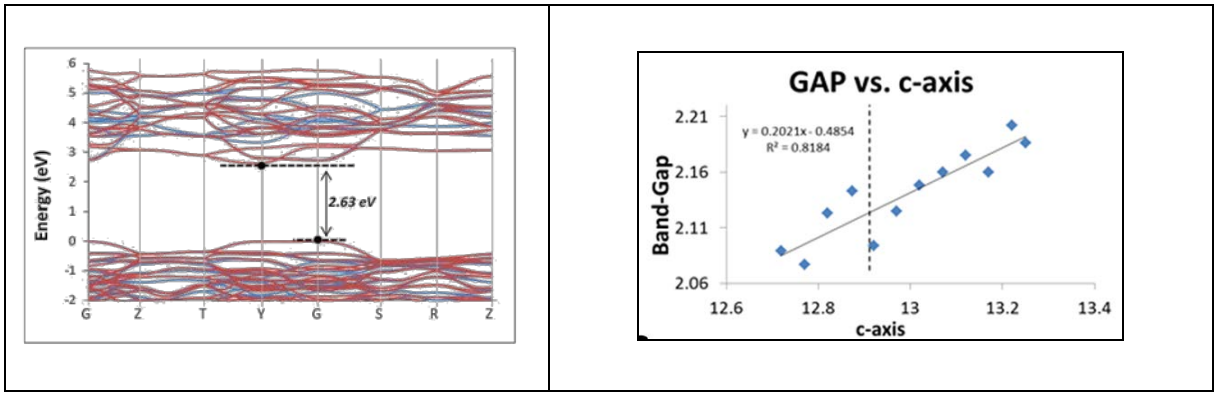

Fig. 5. Theoretical results obtained by DFT+U calculations: left side corresponds to band structure of conventional unit cell of WH1, right side corresponds to electronic valence after c-axis parameter is modified.

The band located at 700 cm^{-1} can be attributed to $\nu(OMo_2)$ and $\nu(OMo_3)$ stretching. The bands located at 400 and 500 cm^{-1} can be assigned to deformation modes. In the case of the band located at 340 cm^{-1}, it corresponds to a $\nu(Mo\text{-}OH_2)$ stretching. Below 300 cm^{-1}, we observe bands that are due to deformation and lattice modes. All assignments can be found in Table 2-I. In Figure 6 (b) shows the Raman spectra for compounds synthetized by microwave radiation. It reveals that all compounds, except MH1m, exhibit three strong peaks at 150, 670 and 800 cm^{-1}, one medium peak at 280 cm^{-1} and one weak peak located at 330 cm^{-1}. The two strong peaks located at 670 and 800 cm^{-1} are due to stretching vibrations ν(W-O-W) of the bridging oxygen atoms, the peak at 330 cm^{-1} is characteristic of ς(O-W-O) deformation mode. Because the solid solutions containing x= 0.25, 0.50, and 0.75 (WM25m, WM50m and WM75m) are quite similar to the x=0 (WH1m), the Raman spectra

shows structural similarity of these samples. When Molybdenum atoms substitutes Tungsten in the crystal lattice, there is a shift in the position of some bands. The bands located at 700 and 800 cm^{-1} gradually shift to 750 and 815 cm^{-1}, respectively, for the WM75m sample. At the same time

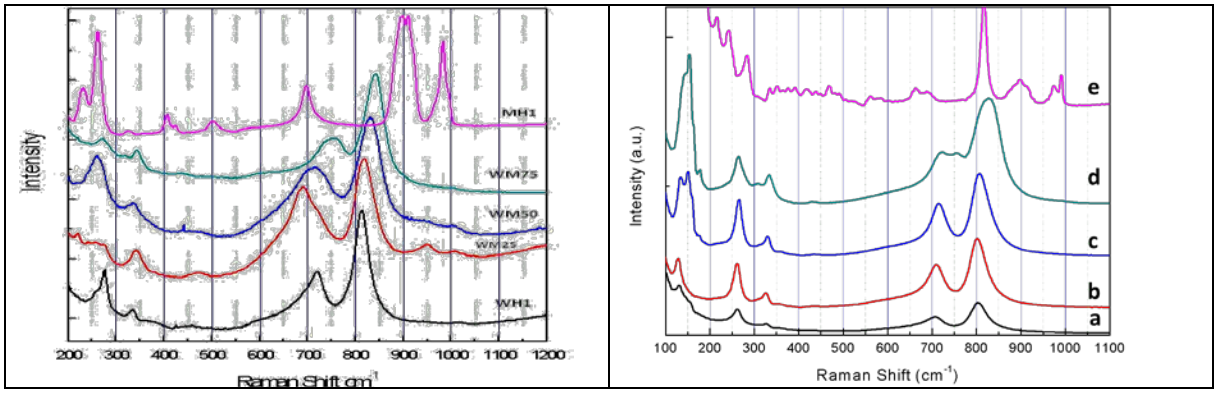

Fig. 6. (Right) Raman shifts of samples synthetized by hydrothermal synthesis: (a) WH1, (b) WM25, (c) WM50, (d) WM75 and (e) MH1. (Left) Raman shifts of samples synthetized by microwave radiation: (a) WH1m, (b) WM25m, (c) WM50m, (d) WM75m and (e) MH1m

Table 2-I: Raman frequencies (cm^{-1}) of $W_{1-x}Mo_xO_3*0.33H_2O$ and $MoO_3*0.55H_2O$ at ambient conditions.

WH1, WM25, WM50 and WM75 (cm^{-1})	$MoO_3*0.55H_2O$ (cm^{-1})	Assignment
	1000-900	ν(Mo=O) stretching ν(O=Mo=O) stretching
1000		W=O stretching
800-700		ν(W-O-W) stretching
	700	ν(OMo_2) stretching ν(OMo_3) stretching
	500-400	Deformation modes
350		ς(O-W-O) deformation
	340	ν(Mo-OH_2) stretching
	< 300	Deformation modes

these peaks become broader, which may be due to either disorder or loss of long distance translational periodicity (of high atomic number atoms) [15].

For the MH1m sample, the representative Raman bands of $MoO_3*0.55H_2O/Mo_2O_5$ (OH) are at the frequency range of 200 to 1000 cm^{-1}. At 900 and 1000 cm^{-1}, we observe two weak bands that correspond to ν(O=Mo=O) and ν(Mo=O) stretching, respectively. We

have a strong band at 800 cm^{-1} that corresponds to ν(Mo–O–Mo) stretching. The weak band located at 700 cm^{-1} can be attributed to ν(OMo_2) and ν(OMo_3) stretching. The bands located below 600 cm^{-1} can be assigned to deformation modes. All assignments can be found in Table 2-II.

Table 2-II. Raman frequencies (cm^{-1}) of $W_{1-x}Mo_xO_3$*0.33H_2O and $MoO_3$0*55H_2O/Mo_2O_5 compounds at ambient conditions.

WH1, WM25, WM50 and WM75 (cm^{-1})	MoO_3*055H_2O/Mo_2O_5 (OH) (cm^{-1})	Assignment
	1000-900	ν(Mo=O) stretching ν(O=Mo=O) stretching
	800	W=O stretching
800-670		ν(W-O-W) stretching
	700	ν(OMo_2) stretching ν(OMo_3) stretching
	<400	Deformation modes
330		ς(O-W-O) deformation

The photocatalityc activity evaluation of the compounds was monitored through the evolution of the hydrogen produced by the dissociation reaction of the water molecule via photocatalysis. Results are shown in Table 3. There was very little production of hydrogen and we believe it is because of the nature of WO_3 itself. We found studies that have shown that WO_3 is a visible light responsive photocatalyst with relatively narrow band-gap energy (2.4-2.8 eV) and a VB potential similar to that of Ag-TiO_2 [16]. Therefore, the oxidizing power of holes in the VB of WO_3 and TiO_2 are considered to be almost the same. However, pure WO_3 is not an efficient photocatalyst toward hydrogen production due its lower CB potential than hydrogen reduction potential, which limits the photocatalyst's ability to react with hydrogen of water molecule [17]. The low CB level also increases the recombination of photo-generated electron–hole pairs leading to minor photocatalytic activity.

Table 3. Photocatalytic hydrogen production through the dissociation of the water molecule under an Hg lamp (250W).

Compound	**Surface area m^2/g**	**H_2/g_{cat} μmoles**	**H_2/m^2 μmoles**	**Compound**	**Surface area m^2/g**	**H_2/g_{cat} μmoles**	**H_2/m^2 μmoles**
WH1	68	10	1.4	WH1m	43	10	2
WM25	46	11	2.3	WM25m	28	11	4
WM50	40	15	3.7	WM50m	19	15	8
WM75	15	20	13	WM75m	6	20	33
MH1	1	5	5	MH1m	6	5	8
Ag-TiO_2	140	180	13	Ag-TiO_2	140	180	13

4. Conclusion and recommendation

We have synthesized a series of $W_{1-x}Mo_xO_3*0.33H_2O$ solid solutions using hydrothermal and microwave radiation with controlled stoichiometry (x = 0, 0.25, 0.50, 0.75). The lattice of WH1 and WH1m ($WO_3*0.33H_2O$) can be substituted with up to 75% Mo without structural alteration. When we increase the content of Mo, the band gap of the $W_{1-x}Mo_xO_3*0.33H_2O$ structure narrowed from 2.62 to 2.10 eV. DFT+U calculations confirmed our experimental data and showed that gap narrow was due to added bands below conductions level of the original WH1 compound. Hydrogen production was reached after 4h of irradiation for each compound. Compound WM75m had the maximum amount produced that was 33 μmoles H_2/g_{cat}. We think that the properties of these enhanced compounds make them suitable for applications like photocatalysis or gas sensing.

Acknowledgments

The authors are thankful with Centro Nacional de Supercomputo (CNS) del Instituto Potosino de Investigacion Cientifica y Tecnologica (IPICyT) for computational resources and with Rodrigo Dominguez, CIMAV NANOTECH for support provided.

References

[1] Ni M, Leung MKH, Sumathy K, Leung DYC. Water electrolysis—a bridge between renewable resources and hydrogen. Proceedings of the International Hydrogen Energy forum, vol. 1, 25–28 May 2004, Beijing, PRC. p. 475–480.

[2] Hodes, G., Fonash, S.T., Heller, A., Miller, B.: In: Gerischer, H. (ed.) Advances in electrochemistry and electrochemical engineering. Wiley, New York (1985)

[3] Hardee, K., Bard, A.: Photoelectrochemical behaviour of several polycrystalline metal oxide electrodes in aqueous solutions. J. Electrochem. Soc. 123, 1024 (1976)

[4] Bahnemann, D.W., Hilgendorff, M., Memming, R.: Charge carrier dynamics at TiO_2 particles: reactivity of free and trapped holes. J. Phys. Chem. B 101, 4265–4275 (1997)

[5] Santato, C., Ulmann, M., Augustynski, J.: Enhanced visible light conversion efficiency using nanocrystalline WO3 films. Adv. Mater. 13, 511 (2001).

[6] Abe, R., Higashi, M., Domen, K.: Facile fabrication of an efficient oxynitride TaON photoanode for overall water splitting into H_2 and O_2 under visible light irradiation. J. Am. Chem. Soc. 132, 11828–11829 (2010)

[7] Hwang, Y.J., Boukai, A., Yang, P.D.: High density n-Si/n-TiO_2 core/shell nanowire arrays with enhanced photoactivity. Nano Lett. 9, 410–415 (2009)

[8] Baeck, S.H., Jaramillo, T.F., Brandli, C., McFarland, E.W.: Combinatorial electrochemical synthesis and characterization of tungsten-based mixed metal oxides. J. Comb. Chem. 4, 563 (2002)

[9] Khader, M.M., Vurens, G.H., Kim, I.K., Salmeron, M., Somorjai, G.A.: Photoassisted catalytic dissociation of water to produce hydrogen on partially reduced alpha.-iron(III) oxide. J. Am. Chem. Soc. 109, 3581 (1987)

[10] L. Zhou, J. Zhu, M. Yu, X. Huang, Z. Li, Y. Wang, and C. Yu, The Journal of Physical Chemistry C 114, 20947 (2010).

[11] F. Harb, B. Gerand, and M. Figlarz, C. R. Acad. Sci. Paris 303, 789 (1986).

[12] H. F., Solid State Ionics 32-3, 84 (1989).
[13] Daniel, M. F.; Desbat, B.; Lassegues, J. C.; Gerand, B.; Figlarz, M. J. Solid State Chem. 1987, 67, 235–247.
[14] Ph. Colomban, Stress- and Nanostructure-Imaging of Ceramic Fibers and Abradable Thermaln Barrier Coatings by Raman Microspectrometry : State of the Art and Perspectives, Ceram. Eng. & Sci. Proc. 21 (2000) 143.
[15] Ph. Colomban, Ceram. Eng. Sci. Proc. 21 (2000) 143.
[16] M. Miyauchi, M. Shibuya, Z. G. Zhao and Z. Liu, J. Phys. Chem. C, 2009, 113, 10642.
[17] M. Miyauchi, Phys. Chem. Chem. Phys., 2008, 10, 6258.

Chapter 1.13. Synthesis, characterization and photocatalytic evaluation of MWO_4 (M = Ni, Co, Cu and Mn) Tungstates

Xiomara A. López[1,2]; Antonio F. Fuentes[2]; Miguel Meléndez Zaragoza[3]; José A. Díaz Guillén[1]; Alejandro Lopez Ortiz[3]; Virginia Collins-Martínez[3]*

[1]Instituto Tecnológico de Saltillo, Blvd. V. Carranza No. 2400, Col. Tecnológico Saltillo, C. P. 25280 Coahuila, México
[2]CINVESTAV del IPN, Unidad Saltillo, C.P. 25900, Ramos Arizpe, Coahuila, México
[3]Centro de Investigación en Materiales Avanzados S. C., Miguel de Cervantes 120, C. P. 31136, Chihuahua, Chih. México

ABSTRACT

Photocatalysis is an technology that can be applied to solve environmental and energy problems such as the production of hydrogen from the dissociation of the water molecule. Tungstates exhibit many potential applications in different areas of technology due their excellent electrical properties. Nanostructured tungstate materials are known for their wide applications in conventional catalysis, as scintillator material, in photoluminescence, optical fibres and as materials in microwave technology. Eventhough these present enough chemical and thermal stability, very scarce reports are found in the literature related to their uses as photocatalysts for hydrogen production through water splitting. The aim of the present study is the synthesis and characterization of family tungstate MWO_4 (M = Co, Cu, Mn and Ni) materials through co-precipitation in order to evaluate their photocatalytic activity towards the production of hydrogen within the visible light range. Characterization consisted in XRD, BET, UV-Vis and SEM, while the photocatalytic evaluation was as follows: 200 mg of $CuWO_4$, $CoWO_4$, $NiWO_4$ and $MnWO_4$ powders were individually suspended in water and methanol, the latter used as a sacrificial agent. The water suspension was placed inside a sealed quartz batch photoreactor under constant stirring and and illuminated by a 250W mercury lamp for 8 h with gas evoultion being monitored by gas chromatography (GC). Preeliminary results indicate that the employed synthesis method was effective to obtain the required crystalline phase. However, optimal conditions are needed to decrease particle size and increase the tungstates surface areas. The bandgap energy of these tungstates was found to be within the visible light spectrum with a variation between 2.24 eV for $CoWO_4$ to 2.56 eV for $MnWO_4$, respetively. Maximum hydrogen production was achieved by sample $MnWO_4$ with 139 $\mu mH_2/g_{cat}$, while the lowest production was observed for sample $CoWO_4$ with 24 $\mu mH_2/g_{cat}$. From these preeliminary results it can be infered that simple and mixed metal transition tungstates can be considerer as potential candidates, as photocatalysts for H_2 production via the splitting of the water molecule under visible light irradiation.

Keywords: H_2 generation; water splitting; photocatalysis; tungstates

---

* Author for correspondence: V. Collins-Martinez, T: +526144391129; E: virginia.collins@cimav.edu.mx

1. Introduction

Catalysis is called to the change in reaction rate due to a participation of an agent called catalyst. This catalyst not only makes possible the chemical reaction to occur in a faster rate, but also lowers the activation its energy, while not being part as a reactant or product. When the catalytic reaction is activated through light absorption it is called phtotocatalysis, [1] and this is defined as a chemical reaction induced by photo iradiation in the presence of a photocatalyst [2]. Such a material facilitates chemical reactions whitout being consumed or transformed. This process starts when a semiconductor material is iluminated with a suitable wavelenght of light that must be equal or higher to the size of the band gap energy of a semiconductor. The general idea of using a fotocatalyst to split the molecule of water consists in use the oxydizing and reducing effect of the charges that are generated in a semiconductor [1]. Photocalysis can be applied to solve enviromental and energy problems [3-5], such as hydrogen production from water splitting. Some of the advantages of the photocatalysys are: low processing costs, the capability of hydrogen and oxygen evolution during the water splitting reaction and suitable small reactor systems for domestic applications, thus providing a huge potential market [2].

Scheelite and wolframite type compounds such as tungstates (AWO_4) are part of an important family of materials from a technogical point of view. According to the literature, Rajagopal et. [6] tungstates present different and interesting properties, that draw attention, because they exhibit potential applications in different technological areas [7], such as; state solid laser [8], microwave, scintillation [9], optoelectronic devices, optic fibers [6], humidity sensors and fluorescent lamps due to their photoluminicense appeling properties, meanwhile some others tungstates are of special interest due to their conductivity and electrical properties [10]. According to the above, these materials could be considered as potential photocatalysts towards the hydrogen production.

Moreover, the coprecipitation synthesis route is a simple, fast and a soft chemical method. Furthermore, it has many advantages such as; low calcination temperature, low cost ,and above all it does not require special operating conditions [11]. This technique is probably the most used to prepare ceramic powders [12]. Garcia-Perez et al. [13] carried out the synthesis of bivalent transition metal tungstates such as; Co^{2+}, Cu^{2+}, Mn^{2+} and Ni^{2+} prepared through coprecipitation, where $CuWO_4$ series presented the greatest photocathalytic activity. Therefore, the objective of the present work is the synthesys, characterization and photocatalytic evaluation of materials of the tungstate family MWO_4 (M=Cu, Co, Ni and Mn) through the water splitting reaction towards the hydrogen production under the visible light irradiation.

2. Experimental

2.1. Synthesis of precursor solutions

The synthesis of MWO_4 compounds was caried out by the reaction in solution method. This technique consists in a disolution-precipitation reaction of salts containing the metals of interest; this method may lead, sometimes, to amorphus materials that through an adequate thermal treatment, can be transformed into crystalline materials with an optimal

morphology and microstructure.

Initially, the equivalent amount of 0.4 moles of $Na_2WO_4 \cdot 2H_2O$ were weighed in grams and dissolved in 1000 mL of distilled water (solution A). Then, four 0.4 M solutions of divalent cations (0.4 mol/1000 mL in distilled water) were prepared separately, using as reactants their hydrated nitrates: $Mn(NO_3)_2 \cdot 4H_2O$, $Cu(NO_3)_2 \cdot 2.5H_2O$, $Co(NO_3)_2 \cdot 6H_2O$ and $Ni(NO_3)_2 \cdot 6H_2O$ (solution B). Next, solution A was slowly added to solution B at room temperature and under vigorous stirring. The general chemical reaction that dictates the dissolution-precipitation method is the following:

$$M(NO_3)_2 + Na_2WO_4 \rightarrow MWO_4\,(\downarrow) + 2\,NaNO_3\,(M = Co^{2+}, Cu^{2+}, Mn^{2+}\ y\ Ni^{2}) \quad (1)$$

When mixing of both solutions in a 1:1 molar ratio took place, a precipitate was spontaneously formed. This was washed four times with DI water and filtered, whereas pH of the solutions was not adjusted. The obtained precipitates were dried at 100°C for 24h, grounded in an agate mortar, and finally calcined at 400°C during 4h. Sample nomenclature was set as follows: (a) $CoWO_4$, (b) $MnWO_4$, (c) $NiWO_4$ and (c) $CuWO_4$.

2.2. Characterization of materials

The MWO_4 (Co^{2+}, Cu^{2+}, Mn^{2+} y Ni^{2+}) powders were characterized using in X-ray diffraction (XRD), Breunner-Emmet-Teller Surface area (BET), diffuse reflectance spectroscopy (UV-Vis) and scanning electron microscopy (SEM) techniques to study their physical and chemical properties.

The synthesized powders were analyzed to determine their crystalline structure, through the X-ray diffraction technique, using a D8 Advance Bruker Axs diffractometer with Cu-Kα (λ = 1.5418 Å) radiation, scintillation detector and a Ni filter. Measurements were performed in a 2θ interval from 10 to 80° and using a step size of 0.016°/sec in an acrylic sample holder. The powders surface area was studied by the nitrogen physisorption technique at a degasification temperature of 180°C, using a Quantachrome Autosorb-1. For the measurement of the bandgap energy a UV-Vis Perkin Elmer (Lambda-10) spectrophotometer equipped with an integration sphere for the diffuse reflectance studies was used. While morphological characterization of the synthetized materials was carried out by scanning electron microscope technique using a SU 3500 HITACHI equipment. While, samples were chemically analyzed by dispersive spectroscopy (EDS) and chemical mapping using secondary electrons (SE) at 2 kX.

2.3. Photocatalytic evaluation

Photocatalytic evaluation of the synthesized samples towards the hydrogen production by water splitting was performed using a 250W mercurial lamp and 0.2 g of tungstate sample suspended in 200 mL of DI water and 4 mL of methanol in the reactor system as sacrificial agent (2% vol). The suspension was placed inside quartz photo reactor with a length and diameter of 19 and 5 cm, respectively, then it was hermetically sealed and placed 7cm away from the 250W mercury lamp. The photoreactor was kept under constant stirring and irradiated for 8h [14]. The reaction was monitored by gas chromatography using a gas chromatograph (GC) Perkin Elmer Clarus 500. The experimental setup employed for carrying out the photocatalytic evaluation of the materials is presented in Figure 1. This setup is composed by a photoreactor, artificial lighting, and GC analysis

equipped with a personal computer data collection. In order to monitor the photocatalytic reaction, gas samples were taken at regular time intervals using a 1mL syringe for gases through a septum located at the upper section of the photoreactor. A sample under darkness was taken at the initial concentration and then the sampling took place every hour up to a total of 8 hours of continuous irradiation.

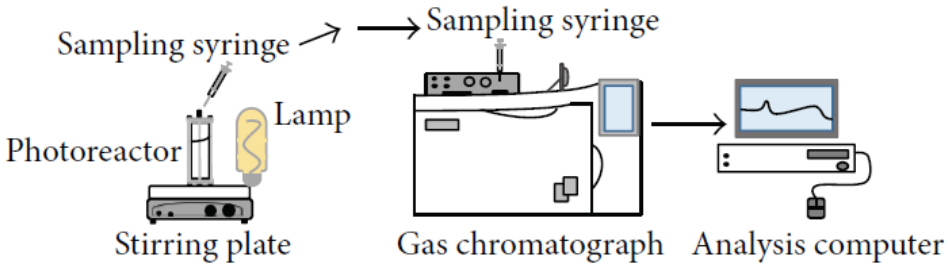

Fig. 1. Experimental setup for the photocatalytic evaluation of the tungstate samples.

3. Results and discussion

3.1. X-ray diffraction tests

Bivalence metal tungstate powders derived from the synthesis by the dissolution-precipitation technique were structurally characterized using XRD. Figure 2 shows the difractogram peaks of the synthetized photocatalysts (Co^{2+}, Cu^{2+}, Mn^{2+} and Ni^{2+}). XRD technique showed that for the four thermally treated metals at 400°C for 4h, the obtained products are crystalline, meaning, that the XRD spectrum of every sample showed the principal reflections reported in the literature [11, 13, 15].

The XRD diffractograms showed that the $CoWO_4$, $NiWO_4$ and $MnWO_4$ powders present a crystalline monoclinic structure [11], whereas $CuWO_4$ powders exhibit a triclinic crystalline structure [11]. The results show evidence that working with a subsequent thermal treatment at 400°C temperature for 4 h, is possible to achieve the formation of the desired tungstate metal samples.

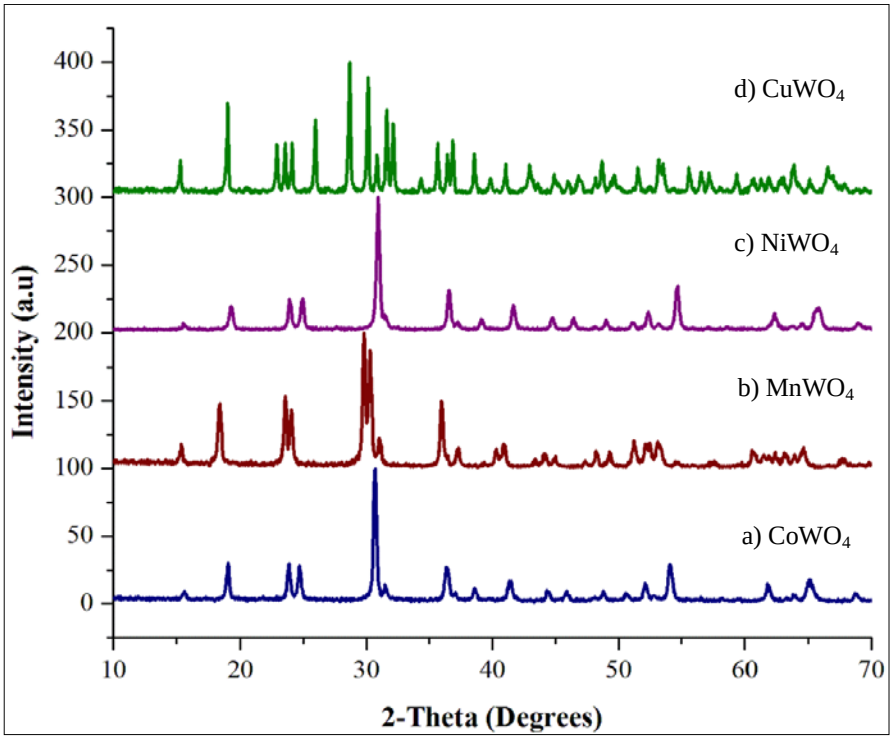

Fig. 2. XRD diffractograms of the synthesized tungstate samples by the dissolution-precipitation technique followed by a thermal treatment at 400°C during 4 h; a) $CoWO_4$, b) $MnWO_4$, c) $NiWO_4$, d) $CuWO_4$.

3.2. UV-Vis Spectra

Figure 3 presents the tungstate diffuse reflectance spectra (UV-Vis) of $CoWO_4$, $MnWO_4$, $NiWO_4$ and $CuWO_4$ samples; results were converted to Kubelka-Munk units [16] through to the following expression:

$$F(R) = \frac{(1-R)^2}{2R} \qquad (2)$$

In order to determine energy band gap of the samples, a lineal region from the inflection point of the diffuse reflectance spectrum is considered, which represents the absorption energy above the border. Extrapolating the lineal slope until the interception to the photonic energy axes (X axes), this point provides the optical band gap value of the material.

The estimated energy band gap values were 2.20 eV (Co), 2.56 eV (Mn), 2.46 (Ni), and 2.24 (Cu), which are similar to the ones reported in the literature for these materials [16-18].

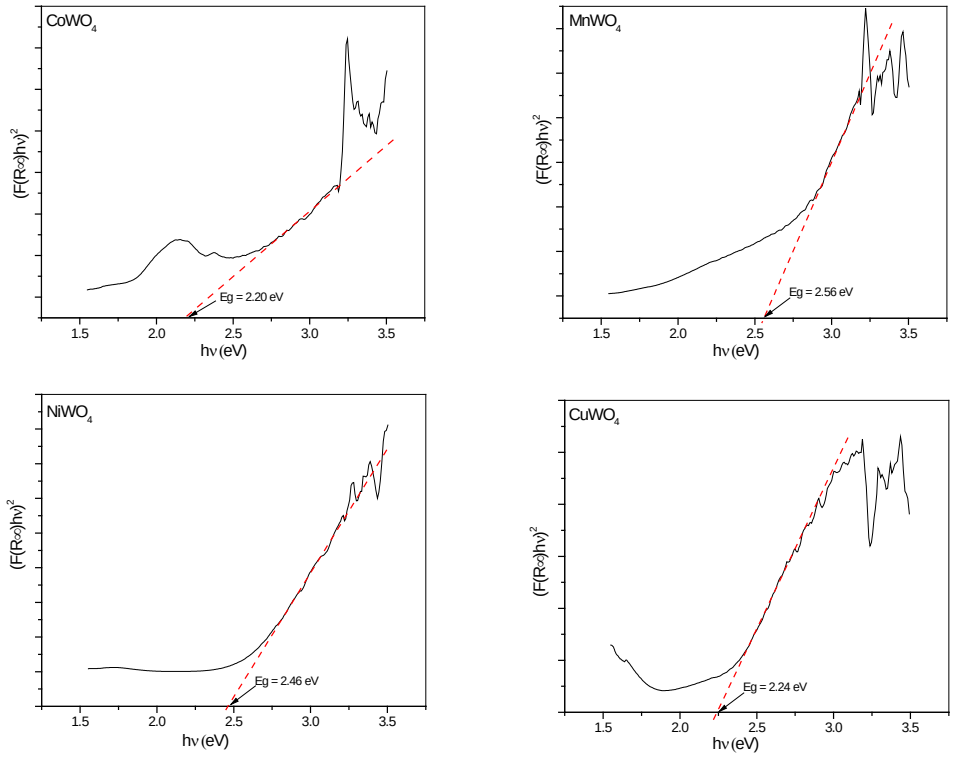

Fig. 3. UV-Vis spectra of samples $CoWO_4$, $MnWO_4$, $NiWO_4$ and $CuWO_4$.

3.3. BET surface area

The specific surface area of the samples was determined by N_2 physisorption. Table 1, presents the materials BET surface areas and band gap energy of the synthesized samples.

The results show the difficulty that exists to obtain large values of surface areas and this will become an issue towards the hydrogen production through water splitting [19].

3.4. Scanning electron microscopy

Scanning electron microscopy provided important information related to their morphology as and well as the apparent particle size and elemental composition present in the samples. Figure 4 shows SEM images of the obtained tungstates treated at 400°C for 4h.

In Figure 4 (a, b and c), similar morphologies were observed, with particles presenting a high degree of agglomeration and large sizes. $CoWO_4$ particles show agglomerates of particles of around 20 µm, while sample $MnWO_4$ show different sizes of agglomerates varying from 10-30 µm. $NiWO_4$ sample show a mixture of small particles of around 5µ to large particle agglomerates of around 30 µm. Finally, sample $CuWO_4$ presents very evident signs of sintering with particles as large as 50 µm with no apparent porosity. While other samples present a rough surface morphology. This behavior can be attributed to the

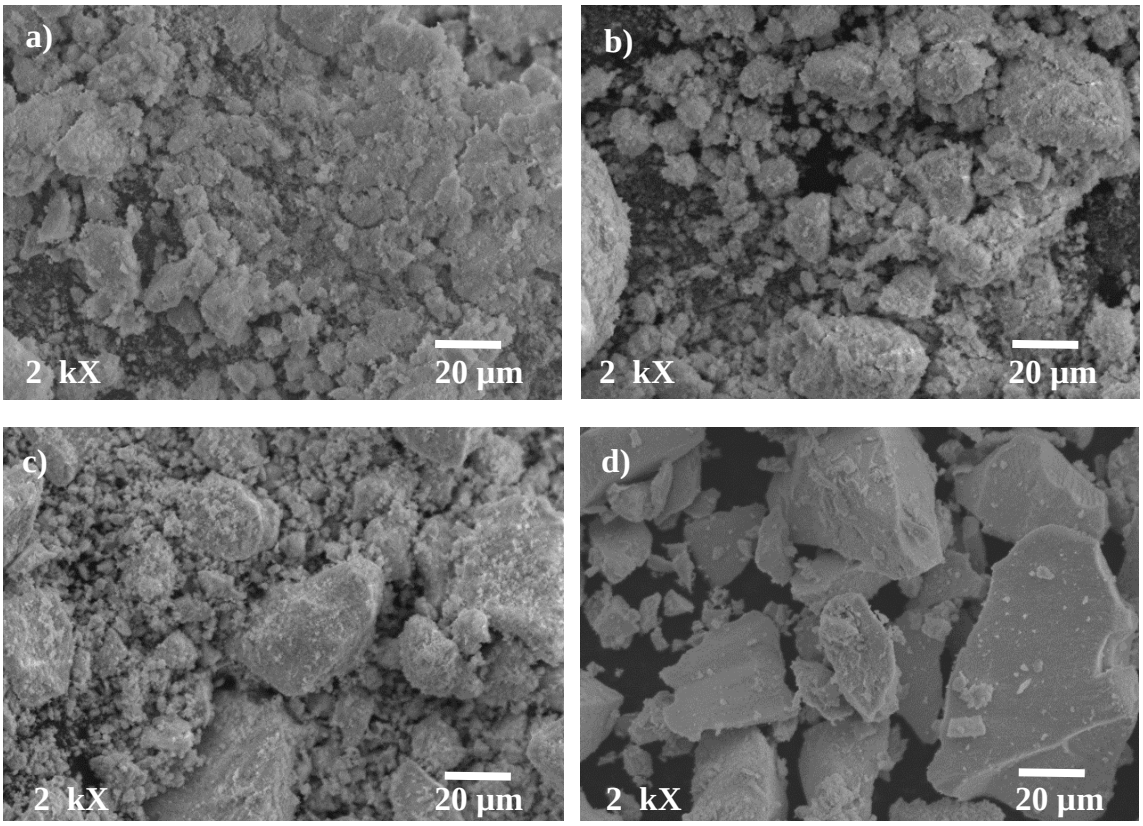

Fig. 4. SEM images of the synthesized tungstates:
a) $CoWO_4$, b) $MnWO_4$, c) $NiWO_4$, d) $CuWO_4$.

intrinsic nature of these materials. Furthermore, the EDS analysis resulted in the expected the molar ratios of the crystalline phase for each sample, thus corroborating the obtained XRD results.

3.5. Photocatalytic evaluation

The photocatalytic evaluation of the different samples was performed by measuring the hydrogen evolution produced by the reaction of the splitting of the water molecule and results are shown in Table 1. The highest hydrogen production was achieved by $MnWO_4$ with 139 µmoles H_2/g_{cat}. While the lowest H_2 produced corresponded to the sample CuWO4 with only 7 µmoles $H_2/g_{cat.}$ Other samples fell in between these values.

The behavior observed in the hydrogen production of the samples can be attributed, presumably, to the particle size here presented, as it was observed in the SEM images, there were agglomerates and large particle sizes, therefore at the irradiation time these particles did not have enough contact time to produce a major hydrogen quantity.

Table 1. BET surface area, band gap energy and hydrogen production for the synthesized samples.

Sample	BET surface area (m^2/g)	Band Gap Energy (eV)	H_2 Production µmoles H_2/g_{cat}
$CoWO_4$	23	2.20	24
$MnWO_4$	22	2.56	139
$NiWO_4$	11	2.46	17
$CuWO_4$	8	2.24	7

4. Conclusion and recommendation

Divalent tungstates of transition metals were successfully synthetized using an effective synthesis method, followed by calcination at 400°C. The photocatalytic activity of $CoWO_4$, $CuWO_4$, $NiWO_4$ and $MnWO_4$ was investigated, obtaining higher H_2 production with compounds $CoWO_4$ and $MnWO_4$. The dissolution-precipitation method allowed to obtain the desired crystalline phase.

However, it is important to optimize conditions to decrease the particle size and increase the available superficial area. The energy band gap of these tungstates fell within the visible light spectrum. Transition metal tungstates can be considered potential candidates for the water splitting of the water molecule under visible light irradiation.

Finally, future work will concentrate in further characterization, to elucidate the decisive properties responsible for the photocatalytic activity of these materials.

References

[1]. Peral J., Ollis D.F. TiO_2 photocatalyst deactivation by gas-phase oxidation of heteroatom organics. Journal of Molecular Catalysis A: Chemical 115 (1997) 347.

[2]. López Chávez E. Guzmán Pantoja J. Peña Castañeda Y. A., Castillo Alvarado F. Nuevos Materiales para el Desarrollo de Celdas de Combustible en México. 137 (2014) 5-205

[3]. Herrmann J.M. Heterogeneous photocatalysis:state of the art and present applications,48 (2005).

[4]. Fujishima A., Honda K., Electrochemical Photolysis of Water at a Semiconductor ElectrodeNature 238 (1972) 37.

[5]. Malato S., Blanco J., Alarcon D.C., Maldonado M.I., Fernandez Ibañez P., Gernjak W., Photocatalytic decontamination and disinfection of water with solar collectors. Catalysis Today 122 (2007) 137.

[6]. Rajagopal S., Nataraj D., Mangalaraj D., Djaoued Y. Robichaud J. Yu O. Nanoscale Ress Lett. 1335 (2009) 1335-1342.

[7]. Naik S.J., Salker A.V. Solid state studies on cobalt and copper tungstates nanomaterials 2065 (2010).

[8]. Jani M.G., Naranjo F.L., Barnes N.P., Murray K.E., Lockard G.E., "Diode-pumped longpulse-length Ho:Tm:YLiF4 laser at 10 Hz. Opt.Lett. 20 (1995).

[9]. Nikl M., Bohacek P., Mihokova N., Kobayashi M., Ishii M., Usuki Y., Babin V., Stolovich A., Zazubovich S., Bacci M.. Excitonic emission of scheelite tungstates AWO_4 (A = Pb, Ca, Ba, Sr). J.Lumin. 87 (2000).

[10]. Montini T. Gombac V. Hameed A. Felisari L. Adami G. Fornasiero P. Synthesis, characterization and photocatalytic performance of transition metal tungstates. Chem Phys Lett 498, (2010).

[11]. Montemayor S. M., Fuentes A. F., Electrochemical characteristics of lithium insertion in several 3D metal tungstates (MWO_4, M=Mn, Co, Ni and Cu) prepared by aqueous reactions. Ceramics International 30 (2004) 393-400.

[12]. Pathank A., Pramanik P. Nano-particles of oxides through chemical methods. Nanomaterials: Special issue of The Indian National Science 51 (2001) 47-70.

[13]. Garcia-Perez U.M., Martinez-de la Cruz A., Peral J., Transition metal tungstates synthesized by co-precipitation method: Basic photocatalytic properties. Electrochimica Acta 81 (2012) 227– 232.

[14]. Guzmán-Velderrain V. Enhanced Photocatalytic Hydrogen Production Under Visible Light over Ag Doped TiO_2. XIV International Congress of the Mexican Hydrogen Society.

[15]. Pourmortazavia S. M. Rahimi-Nasrabadi M. Khalilian-Shalamzari M. Zahedi M. M., Hajimirsadeghi S. S. Omrani I. Synthesis, structure characterization and catalytic activity of nickel tungstate nanoparticles. Applied Surface Science 749 (2012) 745-752.

[16]. Back S. Wenderich K. Mul G. Synthesis of bimetallic tungstates for finding photocatalytic active compounds with a smaller band gap than tungsten oxide. University of Twente Student Theses 5 (2014).

[17]. Doping effect on optical band gap and luminescence of pure and Nd-doped $CoWO_4$ wolframite nanostructure synthesized by chemical precipitation. Chapter 4. 88, 87-104. Avaliable at: http://ir.inflibnet.ac.in:8080/jspui/bitstream/10603/35486/9/09_chapter4.pdf

[18]. Priyanka K. P., Sabu N. A. Sunny A. T. Sheena P. A., Varghese T. Effect of Electron Beam Irradiation on Optical Properties of Manganese Tungstate Nanoparticles. Journal of Nanotechnology 4 (2013) 1-6.

[19]. García Pérez U. M. Síntesis de m-$BiVO_4$ por los métodos de combustión, co-precipitación e hidrotermal en presencia de agentes estructurantes y evaluación de sus propiedades fotocatalíticas. Tesis UANL 5 (2011) 1-200.

Chapter 1.14. Hydrogen production research in Mexico: A Review

V. Collins-Martínez; M. J. Meléndez Zaragoza; A. López Ortiz*

Departamento de Ingeniería y Química de Materiales, Centro de Investigación en Materiales Avanzados, S.C., Miguel de Cervantes 120, Chihuahua, Chih., México, 31136, México.

ABSTRACT

The insertion of the hydrogen technologies into Mexico's energy portfolio is a complex matter. Historically, the government has monopolized the energy sector. However, very recently (August 2014) an energy reform bill approved by the Mexican Congress and ratified as a law by the President allowed foreign investment in the energy sector. In this context, there is a great opportunity for alternative energy and specifically for hydrogen technologies to flourish within Mexico. Specifically, the opportunity for the hydrogen production research activities to contribute to the advance and possible application of the related hydrogen technologies is today of paramount importance. The present paper is aimed to present a review of research activities in the field of hydrogen production in Mexico. Main research activities are reflected in Journal publications and conference proceedings within the last seven years. These resulted in the following topics and contributions: Hydrogen production (HP) from biological processes and wastes 40.4%, followed by HP through conventional and non-conventional fuels (CO_2 capture & Catalysis) 22.4%, HP by photocatalysis & photo-electrocatalysis 14.1%, HP systems and controls 12.2%, theoretical and thermodynamic studies for HP 7.7%, and HP by electrolysis 3.2%. A wide variety of potential applications can be followed by these contributions, while the spread of this research can be a key for future national or international collaborations that may strengthen this important area within the energy sector to take advantage of the upcoming opportunities in the country.

Keywords: Hydrogen production research, Mexico

1. Introduction

Energy is the engine of economic and social development of the world, therefore continuous supply of all forms of energy is of crucial importance to every nation and Mexico as a country is no exception. Hydrogen has become one of the most promising alternative energy carriers in the country, this in view to decentralize the energy production based on oil. The versatility of its new applications, its high calorific value and the fact that it can be used as a clean fuel are some examples of the high potential in new applications and developments. That is the reason why in several European nations as well as in Japan

---

* Author for correspondence: A. López Ortiz, T: +052 614 4394815, E: alejandro.lopez@cimav.edu.mx

hydrogen use in transportation is currently taking place. However, the most abundant element on our planet is not found in its elemental form, but in molecular form (as in oil or water) and consequently in order to be utilized this must be extracted.

At present, there are different methods for producing hydrogen, and these are characterized by their primary source. Among the primary sources are fossil fuels like natural gas and coal as well as renewable sources such as biomass, solar, wind, hydro and nuclear. Additionally, in production technologies there is also many alternatives, such as chemical, biological, electrolytic, photolytic and thermo-chemical processes. The choice of the primary energy source and the technology to produce hydrogen are strongly linked to parameters such as fuel costs as well as environmental and social impacts. Figure 1 show the most employed current technologies to produce hydrogen [1].

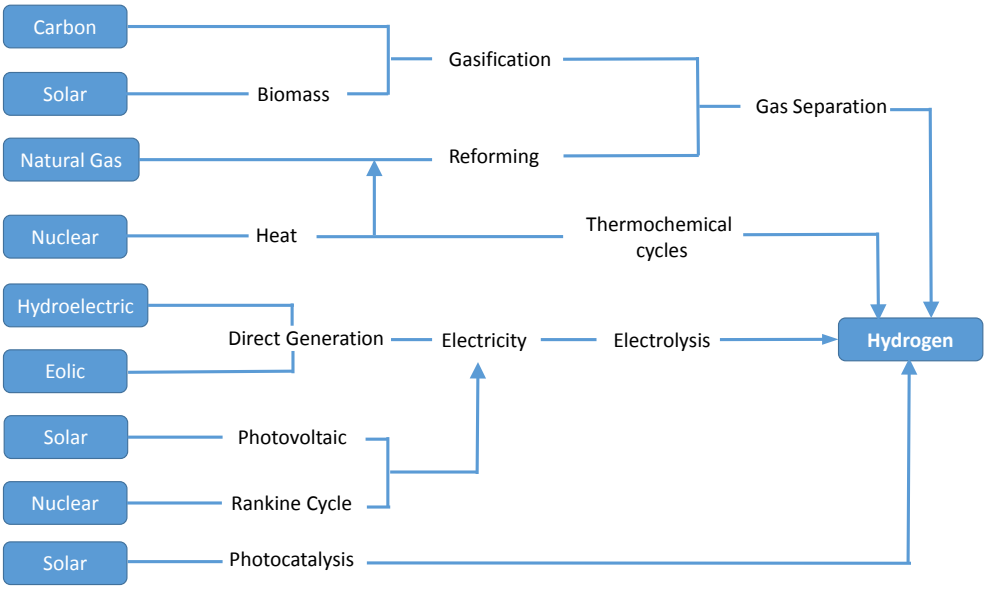

Fig 1. Most employed current technologies to produce hydrogen

In general, electrical and thermal energy can be produced from fossil fuels, nuclear, or recovered energy and renewable energies such as solar, wind, hydro, thermal and biomass. Photonic energy originates from solar irradiation, while biochemical energy is recovered from organic matter. Carbon and biomass (with solar energy as a source) can be gasified to produce syngas (a mixture of H_2 and CO) followed by gas processing and separation to obtain pure hydrogen. Furthermore, natural gas reforming is a mature technology used in many refineries and chemical industries in Mexico for large-scale H_2 production. In some countries (Germany and Japan) small-scale reformers are currently used in demonstration H_2 refueling stations (decentralized production). Reforming options include catalytic steam methane reforming (SMR), partial oxidation (PO) and other variants under development (i.e. CO_2 capture). In SMR, methane reacts with steam at 700°C-950°C to produce syngas, CO is then converted into CO_2, producing additional H_2 by the water-gas shift reaction (WGS). In the POX process, methane reacts initially with pure O_2 to generate syngas [2]. Further purification or gas separation is needed from these processes to obtain pure hydrogen for different needs such as fuel cells in transportation applications.

Hydrogen can be produced using nuclear energy as a source of primary energy, through thermal splitting of the water molecule, electrolysis and thermochemical processes, the three alternatives are free of carbon emissions. The heat obtained from the nuclear reactor is used to achieve the splitting of the water molecule, thus producing hydrogen. Thermochemical cycles were developed already since the 1970s and 1980s when the search for new sources of production of alternative fuels were needed during the petroleum crisis. In thermochemical water splitting, also called thermolysis, heat alone is used to decompose water to hydrogen and oxygen [3]. It is believed that overall efficiencies close to 50% can be achieved using these processes [4]. However, the temperature required for this process is 850 °C; these temperatures are reached only by high temperature reactors [5].

Hydroelectric power has the advantage of being a clean resource that is perpetually renewable and hydrogen production can be carried out by electrolysis. Essentially, this practice is performed to increase the efficiency of hydropower plants through the conversion of water to hydrogen through electrolysis by using the excess energy or wasted energy not yet utilized, and then conversion of hydrogen to electricity via a gas turbine or fuel cells. The electricity produced in the off-peak or no-demand time, or at the time of huge river flows in the spring can be stored in the form of hydrogen, and later, when the peak energy is needed, the hydrogen converted to electricity. One of the advantages of the proposed system is that the resource for production of hydrogen (the water) is available directly at the site. It appears that the conversion of electricity at hydro-power plants to hydrogen, and its utilization via a gas turbine, is technically and economically feasible [6].

Moreover, eolic energy is constantly growing worldwide. In some locations today, wind is cost competitive with conventional, fossil fuel, or nuclear generated electricity. It is the fastest growing renewable energy sector with annual growth of 27%, which means doubling the installed capacity every three years [7]. Direct coupling of an electrolyzer with a wind turbine to produce H_2 implies intermittent operation with a highly variable power output. One particular issue deals with alkaline electrolyzers, when at very low loads the rate at which hydrogen and oxygen are produced (which is proportional to current density) may be lower than the rate at which these gases permeate through the electrolyte, and mix with each other and this may create a hazardous condition inside the electrolyzer [8]. Due to present high costs of electrolyzers and fuel cells, the cost of delivered electricity would be several times higher than the cost of wind-generated electricity [9].

Furthermore, hydrogen production by solar technology can be produced by two methods. Solar energy is converted to electricity in a photovoltaic cell (PV) and hydrogen is generated by electrolysis of water, while the alternative method is carried out in photoelectrochemical cells directly produce hydrogen. Approximately 85% of commercial PV cell technology are based on polycrystalline silicon. Other cells are based on thin plates of amorphous and crystal compounds of group II-IV and I-III-IV of the periodic table [1]. PV based electrolysis process includes photovoltaic (PV) panels, DC bus bar, AC grid, accumulator battery set, electrolyzer and hydrogen storage canisters. PV based electrolysis is one of the most expensive hydrogen production methods; with current technology, the cost of hydrogen from PV electrolysis is about 25 times higher than that of fossil fuel alternatives [10]. However, the cost of this process has been continuously decreasing and this factor is estimated to go down to 6 [11].

Finally, photocatalysis converts photonic energy (solar irradiation) to chemical energy (hydrogen). When a photon encounters the photocatalyst, an electron-hole pair is generated and the obtained electrical charge is employed to dissociate water. In order for a photocatalyst to split water and generate hydrogen, it should have an appropriate band gap and properly located conduction and valance bands for oxidation/reduction reactions. The most studied material so far is TiO_2. In addition to TiO_2, several other semiconductors have been studied, such as, ZnO, Fe_2O_3, $BiVO_4$, and WO_3 [12]. The grand challenge in this technology is to design a catalyst system that can effectively use sunlight and water to generate hydrogen and oxygen [13]. For this technology to be feasible, the development of a photocatalyst must fulfill certain requirements: (a) good (visible) light absorption; (b) high chemical stability in the dark and under illumination; (c) band edge positions that overlap the water reduction and oxidation potentials; (d) efficient charge transport; (e) low overpotentials for reduction/oxidation of water; and (f) low cost [14].

2. Hydrogen production research in Mexico

Hydrogen can be produced from different renewable energy sources, and Mexico is a rich nation in renewable energy resources. Resources, security issues, public acceptance, and appropriate government incentives are the main factors affecting the application of hydrogen technologies as a source of economic growth in Mexico. The inclusion of the hydrogen technologies into Mexico's energy portfolio is a complex matter. Historically, the government has monopolized the energy sector. However, very recently (August 2014) an energy reform bill approved by the Mexican Congress and ratified as a law by the president has allowed foreign investment in the energy sector. In this context, there is a great opportunity for alternative energy and specifically for hydrogen technologies to flourish within Mexico. In 2014, a bill for a general law aimed at the utilization of hydrogen and their related technologies was presented to the Mexican Senate and today this is being analyzed. This bill has the objective to adopt a National Hydrogen Plan with the aim of boosting the energy technological development by hydrogen as a fuel and energy carrier, through scientific and technological research. Therefore, research activities within Mexico are of paramount importance in view of the forecoming utilization of the related technologies. In Mexico, research related to hydrogen technologies is today very active and specifically, one of the major contributions is generated in the field of hydrogen production. In this field major contributions come from the following areas: hydrogen production from biological processes, through conventional and non-conventional fuels (CO_2 capture & Catalysis), by photocatalysis & Photo-electrocatalysis, through systems and controls, theoretical and thermodynamic studies and by Electrolysis. A wide variety of potential applications can be followed by these contributions, while the spread of this research can be a key for Mexico’s future and international collaborations that may strengthen this important area within the energy sector to take advantage of the upcoming opportunities in the country. Therefore, the present paper is aimed to present a review of the hydrogen production research activities in Mexico within the past seven years.

2.1 Biological hydrogen production

Research activities in Mexico focused on biological hydrogen production fall within six main fields: bioreactors their operation and specific applications, microalgae as source for

photosynthetic hydrogen, bacteria and microorganisms, fermentation of organic matter and microbial electrolysis cells (MEC).

2.1.1 Bioreactors

In the field of bioreactors, Torres Zúñiga et al. [15-16] developed a strategy that make use of a Luenberger observer to estimate the glucose and the biomass concentrations inside a fermentative reactor to produce hydrogen. This was established in order to accurately determine unknown inputs, which is a key issue in reactor control of biotechnological systems. Ramos et al. [16a] studied several variables that influence the hydrogen production from the organic fraction of a cafeteria food waste at mesophilic conditions in batch reactors. Main variables studied were the initial pH and the total solids concentration (TS). Their results indicate that the highest specific degradation rate was obtained with the lowest TS concentration and an initial neutral pH. While, it was found that the influence of the TS concentration on hydrogen production was more significant than that of the initial pH for this type of residues. Alzate-Gaviria et al. [17] compared two coupled laboratory scale anaerobic digestion reactors for hydrogen production from an organic fraction of municipal solid waste (OFMSW) and synthetic wastewater. These reactors were a packed bed reactor (PBR) containing OFMSW and an upflow anaerobic sludge bed reactor. The reactors were inoculated with a mixture of non-anaerobic inocula and a hydrogen yield of 37% was reached in mesophilic range. In other work, Espinoza-Escalante et al. [18] performed an optimization analysis of the pretreatments of Tequila's stillages (waste) for volatile fatty acids (VFA's) and hydrogen production. It was found that hydrolyzation of the organic matter present in Tequila's stillages is the adequate treatment to enhance the VFAS's and hydrogen production. While, Buitron et al. [19] studied the H_2 and methane production in a two-stage sequencing batch (SBR) and up-flow anaerobic sludge blanket (UASB) reactors using tequila vinasses achieving an overall organic matter removal of 73–75% and the optimization of such reactors were analyzed in a further study [20]. Furthermore, Carrillo Reyes et al. [21] proposed strategies to cope with methanogens in hydrogen producing UASB reactors by analyzing the community dynamics. In another study, Espinoza Escalante et al [22] analyzed the effect of pH, temperature and hydraulic retention time on the production of hydrogen and methane in the anaerobic digestion of vinasses from the fermentation of Agave tequilana Weber to tequila.

Moreover, other kind of bioreactors studied were stirred tank reactors (CSTR). Cheese whey (CW), as an industrial waste also constituted the object of several studies towards the biological production of hydrogen. That is the case of the study dealing with the improvement of the hydrogen production rate in a continuous CSTR [23]. In that study it was found that continuous fermentative Bio-H_2 production from CW can be significantly enhanced by an appropriate selection of parameters such as hydraulic retention time and organic loading rate. While, start-up and operation analyses were performed on a CSTR for biohydrogen production from restaurant organic solid waste [24]. Furthermore, a biotrickling filter was employed as a bioreactor using oat straw acid hydrolysate with some H_2 production being reported [25]. However, implementation of strategies for biomass control to avoid reactor clogging was needed.

The comparison of in continuous and discontinuous reactors was studied for the production of H_2 in bacterial communities [26]. It was found that the feeding-regime conditioned the diversity and bacterial population abundance, while high H_2 production was

obtained when low diversity was observed. Using a fluidized bed reactor, Muñoz-Paez et al. [27] studied two levels of operational temperatures (ambient and 35 °C) and two organic volumetric loading rates. They found that the H_2 production in the reactor operated at ambient temperature was superior to that of the mesophilic units and showed encouraging results for H_2 production in submerged fermentation of moderate concentration of sucrose. Whereas, biofilm reactors were used to study the biohydrogen production from diary processing wastewater [28] with dried stems of *Opuntia imbricata* were used as substrate along with a pretreated mixed culture for biofilm formation. Hydrogen yield was significantly affected by initial COD concentration, temperature and dairy wastewater pH. Also, the use of anaerobic sludge blanket (UASB) reactor was used for the study of effect of hydraulic retention time (HRT) on the H_2 production employing paper industry wastes [29]. Finally, in a study aimed to evaluate the application of hybrid membranes for the enrichment of hydrogen gas produced in biodigestors Quechulpa-Pérez et al. [30] showed a feasible separation of these gases in a membrane reactor set.

2.1.2 Microalgae

Microalgae are photosynthetic microorganisms that convert solar energy into chemical energy, which can be redirected physiologically to produce hydrogen (H_2). Photosynthetic H2 production by microalgae has many advantages, such as CO_2 sequestration; bioremediation of wastewater when it is used as culture medium to grow algal biomass; microalgae growth is not seasonal; cultures can be installed in non-arable lands; and depending on the microalgae species, valuable byproducts can be obtained. One of the most significant challenges in hydrogen (H_2) production by microalgae is the incompatibility between oxygenic photosynthesis and anaerobic hydrogen production due to the high sensitivity of hydrogenase to oxygen (O_2). Marquez Reyes et al. [31] studied the reduction of photosynthetic O_2 in a culture medium to enhance the production of hydrogen. A remarkable finding of this work is that when the photosynthetic O_2 in the culture medium is depleted (anaerobic conditions), it is possible to produce hydrogen. Moreover, Martin del Campo et al. [32] studied the hydrogen production by *Chlamydomonas reinhardtii* under light-driven and sulfur-deprived conditions, using biomass grown in outdoor photobioreactors at the Yucatan Peninsula, while Marquez-Reyes et al [33] explored the hydrogen production by native species of microalgae isolated from México. Finally, Martin del Campo and Patiño [34] designed a prototype for the bioproduction of H_2 by *Chlamydomonas reinhardtii*.

2.1.3 Microbial hydrogen production

Mexico is a rich country in terms of natural resources. From the exploitation of these resources, an important amount of biological waste is generated, while most of this is not adequately handled towards its utilization in the energy sector. This strategy can be of relevant importance in this critical sector in Mexico's economy. This is the reason why an important research effort is being taking place in the country in order to take advantage of such industrial wastes employing the microbial route for H_2 production.

One important agricultural waste in Mexico is the wheat straw that has been subjected of several important investigations. Diverse microbial consortia were designed in order to efficiently degrade recalcitrant lignocellulosic substrates from wheat straw for hydrogen production [35]. Perez Rangel et al. [36] studied the natural anaerobic consortia

performance for hydrogen production from wheat straw under isolation conditions, while Torres-Aguirre et al. [37] studied the effect of the C/N and C/P ratios over the fermentation of wheat straw. In another study, hydration treatments were performed to increase the biodegradability of native wheat straw for hydrogen production by a microbial consortium [38], while the combined effect of particle size and hydration treatment on the wheat straw biodegradability was studied by Lara Vazquez et al. [39].

Different kinds of bacteria have been employed for the production of H_2, which is the case of diazotrophic Burkholderia species [40]. In another study, Arreola Vargas et al. [41] explored the hydrogen production from acid and enzymatic oat straw hydrolysates in an anaerobic sequencing batch reactor by evaluation of the performance and microbial population analysis. Other bacteria extensively used by Mexican researchers in the H_2 production is *Escherichia coli* using cheese whey as an industrial waste as substrate. In particular, nitrogen sources impact on the hydrogen production was evaluated [42], while maximum yield obtained was comparable to the yield reached in other hydrogen production processes with *Clostridium sp*. or mixed cultures [43], furthermore, the influence of pH control on hydrogen production was studied by Rosales Colunga et al. [44-45].

In other studies, the buffer composition effect over the hydrogen production and the microbial community composition in non-axenic cultures, it was concluded that the formulation of culture media had a strong effect on hydrogen production, kinetics and also on the microbial diversity [46]. The cyanobacteria *Spirulina maxima 2342* was autotrophically obtained in a bioreactor under illumination and air bubbling and analyzed for its photobiological hydrogen production [47], while in a further study the quantification of hydrogen production was performed at different light intensities and through a PEMFC [48].

Moreover, Valdez-Vazquez et al. [49] researched how nutrients related to spore germination improved H_2 production from heat-shock-treated consortia. Cepeda-Rodríguez et al. [50]employed a natural substratum (*Opuntia imbricata*) to immobilize a microbial mixed culture for H_2 production under anaerobic conditions on biofilms. While Herrera Ramirez et al. [51] studied the use of biofilms to produce H_2 by exploring on the influence of pH in the fermentative hydrogen production in batch reactors, by simultaneous saccharification and fermentation (SSF) from paper industry wastes using anaerobic biofilms. Also from industrial paper waste, the study of Morales-García et al. [52] who evaluated different natural microbial consortia for H_2 production from crystalline cellulose. While, Navarro Diaz et al. [53] evaluated the differences in ecological structure between H_2 production under anaerobic digestion consortia.

2.1.4 Fermentation

Plenty biomass from various industries wastes can be used as a source for biohydrogen production where the combination of waste treatment and energy production can be a valuable asset in Mexico's energy portfolio. This section summarizes research activities related to the fermentative biohydrogen production from biomass. Potential biomass that could be the source for biohydrogen generation are glucose wastes, cellulosic materials, dairy wastes, among others, while a special emphasis was given to the microorganisms and factors affecting the biohydrogen production.

Davila-Vazquez et al. [54] used lactose, cheese whey and glucose in batch experiments for the fermentative hydrogen production. Rosales Colunga et al. [55] studied the fermentation of lactose and its constituent sugars by *Escherichia coli* and its impact on the hydrogen production. In addition, this research group explored the estimation of hydrogen production in genetically modified *E. coli* fermentations using an artificial neural network [56]. In another research, anaerobic mixed cultures were evaluated towards the H_2 production among them anaerobic microbial communities and their H_2 production inhibition mechanisms [57].

Whereas, the solid substrate fermentation of agroindustrial wastes and the influence of total solids content and initial pH on batch operation were evaluated by Robledo-Narváez et al. [58]. Furthermore, Moreno-Dávila et al. [59] studied the fermentative hydrogen production by anaerobic biofilms from a pretreated mixed microflora in a continuous fixed bed-reactor, in this research microbial cultured community was mainly formed by lactic acid bacillus from *Phylum firmicutes*. Whereas, Garcia-Lopez et al. [60] used vegetable fermentation products as substrate for hydrogen production by *Rhodopseudomonas palustris*. Alamilla et al. [61] studied the richness, composition and predominance in undefined mixed cultures for fermentative hydrogen production and Montiel-Corona et al [62] explored the effect of flushing method, bicarbonate addition, and outdoor–indoor conditions within the H_2 production by an enriched photoheterotrophic culture using dark fermentation effluent as substrate. Cisneros-Pérez et al [63] employed an inoculum pretreatment to promote differences in hydrogen production performance in EGSB reactors under dark fermentation conditions; they found that inoculum pretreatments allow the selection of bacteria that have better performance in hydrogen production. Finally, Hernández-Rojas et al. [64] reported the effect of the mixed inocula and pH during the dark fermentation process for the production of H_2 using molasses as substrate.

2.1.5 Microbial electrolysis Cells (MEC)

The microbial electrolysis is a biological process that allows the production of hydrogen (H_2) as a result of the cathodic reaction of protons coming from the oxidation of the organic matter contained in waste water. For the application of this technology it is necessary to determine suitable operating conditions that allow to scale-up a microbial electrolysis cell to produce hydrogen efficiently at low cost.

Verea et al. [65] employed a new approach to get high hydrogen production rate in a MEC by achieving in a very short time the process for making the anode's bacteria enrichment for the biofilm formation. In this study, the hydrogen production efficiency was optimized through the change of the electrolyte conductivity and the electrode surface area/electrolyte volume ratio. It was found that the hydrogen production rate increased with the increase of the electrolyte conductivity. In another study, Rivera et al. [66] used a two-chamber microbial electrolysis cell (MEC) to study the organic matter consumption and hydrogen production rate. The chemical oxygen demand (COD) was composed of a mixture of volatile fatty acids (VFAs) present in the effluent of a dark fermentation process. Results indicated that the substrate containing glucose was more slowly degraded because glucose was first transformed into VFAs, and then the VFAs were consumed to produce hydrogen. Finally, Gomez Roquea et al. explored the hydrogen generation in a microbial electrolysis cell (MEC) using two configurations; catalyzed by platinum and biocathode.

2.1.5 Hydrogen production from industrial wastes

Industrial food wastes contain high levels of carbohydrate and protein and these are mostly treated anaerobically. However, lactic acid, biocompost and energy from food wastes can be a valuable strategy for treatment of food wastes. Furthermore, the organic constituents especially carbohydrates in food wastes can be employed as potential substrates for anaerobic hydrogen production [67]. Sugar cane bagasse, cellulosic waste biomass, food waste derived from restaurants, food-processing industries and organic municipal wastes are among the raw materials for the production of hydrogen that Mexican researchers have used in their investigations. Lopez Ortiz et al. [68] used low temperature sugar cane bagasse pyrolysis for the production of high purity hydrogen through steam reforming and CO_2 capture. In this study, slow and low temperature bagasse pyrolysis produced the highest yield of liquid products, while a thermodynamic analysis of acetic acid (main product from this pyrolysis) steam reforming and CO_2 absorption reactions predicted a high purity H_2 gas. Sanchez et al. [69] explored the co-production of ethanol, hydrogen and biogas using agro-wastes. They proposed a conceptual plant design and NPV analysis for mid-size agricultural sectors. Escamilla-Alvarado et al. [70] examined the hydrogen production from organic wastes and re-use of fermented solids to produce holocellulases.

Whereas, Poggi-Varaldo et al [71] reported an overview of hydrogen, fermentation, methane and bioelectricity as key contributions to biorefineries of organic wastes. In another research, Moreno-Andrade et al. [72] evaluated several parameters that affect the H_2 production using organic solid waste in a discontinuous process, such as the hydraulic retention time (HRT), where the *Genus Megasphaera* was found to be the dominant genus in the microbial community.

Escamilla-Alvarado et al. [73] used municipal solid waste biohydrogen production through solid substrate fermentation. They found that in the semi-continuous fermentation, the factors that had significant influence on hydrogen production followed the order: total solids > mass retention time > temperature. While, in the batch fermentation, supplemental nitrogen did not show a significant effect.

2.2 Hydrogen production from conventional and non-conventional fuels

Conventional processes (commercially mature technologies) for H_2 production have been used for years to obtain large-scale hydrogen (steam reforming, coal gasification and partial oxidation of hydrocarbons) are characterized by having high operating costs, be energy intensive, low efficiency and large CO_2 discharges. However, these can be considered as a bridge technology, while new photocatalytic sustainable technologies as water electrolysis, bio-hydrogen, etc., are able to produce H_2 in large quantities with acceptable yields and efficiencies to be used in combination with other alternative energy sources (wind, solar, hydro, etc.). Specifically, traditional methods of H_2 production can be modified by the CO_2 capture at high temperature. Among the most important advantages of this strategy are: the use of extensive experience in operating these processes, as well as the reuse of existing infrastructure in Mexico. Additionally, derived from these modifications, it is possible to reduce emissions of carbon dioxide, resulting in processes that are more efficient. Thus, reducing the effects of global warming. Consequently, changes to conventional processes, which result in greater efficiencies in the production of hydrogen, have become the essential bridge to the hydrogen economy.

Escobedo Bretado et al. [74, 75] studied the absorption enhanced water gas shift (AEWGS), which is a reaction that combines the WGS reaction and CO_2 capture by a solid absorbent to produce high purity H_2 from synthesis gas in one single step. They obtained a 97% H_2 product using calcined dolomite suggesting this last to act as a WGS catalyst. The use of metal oxide to serve as oxygen source for the partial oxidation of hydrocarbons was explored by de los Ríos Castillo et al. [76, 77]. They used $CoWO_4$ as oxygen source promoted with 10% Ni and 10% La_2O_3 in redox cycles of CH_4 and H_2O to evaluate their global kinetics and found that Ni and La_2O_3 resulted in a greater reaction rate with respect to $CoWO_4$ alone. In a similar study, Sosa Vázquez et al. [78] studied the stabilizing effect of Al_2O_3 and ZrO_2 in mixed metal oxides of Cu for hydrogen production through redox cycles. Results showed that these metal oxides were excellent stabilizers for CuO.

The combination of the steam reforming of hydrocarbons and the CO_2 capture by solid oxides is an important research field that has been very active in Mexico in recent years. Aceves Olivas et al. [79, 80] presented results of thermodynamic analysis and experimental evaluation of hydrogen production by steam reforming of ethanol (SRE) combined with CO_2 absorption using a mixture of a solid absorbent (CaO, CaO*MgO and Na_2ZrO_3) and a Ni/Al_2O_3 catalyst. They found that a H_2 concentration of 96.6, 94.1, and 92.2% using CaO, CaO*MgO, and Na_2ZrO_3, respectively can be produced under this reactions scheme. Lopez Ortiz et al. [81] evaluated process variables for the production of hydrogen using calcined dolomite combined with methane reforming. Since the solid CO_2 absorbent is a crucial material in this modified process, Escobedo Bretado et al. [82] performed an experimental and modeling kinetic study of the CO_2 absorption by Li_4SiO_4, a synthetic absorbent. Finally, thermochemical cycles using biomass and carbon were employed by Valverde-Ramírez et al. [83] to produce H_2 at high temperatures.

2.2.1 Catalysis

One of the energy challenges that today's world is facing is the development of practical alternatives to fossil fuels. With increasing levels of global energy demand, as well as climate change triggered by CO_2 emissions, there is an imminent need to find chemical alternatives (energy carriers) to fossil fuels with smaller carbon footprints. Hydrogen, a clean and energetically rich molecule, is one of the most promising candidates. Heterogeneous catalysis is of paramount importance in today's hydrogen production processes from fossil as well as in renewables fuels. The catalytic research performed in Mexico here is presented in terms of their components with emphasis on noble metals deposited over special oxide particles; the emphasis is given in the activity catalysts for the hydrogen production reactions.

Pérez-Hernández et al. [84] proposed the use of Ag nanowires as precursors to synthesize novel Ag-CeO_2 nanotubes for H_2 production in methanol reforming. They found that the catalytic activity was improved as the nanotubes concentration was increased in the catalysts and Ag was found to be the phase mainly responsible of the hydrogen production. Guevara et al. [85] studied the Ni/Ce-MCM-41 mesostructured catalysts for simultaneous production of hydrogen and nanocarbon via methane decomposition. Four types of carbon nanofibers/nanotubes were detected and their formations greatly depend on the reaction temperature, time on steam and degree of the interaction between the metallic Ni and support. The respective mechanisms of the formation of nanocarbons were postulated and

discussed. Galindo-Hernández et al. [86] studied the structural and textural properties of Fe_2O_3/γ-Al_2O_3 catalysts and their importance in the catalytic reforming of CH_4 with H_2S for hydrogen production. They proposed a novel mechanism for the methane reforming with H_2S. Martínez-Salazar et al. [87] performed further studies in this field when they examined the kinetics and modeling over $Mo/La_2O_3–ZrO_2$ catalyst within the hydrogen production by methane and hydrogen sulfide reaction. Further studies examined the high H_2 production from the reforming of CH_4 by H_2S using Mo-Cr supported on heterogeneous catalysts.

In the field of ethanol steam reforming, González Vargas et al. [88] examined the H_2 production over Rh/Ce-MCM-41 catalysts. They found that the incorporation of Ce in the framework of MCM-41 is favorable to the reduction of Rh_2O_3, with the introduction of Ce profoundly enhancing the ethanol conversion and H_2 yield by approximately 2–3 times. Melchor-Hernández et al. [89] studied modification of the nickel supported on La-modified alumina catalysts prepared by sol–gel in ethanol steam reforming. They found that, as lanthanum species are progressively present in the support its contribution to stabilization of the catalyst is certainly related to the enhancement of gasification of carbon residues on the surface of the catalyst but also to a close interaction with nickel particles. Contreras et al. [90] elaborated a complete review on catalysis by the steam reforming of ethanol.

Moreover, Pérez-Hernandez et al [91-93] evaluated the hydrogen production by oxidative steam reforming of methanol over $Ni/CeO_2–ZrO_2$ catalysts and concluded that nickel is the phase mainly responsible of hydrogen production although the CeO_2/ZrO_2 support reduced the CO formation. While, Ortiz et al. [94] evaluated the effect of WOx on catalysts Co, Ni/hydrotalcite to obtain hydrogen from bioethanol and Pt/ hydrotalcite [95].

Furthermore, Lopez et al [96] studied the effect of Cu and Ni impregnation on ZrO_2 and their molecular simulation studies and fou5d that the bimetallic Cu–Ni and core–shell Ni/Cu nanoparticles on the catalysts, suggest that the oxidative steam reforming of methanol reaction may be a structure–sensitive. While other studies examined the effect of Cu loading on CeO_2 [97].

Moreover, Salmones et al. [98] examined the deactivation behavior of Ni-based catalysts for simultaneous production of hydrogen and nanocarbon and the influence of the pore geometry and they found that the catalysts with 15 and 25 wt.% of Ni showed much longer lifetime, which can be explained by assuming a new model related to the pore geometry of the catalysts. In another work, Pérez-Hernández et al. [99] evaluated the effect of the bimetallic Ni/Cu loading on the ZrO_2 support for H_2 production in the autothermal steam reforming of methanol.

Furthermore, in the methane decomposition reaction Zapata et al. [100] studied the effect of Ca, Ce or K oxide addition on the activity of Ni/SiO_2 catalysts. Their results suggest that Ce addition prevents the sintering of nickel particles during the reduction process maintaining a random distribution between the silica and cerium oxide improving the distribution and migration of deposited carbon.

2.3 Hydrogen production from photocatalysis & photoelectrolysis

The need to develop new alternatives for sustainable energy has drawn the attention to emergent clean renewable technologies, since they proceed from natural and lasting sources like solar light. The alternative method of photocatalytic water splitting to produce hydrogen is promising since it involves the absorption of light to produce H_2 and O_2 by irradiating oxide semiconductors. The incorporation of metals or metal oxide nanoparticles

on the surface of semiconductors as co-catalysts has proved to enhance the photoactivity for the water splitting reaction. These photocatalysts must be efficient, stable, harmless, abundant and inexpensive. In this field in Mexico, many research groups intensively work to overcome these challenges. Oros-Ruiz et al. [101] studied the photocatalytic hydrogen production by Au–M_xO_y (MAg, Cu, Ni) catalysts supported on TiO_2 and their results indicate that the electron charge transfer from TiO_2 to the Au–M_xO_y systems and the effect of surface plasmon resonance of gold nanoparticles produce an enhancement of the photocatalytic activity. Also from this research group, the photocatalytic hydrogen production by water/methanol decomposition using Au/TiO_2 prepared by deposition–precipitation with urea was also evaluated [102]. In other studies Galindo Hernandez et al. [103] explored the the role of Fe^{3+} ions in Fe_xO_y/C catalysts for hydrogen production from the photodehydrogenation of ethanol. While, Escobedo Salas et al. [104] evaluated a Pt modified TiO_2 for hydrogen production via water splitting and they found 7.8% quantum efficiency of photon utilization. In Further studies, Perez-Larios et al. [105] improved the hydrogen production from water splitting using TiO_2–ZnO mixed oxides photocatalysts; they found that these solids were resulted in six times more activity than the reference TiO_2 photocatalyst. Torres-Martinez at al. [106] examined the enhanced photocatalytic water splitting hydrogen production on RuO_2/La:$NaTaO_3$ prepared by sol–gel method. The higher activity of the RuO_2/tantalates was attributed to an important reduction in the electron–hole pair recombination due to the effect produced by the presence of La in the $NaTaO_3$ structure as well as by the role of RuO_2 as electron-trap.

Moreover, Valderrama et al. [107] evaluated the photoelectrochemical activity of CIGS thin films for hydrogen production. It was found that under illumination the quantity of hydrogen produced was two orders of magnitude higher than the hydrogen produced in the dark. While, the characterization of screen-printed Ti/CdS and Ti/CdSe photoelectrodes for photoelectrochemical hydrogen production was performed by Morales et al. [108]. Furthermore, Jaramillo et al. [109] showed the application of fiber optics in the hydrogen production by Photoelectrolysis. They proposed an alternative way to transmit concentrated solar energy which may be applied in the hydrogen production by photoelectrolysis. Whereas, Arriaga et al. [110] prepared and characterized (Zn,Cd)S photoelectrodes for hydrogen production.

Furthermore, Huerta-Flores et al. [111] synthesized $SrZrO_3$ powders as photocatalysts for hydrogen evolution from water splitting. Their results confirm that $SrZrO_3$ is a suitable photocatalyst for clean hydrogen generation from water under UV light irradiation, since crystallinity exhibited the greatest effect on the catalytic activity. In other study, Hernández-Gordillo et al. [112] explored the enhanced blue-light photocatalytic H_2 production using a CdS nanofiber. The high photoactivity was attributed to the quantum confinement effect generated by the small particle size of the nanofibers. Ruiz-Gómez et al [113] evaluated the activity of Sm_2GaTaO_7 photocatalyst. They found that the hydrogen evolution activity was enhanced by using 0.2 wt.% of RuO_2 amount, which exceeded 2.4 times compared with the base photocatalyst, Sm_2GaTaO_7. Pérez-Larios et al. [114] used CoO-TiO_2 and WO_3-TiO_2 mixed oxide as photocatalyst for H_2 generation. They found that under visible irradiation, the catalyst with 5.0% TiO_2-CoO produced the best results. Furthermore, this research group also evaluated zeolites type SBA-16 modified with phosphorous as photocatalyst for hydrogen production [115]. Campos Badillo et al. [116] synthesized GaN by hydrothermal method as promising photo-electrocatalyst for hydrogen

production. While, Alvaro-Ruiz et al. [117] evaluated the effect of synthesis parameters over the hybrid zinc sulfide photocatalyst. Mendoza et al. [118] studied the photocatalytic decomposition of H_2O using mixed semiconductor Bi_2S_3/TiO_2. Whereas, Arzola Rubio et al. [119] proposed $W_{1-x}Mo_xO_3 \bullet 0.33H_2O$ as solid solutions as a tunable band gap photocatalytic material for hydrogen production.

In a fundamental study, Collins-Martinez et al. [120] studied the influence of the anatase/rutile ratio on the TiO_2 photocatalytic activity and concluded that the thermal treatment used to induce the formation of rutile by calcination would presumably reduce water adsorption capacity and surface area, leading to a decrease in photocatalytic activity. In an effort to employ cheaper materials and the utilization of the solar light spectrum, Ortega López et al. [121] studied the effect of $CoFe_2O_4$ as a photocatalyst for H_2 production from water and visible light. They found that cobalt ferrite by ball milling had a higher photocatalytic activity and this was attributed to the vacancies generated during the milling process at which the sample was exposed.

2.4 Theoretical studies

Theoretical studies constitute an invaluable tool towards the understanding and discussion of experimental results in a wide variety of research areas where the hydrogen production is the final target.

In this context, Ramírez-Morales et al. [122] proposed an on-line heuristic optimization strategy to maximize the hydrogen production rate in a continuous stirred tank reactor, while, Ramirez-Morales et al. [123] studied the life cycle assessment of hydrogen production from a high temperature electrolysis process coupled to a high temperature gas nuclear reactor. Furthermore, Blanco-Cocoma et al. [124] proposed a mathematical model for a continuous hydrogen production system on a stirred fermenter connected to a biocatalyzed electrolysis cell. Guillen-Arguelles et al. [125] evaluated the implementation of hydrogen-based technologies in the feasibility study on the use of hydrogen technologies by hotels in the Mexican Caribbean. While a study of the sustainable-hydrogen, production in the Yucatan peninsula was performed by Patiño et al. [126] and Bautista et al. [127] performed a theoretical analysis of the direct decomposition of methane gas in a laminar stagnation-point flow in a CO_2-free production of hydrogen.

2.5 Thermodynamic and energy analyses

Chemical equilibrium in a reaction gas mixture is a dynamic process. A spontaneous approach toward equilibrium is observed when the initial partial pressures of the reactants are high and collisions between reactant molecules cause product molecules to form. Once the partial pressures of the products have increased sufficiently, the reverse reaction (forming “reactants” from “products”) begins to occur. As the equilibrium state is approached, the forward and backward rates of reaction become equal and there is no further net change in reactant and product partial pressures. Furthermore, the total Gibbs free energy function governs the forward and backward directions of chemical reactions. The composition at thermochemical equilibrium can be calculated by minimizing the Gibbs free energy, and so such equilibrium calculations provide a means to estimate the extent to which spontaneous chemical reactions will proceed. Equilibrium calculations provide a best-case effective-catalyst scenario for reaction dynamics without the need for complicated kinetic considerations. Throughout the years thermodynamic and energy analyses have

been of paramount importance to assess possible reaction routes and conditions for the proposed hydrogen production processes.

In this context, Romero-Paredes et al. [128] performed an exergy and separately energy analysis of a thermochemical nuclear cycle for hydrogen production. While, Collins-Martinez et al. [129] performed a thermodynamic modeling for the absorption enhanced reforming of light alcohols (methanol and ethanol) for the production of hydrogen. In other study, Gutierrez et al. [130] performed an entropy generation minimization for the thermal decomposition of methane gas in hydrogen using genetic algorithms. Furthermore, Collins-Martínez et al. [131, 132] performed a thermodynamic analysis of the absorption-enhanced autothermal reforming of ethanol.

2.6 Hydrogen production systems

Coupled systems to produce hydrogen and its utilization is a very active research area in view of its implementation in practical energy-related applications. This is the case of the study of Arriaga et al. [133]. They explored the direct coupling of a solar-hydrogen system consisting of a commercial electrolyzer stack and a photovoltaic (PV) solar system of 36 panels (75 W each) of monocrystalline silicon (Siemens) interconnected in a configuration for 2.7 kW power at 48 VDC. In another interesting system, Sanchez-Dirzo et al. [134] proposed a basic system that stores the energy from waves in the form of hydrogen. While, Sebastian et al. [135] modeled a local grid connected integrated solar-hydrogen-fuel cell systems in Mexico. Furthermore, Espinosa-Paredes et al. [136] made a comparative study of the hydrogen generation during a short-term station blackout (STSBO). In addition, Navarro-Solís et al. [137] performed an analysis of the H_2 production by PEM electrolysis, assisted by textile effluent treatment and a solar photovoltaic cell.

Moreover, Aceves et al. [138] proposed safe, long-range, inexpensive and rapidly refuelable hydrogen vehicles with cryogenic pressure vessels. Several other studies have focused on specific applications of hydrogen production and renewable energies [139-140].

Finally, some studies of systems have proposed the utilization of hydrogen as additives to an automobile[142-142] for supplying electrical power to a sustainable housing with a range of 8h/ day and a hydrogen generation system for a PEM fuel cell and performance evaluation using an on-line LabVIEW data acquisition arrangement [143-144], while other research have focused in the use of use of a dielectric-barrier discharge plasma reactor for hydrogen production [145-146], whereas some other systems have proposed the use of recycled waste aluminum for hydrogen generation [147].

2.7 Electrolysis

Ortiz Verdín et al. [148] reported the study of evaluation of rich in nickel alloys for hydrogen generation in an electrolytic alkaline medium. Furthermore, Olvera Vazquez et al. [149] evaluated the electrochemical behavior of mechanical milling synthesized Al_xSn_y in HER (hydrogen evolution reaction). Ortega Chávez et al. [150] performed a mathematical modeling of the the reaction of hydrogen evolution electrodes of Pt/C considering spillovers. In addition, Gutiérrez et al. [151] made an evaluation of electrocatalysts for the production hydrogen from water electrolysis. Finally, Lucatero et al. [152] evaluated the electrocatalytic Properties of NiMo nanoparticles for the hydrogen evolution reaction.

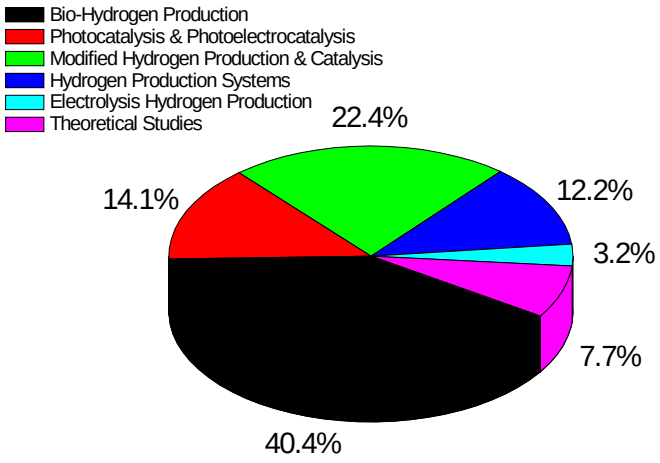

Fig 2. Hydrogen production distribution in terms of research topics in Mexico

3. Conclusion

Figure 2 presents the hydrogen production distribution in terms of research topics in Mexico. From this Figure it can be seen that the distribution of main research activities are quite unique and are reflected in Journal publications and conference proceedings within the last seven years. These resulted in the following topics and contributions: Hydrogen production (HP) from biological processes and wastes 40.4%, followed by HP through conventional and non-conventional fuels (CO_2 capture & Catalysis) 22.4%, HP by photocatalysis & photo-electrocatalysis 14.1%, HP systems and controls 12.2%, theoretical and thermodynamic studies for HP 7.7%, and HP by electrolysis 3.2%. A wide variety of potential applications can be followed by these contributions, while the spread of this research can be a key for future national or international collaborations that may strengthen this important area within the energy sector to take advantage of the upcoming opportunities in the country.

References

[1] Ortega Valencia E., Lacouture J. L. F., Producción De Hidrógeno Mediante Energía Nuclear, Un Escenario Sostenible, Simposio LAS/ANS 2007/2007 LAS/ANS Symposium, Cancún Quintana Roo México, del 1 al 5 de Julio 2007/ Cancún Quintana Roo México, Julio 1-5, 2007.
[2] IEA Energy Technology Essentials: Hydrogen Production & Distribution, OECD/IEA 2007.
[3] Steinfeld A., Solar Thermochemical Production Of Hydrogen-A Review, Solar Energy, vol.78, no.5, pp.603-615, 2005.
[4] Funk J. E., Thermochemical Hydrogen Production: Past And Present, International Journal of Hydrogen Energy,vol.26,no. 3, pp. 185-190, 2001.
[5] National Research Council and National Academy of Engineering. The Hydrogen Economy, The National Academy Press, Washington D.C., United States (2004).
[6] Tarnay D. S., Hydrogen Production at Hydro-Power Plants, International Journal Energy Research 1985, 10,577-584.

[7] Sherif S. A., Barbir F. Veziroglu, T. N., Wind Energy and the Hydrogen Economy—Review Of the Technology, Solar Energy 78, 2005, 647–660.
[8] Sakai, T., Takenaka, H., Torikai, E., 1986. Gas Diffusion in Dried and Hydrated Nafions. J. Electrochem. Soc. 133 (1), 88-92.
[9] Barbir, F., Integrated Renewable Hydrogen Utility System. In: Proc. 1999 DoE Hydrogen Program Annual Review Meeting, Lakewood, CO, May, 1999.
[10] Dincer I. Acar C., Review and Evaluation Of Hydrogen Production Methods For Better Sustainability. International Journal of Hydrogen Energy, Volume 40, Issue 34, 14 September 2015, Pages 11094-11111.
[11] Rand D. A. J., Dell R. M. Fuels - Hydrogen Production: Coal Gasification. Encycl Electrochem Power Sources 2009, 276-92.
[12] Rabbani M., Dincer I., Naterer G. F. Efficiency Assessment of a Photoelectrochemical Chloralkali Process For Hydrogen and Sodium Hydroxide Production. Int J Hydrogen Energy 2014, 39:1941-56.
[13] Sirjoosingh, A., Hammes-Schiffer S. J., Proton-Coupled Electron Transfer versus Hydrogen Atom Transfer: Generation of Charge-Localized Diabatic States. Phys. Chem. A 2011, 115, 2367-2377.
[14] Schneider J., Kandiel T. A., Bahnemann D. W., Solar Photocatalytic Hydrogen Production: Current Status and Future Challenges, Chapter in Materials and Processes for Solar Fuel Production, Volume 174 of the series Nanostructure Science and Technology pp 41-74, 2014.
[15] Torres Zúñiga I., Vargas A. Latrille E. Buitrón G. Robust Observation Strategy To Estimate The Substrate Concentration In The Influent Of A Fermentative Bioreactor For Hydrogen Production, Laboratory For Research On Advanced Processes for Water Treatment, Chemical Engineering Science, Volume 129, 16 June 2015, Pages 126-134.
[16] Villa-Leyva , A. Zhang , I. Torres-Zúñiga, A. Vargas, G. Buitrón, Experimental Validation of a Coupled Nonlinear Observer in a Hydrogen Production Dark Fermenter A, Mexico. XIV International Congress of the Mexican Hydrogen Society, Cancun, Mexico, 2014.
[16a] Ramos C. Buitrón G. Moreno-Andrade I. Rolando Chamy. Effect of the Initial Total Solids Concentration And Initial Ph On The Bio-Hydrogen Production From Cafeteria Food Waste International Journal of Hydrogen Energy, Volume 37, Issue 18, September 2012, Pages 13288-13295.
[17] Alzate-Gaviria L. M., Sebastian P.J., Pérez-Hernández A. Eapen D., Comparison Of Two Anaerobic Systems For Hydrogen Production From The Organic Fraction Of Municipal Solid Waste And Synthetic International Journal of Hydrogen Energy, Volume 32, Issue 15, October 2007, Pages 3141-3146.
[18] Espinoza-Escalante F. M., Pelayo-Ortiz C. Gutiérrez-Pulido H. González-Álvarez V. Alcaraz-González V. Bories A. Multiple Response Optimization Analysis For Pretreatments Of Tequila's Stillages (Waste) For Vfas And Hydrogen Production, Bioresource Technology, Volume 99, Issue 13, September 2008, Pages 5822-5829.
[19] Buitrón G., Kumar G., Martinez-Arce A., Moreno G., Hydrogen And Methane Production Via A Two-Stage Processes (H2-SBR + CH4-UASB) Using Tequila Vinasses Laboratory for Research on Advanced Processes for Water Treatment, International Journal of Hydrogen Energy, Volume 39, Issue 33, 11 November 2014, Pages 19249-19255.
[20] Cardeña R., Moreno G., Buitrón G., Optimization of Photo-Fermentative Hydrogen Production using Volatile Fatty Acids, XIV International Congress of the Mexican Hydrogen Society Cancún 2014.
[21] Carrillo-Reyes J., Celis L.B., Alatriste-Mondragón F., Montoya L., Razo-Flores E., Strategies To Cope With Methanogens In Hydrogen Producing UASB Reactors: Community Dynamics, International Journal of Hydrogen Energy, Volume 39, Issue 22, 24 July 2014, Pages 11423-11432.
[22] Espinoza-Escalante F.M., Pelayo-Ortíz C., Navarro-Corona J., González-García Y., Bories A., Gutiérrez-Pulido H. Anaerobic Digestion of the Vinasses from the Fermentation of Agave Tequilana Weber to Tequila: The Effect Of pH, Temperature and Hydraulic Retention Time on the Production of Hydrogen and Methane, Biomass and Bioenergy, Volume 33, Issue 1, January 2009, Pages 14-20.
[23] Davila-Vazquez G., Cota-Navarro C.B., Rosales-Colunga L.M., de León-Rodríguez A., Razo-Flores E., Continuous Biohydrogen Production Using Cheese Whey: Improving the Hydrogen Production Rate, International Journal of Hydrogen Energy, Volume 34, Issue 10, May 2009, Pages 4296-4304.
[24] Castillo-Hernández A., Mar-Alvarez I., Moreno-Andrade I., Start-Up And Operation Of Continuous Stirred-Tank Reactor For Biohydrogen Production From Restaurant Organic Solid Waste, International Journal of Hydrogen Energy, In Press, Corrected Proof, Available online 7 May 2015.

[25] Arriaga S., Rosas I., Alatriste-Mondragón F., Razo-Flores E., Continuous Production Of Hydrogen From Oat Straw Hydrolysate In A Biotrickling Filter, International Journal of Hydrogen Energy, Volume 36, Issue 5, March 2011, Pages 3442-3449.

[26] Hernández-Mendoza C.E., Moreno-Andrade I., Buitrón G., Comparison Of Hydrogen-Producing Bacterial Communities Adapted In Continuous And Discontinuous Reactors, International Journal of Hydrogen Energy, Volume 39, Issue 26, 3 September 2014, Pages 14234-14239.

[27] Muñoz-Páez K.M., Ruiz-Ordáz N., García-Mena J., Ponce-Noyola M.T., Ramos-Valdivia A.C., Robles-González I.V., Villa-Tanaca L., Barrera-Cortés J., Rinderknecht-Seijas N., Poggi-Varaldo H.M., Comparison of Biohydrogen Production In Fluidized Bed Bioreactors At Room Temperature And 35 °C. International Journal of Hydrogen Energy, Volume 38, Issue 28, 19 September 2013, Pages 12570-12579.

[28] Ríos-González L.J., Moreno-Dávila I.M., Rodríguez-Martínez J., Garza-García Y. Biohydrogen Production From Diary Processing Wastewater By Anaerobic Biofilm Reactors, African Journal of Biotechnology Vol. 10, No 27, 2011.

[29] Mayela I., Moreno Dávila M., Herrera Ramírez E.B., Ríos González L.J., Gutiérrez Rodríguez B., Garza García Y., Rodríguez Martínez J., Hydrogen Production In UASB Reactor Using Enzymatic Hydrolysates from Paper Industry Wastes by Anaerobic Biofilms: Influence of HRT, XI International Congress of the Mexican Hydrogen Society, Cuernavaca 2011.

[30] Quechulpa-Pérez P., Pérez-Robles J.F., Pérez-de Brito A.F., Avilés-Arellano L.M., Hybrid Membranes Prepared by the Sol-Gel Process and based on SilicaPolyvinyl Acetate for Methane Enrichment from Biogas, J Membra Sci Technol 2014, 4:1.

[31] Márquez-Reyes L.A., Sánchez-Saavedra M.P., Valdez-Vazquez I., Improvement Of Hydrogen Production By Reduction Of The Photosynthetic Oxygen In Microalgae Cultures Of Chlamydomonas Gloeopara And Scenedesmus Obliquus, International Journal of Hydrogen Energy, Volume 40, Issue 23, 22 June 2015, Pages 7291-7300.

[32] Martín del Campo J.S., Escalante R., Robledo D., Patiño R., Hydrogen Production By Chlamydomonas Reinhardtii Under Light-Driven And Sulfur-Deprived Conditions: Using Biomass Grown In Outdoor Photobioreactors At The Yucatan Peninsula, International Journal of Hydrogen Energy, Volume 39, Issue 36, 12 December 2014, Pages 20950-20957.

[33] Márquez-Reyes L.A., Sánchez Saavedra M.P., Valdez-Vazquez I., Hydrogen Production By Native Species Of Microalgae Isolated From México, XI International Congress of the Mexican Hydrogen Society, Cuernavaca 2011.

[34] Martín del Campo J.S., Patiño R., Prototipo Para La Bioproducción De H2 Por Chlamydomonas Reinhardtii Cinvestav, X International Congress of the Mexican Hydrogen Society 2010 Toluca.

[35] Pérez-Rangel M., Quiroz-Figueroa F.R., González-Castañeda J., Valdez-Vazquez I., Microscopic Analysis Of Wheat Straw Cell Wall Degradation By Microbial Consortia For Hydrogen Production, International Journal of Hydrogen Energy, Volume 40, Issue 1, 5 January 2015, Pages 151-160.

[36] Pérez-Rangel M., González-Castañeda J., Molina-Guerrero C., Sánchez Carmona A., Valdez-Vazquez I., Evaluation And Isolation Of Natural Anaerobic Consortia For Hydrogen Production From Wheat Straw, XIII International Congress of the Mexican Hydrogen Societym, Aguascalientes 2013.

[37] Torres-Aguirre G., Lara-Vazquez A., Molina-Guerrero C., Sánchez Carmona A., Valdez-Vazquez I., Efecto De La Relación C/N Y C/P Sobre La Producción De Biohidrógeno A Partir De La Fermentación De Paja De Trigo En Reactores, XIII International Congress of the Mexican Hydrogen Society, Aguascalientes 2013.

[38] Lara-Vázquez A.R., Sánchez A., Valdez-Vazquez I., Hydration Treatments Increase The Biodegradability Of Native Wheat Straw For Hydrogen Production By A Microbial Consortium, International Journal of Hydrogen Energy, Volume 39, Issue 35, 3 December 2014, Pages 19899-19904.

[39] Lara-Vazquez A., Sánchez Carmona A., Valdez-Vazquez I., Effect Of Particle Size And Hydration Treatment On The Wheat Straw Biodegradability And Hydrogen Production By A Microbial Consortium, XIII International Congress of the Mexican Hydrogen Society, Aguascalientes 2013.

[40] Terrazas-Hoyos H., Portugal-Marín E., Sánchez-Salinas E., Ortiz-Hernández M.L., Evaluation Of The Potential Hydrogen Production By Diazotrophic Burkholderia Species, International Journal of Hydrogen Energy, Volume 39, Issue 7, 25 February 2014, Pages 3142-3151.

[41] Arreola-Vargas J., Celis L.B., Buitrón G., Razo-Flores E., Alatriste-Mondragón F., Hydrogen Production From Acid And Enzymatic Oat Straw Hydrolysates In An Anaerobic Sequencing Batch Reactor: Performance And Microbial Population Analysis, International Journal of Hydrogen Energy, Volume 38, Issue 32, 25 October 2013, Pages 13884-13894.
[42] Alvarado-Cuevas Z.D., Ordoñez Acevedo L.G., Ornelas Salas J.T., De León-Rodríguez A., Nitrogen Sources Impact Hydrogen Production By Escherichia Coli Using Cheese Whey As Substrate, New Biotechnology, Volume 30, Issue 6, 25 September 2013, Pages 585-590.
[43] Rosales-Colunga L.M., Razo-Flores E., Ordoñez L.G., Alatriste-Mondragón F., De León-Rodríguez A., Hydrogen Production By Escherichia Coli Δhyca Δlaci Using Cheese Whey As Substrate, International Journal of Hydrogen Energy, Volume 35, Issue 2, January 2010, Pages 491-499.
[44] Rosales-Colunga L.M., Razo-Flores E., De León-Rodríguez A., Influence Of Ph Control On Hydrogen Production By Escherichia Coli Δhyca Δlaci Using Cheese Whey As, Journal of Biotechnology, Volume 150, Supplement, November 2010, Pages 152-153.
[45] Muñoz- Páez K.M., Poggi-Varaldo H.M., García-Mena J., Evaluation of Biohydrogen Production from Cheese Whey and Assessment of the Associated Microbial Community, XIV International Congress of the Mexican Hydrogen Society, Cancún 2014.
[46] Davila-Vazquez G., de León-Rodríguez A., Alatriste-Mondragón F., Razo-Flores E., The Buffer Composition Impacts: The Hydrogen Production and The Microbial Community Composition in Non-Axenic Cultures, Biomass and Bioenergy, Volume 35, Issue 7, July 2011, Pages 3174-3181.
[47] A.U. Juantorena, P.J. Sebastian, E. Santoyo, S.A. Gamboa, O.D. Lastres, D. Sánchez-Escamilla, A. Bustos, D. Eapen, Hydrogen Production Employing Spirulina Maxima 2342: A Chemical Analysis, International Journal of Hydrogen Energy, Volume 32, Issue 15, October 2007, Pages 3133-3136.
[48] Juantorena A.U., Sebastian P.J., Lastres O., Hernández, Bustos G.A., Hydrogen Production By Spirulina Maxima 2342 In Different Light Intensities And Quantification Through A PEMFC, XI International Congress of the Mexican Hydrogen Society, Cuernavaca 2011.
[49] Valdez-Vazquez I., Ponce-Noyola M.T., Poggi-Varaldo H.M., Nutrients Related To Spore Germination Improve H_2 Production From Heat-Shock-Treated Consortia, International Journal of Hydrogen Energy, Volume 34, Issue 10, May 2009, Pages 4291-4295.
[50] Cepeda Rodríguez Y., Ríos Gonzáleza L.J., Martínez Luévanos A., Garza García Y., Rodríguez Martínez J., Rodríguez de la Garza J.A., Biohydrogen Production By Biofilms Developed On Opuntia Imbricata Native And Modificated, X International Congress of the Mexican Hydrogen Society, 2010 Toluca.
[51] Herrera Ramírez E.B., Moreno Dávila I.M.M., Ríos González L.J., Gutiérrez Rodriguez B., Garza García Y., Rodríguez Martínez J., Influence Of The Ph On Hydrogen Production By SSF Of Paper Industry Wastes Using Anaerobic Biofilms, XI International Congress of the Mexican Hydrogen Society, Cuernavaca 2011.
[52] Morales-García A.L., Escalante A., Ruiz G.M.L, González Castañeda J., Valdez-Vazquez I., Evaluation Of Different Natural Microbial Consortia For H2 Production From Crystalline Cellulose, XIII International Congress of the Mexican Hydrogen Society, Aguascalientes 2013.
[53] Navarro Díaz M., Valdez-Vazquez I., Escalante A.E., Differences in Ecological Structure Between Hydrogen Producing and Anaerobic Digestion Consortia, XIV International Congress of the Mexican Hydrogen Society, Cancún 2014.
[54] Davila-Vazquez G., Alatriste-Mondragón F., de León-Rodríguez A., Razo-Flores E., Fermentative Hydrogen Production in Batch Experiments Using Lactose, Cheese Whey and Glucose: Influence of Initial Substrate Concentration and pH, International Journal of Hydrogen Energy, Volume 33, Issue 19, October 2008, Pages 4989-4997.
[55] Rosales-Colunga L.M., Razo-Flores E., De León Rodríguez A., Fermentation Of Lactose And Its Constituent Sugars By Escherichia Coli WDHL: Impact On Hydrogen Production, Bioresource Technology, Volume 111, May 2012, Pages 180-184.
[56] Rosales-Colunga L.M., González García R., De León Rodríguez A., Estimation Of Hydrogen Production In Genetically Modified E. Coli Fermentations Using An Artificial Neural Network, International Journal of Hydrogen Energy, Volume 35, Issue 24, December 2010, Pages 13186-13192.
[57] Valdez-Vazque I., Poggi-Varaldo H.M., Hydrogen Production By Fermentative Consortia, Renewable and Sustainable Energy Reviews, Volume 13, Issue 5, June 2009, Pages 1000-1013.

[58] Robledo-Narváez P.N., Muñoz-Páez K.M., Poggi-Varaldo H.M., Ríos-Leal E., Calva-Calva G., Ortega-Clemente L.A., Rinderknecht-Seijas N., Estrada-Vázquez C., Ponce-Noyola M.T., Salazar-Montoya J.A., The Influence Of Total Solids Content And Initial Ph On Batch Biohydrogen Production By Solid Substrate Fermentation Of Agroindustrial Wastes, Journal of Environmental Management, Volume 128, 15 October 2013, Pages 126-137.

[59] Moreno-Dávila I.M.M., Rios-González L. J., Gaona-Lozano J.G., Garza- García Y., Rodríguez-de la Garza J.A., Rodríguez-Martínez J., Fermentative Hydrogen Production By Anaerobic Biofilms From A Pretreated Mixed Microflora, Research Journal of Applied Sciences 5 (6): 376-382, 2010.

[60] García-López D., Adessi A., Olguín E.J., De Philippis R., Vegetable Fermentation Products As Substrate For Hydrogen Production By Rhodopseudomonas Palustris 42OL, XIII International Congress of the Mexican Hydrogen Society, Aguascalientes 2013.

[61] Alamilla Z.L., Escalante A.E., Valdez-Vazquez I., Richness, Composition and Predominance in Undefined Mixed Cultures for Fermentative Hydrogen Production, XIV International Congress of the Mexican Hydrogen Society, Cancún 2014.

[62] Montiel-Corona V., Revah S., Morales M., Hydrogen Production By An Enriched Photoheterotrophic Culture Using Dark Fermentation Effluent As Substrate: Effect Of Flushing Method, Bicarbonate Addition, And Outdoor–Indoor Conditions, International Journal of Hydrogen Energy, In Press, Corrected Proof, Available online 12 June 2015.

[63] Cisneros-Pérez C., Carrillo-Reyes J., Celis L.B., Alatriste-Mondragón F., Etchebehere C., Razo-Flores E., Inoculum Pretreatment Promotes Differences In Hydrogen Production Performance In EGSB Reactors, Dark Fermentation, International Journal of Hydrogen Energy, Volume 40, Issue 19, 25 May 2015, Pages 6329-6339.

[64] Hernández-Rojas M.E., Alemán-Ruiz A., Fajardo-Ortiz C., Baéz-Pimiento S., Dávila-Gómez J.A., Effect Of The Mixed Inocula And The Ph During The Dark Fermentation Process For The Production Of The Hydrogen Using Molasses As Substrate, XIII International Congress of the Mexican Hydrogen Society, Aguascalientes 2013.

[65] Vereaa L., Savadogo O., Verde A., Campos J., Ginez F., Sebastian P.J., Performance Of A Microbial Electrolysis Cell (MEC) For Hydrogen Production With A New Process For The Biofilm Formation, International Journal of Hydrogen Energy, Volume 39, Issue 17, 5 June 2014, Pages 8938-8946.

[66] Rivera I., Buitrón G., Hydrogen Production in a Microbial Electrolysis Cell Fed with Volatile Fatty Acids, SMH Cancún 2014.

[67] Chonga M, Sabaratnam V. Shirai Y. Hassan M. A. Biohydrogen Production from Biomass and Industrial Wastes by Dark Fermentation. International Journal of Hydrogen Energy 34 (2009) 3277–3287.

[68] López Ortiz A., Neri Segura F.J., Sandoval Jabalera R., Marques da Silva Paula M., Arias del Campo E., Salinas Gutiérrez J., Escobedo Bretado M.A., Collins-Martínez V., Low Temperature Sugar Cane Bagasse Pyrolysis For The Production Of High Purity Hydrogen Through Steam Reforming And CO2 Capture, International Journal of Hydrogen Energy, Volume 38, Issue 28, 19 September 2013, Pages 12580-12588.

[69] Sanchez A., Sevilla-Guitron V., Magaña G., Melgoza P. Hernandez H., Co-Production of Ethanol, Hydrogen and Biogas Using Agro-Wastes. Conceptual Plant Design and NPV Analysis for Mid-Size Agricultural Sectors, Computer Aided Chemical Engineering, Volume 29, 2011, pp 1884-1888.

[70] Escamilla-Alvarado C., Ríos-Leal E., Barrera-Cortes J., Esparza-García F., Ponce-Noyola M.T., Poggi-Varaldo H.M., Hydrogen Production from Organic Wastes and Re-Use of Fermented Solids to Produce Holocellulases: A Crucial Combination for Biorefinery of Organic Wastes, SMH Aguascalientes 2013.

[71] Poggi-Varaldo H.M. , Robledo-Narváez P.N., Munoz-Paez K.M., Escamilla-Alvarado C., Ponce-Noyola M.T., Calva-Calva G., Ríos-Leal E., Galíndez-Mayer J., Rinderknecht-Seijas N.F., Estrada-Vázquez C., Ortega-Clemente A., An Overview of Hydrogen Fermentation, Methane and Bioelectricity as Key Contributions to Biorefineries of Organic Wastes, XIII International Congress of the Mexican Hydrogen Society, Aguascalientes 2013.

[72] Moreno-Andrade I., Bujanos-Adame M.C., Biohydrogen Production from Organic Solid Waste in a Discontinuous Process, XIV International Congress of the Mexican Hydrogen Society, Cancún 2014.

[73] Escamilla Alvarado C., Ponce-Noyola M.T., Rios-Leal E., Rinderknecht-Seijas N., Poggi-Varaldo H.M., Biohydrogen Production through Solid Substrate Fermentation of Organic Municipal Wastes : a Multivariable Evaluation, XII International Congress of the Mexican Hydrogen Society Mérida 2012.

[74] Escobedo Bretado M.A., Delgado Vigil M.D., Salinas Gutiérrez J., López Ortiz A., Collins-Martínez V., Hydrogen Production By Absorption Enhanced Water Gas Shift (AEWGS), International Journal of Hydrogen Energy, Volume 35, Issue 21, November 2010, Pages 12083-12090.

[75] Escobedo-Bretado M.A., Ponce-Peña P., Delgado-Vigil M.D., Salinas-Gutiérrez J.M., López Ortiz A., Collins-Martínez V.H., Producción de hidrógeno mediante la combinación de las reacciones de desplazamiento de agua y carbonatación de un absorbente de CO_2, XIV International Congress of the Mexican Hydrogen Society, 2009 Saltillo.

[76] De los Ríos Castillo T., Salinas Gutiérrez J., López Ortiz A., Collins-Martínez V., Global Kinetic Evaluation During The Reduction Of Cowo4 With Methane For The Production Of Hydrogen, International Journal of Hydrogen Energy, Volume 38, Issue 28, 19 September 2013, Pages 12519-12526.

[77] De los Ríos Castillo T., Salinas Gutiérrez J., Delgado Vigil D., López Ortiz A., Collins-Martínez V. Evaluación De La Cinética Global De Reducción Del Cowo4 Con Metano Para La Producción De Hidrogeno, Catalysis Today, Volumes 107–108, 30 October 2005, Pages 831-837.

[78] Aceves Olivas D.Y., Baray Guerrero M.R., Escobedo Bretado M.A., Marques da Silva Paula M., Salinas Gutiérrez J., Guzmán Velderrain V., López Ortiz A., Collins-Martínez V., Enhanced Ethanol Steam Reforming By CO_2 Absorption Using Cao, Cao*Mgo Or Na2ZrO3, International Journal of Hydrogen Energy, Volume 39, Issue 29, 2 October 2014, Pages 16595-16607.

[79] Beltrán-Piña B.B., Delgado-Vigil M.D., Salinas-Gutiérrez J.M., López-Ortiz A., Collins-Martínez V., Reformación De Etanol Combinada Con Absorción De CO_2 Para Producción De Hidrógeno, IX International Congress of the Mexican Hydrogen Society 2009, Saltillo.

[80] Lopez-Ortiz A., Collins-Martinez V., Harrison D.P., SER Process Variable Evaluation For The Production Of Hydrogen Using Calcined Dolomite, XIV International Congress of the Mexican Hydrogen Society, Toluca 2010.

[81] López Ortiz A., Escobedo Bretado M.A., Guzmán Velderrain V., Meléndez Zaragoza M., Salinas Gutiérrez J., Lardizábal Gutiérrez D., Collins-Martínez V., Experimental And Modeling Kinetic Study Of The CO_2 Absorption By Li_4SiO_4, International Journal of Hydrogen Energy, Volume 39, Issue 29, 2 October 2014, Pages 16656–16666.

[82] Escobedo Bretado M. A., González Lozano Ma.A., Guzmán Velderrain V., Pallares Sámano R.B., Salinas Gutiérrez J., Collins-Martínez V., López Ortiz A., Estudio Cinético Y Modelación De La Absorción De CO_2 Por El Li4SiO4 Para La Producción De Hidrógeno, XIV International Congress of the Mexican Hydrogen Society, Aguascalientes 2013.

[83] Valverde-Ramírez A.A., Sánchez-Castro M.E., Carbón Y Biomasa Una Alternativa Para La Obtención De Hidrógeno Por Medio De Procesos Termoquímicos, Catalysis Today, Volume 212, 1 September 2013, Pages 225–231.

[84] Guevara J.C., Wang J.A., Chen L.F., Valenzuela M.A., Salas P., García-Ruiz A., Toledo J.A., Cortes-Jácome M.A., Angeles-Chavez C., Novaro O., Ni/Ce-MCM-41 Mesostructured Catalysts For Simultaneous Production Of Hydrogen And Nanocarbon Via Methane Decomposition, International Journal of Hydrogen Energy, Volume 35, Issue 8, April 2010, Pages 3509-3521.

[85] Galindo-Hernández F., Domínguez J.M., Portales B., Structural And Textural Properties Of Fe2O3/Γ-Al2O3 Catalysts And Their Importance In The Catalytic Reforming Of CH4 With H2S For Hydrogen Production, Journal of Power Sources, Volume 287, 1 August 2015, Pages 13-24.

[86] Martínez-Salazar A.L., Melo-Banda J.A., Domínguez-Esquivel J.M., Martínez-Sifuentes V.H., Salazar-Cerda Y., Coronel-García M.A., Meraz-Melo M.A., Hydrogen production by methane and hydrogen sulphide reaction: Kinetics and modeling study over Mo/La2O3–ZrO2 catalyst, International Journal of Hydrogen Energy, In Press, Corrected Proof, Available online 22 April 2015.

[87] Martínez-Salazar A.L., Melo-Banda J.A., Domínguez-Esquivel J.M., Coronel-García M.A., Reyes de la Torre A.I., High H_2 Production from the Reforming of CH4 by Hydrogen Sulphide Using Mo-Cr Supported on Heterogeneous Catalysts, XIV International Congress of the Mexican Hydrogen Society, Cancún 2014

[88] González Vargas O.A., de los Reyes Heredia J.A., Wang J.A., Chen L.F., Montesinos Castellanos A., Llanos M.E., Hydrogen Production over Rh/Ce-MCM-41 Catalysts via Ethanol Steam Reforming, International Journal of Hydrogen Energy, Volume 38, Issue 32, 25 October 2013, Pages 13914-13925.

[89] Melchor-Hernández C., Gómez-Cortés A., Díaz G., Hydrogen Production By Steam Reforming Of Ethanol Over Nickel Supported On La-Modified Alumina Catalysts Prepared By Sol–Gel, Fuel, Volume 107, May 2013, Pages 828-835.

[90] Contreras J.L., Salmones J., Colín-Luna J.A., Nuño L., Quintana B., Córdova I., Zeifert B., Tapia C., Fuentes G.A., Catalysts For H_2 Production Using The Ethanol Steam Reforming (A Review), International Journal of Hydrogen Energy, Volume 39, Issue 33, 11 November 2014, Pages 18835-18853.

[91] Pérez-Hernández R., Gutiérrez-Martínez A., Palacios J., Vega-Hernández M., Rodríguez-Lugo V., Hydrogen Production By Oxidative Steam Reforming Of Methanol Over $Ni/CeO_2–ZrO_2$ Catalysts, International Journal of Hydrogen Energy, Volume 36, Issue 11, June 2011, Pages 6601-6608.

[92] Pérez-Hernández R., Vega-Hernández M., Rodríguez-Lugo V., Hydrogen Production by Oxidative Steam Reforming of Methanol over $Ni/CeO_2–ZrO_2$ Catalysts, X International Congress of the Mexican Hydrogen Society, Toluca 2010.

[93] Hernández-Pichardo M. L., Valenzuela M. A., Paredes S. P., Díaz C., Escamilla F., Efecto del Método de Síntesis de Catalizadores de Ni/ZrO_2-CeO_2 para la producción simultánea de hidrógeno y nanotubos de carbón, XIV International Congress of the Mexican Hydrogen Society, Toluca 2010.

[94] Ortiz M.A., Contreras J. L., Fuentes G.A., Luna R., Salmones J., Zeifert B., Vázquez A., Efecto Del WOx Sobre Catalizadores de Co, Ni/Hidrotalcita para obtener hidrógeno a partir de bioetanol, XIV International Congress of the Mexican Hydrogen Society, 2009 Saltillo.

[95] Ortiz M.A., Contreras J.L., Fuentes G.A., Luna R., Salmones J., Zeifert B., Hidrógeno A Partir De Bioetanol Sobre Catalizadores De Pt/Hidrotalcita Estabilizados Con WOx. XIV International Congress of the Mexican Hydrogen Society, SMH 2009 Saltillo.

[96] López P., Mondragón-Galicia G., Espinosa-Pesqueira M.E., Mendoza-Anaya D., Fernández Ma.E., Gómez-Cortés A., Bonifacio J., Martínez-Barrera G., Pérez-Hernández R., Hydrogen Production From Oxidative Steam Reforming Of Methanol: Effect Of The Cu And Ni Impregnation On Zro2 And Their Molecular Simulation Studies, International Journal of Hydrogen Energy, Volume 37, Issue 11, June 2012, Pages 9018-9027.

[97] Pérez-Hernández R., Gutiérrez-Martínez A., Gutiérrez-Wing C.E., Effect Of Cu Loading On Ceo2 For Hydrogen Production By Oxidative Steam Reforming Of Methanol, International Journal of Hydrogen Energy, Volume 32, Issue 14, September 2007, Pages 2888-2894.

[98] Salmones J., Wang J.A., Valenzuela M.A., Sánchez E., Garcia A., Pore Geometry Influence On The Deactivation Behavior Of Ni-Based Catalysts For Simultaneous Production Of Hydrogen And Nanocarbon, Catalysis Today, Volume 148, Issues 1–2, 30 October 2009, Pages 134-139.

[99] Pérez-Hernández R., Gutiérrez-Martínez A., Espinosa-Pesqueira M.E., Estanislao Ma.L., Palacios J., Effect Of The Bimetallic Ni/Cu Loading On The Zro2 Support For H2 Production In The Autothermal Steam Reforming Of Methanol, Instituto Nacional de Investigaciones Nucleares.

[100] Zapata B., Valenzuela M.A., Palacios J., Torres-Garcia E.,] Effect Of Ca, Ce Or K Oxide Addition On The Activity Of Ni/Sio2 Catalysts For The Methane Decomposition Reaction, International Journal of Hydrogen Energy, Volume 35, Issue 21, November 2010, Pages 12091-12097.

[101] Oros-Ruiza S., Zanella R., Collins S.E., Hernández-Gordillo A., Gómez R., Photocatalytic Hydrogen Production By Au–MxOy (Mdouble Bond; Length As M-Dashag, Cu, Ni) Catalysts Supported On TiO_2, Catalysis Communications, Volume 47, 5 March 2014, Pages 1-6.

[102] Oros-Ruiz S., Zanella R., López R., Hernández-Gordillo A., Gómez R., Photocatalytic Hydrogen Production By Water/Methanol Decomposition Using Au/TiO_2 Prepared By Deposition–Precipitation With Urea , Journal of Hazardous Materials, Volume 263, Part 1, 15 December 2013, Pages 2-10.

[103] Galindo-Hernández F., Wang J., Chen L., Bokhimi X., Gómez R., Pérez-Larios A., Nava Entzana N., On The Role Of Fe^{3+} Ions In FexOy/C Catalysts For Hydrogen Production From The Photodehydrogenation Of Ethanol, Journal of Hazardous Materials, Volume 263, Part 1, 15 December 2013, Pages 11-19.

[104] Escobedo Salas S., Serrano Rosales B., De Lasa H., Quantum Yield with Platinum Modified TiO_2 Photocatalyst for Hydrogen Production, Applied Catalysis B: Environmental, Volumes 140–141, August–September 2013, Pages 523-536.

[105] Pérez-Larios A., Lopez R., Hernández-Gordillo A., Tzompantzi F., Gómez R., Torres-Guerra L.M., Improved Hydrogen Production From Water Splitting Using TiO_2–ZnO Mixed Oxides Photocatalysts, Fuel, Volume 100, October 2012, Pages 139-143.

[106] Torres-Martínez L.M., Gómez R., Vázquez-Cuchillo O., Juárez-Ramírez I., Cruz-López A., Alejandre-Sandoval F.J., Enhanced Photocatalytic Water Splitting Hydrogen Production On Ruo2/La:Natao3 Prepared By Sol–Gel Method, Catalysis Communications, Volume 12, Issue 4, 15 December 2010, Pages 268-272.

[107] Valderrama R.C., Sebastian P.J., , Pantoja Enriquez J., Gamboa S.A., Photoelectrochemical Characterization Of CIGS Thin Films For Hydrogen Production, Solar Energy Materials and Solar Cells, Volume 88, Issue 2, 15 July 2005, Pages 145-155.

[108] Morales M., Sebastian P.J., Solorza O., Characterization Of Screen Printed Ti/CdS And Ti/CdSe Photoelectrodes For Photoelectrochemical Hydrogen Production, Solar Energy Materials and Solar Cells, Volume 55, Issues 1–2, 23 July 1998, Pages 51-58.

[109] Jaramillo O.A., Arriaga L.G., Sebastian P.J., Fernández A.M., Del Río J.A., Application Of Fiber Optics In The Hydrogen Production By Photoelectrolysis, International Journal of Hydrogen Energy, Volume 23, Issue 11, November 1998, Pages 985-993.

[110] Arriaga L.G., Fernández A.M, Solorza O., Preparation And Characterization Of (Zn,Cd)S Photoelectrodes For Hydrogen Productio, International Journal of Hydrogen Energy, Volume 23, Issue 11, November 1998, Pages 995-998.

[111] Huerta-Flores A.M., Torres-Martínez L.M., Sánchez-Martínez D., Zarazúa-Morín M.E., $SrZrO_3$ Powders: Alternative Synthesis, Characterization, And Application As Photocatalysts For Hydrogen Evolution From Water Splitting, Fuel, Volume 158, 15 October 2015, Pages 66-71.

[112] Hernández-Gordillo A., Tzompantzi F., Oros-Ruiz S., Torres-Martinez L.M., Gómez R., Enhanced Blue-Light Photocatalytic H2 Production Using Cds Nanofiber , Catalysis Communications, Volume 45, 5 February 2014, Pages 139-143.

[113] Ruiz-Gómez M.A., Torres-Martínez L.M., Figueroa-Torres M.Z., Moctezuma E., Juárez-Ramírez I. Hydrogen Evolution from Pure Water over a New Advanced Photocatalyst Sm_2GaTaO_7, International Journal of Hydrogen Energy, Volume 38, Issue 28, 19 September 2013, Pages 12554-12561.

[114] Pérez-Larios A., Hernández-Gordillo A., Tzompantzi F., Gómez R., CoO-TiO_2 And WO_3-TiO_2 Mixed Oxide As Photocatalyst For H2 Generation , XI International Congress of the Mexican Hydrogen Society, Cuernavaca 2011.

[115] Pérez-Larios A., Hernández-Gordillo A., Guzman M.A., Huirache-Acuña R., Gómez R., Zeolites Type SBA-16 Modified With Phosphorous As Photocatalyst For Hydrogen Production, XI International Congress of the Mexican Hydrogen Society , Cuernavaca 2011.

[116] Campos Badillo, Manzo-Robledo A., Vázquez Cuchillo O., ElizondoVillareal N., Arquímedes Cruz-López, Synthesis Of Gan By Hydrothermal Method As Promising Photo-Electrocatalyst For Hydrogen Production Anayancy, XI International Congress of the Mexican Hydrogen Society, Cuernavaca 2011.

[117] Alvaro-Ruiz J. M., Hernández-Gordillo A., Gómez R., Efecto De Parámetros De Síntesis Del Sulfuro De Zinc Hibrido (ZnS(En)0.5) En La Obtención De H2 A Partir De La Disociación Del Agua, XIII International Congress of the Mexican Hydrogen Society, Aguascalientes 2013.

[118] Mendoza C.G., López R., Hernández Gordillo A., Gómez R., Descomposición Fotocatalítica Del H_2O Empleando Semiconductores Mixtos Bi2S3/Tio2, XIII International Congress of the Mexican Hydrogen Society Aguascalientes 2013.

[119] Arzola-Rubio A., Camarillo J., Collins-Martínez V., De la Torre-Sáenz L., Paraguay-Delgado F., W1-Xmoxo3•0.33H2O Solid Solutions With Tunable Band Gap For Hydrogen Production, XIV International Congress of the Mexican Hydrogen Society, Cancún 2014.

[120] Collins-Martínez V. López Ortiz A. Aguilar Elguezabal A. Influence of the Anatase/Rutile Ratio on the TiO_2 Photocatalytic Activity for the Photodegradation of Light Hydrocarbons. International Journal of Chemical Reactor Engineering, Volume 5 2007 Article A92.

[121] Ortega López Y., Medina Vázquez H., Salinas Gutiérrez J., Guzmán Velderrain V., López Ortiz A., Collins Martínez V., Synthesis Method Effect of $CoFe_2O_4$ on Its Photocatalytic Properties for H_2 Production from Water and Visible Light, Journal of Nanomaterials, Volume 2015 (2015), Article ID 985872, 9 pages.

[122] Ramírez-Morales J.E., Torres Zúñiga I., Buitrón G., On-Line Heuristic Optimization Strategy To Maximize The Hydrogen Production Rate In A Continuous Stirred Tank Reactor, Process Biochemistry, Volume 50, Issue 6, June 2015, Pages 893-900.
[123] Giraldi M.R., François J.L., Martin-del-Campo C., Life Cycle Assessment Of Hydrogen Production From A High Temperature Electrolysis Process Coupled To A High Temperature Gas Nuclear Reactor , International Journal of Hydrogen Energy, Volume 40, Issue 10, 16 March 2015, Pages 4019-4033.
[124] Blanco-Cocom L., Guerrero-Álvarez A., Domínguez-Maldonado J., Ávila-Vales E., Alzate-Gaviria L., Mathematical Model For A Continuous Hydrogen Production System: Stirred Fermenter Connected To A Biocatalyzed Electrolysis Cell, Biomass and Bioenergy, Volume 48, January 2013, Pages 90-99.
[125] Guillen-Arguelles E., López-Santiago R., Escobar B., Valenzuela-Muñiz A.M., Carballo-Guillen E.M., Verde Gómez Y., Feasibility Study On The Use Of Hydrogen Technologies By Hotels In The Mexican Caribbean, XIII International Congress of the Mexican Hydrogen Society Aguascalientes 2013.
[126] Patiño R., Sustainable Hydrogen Production in Yucatan, XIV International Congress of the Mexican Hydrogen Society, 2012 Mérida.
[127] Bautista O., Méndez F., Treviño C., Theoretical Analysis Of The Direct Decomposition Of Methane Gas In A Laminar Stagnation-Point Flow: CO_2-Free Production Of Hydrogen, International Journal of Hydrogen Energy, Volume 33, Issue 24, December 2008, Pages 7419-7426.
[128] Romero-Paredes H., Vázquez Rodríguez A., Espinosa Paredes G., Villafan Vidales H.I., Ambriz García J.J., Nuñez-Carrera A., Exergy And Separately Energy Analysis Of A Thermochemical Nuclear Cycle For Hydrogen Production, Applied Thermal Engineering, Volume 75, 22 January 2015, Pages 1311-1320.
[129] Collins-Martinez V., Escobedo Bretado M., Meléndez Zaragoza M., Salinas Gutiérrez J., Lopez Ortiz A., Absorption Enhanced Reforming Of Light Alcohols (Methanol And Ethanol) For The Production Of Hydrogen: Thermodynamic Modeling, International Journal of Hydrogen Energy, Volume 38, Issue 28, 19 September 2013, Pages 12539-12553.
[130] Gutiérrez F., Méndez F., Facultad de Ingeniería, Entropy Generation Minimization For The Thermal Decomposition Of Methane Gas In Hydrogen Using Genetic Algorithms, Energy Conversion and Management, Volume 55, March 2012, Pages 1-13.
[131] Collins-Martínez V., Escobedo Bretado M.A., Salinas Gutiérrez J., Meléndez Zaragoza M., Guzmán Velderrain V., López Ortiz A., Thermodynamic Analysis of the Absorption Enhanced Autothermal Reforming of Ethanol, Journal of New Materials for Electrochemical Systems 16, 229-237 (2013).
[132] Collins-Martínez V., Escobedo Bretado M.A., Salinas Gutiérrez J., Meléndez Zaragoza M., López Ortiz A., Thermodynamic Analysis of the Absorption Enhanced Steam Reforming of Biofuel Model Compounds, Journal of New Materials for Electrochemical Systems 16, 239-251 (2013).
[133] Arriaga L.G., Martínez W., Cano U., Blud H., Direct Coupling Of A Solar-Hydrogen System In Mexico, International Journal of Hydrogen Energy, Volume 32, Issue 13, September 2007, Pages 2247-2252.
[134] Sánchez-Dirzo R., González-Huerta R.G., Mendoza E., Silva R., Sandoval Pineda J.M., From Wave To Jet And From Jet To Hydrogen: A Promising Hybrid System, International Journal of Hydrogen Energy, Volume 39, Issue 29, 2 October 2014, Pages 16628-16636.
[135] Sebastian P.J., Gamboa S.A., Local Grid Connected Integrated Solar-Hydrogen-Fuel Cell Systems In Mexico, International Journal of Hydrogen Energy, Volume 32, Issue 15, October 2007, Page 3109.
[136] Polo-Labarrios M.A., Espinosa-Paredes G., Comparative Study Of The Hydrogen Generation During Short Term Station Blackout (STSBO) In A BWR, Anuals of Nuclear Energy, Volume 83, September 2015, Pages 274-282.
[137] Navarro-Solís I., Villalba-Almendra L., Alvarez-Gallegos A., H_2 Production By PEM Electrolysis, Assisted By Textile Effluent Treatment And A Solar Photovoltaic Cell, International Journal of Hydrogen Energy, Volume 35, Issue 20, October 2010, Pages 10833-10841.
[138] Aceves S.M., Petitpas G., Espinosa-Loza F., Matthews M.J., Ledesma-Orozco E. Safe, Long Range, Inexpensive And Rapidly Refuelable Hydrogen Vehicles With Cryogenic Pressure Vessels, International Journal of Hydrogen Energy, Volume 38, Issue 5, 19 February 2013, Pages 2480-248.
[139] González I.Z., Escobar Morales B., Torres Rivero L., Smit M.A., Verde Gómez Y., Diseño De Un Sistema De Producción y Uso De Hidrógeno Usando Energías Renovables, X Congreso Internacional de la Sociedad Mexicana del Hidrógeno: “Energías Renovables” SMH 2010 Toluca.

[140] Ramírez Minguela J. de J., Rangel Hernández V. H., Analisis Tecnico-Economico De Produccion De Hidrogeno A Traves De Energias Renovables: Energia Solar Fotovoltaica, X Congreso Internacional de la Sociedad Mexicana del Hidrógeno:"Energías Renovables" X International Congress of the Mexican Hydrogen Society, Toluca 2010.
[141] Fonseca Ruiz J.L., Armendáriz Gutiérrez J.R, Hidrógeno En Hidrocarburos De Uso Automotriz, X International Congress of the Mexican Hydrogen Society, Toluca 2010.
[142] Fonseca Ruiz J.L., Armendáriz Gutiérrez J.R., Herrera E., Hydrogen As Additive In Cars With Internal Combustion Engines, XI International Congress of the Mexican Hydrogen Society, Cuernavaca 2011.
[143] González-Huerta R.G., Yunez Cano A., Tufiño Velázquez M., Contreras Puente G., Jiménez Olarte D., Diseño de un Sistema de Hidrógeno para integrar un Sistema Solar-Hidrógeno que suministre Energía Eléctrica a una Vivienda Sustentable con una Autonomía de 8 h/día, XIII Congreso Internacional de la Sociedad Mexicana del Hidrógeno, Aguascalientes 2013.
[144] Citalán-Cigarroa S., Rodríguez-Castellanos A., Pérez-Robles J.F., Solorza-Feria O., Generación de Hidrógeno para una Celda de Combustible Tipo PEM y Determinación de Desempeño Utilizando LabVIEW con una Tarjeta de Adquisición de Datos Ni-USB6009, XIII Congreso Internacional de la Sociedad Mexicana del Hidrógeno, Aguascalientes 2013.
[145] Figueroa Hernández Á.M., Nieto Pérez M.deJ., Use of a Dielectric Barrier Discharge Plasma Reactor for Hydrogen Production, X International Congress of the Mexican Hydrogen Society, Toluca 2010.
[146] Alvab E., Pacheco M., Colín A., Sánchez V., Pacheco J., Valdivia R., Frías H., Soria G., Darío S., Ramos F., Duran M., Hidalgo M., Hydrogen Production From CH4 And NO Treatment With Non Thermal Plasma a Instituto Nacional de Investigaciones Nucleares, XIV International Congress of the Mexican Hydrogen Society, Cancún 2014.
[147] Patiño-Carachure C., Castro I.E., Sierra J.M., Abatal M., Martinez-Vargas S., Figueroa-Ramírez S.J., Hydrogen Generation Using Different Morphologies Of Recycled Aluminum With Alkaline Substance, XIV International Congress of the Mexican Hydrogen Society, Cancún 2014.
[148] Ortiz Verdín A., Ortega Borges R., Trejo Cordova G., Meas Vong Y., Evaluación De Aleaciones Ricas En Níquel Para La Generación Electrolítica De Hidrógeno En Medio Alcalino, IX International Congress of the Mexican Hydrogen Society, 2009 Saltillo.
[149] Olvera Vazquez S.L., Arce Estrada E.M., Comportamiento Electroquímico Del Alxsny Sintetizado Por Molienda Mecánica En La REH (Reacción De Evolución De Hidrógeno, IX International Congress of the Mexican Hydrogen Society, 2009 Saltillo.
[150] Ortega Chávez L., Herrera-Peraza E., Verde-Gómez Y., Modelación Matemática De La Reacción De Evolución Del Hidrógeno En Electrodos De Pt/C Considerando Efectos De Difusión, IX International Congress of the Mexican Hydrogen Society, 2009 Saltillo.
[151] Gutiérrez M.A., Rojas N.Y., Moreno J.C., Evaluación De Electrocatalizadores Para La Producción De Hidrógeno A Partir De Electrólisis De Agua, X International Congress of the Mexican Hydrogen Society, 2010 Toluca.
[152] Lucatero S., Tamayo G., Crespo D., Mariño E., Videa M., Electrocatalytic Properties of NiMo Nanoparticles for the Hydrogen Evolution Reaction, XII International Congress of the Mexican Hydrogen Society, Mérida 2012.

2
Direct oxidation fuel cells

Chapter 2.1. Development of Nickel hollow spheres electrocatalysts for ethanol electrooxidation in alkaline media

A. Altamirano-Gutiérrez[a]; G.E. Martínez-Tapia[a]; L.C. Ordóñez[a,*]

[a]Centro de Investigación Científica de Yucatán, A.C., Parque Científico Tecnológico de Yucatán, Carretera Sierra Papacal – Chuburná Puerto, km 5. Sierra Papacal, Mérida, Yucatán, C.P. 97302.

ABSTRACT

We report the synthesis of nickel hallow spheres and its structural, morphological and electrochemical catalytic evaluation for ethanol oxidation reaction in 1.0 M NaOH. Materials were prepared by the microemulsion method from $NiSO_4 \cdot 6H_2O$, NaOH and using $NaH_2PO_2 \cdot H_2O$ as reducing agent. Dodecyl sodium sulfate (SDS) was used as soft template. The concentration of each component was carefully controlled up to forming colloidal $Ni(OH)_2$ particles which, were reduced to obtain the nickel spheres. The synthesized materials were characterized by X-Ray diffraction (XRD), scanning electron microscope (SEM). The surface morphology was analyzed by atomic force microscope (AFM). Cyclic voltammetry (CV) and electrochemical impedance spectroscopy (EIS) techniques were performed in order evaluate the catalytic activity for the ethanol oxidation reaction in alkaline medium. The synthesized material with microemusion conditions of 96% H_2O-3% SDS -1% pentanol presented the highest current density for ethanol oxidation peak: 147 $mAcm^{-2}$ at 0.722 V. Results indicate that metallic Ni microspheres with diameters between 0.2 and 1.4 micrometers are potential candidates for it use as anodes in alkaline direct alcohol fuel cells (A-DAFCs).

Keywords: Nickel hollow microspheres, Microemulsion, Ethanol electrooxidation, Alkaline direct alcohol fuel cells

---

* Author for correspondence: Luis Carlos Ordóñez López, E: lcol@cicy.mx

1. Introduction

In recent years, there has been an interest in the synthesis of micrometer and nanometer structures with specific morphologies and functions such as core-shell particles, nanotubes and hollow particles [1-4]. Hollow architecture can exhibit novel properties substantially different from their solid counterparts in the fields of: chemistry, physics, biotechnology and materials science, making them attractive for scientific and technological applications [5-6]. The preparation of hollow spheres with controlled morphology is especially interesting for applications in catalysts, chemical sensors, photonic crystal, adsorbents,

controlled delivery agents, low density materials and optical, electronic and magnetic devices [7], Direct alcohol fuel cells (DAFCs) based on liquid fuels such as methanol and ethanol have attracted enormous attention in the last years [8]. Pd, Au, Ag and Ni have been used as anodic electrocatalysts for alcohol electrooxidation [9-10]. Here we synthesized nickel hollow microspheres and study their behavior as catalysts for ethanol oxidation in alkaline media.

2. Materials and Methods

2.1. Preparation and structural characterization of the catalysts

Ni microspheres were prepared by the microemulsion method using a ternary system of H_2O-SDS-1-pentanol. 3 g of $NiSO_4 \cdot 6H_2O$, 0.902 g NaOH and 4.011 g $NaH_2PO_2 \cdot H_2O$ were separately dissolved in 25 mL of deionized water. 4 different ratios for the microemulsion system of H_2O-SDS-1-pentanol were performed: a) 60%-30%-10%, b) 70%-20%-10%, c) 80%-15%-5% d) 96%-3%-1%. Maintaining the ternary system with vigorous stirring at 80 ^oC, it was added dropwise the $NiSO_4 \cdot H_2O$ solution and subsequently the NaOH solution. Color changes were observed in the reaction mixture from bright green to green milky due to the formation of a thin gel of $Ni(OH)_2$. Finally, it was added dropwise the $NaH_2PO_2 \cdot H_2O$ solution. After an contact time it was observed a hydrogen gas evolution accompanied by the precipitation of fine dark gray particles. The reaction was allowed for 2 hours. Precipitate was separated by centrifugation (Orto Alresa Centrifuge, digicen 21R) at 3000 rpm for 10 minutes, washed several times with deionized water. The product was dried in a vacuum oven (Lab-Line Duo-Vac-Oven) at 80 ^oC for 24 hours. Subsequently, the recovered black fine powder was thermally treated in a horizontal oven for 4 h at 300 ^oC under a constant N_2 (Infra 99.9%) flow and using a heating rate of 10 ^oC/min. Morphological characterization was performed by scanning electron microscope (SEM) on a Jeol JSM-6360LV microscope. The elemental chemical composition was determinated on a Philips microscope XL30ESEM. The surface morphology was analyzed by an atomic force microscope (AFM) Bruker Multimode 8. XRD was carried out on a diffractometer D-5000 Siemmens (CuKa radiation, $\lambda = 1.5405$ Å).

2.2. Electrode preparation

The working electrode was prepared by mixing 2.0 mg of corresponding material and 4.6 mg of Vulcan XC-72R with 100 μL of isopropanol and 80 μL of 5 wt. % Nafion® solution. These components were homogenized in an ultrasonic bath for 10 min. A 2.0 μL aliquot of the resulting ink was deposited on a glassy carbon electrode with a 0.0701 cm^2 geometric area.

2.3. Electrochemical characterization of the catalysts

Electrochemical measurements were performed at room temperature in a potenciostat/galvanostat (Autolab PGSTAT302N) using a typical three electrode electrochemical cell. A graphite bar was used as counter electrode. As a reference a mercury/mercuric oxide (Hg/HgO, 1.0 M NaOH) electrode and as working electrode each synthesized material deposited on a glassy carbon electrode. The electrolyte was 1.0 M NaOH. Cyclic voltammetry (CV) measurements were performed in a potential range of -1.0

to 0.8 V vs Hg/HgO. The supporting electrolyte was deoxygenated with N_2 for 30 minutes. Then, 30 cycles were performed at a scan rate of 50 $mVs^{-1}$and the last was selected. The open circuit potential (OCP) was measured at the beginning and end of cycle. Subsequently, the CV was performed in the presence of 1.0 M ethanol + 1.0 M NaOH, with a scan rate of 10 mVs^{-1}.

3. Results and discussion

For purposes of abbreviations, the following keys are used to refer to new materials throughout the manuscript. Microemulsions in which the materials were synthesized: 60%H_2O-30%SDS-10%-1-pentanol as N1, 70%H_2O-20%SDS-10%-1-pentanol as N2, 80% H_2O-15%SDS-5%-1-pentanol as N3 and 96%H_2O-3%SDS-1%-1-pentanol as N4.

3.1. Structural characterization

Figure 1 presents the SEM images of nickel materials synthesized by microemulsion. The microemulsion conditions has a strong influence on particle morphology. However, it was observed in all cases the formation of spherical structures of Ni. Samples of the systems N1 and N2 shows well defined microspheres of nickel and greater presence in the observed area compared to samples of the N3 and N4 systems.

N1

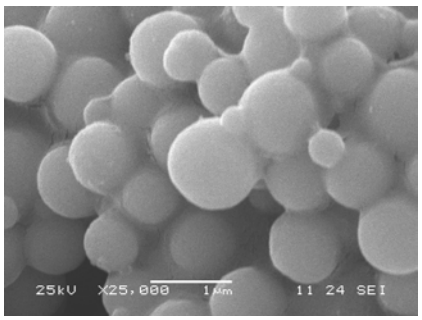

N2

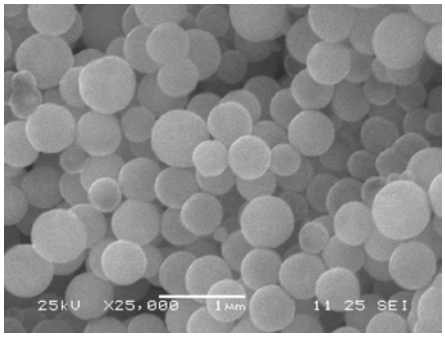

N3

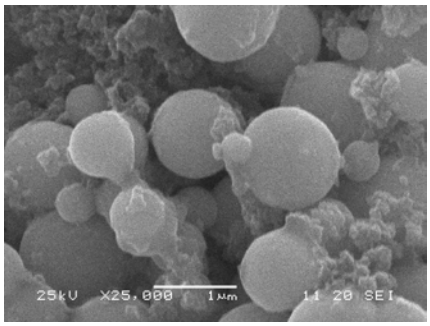

N4

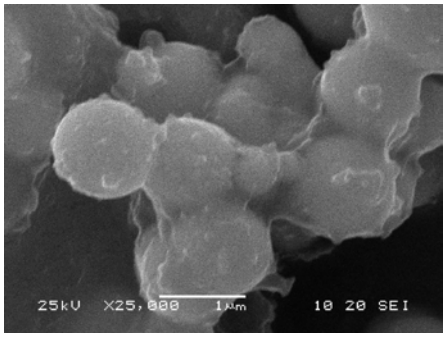

Figure 1. SEM micrographs of the hollow nickel microspheres prepared by microemulsion under the following conditions: N1 (60% H_2O-30% SDS-Pentanol 10%); N2 (70% H_2O-20% SDS-Pentanol 10%); N3 (80% H_2O-15% SDS-5% Pentanol) and N4 (96% H_2O-3% Pentanol 1% SDS), heat treatment at 300 °C under N_2, t = 4 h.

The latter samples also presented nickel spheres and additionally, small particles of irregular shape around it. N1, N3 and N4 samples presented a microsphere diameter ranging between 0.930 and 1.350 microns. N2 sampls had a diameter range between 0410-0680 microns.

AFM analysis was performed using the technique of magnetic force microscopy (MFM), considering that the material had magnetic properties, this technique uses a combination of TappingMode and LiftMode. The TappingMode topography of the sample was determined by analyzing an area of 25 μm^2. The images were obtained while the cantilever and the tip intermittently range near the resonance frequency (60-100 kHz). The points used were the MESP model antimony doped silicon material of 0.01 to 0.025 ohm-cm. Surveyed signals are detected by the scanner mounted on the piezoelectric AFM. Figure 2 shows representative AFM images of samples N1 and N4. Ni microspheres can be detected and amorphous regions, this supports the results obtained by the SEM technique. The N1 sample has a roughness factor Ra of 77.6 nm greater than sample N3,1.0 nm Ra.

N1 N4

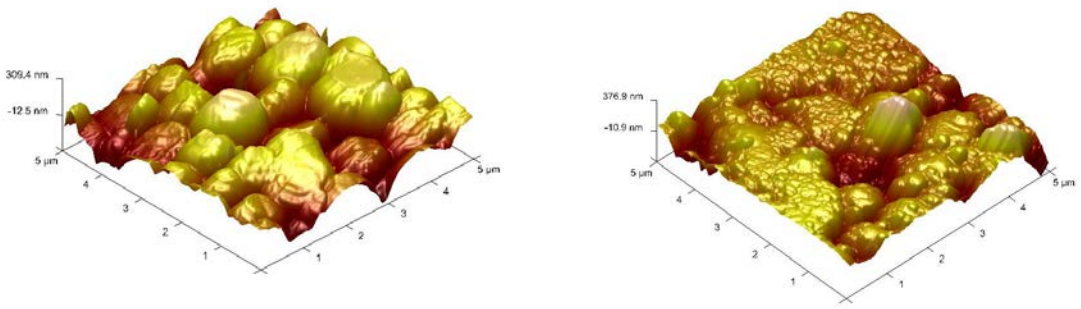

Fig. 2. AFM images representative of the nickel hollow microspheres: N1 and N4, heat treated at 300 ° C under N_2, for t = 4 h.

The chemical composition of the nickel hollow spheres thermally treated at 300 ^oC under nitrogen, for 4 hours was determinated by EDX studies (Table 1). The Ni weight percentage ranges between 71 to 86% for the four samples. Phosphorus weight percentage was between 8 and 11%. This was attributed to the sodium hypophosphite used, despite making several washes failed to eliminate in the process of synthesis. Moreover, a weight percentage of significant oxygen between 5 and 13%, probably attributed to the surfactant (SDS) which has not been complete removed from the interior of the nickel microspheres despite the heat treatment.

Table 1. Chemical composition of the catalysts prepared under the following conditions: N1 (60%H_2O-30%SDS-10%Pentanol); N2 (70%H_2O-20%SDS-10%Pentanol); N3 (80%H_2O-15%SDS-5%Pentanol) y N4 (96%H_2O-3%SDS-1%Pentanol), heat treatment at 300 ^oC in atmosphere of N_2, during 4 h.

	Heat treatment		
Catalyst	**Ni (Wt. %)**	**P (Wt. %)**	**O (Wt. %)**
N1	86.72	8.27	5.01
N2	78.82	11.39	9.79
N3	71.96	11.90	16.14
N4	74.54	11.78	13.68

Figure 3 shows XRD patterns of the nickel N1, N2, N3 and N4 samples. It is possible to observe the characteristic peaks of the face-centered-cubic (fcc) of polycrystalline Ni (JCPDS, PDF # 04-0850), corresponding to the (111), (200) and (220) planes located at 44.5°, 76.3° and 51.8°, respectively. In all cases, are observed reflections associated to Ni3P with a body centered tetragonal structure (JCPDS, PDF # 34-0501). The corresponding planes: (031), (231), (330), (112), (240), (141), (222), (132) and (233) located at 36.4°, 41.7°, 42.8°, 43.6°, 45.2°, 46.6°, 50.5°, 75.3° and 52.7°, respectively. The formation of Ni_3P occurred by the heat treatment at 300 ^oC in N_2, similarly to Bernardi C. *et al.* They obtained by heat treating the compound Ni_3P [7], it is noteworthy that the Ni_3P diffraction peaks are more intense than the peaks of nickel (Fig. 3). N4 sample presented the best defined N4 diffraction peaks.

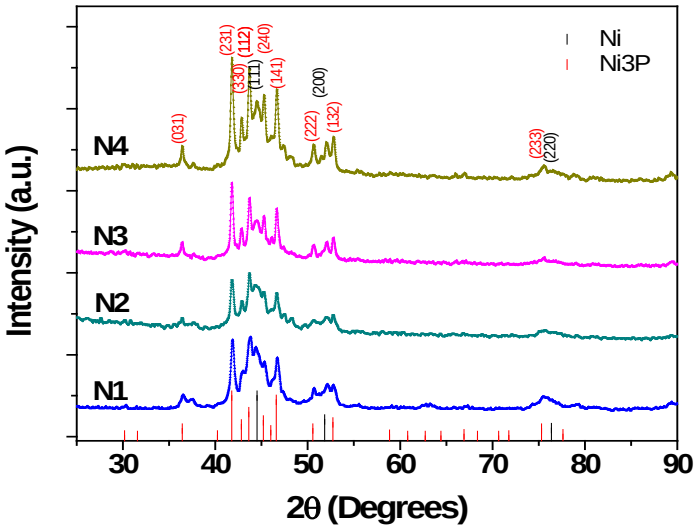

Fig. 3. X-ray diffraction pattern of the hollow Ni microspheres prepared by microemulsion with different conditions N1, N2, N3 y N4, at 300 °C in atmosphere of N_2, t = 4 h.

Table 2 shows the crystal size of the hollow spheres composed of nickel and Ni_3P calculated from the full-width at half-maximun (FWHM) of the diffraction peaks, according to the Scherrer equation [13]. Nanoparticles were obtained in all cases, the size was analyzed peak intense compound Ni_3P diffraction, it was not possible to determine the crystal size of nickel by this method because there is an overlap in the diffraction peaks of both compounds Ni and Ni_3P.

Table 2. Crystal size of the materials synthesized of nickel by microemulsion, with heat treatment at 300 ^oC in atmosphere of N_2 during 4 h.

Material	***Ni_3P (nm)***
N1: 60%H_2O-30%SDS-10%Pentanol	20.8
N2: 70%H_2O-20%SDS-10%Pentanol	9.8
N3: 80%H_2O-15%SDS-5%Pentanol	13.9
N4: 96%H_2O-3%SDS-1%Pentanol	21.1

3.2 Electrochemical characterization

Figure 4 shows the CVs of the hollow microspheres of nickel with and without 1.0 M C_2H_5OH.

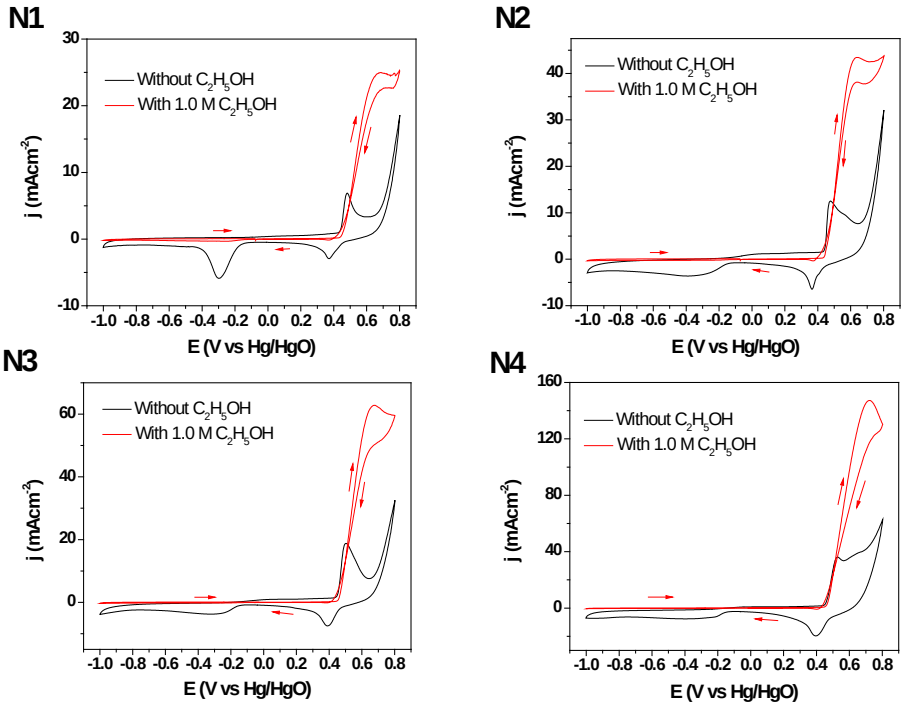

Fig. 4. Cyclic voltamperograms of the electrocatalysts prepared under the following conditions, in N_2 saturated 1.0 M NaOH: N1; N2; N3 y N4, in the absence and presence of 1.0 M ethanol solution. Scan rate 50 and 10 mV s^{-1}, respectively.

The shape evaluation of the CVs in the absence of ethanol show the characteristic peaks related to the formation of nickel oxides and nickel hydroxides in 0.49 V vs. Hg/HgO in the forward sweep and in 0.4 V in the return sweep. At 0.7 V start the oxygen evolution reaction [14]. In the presence of ethanol, a single peak appears at 0.7 V attributed to oxidation of ethanol; N4 catalyst has the highest current density of 147 $mAcm^{-2}$ at 0.72 V compared to N1 with a peak current density of 8.24 $mAcm^{-2}$ at 0.68V.

4. Conclusione

Nanostructures of hollow Ni-P microspheres were synthesized by autocatalytic reduction microemulsion method, in aqueous solution at 80 ^{o}C. Depending on the concentrations of the components of the microemulsion was possible to obtain different diameters of the nickel spheres from 0.4 to 1.35 microns. The synthesis conditions are an important factor in the structure and catalytic activity of the materials. The best catalyst was obtained with our N4 material with a current density performance of 147 $mAcm^{-2}$ at 0.72 V for the oxidation reaction in alkaline ethanol.

Acknowledgements

The authors acknowledge the financial support received from CONACYT-181106 and hydrogen thematic network (252003). Alejandro Altamirano Gutiérrez thanks to the postdoctoral scholarship. Authors acknowledge Dra. María Goreti Campos and Q. Silvia Beatriz Andrade for SEM images, to M.C. Enrique Escobedo Hernández for AFM. XRD, FE-SEM analysis were performed at LANNBIO- Cinvestav Unidad Mérida, (financially supported by CONACYT-FOMIX-Yucatán, 2008-1081160) and authors acknowledge the technical collaboration of Dra. Patricia Quintana Owen, M.C. Daniel Aguilar, M.C. Dora A. Huerta y Q. Ana Ruth Cristóbal, respectively.
Authors thanks to the scholarship for participation in the XV International Congress of the Mexican Hydrogen Society, 2015.

References

[1] Deng Y., Zhao L., Liu L., Shen B., Hu W., Mater. Res. Bull. 2005; 40: 1864-1870.
[2] Davis S.A., Burkett S.L., Mendelson N.H., Mann S., Nature, 1997; 385: 420.
[3] Kaltenpoth G., Himmelhaus M., Slansky L., Gruzen M., Adv. Mater., 2003; 15: 1113.
[4] Sun Y, Xia Y., Science, 2002; 298: 2176.
[5] Bao J., Liang Y., Xu Z., Si L., Adv. Mater., 2003; 15: 1832-1835.
[6] Liu Q., Liu H., Han M., Zhu J., Liang Y., Xu A., Song Y., Adv. Mater., 2005; 17: 1995-1999.
[7] Bernardi C., Drago V., Bernardo F.L., Giraldi D., Klein N., J. Mater Sci 2008; 43: 469-474.
[8] Xu C., Hu Y., Rong J. Jiang S.P., Liu Y., Electrochem. Commun., 2007; 9: 2009-2012.
[9] Xu C.W., Cheng L.Q., Shen P.K., Liu Y.L., Electrochem. Commun., 2007; 9: 997.
[10] Xu C.W., Sheng P.K., Liu Y.L., J. Power Sources, 2007; 164: 527.
[11] Guo D.J., Li H.L., Carbon, 2005; 43: 1259.
[12] Zhang K. F., Guo D.J., Liu X., Li J., Li H.L., Su Z.X., J. Power Sources 2006; 162: 1077.
[13] Cullity B.D. Elements of X-ray Diffraction. Addison-Wesley; 1978.
[14] Muench F., Oezaslan M., Rauber M., Kaserer S., Fuchs A., Mankel E., et al., J. Power Sources 2013; 222: 243-252.

Chapter 2.2. Methanol Oxidation on Au@Pt and Cu@Pt Core-Shell Electrocatalysts

N. Chávez-Pineda[a]; G. Vázquez-Huerta[a,*]; S. Corona-Avendaño[a]

[a] Materials Department, Universidad Autónoma Metropolitana, Av. San Pablo 180, Reynosa Tamaulipas, C.P. 02200, México D.F., México.

ABSTRACT

In this work, the methanol oxidation on core-shell Au@Pt and Cu@Pt electrocatalysts is studied. For this purpose, the core-shell nanoparticles supported on carbon Vulcan XC-72R were prepared by using a two-step colloidal method. The electrochemical behavior of Au@Pt/C and Cu@Pt/C was evaluated by using anodic stripping voltammetry, cyclic voltammetry and chronoamperometry (in a three-electrode electrochemical cell and 0.5 M H_2SO_4 + 1 M methanol as working solution). The physical characterization by scanning-transmission electron microscopy (STEM) showed that the synthesis procedure generates quasi-spherical nanoparticles of ~22 nm for Au@Pt and 12 nm for Cu@Pt/C. X-ray diffraction (XRD) results showed that in both cases, Au@Pt and Cu@Pt, the crystallographic structure of the core is maintained, inferring that an Pt epitaxial growth is produced. The electrochemically active surface area (ECSA) was evaluated in all cases by using anodic stripping voltammetry; the values of ECSA were used to normalize the currents obtained during methanol oxidation experiments. From cyclic voltammetry results it was found that Au@Pt/C catalyst presented the highest values of current density for methanol oxidation, also the peak potentials ($E_{p,1}$ and $E_{p,2}$) of methanol oxidation are less positive than those showed on Cu@Pt/C which indicates that a smaller activation energy is needed on Au@Pt/C for methanol oxidation to occur. Similar results were obtained from chronoamperometric experiments; the steady-state current density (i_{ss}) of methanol oxidation is higher when Au@Pt/C catalyst is used. For comparison purposes, Pt/C was also prepared, and in chronoamperometric experiments the current density obtained for methanol oxidation, at initial times, was higher on Pt/C than on the other catalysts; however after 1200 s, it diminishes below the i_{ss} value showed by Au@Pt/C, this behavior could be related to the poisoning effect of CO on Pt, the poisoning effect is diminished on Au@Pt/C electrocatalyst.

Keywords: Methanol oxidation, Core-shell nanoparticles, Gold-platinum, Copper-platinum

1. Introduction

Up to date, the energetic situation is conditioned by facts such as fossil fuel scarcity and environmental issues [1], fuel cells are among the alternative technologies for energy

---

* Corresponding author:
G. Vázquez-Huerta, T: 52 (55) 53189356, E: gvh@correo.azc.uam.mx

production, they present the advantage of clean energy production, no noise, high efficiency, reliability and good performance [2]. Also, a great interest for the use of hydrogen-containing fuels such as methane and methanol has arisen [3]. In fuel cell technology, platinum has traditionally been considered as an excellent electrocatalyst for methanol oxidation [4], however the electrochemical activity of platinum diminishes because of the generation of strongly CO-like intermediates during methanol electrooxidation [4-5] which poison Pt catalysts. In order to improve Pt-based catalysts with antipoisoning properties several approaches have been used, among them are Pt-alloys with metals such as Ru, Au, Sn, Ni, Bi, W, Os [6-10]. Another approach for fabrication of lower-cost and improved tolerance to CO poisoning electrocatalysts is by using the so-called core-shell nanoparticles. Core-shell nanoparticles allow positioning Pt atoms on the surface (where they are needed) while the core is made of a cheaper transition metal. Furthermore, the nanoscopic size of core-shell particles gives them unique electronic properties that result in changes in the electrocatalytic activity, and it is commonly accepted that a correlation must exist between electrocatalytic activity and stability of bimetallic catalysts with a combination of electronic and geometric parameters such as lattice parameter, particle size, d-band vacancy, and surface [11]. Since the core metal plays a relevant role for the activity of Pt, varying the core metal may result in a tuning effect of methanol oxidation reaction (MOR). In this work, the effect of core metal in Au@Pt and Cu@Pt catalysts compared to Pt for MOR is analyzed. Several techniques have been used to physically characterize the electrocatalysts among them are the scanning-transmission electron microscopy (STEM) and X-ray diffraction, XRD. The electrochemical response of the electrocatalysts supported on carbon Vulcan XC-72R (Au@Pt/C, Cu@Pt/C and Pt/C) was measured by using electrochemical techniques such as cyclic voltammetry, chronoamperometry and anodic stripping voltammetry.

2. Materials and Methods

2.1 Electrocatalysts synthesis.

Au@Pt, Cu@Pt and Pt nanoparticles were synthetized by using gold (III) chloride hydrate ($HAuCl_4 \cdot xH_2O$) (Sigma-Aldrich), copper nitrate trihydrated ($CuNO_3 \cdot 3H_2O$) (Sigma-Aldrich) and sodium tetrachloroplatinate(II) hydrate ($Na_2PtCl_4 \cdot xH_2O$) (Sigma-Aldrich) as precursors. Trisodium citrate dihydrate ($C_6H_5Na_3O_7 \cdot 2H_2O$) or sodium borohydride ($NaBH_4$) (Sigma-Aldrich) were used as reducing agents; Carbon Vulcan XC-72R (Cabot) was used as the carbon support. All the chemicals were used as-received. Au@Pt and Cu@Pt nanoparticles were synthesized following a two-step method; i.e. *i)* first, the core (Au or Cu) was formed by reducing the corresponding precursor salt with $C_6H_5Na_3O_7 \cdot 2H_2O$ or $NaBH_4$, and *ii*) the core was covered with Pt to form the core-shell structure (Au_xCu_y@Pt). Briefly, 3.8 mL 0.01M $HAuCl_4 \cdot 3H_2O$ was added to 200 mL deionized water in an Erlenmeyer flask, the solution was heated to its boiling point maintaining with a vigorous stirring, then 5.7 mL of 0.1 M $C_2H_5Na_3O_7$ were added and after a while the solution color changes from pale-yellow to ruby-red indicating that Au nanoparticles have been formed, the colloidal solution containing Au- nanoparticles is allowed to cool down to ~40ºC and an aliquot of $2.5X10^{-2}$ M $Na_2PtCl_4 \cdot 6H_2O$ is added, the atomic rate of Au to Pt is 1:1. Once the Au@Pt core-shell nanoparticles are obtained they

are supported on 40 mg of carbon Vulcan XC-72R, the material is now designated as Au@Pt/C. Cu@Pt/C catalyst was prepared in a similar way as Au@Pt/C but using $NaBH_4$ as reducing agent. Pt nanoparticles were formed by using $Na_2PtCl_4 \cdot 6H_2O$ as precursor salt and $C_2H_5Na_3O_7$ as reducing agent. 10 mL of Au@Pt, Cu@Pt and Pt hydrosols were taken and reserved for STEM characterization.

2.2 Scanning transmission electronic microscopy and XRD characterization.

Particle size, morphology and size distribution of Au@Pt and Cu@Pt were evaluated by using a JEM-1200EX SUPRA 55PV equipment from JEOL-Carl-Zeiss (working in STEM mode). Catalysts were also examined by X-ray diffraction (XRD), the experiments were performed in a Brucker 2000 diffractometer with a step scan of 0.02°, 2θ and 15 seconds per step, between 30° and 90° 2θ, at 35 kV and 30 mA, using Cu K_α radiation, 1.54056 Å.

2.3 Electrochemical procedure.

Working electrodes were prepared by weighing 3 mg of the supported catalyst in a 2.0 mL vial, then 200 µL of deionized water and 20 µL of Nafion 5% V/V solution were added into the vial and placed in ultrasonic bath for 10 minutes until a homogeneous suspension (or catalytic ink) was obtained. An aliquot of 20 µL of this ink was applied onto a freshly polished surface of a glassy carbon electrode with geometric area = 0.196 cm^2 and was left to dry in an oven at 60 ºC for 10 min. The electrochemical signals were recorded with a VersaSTAT4 from Princeton Applied Research (PAR), using 0.5 M H_2SO_4 as electrolytic solution or 0.5 M CH_3OH + 0.5 M H_2SO_4 as working solution for methanol oxidation experiments. In all the electrochemical measurements a conventional three-electrode cell was used; electrode potentials were measured and reported against the Hg/Hg_2SO_4 electrode (SSE) placed close to the working electrode. A graphite bar served as counter electrode, while the working electrode was Au@Pt/C, Cu@Pt/C or Pt/C. The electrochemical experiments were performed within the −0.70 to 0.60V as potential range, at 50 mVs^{-1} scan rate. In order to calculate the electrochemically active surface area (easa), CO-stripping voltammograms were measured in 0.5 M H_2SO_4 solution, the catalyst surface was previously saturated with CO by bubbling CO in the electrolyte solution and polarizing the electrode at -0.45 V/SSE for 15 minutes; after which, the remaining-CO dissolved was purged by bubbling N_2 for 15 minutes, immediately after an I vs E plot of CO stripping was performed (scan rate = 50 mVs^{-1}). The charge associated with CO stripping was used to measure the easa [12].

3. Results and Discussion

3.1 Scanning transmission electronic microscopy and XRD results.

The micrographs of Au@Pt, Cu@Pt and Pt nanoparticles by using scanning transmission electron microscopy (STEM) are shown in Fig 1. In all cases, the synthesis procedure generates quasi-spherical nanoparticles with a narrow size distribution, the average particle size of Au@Pt is 18 nm (Fig 1a), Cu@Pt is 15 nm (Fig 1b) and Pt is 22 nm (Fig 1c). The crystal structures of the catalysts were obtained from XRD measurements, Fig. 2 presents the XRD patterns of: *a)*Au@Pt/C and *b)*Cu@Pt/C, the peaks corresponding to Pt are also shown. The diffraction pattern of Au@Pt in Fig. 2*a*, shows diffraction peaks

at 2θ = 38.1º, 43.9º, 64.2º, 77.2º and 81.2º which can be indexed to the (111), (200), (220), (311) and (222) lattice planes of the Au face-centered cubic (fcc) structure, respectively (JCPDS 04–0784). Cu@Pt diffraction pattern is shown in Fig. 2*b*, and the peak at 42.9º can be attributed to the Cu (111) lattice plane (fcc structure) according with JCPDS 04–0836. The broad diffraction peak at 25.1º in each XRD pattern corresponds to the graphite (002) plane (JCPDS, No. 74-2330) from the carbon Vulcan XC-72R support. Dotted lines have been added to the diffraction patterns to indicate (111) lattice planes of pure Au, Cu and Pt. The broadening phenomenon of diffraction peaks is due to the nanometer scale of catalyst.

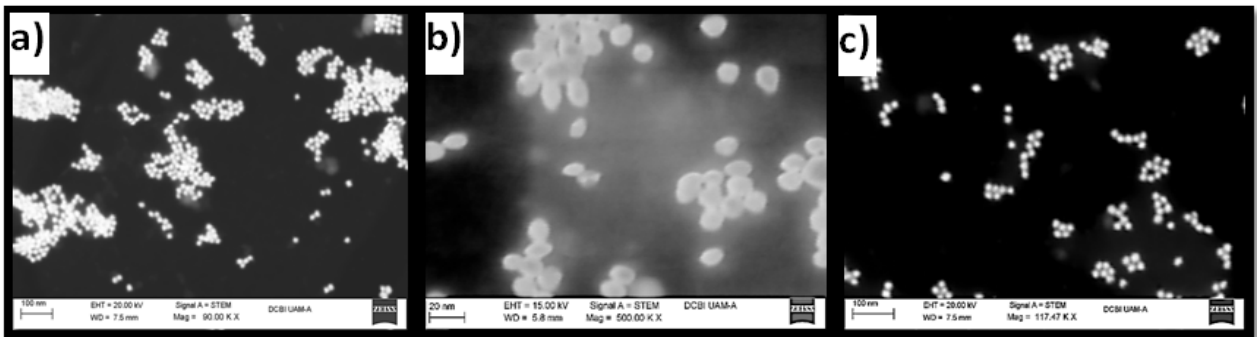

Fig. 1. STEM images of: *a)* Au@Pt, *b)* Cu@Pt and *c)* Pt.

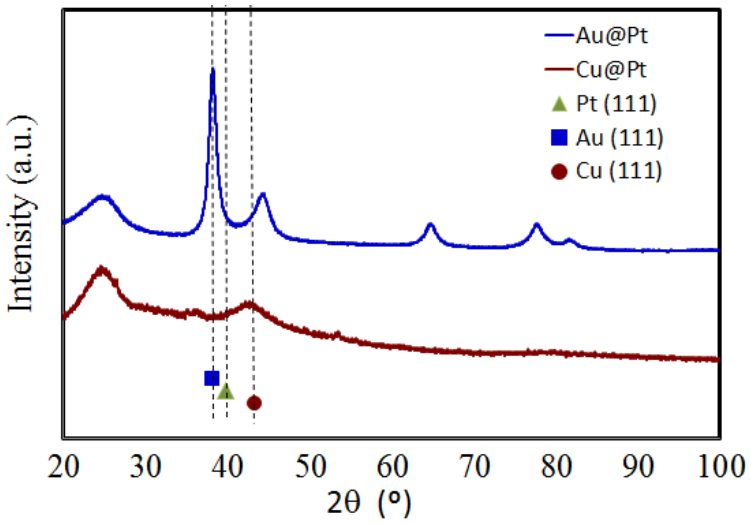

Fig. 2. X-ray diffraction patterns of Pt-based catalysts.

3.2 Electrochemical results.

The methanol oxidation reaction on Pt is a complex multi-step process; and many investigations have been conducted in order to elucidate the complete mechanism. Reactions 1-3 represent the methanol oxidation [13], eq. 1 is the dissociative adsorption of methanol, R2 is the formation of oxygen-containing species from water and R3 is the reaction of the oxygen-containing species with CO_{ads} to generate CO_2.

$$CH_3OH \rightarrow CO_{ads} + 4H^+ + 4e^- \quad (1)$$

$$H_2O \rightarrow OH_{ads} + H^+ + e^- \quad (2)$$

$$CO_{ads} + OH_{ads} \rightarrow CO_2 + H^+ + e^- \quad (3)$$

By tracking isotopes [14] more intermediates have been identified and other reactions have been proposed for the dissociative adsorption of methanol (equations 4-6).

$$CH_3OH \rightarrow CH_3OH_{ads} \quad (4)$$

$$CH_3OH \rightarrow CH_3O_{ads} + H^+ + e^- \quad (5)$$

$$CH_3OH \rightarrow COH_{ads} + 3H^+ + 3e^- \quad (6)$$

The overall reaction for methanol oxidation can be obtained by combining reactions 1-3 to give (eq.7):

$$CH_3OH + H_2O \rightarrow CO_2 + 6H^+ + 6e^- \quad (7)$$

The voltammograms in Fig. 3 present the electrochemical behavior of Au@Pt/C, Cu@Pt/C and Pt/C catalysts in 0.5 M methanol + 0.5 M H_2SO_4, the I vs E plots show the well-known oxidation profile characterized by two oxidation peaks [15] during the forward and backward sweeps. In Au@Pt/C (Fig 3a), an anodic peak ($E_{p,1}$) appears at 0.26 V during the positive sweep, the peak is associated to the oxidation of methanol molecules [16]. During the negative potential sweep, the Pt oxide is reduced; this last process reactivates the surface and an oxidation reaction occurs as indicated by the presence of an intense anodic peak ($E_{p,2}$). All Au@Pt/C, Cu@Pt/C and Pt/C catalysts show a similar behavior during methanol oxidation with some differences; for example, the anodic peak potential, $E_{p,1}$ is less positive for Au@Pt/C than that on Cu@Pt/C and Pt/C; similarly the peak current densities (during the forward and backward sweep) are greater for Au@Pt/C than those on Cu@Pt/C and Pt/C, this means that the highest peak current density occur on Au@Pt/C at the smaller $E_{p,1}$, indicating that Au@Pt/C is better catalyst than Cu@Pt/C and Pt/C (It is worth to mention that in all cases, the electrochemical active surface area (easa) was obtained from CO-stripping experiments, the experiments were carried out by applying a E_{pulse} = -0.45V while CO is bubbled (15min), after that N_2 was bubbled maintaining E_{pulse} for another 15 min, then the cyclic voltammogram was acquired, from charge associated to CO desorption, the easa was calculated and used to normalize the voltammograms in Figures 3 and 4).

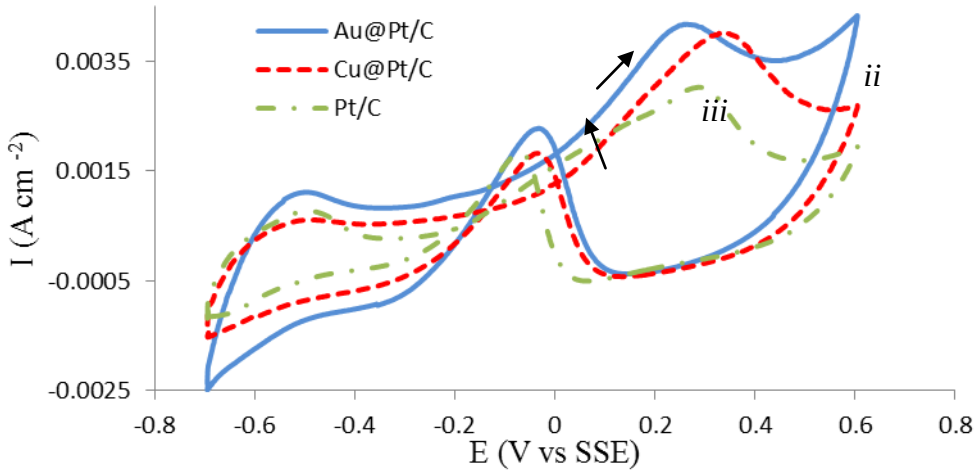

Fig. 3. I vs E plots of Pt-based catalysts in 0.5 M CH_3OH + 0.5 M H_2SO_4, sr = 50 mVs^{-1}. *i)* Au@Pt/C, *ii)* Cu@Pt/C and *iii)* Pt/C.

3.3 I vs t plots of methanol oxidation.

Figure 4 shows the I vs t plots of methanol oxidation on Au@Pt/C, Cu@Pt/C and Pt/C catalysts, the applied potential is 0.30 V vs SSE during 1200s, at the end of which all the plots present a constant value associated to the steady-state current density (I_{ss}), in Fig 4 the value of I_{ss} depends on the type of catalyst, *i.e.*, the I_{ss} values are 2.52, 0.18 and 1.63, mA cm^{-2} for Au@Pt/C, Cu@Pt/C and Pt/C, respectively. From this behavior, it is evident that the presence of Cu in Cu@Pt/C disfavors the kinetics of methanol oxidation, while the gold content in Au@Pt/C increases the current density even more than that obtained on Pt/C.

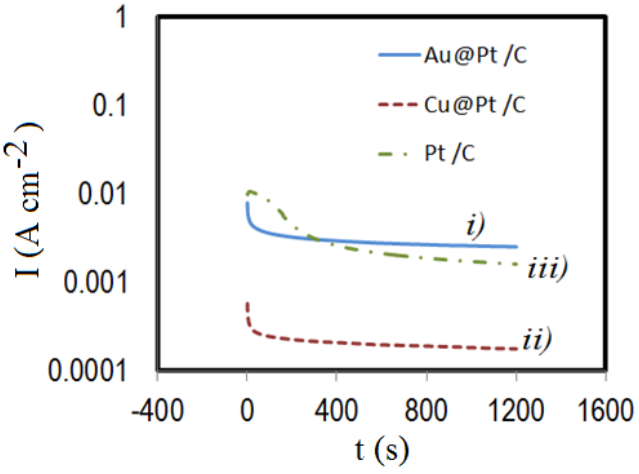

Fig. 4. I vs t plots of: *i)* Au@Pt/C, *ii)* Cu@Pt/C and *iii)* Pt/C, in 0.5M H_2SO_4 + 0.5 M CH_3OH (E_{pulse} = 0.30 V vs SSE).

4. Conclusion

Au@Pt/C, Cu@Pt/C and Pt/C catalysts have been prepared in order to evaluate their electrochemical behavior for the methanol oxidation reaction. From morphological analysis it was found that the synthesis method produces quasi- spherical core-shell nanoparticles. The I_{ss} values are 2.52, 0.18 and 1.63, mA cm^{-2} for Au@Pt/C, Cu@Pt/C and Pt/C, respectively. The value of I_{ss} depends on the type of catalyst and from this behavior, it is evident that the presence of Cu in Cu@Pt/C disfavors the kinetics of methanol oxidation, while the gold content in Au@Pt/C increases the current density even more than that on Pt/C.

Acknowledgements

The authors are thankful to the Department of Materials at UAM-A for financing the present research and the Laboratory of Microscopy of the D-CBI, UAM-Azc, for STEM images.

References

[1] Mayandía-Aguirre A. Descripción y Modelado de una pila de combustible de Membrana de Intercambio Protónico. [cited 2015 July 29]. Available from: URL: http://e-archivo.uc3m.es/bitstream/handle/10016/6055/PFC_Antonio_Mayandia_V2.pdf?sequence=1

[2] Escobedo-Hernández E., Zamora Campos L. A. Modelado dinámico de celdas de combustible. [cited 2015 July 29]. Available from: URL: http://www.cenidet.edu.mx/subaca/web-mktro/submenus/investigacion/tesis/25-26%20Enrique%20Escobedo%20Hernandez%20-%20Luis%20Alberto%20Zamora%20Campos.pdf

[3] K. D. Kreuer. On the Development of Proton Conducting Polymer Membranes for Hydrogen and Methanol Fuel Cells. Journal of Membrane Science 2001; 185:29-39. [cited 2015 July 30]. Available from: URL: http://dns2.asia.edu.tw/~ysho/ysho-english/1000%20ce/pdf/j%20mem%20sci185,%2029.pdf

[4] Zhao X., Yin M., Ma L., Liang L., Liu C., Liao J., Lu T., Xing W. Recent advances in catalysts for direct methanol fuel cells. Energy Environ. Sci. 2001; 4:2736-2753.

[5] Alcaide F., Álvarez G., Cabot P. L., Grande H. J., Miguel O., Querejeta A. Testing of carbon supported Pd–Pt electrocatalysts for methanol electrooxidation in direct methanol fuel cells. Int. J. Hydrogen Energy 2001; 36:4432-4439.

[6] Luo J., Njoki P. N., Lin Y., Mott D., Wang, Zhong C. J. Characterization of Carbon-Supported AuPt Nanoparticles for Electrocatalytic Methanol Oxidation Reaction. Langmuir 2006; 22:2892-2898.

[7] Lin Y., Cui X., Yen C. H., Wai C. M. PtRu/Carbon Nanotube Nanocomposite Synthesized in Supercritical Fluid: A Novel Electrocatalyst for Direct Methanol Fuel Cells. Langmuir 2005; 21:11474-11479.

[8] Park K. W., Choi J. H., Sung Y. E. Structural, Chemical, and Electronic Properties of Pt/Ni Thin Film Electrodes for Methanol Electrooxidation. J. Phys. Chem. B 2003; 107:5851-5856.

[9] Huang J., Yang H., Huang Q., Tang Y., Lu T., Akins D. L. Methanol Oxidation on Carbon-Supported Pt-Os Bimetallic Nanoparticle Electrocatalysts. J. Electrochem. Soc. 2004; 151:A1810-A1815.

[10] Umeda M., Ojima H., Mohamedi M., Uchida I. Methanol electrooxidation at Pt–Ru–W sputter deposited on Au substrate. J. Power Sources 2004; 136:10-15.

[11] Joo S. H., Kwon K., You D. J., Pak C., Chang H., Kim J. M. Preparation of high loading Pt nanoparticles on ordered mesoporous carbon with a controlled Pt size and its effects on oxygen reduction and methanol oxidation reactions. Electrochim. Acta 2009; 54:5746-5753.

[12] Chen D., Tao Q., Liao L., Liu S., Chen Y., Ye S. Determining the Active Surface Area for Various Platinum Electrodes. Electrocatalysis 2011; 2:207-219

[13] Lamy C., Lima A., LeRhun V., Delime F., Coutanceau C., Léger J. M. Recent advances in the development of direct alcohol fuel cells (DAFC). J. Power Sources 2002; 105:283-296.
[14] Franaszczuk K., Herrero E., Zelenay P., Wieckowski A., Wang J., Masel R. I. A comparison of electrochemical and gas-phase decomposition of methanol on platinum surfaces. J. Phys. Chem. 1992; 96:8509-8516.
[15] Feng R., Li M., Liu J. Synthesis of core–shell Au@Pt nanoparticles supported on Vulcan XC-72 carbon and their electrocatalytic activities for methanol oxidation. Colloids Surf. A, 2012; 406:6-12.
[16] Zerihun T., Gründler P. Oxidation of formaldehyde, methanol, formic acid and glucose at ac heated cylindrical Pt microelectrodes. J. Electroanal. Chem. 1998; 441:57-63.

Chapter 2.3. Formic Oxidation on Core-Shell Au@Pt$_x$/C Electrocatalyst

L. U. Martínez-Fernández[a]; G. Vázquez-Huerta[a,*]; S. Corona-Avendaño[a]

[a] Materials Department, Universidad Autónoma Metropolitana, Av. San Pablo 180, Reynosa Tamaulipas, C.P. 02200, México D.F., México.

ABSTRACT

Pt is the best up-to-date known catalyst; however platinum can be easily poisoned with CO which is produced during formic acid oxidation. To solve this problem, core-shell nanocatalysts (Au@Pt$_x$) with variable Pt-thickness are synthesized by using a two-step colloidal method, the synthesized catalysts were prepared using the following Au:Pt proportions: 2:1, 1:1, 1:2 and 1:4. The electrochemical behavior of Au@Pt catalysts supported on carbon Vulcan XC-72R (denominated Au@Pt$_x$/C) was evaluated with electrochemical techniques in a three-electrode electrochemical cell and 0.5M H_2SO_4 + 0.5M HCOOH as working solution. The physical characterization of Au@Pt$_x$/C catalysts was carried out by scanning-transmission electron microscopy (STEM) and X-ray diffraction (XRD). Electrochemical results from *I vs E* curves showed that 2:1 Au@Pt/C electrocatalyst produced the highest current density in comparison with 1:1, 1:2 and 1:4 Au@Pt$_x$/C catalysts. The electrochemically active surface area (ECSA) was evaluated in all cases by using anodic stripping voltammetry; the values of ECSA were used to normalize the currents obtained during the formic acid oxidation experiments. The physical characterization by scanning-transmission electron microscopy (STEM) showed that the synthesis procedure generates quasi-spherical nanoparticles of 18nm, 16 nm, 18nm y 21 nm for 2:1, 1:1, 1:2 and 1:4 Au@Pt$_x$/C catalysts. XRD results showed that in all cases the crystallographic structure of gold-core is maintained inferring that an epitaxial growth of Pt on Au is produced.

Keywords: Formic acid oxidation, Gold-platinum, Core-shell catalysts

1. Introduction

Fuel cells are electrochemical devices that directly and continuously convert the chemical energy of a fuel into electrical energy, they represent an alternative to produce clean energy [1], the basic structure of a fuel cell consists of two electrodes (anode and cathode) separated by a solid electrolyte (membrane). In the anode, the oxidation reaction takes

---

* Author for corresopndence: G. Vázquez-Huerta, T: 5255 53189356, E: gvh@correo.azc.uam.mx

place, the generated electrons are conducted through an external electric circuit to the cathode, where the reduction reaction takes place and the oxidant species (usually oxygen) is reduced. The generated products depends on the type of fuel cell [2]. Formic acid fuel cell (FAFC) coverts the chemical energy of formic acid into electrical energy, the global reaction is represented in equation 1 [3].

$$HCOOH + 1/2\ O_2 \leftrightarrow CO_2 + H_2O + \text{Energy} \quad (1)$$

In the literature, the oxidation reaction of formic acid on Pt is considered to follow a dual path mechanism, *i.e.* dehydrogenation and dehydration [3-4]. Dehydrogenation process takes place without carbon monoxide (CO) generation and produces carbon dioxide directly (equation 2).

$$HCOOH \rightarrow CO_2 + 2H^+ + 2e^- \quad (2)$$

However, dehydration produces CO which is a poisoning intermediate [3-4].

$$HCOOH + Pt^0 \rightarrow Pt\text{-}CO + H_2O \quad (3)$$

$$Pt^0 + H_2O \rightarrow Pt\text{-}OH + H^+ + e^- \quad (4)$$

$$Pt\text{-}CO + Pt\text{-}OH \rightarrow CO_2 + H^+ + e^- \quad (5)$$

$$HCOOH \rightarrow CO_2 + 2H^+ + 2e^- \quad (6)$$

CO production involves a strongly bonded CO to Pt, the amount of CO produced by this reaction may block the reaction sites, poisoning Pt catalyst [5]. In this sense, Pt-based catalysts with antipoisoning properties must be developed. In the literature, Pt-alloys has been studied to minimize the poisoning of Pt and with this purpose different metals such as Ru, Au, Sn, Ni, Bi, W, Os [6-10] have been used. Another approach for fabrication of lower-cost and improved tolerance to CO poisoning electrocatalysts is by using the so-called core-shell nanoparticles. Core-shell nanoparticles allow positioning Pt atoms on the surface (where they are needed) while the core is made of a cheaper transition metal.

Additionally, the unique electronic properties of core-shell nanoparticles result in changes of the stability, electrocatalytic activity, d-band energy and lattice parameter [11]. Varying the shell thickness may also result in a tuning effect of Pt surface properties that can be used as a tool for the design of more efficient electrocatalysts for fuel cells technology. In this work, the effect of varying the shell thickness of $Au@Pt_x$ has been investigated for formic acid oxidation, the atomic rates of Au:Pt are 2:1, 1:1, 1:2 and 1:4.

Physical techniques have been used to characterize the electrocatalysts among them are the scanning-transmission electron microscopy (STEM) and X-ray diffraction, XRD. The electrochemical response of the electrocatalysts supported on carbon Vulcan XC-72R ($Au@Pt_x/C$) was measured by using electrochemical techniques such as cyclic voltammetry, chronoamperometry and anodic stripping voltammetry.

2. Materials and Methods

2.1 Electrocatalysts synthesis

$Au@Pt_x$ core-shell nanoparticles were synthetized by using gold (III) chloride hydrate ($HAuCl_4 \cdot xH_2O$) (Sigma-Aldrich) and sodium tetrachloroplatinate(II) hydrate ($Na_2PtCl_4 \cdot xH_2O$) (Sigma-Aldrich) as precursors. Trisodium citrate dihydrate ($C_6H_5Na_3O_7 \cdot 2H_2O$) was used as reducing agent; Carbon Vulcan XC-72R (Cabot) was used as the carbon support. All the chemicals were used as-received. $Au@Pt_x$ nanoparticles were synthesized following a two-step method; i.e. *i)* first, the core (Au) was formed by reducing the gold precursor salt with $C_6H_5Na_3O_7 \cdot 2H_2O$, and *ii*) the core was covered with Pt to form the core-shell structure ($Au@Pt_x$). Briefly, Au:Pt (1:1) was as follows, 3.8 mL 0.01M $HAuCl_4 \cdot 3H_2O$ was added to 200 mL deionized water in an Erlenmeyer flask, the solution was heated to its boiling point maintaining a vigorous stirring, then 5.7 mL of 0.1 M $C_2H_5Na_3O_7$ were added and after a while the solution color changes from pale-yellow to ruby-red color, indicating that Au nanoparticles have been formed. The colloidal solution containing Au- nanoparticles is allowed to cool down to ~40ºC and a proper amount to form Au:Pt (1:1) atomic percentage of $2.5X10^{-2}$ M $Na_2PtCl_4 \cdot 6H_2O$ is added. Once the Au@Pt (1:1) nanoparticles are obtained, 40 mg of carbon Vulcan XC-72R are added to support them, the material is now designated as Au@Pt/C. Au:Pt 2:1, 1:2 and 1:4 compositions are prepared in a similar way but adding the proper amount of Pt solution.

2.2 Scanning transmission electronic microscopy and XRD characterization.

Particle size, morphology and size distribution of $Au@Pt_x$ were evaluated by using a JEM-1200EX SUPRA 55PV equipment from JEOL-Carl-Zeiss (working in STEM mode). Catalysts were also examined by X-ray diffraction (XRD), the experiments were performed in a Brucker 2000 diffractometer with a step scan of 0.02°, 2θ and 15 seconds per step, between 30° and 90° 2θ, at 35 kV and 30 mA, using Cu K_α radiation, 1.54 Å.

2.3 Electrochemical procedure

Working electrodes were prepared by weighing 3 mg of the supported catalyst in a 2.0 mL vial, then 200 μL of deionized water and 20 μL of Nafion 5% V/V solution were added into the vial and placed in ultrasonic bath for 10 minutes until a homogeneous suspension (or catalytic ink) was obtained. An aliquot of 20 μL of this ink was applied onto a freshly polished surface of a glassy carbon electrode with geometric area = 0.196 cm^2 and was left to dry in an oven at 60 ºC for 10 min. The electrochemical signals were recorded with a VersaSTAT4 from Princeton Applied Research (PAR), using 0.5 M H_2SO_4 as electrolytic solution or 0.5 M HCOOH + 0.5 M H_2SO_4 as working solution. In all the electrochemical measurements, a conventional three-electrode cell was used; electrode potentials were measured and reported against the Hg/Hg_2SO_4 electrode (SSE). A graphite bar served as counter electrode, while the working electrode was $Au@Pt_x/C$. The electrochemical experiments were performed within -0.60 a 0.55V as potential range, at 50 mVs^{-1} scan rate. In order to calculate the electrochemically active surface area (easa), CO-stripping voltammograms were measured in 0.5 M H_2SO_4 solution, the catalyst surface was previously saturated with CO by bubbling CO in the electrolyte solution and polarizing the electrode at -0.45 V/SSE for 15 minutes; after which, the remaining-CO dissolved was

purged by bubbling N_2 for 15 minutes, immediately after an I vs E plot of CO stripping was performed (scan rate = 50 mVs^{-1}). The charge associated with CO stripping was used to measure the easa [12].

3. Results and Discussion

3.1. Scanning transmission electron microscopy results.

Micrographs of Au@Pt_x with Au:Pt, 2:1, 1:1, 1:2 and 1:4 were obtained from scanning transmission electron microscopy (STEM) and are shown in Fig 1. The synthesis procedure generates quasi-spherical nanoparticles with small dispersion in size. In Figure 1, the average particle sizes are of 16nm, 16 nm, 18nm and 21 nm for Au:Pt, 2:1, 1:1, 1:2 and 1:4 catalysts, respectively.

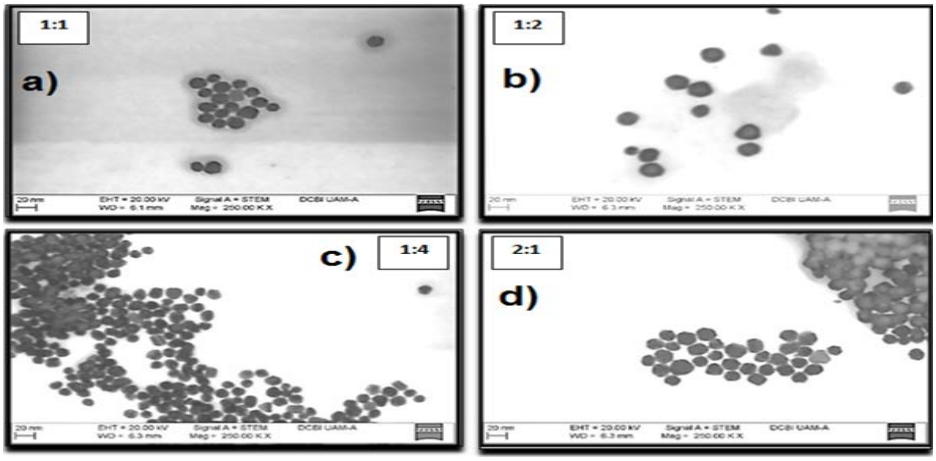

Fig. 1. STEM images of: *a)* Au@Pt (1:1), *b)* Au@Pt (1:2), *c)*Au@Pt (1:4) and *d)*Au@Pt (2:1).

3.2. X-ray diffraction results.

Crystalline structures of the catalysts were analyzed from XRD measurements, the diffraction patterns of Au@Pt_x with Au:Pt, 2:1, 1:1, 1:2 and 1:4 are shown in Fig. 2. Figure 2 corresponds to Au@Pt 1:1 and shows five peaks located at 2θ= 38.28°, 44.18.4°, 64.69°, 77.61° and 81.81 which correspond to those expected for a gold sample (JCPDS, card no. 04-0784), the peaks can also be identified with (111), (200), (220), (311) and (222) crystallographic planes of an FCC structure; these results allow inferring that platinum atoms may have an epitaxial growth on gold core and the FCC crystalline structure is maintained. A similar behavior is presented by Au:Pt 2:1, 1:2 and 1:4 samples. Additionally, the broad diffraction peak at 25.1º in each XRD pattern corresponds to the graphite (002) plane (JCPDS, No. 74-2330) from the carbon Vulcan XC-72R support, the broadening phenomenon of diffraction peaks is due to the nanometer scale of catalysts.

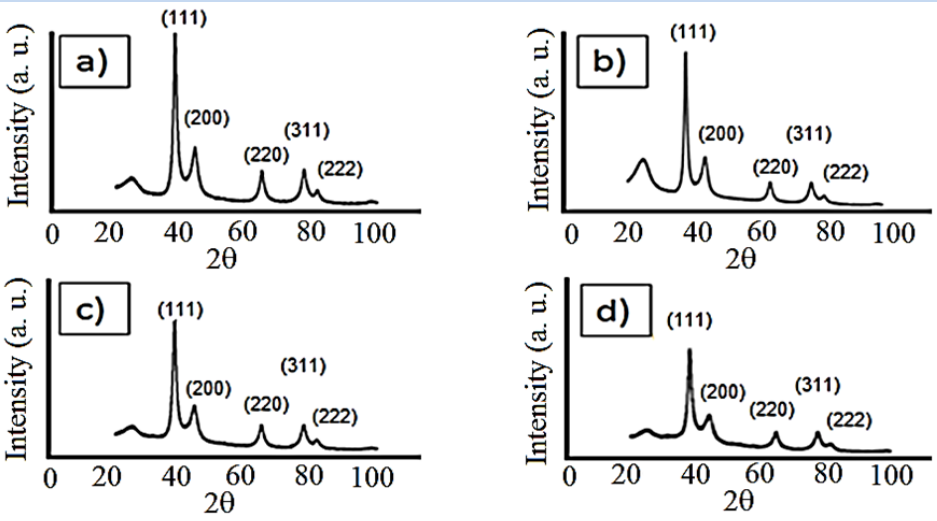

Fig. 2. X-ray diffraction patterns of: *a)* Au@Pt (1:1), *b)* Au@Pt (1:2), *c)*Au@Pt (1:4) and *d)*Au@Pt (2:1).

3.3 CO_{ads} stripping voltammetry

In order to determine the easa of Au@Pt_x/C catalysts CO-stripping experiments were performed, the experiments were carried out by applying a E_{pulse} = -0.45V while CO is bubbled (15min); after that, N_2 was bubbled maintaining E_{pulse} for another 15 min, then a cyclic voltammogram was acquired, from the charge associated to CO desorption (shadowed area in Figure 3) the easa was calculated and used to normalize the voltammograms in Figures 4 and 5.

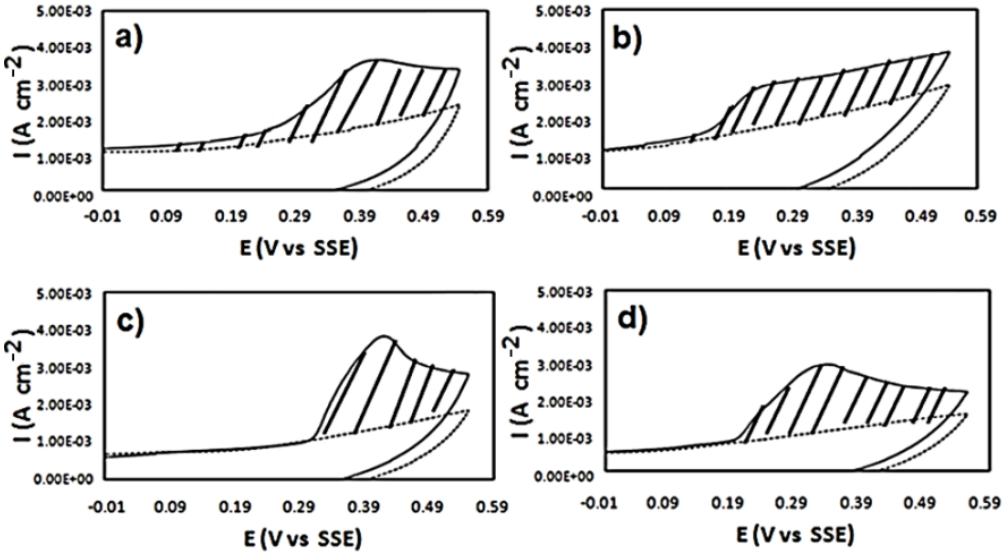

Fig. 3. CO-stripping voltammograms of Au@Pt_x/C in 0.5 M H_2SO_4, sr = 50mVs^{-1}. *a)* Au@Pt (1:1), *b)* Au@Pt (1:2), *c)*Au@Pt (1:4) and *d)*Au@Pt (2:1). (In all cases, the first cycles are shown as solid lines while the second ones in dashed lines).

3.4 Cyclic voltammetry of HCOOH.

Previous to the electrochemical characterization, the working electrode was electrochemically cleaned by carrying out 100 cycles within the potential range of -0.6 to 0.55 V vs SSE. Once the working electrode is clean and activated, its electrocatalytic activity for HCOOH oxidation in 0.5 M H_2SO_4 was measured. Figure 4 shows the electrochemical behavior of Au@Pt_x/C electrocatalyst, all of them present the well-known oxidation profile characterized by two oxidation peaks [13], in Figure 4a, an anodic peak between -0.43 y 0.33 V vs SSE appears during the forward sweep, this peak is associated to formic acid oxidation, while during the backward sweep another anodic peak is present, this second peak is associated to intermediary species generated from incomplete oxidation of HCOOH in the forward sweep.

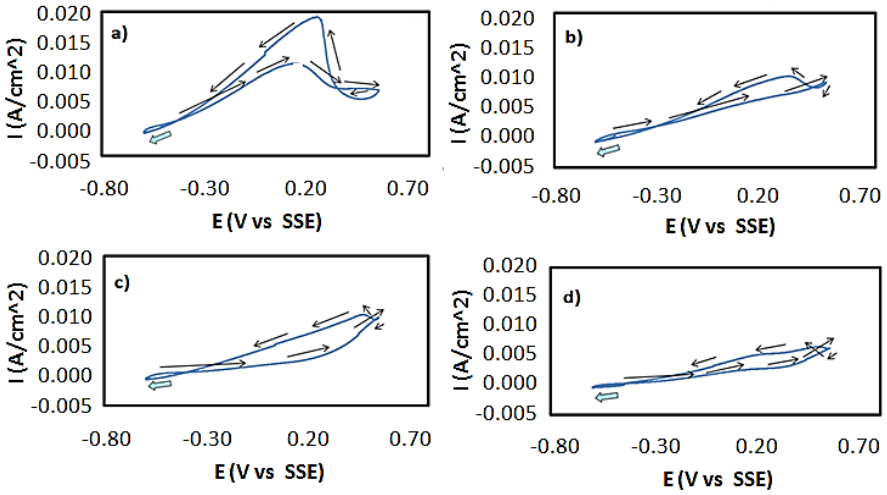

Fig. 4. Cyclic voltammperograms of : a) Au@Pt 2:1, b) Au@Pt 1:1, c) Au@Pt 1:2 and d) Au@Pt 1:4, in 0.5 M H_2SO_4, + 0.5 M HCOOH, scan rate 50 mVs^{-1}.

In all cases, the peak current density and the potential peak of the forward sweep diminishes as the quantity of Pt_{shell} increases, this indicates that the gold core within Au@Pt_x favors positively the electrocatalytic properties of Pt_{shell} atoms avoiding the poisoning effect, the more the Pt content the lesser the electrochemical current.

3.5 I vs t plots of HCOOH oxidation

I vs t plots of formic acid oxidation on Au@Pt_x/C, in 0.5 M H_2SO_4, + 0.5 M HCOOH are shown in Figure 5. The applied potential in these experiments is 0.10 V, during 200s, at the end of which all the I vs t curves present a constant value associated to the steady-state current density (I_{ss}). The steady state current density (I_{ss}) for: Au@Pt (2:1), Au@Pt (1:1), Au@Pt (1:2) and Au@Pt (1:4) are $7.59x10^{-3}$, $6.84\ x10^{-3}$, $3.13\ x10^{-3}$ and $2.11\ x10^{-3}$ A cm^{-2}, respectively. Clearly the current density diminishes as the Pt amount on the shell increases, a possible explanation for this is that the presence of gold in the core modifies the electronic properties of Pt_{shell} which diminishes the CO-Pt bond allowing liberation of active sites, which in turns allows the oxidation of more HCOOH molecules, while the

increment in the amount of Pt_{shell} atoms results in the poisoning of the catalyst caused by the generation of CO_{ads} during HCOOH oxidation.

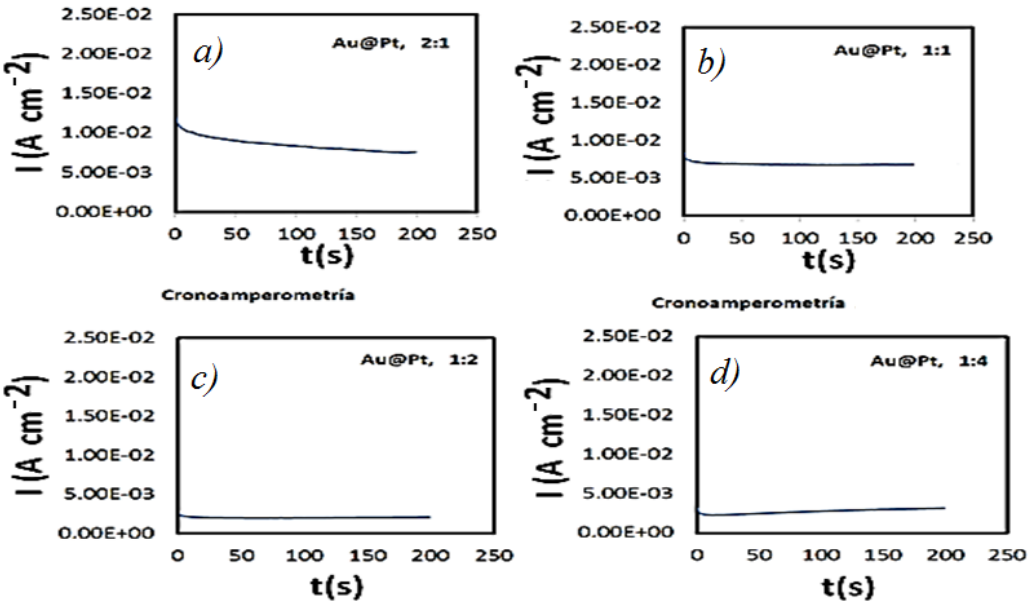

Fig. 5. I vs t plots of : a) Au@Pt 2:1, b) Au@Pt 1:1, c) Au@Pt 1:2 and d) Au@Pt 1:4, in 0.5 M H_2SO_4, + 0.5 M HCOOH (E_{pulse} = 0.10 V vs SSE).

4. Conclusion

Core-shell $Au@Pt_x$ with variable Pt-thickness were synthesized by using a two-step colloidal method, the prepared catalysts have Au:Pt proportions: 2:1, 1:1, 1:2 and 1:4. The physical characterization by scanning-transmission electron microscopy (STEM) showed that core-shell nanoparticles are nearly spherical in all cases and the average particle sizes are 16nm, 16 nm, 18nm and 21 nm for 2:1, 1:1, 1:2 and 1:4 $Au@Pt_x/C$ catalysts. XRD diffraction patterns showed that in all cases $Au@Pt_x$ nanoparticles maintain an FCC crystallographic structure. Cyclic voltammetry evaluation shows that Au@Pt (2:1) produces the highest current density (0.019 A cm^{-2}) at the smaller potential peak (0.24 vs SSE), in comparison with Au@Pt 1:1, 1:2 and 1:4. Also, from chronoamperometric results, it was found that Au@Pt (2:1) produces the highest steady-state current density (7.59 A cm^{-2}) in comparison with the other catalysts. The latter may be due to the presence of gold in the core which modifies the electronic properties of Pt_{shell} favoring the liberation of active sites and allowing the oxidation of more HCOOH molecules.

Acknowledgements

The authors are thankful to the Department of Materials at UAM-A for financing the present research and the Laboratory of Microscopy of the D-CBI, UAM-Azc, for STEM images.

References

[1] Appleby A.J., Fouldes F.R., "Fuel Cell Handbook", van Nostrand-Reinhold, New York, USA, 1989.

[2] Cano-Castillo U., Las celdas de combustible: verdades sobre la generación de electricidad limpia y eficiente vía electroquímica. Boletín iie, 1999.

[3] Lović J.D., Tripković A.V., Gojković S.Lj., Popović K.Dj., Tripković D.V., Olszewski P., Kowal A., Kinetic study of formic acid oxidation on carbon-supported platinum electrocatalyst. J. Electroanal. Chem., 2005; 581: 294-302.

[4] Rice C., Ha S., Masel R.I., Wieckowski A., Catalysts for direct formic acid fuel cells. J. Power Sources, 2003; 115: 229-235.

[5] Vázquez-Huerta G., Hernández-Rojas M. E., Dávila-Gómez J. A. Desarrollo de una celda de combustible tipo PEM alimentada con oxígeno del aire e hidrógeno parcialmente purifica, Rev Cuba Quim, 2012; 24: 212-214.

[6] Luo J., Njoki P. N., Lin Y., Mott D., Wang, Zhong C. J. Characterization of Carbon-Supported AuPt Nanoparticles for Electrocatalytic Methanol Oxidation Reaction. Langmuir 2006; 22:2892-2898.

[7] Lin Y., Cui X., Yen C. H., Wai C. M. PtRu/Carbon Nanotube Nanocomposite Synthesized in Supercritical Fluid: A Novel Electrocatalyst for Direct Methanol Fuel Cells. Langmuir 2005; 21:11474-11479.

[8] Park K. W., Choi J. H., Sung Y. E. Structural, Chemical, and Electronic Properties of Pt/Ni Thin Film Electrodes for Methanol Electrooxidation. J. Phys. Chem. B 2003; 107:5851-5856.

[9] Huang J., Yang H., Huang Q., Tang Y., Lu T., Akins D. L. Methanol Oxidation on Carbon-Supported Pt-Os Bimetallic Nanoparticle Electrocatalysts. J. Electrochem. Soc. 2004; 151:A1810-A1815.

[10] Umeda M., Ojima H., Mohamedi M., Uchida I. Methanol electrooxidation at Pt–Ru–W sputter deposited on Au substrate. J. Power Sources 2004; 136:10-15.

[11] Joo, S. H., Kwon, K., You, D. J., Pak, C., Chang, H., Kim, J. M., Preparation of high loading Pt nanoparticles on ordered mesoporous carbon with a controlled Pt size and its effects on oxygen reduction and methanol oxidation reactions. Electrochim. Acta 2009; 54:5746-5753.

[12] D. Chen, Q. Tao, L. Liao, S. Liu, Y. Chen, S. Ye, Determining the Active Surface Area for Various Platinum Electrodes, Electrocatalysis, 2 (2011) 207-219.

[13] Hu Sh., Munoz, F. Noborikawa, J., Haan J., Scudiero L., Ha S., Carbon supported Pd-based bimetallic and trimetallic catalyst for formic acid electrochemical oxidation; Applied Catalysis B: Environmental 180 (2016) 758–765.

Chapter 2.4. Synthesis and characterization of Sn@Pt/C and Ru@Pt/C core-shell nanocatalysts for the EOR

D. González-Quijano[a]; W.J. Pech-Rodríguez[a]; J.I. Escalante-García[a,b]; G. Vargas-Gutiérrez[a,b]; F.J. Rodríguez-Varela[b,c,*]

[a]Ingeniería Metalúrgica e Ingeniería Cerámica
[b]Sustentabilidad de los Recursos Naturales y Energía
[c]Programa de Nanociencias y Nanotecnología
Cinvestav Unidad Saltillo, Av. Industria Metalúrgica 1062, Parque Industrial Ramos Arizpe.
Ramos Arizpe, Coahuila, C.P. 25900, México.

ABSTRACT

Pt-alone anodes have shown low performance for the complex oxidation of alcohols to CO_2. It involves the breaking of C-C bonds during their dissociative adsorption producing intermediates (i.e. CO-like species) that strongly adsorb on Pt active sites, depolarizing it. Core-shell nanostructures have shown high catalytic activity for the oxidation of alcohols. In this work, M@Pt/C core-shell catalysts (where M: Sn and Ru) with nominal Pt:M atomic ratio of 1:1 were synthesized by a polyol reduction process in two successive steps. The Metal:Vulcan support ratio was 20:80 (wt. %). The electrocatalytic activity of the catalysts was studied in acid media for the Ethanol Oxidation Reaction (EOR). XRD characterization of Sn@Pt/C and Ru@Pt/C shows the typical peaks of carbon and fcc Pt. The particle size calculated with the Scherrer equation was 2.47 and 1.96 nm for Sn@Pt/C and Ru@Pt/C, respectively. Chemical analysis by EDS indicated that the atomic ratio was higher than the expected: 2.4:1 in the case of Sn@Pt and 2.5:1 for Ru@Pt. The CO stripping experiments indicated that the core-shell catalysts adsorb the CO at lower potentials than Pt/C. The EOR characterization showed that the reaction started at lower onset potentials (404 mV) in the case of Sn@Pt/C, with a maximum peak current density of 313.40 mA mg_{Pt}^{-1}. The values for Ru@Pt/C were 322 mV and 266.71 mA mg_{Pt}^{-1}, while those of Pt/C were 450 mV and 427.57 mA mg_{Pt}^{-1}. After accelerated degradation test, the core-shell catalysts did not show Electrochemically Active Surface Area losses, demonstrating their high stability. Furthermore, the chronoamperometry measurements showed that the catalysts have a similar behavior than Pt/C. These results demonstrated that the core-shell catalysts have better performance and stability during the EOR than the Pt/C catalyst.

Keywords: Core-Shell catalysts, Sn@Pt and Ru@Pt, EOR, Direct alcohol fuel cells

---

* Author for correspondence:
F.J. Rodriguez-Varela, T: 52(844)438-9600 ext. 8526, E: javier.varela@cinvestav.edu.mx

1. Introduction

Direct Alcohol Fuel Cells (DAFCs) have been widely investigated worldwide [1,2]. One of the main challenges for their massive commercialization is the low performance of Pt-alone (Pt/C) catalysts for the oxidation of organic molecules, such as alcohols, to CO_2 [1,2]. The complete oxidation of alcohols involves the breaking of C-C bonds during their dissociative adsorption producing reaction intermediates (for example CO-like species) that strongly adsorb on Pt active sites, depolarizing the electrode [1–6].

Several Pt-based alloys such as Pt-Ru/C and Pt-Sn/C, have shown high catalytic activity for the oxidation of alcohols, i.e., the onset potential is more negative and the current density is higher during the Oxidation Reaction [7–13]. These catalysts are more tolerant to the poisoning effect by CO. The co-catalyst modifies the Pt atomic structure promoting the bi-functional mechanism and the ligand effect [9, 10, 14]. The ligand effect contributes to weaken the adsorption energy of CO and facilitates the C–C bond cleavage of adsorbed alcohols. Meanwhile, in the bi-functional mechanism the co-catalyst provides –OH species that facilitate the alcohol oxidation at lower potentials than Pt/C catalysts [1, 2, 15]. The study of the effects of these mechanisms on the behavior of Pt-catalysts, can give an insight on their contribution to the oxidation reaction. However, such differentiation is not an easy task.

The contribution of the bi-functional mechanism could be limited by depositing a thin Pt layer on the surface of a co-catalysts, preventing its direct participation in the reaction. Nanostructures having such morphology have been developed in recent years and are known as core-shell. Some research groups have attempted to differentiate the two effects on the electrooxidation of organic molecules. Muthuswamy et al. observed a strong dependence of tolerance to CO poisoning and catalytic activity for the Methanol Oxidation Reaction (MOR) on the shell composition [16]. Ochal et al. characterized Ru@Pt/C core-shell catalysts by CO stripping, determining their good balance between activity and stability [17]. Zhang et al. prepared Ru@Pt anodes by the microwave irradiation technique, demonstrating their higher electrocatalytic activity compared to commercial Pt/C for the hydrogen oxidation in the presence of CO [18]. Overall, core-shell catalysts have shown a high tolerance toward CO poisoning. However, the synthesis of core-shell anodes is complex and the procedure to obtain them may have an important effect on their physicochemical and electrocatalytic characteristics.

Considering the importance of developing high performance anode catalysts for DAFC applications, the optimal synthesis conditions to obtain Pt-Sn/C alloys via the polyol method has been reported by our group [7]. In this work, we report the synthesis of Sn@Pt/C and Ru@Pt/C core-shell nanocatalysts using the best solution ratio previously determined. The anodes have been characterized by XRD, EDS, and their catalytic activity for the Ethanol Oxidation Reaction (EOR) evaluated by CV and chronoamperometry.

2. Materials and Methods

2.1 Reactants and gases

Analytical grade chemicals were purchased from Aldrich and used as received. $H_2PtCl_6 \cdot 6H_2O$, $SnCl_2 \cdot 2H_2O$, and $RuCl_3$ were used as metallic precursors. Vulcan XC-72

(Cabot Corp) was the catalysts support. Ethanol (EtOH), ethylene glycol (EG), 2-Propanol, NaOH, and H_2SO_4 were used in the catalysts synthesis and electrochemical characterization. Nafion® solution (5 wt. %) was used for the catalytic ink preparation. Ultra high purity (> 99 %) N_2 purchased from Infra gas was used to control the atmosphere of the electrochemical cell.

2.2 Synthesis of the catalysts

Sn@Pt/C and Ru@Pt/C catalysts, having 20 wt. % metal loading and Pt:M atomic ratio of 1:1 were synthesized by the polyol method, using a two-successive steps as described in a previous work [7]. First, the core (Sn or Ru metal) was synthesized in an EG:EtOH:H_2O solution with a 96:4:0 (v/o) ratio while the temperature was kept at 130 °C for 3 h., after, the powders was washed and filtered [7].

Afterwards, the cores (separately) were dispersed 30 min by ultrasound in a solution containing 38 mL of EG, while the required amounts of $H_2PtCl_6 \cdot 6H_2O$ and Vulcan were dissolved in 2 mL of EG and 8 mL EG + 2 mL EtOH, respectively. Then, the metallic core and the Pt precursor were mixed and magnetically stirred for 1 h. The solution was adjusted to a pH of 12 and heated to 130 ºC for 2 h under refluxing conditions. After this time, the Vulcan was added, maintaining stirring and temperature conditions for 1 h. The mixture was left to cool down to room temperature keeping stirring conditions for 3 h. Subsequently, the pH was adjusted to 2 and the obtained powder was filtered, washed, and dried. For comparison purposes, a Pt/C catalyst was synthesized as follows: the $H_2PtCl_6 \cdot 6H_2O$ salt was dissolved in 2 mL of H_2O and the Vulcan support in 48 mL of EG. The solutions were sonicated separately for 30 min followed by mixing and stirring for 1 h, followed by the heating and pH adjustments described above.

2.3 Physicochemical characterization

X-ray diffraction (XRD) patterns were obtained using an X'pert Philips diffractometer, with a Cu Ka radiation source (λ = 1.54 Å) over a range of 10-100° (2θ). The chemical composition of the catalysts was obtained by Energy Dispersive Spectroscopy (EDS) analyses in a Philips XL30 Scanning Electron Microscope (SEM) apparatus, using an accelerating voltage of 20 keV.

2.4 Electrochemical set-up and characterization

The catalytic inks were prepared as described in previous work [7]. Briefly, 10 mg of the catalysts were dispersed in a mixture of 1 mL propanol and 5 µL Nafion®, with a subsequent sonication for 30 min. The electrochemical measurements were performed in a VoltaLab PGZ 301 potentiostat/galvanostat in a standard three-electrode cell. The working electrode was a glassy carbon disk (5 mm diameter) containing 10 µL of the corresponding catalytic ink. A Pt foil was the counter-electrode and an Ag/AgCl was the reference electrode, although all potentials were referred in this work to the Standard Hydrogen Electrode (SHE).

Cyclic voltammograms (CVs) were performed in 0.5 M H_2SO_4 electrolyte saturated with N_2 at a scan rate was of 20 mV s^{-1}. The potential interval was from 50 to 1200 mV/SHE for Pt/C and Sn@Pt/C, while that of Ru@Pt/C was from 50 to 800 mV/SHE to avoid the formation of irreversible oxides and the Ru particle growth. Afterwards, CVs of the EOR were conducted in the same N_2-saturated electrolyte with 0.5 M of EtOH at the

same potential ranges described here above. To evaluate the stability of the catalysts, Accelerated Degradation Tests (ADT) were carried out in N_2-saturated electrolyte by acquiring 500 cycles with a scan rate of 100 mV s^{-1} followed by three cycles at 20 mV s^{-1}. The potential scanned was the same for each catalyst as described above. Electrochemically Active Surface Area (ECSA) losses were determined by comparing the CVs before and after ADT. Chronoamperometric curves of the EOR were acquired in fresh N_2-saturated electrolyte containing 0.5 M EtOH by applying a static potential of 600 mV/SHE for 30 min.

3. Results and Discussion

3.1 Physicochemical characterization

Fig. 1 shows the XRD patterns of the Pt/C, Sn@Pt/C and Ru@Pt/C catalysts. Pt/C shows the typical face-centered-cubic (fcc) crystallographic structure of Pt (JCPDS # 040802), with reflections corresponding to the (111), (200), (220), and (311) planes. The peak located at around 26° (2θ) corresponds to the (002) plane of the hexagonal structure of graphite due to the presence of Vulcan. The patterns of Sn@Pt/C and Ru@Pt/C also show the peaks attributed to Pt and Vulcan, with a higher intensity of the (200) reflection.

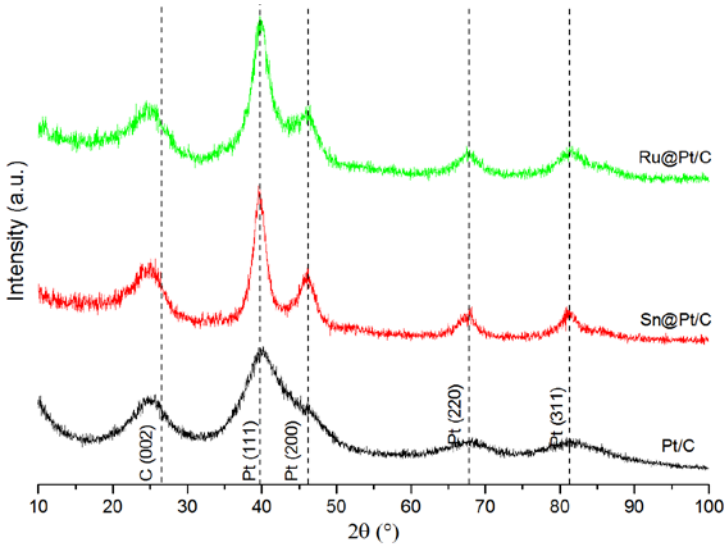

Fig. 1. XRD patterns of Pt/C, Sn@Pt/C and Ru@Pt/C.

The analysis of the (220) peaks using the Scherrer equation reveals particle sizes of 2.47, 1.96, and 1.90 nm for Sn@Pt/C, Ru@Pt/C, and Pt/C, respectively (Table 1). The EDS results indicate a chemical composition of Pt/C practically equal to the nominal, i.e., 19.2 wt. % Pt, compared to a theoretical 20 wt. % (Table 1). The core-shell catalysts have a Vulcan content of 80 wt. %, which is the expected value. However, the Sn and Ru content are 2.89 and 2.61 wt. %, respectively. Such values are higher than calculated. The core-shell anodes also show presence of O_x species that are believed to be in part due to the presence of SnOx or RuOx (even though this could not be confirmed by XRD). The chemical composition of Pt/C did not show the formation of PtO_x, despite the fact that it

has been synthesized in the presence of relatively large amounts of water (4 v/o). The Pt:Sn ratio is 2.4:1 and the Pt:Ru ratio is 2.51, higher than the theoretical 1:1 (Table 1).

Table 1. Chemical composition and particle size of the catalysts.

Catalyst	Pt	Sn or Ru (wt. %)	C	O_X	Pt:M ratio (at. %)	Particle size (nm)
Pt/C	19.20	-	80.80	-	-	1.90
Sn@Pt/C	11.34	2.89_{Sn}	80.63	5.14	2.4:1	2.47
Ru@Pt/C	12.34	2.61_{Ru}	80.07	4.98	2.5:1	1.96

3.2 Electrochemical characterization

Figures 2(a), (b), and (c) show the CVs of Pt/C, Sn@Pt/C, and Ru@Pt/C, respectively, before and after ADT. The ECSA losses after ADT are 34.23 % for Pt/C and 21.75 % for Sn@Pt/C, demonstrating the higher stability of the core-shell nanocatalyst (Table 2). In the case of Ru@Pt/C it is not possible to calculate ECSA values due to the absence of a $H_{ads/des}$ region. However, the CVs before and after ADT of the later present no differences, indicating its high stability under the experimental conditions of this study.

Figure 2(d) shows the polarization curves of the EOR at Pt/C, Sn@Pt/C and Ru@Pt/C in acid media. The current densities in the figure have been normalized with respect to the Pt mass content in the catalysts using the chemical composition obtained by EDS. The core-shell catalysts have a high catalytic activity for the EOR, showing an onset potentials of the EOR of 404 and 322 mV (Sn@Pt/C and Ru@Pt, respectively), more negative than 450 mV of Pt/C.

Moreover, the maximum peak current density (in the forward scan) is located at 852 mV for Sn@Pt/C and 848 mV for Ru@Pt, also more negative than the 1002 mV of Pt/C. The electrocatalytic parameters of the EOR at the nanocatalysts are given in Table 3.

The chronoamperometric behavior of the core-shell and Pt/C catalysts during the EOR is shown in Figure 3. Within the first few minutes, the catalysts show a fast current density decay. After ca. 2.5 min, Pt/C reaches a quasi-stable current density, which is higher than the current densities of Sn@Pt/C and Ru@Pt/C, demonstrating a better time-dependent performance.

Table 2. Parameters before and after ADT for Pt/C, Sn@Pt/C and Ru@Pt/C.

Catalyst	Pt_{Load} (mg)	Q (μC)	ECSA ($m^2\ g^{-1}$ Pt)	Q^* (μC)	$ECSA^*$ ($m^2\ g^{-1}$ Pt)	Variation in ECSA (%)
Pt/C	0.0193	13.76	66.45	9.44	43.70	34.23
Sn@Pt/C	0.0118	1.90	14.94	1.48	11.69	21.75
Ru@Pt/C	0.0124	-	-	-	-	-

*Value after ADT.

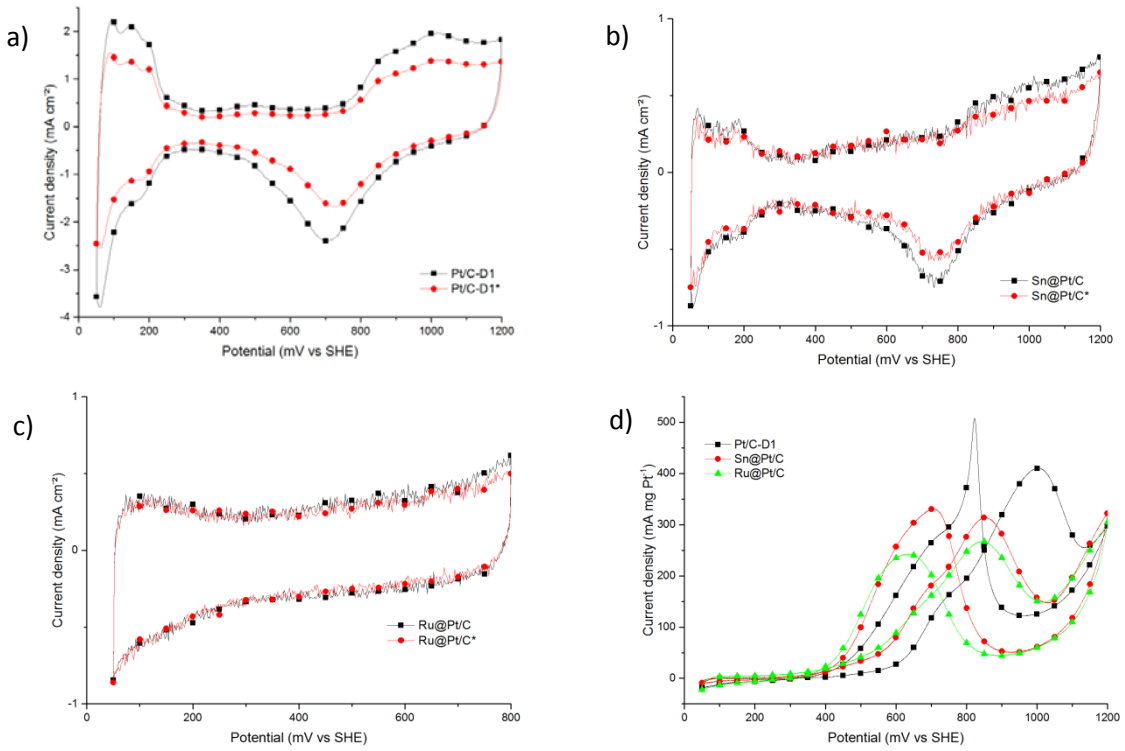

Fig. 2. CVs before and after ADT of a) Pt/C, b) Sn@Pt/C and c) Ru@Pt/C. Electrolyte: N_2-saturated 0.5 M H_2SO_4. d) Polarization curves of the EOR at the three catalysts. Electrolyte: N_2-saturated 0.5 M H_2SO_4 + 0.5 M EtOH. Scan rate: 20 $mV \cdot s^{-1}$.

Table 3. Electrochemical parameters of the EOR at Pt/C, Sn@Pt/C and Ru@Pt/C.

Catalyst	Onset potential (mV)	Peak current density (mA mg^{-1} Pt)
Pt/C	450	427.57 at 1002 mV
Sn@Pt/C	404	313.40 at 852 mV
Ru@Pt/C	322	266.71 at 848 mV

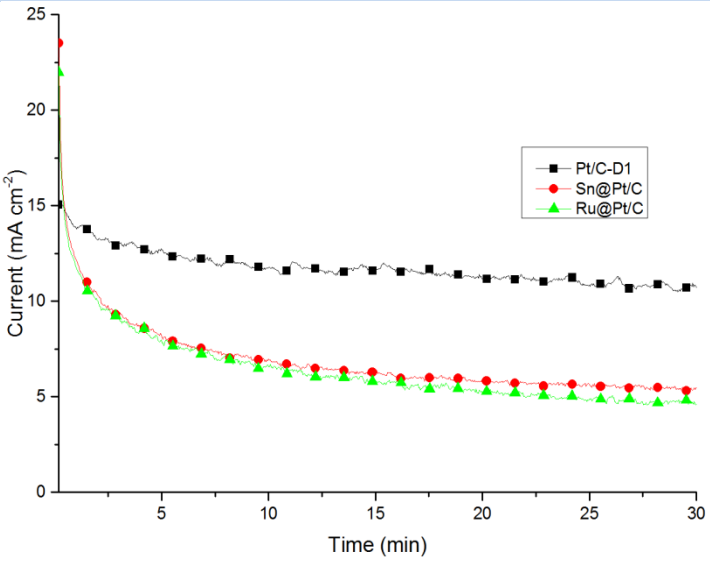

Fig. 3. Chronoamperometric curves of the EOR of Pt/C, Sn@Pt/C and Ru@Pt/C. Static potential: 600 mV/SHE.

4. Conclusion

The XRD patterns of the three catalysts showed the typical peaks corresponding to Pt fcc structure. The (200) peak was more intense at the core-shell anodes. The particle size was 2.47 and 1.96 nm for Sn@Pt/C and Ru@Pt/C, respectively, while Pt/C showed the smaller size (1.9 nm). The EDS analyses showed that Sn@Pt/C and Ru@Pt/C are Pt-rich catalysts with atomic ratios of 2.4:1 and 2.5:1, respectively.

The electrochemical characterization demonstrated that the core-shell catalysts have higher catalytic activity for the EOR, promoting the reaction at significantly lower onset potential than Pt/C. Even though the maximum peak current densities of the bimetallic catalysts were lower than that of Pt/C, the former showed a best performance in the 50 to 700 mV/SHE potential interval.The ADT tests indicated that Sn@Pt/C and Ru@Pt/C are stable catalysts compared to Pt/C because of smaller ECSA losses. However, the chronoamperometric curves demonstrated that their electrochemical stability must be improved.

Acknowledgements

The authors wish to thank the Mexican National Council for Science and Technology (CONACyT) for financial support of this work through projects 252079, 241526, and 252003 and for Doctoral scholarships granted to DGQ and WJPR. Special thanks are due to the MHS for the support provided to DGQ and WJPR to attend the XV International Congress.

References

[1] Chatterjee M., Chatterjee A., Ghosh S., Basumallick I. Electro-oxidation of ethanol and ethylene glycol on carbon-supported nano-Pt and -PtRu catalyst in acid solution. Electrochim Acta 2009;54:7299–304.

[2] Sieben J.M., Duarte M.M.E. Methanol, ethanol, and ethylene glycol electro-oxidation at Pt and Pt–Ru catalysts electrodeposited over oxidized carbon nanotubes. Int J Hydrogen Energy 2012;37:9941–7.

[3] Léger J., Rousseau S., Coutanceau C., Hahn F., Lamy C. How bimetallic electrocatalysts does work for reactions involved in fuel cells? Example of ethanol oxidation and comparison to methanol. Electrochim Acta 2005;50:5118–25.

[4] Neto A.O., Dias R.R., Tusi M.M., Linardi M., Spinacé E.V. Electro-oxidation of methanol and ethanol using PtRu/C, PtSn/C and PtSnRu/C electrocatalysts prepared by an alcohol-reduction process. J Power Sources 2007;166:87–91.

[5] Zhou W.J., Song S.Q., Li W.Z., Sun G.Q., Xin Q., Kontou S., Poulianitis K., Tsiakaras P. Pt-based anode catalysts for direct ethanol fuel cells. Solid State Ionics 2004;175:797–803.

[6] Zhu J., Cheng F., Tao Z., Chen J. Electrocatalytic Methanol Oxidation of Pt 0.5 Ru 0.5- x Sn x /C (x = 0−0.5). J Phys Chem C 2008;112:6337–45.

[7] González-Quijano D., Pech-Rodríguez W.J., Escalante-García J.I., Vargas-Gutiérrez G., Rodríguez-Varela F.J. Electrocatalysts for ethanol and ethylene glycol oxidation reactions. Part I: Effects of the polyol synthesis conditions on the characteristics and catalytic activity of Pt–Sn/C anodes. Int J Hydrogen Energy 2014;39:16676–85.

[8] Villanueva A.F.C., Ramirez A.M., Gutiérrez G.V., Torres L.A., Varela F.J.R. Synthesis of Unsupported Pt-based Electrocatalysts and Evaluation of Their Catalytic Activity for the Ethylene Glycol Oxidation Reaction. J New Mater Electrochem Syst 2013;16:171–6.

[9] Spinacé E.V., Neto A.O., Linardi M. Electro-oxidation of methanol and ethanol using PtRu/C electrocatalysts prepared by spontaneous deposition of platinum on carbon-supported ruthenium nanoparticles. J Power Sources 2004;129:121–6.

[10] Rodríguez Varela F.J., Savadogo O. Ethanol-tolerant Pt-alloy cathodes for direct ethanol fuel cell (DEFC) applications. Asia-Pacific J Chem Eng 2009;4:17–24.

[11] Sieben J.M., Duarte M.M.E. Nanostructured Pt and Pt–Sn catalysts supported on oxidized carbon nanotubes for ethanol and ethylene glycol electro-oxidation. Int J Hydrogen Energy 2011;36:3313–21.

[12] Neto A.O., Vasconcelos T.R.R., Da Silva R.W.R.V., Linardi M., Spinacé E.V. Electro-oxidation of ethylene glycol on PtRu/C and PtSn/C electrocatalysts prepared by alcohol-reduction process. J Appl Electrochem 2005;35:193–8.

[13] Livshits V., Peled E. Progress in the development of a high-power, direct ethylene glycol fuel cell (DEGFC). J Power Sources 2006;161:1187–91.

[14] Yan S., Sun G., Tian J., Jiang L., Qi J., Xin Q. Polyol synthesis of highly active PtRu/C catalyst with high metal loading. Electrochim Acta 2006;52:1692–6.

[15] Qian Q.Y., Yang C., Zhou Y.G., Yang S., Xia X.H. Efficient C-C bond cleavage in ethanol electrooxidation on porous Pt catalysts. J Electroanal Chem 2011.

[16] Muthuswamy N., de la Fuente J.L.G., Tran D.T., Walmsley J., Tsypkin M., Raaen S., Sunde S., Rønning M. Chen, D. Ru@Pt core–shell nanoparticles for methanol fuel cell catalyst: Control and effects of shell composition. Int J Hydrogen Energy 2013;38:16631–41.

[17] Ochal P., Gomez de la Fuente J.L., Tsypkin M., Seland F., Sunde S., Muthuswamy N., Rønning M., Chen, D. Garcia S., Alayoglu S. CO stripping as an electrochemical tool for characterization of Ru@Pt core-shell catalysts. J Electroanal Chem 2011;655:140–6.

[18] Zhang L., Kim J., Chen H.M., Nan F., Dudeck K., Liu R-S., Botton G.A., Zhang J. A novel CO-tolerant PtRu core–shell structured electrocatalyst with Ru rich in core and Pt rich in shell for hydrogen oxidation reaction and its implication in proton exchan ge membrane fuel cell. J Power Sources 2011.

Chapter 2.5. Micro-direct methanol fuel cells

P. Mendoza-Correa[a]; V. Galvan[b]; K. Domalon[b]; S. Sotez[b]; F. Gomez[b]; M. Hinojosa[a]

[a]Facultad de Ingeniería Mecánica y Eléctrica, Universidad Autónoma de Nuevo León, Pedro de Alba S/N, Ciudad Universitaria, 66450 San Nicolás de Los Garza, NL, Mexico.
[b]California State University, Los Angeles, 5151 State University Drive, Los Angeles, CA, 90032-8202.

ABSTRACT

The development of advanced technologies to generate alternative energy sources at low cost, which does not require the use of fossil fuels and can be used in small portable devices, has significantly increased. For example, fuel cells are simple to operate, have high energy conversion and cause no harm to the environment. One of the newest developments in this field is the microfluidic fuel cells (MFCs). The MFC paper-based works in a standard lateral flow test format, the porosity of the material allows separating the fuel and oxidant species throughout two parallel streams without an ionic exchange membrane or external pumps.
This work describes its fabrication using a paper microfluidic platform. The fuel cells use formate as the anode fuel and hydrogen peroxide as cathode oxidant. By using these materials has been achieved a maximum power density of nearly 1.2 mW mg^{-1} Pd. The MFC achieves a current density of 3.5 mA cm^{-3}. It is also demonstrated that the MFC does not require continuous flow of fuel and oxidant to produce power.

Keywords: Fuel cells, Microfluidics, Membraneless, Laminar flow

1. Introduction

Technological growth and the necessity to optimize processes without losing the essence of getting real results in a short time has led to increased knowledge in the field of portable devices which operate rapidly and efficiently through an electronic circuit and a battery formed by a paper-based fuel cell.

The PEM fuel cell is a device which provides electrical energy through a chemical oxidation-reduction reaction that takes place at the anode and cathode, respectively. The main benefit when using this type of cells is that they are self-rechargeable, thus are constantly generating electricity. Between anode and cathode there is a membrane able to separate the hydrogen atoms provided by the fuel at the anode, allowing the passage of

---

* Author for correspondence: P. A. Mendoza Correa, T: 044 811 216 8955, E: paolaamendoza@gmail.com

electrons to a circuit providing electrical power and output protons towards the cathode where they react with the room air and has water as a residue.

Most of this kind of cells produce clean energy without emitting gases that may affect the environment or some other harmful emissions. The inconvenience you have with them is the membrane degradation over time as it creates a constant reaction. Also takes into mind the high cost of materials that do not greatly benefits these devices when it comes to marketing.

Microfluidic fuel cells provide the opportunity to be similarly used as the PEM since they not require a solid membrane for chemical conversion into electricity. These cells operate using a laminar flow through a micro channel in which the chance of fuel leakage is eliminated, also, they have an estimated cost of $ 2 USD for each cell, which introduced them to the market as prospects for the electronics industry. They are compact and small, ideal for use in point-of-care devices.

2. Materials and Methods

Portable point-of-care devices are replacing the traditional diagnosis tests due to its facility to use allowing the patients to monitor their health at home. They not only give information about the current health status but also can help to prevent any further diseases. There are a few which may be single use and others that can be reused several times. Also it is important to mention that these devices shouldn't depend on a pumping system to provide fuel to make them work properly. They require materials that are environmental friendly for its manufacture and does not generate any pollution once they are thrown away.

Microfluidic fuel cells play an important role in this area since they are conform on a paper matrix with a Y-shaped form. The streams are loaded with fuel and other with the oxidant, e, g. formic acid, methanol, peroxide hydrogen, among others. In the middle of the channel, the anode and cathode are arranged where they reach the fuel and oxidant, respectively, by capillary action.

There were created three types of chips using Whatman 3 filter paper each one with different width and length (Fig. 1). A basic Y-shape was used to maintain separating the flow of the reactants until they join in the lateral column. The anode is conformed of a solution of Pd (0.007gr), C (0.003gr), 20 mL of H2O, dispersed Nafion solution (0.06 mL) and isopropyl alcohol (0.7 mL). The cathode is a mixture of paint (1.5479gr), carbon black (0.0751gr) and active carbon (0.2006 g).

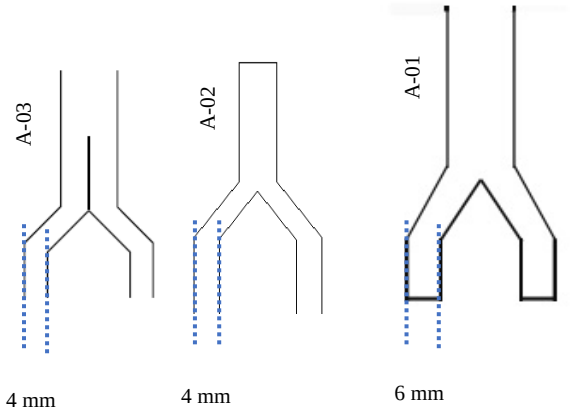

Fig. 1. Types of paper-based microfluidic fuel cells.

Table 1. Paper-based microfluidic fuel cells properties.

Sample	**Width**	**Length**
A-01	2.5 cm	4.9 cm
A-02	2.2 cm	4.5 cm
A-03	2.1 cm	3.6 cm

3. Results and Discussion

It is important to emphasize that in order to design an electronic device or system is required to know the current density generated by the material. The current density is expressed as the electrical current per unit area. It is also recommended that it remains low to prevent deterioration or degradation of the material.

For the testing, the electrodes were secured by brass mesh clips linked by silver epoxy to the anode and cathode (Fig. 2). The chip or microfluidic was placed vertically allowing flow entrance of fuel (20 mL formic acid) and oxidant (20 mL hydrogen peroxide) through two streams. Both species were disposed in glass vials. The flow raised by capillary action until it reached the anode and cathode, and it was left for 10 minutes to get a full cover.

The electrochemical measurements were placed in a Potentiostat 263A from Princeton Applied Research (Fig. 3) operating with two electrodes. Tests were increased to 10 mV in 40 mV steps at 2s intervals under continuous flow at room temperature (23 ºC).

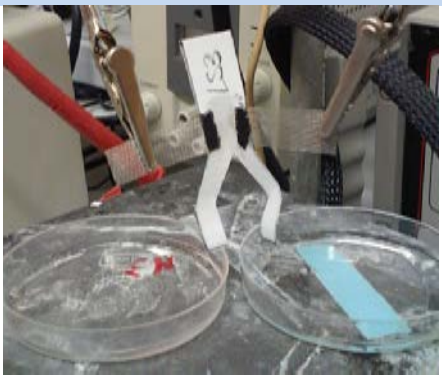

Fig. 2. A microfluidic fuel cell, with anode at the left and cathode at the right.

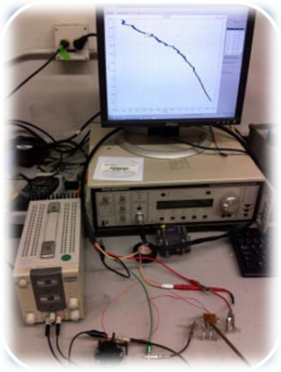

Fig. 3. Potentiostat 263A from Princeton Applied Research.

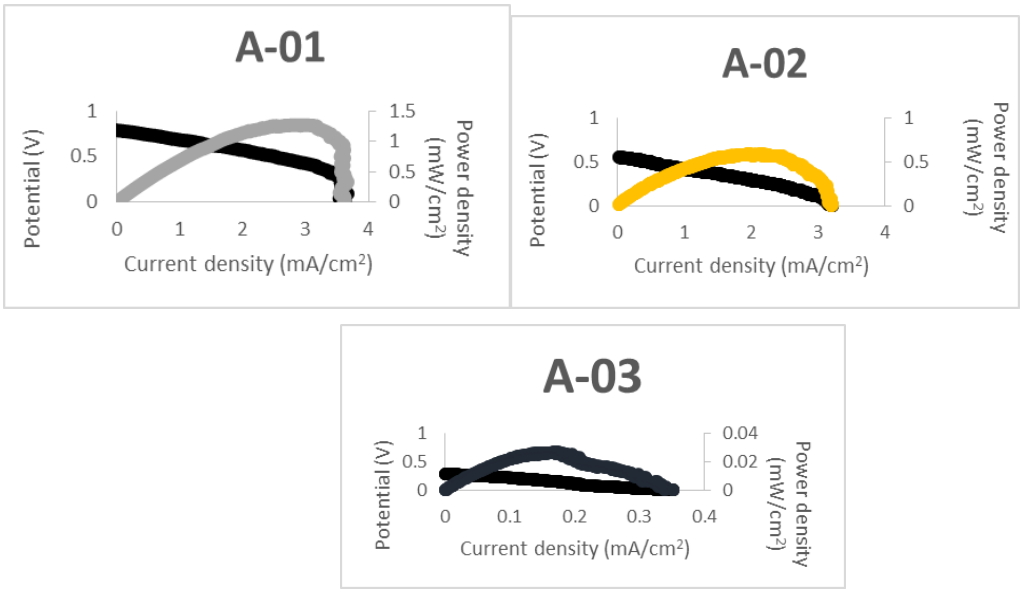

Fig. 4: Paper-based microfluidic fuel cell performance. (a) Sample A-01 polarization curves. (b) Sample A-02 polarization curves. (c) Sample A-03 polarizarion curves.

The results expressed in polarization curves show that in open circuit, the MCF A-01 (4.9 x 2.5 cm) achieved a voltage of about 0.8 V and a current density of 3.5 mA/cm^3. On a smaller size, the cell A-02 (4.5 x 2.2 cm) generates a current density a little bit lower, 3.3 mA/cm^3 and as the maximum current, 0.7 V. For the smallest cell A-03 (3.6 x 2.1 cm), it has a similar voltage but lower current density of 0.35 mA/cm^3 (Fig. 4).

4. Conclusion

It has been described the method for creating a paper-based microfluidic fuel cell using formic acid as a fuel at the anode and hydrogen peroxide as the oxidant at the cathode. These materials have generated a current of about 0.7 V for the different cells and a current density ranging from 3.5 to 0.35 mA/cm^3. The MFC's did not require a continuous flow of fuel and oxidant to generate power and they remained operating for 24 hours without any significant change in their voltage.

Acknowledgements

The research has been supported by California State University, Los Angeles, which provided the material and equipment necessary to develop these fuel cells. Prof. Frank Gomez and Prof. Moises Hinojosa played an important role on this work by bringing their knowledge and time. Also Prof. Virginia Collins who has been supportive on the promotion of the new materials for green energy.

References

[1] Esquivel J.P., Del Campo F.J., Gómez de la Fuente J.L., Rojas S., Sabaté N., Microfluidic fuel cells on paper: meeting the power needs of next generation lateral flow devices. Energy Environ. Sci., 2014, 7, 1744-1749.

[2] Venugopalan, S. Micro Fuel Cells. Recent Trends in Fuel Cell Science and Technology. By Suddhasatwa Basu. New York: Springer, 2007, 137-56.

[3] Copenhaver, T. S.; Purohit, K. H.; Domalaon, K.; Pham, L.; Burgess, B. J.; Manorothkul, N.; Galvan, V., Sotez, S.; Gomez, F. A.; Haan, J. L. A Microfluidic Direct Formate Fuel Cell on Paper. Electrophoresis, 2015, 8, 1825-29.

[4] Gomez A. F,. The future of microfluidic point-of-care diagnostic devices. Bioanalysis 2013, 5, 1-3.

[5] Ho B., Kjeang E., Microfluidic Fuel Cell Systems. Central European Journal of Engineering. 2011, 1, 123-131.

3
Fuel cells components and stacks

Chapter 3.1. Optimization of stack performance of low power PEM fuel cells

R. Moreno-Flores[a]; E. Escobedo*[a]; D. Pacheco[a]; M. Smit[a]

[a]Unidad de Energía Renovable, Centro de Investigación Científica de Yucatán. Calle 43#130 Col. Chuburna de Hidalgo,CP. 97200, Mérida Yucatán, México.

ABSTRACT

For a PEMFC under operation, different causes of performance loss exist. Performance loss can increase when the system is scaled up to higher power. In this work the performance of low-power stacks manufactured in CICY is optimized through studies of the behavior and performance of single cells and stacks of own fabrication, and results are compared to commercial cells. Several electrochemical techniques are used, such as: polarization curves, electrochemical impedance spectroscopy, cyclic voltammetry. These provide insight into the performance of the cell and stack in operation, as well as into the different causes of losses, such as electrical resistance and fuel crossover. In addition to these techniques, SEM is used to evaluate the morphology and uniformity of the catalytic layer. In the first stage of work scaling and operating conditions of the single cell were analyzed in detail, the second stage focused on the manufacturing process, the design and materials of the components of the stack were established. The results demonstrate that for cells with catalyst layers deposited by electrospray the maximum power density of the single FC is higher than for cells prepared with the technique of dropping. The increase is significant, from 208 to 270 mW/cm^2. Also, the optimization of the hot-pressing process of the MEA resulted in an improvement of the maximum power density up to 310 mW/cm^2, while minimizing the canal-rib ratio improved the FC performance with about 16%. Compared to commercial PEMFC's, the performance however, is still low, which is likely related to the type of materials used.

Keywords: Proton exchange membrane fuel cell, Stack, Electrochemical techniques

1. Introduction

The fuel cell proton exchange membrane (PEMFC) is an electrochemical device that transforms the chemical energy of a reaction into electrical energy with high efficiency. The high power density at low temperatures and long life makes it attractive to DC to be used in stationary, mobile and portable systems, such as for backup systems energy, automotive and electronic entertainment equipment industry, respectively.

---

* Author for correspondence:
E.Escobedo, Unidad de Energía Renovable, Centro de Investigación Científica de Yucatán. Calle 43#130 Col. Chuburna de Hidalgo,CP. 97200, Mérida Yucatán, México.

The fuel cell is mainly composed of five parts: end plates, current collector plates, gaskets, bipolar plates and membrane electrode assembly. The union of anode-membrane-cathode is known as MEA, it is considered the heart of the cell because it is in the catalytic layer where the electrochemical reactions take place. On the surface of the anode hydrogen is oxidized, while oxygen is reduced at the cathode. The catalytic layer is basically the joining of a catalyst, a carbonaceous support and ionic conductor; typically this layer can be applied on the membrane or on the gas diffuser.

Generally the most used materials for the MEA is carbon supported platinum catalyst, Nafion®, electrolyte membrane, paper or carbon cloth as a gas diffuser. There are several ways to apply the catalytic layer as a liquid mixture of catalyst and solvent in the electrolyte solution through the dropping technique that involves depositing ink, with a micropipette, drop by drop to the diffuser; Another way is by electrospray technique of applying the same way that ink dropping but applying a potential difference (10 to 11 kV) between metal needle pipette and the diffuser surface.

Arrangements FC connections in series are to raise a potential difference and put this potential for practical use. Such connections are provided and are improved by bipolar plates. Other functions of the plates are: being a way by which the heat is removed and water, provide mechanical support to the cells, provide a thermal contact between the coolant, driving electrons generated in the reactions, the reactant gases lead to all cells and all your work surface through channels[1][2]. It is important that the materials plates have high electrical conductivity such as metals, polymers or composite graphite whit flow channels of different configurations for conducting the fuel and oxidant.

Individual PEMFC is characterized by delivering direct current at low potential difference, relatively, this means that to get a potential to use in conventional electrical equipment is required series connection of the cells. Each cell produces a voltage of 1.23V theoretically, this potential is ideal, in a real cell performance losses are various causes, under standard operating conditions and may be increased if more cells connected in series are added[3] to learn the electrical performance of the electrochemical cell operation polarization curve technique is used.

2. Materials and methods

The materials used were diffusers carbon cloth BASF Fuel Cell Inc. A6NCV2.1 ELAT and carbon paper EC-TP1-060T, Nafion® membrane (DuPont), Nafion® Solution 5% (SIGMA ALDRICH), catalyst Pt/C 20% and 2-propanol (reagent grade). The only known diffusers carbon cloth have Teflon coated fabric, a microporous carbon layer vulcan and measured 0.36mm thick; carbon paper is treated with 30% Teflon® and 0.19mm thickness, these data are given by the manufacturer[4].

The electrochemical characterization made to all cells in all tests were through a polarization curve using the testing station (FCT-50, BioLogic) for controlling the operating conditions and the potentiostat / galvanostat (VSP BioLogic) with booster 10 A - 20 V (BioLogic, VMP3B-10) for the polarization curves, they were conducted with a scan rate of 10mV / s OCP to 0V and operating conditions, which we will call conditions standard in this work, were 60 ° C, 50 ML / min / cm^2 flow of gases (H_2 / O_2) to 100% relative humidity (RH).

2.1. Materials comparison for diffusers

Two MEAs of 1cm^2 were prepared with platinum loading of 0.5 mg/cm^2, both with parameters membrane electrode assembly EROSA(2011) [5], temperature 120°C, 4 minutes pressing time and 1814.4 kgf / cm^2 (4000 lbf / cm^2), a diffuser MEA carbon cloth and the other of carbon paper. The obtained MEAs were placed in the hardware with flow field single serpentine configuration, both cells under standard conditions for evaluation by polarization curve operated.

2.2. Catalytic ink deposition method comparison

The method of dropping was selected to be simple to implement in very small cells and electrospray by to be controlled deposition. Two MEAs were prepared with platinum loading 0.5 mg/cm^2, one for each method, using hot-pressing parameters (temperature, pressure and time) proposed by EROSA (2011) whit carbon paper diffusers. Two MEAs obtained were placed on the same hardware in the previous section and is operated under standard conditions. The electrochemical characterization was by a polarization curve.

2.3. Comparison of method of membrane-electrode assembly

To carry out the comparison of two methods of membrane assembly electrode with optimized parameters for each author, two MEAs of 4 cm^2 were prepared with platinum loading of 0.5 mg/cm^2, one with each method, was used electrospray to apply the catalyst ink in the diffuser of carbon paper. The membrane electrode assembly parameters of OKUR(2013)[6] are: temperature 97 °C, 3.6 minutes, 66 kg/cm^2 (145.5051 lbf/cm^2) of pressure press and the method of EROSA(2011) are: temperature 120°C, 4 minutes pressing time and 1814.4 kgf/cm^2 (4000 lbf/cm^2)

For electrochemical characterization of obtained MEAs, was used a hardware with flow field single serpentine configuration and were electrochemically characterized by polarization curve, both cells operated at standard conditions.

2.4. Comparison of electrical contact ratio

To know the effect of the electrical contact ratio (ECR) variation of the flow field in the cell performance, mainly resistance electrical contact and diffusion of gases, were evaluated electrochemically two designs of flow fields with two different reasons of electrical contact. ECR for plates were 0.2 and 0.5, the depth of channel designs were both 1 mm, the channel width and rib were variable in both designs according to the limitations of the tools and materials used for the manufacture of plates. Cells were characterized electrochemically by polarization curves operated at standard conditions.

2.5. Characterization of optimized MEAs in the stack

Graphite diffuser plates were made (two end plates and two bipolar plates), and three MEAs and the others components were made to use in the stack according the results of this work. The polarization curves were run simultaneously to all cells in the stack to standard operating conditions. The range was from open circuit potential to 0 V at a scan rate of 10 mV/s, were performed graphs current density versus potential (I-V).

3. Results and discussion

3.1. Carbon cloth and carbon paper as diffusers

In the first part of this work was to study what diffuser which offered higher power density, as shown in the polarization curve in Figure 1 a) the MEA made with carbon cloth diffuser showed better performance than MEA paper diffuser, showing that the peak power density of the MEA with carbon cloth and the MEA with carbon paper was 214 and 208 mW/cm^2, respectively. Likewise, it can be seen that the performance of the MEA with paper falls faster than the MEA with cloth, especially in the region of higher current density. This could indicate a problem of diffusion of gases through the diffuser of the MEA with paper and attributed to the highly disorganized, irregular and compact structure of carbon paper severely limits mass transport when the cell operates at high relative humidity; in addition, its relatively smooth surface makes the water drop separating harder, resulting in water on the cover surface so therefore increased waste mass transfer[7]. Some studies report that the high porosity of the material used as diffusers are necessary to improve the operation of the FC[8], others report that diffusers with low amounts of Teflon in its structure are best to increase cell performance[9][10][11][12].

3.2. Dropping and electrospray

In the results of the comparison of deposition techniques catalyst ink, in Figure 1 b), it can be seen that the MEA made with the ink by electrospray shows the best performance with maximum power density of 266 mW/cm^2 compared to the value obtained by the drooping method was 208 mW/cm^2. Also, the potential of the MEA-DROP falls faster than the polarization curve in areas of higher current densities (from 400 mA/cm^2). This behavior could be due to a lower gas diffusion more sites of the catalytic layer, it mean, greater charge transport resistance, the porosity of the structure of the catalyst layer could be a factor that causes the variation of the operation, other words, it is possible that deposits made by dropping clusters exist that block catalytic active sites.

3.3. EROSA and OKUR and Okur

The effects of varying the parameters of the hot-pressing technique are shown in Figure 1 c), the OCP obtained MEA-OKUR is 1.008 V and the MEA-EROSA is 0.98 V, a higher OCP is one result of a better contact between the catalyst layer and the membrane[6]. Furthermore, the power density of the MEA-OKUR show be greater than the MEA-EROSA, 310 mW/cm^2 for the first and 270 mW/cm^2 for the second; the maximum current density of MEA-OKUR 1413 mA/cm^2, while the MEA is 1113 EROSA mA/cm^2. The highest value of the current density and maximum power is presented by the MEA-OKUR that can result in a more porous structure of the catalyst layer of the MEA-EROSA, however, other factors may be influencing that behavior.

The decay of the power density may be due to a change in the structure of the MEA caused by high temperatures and pressures when preparing them. High pressures affecting the catalytic structure, which reduces the electron conductive network and causes mass transport problems[6], in other words, a higher pressure will result in the compaction of the porous structure, which affect the cell performance by mass transport problems, limiting the flow of the reactant gases through the active sites of the catalyst layer.

3.4. Electrical contact ratio, ECR 0.5 and ECR 0.2

In comparing of the electrical contact ratios in the flow field of graphite plates, the results shown in Figure 1 d) which shows that the single cell with ECR 0.2 provides better performance than obtained of the ECR 0.5, particularly at low potential (mass transfer losses). The maximum power density of ECR0.2 increased 11%, from 261 to 290 mW/cm^2 compared to 0.5 ECR design, it increases with decreasing electrical contact ratio, in other words, to increase the area of gas contact with the diffuser, a smaller channel area means a wider rib, and gas diffusion behind the ribs becomes more difficult, it is also possible that water retention is higher.

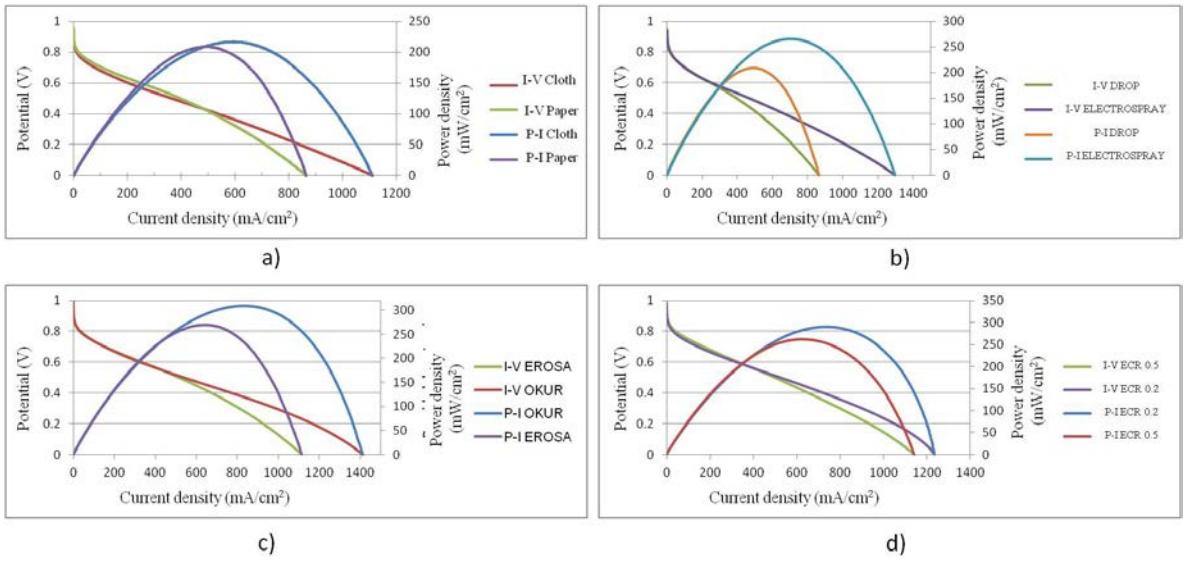

Fig. 1. Curves of current density-potential and current density and power density, operated under standard conditions of monocells: (a) of 1 cm^2 with cloth and paper diffuser, (b) of 1 cm^2 made by the dropping and electrospray techniques, (c) made by EROSA and OKUR method, (d) made by two plates diffuser designs, ECR0.2 ad ECR 0.5.

3.5. Characterization in the stack of optimized MEAs

In figure 2 the polarization curves of the three cells in the first two loss zones (ohmic and activation) are very similar; the difference between cells highest OCP is 0.008 V (8 mV), while at 500 mA/cm^2 the difference is 0.022 V (22 mV); cell C1 has the highest potential and the cells C2 and C3 of less at 500 mA/cm^2, these values can be seen in table 1. Furthermore, in the concentration loss zone behave very different, the difference between the highest potential cell at 800 mA/cm^2 and the less is 0.170 V (170 mV), the cell potential was greater C1, followed by C2 and C3 in the same order from highest to lowest. In the table 1, the potential cell and stack are observed in three different points of each curve, OCP, 500 mA/cm^2 and 800 mA/cm^2.

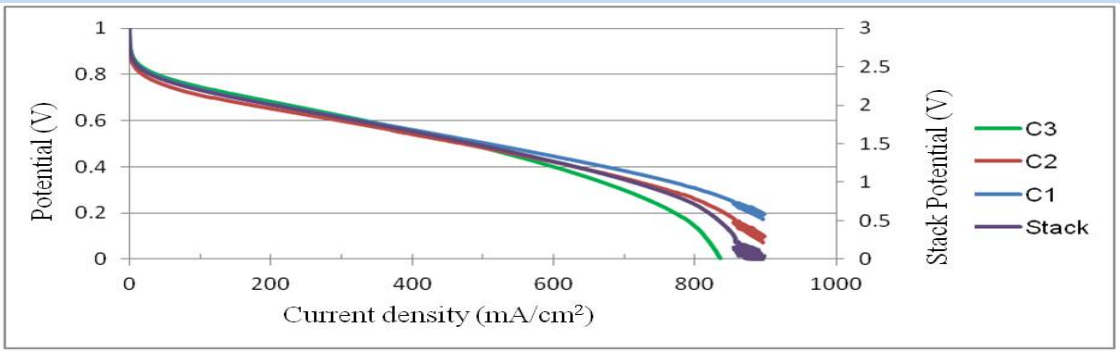

Fig. 2. Polarization curves measures to stack and its three cells simultaneously. The tests were conducted under standard operating conditions.

Table 1. Potential stack and potential cells at three different current densities representative of losses zones (activation, ohmic and mass transport) of the polarization curve.

Current density	**Potential (V)**			
	Stack	**C1**	**C2**	**C3**
0 mA/cm^2 (at OCP)	2.999	0.996	1.000	1.004
500 mA/cm^2	1.475	0.505	0.483	0.483
800 mA/cm^2	0.710	0.309	0.259	0.139

Different behavior between the performances of the three cells at high current densities is observed, particularly, in the concentration losses zone. The inputs of both gases of the stack were sided in one side, near to C1; there could be within the stack has bad distribution gas flow that difficult the arrival of one or both gases to the cells, causing an absence of fuel or the oxidant.

Linked to poor gas distribution, it could also be added, low elimination of water produced by reactions in cells that do not arrive gases; that reason affect the pores of electrode surface, obstructing the gases flow through the catalytic layer. Another reason that can be attributed that difference is the lack of standardization of manufacturing and assembling the components of the cell, starting from the MEA, diffusers graphite plates, seals, etc; emphasizes that in developing the MEAs, to press them with heat, the membranes were dehydrated and loss their original shape.

4. Conclusion

The electrospray technique allowed depositing catalytic layer on the diffuser homogeneous and scalable compared to the dropping technique. In addition, it was possible to increase the maximum power density only by varying the deposition technique from 208 to 270 mW/cm^2, the optimized method OKUR (2013) for the development of MEAs allowed improving yields of these, the reduction of electrical contact ratio of the flow field allowed to increase the maximum power by 11%.

Stack maximum power was 762 mW/cm^2, and each one of its cells was 270, 254 and 243 mW/cm^2. The potential in the polarization curves of the three cells of the stack at 500 mA/cm^2 were 0.50, 0.48, 0.48 V, a difference of potential between the highest and lowest cell of 22 mV. The cells in the stack had a very similar behavior due to the selection of materials and methods suitable for preparation of homogeneous cell components.

Acknowledgments

The authors thank the Centro de Investigación Científica de Yucatán (CICY) to facilitate their laboratory and equipment and the Programa Redes Temáticas CONACYT/RTH2.

References

[1] S. S. Dihrab, K. Sopian, M. a. Alghoul, and M. Y. Sulaiman, "Review of the membrane and bipolar plates materials for conventional and unitized regenerative fuel cells," *Renewable and Sustainable Energy Reviews*, vol. 13, no. 6–7, pp. 1663–1668, Aug. 2009.

[2] R. a. Antunes, M. C. L. Oliveira, G. Ett, and V. Ett, "Corrosion of metal bipolar plates for PEM fuel cells: A review," *International Journal of Hydrogen Energy*, vol. 35, no. 8, pp. 3632–3647, Apr. 2010.

[3] A. Dicks, *Fuel Cell Systems Explained*, Second Edi. John Wiley & Sons Ltd, 2003.

[4] A. Pfrang, D. Veyret, F. Sieker, and G. Tsotridis, "X-ray computed tomography of gas diffusion layers of PEM fuel cells: Calculation of thermal conductivity," *International Journal of Hydrogen Energy*, vol. 35, no. 8, pp. 3751–3757, Apr. 2010.

[5] E. Renovable, "Centro de Investigación Científica de Yucatán , A . C . ESTANDARIZACIÓN DEL MÉTODO DE FABRICACIÓN DE ENSAMBLES MEMBRANA- TIPO PEM Tesis que presenta JUANA ARELY EROSA SOLIS En opción al título de MAESTRO EN CIENCIAS EN ENERGÍA RENOVABLE," 2011.

[6] O. Okur, Ç. İyigün Karadağ, F. G. Boyacı San, E. Okumuş, and G. Behmenyar, "Optimization of parameters for hot-pressing manufacture of membrane electrode assembly for PEM (polymer electrolyte membrane fuel cells) fuel cell," *Energy*, vol. 57, pp. 574–580, Aug. 2013.

[7] Y. Wang, C. Wang, and K. S. Chen, "Elucidating differences between carbon paper and carbon cloth in polymer electrolyte fuel cells," vol. 52, pp. 3965–3975, 2007.

[8] B. Millington, S. Du, and B. G. Pollet, "The effect of materials on proton exchange membrane fuel cell electrode performance," *Journal of Power Sources*, vol. 196, no. 21, pp. 9013–9017, Nov. 2011.

[9] K. Wikander, H. Ekström, A. E. C. Palmqvist, and G. Lindbergh, "On the influence of Pt particle size on the PEMFC cathode performance," *Electrochimica Acta*, vol. 52, no. 24, pp. 6848–6855, Aug. 2007.

[10] L. Giorgi, E. Antolini, A. Pozio, E. Passalacqua, C. R. Casaccia, V. Anguillarese, and S. M. Galeria, "Influuence of the PTFE content in the diffusion layer of low-Pt loading electrodes for polymer electrolyte fuel cells," vol. 43, no. 24, pp. 3675–3680, 1998.

[11] E. Antolini, R. R. Passos, and E. A. Ticianelli, “Effects of the cathode gas diffusion layer characteristics on the performance of polymer electrolyte fuel cells,” pp. 383–388, 2002.

[12] J. Lobato, P. Cañizares, M. a. Rodrigo, C. Ruiz-López, and J. J. Linares, “Influence of the Teflon loading in the gas diffusion layer of PBI-based PEM fuel cells,” *Journal of Applied Electrochemistry*, vol. 38, no. 6, pp. 793–802, Feb. 2008.

Chapter 3.2. Effect of porosity on IEC and water distribution for sulfonated poly(styrene-co-acrylic acid) PEM copolymer

L. Melo[a]; R. Benavides[a]; G. Martínez[a]; D. Morales[a]; MMS Paula[b]; L. Da Silva[b]

[a]Centro de Investigación en Química Aplicada, Blvd. Enrique Reyna H. 140, Saltillo, Coahuila, México.
[b]Universidade do Extremo Sul Catarinense (UNESC), Av. Universitária, 1105 - Cx.P. 3167, Criciúma, SC. Brazil, 88.806-000

ABSTRACT

Polystyrene-acrylic acid copolymers were synthesized by radical solution copolymerization reactions involving two different crosslinking agents (divinyl benzene-DVB or trimethylol propane trimethacrylate-TMPTMA) and further sulfonated with sulfuric acid catalyzed with silver sulfate. Casting procedures to obtain membranes consisted in dissolving copolymers in THF and the mixture THF/DMSO (DMSO at two levels: 55 and 110 %mol) followed by slow evaporation. Copolymers are miscible in the solvents mixture despite are immiscible in neat DMSO. Characterization of membranes was carried out by ion exchange capacity (IEC) measured by titration, water uptake (WU) measured gravimetrically, gas chromatography with mass detector (GC-MS) for measuring residual DMSO and scanning electron microscopy (SEM) to observe membrane structure. SEM images show considerably higher amount of pores for the THF/DMSO casted membranes, comparing with the ones obtained from neat THF. High amount of DMSO in the solvent mixture enhance IEC values (from 0.14 to 0.55 meq/g for DVB copolymer and from 0.08 to 0.9 meq/g for TMPTMA copolymer) as well as WU (from 15 to 105 % and from 14 to 139 % respectively) with no residual DMSO as measured by GC-MS. These important differences do not correlate with a relatively small difference in dimensional changes after membrane hydration (from 2.5 to 8 %). The pore formation is a consequence of differences in molecular weights between THF and DMSO (72 and 78 g/mol respectively) but most important to evaporation temperature differences (66 and 189 ºC respectively). The general effect of using a solvent mixture for the casting procedure is the promotion of differences in the microscopic hydrophilic/hydrophobic domains into the molecular structure of the polyelectrolyte. Once the THF evaporates, DMSO itself has no salvation possibilities and remains longer into the copolymer matrix as bubbles, leaving pores after its final extraction. IEC and WU values increase due to the higher possibilities for water to remain into de membranes after hydration, since pores allow more water inside with lower dimensional changes. The latter in turn will allow protons to exchange easily, enhancing IEC value.

Keywords: Porosity, IEC, Water uptake

---

* Author for correspondence:
Roberto Benavides, +52(844)438 9830 xt. 1322, fax: +52(844)438 9839, roberto.benavides@ciqa.edu.mx

1. Introduction

A Proton Exchange Membrane must have high proton conductivity, which depends on the number of available acid groups and their dissociation capability in water [1]. Considering that, water uptake is an important issue in the development of polymer electrolyte membranes, since proton conduction is a water-assisted mechanism. A low water uptake reduces the proton conductivity and reduces the fuel cell performance [2].

In order to optimize fuel cell performance, perfluorinated polymer-based composite membranes have been modified with ceramic/inorganic fillers, namely, SiO_2, TiO_2, ZrO_2, clay, and activated carbon, to promote proton conduction in the membranes at elevated temperatures or under low relative humidity. The inorganic filler materials have high affinity to water and assist proton transport across the electrolyte membrane [3].

Proton Conduction is also affected by the chemical structure, morphology of the membrane, and operation temperature [4]. Morphology of the membrane is very important, especially when the microphase separation of hydrophilic and hydrophobic domains occur, which is typical for block copolymers [5]. However, copolymers that are not block type but contain acidic groups across the polymer chain, such as Nafion, can also result in membranes with different characteristics depending on the solvent used for their preparation [1]. In our research group, mixtures of solvents during the casting procedure has been used, obtaining membranes with different porosities, more water uptake and IEC values.

2. Materials and Methods

2.1. Materials

Styrene (St, 99%, Aldrich) was purified by washing with NaOH (20%), dried with $CaCl_2$ and distilled at reduced pressure. Phenothiazine was added to the acrylic acid (AA, 99%, Aldrich) and further distilled. Benzoyl peroxide (BPO) was used as initiator. Nafion 117 membrane (Aldrich), H_2SO_4 (J.T.Baker), hydrochloric acid 36.5-38% (Sigma Aldrich), Nitric acid 70% (CTR Scientific), Silver Nitrate ≥99.0% (CTR Scientific), Sodium chloride (J.T. Baker), sodium hidroxide (Aldrich), inhibitor free tetrahydrofuran ≥99.9% (THF, Aldrich), dimethylsulfoxide ≥99.5% (DMSO, Sigma Aldrich) and anhydride dichloromethane ≥99.8% (Aldrich).

2.2. Methods

2.2.1. Polymerization procedure

Two different copolymers of poly(styrene-co-acrylic acid) were previously synthesized with 94 %mol of St and 6 %mol of AA. The reactions were carried out by conventional solution free radical polymerization, using diethylbenzene as solvent. Benzoyl peroxide was used as radical initiator at 0.045 %mol, and partially crosslinked (crosslinking agent at 0.25 mol%) with divinylbenzene (DVB) or trimethylol propane trimethacrylate (TMPTMA) to improve them mechanical resistance. The initiator and crosslinking agent concentrations used were selected from previous experiments made in our research group. The random PS-PAA copolymer D (crosslinked with DVB) exhibits a Mn = 68,012, Mw =

259,095, Đ = 3.8 and 1.6 % weight of insoluble material in THF; and the random PS-PAA copolymer T (crosslinked with TMPTMA) presents a Mn = 54,068, Mw = 302,607, Đ = 5.6 and 2.2 % weight of insoluble material in THF. This polymerization procedure was described and reported previously [6].

2.2.2. Sulfonation procedure

D and T copolymers were sulphonated with a theoretical molar quantity of sulfuric acid (H_2SO_4 = 170% mol) employing silver sulfate as catalyst (Ag_2SO_4 = 0.11 or 0.055% mol). Each copolymer was dissolved in dichloromethane under a N_2 atmosphere at 200 rpm and 40°C by 40 minutes. The sulfonating agent and catalyst concentrations used were selected from previous experiments made in our research group. The theoretical amount of Ag_2SO_4 was dissolved in the H_2SO_4 and subsequently added to the dissolved copolymer, the sulphonation reaction was left to proceed during 2 or 4 hours (for the T and D copolymer respectively). The reaction was ended removing the solvent and adding cold distilled water. The sulfonated copolymer was washed with more distilled water until reaching the pH ≈ 7. Finally, the polymer was dried at room temperature with an airstream during 48 hours.

2.2.3. Casting procedures

Three membranes by casting were prepared from each sulfonated copolymer employing different solvent or mixture of solvents. The ratio copolymer mass/solvent volume/area membrane employed was 0.4g/2mL/16cm^2. The composition of the first solution casting was: sulphonated copolymer+THF. The second was sulphonated copolymer+THF+DMSO (55% weight) and the third was copolymer+THF+110%DMSO. Evaporation of the solvent proceeded very gradually at room temperature during 7 days, keeping the molds partially covered to allow the solvent vapor to escape.

2.2.4. Membrane activation

Membranes were activated before further characterization. The membranes were unmolded and immersed in distilled water by two days, changing the water every 4 hours to eliminate the DMSO. Subsequently the membrane was immersed in HNO_3 0.5 M by 24 hours. Afterward the membrane was submerged 1 hour in H_2O_2 (5% vol) at 80°C, 1 hour in H_2SO_4 0.5 M at 80°C and 1 hour in distilled water at 80°C.

2.3. Characterization

Ion-exchange capacity (IEC) was measured for membranes using a titration method. The cation-exchange membrane was soaked in 1 M HCl solution for 24 hours. After that, the membrane was washed with distilled water to remove excess HCl and then was immersed into 1M NaCl solution for 24 hours. The number of displaced protons from the membrane was determined by titration of the NaCl solution with 0.005 M NaOH solution using a pH-meter. Then the ion-exchange membrane was soaked in 1 M HCl solution for 24 h or more. After that, the membrane was washed with distilled water and water on the surface was wiped off with tissue paper to measure the wet weight of membrane (Wwet). Then the membrane was placed in an oven at 44 ◦C for 24 h and then the dry weight of membrane was then measured (Wdry). The percentage of water absorption was calculated by differences between dry/wet weights.

The IEC and U of membranes was calculated using Eqs. (1) and (2) [2, 7-9].

$$IEC = abW_{dry} \quad (1)$$

$$U\ (\%mass) = (W_{wet} - W_{dry}/W_{dry}) \times 100 \quad (2)$$

where a is the concentration of NaOH solution used (mmol/mL ~ meq/mL), b is the volume of NaOH solution used (mL), W_{dry} is the dry weight of the membrane (g) and W_{wet} is the wet weight of the membrane (g).

Porosity of the membranes was investigated after the specimens were fractured in liquid nitrogen. SEM micrographs were obtained using 2 kV and working distance of 14.7 mm with a JEOL JSM-7401F Scanning electron microscope.

Membranes were analyzed by GC-MS to evaluate the presence of residual solvent, a gas chromatograph instrument AGILENT was used, with a column HP-5M5 30 m x 0.25 mm, employing helium as a carrier gas at 1.5 mL/min and the following conditions: Inyector temperature= 200°C, Oven temperature= 70°C. Membranes were poured into a 30-mL glass container and exposed at 200°C during 1 hour to evaporate all remaining solvent.

3. Results and Discussion

Membranes were obtained by casting using THF as solvent and the procedure mentioned above. These membranes have a thickness similar than Nafion (Table 1) and IEC and U were determined and compared versus Nafion. Table 1 shows the values obtained. Thickness of the membranes D and T sulfonated after being hydrated didn't change a lot, just 2.5 and 3.1% respectively. Low dimensional change is favorable in a Membrane Electrode Assembly (MEA), to maintain good contact the components. But on the other hand D and T copolymers show very low IEC and U values that are not competitive with Nafion. Such values are directly related with the proton conductivity in a PEM. For that reason it is essential to have high IEC and U values before proceeding with the evaluation of other characteristics in the membranes.

Table 1.Thickness, IEC and U of Nafion and sulfonated D and T membranes obtained by casting (THF).

Membrane	Thickness Dry (mm)	Thickness Wet (mm)	Thickness Increment (%)*	IEC (meq/g)	U (% mass)
D sulfonated	0.157	0.161	2.5	0.14	15.2
T sulfonated	0.196	0.202	3.1	0.08	13.6
Nafion	0.189	0.230	21.7	0.87	23.2

* Thickness increment (%) when dry membrane thickness is equal to 100%

Silva et al. [1] reported the influence of the solvents ethylene glycol (EG), dimethyl sulfoxide (DMSO) and dimethylformamide (DMF) during Nafion dissolution, on the conductivity, density, solubility, equivalent weight and water uptake of the casted membranes. Results show that the choice of the solvent is of paramount importance. The perfluorosulfonate ionomer dispersion prepared showed to play a significant role in conductivity of the cast membranes (conductivity trend: DMF > EG > DMSO) and in the

water uptake results (DMF>DMSO>EG). Silva also mentioned, as a hypothetical reason for these results is that a continuity of clusters retains more water than isolated clusters full of acidic groups.

Taking as a basis the above reasoning, we chose to use a different solvent for the casting of the membranes with the copolymers D and T, which consists of a mixture of solvents: THF and DMSO. Casting procedure was described in the methodology. Figure 2 shows the IEC values obtained from the membranes obtained by casting with the solvent mixture.

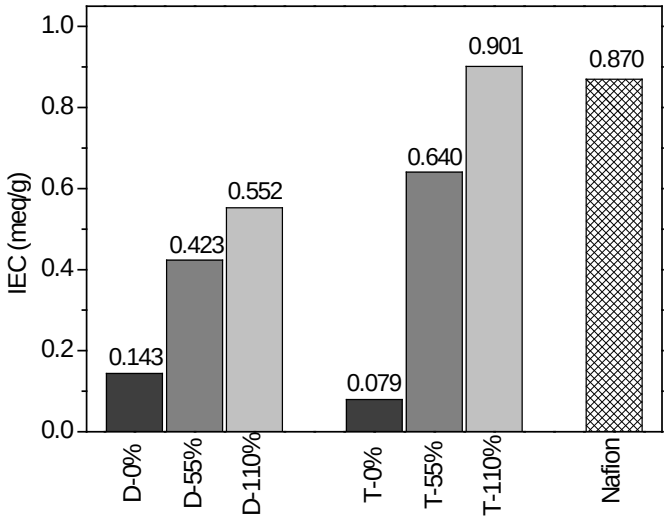

Fig. 2. IEC values from membranes obtained by casting with some solvent mixtures.

The IEC values increase when DMSO is used in the casting mixture showed as D-55%, D-110%, T-55% and D110% (figure 2), even IEC value of the membrane obtained using the mixture copolymer+THF+110%DMSO (110% weight) is slightly greater than the value of Nafion.

Water uptake and thickness of those membranes were measured too (figure 3). Thickness of D and T membranes increase from dry to wet 7.9% as maximum (T-110%), unlike Nafion that increases 21.7%. However despite this small increase in thickness of the membranes when hydrated, the weight gain by the water uptake (U) is much higher in the membranes D and T prepared with DMSO, comparing with Nafion.

Given the disagreement found between low increase in membrane thickness and the amount of water absorbed by the same material, especially when comparing 0% type membranes with type 110%, its morphological structure was analyzed. Figure 4 shows cross-section microphotographs of each membrane. Characterization by SEM shows that Nafion, D-0% and T-0% membranes practically do not have pores, in comparison with those prepared with DMSO that have high amount of pores of different dimensions.

Pores are generated because DMSO molecule is heavier than THF (78.13 and 72.11g/mol respectively) and it evaporates more slowly (189 and 66 °C respectively). Once the THF is evaporated, DMSO remains in the membrane occupying a volume, and after it is extracted the presence of pores is evident.

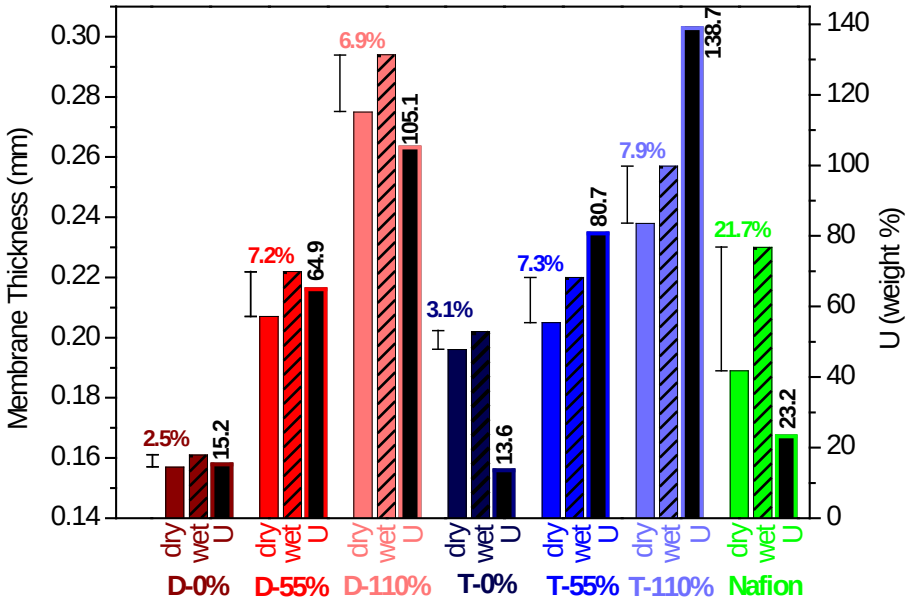

Fig. 3. Thickness and water uptake of the membranes. Colored bars: dry membranes thickness, dashed bars: wet membranes thickness, percent above the bar: increment of thickness of the membranes, black bars: weight percent gained by the membranes after hydrated.

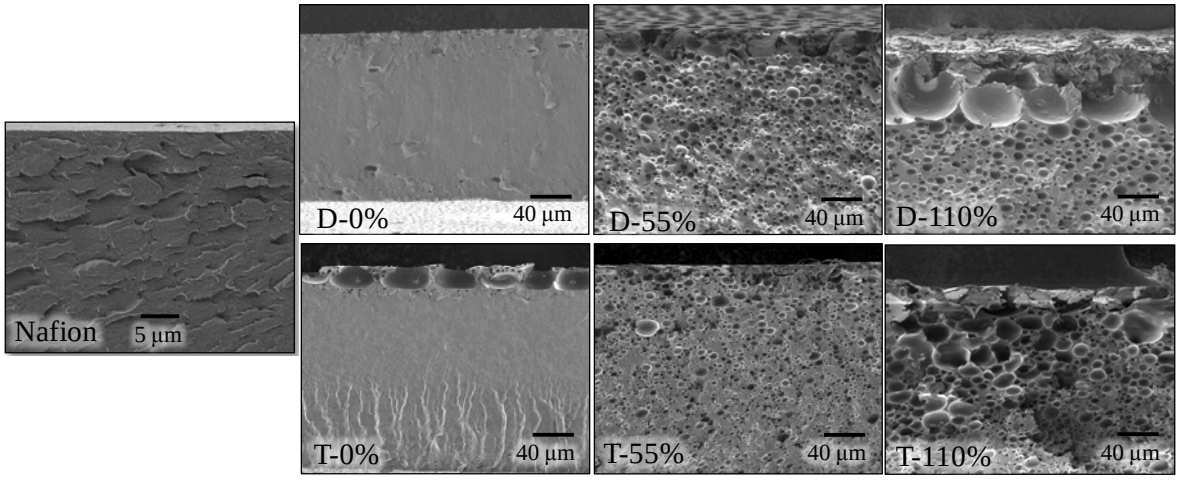

Fig. 4. SEM images of Nafion, and membranes of D and T sulfonated copolymers obtained from solvent evaporation method employing different solvent composition.

4. Conclusion

The preparation of membranes of the sulfonated polymers D and T by casting using mixture of solvents, results in significant differences in the morphology of the membrane, which in turn affect other characteristics. Pore formation is related with the way that water

is distributed in the membrane, when the membranes are submerged inside an aqueous solution, water must penetrates among the polymer chains and fills the pores as well. Such phenomenom cause an increase in the water uptake value without considerable change in thickness. Regarding the effect on IEC, the acid groups must be more available to exchange. More evaluations are needed to make better conclussions

Acknowledgements

The authors would like to thank M.C. María Concepción González Cantú for her assistance in the laboratory, Lic. Marcelo Ulloa Pérez for GC-MS analysis and L. Melo would also like to express thanks to CONACYT (National Council of Science and Technology) to provide the funding the research for her PhD scholarship.

References

[1] Silva R.F., De Francesco M., Pozio A. Solution-cast Nafion ® ionomer membranes: preparation and characterization. Electrochimica Acta 2004, 49, 3211–3219
[2] Zhou S., Hai S.D., Kim D. Cross-linked Poly(arylene ether ketone) Proton Exchange Membranes with High Ion Exchange Capacity for Fuel Cells. Fuel Cells 2012, 12(4), 589–598
[3] Fang J., Qiao J., Wilkinson D. P., Zhang J. in Electrochemical Polymer Electrolyte Membranes. CRC Press 2015
[4] Wilkinson P. D., Zhang J., Hui R., Fergus J., Li X. in Proton Exchange Membrane Fuel Cells: Materials Properties and Performance. CRC Press 2010
[5] Gross M., Maier G., Fuller T., MacKinnon S., Gittleman C. in Handbook of Fuel Cells: Fundamentals Technology and Applications. John Wiley & Sons 2010
[6] Melo L., Benavides R., Martínez G., Da Silva L., Paula M.M.S. Degradation reactions during sulphonation of poly(styrene-co-acrylic acid) used as membranes. Polymer Degradation and Stability 2014, 109, 343-352
[7] Klaysom C., Ladewig B.P., Lu G.Q.M., Wang L. Preparation and characterization of sulfonated polyethersulfone for cation-exchange membranes. Journal of Membrane Science 2011, 368, 48–53.
[8] Liu F., Yi B., Xing D., Yu J., Zhang H. Nafion/PTFE composite membranes for fuel cell applications. Journal of Membrane Science 2003, 212, 213–223
[9] Jun M., Choi Y., Kim J. Solvent casting effects of sulfonated poly(ether ether ketone) for Polymer electrolyte membrane fuel cell. Journal of Membrane Science 2012, 396, 32– 37

Chapter 3.3. Polystyrene-co-acrylic acid proton exchange membranes: morphology and mechanical properties

L. Melo[a]; R. Benavides[a]; G. Martínez[a]; M.L. López[a]; MMS Paula[b]; L. Da Silva[b]

[a]Centro de Investigación en Química Aplicada, Blvd. Enrique Reyna H. 140, Saltillo, Coahuila, México.
[b]Universidade do Extremo Sul Catarinense (UNESC), Av. Universitária, 1105 - Cx.P. 3167, Criciúma, SC. Brazil, 88.806-000

ABSTRACT

Two random copolymers of poly(styrene-co-acrylic acid) (PS-AA) were synthesized in solution (diethylbenzene) by radical polymerization and partially crosslinked by adding, either the tryfunctional monomer trimethylol propane trimethacrylate (TMPTMA) or the difunctional monomer divinylbenzene (DVB) to improve mechanical resistance. Crosslinked copolymers were also dissolved in dichloromethane and sulfonated with theoretical molar quantities of sulfuric acid (H_2SO_4 = 170%) and two different amounts of silver sulfate (Ag_2SO_4 = 0.11 or 0.055%) as a sulfonation reaction catalyst. Materials (neat and sulfonated) were dissolved in three different solvent compositions: copolymer+THF, copolymer+THF+55%DMSO and copolymer+THF+110%DMSO and then membranes prepared by casting from them. Membranes were fully activated by immersing them in HNO_3, followed by H_2O_2 and finally in H_2SO_4. Thermomechanical Analysis (TMA), Ionic Exchange Capacity (IEC), Water Uptake (WU) and Scanning Electron Microscopy (SEM) were used to evaluate membranes. Addition of DMSO to THF as a mixture of solvents during casting procedure for the same sulphonated copolymer has an important increment on IEC and WU results. However, mechanical resistance measured by flexure modulus (ASTM D790) in a TMA is considerably reduced. SEM images show almost no pores in the membranes casted from THF alone, while increasing the amount of DMSO mixed with THF for casting, an increment in porosity is clearly seen. 55% DMSO materials have an important amount of pores, but for the 110% DMSO membranes, SEM images show them side-by-side. Such phenomenon is responsible for the lowest mechanical property (brittleness), as seen by TMA results for the same membranes. In general, the mixture of solvents THF+DMSO enhance water uptake and ionic properties but reduce mechanical resistance of PS-AA copolymers.

Keywords: Copolymers, Casting, Flexure modulus, Porosity

1. Introduction

There is a great interest in discovering new polymeric ionic materials for the preparation of ion exchange membranes. Traditionally, a membrane is evaluated according to their

---

* Author for correspondence: R. Benavides, T: 52(844)4389830 x 1322, E: roberto.benavides@ciqa.edu.mx

polyelectrolyte performance, characteristics as ion exchange conductivity (IEC), water uptake (WU or U) and proton conductivity. However, membranes must also possess mechanical stability to withstand the processes to which they are exposed; those include processing (extrusion, casting, etc.), incorporation of catalysts, compression during formation of the MEA, pressure during PEMFC closure to test performance, dimensional changes during hydration and dehydration of the membrane, and pressure generated by the fuel, either gaseous or liquid.

The mechanical properties of polymeric membranes are governed by its own chemical nature as well as by external factors. A polymeric material tends to be brittle if: has low molecular weight, a rigid chemical structure or no branching. Furthermore, an increase in the degree of sulfonation improves water uptake and conductivity, but reduces mechanical performance. The latter also reduce the long-term stability of the membrane in the fuel cell [1]. Mechanical degradation of mechanical properties in polymeric membranes occur in many forms, such as cracks, tears, punctures, or pinhole blisters. Hence, adequate care must be taken during membrane preparation to prevent no uniform pressure between membrane electrode assembly and bipolar plates during operation [2].

Mechanical properties of Nafion are influenced by hydration, although high conductivities require the presence of moisture. Nevertheless, when Nafion is soaked in water or any solvent, its Young's modulus decreases; the solvent have a direct impact on the stress-strain relationship. The high solvent (water) content swells the membrane, reduces the intermolecular forces and increase the degree of elongation, making the Nafion membrane more ductile and susceptible to permanent deformation, gradual weakening, and eventual failure in fuel cell when exposed to pressure gradients and pressure pulses [3,4]. Considering all the above aspects, it is of high importance the evaluation of mechanical properties for new synthesized materials pretending to be employed as ion exchange membranes.

2. Materials and Methods

2.1. Materials

Styrene (St, 99%, Aldrich) was purified with NaOH, dried with $CaCl_2$ and distilled at reduced pressure. Phenothiazine was added to the acrylic acid (AA, 99%, Aldrich) and distilled at reduced pressure. Benzoyl peroxide (BPO) as initiator. Nafion 117 membrane (Aldrich), H_2SO_4 (J.T.Baker), chlorihidric acid 36.5-38% (Sigma Aldrich), Nitric acid 70% (CTR Scientific), Silver Nitrate ≥99.0% (CTR Scientific), Sodium chloride (J.T. Baker), sodium hidroxide (Aldrich), inhibitor free tetrahydrofuran ≥99.9% (THF, Aldrich), dimethylsulfoxide ≥99.5% (DMSO, Sigma Aldrich) and anhydride dichloromethane ≥99.8% (Aldrich). Trimethylol propane trimethacrylate (TMPTMA, Aldrich) and Divinyl benzene (DVB, Aldrich) as crosslinking agents.

2.2. Methods

2.2.1. Polymerization procedure

Two different copolymers of poly(styrene-co-acrylic acid) (PS-AA) were previously

synthesized with 94 %mol of St and 6 %mol of AA. The reactions were carried out by conventional solution free radical polymerization, using diethylbenzene as solvent. Benzoyl peroxide was used as radical initiator at 0.045 %mol, and partially crosslinked (crosslinking agent at 0.25 mol%) with divinylbenzene (DVB) or trimethylol propane trimethacrylate (TMPTMA) to improve the mechanical resistance. The initiator and crosslinking agent concentrations used were selected from previous experiments made in our research group. The random PS-PAA copolymer D (crosslinked with DVB) exhibits a Mn = 68,012, Mw = 259,095, and the random PS-PAA copolymer T (crosslinked with TMPTMA) presents a Mn = 54,068, Mw = 302,607. The polymerization procedure was described and reported previously [5].

2.2.2. Sulfonation procedure

D and T copolymers were sulphonated with a theoretical molar quantity of sulfuric acid (H_2SO_4 = 170% mol) employing silver sulfate as catalyst (Ag_2SO_4 = 0.11 or 0.055% mol). Each copolymer was dissolved in dichloromethane under a nitrogen atmosphere at 200 rpm and 40°C by 40 minutes. The theoretical amount of Ag_2SO_4 was dissolved in the H_2SO_4 and subsequently added to the dissolved copolymer, the sulphonation reaction was left to proceed during 2 or 4 hours (for the T and D copolymer respectively). The reaction was ended removing the solvent and adding cold distilled water. The sulfonated copolymer was washed with more distilled water until reaching the pH ≈ 7. Finally, the polymer was dried at room temperature with an airstream by 48 hours.

2.2.3. Casting procedures

Three membranes were prepared by casting from each copolymer, employing a specific solvent or mixture of solvents. The ratio copolymer mass/solvent volume/area membrane employed was 0.4g/2mL/16cm^2. The composition for the first casting was: sulphonated copolymer+THF; the second was sulphonated copolymer+THF+DMSO (55% weight) and the third was copolymer+THF+110%DMSO. Evaporation of the solvent proceeded gradually at room temperature during 7 days, keeping the molds partially covered to allow solvent vapor to escape.

2.2.4. Membrane activation

Membranes were activated before further characterization. The membranes were unmolded and immersed in distilled water by two days, changing the water every 4 hours to eliminate the DMSO. Subsequently the membrane was immersed in HNO_3 0.5 M by 24 hours. Afterward the membrane was submerged 1 hour in H_2O_2 (5% vol) at 80°C, 1 hour in H_2SO_4 0.5 M at 80°C and 1 hour in distilled water at 80°C.

2.2.5. Ion-exchange capacity (IEC) and water uptake (U) for membranes

Ion-exchange capacities were measured using a titration method. The cation-exchange membrane was soaked in 1 M HCl solution for 24 hours. After washing with distilled water they were immersed into 1M NaCl solution for 24 hours. The number of displaced protons from the membrane was determined by titration of the NaCl solution with 0.005 M NaOH solution using a pH-meter.

The membranes were then soaked in 1 M HCl solution for 24 h or more. After that, the membrane was washed with distilled water and water on the surface was wiped off with

tissue paper to measure the wet weight of membrane (W_{wet}). Finally the membranes were placed in an oven at 44 ◦C for 24 h and then the dry weight of membrane was then measured (W_{dry}). The percentage of water absorption was calculated by differences between dry/wet weights.

The IEC and water uptake (U) of membranes were calculated using Eqs. (1) and (2) [6-9].

$$IEC = abW_{dry} \quad (1)$$

$$U\ (\%mass) = (W_{wet} - W_{dry}/W_{dry})\ x\ 100 \quad (2)$$

Where a is the concentration of the NaOH solution (mmol/mL ~ meq/mL), b is the volume of NaOH solution used (mL), W_{dry} is the dry weight of the membrane (g) and W_{wet} is the wet weight of the membrane (g).

2.2.6. Thermomechanical Analysis (TMA)

The modulus was determined by the flexural test in rectangular bars directly cut from the membranes. These test methods utilize a three-point bending system applied to a simple supported beam. The Modulus of Elasticity or Tangent Modulus of Elasticity is the ratio, within the elastic limit, of stress to the corresponding strain. It is calculated by drawing a tangent to the steepest initial straight-line portion of the load-deflection curve and using Eq (3) [10], the maximum Force applied is equal to 1 N and the velocity is equal to 0.15N/min.

$$EB = L^3 m / 4bd^3 \quad (3)$$

Where EB is the modulus of elasticity in bending (MPa), L is the support span (m), b is the width of beam tested (m), d is the depth of beam tested (m) and m is the slope of the tangent to the initial straight-line portion (N/m).

2.2.7. Morphology of the membranes

Morphology surface topography of the membranes was observed using scanning electron microscopy (SEM) JEOL JSM-7401F at 3 kV with a working distance of 5.7 mm.

3. Results and Discussion

3.1. Ion exchange capacity and water uptake

The ion-exchange capacity (IEC) is an important factor related to the conductivity and ion transport properties of the membranes. The water uptake (U), ion-exchange capacity and thickness of the sinthesized membranes are summarized in Table 1. Generally the IEC and water uptake increases with higher degree of sulfonation, due to the presence of more hydrophilic sulfonic acid groups in the polymer matrix. Moreover, Table 1 also show that is possible to get different IEC values with the same polymer by changing the casting procedure. The higher concentration of DMSO in the mixture with THF for preparation of membranes by casting generates higher values of IEC and U.

Table 1. Ion exchange capacity and water uptake of the membranes casted from different solvent composition.

Sulfonated copolymer	Solvent composition to the casting procedure	Label	IEC (meq/g)	U (%)
D	THF-0% DMSO	D-0%	0.1439	15.2210
	THF-55% DMSO	D-55%	0.4231	64.9186
	THF-110% DMSO	D-110%	0.5524	105.1195
T	THF-0% DMSO	T-0%	0.0795	13.6132
	THF-55% DMSO	T-55%	0.6405	80.7000
	THF-110% DMSO	T-110%	0.9015	138.9580
Nafion 117	-	Nafion	0.87	23.2

This effect seems related with chemical structure size of solvents, since DMSO is heavier than THF (78.13 and 72.11 g/mol) and its boiling point as well (189 ° C and 66 ° C respectively). DMSO evaporates slower than THF, even some DMSO remains among the chains of the sulfonated copolymer membranes, so it was necessary to immerse the membranes in distilled water for 2 days before activation.

The polymer membranes morphology depends on the chemical nature of the polymer, but is affected by external factors, including the method of membrane preparation (solution casting, compression molding and extrusion) [11]. Peckham et al. observed that the more akin is the solvent with the copolymer in the casting, a higher morphological arrangement in the membrane is generated, however he found no obvious correlation properties of the solvent used and the morphology adopted by the copolymer [12].

3.2. Physical performance of the polymers.

The tests were made in a termomechanical analyzer (TMA) with a flexure accessory and calculating Modulus of Elasticity following the ASTM D790. Figures 1 and 2 show the curves of Force vs Deformation and the Modulus of Elasticity obtained from the different membranes obtained, for both D and T copolymers prepared by casting with different solvent composition. Nafion 117 mechanical behavior is shown as a reference.

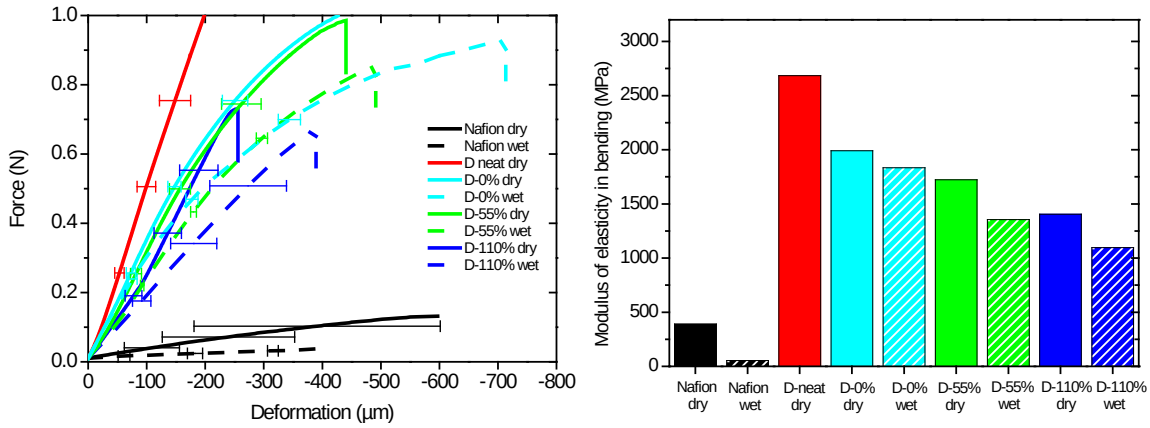

Fig. 1. Mechanical behavior of D membranes, neat and sulfonated copolymer obtained from casting procedures (dry and wet state).

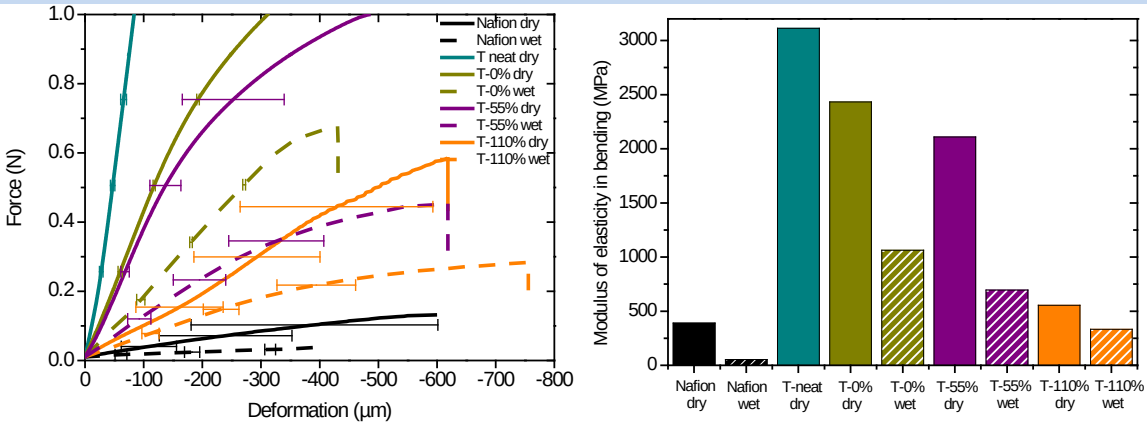

Fig. 2. Mechanical behavior of T membranes, neat and sulfonated copolymer obtained from casting procedures (dry and wet state).

Results indicate that the Modulus of Elasticity (E_B) for dry and wet membranes obtained from the D and T copolymers are higher than Nafion E_B, which means that all those membranes are harder than Nafion. It is also clear that E_B values from the sulfonated membranes are smaller than neat (unsulfonated) copolymers D and T; this effect is observed by comparing the E_B of the membranes D-neat vs D-0%, as well as T-neat vs T-0%. Such values were obtained from THF casting solution membranes. Reduced E_B and the difference in the mechanical behavior could be attributed to a different chain arrangement of the neat polymer comparing with the sulphonated polymer. Both types of materials (neat and sulphonated) have different steric hindrance, different chemical environment and chemical interaction with the solvent, mainly by the presence of the sulfonic group.

There is another observation in the Force vs Deformation graphs clearly seen (Figure 1 and 2) regarding linearity of traces; while neat materials get an straight line, sulfonated material are more related to curved traces. The reason could be related with the amount of pores in the sulfonated membranes, which in turn results in a stochastic cracking. Such fracture type implies multiple cracking of inter-porous bridges and, as a result, nonlinearity of the stress-strain diagrams of these materials [13].

3.3. Structural analysis

Figure 5 shows SEM of the membranes prepared from D and T sulphonated copolymers employing different solvent composition (THF-0%DMSO, THF-55%DMSO and THF-110%DMSO). The difference in the solvent employed causes changes in the topography and porosity of the membranes of the same polymer.

As mentioned earlier, high-porous materials tend to fracture by stochastic cracking. Such fracture type implies multiple cracking of interporous bridges and, as a result, nonlinearity of the stress-strain diagrams of these materials.

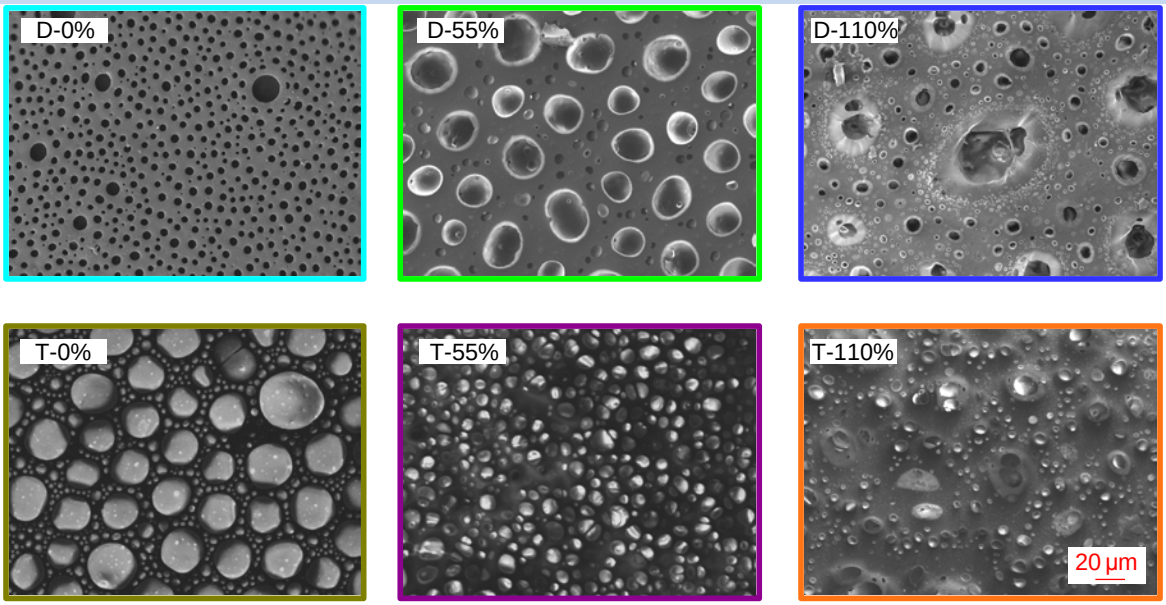

Fig. 5. SEM images of D and T sulfonated copolymers obtained from solvent evaporation method employing different solvent composition.

Microphotographies show membranes with porous of different sizes; even the membranes obtained using 110% of DMSO show pores with irregular shapes. The critical defect size is associated with the crack size, according to the theory of fracture mechanics. Pores with shape different from the ideal sphere shape, means a critical defect. With the application of load during TMA experiments, the bridges break between the nearest pores at first, then as the load increases, the pores located at a greater distance are involved in the cracking process, and so on up to the complete fracture of the material [13].

The copolymers D and T were synthesized with styrene and acrylic acid mainly. Both monomers can generate brittle homopolymers, therefore a copolymer made of PS and PAA will be a brittle material too. Besides that, the membranes prepared have a large quantity of pores. It is known that materials with small porosity also fracture by a propagation of a single cracks, while materials with middle and large porosities suffer fracture by stochastic cracking of separated interporous bridges. The mechanism for crack propagation in brittle high-porous materials changes with the amount of porosity. A brittle crack in a porous material has two alternatives for propagation: by a linear or by a curved trajectory via the break of interparticle bridges and the confluence of the neighboring pores [13]. Therefore, the presence of pores could increase the IEC and U of the membranes but this feature decreases the resistance of the materials during bending and in turn causing fragility

4. Conclusion

Membranes of copolymers of partially crosslinked PSAA were prepared and sulfonated; casting procedure involving a mixture of solvents have an notorious influence for obtaining different morphologies. The method also increase porosity in membranes and an increasing accessibility to the functional groups on of the polymer structure, which in

turn enhance IEC and water uptake values. As a consequence, mechanical properties are reduced and membranes become brittle. More experiments are needed to obtain equilibrium among electrochemical properties enhanced with low loss of mechanical resistance.

Acknowledgements

The authors would like to thank M.C. María Concepción González Cantú for her assistance in the laboratory, M.C. Marcelina Sanchez Adame for technical support in TMA analysis and L. Melo would also like to express thanks to CONACYT (National Council of Science and Technology) for her PhD scholarship and to SMH for the grant to attend the XV Congress of the Mexican Hydrogen Society.

References

[1] Reyna-Valencia A.; Kaliaguine S.; Bousmina M. Tensile Mechanical Properties of Sulfonated Poly(Ether Ether Ketone) (SPEEK) and BPO 4/SPEEK Membranes . *Journal of Applied Polymer Science* **2005**, 98, 2380 –2393.

[2] Zaidi S. M. J.; Matsuura T. in *Polymer Membranes for Fuel Cells*. Springer 2009

[3] Kundu S.; Simon L. C.; Fowler M:; Grot S. Mechanical properties of Nafione electrolyte membranes under hydrated conditions. *Polymer* **2005**, 46, 11707–11715

[4] Kawano Y.; Wang Y.; Palmer R. A.; Aubuchon S. R. Stress-strain curves of Nafion membranes in acid and salt forms *Polímeros* **2002**, 12(2), 96–101.

[5] Melo L., Benavides R., Martínez G., Da Silva L., Paula M.M.S. Degradation reactions du ring sulphonation of poly(styrene-c o-acrylic acid) used as membranes. *Polymer Degradation and Stability* **2014**, 109, 343-352.

[6] Zhou S.; Hai S.D.; Kim D. Cross-linked Poly(arylene ether ketone) Proton Exchange Membranes with High Ion Exchange Capacity for Fuel Cells. *Fuel Cells* **2012**, 12(4), 589–598.

[7] Klaysom C.; Ladewig B. P.; Lu G.Q.M.; Wang L. Preparation and characterization of sulfonated polyethersulfone for cation-exchange membranes. *Journal of Membrane Science* **2011**, 368, 48–53.

[8] Liu F.; Yi B.; Xing D.;Yu J.; Zhang H. Nafion/PTFE composite membranes for fuel cell applications. *Journal of Membrane Science* **2003**, 212, 213–223

[9] Jun M.; Choi Y.; Kim J. Solvent casting effects of sulfonated poly(ether ether ketone) for Polymer electrolyte membrane fuel cell. *Journal of Membrane Science* **2012**, 396, 32– 37

[10] ASTM D790-07e1, Standard Test Methods for Flexural Properties of Unreinforced and Reinforced Plastics and Electrical Insulating Materials, ASTM International, West Conshohocken, PA, **2007**.

[11] Yang Y.; Siu A.; Peckham T.; Holdcroft S. Structural and Morphological Features of Acid-Bearing Polymers for PEM Fuel Cells. *Advanced Polymer Science* **2008**, 215, 55-126

[12] Peckham T.J. and Holdcroft S. Structure-Morphology-Property Relationships of Non-Perfluorinated Proton-Conducting Membranes. *Advanced Materials* **2010**, 22, 4667–4690

[13] Borysovska K., Verbylo D., Podrezov Yu., Szafran M. The structural optimization of ceramic-organic composites. *Archives of Metallurgy and Materials* **2009**, 54(4), 875-879.

Chapter 3.4. Pneumatic-Thermic press for manufacturing fuel cell electrodes

L. Belin-Sandoval[a]; B. Escobar[b]; L.A. Soto-Ramirez[c]; J.C. Cruz[c]; Victor M. Sanchez[a]; G. R Barbosa Pool[a,*]

[a]Universidad de Quintana Roo, Boulevar Bahía s/n, Chetumal 77019, Q. Roo, México
[b]Catedra CONACYT, Centro de Investigación Científica de Yucatán, A.C., Calle 43 No. 130 Colonia Chuburná de Hidalgo, Mérida, Yucatán 97200, México.
[c]Instituto tecnológico de Chetumal, AV. Insurgentes s/n, Chetumal, Quintana Roo 77013, México

ABSTRACT

This document describes the process of conceptualization, design and implementation of an electro-pneumatic hot-pressing system, for the production of porous electrodes and membrane electrode assemblies. The pressing system is controlled by a programmable logic control system (PLC) via analog and digital signals. The pressures and temperatures of operation of the pressing system are established according to past experiences and literature, as well as market research of the components that were selected according to the specific needs of the project. The integral design of the prototype was made in SolidWorks 2014 ©, but the construction stage is not yet reached. Finally, a cost comparison between the proposed design regarding trademark presses with similar design is presented.

Keywords: PEMFC electrodes, Assembly process, Control system, Hot-pressing

1. Introduction

Due to its wide range of applications, hydrogen is viewed as the fuel of the future [1]. In this scenario, it is expected that the Proton Exchange Membrane Fuel Cells (PEMFC) play an important role in the future "hydrogen economy", especially in its application in the automotive industry, residential and mobile applications such as cell phone, laptops, etc. [2, 3].

One of the main components of the PEMFC is the catalytic layer (CL). Composed of micro or heterogeneous nanoreactors, the catalytic layer is possibly the most complex element of the cell. CL is formed by a conductive material that supports the nanostructured catalyst, which must also be in contact with a dispersed electrolyte. This is, in a three-dimensional region, the coexistence of the conductor, its support, catalyst, electrolyte in dispersed form and a reactant gas. This three-dimensional region must be porous to allow access of the reactant gases and to remove the product formed throughout the reaction, i.e.

---

* Author for correspondence:
Dr. Gliserio Romeli Barbosa Pool, +983 156 6032, romelix1@gmail.com

water in vapor and liquid form. These regions of nanometric thickness are where the electrochemical reactions and mass transport, which determines the end performance of the fuel cell, take place. The effectiveness of the physical and electrochemical properties of this component is significantly dependent on its microstructure, which can be manipulated or induced through different manufacturing strategies.

The electrode manufacturing technique greatly influences the formation of the internal microstructure, modifying the effective transport coefficient (ETC) directly. This also influences the overall thickness of the CL, which directly affects the macroscopic performance. Currently, the most used strategy is to deposit a solution containing the primary elements onto a substrate to be subsequently pressed. The solution is referred to as "catalyst ink", which should be as “homogeneous” as possible, to ensure a uniform structure at "macro" level. [4, 5-10 149-154]. The deposition method and the material used at the same time as a substrate define the different conditions of manufacturing. Some deposition techniques based on this methodology can include: Airbrush deposit or by "spray" [11, 10], by brush [7-9], electro-spray [6] and screen printing [5, 12]. Regarding the substrate we can mention some of the following apply methods: directly on the membrane [5, 8-9] on the diffusion layer [6-7, 10] or over an "inert" substrate (technically known as Decal) [12-14].

The final process in the manufacture of electrodes consist of a hot pressing process. In this process, the pressure, temperature and the pressing time are the most important factors [16-17]. The pressure applied and the mechanical effort ressistance of the materials used, affect the porosity and the thickness of the CL and they influence the "membrane electrode" adhesion. The pressure ranges s used in the literature are relatively large between 1-100 kg/cm2. Regarding the temperature ranges, it influences the pore formation, and solvent and/or pore promoter removal. The highest temperature of a hot-pressing process is limited by the vitreous transition of Nafion (~ 125 ° C) while the lowest, depending on the MEA’s adhesion, commonly ranges between 80 and 125 °C. Pressing time affects the degree of CL deformation, where the minimum time is conditioned by the MEA’s adhesion and the maximum time is defined by the desired degree of microstructural deformation, commonly between 1 to 6 minutes.

One of the main challenges of designing an automated manufacturing system is to define the components that integrate this mechanism. In Mexico there are several companies that provide mechanical, pneumatic and electronic equipment that can be potentially used for the construction of the press at, however, a high cost.

Although the purpose of the press is to modify and control the microstructure of the electrodes to improve efficiency and effectiveness of the porous layers of a PEMFC, this paper does not focus on theoretical analysis of the transport phenomena occurred in the electrode. This document covers the technical challenges of design, construction and costs of the press and its components.

2. Technical specifications of the press

The main boundaries on the features of the press are conditioned by the power of the cells to be manufactured. The system studied in this work is defined for a maximum electrode area of 20 cm^2, which defines the compression area for mainly rectangular electrodes about 2 cm wide by 10 cm long. The work area was defined to be 5 cm wide by

15 cm long. The control system and actuators allow force ramps from 0.5 kN to 20 kN, with precision of 10 N and speeds from 10N / s up to 1000 N / s, defining the maximum force to be 2 Ton. The piston stroke allows a maximum distance between compression plates of 10 cm. To heat the electrodes to be manufactured, a steel plate is heated by electric resistors cartridges coupled to the control system. The temperature heating ramps allow 1 ° C / s, the maximum temperature the steel plate can get is 120 ° C. The central control module is a FESTO CEPX PLC, which can be connected to a computer to be operated in real time or ir can be programmed and operated by the module through free software "CoDeSys". Figure 1 shows the general diagram of the system.

Fig. 1. Front view and some angles of the pneumatic hot-press prototype

2.1. Pneumatic system

Among the most important features of the pneumatic circuit is the control of the pressure on the thermal plates. The most important criteria to keep in consideration are: 1) the pressure changes the microstructure and 2) errors in the distribution of forces involve a decline in the assembly quality. The pneumatic circuit will allow assemblies with different surface areas and different side measures, always staying within a maximum surface area of 20 cm2. It is required to produce a pressure of 100 kg/cm2 (around 9,807 N/mm2), so that for the area specified before, the press will apply maximum force of approximately 2 tons. In this work, the chosen strength source is a Festo ADNH-100-150 pneumatic piston controlled by a proportional valve, which regulates the pneumatic pressure supplied to the piston in order to have a gradual increase/decrease of mechanical strength. The process of modulating pressure control is to achieve a positive/negative pressure ramp. During the positive phase of the cycle, the piston can reach up to 18 kN. In a beginning it was defined a force increase rate of 100 N / s (≈ 9.81 kgf/s).

For the hot-pressing process to achieve efficiently, it is necessary to implement a programmable logic controller (PLC) which will manage the proportional valve, bidirectional valve, the heating elements and monitoring input/output data, resulting in an indirect control of mechanical pressure applied to the assemblies. The PLC will conduct the

monitoring of the analog input signals and the sending of new modulated output signal to the proportional control valve VPPX. This system will also receive and send digital signals (on/off) to and from the bidirectional valve that will be responsible for directing the flow of the working gas.

The actuation system comprises all pneumatic hardware, which manages supply, application and exhaust of the working fluid (FDT). Figure 2 describes the basic components that make up the pneumatic system.

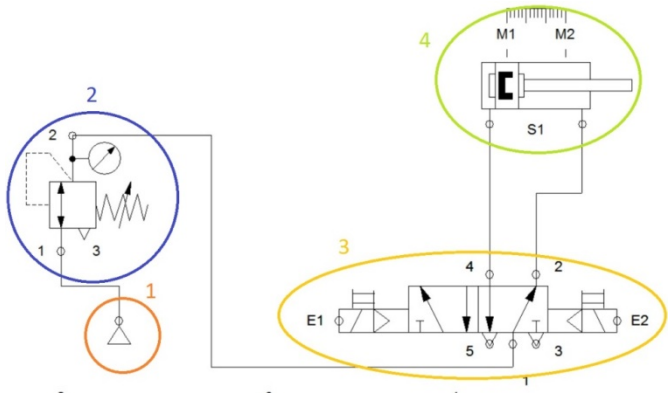

Fig. 2. Pneumatic system: 1) Service unit, supply of the FDT, 2) proportional control valve VPPX, 3) bidirectional valve and 4) Festo ADNH-100-150 pneumatic piston.

The phases of the working cycle of the press system is described in the following. The first phase of the cycle is the phase of delivery of working fluid at the specified pressure, which must be constant at all times during the operation of the press. The working fluid can be compressed air or an inert gas. The supplied pressure will be regulated by the maintenance unit and must be between 6 bar to 10 bar.

The increase of barometric pressure applied to the piston is effected by the proportional valve, which modulates such increment according to the signal strength, voltage (V) or current (I), sent by the controller. Thus, it is intended to control the increase in the force exerted on the tip of the rod of the pneumatic piston. Figure 3 shows a representation of the profile of the ramps of pneumatic pressure and mechanical force.

The proportional valve contains its own control system which monitors the output pressure at all times, comparing it with the indicated input value. Figure 4 shows the system of internal control VPPX.

Figure 4 shows a closed control loop , the reference magnitude w (set point, p / e 5 V or 8 mA) first strikes into a comparator , the measuring device emits the signal corresponding to the controlled magnitude x (real value, e.g. 3 bar) as r magnitude feeds back, which is received by the comparator. The regulatory element detects the deviation e and avtivates the final element of control. The output signal of the final element of control affects the regulation path. Thus, the regulatory element, using the final element of control tries to compensate for the difference between the reference magnitude w and the controlled magnitude x .

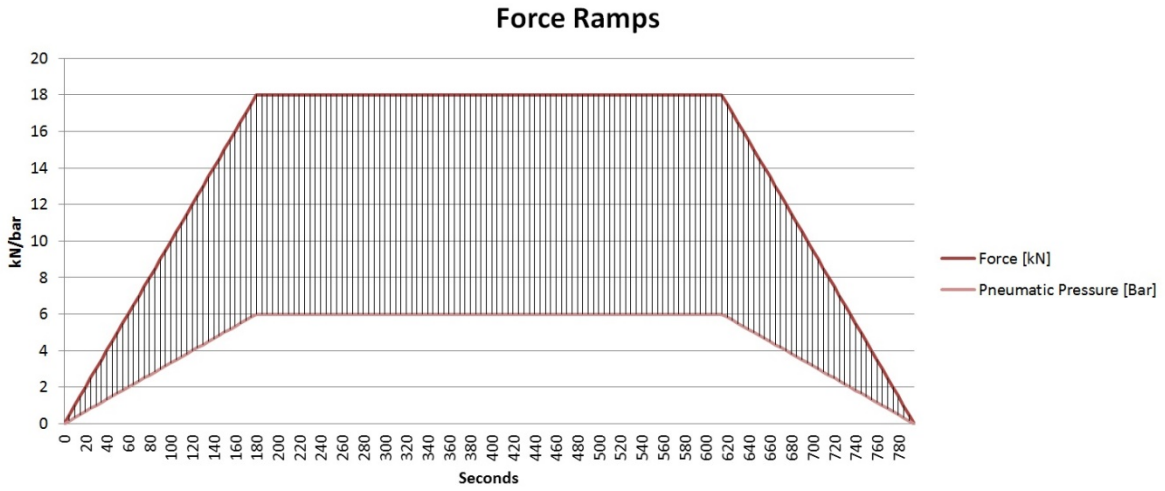

Fig. 3. Relationship between pneumatic pressure (pink line) vs mechanical pressure (red line) ramps, in relation to time (s)

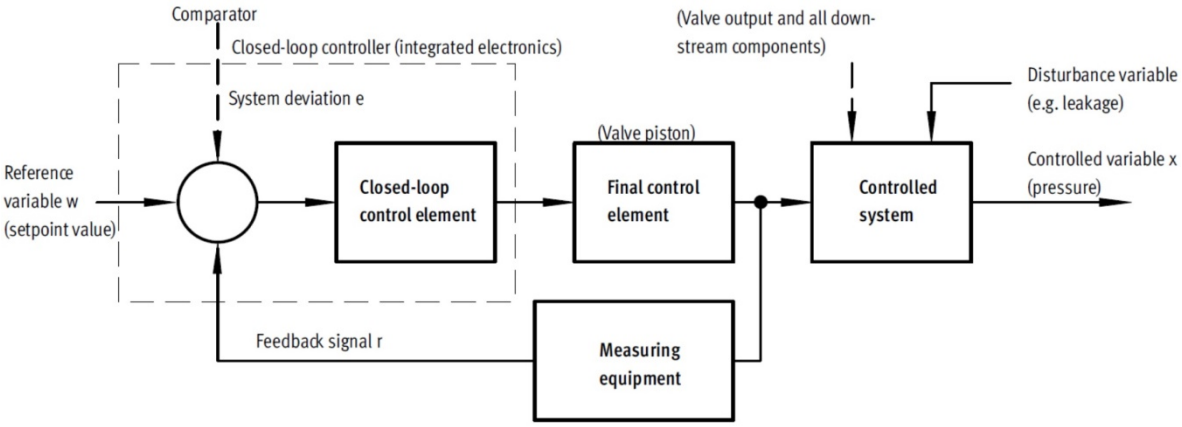

Fig. 4. Block diagram of the proportional valve FESTO VPPX control system.

The operation of the VPPX is based on a temporal input signal; the valve stores the set point and maintains regulation based on that value. If the comparator receives a different reference value w, this will erase the memory of the previous value and store the new data, restarting the cycle regulation on the new input value.

The regulated pressure output is guided directly towards the FESTO JMFH 5/2 valve, which, initially, maintains the output pressure to the retraction of the piston. When the duty cycle starts, the controller sends a pulse signal to the bidirectional valve and this valve will change its position to direct the pressure supply to the advancement of the stem. Simultaneously, the controller will send an analog signal to the proportional valve to initiate the pressure increase. The proportional valve needs enough pressure to start the advance of the piston, afterwards the pressure will be gradually increasing depending on the desired set point. The proportional valve opens or closes the diaphragm causing "leakage"

of pressure proportional to the input signal, thereby generating a linear increase in barometric pressure.

The system of the proportional valve always detects any change in the reference magnitude. It also produces a deviation if the reference magnitude remains constant and changes the controlled variable. This is the case when the delivery flow varies throughout the valve due to a switching operation, a movement of the cylinder or a load change. Moreover, the disturbance magnitude z may cause a deviation; for example, a pressure drop in the air supply system. The disturbance magnitude z does not intentionally influences the controlled magnitude x. In all these cases, the regulator attempts to modify the magnitude x to match the reference magnitude w.

2.2. Thermal system

In the process of microstructural formation of the porous electrodes, it is necessary to apply a temperature increase during the compression process. Initially this heat will be supplied by three electric cartridge type resistance 250W, 120V each, resulting in an 750W electro-resistive system. Each cartridge has 9.5 mm (3/8") in diameter and 152.0 mm (6 in) in length. This system is installed in a T304 stainless steel plate 100.0 mm wide by 200.0 mm long by 30.0 mm thick. The heating elements are uniformly distributed with a spacing of 22.5 mm from the center of the circumference of each cross section.

Initially the maximum temperature will be admitted to all set points which will be received by the PLC via PT100 temperature sensor. The CEPX controller will then compare the output signal of the sensor, with temperature set point and send a signal to the power source. The three thermo- resistance increase temperature evenly receiving power from the source according to the temperature sensed by the PT100. As the heating elements are in contact with the steel, the plate heats up at a rate determined by its heat transfer coefficient. The challenges of this system lie in a good heat transfer and dissipation.

The heating cycle must be synchronized with the pressure cycle so that the first of them start in a specific stage of pressing. This delay or advance of the start of the heating cycle allows greater versatility when pressing, since one will be able to define the starting point and increase rate of heating of the compression phase. This is applicable only when considering the heat transfer coefficient of the material as the limited value for the maximum rate of temperature increment when the resistors are heated at full power.

3. Analysis strategy

In order to perform the functions of a press, the pneumatic cylinder must be secured to a structure, it serving as a solution for the piston position and the heating plates and it is mainly a mechanical support that absorbs the reaction forces occurred when the piston is in the compression phase.

The pneumatic piston generates mechanical stress so that the analysis should start from this point. When the press is in the phase of maximum power duty cycle, the pneumatic piston rod supports a compressive force equivalent to 18.3 kN (~1.8 ton). It is known that the pressure (P) is directly proportional to the force (F), and inversely proportional to the area of compression (A) (equation 1).

$$P = F / A \quad (1)$$

In the case of piston rod, which has a diameter of 2.5 cm, the pressure of the maximum force (18.3 kN) is 37.3 MPa. For the upper end of the piston, a square area is considered with sides of 0.1135 m each, the exerted pressure is 1.4 MPa.
This compressive force is applied by the rod and projected directly onto the back cover of the piston body, which is attached to a black A36 steel plate supported by four T304stainless steel rods. As a result of reaction, the piston body tend to go in opposite direction to the movement of the rod when the latter cannot move forward but the pressure inside the piston continues to increase. When this happens, the plate 1 will transfer the force exerted by the piston body around 4 rods fixed in the corners, turning the compression force in tensile strength. In this case, the force received by the plate will be divided according to the number of fixed supports. The rods are flat headed at an upper end and standard thread at the lower and fixed on the plate 2, which supports the lower rods and the piston surface facing below.

In the case of the forces exerted on the upper support plate, the center of gravity of the piston's upper surface area is obtained to define a single point of application of force; the force is distributed evenly among the 4 points where the 4 support T304 stainless steel rods absorb the generated stress. It is considered that the system is in equilibrium, so that the sum of all external moment vectors acting on the system is equal to zero. Applying this concept, the force produced by the piston is distributed equally in four points (Equation 2).

$$FVA = Fp / n = 18.3\ kN / 4 = 4.6\ kN \quad (2)$$

where Fp is the maximum piston force, n the number of support points evenly distributed.

In order to dimension the design, material selection and determine safety ranges, the mechanical and thermal conditions were simulated in SolidWorks 2014. Because the reaction forces are absorbed by the structure supporting the piston, the efforts system can be interpreted as a closed cycle. The simulation was performed under static loading conditions. The study was to analyze each piece individually, as well as the conditions required for assemblies in order to identify the factors involved during the pressing process more precisely.

When the pneumatic cylinder is at its point of maximum pressure, it will be applying its nominal maximum force on the heating plate. Inside the cylinder, the air pressure will cause the advance of multiple plunger until reaching a point where it can advance no more; at that moment, since the pneumatic pressure exerts its action in all directions, the top of the cylinder is pressed against the upper plate generating fatigue on the element.

For the simulation of all elements, a 4-Jacobians-points solid mesh was created with elements of 5.00 mm with a tolerance of 0.25 mm. In Figure 5 and 6 meshing elements of designed press are shown.

Table 1. Thermo-mechanical properties of the materials used to build the armature and pressing system.

Name	Properties	
ASTM A36 Steel 	Model type	Isotropic linear elastic
	Default error criteria	Von Mises max. tension
	Elastic limit	250 N/mm^2
	Traction limit	400 N/ mm^2
	Elastic modulus	200000 N/ mm^2
	Poisson	0.26
	Density	7850 g/cm^3
	Shear modulus	79300 N/ mm^2
AISI 304 Stainless steel 	Model type	Isotropic linear elastic
	Default error criteria	Von Mises max. tension
	Elastic limit	206.807 N/ mm^2
	Traction limit	517.017 N/ mm^2
	Elastic modulus	190000 N/ mm^2
	Poisson	0.29
	Density	8000 g/cm^3
	Shear modulus	75000 N/ mm^2
	Thermal expansion coefficient	1.8 x 10 005 /Kelvin

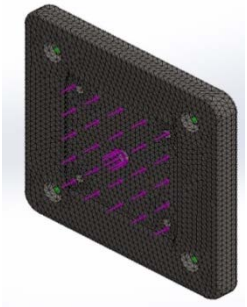

Fig. 5. View of the upper plate's mesh for simulation, with its respective arrows to describe the forces applied over the piece.

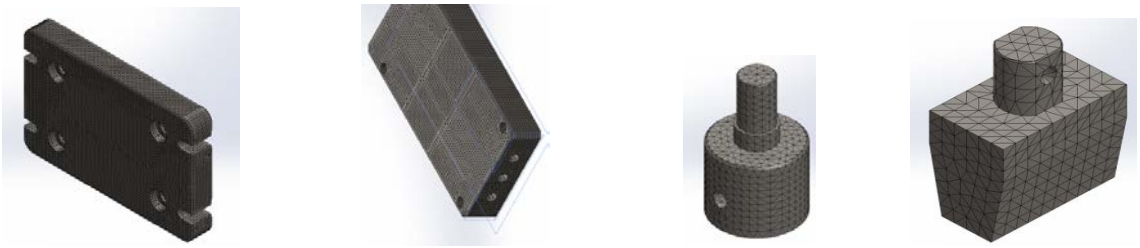

a) **b)** **c)** **d)**

Fig. 6 Mesh tracing of the **a)** lower plate, **b)** heating plate, **c)** compressor support bit, and **d)** compressor head.

4. Results

The results of the simulation efforts were satisfactory for all elements of the structure, the compression and heating components. From the results, it was found that the element is exposed to greater fatigue in the bottom plate. This is because the plate absorbs three different types of forces in the same line of action but in different directions and distances of separation. In addition, the points of greatest fatigue and possible failure of all elements in the event of a sudden increase in the force applied to the system were identified.

The top plate is the element that receives the direct force of recoil cylinder during the compression cycle. In Figure 7 and Table 2, the tension present during the displacement cycle of maximum strength is demonstrated.

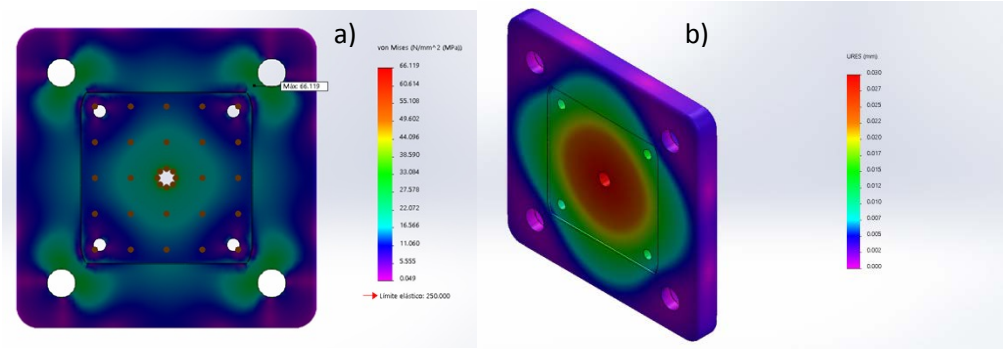

Fig. 7. Upper plate – Static Analisys. a) Tensions and b) displacement.

Table 2. Von Mises tensions analysis for the upper and displacement analysis of the plate during the max yield strength point.

Name	Type	Min	Max
Effort analisys	VON: Von Mises tensions	0.0486 N/mm^2 (MPa) Node: 61813	66.1195 N/mm^2 (MPa) Node: 64227
Displacement	URES: Total displacement	0 mm Node: 4	0.0298 mm Node: 65827

The top plate distributes force evenly unto four rods arranged one on each corner of the plate. The analysis of the efforts distributed in one of the rods is shown below in Fig. 8. Minimum and maximum tensions were determined in node 13240 and 23216, respectively. In Table 3, the Von Mises tensions and displacement analysis is showed for the rods.

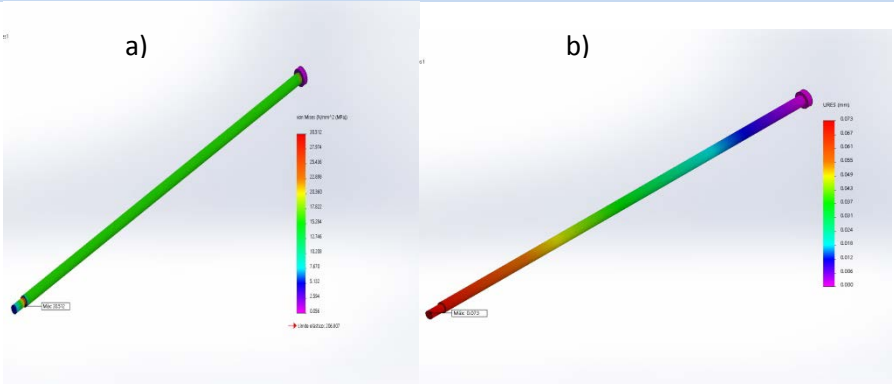

Fig. 8. Upper stem – Static Analisys. a) tensions and b) displacement.

Table 3. Von Mises tensions and displacement analysis of the upper stem.

Name	Type	Min	Max
Effort analisys	VON: Von Mises tensions	0.0556 N/ mm^2 (MPa) Node: 13240	30.5124 N/ mm^2 (MPa) Node: 23216
Displacement	URES: Total displacement	0 mm Node: 225	0.0732682 mm Node: 1

The intermediate plate is the part where all tension rods are threaded, which undergoes cutting and bending stresses during the compression phase. In addition, the front face of the cylinder rests so it has a larger drilled point in the center to allow the smooth running of the rod and accessories. As the image describes, the plate suffers efforts from both sides because, even though the whole system of rods exerts force on the same line of action, exert in opposite directions, hence the intermediate plate suffers the most displacement at the ends. Then proceeding with the simulation, the result of the displacement approaches zero, indicating a proper functioning of the part. The maximum and minimum tension and displacement, and the results present during the displacement cycle of maximum strength are showed in Table 4.

Table 4. a) Von Mises tensions analysis, and b) displacement analysis of the middle plate.

Name	Type	Min	Max
Middle plate	VON: Von Mises tensions	0.0890 N/ mm^2 (MPa) Node: 2213	26.8026 N/ mm^2 (MPa) Node: 2679
Displacement	URES: Total displacement	0 mm Node: 329	0.0157 mm Node: 2396

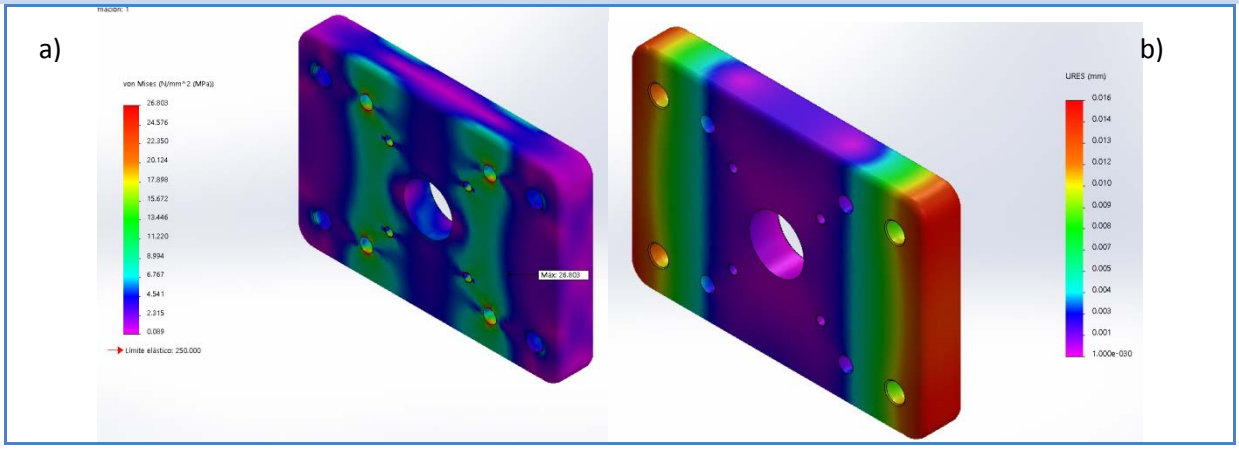

The lower rods are much shorter than the top ones, and a slightly larger cross section area. These is with the purpose of moving the center of mass of the entire structure towards the bottom and thus improve the stability of the device, increasing the security of the system, reducing the risk of accidental falling. In addition, the tensioning effort, is not much larger than thatat of the intermediate plate, and is much lower than the yield strength of the material (stainless steel T304); displacements are also very low, which confirms the functionality of the component's design.

Table 5. a) Von Mises tensions analysis, and b) Displacement analysis for the lower rods in max force cycle.

Name	Type	Min.	Max.
Effort analisys	VON: Von Mises tensions	0.2110 N/mm^2 (MPa) Node: 1745	28.4976 N/mm^2 (MPa) Node: 38207
Displacement	URES: Total displacement	0 mm Node: 309	0.0167 mm Node: 7

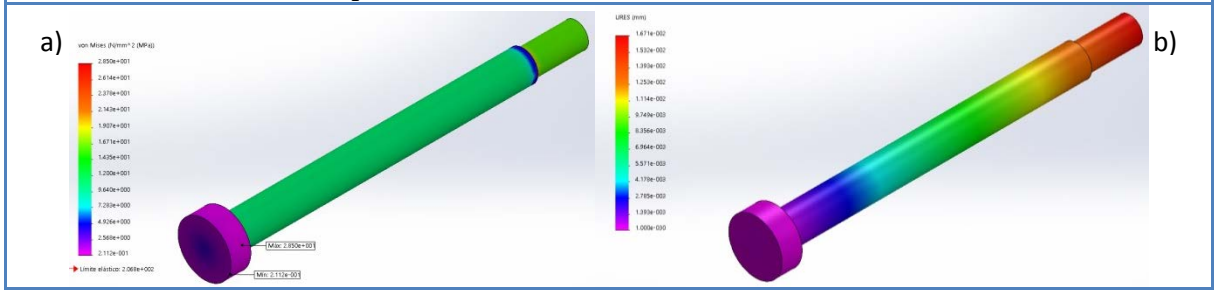

The bottom plate is the element that suffers more fatigue as it is subjected to compressive stresses in the central area (besides increasing temperature by indirect driving of the heating plate), while supporting the four lower rods which generate an effort in the opposite direction of compressive stress . Finally, the plate is fastened at each corner by a mock, to minimize distortion. It is worth mentioning that the initial design of the lower plate was conceived with a thickness of 30.0 mm, but the simulation showed high levels of deformation (over 4 mm). Because of this, the plate thickness was increased by 10 mm.

With this action, the displacement of the piece was reduced to nearly zero, validating the design of the piece.

Table 6. a) Von Mises tensions analysis and b) Displacement analysis for the lower plate at max force point.

Name	Type	Min.	Max.
Effort analisys	VON: Von Mises tensions	0.0155 N/mm^2 (MPa) Nodo: 331517	15.6894 N/mm^2 (MPa) Nodo: 329071
Displacement	URES: Total displacement	0 mm Nodo: 381	0.00956695 mm Nodo: 43
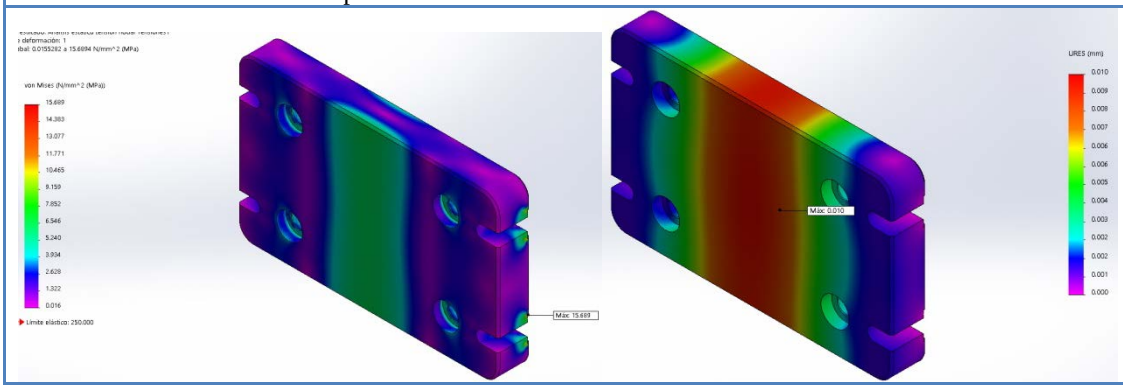			

Regarding the "thermal module", this system is installed in a T304 stainless steel plate of 100 mm wide by 200 mm long and 30 mm thick. Heating cartridges are uniformly distributed with a spacing of 22.5 mm from the center of the circumference of each cross section. Initially, the set point of maximum temperature will be submitted by the user into the PLC.

When the heating elements are in contact with the steel plate, it will tend to heat up at a rate determined by its heat transfer coefficient. It is required that the temperature of the heating plate increases and dissipates relatively quickly, being ready for a new cycle. The analysis in SolidWorks delimits the phenomenon of conduction. Table 7 summarizes the boundary conditions and the simulated material.

Table 7 shows the temperatures achieved by the heating plate in the simulation fully meet the maximum temperature needs, reaching a point above the required temperature, so the hysteresis defined in the control system must be well located, not to exceed the permissive thermal limit in order to perform a correct preparation of the electrode. It is worth mentioning that respect to thermal simulation, convection coefficient was taken with zero wind conditions and constant temperature of 25 ° C as boundary conditions.

Table 7. Thermal properties of the hot-plate´s components

Name	Values	Component
Solid model: Thermic Plate	Mass: 4.3302 kg Volume: 0.000541274 m^3 Density: 8000 kg/m^3 Wheight: 42.4359 N Thermal conductivity:500 J/(kg.K) Specific heat 8000 kg/m^3	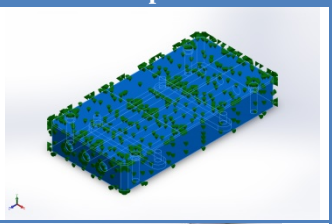
Solid model: Heat generating element	Individual power: 250 W Entities: 3 Total power: 750 W	
Flow model: Convection heat discipation	Convection coefficient:375W/(m^2.K) Room temperature: 300 Kelvin	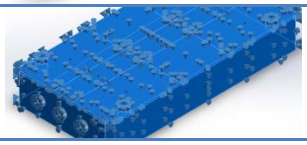
Default error criteria	16 W/(mK)	ALL
Results Tmax: 170°C Tmin: 46°C	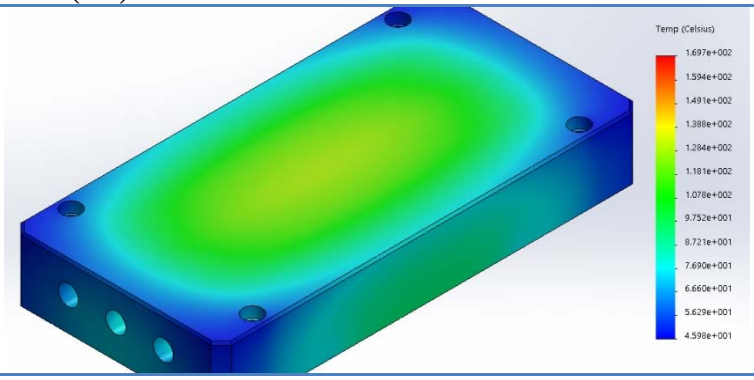	

4. Conclusion

It is very important to have a full control over mechanical reactions on the elements of the thermo-electro-pneumatic press, assuring safety for users and achieving a uniform pressing throughout the electrode area, ensuring a correct ordering of the microstructure of the latter. With this simulation, not only the theoretical calculations of the dimensioning of the support frame is confirmed, but also possible failures in specific areas can be foreseen considering long term usage of the designed equipment.

With these results, the second phase of the project can be proceeded, which is the manufacturing of the parts of the support frame, and the integration of these with the other subsystems that make up the press. While the support frame is not part of the control system and uses no moving parts, its presence in the press is essential to achieve the objectives of microstructural modification. Once the press system is fully constructed, manufacturing test will be performed adjusting pressing times, pressure and temperature ramps, and heating time, to verify the microstructure changes of the porous electrodes. The

scope of this paper, however, does not cover the verification of the effect of the microstructurall changes on the MEAs' efficiencies.

Acknowledgements

The authors would like to thank *SEP-CONACYT* for the support of this project under Grant CB-2013/221988 and project 252003 "*Programa de Redes Temáticas (RTH2)*". B. Escobar wishes to thank the *Cátedras-CONACYT* program

References

[1] Andrews, J. and Shabani, B. Re-envisioning the role of hydrogen in a sustainable energy economy. Int. J. Hydrogen Energy (2012) in press.
[2] Hajimiragha, A.H., et al. Sustainable convergence of electricity and transport sectors in the context of a hydrogen economy. Int. J. Hydrogen Energy (2012) 36: 6357-6375.
[3] Dougherty, W., et al. Greenhouse gas reduction benefits and costs of a large-scale transition to hydrogen in the USA. Energy Policy (2009) 37: 56-67.
[4] Litster S. and McLean G. PEM fuel cell electrodes review. J. Power Sources (2004) 130: 61-76.
[5] Rajalakshmi N. and Dhathathreyan K.S. Catalyst layer in PEMFC electrodes- fabrication, characterization and analysis. Chemical Engineering Journal (2007) 29: 31-40.
[6] Chaparro A.M., et al. Catalyst layers for proton exchange membrane fuel cells prepared by electrospray deposition on Nafion membrane. J. Power Sources (2011) 196: 4200-4208.
[7] Kadjo A.J.-J., et al. Improvement of PEMFC electrical performance by optimization of operating parameters and electrodes preparation. J. Power Sources (2007) 172: 613-622.
[8] Andrade A., et al. Fabrication of high precision PMEFC membrane electrode assemblies by Sieve printing method. J. Fuel Cell Sci. and tech. (2009) 6: (021305)1-(0213005)3.
[9] Towne S., et al. Fabrication of PEMFC MEAs utilizing inkjet print technology. J. Power Sources (2007) 171: 575-584.
[10] Sengul E., Erkan S. Effects of gas diffusion layer characteristics and addition of pore-forming agents on the performance of PEMFC. Chemical Engineering Communications (2009) 196: 161-170.
[11] Fernández R., et al. PEMFC electrode preparation: Influence of the solvent composition and evaporation rate on the catalytic layer microstructure. J. Power Sources (2005) 151: 18-24.
[12] Tang H., et al. A comparative study of CCM and hot-pressed MEAs for PEMFC. J. Power Sources (2007) 170: 140-144.
[13] Jeon S., et al. Effect of ionomer content and relative humidity on polymer electrolyte membrane fuel cell (PEMFC) performance of membrane-electrode assemblies (MEAs) prepared by decal transfer method. Int. J. Hydrogen Energy (2010) 35: 9678-9686.
[14] Cho H.J., et al. Development of a novel decal transfer process for fabrication of high-performance and reliable membrane electrode assemblies for PEMFCs. Int. J. Hydrogen Energy (2011) 36: 12465-12473.
[15] Alvarez A., et al. Composite membranes based on micro and mesostructured silica: A comparison of physicochemical and transport properties. J. Power Sources (2011) 196: 5394-5401.
[16] Nakrumpai B., et al. Optimum condition of membrane electrode assembly fabrication for PEMFC. Korean J. Chem. Engineering (2006) 23: 570-575.
[17] Therdthianwonga A., et al. Investigation of membrane electrode assembly (MEA) hot-pressing parameters for PEMFC. Energy (2007) 2400-2411.

Chapter 3.5. An optimization study of the EPD parameters of Pt/C to fabricate PEM fuel cell electrodes using non-asymmetric AC electric field

W.J. Pech-Rodríguez[a]; D. González-Quijano[a]; G. Vargaz-Gutierrez[a,b]; J.I. Escalante-Garcia[a,b]; F.J. Rodríguez-Varela[b,c,*]

[a]Ingeniería Metalúrgica e Ingeniería Cerámica
[b]Sustentabilidad de los Recursos Naturalez y Energía
[c]Programa de Nanociencias y Nanotecnología
Cinvestav Unidad Saltillo, Av. Industria Metalúrgica 1062, Parque Industrial Ramos Arizpe, Ramos Arizpe, Coahuila, C.P. 25900, México

ABSTRACT

PEM Fuel Cell electrodes were fabricated by electrophoretic deposition (EPD) under Non-Asymetric AC electric field, by deposition of a catalytic layer of home-synthesized Pt/C nanoparticles on commercial carbon cloth as support. The experiments were carried out based on a L9 orthogonal Taguchi experimental design array with four factor control at 3 levels. The effect of various parameters such as applied voltage, deposition time, asymmetric factor and Nafion content has been studied. The obtained layers were characterized by Scanning Electron Microscopy to investigate the dispersion of the catalyst. The results indicated that EPD is an effective method to fabricate PEM fuel cell electrodes with thin and homogenoeus catalytic layer. Electrochemical studies of the EOR in acid media demonstrated a high electrocatalytic activity for the EOR of the electrodes fabricated using the EPD technique.

Keywords: EPD, Fuel Cell Electrodes, EOR, Optimization

1. Introduction

Direct ethanol fuel cells (DEFC) are electrochemical devices that have received increasing interest as an alternative power source [1, 2]. Ethanol is a promising fuel due to its low toxicity, high energy density, and may be produced from biomass such as raw material rich in sugar. Additionally, ethanol is very advantageous because it is easy to store and handle [3-5]. At present, one challenge for DEFC is to improve the Pt utilization at the catalysts layer, which would result in a decrease of metal loading on the electrodes [6, 7]. Several methods for electrode preparation has been proposed including: spraying, hand brushing, direct printing, screen printing, decal transfer, electrochemical deposition and

---

* Author for correspondence:
F.J. Rodríguez-Varela, T: 52(844)438-9600 x 8526, E: javier.varela@cinvestav.edu.mx

EPD, among others [8]. The EPD technique is a highly versatile method for production of a wide range of coatings and films from colloidal suspensions [9-11]. The EPD process is achieved by the movement of charged particles dispersed in a solvent toward an oppositely charged electrode under an applied electric field [12, 13].

Modulated electric field has been proposed as a method to form uniform and homogenous deposits [14, 15]. Adilbish and coworkers studied the activity of Pt/C catalysts deposited by using pulsed EPD and demonstrated that the morphology of the electrodes could be controlled by changed the duty cycle [16]. Also, it has been demonstrated that the particle size growth of Pt nanoparticles may be overcome by using pulsed electrophoretic deposition [7]. In this work, we study the effect of electrophoretic parameters such as applied voltage, deposition time, asymmetric factor and Nafion® content on the characteristics of Pt/C catalytic layers on commercial carbon cloth electrodes. The catalytic activity of the fabricated fuel cell electrodes is evaluated for the EOR in acid electrolyte.

2. Materials and Methods

2.1.Materials.

A commercial ELAT® LT-1200W (BASF) with a Micro-Porous Diffusion Layer (MPDL) on one side was used as carbon matrix. Commercial 20 wt. %. Pt/C (E-tek) was used as catalyst powder for the EPD. Nafion® solution (5 wt. %, Sigma Aldrich) was used as surfactant to ensure a negative surface charge of the Pt/C nanoparticles and as ionic conductor to enhance the three phase boundary (TPB). A mixture of isopropil alcohol and acetone (Sigma Aldrich) was used as solvent. The electrical conductivity of the solution was enhanced by adding 0.1 M H_2SO_4 (Sigma Aldrich).

2.2. Fabrication of the Pt/C electrodes.

Homogeneous and stable suspensions of Pt/C (0.16 mg mL^{-1}) were prepared by mixing the catalysts powders in an ethanol-acetone solution (50:50 v/v) in an ultrasonic bath. Then, the corresponding amount of Nafion® solution was added in the slurry, keeping stirring for 10 min. With the aim to enhance the electrical conductivity of the mixture, 0.1 mL of 0.1 M H_2SO_4 solution were added.

The EPD were carried out using the setup illustrated in Figure 1(a). It consisted of two fixed electrodes placed inside a glass cell with a distance between electrodes of 1 cm. The working electrode holder had a circular window where the carbon cloth was fixed. The counter electrode was a stainless steel electrode mounted on a glass support (Radiometer) The EPD was carried out using a BIO-RAD Power Pac 3000 power supply. The device included an electronic circuit designed to control the cycles applied to the system, with the capability of changing the polarity of the pulses. The experiments were performed using a square-shaped asymmetric waveform, as shown schematically in Figure 1(b). To avoid particle sedimentation, slow magnetic stirring was imposed to the cell. The weight of the deposited coatings was determined by measuring the weight difference between the coated and the uncoated carbon cloth samples.

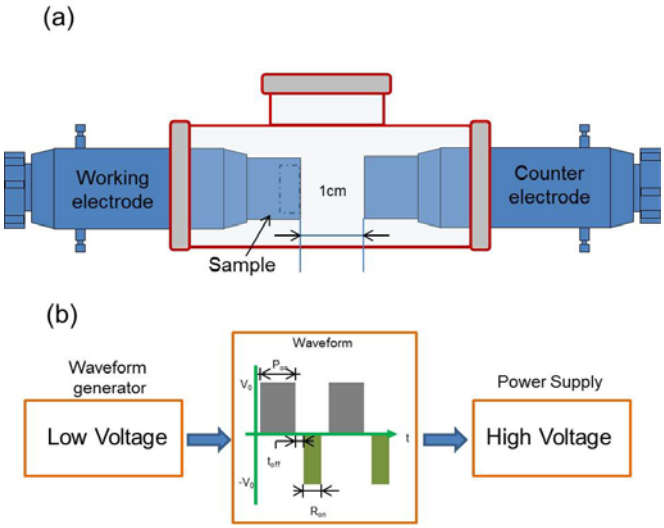

Fig. 1. Schematic diagrams of the a) electrophoretic deposition setup; b) waveform and conditioning circuit.

2.3. Taguchi design of experiments.

The effect of several EPD factors during the fabrication of Pt/C electrodes was studied by employing the Taguchi method. Such design of experiments allowed to determine the relevance of different parameters simultaneously, with the aim of reducing the time and cost of EPD experiments. Table 1 shows the full L9 orthogonal array design, which was selected with non-interaction between factors. The obtained electrodes were labeled as A1 through A9.

Table 1. The Taguchi L9 orthogonal array

Sample	Factor Levels			
	Voltage / V	Time / min	Asymmetric Factor	Nafion® loading / wt. %
A1	60	15	2	20
A2	60	20	3	30
A3	60	30	4	35
A4	90	15	3	35
A5	90	20	4	20
A6	90	30	2	30
A7	120	15	4	30
A8	120	20	2	35
A9	120	30	3	20

2.4. Characterization of the electrodes containing deposited Pt/C catalysts layers.

The morphology and chemical composition of the Pt/C electrodes was carried out in a Philips XL30 SEM-EDS apparatus, operating at 20 kV.

Electrochemical measurements were performed with a Voltalab PGZ 301 potentiostat/galvanostat in a standard three electrode cell. The working electrode was a deposited Pt/C electrode disk inserted into a Teflon holder. The electrode geometrical area

exposed to the electrolyte was 0.75 cm^2. An Ag/AgCl reference electrode was placed in a Luggin capillary that ended up close to the working electrode. A platinum foil was used as the counter electrode. Cyclic voltammetry and chronoamperometric curves were carried out in N_2-saturated 0.5 M H_2SO_4 without and with 0.5 M ethanol. The constant potential during chronoamperometry measurements was 0.87 V vs. RHE. The CV curves were obtained at a scan rate of 20 mV s^{-1}.

3. Results and Discussion

3.1. Characterization of the Pt/C electrodes.

Figure 2 shows the SEM micrographs at two magnifications of the Pt/C catalyst layers deposited on carbon cloth under non-asymmetric AC electric field. It is found that the thickness of the catalysts layer is less than 12 μm. As can be seen, the deposited electrodes show a porous morphology, a feature that is very important for the diffusion of the fuel to the Pt sites. In the micrographs of Figure 2, cracks at the MPDL can be observed. The A1 electrode presents non-uniform deposition of Pt/C and large regions where no catalyst or only small amounts of Pt/C cover the MPDL. Meanwhile, the A5 sample displays a high dispersion of the Pt/C MPDL, covering the surface of the carbon cloth. The A9 electrode shows larger amount of catalyst, but it is also clear that forms a thicker layer, with areas of significant agglomeration.

Figure 3 shows cross sectional views of SEM micrographs corresponding to the A1, A5 and A9 electrodes. The images reveal that dense films with varying thickness are formed. A good adhesion between the MPDL and the uniformly deposited Pt/C film has been observed.

The morphology in Figure 3(a) indicates that the non-cover areas of sample A1 in Figure 2, are isolated regions in the surface microstructure. Such electrode presents the thinner layer, about 2-3 μm thickness. Meanwhile, the morphology of electrodes A5 (Figure 3b) and A9 (Figure 3c) display thicker layers, with thickness around 10-11 μm, features attributed to the deposition parameters (Table 1)

3.2 Electrochemical characterization.

Figure 4 shows the CVs of the A1, A5 and A9 Pt/C electrodes. The samples have the general features of Pt catalysts, although A1 shows less intense current densities over the potential region scanned [17]. A9 show the largest hydrogen adsorption/desorption region, followed by A5. The real Pt surface area (ECSA) can be determined from the CVs of the deposited electrodes. The average (Q_H) of the charge associated to the hydrogen adsorption (Q_a) and desorption (Q_d) processes after double layer subtraction has been obtained. The obtained Q_H values have been converted into real surface areas using the well-known factor of 210 μC cm-2 associated to the adsorption of one monolayer of hydrogen at a smooth Pt electrode [18-20].

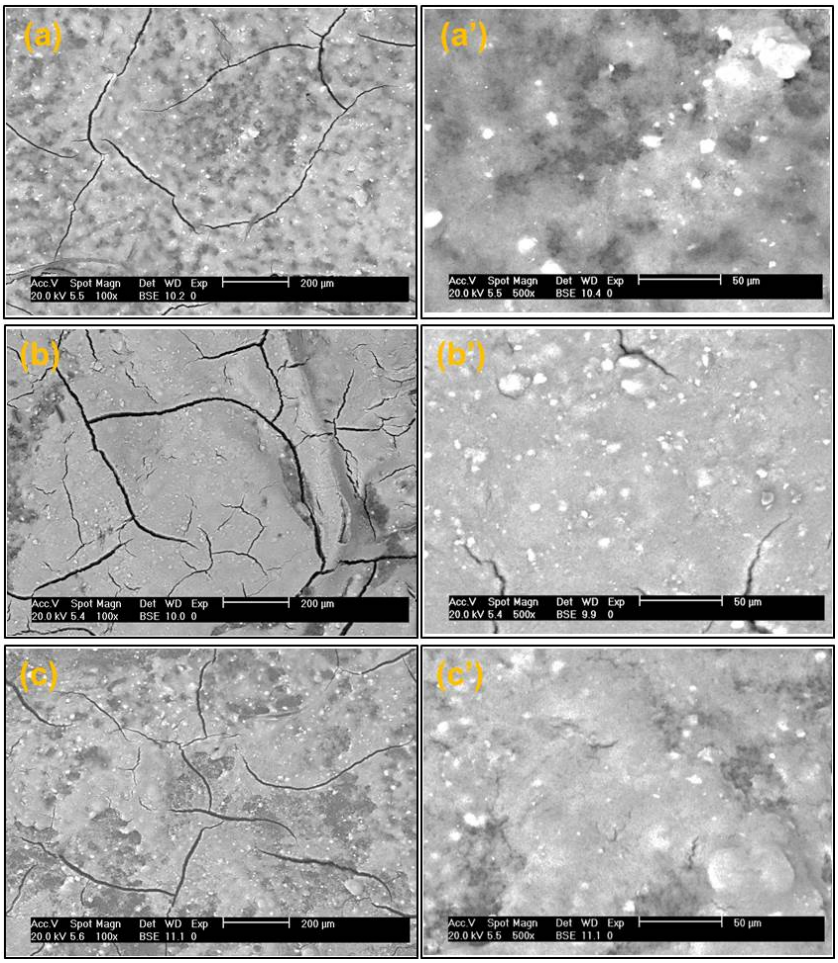

Fig. 2. Surface microstructure of the Pt/C electrodes prepared by EPD. A1 (a-a'), A5 (b-b') and A9 (c-c').

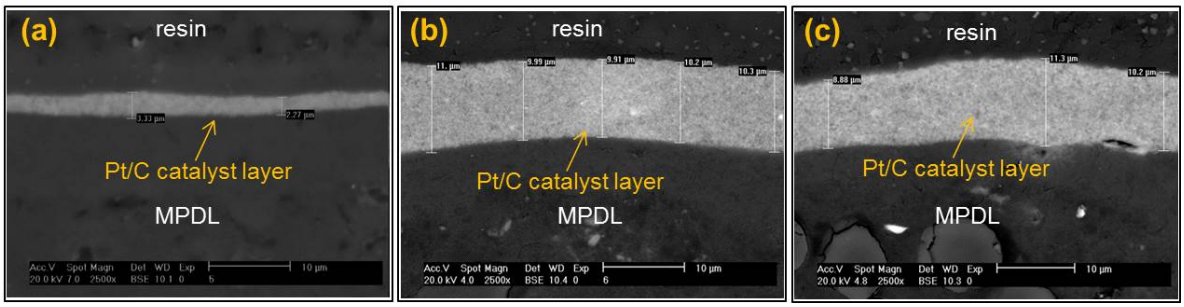

Fig. 3. Cross-sectional SEM image of Pt/C electrodes deposited on carbon cloth substrate. A1 (a), A5 (b) and A9 (c)

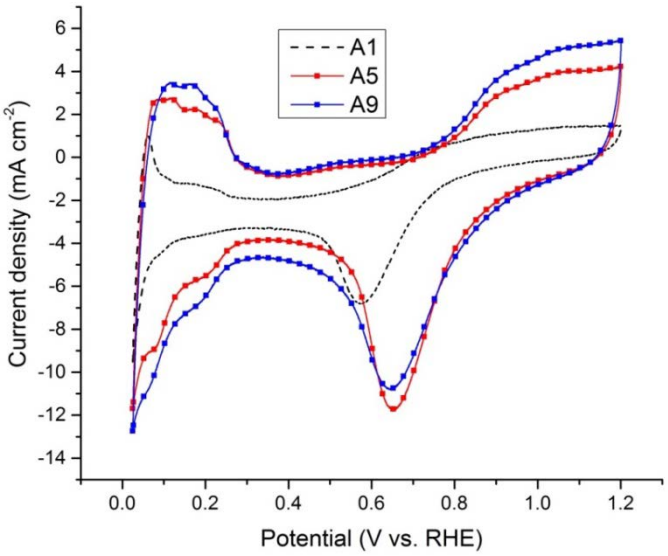

Fig. 1. CVs of Pt/C electrodes prepared under different conditions in Non-Asymmetric EPD. Scan rate of 20 mV s^{-1} at room temperature in 0.5 M H_2SO_4.

Table 2 summarizes the charges calculated for A1, A5 and A9. The results show that the A9 has a larger ECSA, followed by A5. A1 shows a significantly smaller ECSA. Table 2 also shows the Yield, i.e., the amount of Pt/C plus Nafion® deposited at each electrode. The maximum Yield has been measured for A9.

Table 2. Specific surface area and Pt loading estimated for the electrodes

Electrode	Yield (*mg*)	Hydrogen adsorption/desoption			ECSA / cm^2
		Q_a / mC cm^{-2}	Q_d / mC cm^{-2}	Q_H /mC cm^{-2}	
A1	0.45	11.2	10.48	10.8	39.0
A5	1.6	33.9	32.8	33.4	120.0
A9	1.9	37.2	35.6	36.4	130.0

The CV features and the ECSA values of A1, A5 and A9 correlate well with their morphological characteristics (Figures 2 and 3), and can be associated to the experimental parameters used for EPD (Table 1).

Figure 5 shows the polarization curves of the EOR. At low overpotentials, A5 and A9 show similar performances. The onset potential of the EOR at A9 is 0.24 V, slightly lower than 0.25 V of A5 (Table 3). Between ca. 0.6 and 0.8 V/RHE, A5 shows a broad current density shoulder not present at A9, followed by similar current density-potential behavior of these two electrodes. At potentials above ca. 0.91 V/RHE, A9 delivers a higher current density. The oxidation peak around 0.81 mV is due to the removal of absorbed species that are not oxidized in the forward scan [21, 22]. The A1 sample shows an overall poorer performance for the EOR, compared to A5 and A9. The higher performance of A5 and A9 for the EOR can be attributed to the better homogeneous dispersion of the Pt/C nanoparticles, the thickness of the catalyst layer and the Yield at the carbon cloth.

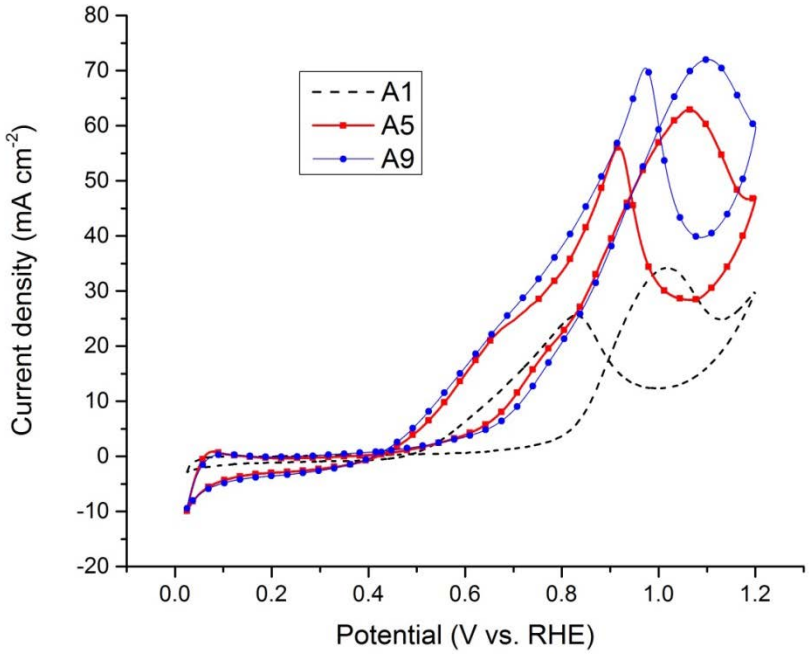

Fig. 2. CVs of the EOR at the A1, A5 and A9 electrodes. Electrolyte: N_2-saturated 0.5 M H_2SO_4 + 0.5 M C_2H_6O

Table 3. Electrocatalytic parameters of the EOR at the Pt/C electrodes

Catalyst	Onset potential / *V*	Peak current density / mA cm^{-2}
A1	0.30	34.2
A5	0.25	62.5
A9	0.24	71.6

In order to study the stability of the electrodes for the EOR, chronoamperometric measurements have been performed in 0.5 M H_2SO_4 + 0.5 M EtOH. The curves are shown in Figure 6. The A5 and A9 electrodes have significantly more stable current densities after 10 min compared with A1.

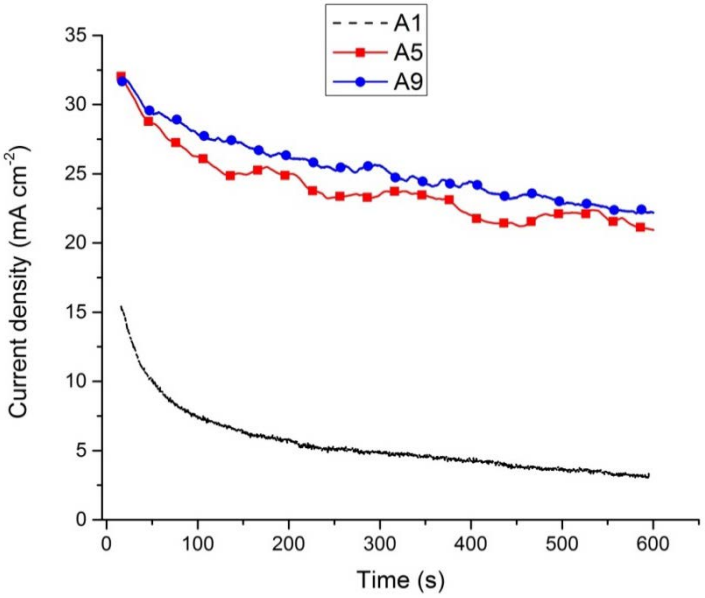

Fig. 3. Chronoamperometric curves at the Pt/C electrodes. Electrolyte: 0.5 H_2SO_4 + 0.5 M EtOH. Applied potential: 0.87 V/RHE

4. Conclusion

Pt/C catalyst layers have been successfully deposited on carbon cloth electrodes by EPD under Non asymmetric AC electric field. A dense layer has been obtained under all parameter used to fabricate the electrodes. The electrochemical characterization indicates that the performance of Pt/C electrodes catalysts is influenced by the EPD parameters. The A5 and A9 electrode show the highest catalytic activity for the EOR among the materials studied in this work.

Acknowledgements

This work was financially supported by the Mexican National Council for Science and Technology (CONACYT) through grants 252079, 241526 and 252003. We thank CONACYT for doctoral scholarships provided to WJPR and DGQ.

References

[1] Wang Y, Song S, Andreadis G, Liu H, Tsiakaras P. Understanding the electrocatalytic activity of PtxSny in direct ethanol fuel cells. J Power Sources. 2011;196:4980-6.
[2] Silva JCM, De Souza RFB, Parreira LS, Neto ET, Calegaro ML, Santos MC. Ethanol oxidation reactions using SnO2@Pt/C as an electrocatalyst. Appl Catal, B. 2010;99:265-71.
[3] De Souza RFB, Parreira LS, Rascio DC, Silva JCM, Teixeira-Neto E, Calegaro ML, et al. Study of ethanol electro-oxidation in acid environment on Pt3Sn/C anode catalysts prepared by a modified polymeric precursor method under controlled synthesis conditions. J Power Sources. 2010;195:1589-93.

[4] Baranova E, Amir T, Mercier PJ, Patarachao B, Wang D, Page Y. Single-step polyol synthesis of alloy Pt7Sn3 versus bi-phase Pt/SnOx nano-catalysts of controlled size for ethanol electro-oxidation. J Appl Electrochem. 2010;40:1767-77.
[5] Rao L, Jiang Y-X, Zhang B-W, Cai Y-R, Sun S-G. High activity of cubic PtRh alloys supported on graphene towards ethanol electrooxidation. Phys Chem Chem Phys. 2014;16:13662-71.
[6] Liu B, Chia Z-W, Lee Z-Y, Cheng C-H, Lee J-Y, Liu Z-L. The importance of water in the polyol synthesis of carbon supported platinum–tin oxide catalysts for ethanol electrooxidation. J Power Sources. 2012;206:97-102.
[7] Yu Y-T, Song J-C, Kim J-H, Kim Y-S, Lee H-G. Nano-architecture platinum catalyst layer prepared by electrophoresis deposition for PEM fuel cells. J Solid State Electrochem. 2012;16:1377-81.
[8] Hayashi K, Furuya N. Preparation of Gas Diffusion Electrodes by Electrophoretic Deposition. J Electrochem Soc. 2004;151:A354-A7.
[9] Besra L, Liu M. A review on fundamentals and applications of electrophoretic deposition (EPD). Prog in Mater Sci. 2007;52:1-61.
[10] Du C, Heldebrant D, Pan N. Preparation of carbon nanotubes composite sheet using electrophoretic deposition process. J Mater Sci Lett. 2002;21:565-8.
[11] Boccaccini AR, Zhitomirsky I. Application of electrophoretic and electrolytic deposition techniques in ceramics processing. Current Opinion in Solid State and Materials Science. 2002;6:251-60.
[12] Meng X, Kwon T-Y, Yang Y, Ong JL, Kim K-H. Effects of applied voltages on hydroxyapatite coating of titanium by electrophoretic deposition. Journal of Biomedical Materials Research Part B: Applied Biomaterials. 2006;78B:373-7.
[13] Wu DC, Shen L, Low JE, Wong SY, Li X, Tjiu WC, et al. Multi-walled carbon nanotube/polyimide composite film fabricated through electrophoretic deposition. Polymer. 2010;51:2155-60.
[14] Ammam M. Electrophoretic deposition under modulated electric fields: a review. RSC Advances. 2012;2:7633-46.
[15] Chávez-Valdez A, Boccaccini AR. Innovations in electrophoretic deposition: Alternating current and pulsed direct current methods. Electrochim Acta. 2012;65:70-89.
[16] Adilbish G, Kim J-W, Lee H-G, Yu Y-T. Effect of the deposition time on the electrocatalytic activity of Pt/C catalyst electrodes prepared by pulsed electrophoresis deposition method. Int J Hydrogen Energy. 2013;38:3606-13.
[17] Guo JW, Zhao TS, Prabhuram J, Wong CW. Preparation and the physical/electrochemical properties of a Pt/C nanocatalyst stabilized by citric acid for polymer electrolyte fuel cells. Electrochim Acta. 2005;50:1973-83.
[18] Kim H, Subramanian NP, Popov BN. Preparation of PEM fuel cell electrodes using pulse electrodeposition. J Power Sources. 2004;138:14-24.
[19] Prabhuram J, Zhao TS, Wong CW, Guo JW. Synthesis and physical/electrochemical characterization of Pt/C nanocatalyst for polymer electrolyte fuel cells. J Power Sources. 2004;134:1-6.
[20] Watt-Smith MJ, Friedrich JM, Rigby SP, Ralph TR, Walsh FC. Determination of the electrochemically active surface area of Pt/C PEM fuel cell electrodes using different adsorbates. J Phys D: Appl Phys. 2008;41:174004.
[21] Cheng F, Dai X, Wang H, Jiang SP, Zhang M, Xu C. Synergistic effect of Pd–Au bimetallic surfaces in Au-covered Pd nanowires studied for ethanol oxidation. Electrochim Acta. 2010;55:2295-8.
[22] Ye W, Yan J, Ye Q, Zhou F. Template-Free and Direct Electrochemical Deposition of Hierarchical Dendritic Gold Microstructures: Growth and Their Multiple Applications. J Phys Chem C. 2010;114:15617-24.

Chapter 3.6. Electrocatalytic Oxygen Reduction Reaction (ORR) on nanostructured Pt-$NiTiO_3$/C catalyst in alkaline media

A. Hernández-Ramírez[a]; M. E. Sánchez-Castro[a,b]; Kalasapurayil Kunhiraman Aruna[c]; Palanisamy Karthikeyan Manoharan[c]; F. J. Rodríguez-Varela[a,b,*]

[a]Programa de Nanociencias y Nanotecnología, Cinvestav Unidad Saltillo, Av. Industrial Metalúrgica No. 1062, Parque Industrial Saltillo-Ramos Arizpe, Ramos Arizpe, Coah., México, 25900.
[b]Grupo de Sustentabilidad de los Recursos Naturales, Cinvestav Unidad Saltillo, Av. Industrial Metalúrgica No. 1062, Parque Industrial Saltillo-Ramos Arizpe, Ramos Arizpe, Coah., México, 25900.
[c]Electrochemical Energy Materials Laboratories, Nanotech Research Facility, PSG Institute of Advanced Studies, Coimbatore, India 641 004

ABSTRACT

The catalytic activity for the ORR on carbon suppported Pt-$NiTiO_3$ catalyst was evaluated in 0.5 M KOH elecrolyte. $NiTiO_3$ nanoparticles were synthesized via a wet-chemical method. Then, 20% Pt-$NiTiO_3$ catalyst (Pt:$NiTiO_3$ ratio of 1:1) was obtained by the microwave assited polyol method. XRD analysis confirmed a nanocrystalline $NiTiO_3$ with a particle size around 25 nm. TEM results showed homogenously dispersed nanoparticles of Pt/C and Pt-$NiTiO_3$ on the carbon support with a narrow particle size distribution of around 2-3 nm. The titanate-containing catalyst showed a high cataytic activity for the ORR in 0.5 M KOH electrolyte. Koutecky-Levich plots indicate that the reaction proceeds through a four-electron transfer mechanism. Moreover, thesecathode showed enhanced tolerance to methanol and ethanol, compared to Pt/C. These results demonstrate that Pt-$NiTiO_3$/C electrocatalyst are excellent candidate for Alkaline Fuel Cells applications.

Keywords: Pt-$NiTiO_3$/C catalyst, Oxygen reduction reaction, Alkaline media, Tolerance to organic molecules

1. Introduction

Polymer Electrolite Membrane Fuel Cells (PEMFCs) are been considered as a promising technology for energy production with high conversion efficiency and very low emission of greenhouse pollutants [1-2]. It is well known that H_2 is a high power density fuel. However, there are still significant challenges in production, transporting, storing and handle gaseous H_2. For this reason, liquid fuels such CH_3OH or CH_3CH_2OH have become an attractive alternative to H_2. Hence direct alcohol fuel cells (DAFC) have been extensively studied in the past few decades [3-6].

---

* Author for correspondence:
F.J. Rodríguez-Varela, Phone number: +52(844)438-9600 Ext. 8526, E-mail: javier.varela@cinvestav.edu.mx

Recent advances in the synthesis of chemically stable anion-exchange membranes have open the opportunity for the development of the alkaline direct alcohol fuel cells (A-DAFCs) [7,8-11]. In this context alkaline A-DAFCs are interesting because have been demonstrated that the reactions kinetics and catalytic activities in alkaline media are significantly higher than those in acid conditions and the less corrosive alkaline environment ensure a longer life of the cell [12-17].

The catalyst layer is one of the most important constituents of the cell, Pt-based electrocatalyst are still widely used due to their high catalytic activity [11,18-23]. Nevertheless, the amount of noble metals used as catalysts in PEMFCs and A-DAFCs must be decreased in order to reduce the costs of the fuel cell devices. In addition, in the case of A-DAFCs the efficicency losses due to the crossover effect. Therefore, the cathode electrocatalyst must also show a high tolerance to the presence of organic substances [17,19,24].

This study focuses in the use of $NiTiO_3$ as co-catalyst for ORR. To the best of the author´s knowledge, this is the first time that the titanates has been used as cathodes in fuel cells.

2. Materials and Methods

2.1 Reactants and gases

Chemicals of analytical grade were used as acquired without any purification or pretreatment: $Ni(OCOCH_3)_2{\cdot}4H_2O$, $Ti[OCH(CH_3)_2]_4$, $H_2PtCl_6{\cdot}H_2O$, ethylene glycol (EG), KOH, 2-propanol, CH_3OH and C_2H_5OH (Aldrich), UHP grade O_2, N_2 (Infra, purity ≥ 99.999%) and Vulcan XC-72 was obtained from Cabot Corp.

2.2 Physicochemical characterization

X-ray diffraction analysis were performed in an Phillips X´Pert (PANalaytical) apparatus with a Ni-filtered Cu Kα radiation. Diffraction patterns were collected in the range of 10° to 80° (2θ) for $NiTiO_3$ powders and from 10° to 100° (2θ) for the Pt-$NiTiO_3$ electrocatalyst. Chemical composition by EDS was obtained in a Philips XL30 SEM equipment having an accelerating voltage of 20 kV. TEM images were obtained in a Jeol 2100 microscope with 200 kV accelerating voltage. The particle size distribution of the supported electrocatalysts was determined by measuring approximately 300 nanoparticles using the Image-Pro Plus software.

2.3 Synthesis of $NiTiO_3$ nanoparticles and Pt-$NiTiO_3$/C catalyst

$NiTiO_3$ nanoparticles were obtained by a wet-chemical procedure [25]. Stoichiometric amounts of $Ni(OCOCH_3)_2{\cdot}4H_2O$ and $Ti[OCH(CH_3)_2]_4$ were separately dissolved in methanol. Citric acid was added to the titanium solution under magnetic stirring until a transparent phase was achieved and nickel solution was added to this mixture. Then, the solution containing Ti and Ni precursors was heated at 90°C for 12 h to remove the solvent and promote the formation of metal-citrate complex. The precursor was calcinated in air atmosphere for 3 h at 700° C. After cooling down to room temperature, the $NiTiO_3$ nanoparticles were obtained.

The 20% Pt-$NiTiO_3$/C catalyst with Pt:$NiTiO_3$ nominal ratio 1:1 was synthesized by the microwave assisted polyol method. $H_2PtCl_6{\cdot}H_2O$, $NiTiO_3$ and Vulcan powders were

separately dispersed in EG by ultrasound for 30 min. The solutions were put together under magnetic stirred and a EG solution of NaOH was added to adjust the pH to 11. Subsequently, the mixture was heating by applying microwave irradiation on/off pulses of 1 min each one until reach to 4 min of effective irradiation. After cooling to room temperature, H_2SO_4 in EG was used to adjust the pH to 2, maintaining stirring for 1 h. The product was then filtered and dried in a dessiccator overnight. A 20% Pt/C electrocatalyst was synthesized under the same conditions.

2.4 Electrode preparation and electrochemical set-up

The catalytic inks were prepared with 10 mg of the catalyst, 1 mL 2-propanol and 5 µL Nafion® solution, the mixture was dispersed by ultrasound for 30 min. To form the working electrode, an aliquot of 10 µL of the ink were dispersed on a glassy carbon electrode (5 mm in diameter), which is placed in a rotating disc set-up (Pine Inst.). The current density in the electrochemical results is given in terms of the geometrical area of the working electrode. Electrochemical measurements were carried out in a standard three-electrode cell using a potensiostat (Pine Inst.). A Pt wire was used as the counter electrode and a Ag/AgCl (sat. KCl) electrode coupling to a Luggin capillary was employed as the reference electrode. All the potentials have been reported with respect to the reversible hydrogen electrode (RHE) according to the Nerst equation:

$$E_{RHE} = E_{Ag/AgCl} + 0.059\ pH + E°_{Ag/AgCl} \quad (1)$$

where $E_{Ag/AgCl}$ is the potencial measured, pH of the 0.5 M KOH electrolyte is 13.96 and $E°_{Ag/AgCl} = 0.197$ V.

Cyclic voltammetry (CV) measurements were performed in Ar-satured 0.5 M KOH. The CVs were obtained at a scan rate of 20 mV s^{-1} in the 0.5 to 1.2 V range (vs. RHE). Afterwards, To evaluate the catalytic activity of the synthesized electrocatalysts for the ORR, CV curves in O_2-satured electrolyte were obtained at different rotation rates (400, 800, 1200, 1600 and 2000 rpm), at the scan rate of 5 mV s^{-1} from 0.5 V to 1.2 V (vs. RHE). To eliminate any contributions of capacitive current CV curve in Ar-satured electrolyte at a scan rate of 5 mV s^{-1} at 2000 rpm was obtained. This background current was substracted from the experimental ORR current densities.

The tolerance behavior of the nanomaterials was studied obtaining polarization curves at 2000 rpm in the presence of 0.1 y 0.5 M CH_3OH or CH_3CH_2OH under O_2 atmosphere.

3. Results and Discussion

3.1 Physicochemical characterization

The high cristallinity of the titanate can be confirmed by the XRD results showed in figure 1(a), all the reflections can be assigned to the rhombohedral structure of pure $NiTiO_3$ and the characteristic crystalline planes are identified. Furthermore EDS analysis confirmed a Ni:Ti atomic ratio of 1:1. Figure 1(b) and 1(c) shows the diffraction patterns of Pt/C and Pt-$NiTiO_3$/C catalysts, respectively. In both difractograms can be observed the (111), (220) and (311) characteristic planes of crystalline face centered cubic structure of Pt. The peak located at 25° (2θ) corresponding to the carbon support are attributed to (002) crystalline graphite plane.

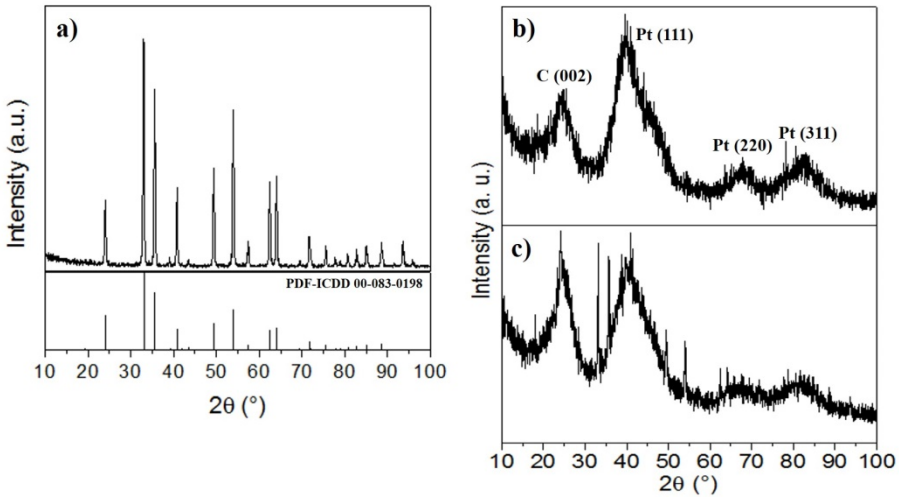

Fig. 1. XRD patterns of a) $NiTiO_3$, (b) Pt/C and (c) Pt-$NiTiO_3$/C.

The crystallite size was determinated with the (311) plane of the Pt/C and Pt-$NiTiO_3$/C difractograms using the Scherrer equation. The estimated crystallite sizes were 1.4 and 1.7 nm to Pt/C and Pt-$NiTiO_3$/C, respectively (Table 1). The EDS analysis demonstrate that the real compositions is very close from nominal calculations. The Pt:$NiTiO_3$ ratio is 0.95:1 and the catalyst amount is approximately 20 wt. %. On the other hand, the Pt content in the Pt/C catalyst results to be around 16 wt. %.

Table 1. Physical characterization of Pt/C and Pt-$NiTiO_3$/C catalyst.

Catalyst	Crystallite size, XRD (nm)	Particle size, TEM (nm)	Chemical composition (wt. %)			Pt:$NiTiO_3$ ratio
			Pt	$NiTiO_3$	C	
Pt/C	1.4	2.2	16.39	-	83.61	-
Pt-$NiTiO_3$/C	1.7	2.3	10.37	8.65	80.98	0.95:1

TEM and HRTEM images of Pt/C (Figures 2 a-c) and Pt-$NiTiO_3$/C (Figures 2 d-f) have been analyzed shows the highly homogeneous dispersed nanoparticles of both electrocatalysts. The insert in figure 2(b) show the SAED analysis. A distance between lattice fringes of 0.22 nm attributed to the Pt(111) plane has been determinated [26, 27 de mi articulo]. The SAED pattern in figure 2(d) illustrates different rings of Pt-$NiTiO_3$/C. The average particle size of Pt/C is 2.2, while that of Pt-$NiTiO_3$/C is 2.3 nm (Figures 2(c) and 2(f), repectively).

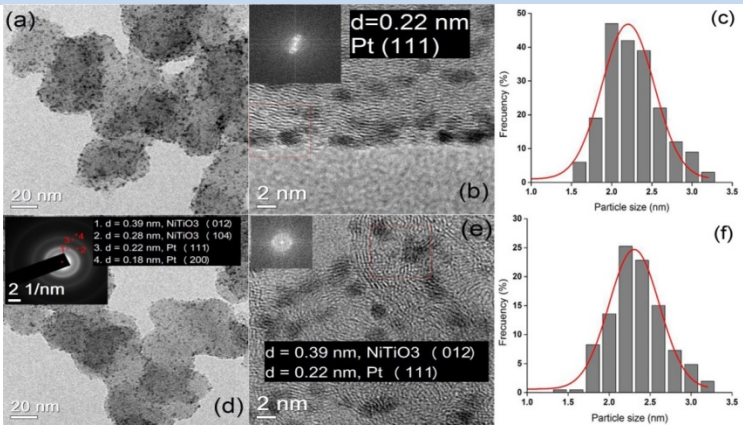

Fig. 2. TEM and HRTEM images of Pt/C (a-c) and Pt-$NiTiO_3$/C (d-e). The histograms of particle size distribution of each catalyst are shown in (c) and (f), respectively.

3.2 Electrochemical characterization and catalytic activity for the ORR

The CVs profiles of Pt/C and Pt-$NiTiO_3$/C (Figure 3) shows the characteristic regions of the Pt-based electroctalysts, i.e., the hydrogen adsorption/desorption ($H_{ads/des}$), double layer and Pt-oxides formation/reduction regions.

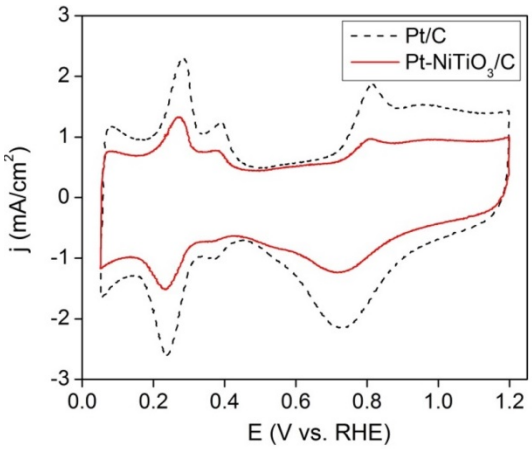

Fig. 3. CVs of the Pt/C and Pt-$NiTiO_3$/C catalysts. Ar-satured 0.5 M KOH electrolyte at a scan rate of 20 mV s^{-1}.

The ORR curves of Pt/C and Pt-$NiTiO_3$/C are presented in Fig. 4. The insert in each figure corresponds to the CVs obtained in Ar and O_2-satured electrolyte before current density correction. This results shows that the titanate-containing catalyst has a catalytic activity comparable to the monometallic material.

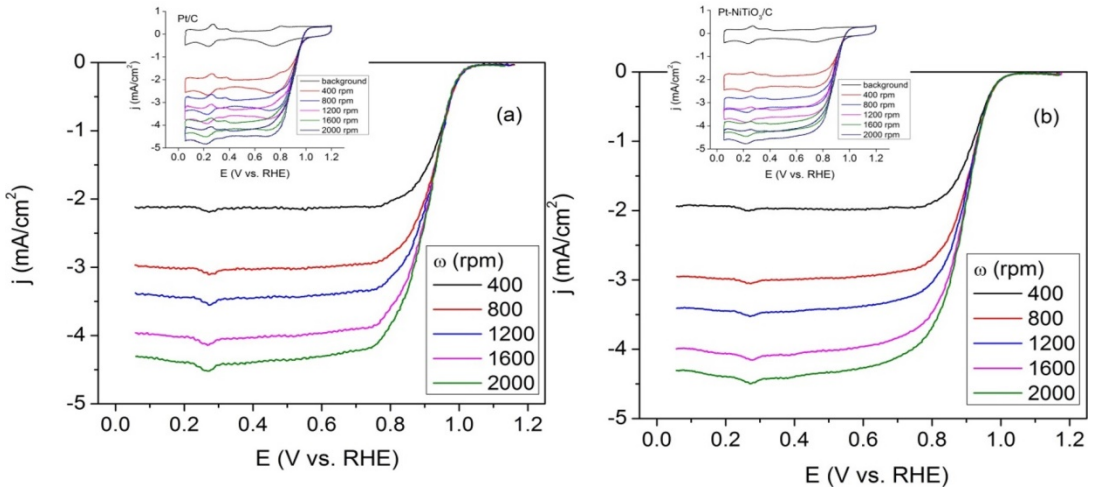

Fig. 4. Polarization curves for the ORR a) Pt/C and b) Pt-$NiTiO_3$/C catalysts obtained in O_2-satured 0.5 M KOH electrolyte at a scan rate of 5 mV s^{-1}. Inserts: CVs in Ar and O_2-satured electrolyte before current density correction.

The Koutecky-Levich plots of Pt/C and Pt-$NiTiO_3$/C at different potentials are presented in Fig. 5(a) and (b), respectively. The plots shows linearity and parallelism, indicating first-order kinetics with respect to O_2, which means that the number of electrons transferred during the ORR do not change within the potential range scanned [26-28]. In both cases, the plots fall close to that corresponding to a theoretical 4e- transfer slope (included in the figure). This indicates that the ORR in this catalyst follows mainly a process that involve a four electron transfer, meaning that the home-prepared Pt-$NiTiO_3$/C catalyst perform a nearly complete reduction of O_2.

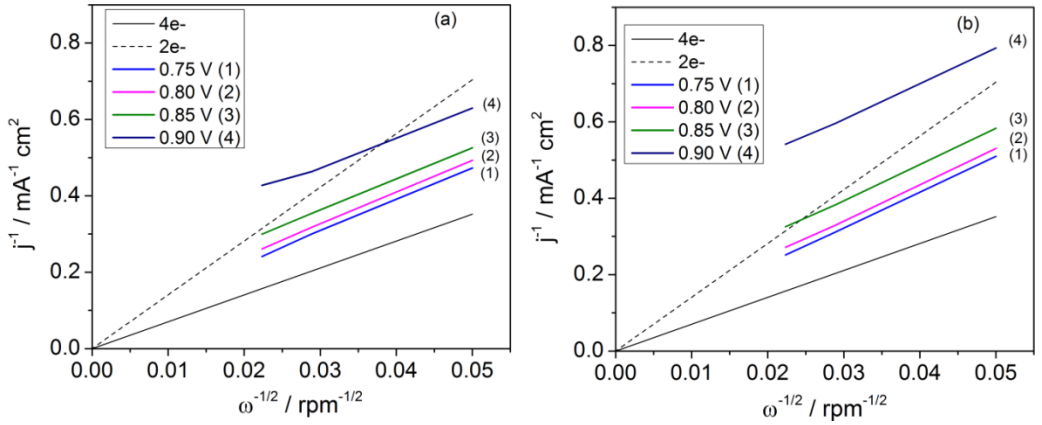

Fig. 5. Koutecky-Levich plots of the ORR at different potentials on: (a) Pt/C and (b) Pt-$NiTiO_3$/C.

3.3. Evaluation of tolerance of Pt/C and Pt-$NiTiO_3$/C to the presence of methanol and ethanol

It is well known that the Pt-based cathodes are depolarized by the presence of organic molecules, with a loss of catalytic activity of the cathode. Then, it is important to study the

electrochemical behavior of the catalysts in the presence of this substances. Fig. 6(a) and (c) show the polarization curves of Pt/C and Pt-$NiTiO_3$/C catalysts during the ORR in the absence and presence of 0.1 and 0.5 M CH_3OH and CH_3CH_2OH. At 0.5 M both catalysts show high current oxidation densities but clearly Pt-$NiTiO_3$/C is less active for oxidation of methanol and ethanol. At lower concentration of fuels, presented in figures (b) and (d), shows that the Pt/C catalyst show higher current densities corresponding to the oxidation of the organic substances than Pt-$NiTiO_3$/C.

These results indicate that the presence of titanate increases the catalytic selectivity towards ORR over methanol and ethanol oxidation.

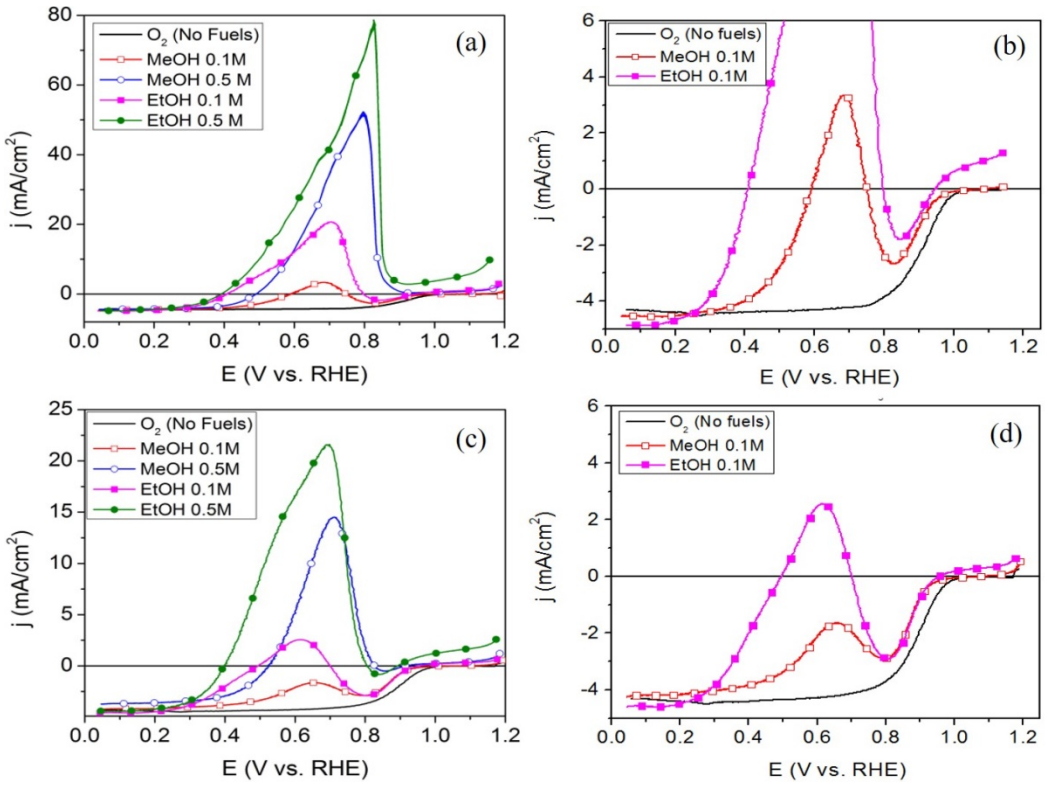

Fig. 6. Polarization of the ORR at different potentials on: (a) Pt/C and (b) Pt-$NiTiO_3$/C catalysts in the absence and presence of 0.1 y 0.5 M of CH_3OH and CH_3CH_2OH. A zoom of polarization curves with 0.1 M of MeOH and EtOH on: (b) Pt/C and (d) Pt-$NiTiO_3$/C. Scan rate 5 mV s-1 and ω= 2000 rpm in O_2-satured 0.5 M KOH electrolyte.

4. Conclusion

Nanostructured Pt-NiTiO3/C catalyst (Pt-NiTiO3 ratio of 0.95:1) was successfully shynthesized by the microwave-assisted poliol method. The catalyst showed homogeneously dispersed nanoparticles on the support. Its particle size was calculated in the order of 2 nm by XRD and TEM analysis. The catalytic activity of Pt-NiTiO3/C for the ORR in alkaline media (0.5 M KOH) was comparable with Pt/C. The Koutecky-Levich plots suggested that the mechanism on this catalyst follow a 4e- mechanism transfer leading to a nearly complete ORR. The tolerance tests demonstrates that a lower fuel concentrations

(0.1 M of methanol or ethanol) Pt-$NiTiO_3$/C catalyst can be a potential candidate as cathode material for A-DAFC applications.

Acknowledgements

The authors thank the Mexican Council for Science and Technology (CONACYT) for financial support through grants 252079, 241526 and 252003. We also thank the financial support from DST (Nano Mission) and DST (Indo-Mexican Bilateral programme), India. AHR acknowledge the support from CONACYT through the Doctoral scholarship.

References

[1] Gasteiger H., Kocha S., Sompalli B., Wagner, F. Activity benchmarks and requirements for Pt, Pt-alloy, and non-Pt oxygen reduction catalysts for PEMFCs. Appl. Catal. B: Environm. 2005; 56:9-35.
[2] Chen Z., Xu L., Li, W., Waje M., Yan Y. Polyaniline nanofibre supported platinum nanoelectrocatalyst for direct methanol fuel cells. Nanotechnology. 2006; 17:5254-5259.
[3] Zhao T,. Li S., Shen Y. Anion-exchange membrane direct ethanol fuel cells: Status and perspectives. Front. Enery Power Eng. 2010; 4:443-458.
[4] Tiwari J., Tiwari R., Sigh G., Sim K. Recent progress in the development of anode and cathode catalysts for direct methanol fuel cells. Nano Energy. 2013; 2:553-578.
[5] Krewer U., Koch T., Struckmann L. Electrochemical oxidation of carbon containing fuel and their dynamics in low temperature fuel cells. Chem Phys Chem. 2011; 12:2518-2544.
[6] Antolini E., Lopes T., González E. An overview of platinum-based catalysts as methanol-resistant oxygen reduction materials for direct methanol fuel cells. A. Alloy Compd. 2008; 461:253-262.
[7] Perry M., Fuller T. A historical perspective of fuel cell technology in the 20th century. J. Electrochem. Soc. 2002: 149:S59-S67.
[8] Merle G., Wessling M., Nijmeijer K. J. Anion exchange membranes for alkaline fuel cells: A review. Membrane Sci. 2011; 377:1-35.
[9] Lin B., Kirk D., Thorpe S. Performance of alkaline fuel cells: A possible future energy system?. J. Power Sources. 2006; 161:474-483.
[10] Slade R., Kisewski J., Poynton D., Zeng R., Varcoe J. Fuel Cells, Selected Entries from the Encyclopedia of Sustainability Science and Technology. New York. Springer; 2012.
[11] Corti H., Gonzalez E. Direct Alcohol Fuel Cells. Materials, Performance, Durability and Applications. New York. Springer; 2014.
[12] Li Y., Zhao T. A high-performance integrated electrode for anion-exchange membrane direct ethanol fuel cells. Int. J. Hydrogen Energy. 2011; 37:7707-7713.
[13] Yu E., Scott K. Development of direct methanol alkaline fuel cells using anion exchange membranes. J. Power Sources. 2004; 137:248-256
[14] An L., Zhao T. Performance of an alkaline direct ethanol fuel cell with hydrogen peroxide as oxidant. Int. J. Hydrogen Energy. 2014; 39:2320.2324.
[15] Carrete L., Friedrich K., Stimming U. Fuel Cells – Fundamentals and applications. Fuel Cells. 2001; 1:5-
[16] An L., Zhao T. An alkaline direct ethanol fuel cell with a cation exchange membrane. Energy Environm. Sci. 2011; 4:2213-2217.
[17] Antolini E., Gonzalez E. Alkaline direct alcohol fuel cells. J. Power Sources. 2010; 195:3431-3450.
[18] Varcoe J., Slade R., Wright G., Chen Y. Steady-state dc and impedance investigations of H2/O2 alkaline membrane fuel cells with commercial Pt/C, Ag/C, and Au/C cathodes. J. Phys. Chem. B. 2006; 110:21041-21049.
[19] Varcoe J. Slade R. Prospects for alkaline anion-exchange membranes in low temperature fuel cells. Fuell Cells. 2005; 5:187-200.
[20] Wang Z., Xin L., Zhao X., Qiu Y., Baturina O., Li W. Carbon supported Ag nanoparticles with different particle size as cathode for anion exchange membrane direct glycerol fuel cells. Renewable Energy. 2014: 62:556-562.

[21] Sigh R., Awasthi R., Sharma C. Review: An overview of recent development of platinum-based cathode materials for direct methanol fuel cells. Int. J. Electrochem. Sci. 2014; 9:5607-5639.
[22] Yu E., Krewer U., Scott K. Principles and materials aspects for direct alkaline alcohol fuel cells. Energies. 2010; 3:1499-1528.
[23] Xie S., Chen S., Liu Z., Xu C. Comparison of alcohol electrooxidation on Pt and Pd electrodes in alkaline medium. Int. J. Electrochem. Sci. 2011; 6:882-888.
[24] Demarconnay L., Countanceau C., Léger J. Electroreduction of dioxygen (ORR) in alkaline medium on Ag/C and Pt/C nanostructured catalysts - effect of the presence of methanol. Electrochimi. Acta. 2004; 49:4513-4521.
[25] Vijayalakshmi R., Rajendran R.. Effect of the reaction temperature on size and optical properties of $NiTiO_3$ nanoparticles. E-Journal of Chemistry. 2012; 9:282-288.
[26] Sekol R., Li X., Cohen P. Doubek G., Carmo M., Taylos A. Silver palladium core-shell electrocatalyst supported on MWNTs for ORR in alkaline media. Appl. Catal. B: Envirom. 2013; 138-139:285-293.
[27] Duron S., Rivera R., Nkeng P., Poillerat G., Solorza O. Kinetic study of oxygen reduction on nanoparticles of ruthenium synthesized by pyrolysis of $Ru_3(CO)_{12}$. J. Electroanal. Chem. 2004; 566:281-289.
[28] Meng H., Shen P. Novel Pt-free catalyst for oxygen electroreduction. Electrochem. Commun. 2006; 8:588-594.

Chapter 3.7. Synthesis and characterization Pt/WO_3 supported on CNT for oxygen reduction reaction

E. Oseguera[a,b]; C. Cortés-Escobedo[a]; R. de G. González-Huerta[b*]

[a]Centro de Investigación e Innovación Tecnológica del Instituto Politécnico Nacional, Cda. Cecati s/n, Col. Sta. Catarina, CP 02250 Azcapotzalco, D.F., Mexico
[b]ESIQIE-Instituto Politécnico Nacional, Laboratorio de Electroquímica y Corrosión, UPALM, CP 07738 DF, Mexico

ABSTRACT

In recent years, extensive research work has been carried out and reported on improving the performance of catalysts for both anode and cathode of polymer electrolyte membrane fuel cell (PEMFC). The electrochemical performance of cabon nanowall tubes (CNT) supported Pt–WO3 electrocatalysts was investigated. WO3 was tipically deposited from tungstate, the deposition of which is induced by a pH change according to the reaction $WO_4^{2-} + 2H^+ \rightarrow WO_3 \cdot H_2O$ by adding HCl. Platinum nanocatalysts on tungsten have been synthesized and characterized as catalysts for oxygen reduction reaction in 0.5 mol dm^{-3} H_2SO_4 solution, at 25 °C. Pt nanoparticle-tungsten trioxide/multi-walled carbon nanotube (Pt–WO_3/MWCNT) materials were synthesized by polyol method. These composite materials were employed as cathode electrocatalysts for oxygen reduction reaction (ORR). The surface morphology of the carbon nanotubes and the prepared catalysts was examined by scanning electron microscopy (SEM). The SEM images revealed the preferential growth of aligned MWCNTs. The support surface of Pt–WO3/MWCNT catalysts was characterised using Raman spectra. Their electrocatalytic properties toward the ORR were investigated in acid media using the rotating disk electrode (RDE) technique. The ORR activity of Pt–WO3/MWCNT was compared with that of commercial Pt/C catalyst. Pt/WO3/CNT catalysts exhibited better catalytic activity, expressed in terms of kinetic current density at the constant, in comparison with Pt/C catalyst.

Keywords: Multi-walled carbon nanotubes, Polyol method, PEM fuel cell

1. Introduction

Overcoming fuel cell commercialization and mass-production challenges by developing catalyst materials with satisfactory activity and stability is of great interest [1-2]. Several factors compromise the fuel cell durability, such as loss of conductivity, membrane degradation and corrosion of carbon support. These issues should be solved for further

---

* Author for correspondence: R. de G. González-Huerta, E: rosgonzalez_h@yahoo.com.mx

implementation in automotive fuel cell application. Fuel cell catalyst electro-active area decreases as a result of carbon support corrosion which leads to agglomeration and migration of Pt particles at potentials higher than 0.9 V vs. reversible hydrogen electrode (RHE) [3]. Therefore a great number of alternative catalyst support materials have been proposed in recent studies [1-2].

The development of CO-tolerant electrocatalysts and the lowering of Pt loading for cost-effectiveness are some of the critical issues facing commercialization of fuel cells [1–3]. The addition of a second or third metal has demonstrated to be effective in increasing performance as a function of Pt loading, as well as improving the resistance to CO poisoning. According to the bi-functional mechanism, the CO intermediate formed on the Pt sites can be oxidized by an oxygen-containing species on the neighbouring co-catalyst metal [2]. A promising cost-effective alternative is WO_3, which has been extensively studied for promoting the electrocatalytic activity of Pt. The costs saving effectiveness, however, should be compared in terms of both current and voltage output. Tseung's group demonstrated the hydrogen spill-over effect for typical fuel cell anode reactions on Pt/WO_3 electrocatalyst whenWO_3 forms a conducting, blue hydrogen tungsten bronze, H_xWO_3, when receiving protons in acidic media at the potential region of 0–0.55V vs. RHE, as shown in the reaction.

$$H_xWO_3 \leftrightarrow WO_3 + xH^+ + xe^- \quad (1)$$

The formation of H_xWO_3 has attracted attention due to its beneficial features, such as chemical stability in strong acids, pseudometallic conductivity and reversible redox transition [10]. In this work, this oxide is of particular interest since WO_3 surfaces catalyze reduction reactions, for instance the electroreduction of oxygen or methanol oxidation [1-3]. It is generally accepted that these properties arise from the presence of nonstoichiometric tungsten oxide species: hydrogen bronzes (H_xWO_3, $0 < x < 1$) and/or substoichiometric lower oxide (WO_{3-y}, $0 < y < 1$) [3]. The role of these centers seem to be related with its capability to extract oxygen atoms from the substrates and to increase hydrogen spillover [4]. The hydrogen spillover favors the formation of tungsten bronzes and increases the conductivity, therefore the transfer of electrons to the platinum active sites is also increased.

As tungsten oxide has limited electrical conductivity the electroactivity can be adversely affected when WO_3 is present as larger particles. This in turn may affect the promotion of Pt and the ability to remove CO.

In this study, WO_3/CNT nanocomposites were firstly synthesized is typically deposited from tungstate, the deposition of which is induced by a pH change according to the reaction

$$WO_4^{-2} + 2H^+ \rightarrow WO_3 \cdot H_2O \quad (2)$$

and Pt nanoparticles were then deposited onto the nanocomposites by polyol method using dyethylene glycol (DEG) as both the reducing agent and solvent to obtain $Pt–WO_3/C$ electrocatalysts. CNT with or without chemical treatment were employed as the support for the electrocatalysts. Influence of the preparation parameters of WO_3/C nanocomposites and

CNT supports on the morphology, ORR performances of the Pt–WO_3/C electrocatalysts were investigated. In this work, carbon nanotubes Pt–WO_3 electrocatalysts with 1:1 and 1:0.5 ratio compositions of Pt–WO_3 as weight percentage were compared.

2. Materials and Methods

Platinum dichloride ($PtCl_2$, 99%), dyethylene glycol (99.9+%), hydrochloric acid (37% solution in water), were obtained from Sigma-Aldrich. CNT pristine from Bayer AG as catalyst support.

2.1 Exfoliation treatment

Exfoliated carbon nanotubes (ex-CNT) were prepared by dispersing 0.25g CNT into 15 mL concentrated H_2SO_4, stirred for 1 hr and heated to 50 ° C. Then 1.5 g of $KMnO_4$ was added. When all the $KMnO_4$ was consumed, the reaction was quenched by adding 30 mL deionized water and 3 mL 30% H_2O_2. The ex-CNT were extracted by centrifugation, which was operated at 2500 rpm for 20 min to separate nanotubes and remove solvents in addition to eliminate oxidants were washed with deionized water.

2.2 Functionalization treatment

1g of CNT were dispersed in 50 mL solution 1:1 HNO_3-H_2O and heated to 120 °C in constant reflux for 2 hrs. Then they filtered, washed and dried at 80 ° C for 24 hours to obtain f-CNT.

2.3 Preparation of the WO_3/CNT nanocomposites, Pt/CNT and Pt–WO_3/CNT catalysts

WO_3/CNT was prepared as follows. Carbon nanotubes were first ultrasonically stirred with milli Q water (1 h). A stock solution with the tungsten species was added in the suspension and mixed 1 h. To precipitate tungsten trioxide WO_3, 4 mL of hydrochloric acid were added drop by drop and left under stirring 6 h. This synthesis process was performed at 80 °C. To obtain stable WO3/C, the resultant was transferred into a tubular oven and heat-treated at 400 ◦C for 2 h in air atmosphere. The substrate powder obtained was then used to deposit platinum particles by polyol method.

For catalyst Pt/CNT the desired Pt loading was 10 wt%. Briefly, $PtCl_2$ was dispersed in 80 mL DEG by sonication for 15 min, this solution was heated to boiling point (220°C) for 3 under continuous stirring. After cooled to room temperature, the mixture was filtered and washed thoroughly by ethanol, then dried at 100 °C for 2 h under argon atmosphere and the Pt/C electrocatalyst was obtained.

Preparation of Pt–WO_3/C was done as follows. First, an appropriate amount of $PtCl_2$ was dissolved in DEG solution, and then was thoroughly mixed with the WO_3/C support by sonication and agitation. The mixture was kept to boiling point (220 °C). Subsequently, the suspension was filtered and washed with deionized water, and then dried at 80 ◦C for 6 h to obtain the Pt–WO3/CNT (10%Pt/10%WO_3 wt%) and Pt–WO3/C-2 (10%Pt/5%WO_3 wt%) was prepared in the same way.

3. Results and Discussion

In Fig. 1 it is noted that the ex-CNT show generates higher current density in all potential range. Higher current density in the VC indicates a higher interfacial activity between the electrode and the electrolyte, also indicates a better catalyst support because a higher number of charged sites exists and these are closer to each other. Also the capacitance is directly proportional to the electrochemically active area that can provide support for the metal particles can anchor.

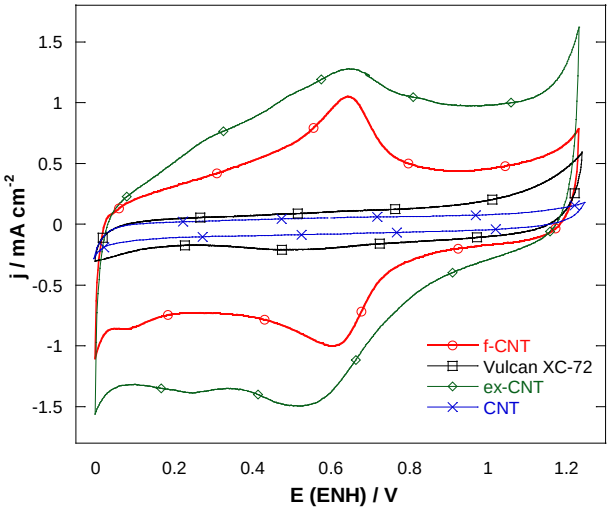

Fig. 1. Cyclic voltammograms support comparison.

VC profiles have two shoulders about 0.8 V, more marked in the NTC-f and ex-CNT. Such signals may be associated with pseudo-capacitive contributions of oxygenated functional groups present in the walls of treated CNT. The presence of oxygenated functional groups on the surface of carbon nanotubes affects the response of the VC, as the pseudo-capacitance increases as the number of oxygen functional groups on the surface is increased, some authors report that the signals observed in the f-CNT are because the carbonyl groups. These contributions, in acid medium, are governed by the equation:

$$C_xO + H^+ + e^- \leftrightarrow C_xOH \qquad (3)$$

The increase in the current-density profiles indicates the interfacial activity has increased, therefore more active electrode surface. Shoulders appreciated in ex-CNT and f-CNT show a pseudo-capacitive contribution.

TEM micrographies of catalysts 10%Pt/10%WO_3/f-CNT and 10%Pt/10%WO_3/ex-CNT are showed in Fig. 2. The metal phase distribution is observed, particles having spheroidal shape and show good dispersion in both micrographs. The ex-CNT sample has smaller size and better particle distribution respect to the sample supported on f-CNT. Figure 3 shows a comparison of the VC for catalysts 10%Pt/10%WO_3/f-CNT and 10%Pt/10%WO_3/ex-CNT, a similar behavior is observed, however by adding tungsten phase is a lower current density is obtained over the entire potential range, this is attributed to the tungsten is blocking active sites of platinum, which influence the catalytic activity of the RRO.

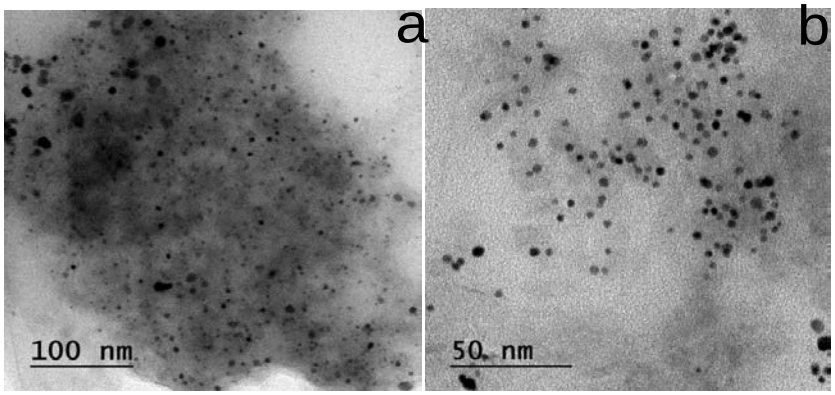

Fig. 2. TEM images 10%Pt/10%WO_3/f-CNT and 10%Pt/10%WO_3/ex-CNT catalyst.

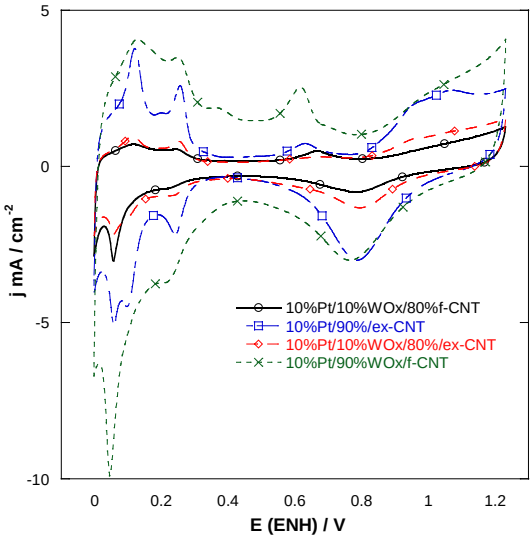

Fig. 3. Cyclic voltammogram catalyst comparison

For the kinetics of the reduction reaction of oxygen with tungsten catalysts linear voltammetry was obtained. Figure 4 shows the polarization curves at 1600 rpm, shows that the Pt-Etek showed a higher current density, reaching -2.7 mA cm^{-2} approximately, as already mentioned the higher current density, there active sites better distributed in the electrode surface adsorbing oxygen dissolved in the electrolyte to produce a reduced and subsequently faradaic current.

Tungsten catalysts have lower current density in the polarization curves, indicating lower catalytic activity, this is attributed to blocking of active sites by the tungsten which prevent carrying out the process of oxygen reduction so efficient, since according to the kinetic curves is slow and is not reached to have a reaction rate to provide a constant high overpotentials diffusional control.

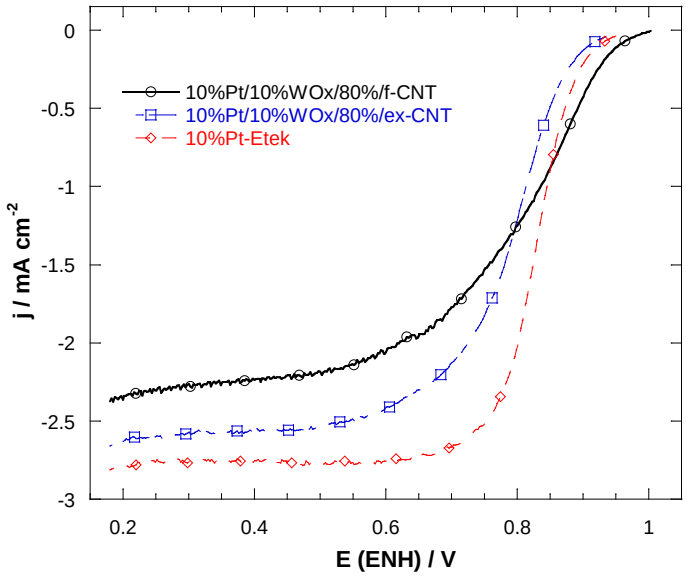

Fig. 4. Tungsten catalysts ORR polarization curves comparison.

4. Conclusion

10% wt Pt/CNT catalyst showed higher kinetic activity towards ORR, it was supported on carbon nanotubes with exfoliation treatment. 10%Pt/10%WO_3/f-CNT and 10%Pt/10%WO_3/ex-CNT electrocatalysts generated higher current density than commercially Pt-Etek. The synthesis of electrocatalysts with WO_x showed low catalytic activity towards ORR, which was attributed to the W-DEG complex is very stable and tough to reduce by polyol method, which obstructs platinum active sites.

Acknowledgements

This work has been supported by multidisciplinary project IPN-SIP 1683 and Programa Redes Temáticas CONACYT/RTH_2.

References

[1] K. Jukk, N. Kongi, A. Tarre, A. Rosental, A.B. Treshchalov, J. Kozlova, P. Ritslaid, L. Matisen, V. Sammelselg, K. Tammeveski Electrochemical oxygen reduction behaviour of platinum nanoparticles supported on multi-walled carbon nanotube/titanium dioxide composites Journal of Electroanalytical Chemistry 2014; 735: 68–76.

[2] Chunzhen Yanga, Nicole K. van der Laaka, Kwong-Yu Chana, Xin Zhang Microwave-assisted microemulsion synthesis of carbon supported Pt-WO_3 nanoparticles as an electrocatalyst for methanol oxidation Electrochimica Acta 2012; 75: 262–272.

[3] Kulesza PJ, Faulkner LR. Reactivity and charge transfer at the tungsten oxide/sulfuric acid interfaces: Nonstoichiometric tungsten (VI,V) oxide films as powerful electroreduction catalysts. Colloids and Surf 1989;41:123-134.

[4] Kulesza PJ, Grzybowska B, Malik MA, Galkowski M. Tungsten Oxides as Active Supports for Highly Dispersed Platinum Microcenters: Electrocatalytic Reactivity Toward Reduction of Hydrogen Peroxide and Oxygen. J Electrochem Soc 1997;1997: 1911-1917.

Chapter 3.8. $CoTiO_3$ deposited by laser ablation on a commercial alkaline membrane: electrochemical performance for the ORR reaction in alkaline media

R. Basurto Sánchez [a]., T. Romero Castañon[b], L.Escobar Alarcon[c], M. A. García Contreras[a], J. Bonifacio Martínez[a], E. Ordoñez-Regil, S. M. Fernández Valverde*.

[a] Depto. de Química, Instituto Nacional de Investigaciones Nucleares, A.P. 18-1027, Mexico D.F. C.P.11801, Mexico. Tel. 5553297200 ext 12277 [b] Gerencia de Energías No Convencionales, Instituto de Investigaciones Eléctricas (IIE), Av. Reforma 113, Col. Palmira 62490, Cuernavaca, Mor., México

ABSTRACT

Oxygen electrochemistry is at the basis of renewable energy technologies, one of the major challenges is the search of stable and high efficiency membranes-electrocatalyst for alkaline fuel cells. The objective of this work was to test the pulsed laser deposition (PLD) technique to prepare an assembly membrane-electrode with a commercial zirfon membrane and $CoTiO_3$ electrocatalyst obtained by Mechanical Alloying and tested for the Oxygen Reduction Reaction (ORR) in alkaline media. $CoTiO_3$ was synthesized by MA technique mixing Co_3O_4 and commercial titanium oxide. The physical and chemical characterization was done by: XRD in a Siemens D5000, SEM and EDX in a JEOL-JSM-5900 LB with an EDAX microprobe. Binding energies were determined in a Thermo Scientific K-Alpha XPS, BET analysis and pore diameter was obtained in a Bel Sorp max Bel Japan Inc. The ORR was performed in 0.5 M KOH solution, in a conventional three electrode cell; the reported current densities are referred to the geometric surface area of working electrodes. The specific area was $2.81x10^{-2}$ m^2g^{-1} and the total pore volume was $8.13x10^{-4}$, the current density was 6.5 $mAcm^{-2}$ at 0.8 mV and 1600 rpm. This value was constant for different experiments therefore $CoTiO_3$ is stable for the ORR. The Kinetic parameters are reported. Ti(III), TI(IV), Co(III) and Co(II) were determined by XPS.. This material was deposited on the zirfon membrane by PLD, the Raman spectra of $CoTiO_3$-zifon membrane of the deposited film correspond to $CoTiO_3$ structure assembly was tested in the same experimental conditions described before for the ORR.

Keywords: ORR in alkaline media, Alkaline membranes, $CoTiO_3$,Laser deposition

1. Introduction

One of the bigger tasks in fuel cell development is the search of good electrocatalysts for the oxygen reduction reaction; trying to achieve such an important goal have been many

---

*Author for correspondence: Dr. Suilma M. Fernández-Valverde, +52 01 55 53 29 72 00 ext. 12277
suilma.fernandez@inin.gob.mx

proposals. For the oxygen reduction reaction (ORR) platinum is still the leader metal, whether or not, combined in alloys [1-3], and supported upon different materials [4-5].
In the search of electrocatalyst for Alkaline Fuel Cells, oxides of transition metals is a very active field of research, this materials works in alkaline medium and can be more active than electrocatalysts for acid media [1,3,6]. The goal of this work was to test the pulsed laser deposition (PLD) technique to prepare an assembly membrane-electrode with a commercial zirfon membrane and CoTiO3 electrocatalyst obtained by Mechanical Alloying and test assembly for the Oxygen Reduction Reaction (ORR) in alkaline media

2. Materials and Methods

2.1 Synthesis of $CoTiO_3$

Mechanical alloying technique allows the synthesis of cobalt titanate as reported before, briefly mixing Co_3O_4 also obtained by mechanical alloying plus commercial titanium oxide and urea. After the alloying, the mixture was dried and heated at 900 ^{O}C.

2.2 Laser deposition of $CoTiO_3$ assambly zirfon-membrane

Thin films were grown onto commercial zifon membrane substrate at room temperature by pulsed laser deposition[7]. The targets were high purity $CoTiO_3$ powder pressed at 5 tons to make a disk of 2 mm thick and 13 mm diameter, then sinter at 500 ^{O}C during 2 h. Target and substrates placed inside a vacuum chamber with a turbomolecular pump yielding pressures close to $6x10^{-3}$ Pa. The $CoTiO_3$ target disc was rotated at 10 rpm with an electric motor to avoid depletion of material at any given spot. Substrates (zirfon membranes of different sizes) were placed 5.5 cm from the target to obtain homogenous films. The deposition time was 6 min. The energy source used in these experiments was a pulsed Nd:YAG laser with emission at the fundamental line (1064 nm) and 5 ns pulse duration. Deposits were performed at a laser fluence close to 3.5 J/cm^2 at a repetition rate of 10 Hz.

2.3. Physical and Chemical Characterization

2.3.1. Electrocatalyst

The electrocatalyst was characterized by X-ray diffraction (XRD) by using a diffractometer SIEMMENS D5000 with CuKα radiation. Morphology and particle size were analyzed employing a JEOL JSM-6300 scanning microscope (SEM), equipped with an energy dispersive X-ray analyzer (EDAX) microprobe. The specific surface area of the electrocatalyst was determined by N_2 adsorption with a BEL JAPAN apparatus, BELSORP

MAX-MP. Binding energies were obtained with a Thermo Scientific K-Alpha X-ray Photoelectron Spectrometer, with the Al Kα X-ray. The analysis was done with the Avantage software. Experimental peaks were decomposed into components using mixed Gaussian–Lorentzian functions and a non-linear squares fitting algorithm. Shirley background subtraction was applied. Binding energies were reproducible to within 0.2 eV and the C 1s peak at 284.6 eV was used as a reference from adventitious carbon.

2.3.2 Electrode assembly

Micro-Raman Spectroscopy characterized the target, deposited film and zirfon substrate. The Raman spectra recorded using an HR LabRam 800 system, equipped with an Olympus BX40 confocal microscope. A Nd:YAG laser beam (532 nm) was focused by an 50X microscope objective onto an ≈1μm diameter spot on the sample surface. The laser power at the sample was close to 1 mW. A cooled CCD camera was used to record the spectra, usually averaged for 20 accumulations in order to improve the signal to noise ratio. All spectra calibrated using the 521 cm^{-1} line of silicon.

.

2.3.3 Electrocatalytic activity measurements

The electrochemical performance for the ORR made in 0.5 M KOH solution in a conventional three- electrode cell coupled to an E&G Model 273 potensiostat/galvanostat. A unit for speed control E&G Model 636 used for linear voltammetry with a rotating disk electrode. The reported current densities referred to the geometric surface area of working electrodes. Circles of 0.5 cm of diameter were cut from the deposited membrane and put over a conductive Leit C carbon in a from Neubauer chemikalien over pressed graphite put inside Teflon cylinders with a concentric hole utilized as holders for working electrodes, the circle was fixed with a special glue and dried for 24 hours before electrochemical determinations.

4. Results and Discussion

The XRD pattern of the electrocatalyst is reported in **Fig. 1** all observed reflections corresponds to JCPDS card 00-015-0866 of $TiCoO_3$ however some reflections does not have exactly the same intensity of the diffraction pattern of the $CoTiO_3$. This difference can be attributed to preparation technique. The specific area determined by BET was $2.81X10^{-2}$ m^2g^{-1} and the total pore volume was $8.13X10^{-4}$.

The structure of $CoTiO_3$ as determined using the Crystal Maker software package with the lattice structure of iron titanate and changing the cobalt instead of iron is shown in **Fig. 2** The X ray diffraction pattern determined with the same softwere shows some little differences in the peak intensity in relation with that obtained with iron titanate.

The structure of $CoTiO_3$ as determined using the Crystal Maker software package with the lattice structure of iron titanate and changing the cobalt instead of iron is shown in **Fig. 2** The X ray diffraction pattern determined with the same softwere shows some little differences in the peak intensity in relation with that obtained with iron titanate.

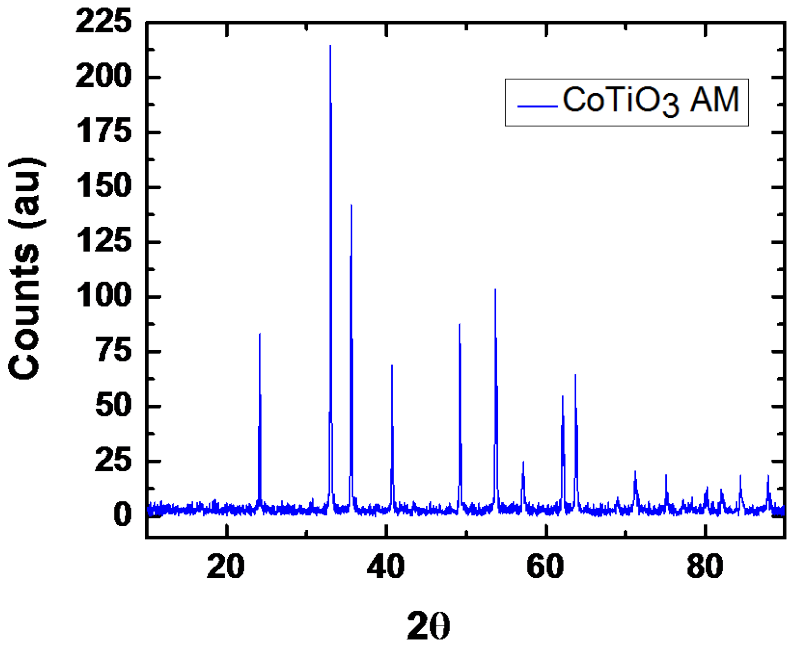

Fig 1. XRD diffraction pattern of $CoTiO_3$ obtained by mechanical alloying, corresponds to JCPDS card 00-015-0866 of TiCoO3

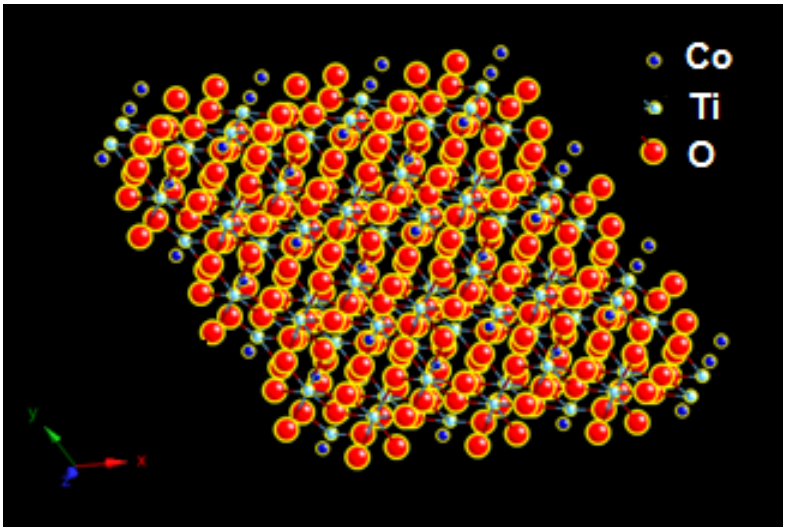

Fig. 2. Crystal structure of. $CoTiO_3$

Fig. 3 shows the SEM image of the $CoTiO_3$. This titanate is composed of nanometric particles of 63 nm forming micrometric agglomerates with sizes between 4.8 to 8.3 μM.

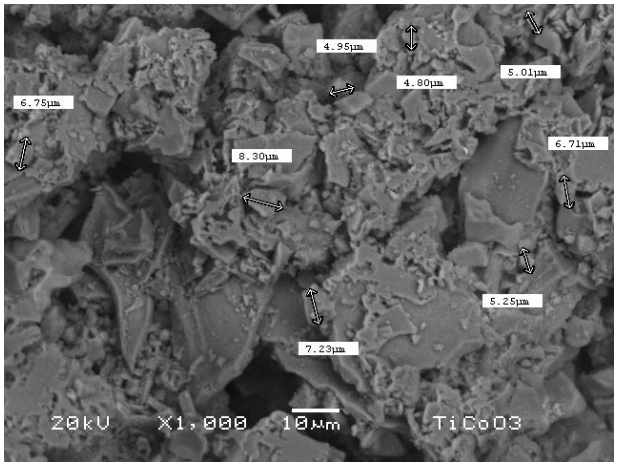

Fig. 3. SEM image of $CoTiO_3$

The chemical EDAX analysis only shows the energies of titanium cobalt and oxygen, in the atomic percentages corresponding to $CoTiO_3$

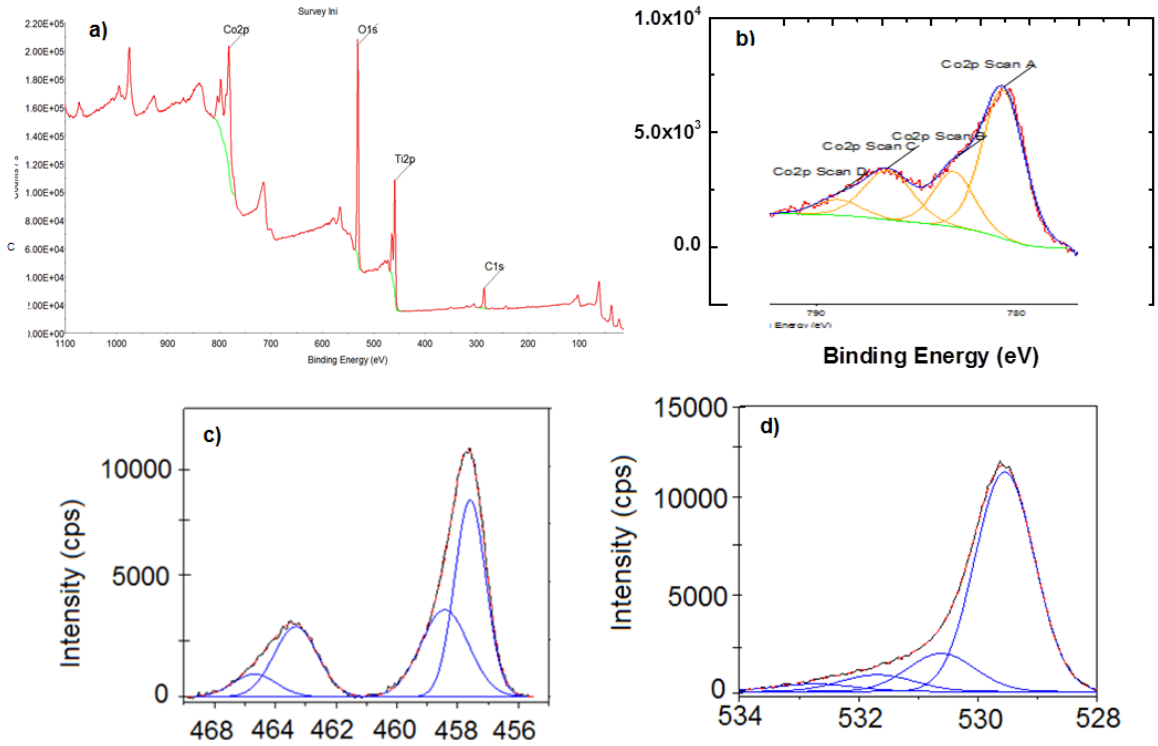

Fig. 4. X-ray photoelectronic spectra of $TiCoO_3$ a) Survey and b) Co 2p signal, c) titanium signal, and d) oxygen

The XPS of $TiCoO_3$ is shown in Fig. 4. The survey presents the binding energies of Ti, Co, O and adventicious carbon Fig. 4 a). The deconvolution of XPS spectra of cobalt in Fig. 4 b) shows the BE of Co(III) and Co(11). In titaniun deconvolution of Fig 4 c) the peak at 457.58 was asigned to the 3/2 p of Ti(III) and that of 458.42 to the 3/2 p peak of Ti(IV)[8]. The $TiCoO_3$ obtained by MA is a double mixed oxide compound of titanium and cobalt.

Figure 5 shows the Raman spectra corresponding to the deposited film (spectrum (a)), the $CoTiO_3$ target (spectrum (b)), and the zirfon membrane (spectrum (c)) the spectra agrees well with the tetragonal phase of ZrO3 [9]. The spectra of the film and target show the same Raman peaks at 209, 234, 265, 332, 383, and a strong Raman mode at 696 cm^{-1}. These signals agrees very well with the vibrational modes reported for $CoTiO_3$[8,10]. Some additional features, attributed to the zirfon membrane are observed in the Raman spectrum of the film, confirming the deposition of the $CoTiO_3$ in the same chemical form.

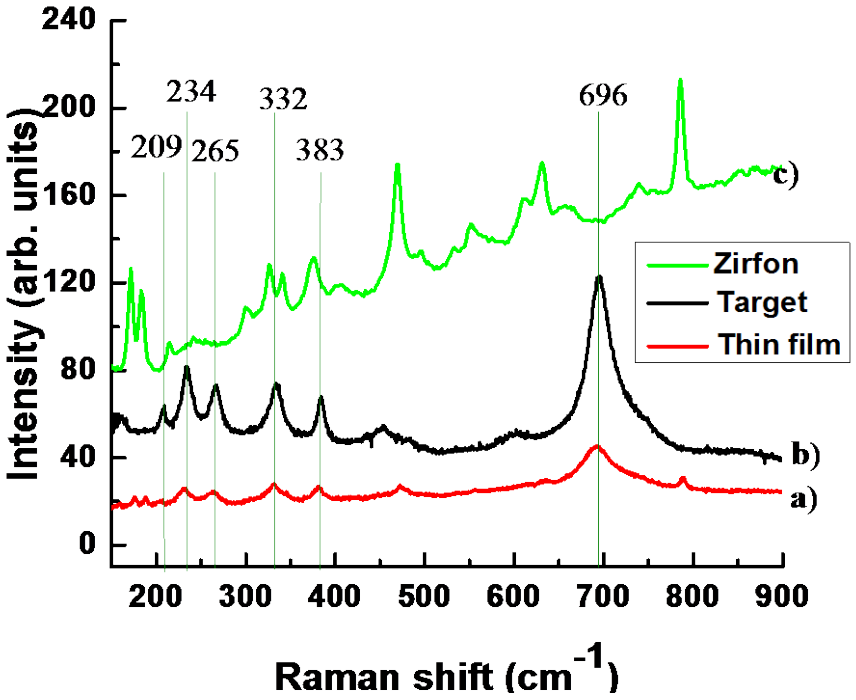

Fig. 5. Raman spectra of a) thin film, b) $TiCoO_3$ obtained by MA and zirfon commercial membrane

The linear scan voltammograms obtained for the catalysts at 25 ^{O}C are shown in **Fig. 6** at different revolutions per minute (RPM). In this figure, it can be seen that: the ORR on all catalysts is controlled by mixed diffusion kinetic in the potential region from- 0.05 to -0.5 V. $TiCoO_3$ and the current density was 6.5 $mAcm^{-2}$ at 0.8 mV and 1600 rpm. This value is equivalent to the best-reported current density for the ORR reaction.

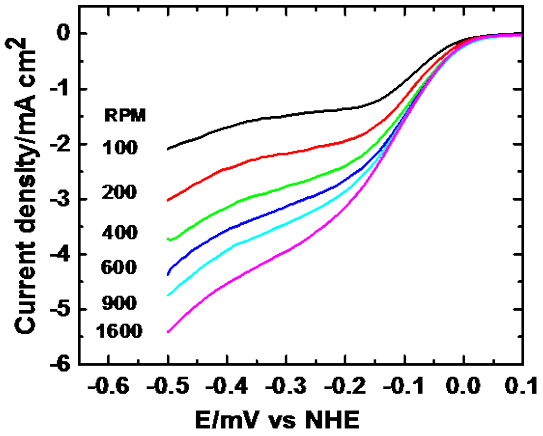

Fig. 6. Polarization curves for the ORR of $TiCoO_3$ at different rotation rates and T=25 ^oC

The kinetic parameters obtained or the ORR for both the TiCoO3 in Vulcan and for the assembly zirfon membrane-$CoTiO_3$ deposited by Laser are in **Table 1**. The exchange current density is higher for the assembly zirfon membrane-$CoTiO_3$ than that of $CoTiO_3$ in vulcan, the symmetry factor α and the Tafel slope are lower.

Table 1. Kinetic Parameters for the oxygen reduction reaction on $TiCoO_3$ in alkaline media

	Io ($mAcm^{-2}$)	α	b ($mVdec^{-1}$)
On Vulcan	**5.96×10^{-4}**	**0.25**	**239**
On zirfon membrane	**1.1×10^{-3}**	**0.2**	**69**

Finally, the linear scan voltammograms obtained for the assembly zirfon membrane - $TiCoO_3$ deposited by Laser at different temperatures and RPM are shown in **Fig 7.**

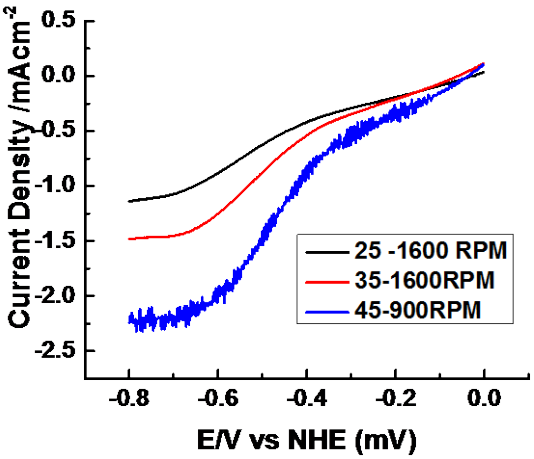

Fig.7. Polarization curves for the ORR on TiCoO3 - Zirfon at 25 ^OC, 35 ^OC and 45 ^OC

4. Conclusion

The obtained materials are nanocrystalline with a very good electrocatalyic activity for the ORR in alkaline media. The assembly has good performance for the oxygen reduction reaction in alkaline media; although the preparation of the electrode needs to be improved to increase, the current density also the changes observed in the electrode response with temperature needs to be clarified. Alternatively, the characterization in a single cell is the next research step.

Acknowledgements

ININ and CONACYT sponsored this work. Suilma M. Fernandez thanks the SMH and CONACYT for financial support. This work is part of Projects CB-906 and CB-304 of the Chemistry Department of the ININ. The authors thank the technicians of the chemistry laboratory at ININ for their technical help and J. Perez for SEM and EDAX analysis and Isidoro Martinez for the XRD diffraction spectra.

References

[1] Lima F. H. B., Salgado J. R. C., Gonzalez E. R., Ticianelli E. A.; Electrocatalytic Properties of PtCo/C and PtNi/C alloys for the Oxygen Reduction Reaction in Alkaline Solution; J. Electrochem. Soc., 154 _4_ A369-A375, 2007.

[2] Koh Sh., Yu Ch., Mani P., Srivastava R., Strasser P.; Activity of ordered and disordered Pt-Co alloy phases for the electroreduction of oxygen in catalysts with multiple coexisting phases; J. Power Sources 172, 50–56, 2007.

[3] García-Contreras, M. A. Fernández-Valverde. S. M, Basurto-Sánchez R. Investigation of oxygen reduction in alkaline media on electrocatalysts prepared by the mechanical alloying of Pt, Co, and Ni. J. Appl. Electrochem. In press juin 2015.

[4] Kim D.S., Abo Zeid E.F., Kim Y.T.; Additive treatment effect of TiO_2 as supports for Pt-based electrocatalysts on oxygen reduction reaction activity; Electrochim. Acta 55, 3628–3633, 2010.

[5] Vracar Lj.M., Krstajic N.V., Radmilovic. V.R., Jaksic M.M.; Electrocatalysis by nanoparticles – oxygen reduction on Ebonex/Pt electrode; J. Electroanal. Chem. 587, 99–107, 2006

[6] Xiaoming Ge X., Sumboja A., Wuu D., An T., Li B., Thomas Goh F.W., Andy Hor T.S., Zong Y., and Zhaolin L. Oxygen Reduction in Alkaline Media: From Mechanisms to Recent Advances of Catalysts; ACS Catal., 5, 4643–4667, 2015

[7] Chrisey, D.B., Hubler, G.K. (Eds.), Pulsed Laser Deposition of Thin Films, John Wiley & Sons, New York, 1994.

[8] Zhow G.W., Lee D.K., Young H.K., Woo Kan C., Soo Kang Y.; Preparation and characterization of Ilmenite-Type $CoTiO_3$ nanoparticles. Bull. Korean Chem. Soc. 27, 368-372, 2006.

[9] Naumenko A.P, Berezovska N.I., Biliy M.M., Shevchenko O.V. Vibrational Analysis and Raman Spectra of Tetragonal Zirconia Phys and chem of solid state. T. 9, № 1 C. 121-125, 2008.

[10] Baraton M. I., Busca G., Prieto M.C., Ricchiardi G., Sanchez Escribano V.; On the vibrational spectra and structure of $FeCrO_3$ and of the ilmenite-type compounds $CoTiO_3$ and $NiTiO_3$; J. of solid state chem. 112, 9-14, 1994.

4
Modeling and design

Chapter 4.1. Design of a microfluidic system in a PEMFC cell

L. M. Ponce-Herrera[a]; G. Carbajal-De la Torre[a*]; S. A. Gamboa-Sánchez[b]; K. Suarez-Alcantara[c]; M. Villagómez-Galindo[a]; M. A. Espinosa-Medina[a]

[a]Universidad Michoacana de San Nicolás de Hidalgo, Edificio W, Ciudad Universitaria, Francisco J. Mújica S/N C.P. 58030, Morelia Michoacán, México,(443)3223500 ext. 3148, gctorre@umich.mx.
[b]Instituto de Energías Renovables, UNAM, Priv. Xochicalco S/N Temixco C.P. 62580, Morelos México.
[c]Instituto de Investigaciones en Materiales, UNAM, Ant. Carretera a Pátzcuaro 8701 C.P. 58341, Morelia Michoacán, México.

ABSTRACT

In this paper, it is presented the design and simulation of a prototype proton exchange fuel cell (PEMFC) micro scale with the ultimate goal of providing electricity in mobile applications which are almost indispensable in our daily use development. A numerical analysis was done by simulating computational fluid dynamics flow field using the COMSOL Multiphysics software, taking into consideration that our fluid flow with a physical model of creeping flow (Re <400), with which reached analysis to find the pressure distribution and flow rate within two proposals flow plate coil geometric arrangement, concluding that would be used for further study of the proposals, the cell that is located a discarded pressure drop due to the arrangement of the flow plate, thereby achieving optimal distribution of the reagents on the active surface of the fuel cell to the proposed scale. Taking the final proposal plate electrochemical flow analysis was performed, making the assembly of the physical model using physical Secondary Current Distribution (SIEC) to assess the conservation of electric charge inside the cell and to evaluate conservation physical model species Reactive Flow in Porous Media (RFCs) for anode and cathode. To evaluate the electrical performance of the polarization curves given fuel cell were obtained, i.e. the graph cathode electric potential depending on the electric current density and the graph of the electrical power density based on the density electric current, with which the result and efficiency compared with the theoretical curve of a PEMFC cell polarization observed that achieved by the simulation results shown are acceptable.

Keywords: Proton exchange fuel cell (PEMFC), Creeping flow, Secondary current distribution (SIEC), Reactive flow in porous media (RFCs)

1. Introduction

The search for new sources of clean energy and replace fossil sources use has been extensively studied in recent decades (1). Considering fuel cells as a source of clean energy

---

* Author for correspondence:
G. Carbajal-De la Torre, T:(443)3223500 ext. 3148, E: gctorre@umich.mx.

generation, we have many choices within the same frame: (alkali fuel cell, AFC, phosphoric acid, PAFC, molten carbonate, MCFC, solid oxide SOFC) (2), in this paper proton exchange membrane is considered, PEMFC. PEMFC is considered one of the cells with greater efficiency for mobile devices, as it works at low temperatures (40-80 ° C), can use oxygen as fuel and high current density (1) compared to electrochemical cells business.

With the aim of mobile applications in the past decade there have been efforts for technological research to release a miniaturization and thereby improve the electrochemical performance (3). For PEMFC mobile application as already mentioned, it is important to generate high current densities which can achieve adequate hydration of the membrane, the distribution of reagents and materials that make the (4; 5; 6; 7; 8), among other conditions.

Computational fluid dynamics (CFD) has become a powerful tool for the simulation and optimization of fuel cells, allowing us a good fit between the physical operation involving, as is the distribution of anode current and cathode transport of species between porous media (5) and thereby achieve an improvement in future models.

This research focuses on the design of a microfluidic system in a PEMF cell, for which is considered important for the performance of it by changing the geometry several studies have been conducted on this topic: parallel and interdigitated flow arrangements, serpentine shape (9; 10; 11; 12; 13; 14), more complex designs such as the Sierpinski (circular shape) (15) and the Hilbert fractal shape (16). The geometric arrangement showing better performance is the serpentine in which we are working with, as it has a better distribution of reactive and therefore its consumption also in water management is improved with this arrangement (17).

Taking into account the literature on the geometrical arrangement of flow plates will start with two settlement proposals serpentine, with the difference between each start for the distribution of reagents within them, using elbow 90 in one and the other radial side, showing by this falling pressure and thereby determine pressure drops within them, having chosen a final proposal is reached the electrochemical analysis and obtain the polarization curves of the cell.

The structure of the article is as follows: in the second section will be given a description and modeling of PEMFC, in the third section the model results and conclusions are presented.

2. Design of the micro-PEMFC and model description.

In Fig. 1, the composition of the two proposals micro PEMFC, which consist of 6 layers each shown. Prototypes are drawn using SolidWorks® as shown listed: 1 and 6, flow plate engraved in a polymer " Polymethyl methacrylate " with a depth of 300μm and 300μm width; 2 anode gas diffusion layer of carbon paper hydrophobic with no less than 200μm thick; 3 catalyst plate formed by a plate load of 0.5 mg/cm^2; 4 perfluorosufonada Nafion® 117 membrane with a thickness of 180μm; 5, cathode gas diffusion layer of hydrophobic carbon paper weighing less than 200μm thick.

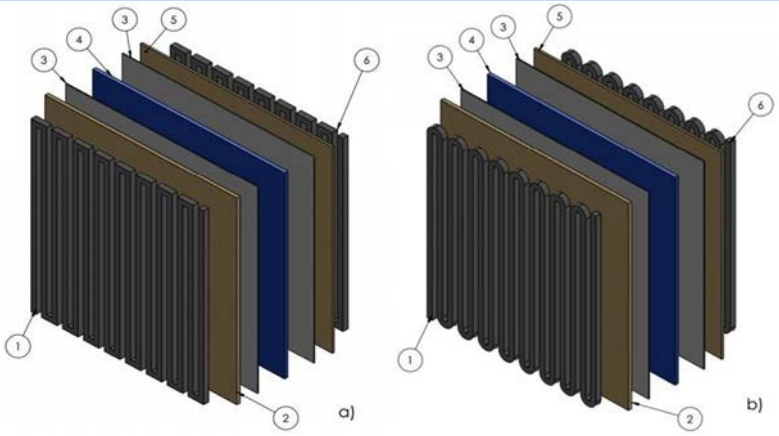

Fig. 1. Isometric view of a cell PEM a) 90° elbow serpentine shape, b) radial elbow serpentine shape.

The flow plate has 17 channels, the channel to rib ratio CR = 1, i.e. the channel and the width of post is 300μm, aspect ratio AR = 1, the active area of the plate flow A = 1cm^2, electronic conduction area is 0.5 cm^2, the total length of the channels is L≈162mm, for the hydraulic connection commercial stainless steel needle of 0.8 mm diameter are used.

Influencing phenomena involved in the operation of the PEMFC are mass transport of different species (H_2, O_2, H_2O, N_2), fluid flow, the electrochemical reaction and heat transfer.

To make the mathematical model are partial differential equations that describe the phenomena described above, for which the following assumptions are made:

- steady state,
- ideal gas,
- one phase (gas phase),
- isotropic materials,
- isothermal behavior,
- laminar flow (Re<400),
- incompressible flow.

2.1 Hydrodinamic Considerations.

In the analysis and design of the plates the hydrodynamic analysis was performed, considering that the size of the channels is comparable with, λ, mean free path of the gas molecules with the Knudsen number, Kn, determine the degree of thinning of gas, and the characteristic length, L, which is equal to the hydraulic diameter, Dh, (18) the above terms can relate to the Eq. 1 (19):

$$Kn = \frac{\lambda}{L} \qquad (1)$$

To calculate the number of Knudsen you can get from the logarithmic plot of the Knudsen number based on the hydraulic diameter of microchannels different shown in Fig. 2 (20):

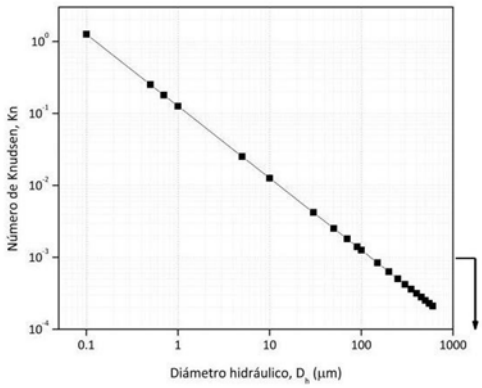

Fig 2. Log plot Knudsen number based on the hydraulic diameter of different microchannels.

In conventional thermodynamic systems in which gas at standard conditions of temperature and pressure are used , the characteristic length is much greater average free path of the gas , and the Knudsen number is essentially zero. For such systems , the physical domain is large compared with the mean free path of the fluid, $L >> \lambda$, for which can be seen as an ongoing matter where their local properties can be determined from the averaged value of the molecular properties such as mass, velocity and energy.

2.2 Governing differential equations.

To start with the equations governing the model of micro-PEMFC, we have the following conservation equations: Eq. 2 of conservation of mass and Eq. 3 Momentum conservation.

$$\nabla * u = \frac{Q}{\rho} \tag{2}$$

$$\rho u * \nabla u = \nabla\{-pI + \mu[\nabla u + (\nabla u)^T]\} \tag{3}$$

where u, is the velocity of the gas mixture (m/s), ρ is the mixture density (kg/m^3), Q, is the source term (kg/m^{3}s), p, is the pressure (N/ m^2), and μ, is the dynamic viscosity of the mixture (kg /m s) which is calculated using Eq. 4 (21):

$$\mu = \sum_{\bar{i}} x_{\bar{i}}\, \mu_{\bar{i}} \tag{4}$$

In the gas diffusion layer (GDL), the pressure drop is proportional to the gas velocity if the flow is laminar, and is modeled as Eq. 5 (21):

$$(\mu/\kappa)u = \nabla\{-pI + (1/\varepsilon)\mu[\nabla u + (\nabla u)^T]\} \quad (51)$$

where κ, is the permeability of the GDL (m^2) and ε, is the porosity of the GDL.

Multispecies mass transport is in whole computational domain, including flow channels and gas diffusion layer which are described by the Stefan-Maxwell equation. Which resolves flows in terms of mass fraction. The general form of the Stefan-Maxwell equation shown in Eq. 6 (21).

$$\nabla\left\{-\rho w_i \sum_{j=1}^{N} D_{ij}\left[\frac{M}{M_j}\left(\nabla w_j + w_j\frac{\nabla M}{M}\right) + \left(x_j + w_j\right)\frac{\nabla P}{P}\right] + w_i\rho\vec{u}\right\} = R_i \quad (6)$$

where D_{ij}, is the binary diffusion coefficient, x, is the mole fraction, w, is the mass fraction, M, is the molar mass, R, is the universal gas constant (8.314 J/mol K), T, is the operating temperature of the cell (K), ρ, it is the density of the gas mixture, which is described by Eq. 7 (21).

$$\rho = \left(\sum_i x_i\,\mu_i\right)P/(R * T) \quad (7)$$

Subscripts i and j represent different species, R_i, is the reaction rate, which explains reagent consumption and product production during the electrochemical reactions in the catalyst layer, for calculating the R_i is used Eq. 8 (21).

$$\begin{aligned} R_{H_2} &= -\frac{j_a}{2F}M_{H_2} \\ R_{O_2} &= -\frac{|j_c|}{4F}M_{O_2} \\ R_{H_2O} &= -\frac{|j_c|}{2F}M_{H_2O} \end{aligned} \quad (8)$$

On the cathode side, only the oxygen and water mass fraction is replaced, since the third species can always be obtained from mass balance Eq. 9 (21).

$$w_{N_2} = 1 - w_{O_2} - w_{H_2O} \quad (9)$$

On the anode side, the mass fraction of hydrogen thereby obtain the mass fraction of water as is used Eq. 10 (21).

$$w_{H_2O} = 1 - w_{H_2} \quad (10)$$

The D_{ij} binary diffusion coefficient used in the Stefan-Maxwell equation is calculated from an empirical correlation with Eq. 11 (22).

$$D_{ij} = D_{ij\_0}\left(\frac{T}{T_0}\right)^{1.5} \quad (11)$$

where T_0 is the reference temperature and D_{ij-0} is the binary diffusion coefficient reference. In porous media binary effective diffusion coefficient amending Eq. 12 to take into account the effect of the porosity of the GDL, is calculated with Eq. 12 (23).

$$D_{ij} = D_{ij\_0}(\varepsilon)^{1.5} \quad (12)$$

In a PEMFC, the current can be divided into two parts: ion current and the electron current. When protons travel through the membrane to form an ion current, while the electrons are transferred only through the solid matrix of electrodes, which is an electronic current. The current continuity equations are obtained using Ohm's law, which is in Eq. 13 (21).

$$\nabla * (-\sigma_s \nabla * \phi_s) = S_s$$
$$\nabla * (-\sigma_m \nabla * \phi_m) = S_m \quad (13)$$

Where ϕ, is the potential phase, σ, is the effective conductivity (S/m), S, is the density of volumetric flow rate (A/ m^3), the subscript s indicates the characteristic of the solid phase while m, the membrane. The terms equations based on electron and proton transport are the result of the electrochemical reaction, which occurs only in the catalyst layers of both anode and cathode, and are obtained with Eq. 14 (21).

$$Capa\ Catalizadora\ ánodo\ \ S_m = j_a \qquad S_s = -j_a$$
$$Capa\ Catalizadora\ ánodo\ \ S_m = j_c \qquad S_s = -j_c \quad (14)$$

where j_a and j_c are the current density transfer corresponding to the electrochemical reaction in the catalyst layers of the anode and cathode, respectively.

The source terms in both species and load equations are related to the current density transfer (j_a and j_c) and is calculated by Eq. 15 and Eq. 16, the Butler- Volmer equation (21).

$$j_a = ai_{0,a}^{ref}\left(\frac{C_{H_2}}{C_{H_2 ref}}\right)^{0.5}\left(\frac{\alpha_a + \alpha_c}{RT} F\eta_a\right) \quad (15)$$

$$j_c = ai_{0,c}^{ref}\left(\frac{C_{O_2}}{C_{O_2 ref}}\right) exp\left(-\frac{\alpha_c}{RT} F\eta_c\right) \quad (16)$$

Where η represents the power differential between the solid matrix and the electrolyte and is defined by Eq. 17 (21).

$$\text{Ánodo: } \eta_a = \phi_s - \phi_e$$
$$\text{Cátodo: } \eta_c = \phi_s - \phi_e - U_{oc} \quad (17)$$

2.3 Computational Method

To solve the above equations numerically, it was used COMSOL Multiphysics® software, which based its solution in finite element computer model discretizing the elementary volumes. The mesh of the computational model was performed using a structured mesh, using a free tetrahedral for the section of the channels, making a refined corners because elbows of geometry, to the remaining section a type of triangular mesh free was used because geometry has less complexity (see Fig. 3).

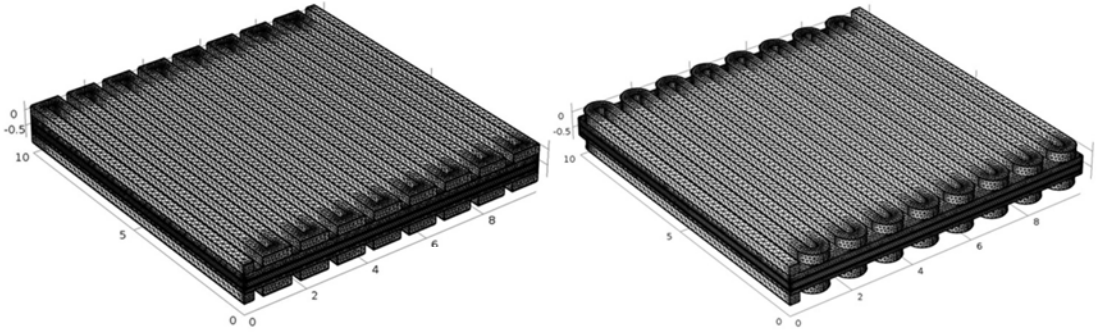

Fig. 3. Isometric view of structured mesh, a) 114273 elements 90° elbow serpentine shape b) 466 061 elements radial elbow serpentine shape.

2.4 Boundary and initial conditions

For operation of the cell, it has an inlet volumetric flow rate of 1.667E-7 m^3/s applied to H_2 and O_2. H_2 a mass fraction of 0.8 at the anode, to O_2 and H_2O respectively 0.2 and 0.1 in the cathode. A pressure of 1 atmosphere, at 27 °C it has which are operating conditions of the cell.

3. Simulation results and discussion

Using the parameters and properties as mentioned above (geometry and materials), the pressure distribution analysis was performed on the section of the channels, using a volumetric flow Q = 10 ml/min, which is the influence of known form of settlement between the coil forms (elbow 90 degrees and radial elbow). These results are not considered electrochemical reactions.

In Fig. 4 the distribution of pressure (static) in the channels, in which one can observe the scale contours shown the static pressure gradient (a) was 2215-0 Pa and if (b) it was to 2186-0 Pa, applying greater pressure drop in (a) unlike (b) with which we can conclude that the pressure drop can provoke flooded channels, would affect FC performance.

In the analysis of the dynamic pressure, the pressure gradient (a) a zero pressure drop is observed at the corners of the model, furthermore a more stable pressure within the channel (b) behavior were reported (see Fig. 5).

With this study of pressure distribution within a single cell we conclude that determining a geometry where the pressure drop is less, being part plate flows critical to the performance of the cell. When choosing a suitable geometric arrangement we will ensure that the reagents within the cell ARE as long as possible within the same and that is made more effective chemical reactions.

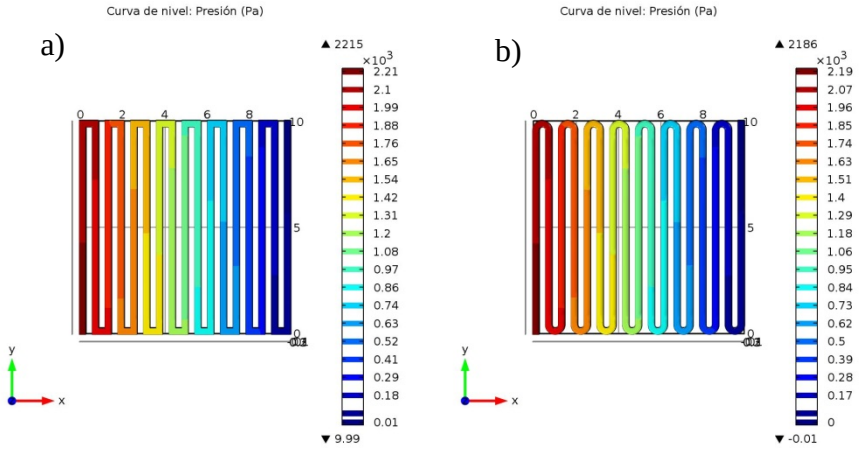

Fig. 4. Contours of static pressure a) 90° elbow serpentine shape b) radial elbow serpentine shape.

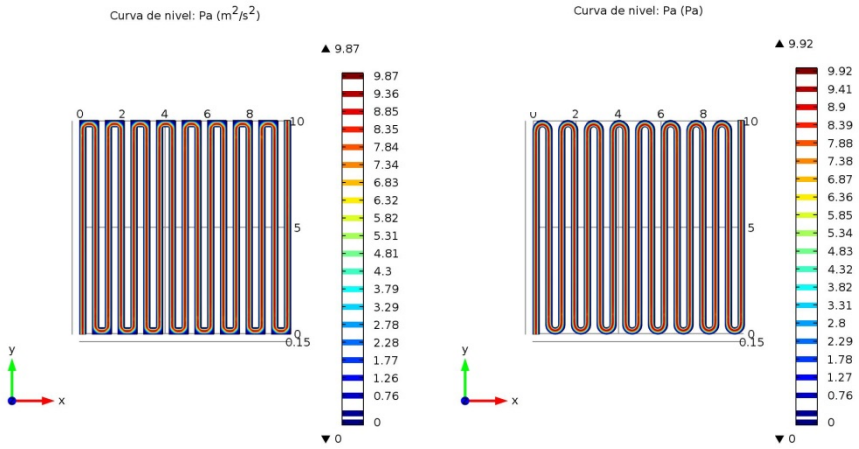

Fig. 5. Contours of dynamic pressure a) 90° elbow serpentine shape b) radial elbow serpentine shape.

References

[1] Sammes, Nigel. *Fuel Cell Technology: Reaching Towards Commercialization.* Springer Science & Business Media, 2006.

[2] C., Mandil. Prospects for Hydrogen and Fuel Cells. International Energy Agency, 2005.

[3]. Wang Y, Chen KS, Mishler J, Cho SC, Cordobes Adroher X. *A review of polymer electrolyte membrane fuel cells: technology, applications, and needs on fundamental research.* Appl Energy. 981-1007.

[4] Jiao K, Li X. *Water transport in polymer electrolyte membrane fuel cells.* Prog Energy Combust Sci, 2011; 37: 221-91.

[5] C, Siegel. *Review of computational heat and mass transfer modeling in polymer-electrolyte-membrane (PEM) fuel cells.* Energy, 2008, 33: 1331-52.

[6] Wang XD, Duan YY, Yan WM, Peng XF. *Local transport phenomena and cell performance of PEM fuel cells with various serpentineflow field designs.* J Power Sources, 2008, 175: 397-407.

[7] Wang XD, Zhang XX, Yan WM, Lee DJ, Su A. *Determination of the optimal active area for proton exchange membrane fuel cells with parallel, interdigitated or serpentine designs.* Int J Hydrogen Energy, 2009, 34: 23-32.

[8] Wang XD, Huang YX, Cheng CH, Jang JY, Lee DJ, Yan WM. *Flow field optimization for proton exchange membrane fuel cells with varying channel heights and widths.* Electrochim Acta, 2009, 55: 22-30.

[9] Tüber K, Oedegaard A, Hermann M, Hebling C. *Investigation of fractal flow-fields in portable proton exchange membrane and direct methanol fuel cells.* J Power Sources, 2004, 131:75-81.

[10] Yan WM, Li HY, Chiu PC, Wang XD. *Effects of serpentine flow field with outlet channel contraction on cell performance of proton exchange membrane fuel cells.* J Power Sources, 2008, 178: 74-80.

[11] Huang CH, Chen LY, Kim S. *An inverse geometry design problem in optimizing the shape of the gas channel for a proton exchange membrane fuel cell.* J Power Sources, 2009, 187: 36-47.

[12] Wang XD, Huang YX, Cheng CH, Jang JY, Lee DJ, Yan WM. *An inverse geometry design problem for optimization of single serpentine flow field of PEM fuel cell.* Int J Hydrogen Energy, 2010, 35: 47-57.

[13] Lobato J, Canizares P, Rodrigo MA, Pinar FJ, Mena E, Ubeda D. *Three-dimensional model of a 50 cm2 high temperature PEM fuel cell. Study of the flow channel geometry influence.* Int J Hydrogen Energy, 2010, 35: 10-20.

[14] Wong CW, Zhao TS, Ye Q, Liu JG. *Experimental investigations of the anode flow field of a micro direct methanol fuel cell.* J Power Sources, 2006, 155: 1-6.

[15] Chang JY, Kuan YD, Lee SM, Lee SR. *Characterization of a liquid feed direct methanol fuel cell with sierpinski carpets fractal current collectors.* s.l. : J Power Sources, 2008, 184: 80-90.

[16] Kuan YD, Chang JY, Lee SM, Lee SR. *Characterization of a direct methanol fuel cell using Hilbert curve fractal current collectors.* s.l. : J Power Sources, 2009, 187:12-22.

[17] Imran S, Xianguo L. *Review of bipolar plates in PEM fuel cells: flow-field designs.* 2005, 30: 359-371.

[18] Emerson, R.W. Barber & D.R. *The influence of Knudsen number on the hydrodynamic development length within parallel plate micro-channels.* Southampton, UK : Advances in Fluid Mechanics IV, 2002, 207-216.

[19] George Karniadakis, Ali Beskok, Narayan Aluru. *Microflows and Nanoflows: Fundamentals and Simulation.* s.l. : Springer, 2005. 0-387-22197-2.

[20] *Fabrication and characterization of a micro-fuel cell made of metallized PMMA.* J.A. Alanís-Navarroa, C. Reyes-Betanzob, J. Moreirac, P.J. Sebastiana. Journal of Power Sources, 2013, 242: 1-6.

[21] *Three-Dimensional Modeling and Experimental Study of a High Temperature PBI-Based PEM Fuel Cell.* E. U. Ubong, Z. Shi, X. Wang. Journal of The Electrochemical Societ, 2009, vol. 156.

[22] R. B. Bird, W. E. Stewart, and E. N. Lightfoot. *Fenomenos de Transporte* . John Wiley & Sons, 1960.

[23] Buchlin, J. Bear and J. M. *Modelling and Applications of Transport Phenomena in Porous Media.* Boston : Kluwer Academic, 1991. 978-94-010-5163-7.

Chapter 4.2. Design and analysis of photovoltaic-hydrogen system for illumination and fuel cell characterization

J. Olmedo-González[a*]; R. de G. González-Huerta[a]; M. Tufiño-Velázquez[b]; G. Contreras-Puente[b]

[a]ESIQIE-IPN, Laboratorio de Electroquímica y Corrosión, UPALM, CP 07738, México, D.F.
[b]ESFM-IPN, Laboratorio de Física Avanzada, UPALM, CP 07738, México, D.F.

ABSTRACT

At the present time hydrocarbon resources are the principal source of energy. However, they have not been friendly to the environment and we have to consider that the demand of energy has been growing in the last decades. So, it is so important to develop new ways to produce energy. Renewable energy sources such as solar or wind energy are cleaner than hydrocarbon/fossil fuel based energy, and they could satisfy the demand of energy, when the energy is administered in a correct way. One of the problems of these primary sources is the intermittence; H_2 could be a good solution for this problem. In this work is proposed a photovoltaic-hydrogen system, in the hybrid system photovoltaic modules are used to provide energy for a PEM electrolyser producing hydrogen and oxygen gases through the water electrolysis, gases produced are stored in a variable volume tanks, so they are supplied into a PEM fuel cell to generate electrical energy. The design was developed in order to produce enough hydrogen for the two requirements, illumination or for analyses of new PEM fuel cells. It was considered the period of time for illumination and the flow rate of hydrogen and oxygen that the new PEM fuel cells could require. The analysis of the system was based on material and energy balances. It shows the period of time for gases production and it permits understand their efficiency and efficacy of the system. It was found that the system has a good behaviour when it is designed in order to be a flexible system, it improve the use of energy produced increasing its efficacy. Storing part is really efficient because auxiliary energy to store gases is not necessary.

Keywords: Photovoltaic-hydrogen system, PEM fuel cell applications, Hydrogen Storage

1. Introduction

We live in a world where technology is growing rapidly and society increasingly depends on this, it is very important to innovate in sustainable energy sources in order to

---

* Author for correspondence:
J. Olmedo-González, T:+52 5527092864; E: jolmedog0900@alumno.ipn.mx

satisfy the energy demand, therefore it permits to reduce emission pollutant gases that create problems for the development of flora and fauna.

We have the challenge of the optimal development of primary energy sources such as wind and solar energy, which due to its natural intermittency is necessary to develop ways to correct this problem, in relation to a constant demand of electricity by society.

However, it is so important to understand and take into account that society have to learn the correct manage of electricity consumption in relation to the capacity power generation systems with these characteristics compared with power generation systems that is based in hydrocarbons.

Storing the electrical energy produced by the photovoltaic system (PS) promises to be a solution to the intermittence of the primary source, the sun. It is possible to store this energy as a hydrogen (H_2) using, in this case, a PEM electrolyser (PEME) which produces hydrogen and oxygen (O_2 and H_2) of high purity from electrolysis of the water.

In order to have a feasible process at least H_2 and in some cases like this the O_2 must achieve to be stored safely and efficiently under the predetermined conditions of use by the system, which in the proposed system is at conditions of temperature and pressure of Mexico City.

The main goal of storing energy as H_2 is generating electrical energy with PEM fuel cells (PEMFC), according to a predetermined user demand. The proposed system allows to analyse the production of electrical energy to power a PEMFC for two luminaries. However, the system also allows to evaluate and characterize different PEMFC's helping this to become friendlier with the environment.

That is why the analysis of the performance of each of the stages of this hybrid system is of great importance, allowing to understand the challenges of design and adaptation necessary for an efficient, effective and safe use.

The study of each of the equipment allows to understand their behaviour at different operating conditions thus achieving determine optimum operating conditions, increasing the efficiency and effectiveness of the system.

2. Materials and Methods

It was developed a PV-hydrogen hybrid system in order to illuminate a work area for the development of PEM fuel cells (PEMFC) and for the analysis in a test bench of these in the Sustainable Energies laboratory at Escuela Superior de Ingeniería Química e Industrias Extractivas IPN.

The system is explained in five main stages for further analysis. The first step is the generation of electricity by a PS.

The primary source is the sun and it is used a PS, which was designed based on the study of the energy required by the PEME and the behaviour of sunlight in Mexico City, where the average peak sunlight is 5 hours, it showed in figure 1.

Mexico City has an acceptable geographic position to capture sunlight, one of these reasons is that it is near of the equator, where daylight hours are relatively constant in all seasons and months therefore peak hours of sunlight either do it, which it allows a stable PS.

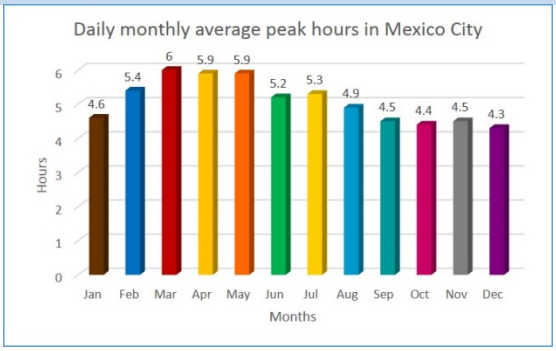

Fig. 1. Daily monthly average peak hours in Mexico City

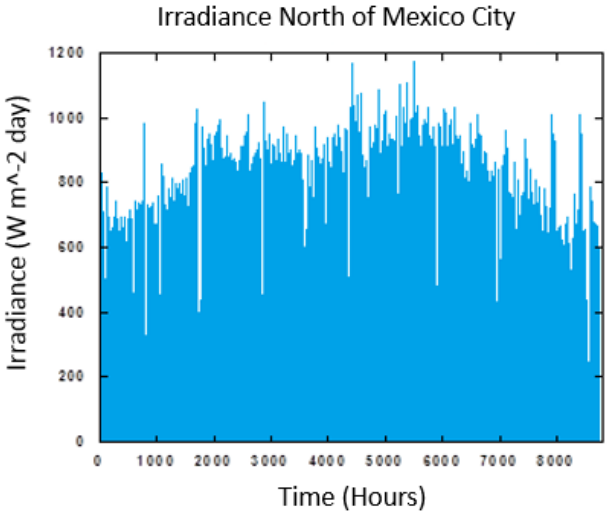

Fig. 2. Irradiance in north of Mexico City

It was studied the irradiance in the north of Mexico City where is located the university as we can see in figure 2. This information permits to understand the maximum and minimum energy that the PS is able to produce during the year, where the average is 800W m^{-2}.

The PS consists of 6 modules of polycrystalline silicon (rigid panels) of 85 W each one, these modules are connected in a series-parallel arrangement to produce 510 W at optimum sunlight and they are able to generate 2.55KWh / day when the irradiance is 1000W m^{-2}. The PS type island, which is independent of the mains, it requires a DC/DC regulator, an inverter and batteries only to achieve steady power generation during the period of the hydrogen production. The efficiency and effectiveness of PS in Mexico City was studied in relation to the electrical behaviour with PEME.

The electrical specifications of the solar panels, DC/DC controller and inverter are presented in Table 1.

Table 1. Electrical Specifications of PS

Electrical Performance under Standard Test Conditions each panel		DC/DC Regulator	
Maximum Power	87W (+10%/ -5%)	Nominal Voltage	12/24V
Maximum Power Voltage	17.4V	Maximum Current	20A
Maximum Power Current	5.02A	Inverter	
Open Circuit Voltage	21.7	Output Voltage	120VAC
Short Circuit Current	5.34A	Output Frequency	60Hz
*STC: Irradiance 1000W/m^2 AM1.5 Spectrum, module temperature 25°C			

The second step is the generation of H2 and O2, which are produced with a commercial PEME (Peak Scientific PH300), this device produces H_2 in a range of 30 to 300ml min-1 at pressures from 7 kPa to 827 kPa, with consumption of 340W, alternating current (AC).

The proper analysis of the internal elements, especially the electrolytic cell (EC) is essential to understand the behaviour of the PEME that works with AC in order to adapt it in a correct way. The elements are illustrated in Figure 3 and described in Table 2.

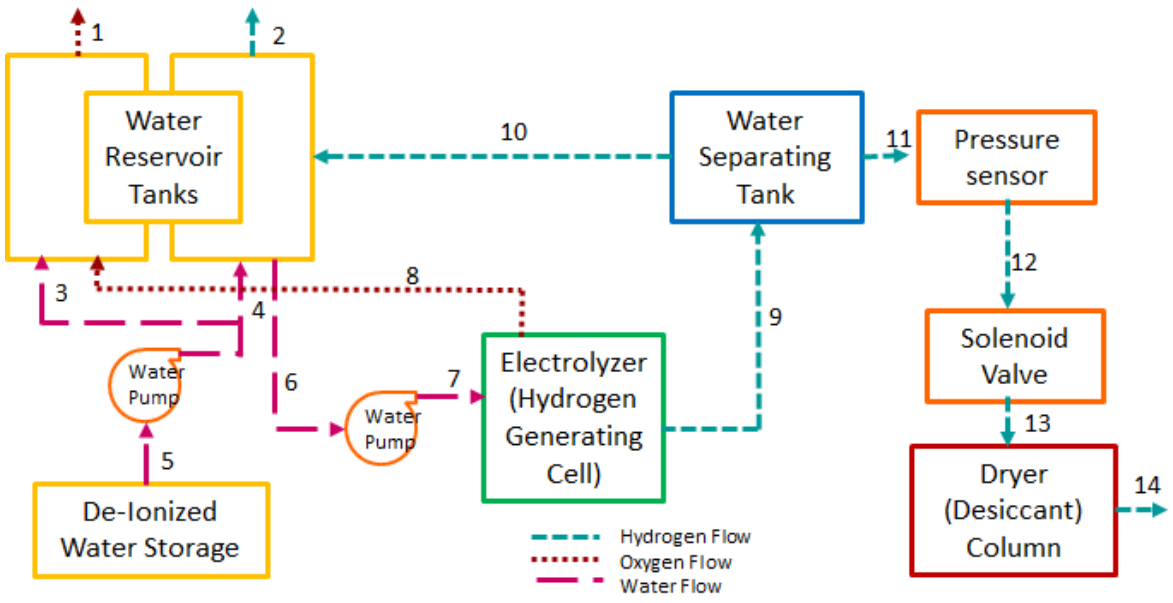

Fig 3. PEM Electrolyser PEAK Scientific PH300 System

EC behaviour was analysed, obtaining performance curve current vs voltage (VvsI) at different pressures, it was also analysed the quantity of H_2 produced as a function of the current applied into the EC (Flow vs. current) at different pressures., which was evaluated with the Michael Faraday law, equation 1.

$$m = ItEe \quad (1)$$

Table 2. PEM electrolyser PEAK Scientific PH300 System

Flow	Typology	Flow	Typology	Flow	Typology
1	O_2 Delivery	6	H_2O	11	H_2
2	H_2 Vent	7	H_2O	12	H_2
3	H_2O	8	$O_2 + H_2O$	13	H_2
4	H_2O	9	$H_2 + H_2O$	14	H_2 Delivery
5	H_2O	10	$H_2 + H_2O$		

for this case of study, where
m is the mass of H2 produced; I is the applied current; t is the time; and Ee is the electrochemical equivalent

It expresses *"The mass in grams of a substance deposited or released is directly proportional to the current intensity and the duration of electrolysis"*.

The third stage is the storage of H_2 and O_2. The storage system (SS) was designed in relation with the demand of the PEMFC, it is worth noting that the H_2 has the highest energy content per unit of weight, but not per unit volume. This relatively low volumetric energy content is an important scientific and technological challenge for store H_2. The H_2 storage system stationary may occupy a relatively large volume and it is able to operate at lower temperatures and pressures where the refuelling time can be large, in the right conditions. The SS was designed in order to save energy, storage systems such as pressurized tanks at high pressures requires a compressor to store the gases entails to increased energy consumption, likewise hydride systems for storing H_2 are really efficient however, these systems are often expensive and require significant care, these are the reasons that it was designed a variable volume system at Mexico City conditions (25 ° C, 585mmHg).

The SS illustrated in Figure 4 is composed of a main acrylic manufactured container which contains water, within this two floating capsules are of the same material, where H_2 and O_2 are stored in each one of these. System capacity is 15 l of O_2 and 30l of H_2. The system was designed in order to be safe as the water protects gases to escape through the bottom of the container. Connections were designed especially for the safe handling of H_2, based on the Hydrogen Technologies Code NFPA standard.

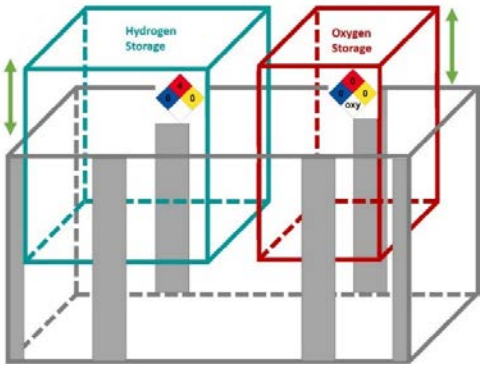

Fig 4. Storage System

The residence time or duration of the gases in the SS according to consumption was analysed, allowing to understand the operating time of the PEMFC proposed to lighting and the time available for analysis of different PEMFC's according to the consumption of these in the analyses tests. The power available by the H_2 stored in the SS according with the environmental conditions was analysed.

The fourth step is the generation of electricity by the PEMFC's, the system was designed to operate a PEMFC which was designed at the CINVESTAV-IPN Zacatenco by a group of experts in the area.

PEMFC comprises a bipolar plates, outer plates, membrane electrode assemblies (MEA) and gas diffusion layers (GDL). Among the constituents of the PEMFC, the bipolar plate is a key component that collects and conducts current from cell to cell. The bipolar plates and end plate are of low porosity graphite.

The PEMFC designed for this project (Figure 5) contains 20 individual cells, each with an active area of 0.0035m2. The cells are stacked in a series configuration with current collectors placed in the anode and cathode sides. The components considered in the volume size restriction are: end plates, current collectors, bipolar plates, all seal materials and MEAs. The dimensions of the PEMFC are 0.13mx 0.075 m 0.140 m when it is fully assembled, its weight is 1.6 kg.

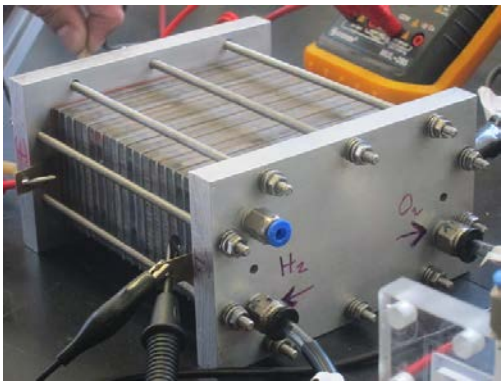

Fig 5. PEM Fuel Cell

PEMFC is expected to consume 800 ml min-1 of H2 and 400ml min-1 O2 at a pressure of 0.45 bar to generate 50W of power. It was designed an automatic regulation system of gases in to the PEMFC, which enables different PEMFC's for future experiments having a constant and controlled feed.

It was analysed and confirmed the generation of electricity supply with different gas flows, taking into account that these are based on current consumption in relation with Michael Faraday law, equation 1.

The fifth step consists in the electrical charges energized by the PEMFC which in this case is two LED lamps of 25W each one with a predetermined time interval work. Power consumption LED lamps was analysed in relation to the amount of energy that the PEMFC can provide. It permits to determine the adjustments required by the system for proper operation.

The five principal steps of the global system are showed in the schematic diagram, figure 7, and described in table 3 where the different connections and lines have been detailed that de global system requires for a correct and safe operation.

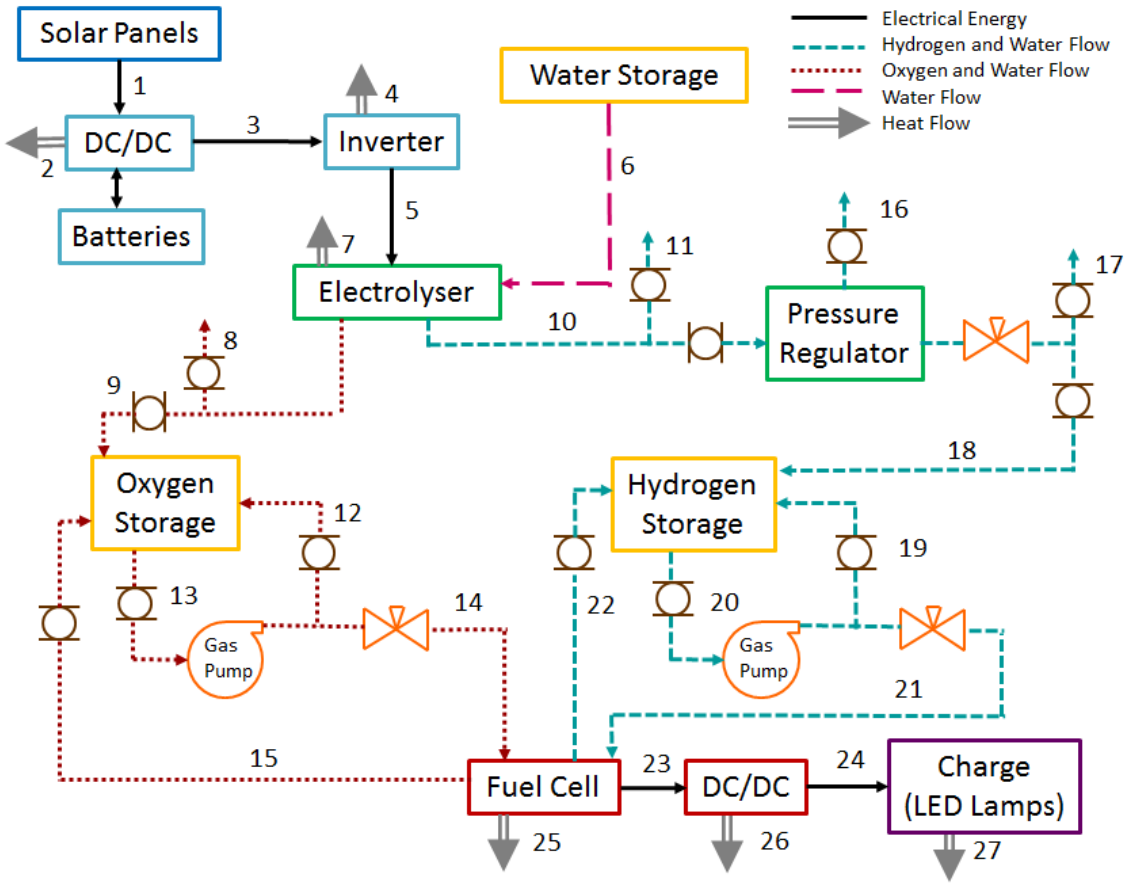

Fig 7. Photovoltaic-hydrogen system schematic diagram

Table 3. Information of photovoltaic-hydrogen system schematic diagram

Flow	Typology	Flow	Typology	Flow	Typology
1	Electrical Energy	10	H_2	19	H_2 Recirculation
2	Heat Flow	11	Purge	20	H_2
3	Electrical Energy	12	O_2 Recirculation	21	H_2 Regulated
4	Heat Flow	13	O_2	22	$H_2 + H_2O$ Recirculation
5	Electrical Energy	14	O_2 Regulated	23	Electrical Energy
6	H_2O	15	$O_2 + H_2O$ Recirculation	24	Electrical Energy
7	Heat Flow	16	Purge	25	Heat Flow
8	Purge	17	Purge	26	Heat Flow
9	O_2	18	H_2	27	Heat Flow

In colour blue is shown the first step PS, in colour green the second step the PEME, in colour yellow the third step SS, in colour red the fourth step PEMFC and the fifth step in colour purple the charges.

3. Results and Discussion

It was found that the PS is able to produce energy for the presented requirements, the PEME, in relation with the insolation in the location where the hybrid system is developed, we found that the system is able to produce 417.6Wh owing the average insolation is 800 W m^{-2}. It is important to mention that this capacity could be higher or lesser depending on the weather each day.

PS energy demanded by the PEME was analysed, which is the consumption by the EC and the auxiliary energy, it is showed in Figure 8. It was obtained that the period of time that the PEME operates is 4.7 hours each day.

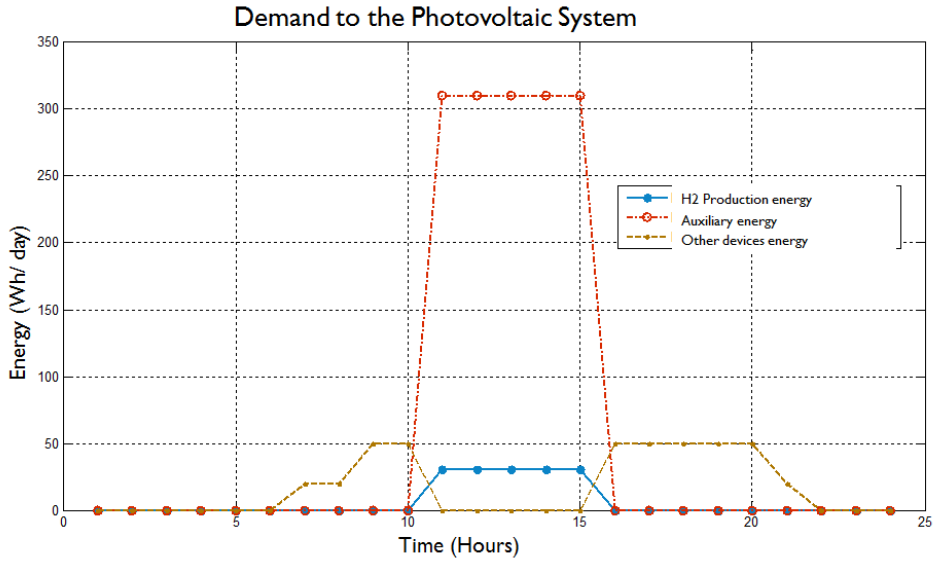

Fig 8. Demand to the photovoltaic system

The PEME works with AC increasing the energy consumption in relation with a direct current (DC) PEME. In Figure 8 we can observe the energy consumed by the PEME only for H_2 production compared to the charge of the auxiliary energy conversion from AC to DC and the control system, which turns out to be much higher than required only for 90ml min-1 of H_2 production.

In figure 9 we can see the relation between auxiliary power consumption with respect to the consumption of energy used for producing H_2 at different production flow rates of H_2.

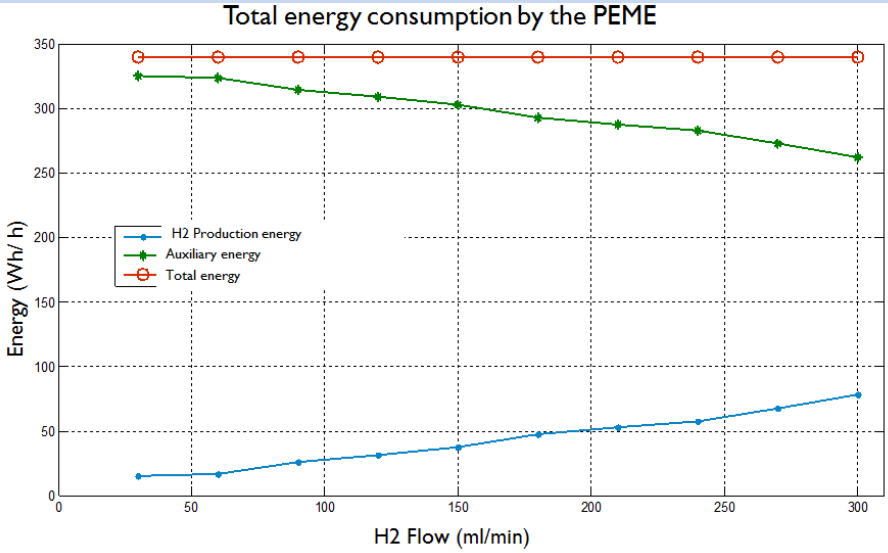

Fig 9. Total energy consumption by the PEME

This analysis proves to be of great importance, it determines that the implementation of a DC PEME is more suitable than one that works with AC. However, the energy required for the conversion from AC to DC is not directly involved with the production of hydrogen, which can be omitted with the PEME efficiency analysis.

The electrical behaviour of the PEME was studied at three different pressures and different flows, Figure 10.

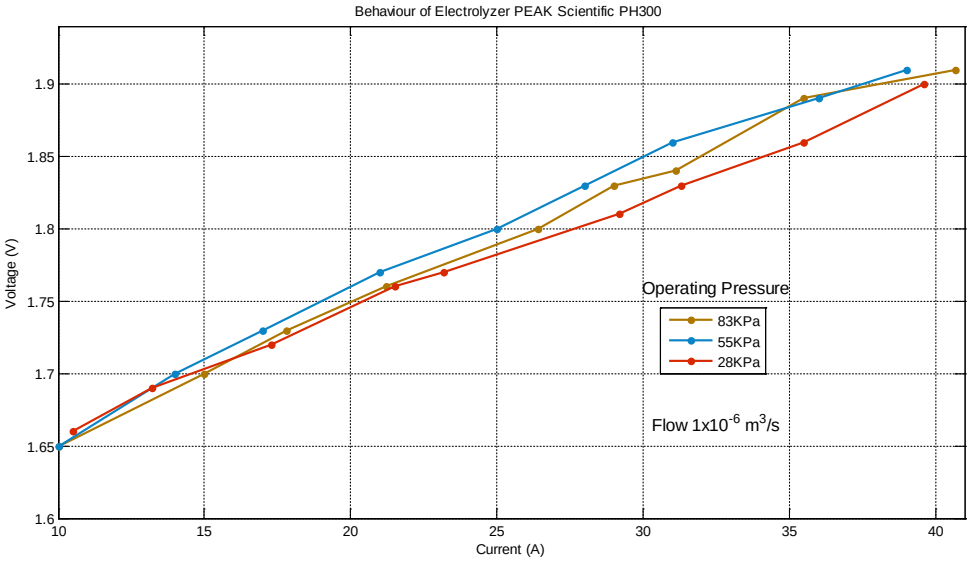

Fig 10. Electrolyser PEAK scientific PH300 electrical behaviour

Based on Figure 10 it is shown that the behaviour of current versus voltage in H_2 production at different pressures is very similar, so the H_2 gas production is not dependent on the system pressure, corroborating thus Michael Faraday's Law described in equation 1.

The curves in Fig. 10 also permit to understand the energy required to produce H_2 complementing with figure 11.

Hydrogen production as a function of the current applied to the EC was studied, obtaining H_2 production depends on the current supplied in this, being directly proportional as shown in Figure 11.

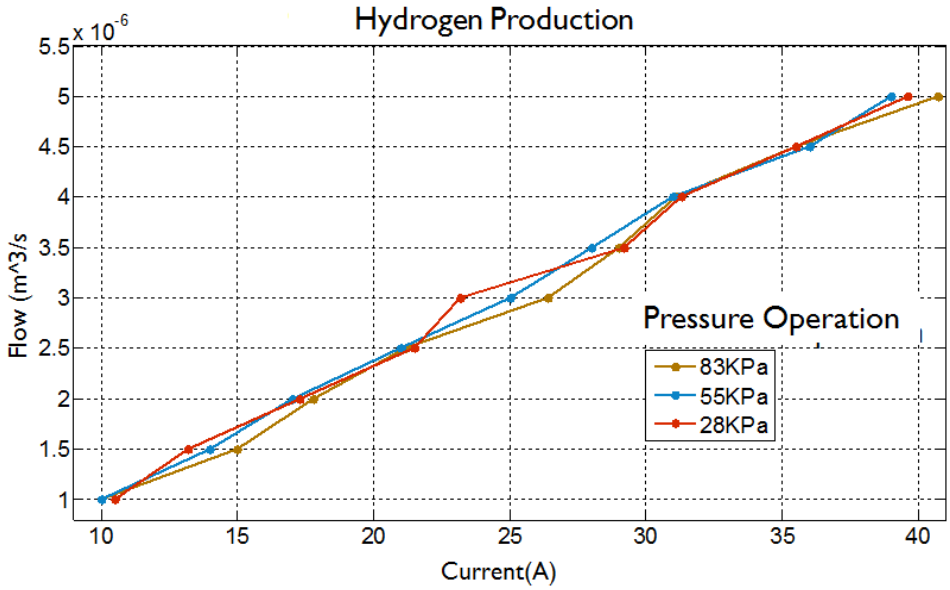

Fig 11. Hydrogen production

It was determined that the current variation is given by internal electronics in relation to the pressure difference between the desired pressure and the actual pressure.

It was found that the PEME is really important to operate between 10% and 30% of hydrogen production, 30-90 ml min-1, for safety and durability of the equipment. In consideration with this and with the PS capacity the PEME has to work for 4.7 hours to fill the SS.

The development of the graphic shown in Figure 12 allows to understand the time available regarding H_2 consumption of the SS. This graph is of great importance when using the SS for analyses of different PEMFC's, which come to have different gas consumption in relation to the power and type of loads connected on them.

We can observe that the PEMFC for lighting, with the proposed conditions is able to operate for 45 minutes which are appropriate for the work because it is used in illumination for a few time. When it is used for analyses of PEMFC's we found that the SS is suitable for PEMFC that requires 600 ml min^{-1} of H_2 or less. However depending on the analysis the system could operate with greater flows of 600 ml min^{-1} of H_2.

H_2 storage is a technological challenge, it is one of the most important factors to consider for proper sizing of H_2 systems.

It was analysed the available power of H_2 stored in the SS according to the environmental conditions shown in Figure 13. It is so important to note that system analysis

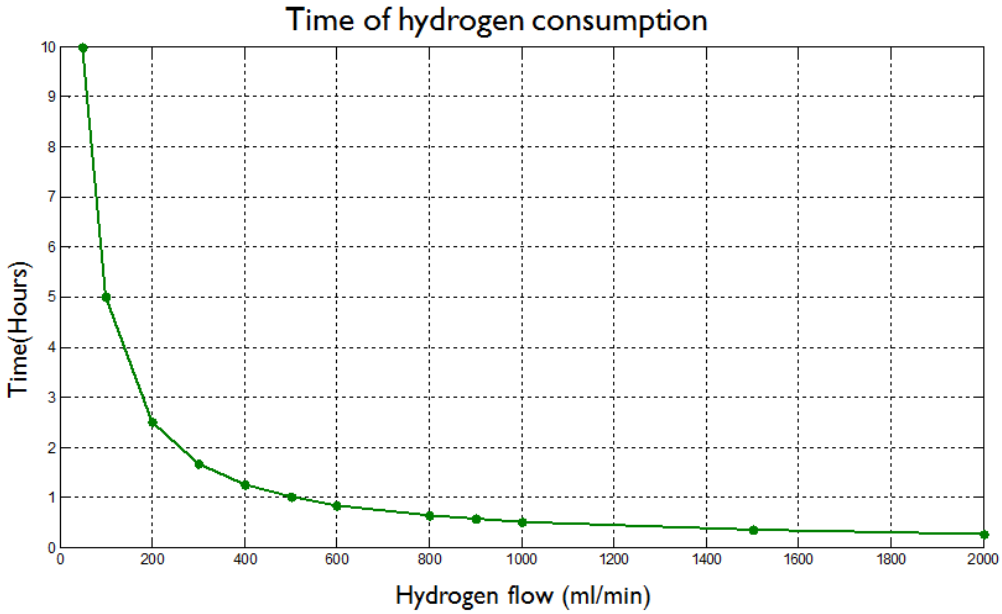

Fig 12. Time of H_2 consumption

should be performed under normal conditions, nevertheless the power available for the H_2 will depend on the operating conditions of pressure and temperature but it is not the only factors that we have to consider.

In relation with the obtained information H_2 gas has lower power available in the stored conditions and it could impact in the efficiency of the PEMFC. However it is so important to note that the optimal operation of the PEMFC includes the diffusivity of the gases, operating temperature, 60 °C and the pressure, with these aspects in spite of being an exothermic reaction having a low temperature it is not good for the PEMFC because it is affected the transport phenomena's inside the PEMFC so the energy available from the hydrogen is not the only factor to take into account to determinate the PEMFC efficiency.

In Fig. 14 the PEME power curve and the PEMFC power curve are presented. We can see that the PEME power curve is above of the PEMFC because there are energy losses in the process of production of H_2 and during the process of generating electricity in the PEMFC.

It is noteworthy that in order to carry out this comparison it is properly to analyse a single cell of the 20 cells of the PEMFC because each one of them generates the same amount of current, however, the assembly in series is performed to obtain a higher voltage ($18V_{DC}$).

It was analysed the energy consumption by LED lamps compared to the energy production of PEMFC shown in Figure 15, we can determine that consumption of the LED lamps is slightly higher than the expected nominal power so the H_2 consumption is greater than planned.

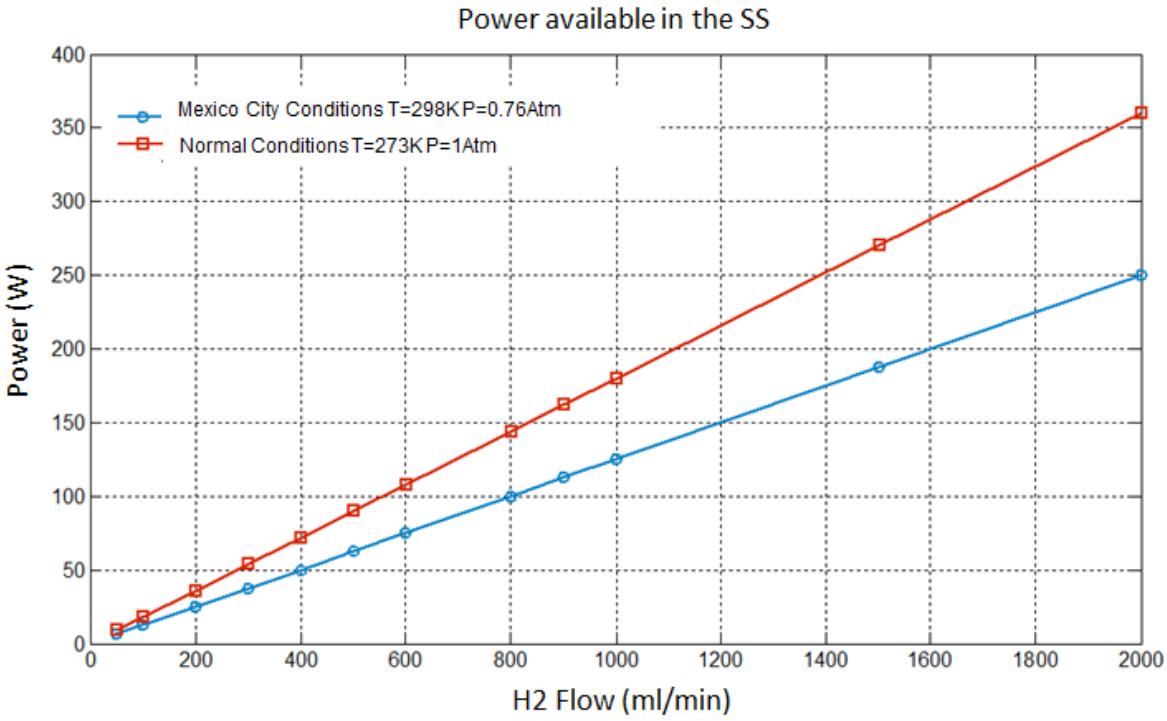

Fig 13. Power available in the SS

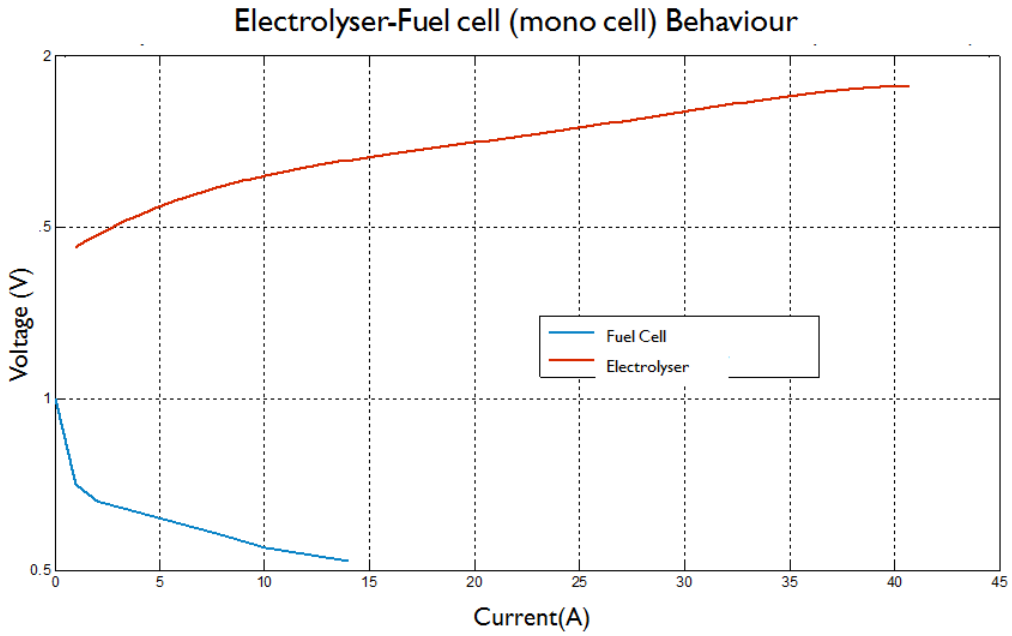

Fig 14. Electrolyser-Fuel cell (mono cell) Behaviour

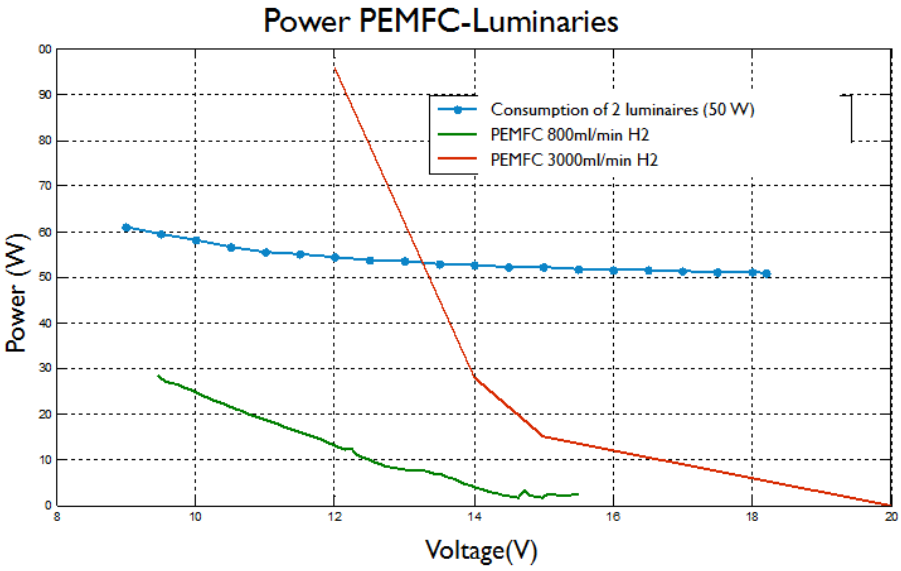

Fig 15. Power PEMFC-Luminaries

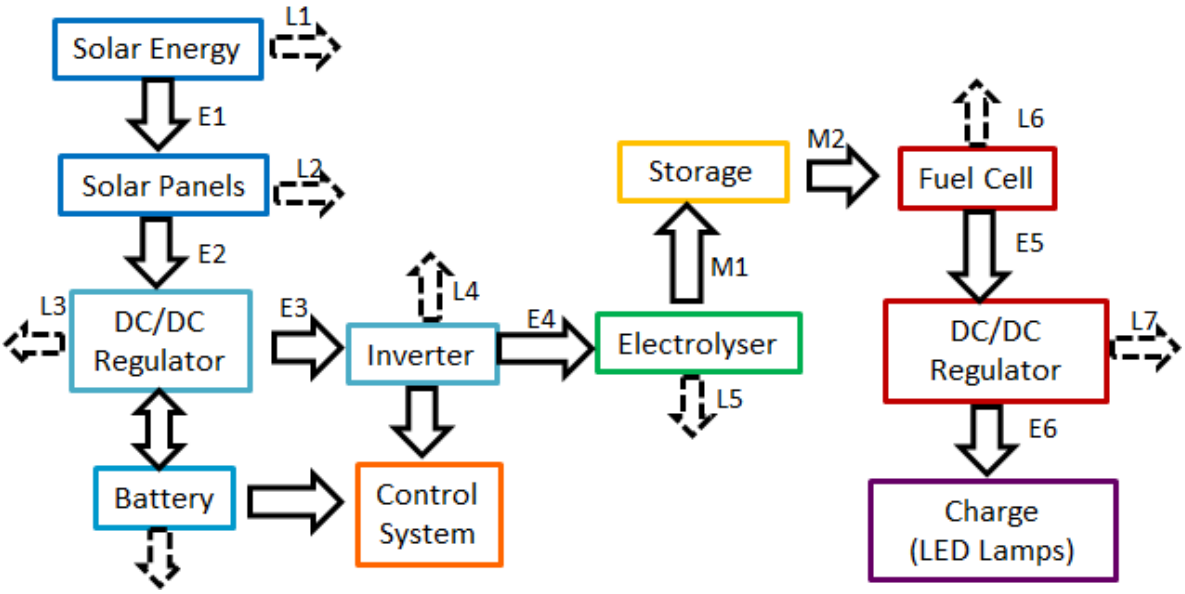

Fig 15. Energy flows in the system

Table 4. Energy flows in the system

Flows	Energy	Flows	Energy
E1	800 Wh/m^2	M1	18.9Wh
E2	417.6 Wh	M2	18.9Wh
E3	375.84 Wh	E5	50Wh
E4	340 Wh	E6	50Wh

For a correct performance with the operating conditions it is necessary to modify the design of the LED lamps to suit the power of 50W planned for this system. Other alternative is working with a higher gases flow but we will have less time for illumination.

It was developed a diagram shown in Fig. 16 and Table 4 where it is possible to analyse the energy involved in the process. This diagram permits to understand loses of energy in each step.

The balance permits to understand the system requires a lot of energy for the electrolysis process due it is used a AC electrolyser with 90ml/min of flow production, it is really important to solve this problem, for example increasing the H_2 flow production.

The most important thing in this system is the flexibility of energy, where it is possible to use H_2 energy when it was required.

4. Conclusion

We can conclude the following:

1. The design of a solar-hydrogen hybrid system is of great current importance, allowing to understand and solve the challenges of sizing for optimal and safe use.

2. The optimum hydrogen production and safe storage is very important in a power generation system based on hydrogen, therefore it is possible to determine with the analysis that the adaptation of a commercial PEM electrolyser is feasible for this purpose.

3. The development of a variable volume storage reduces energy consumption to only require the pressure of H2 and O2 production electrolyser avoiding auxiliary systems to perform this task. However, for systems that require greater amount of H2 it is impractical a system of this type in relation to size, increasing the risk of storage.

4. The uptime of hydrogen and oxygen in the tanks is really important to manage a system of power generation, which must be able to provide enough energy over proposed time.

6. The limitations of hydrogen storage requires dimension and design the energy consumption with great rigor, so systems of this type could proliferate in the society only changing the philosophy of energy, having to learn to manage it in a systematic and orderly way.

Acknowledgements

Authors thank CONACYT to the Programa de Redes Temáticas (RTH2) projects 252003 and 249795; and IPN SIP multidisciplinary project 1683.

References

[1] Geophysics Institute, Radiación Solar Promedio Disponible en la Ciudad de México, UNAM., Mexico., 2005.

[2]Fernández JM. Compendio de Energía Solar, Fotovoltaica, Térmica y Termoeléctrica. 1st ed. Madrid:

Mundi-Prensa AMV Ediciones; 2010.
[3] PH User Manual, PEAK Scientific, Scotland., 2011.
[4] Mompin P. Energía Solar Fotovoltaica. 2nd ed. Barcelona: Marcocombo; 1985.
[5] Aguer M , Miranda A. El Hidrógeno, Fundamento de un futuro equilibrado. 1st ed. España: Ediciones Díaz de Santos; 2005.
[6] Couper JR, Penney W, Fair J, Walas S. Chemical Process Equipment, Selection and Design. 2nd ed.; USA: Elsevier, Inc; 2010.
[7] Sinnot R, Towler G. Diseño en Ingeniería Química. 5th ed. Barcelona: Revarte; 2012.
[8] Hoogers G. Fuell Cell Techonology, Handbook. 1st ed. USA: CRC Press LLC; 2003.
[9] Barbir F. PEM Fuel Cells, Theory and Practice. 2nd ed. USA: Elsevier, Inc; 2013.
[10] Corbo P, Migliardini F, Veneri O. Hydrogen Fuel Cell for Road Vehicles. 1st ed. London: Springer-Verlag; 2011.
[11] Smith JM, Van Ness HC, Abbott MM. Introducción a la termodinámica en Ingeniería Química. 7th ed. Mexico: Mc Graw Hill; 2007.

Chapter 4.3. Dissociative mechanism of oxygen reduction reaction (ORR) on Pd-Cu disordered binary alloy metal surfaces: A theoretical study

E. López-Chávez[a,*]; A. García-Quiroz[a]; G. González-García[a]; Y. A. Peña-Castañeda[a]; J. A. I. Díaz-Góngora[b]; F. L. Castillo-Alvarado[c]

[a]Autonomous University of Mexico City. Av. Fray Servando Teresa de Mier 92-110.Col. Centro Histórico, Del. Cuauthémoc, CP 06080 México, D.F.
[b]Research center in applied science and advanced technology of National Polytechnic Institute. Legaria 694, Col Irrigación, Miguel Hidalgo, 11500 Ciudad de México, Distrito Federal, Mexico.
[c] School of Physics and Mathematics of the National Polytechnic Institute. Edificio 9 de la UPALM, Zacatenco, Col. Lindavista, Gustavo A. Madero, CP. 07738, México, Distrito Federal.

ABSTRACT

Density functional theory (DFT) in conjunction with virtual crystal approximation is used to study the oxygen reduction reaction (ORR) as a function of the cooper concentration in Pd-Cu disordered binary alloy metal surfaces. Reactivity is evaluated on the basis of an oxygen reduction reaction (ORR) dissociative mechanism of four steps, it involves the splitting of the O–O bond in O_2 after its adsorption, followed by hydrogenation of atomic O to OH. Then, the OH species undergoes another hydrogenation to yield H_2O. For each concentration of Cu, results for low oxygen coverage are presented at zero cell potential (U = 0), at the equilibrium potential (U = 1.23 V), and at the highest potential (U = 0.80 V) where all reaction steps are exothermic. The results indicate that at the ORR equilibrium potential of 1.23 V, the reactivity of all surfaces is shown to be limited by the rate of OH removal from the surface, while that at a cell potential of 0.80 V, the ORR reactivity of different surfaces is dictated by the strength of oxygen adsorption. The results are compared with other non-Pt alloys.

Keywords: Catalysis, Binary alloy, Oxyen reduction reaction, Dissociative mechanism

1. Introduction

During the past few years, proton exchange membrane (PEM) fuel cells, at low temperature, have attracted attention for application in vehicles. However, it is still required solving some scientific and technical problems, including low reaction rate of oxygen reduction which takes place at the cathode of the fuel cell. Added to this, the development of new materials in order to reduce or eliminate the amount of platinum is necessary to make the fuel cell technology more feasible. For several years, both experimental [1] and theoretical [2] studies have been performed with the intention of achieve these goals.

---

* Author for correspondence: Ernesto López-Chávez, T: 5255 51349804 x 11110, E: elopezc_h@hotmal.com

The problem has been addressed in two ways, the first of which is to replace the Pt with another less expensive precious metal, such as palladium [3]. The second one is to use non-precious metal catalysts (NPMC). Bashyam and Zelenay have examined the cobalt–polypyrrole–carbon (Co–PPY–C) composite [7]. This catalyst exhibits good activity and stability in PEM fuel cells with a Co loading of 6.0 x 10^{-2} mg cm^{-2} and it generates 0.2A/cm^2 at 0.50 V and a peak power density of 0.14 W/cm^2, after Fernandez et al. Some studies are focused on heat-treated Fe and Co–N/C catalysts, of which a review is given by Bezerra et al. [5].

Some authors have made combination of DFT studies and an array of experimental techniques in order to identify, synthesize and test successfully, a new class of materials for ORR that are based on monolayers of Pt deposited on different late transition metals (Au, Pd, Rh, Ir, Ru) [6]. The enhanced reactivity of these catalysts has been attributed to the modifications in the electronic structure of surface Pt atoms effected by the metal substrate through both geometric and ligand variations. In particular, the center of the d-band of surface Pt atoms and the binding energy of atomic oxygen (BE_O) on these surfaces were shown to correlate with their experimentally measured ORR activity.

In this work, we have used a scheme originally proposed by Norskov and co-workers [2] so as to study catalytic activity of Pd-Cu disordered binary alloy metal surfaces for the ORR. The approach accounts for a variety of factors, including that of potential bias. This approach has been applied successfully for studying ORR on various materials [6, 8] and has established important insights regarding the respective reaction mechanisms. In this study, we have used approach virtual crystal in order to simulate the compositional disorder of Pd-Cu alloy.

2. Materials and Methods

Here, we apply the approach suggested by Norskov in order to determine the free energies of different intermediate reactions on disordered binary alloys of Pd_xCu_{1-x} at concentrations x= 0.80, 0.85, 0.90. 0.95. Subsequently, we construct the free energy diagrams (FED). Finally, by performing a Sabatier analysis, the free energy changes and activation energy barriers for relevant steps are used to estimate the relative activity of these catalysts at cell potentials of 0, 0.80 and 1.23 V.

The calculations were done on a (3 x 2) three-layer FCC (111) slab at the Perdew–Burke–Ernzerhof (RPBE) [9] level theory. The bottom two layers were fixed, and the top layer was allowed to relax. The plane wave cutoff was 340 eV, and the density was treated on a grid corresponding to a plane wave cutoff at 500 eV. The OH adsorption energies were calculated on (2 x 2) four-layer slabs with the top two layers relaxed. A 4 x 4 x 1 Monkhorst-Pack k-point sampling was used, with maximum symmetry applied to reduce the number of k points in the calculations.

The dipole corrections, the effect of a bias on all states, the effect of the water layer on adsorbed intermediates, and entropies and zero point energies contributions were used in all cases. The plane wave cutoff was 340 eV for OH, 350 eV for H, and 450 eV for the O adsorption calculations. The binding energies (BE) were calculated by means of formula:

$$BE = E_{Total} - E_{Slab} - E_{gas-adsorbate} \quad (1)$$

Following the approach proposed by Norskov et al., the free energies of different reaction intermediates were calculated at 1 bar and 300 K. Zero-point energy (ZPE) and entropic (TDS) corrections have been added to the free energies of all reaction intermediates. In this study, we have used a coverage equal to zero.

3. Results and Discussion

The individual steps in the ORR mechanism developed in this study are:

Step 1, adsorption of $\frac{1}{2}O_2$ on surface of Pd-Cu: $\frac{1}{2}O_2 + * \rightarrow O^*$ (2)

Step 2, hydrogenation of O^*: $O^* + H^+ + e^- \rightarrow HO^*$ (3)

Step 3, hydrogenation of HO^*: $HO^* + H^+ + e^- \rightarrow H_2O + *$ (4)

where * is a site on the surface of alloy.

Using the procedure outlined above, we constructed the free energy diagram at several electrode potentials *U*. Free energy diagrams for U=0, 0.80 and 1.23 V and concentrations x=0.80, 0.85. 0.90 and 0.95 are show in figures 1, 2a and 2b, respectively. We considered the case where the oxygen coverage is zero. Further, within our approaches, we assume that the electrode potential is measured against the standard hydrogen potential. It is equal to the potential of the fuel cell if we assume the anode reaction to be in equilibrium and neglect ohmic losses.

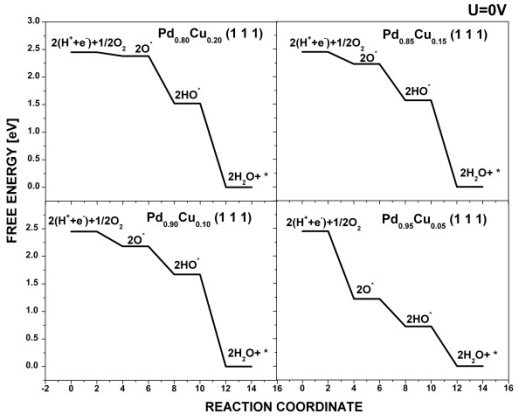

Fig. 1. Free energy diagrams for U=0 V and concentrations of x=0.80, 0.85. 0.90 and 0.95.

In Fig. 1, it can be observed that all elementary steps are strongly exothermic. The situation at *U* = 0 V corresponds to the reaction running by short circuiting the cell. This situation is roughly equivalent to the gas-phase hydrogen oxidation reaction. For potential *U* = 0, the rate determining step is hydrogenation of HO^*, since in this step, more energy is released; the other step of hydrogenation is relatively easier. For $OH^* + H^+ + e^- \rightarrow H_2O + *$ step, we observed that the largest amount of energy is released in the concentration *x = 0.90*; while

for $x = 0.95$ have the least amount of energy released. This means that, for potential $U = 0$, the most suitable concentration for the design of *Pd-Cu* catalysts is $x = 0.95$.

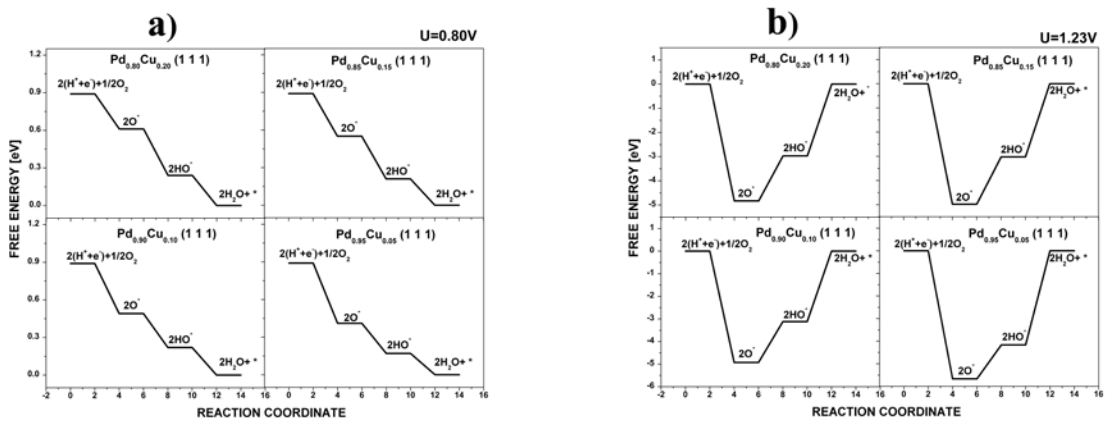

Fig. 2. (a) Free energy diagrams for U=80 V and concentrations of x=0.80, 0.85. 0.90 and 0.95. The effect of the water environment, the formation of electric field and the bias practically nullify the effect of the concentration.(b) Free energy diagram for ORR on Pd-Cu(111) for concentrations different at potential U=1.23 V.

For the case of V = 0.80 V, shown in figure 2a, all steps are also exothermic type in the reaction mechanism of oxygen reduction on the surface. We also may notice little variation in the release of energy for different concentrations, that means that the effect of the water environment, the formation of electric field and the bias practically nullify the effect of the concentration.

I n figure 2b, we shift the chemical potential of the electrons by the equilibrium potential of U= 1.23 V, corresponding to the situation where the fuel cell has the maximum potential allowed by thermodynamics, in this figure, we observed that both electron/proton-transfer steps become uphill. The barriers for the step of OH removal from the surface are greater than the corresponding to the O* hydrogenation, which means that the reactivity of all surfaces is shown to be limited by the rate of OH removal from the surface, OH removal from surface is the rate-limiting step.

4. Conclusion

In summary, we have systematically studied ORR on disordered binary alloy surfaces of Pd_xCu_{1-x}, with x=0.80, 0.85, 0.90 and 0.95 by employing density functional theory to obtain relevant free energy diagrams. Our studies reveal that OH removal is the rate-limiting step for the most likely reaction mechanism at the ORR equilibrium potential of 1.23 V. At a cell potential of 0.80 V, the proton/electron transfer steps become easier and all steps are also exothermic type in the reaction mechanism of oxygen reduction on the surface. For potential $U = 0$, the rate determining step is hydrogenation of HO^*, since in this step, more energy is released; the other step of hydrogenation is relatively easier.

These results are in excellent agreement with recent theoretical and experimental studies realized by others researcher [2,6,7], and provide additional insights into the ORR mechanism for disordered binary alloys surfaces of Pd-Cu.

Acknowledgements

The authors thank the National Research System through the National Council of Science and Technology of Mexico (SNI-CONACyT). Also we acknowledge CONACyT through the 252003 project [called "RED NACIONAL DEL HIDRÓGENO; Subprograma de Teoría, Modelación y Simulación; TeMoSi], CINVESTAV-Saltillo and UACM for their partial financial support and facilities. We are pleased with SMH and XV International Congress of the Mexican Hydrogen Society for the correspondent given support.

References

[1] Zhang, J., Mo Y., Vukmirovic M.B., Klie R., Sasaki K., Adzic R.R. Platinum Monolayer Electrocatalysts for O_2 Reduction: Pt Monolayer on Pd(111) and on Carbon-Supported Pd Nanoparticles. J. Physical Chemistry B 108(30), 2004; 10955.

[2] Norskov J.K., Rossmeisl J., Logadottir A., Lindqvist L., Kitchin J.R., Bligaard T., Jonsson H., Origin of the Overpotential for Oxygen Reduction at a Fuel-Cell Cathode. J. Physical Chemistry B 108(46), 2004; 17886.

[3] Debe MK. Advanced cathode catalysts and supports for PEM fuel cells. 2010 Hydrogen program annual merit review and peer evaluation meeting. Washington, DC, 2010.

[4] Fernández J.L., Raghuveer V., Manthiram A., Bard A.J., Pd–Ti and Pd–Co–Au electrocatalysts as a replacement for platinum for oxygen reduction in proton exchange membrane fuel cells, J. Am Chem Soc. 127(38), 2005; 13100-13101.

[5] Bezerra C.W.B., Zhang L., Lee K.C., Liu H.S., Marques A.L.B., Marques E.P., Wang H.J., Zhang J.J. A review of Fe–N/C and Co–N/C catalysts for the oxygen reduction reaction. Electrochimica Acta 53(15) , 2008; 4937-4951.

[6]. Nilekar A. U., Mavrikakis M. Improved oxygen reduction reactivity of platinum monolayers on transition metal surfaces. Surf. Sci. 602(14), 2008, L89-L94, 2337-2622.

[7]. R. Bashyam, P. Zelenay P. A class of non-precious metal composite catalysts for fuel cells. Nature, 443 (7107), 2006; 63-66.

[8]. Stamenkovic V., Mun B.S., Mayrhofer K.J.J., Ross P.N., Markovic N.M., Rossmeisl J., Greeley J., Norskov J.K., Changing the Activity of Electrocatalysts for Oxygen Reduction by Tuning the Surface Electronic Structure. Angewandte Chemie International Edition 45(18), 2006; 2897-2901.

[9] Yang K., Zheng J., Zhao Y., Truhlar D.G., Tests of the RPBE, revPBE, τHCTHhyb, ωB97X-D, and MOHLYP Density Functional Approximations and 29 Others Against Representative Databases for Diverse Bond Energies and Barrier Heights in Catalysis. J. Chemical Physics 132, 2010; 164117/1-10.

Chapter 4.4. Numerical study of heat transfer in a PEM fuel cell with different flow- fields

J. Macedo-Valencia[a]; J. M. Sierra[a,*]; S. Figueroa-Ramírez[a]; H. Mandujano[a]; M. Meza[a]

[a]Facultad de Ingeniería, Universidad Autónoma del Carmen, Cd. del Carmen, Campeche C.P. 24115, México.

ABSTRACT

The heat generated in a proton exchange membrane fuel cell (PEMFC) may represent 50% of the total energy produced in these devices. This heat is produced mainly for three reasons: the electrochemical reactions, ohmic heating and water condensation in the fuel cell. Proper manage of these mechanisms is a critical problem to solve in the fuel cell. In this regard, a 3D numerical study of heat transfer in a PEMFC is presented in this work. The governing equations were solve using a commercial code of Computational Fluid Dynamics (CFD). Conventional and non-conventional designs of flow fields with an active area of 50 cm^2 were evaluated to understand two issues i) how the temperature is distributed inside the fuel cell and 2) which flow field design removes more effectively the heat from the fuel cell. Normal operating conditions of pressure and temperature were set. Dry oxygen and hydrogen were supplied to the fuel cell to avoid non desired processes as well as the appearance of liquid water on the anode side. Distributions contours of temperature, species and current density were obtained in this study. Numerical results showed that designs with multiple parallel channels dissipate more heat than conventional designs, also some non conventional designs showed better results than conventional designs. Furthermore it was found that the cathode compartment presents higher temperatures than the anode compartment. The results were validated by polarization curves and experimental data reported in the literature. From this study relevant information of heat transfer processes was obtained to improve the design of the fuel cell.

Keywords: Heat transfer, PEM Fuel Cell, Flow fields, CFD

1. Introduction

One of the most promising technologies at the new hydrogen economy are the fuel cells (FC's). These are characterized by their high conversion efficiency, modularity and zero pollution. Their advantages have made them a leading technology that can replace the internal combustion engines in transportation and batteries in portable applications [1]. Currently there are different types of fuel cells, which are distinguished by the operating temperature and the electrolyte. However, the proton exchange membrane (PEM) fuel cell

---

*Author for correspondence: J.M. T. Sierra Grajeda, T: 52 777 184 35 85, E: juanmsg@live.com.mx

has gained more attention by their low operating temperature and high efficiency. The operation of a fuel cell is simple, hydrogen and oxygen are supplied separately to the cell and they react electrochemically to generate electricity, the only products obtained are water and heat. The water generated in the fuel cell is one of the main problems in the cell because it floods the gas diffusion layer. The water drops produced by the cathode reaction avoid that oxygen reaches the active sites of the catalyst layers. This affects the performance of the fuel cell. However, the water usually is removed by the air flow and oxygen fed into the cathode. Furthermore, different designs of flow fields have been proposed to solve this problem; the most common are the parallel channel design and interdigitated; which efficiently expel water from the cell [2].

One of the most important problems in these devices is the heat generated by the fuel cell, which may represent 50% of the total energy produced in these devices [1]. This heat is produced mainly for three reasons: the electrochemical reactions, ohmic heating and water condensation. Proper manage of these mechanisms is a critical problem to solve. To understand these processes different experimental studies and numerical methods have been employed to study the physical phenomenon within a fuel cell such as mass, heat and energy transport, electrode kinetics and potential fields. Wang and Ouyang [3] developed a three-dimesional model for an air-breathing proton exchange membrane fuel cell using non-dimensional heat/mass transfer coefficients. The Navier Stokes and energy equations were solves using a commercial CFD tool STAR-CD. The model was built considering assumptions including steady state and non-isothermal. The anode and cathode channel arranged as intercross flow mode. However, disadvantages of their model were the assumptions of a solid membrane and the neglect of the ohmic heating and ohmic resistance in the bipolar plates. Hashemi et al [4] proposed a three-dimensional model for a PEMFC with straight and serpentine flow fields. The model findings revealed that the serpentine flow field shows better distribution of current density and temperature. The simulation result were compared with the experimental data reported in literature showing good agreement between the model and experimental results. However, in high current densities the modeling results deviate from experimental results because of the assumption of one-phase model which neglects the water flooding in cathode and drying in anode. Masher and Sadiq [5] developed a three-dimensional, multi-phase, non-isothermal computational fluid dynamics model of a proton exchange membrane fuel cell to investigate the displacement, deformation, and stresses inside the cell due to the changes of temperature and relative humidity. They results show that the non-uniform distribution of stresses, caused by the temperature gradient in the cell, induces localized bending stresses, which can contribute to delaminating between the membrane and the gas diffusion layers.

In this regard, a 3D numerical study of heat transfer in a PEMFC is presented in this work. Conventional and non-conventional designs of flow fields were evaluated to understand two issues: i) how the temperature is distributed inside the fuel cell and 2) which flow field design removes more effectively the heat from the fuel cell. To achieve these goals the first analysis consisted of studying the temperature variation as function of the current density, as well as the temperature distribution through the membrane electrode assembly. The second analysis was to identify the main factors affecting the distribution of heat in the fuel cell. The third analysis was done to evaluate different flow fields to know what type of design removes better the heat generated by the fuel cell.

2. Description of the computational model

The computational models evaluated in this work consist of six types of flow fields (Fig. 1): (a) serpentine - A, (b) serpentine - B, (c) serpentine - C, (d) straight channels, (e) pin type, and (f) branched channels [5]. The fuel cell models include gas diffusion layers (GDL), catalyst layers (CL), membrane (MEM) and monopolar plates (MP). The flow fields were designed with an active area of 50 cm^2, and designs for both anode and cathode were the same. The plates were located in such a way that the gases were fed in the same direction of flow [6]. The dimensions of the components are specified in Figure 1.

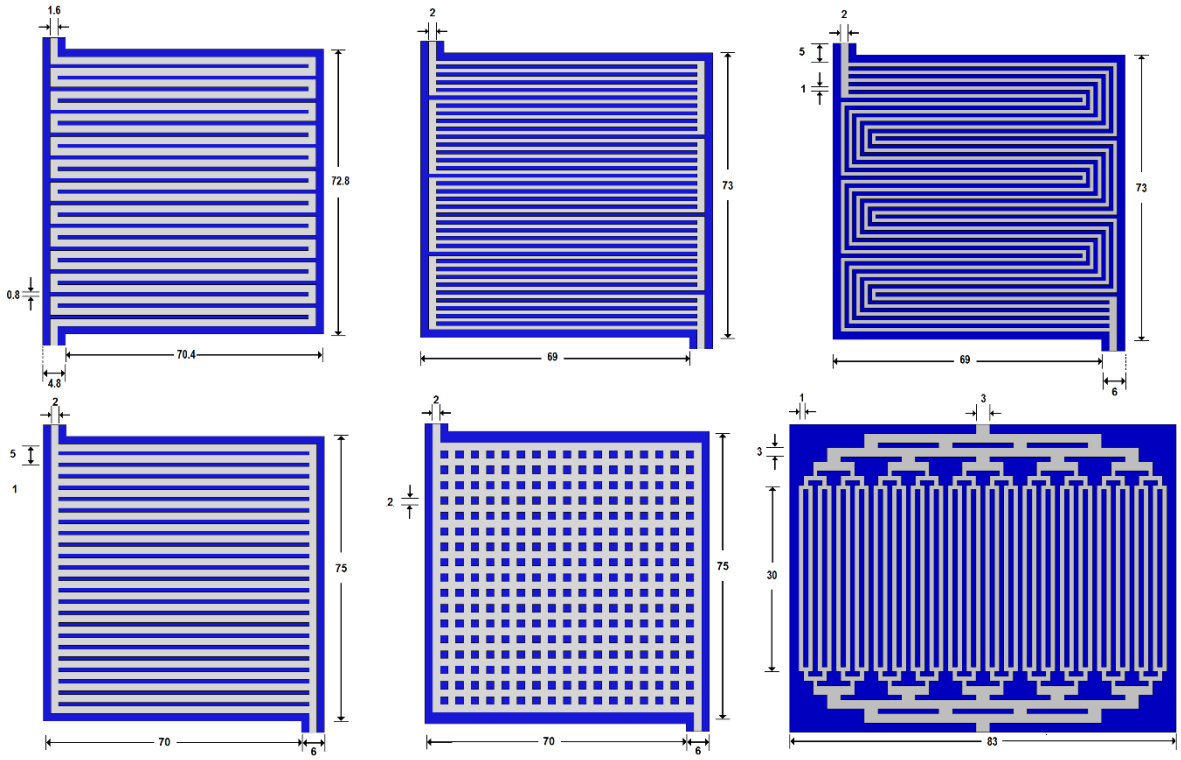

Fig. 1. Designs of the flow fields (a) serpentine - A, (b) serpentine - B, (c) serpentine - C, (d) straight channels, (e) pin type, and (f) branched channels.

In order to establish the accuracy of the results and to ensure that they were independent of the grid, previous simulations were performed. The reference parameter used to do the analysis was the average current density. The final mesh (Fig.2) used in the models had the following intervals: channels and plates (0.2), GDL's (0.035), MEM (0.007), and CL's (0.0014). The mesh elements obtained in the models was around 1.2 million. The computational time calculated per each polarization curve was about 80 hrs.

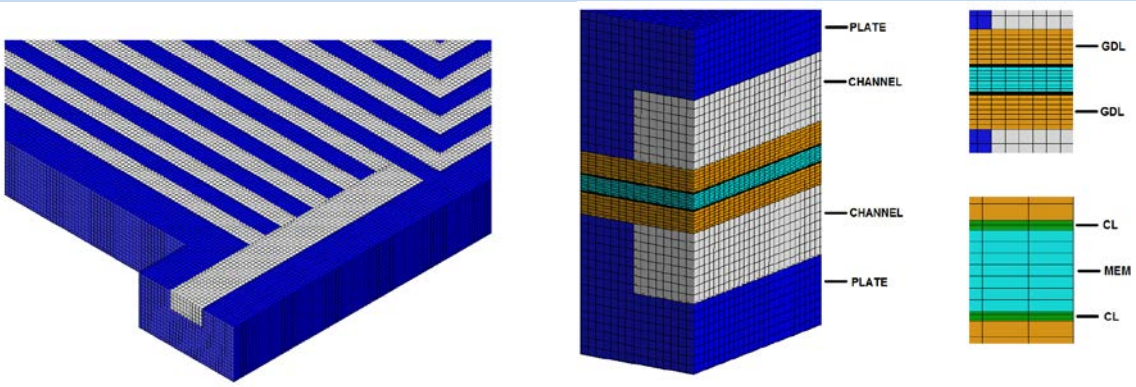

Fig. 2. Mesh visualization and components of single fuel cells with 50 cm^2 of active area.

The assumptions considered to carry out the numerical simulation of the computational models were the following: (a) steady state conditions, (b) laminar flow in channels, (c) isotropic porous zones, (d) the electrochemical reactions take place on the catalyst layer surface, (e) transport of species in the gas phase, and (f) the transport of liquid water in the membrane is controlled by diffusion mechanisms and electro-osmotic drag.

3. Mathematical Model

Transport phenomena occurring inside a PEM fuel cell are represented by the governing equations of mass conservation, momentum, energy, species and charge transport. These equations are described below.

3.1. Continuity equation

The continuity equation represents the mass conservation for all transport processes that take place in the fuel cell, such as fluid flow, mass diffusion, phase change and electrochemical reactions. This equation is written in a simplified form (steady state) as:

$$\nabla \cdot (\rho \vec{v}) = S_m \tag{1}$$

where ρ is the fluid density, $\vec{v}$ is the vector velocity and S_m is the source term for the species balance.

3.2. Momentum transport

The momentum transport equation in a steady state is described by:

$$\nabla \cdot (\rho \vec{v}\vec{v}) = -\nabla p + \nabla \cdot (\mu^{eff} \nabla \vec{v}) + S_v \tag{2}$$

where p is the static pressure, μ_{eff} is the average viscosity of the mixture and S_p is a source term that contains the physical characteristics of porous media and it is defined as:

$$S_v = -(\mu/k)\vec{v} \tag{3}$$

where μ is the gas viscosity (kg/m·s), *k* is the permeability (gas diffusion layers and catalyst layers), and $\vec{v}$ is the superficial vector velocity at the porous media (m/s) [7].

3.3. Species transport

The species transport equation represents the mass conservation for each individual species of a gas. To determine the local mass fraction of each species *yi*, the following equation is used:

$$\nabla \cdot (\rho \vec{v} y_i) = -\nabla \cdot \vec{J}_i + S_i \quad (4)$$

where S_i is the source term for each phase, $\vec{J}_i$ is the flux diffusion for the species *i*, which is calculated for a laminar flow as:

$$\vec{J}_i = -\rho D_i \nabla \cdot y_i \quad (5)$$

where D_i is the diffusion coefficient for the species *i*.

3.4. Energy

The energy equation for steady state is expressed by:

$$\nabla \cdot [\vec{v}(\rho E + p)] = \nabla \cdot \left(k_{eff} \nabla T - \sum_i h_i \vec{J}_i\right) \quad (6)$$

where *E* is the total energy, k_{eff} is the effective conductivity and $\vec{J}_i$ is the flux diffusion for the species *i*.

3.5. Electrochemical model

The fluid dynamics equations preceding this section are coupled to the electrochemical model implemented in Ansys-Fluent®. This set of equations allows to solve the transport phenomena and electrochemical processes occurring in the fuel cell. This model consists of two equations for solving the two potential fields: equation (7) associated with the transport of electrons in the catalyst layers, the gas diffusion layers and the plates and, equation (8) associated to proton transport through the membrane and the catalyst layers.

$$\nabla \cdot (\sigma_{sol} \nabla \varphi_{sol}) + R_{sol} = 0 \quad (7)$$

$$\nabla \cdot (\sigma_{mem} \nabla \varphi_{mem}) + R_{mem} = 0 \quad (8)$$

where σ is the electric or ionic conductivity, φ is the cell potential and *R* is the transfer current; the subscripts sol and mem correspond to the solid and the electrolyte phases, respectively.

The transfer current or source terms in equations 7 and 8 are determined from the general Butler-Volmer formulation, which is used to calculate the local current density on the catalyst layers by the following equations:

$$R_{an} = j_{an}^{ref}\left(H_2/H_{2.ref}\right)^{\gamma_{an}}\left(e^{\alpha_{an}F\eta_{an}/RT} - e^{\alpha_{ca}F\eta_{an}/RT}\right) \quad (9)$$

$$R_{ca} = j_{ca}^{ref}\left(O_2/O_{2.ref}\right)^{\gamma_{ca}}\left(-e^{\alpha_{an}F\eta_{ca}/RT} + e^{-\alpha_{ca}F\eta_{ca}/RT}\right) \quad (10)$$

where j^{ref} is the exchange current density, H_2 y $H_{2,ref}$, are the local and reference species concentrations, γ is the concentration coefficient, α is the transfer coefficient, η is the activation losses defined in equations 11 and 12, and F is the Faraday constant (9.65×10^7 C kg^{-1} mol^{-1}).

The reaction kinetics is controlled by the local surface overpotential, η, known as activation losses, which is associated with the difference of surface potentials between the electrode and the electrolyte φ_{sol} and φ_{mem}. This overpotential is calculated for both the anode and the cathode, including as last term the open circuit voltage (VOC) and thus establishing the potential difference between both electrodes.

$$\eta_{an} = \varphi_{sol} - \varphi_{mem} \quad (11)$$

$$\eta_{ca} = \varphi_{sol} - \varphi_{mem} - V_{oc} \quad (12)$$

The membrane is modeled as a porous zone and its properties such as ionic conductivity σ_{mem} and the electro-osmotic drag coefficient are evaluated as a function of the water content λ.

$$\sigma_{mem} = (0.00514\lambda - 0.00326)e^{1268\left(\frac{1}{303} - \frac{1}{T}\right)} \quad (13)$$

$$\lambda = 0.043 + 17.81a - 39.84a^2 + 36a^3 (a < 1) \quad (14)$$

$$\lambda = 14 + 1.4(a-1)(a > 1)$$

where a is the water activity. The saturation model is used to model the formation and transport of liquid water in the membrane-electrode assembly.

From these equations (7-14) both potential fields are solved, also the electrochemical process that causes the three potential losses in a fuel cell are included, which are known as: activation overpotential, ohmic overpotential and concentration overpotential.

The operating conditions and the electrochemical parameters used in the simulation were taken from experimental data and literature data [6, 8]. These values are shown in Table 1.

4. Results and Discussion

Based on the simulations performed in the commercial code Ansys Fluent®, distribution contours were obtained at the anode and cathode interfaces (GDL/CL) of the fuel cell. The variables studied were temperature, species concentration and current density. Normal operating conditions of pressure (1 atm) and temperature (298 K) were set in the boundary conditions to develop the numerical simulations. Dry oxygen and hydrogen were

Table 1. Operating conditions and electrochemical parameters.

Parameter	symbol	unit	value
Pressure	P	atm	1
Cell temperature	T_C	K	300
Relative humidity (H_2, O_2)	HR_a	%	0
Ref. exchange current density (anode)	$j_{ref,an}$	A cm^{-2}	0.2
Ref. exchange current density (cathode)	$j_{ref,an}$	A cm^{-2}	1×10^{-4}
Charge transfer coefficient (anode)	$\alpha_{,an}$	-	1
Charge transfer coefficient (cathode)	$\alpha_{,ca}$	-	0.5
Concentration exponent (anode)	$\gamma_{,an}$	-	0.5
Concentration exponent (cathode)	$\gamma_{,ca}$	-	1
GDL porosity	ε_{GDL}	-	0.4
GDL viscous resistance	$v_{R,GDL}$	$1/m^2$	1×10^{12}
CL porosity	ε_{CL}	-	0.2
CL viscous resistance	$v_{R,CL}$	$1/m^2$	4×10^{12}

supplied to the fuel cell to avoid non desired processes as well as the appearance of liquid water on the anode side.

Fig. 3. shows the temperature contours for serpentine design at the cathode interface GDL/CL. These results were obtained at different current densities. The distribution contours show that the temperature increases when the cell potential decreases, this is because the temperature is directly related to current density, which can be explained by Joule heating. However, another important aspect that can be observed in the results is that highest temperature is exhibited in the flow channels, so the heat generated by the cell is removed by the own flow. The electrochemical reactions that take place in electrodes are exothermic and they release energy as heat (48.68 kJ mol^{-1}), this heat is reflected in a temperature increase, which is dissipated by convection mechanism of reactant gases.

Also, the temperature distribution is not uniform throughout the active area of the cell, higher temperature values are shown near to the inlet flow, and the lower temperature values are shown at the outlet, this happens due to the water concentration in the fuel cell. In zones where water is accumulated the temperature decreases, in areas where the water is not present the temperature rises. Moreover, it was observed that in cathode compartment, the temperature is always higher than anode compartment, about < 2 degrees Celsius, as reported in the literature [9].

In Figure 4, the temperature contours for different flow fields are presented. These results were obtained at the cathode interface GDL/CL for a potential of 0.2V. The scale was set in the range of 300-336 K, which corresponds to the minimum and maximum temperature reached by the models. Distribution contours demonstrate that pin type and serpentine - A designs showed the highest values of temperature, then the design of straight channels, branched channels, and finally the serpentine with five parallel channels. This last design dissipates the heat generated by the electrochemical reactions and the joule heating efficiently. This is because the gases are distributed evenly through the parallel channels and they can remove the heat produced in the electrodes by convection mechanism.

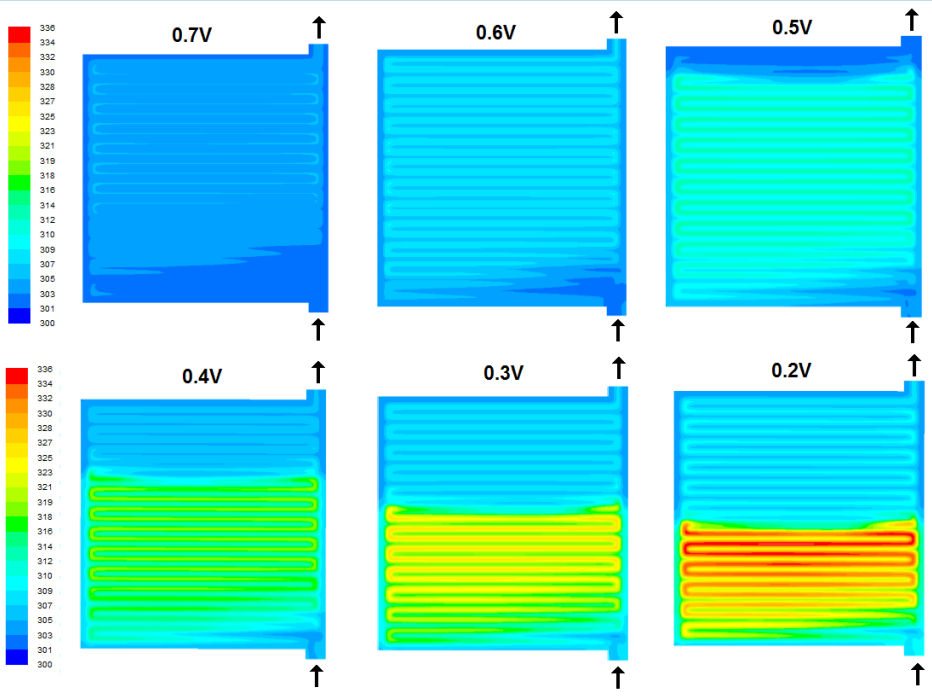

Fig. 3. Temperature contours (K) at the cathode interface GDL/CL for different operating voltages.

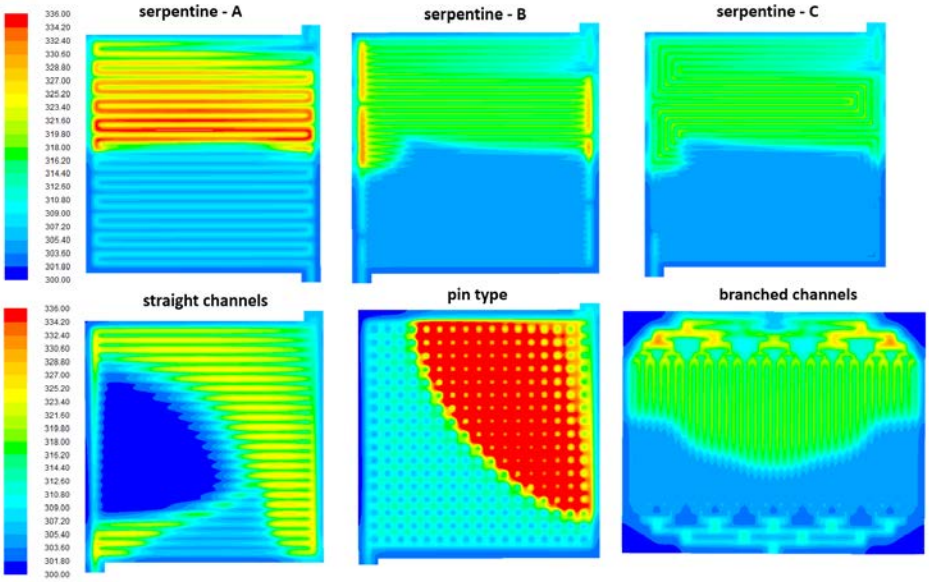

Fig. 4. Temperature contours (K) at the cathode interface GDL/CL for different flow fields.

Fig. 5a shows the polarization curves obtained for different designs of flow fields, as well as the temperature variation as a function of the current density (Fig. 5b). These plots indicate that serpentine design presents the best performance and the parallel channels design showed the lowest performance.

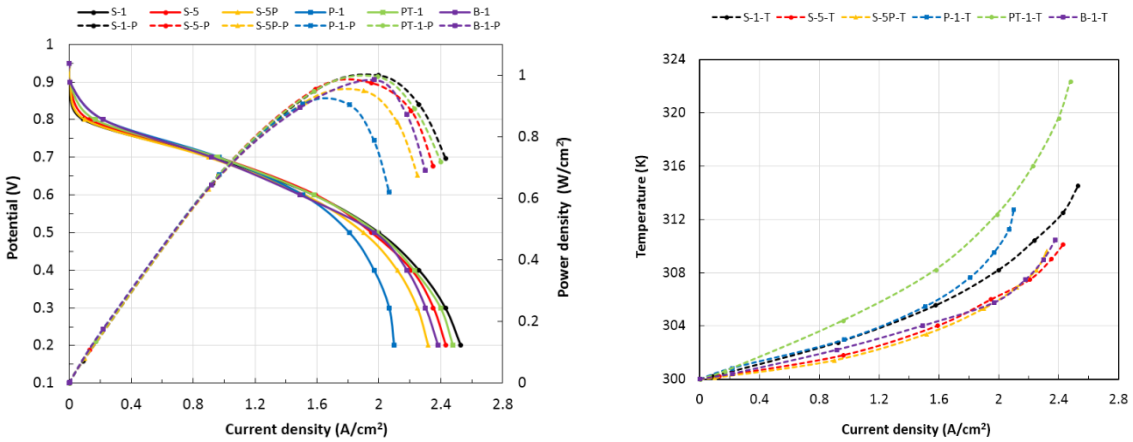

Fig. 5. (a) Polarization curves, and (b) temperature plots for different flow fields.

However, the difference between them is only at high current densities values. The significant variations were presented for the temperature values. In Fig. 5b, the results indicate that flow fields of pin type, serpentine and parallel channels show the highest temperatures, and flow fields with branched channels, serpentine with five channels and serpentine with five parallel channels show the lower temperatures. This demonstrate that the use of multiple channels favors the distribution of gases over the electrodes and the heat dissipation from the fuel cell.

5. Conclusion

A 3D numerical study of heat transfer in a PEMFC was presented in this work. From this study was demonstrated that temperature is directly related to the current density of the fuel cell. The higher temperature values are shown near to the inlet flow, and the lower temperature values are shown at the outlet, this is due to water concentration in the fuel cell. Also from the simulation results was demonstrated that heat generated by the electrochemical reactions and ohmic heating is removed by the convection mechanism through channels. The use of channels in parallel form helps to dissipate heat from the fuel cell.

Acknowledgements

The authors gratefully acknowledge to UNACAR for the granted support to perform the numerical simulations in their computing equipment and the use of Ansys-Fluent® software license. In addition, the author gratefully acknowledges the financial support from the project 252003 “Programa de Redes Temáticas (RTH2)”.

References

[1] F. Barbir, PEM Fuel Cells – Theory and Practice, Academic Press, Elsevier, 2005.
[2] Xianguo Li. Imran Sabir, Review of bipolar plates in PEMFCs: Flow-field designs. Int. Journal of Hydrogen Energy 2005; 30: 359 - 71.
[3] Ying Wang. Mingao Ouyang. Three-dimensional heat and mass transfer analysis in an air-breathing proton exchange membrane fuel cell. Journal of Power Sources 2007; 164: 721-729.
[4] F. Hashemi, S. Rowshnzamir, M. Rezakazemi. CFD simulation of PEM fuel cell performance: Effect of straight and serpentine flow fields. Mathematical and Computer Modelling. 2012; 55: 1540-1557.
[5] Bladimir Ramos-Alvarado, Abel Hernandez-Guerrero, Daniel Juarez-Robles, Peiwen Li., Numerical investigation of the performance of symmetric flow distributors as flow channels for PEM fuel cells. Int. Journal of Hydrogen Energy 2012; 37: 436-48.
[6] J.M. Sierra, J. Moreira, P.J. Sebastian, Numerical analysis of the effect of different gas feeding modes in a proton exchange membrane fuel cell with serpentine flow-field. J. Power Sources 2011; 196: 5070-5076.
[7] Ansys Manual 15.0. 20013.
[8] J. M. Sierra, S. J. Figueroa Ramírez, S.E. Díaz, J. Vargas, P. J. Sebastian, Numerical evaluation of a PEM fuel cel with conventional flow fields adapted to tubular plates. Int. Journal of Hydrogen Energy 2015; 39: 16694 - 16705.
[9] S. G. Kandlikar, Z. Lu. Thermal management issues in a PEMFC stack – A brief review of current status. Applied Thermal Engineering. 2009; 29: 1276-1280.

Chapter 4.5. Numerical evaluation of a PEM electrolyzer using computational fluid dynamics

B. A. Flores-Argáez[a]; J. M. Sierra[a,*]; S. Figueroa-Ramírez[a]; O. Meza-Cruz[a]; C. Patiño[a]

[a]Facultad de Ingeniería, Universidad Autónoma del Carmen, Cd. del Carmen, Campeche C.P. 24115, México.

ABSTRACT

In this research a 3D computational fluid dynamics study in a proton exchange membrane electrolyzer is presented. The aim of this work was to model the transport phenomena that take place inside the electrolyzer, such as species distributions, and temperature variations in the electrodes. The governing equations of continuity, momentum, energy, species transport, and the Butler-Volmer model for the electrochemical reactions were solved using a commercial code. The operating conditions set in the model were 2 atm and 75 °C, for pressure and temperature, respectively. Two flow field designs were simulated in a single model of electrolyzer. Both designs are constituted by a membrane, electrodes and monopolar plates. Contours of pressure, mass fraction, temperature, current density and ionic conductivity were obtained by numerical simulation. These results showed that the distribution of pressure, velocity and temperature are not uniform across the active area, these parameters vary from the inlet to the outlet and they are directly related to the design of the channels. Likewise, results demonstrated that electrolyzer performance is sensitive to reactants flow rate, therefore is absolutely necessary that the electrodes receive the same amount of water. Accumulation of gas and hot spots in non desired areas will be avoided when water distribution is homogeneous. Numerical polarization curves were obtained and validated by experimental data reported in the literature. In this study, it was possible to obtain relevant information on the mass transport, heat transfer and electrochemical reactions that take place in the PEM electrolyzer. These results can be used as criteria to improve the design and performance of the PEM electrolyzer.

Keywords: PEM electrolyzer, Flow field, CFD

1. Introduction

The quality of human life depends greatly on the availability of energy resources and the ability to transform them into useful energy. Hydrogen is regarded as the fuel of the future due to its high energy density (33.3 kWh/kg). The hydrogen technology play an important role in renewable energy and these are suitably combined with solar and wind energy.

Water electrolysis is the most attractive method for producing hydrogen. Water is decomposed into hydrogen and oxygen from the passage of an electric current.

---

*Author for correspondence: J.M.T. Sierra Grajeda, T: 52 777 184 35 85, E: juanmsg@live.com.mx

The standard potential of a water electrolysis cell is 1.23V, and electrical energy can be obtained from photovoltaic panels or wind turbines, among others.

Although there are many studies reported in literature about theoretical analysis of fuel cells [1-5], few studies are focused on the PEM (proton exchange membrane) electrolysis cells. In order to improve the performance of electrolysis cells, analytical and numerical models for the device are necessary to optimize their design. For example, Diego de Haro Ruiz et al [6] developed a mathematical and numerical framework for PEM electrolyzers. They studied the fundamental issues associated with mass transport, energy and electrochemical processes. Also they worked in the development and integration of various flow channel designs for high performance hydrogen production. A single-domain model was implemented in the commercial CFD code ANSYS Fluent. The results suggested that multiple-serpentine channel design performs better in term of hydrogen production and uniformity of temperature with reasonable pressure drop. Otherwise, Zhang et al [7] developed a system for hydrogen production a PEM electrolyzer based on semi-empirical equations, thermodynamic-electrochemical modeling of water splitting reaction. They confirmed that the joule heat resulting from the irreversibilities inside the PEM electrolyzer was larger than that needed in the water splitting process in the whole region of the electric current density. Some alternative configurations were designed to improve the overall performance of the system and the corresponding expressions of the efficiency were also derived. Recently, Han et al. [8] performed a comprehensive computational model for a PEM electrolyzer cells introducing a new ohmic loss model. The interfacial resistance between the membrane and electrode had been found to play an important part for electrolyzer performance and an overpotential was increased significantly with the interfacial resistance.

In this research a 3D computational fluid dynamics (CFD) study in different flow fields of a PEM electrolyzer is presented. The aim of this work is focused on the heat and mass transfer that take place inside the electrolyzer, such as water distribution, and temperature variations in the porous media. The flow fields evaluated on this investigation were the multichannels serpentine, straight channels and pin type design (Fig. 1). The standard equations of fluid mechanics, such as mass conservation equation, momentum and energy were solved using a commercial code Ansys - Fluent® 15.0. The operating conditions set in the model were 2 atm and 75 °C, for pressure and temperature, respectively. The flow fields were simulated in a single model of electrolyzer. The models are constituted by porous media, channels and monopolar plates as can be seen in Fig. 2.

In order to establish the accuracy of the results, a grid independence study was realized. The total number of hexaedral elements in the models was about 500,000 with a grid size of 0.2 for channels and ribs, 0.035 for gas diffusion layer, and 0.007 for catalyst layer.

Consecutively to solve the model, it was considered the following assumptions: (i) the electrolysis cell operates under steady-state and non-isothermal conditions; (ii) based on Reynolds number calculation a laminar flow was considered in the channels; (iii) the porous zones were assumed to be isotropic; (iv) the electrochemical reactions were not considered in electrodes.

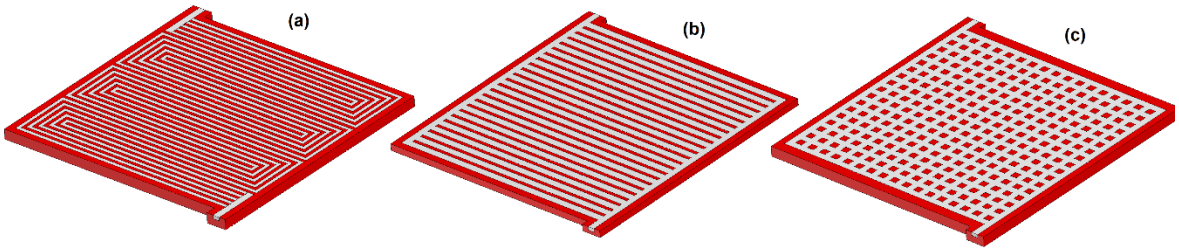

Fig. 1. Designs of the flow fields with 50cm^2 of active area, (a) multichannel serpentine, (b) straight channels, and (b) pin type design.

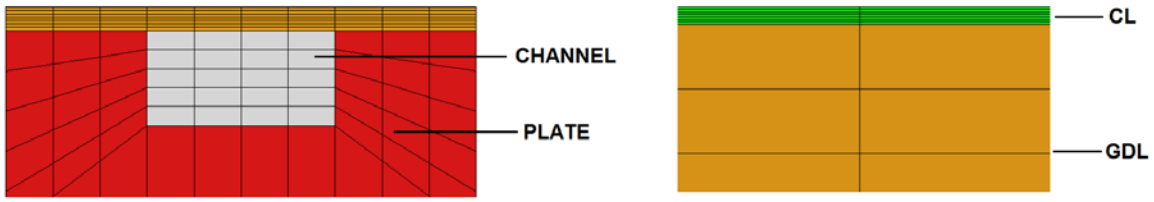

Fig. 2. Mesh visualization and components of PEM electrolyzer model.

The boundary conditions used in the simulation were taken from literature data [6, 9, 10]. The mass flow rate used in this study was obtained from experimental results and it vary from 1×10^{-5} to 1×10^{-3} kg/s. These values are shown in Table 1.

Table 1. Boundary conditions used in the model.

Parameter	symbol	unit	value
Pressure	P	atm	2
Flow temperature	T_C	K	348
Mass flow inlet	$\dot{m}$	kg/s	1×10^{-5}
Water viscosity	μ	kg/m·s	3.78×10^{-4}
Water density	ρ	kg/m^3	974.68
GDL porosity	ε_{GDL}	-	0.4
GDL viscous resistance	$v_{R,GDL}$	1/m^2	1×10^{12}
CL porosity	ε_{CL}	-	0.2
CL viscous resistance	$v_{R,CL}$	1/m^2	4×10^{12}

3. Mathematical Model

Mass transport occurring inside a PEM electrolyzer are represented by the governing equations of mass conservation, momentum and energy. These equations are described below.

3.1. Continuity equation

The continuity equation represents the mass conservation for all transport processes that take place in the fuel cell, such as fluid flow and mass diffusion. This equation is written in a simplified form (steady state) as:

$$\frac{\partial(\rho u)}{\partial x}+\frac{\partial(\rho v)}{\partial y}+\frac{\partial(\rho w)}{\partial z}=S_m \tag{1}$$

where ρ is the fluid density, u, v and w are the vector velocities and S_m is the source term that contains the characteristics of porous media, its values is zero in the flow channels. This equation states that the mass flow rate contained in a control volume is exactly equal to the net flow of mass towards the same volume control.

3.2. Momentum transport

The principle of conservation of momentum is an application of Newton's second law to a fluid element and states that speed at which the momentum of a fluid volume is changing is equal to the net external force acting on mass.
The momentum transport equation in a steady state is described by:

$$\begin{aligned}
u\frac{\partial(\rho u)}{\partial x}+v\frac{\partial(\rho u)}{\partial y}+w\frac{\partial(\rho u)}{\partial z}&=-\frac{\partial p}{\partial x}+\frac{\partial}{\partial x}\left(\mu\frac{\partial u}{\partial x}\right)+\frac{\partial}{\partial y}\left(\mu\frac{\partial u}{\partial y}\right)+\frac{\partial}{\partial z}\left(\mu\frac{\partial u}{\partial z}\right)+S_{px}\\
u\frac{\partial(\rho v)}{\partial x}+v\frac{\partial(\rho v)}{\partial y}+w\frac{\partial(\rho v)}{\partial z}&=-\frac{\partial p}{\partial y}+\frac{\partial}{\partial x}\left(\mu\frac{\partial v}{\partial x}\right)+\frac{\partial}{\partial y}\left(\mu\frac{\partial v}{\partial y}\right)+\frac{\partial}{\partial z}\left(\mu\frac{\partial v}{\partial z}\right)+S_{py}\\
u\frac{\partial(\rho w)}{\partial x}+v\frac{\partial(\rho w)}{\partial y}+w\frac{\partial(\rho w)}{\partial z}&=-\frac{\partial p}{\partial z}+\frac{\partial}{\partial x}\left(\mu\frac{\partial w}{\partial x}\right)+\frac{\partial}{\partial y}\left(\mu\frac{\partial w}{\partial y}\right)+\frac{\partial}{\partial z}\left(\mu\frac{\partial w}{\partial z}\right)+S_{pz}
\end{aligned} \tag{2}$$

where p is the static pressure, μ_{eff} is the average viscosity of the mixture and S_p is a source term that contains the physical characteristics of porous media and it is defined as:

$$S_p=-(u/k)v \tag{3}$$

where μ is the gas viscosity (kg/m·s), k is the permeability (gas diffusion layers and catalyst layers), and v is the superficial vector velocity at the porous media (m/s) [7].

This last equation corresponds to Darcy's law, which represents the pressure drop through the porous media. With this set of equations the mass transport in channels and porous media is calculated. From these solutions velocity fields and pressure distributions are obtained in different components of the electrolyzer.

3.3. Energy equation

The energy equation for steady state is expressed by:

$$u\frac{\partial(\rho CT)}{\partial x}+v\frac{\partial(\rho CT)}{\partial y}+w\frac{\partial(\rho CT)}{\partial z}=\frac{\partial}{\partial x}\left(k\frac{\partial T}{\partial x}\right)+\frac{\partial}{\partial y}\left(k\frac{\partial T}{\partial y}\right)+\frac{\partial}{\partial z}\left(k\frac{\partial T}{\partial z}\right)+S_h \quad (4)$$

where C is the specific heat, k is the thermal conductivity and S_h is a source term that contains any source of heat. From these equations, heat and mass transfer in channels and porous media are solved in the model of PEM electrolyzer.

4. Results and Discussion

In this section the numerical results for two flow fields of PEM electrolyzer are presented. Likewise, a comparison between serpentine multichannel, straight channels and pin type designs with 50 cm^2 of active area was carried out. Distributions of various physical parameters were obtained at the interface of the gas diffusion layer/catalyst layer (GDL/CL). The operating conditions set in the simulation were 2 atm of pressure and 348 K of temperature. The mass flow rate of water supplied to the electrolyzer was from 1×10^{-5} to 1×10^{-3} kg/s. Based on a calculation of Reynolds number a laminar flow was considered in the channels (Re < 2300).

4.1 Pressure drops

The results of pressure drops (Pa) for different flow fields are ilustrated in Fig. 3. In the contours it can be seen that pressure is reduced from the inlet to the outlet and the pin type design showed the smallest pressure drops with values up to 1.2 Pa. Although the multichannel serpentine has five channels in parallel configuration, the pressure drop (8 Pa) through it is slightly higher than straight channels (2 Pa) and pin type design. This happens due to the path length and the bends of the channel.

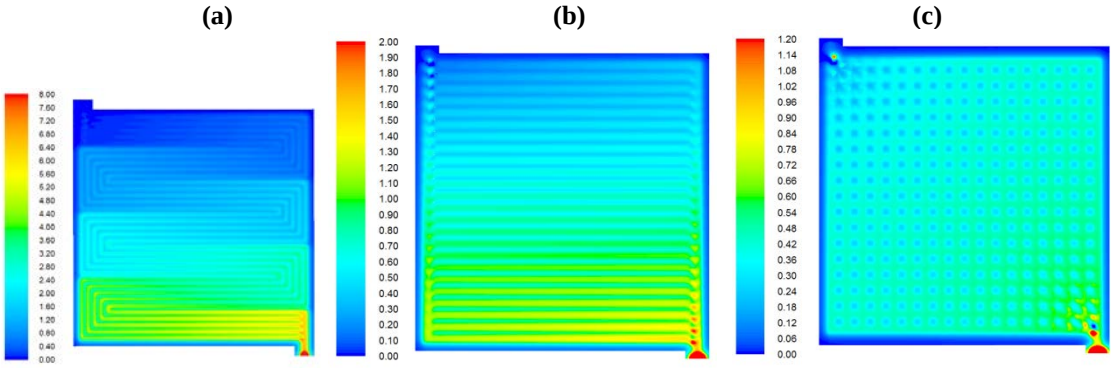

Fig. 3. Pressure distributions (Pa) at the GDL/CL interface for (a) multichannel serpentine (b) straight channels and (c) pin type design.

4.2 Velocity distributions

Fig. 4. shows the velocity distributions for three flow fields at the cathode interface GDL/CL. In these results the multichannel serpentine showed higher velocities (1×10^{-5} m/s) than the straight channels (2×10^{-6} m/s) and pin type design (1×10^{-6} m/s), about one order of magnitude larger. The velocity of water flow always is reduced from the inlet channel to the outlet channel. For these results the multichannel serpentine design shows an

even distribution of water throughout the gas diffusion layer. Water travels over the entire flow field and its velocity is gradually reduced.

However, the flow field with straight channels and the pin type design showed more uniform velocity distributions across the gas diffusion layer. In contrast to a fuel cell that uses hydrogen and oxygen, the serpentine design is the best flow field, however, these designs favor the distribution of liquid water for an electrolysis cell.

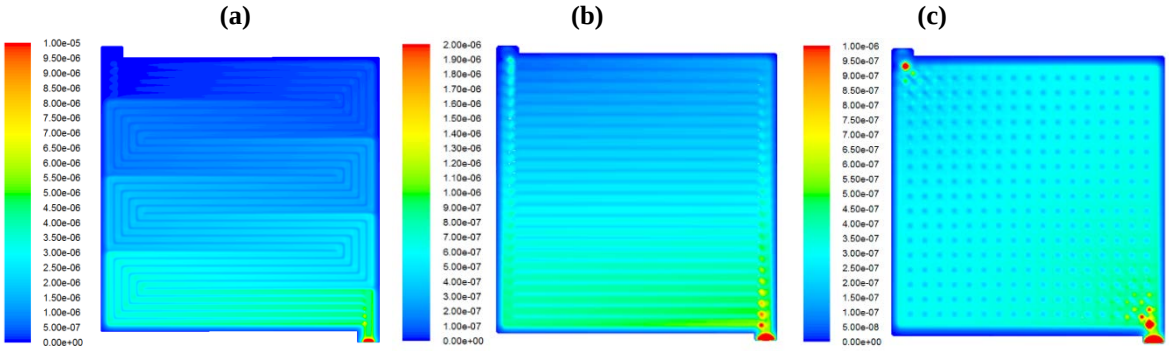

Fig. 4. Velocity distributions (m/s) at the GDL/CL interface for (a) multichannel serpentine, (b) straight channels, and (c) pin type design.

4.3 Temperature distributions

The temperature distribution at interface GDL/CL for three base designs is presented in Fig. 5. Water was supplied to the cell at 348 K and the flow field is responsible for dissipating heat through the porous media. The temperature is slightly uniform on catalyst layer for (b) and (c), however, for serpentine design (a) the temperature distribution is high at inlet channel and lower near to the outlet channel. Moreover, this design showed higher temperature values, from 310 - 328 K, compared with other designs 304 - 324 K. Then, the heat is better distributed in the porous media by straight channels flow field and pin type design than the multichannel serpentine. Therefore, accumulation of hot spots in non desired areas can be avoided when water distribution is homogeneous in the flow field.

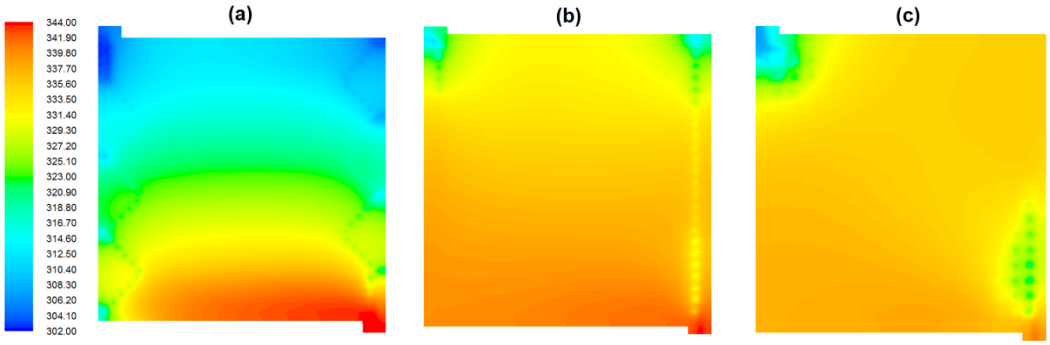

Fig. 5. Temperature distributions (K) at the GDL/CL interface for (a) multichannel serpentine, (b) straight channels, and (c) pin type design.

5. Conclusion

A 3D numerical analysis of a PEM electrolyzer has been developed in order to study the effect of three flow fields on the heat and mass transfer processes. Different mass flow rates were used to maximize the effect of the flow field on distributions of pressure, velocity and temperature at the interface GDL/CL. From this study was demonstrated that straight channels flow field and pin type design has the best performance. The pressure, velocity and temperature are most uniform on catalyst layer for this last designs. These factors can be considered to avoid a catalyst degradation in the electrolyzer. In contrast to a PEM fuel cell that uses hydrogen and oxygen, the serpentine design is not the best flow field for a PEM electrolyzer.

Acknowledgements

The authors thanks the National Council for Science and Technology for the financial support from the project 252003 “Programa de Redes Temáticas (RTH2)”. Also the author gratefully acknowledges to UNACAR for the granted support to perform the numerical simulations in their computing equipment and the use of Ansys-Fluent® software license.

References

[1] S. Shimpalee, and J.W. Van Zee, The impact of channel path length on PEMFC flow-field design. J. Power Sources 2006; 160: 398-406.
[2] N. Djilali, and T. Berning, Computational model of a PEMFC with serpentine gas flow channels. J. Power Sources 2004; 130: 149-157.
[3] T. Berning and N. Djilali, Three-dimensional computational analysis of transport phenomena in a PEM fuel cell, a parametric study. J. Power Sources 2003; 124: 440-452.
[4] J. M. Sierra, S. J. Figueroa, S. E. Díaz, J. Vargas, P. J. Sebastian, Numerical evaluation of a PEM fue cell with conventional flow fields adapted to tubular plates. Int. Journal of Hydrogen Energy 2014; 39: 16694-16705.
[5] A. P. Manso, F.F. Marzo, J. Barranco, X. Garikano, M. Garmendia Mujika, Influence of geometric parameters of the flow fields on the performance of a PEM fuel cell. A review. Int. Journal of Hydrogen Energy 2012; 37: 15256-15287.
[6] Diego de Haro Ruiz, Agus P. Samito, Tariq Shamim. Numerical Investigation of the High Temperature PEM Electrolyzer: Effect of Flow Channel Configurations; ECS Transactions 2013; 58: 99-112.
[7] Houcheng Zhang, Shanhe Su, Guoxing Lin, Jincan Chen. Efficiency Calculation and Configuration Design of a PEM Electrolyzer System for Hydrogen Production, Int. J. Electrochem. Sci. 2012; 7: 4143-4157.
[8] Bo Han, Stuart M. Steen III, Jingke Mo, Feng-Yuan Zhang. Electrochemical performance modeling of a proton exchange membrane electrolyzer cell for hydrogen energy, Int. J. Hydrogen Energy 2015; 40: 7006-7016.
[9] N. Briguglio, G. Brunaccini, S. Siracusano, N. Randazzo, R. Ornelas, Design and testing of a compact PEM electrolyzer system. Int. Journal of Hydrogen Energy, 2013; 38:11519-11529.
[10] H. Ito, T. Maeda, A. Nakano, Y. Hasegawa, Effect of flow regime of recirculating water on a PEM electrolyzer. Int. Journal of Hydrogen Energy, 2010; 35: 9550-9560.

Chapter 4.6. APQP methodology applied in the design and manufacture of an alkaline electrolyzer

M. Horcasitas-Verdiguel[a,*]; R. G. Gonzalez-Huerta[b]; J. M. Sandoval Pineda[a]

[a]ESIME-IPN UA, Sección de posgrado, Av. de las Granjas 682, C.P. 02250, México, D.F.
[b]ESIQIE-IPN, Laboratorio de Electroquímica y Corrosión, UPALM, 07738, México D.F.

ABSTRACT

This communication analyzes the main main problems of the alkaline electrolysis, i.e., the process of manufacturing, geometry and materials, its requirements for a design that allows control parameters such as electric current, gas outlet, optimal level of electrolyte, corrosion, sealing system, etc., this with an objective, manufacture and get to get an electrolyzer with maximum efficiency. Therefore the use of Hydrogen produced from electrolysis of water may be used as an additive with fossil fuels for transport that can reduce certain parameters such as CO and CO_2 pollutants., And its overall objective to reduce automotive emissions. Hydrogen is of particular interest as secondary energy carrier because it has the potential to be generated in situ, stored and transported. Due to the particular application allows Oxyhydrogen gas generation in situ and is not be high purity, as this gas will be injected into internal combustion engines as an additive to the mixture air-fuel (gasoline or diesel). This paper focuses on the APQP methodology for the design of an alkaline electrolyzer. APQP is an analytical methodology used to ensure potential problems are considered and addressed through the process of product development and process (APQP -Planning advanced quality of a product). With gas generation technology Oxyhydrogen by alkaline electrolysis, the Methodology application and appropriate manufacturing it is possible to develop a more efficient reactor in all its features and a better design with optimal materials and special components. Good design and manufacture of the components of the electrolyzer substantially improve the performance thereof, as well as the efficiency current and voltage as a good internal connection between each electrode decreases overpotential and the distance between anode and cathode reduce the resistance.

Keywords: Hydrogen, APQP, Alkaline electrolysis, Manufacturing

1. Introduction

Akansu S.O., Dulger A., Kahraman N. (2004) have demonstrated that most of the energy consumed across societies is furnished by fossil fuels. Burning fossil fuels generates residues, predominantly emissions, which reach the atmosphere in the form of gas, dust and

---

* Author for correspondence: M. Horcasitas-Verdiguel, E: hove_lenuma@hotmail.com

ashes classified as particles regarding pollution [1]. Finding new fuels such as hydrogen is therefore essential. However, for hydrogen to be sustainable, it must be drawn from the water, thus avoiding the need for hydrocarbons.

The energy produced by the electrochemical decomposition of water is relatively high, as the H2O molecules are characterized by a stable structure at room temperature [2].

H. Matsushima, T. Nishida, Y. Konishi, Y. Fukunaka, Y. Ito, K. Kuribayashi (2003) have revealed that, in terms of thermodynamics, a theoretical voltage of 1.23 V is required to break the bonds between hydrogen and oxygen atoms. This voltage is also known as offset voltage. However, considerably higher voltage levels are used in industrial electrolysis cells: from 1.48 V to 3 V and beyond for a single cell. The excess voltage is known as reaction "overpotential" [3].

Once produced, hydrogen provides clean fuel: when burned with oxygen, its only exhaust fumes consist of water vapor; however, when burned with air, hydrogen lean mixtures are required to avoid the formation of nitrogen oxides. For hydrogen to be considered a form of clean energy worlwide, it must be derived from renewable primary energy allowing to split water in an electrolysis process [4,5].

J.M. Gomes Antunes, R. Mikalsen, A.P. Roskilly (2008) have reported the results of experimental research on operating a CI engine by means of Compression (EC) in the power mode through homogeneous-charge compression ignition (HCCI) using hydrogen fuel. Their analysis included factors such as motor efficiency, emissions and mechanical loads. If greater efficiency is to be attained in the use of oxyhydrogen, it is essencial to conduct further testing and evaluation regarding the performance and optimization of alkaline electrolysers with the view of incorporating them into CI engines. This requires configuration adjustments vis-à-vis their original operating parameters [6].

Research has indicated that it is possible to mix hydrogen with fossil fuels, such as to reduce automotive emissions while maintaining the power obtained with gasoline.

H. An, W.M. Yang, A. Maghbouli, J. Li, S.K. Chou, K.J. Chua, J.X. Wang, (2014) have conducted experiments and performed simulations with a diesel engine fueled by biodiesel with additional hydrogen inductions of 0.5%, 1%, 2% and 3% vol of H_2 in the air. They developed a reaction mechanism to include the hydrogen and biodiesel kinetics reaction with CO, NOx [7].

O. H. Mohammad, Mohamed Y.E. Selim, Salah-A.B. Al-Omari, Emad Elnajjar (2014) have conducted experimental research on the behavior of the compression ignition engine (EC). They promoted combustion by enriching the air intake manifold with a hydrogen supplement at atmospheric conditions. The study showed the engine's thermal efficiency, NOx emissions and exhaust temperature by varying the hydrogen content, engine speed and ignition timing. Results indicated that the thermal efficiency of the compression ignition engine rises with the hydrogen content in the intake air for the same diesel mass flow rate. The impact of the hydrogen supplement on the efficiency of the engine is more pronounced at a lower engine speed with partial load. It produces greater NOx emissions attributable to the rising temperature of combustion, and a drop in CO emissions [8].

Tuan Anh Nguyen, Masato Mikami (2013) researched the noise characteristics of combustion in a diesel engine with hydrogen added to the intake air. The noise of the engine with the addition of 10% more hydrogen in volume in intake air was less than that obtained with diesel fuel [9].

2. Materials and Methods

2.1. Alkaline electrolyzer design considerations

The APQP analytical methodology permits generating a base system to follow the manufacturing process of an alkaline electrolyzer step by step, through a detailed analysis of each one of the manufacturing materials and processes of its components. It comprises considerations related to materials, leaks, corrosion, stacking of electrodes and series-parallel arrangement.

2.2. Quality and reliability objectives

Figure 1 illustrates the different points that should be considered for good manufacturing of an electrolyzer, including matters of security and economics.

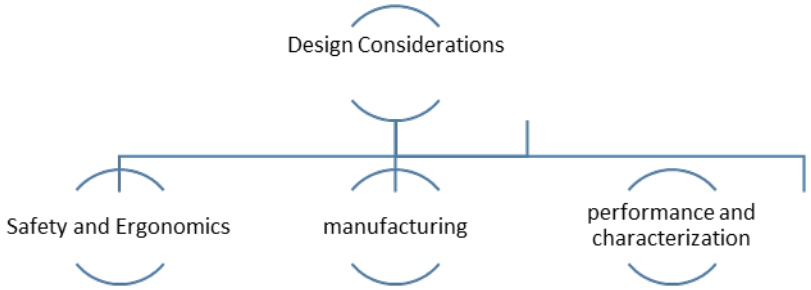

Figure 1. Main design and manufacturing considerations.

2.3 Electrolyzer design and development

Subsequent to achieving a good design, a manufacturing and development process was proposed for the alkaline electrolyzer in order to obtain laboratory trial results and, hence, actual performance data in the field of application and possible failures.

2.4 Considerations on manufacturing, assembly and serviceability

Principles have been established based on experience, with innovative improvements evolving continuously in design and manufacturing techniques for raising productivity and quality and increasing the security system of the electrolyzer. Among others, the denominated Poka Yoke process has contributed to minimize the risk for errors and connect parts correctly.

2.5. Failure Mode and Effect Analysis (AMEF)

Application of *FMEA* for analyzing alkaline elecrolizer manufacturing centered on elements and materials with certain characteristics and failure modes valued.

2.6. Design verification and review

In this area, a functionality analysis was performed for each one of the elements of the electrolizer. This method was carried out in order to prevent problems and

misunderstandings in an engineering inspection of the design: functionality, reliability, service cycles, experiment design and trial failures.

2.7. Characterization of the oxyhydrogen reactor

At this stage, the previously designed electrolyzers were characterized in order to register their characteristic performance curves, and calculate their voltage and current efficiency based on the corresponding equations. Faraday laws were applied to calculate the theoretical and actual volume of an alkaline electrolizer with the view of determining the efficiency of the electrolizer. The following equation was used to calculate actual volume:

$$V_{CE} = V_1 \frac{(P - P_V)}{760} \frac{298}{T + 273} \quad (1)$$

Therefore, Equation 2 was used to calculate the volume in standard conditions, and Equation 3 to calculate the volume in normal conditions:

$$V_T = 1.899x10^{-4}\, I\, t \quad (2)$$

$$V_T = 1.7399\, x\, 10 - 4\, I\, t \quad (3)$$

Where:

V_{ce} → Actual volume
V_1 → Volume in liters (Cd.de conditions of Mexico)
P → Atmospheric pressure (585 mm Hg)
P_v → Vapor pressure of 18 mm Hg
T → Ambient temperature (° C)

2.8. Theoretical study of the oxyhydrogen reactor in internal combustion engines

Analysis for quantifying the amount of oxyhydrogen gas furnished during the combustion process in an engine is based not only on the volume generated by the reactor and the percentage of enrichment desired to fuel the combustion process, but also on the characteristics and size of the motor being studied.

The following equation was used to define the volume percentage of the oxyhydrogen injected in the air intake system:

$$\alpha_{2H2/O2} = [V_{0H2}/(V_{0H2} + V_{air})]x\ 100\% \quad (4)$$

The following equation was used to perform calculations based on the percentage of oxyhydrogen gas:

$$V_{OH2} = \frac{V_{aire}}{\left(\frac{1}{\alpha_{2H2O/O2}} - 1\right)} \quad (5)$$

Where:

$\alpha_{2H2/O2}$ → Porcentaje de volumen oxyhydrogen
V_{0H2} → Volumen de oxyhydrogen
V_{aire} → Volumen de aire

Reference is made to charaacteristic equations for the calculation of the volume of air, according to the specific case, and the type of motor based on the Diesel or the Otto cycle not included in this work.

3. Results and Discussion

3.1. Alkaline electrolyzer design and construction

The cooperative used of design and manufactauring tools has led to a more detailed analysis for the manufacturing of the alkaline electrolyzer. Figure 2 dhows the technology involved in the use of computers to carry out the tasks of creation, modification, analysis and optimization of the design of the elements comprised by the electrolyzer.
Post fabrication electrolyser proceeded to a detailed process for calculating the concentration study electrolytic solutions 5%, 15% and 30% by weight were analyzed.

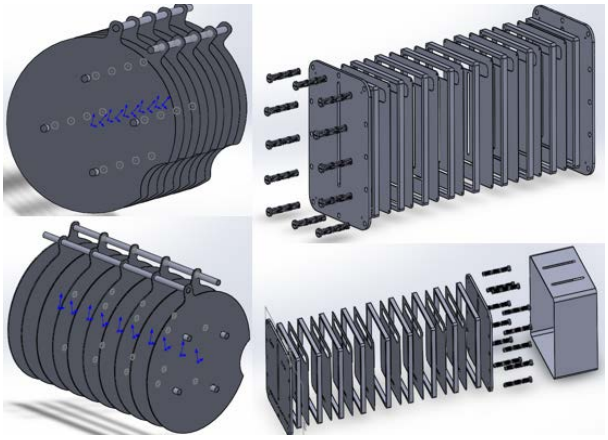

Fig. 2. Electrolyzer design.

To calculate entrainment gases generated in electrolyte solutions at 5%, 15% and 30% by weight NaOH conductance of the water contained in a bubbler was obtained at the outlet of the electrolyzer after 2 hours of operation were prepared. Figure 3 shows the performance curve of electrolyzed shown, the test system consisted of an electrolyzer

connected in parallel with stainless steel plates, the energy supply using a power source Matrix 10A-30V, a sweep current was applied current from 0.5 A to 3.5 a, recording the voltage required by the system.

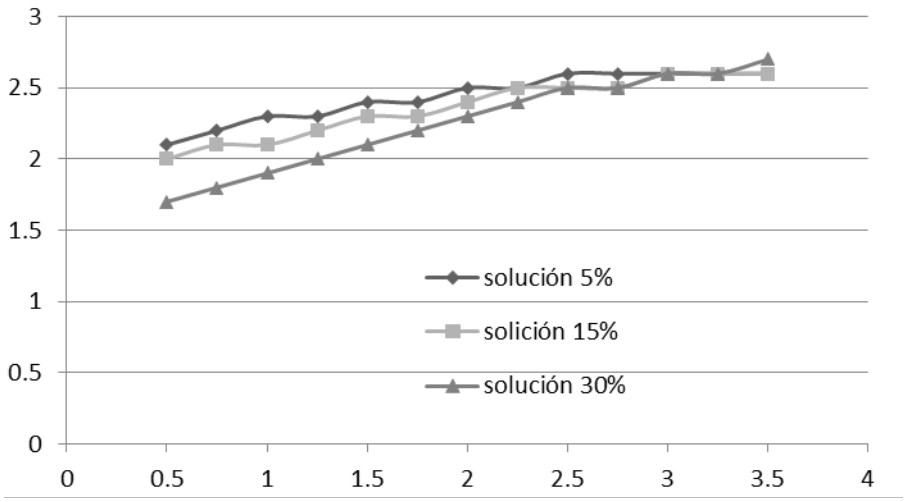

Fig. 3. Electrolyzer performance with different concentrations of electrolyte

Figure 3 shows that at low currents (i <2 A) the required voltage is lower for the 30% solution, in all cases this is due to the resistance imposed by low conductance of the electrolyte, generating an envelope-potential in the overall performance of the electrolyzer, which results in increased energy consumption. A higher current intensity (i> 2 A) the required potential is almost the same, this is because the efficiency of the electrolyzer increases with increased current intensity, attributed to increased temperature in the electrode-electrolyte is applied, looking more this increased efficiency with 5% electrolyte, together with the drag was lower, with an increase in the water conductivity of 0.5 µS bubbler 10 µS after two hours of operation, while in the solution 30% increase water conductivity increase up to 40 µS.

Tests were performed by varying the area and the number of electrodes for its performance curves. Figure 4 shows the current vs voltage curve of the systems that were tested.

In the process of characterizing the electrolyzer the actual volume and the theoretical volume is calculated, which are raised by the equations set (1) and (2), this calculation is useful to determine the efficiencies.

In order to meet its performance curve and comparing their efficiency to determine which had the best manufacturing process

$$\eta_I = \frac{v_{real}}{v_{teórico}}(100) \tag{6}$$

$$\eta_v = \frac{1.48_v}{E\exp_v}\eta_I \quad (7)$$

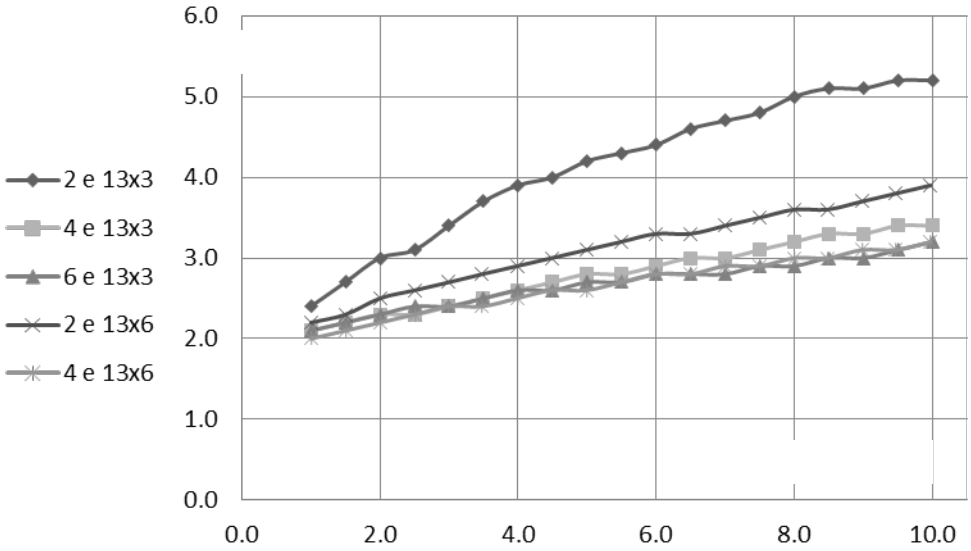

Fig. 4. Electrolyzer performance with different concentrations of electrolyte

where:

η_I → Power efficiency

η_v → Voltage efficiency

$E\exp_v$ → Experienced voltage

v_{real} → Actual volume

$v_{teórico}$ → Theorecal volume

Table 1 shows a comparison of performance electrolyzer efficiency for a given expenditure during working time.

Table 1. Comparison between actual and theoretical volume.

Flow ml/min	Actual volume (Nml)	Ampere	Theorecal volume	η_I	η_V
12.7	8.84	1.0	11.34	77.91	70.48
26.4	13.36	2.0	22.68	80.98	64.35
41.3	28.73	3.0	34.02	84.46	61.67
69.4	48.28	5.0	56.70	85.15	54.81
114	79.31	8.0	90.72	87.42	51.03
147	102.27	10	113.40	90.18	46..25

4. Conclusion

It was determined that the overpotential required for the overall system depends on the electrode material, current density (current is proportional to the overpotential), temperature (increasing temperature decreases overpotential system), this means that the flow hydrogen mass increases with increasing temperature and electrolyte concentration, higher temperature decreases the potential required to break the water molecule. Good design and manufacture of the components of the electrolyzer substantially improve the performance thereof, as well as its current efficiency and voltage as a good internal connection between each electrode decreases overpotential and the distance between anode and cathode reduce resistance.

Acknowledgements

We thank the IPN-SIP for the support given to multidisciplinary project 1683.

References

[1] S.O. Akansu, Z. Dulger, N. Kahraman, T. N. Veziroglu, *Internal combustion engines fueled by natural gas—hydrogen mixtures, International Journal of Hydrogen Energy*, p. 1527-1539, Vol. 29, Issue 14, November (2004).

[2] F.N Lin, W.I. Moore, S.W. Walker, *Economics of liquid hydrogen from water electrolysis, International Journal of Hydrogen Energy*, p.811–815, Vol. 10, Issue 12, (1985).

[3] H. Matsushima, T. Nishida, Y. Konishi, Y. Fukunaka, Y. Ito, K. Kuribayashi, *Water electrolysis under microgravity Part 1. Experimental technique, Electrochimica Acta*, p. 4119-4125 Vol. 48, Issue 28, December (2003).

[4] J. Sigurvinsson, C. Mansilla, B.Arnason, A. Bontemps, A.Maréchal, T.I. Sigfusson, F.Werkoff, *Heat Transfer Problems for the Production of Hydrogen from Geothermal Energy, Energy Convesion. Management*, p. 3543-3551, Vol. 47, issue 20, December (2006).

[5] C. J Winter, J.Nitsch, *Hydrogen as an Energy Carrier: Technologies, Systems, Economy* ISBN: 978-3-642-64872-4, Springer, (1988)

[6] J.M. Gomes Antunes, R. Mikalsen, A.P. Roskilly, *An investigation of hydrogen-fuelled HCCI engine performance and operation, International Journal of Hydrogen Energy*, p. 5823-5828, Vol. 33, Issue 20, October (2008).

[7] H. An, W.M. Yang, A. Maghbouli, J. Li, S.K. Chou, K.J. Chua, J.X. Wang, L. Li, *Numerical investigation on the combustion and emission characteristics of a hydrogen assisted biodiesel combustion in a diesel engine, Journal Fuel*, p. 186-194, (2014)

[8] O. H. Mohammad, Mohamed Y.E. Selim, Salah-A.B. Al-Omari, Emad Elnajjar, *"Hydrogen supplement co-combustion with diesel in compression ignition engine", Renewable Energy*, p. 1-7, (2014)

[9] Tuan Anh Nguyen, Masato Mikami, *Effect of hydrogen addition to intake air on combustion noise from a diesel engine, International Journal of Hydrogen Energy*, p. 4153-4162, Vol. 38, (2013)

Chapter 4.7. Thermodynamic analysis of the autothermal partial oxidation/steam reforming of ethanol by MeO (Me = Ni, Cu) with CO_2 capture

V. Collins-Martínez; M. J. Meléndez-Zaragoza; A. López-Ortiz*

Departamento de Ingeniería y Química de Materiales, Centro de Investigación en Materiales Avanzados, S.C., Miguel de Cervantes 120, Chihuahua, Chih., México, 31136, México.

ABSTRACT

Hydrogen is generally considered as a clean and high efficient energy carrier that can be employed for power generation through fuel cell units, with innocuous water as the only by-product, to decrease the release of pollutants into the atmosphere. Today, there is a developing interest for hydrogen generation from renewable sources such as bio-oil, bio-gas, bio-ethanol or bio-butanol etc. Among the different renewable feedstock options, ethanol has been viewed as an appealing feedstock because of its relatively high hydrogen content, accessibility, nontoxicity, ease of handling and safety. The present thermodynamic analysis is aimed to explore autothermal conditions at equilibrium for a high H_2-syngas production under the combined ethanol steam reforming (SRE), chemical looping partial oxidation (CLPOX) and CO_2 solid absorption reaction system. SRE studied conditions were H_2O/C_2H_6O = 3-6 molar ratio, CLPOX employed NiO or CuO as metal oxide (MeO) oxygen carriers from MeO/C_2H_6O = 0.05-1.5 molar ratio, while 2 kmols of CaO were used for CO_2 capture in a T range of 100-900 °C at 1 atm. NiO most favorable adiabatic conditions ($T \geq 500$ °C and $C \leq 0.1$ kmols) were: H_2O/C_2H_6O = 3 and NiO/C_2H_6O = 0.05-0.5. While, for CuO was at H_2O/C_2H_6O = 4, CuO/C_2H_6O = 0.5 and T_{adiab} = 529 °C. These favorable reaction conditions are the product of the combination of the exothermic carbonation reaction and its influence over the thermodynamic equilibrium over the POX and SRE endothermic reactions.

Keywords: Combined SRE CLPOX and CO_2 capture, Autothermal thermodynamic conditions

1. Introduction

Hydrogen is generally considered as a clean and high efficient energy carrier that can be employed for power generation through fuel cell units, with innocuous water as the only by-product, to decrease the release of pollutants into the atmosphere [1]. Hydrogen presents an energy content of 143 MJ/kg, which is approximately three times higher than any liquid

---

* Author for correspondence:
Dr. Alejandro López-Ortiz, T:52 614 4394815, E: alejandro.lopez@cimav.edu.mx

hydrocarbon based fuel [2]. Furthermore, other benefits for hydrogen utilization are plenty availability, use of a wide diversity of feedstocks and a variety of production technologies [3]. Other uses of hydrogen include the manufacture of ammonia and other fertilizers (e.g. urea), to upgrade heavy oils, and to produce a wide variety of chemicals and fuels.

Currently, new approaches are being investigated in order to produce hydrogen in a mass scale such as water electrolysis, hydrocarbon reforming, photocatalytic water splitting and biological processes etc [4-6]. Nevertheless, steam reforming of fossil based hydrocarbons, mainly natural gas, is the most common process for hydrogen production worldwide, but generally ignoring the high costs in terms of damage to the environment [7]. Furthermore, the use of fossil fuels for supplementary energy production is non-sustainable.

Considering the sustainable advance, there is a developing interest for hydrogen generation from renewable sources such as bio-oil, bio-gas, bio-ethanol or bio-butanol etc. [8]. Among the different renewable feedstock options, ethanol has been viewed as an appealing feedstock because of its relatively high hydrogen content, accessibility, nontoxicity, ease of handling and safety [9].

Moreover, steam reforming (SR), partial oxidation (POX) and autothermal steam reforming (ATR) are the most important studied processes for hydrogen production from ethanol.

$$C_2H_5OH + 3H_2O \rightarrow 6H_2 + 2CO_2 \qquad \Delta H^0 = 173.3 \text{ kJ/mol} \qquad (1)$$

Ethanol SR (Eq. (1)) is the most widely studied route since it generates the highest hydrogen yield. This process is typically considered as a combination of ethanol SR to syngas followed by water–gas shift (WGS, Eq. 2).

$$CO + H_2O \rightarrow H_2 + CO_2 \qquad \Delta H^0 = -41.138 \text{ kJ/mol} \qquad (2)$$

Thermodynamic analysis indicates that equilibrium H_2 yield can be as high as 70 mol% for ethanol SR at 700 °C with a stoichiometric molar feed ratio (H_2O/C_2H_5OH) of 3 [10,11]. However, ethanol SR is highly endothermic, demanding a large amount of energy, which increases operating costs. This serious disadvantage significantly hinders the practical hydrogen production, particularly for on-board applications.

$$C_2H_5OH + 1.5O_2 \rightarrow 3H_2 + 2CO_2 \qquad \Delta H^0 = -552.2 \text{ kJ/mol} \qquad (3)$$

POX of ethanol (reaction 3) is an alternative process for hydrogen production. Compared to ethanol SR, POX is exothermic and fast, and very appropriate for handling rapid loading variations, such as those usually demanded by on-board reformers, which frequently perform under variable conditions. In the meantime, benefits of this oxidative process are its lower reaction temperature and fewer tendency for carbon formation due to the oxygen addition. Though, an excess in oxygen content oxidation may lead to lower hydrogen yield compared to the SR process.

$$C_2H_5OH + 1.8H_2O + 0.6O_2 \rightarrow 4.8\ H_2 + 2CO_2 \qquad \Delta H^0 = -116.9 \text{ kJ/mol} \qquad (4)$$

ATR of ethanol, is a combination of SR and POX represents a compromise between energy efficiency and hydrogen yield. Oxygen from the feed may provide the necessary heat for the endothermic ethanol SR due to the exothermic nature of the partial oxidation of ethanol [12].

Therefore, with a stoichiometric feed ratio ($H_2O/C_2H_5OH/O_2$ = 3/1/0.6), the overall reaction can be thermally neutral (ΔH^0 =+4.4 kJ/mol) and the dry H_2 content can reach ~70 mol% in the product stream [13]. This means that ethanol ATR not only alleviate the heat demand of the system, but leads to a reasonably high hydrogen yield. Moreover, the presence of oxygen also eases the removal of carbon deposition formed during the reactor operation.

Thermodynamic analysis of ethanol SR process shows high values of equilibrium constant for temperatures above 323 °C and an increase in temperature prevents methane formation (the main byproduct consuming H_2) [14]. Increasing space time enhances the ethanol conversion and hydrogen selectivity together with the reduction of the intermediates formation [15]. In general, an increase in water in the reactants favors the ethanol conversion and H_2 production. The increase of CO_2 concentration together with the decrease of CO implies that the addition of water also promotes the WGS reaction. The presence of oxygen in the feed may promote the initial ethanol conversion. However, H_2 concentration decreased due to the partial oxidation. Moreover, coke formation significantly reduces with the increase in H_2O/C_2H_5OH or O_2/C_2H_5OH ratios considering the contribution of the carbon gasification by H_2O or O_2. ATR is a convenient reaction for the on-board H_2 production for portable applications requiring high H_2 selectivity and fast response (startup). With suitable precursors and process control, the ATR has been used for the production of other chemicals as well [16]. However, one of the main disadvantages of this ATR reaction system is the need for a pure source of O_2.

Moreover, chemical looping partial oxidation (CLPOX) is a novel POX process that avoids the use of pure O_2 consumption [17]. In this process the O_2/fuel ratio is kept low to prevent complete oxidation to CO_2 and H_2O. This CLPOX process makes possible to obtain a N_2 free Syngas from the POX reactor avoiding the O_2/N_2 separation step in the conventional POX process. This CLPOX process involves the use of an oxygen carrier, which transfers oxygen from air to the fuel, avoiding the direct contact between them. This process is composed of two interconnected reactors; a fuel reactor (I) and an air reactor (II), as described in Figure 1. In the fuel reactor a hydrocarbon-based fuel (ethanol) is partially oxidized to produce Syngas (CO + H_2) by a metal oxide (MeO) that is reduced to a metallic state (Me) or to a reduced form of the MeO. The metal or reduced oxide (Me) is further transferred to the air reactor where it is oxidized back to MeO with air, and the regenerated material is then sent back to the fuel reactor to start a new cycle. The flue gas leaving the air reactor contains N_2 and unreacted O_2, while the exit gases from the fuel reactor contains Syngas, CO_2 and H_2O.

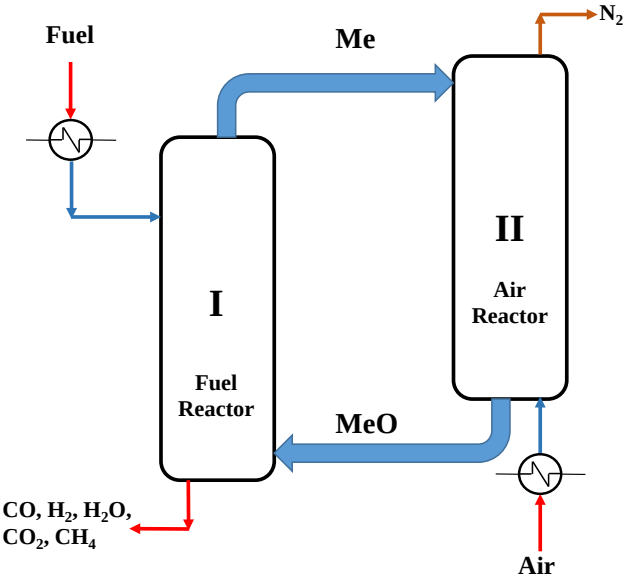

Fig. 1. Conceptual design of CLR process [18]

1.1. The oxygen Carrier in the CLPOX Process

A key component of the CLPOX process is the selection of a suitable oxygen carrier with desirable properties such as: high reactivity, resistant to coke formation, resistant to attrition and sintering through a continuous cycle to cycle operation leading to an extended durability [19].

Some authors have studied several metals such as Fe, Ni, Cu, Co and Mn as oxygen carriers supported in different ceramics like α-Al_2O_3, γ-Al_2O_3, $MgAl_2O_4$, SiO_2, and Mg-ZrO_2 prepared through different techniques [20]. Zatar et al [21] found higher reactive particles composed by Fe, Mn, Ni and Cu supported on $MgAl_2O_4$ compared to those supported on SiO_2. Furthermore, Kale et al [18] reported that CuO happened to be a good oxygen carrier, since showed a complete conversion of ethanol withy easy regenerability.

CuO as oxygen carrier has been extensively studied due to its high reactivity, oxygen transport capacity and lack of thermodynamic limitations to completely oxidize a fuel [22]. While several supports have been successfully tested for CuO as oxygen carrier, Al_2O_3 has been the most often employed [23]. Furthermore, one of the advantages of the use of metals such as Cu and Ni is the fact that they are able to catalyze the SR nad POX reaction, while the mayor disadvantage of NiO resides in its propensity to produce carbon deposits. Therefore, a careful selection of the oxygen carrier is of paramount importance in this CLPOX process.

Several studies have determined the amount of hydrogen yield and carbon formation for the most thermodynamically viable oxygen carriers in CLPOX technology, and these include Fe_3O_4, Mn_2O_3, CoO, CuO and NiO [24]. Recent studies have reported that from most of metal oxides available NiO, CuO and CoO are the oxygen carriers that present the highest amount of O_2 (0.5 mols) per mol of metal [21-26]. Furthermore, they reported that the order from highest to lowest H_2 production was: Fe_3O_4 > CoO > NiO = CuO > Mn_2O_3. However, carbon formation increased in the order: Mn_2O_3 > Fe_3O_4 > CoO > CuO = NiO.

Therefore, a suitable metal oxide to be used in the present thermodynamic analysis can be either NiO or CuO or even a mixture of them.

Another important issue towards the selection of the oxygen carrier is its melting point. The melting point should be high enough to withstand the CLPOX reaction temperature process and to avoid sintering of the circulating particles. Rydén et al [26] found that Cu melting point was too low to withstand the high temperatures required by the CLPOX process, unless this is dispersed in suitable support. While, iron and Mn oxides are known to be hard to reduce and to produce significant amount of carbon compared to other oxides at the same conditions. Also, Ni in known to withstand high temperatures when used as a reforming catalyst supported in a ceramic material. Therefore, based on previous studies it is possible to select Cu and Ni or even a mixture of both to be used in the following proposed reaction system.

1.2. Chemical Looping Autothermal Ethanol Reforming with CO_2 Capture System

Studies in the field argue that even though steam can be added to the fuel (ethanol) to enhance the highly endothermic SR reaction, this could cause the SRE to dominate over the POX process causing a great heat demand in the reaction system. However, the introduction of the exothermic nature of the POX reaction through an oxygen carrier is intended to balance the heat demand to make this process autothermal in nature.

Nevertheless, one disadvantage of the use of Ni as an oxygen carrier is that its POX reaction with ethanol as a fuel is of endothermic nature. On the opposite for CuO this reaction is exothermic if a proper amount of oxides are provided:

$$C_2H_5OH + 3NiO \rightarrow 3H_2 + 2CO_2 + 3Ni \qquad \Delta H^0 = +166.9\ kJ/mol \qquad (5)$$

$$C_2H_5OH + 3CuO \rightarrow 3H_2 + 2CO_2 + 3Cu \qquad \Delta H^0 = -84.8\ kJ/mol \qquad (6)$$

while a complete list of possible involved reactions are reported elsewhere [27]

Furthermore, the introduction of a CO_2 absorbent in the system will presumably shift the equilibrium of the above POX reactions towards a higher H_2 production by:

$$C_2H_5OH + 3NiO + 2CaO \rightarrow 3H_2 + 2CaCO_3 + 3Ni \qquad \Delta H^0 = -189.5\ kJ/mol \qquad (7)$$

$$C_2H_5OH + 3CuO + 2CaO \rightarrow 3H_2 + 2CaCO_3 + 3Cu \qquad \Delta H^0 = -441.2\ kJ/mol \qquad (8)$$

These reactions are both exothermic and then combined with the endothermic nature of the ethanol reforming reaction (1) will result in the overall reaction system to eventually reach a thermoneutral state (autothermal operation) at suitable operation conditions. Therefore, the target is to generate hydrogen/Syngas in the fuel reactor by the combination of the POX, SER and CO_2 capture reactions through:

$$C_2H_5OH + NiO + CaO + H_2O \rightarrow CO + 4H_2 + CaCO_3 + Ni \qquad \Delta H^0 = +34.1\ kJ/mol \quad (9)$$

$$C_2H_5OH + CuO + CaO + H_2O \rightarrow CO + 4H_2 + CaCO_3 + Cu \qquad \Delta H^0 = -49.8\ kJ/mol \quad (10)$$

Even though, these reactions are endothermic or exothermic in nature, proper amounts of NiO and/or CuO would make these thermoneutral. Furthermore, regeneration of the oxygen carriers and CO_2 absorbent are to be performed at the air reactor, where the following reactions are expected to take place:

$$2Ni + 2CaCO_3 + O_2 = 2CO_2 + 2NiO + 2CaO \qquad \Delta H^0 = -123.1 \text{ kJ/mol} \qquad (11)$$

$$2Cu + 2CaCO_3 + O_2 = 2CO_2 + 2CuO + 2CaO \qquad \Delta H^0 = +44.8 \text{ kJ/mol} \qquad (12)$$

The amount of metal oxide (CuO or NiO) and/or CO_2 absorbent (CaO) in order to make this reaction system suitable to operate at the highest possible H_2/Syngas production and at thermoneutral conditions is not an obvious issue. Therefore, the aim of the present thermodynamic study is to explore possible ethanol chemical looping partial oxidation-steam reforming with CO_2 absorption (CLPOX-SR-CO_2A) to produce H_2/Syngas at autothermal and efficient conditions. This reactions system will make use of CuO and NiO as oxygen carrier materials, while CaO will be employed as a CO_2 absorbent.

2. Simulation Methodology: Thermodynamics Method

Thermodynamic calculations employed the Gibbs free energy minimization technique. In a reaction system where many simultaneous reactions take place, equilibrium calculations can be performed through the Gibbs energy minimization approach (also called the nonstoichiometric method). Details of this technique can be found elsewhere [28]. All calculations were performed using the equilibrium module of the HSC chemistry software for windows [29]. HSC calculates the equilibrium composition of all possible combination of reactions that are able to take place within the thermodynamic system. These equilibrium calculations make use of the equilibrium composition module of the HSC program that is based on the Gibbs free energy minimization technique. The GIBBS program of this module finds the most stable phase combination and seeks the phase compositions where the Gibbs free energy of the system reaches its minimum at a fixed mass balance, constant pressure and temperature. Within the ethanol CLPOX-SR-CO_2A system the gaseous species included were: ethanol, ethylene, ethane, acetone, acetaldehyde, acetic acid, C_2H_6O, CO, CH_4, CO_2, H_2, and H_2O, while solid species were: C, CaO, $CaCO_3$, Cu, CuO, Ni and NiO.

During the thermodynamic simulation work the reaction temperature was varied in the range of 100-1000 °C at 1 atm. H_2O/C_2H_5OH molar ratio was allowed to change from 3:1 to 6:1, carbonate to ethanol molar ratio ($CaCO_3$/ C_2H_5OH) was varied from 1:1 to 2:1 while CuO/C_2H_5OH and NiO/C_2H_5OH molar ratios varied from 0.05:1 to 1.5:1 (all these values were determined according to the stoichiometric numbers from reactions 9 and 10). It is important to notice that all the ratios will be allowed to vary in order to find a thermoneutral (autothermal) point that favors the H_2/syngas production. Furthermore, the conditions here determined in the present thermodynamic analysis are based on theoretical considerations and these are to be taken as a guide to further experimental evaluation of the reaction system, since no heat and mass diffusional limitations as well as kinetics effects were taken into account for the conformation of the present thermodynamic analysis.

3. Results and Discussion

3.1 Thermodynamic Analysis

Table 1 presents results of the equilibrium molar content (H_2, CO, CO_2, CH_4 and C) for the steam reforming of ethanol (SRE) at the maximum hydrogen production and using H_2O/C_2H_6O molar ratios from 3 to 6. Here it can be seen that hydrogen production increased as the H_2O/C_2H_6O ratio also augmented, while the temperature for the maximum H_2 content decreased from 740°C at H_2O/C_2H_6O = 3 to 698 °C at H_2O/C_2H_6O = 6. Furthermore, CO_2 mols followed the same trend as H_2 content, while CO and CH_4 content decreased. This behavior is consistent with the promotion of the water gas shift (WGS, $CO + H_2O = CO_2 + H_2$) and the methane steam reforming (SMR, $CH_4 + 2H_2O = CO_2 + 4H_2$) reactions as temperature increased. It is important to address that no carbon formation is thermodynamically possible at the maximum H_2 production conditions. These results are in agreement with previous studies where higher H_2 yields resulted at molar feed ratios (H_2O/C_2H_6O) greater than 3 [30-32].

Table 1. Equilibrium molar content (H_2, CO, CO_2, CH_4 and C) at maximum hydrogen production and adiabatic conditions for the SRE reaction system.

Molar Feed			T °C	Max H_2 Production, Equilibrium Content, kmols					T_{adiab} °C	Adiabatic T Equilibrium Content, kmols				
H_2O/C_2H_5OH	NiO	CaO		H_2	CO	CO_2	CH_4	C		H_2	CO	CO_2	CH_4	C
3	0.0	0	740	4.47	1.37	0.580	0.0360	0.0000	338	0.3308	0.00267	0.58071	1.4166	0.000
4	0.0	0	740	4.71	1.22	0.770	0.0180	0.0000	298	0.2471	0.00087	0.56111	1.4380	0.000
5	0.0	0	705	4.88	1.00	0.968	0.0270	0.0000	272	0.1919	0.00035	0.54772	1.4519	0.000
6	0.0	0	698	5.03	1.10	0.879	0.0210	0.0000	254	0.1633	0.54068	0.00018	1.4591	0.000
0	0.8	0	900	2.86	1.59	0.049	0.0108	0.3520	343	0.2156	0.00105	0.16360	0.6563	1.179
0	0.9	0	900	2.84	1.63	0.063	0.0085	0.2960	325	0.1707	0.00063	0.16563	0.6306	1.203
0	1.0	0	900	2.81	1.66	0.080	0.0066	0.2489	298	0.1165	0.00028	0.16271	0.6046	1.232
0	1.1	0	900	2.77	1.68	0.100	0.0051	0.2109	281	0.0880	0.00015	0.16524	0.5713	1.263
0	1.2	0	900	2.73	1.69	0.124	0.0040	0.1805	255	0.0557	0.00006	0.16269	0.5349	1.302
0	1.3	0	900	2.68	1.69	0.150	0.0032	0.1565	237	0.0398	0.00003	0.49569	0.1656	1.339
0	1.4	0	900	2.63	1.68	0.178	0.0025	0.1374	210	0.0230	0.00001	0.16289	0.4514	1.386
0	1.5	0	900	2.58	1.67	0.207	0.0020	0.1219	188	0.0125	0.00000	0.15972	0.4035	1.437

Also in Table 1 results for equilibrium SRE at the adiabatic temperature (T_{adiab}, $\Delta H \approx 0$) are shown. As stated earlier it is possible for the SRE reaction system to reach autothermal conditions. Here, it can be seen that at all adiabatic SRE conditions temperatures and H_2 content are low, consequently CO_2 and CH_4 content are high as the reverse WGS and SMR are favored with no carbon formation. This result was expected, since the nature of the SRE reaction (1) is endothermic.

Furthermore, in Table 1 the equilibrium content at the maximum H_2 production temperature for the partial oxidation of ethanol using NiO as an oxygen source is presented. Here, the NiO/C_2H_6O molar ratio was varied from 0.8-1.5. Results indicate that the maximum H_2 production was found at the end upper temperature limit of 900 °C, with only an average H_2 content of 2.74 kmols disregarding the amount of oxygen content on NiO in the reaction system. In fact, as the NiO/C_2H_6O molar ration increased, there is a slight reduction of the amount of H_2 produced at 900 °C. This is consistent with the partial oxidation of ethanol to syngas and the Boudouard reactions:

$$C_2H_5OH + NiO \rightarrow 3H_2 + 2CO + Ni \qquad \Delta H^0 = +253.4 \text{ kJ/mol} \qquad (13)$$

$2CO \rightarrow CO_2 + C$ $\Delta H^0 = -175.81$ kJ/mol (14)

at these conditions, the concentration of CO_2 is small and there is a large amount of C being formed. Even though, there exists an excess of NiO in the reaction system the formation of C is still present, this in contrast with the SRE system, where the presence of steam prevents the formation of carbon deposits. Furthermore, in Table 1 the equilibrium content at adiabatic conditions (T_{adiab}, $\Delta H \approx 0$) is shown for the ethanol POX with NiO. At these adiabatic conditions the maximum H_2 content was of 0.216 kmols at 343 °C and $NiO/C_2H_5OH = 0.8$. Greater amounts of NiO will generate lower adiabatic temperatures and H_2 production, while greater amounts of carbon and carbon dioxide (through the Boudouard reaction) are present. This behavior is expected, since POX reactions with NiO (5 and 13) are both endothermic in nature.

Based on the results described above it is evident the need an additional reaction in order to balance out the SRE and POX reaction (both endothermic) with another highly exothermic reaction. This reaction is the CO_2 absorption with CaO:

$CaO + CO_2 \rightarrow CaCO_3$ $\Delta H^0 = -178.17$ kJ/mol (15)

This reaction will not only alleviate the heat needed for the reaction system for a possible autothermal operation, but will reduce the CO_2 content in the gas product by modifying the thermodynamics of both SER and POX reactions towards a greater H_2 production.

Table 2 presents results of the equilibrium molar content (H_2, CO, CO_2, CH_4 and C) for the combination of SRE, POX and CO_2 absorption (reaction 9) of ethanol at the maximum hydrogen production using $NiO/C_2H_5OH = 1$ and varying the H_2O/C_2H_5OH ratio from 3 to 6.

The CaO feed was kept at 2 kmols to insure the complete CO_2 absorption in the reaction system. Here, it can be observed that the maximum H_2 content occurred in a very narrow temperature range from 625 to 679 °C at H_2O/C_2H_5OH ratios of 6 and 3, respectively. In this region syngas production (CO + H_2) is favored as reaction (13) is thermodynamically feasible. Also, the CO_2 content is low due to CaO carbonation reaction (15) being promoted, shifting the equilibrium towards greater H_2 production in reaction (9). This carbonation reaction did not only had an effect on the H_2 production, but also on reduction of carbon formation as can be seen in Table 2.

. Also, in Table 2, the equilibrium content at adiabatic conditions (T_{adiab}, $\Delta H \approx 0$) is shown for the combined ethanol of SRE, POX and CO_2 absorption reaction system at $NiO/C_2H_5OH = 1$ and H_2O/C_2H_6O from 3 to 6. At these conditions, the adiabatic temperature varied from 466 to 382 °C at H_2O/C_2H_6O ratios of 3 and 6, respectively. Hydrogen production at adiabatic conditions do not differ significantly with respect to the values found at the higher temperatures of the maximum hydrogen production. This can be explained in term that at the adiabatic temperatures (382-466 °C) the carbonation reaction is even more thermodynamically favored and this being reflected in very small CO_2 concentrations as seen in Table 2 for these conditions.

Table 2. Equilibrium molar content (H_2, CO, CO_2, CH_4 and C) at maximum H_2 production and adiabatic conditions for the SRE, CLPOX and CO_2 capture combined process reaction system using NiO as oxygen carrier.

Molar Feed			T °C	Max H_2 Production, Equilibrium Content, kmols					T_{adiab} °C	Adiabatic T Equilibrium Content, kmols				
H_2O/C_2H_5OH	NiO	CaO		H_2	CO	CO_2	CH_4	C		H_2	CO	CO_2	CH_4	C
3.0	1.00	2	679	4.19	0.34	0.241	0.0520	0.1306	466	3.85	0.00054	0.00145	0.27390	0.02795
3.5	1.00	2	670	4.33	0.41	0.328	0.0450	0.1000	449	4.02	0.00026	0.00097	0.23826	0.01718
4.0	1.00	2	661	4.45	0.24	0.255	0.0400	0.0780	431	4.15	0.00012	0.00060	0.20908	0.01067
4.5	1.00	2	652	4.54	0.20	0.255	0.0350	0.0620	418	4.25	0.00008	0.00052	0.18332	0.00793
5.0	1.00	2	643	4.61	0.17	0.250	0.0316	0.0500	405	4.34	0.00003	0.00029	0.16389	0.00497
5.5	1.00	2	634	4.67	0.14	0.243	0.0280	0.0410	391	4.41	0.00001	0.00015	0.14757	0.00309
6.0	1.00	2	625	4.72	0.11	0.233	0.0263	0.0350	382	4.47	0.00001	0.00012	0.13280	0.00233
3.0	0.05	2	732	4.78	0.91	0.289	0.0597	0.0122	502	4.06	0.00236	0.00288	0.47066	0.00404
3.0	0.10	2	732	4.75	0.89	0.295	0.0553	0.0229	502	4.06	0.00237	0.00297	0.45625	0.00795
3.0	0.15	2	723	4.72	0.81	0.282	0.0637	0.0365	502	4.06	0.00237	0.00306	0.44224	0.01163
3.0	0.25	2	723	4.65	0.77	0.292	0.0550	0.0525	493	4.04	0.00163	0.00239	0.41920	0.01578
3.0	0.50	2	705	4.50	0.51	0.274	0.0580	0.0930	484	4.00	0.00113	0.00204	0.36352	0.02384
3.0	1.00	2	679	4.19	0.34	0.241	0.0520	0.1306	466	3.85	0.00054	0.00145	0.27390	0.02795
3.0	1.50	2	661	3.87	0.22	0.222	0.0388	0.1311	444	3.63	0.00025	0.00101	0.20475	0.02507
4.0	0.05	2	697	5.13	0.56	0.303	0.0637	0.0076	467	4.58	0.00058	0.00144	0.34296	0.00137
4.0	0.10	2	687	5.09	0.49	0.283	0.0721	0.0161	467	4.56	0.00059	0.00148	0.33377	0.00276
4.0	0.15	2	688	5.06	0.48	0.286	0.0675	0.0229	458	4.54	0.00039	0.00108	0.32690	0.00348
4.0	0.25	2	687	4.99	0.46	0.292	0.0593	0.0342	458	4.50	0.00039	0.00115	0.30967	0.00562
4.0	0.50	2	679	4.81	0.37	0.281	0.0520	0.0565	449	4.40	0.00026	0.00093	0.27211	0.00876
4.0	1.50	2	643	4.07	0.15	0.225	0.0301	0.0819	413	3.85	0.00005	0.00038	0.15867	0.00974
5.0	0.05	2	670	5.37	0.35	0.295	0.0572	0.0047	431	4.90	0.00012	0.00056	0.26259	0.00051
5.0	0.10	2	670	5.33	0.34	0.297	0.0539	0.0092	431	4.88	0.00012	0.00057	0.25614	0.00105
5.0	0.15	2	661	5.29	0.29	0.273	0.0603	0.0142	426	4.85	0.00012	0.00059	0.24981	0.00156
5.0	0.25	2	661	5.21	0.28	0.277	0.0537	0.0217	422	4.79	0.00008	0.00043	0.23909	0.00214
5.0	0.50	2	652	5.01	0.23	0.260	0.0475	0.0368	413	4.65	0.00005	0.00033	0.21198	0.00337
5.0	1.50	2	625	4.20	0.11	0.214	0.0242	0.0546	387	3.99	0.00001	0.00017	0.12576	0.00454
6.0	0.05	2	652	5.53	0.24	0.289	0.0454	0.0029	396	5.12	0.00002	0.00017	0.20943	0.00019
6.0	0.10	2	652	5.49	0.23	0.290	0.0430	0.0059	396	5.08	0.00002	0.00018	0.20459	0.00040
6.0	0.15	2	652	5.44	0.23	0.291	0.0408	0.0087	396	5.05	0.00002	0.00018	0.19984	0.00060
6.0	0.25	2	643	5.36	0.19	0.267	0.0430	0.0142	400	4.99	0.00002	0.00019	0.19058	0.00099
6.0	0.50	2	625	5.14	0.21	0.301	0.0280	0.0224	396	4.83	0.00002	0.00022	0.16881	0.00190
6.0	1.50	2	617	4.28	0.08	0.218	0.0176	0.0375	369	4.09	0.00001	0.00010	0.10195	0.00259

Also, CO and C content are reduced at adiabatic conditions. All these features make a very attractive operating conditions for reaction (9). However, kinetic and catalytic limitations have been reported for the steam reforming of ethanol at temperatures below 500° C as reported elsewhere [31, 32]. Therefore, even though favorable adiabatic conditions exist at NiO/C_2H_5OH = 1 and H_2O/C_2H_5OH from 3 to 6, it is required to find (at least from a thermodynamic point of view) conditions for adiabatic temperatures greater than 500 °C.

Furthermore, Table 2 presents results for the SRE, POX and CO_2 absorption combined system fixing the H_2O/C_2H_5OH ratio at 3, 4, 5 and 6, while varying the NiO/C_2H_5OH ratio from 0.05 to 1.5, while keeping the CaO/C_2H_6O = 2.

Generally, from results of Table 2, it can be observed that the maximum H_2 production, occurred at $NiO/C_2H_6O < 1$ and this is increased as the H_2O/C_2H_6O also grew. More than 5 kmols of hydrogen are produced at $H_2O/C_2H_6O \geq 4$ and at temperatures between 620 and 700 °C. Even though at all these conditions there exist some carbon formation and this is relatively small with respect to other species. It is important to underline that selected conditions of the present study were chosen in order to minimize the carbon formation, but the combination of adiabatic conditions and high H_2 production resulted in only marginal C formation. Moreover, due to the configuration of the reaction process, the carbon deposited in the fuel reactor and ultimately over the catalyst, will be adequately removed in the air reactor (regenerator reactor) where the reduced Me is to be reoxidized back to MeO (see

Figure 1). This operation mode, in which deposited carbon is removed by another oxidizing reactor is well documented in the commercial FFC catalytic reactors [33] and in the CALCOR and Catforming commercial processes for ethanol dry reforming [34, 35]. However, kinetic may play a significant role at these reaction conditions, since there are some studies that report the kinetic propensity of Ni to form carbon deposits [36].

Table 2 additionally presents adiabatic equilibrium conditions for the combined SRE, POX and CO_2 absorption reaction system. Most favorable reactions conditions were encountered at H_2O/C_2H_5OH = 3 and NiO/C_2H_5OH ratios in the range of 0.05-0.25, where the adiabatic temperature is equal or greater than 500 °C. At these conditions there is a reasonable high concentration of H_2 at equilibrium with respect to other gaseous species and a relatively small amount of carbon formation, with the exception of CH_4, which is the other more concentrated specie in the gas product. However, experimental findings have concluded that at SRE of ethanol combined with CO_2 absorption reaction system conditions, methane formation is kinetically limited as a recent study have reported [37]. It is important to point out that these favorable reaction conditions are the product of the combination of the exothermic carbonation reaction and its influence over the thermodynamic equilibrium over the POX and SRE endothermic reactions.

Moreover, Table 3 presents results of the equilibrium molar content (H_2, CO, CO_2, CH_4 and C) for the combination of SRE, POX and CO_2 absorption (reaction 10) of ethanol at the maximum hydrogen production using CuO/C_2H_5OH = 1 and varying the H_2O/C_2H_5OH ratio from 3 to 6. Again, here, CaO feed was kept at 2 kmols to insure the complete CO_2 absorption in the reaction system. From this table it can be observed that the maximum H_2 content occurred, similarly as in the case of with NiO, in a very narrow temperature range from 625 to 688 °C at H_2O/C_2H_5OH ratios of 6 and 3, respectively. In this region Syngas production (CO + H_2) is favored as the following reaction is thermodynamically favored:

$$C_2H_5OH + CuO \rightarrow 3H_2 + 2CO + Cu \qquad \Delta H^0_{298} = +169.5 \text{ kJ/mol} \qquad (16)$$

as well as CO_2 is produced as the exothermic reaction (6) is favored, while methane and carbon content are rather small in this region. Also in this Table, it is important to indicate that adiabatic temperatures present values greater than 500 °C (519-590). However, at these conditions CO_2 and CH_4 content are rather high as Solunke and Vesser have reported in their thermodynamic calculations [38]. This feature can create an additional purification step for H_2 and or syngas.

Table 3 additionally presents maximum H_2 production equilibrium conditions for the combined SRE, POX and CO_2 absorption reaction fixing the H_2O/C_2H_5OH ratio at 3, 4, 5 and 6, while varying the CuO/C_2H_5OH ratio from 0.05 to 1.5, and keeping the CaO/C_2H_5OH = 2. From results of Table 3, it can be observed that the maximum H_2 production, occurred at $CuO/C_2H_5OH < 1$ and this is increased as the H_2O/C_2H_5OH also grew. More than 5 kmols of hydrogen are produced at $H_2O/C_2H_5OH \geq 4$ and at temperatures between 634 and 697 °C. Even though at all these conditions there exist some carbon formation and this is relatively small with respect to other species.

Also, Table 3 shows adiabatic equilibrium conditions for the combined SRE, POX and CO_2 absorption reaction system. Most favorable reactions conditions; $T \geq 500$ °C and small carbon formation, $C \leq 0.1$ kmols, were encountered at several regions: i) at H_2O/C_2H_5OH = 3 and all CuO/C_2H_5OH ratios (0.05-1.5), ii) at H_2O/C_2H_6O = 4 and CuO/C_2H_5OH ratios of

0.25-1.5, and finally iii) at H_2O/C_2H_5OH = 5 and 6 with a CuO/C_2H_5OH ratio of 1.5. At all these adiabatic conditions, hydrogen production higher than 4 kmols at equilibrium occurred at all H_2O/C_2H_5OH ratios, with the exemption of H_2O/C_2H_5OH = 3 and CuO/C_2H_5OH = 1.5, while maximum H_2 production at adiabatic conditions was found at H_2O/C_2H_5OH = 4, CuO/C_2H_5OH = 0.5 and T_{adiab} = 529 °C, where 4.48 kmols of H_2 are produced at equilibrium. At this condition, very small amount of carbon oxides are generated as well as carbon formation (C = 0.032 kmols). Again, these favorable reaction conditions are the product of the combination of the exothermic carbonation reaction and its influence over the thermodynamic equilibrium over the POX and SRE endothermic reactions.

Furthermore, the production of hydrogen and equilibrium molar content of CO, CO_2 and C at a temperature range of 100-900 °C and CuO/C_2H_5OH molar ratios from 0.05 to 1.5 (CaO feed of 2 kmols) are presented in Figure 2. This Figure shows the equilibrium content for H_2 and CO while Figure 3 for CO_2 and CH_4.

Table 3. Equilibrium molar content (H_2, CO, CO_2, CH_4 and C) at maximum H_2 production and adiabatic conditions for the SRE, CLPOX and CO_2 capture combined process reaction system using CuO as oxygen carrier.

Molar Feed			T °C	Max H_2 Production, Equilibrium Content, kmols					T_{adiab} °C	Adiabatic T Equilibrium Content, kmols				
H_2O/C_2H_5OH	CuO	CaO		H_2	CO	CO_2	CH_4	C		H_2	CO	CO_2	CH_4	C
3.0	1.00	2	688	4.19	0.39	0.265	0.0440	0.1233	590	4.04	0.05301	0.05930	0.16261	0.12894
3.5	1.00	2	670	4.33	0.29	0.251	0.0453	0.1001	581	4.19	0.04363	0.06120	0.14205	0.09711
4.0	1.00	2	661	4.44	0.24	0.255	0.0397	0.0783	564	4.30	0.02728	0.05010	0.13350	0.07022
4.5	1.00	2	652	4.53	0.20	0.255	0.0352	0.0625	555	4.40	0.02175	0.04866	0.11819	0.05499
5.0	1.00	2	643	4.61	0.17	0.250	0.0315	0.0508	537	4.46	0.01287	0.03691	0.11238	0.04057
5.5	1.00	2	634	4.66	0.14	0.243	0.0285	0.0419	528	4.52	0.00997	0.03412	0.10151	0.03263
6.0	1.00	2	625	4.71	0.11	0.233	0.0261	0.0351	519	4.57	0.00765	0.03095	0.09257	0.02652
3.0	0.05	2	732	4.78	0.91	0.289	0.0596	0.0126	511	4.07	0.00343	0.00390	0.46740	0.00486
3.0	0.10	2	723	4.75	0.83	0.278	0.0686	0.0267	520	4.08	0.00493	0.00540	0.44889	0.01092
3.0	0.15	2	723	4.72	0.81	0.283	0.0635	0.0369	528	4.09	0.00702	0.00740	0.42936	0.01828
3.0	0.25	2	723	4.65	0.77	0.293	0.0549	0.0529	537	4.10	0.00986	0.01032	0.39397	0.03251
3.0	0.50	2	706	4.50	0.58	0.275	0.0579	0.0934	555	4.10	0.01855	0.01977	0.30985	0.06879
3.0	1.00	2	688	4.19	0.39	0.265	0.0440	0.1233	590	4.04	0.05301	0.05930	0.16261	0.12894
3.0	1.50	2	661	3.86	0.22	0.222	0.0386	0.1310	617	3.83	0.09328	0.11695	0.07380	0.13998
4.0	0.05	2	697	5.13	0.55	0.303	0.0635	0.0080	467	4.58	0.00058	0.00144	0.34252	0.00144
4.0	0.10	2	688	5.09	0.49	0.283	0.0718	0.0165	476	4.57	0.00088	0.00208	0.33115	0.00331
4.0	0.15	2	688	5.06	0.48	0.286	0.0672	0.0232	485	4.56	0.00132	0.00296	0.31950	0.00568
4.0	0.25	2	688	4.98	0.46	0.292	0.0591	0.0345	502	4.54	0.00288	0.00585	0.29500	0.01221
4.0	0.50	2	679	4.81	0.37	0.282	0.0518	0.0567	529	4.48	0.00840	0.01569	0.23667	0.03215
4.0	1.50	2	644	4.06	0.15	0.225	0.0299	0.0818	599	4.04	0.06354	0.11775	0.05716	0.08616
5.0	0.05	2	670	5.37	0.35	0.295	0.0569	0.0050	440	4.91	0.00019	0.00081	0.26065	0.00065
5.0	0.10	2	670	5.33	0.34	0.297	0.0537	0.0096	449	4.89	0.00030	0.00120	0.25248	0.00152
5.0	0.15	2	661	5.29	0.29	0.273	0.0600	0.0145	458	4.87	0.00046	0.00176	0.24420	0.00265
5.0	0.25	2	661	5.21	0.28	0.277	0.0534	0.0220	466	4.82	0.00071	0.00261	0.22946	0.00502
5.0	0.50	2	652	5.01	0.23	0.260	0.0472	0.0370	493	4.71	0.00237	0.00777	0.19070	0.01437
5.0	1.50	2	625	4.19	0.11	0.214	0.0240	0.0545	572	4.15	0.03361	0.09314	0.05117	0.05549
6.0	0.05	2	652	5.52	0.24	0.289	0.0451	0.0032	405	5.12	0.00003	0.00026	0.20792	0.00025
6.0	0.10	2	652	5.48	0.23	0.290	0.0428	0.0062	413	5.09	0.00006	0.00040	0.20187	0.00061
6.0	0.15	2	644	5.44	0.20	0.265	0.0476	0.0094	422	5.06	0.00009	0.00060	0.19580	0.00108
6.0	0.25	2	644	5.36	0.19	0.267	0.0428	0.0144	440	5.01	0.00023	0.00135	0.18351	0.00249
6.0	0.50	2	634	5.14	0.16	0.247	0.0383	0.0247	467	4.86	0.00085	0.00436	0.15527	0.00755
6.0	1.50	2	617	4.27	0.08	0.218	0.0174	0.0375	555	4.23	0.02133	0.08099	0.04302	0.03822

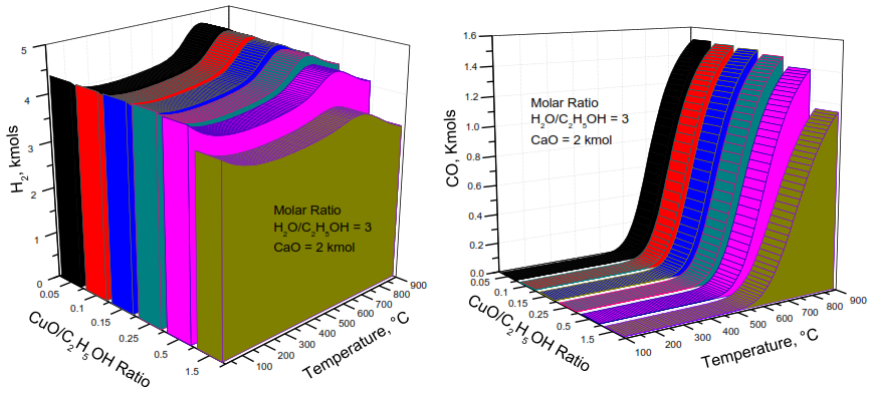

Fig 2. Equilibrium content of H_2 and CO for the SRE, CLPOX and CO_2 capture combined process

In Figure 2 it is evident that H_2 mols at equilibrium are always greater than 4 kmols and this is due to the shift in equilibrium towards a greater hydrogen production in reaction (10). A maximum H_2 can be found at a temperature range from 661-732 °C as also can be seen in results from Table 3. While in Figure 2, CO concentration is kept low for the temperature range from 100-550 °C and this is due to the combination of the water gas shift and the CO_2 carbonation reactions, thus producing more H_2 and CO_2 (through WGS), which is finally trapped in $CaCO_3$. Greater values of 550 °C will hamper the ability of CaO to capture CO_2, since greater carbon dioxide partial pressures will shift the equilibrium of reaction (15) towards decarbonation of $CaCO_3$. This behavior is reflected in Figure 3 where the CO_2 content is shown to be negligible in the temperature range from 100-550 °C at all CuO/C_2H_5OH molar ratios. Meanwhile, CH_4 content (Figure 3) results in values less than 0.5 kmols at a temperature range from 100-650 °C, where the endothermic steam methane reaction takes over the reaction system to produce more hydrogen and CO_2 at higher temperatures.

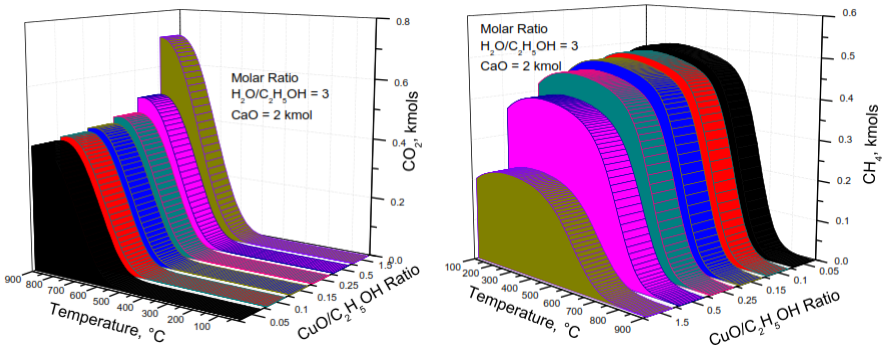

Fig 3. Equilibrium content of CO_2 and CH_4 for the SRE, CLPOX and CO_2 capture combined process

Finally, Figure 4 presents the carbon content at equilibrium for the reaction system. In this plot it is clear that in a temperature range 100 – 500 °C carbon formation is almost negligible at all CuO/C_2H_6O molar ratios. Here it can be seen that as CuO/C_2H_5OH increases carbon formation will grow. However, the carbon formed at equilibrium in Figure 4 is always less than 0.15 kmols at all presented conditions. All the previous results are in agreement with thermodynamic analysis data reported by Wang and Cao [27] for similar reaction conditions.

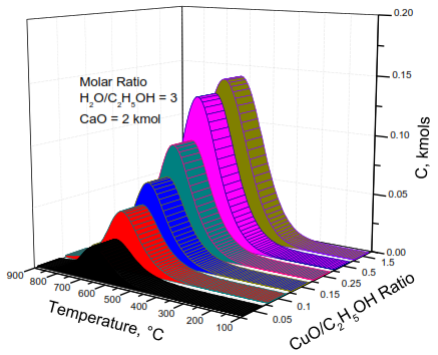

Fig 4. Equilibrium content of C for the SRE, CLPOX and CO_2 capture combined process

Figure 5 presents two plots for the adiabatic temperature (°C) and the equilibrium molar content at H_2O/C_2H_5OH = 3 and the corresponding adiabatic temperature as a function of NiO/C_2H_5OH (Figure 5) and CuO/C_2H_5OH (Figure 5). In this it is evident that for the NiO/C_2H_5OH range of 0.05-0.15 adiabatic temperatures are ≥ 500 °C, whereas higher molar ratios will lead to lower adiabatic temperatures. At this condition (T ≥ 500 °C) it is clear that values of H_2 content are ≥ 4 kmols. Lower adiabatic temperatures and H_2 content will arise when NiO/C_2H_5OH > 0.15. This attractive operating adiabatic range (T ≥ 500 °C and NiO/C_2H_5OH = 0.05-0.15) can be explained in terms of the combined effects of the highly endothermic nature of the SRE and POX reactions and the counter effect achieved by the highly exothermic CaO carbonation reaction. This effect is even clearer, since at this region CO_2 concentrations are almost negligible in Figure 5.

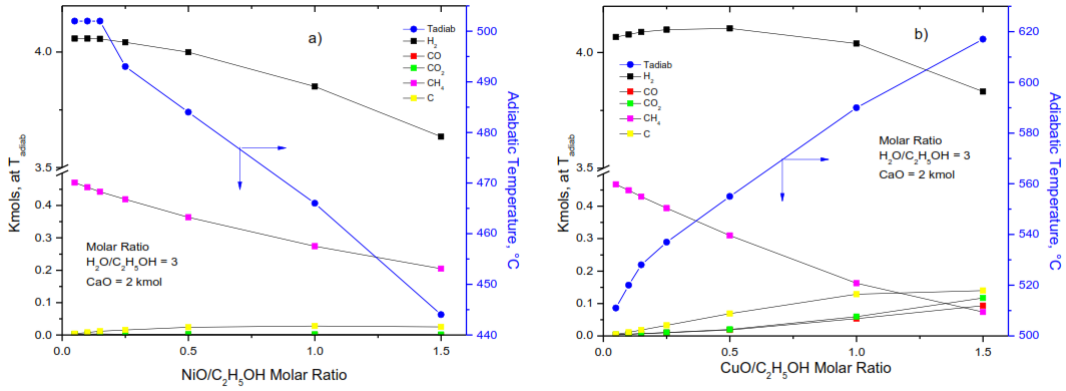

Fig 5. Adiabatic temperature and species equilibrium content as a function of metal oxide and steam content.

Moreover, Figure 5 shows the adiabatic temperature (°C) and the equilibrium molar content at H_2O/C_2H_5OH = 3 and the corresponding adiabatic temperature as a function of CuO/C_2H_5OH. In this plot it is interesting to realize that as the NiO/C_2H_5OH increases, the adiabatic temperature also rises. This can be explained in terms of the combined nature of reactions (6) and (8), which both are exothermic in nature. This is the reason why the NiO adiabatic temperature curve from Figure 5 (a) presents an opposite trend with respect to the use of CuO as oxygen carrier in Figure 5 (b). Furthermore, it is important to mention that all adiabatic temperature values presented in Figure 5 (b) are greater than 500 °C and that in a CuO/C_2H_5OH range of 0.05-0.15 hydrogen production is always greater than 4 kmols at equilibrium.

4. Conclusion

In the present work a thermodynamic analysis was performed to explore reaction conditions at equilibrium for a high syngas-H_2 production and adiabatic temperatures, under the combined ethanol steam reforming (SRE) , chemical looping partial oxidation (CLPOX) and CO_2 solid absorption reaction system. SRE studied conditions were in a range of H_2O/C_2H_5OH = 3 to 6 molar ratio, CLPOX employed NiO and CuO as oxygen carriers and varied from MeO/C_2H_5OH = 0.05 to 1.5 molar ratio, while 1 kmols of CaO were used for CO_2 Capture in the reaction system in temperature range of 100-900 °C at atmospheric conditions. Results indicate that for NiO the maximum H_2 content occurred in a T range of 625 to 679 °C at H_2O/C_2H_5OH ratios of 6 and 3, respectively and most favorable reactions conditions ($T \geq 500$ °C and small carbon formation, $C \leq 0.1$ kmols) were encountered at H_2O/C_2H_5OH = 3 and NiO/C_2H_5OH ratios in the range of 0.05-0.25, where the adiabatic temperature is equal or greater than 500 °C. At these conditions there is a reasonable high concentration of H_2 at equilibrium with respect to other gaseous species and a relatively small amount of carbon formation. While, for CuO as oxygen carrier, the maximum H_2 content occurred, similarly as in the case of with NiO, in a T range from 625 to 688 °C at H_2O/C_2H_6O ratios of 6 and 3, respectively. Alternatively, Most favorable adiabatic reactions conditions with CuO were encountered at several regions: i) at H_2O/C_2H_6O = 3 and all CuO/C_2H_5OH ratios (0.05-1.5), ii) at H_2O/C_2H_5OH = 4 and CuO/C_2H_5OH ratios of 0.25-1.5, and finally iii) at H_2O/C_2H_5OH = 5 and 6 with a CuO/C_2H_5OH ratio of 1.5. Finally, it was concluded that these favorable reaction conditions are the product of the combination of the exothermic carbonation reaction and its influence over the thermodynamic equilibrium over the POX and SRE endothermic reactions.

References

[1] Dou B. L., Song Y.C., Wang C., Chen H.S., Xu Y.J., Hydrogen production from catalytic steam reforming of biodiesel byproduct glycerol: issues and challenges. Renewable Sustainable Energy Rev, 30 (2014), pp. 950–960.

[2] Mazloomi K., Gomes C. Hydrogen as an energy carrier: prospects and challenges. Renewable Sustainable Energy Rev, 16 (2012), pp. 3024–3033.

[3] Chaubey R., Sahu S., James O.O., Maity S. A review on development of industrial processes and emerging techniques for production of hydrogen from renewable and sustainable sources. Renewable Sustainable Energy Rev, 23 (2013), pp. 443–462.

[4] Taboada E., Angurell I., Llorca J. Dynamic photocatalytic hydrogen production from ethanol–water mixtures in an optical fiber honeycomb reactor loaded with Au/TiO_2. J Catal, 309 (2014), pp. 460–467.
[5] Ni M, Leung MKH, Leung DYC, Sumathy K. A review and recent developments in photocatalytic water-splitting using TiO_2 for hydrogen production. Renewable Sustainable Energy Rev, 11 (2007), pp. 401–425.
[6] Marone A., Izzo G., Mentuccia L., Massini G., Paganin P., Rosa S., Varrone C., Signorini A. Vegetable waste as substrate and source of suitable microflora for bio-hydrogen production. Renewable Energy, 68 (2014), pp. 6–13.
[7] Faria E.C., Neto R.C.R., Colman R.C., Noronha F.B. Hydrogen production through CO2 reforming of methane over Ni/$CeZrO_2$/$Al2O_3$ catalysts. Catal Today, 228 (2014), pp. 138–144.
[8] Ni M., Leung D.Y.C., Leung M.K.H., Sumathy K. An overview of hydrogen production from biomass. Fuel Process Technol, 87 (2006), pp. 461–472.
[9] Augusto B.L., Costa L.O.O., Noronha F.B., Colman R.C., Mattos L.V. Ethanol reforming over Ni/CeGd catalysts with low Ni content. Int J Hydrogen Energy, 37 (2012), pp. 12258–12270.
[10] Li J., Yu H., Yang G., Peng F., Xie D., Wang H. Steam reforming of oxygenate fuels for hydrogen production: a thermodynamic study. Energy Fuels, 25 (2011), pp. 2643–2650.
[11] Díaz Alvarado F., Gracia F. Steam reforming of ethanol for hydrogen production: thermodynamic analysis including different carbon deposits representation. Chem Eng J, 165 (2010), pp. 649–657.
[12] Guil-López R., Navarro R.M., Peña M.A., Fierro J.L.G. Hydrogen production by oxidative ethanol reforming on Co, Ni and Cu ex-hydrotalcite catalysts. Int J Hydrogen Energy, 36 (2011), pp. 1512–1523.
[13] Kugai J., Subramani V., Song C., Engelhard M.H., Chin Y.H. Effects of nanocrystalline CeO_2 supports on the properties and performance of Ni–Rh bimetallic catalyst for oxidative steam reforming of ethanol. J Catal, 238 (2006), pp. 430–440.
[14] Ramírez de la Piscina P., Homs N. Use of biofuels to produce hydrogen (reformation processes). Chem Soc Rev, 37 (2008), pp. 2459–2467.
[15] Silva A.M., Costa L.O.O., Souza K.R., Mattos L.V., Noronha F.B. The effect of space time on Co/CeO2 catalyst deactivation during oxidative steam reforming of ethanol. Catal Commun, 11 (2010), pp. 736–74.
[16] Nishiguchi T., Matsumoto T., Kanai H., Utani K., Matsumura Y., Shen W. J., Imamura S. Appl Catal A-Gen, 2005, 279(1-2): 273.
[17] Mattisson T., Lyngfelt A. Applications of chemical looping combustion with capture of CO_2. In: Proc. 2nd Nordic Minisymposium on Carbon Dioxide Capture and Storage. Göteborg, Sweden; 2001.
[18] Kale G.R., Kulkarni B.D., Bharadwaj K.V. Chemical looping reforming of ethanol for syngas generation: a theoretical investigation. International Journal Energy Research 2013; 37:645–656.
[19] Adanez J., Abad A., Garcia-Labiano F., Gayan P., de Diego L.F. Progress in chemical-looping combustion and reforming technologies. Progress in Energy and Combustion Science 2012; 38:215–82.
[20] Ortiz M., Abad A., de Diego L.F., García-Labiano F., Gayán P., Adánez J. Optimization of hydrogen production by chemical-looping auto-thermal reforming working with Ni-based oxygen-carriers. International Journal of Hydrogen Energy 2011; 36:9663–72.
[21] Zafar Q., Mattisson T., Gevert B. Redox investigation of some oxides of transition-state metals Ni, Cu, Fe, and Mn supported on SiO2 and $MgAl_2O_4$. Energy and Fuels 2006; 20:34–44.
[22] Arjmand M., Azad A.M., Leion H., Lyngfelt A., Mattisson T. Prospects of Al_2O_3 and $MgAl_2O_4$-supported CuO oxygen carriers in chemical-looping combustion (CLC) and chemical-looping with oxygen uncoupling (CLOU). Energy and Fuels 2011; 25:5493–5502.
[23] de Diego L.F., García-Labiano F, Gayán P, Celaya J, Palacios J.M., Adánez J. Operation of a 10 kWth chemical-looping combustor during 200 h with a CuO/Al_2O_3 oxygen carrier. Fuel 2007; 86:1036–1045.
[24] Kale G.R., Kulkarni B.D., Bharadwaj K.V. Chemical looping reforming of ethanol for syngas generation: A theoretical investigation. International Journal of Energy Research 2013, Volume 37, Issue 6, pages 645–656.
[25] Comas J., Laborde M., Amadeo N. Thermodynamic analysis of hydrogen production from ethanol using CaO as a CO_2 sorbent. Journal of Power Sources 2004; 138:61–67.
[26] Rydén M., Lyngfelt A.,Mattisson T. Synthesis gas generation by chemical-looping reforming in a continuously operating laboratory reactor. Fuel 2006; 85:1631–1641.

[27] Wang W. Cao Y. A combined thermodynamic and experimental study on chemical-looping ethanol reforming with carbon dioxide capture for hydrogen generation. International Journal of Energy Research Int. J. Energy Res. 2013; 37:25–34.
[28] Collins-Martínez V. Escobedo Bretado M., Meléndez Zaragoza M., Salinas Gutiérrez J., López Ortiz A. Absorption enhanced reforming of light alcohols (methanol and ethanol) for the production of hydrogen: Thermodynamic modeling, Int J Hydrogen Energy 2013; 38:12539–553.
[29] Roine A. Chemical reaction and equilibrium software with extensive thermo-chemical database. Outokumpu HSC 6.0 Chemistry for windows; 2010.
[30] Collins-Martinez V., Escobedo Bretado M., Meléndez Zaragoza M., Salinas Gutiérrez J., López Ortiz A. Absorption enhanced reforming of light alcohols (methanol and ethanol) for the production of hydrogen: thermodynamic modeling. Int J Hydrogen Energy 2013; 28:12539-53.
[31] Fatsikostas A.N., Verykios X.E. Reaction network of steam reforming of ethanol over Ni-based catalysts. J Catal 2004; 225:439-52.
[32] Frusteri F., Freni S., Chiodo V., Spadaro L., Di Blasi O., Bonura G.. Cavallaro, steam and auto-thermal reforming of bio-ethanol over MgO and CeO2eNi supported catalysts. Int J Hydrogen Energy 2006; 31(15):2193-9.
[33] Sugungun M.M., Kolesnikov I.M., Vinogradov V.M., Kolesnikov S.I. Kinetic modeling of FCC process, Catalysis Today, Volume 43, Issues 3–4, 27 August 1998, Pages 315–325.
[34] Solh E., T., Jarosch, K., de Lasa, H. Catalytic Dry Reforming of Methane in a CREC Riser Simulator Kinetic Modeling and Model Discrimination. Ind. Eng. Chem. Res. 2003; 42; 2507.
[35] Teuner, St. C. Neumann, P. Von Linde, F. The Calcor Standard and Calcor Economy Processes. Oil Gas Eur. Mag. 2001; 3; 44.
[36] Youn M. H., Seo J. G., Cho K. M., Park S., Park D. R., Jung J. C. Hydrogen production by auto-thermal reforming of ethanol over nickel catalysts supported on Ce-modified mesoporous zirconia: effect of Ce/Zr molar ratio. Int J Hydrogen Energy 2008; 33:5052–9.
[37] Aceves Olivas D.Y. Baray Guerrero M.R., Escobedo Bretado M.A., Marques da Silva Paula M., Salinas Gutiérrez J., Guzmán Velderrain V., López Ortiz A. Collins-Martínez V. Enhanced ethanol steam reforming by CO_2 absorption using CaO, CaO*MgO or Na_2ZrO_3. Int J Hydrogen Energy 2014; 39:16595–16607.
[38] Solunke R. D. and Veser G. Hydrogen Production via Chemical Looping Steam Reforming in a Periodically Operated Fixed-Bed Reactor, Ind. Eng. Chem. Res. 2010, 49, 11037–11044.

5
Renewable energy systems

Chapter 5.1. Hydrodeoxygenation of oxygenated organic compounds using Ni / γ-Al2O3 performed by the wet impregnation incipient method

B. N. López-García[a,*]; M. Sánchez-Cárdenas[a]; J. Medina-Valtierra[b]

[a]Universidad Politécnica de Aguascalientes, Calle Paseo , San Gerardo, 207, Aguascalientes, Ags., México, 20342.
[b]Instituto Tecnológico de Aguascalientes, Av. Adolfo López Mateos Ote. No. 1801, Fracc. Bona Gens, Aguascalientes, Ags., México, 20256

ABSTRACT

A supported Nickel catalyst on gamma alumina synthesized by the wet impregnation incipient method was tested for the hydrodeoxygenation of oleic acid which is considered as a model molecule of oxygenated organic compounds. The catalyst was synthisized by a physical method of Bohemia and a solution of Nickel (II) tetrahydrate acetate until a homogeneous paste which was left to be dried at a current temperature. After drying the paste, it was performed a process of extrusion to obtain tablets of the same size. Finally the tables were calcined at 510 ° C in oxygen to obtain at the end nickel oxide deposited on gamma alumina. The reduction of the catalyst in the reactor was performed by applying a flow of hydrogen at 400 ° C, whereby Ni / γ-Al_2O_3 was obtained.
The hydrotreating experiments were performed in a tubular reactor of stainless steel by using batches at 320 ° C, 20 bar H2 pressure, 200 rpm and 5 hours of reaction. Data conversion of oleic acid and yields alkanes n-C_{17} and n-C_{18} were calculated from GC.
By analyzing the products of oleic acid hydrotreating using a catalyst with 3% in weight of Ni, it was obtained a percent conversion of oleic acid of 55.3% and a yield molar total n-C_{17} + n-C_{18} of 48.7%. By performing an analysis of the amount of n-alkanes even and odd generated in the reaction, it was obtained a relationship of (decarboxylation + decarbonylation)/hydrodeoxygenation of 1.59. This process indicates that Nickel is an appropriate active phase to accelerate and direct the actions of hydrodeoxygenation as well as to obtain alkanes n-C_{18} considering that the overall reaction remains a slight domain to the decarboxylation + decarbonylation reactions for this catalyst.

***Keywords*:** Hydrodeoxygenation, Decarboxylation, Decarbonylation, Oleic Acid

1. Introduction

In the present day, about 80% of the world energy demand is obtained by burning fossil fuels. This leads to a depletion of fossil energy resources, which are limited, causing that the use of fossil fuels is identified as the main cause of global climate change due to the emission of pollutants as a result of combustion [1].

---

* Author for correspondence:
López García Brenda Nayeli, (0449)-449-187-98-29, up120083@alumnos.upa.edu.mx

One option for reducing the consumption of fossil fuels and their impact on the environment is the use of renewable energy based on biomass processing because they have a huge energy potential, and they can contribute to the reduction of emissions of greenhouse, such is the case of biodiesel. The method of application of biodiesel fuel and its mixtures with petroleum-based diesel can be used in diesel engines without any significant modification of the engine [2].

The disadvantages encountered in the application of biodiesel obtained by transesterification are: the susceptibility to oxidation, under low temperature performance, and high emissions of NOx. Solving these disadvantages has sparked interest in developing catalyst preparation methods Ni for application in processes of catalytic hydrodeoxygenation of methyl esters from vegetable oils and animal fats, so that they can transform a condition of polyunsaturated to monounsaturated. This new oxygen free biodiesel is considered a high-energy biofuel.

Yang and colleagues synthesized catalysts supported nickel phosphide on SBA-15 programmed reduction of a nickel phosphide temperature, performed by varying the atomic molar ratio P / Ni for different active phases, Ni_2P, $Ni_{12}P5$ or Ni_3P. All catalysts were evaluated nickel phosphide in the hydrodeoxygenation of methyl oleate on a continuous flow reactor to 30 bar and a temperature range of 250 ° C to 340 ° C.

Analysis of the products showed that the hydrodeoxygenation activity and selectivity are affected significantly by the atomic molar ratio Ni / P. The maximum conversion is achieved for the catalysts prepared with an initial ratio Ni / P 1, while the selectivity to C18 is higher for the catalyst with an initial ratio Ni / P of 2. These catalysts contain predominantly Ni_2P phase appears the most active for this process, although the presence of $Ni_{12}P_5$ in the case of catalysts with Ni / P = 2 also appears to be favorable. (Yang y col., 2015).

In this paper we attempted to overcome the disadvantages presented by the conventional biodiesel with the design of a process to get biodiesel free of oxygen from oleic acid, considered as a model of oxygenated organic compound molecule through a catalytic process of hydrodeoxygenation where they were used the Ni catalysts deposited on γ-Al_2O_3, 10% by weight relative to the load of oxygenated organic compounds. It was done for accelerating and directing the reaction towards the production of n-alkanes.

2. Experimentation

2.1 Reagents

- Hydrogen
- Oleic acid
- Nickel catalyst on gamma alumina
- Water

2.2 Equipment

- Reactor

- Digital thermometer

Figure 1 shows the process of hydrodeoxygenation of oleic acid.

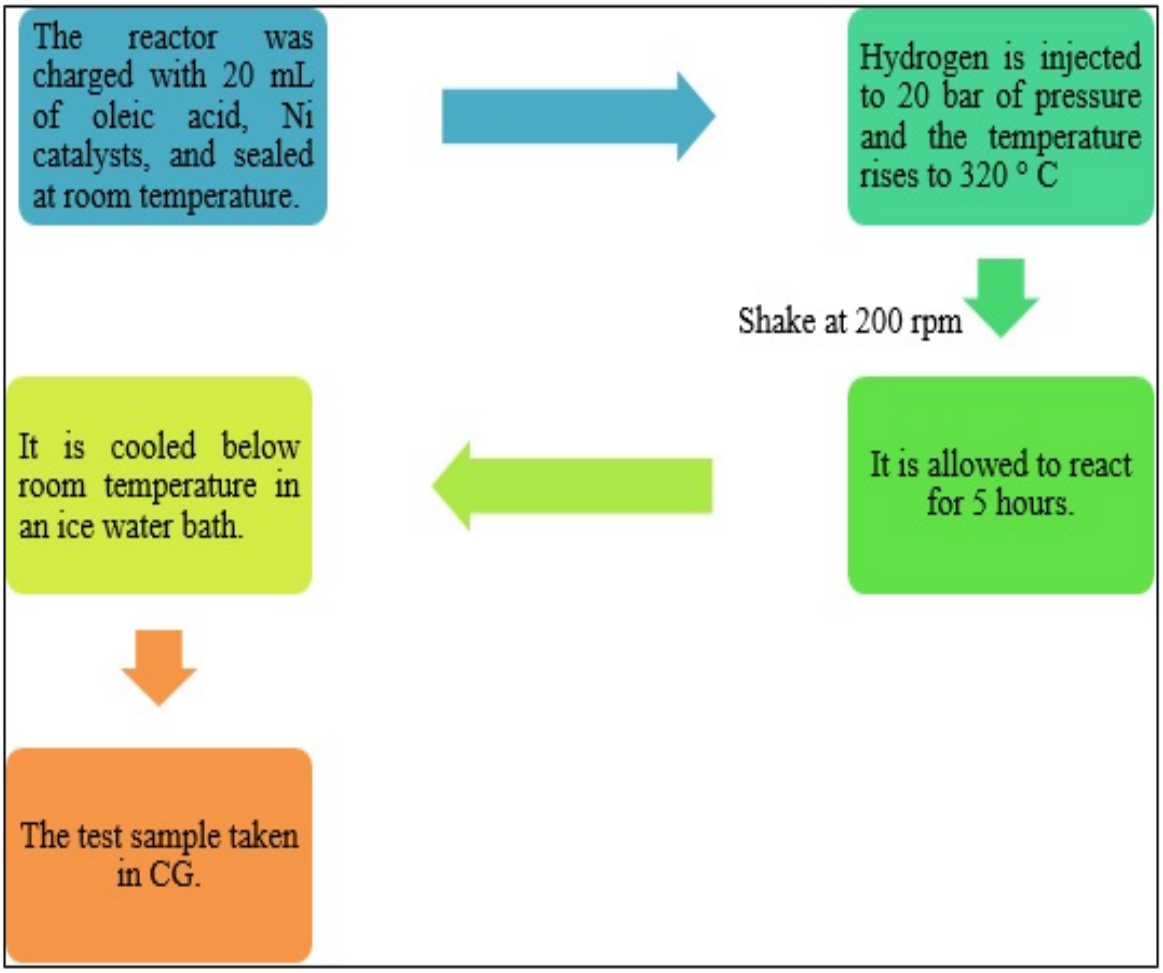

Fig. 1. Process of hydrodeoxygenation of oleic acid.

3. Results and Discussion

Fig. 2 shows the image obtained by transmission electron microscopy of Ni / γ-Al_2O_3 3%, where nanoparticles ranging in size within a range of 2 to 6 nm, with a suitable dispersion shown observed Ni metal nanoparticles in the catalyst support. These results are reinforced by those obtained in the EDS analysis, where a percentage of Ni of 3.21% and an atomic proportion of 1.15 were obtained, confirming that the impregnation technique is suitable for physically obtaining the percentages of active phase of Ni calculated. By analyzing products of oleic acid hydrotreating catalyst using a 3 wt% Ni, a maximum conversion rate of 55.3% oleic acid, and a total molar yield n-C_{17} + n-C_{18} 48.7% were

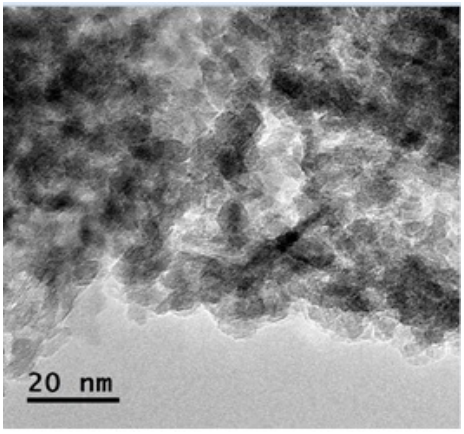

Fig. 2. Transmission electron microscopy of nickel catalysts deposited on gamma alumina with 3% by weight of active phase.

obtained. It is noteworthy that the greatest progress of the reaction occurs in the first two hours, one of the causes is the release of oxygen from the oleic acid, thus affecting the activity of the active metal phase.

While performing an analysis of the amount of n-alkanes even and odd generated in the reaction, a ratio (decarbonylation + decarboxylation) / hydrodeoxygenation of 1.59 to 5 hours of reaction was obtained. It indicates that the Ni is a suitable active phase for accelerating and directing hydrodeoxygenation reactions and obtaining n-C_{18} alkanes. It is also considered that the overall reaction remains a slight domain to the reactions of decarboxylation + decarbonylation for this catalyst.

Fig. 3 displays the analysis hydrodeoxygenation reaction of oleic acid with Ni / γ-Al_2O_3 with 3% by weight, at 20 bar and 320 °C.

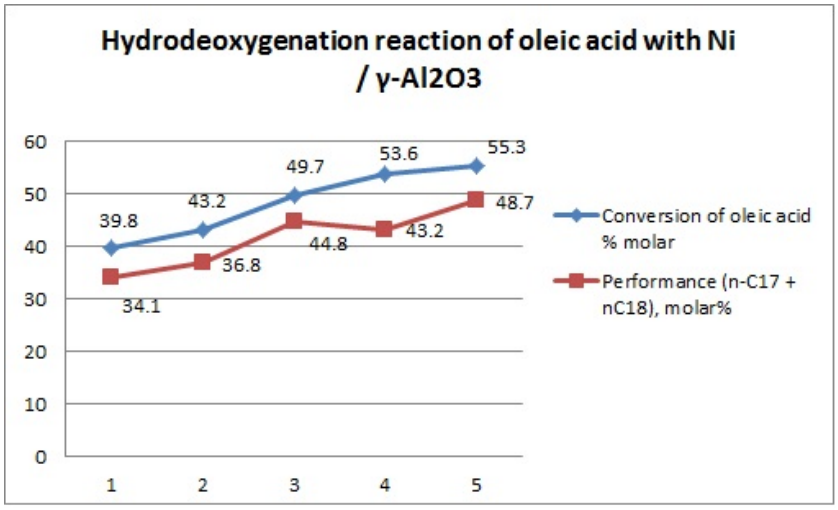

Fig. 3. Graph of the analysis hydrodeoxygenation reaction of oleic acid with Ni / γ-Al_2O_3 with 3% by weight, at 20 bar and 320 °C.

4. Conclusion

With the TEM and EDS characterization techniques it was found that the method of incipient wetness impregnation is suitable for deposition of Ni on γ-Al_2O_3.
The catalytic activity of Ni catalysts on γ-Al_2O_3 showed that the catalysts are suitable to accelerate and direct hydrodeoxygenation reactions of oxygenated organic compounds. The performance obtained after 5 h of reaction is promising and opening the possibility of changing some control factors such as, temperature, H_2 pressure, and amount of catalyst to increase the rates of oleic acid conversion and performance to C_{17} and C_{18} alkanes.

Finally, the analysis of alkanes C_{17} and C_{18} indicates that the Ni favors a balanced way hydrodeoxygenation reactions, but still with a slight domain to decarboxylation + decarbonylation reactions.

5. Acknowledgements

Thanks to Dr. Fernando Trejo Zarraga from CICATA - Legaria IPN, for his support in the characterization of materials.

6. References

[1] D. Dasa, T. NejatVeziroglu,"Hydrogen production by biological processes: a survey of literature‘‘, International Journal of Hydrogen Energy, 2001; 26;13-28.
[2]G. Knothe, J.H. Van Gerpen, J. Krahl, The Biodiesel Handbook, AOCS Press, Champaign, Illinois, 2005.
[3]Y. Yang, C.Ochoa, P. Pizarro, V. A. de la Peña, J. M. Coronado, D. P. Serrano, Influence of the Ni/P ratio and metal loading on the performance of NixPy/SBA-15-catalysts for the hydrodeoxygenation of methyl oleate, Fuel, 144 (2015) 60-70.

Chapter 5.2.Energy balance analysis of a solar-hydrogen hybrid system integrated to a sustainable house

A. Yunez Cano[a]; R. de G. González Huerta[b]; R. Barbosa Pool[c]; M. Tufiño Velázquez[d]*; B. Escobar[e]

[a]CIITEC-IPN, Cda. Cecati s/n, Col. Sta. Catarina, CP 02250 Azc., México D.F.
[b]ESIQIE-IPN, Lab. Electroquímica y Corrosión, UPALM, CP 07738, México, D.F.
[c]Universidad de Quintana Roo, Boulevar Bahía s/n, chetumal 77019, Q. Roo, México
[d]ESFM-IPN, Laboratorio de Física Avanzada, UPALM, CP 07738, México, D.F.
[e]CICY, A.C., Calle 43 No. 130 Col. Chuburná de Hidalgo, Mérida, Yucatán 97200, México.

ABSTRACT

One of the most interesting developments of energy systems based on the utilization of hydrogen is their integration with renewable sources of energy. In fact, hydrogen can operate as a storage and carrier of the energy produced by these primary sources. The design and operation of the system change noticeably depending on the type and availability of the primary source. Here we describe the performance of a stand-alone energy system that uses solar energy as the primary source, which comprises PV solar panels, an electrolyzer, a hydrides storage tank and a proton exchange membrane fuel cell (PEMFC). The sizing and design of these technologies need to meet the local microclimate in order to reach high efficacies. An analytical model to size, analyze and assess the performance of a hybrid photovoltaic/hydrogen (PV/H_2) energy conversion system using real weather data is presented in this work. The analysis includes an energy balance and a description of the behavior of electrical variables of the system components; the subsystems efficacy is calculated and from the obtained results, improvements to increase the efficiency by the use of surplus energy produced by the hybrid system are proposed. We used solar radiation measurements from a meteorological monitoring station placed on the roof of the sustainable house located in the north side of Mexico City. PV solar panels supply the electric power to satisfy the electric load. Surplus energy is delivered to an electrolyzer to produce the hydrogen to be stored in a hydrides tank. In energy deficit hours a PEMFC covers partially the electric demand; therefore the hybrid system efficacy is calculated based on the level of energy stored and the fulfillment of the electric load.

Keywords: Energy balance analysis, Solar-hydrogen hybrid system, Sustainable house

1. Introduction

One of the most interesting developments of energy systems based on the utilization of hydrogen is their integration with renewable sources of energy.

---

* Author for correspondence:
Miguel Tufiño Velázquez, (+52) 55 57296000 ext. 46138, mitufinovel@gmail.com

To realize a sustainable energy system we should change the whole energy chain: from the supply sector to the energy endues technologies. The crucial mission of energy research is the promotion and implementation of methods, technologies and processes to develop clean (no resources consumption and zero pollutant emissions), efficient, appropriate (to different local conditions), safe and convenient energy systems. This is particularly true for household, which is the third energy sector of energy consumption in Mexico as shown in Fig. 1 [1].

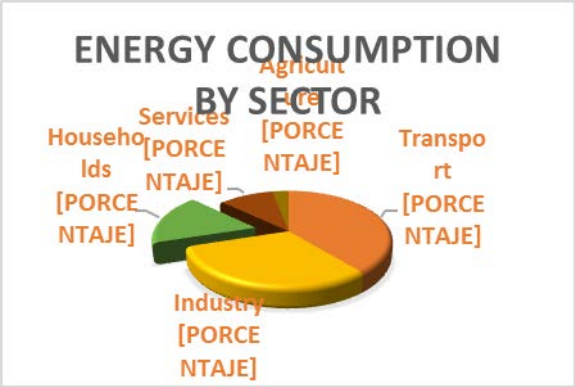

Fig. 1. Energy consumption by sector in Mexico.

Moreover, if from one side the diffuse structure of residential energy consumption can be difficult to be changed, on the other side it is an appropriate structure to implement distributed energy generation systems sourced by local renewable energy [2-7]. The development of integrated energy efficient systems formed by renewable energy sources and hydrogen technologies can play an important role in reducing both the energy consumption from fossil fuels and the emission of pollutants. If this type of integrated systems are to be developed, improving the security in the production of energy becomes an important task.

Renewable energy has received more attention recently. Solar radiation is considered the most preferred renewable energy source for its availability and inexhaustibility [1]. However, due to the selective geographical availability and intermittency of solar radiation, it has been a challenge to generate a highly reliable power source with photovoltaic (PV) modules [2]. To overcome this limitation, we propose the use of a PV-Hydrogen hybrid power system (PV-H2) to supply electricity to a mobile house.

Over the past decade several RSE-H2 systems have been discussed in literature; the most importants were: Erkan Dursun et al. report a modeling of hydrogen production with a stand-alone renewable hybrid power system [2]; Mehmed Eroglu et al. report a mobile renewable house using PV/wind/fuel cell hybrid power system [3]; Massimo Santarelli et al. report the design and analysis of stand-alone hydrogen energy systems with different renewable sources [4]; E. Bocci et al. report a renewable and hydrogen energy integrated house [5]; Beatriz Escobar et al. report an analytical model for the sizing of a hydrogen production system based on renewable energy, applied to the Mexican Caribbean as a case

of study [6] and Romeli Barbosa et al. report a sizing of a solar/hydrogen system for high altitude long endurance aircrafts [7].

The aim of this paper was tohe design and analysis of a stand-alone energy system fulfilling the electricity needs (1825 kWh/year), during a complete year of operation, of an isolated mobile house situated in a selected site (North Valley DF-Mexico). The system operates using a combination of a renewable source of energy (RSE) and a hydrogen system, HS; the RSE utilizes solar radiation as the primary source through an array of PV panels; the HS system consists of a proton exchange membrane electrolyzer (PEME), a hydrides storage tank and a PEM fuel cell (PEMFC), without integration of traditional energy devices based on fossil fuels (CFE network).

This work considers as a case of study a 24 square meters isolated mobile house where two persons may live comfortably, located in Mexico City: 19° 30´ North; 99° 07´ West, figure 3. During July 2014 to June 2015, the PV system energy supply to meet the electrical loads was analyzed, Fig. 2. Finally, the hydrogen backup system (electrolyzer, metal hydrides and fuel cell) is analyzed, taking into consideration its dynamic behavior, experimentally determined, and giving some remarks in the conclusions. This paper focuses on the integration of PV-H2 technologies for which market available commercial devices were used; thus it highlights the most important points.

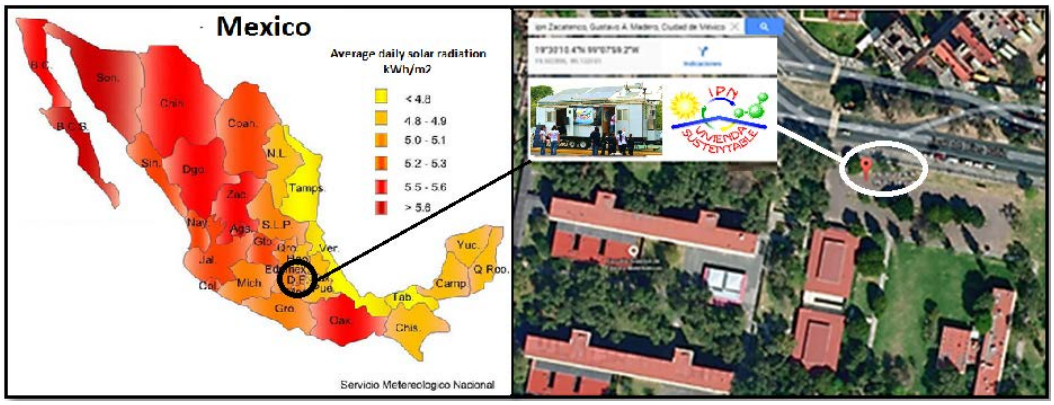

Fig. 2. Independent sustainable housing located in Mexico D.F.

The energy balance analysis of the hybrid system has to be done by considering the steady state system behaviour, unsteady profiles of the site energy source and the electricity loading demand. The overall configuration of the PV-H2 hybrid system developed for a grid independent house is shown in Fig. 3.

This system consists of a PV panels system, a PEWE, two PEMFC, a power control system, and a hydrides storage tank. If the total power generated by the primary system (PV) is higher than the electrical demand, the surplus energy is used by a PEWE to produce hydrogen which is stored in a hydrides tank as long as it is not necessary to be used [2-6]. If the primary system is not sufficient to meet the loading, the energy required will be provided from the hydrogen stored in the hydrides tank fed to the PEMFC; this may continue as long as the power deficit exists. Nominal power of the subsystems should be carefully selected to satisfy the electric demand but without oversizing the system.

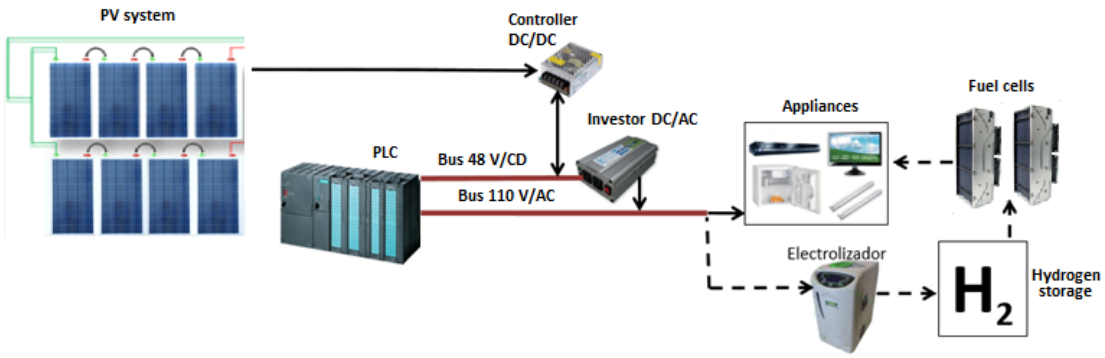

Fig. 3. The PV/H2 hybrid power system to supply electricity to the mobile house.

2. Theory and calculation of experimental profiles

The system operation features allow us to define the "efficacy" term (functionality) of the system in both conditions (undersizing or oversizing) [6]. Undersizing conditions exist when the electric demand is not entirely fulfilled, and oversizing will be when the input energy is not completely useful. Eq. (1) determines the "load efficacy" (η_L),

$$\eta_L = \varepsilon_{L,actual} / \varepsilon_{L,nom} \quad (1)$$

Where $\varepsilon_{L,actual}$ is the actual consumed energy and $\varepsilon_{L,nom}$ the nominal demanded energy. The "useful efficacy" (η_U) is determined by Eq. (2),

$$\eta_U = (\varepsilon_{L,actual} + \varepsilon_S) / \varepsilon_{in} \quad (2)$$

where ε_S is the energy stored and ε_{in} the input energy. System's global efficacy can be determined by a “mixed efficacy" (η_M),

$$\eta_M = \eta_L \eta_U \quad (3)$$

The design strategy consisted of a parametric combination of the subsystems power using experimental profiles along the time. Average of the instantaneous efficacies helps to select the best combination. Instantaneous system behavior will be determined by an energy balance analysis.

2.1. Energy input

Technical characteristics of the PV system are: a serial-parallel arrangement was installed, which generates 1.08 kW (instant nominal power generated) with 8 rigid panels of polycrystalline silicon (maximum power 70.7 V and 15.5 A DC) with a DC-DC charge controller (12-60 V and 60 A). The input energy (ε_{in}) of the hybrid system is the electrical output energy of the PV system:

$$\varepsilon_{in} = \varepsilon_{PV} \quad (4)$$

where ε_{PV} is the output energy of the PV; this energy is according to the solar abundance of the site and the physical characteristics of the devices. Instantaneous electric output energy from a PV (ε_{PV}) is given for the following equation:

$$\varepsilon_{PV} = \eta_{PV} A_{PV} G_i \quad (5)$$

where η_{PV} is the PV instantaneous efficiency, A_{PV} the total area of the PV and G_i equals to instantaneous solar radiation per incident area on the PV surface. Strictly, η_{PV} is dependent on three parameters: the temperature, the packing factor and the module reference efficiency. However, the efficiency used in this work is a global parameter of a theoretical PV (η_{PV} = 11%). A_{PV} was 7.4 m^2. The solar irradiance, Gi, is based on real data, which was obtained from a meteorological station located on the roof of the house, Fig. 4.

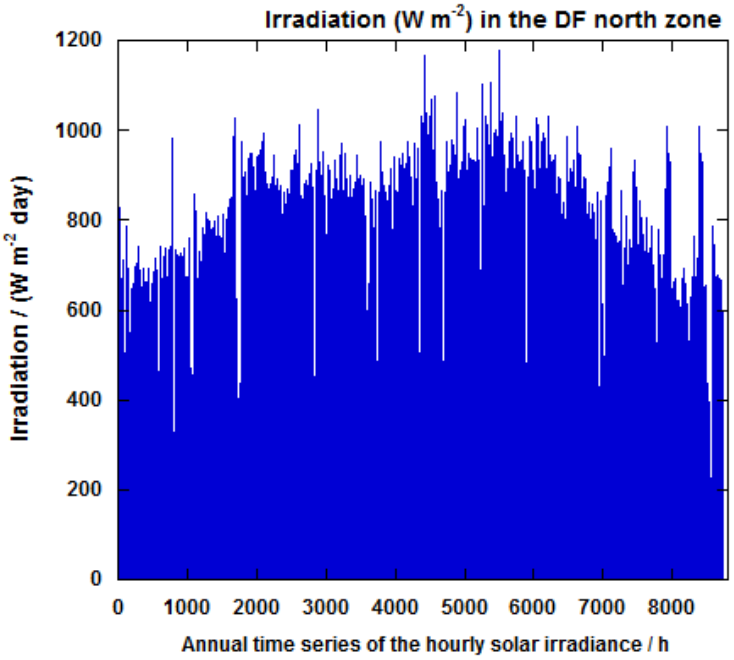

Fig. 4. Annual time series July 2014-June 2015 of hourly solar irradiance.

The net hourly electrical power according to the solar irradiance in Mexico City north zone was determined from experimental data, including the average of one period of time: July 2014-Jun 2015. This annual average behavior is shown in Fig. 5.

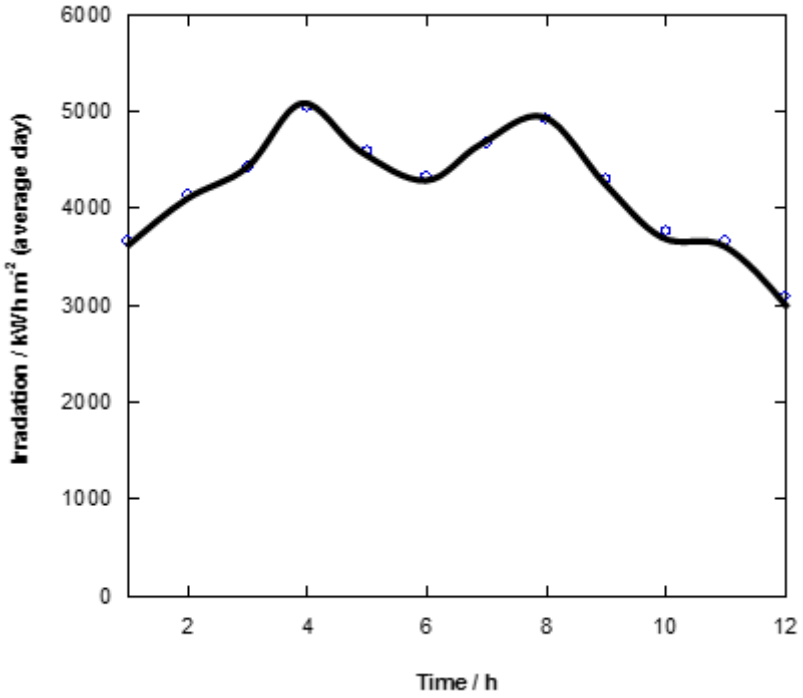

Fig. 5. The average solar irradiance in Mexico City north zone.

2.2. Energy storage

An entire carbon-free and pollution free hydrogen storage process is made by using a metal hydrides canister. These can be supplied with hydrogen produced by an electrolysis process. In this work, we used 2 hydrides tanks, the first one has a nominal capacity of 81 g (0.9 Nm^3) of hydrogen, internal volume of the cylinder is 1.5 L and mass system is 7 kg; the second one has a nominal capacity of 270 g (3 Nm^3) of hydrogen, internal volume of the cylinder is 5 L and mass system is 22 kg. The storage tanks capacity is considered to meet up to 3 autonomous operation days at a rated load. This maximum storage capacity was taken to satisfy a critical shortage of energy after an emergency situation. Electrical energy stored (E_{NHs}) can be determined by the balance of energy in the storage subsystem, fig. 6.

$$E_{NHs} = E_{NHg} - E_{NHc} \quad (6)$$

where E_{NHs} is the energy of the stored hydrogen, E_{NHg} is the energy of the hydrogen generated by the electrolyzer and E_{NHc} is the energy produced by the hydrogen consumed in the fuel cell.

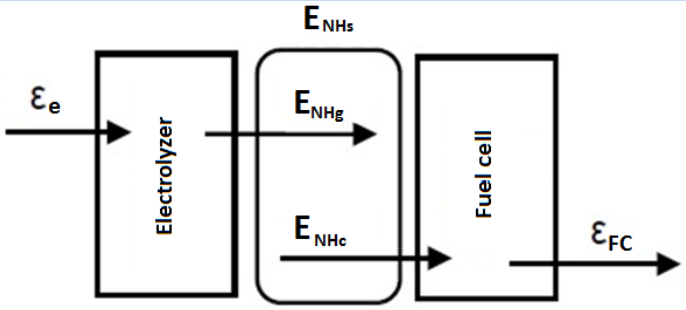

Fig. 6. Electrical energy stored, E_{NHs}

Hydrogen production is performed by a PEM electrolyzer type (proton exchange membrane electrolyzer), which generates from 50 to 300 cm^3 min^{-1} of high purity hydrogen. In a PEME, E_{NHg} can be determined by the electrolyzer efficiency (η_e),

$$\eta_e = E_{NHg} / \varepsilon_e \quad (7)$$

where ε_e is the energy consumed by the electrolyzer. In electrical terms, the energy consumed by the electrolyzer (ε_e) is:

$$\varepsilon_e = I_e V_e t \quad (8)$$

where Ie is the applied current, Ve is the applied voltage and t is the operating time.

Two PEMFC type (proton exchange membrane fuel cell) which have a maximum output of 500 W each one were used. PEMFC are open cathode with 24 mono-cells; that is, they take oxygen from the air. The power generated by the cells can controlled by regulating the hydrogen flow; in order to achieve the maximum electric power, a 6.5 L/min flow is required. The PEMFC stack efficiency (η_{FC}) can be defined thermodynamically by,

$$\eta_{FC} = \varepsilon_{FC} / E_{NHc} \quad (9)$$

where ε_{FC} is the energy produced by the fuel cell and E_{NHc} is the energy produced by the hydrogen consumed in the fuel cell. On the other hand, in electrical terms, the energy produced by the PEMFC stack (ε_{FC}) depends on the operating time (t), the total current produced (I_{FC}) and the total potential produced of the stack (V_{FC}),

$$\varepsilon_{FC} = I_{FC} V_{FC} t \quad (10)$$

The PEMFC and PEWE efficiencies depends on their potentials, Fig. 7 shows the performance of a single-cell PEMFC and PEWE used in this work, which are experimental polarization curves carried out in our laboratory.

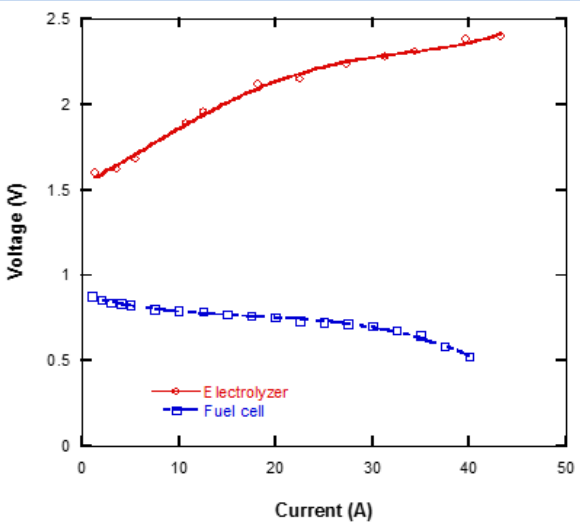

Fig. 7. Performance of a single-cell PEMFC and PEWE.

2.3. Energy output

The electrical output of the hybrid system is equal to the power consumed by the electrical load. Concerning the user, the profile of the electric power demand has been defined by using statistical data for a CFE type 1 house. The electricity demand has been evaluated during one complete year of operation; for each month a reference day has been established, and in the reference day the electricity demand is given for every hour of operation. The nominal load profile proposed corresponding to the real consumption of a house is shown in Fig. 8.

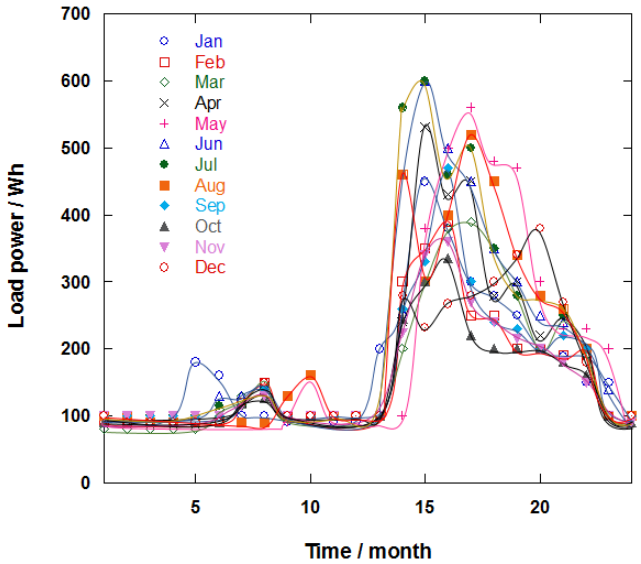

Fig. 8. Monthly average of the electricitydemand of the user,

The nominal output energy can be obtained by the curve integration in the required time of period, $\varepsilon_{L,actual}$, Fig. 9.

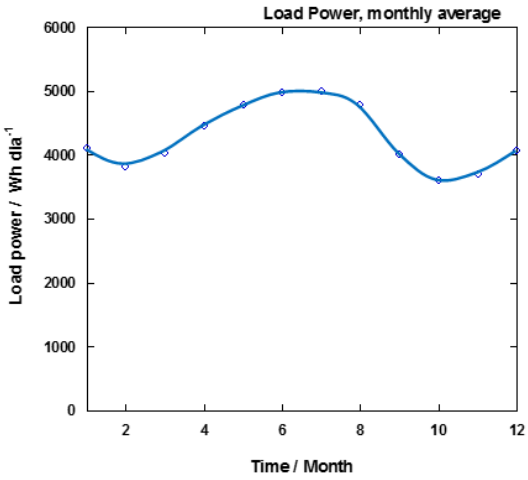

Fig. 9. Monthly average of the nominal output energy.

3. Results and Discussion

Mixed efficacy is evaluated every hour using a parametric combination of nominal values: the nominal power of PV (PPV), the nominal power of PEMFC (PFC), the nominal power of PEWE (PE) and the nominal hydrogen storage capacity of tanks (EHS). Minimum and maximum limits are listed in Table 1, there are found ten points between these limits.

Table 1. Limits of the combination.

	PPV (W)	PE (W)	EHS (Wh)	PFC (W)
Minimum	730	220	430	130
Maximum	3000	1660	8500	1300

In this work the analysis of secondary devices (i.e., sensors, actuators, valves, controllers, batteries bank, Peltier cell-based system heats or cools the tanks, etc) is not included.

The energy input (subject to experimental data and evaluated by Eq. (5)), the energy stored (evaluated by Eq. (6)) and the strategy to evaluate the actual energy consumed, allow to determinate the mixed efficacy (η_M, Eq. (3)) with several nominal powers (Table 1). The hourly efficacy is averaged to evaluate annual behaviors and then compared in order to found the best solution. Fig. 10 shows the dependence of the mixed efficacy respects to PPV. In this Figure, the "points" are plotted for all possible combinations, where the minimum and maximum rated powers correspond to Table 1.

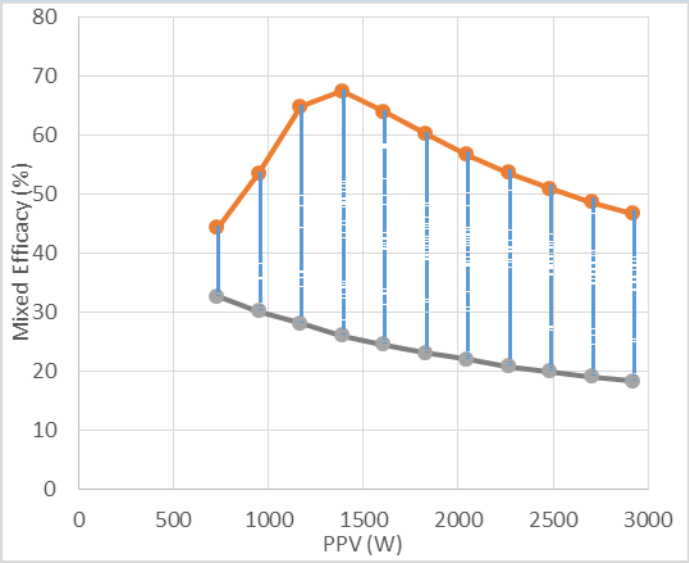

Fig. 10. Dependence of the mixed efficacy (η_M) with respect to Nominal power of photovoltaic array.

Depending on PPV, η_M reaches different value. Mixed efficacy increases because load efficacy (η_L) is higher with the input power increment (i.e. PPV increment), but when the surplus energy of the system exceeds the maximum energy level, useful efficacy (η_U) decreases to have a surplus that is not used, this suggests that the system is "oversizing". In addition, it can also observe that mixed efficacy decreases because electrical demand is not entirely fulfilled, then an undersizing condition exists.

Mixed efficacy (η_M) versus EHS is showed in Fig. 11. The lines correspond to the minimum and maximum rated powers correspond to Table 1 and to three conditions selected from Fig. 10: PPV=1400 W, PPV=1600 W and PPV=1800 W.

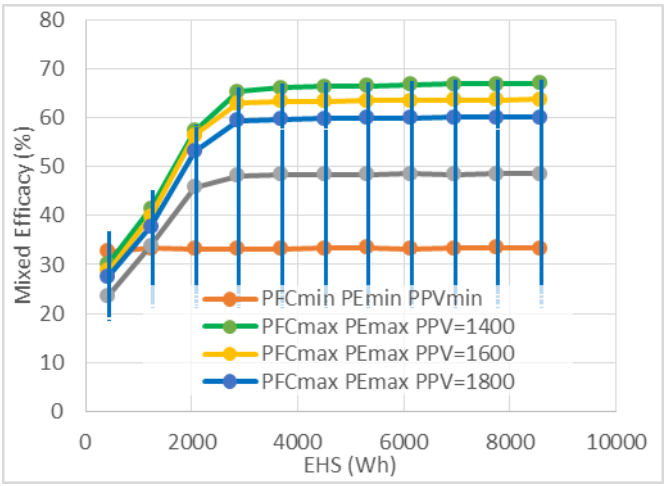

Fig. 11. Dependence of the mixed efficacy (η_M) with respect to electrical energy stored

From the trajectory of the plots in Fig. 11, we can see that η_M increases while EHS increases. Nevertheless, it should be noticed that η_M changes only 2.3 % from 2900 Wh (~65 %) to the maximum limit studied, 8600 Wh (67 %). Then, any local maxim point can be selected for further comparison. Mixed efficacy (η_M) versus PFC is showed in Fig. 12.

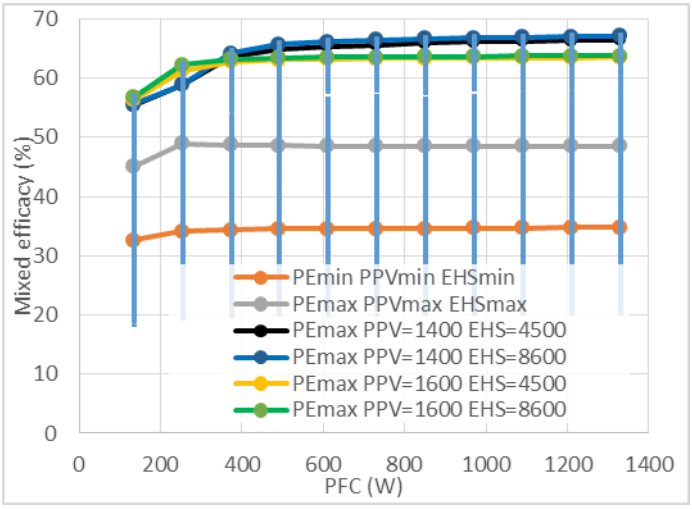

Fig. 12. Dependence of the mixed efficacy (η_M) with respect to Nominal power of fuel cell

Also it should be noticed that ηM increases while PFC increases. The six lines indicate different conditions of PPV and EHS when PE is the maximum limit studied in table 1. Mixed efficacy (ηM) versus PE is showed in Fig. 13.

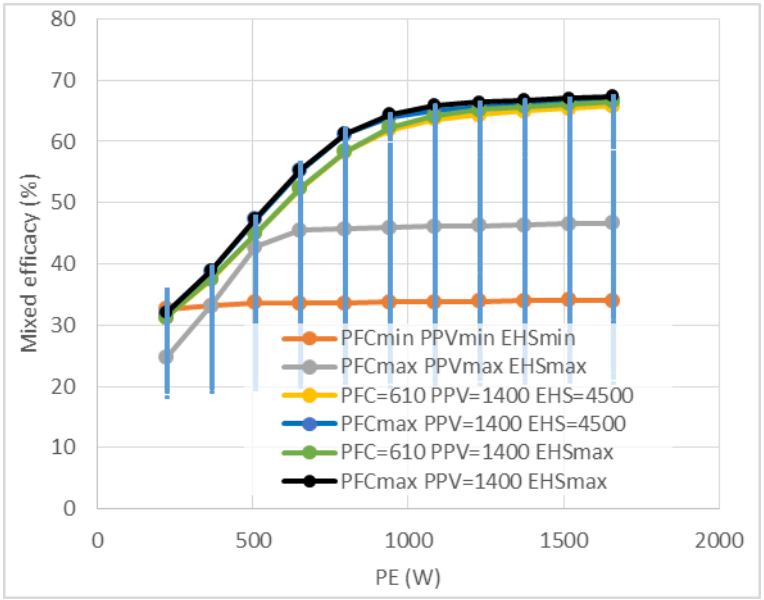

Fig. 13. Dependence of the mixed efficacy (η_M) with respect to Nominal power of the electrolyzer.

The same pattern was observed in Figs. 11, 12 and 13, the ηM increases while the nominal power increases. This is an expected behavior because of the high nominal power of the electrochemical system is capable of meet an improved efficiency.

4. Conclusion

Theoretical efficacy, of a hybrid solar-hydrogen system of a sustainable house, was determined using an energy balance analysis. Real electrical performance of the house, real electrochemical characteristics of the hydrogen systems and real microclimate data of solar resource, from north side of Mexico City, were used to determine ηM at different scenarios. Results shows that the highest PPV not always meet the highest efficacy of the hybrid system, therefore the model allows determine the best subsystems configuration to avoid the oversizing or undersizing. The simulation data applied different scenarios show the ηM, around the 65 % at 1400 W of PPV, 4500 Wh of EHS, ~600 W of PFC and ~1000 W of PE. Based on the results, using the analytical model proposed is possible make decisions to choose strategies which allow sizing hydrogen hybrid systems with the high efficacy.

Acknowledgements

This work has been supported by the IPN projects SIP-20150073, multidisciplinary project IPN-SIP 1683 and 1725, Programa Redes Tematicas CONACYT/RTH2. R. Barbosa would like to thank PRODEP UQROO-PTC-119 and B. Escobar wishes to thank the Catedras-CONACYT program.

References

[1] http://www.sener.gob.mx/
[2] Erkan Dursun, Bora Acarkan, Osman Kilic Modeling of hydrogen production with a stand-alone renewable hybrid power system. Int. J. Hydrogen Energy 2012, 37, 3098-3107.
[3] Mehmed Eroglu, Erkan Dursun, Suat Sevencan, Junseok Song, Suha Yazici, Osman Kilic. A mobile renewable house using PV/wind/fuel cell hybrid power system. Int. J. Hydrogen Energy, 2011, 36, 7985-7992.
[4] Massimo Santarelli, Michele Cal, Sara Macagno. Design and analysis of stand-alone hydrogen energy systems with different renewable sources. Int. J. Hydrogen Energy 2004, 29, 1571-1586.
[5] E. Bocci, F. Zuccari, A. Dell'Era. Renewable and hydrogen energy integrated house. Int. J. Hydrogen Energy 2011, 36, 7963-7968.
[6] Beatriz Escobar, José Hernández, Romeli Barbosa, Ysmael Vrerde-Gómez. Analytical model as a tool for the sizing of a hydrogen production system based on renewable energy: The Mexican Caribbean as a case of study. Int. J. Hydrogen Energy 2013, 38, 12562-12569.
[7] Romeli Barbosa, B. Escobar, Victor M. Sanchez, J. Hernández, R. Acosta, Y. Verde. Sizing of a solar/hydrogen system for high altitude long endurance aircrafts. Int. J. Hydrogen Energy 2014, 39, 16637-16645.
[8] Armando Yunez Cano, (Acta de examen 17740) "Modelado 3D e integración de una casa sustentable solar-hidrógeno", Tesis de Licenciatura ESIQIE, 7 de febrero de 2013.

Chapter 5.3.Reactor with agitation of double twist for hydrotreating of oxygenated organic compounds

S. L. Zamorano-Murillo[a,*]; M. Sánchez-Cárdenas[a]; J. Medina-Valtierra[b]; R. A. Ortiz-Medina[a], Z.J. Pineda-Hernández[a]

[a] Universidad Politécnica de Aguascalientes, Calle Paseo , San Gerardo, 207, Aguascalientes, Ags., México, 20342.
[b]Instituto Tecnológico de Aguascalientes, Av. Adolfo López Mateos Ote. No. 1801, Fracc. Bona Gens, Aguascalientes, Ags., México, 20256

ABSTRACT

A stainless steel reactor for hydrotreating of waste oils and their conversion to biodiesel has been designed and build. The reactor can run by batches or continuous flow. It has the capacity to convert 100 mL of waste oil at temperatures exceeding 400 degrees Celsius and at H_2 pressures of up to 20 MPa. The stainless steel cylindrical reactor is introduced to a jacket containing a heating tape connected to a temperature controller. In the inside of the reactor there is a mechanism consisting of a roller bearing that was placed at the top, that intended to facilitate the rotation and bring stability in the assembly of the reactor with the heating jacket. At the bottom of the reactor, there are agitation blades that gives homogeneity to the agitation of the mixture. On the outside, the reactor has a turmoil mechanism where is connected with a shaft and assembled to an engine. The engine controls speed and rotation, and allows agitation with full and half turns of the shaft.
To ensure good performance and safety of operation, a simulation study was carried out in order to determine the vulnerabilities of the reactor in critical or nominal working conditions. It takes into account the strenghth of the material and its posible deformation for such conditions. The study simulates the loads and pressures that the reactor will be subject to and determinates the way that the material will answer, taking into account the geometry of the whole reactor. The pressure is estimated to be at 40 KPa as a maximum allowed for this reactor, whereas the pressure of work for the hydrotreating processes is well below this limit, which is acceptable to the established range. Studies of Von Mises stress applied to the structure of the simulated solid are located below the elastic limit of the material, so the structure of the reactor remains stable and safe.Tests were carried out to the hidrodeoxygenation of the oleic acid using Pt and Ni catalyst supported on γ- Al_2O_3.
In the experiments, it was observed that the catalyst with 2% by weigth of Pt presented a (descarbonylation + decarboxylation) / Hydrogenation ratio of 18.2, which in comparison with the 2% by weight Ni catalyst with a 1.23 ratio shows that the Pt catalyst has a bigger acceleration reaction for descarbonylation and descarboxylation.

***Keywords*:** Hydrotreating, Reactor, Agitation

---

*Author for correspondence: Zamorano Murillo Saira Lizette, (0449)-449-142-39-48
up130248@alumnos.upa.edu.mx

1. Introduction

Currently approximately 80% of world energy demand is obtained by burning fossil fuels. This leads to a depletion of fossil energy resources, which are limited. This has caused that the use fossil fuels is now identified as the main cause of global climate change due to emissions of pollutants agents as a result of its combustion [1].

An option to reduce the consumption of fossil fuels and their impact on the environment is the use of renewable energies based on biomass processing, because they have a huge energy potential and can contribute to the reduction of greenhouse gases emissions [2]. This has led that investigations continue around obtaining a highly compatible fuel with conventional diesel, with a good performance in cold weather and does not affect conventional engines [3].

The interest is also attracted by the development of catalytic processes of hydrodeoxygenation of methyl esters from vegetable oils and animal fats, so that they can transform a condition of polyunsaturated to monounsaturated. This new biodiesel is what is known as second-generation biodiesel [4].

The preparation of some kind of catalyst for the hydrodeoxygenation of biodiesel requires a preview process of reduction of hydrogen, so that it needs to implement a reactor that will make the process of hydrodeoxygenation of biodiesel. Also, the process requires that the reactor have special characteristics so it can inject hydrogen pulses in specific conditions, for this reason is essential to design a reactor that meets this requirements.
The hydrodeoxygenation is a chemical reaction in which a carboxyl group its removed in the presence of hydrogen compound producing water. The preparation of the catalyst used to activate the reaction of hydrodeoxygenation of biodiesel, requires previous preparations as a part of the elaboration, which consist in a reduction trough hydrogen pulses. For this reason the reactor must have the capacity of make this process and do not need any special equipment.

For this operation a reactor is designed and built, with all this capacities to optimize and produce biodiesel of second generation from the hydrodeoxygenation of first generation diesel. The reactor has the entire operative and safety features required to make the process of organic oxygenates of hydrodeoxygenation compounds. This project focused on the design of the reactor, for it to have the functional and operative features required for the process.

It is proposed to innovate in hydrodeoxygenation by means of a reactor that has positive results with the control of the reaction and at the same time obtain a more environmental friendly biodiesel.

2. Materials and Methods

The reactor contains the principal and needed components for carry out the process of hydrodeoxygenation with reference to an existing chemical reactor. The latest to being able to define the accessories that was required to add, change and modify as well as the dimensions in the structure of the reactor.

A model of the reactor in its whole was made, containing the dimensions and specifications to establish the necessary procedures and materials for it. It is worthy to distinguish that the mechanic and physics possibilities were taken account, as well as the economics.

The reactor to be used has the following specifications.

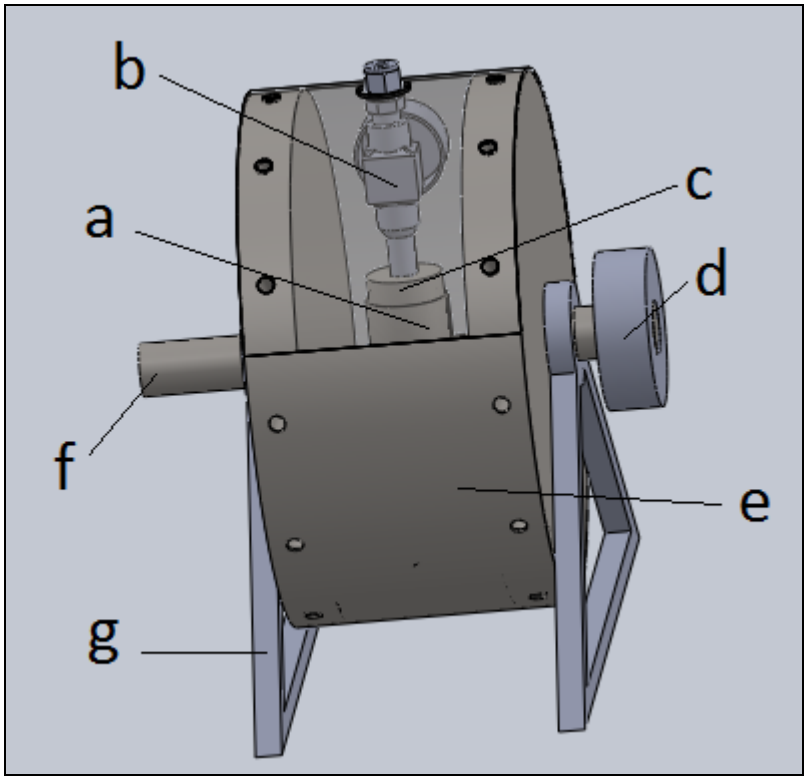

Fig. 1. Assembly of the cylindrical reactor of half twist: a) cylindrical reactor of stainless steel where the reaction is performed, b) valve of hydrogen feeding, c) screw cap of the reactor for catalyst feeding and oxygenated organic compounds, d) mechanical system for moving the reactor through a chain or belt, e) fixed lower cap of reactor, f) shaft of rotation of reactor and g) base of reactor.

This method for hydrodeoxygenation of biodiesel is shown on Figure 2.

3. Results and Discussion

The implementation of the simulation study, focus on determinate the vulnerabilities of the reactor on critical conditions or conditions that exceed the rated work, that is why the material resistance and its possible deformation in those conditions are taken account.

The study simulates loads and/or pressures to which the reactor will be subject and determinates the response of the material taking account the geometry of the piece. This

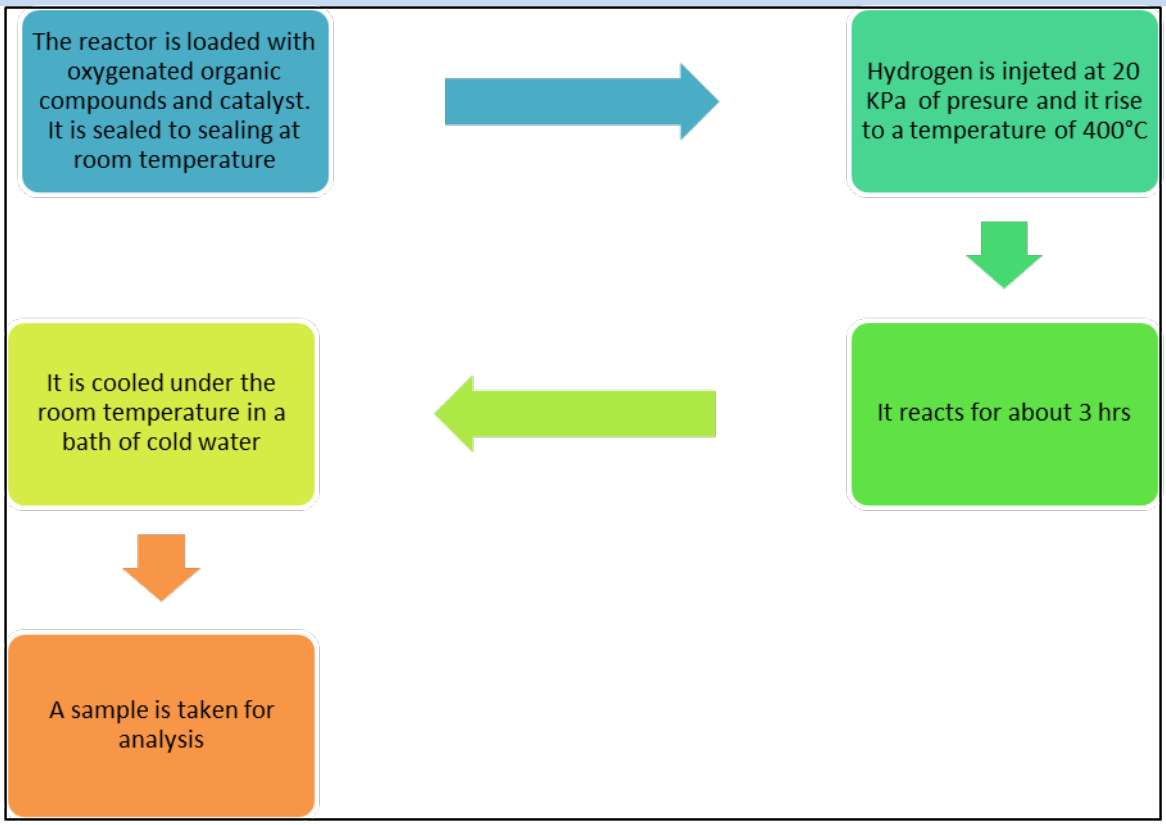

Fig. 2. Process for hydrodeoxigenation of oxygenated organic compounds.

pressure is estimated at 20 KPa as maximum allowed for the reactor, considering that the pressure of work for the hydrodeoxygenation process is below that limit. Given this the established range is acceptable.

The study of Von Mises stress was obtained for the simulated solid structure. This stress is a physical magnitude proportional to the distortion energy. In structural engineering, the Von Mises stress is used in the context of the failure theories as an indicator of a good design for ductile materials. The obtained results are represented as a color change in the zone where the larger tension is applied. The colors close to the blue represents a lower Von Mises stress, as the colors that are closer to the red tones show a larger stress. It is important to point out that all the shown stresses in the study are below the elastic limits of the material so that the structure remains safe and steady.

The zone where the reactor has a larger vulnerability to deformations or alterations on the material is given in a higher condition that the one in the simulation, and it would be at a pressure over 10,000 KPa.

The results of the hydrodeoxygenation reactions of the oleic acid made in the reactor with platinum and nickel catalysts with a weight percentage of 2% of metal active phase are shown in table 1. This results are given by (descarbonylation + decarboxylation) / hydrogenation, that is an indicative of the capacity that each metal active phase has to

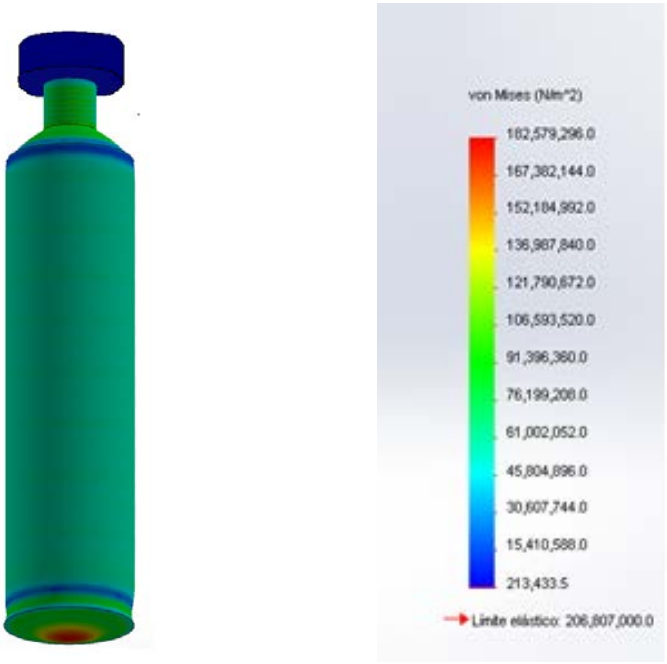

Fig.3 Study of Von Mises stress.

accelerate and lead the obtaining of n-C_{17} y n-C_{18} alkanes. In the analysis of the products made by gas chromatography, a relation of 18.2 is observed for the Pt/ γ- Al_2O_3 catalyst, and for the Al_2O_3 catalyst it was 1.23, much less than platinum.

The result indicates that Ni is better that Pt for this purpose, because Ni have a relation that indicates that the obtaining n-C_{18} alkane is easier.

Table 1. Relationships obtained by the relation descarbonylation + decarboxylation) / hydrogenation

	% in weight of metallic active phase	**(decarbonylation + decarboxyilatcion) / hydrogenation**
Platinum (Pt)	**2**	**18.20**
Nickel (Ni)	**2**	**1.23**

4. Conclusion

The process of hydrodeoxygenation of biodiesel presents very difficult parameters to manage for most of the chemical reactors, where high temperatures combined with the pressurizing of gaseous hydrogen generates a risky environment for the reactor operator and for the stability of the reactor structure. It is noteworthy that a continuous agitation medium is required, that is the reason for not using common reactor and it is where the need arises a new design of reactor to fulfill the work conditions. This innovative reactor, represents an advance for the development of applied technology to chemical processes, since it meets all the operational conditions and the adequate security for the handled temperatures in a pressurized hydrogen atmosphere. So that can be used for many types of chemical reactions processes that are within the ranges of reactor operation.

In the reactions of this work the weight percentage of 2% of metal active phase was used for the platinum and nickel, which were presented in the relation (descarbonylation + decarboxylation) / hydrogenation for indicate that the nickel is better in acceleration and leading capacity for the obtaining of n-C_{17} y n-C_{18} alkanes. In the analysis of the products made by gas chromatography, it was observed that for the Al_2O_3 catalyst the relation was 1.23, that is better that the one obtained for the Pt/ γ- Al_2O_3 catalyst with a relation of 18.2.

Acknowledgements

We acknowledge Dr. Jorge Medina Valtierra for his contribution and support during this project.

References

[1] Levenspiel, O. (2002). *El omnilibro de los reactores químicos.* Barcelona: Reverté.
[2] Lenoir, C. (2010). *Análisis de la producción de biodiesel.* Buenos Aires, Argentina: Agrolluvia.
[3] Martínez Romero, D. (2011). *Obtención de combustibles renovables mediante hidrotratamiento catalítico de aceites vegetales y gasóleo.* México, D.F.: Instituto Politécnico Nacional.
[4] Sivasamy, A., Cheah, K., Fornasiero, P., Kemausuor, F., Zinoviev, S., & Miertus, S. (2009). *Catalytic applications in the production of biodiesel from vegetable oils.* ChemSusChem.

Chapter 5.4. Improvement of novel microbial fuel cell design for wastewater treatment

Angel Rodrigo M. Ochoa[a]; K. Sathish-Kumar[a]; O. Solorza-Feria[b]; J. Tapia-Ramírez

[a]Universidad Politécnica de Aguascalientes, Ingeniería en Energía Calle Paseo San Gerardo No. 207. Fracc. San Gerardo. Aguascalientes, Ags. México, 20342.
[b]Centro de Investigación y de Estudios Avanzados del Instituto Politécnico Nacional, Departamento de Química, Av. Instituto Politécnico Nacional 2508, Col. San Pedro Zacatenco, Delegación Gustavo A. Madero, México D.F. 07360.
[c]Centro de Investigación y de Estudios Avanzados del Instituto Politécnico Nacional, Departamento de Genéticas y Biología Molecular

ABSTRACT

In our previous report, we proposed the novel microbial fuel cells (MFCs) design from pencil (SMH2014). Furthermore, we known the 6M sulfuric acid treated pencil based integrated MFCs exhibit better performance. At the continues of that point, we have tried to improve the performance of pencil based intergrated MFCs by increasing the anodic current collector surface area. In pencil, the graphite rod could act as anode besides submerged with wooden portion into the raw high concentrated wastewater solution, and remained wooden portion bound with Pt/Carbon cloth (Cathode) exposed to air. Raw high concentrated waste waters was used both as inoculum to form electrochemically active bacteria on graphite based anode and also as the medium to be treated. Later we applied the graphite felt on the anodic current collector (graphite rod) of pencil based integrated MFCs. The highest maximum power density (191.6mW/m^3) is obtained in graphite felt anode, which is 65.49 % higher than that of graphite rod as anode (66.1 mW/m^3) in pencil based integrated MFCs. The large surface area properties of the graphite felt anode play a rather important role in anodic reaction. Batch operation of graphite felt anode showed the average power density 1.52 mW/m^3, which is 54.38 % higher than that of graphite rod as anode 0.83 mW/m^3. The average COD removal efficiencies were 91.77 % and 82.65 % in the graphite felt anode and graphite anode, respectively. Further, we powered the 3 digital clock by 3 serially connected graphite felt anode as MFCs, which exhibited the average power density 10.3 mW/m^3 and potential 1.1487 V. These results show graphite felt is suitable for pencil based integrated MFCs as anode could increase the extracellular electron transfer in that way increase power production in MFCs.

Keywords: Microbial fuel cells, Graphite felt, pencil, Air cathode

1. Introduction

Microbial fuel cells are generating electrical energy from the wastewater, while at the same time the wastewater is treated. The power output from the MFCs over the years by several

---

* Author for correspondence: Kamaraj Sathish-Kumar, +01 (449) 442 1400 ext: sathish.bot@gmail.com,sathish-kumar.kamaraj@upa.edu.mx

orders of magnitude is improving. MFCs improving performance is likely to the results from the optimized component properties such as anode, cathode, separator and reactor configurations [2, 3]. In general, the power production has shown to increase with higher surface area electrodes, such as graphite granules, graphite felt, and graphite fiber brushes [4, 5, 6]. They have a good stability, microbial accessibility, high conductivity and relatively high specific area [7]. Separators /membranes are one of the most important components in MFCs as they physically separate the anode and cathode compartment, thereby avoiding undesirable crossover, while allowing protons to pass through to cathode. Nafion 117 membrane is one of the most commonly used membrane/ separator, though it has number of problem associated with oxygen leakage from cathode to anode, cation transport and biofouling, while using wastewater as sole source [8, 9, 10, 11].

Among these issues, one of the main constrain is cost per power production higher. Scaling up of MFCs system for real word wastewater utilities is facing challenges on configuration of reactor and cathodic type [12, 13]. Whereas, use of liquid catholyte hardly impossible for such applications, due to cumbersome maintenance of reactors. However, utilization of oxygen as the electron acceptor has been considered as more attractive sustainable air-cathode for MFCs real world applications [12]. Though, the structure of air-cathode has been complicated, the cost has been high, and the power output remains low compared with other type of cathodes [14, 15, 16]. MFCs stacks has generally needed to provide higher voltage or current for application of small electronics. More importantly, they can be either connecting in series or parallel, depends on the application requirement.

Construction of larger scale reactors by increasing the electrode area and reactor volume can resulted in decrease of volumetric power output, compared to the smaller lab scale reactors [17, 18]. The use of high numbers of smaller electrodes in stacks with hydraulically coupled reactors has been proposed as an effective method for scale-up MFCs [19, 20]. Among the MFCs components, MFCs reactor configurations is one of the crucial determinant to high power production and improving its performance is critical to continued development of practical applications.

The objective of this work was to improve the softwood materials of pencil based integrated MFCs design by placing the graphite felt at the anodic current collector, would significantly provide the higher surface area. Further, we connected in series of pencil based integrated MFCs to power the digital clock. These integrated MFCs design would simplify the MFCs application to the real world wastewater treatment process. By inserting the integrated MFCs to the wastewater treatment process without much changing the traditional wastewater treatment plant can effectively treat the wastewater; meanwhile we can produce the electrical energy. This also could reduce the maintenances in operation of MFCs. More importantly, these integrated pencil based MFCs system avoid the usage of the commercial Nafion.

2. Materials and Methods

2.1 Collection of Inoculum

Wastewater was collected from a Universidad Politécnica de Aguascalientes (UPA) and stored in refrigerator at 4°C. The wastewater served as inoculum in anode and also as medium to be treated.

2.2 Construction of novel softwood microbial fuel cell and operation

We constructed the pencil based integrated MFCs from the Koh-i-Noor Hardtmuth pencil (Koh-i-Noor Hardtmuth a.s. is a Czech manufacturer and one of the world's largest producers and distributors of a full line of pencils, pens, and art supplies [12]). These pencils were treated with 6 M sulphuric acid for overnight. Further, we removed the pencil protective/softwood layer up to 4.2 cm and remaining graphite (4.2 cm) act as anode along with submerged protective/softwood portion (4.2 cm) into the wastewater, persisted protective/softwood layer exposed to air, where we bound the Pt/Carbon cloth (0.5 mg/cm^2) could act as cathode (Figure 1.) [1]. conspicuously, in our study didn't utilize any external power source for the agitation, circulation and air purging.

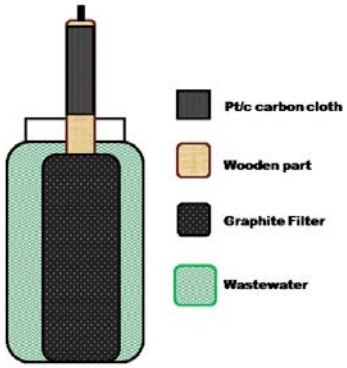

Fig 1. Schematic representation of novel softwood Microbial fuel cell

2.3 Electrochemical characterization of novel softwood microbial fuel cells

Novel softwood microbial fuel cell was characterized by linear sweep voltammetry (LSV) and electrochemical impedance spectroscopy (EIS). Liner sweep voltammetry (LSV) was performed in a Gamry Reference 600 Potentiostat/Galvanostat, run at a recommended scan rate of 0.1 mV s^{-1}, starting from the measured open circuit potential up to +50 mV [21, 22]. Impedance spectra of microbial fuel cells were obtained at the open circuit potential (E_{ocp}). The amplitude of the signal perturbation was 10 mV, scanned in the frequency range from 100 kHz to 10 mHz. Data fitting was accomplished by Z-view software [1].

2.4 Analyses

Chemical oxygen demand of the feed and MFC liquor and pH were determined according to the Standard Methods [23]. COD removal efficiency η_{COD} and coulombic efficiency η_{coul} were calculated as reported elsewhere [24]. All the experiments were duplicated.

3. Results and Discussion

Our previous report in the SMH2015, we had optimized the sulfuric acid treated pencil at 6 M would improve the power production in Pencil integrated MFCs (as standard PI-MFCs) via vertical proton hopping process. At the extension of that work, we concentrate the anodic side, by increasing the surface area of the graphite rod electrode. We placed the graphite felt as current collector in the anodic side, designated as GF-PI-MFCs. Raw high concentrated wastewater collected from our polytechnic university of Aguascalientes was used both as inoculum to form electrochemically active bacteria and also as medium to be treated. The standard PI-MFCs exhibit the maximum volumetric power density of 66.1 mW/m^3 at the maximum current density of 238.91 mA/m^3 0.270 Voltage. GF-PI-MFCs showed maximum power density of 191.6 mW/m^3 at the current density of 658.04 mA/m^3 Voltage of 0.290. Graphite felt incorporated PI-MFCs reveals the 65.49 % of improved power production than the standard PI-MFCs. This could be speculated that the increment of anodic surface area would accommodate more space to the electrochemically active microbes [ ] as a result, we could obtain the maximum power production in GF-PI-MFCs. The average COD removal efficiencies were 91.77 % and 82.65 % in the graphite felt anode and graphite anode, respectively.

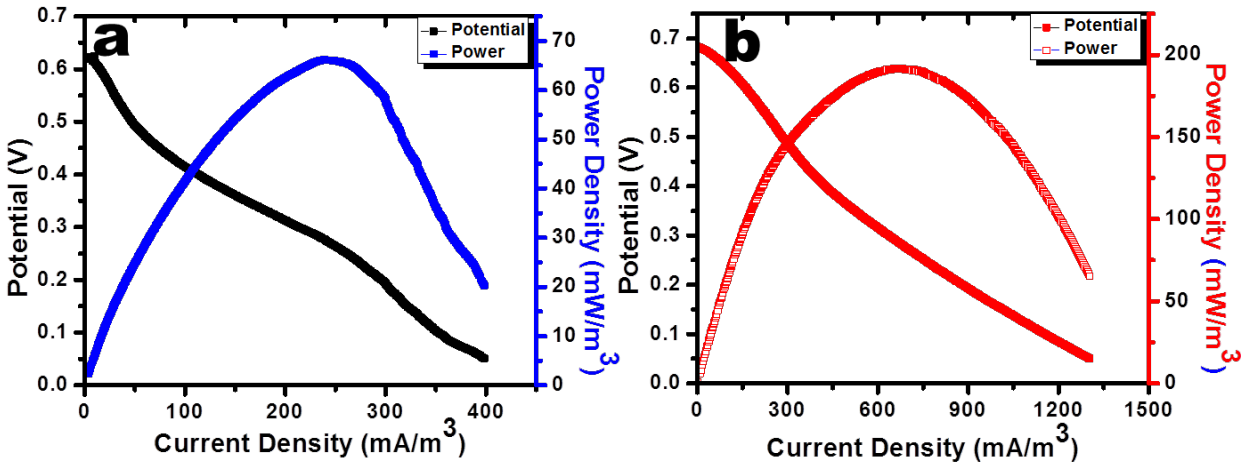

Fig. 2. Polarization curve image of pencil integrated MFCs. (a) standard pencil integrated MFC; (b) Graphite felt pencil integrated MFC.

The Tafel plots were fitted reasonably well ($R^2 \geq 0.999$) at the overpotential, where $|(F\eta)/(RT)| > 1$ [25] [Fig 3.]. The exchange current (i_0) of 1.453 µ A and 8.578 µ A were calculated for standard cell using graphite rod as anode and graphite felt as anode, respectively. The i_0 represents the exchange rate between the reactant and product states at equilibrium. Interestingly, graphite felt as anode PI-MFCs exhibited the higher value means a faster reaction rate, following a lower activation energy barrier of forward reaction, as a result of higher surface area electrode.

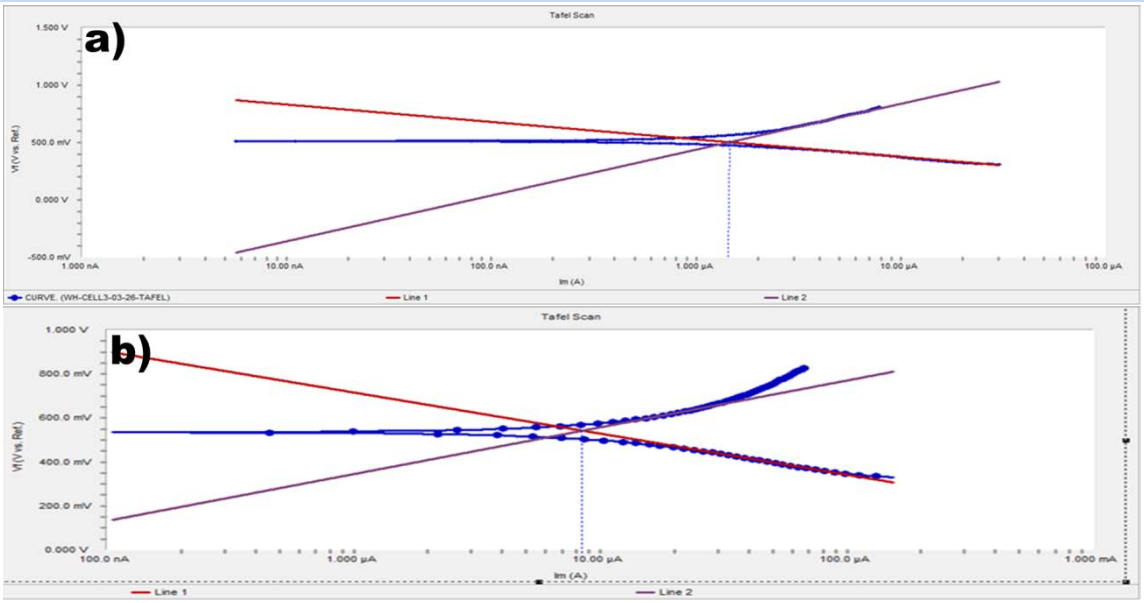

Fig. 3. Tafel plot of pencil integrated MFCs. (a) standard pencil integrated MFC; (b) Graphite felt pencil integrated MFC.

The whole cell configuration Nyquest plot was shown in Fig 4. and inset of the image explicit the equivalent circuit used to fit the model [26]. The total internal resistance is sum of anode resistance (R_a), separator resistance (R_s) and cathode resistance (R_c). Standard cell with graphite rod reveals the R_a 3000 ohms, R_s 24000 and R_c 22000. PI-MFC with graphite felt anode exhibit the 425 ohms for R_a, 5500 ohms for R_s and 1200 ohms for R_c. Moreover, the graphite felt as anode reveals the less resistance than the graphite rod. This would be an additional evidence to justify the maximum power production in high surface area anode. In the case of whole cell MFCs resistance greatly depends on the design and configuration of the MFC along with the microbial population in the anode [27] and cathodic reaction. [28, 29] realized the high surface area anode material would enhance both the electrochemical activity and electron transfer are enhanced remarkably, leading to improve the power production in MFCs [28, 29].

Later, we constructed the each three of the PI-MFCs standard cell and graphite felt connected in series to power the Digital clock.

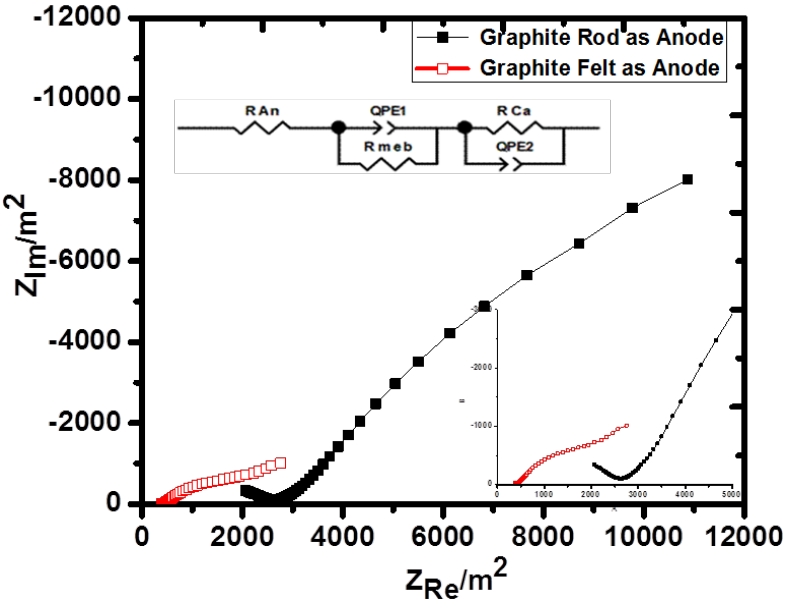

Fig. 4. Electrochemical Impedance Spectroscopy of pencil integrated MFCs. (a) standard pencil integrated MFC (GR as anode); (b) Graphite felt pencil integrated MFC (GF as anode).

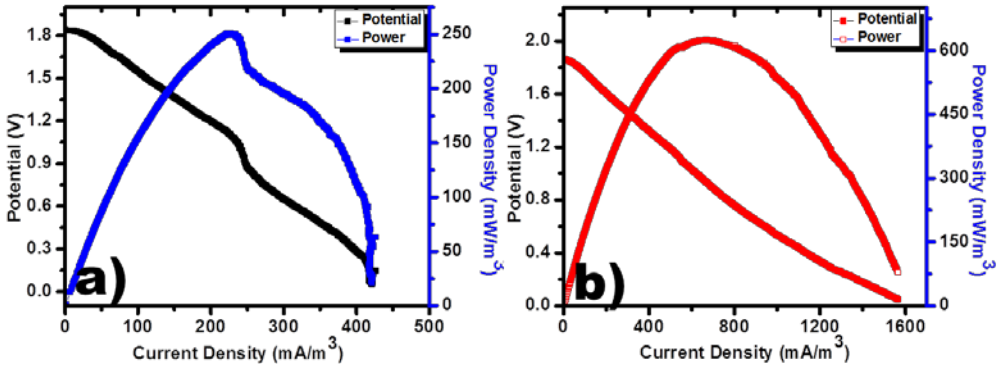

Fig. 5. Polarization curve of three PI-MFCs connected in series (a) standard pencil integrated MFC; (b) Graphite felt pencil integrated MFC.

Fig 5 shows the polarization curve of the three standard cells of PI-MFCs and three graphite felt PI-MFCs connected in series. Standard cell of PI-MFCs exhibit the maximum volumetric power density 250.93 mW/m^3 of current density 222.5 mA/m^{3}at 1.13 V. Graphite felt PI-MFCs reveals the maximum volumetric power density 624.75 mW/m^3 of current density 665.82 mA/m^3 at 0.94 V. Further, long term operation of PI-MFCs of standard cell and graphite felt were presented in Fig 6, Table 2 and 3. Graphite felt PI-MFCs demonstrate the 2.4 times higher the volumetric power density than the standard PI-MFCs. Moreover, both of the cells realized the stable power production up to 300 hrs with the COD removal of 82 % in standard cell and 91 % in graphite felt cells (Table 2 and 3).

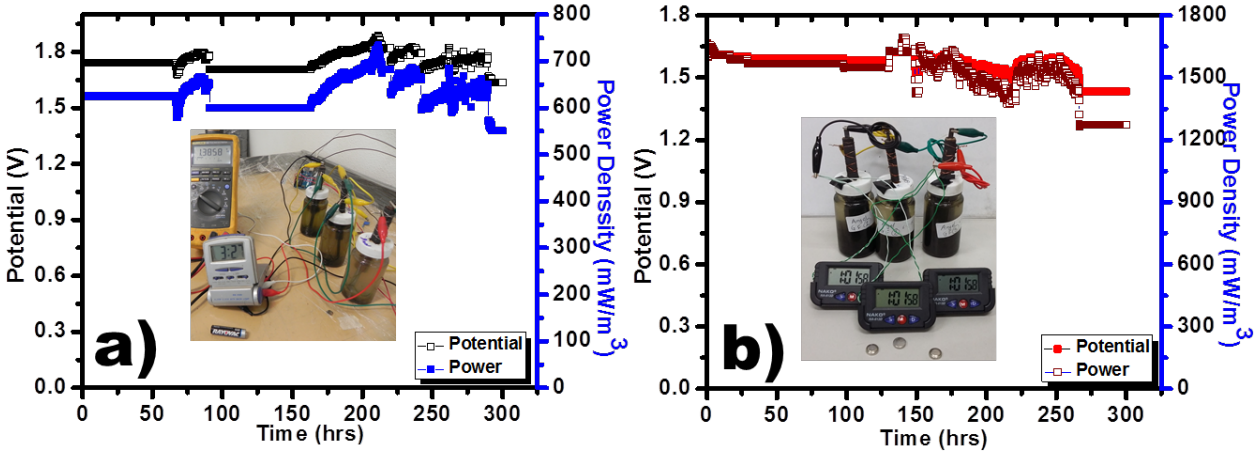

Fig. 6. Long term operation of pencil integrated MFCs with Digital clock (a) standard pencil integrated MFC; (b) Graphite felt pencil integrated MFC.

This could confirm the stability of the anodic current collector for the real time wastewater treatment process, with the interest of long term operations. Hence, this attractive feature could scale up the integrated MFCs for wastewater treatment process.

Table 1. Average parameters values of long term operation of the standard PI-MFCs with Digital clock

Parameters	GR 1	GR 2	GR 3	GR Series
P^a (mW/m^2)	42.93 ± 3.34	51.36 ± 1.56	58.95 ± 5.89	119.37 ± 5.95
$P_V{}^b$ (mW/m^3)	174.87 ± 13.6	209.2 ± 6.37	240.12 ± 24.0	629.39 ± 31.4
P^c (mW)	0.019 ± 0.0014	0.023 ± 0.0007	0.026 ± 0.0026	0.011 ± 0.0005
I (mA/m^2)	80.67 ± 3.18	88.28 ± 1.33	94.48 ± 4.61	68.28 ± 1.7
I (mA/m^3)	328.63 ± 12.95	359.57 ± 5.44	384.81 ± 18.79	360.01 ± 8.96
I^d (mA)	0.036 ± 0.0014	0.039 ± 0.0006	0.042 ± 0.002	0.0063 ± 0.00015
E^e (V)	0.53 ± 0.02	0.58 ± 0.008	0.62 ± 0.03	1.74 ± 0.04
$\eta_{COD}{}^f$ (%)	82.65	82.65	82.65	82.65
$\eta_{Coul}{}^g$ (%)	35.2	38.2	40.1	61.4

Notes: [a] surface area power density; [b] volumetric power density; [c] average power; [d] average current; [e] average potential; [f] chemical oxygen demand removal efficiency; [g] coulombic efficiency.

Table 2. Average parameters values of long term operation of the graphite felt PI-MFCs (3cells connected in series) with Digital clock.

Parameters	GF 1	GF 2	GF 3	GF Series
P^a (mW/m^2)	11.38 ± 1.11	18.09 ± 3.73	13.09 ± 2.92	35.94 ± 2.41
$P_V{}^b$ (mW/m^3)	481.38 ± 47	765.01 ± 157.78	553.37 ± 123.52	1519.37 ± 101.9
P^c (mW)	0.05 ± 0.005	0.084 ± 0.017	0.06 ± 0.013	0.023 ± 0.00154
I (mA/m^2)	22.32 ± 1.06	28.04 ± 2.78	23.84 ± 2.43	22.91 ± 0.79
I (mA/m^3)	943.74 ± 47.57	1185.38 ± 117.82	1007.9 ± 102.88	968.6 ± 33.38
I^d (mA)	0.1 ± 0.004	0.13 ± 0.017	0.11 ± 0.011	0.0143 ± 0.0005
E^e (V)	0.5 ± 0.02	0.64 ± 0.06	0.54 ± 0.05	1.56 ± 0.053
$\eta_{COD}{}^f$ (%)	91.77	91.77	91.77	91.77
$\eta_{Coul}{}^g$ (%)	46.2	55	43.7	64.45

Notes: [a] surface area power density; [b] volumetric power density; [c] average power; [d] average current; [e] average potential; [f] chemical oxygen demand removal efficiency; [g] coulombic efficiency.

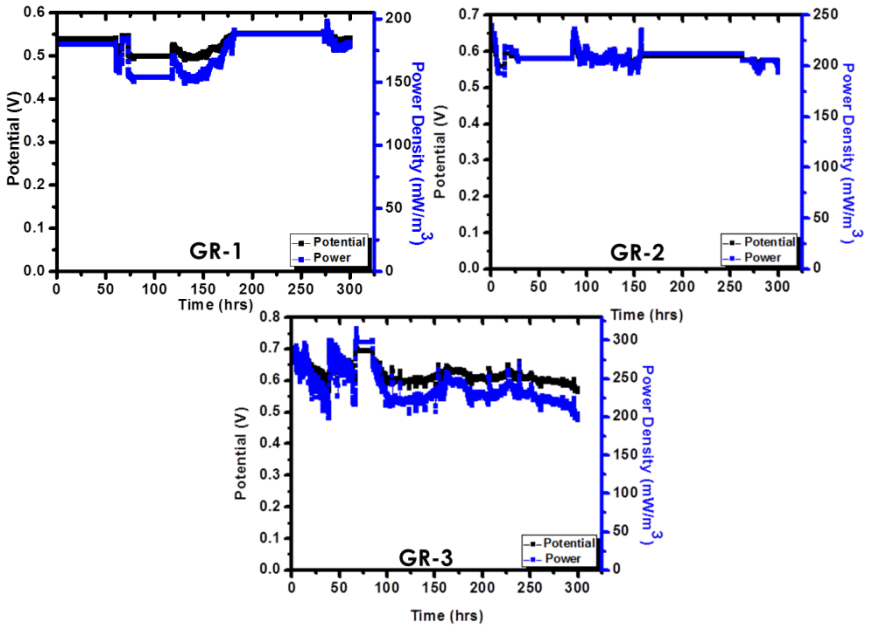

Fig. 7. Long term operation of individual standard PI-MFCs (graphite rod as anode-GR).

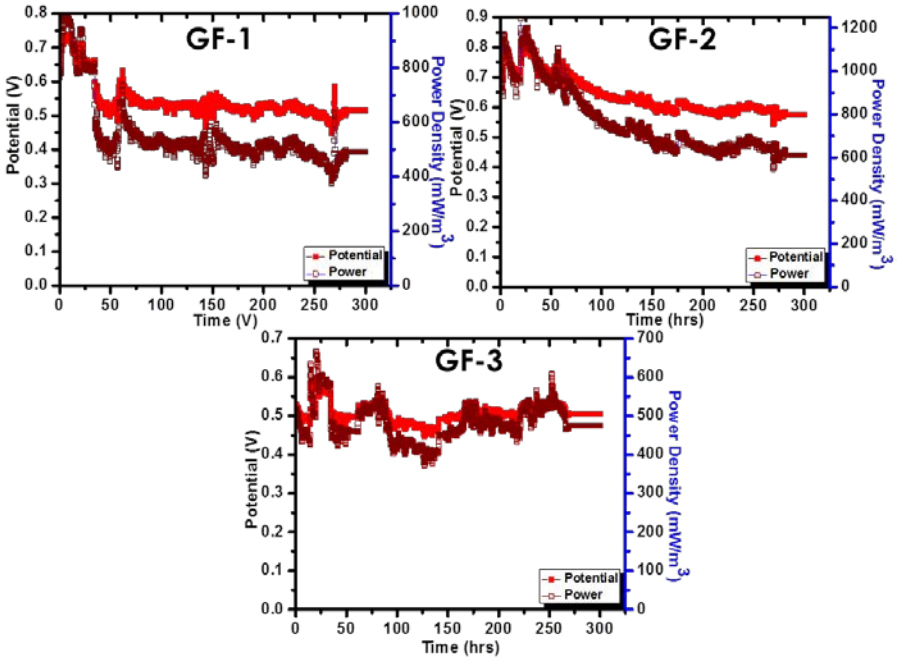

Fig. 8. Long term operation of individual Graphite felt PI-MFCs.

Harnessing the useful power from the MFCs stacks is one of the main challenges for scaling up the MFCs process, this could be avoid by the voltage reversal i.e., reversal in polarity of one or more cells and a loss of power generation. As a result of fuel starvation leading to loss of bacterial activity and internal resistance variation, it often occurs in stacked MFCs, which are connected in series and operated under fed-batch mode or during a sudden change of fuel demand [30, 31, 32] leads to the voltage reversal. Interestingly, in this study, during the long term operation of the PI-MFCs stack avoided the potential for substrate conditions at the feed for each unit, and the voltage reversal was not observed throughout the 300 hrs of operations (Fig 7 and 8 Table 1 and 2).

4. Conclusion

In our previous report, we proposed the novel microbial fuel cells (MFCs) design from pencil (SMH2014). Furthermore, we known the 6M sulfuric acid treated pencil based integrated MFCs exhibit better performance. At the continuation of that point, we have tried to improve the performance of pencil integrated MFCs (PI-MFCs) by increasing the anodic current collector surface area by adding the graphite felt as anode. Raw high concentrated wastewater was used both as inoculum to form electrochemically active bacteria and also as the medium to be treated at the anode. The maximum volumetric power density (191.6mW/m^3) was obtained in graphite felt anode, which is 65.49 % higher than that of graphite rod as anode (66.1 mW/m^3) in PI-MFCs. The Tafel plot of graphite felt anode exhibit the highest exchange current (i_o) than the standard graphite rod anode. From these results speculated that the higher surface area anode could facilitate the faster electron transfer via electrochemically active bacteria enhancing the power production. Later, we

connected the three graphite rod PI-MFCs in series and three of graphite felt PI-MFCs in series, in order to power the digital clocks. From that, graphite felt PI-MFCs exhibited the 59.8 % higher power production with the 9.93% COD removal and 4.73 % columbic efficiency than the graphite rod PI-MFCs in long term operation. These results encouraging the use of graphite felt as anode for the PI-MFCs.

Acknowledgements

The authors would like to acknowledge the fellowship from the SMH and extended our gratitude to the XV International Congress of the Mexican Hydrogen Society. KSK would like to acknowledge the funding agency of Secretaria de Educacion Pubica (SEP), Mexico for the project DSA/103.5/14/10671 and extended to Conacyt for SNI.

References

[1] Angel Rodrigo M. Ochoa., Sathish-Kumar K., Solorza-Feria O.,Tapia-Ramirez J. Novel microbial fuel cell design for raw high organic load waste water treatment. Proceeding of the International Hydrogen Congress 2014.,

[2] Sathish-Kumar K., Solorza-Feria O., Vázquez-Huerta G., Luna-Arias J., Poggi-Varaldo H.M. Electrical Stress-directed Evolution of Biocatalysts Community Sampled from A Sodic-saline Soil for Microbial Fuel Cells. Int. J. New Mat. Electrochem. Systems 2012; 15:181-186.

[3] Vázquez-Larios A.L., Solorza-Feria O., Vázquez-Huerta G., Esparza-García F., Rinderknecht-Seijas N., Poggi-Varaldo H.M. Effects of architectural changes and inoculum type on internal resistance of a microbial fuel cell designed for the Treatment of leachates from the dark hydrogenogenic Fermentation of organic solid wastes. Int. J. Hydrogen Energy 2011; 36:6199-6209.

[4] Rabaey K., Lissens G., Siciliano S.D., Verstraete W. A microbial fuel cell capable of converting glucose to electricity at high rate and efficiency. Biotechnology Letters 2003; 25(18):1531-5.

[5] Ringeisen B.R., Ray R., Little B. A miniature microbial fuel cell operating with an aerobic anode chamber. J. Power Sources 2007; 165(2): 591-7.

[6] Logan B., Cheng S., Watson V., Estadt G. Graphite fiber brush anodes for increased power production in air-cathode microbial fuel cells. Environ. Sci. Technol 2007; 41(9):3341-6.

[7] Chaudhuri S.K., Lovley D.R. Electricity generation by direct oxidation of glucose in mediatorless microbial fuel cells, Nature Biotechnology 2003; 21:1229–1232.

[8] Liu H., Cheng S., Logan B.E. Power Generation in Fed-Batch Microbial Fuel Cells as a Function of Ionic Strength, Temperature, and Reactor Configuration. Environ. Sci. Technol 2005; 39:5488-5493.

[9] Kim J.R., Min B., Logan B.E. Evaluation of procedures to acclimate a microbial fuel cell for electricity production. Appl. Microbiol. Biotechnol. 2005; 68:23-30.

[10] Zhang X., He W., Ren L., Stager J., Evans P.D., Logan B.E. COD removal characteristics of air-cathode microbial fuel cells. Biores. Technol 2015; 176:23-31.

[11] Kamaraj S.-K., Romano S.M., Moreno V.C., Poggi-Varaldo H.M., Solorza-Feria O. Use of Novel Reinforced Cation Exchange Membranes for Microbial Fuel Cells. Electrochimica Acta 2015; 176:555-566.

[12] Li W.-W., Yu H.-Q., He Z. Towards sustainable wastewater treatment by using microbial fuel cells-centered technologies. Energy Environ. Sci. 2014; 7 (3):911–924.

[13] Wang H., Ren Z.J. A comprehensive review of microbial electrochemical systems as a platform technology. Biotechnol. Adv. 2013; 31:1796–1807.

[14] Zhuang L., Zhao Y., Zhou S.G., Yuan Y., Yuan H., Chen Y. Scalable microbial fuel cell (MFC) stack for continuous real wastewater treatment. Bioresour. Technol. 2012; 106:82–88.

[15] Forrestal C., Huang Z., Ren Z.J. Percarbonate as a naturally buffering catholyte for microbial fuel cells. Bioresour. Technol. 2014; 172:429–432.

[16] Zhang F., Saito T., Cheng S., Hickner M., Logan B. Microbial fuel cell cathodes with poly (dimethylsiloxane) diffusion layers constructed around stainless steel mesh current collectors. Environ. Sci. Technol. 2010; 44:1490–1495
[17] Ieropoulos I., Greenman J., Melhuish C. Microbial fuel cells based on carbon veil electrodes: Stack configuration and scalability. Int. J. Energy Research 2008; 32:1228-1240.
[18] Rader G.K., Logan B.E. Multi-electrode continuous flow microbial electrolysis cell for biogas production from acetate. Int. J. Hydrogen Energy 2010; 35:8848-8854.
[19] Ahn Y., Logan B. A multi-electrode continuous flow microbial fuel cell with separator electrode assembly design. Applied Microbiology and Biotechnology. 2012; 93:2241-2248.
[20] Gálvez A., Greenman J., Ieropoulos I. Landfill leachate treatment with microbial fuel cells; scale-up through plurality. Bioresource Technology 2009; 100:5085-5091.
[21] Velasquez-Orta S.B., Curtis T.P., Logan B.E. Energy from algae using microbial fuel cells. Biotechnol Bioeng 2009; 103(6):1068-76.
[22] Watson V.J., Logan B.E. Analysis of polarization methods for elimination of power overshoot in microbial fuel cells. Electrochem Commun 2011; 13(1):54-6.
[23] APHA. Standard methods for examination of water and wastewater. 17th ed. Washington DC: American Public Health Association; 1981.
[24] Fornero J.J., Rosenbaum M., Angenent L.T. Electric Power Generation from Municipal, Food, and Animal Wastewaters Using Microbial Fuel Cells: Electroanalysis 2010; 22:832-843.
[25] Bagotsky V.S., Fundamentals of Electrochemistry, in: Polarization of Electrodes John Wiley and Sons, 2006; 79-99.
[26]Lepage G., Albernaz F.O., Perrier G., Merlin G. Characterization of a microbial fuel cell with reticulated carbon foam electrodes: Bioresour Technol. 2012; 124:199-207.
[27] Logan BE., Regan JM. Microbial fuel cells-challenges and applications: Environ Sci Technol 2006; 40: 5172-5180.
[28] He Y.-R., Xiao X., Li W.-W., Sheng G.-P., Yan F.-F., Yu H.-Q., Yuan H., Wu L.-J. Enhanced electricity production from microbial fuel cells with plasma-modified carbon paper anode: Physical Chemistry Chemical Physics 2012; 14:9966-9971.
[29] Zhao Y., Watanabe K., Hashimoto K. Hierarchical micro/nano structures of carbon composites as anodes for microbial fuel cells: Physical Chemistry Chemical Physics 2011; 13:15016-15021.
[30] Aelterman P., Rabaey K., Pham T.H., Boon N., Verstraete W. Continuous electricity generation at high voltages and currents using stacked microbial fuel cells: Environ. Sci. Technol. 2006; 39:3388–3394.
[31] Ieropoulos I., Greenman J., Melhuish C. Microbial fuel cell based on carbon veil electrodes: stack configuration and scalability. Int. J. Energy Res. 2008; 32:1228–1240.
[32] Oh, S.E., Logan, B.E., Voltage reversal during microbial fuel cell stack operation. J. Power Sources 2007; 167:11–17.

Chapter 5.5. Use of Clay tube as integrated Microbial fuel cell for wastewater treatment

Alberto de Jesús Robledo Ruiz[a]; K. Sathish-Kumar[a,]; O. Solorza-Feria[b]; J. Tapia-Ramírez[c]

[a]Universidad Politécnica de Aguascalientes, Ingeniería en Energía Calle Paseo San Gerardo No. 207. Fracc. San Gerardo. Aguascalientes, Ags. México, 20342.
[b]Centro de Investigación y de Estudios Avanzados del Instituto Politécnico Nacional, Departamento de Química, Av. Instituto Politécnico Nacional 2508, Col. San Pedro Zacatenco, Delegación Gustavo A. Madero, México D.F. 07360.
[c]Centro de Investigación y de Estudios Avanzados del Instituto Politécnico Nacional, Departamento de Genéticas y Biología Molecular

ABSTRACT

Simplified Microbial fuel cells (MFCs) design attracts the attention of researcher, in order to scale up the process. In this context, we have proposed the simplified MFCs design from clay tube based integrated MFCs, which utilizes the real wastewater collected from the polytechnic university of Aguascalientes served as waste tobe treated as well as biocatalyst. Clay materials are commonly phyllosilicates or layer silicates.It's cation exchange capabilities, low permeability, and long term structural stability triggers the interest. Moreover, partially submerged clay tube into the water would arise on the lateral direction through capilary force. We could exploite this process along with proton hopping facilitate the proton mobility towards vertical direction on the clay tube. Remarkably, we could optimize the level of submerged clay tube into wastewate. Since we performed the two kinds of experiments. First, we could submerged the 2 part of clay tube into the wastewater and 1 part of the clay tube exposed to the air (2:1 ratio). Later experiment, we performed the submerged 3 part of the clay tube and 2 part of clay exposed to air (3:2). From that 3: 2 ratio integrated clay tube MFCs exhibited highest power density 17.54 mW/m^3, currend density 55.97 mA/m^3 at 0.313 V potential. Moreover, it exhibit the higest COD removal of 91 %. Further, we connected the three 3:2 ratio integrated clay tube MFCs in series and powered the Digital Clock. Hence, Our simplified MFCs design could possible scale up the process and more importantly without using any additional input energy (purging, agitation, temperature, circulation and etc…) [Patent Pending].

Keywords: Clay, Proton transfer, Wastewater, Proton hopping

1. Introduction

The present wastewater treatment process requires considerably high energy demand. The seven most important wastewater treatment plants (WTP) in the state of

---

* Corresponding author: Kamaraj Sathish-Kumar, +01 (449) 442 1400 ext: sathish.bot@gmail.com,sathish-kumar.kamaraj@upa.edu.mx

Aguascalientes, Mexico, treated 1948 Ls(-1), [1]. A significant amount of this municipal energy was spending to the wastewater treatment facilities. With pumps, motors, and other equipment operating 24 hours a day, seven days a week, water and wastewater facilities can be among the largest consumers of energy in a community. Electricity use accounts for 25–40 percent of the operating budgets for wastewater utilities. Subsequently, the need for an efficient source of inexpensive energy has driven technological advancements in the area of utilizing organic matter as an energy source. Plentiful amounts of energy can be found in organic matter such as carbohydrates, which are found in municipal waste. Municipal waste can constitute as much as 80 percent organic materials. Energetic valorization of organic matter has been accomplished by conversion of the organic matter for the production of biofuels, such as ethanol, and by conversion to hydrogen; however, alternate ways to extract energy directly out of biomass exist, that technology called as Microbial fuel cells (MFCs). A microbial fuel cell is a device that directly utilizes the metabolic output of microbial activity to produce electrical power. This electrical energy is produced by coupling the oxidation of substrates (organic or inorganic) by the microbe (biocatalyst) to the chemical reduction of an oxidant. These biological fuel cells have received considerable attention because they can provide access to an economically feasible “green” energy source from the wastewater, meanwhile to produce the clean water.

In MFCs, the Nafion®117 membranes is one of the most commonly used PEM, though a number of problems associated with Nafion®117 arise, such as oxygen leakage from cathode to anode, substrate loss, cation (rather than protons) transport, and biofouling. Among these issues, one of the main problems is the oxygen leakage into the anode chamber, which can either inhibit the growth of obligate anaerobes or facilitate aerobic respiration by facultative bacteria, thus resulting in lower energy recovery, due to the substrate losses [2, 3, 4].

To reduce the capital cost of MFCs, it is an urgent need to develop economical electrodes and produce cheaper separator material, which is effective in proton transfer, offer negligible substrate loss from anodic chamber, offer minimum oxygen diffusion and resist fouling to support long term stable wastewater treatment. The major disadvantage of using Nafion membrane in MFC is high cost and low stability as it contains sulfonic acid groups, which get easily combined with ammonia present in wastewater [5]. For enhancing the MFCs performance, an ideal material would form both the structural frame and the means for ion exchange, and in such a case, the porous ceramic material appears to be a highly promising separator. A porous ceramic material works as a separator in an electrochemical system because it enables separation of anolyte and catholyte, whilst permitting mobility of ions in solution [6], which in turn facilitates electron flow through an external circuit. Park and Zeikus was first used the ceramics in MFCs [7]. They utilized a porcelain septum separator. Later, Seo et al. prepared a porous porcelain membrane and more recently Behera et al. [8, 9] adapted and successfully operated an earthen pot as MFC using the reactor wall as separator.

The objective of this study is to design and optimize the vertical clay tube integrated MFCs for wastewater treatment. Furthermore, we powered the LED and Digital clock via series connection of optimized clay tube integrated MFCs.

2. Materials and Methods

2.1 Collection of wastewater

Wastewater was collected from a Universidad Politécnica de Aguascalientes (UPA) and stored in refrigerator at 4°C. The wastewater served as inoculum in anode and also as medium to be treated.

2.2 Construction of clay tube integrated MFCs

We procured the clay soil from the local merchant of Aguascalientes, Mexico, then prepared the tube and backed inside the furnace at 700° C for 2 hrs. It's ion exchange capabilities and long term structural stability triggers an interest, to exploit as separator. Moreover, partially submerged clay tube into the water would arise on the lateral direction through capillary force. First phase of the MFCs optimization, we could find the optimal length insertion of clay tube into wastewater, where we placed the graphite felt act as anode and rest of the tube on the top convert with catalyst to facilitate the oxygen reduction reaction. We varied the insertion of tube by submerge the 2 part of clay tube into the wastewater and 1 part of the clay tube exposed to the air (2:1 ratio). Later, we performed the submerged 3 part of the clay tube and 2 part of clay exposed to air (3:2). From that we selected the maximum power produced clay tube for the second stage of optimization process, where we proposed the used battery catalyst as cathode, in order to reduce the cost of the MFCs. In all the case, we fixed the thickness of tube (3 mm), Volume of the container (82 ml), anode (0.021/m^2) and cathode (0.014/m^2) area. At final, we developed the prototype to power the LED and digital clock utilize the wastewater of polytechnic university of Aguascalientes.

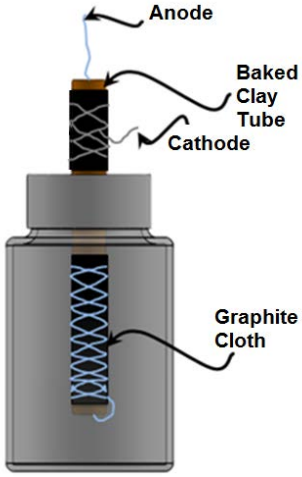

Fig 1. Schematic representation of the clay tube integrated MFCs

2.3 Electrochemical characterization of clay tube microbial fuel cells

Clay tube microbial fuel cell was characterized by linear sweep voltammetry (LSV) and electrochemical impedance spectroscopy (EIS). Liner sweep voltammetry (LSV) was performed in a Gamry Reference 1000 Potentiostat/Galvanostat, run at a recommended scan rate of 0.1 mV s^{-1}, starting from the measured open circuit potential up to +50 mV [10,

11]. Impedance spectra of microbial fuel cells were obtained at the open circuit potential (E_{ocp}). The amplitude of the signal perturbation was 10 mV, scanned in the frequency range from 100 kHz to 10 mHz. Data fitting was accomplished by Z-view software [12].

2.4 Analyses

Chemical oxygen demand of the feed and MFC liquor and pH were determined according to the Standard Methods [13]. COD removal efficiency η_{COD} and coulombic efficiency η_{coul} were calculated as reported elsewhere [14]. All the experiments were duplicated.

3. Results and Discussion

In a first optimization stage of clay tube integrated MFCs (CT-MFCs), we focus the optimal submerged level of clay tube into the wastewater. Generally, submerge of clay tube into water, it could arise the water content on the lateral direction through capillary force/water coherence. Our previous report, exploited the proton hopping along with the vertical arise of water content [15] for the air cathodic MFCs . Since, we can employ that concept in clay tube, to design and construction of simplified integrated MFCs for raw wastewater applications.

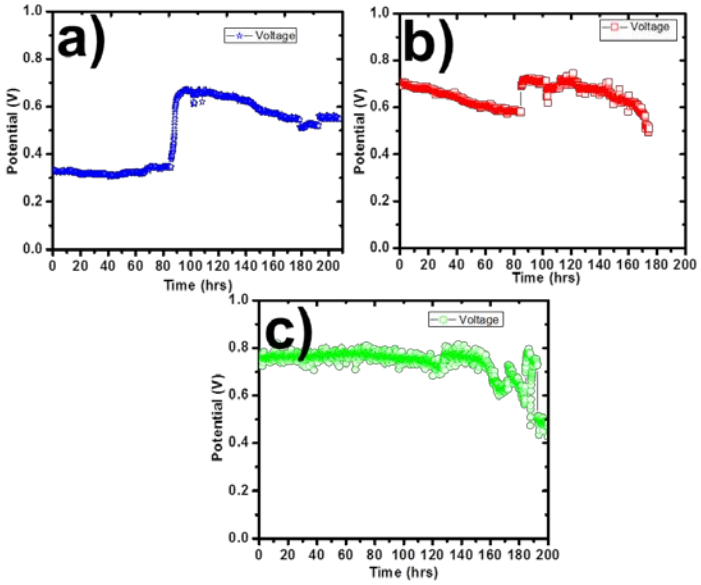

Fig. 2. Open Circuit Potential of the Clay tube Integrated MFCs: (a) 2:1 ratio Cell (b)3:2 ratio cell (c) 3:2 ratio cell with used battery catalyst

As mentioned detailed in materials and method section, we proposed two ration of submerge (2:1 and 3:2) CT-MFCs. Open circuit potential (OCP) of CT-MFCs 2:1 and 3:2 showed in Fig 1. Which can infers the stability and time to obtain the maximum open circuit potential of MFCs. Further we can characterize the electrochemical behavior of MFCs at the Maximum OCP. During the initial time interval, CT-MFCs of 2:1 exhibit the low OCP than 3:2 CT-MFC, more later it would attain the maximum OCP. But in the case of 3:2 CT-MFC attained the maximum OCP in the early stage of operation and more stable

along the operation. CT-MFCs polarization curves were presented in Fig 3. CT-MFC of 2:1 reveals the maximum volumetric power density of 17.54 mW/m^3 at 0.313 V. The volumetric power produced from the 3:2 CT-MFC was nearly 8 times (138.52 mW/m^3 at 0.382 V) higher than the 2:1 CT-MFCs. Which could be either shortage of water arise or strong water arise towards the cathodic chamber. Therefore, both of processes are hindering the cathodic reaction by carrying the insufficient proton hopping or strong water blocks the oxygen reduction reaction. Possibly, 3:2 CT-MFCs would facilitate the optimal proton hopping process facilitate the oxygen reduction reaction in the air cathode, as a result of this could exhibit the higher power. Clayware ceramic separator as membrane to reduce fabrication cost of MFCs and obtained a maximum power density of 16.8 W/m^3 by Behera et al. (2010).However, they used the stainless steel mesh as anode and more importantly they used the KMnO4 as cathodic electrolyte [9].Moreover, we used the wastewater as sole organic source with sustainable air cathode makes attractive.

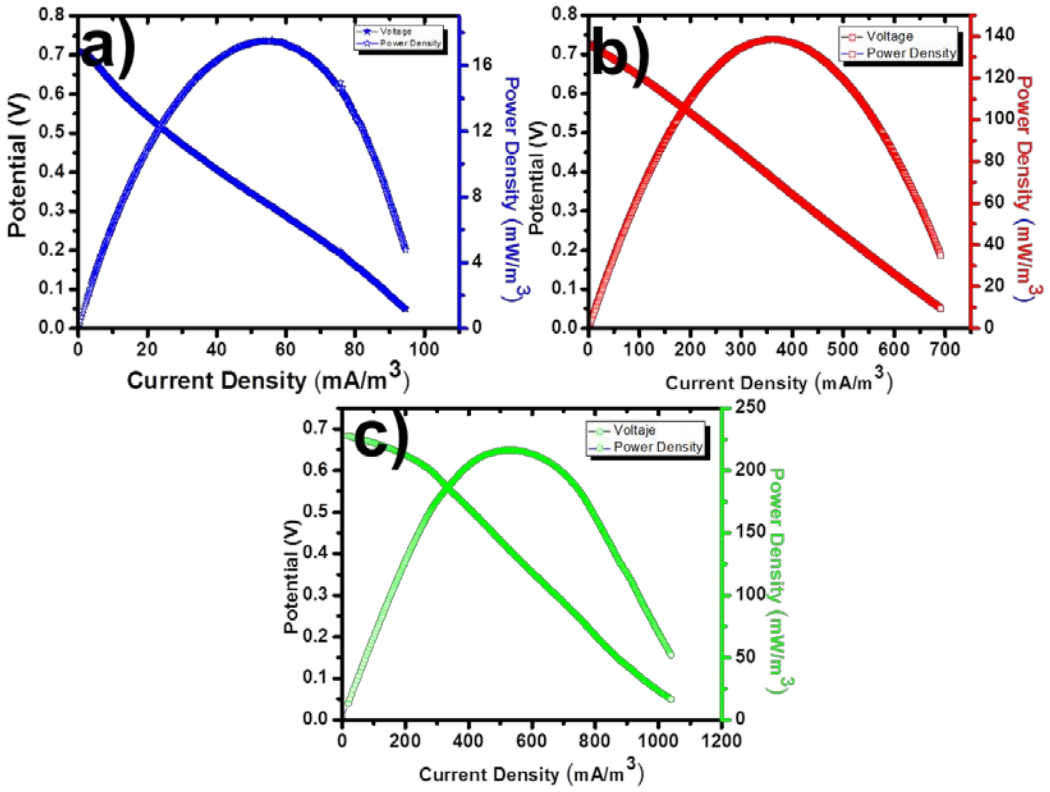

Fig. 3. Polarization curve of the clay tube integrated MDCs: (a) 2:1 ratio Cell (b) 3:2 ratio cell (c) 3:2 ratio cell with used battery catalyst.

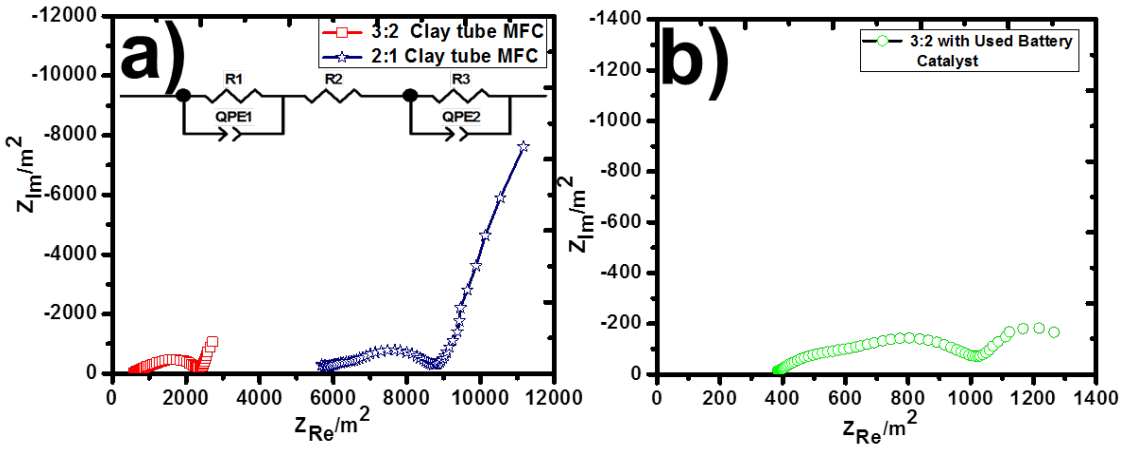

Fig. 4. Electrochemical Impedance Spectroscopy of the clay tube integrated MFCs: (a) 2:1 ratio Cell and 3:2 ratio cell (b) 3:2 ratio cell with used battery as cathode catalyst.

Electrochemical impedance spectroscopy of the whole cell CT-MFCs showed in Fig 4. From the equivalent circuit, R1, R2 and R3 represent the anode, separator, and cathode resistance, respectively (Fig 4 inset). CT-MFC 2:1 represents the total internal resistance of 12600 Ω from that anode (4000 Ω), separator (3900 Ω) and cathode (4700 Ω). Internal resistance of 3:2 CT-MFC shows the 8375 Ω, anode, separator and cathode are 5800 Ω, 525 Ω, and 2050 Ω respectively. Excitingly, 3:2 CT-MFC showed the less separator resistance, which would infers the proton hopping facilitate to increase the ionic conductivity as a result fewer resistance. Moreover, this can reflex in the enhancement of power production in 3:2 CT-MFCs (Fig 3.).

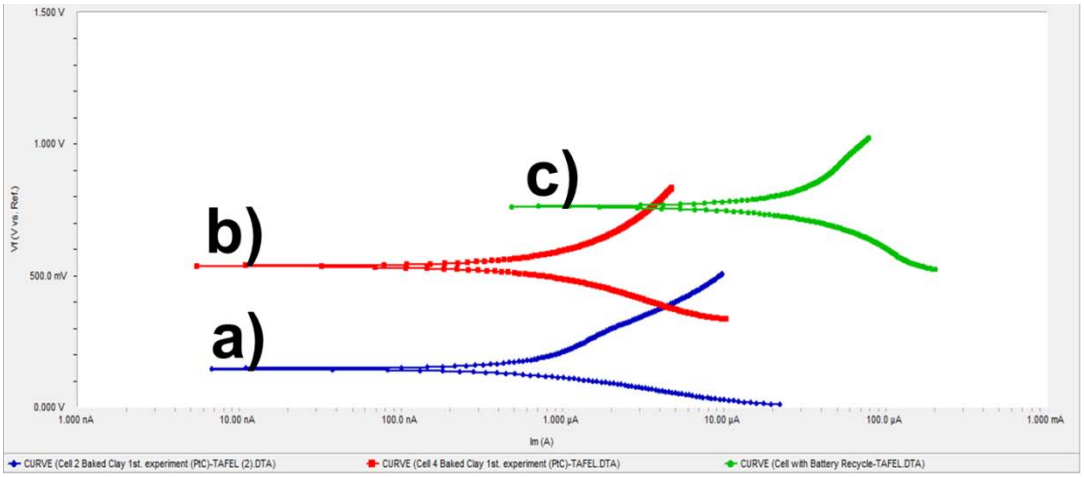

Fig. 5. Tafel Plot of (a) 2:1 ratio Cell (b) 3:2 ratio cell (c) 3:2 ratio cell with used battery material as cathode catalyst

Further, Tafel plot for CT-MFCs shown in fig 5. CT-MFC of 3:2 display the high exchange current (i_0-1.09 µA) than the 2:1 CT-MFC (i_0-0.783 µA). The exchange current also justifies the exchange rate between the reactant and product states at equilibrium in 3:2 CT-MFC could enhance the performance of the MFCs [16].

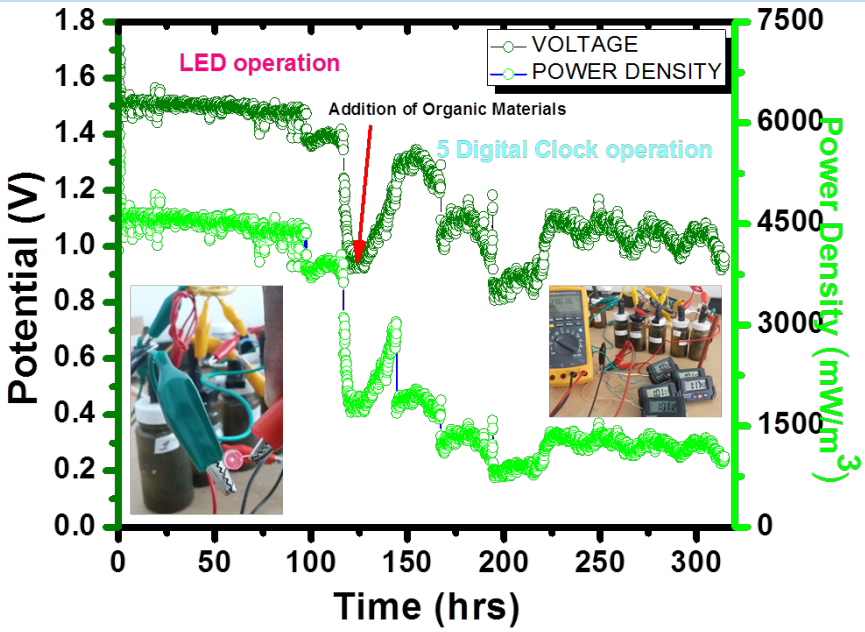

Fig. 6. Batch Operation of 3:2 MFCs used battery material as cathode powered LED and Digital clock (inset)

Second stages of optimization focus the cathode, where we applied the used battery material as cathode in 3:2 CT-MFC instant of Pt/carbon, in order to make the sustainable power production in MFCs. This cell attained the maximum OCP in the early stage of operation and more stable along the long term operation, which resembles the Pt/carbon as cathode in 3:2 CT-MFC (Fig 2.).

The used battery material as cathode reveals the maximum volumetric power density of 216.22 mW/m^3 and 525.14 mA/m^3 of Current density at 0.412 V. This performance is slightly higher than the Pt/carbon cathode of 3:2 CT-MFC performance (Fig 3). Further, it exhibited the very less internal resistance of (1740 Ω) and significantly reduce the separator resistance (375 Ω), in terms fewer resistance in cathode (470 Ω). This could be due to the enhanced oxygen reduction reaction at the air cathode, facilitate the higher power production in used battery material as cathode (Fig 4). Furthermore, the higher current exchange (i_0) of 21.60 µA can facilitate to obtain the higher power density in MFC (Fig 5.).

Final stage, we construct the five used battery cathode 3:2 CT-MFCs in series connection in order to develop prototype energize with LED and five digital clocks during the batch operation. Their performances are in Table 1 (Fig 6.). During the LED operation, average potential of 1.39 V produced and maintained constantly 120 hrs, later due to the depletion of organic material the potential reduces. After the 125 hrs, addition of wastewater again the potential suit-up and reaches the average potential of 1.06 powered five digital clocks. Interestingly, second batch operation columbic efficiency slightly improving that could confirm the presence of effective electrochemically active bacterium [17].

Table 1. Batch operation average parameters values of prototype energize with LED and Digital clocks.

Parameters	LED Operation	Five Digital Clocks Operation
P^a (mW/m^2)	186.17 ± 43.37	60.50 ± 14.1
P_V [b] (mW/m^3)	2958.49 ± 6.23	1289.81 ± 30.9
I (mA/m^2)	131.43 ± 17.26	56.26 ± 6.5
I (mA/m^3)	2088.66 ± 27.34	1199.31 ± 13.72
E [c]	1.39 ± 0.18	1.06 ± 0.12
η_{COD} [d] (%)	88.27%	77.6%
η_{Coul} [e] (%)	31.5%	32.5%

Notes: [a] surface area power density; [b] volumetric power density; [c] average potential; [d] chemical oxygen demand removal efficiency; [e] coulombic efficiency.

Clay materials as membranes have long life spans in comparison to electrolytic cells [18] and water filtration [19]. Here in, we report the long term batch operation of CT-MFCs prototype directly energize the LED and digital clocks (5 nos.). This could particularly interesting in term of extended longevity and self-sustainability of MFC systems operating in rural areas. Moreover, the commercial high cost and less porous structures such as Nafion, this can have a detrimental effect over time [20], but in the case of clay ceramic material it might benefit for long term operation, structural stability and easy handling would be an attractive feature.

4. Conclusion

We have proposed the simplified MFCs design from CT-MFCs, which utilizes the real wastewater collected from the polytechnic university of Aguascalientes served as waste to be treated as well as biocatalyst. Clay materials are commonly phyllosilicates and their ion exchange capabilities, low permeability, and long term structural stability triggers an interest. Moreover, partially submerged clay tube into the water would arise on the lateral direction through capillary force/water coherence. We could exploited this process along with proton hopping facilitate the proton mobility towards vertical direction, where reduction of oxygen in the air occurs, with the aid of electrocatalysts. In a first optimization stage of CT-MFCs, we focus the optimal submerged level of clay tube into the wastewater. Since, we performed the two kinds of experiments. First, we could submerge the 2 part of clay tube into the wastewater and 1 part of the clay tube exposed to the air (2:1 ratio). Later experiment, we performed the submerged 3 part of the clay tube and 2 part of clay exposed

to air (3:2). From that the maximum volumetric power was registered in 3:2 CT-MFC. This was nearly 8 times (138.52 mW/m^3 at 0.382 V) higher than the 2:1 CT-MFCs. Further, analysis from the EIS and Tafel plot also confirm the higher power production by the less internal resistance especially in separator and high current exchange (i_0) value. Second stages of optimization focus the cathode, where we applied the used battery material as cathode in 3:2 CT-MFC instant of Pt/carbon. The used battery material as cathode reveals the maximum volumetric power density of 216.22 mW/m^3 and 525.14 mA/m^3 of Current density at 0.412 V. This performance is slightly higher than the Pt/carbon cathode of 3:2 CT-MFC performance. At the final stage, we developed the prototype energize the LED and five digital clocks in a batch operation by connected the five used battery material as cathode 3:2 CT-MFCs in series. Our simplified MFCs design could possible scale up the process, more importantly without using any additional input energy and easy handling.

Acknowledgements

The authors would like to acknowledge the fellowship from the SMH and extended our gratitude to the XV International Congress of the Mexican Hydrogen Society. KSK would like to acknowledge the funding agency of Secretaria de Educacion Pubica (SEP), Mexico for the project DSA/103.5/14/10671 and extended to Conacyt for SNI. We kindly acknowledge the clay soil gift from the Sr. Saul.

References

[1] Torres-Guzmán F., Avelar-González F.J., Rico-Martínez R. An assessment of chemical and physical parameters, several contaminants including metals, and toxicity in the seven major wastewater treatment plants in the state of Aguascalientes, Mexico. Journal of Environmental Science and Health, Part A 2010; 45:2-13.

[2] Zhang X., He W., Ren L., Stager J., Evans P.D., Logan B.E. COD removal characteristics of air-cathode microbial fuel cells. Biores. Technol 2015; 176: 23-31.

[3] Mauritz K.A., Moore RB. State of Understanding of Nafion. Chem. Rev 2004; 104: 4535-4585.

[4] Rozendal R.A., Hamelers H.V.M., Buisman C.J.N. Effects of membrane cation transport on pH and microbial fuel cell performance. Environ Sci Technol. 2006; 40: 5206-5211.

[5] Rabaey K., Lissens G., Verstraete W. Microbial fuel cells: performances and perspectives. Biofuels for fuel cells: renewable energy from biomass fermentation. IWA publishing, UK, pp. 2005; 377–399.

[6] Cai Z. Characterisation of electrochemically activated solutions for use in environmental remediation. PhD thesis, University of the West of England, Bristol. 2005.

[7] Park D.H., Zeikus J.G. Improved fuel cell and electrode designs for producing electricity from microbial degradation. Biotechnol Bioeng 2003; 81:348–355.

[8] Seo H.N., Lee W.J., Hwang T.S., Park D.H. Electricity generation coupled with wastewater treatment using a microbial fuel cell composed of a modified cathode with a ceramic membrane and cellulose acetate film. J Microbiol Biotechnol 2009; 19:1019–1027.

[9] Behera M., Jana P.S., Ghangrekar M.M. Performance evaluation of low cost microbial fuel cell fabricated using earthen pot with biotic and abiotic cathode. Bioresour Technol 2010; 101:1183–1189.

[10] Velasquez-Orta S.B., Curtis T.P., Logan B.E. Energy from algae using microbial fuel cells. Biotechnol Bioeng 2009;103(6): 1068-76.

[11] Watson V.J., Logan B.E. Analysis of polarization methods for elimination of power overshoot in microbial fuel cells. Electrochem Commun 2011;13(1): 54-6.

[12] Sathish-Kumar K., Solorza-Feria O., Vázquez-Huerta G., Luna-Arias J., Poggi-Varaldo H.M. Electrical Stress-directed Evolution of Biocatalysts Community Sampled from A Sodic-saline Soil for Microbial Fuel Cells. Journal of New Materials for Electrochemical Systems 2012;15:181-186.

[13] APHA. Standard methods for examination of water and wastewater. 17th ed. Washington DC: American Public Health Association; 1981.
[14] Fornero J.J., Rosenbaum M., Angenent L.T. Electric Power Generation from Municipal, Food, and Animal Wastewaters Using Microbial Fuel Cells. Electroanalysis 2010;22:832-843.
[15] Montes-Ochoa A.R., Sathish-Kumar K., Solorza-Feria O., Tapia-Ramirez J., Novel microbial fuel cell design for raw high organic load wastewater treatment. Proceeding of the International Hydrogen Congress 2014.
[16] Karthikeyan R., Sathish-Kumar K., Murugesan M., Berchmans S., and Yegnaraman V. Bioelectrocatalysis of Acetobacter Aceti and Gluconobacter Roseus for Current Generation. Environmental science & technology 43, 2009; 22:8684-89.
[17] Kamaraj S.K., Romano S.M., Moreno V.C., Poggi-Varaldo H.M., Solorza-Feria O. Use of Novel Reinforced Cation Exchange Membranes for Microbial Fuel Cells. Electrochimica Acta 2015; 176:555-566.
[18] Cai Z. Characterisation of electrochemically activated solutions for use in environmental remediation. PhD thesis, University of the West of England, Bristol 2005.
[19] Guerra K., Pellegrino J., Drewes J.E. Impact of operating conditions on permeate flux and process economics for cross flow ceramic membrane ultrafiltration of surface water. Sep Purif Technol 2012; 87:47–53.
[20] Chae K.J., Choi M., Ajayi F.F., Park W., Chang I.S., Kim I.S. Mass transport through a proton exchange membrane (Nafion) in microbial fuel cells. Energy Fuel 2008; 22:169–176.

Chapter 5.6. Instant disposable microbial-battery from paper cup for electronic applications

María Catalina Vega Reyes[a]; Angel Rodrigo M. Ochoa[a]; K. Sathish-Kumar[a,*]; O. Solorza-Feria[b]; J. Tapia-Ramírez[c]

[a]Universidad Politécnica de Aguascalientes, Ingeniería en Energía Calle Paseo San Gerardo No. 207. Fracc. San Gerardo. Aguascalientes, Ags. México, 20342.
[b]Centro de Investigación y de Estudios Avanzados del Instituto Politécnico Nacional, Departamento de Química, Av. Instituto Politécnico Nacional 2508, Col. San Pedro Zacatenco, Delegación Gustavo A. Madero, México D.F. 07360.
[c]Centro de Investigación y de Estudios Avanzados del Instituto Politécnico Nacional, Departamento de Genéticas y Biología Molecular

ABSTRACT

Herein, we present a paper cup based integrated microbial fuel cell (PC-MFC) for instant power production. We placed the graphite felt electrode to the inside of the paper cup that act as a anode. Raw high concentrated wastewaters collected from the Polytechnic University of Aguascalientes was used both as inoculum to form electrochemically active bacteria and the medium to be treated. These wastewater poured into paper cup. Outer portion of the paper cup was tied with Pt/Carbon cloth exposed to air as cathode. This MFC exhibited the maximum power density 18.15±5.19 mW/m^3 and current density 82.64±48.60 mA/m^3 at 0.22 V. Further, we serially connected the two instant PC-MFCs to power the digital clock. This serially connected MFCs were showed the average volumetric power density of 318.75±149.7 mW/m^3 at 1.164±0.21V during the 550 hrs of operation. Individual PC-MFC-1 and PC-MFC-2 were revelaed the average volumetric power density of 0.460±0.14 mW/m^3 and 0.513±0.31 mW/m^3 repectively. Moreover, PC-MFC-1 and PC-MFC-2 exhibit the COD removal of 33.66 % and 33.84 %. This PC-MFCs has the advanges of ease of use for the small electronics applications and high portabililty (Patent pending).

Keywords: Bio-battery, paper cup, Wastewater, Graphite felt

1. Introduction

Development of energy resource is an important for the survival and progress of human society. Due to the constant increase of the energy demand and the consequential

---

* Author for correspondence: Kamaraj Sathish-Kumar, +01 (449) 442 1400 sathish.bot@gmail.com,sathish-kumar.kamaraj@upa.edu.mx

environmental problems, the need to clean, sustainable energy sources have been receiving considerable attention. One of the promising fields for the alternative green energy technologies that utilize the microbial consumption of organic materials direct generation of electricity by the name of Microbial fuel cells (MFCs)[1, 2]. MFCs have attracted the considerable interest of many of the researcher's, due to numerous applications, including wastewater treatment[3], environmental monitoring power sources[4], desalination [5], biogas production [6] and bioremediation [7]. There have been done many works to improve MFCs performance by exploring the carbon sources [8], optimum operating conditions [9], device configurations and engineering of electrode [10, 11] and separators [1].

Although many of the researchers successfully demonstrated substantial increase in power density and energy efficiency, but the MFCs performance is inadequate for potential applications[2, 12]. In their present form, MFCs are not a good alternative for conventional energy technologies. The complexity of MFCs makes it difficult to improve its performance. So far, almost most of the researchers on MFCs are still focused on the structure or material option of the microbial fuel cell itself, to realize the portable application of small electronics[13]. At this point, usage of the cost effective materials have considerable attention for sustainable power production. One of the most abundant materials in the world is cellulose. The cellulose-based material is still common place in everyday life in the form of paper and waste is still an issue. Paper has the following advantage for use in Bioelectrochemical systems (i) Ubiquitous nature with cost effective; (ii) easily disposable and biodegradable; (iii) Light weight, thin, flexible and high surface area for reagent to be stored [14, 15]; (iv) it is ability to wick fluids through capillary action, therefore, microfluidic paper devices have a distinct advantage in that no external pumps are needed to transport liquid through the patterned fluidic pathways in the paper.

Owing to these advantages, paper-based disposable biosensors have attracted more and more interest and have shown remarkable potential applications in many areas [16].
This current work demonstrates the feasibility of using a simple, cost effective and used paper cup to fabricate the instant microbial fuel cell. In a standard paper cup based microbial fuel cells (PC-MFCs) used the Pt/carbon cloth as cathode. In order to minimize the use of Pt associated cost issues. We applied the sustainable materials excreted from the used battery as cathode. Further we optimized the used battery catalyst loading rate (1, 2 and 3 grams per cm^2) on PC-MFCs. The final stage of this work was to interconnect the PC-MFCs into a stack and directly energize practical applications of digital clocks. This work demonstrates the potential realization of practical applications, where we generate instant electricity directly from the wastewater with the aid of used/death battery. It could be a useful power source for the environmental monitoring sensors in the less human activity area.

2. Materials and Methods

2.1 Collection of wastewater

Wastewater was collected from a Universidad Politécnica de Aguascalientes (UPA) and stored in refrigerator at 4°C. The wastewater served as inoculum in anode and also as medium to be treated.

2.2 Construction of paper cup cell MFCs

We procured the used paper cup from our polytechnic university campus. Then we gently rinsed paper cup with tap water in order to clean. Inside of the paper cup placed the graphite felt act as anode and the outside of the paper cup wrapped with Pt/c act as cathode .This could be as standard cell PC-MFCs (Fig 1.). We excreted the battery materials from the used battery. Later we painted different weight percentage (1 g- 11.73 mg/cm^2, 2 g-23.46 mg/cm^2 and 3 g-35.19 mg/cm^2)of battery material on the outside of the paper cup. This could follow the notation as 1-PC-MFC, 2-PC-MFC and 3-PC-MFC respectively.

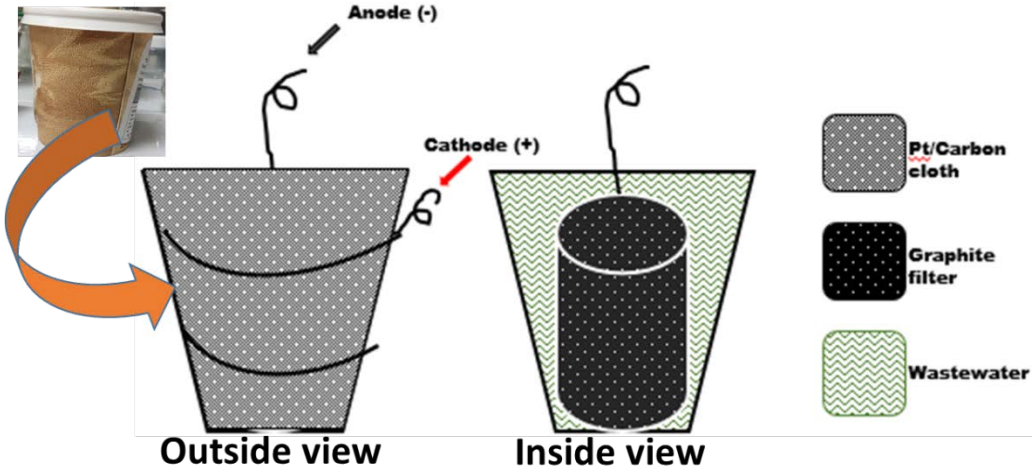

Fig 1. Schematic representation of the paper cup integrated MFCs

2.3 Electrochemical characterization of the paper cup microbial fuel cells

Novel PC-MFCs was characterized by linear sweep voltammetry (LSV) and electrochemical impedance spectroscopy (EIS). Liner sweep voltammetry (LSV) was performed in a Gamry Reference 600 Potentiostat/Galvanostat, run at a recommended scan rate of 0.1 mV s^{-1}, starting from the measured open circuit potential up to +50 mV [17, 18]. Impedance spectra of microbial fuel cells were obtained at the open circuit potential (E_{ocp}). The amplitude of the signal perturbation was 10 mV, scanned in the frequency range from 100 kHz to 10 mHz. Data fitting was accomplished by Z-view software [3].

2.4 Long term operation of PC-MFCs with Digital clocks

Two PC-MFCs are connected in series to directly power the digital clocks. We measured the potentials between the anodes and the cathodes with Arduino acquisition system, and recorded the potential every 300 s via a customized homemade interface. We obtained the current flow through the cells by Ohm's law (I = V/R).

2.5 Analyses

Chemical oxygen demand of the feed and MFC liquor and pH were determined according to the Standard Methods [19]. COD removal efficiency η_{COD} and coulombic efficiency η_{coul} were calculated as reported elsewhere [20]. All the experiments were duplicated.

3. Results and Discussion

We begin the discussion of our reports, above, with an overview of the fundamental principles behind a paper-based MFC. Therefore, a basic understanding of MFCs is first required. MFCs are typically comprised of anodic and cathodic chambers separated by a proton exchange membrane, so that protons can pass from the anode to the cathode. A paper cup is a cup made out of paper and often lined with plastic or wax to prevent liquid from leaking out or soaking through the paper. [21].Here, paper cup cellulose material was used the separator. It could physically separate the anodic and cathodic compartment, also its porous structure allows for proton transportation across the paper [9].

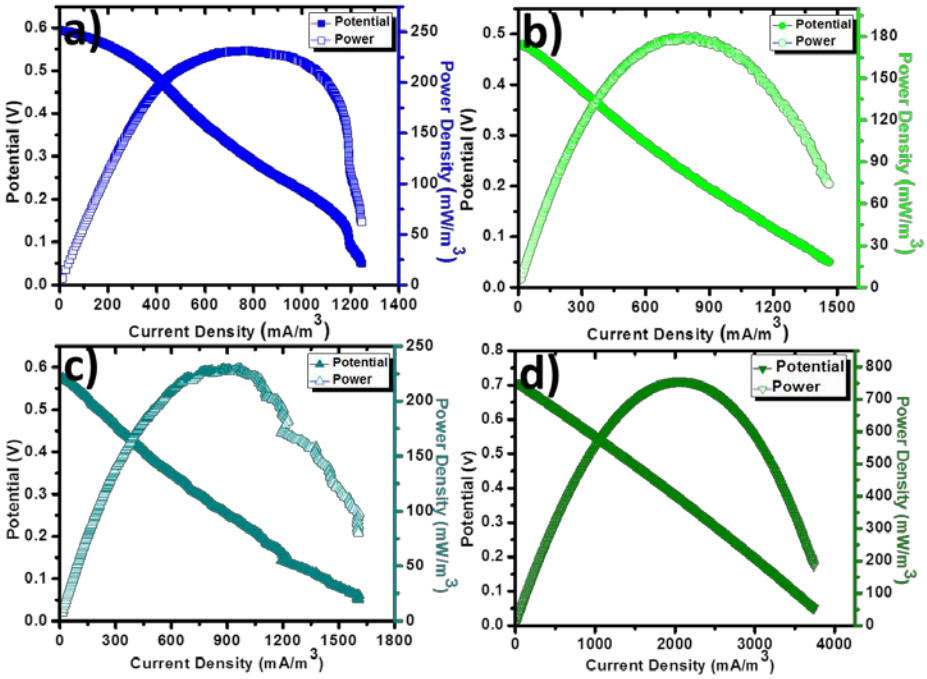

Fig. 2. Polarization curve of the paper cup microbial fuel cells. (a) Standard PC-MFC (Pt as cathode); (b) 1 g-PC-MFC; (c) 2 g-PC-MFC; (d) 3 g-PC-MFC.

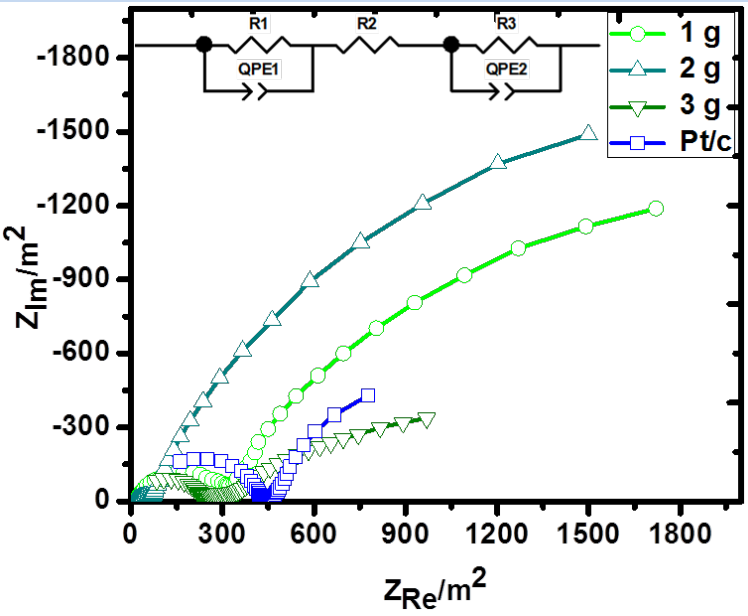

Fig 3. Electrochemical impedance spectroscopy of the PC-MFC. Standard PC-MFC (Pt as cathode); 1 g-PC-MFC; 2 g-PC-MFC; 3 g-PC-MFC

Standard PC-MFCs shows the maximum volumetric power density of 231.56 mW/m^3.(Fig 2).In the case of used battery material as cathode PC-MFCs, follows the order of maximum volumetric power density 3-PC-MFC (757 mW/m^3) > 2-PC-MFC (229.56 mW/m^3)>1-PC-MFC (180.59 mW/m^3) (Fig 2). Remarkably, used battery material as cathode 3-PC-MFC was exhibit the 3 times higher volumetric power density than Pt cathode. Moreover increasing catalyst loading could significantly improve the power production in PC-MFCs. Further studies required for the material composition characterization of used battery material. EIS represent in the Fig 3. Their corresponding equivalent circuit (inset of Fig 3.) parameters are tabled in 1. Where, R1, R2 and R3 represent that the anode (R_{an}), separator (R_{sep}) and cathodic resistance (R_{cat}). When compare all the resistance, anodic resistance would be higher in all the case. That could be possible raw wastewaters to reveals the less electrochemically active bacteria presence. Next rate-limiting part was cathodic, where Pt cathode shows higher cathodic resistance, hence it exhibit the lesser power density in PC-MFC, might be unspecific ions transport over the cellulose based paper separator hindering the cathodic reaction. However, used battery material exhibit the higher tolerance of other ion transport towards the cathode might sustain the cathodic oxygen reduction reaction, could produce higher power density in PC-MFCs and reveals less resistance in all the used battery material as cathode [9]. Fig 4. Was explicit the tafel plot. Where the exchange current (i_0) follows the order as: 3-PC-MFC (28.18 µA) > 2-PC-MFC (16.89 µA) > Pt-PC-MFC (12.2 µA) > 1-PC-MFC (11.5 µA).Higher exchange current can facilitate to achieve the higher power density in PC-MFCs. Furthermore increasing the catalytic loading of used battery material can enhance the cathodic reaction, reflect in higher power. .This value follows the order of maximum power production PC-MFCs.

Table 1. Parameters calculated from the equivalent circuit of EIS for PC-MFCs.

Parameters	1-PC-MFC	2-PC-MFC	3-PC-MFC	Pt/C cloth
R_{an}	1500	1500	1240	8650
R_{sep}	10	10	45	4360
R_{cat}	350	78	85	49000
QPE1-Q	0.01	0.01	0.001	0.07
QPE1-n	0.80	0.50	0.58	0.6
QPE2-Q	0.0075	0.045	0.085	0.006
QPE2-n	0.75	0.6	0.69	0.495

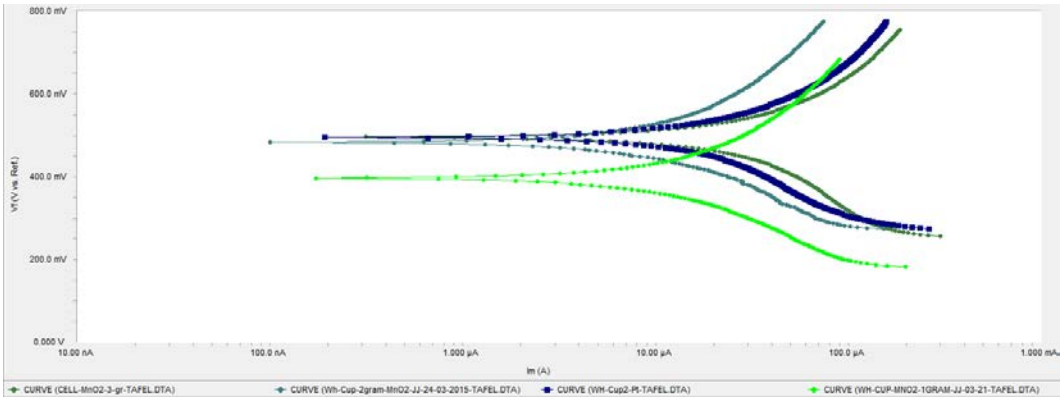

Fig 4. Tafel plot for paper cup microbial fuel cells

At final, we connected the PC-MFCs of standard PC-MFCs and 3-PC-MFCs each of two cells in series, and their polarization curve was presented in Fig 5. Two of the standard PC-MFCs connected in series reveal the maximum volumetric power density of 488.94 mW/m^3 and current density of 956.93 mA/m^3 at 0.51 V. 3-PC-MFC of 2 cells were connected in series shows the maximum volumetric power density of 1328.48 mW/m^3 and current density of 1840 mA/m^3 at 0.722 V. Later with standard PC-MFCs connected the single digital clock for the long term operation of up to 350 hrs (Fig 6.(a)). It gradually reached the maximum potential of 1.5 V at 50 hrs, and produce average power density of 734.45 mW/m^3 with average potential of 1.3 V (Table 2.). After the 250 hrs of operation, the potential gradually decreases and finally it represents the 56 % of COD removal with 83 % of columbic efficiency. We also monitor the individual standard PC-MFC cell 1 and 2 and their electrochemical performances were in table 2. Both of the cells were exhibit the more or less average power density and average potential.

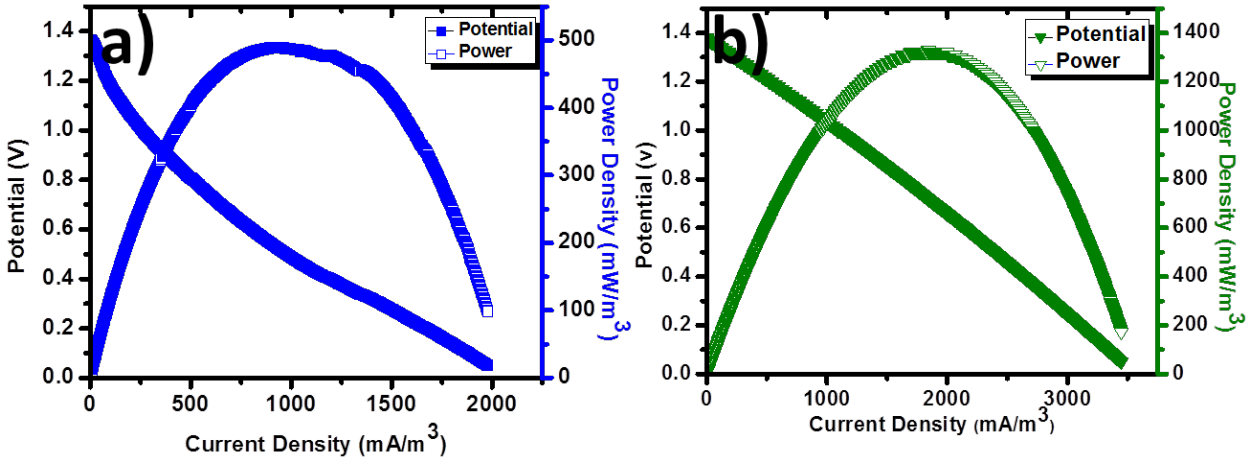

Fig 5. Polarization curve of serially connected (a) standard PC-MFCs and (b) 3-PC-MFCs

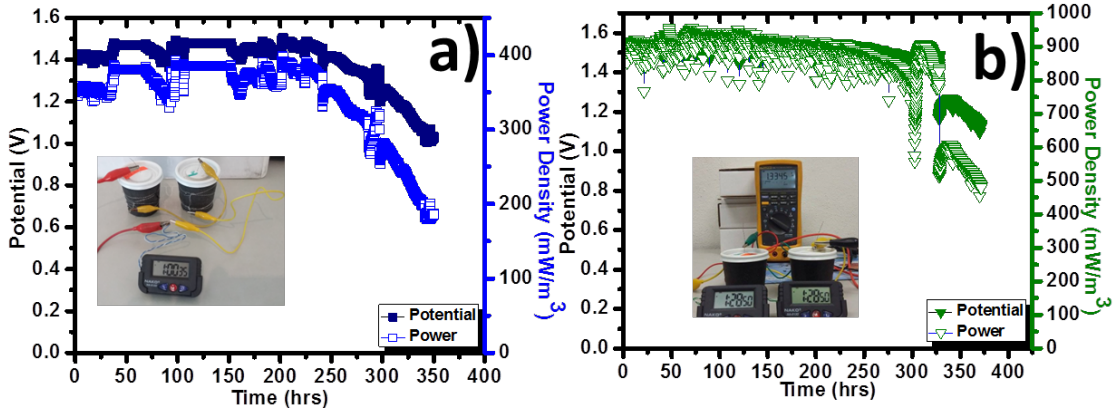

Fig 6. Long term operation of serially connected (a) standard PC-MFCs and (b) 3-PC-MFCs directly powered digital clocks

Thus it confirms that the less possibility of voltage reversal in this system would encourage the prototype for direct small electronic applications. Individual 3-PC-MFC electrochemical performances were in Table 3. This show the average volumetric power density of 395.75 and 403.05 mW/m^3 for 3-PC-MFC cell 1 and 2 respectively. Also it equally shares the average potential of 0.73 V to enhance the power to directly energize the two of the digital clocks. More importantly, used battery material cathode also exhibit the higher stability than Pt cathode and enhance to direct power the two digital clocks over the period of 350 hrs. One of the main challenges for scaling up the MFCs process is to harnesses the useful power from the MFCs stacks; this could be affected by the voltage reversal process. This process can change the polarity of one or more cells connected in series as a result loss of power generation. Moreover, the fuel starvation leading to loss of bacterial activity and variation in internal resistance can affect the stacked MFCs performance [22, 23]. Remarkably, 3-PC-MFCs connected in series was not observed any of the voltage reversal problem and we can convert the electrical energy produced from the MFCs into direct useful energize applications (Table 3).

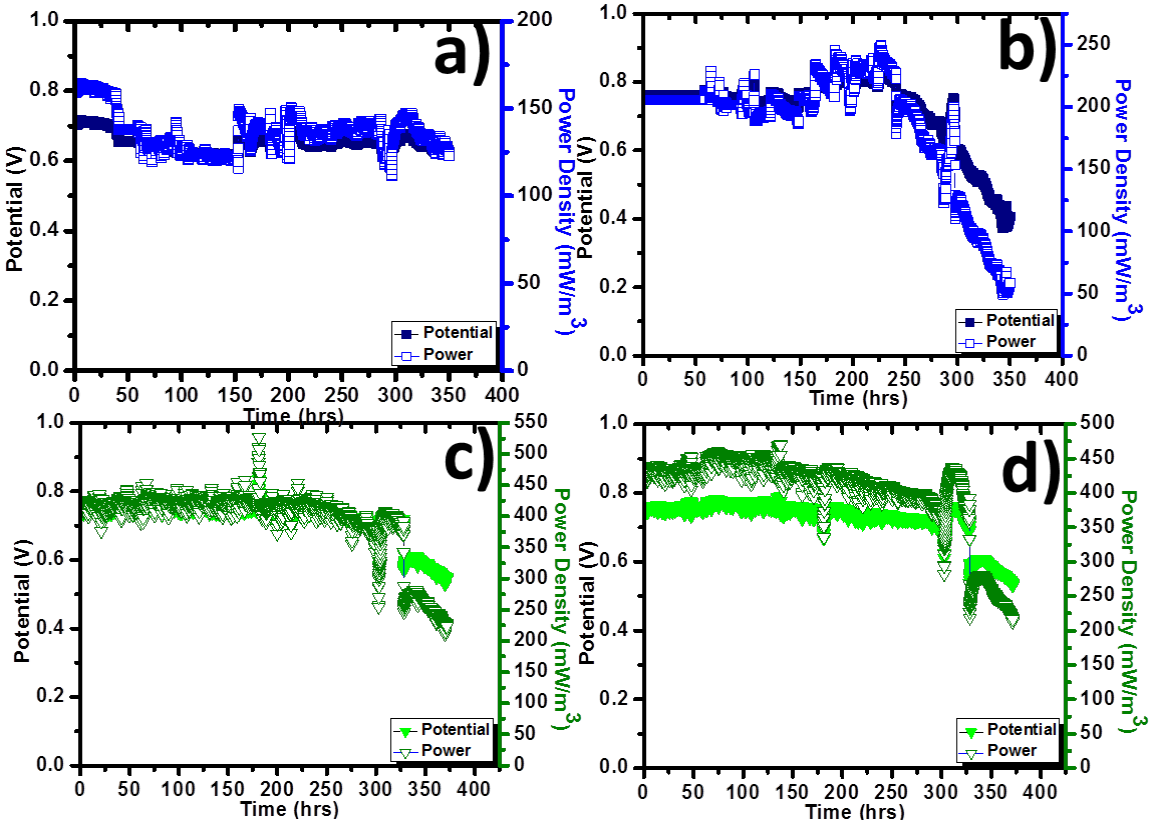

Fig 7. Performance of serially connected each PC-MFCs operation (a) standard PC-MFC 1 (b) standard PC-MFC 2; (c) 3-PC-MFC 1;(d) 3-PC-MFC 2

Table 2. Electrochemical parameters of long term operation of serially connected standard PC-MFCs

Parameters	Pt/C cloth 1	Pt/C cloth 2	Pt/C cloth 2series
P^a (mW/m^2)	1.56 ± 0.12	1.95 ± 0.47	3.58 ± 0.54
$P_V{}^b$ (mW/m^3)	136.7 ± 11.02	187.35 ± 46	343.87± 52.66
P^c (mW)	0.015± 0.001	0.018 ± 0.004	0.034 ± 0.005
I (mA/m^2)	2.49 ± 0.09	2.65 ± 0.37	2.55± 0.021
I (mA/m^3)	209.38 ± 8.34	254.7 ± 36.45	245.63 ± 20.39
I^d (mA)	0.023 ± 0.0009	0.025 ± 0.0036	0.024 ± 0.002
E^e (V)	0.65 ± 0.025	0.72 ± 0.1	1.39 ± 0.115
$\eta_{COD}{}^f$ (%)	56.3	56.3	56.3
$\eta_{Coul}{}^g$ (%)	37.7	39.7	39.1

Notes: [a] surface area power density; [b] volumetric power density; [c] average power; [d] average current; [e] average potential; [f] chemical oxygen demand removal efficiency; and [g] coulombic efficiency.

Table 3. Electrochemical parameters of long term operation of serially connected 3-PC-MFCs

Parameters	3-PC-MFC 1	3-PC-MFC 2	3-PC-MFCs in series
P^a (mW/m^2)	4.12 ± 0.56	4.19 ± 0.61	8.9 ± 1.2
P_V [b] (mW/m^3)	395.75 ± 53.8	403.05 ± 58.82	854.41 ± 116.09
P [c] (mW)	0.039 ± 0.0053	0.04 ± 0.0058	0.085 ± 0.011
I (mA/m^2)	5.67 ± 0.42	5.72 ± 0.45	5.89 ± 0.43
I (mA/m^3)	545.02 ± 40.44	549.79 ± 43.82	566.27 ± 41.93
I [d] (mA)	0.054 ± 0.004	0.054 ± 0.004	0.056 ± 0.004
E [e] (V)	0.72 ± 0.053	0.73 ± 0.05	1.5 ± 0.11
η_{COD} [f] (%)	66.9	66.9	66.9
η_{Coul} [g] (%)	89.6	89.8	89.2

Notes: [a] surface area power density; [b] volumetric power density; [c] average power; [d] average current; [e] average potential; [f] chemical oxygen demand removal efficiency; and [g] coulombic efficiency.

4. Conclusion

We successfully designed the air cathodic PC-MFCs system. From this, cellulose based paper material can act as separator to facilitate the air cathodic reaction on the outside of the paper cup, wrapped by Pt/carbon cloth as standard cell. Standard PC-MFCs shows the maximum volumetric power density of 231.56 mW/m^3. Further we applied the used battery material as cathode in different catalyst loading rate of 1, 2 and 3 grams per cm^2, in order to avoid the usage of Pt and to prepare the cost effective real time electronic applications. In the case of used battery material as cathode PC-MFCs, follows the order of maximum volumetric power density 3-PC-MFC (757 mW/m^3) > 2-PC-MFC (229.56 mW/m^3)>1-PC-MFC (180.59 mW/m^3). Remarkably, used battery material as cathode of 3-PC-MFC was exhibit the 3 times higher volumetric power density than Pt cathode. Moreover increasing catalyst loading could significantly improve the power production in PC-MFCs. At final, we connected the PC-MFCs of standard PC-MFCs and 3-PC-MFCs each of two cells in series. Two of the standard PC-MFCs connected in series reveals the maximum volumetric power density of 343.87 mW/m^3. 3-PC-MFC of 2 cells were connected in series shows the maximum volumetric power density of 1328.48 mW/m^3. At the final stage we directly powered the one digital clock with two standard PC-MFCs serially connected and it reveals the average volumetric power density of 343.87 mW/m^3. Two of the 3-PC-MFCs were connected in series directly power the two digital clocks and produce the average power density of 1328.48 mW/m^3. This work demonstrates the potential realization of practical applications, where we generate instant electricity directly from the wastewater with the aid of used/death battery.

Acknowledgements

The authors would like to acknowledge the fellowship from the SMH and extended our gratitude to the XV International Congress of the Mexican Hydrogen Society. KSK would

like to acknowledge the funding agency of Secretaria de Educacion Pubica (SEP), Mexico for the project DSA/103.5/14/10671 and extended to Conacyt for SNI.

References

[1] Kamaraj S.-K., Romano S.M., Moreno V.C., Poggi-Varaldo H.M., Solorza-Feria O. Use of Novel Reinforced Cation Exchange Membranes for Microbial Fuel Cellss. Electrochimica Acta 2015; 176:555-566.
[2] B. E. Logan. Appl. Microbiol. Biot., 2010; 85-1665..
[3] Sathish-Kumar K., Solorza-Feria O., Vázquez-Huerta G., Luna-Arias J., Poggi-Varaldo H.M. Electrical Stress-directed Evolution of Biocatalysts Community Sampled from A Sodic-saline Soil for Microbial Fuel Cells. Journal of New Materials for Electrochemical Systems 2012; 15:181-186.
[4] T. Ewing, P. T. Ha., J. T. Babauta., N. T. Tang., D. Heo and H. Beyenal, J. Power Sources, 2014; 272:311–319.
[5] Y. Kim and B. E. Logan, Desalination, 2013; 308:122–130.
[6]A. Kadier, Y. Simayi., M. S. Kalil., P. Abdeshahian and A. A. Hamid, Renewable Energy, 2014; 71:466–472.
[7]W. Li and H. Yu, Biotechnol. Adv., 2015; 33:1–12.
[8] A. P. Borole., G. Reguera, B. Ringeisen, Z. Wang., Y. Feng and B. H. Kim. Energy Environ. Sci., 2011; 4:4813–4834.
[9] A. Fraiwan., S. P. Adusumilli, D. Han., A. J. Steckl., D. F. Call., C. R. Westgate and S. Choi., Fuel Cells, 2014; 14:801–809.
[10] J. B. A. Arends and W. Verstraete. Microb. Biotechnol. 2012; 5:333–346.
[11] V. B. Oliveira., M. Simoes., L. F. Melo and A. M. F. R. Pinto, Biochem. Eng. J. 2013; 73:53–64.
[12] J. Babauta, R. Renslow, Z,. Lewandowski and H. Beyenal, Biofouling, 2012; 28:798–812.
[13] Winfield J., Chambers L.D., Rossiter J., Greenman J., Ieropoulos I. Urine-activated origami microbial fuel cells to signal proof of life. Journal of Materials Chemistry A. 2015; 3:7058-7065.
[14] E. J. Maxwell., A. D. Mazzeo., and G. M. Whitesides. Paper-based electroanalytical devices for accessible diagnostic testing. Mater. Res. Soc. Bull. 2013; 38(4):309–314.
[15] J. P. Metters., S. M. Houssein., D. K. Kampouris, and C. E. Banks. Paperbased electroanalytical sensing platforms. Anal. Methods. 2013; 5(1):103–110.
[16] Nguyen T.H., Fraiwan A., Choi S. Paper-based batteries: A review. Biosensors and Bioelectronics 2014; 54:640-649.
[17] Velasquez-Orta S.B., Curtis T.P., Logan B.E. Energy from algae using microbial fuel cells. Biotechnol Bioeng 2009; 103(6):1068-76.
[18] Watson V.J., Logan B.E. Analysis of polarization methods for elimination of powe overshoot in microbial fuel cells. Electrochem Commun 2011;13(1):54-6.
[19] APHA. Standard methods for examination of water and wastewater. 17th ed. Washington DC: American Public Health Association; 1981.
[20]Fornero J.J., Rosenbaum M., Angenent L.T. Electric Power Generation from Municipal, Food, and Animal Wastewaters Using Microbial Fuel Cells. Electroanalysis 2010;22:832-843.
[21] Maying Soong. Chinese Paper Folding for Beginners. Courier Dover Publications. pp. 6–7. ISBN 0-486-41806-5. – How to make a paper cup out of a square of paper using origami. 2002.
[22] Aelterman P., Rabaey K., Pham T.H., Boon N., Verstraete W. Continuous electricity generation at high voltages and currents using stacked microbial fuel cells: Environ. Sci. Technol. 2006; 39:3388–3394.
[23] Ieropoulos I., Greenman J., Melhuish C. Microbial fuel cell based on carbon veil electrodes: stack configuration and scalability. Int. J. Energy Res. 2008; 32:1228–1240.

Chapter 5.7. Oxyhydrogen gas production for fuel enriched in internal combustion engine

J.A. Fuentes Coutiño[a,b]*; J.M. Pineda Sandoval[a]; R.G. González-Huerta[b]

[a]IPN-ESIME-Azc, SEPI, Av. De las Granjas, N°.682, Azcapotzalco. CP. 02250. México DF.
[b]ESIQIE-IPN, Laboratorio de Electroquímica y Corrosión, UPLAM, CP 07738, México, D.F

ABSTRACT

The limited fossil fuel reserves and severe environmental pollution have pushed studies on fuel economy in internal combustion engines (ICE). This paper investigated the effect of hydrogen and oxygen blends (oxyhydrogen gas) addition on the performance of gasoline engine. In this proposal, an alkaline electrolyzer prototype was design and constructed for oxyhydrogen production to enrich gasoline used in an ICE. There are two alkaline electrolysis cell configurations, namely, the monopolar and the bipolar. From the manufacturing point of view, the monopolar configuration is simple and easy to fabricate and maintain but suffers from high electrical currents at low voltages, causing large ohmic losses. The bipolar configuration reduces the ohmic losses on the electrical circuit connecters but demands much greater precision in design and manufacturing to prevent the electrolyte and gas leakage between cells. Methodologies and manufacturing processes are analyzed, prototype development is detailed, including materials selection, handling and security, manufacturing process and efficiency. In this work, we use monopolar configuration, regarding it product could be marketed in the short term.
The test was performed on a modified CIE (a piston to 125 cc) equipped with an oxyhydrogen gas injection system. The engine was run at a typical city-driving speed of 1000 and 2000 rpm with various excess air ratios and five standard oxyhydrogen volume fractions in the total intake gas of 0%, 5%, 10%, 15% and 20%, it was done an analysis about reduce gasoline consumption. The engine performance, service life and reducing the use of gasoline are analyzed, a perspective of the pollutants reduction and environmentally damaging emissions is done. Security measures at every stage are considered. 5% oxyhydrogen enriched, produce around 10% less gasoline consumption and a reduction of greenhouse gases such as carbon monoxide (CO) and carbon dioxide is also reduced in 5% to 10% approximately.

Keywords: Alkaline Electrolyzer, Oxyhydrogen gas, Internal combustion engines, Saving gasoline

1. Introduction

The limited fossil fuel reserves and severe environmental pollution have pushed studies on fuel economy in internal combustion engines (ICE), and it has generated the need for

---

* Author for correspondence: Jesus Adrian Fuentes Coutiño; (55)5533876682; E-mail: j_fuentesc@hotmail.com

clean, renewable and alternatives energies. Hydrogen generation offers the possibility to reverse the impact somewhat generated in the use of fossil fuels on the environment and have an alternative as hydrocarbons run out so we can deal with the high demand for fuel and energy Current [1] society. Hydrogen can be used as fuel directly in internal combustion engine (ICE), a stove, etc. or in a first stage adapting existing technology, it is possible enrichment hydrocarbon in ICE. Everything points to a new energy system is starting: The hydrogen era as an energy carrier and fuel clean and friendly environment has started. It is need to generate new designs and process improvements, equipment and methodologies for the generation, storage and use of hydrogen. Similarly the technology development and tools for safe use hydrogen is required [2-6].

2. Experimental Methodology

A manufacturing process of an alkaline electrolyzer (AE) using a design pattern known as "technology transfer" was established, in which new devise is developed through a logical process. It began with a preliminary design proposed, this devise was testing and their components optimised, selecting the best materials, making the required change and manufacturing each component. Models and simulations were development using specialist software, as is solid-Works.

2.1. Development electrolyzer

2.1.1. Establishment of geometries

A general analysis of the geometries of the plates (electrodes) was first performed in existing electrolyzers and also subsequently propose a new geometry taking into account the performance of the electrolyzer, the electrolyte and operating conditions. Electrolyte medium is a highly corrosive alkaline solution with operating temperatures from 30-80 ° C at 30 psi. Square or rectangular geometries electrodes generate a lot of stress concentration at edges or corners, it produces wear faster in electrodes. So, circular electrodes were proved, when they are in contact with the solution to the above conditions the wear rate is reduced on the plates and their time life is increased. Similarly it was concluded that for better clamping between plates and pressure distribution more uniform in the stack and reduce lateral and lower leakage outer end plates must have a greater than the inner plates thickness, in order to avoid overcome the yield strength of the material module and this yields to the pressure and bend, thereby generating spaces between plates and therefore leakage.

2.1.2. Selection of materials

For a longer life of the components of the electrolyzer, an analysis of each was carried out and the role they had in the electrolyzer as a global system in order to meet its performance was analyzed and if necessary propose actions corrective from a simple modification to its total change of material. The design methodology “ASHBY-Selection of Materials in the Mechanical Design” for the selection of suitable materials was taken into account for each of the components. Where it is explained that the selection of the material may not be independent of the selection of the manufacturing process and product costs depend on the material selection and therefore the selection of the manufacturing process.

Figure 1 shows a schema design methodology, it is proposed ASHBY where each step was analyzed, and performance was obtained for select the best material according their functionality

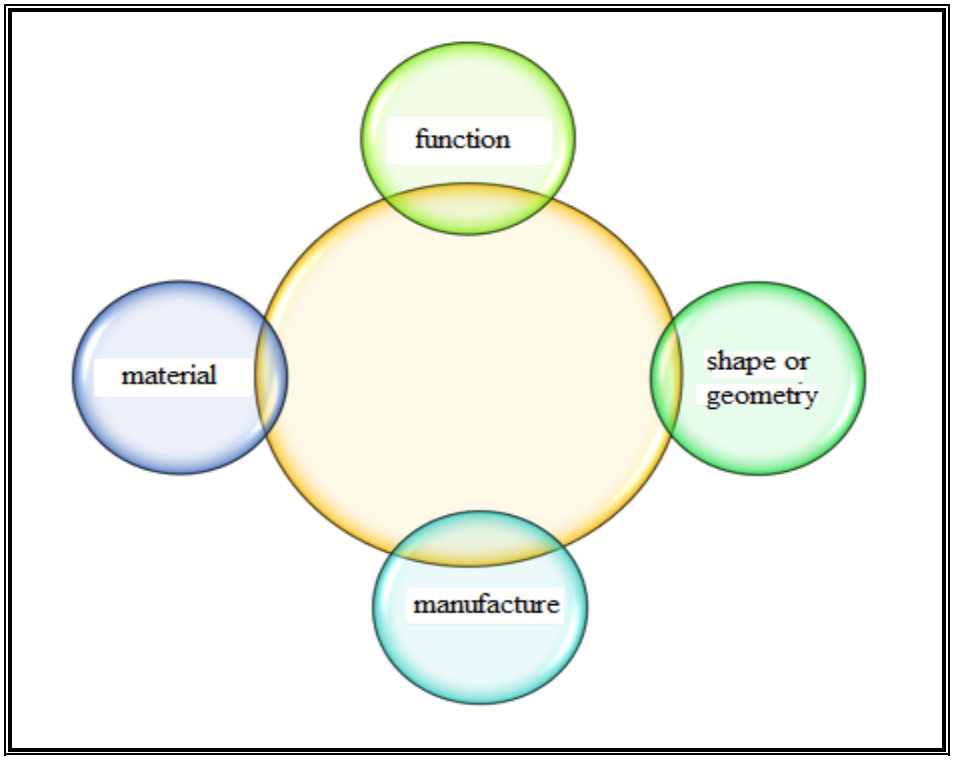

Fig. 1. ASHBY scheme of the methodology

2.1.3. Coupling the motor bike

By using Faraday's laws theoretical calculations of the necessary flows were performed to obtain the percentage of enrichment to each of the specific analyzing speed and efficiencies for both current and voltage specification tables they are also calculated using the following formulas and motor:

$$V_{CE} = V_1 \frac{(P-P_V)}{760} \frac{298}{T+273} \quad (1)$$

where:
V_{CE} is actual volume
P is atmospheric pressure (mm Hg)
T is ambient temperature (° C)
P_v is vapor pressure of 18 mm Hg
V_1 is volume in liters (Cd.de conditions of Mexico)
Volume to standard conditions (V_T) is:

$$V_T = 1.899x10^{-4} I\, t \quad (2)$$

where I is current that goes through the system and t is time
Normal volume:

$$V_T = 1.7399\, x\, 10 - 4\, I\, t \qquad (3)$$

The volume fractions of the Oxyhydrogen $\alpha_{2H2/O2}$ in the total intake air injection are defined as:

$$\alpha_{2H2/O2} = [V_{0H2}/(V_{0H2} + V_{air})]x\ 100\% \qquad (4)$$

where V_{OH2} is oxyhydrogen gas flow produced and V_{air} is flow engine intake air

For calculations based on the percentage of gas Oxyhydrogen it is based on the following equation:

$$V_{OH2} = \frac{V_{aire}}{\left(\frac{1}{\alpha 2H2O/02} - 1\right)} \qquad (5)$$

3. Results and Discussion

The following graphs show the percentage amount of oxyhydrogen gas enriched in the engine at certain speeds and flows 1 – 2 (lt/min).

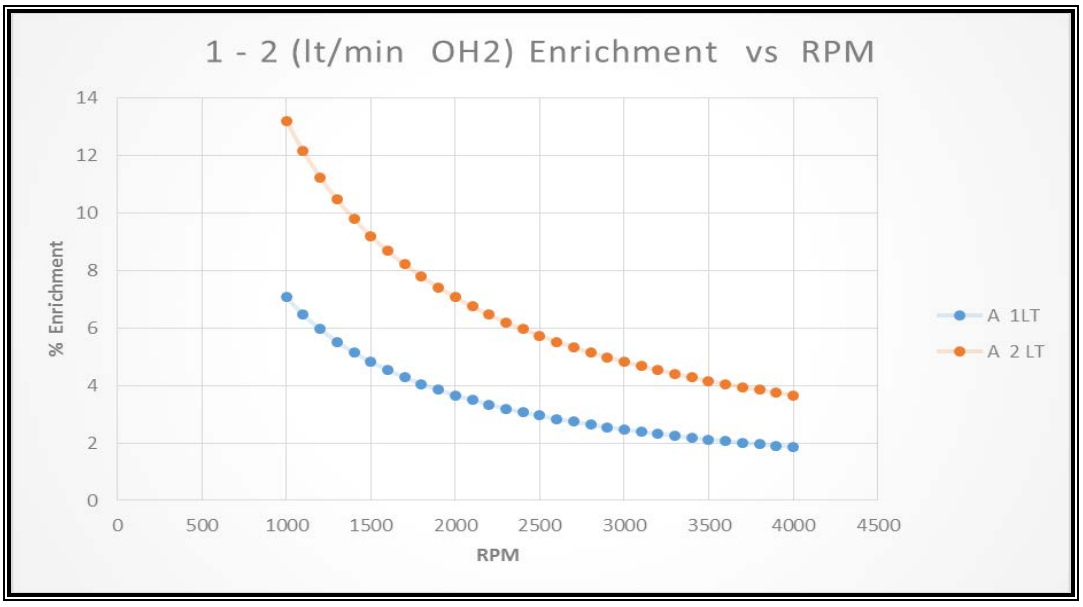

Fig. 2. Graphic percentage oxyhydrogen enriched gas

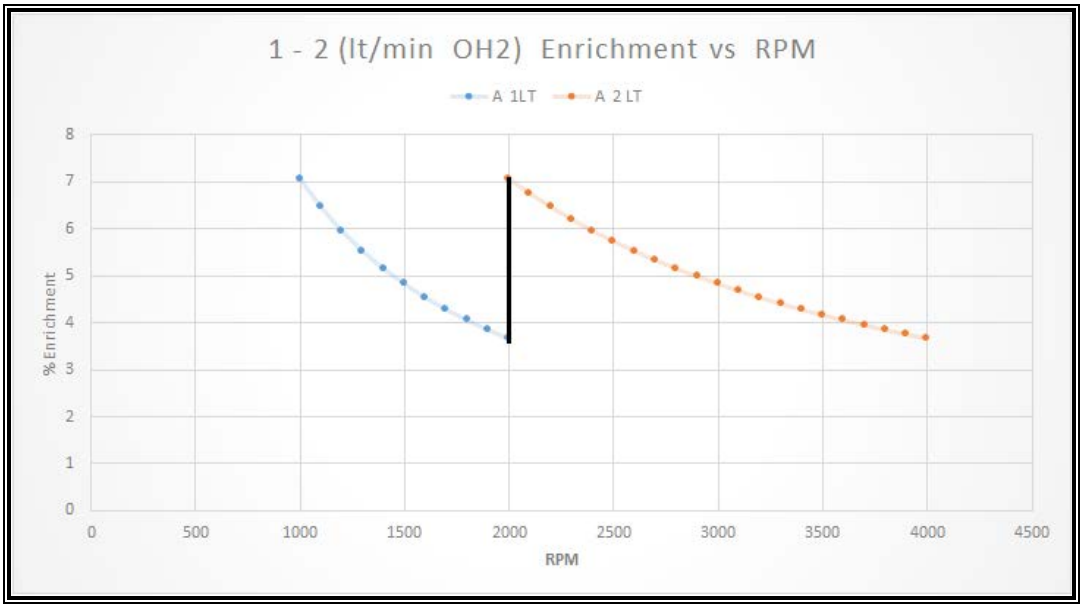

Fig. 3. Percentage graphs oxyhydrogen enriched gas in two specific points of 1000 RPM to 2000 RPM

In the following graphic the percentage of gasoline saved enrichment 1-2 flows in the motor shown

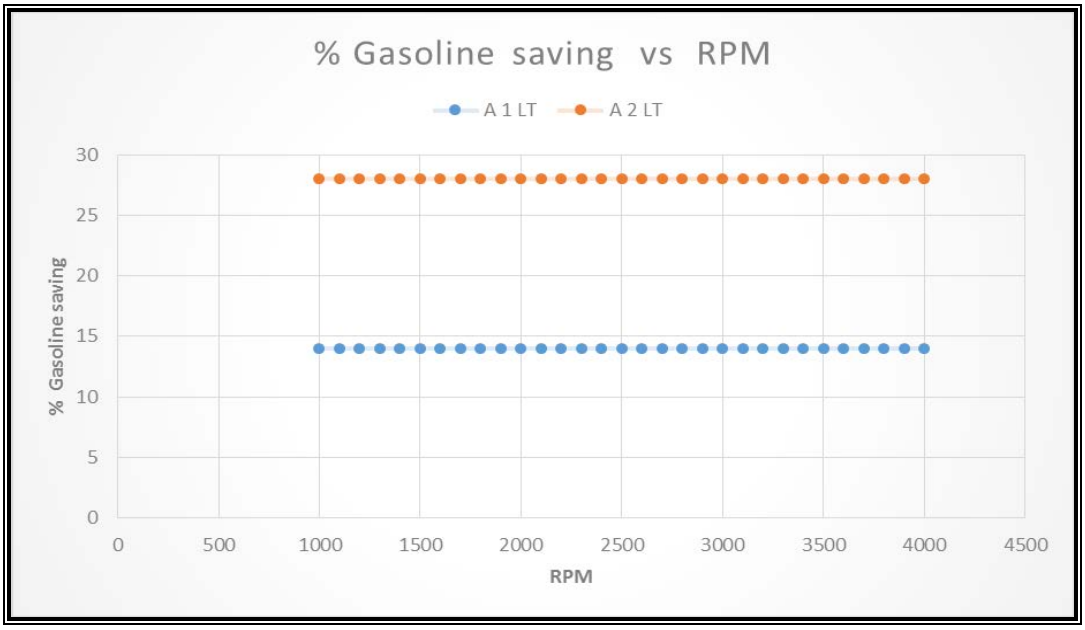

Fig. 4. Percentage of gasoline saved (1-2 lt/min)

In Figure 5, the result of the final optional proposal together with its component is to implement official and generally, since it meets all the requirements, changes and modifications necessary for the characteristics required of a prototype electrolyser shown

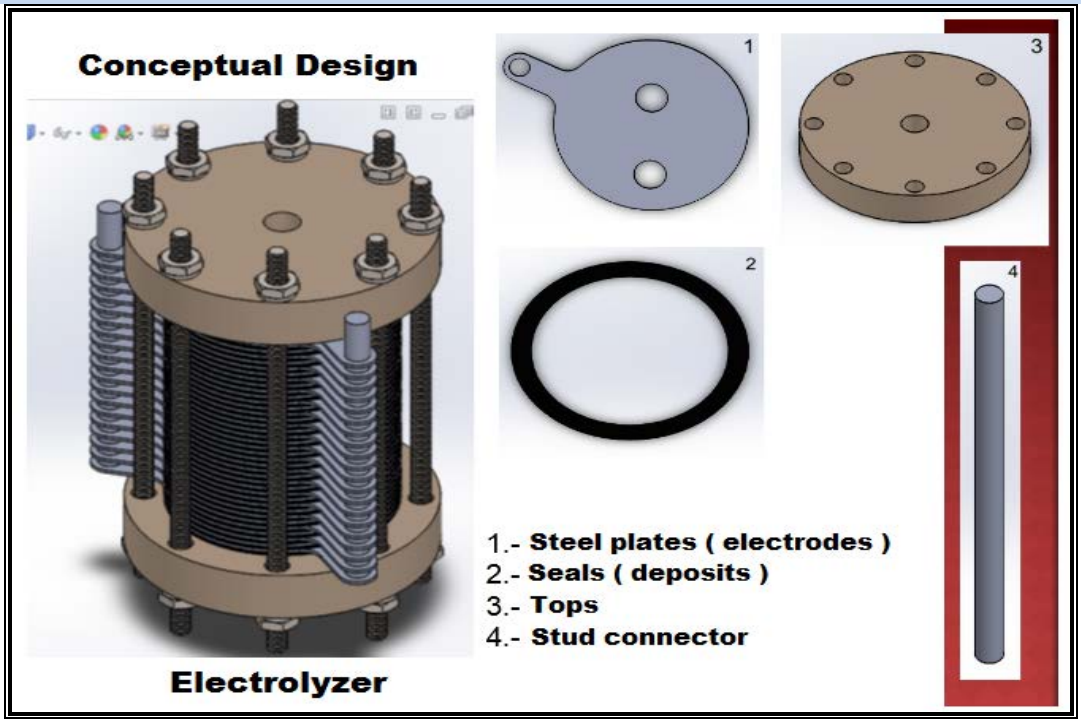

Fig. 5. Views of the prototype and its components

4. Conclusion

In this paper we have presented the evaluation of each of the components of an alkaline electrolyzer and its manufacturing processes, the choice of materials and manufacturing performance , so modifying each established their manufacturing processes, forms and existing geometries and materials use, in order to achieve greater efficiency and the specifics required along with the elimination of existing damage , thus achieving a better and more efficient prototype, no damage (leak) and leave a formal proposal and professional design and manufacture for complete installation and comparison of theoretical and experimental results.

Acknowledgements

This work has been supported by multidisciplinary project IPN-SIP 1683 and Thematic Networks program CONACYT/RTH2

References

[1] Shoufeng Wang, Changwei Ji, Jian Zhang, Bo Zhang, *Comparison of the performance of a spark-ignited gasoline engine blended with hydrogen and hydrogene-oxygen mixtures*, Energy 36, p. 5832, (2011).
[2] S. Thomas, M. Zalbowitz, Fuel Cells: Green Power, Los Alamos National Laboratory, The 3M Foundation, Reporte LA-UR-99-3231(1999).

[3] Hydrogen & Fuel Cells, Review of National R&D programs, International Energy Agency, OECD/IEA, 2004.
[4] Kai Zeng, Dongke Zhang, RECENT PROGRESS IN ALKALINE WATER ELECTROLYSIS FOR HYDROGEN PRODUCTION AND APPLICATIONS, Progress in Energy and Combustion Science 36, p.p. 307–326, 2010.
[5] Shuofeng Wang, Changwei Ji, Jian Zhang, Bo Zhang, Improving the performance of a gasoline engine with the addition of hydrogene-oxygen mixtures, Int. J. Hydrogen Energy, 36, 11164-11173, 2011
[6] Chenglong Tang, YingjiaZhang, ZuohuaHuang, Progress in combustion investigations of hydrogen enriched hydrocarbons, Renewable and Sustainable Energy Reviews, 30, 195–216, 2014.

Chapter 5.8. Simulation process of alkaline electrolysers to save natural gas in food dehydration plant

J.A. Gutiérrez Rodríguez[1,2,*]; S.A. Romo Ríos[1,2]; R. de G. González Huerta[2]

[1]UNAM-Facultad de Química, C. Universitaria, Circuito Exterior S/N, CP 04510, México D.F.
[2] IPN-ESIQIE, Lab. Electroquímica y Corrosión, UPALM, CP 07738, México D.F.

ABSTRACT

Nowadays, world starts to live the decrease of oil production. This is reflected on the constant costs increase in hydrocarbon products. For instance the liquefied gas in México shown a 20% of increase in its cost in only three years (2012-2015). Therefore, it is necessary to search for alternative energies that can be useful in the existing infrastructure and also work independent from the conventional energies. Hydrogen has been recognized as the most promising future energy carrier. At present, industrial hydrogen production processes are not independent of traditional energy resources, which could easily cause secondary pollution. Mexico has abundant solar energy resources and the installed capacity of solar power (photovoltaics system-PV) grows every year .
In this paper, solar power is used in water-electrolytic process, which will contribute to the development of green economy and low carbon economy in Mexico. We produce oxyhydrogen gas (oxygen ang hydrogen mix) obtained from alkaline electrolysis in order to save natural gas in food dehydration plant. The sizing of a hybrid system (solar-hydrogen) has to consider the steady state characteristics, unsteady profiles of the site energy source and the electricity loading demand. Although these profiles restrict the power of the subsystems to a limited range of possibilities, the numbers of possible combinations are numerous. So first, small alkaline electrolyzers prototypes were desing, performance (voltage vs current curves) and oxyhydrogen gas production were obtained. Second, this allows design bigger electrolizer for enrichment of hydrocarbon lines in industrial processes which spend much energy. Finally, a simulation process was developed to integrate a hybrid system (PV-alkaline electrolyzer) with a food dehydration plant. Authors thank CONACYT to the Programa de Redes Temáticas (RTH2) proyects 252003 and 249795; and IPN SIP multidisciplinary project 1683.

Keywords: Hydrogen production, Hydrogen applications, Alkaline electrolysis, Save fossil fuel

1. Introduction

Nowadays, world starts to live the decrease of oil production. This is reflected on the constant costs increase in hydrocarbon products. For instance the liquefied gas in México

---

* Author for correspondence:
Juan Antonio Gutiérrez Rodríguez, +52-1(55) 284 72 617, j.antoniogr92@gmail.com

shown a 20% of increase in its cost in only three years (2012-2015). Therefore, it is necessary to search for alternative energies that can be useful in the existing infrastructure and also work independent from the conventional energies. Hydrogen has been recognized as the most promising future energy carrier. At present, industrial hydrogen production processes are not independent of traditional energy resources, which could easily cause secondary pollution. Mexico has abundant solar energy resources and the installed capacity of solar power (photovoltaics system-PV) grows every year .

Conventional energies have produced serious environmental problems worldwide. Mexico is not excluded; Mexico City is one of the most polluted cities in the world causing problems not only to the environment, also to its citizen. Renewable energy is part of the solution to these problems, nevertheless it has a flaw: it is intermittent energies although this problem can be solved with the use of hydrogen as an energy carrier in a chemical form [1].

Ankica Dukic and Mihajlo Firak from Zagreb University show in article called "Hydrogen production using alkaline electrolyzer and photovoltaic (PV) module production" a model of hydrogen avoiding CO2 emissions- It is using alkaline electrolyzer coupled to a photovoltaic system. This could be useful to avoiding the use of electrical energy from conventional energy in hydrogen generation [2].

Alkaline electrolysis is a electrochemical reaction carried out by external electrical current and higher voltage than reversible cell potential. The basic units in an electrolyzer are electrodes (cathode and anode), power source, electrolyte (basic pH) and a container system. There are two kinds of electrolysers: monopolar arrangement wherein the total system voltage is the same for all electrodes and bipolar arrangement, where only two electrodes are connected to the power source and every two adjacent electrodes are making a cell unit wherein the total voltage is the sum of each cell [4].

Serial arrangement was used in this work because gas production is higher than parallel arrangement per unit of electrical power supplied. Once defined the type under study, was obtained from a prototype characteristics an algorithm for the design of equipment with greater capacity. Some parameters of the prototype considered as scalable without significant variation and extrapolation mathematical model was developed to predict the behavior of parameters that have significant changes according with electrolyzer size. Data of hydrogen gas quantity required for energy enrichment of 10% to a LP gas line (GLP) in a real dehydration plant food located in State of Mexico was used to illustrate the operation of the algorithm. From this data the design of equipment that meets the needs of gas production and a photovoltaic system capable of feeding the alkaline electrolyser was performed. Dimensioning includes number of electrodes reached, distance between them, effective area and electrical characteristics of them as voltage and amperage.

2. Materials and Methods

2.1 Characterization of alkaline electrolyzers

In this work an alkaline electrolyzer (AE) was characterized in the Laboratory of Electroquímica y Corrosión of the ESIQIE – IPN, starting with the assumption that the electrolyzer has a good electrochemical response and it is an ideal equipment for scaling.

The material of the electrodes are of stainless steel 304 and between electrode and electrode exist a spacing of 0.5 cm. The AE of this experiment counts with 7 cells with the bipolar configuration. The effective area of the AE is of 1152 cm^2. The AE electrolytic solution of NaOH 5% weight was used for the experiments. The measurements were taken under ambient pressure and temperature.

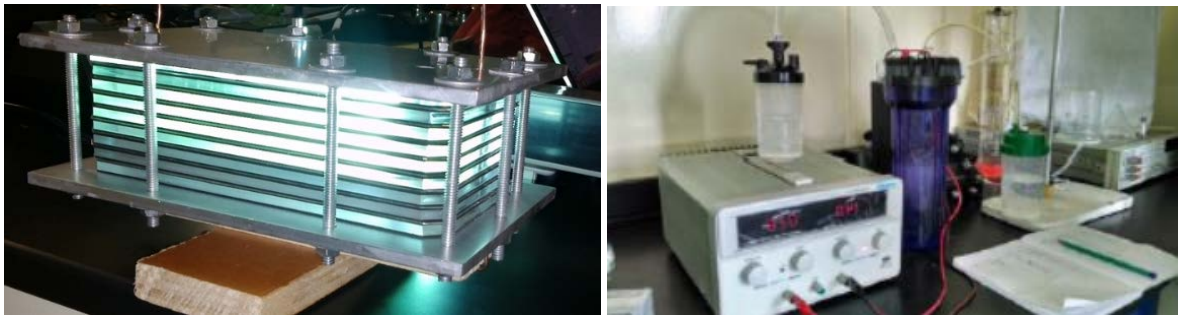

Fig. 1. a) Alkaline electrolyzer b) Test system.

The extreme electrodes of the AE were connected to a direct current (DC) power supply, consequently different values of electrical current were fed to the AE, starting for 0.01 A to 5.0 A. The values of oxyhydrogen gas produced and voltage were taken account. The values of amperage, voltage and volume of oxyhydrogen gas produced are presented in Table 1 (I vs V) and Table 2 (I vs Oxyhydrogen production).

Table 1. Values of electrical current and voltage of the AE.

Amperage	Voltage	Amperage	Voltage
0.00	0.00	0.80	14.27
0.01	11.33	1.00	14.50
0.10	12.83	1.40	14.83
0.30	13.40	2.00	15.27
0.40	13.53	3.00	15.83
0.50	13.90	5.00	16.87

Table 2. Values production of oxyhydrogen gas

Amperage	Oxyhydrogen production (ml/min) Standard conditions
1.00	95.43
2.00	197.33
5.00	560.66

Figure 2 shows characteristic curve I vs V of the AE, we can see two regions, firt one is observed at low currente, voltage has a exponential behavior, between 0 and 1 A at 14.5 V; the second one shows a linear relationship between current and voltage, from 1 A to 5 A

between 14.5 V and 17 V, which is known as ohmic area, in this region alkaline electrolyzer has to used at minima efficiency of 50%.

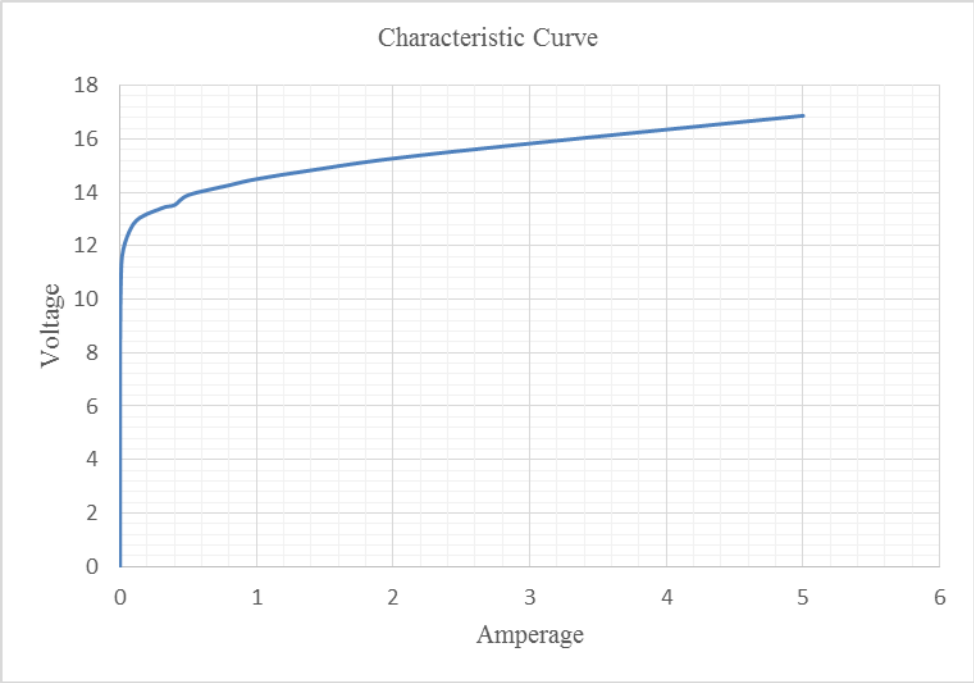

Fig. 2. Characteristic Curve I vs V of the AE.

3. Results and Discussion

3.1 Algorithm Method for Scaling Alkaline Electrolyzers

The electrolyzers design algorithm from a prototype is shown in Figure 3. The meaning of the boxes in the diagram is: rectangle corresponds to operción or mathematical calculation, trapeze is information fed and semi ovals are data produced by the algorithm. Below is explained a iteration for this algorithm.

3.2 Conditions and Requirements in the food dehydration plant

The food dehydration plant is located in the Estado de Mexico. It is necessary to stand out several data from the company, which would define the project scope and the proper use of the algorithm method proposed in order to provide a good design of alkaline electrolyzer that achieve the requirements (enrichment 2-10% of natural gas). Adding to this information, it is known that the geographic location of the plant has an average annual solar hours equivalent to 5.72 hours per day, this is important since the scope of the project is generate oxyhydrogen gas from a renewable source, in this case photovoltaic energy.

Figure 4 is shows a schematic process diagram of the dehydration plant.

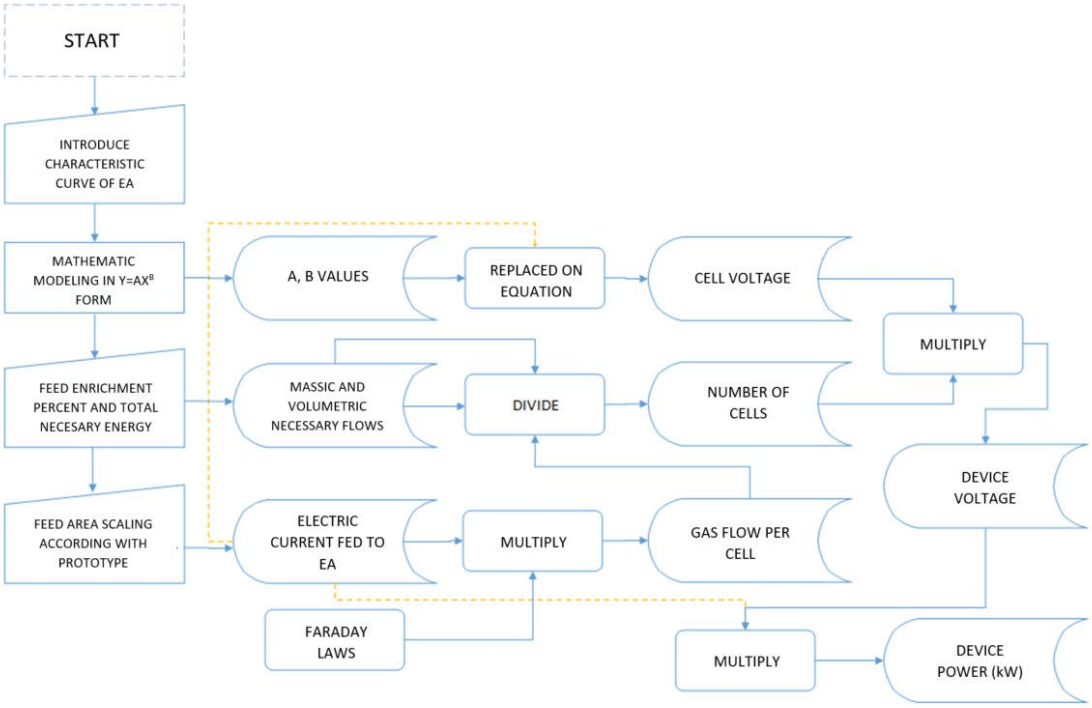

Fig. 3. Algorithm from a design prototype.

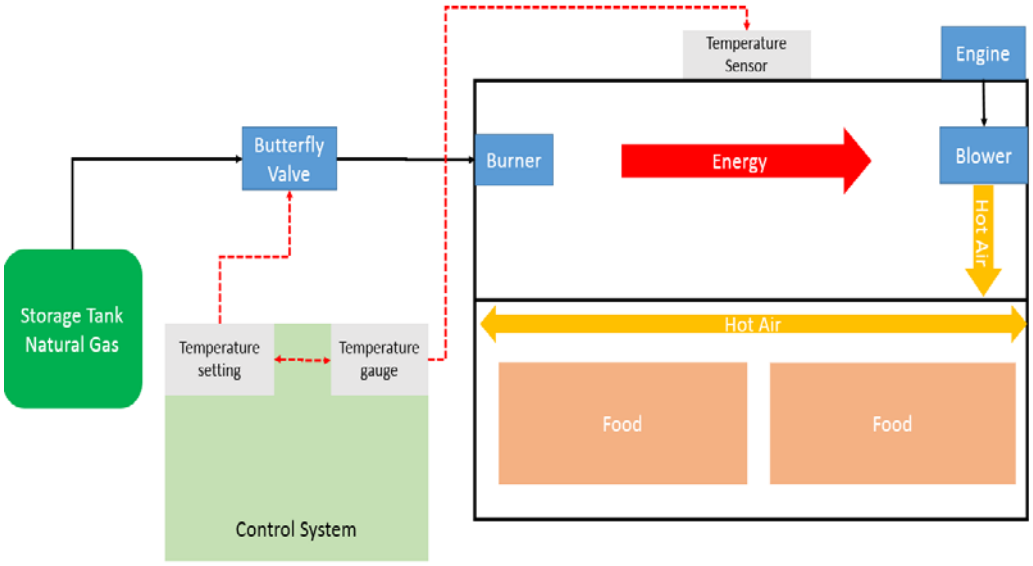

Fig. 4. Schematic process diagram.

The figure 4 provides the main step process of the dehydration plant. Firstly the blower turns on accompanied by a pilot flame on the burner, this action creates a vacuum

that is detected on the room and send a signal to the butterfly valve that allows the volumetric flow of the natural gas. The temperature inside the dehydration room will be function of the climate conditions and the amount of natural gas burned per unit of time. The butterfly valve will increase/decrease the amount flow of natural gas in order to ensure the adjusted temperature set by the operator.

Table 3 describes the main machines and accessories that allow the operation of the plant. The technical characteristics such as electric consumption and hours of work per day allow the calculation of a electric consumption balance in order to known the electric energy availability that will feed the AE.

Table 3. Machines and Accessories in the plant.
(Hp = horsepower)

Machine/Accessory	Quantity
Butterfly Valve	3
Engine 30 Hp	1
Windmill 30 Hp	3
Mixer 15 Hp	1
Engine 10 Hp	1
Engine 3 Hp	3
Engine ¼ Hp	3
Blower ¼ Hp	2

Dehydration plant has an agreement with CFE (Comisión Federal de Electricidad) for energy supply of 100 kW/month of medium voltage. From the information in the Table 3 allows to make a maximum load analysis, the results are shown in the table 4.

Table 4. Maximum Load Analysis.

Machine	Quantity	Unit Power (kW)	Maximum simultaneous operation	Power demand (kW)
Engine 30 Hp	1	22.380	1	22.380
Windmill 30Hp	3	22.380	2	44.760
Mixer 15 Hp	1	11.190	-	-
Engine 10 Hp	1	7.4600	-	-
Engine 3 Hp	3	2.2400	1	2.24
Engine ¼ Hp	3	0.1860	-	-
Blower ¼ Hp	2	0.1860	2	0.372

From Table 4 it is possible to make an energy balance in order to know the quantity of energy available in the plant. The sum of the values of power demand provide the load that it is used in the dehydration plant and it is 69.75 kW from the rest of the total energy supply of CFE it is known the amount of electric energy free in the plant and it is 30.25 kW.

Another thing is really important in the operation process in order to ensure a good design. This consist in determine the frequency of use of the room dehydration process. In the Figure 5 it is presented the natural gas consumption reported in the plant.

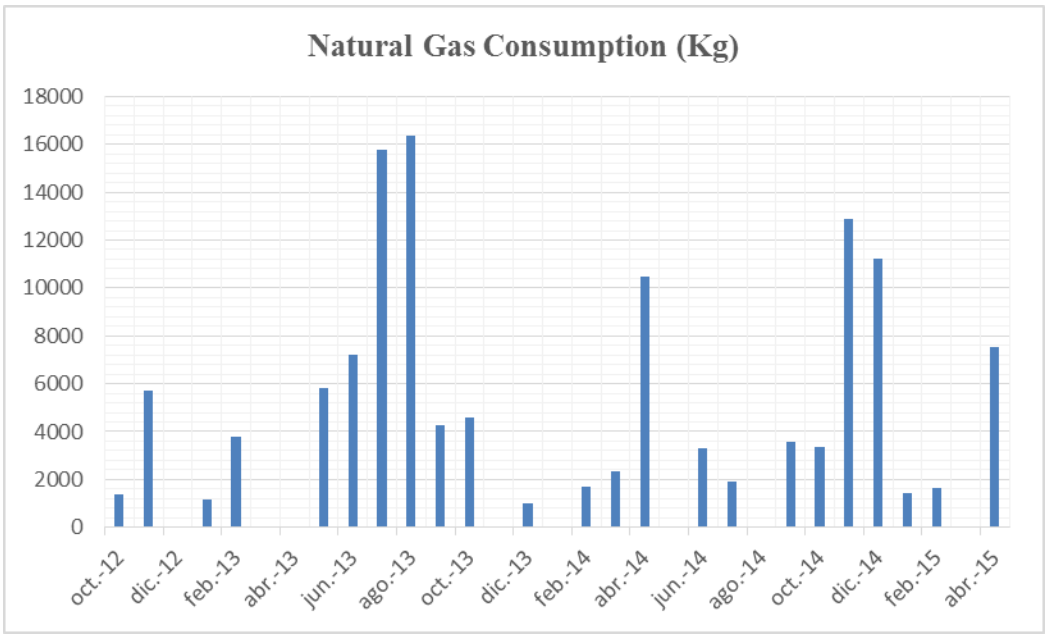

Fig. 5. Natural Gas Consumption in time.

The plant operators report that the consumption of natural gas per hour of operation is 27.5 kg. And the providers of natural gas report that the energy density of the natural gas that the plant consume is 46.29 MJ/kg. Figure 6 show images of the dehydration plant.

Fig. 6. Food dehydration plant. a) Blower b) Food.

3.3 Simulation Solution

Starting from the explanation of the correct use of the algorithm method for scaling alkaline electrolyzers and the current operation conditions of the dehydration plant it is possible to make a simulation of the alkaline electrolyzer required for the process. A proposal solution of the problem is to design the AE starting from the amount of free electricity energy of the plant. In that way the AE would be feed by the free load supply of CFE, in order to ensure that the process is sustainable, a photovoltaic system will be design

to return the amount of energy that the AE will be consuming. In order to determine the size of the photovoltaic system it is necessary to calculate the hours of use of the AE. From figure 5 and knowing that the consumption of natural gas per hour of operation is 27.5 kg, it is possible to know the operation hours of the burner per month, Figure 7.

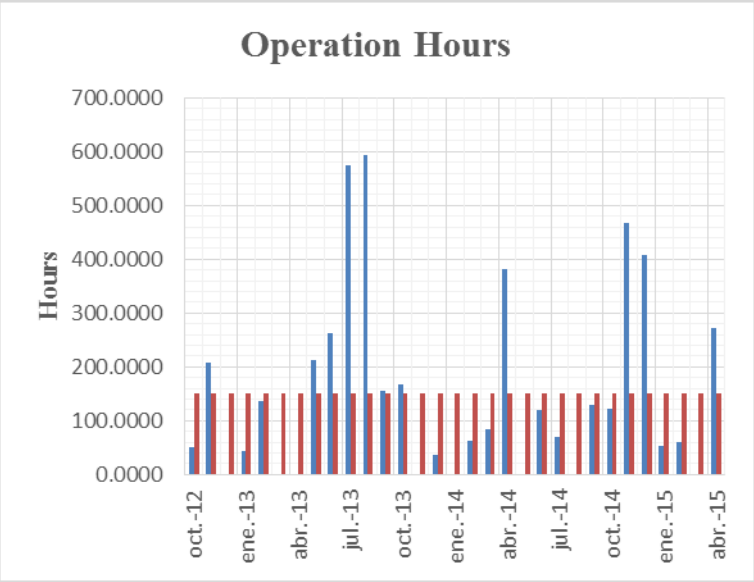

Fig. 7. Operation Hours of natural gas burner.

Figure 7 shows the non stationary operation conditions in the plant, due the fact that the plant works in function of the market and the clients. Blue bar indicates the operation hours of the natural gas burner per month and red bar indicates the average operation hours of the natural gas burner obtained from 31 months sampled. The average operation hours per month is 168 hours. For this first design proposal it is a good approximation. Due the fact that the plant have a month contract with CFE the photovoltaic system must be designed in order to feed the electricity consumption from the AE in that month. Following that logic we obtain 5040 kWh/month as the consumption of electricity that must be covered by the photovoltaic system.

Taking into account that the geographic location of the plant provides 5.72 hours of solar irradiation and considering the use of 300 W solar panels we can obtain the design of the photovoltaic system. The size of the photovoltaic system would be of 110 solar panels of 300 W each one, arranged in (11 parallel X 10 series), the amperage and voltage of the line would be of 90.2 A and 366 V.

The proper way to feed the AE simulated is by the use of equipment that can set values of amperage and voltage in order to create a steady state point of operation in the electrolyzer, for this reason it is proposed to use a direct current (DC) power supply, in the market it is common to find out power supplies with power supplies of 30 kW and is the best option because the higher values of power supplies, higher oxyhydrogen gas production and higher saving of natural gases.

Since the power supply in this paper is assumed to be of 30kW. It is possible to know the limits enrichment of natural gas with oxyhydrogen gas. From the technical characteristics of power sources of 30 kW enrichment limits were obtained starting from (4% to 6.2%). The selected enrichment will be function of the feeding amperage and voltage to AE. For this paper it is consider 78 A and 375 V as the correct values to set the operation point in the AE and represents a 5.4% of enrichment.

Due the fact that the AE will be working at 78 A and 375 V the AE simulated using the Algorithm Method for Scaling Alkaline Electrolyzers the size of the machine is determined. The effective area per electrode of the AE must be 390 cm^2, 3 times the size of the AE prototype. The number of cells would be of 130. The final dimension of the AE simulated would be of 55.3 height, 30 width and 334 thickness.

The main equipment for the proper operation of the AE and photovoltaic system are the next list.

- 30 kW Inverter (AC-DC)
- 300 W Solar Panel
- 30 kW Direct current (DC) power supply
- AE Simulated

4. Conclusion

- Starting from a lab prototype of Alkaline Electrolyzer and it electrochemical characterization it was obtained an Alkaline Electrolyzer simulated that theoretically enrich a natural gas line in 5.4%, the consumption of natural gas implicates a decreasing of greenhouse gas emissions.
- Using computational techniques as shown in this paper is possible to decrease the number of manufacturing needed to predict the equipment performance at different scaling levels referring first prototype design.
- Future works would develop a more strong computational algorithms in better software than Excel. It will do faster the calculation, also in different paths. For example, feeding different parameters as voltage and electrical current available on site to obtain maximum possible enrichment for some energy requirement.

Acknowledgements

This work has been supported by multidisciplinary project IPN-SIP 1683 and Programa Redes Temáticas CONACYT/RTH2.

References

[1] Das D., Veziroglu T.N. Hydrogen production by biological processes: a survey of literature. Int J. Hydrogen Energy 2001; 26:13-28.

[2] Vázquez-Larios A.L., Solorza-Feria O., Vázquez-Huerta G., Esparza-García F., Rinderknecht-Seijas N., Poggi-Varaldo H.M. Effects of architectural changes and inoculum type on internal resistance of a microbial fuel cell designed for the Treatment of leachates from the dark hydrogenogenic Fermentation of organic solid wastes. Int. J. Hydrogen Energy 2011; 36:6199-6209.

[3] Valdez-Vázquez I., Ríos-Leal E., Esparza-García F.J., Cecchi F., Poggi-Varaldo H.M. Semi-continuous solid substrate anaerobic digestors for H_2 production from organic waste: Mesophilic versus thermophilic regime. Int. J. Hydrogen Energy 2005; 30:1383-1391.

[4] Morse S.S. Factors in the emergence of infectious diseases. Emerg Infect Dis [serial online] 1995 Jan-Mar [cited 1996 Jun 5]; 1(1): [24 screens]. Available from: URL: http://www.cdc.gov/ncidod/eid/index.htm.

[5] Norman I.J. Redfern SJ, editors. Mental health care for elderly people. New York: Churchill Livingstone; 1996.

Chapter 5.9. Evaluation a stand-alone hybrid system PV-WT-FC and batteries in Mexico

A.M. Martínez-Bañuelos[a]; J. C. Jaime-Dominguez[a]; J. R. Espinoza-Lumbreras[a]; S. M. Durón-Torres[a*]; C. Guzmán[b]

[a]UACQ–UAZ, CU Siglo XXI Edificio 6, Km 6 Carr. Zac–Gdl, La Escondida Zacatecas, Zac, C.P. 96160, México.
[b]Facultad de Ingeniería, Universidad Autónoma de Querétaro, Cerro de las Campanas, C.P. 76000, Santiago de Querétaro, Qro., México.

ABSTRACT

The use of renewable energy sources such as solar radiation in photovoltaic (PV) and wind speed wind turbine (WT) to provide the energy demand in isolated places has been possible due to their use altogether, this type of system is known as hybrid power system. However one of the main problems with the isolated hybrid power systems is its intermittency due to fluctuating weather condition, For this reason sought different energy systems that can help power generation to achieve also have a stable power generation is very important.
For that reasson the objetive of this work was the use of fuel cells (FC) as a secondary power generation system, it is performed to compare a PV hybrid system of 1.2 kW, a WT of 900 W, laboratory feeding the load varies throughout the day, with a bank of batteries 48 V @ 450 Ah, and the same system by adding FC 1 kW and removing the battery bank and evaluation using a set system (FC, WT, FC and battery bank), which the electrical parameters (voltage and current) are monitored, so by implementing genetic algorithms, make decisions connect and disconnect systems, the system with more elements is the best performance because the fuel cell power to supplement the battery bank, and these allow stabilize the input voltage of the inverter.

Keywords: Hybrid system, Fuel cell

1. Introduction

Today global dependence on petroleum oils are high, so much so that the proven oil reserves are for the following 53.3 years [1]. In Mexico the situation is not very favorable in this sense, as the proven reserves are close to 10.6 years. One of the major economic and environmental problems encountered in this fuel is increasing its price for its imminent extinction, in addition to the pollution generated, which has a tangible impact on the world, for 40% of CO2 generation is thanks to the production of electricity in which this

---

*Author for correspondence: S. Durón, duronsm@prodigy.net.mx

hydrocarbon is used [2], [3], so the search for systems that can take advantage of other sources of energy has become one of the main research topics.

Renewable energy can meet the needs and avoid the problems mentioned above, but these systems have the problem of being intermittent and seasonal, so that a single system may not satisfy the needs of each location. It is therefore necessary to know the climatic and geographical conditions in order to make a proper choice of systems that will be used to supply the system demand. This type of system in which two or more technologies are used to obtain stable electric power are known as hybrid power systems. The analysis of economic, technical, control and efficiency of renewable energies such as solar and wind generators have viable results for installation [4]–[7]. Hybrid power systems have the advantage that can work under different conditions. Both may be in connection with public power grids or isolated as an autonomous system. The use of an autonomous hybrid system is a solution to avoid using any hydrocarbons for electricity generation, but these systems need storage systems that can ensure electrical stability required [8]–[10].

Energy storage may be accomplished by different technologies, one of them is based on the production of hydrogen obtained by electrochemical processes in water. The hydrogen is stored and then use in fuel cells (FC for its acronym in English) for electricity generation [11], [12]. The most important advantages in this type of storage is the efficiency of the process that is 40-60%, is a fuel extracted from water, which is an abundant and inexhaustible resource in the world, the combustion of hydrogen with air It is clean, thus avoiding contamination of the environment.

One of the problems with using a system with a hydrogen storage system is that the FC operation requires compliance with predetermined starting lapses, so that adequate control in the coupling of an FC to a wind hybrid system Solar should consider non-linear factors such as the energy consumption of the place [13], [14], which varies throughout the day and every day is a different behavior, making it necessary to find parameters that allow the systems to work together or disconnect any of the factors which enable a more efficient operation of the system, so a classic control system does not allow to consider all these parameters and make the system work optimally.

The use of fuzzy logic provides the basis for representing knowledge and the development of mechanisms to infer the essential decisions on appropriate actions to be taken to control a fuel cell. This structure is the most useful in practice. Human reasoning applies rules of such control. The number of fuzzy rules or statements to control a system varies greatly according to the complexity.

Fuzzy sets can be considered as a generalization of the classical ensembles, classical set theory only provides membership or non-membership of one element to a set, but the fuzzy set theory provides partial membership an element to a set ie each element has a degree of membership in a fuzzy set that can take any value between 0 and 1. This degree of membership is defined by the characteristic function associated with the fuzzy set Fig. 1.

Currently the programmable logic controller (PLC) is used in industry for control and for event based control of continuous processes by methods discrete time systems. This is due to the capabilities that have the PLC to process analog and digital signals. From this investigation it has detached from the constraints and the ability of the PLC for discrete control in a time shorts enough (real time).

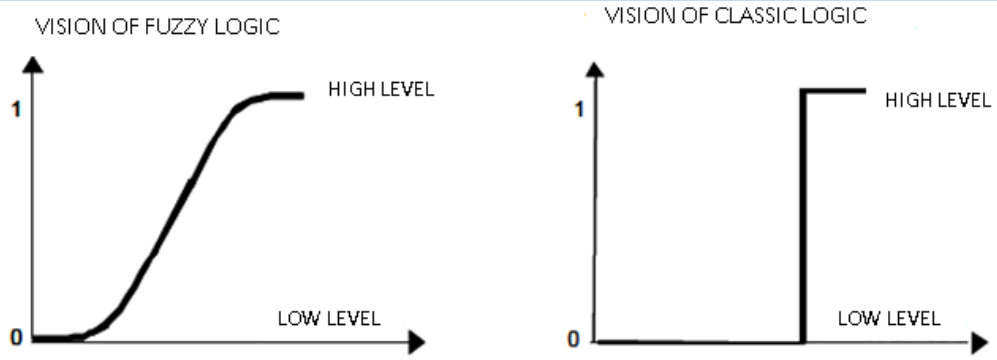

Fig. 1. Comparative Fuzzy Logic vs Classic

This in n can implement advanced controllers for complex industrial processes, taking advantage of the equipment installed, without requiring a special driver.

2. Materials and Methods

The hybrid systems studied has two types of technologies in the photovoltaic (PV's), solar panels mono-crystalline silicon and CIGS (copper, indium, gallium and selenium). These although each module has the same production capacity of 140 W operating characteristics vary between each module, as shown in Table 1

Table 1. Electrical characteristics of the PV modules

Technology	CIGS	Mono-Si
Maximum power (W)	140	140
Short circuit Current I_{sc} (A)	6.93	4.113
Open circuit voltaje V_{oc} (V)	38.7	42.96
Maximum power current I_{mp} (A)	5.44	3.88
Maximum power voltaje V_{mp} (V)	26	36.40

In each of the technologies has 6 modules which generate 840 W, due to its characteristics, it was decided to make the connection of a 2s x 3p arrangement modules mono-crystalline silicon and the connection used with the technology of CIGS it was decided that it was 3s x 2p as can be seen in Fig. 2.

These arrangements are placed in parallel with which a 1687.18W ideal total power, however the real power obtained was 1622.34 W, which due to this voltage peak power under CIGS has to adapt to the voltage panels mono-crystalline silicon, changing 78 V to 72.04 V (Table 2.).

Wind turbines perform the conversion of wind kinetic energy into electrical energy. The WT classification is related to the power generation capacity, which is considered the nominal power. A subdivision of small turbines is the micro-turbines (0-5 kW) and the mini-turbines (5-80 kW). In this paper, a commercial micro WT (Whisper 100) was coupled to the hybrid power system. This device is a horizontal axis WT (HAWT), and its technical specifications are described in Table 3.

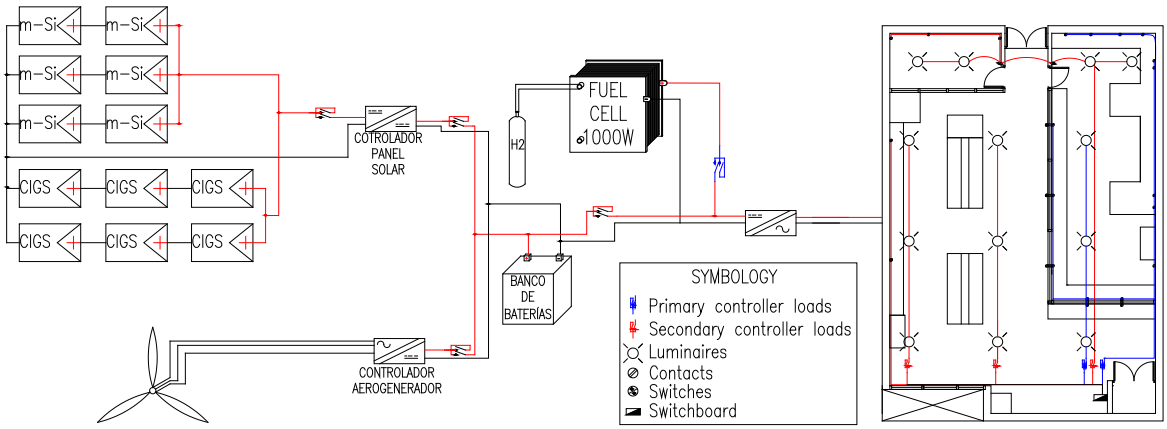

Fig. 2. Interconnection diagram of the hybrid system (Left), and electrical diagram showing the location of the drivers load (right).

Table 2. Electrical properties calculated for PV conection

Parameter	CIGS	Mono-Si	Total (Ideal)	Total (parallel)
Current (A)	10.88	11.64	22.52	22.52
Voltge (V)	78	72.04	72.04	72.04
Power (W)	848.64	838.54	1687.18	1622.34

Table 3. Technical specifications of the micro WT Whisper 100

Parameter	Specifications
Rotor diameter	2.1 m
Weight	21 kg
Start-up wind speed	3.2 m s^{-1}
Voltage	12, 24 36 48 V_{CD}
Rated power	900 W @ 12.5 m s^{-1} (28 mph)
Body	Cast aluminum
Blades	3- carbón reinforced fiberglass
Producion	100 kWh/mo @ 5.4 m s^{-1}
Survival wind speed	55 m s^{-1}

The storage system is using a battery bank, which consists of 8 Pb-acid batteries 6 V @ 360 Ah connected in series. Besides the hybrid system is to support a stack of FC 1 kW (Table 4), which comes into operation when the control program analyze meteorological and electrical parameters, so as to allow it to function as a backup for the hybrid system on controlled conditions.

Table 4. Technical specifications Fuel cell 1000 W

Parameter	Specifications
Type of fuel cell	PEM
Number of cells	48
Rated power	1000 W
Performance	28.8 V @ 35[a]
Reactants	Hydrogen and Air
External Temperature	5 – 30 °C
Max Temperatue stack	65 °C
H_2 pressure	0.45 - 0.55 bar
Dimension	21.9 x 26.8 x 12.3 cm
Flow rate at max output	13 L min^{-1}
Efficiency off stack	40% @28.8 V

3. Results and Discussion

To make an appropriate coupling for interconnecting the FC hybrid system so far has made the characterization of the same, using the methodology suggested by the manufacturer, as well as improvements in the hydration process and operation can be observed (fig. 3). The system with this procedure has a higher presented in the manual factory behavior.

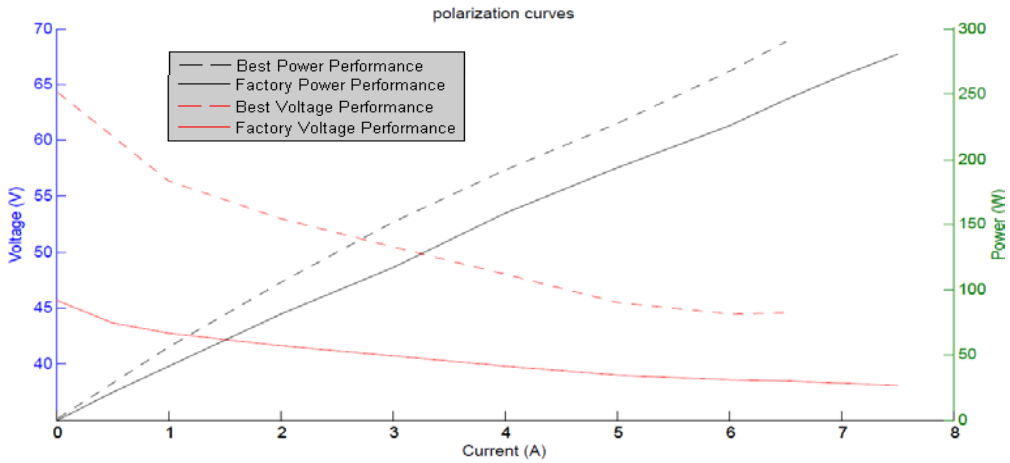

Fig. 3. Polarization curves of the fuel cell up to 300 W factory where the signal is compared with the best response of the system in operation.

A methodology was established to make an interconnection to the general system based on the operation of the FC, and the data that the fuzzy controller has to consider the methodology shown in Fig. 4 which is made using the LabView program as the basis for data collection and decisions, where only signals connection and disconnection of the FC system is expected, as well as determine the right time on and off.

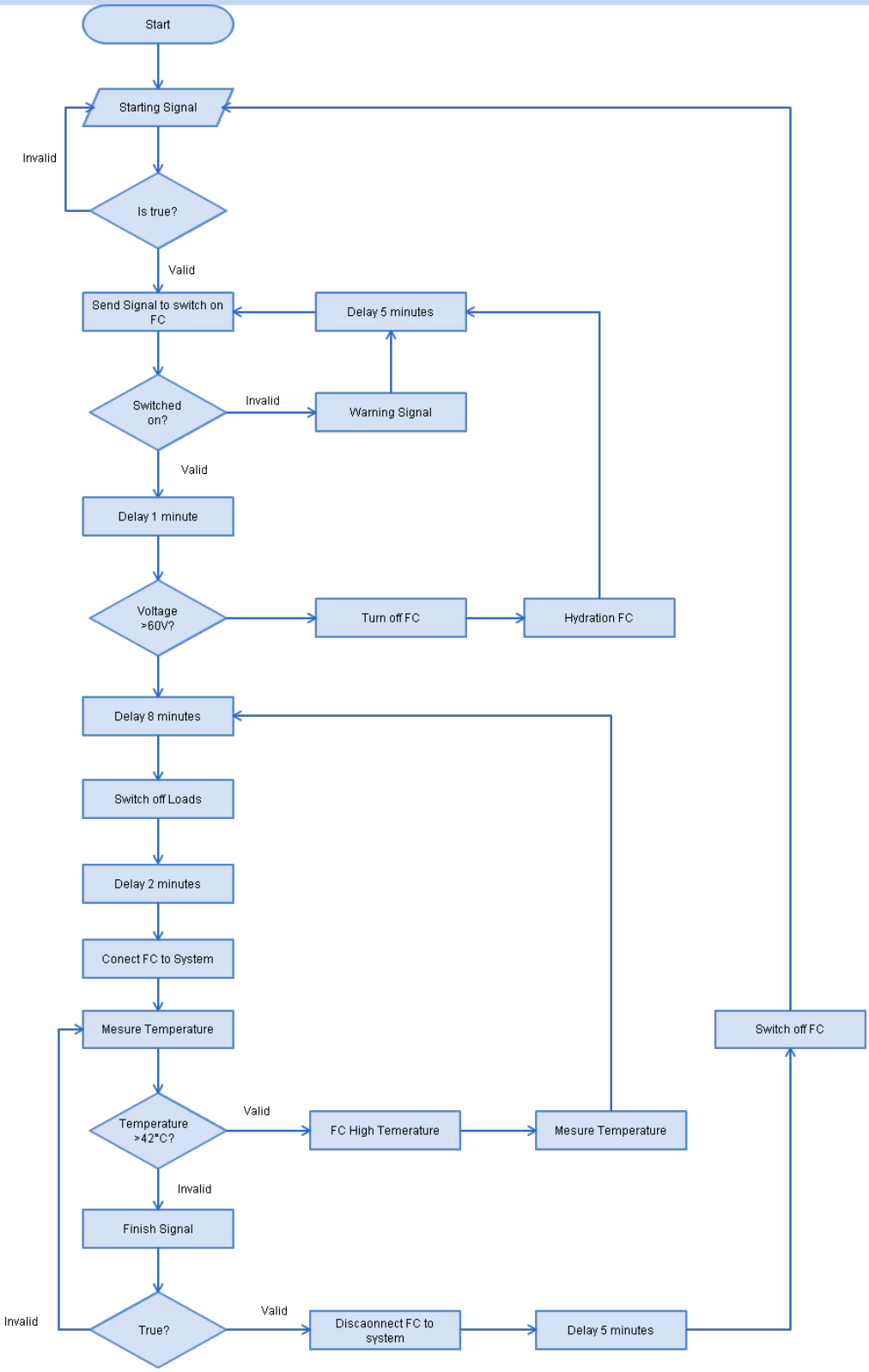

Fig. 4. Flow diagram of the hybrid system FC

4. Conclusion

The wind-solar-hybrid system battery bank has characterized their overall performance, while the fuel cell is characterized in its individual form, so that the work performed is the interconnection of the FC hybrid system, considering that the FC work as a backup system, for which the control will be performed using fuzzy logic based on solar radiation, state of charge (SOC) of the batteries and power consumption of the laboratory and based on this make the control system loads.

References

[1] bp.com/statisticalreview, «BP Statistical Review of World Energy June 2015». [En línea]. Disponible en: http://www.bp.com/content/dam/bp/pdf/Energy-economics/statistical-review-2015/bp-statistical-review-of-world-energy-2015-full-report.pdf. [Accedido: 14-ago-2015].

[2] S. Secretaría de Energía, «SECTOR ELECTRICO NACIONAL». .

[3] SENER, «Balance Nacional de Energía 2013», 2014. [En línea]. Disponible en: http://www.sener.gob.mx/res/PE_y_DT/pub/2013/Balance_2013.pdf. [Accedido: 14-ago-2015].

[4] A. U. Chávez-Ramírez, J. C. Cruz, R. Espinosa-Lumbreras, J. Ledesma-García, S. M. Durón-Torres, y L. G. Arriaga, «Design and set up of a hybrid power system (PV-WT-URFC) for a stand-alone application in Mexico», *Int. J. Hydrog. Energy*, vol. 38, n.º 28, pp. 12623-12633, sep. 2013.

[5] J. Lagorse, D. Paire, y A. Miraoui, «Sizing optimization of a stand-alone street lighting system powered by a hybrid system using fuel cell, PV and battery», *Renew. Energy*, vol. 34, n.º 3, pp. 683-691, mar. 2009.

[6] B. Guinot, B. Champel, F. Montignac, E. Lemaire, D. Vannucci, S. Sailler, y Y. Bultel, «Techno-economic study of a PV-hydrogen-battery hybrid system for off-grid power supply: Impact of performances' ageing on optimal system sizing and competitiveness», *Int. J. Hydrog. Energy*, vol. 40, n.º 1, pp. 623-632, ene. 2015.

[7] V. Dash y P. Bajpai, «Power management control strategy for a stand-alone solar photovoltaic-fuel cell–battery hybrid system», *Sustain. Energy Technol. Assess.*, vol. 9, pp. 68-80, mar. 2015.

[8] S. Diaf, M. Belhamel, M. Haddadi, y A. Louche, «Technical and economic assessment of hybrid photovoltaic/wind system with battery storage in Corsica island», *Energy Policy*, vol. 36, n.º 2, pp. 743-754, feb. 2008.

[9] M. S. Behzadi y M. Niasati, «Comparative performance analysis of a hybrid PV/FC/battery stand-alone system using different power management strategies and sizing approaches», *Int. J. Hydrog. Energy*, vol. 40, n.º 1, pp. 538-548, ene. 2015.

[10] W. Wu, V. I. Christiana, S.-A. Chen, y J.-J. Hwang, «Design and techno-economic optimization of a stand-alone PV (photovoltaic)/FC (fuel cell)/battery hybrid power system connected to a wastewater-to-hydrogen processor», *Energy*, vol. 84, pp. 462-472, may 2015.

[11] A. S. Joshi, I. Dincer, y B. V. Reddy, «Solar hydrogen production: A comparative performance assessment», *Int. J. Hydrog. Energy*, vol. 36, n.º 17, pp. 11246-11257, ago. 2011.

[12] P. Moriarty y D. Honnery, «Hydrogen's role in an uncertain energy future», *Int. J. Hydrog. Energy*, vol. 34, n.º 1, pp. 31-39, ene. 2009.

[13] N. Bizon, M. Oproescu, y M. Raceanu, «Efficient energy control strategies for a Standalone Renewable/Fuel Cell Hybrid Power Source», *Energy Convers. Manag.*, vol. 90, pp. 93-110, ene. 2015.

[14] A. Sakhare, A. Davari, y A. Feliachi, «Fuzzy logic control of fuel cell for stand-alone and grid connection», *J. Power Sources*, vol. 135, n.º 1-2, pp. 165-176, sep. 2004.

Chapter 5.10. Biological production of CO_2-free hydrogen by anaerobic microbial mixed microflora in an upflow anaerobic sludge blanket (UASB) reactor

I.M.M. Moreno-Dávila[a]; E.B. Herrera-Ramírez[a]; L.J. Ríos González[a*]; Y. Garza-García[a]

[a] Departament of Biotechnology, Facultad de Ciencias Químicas, Universidad Autónoma de Coahuila. Blvd V.Carranza y José Cárdenas Valdez, Col. República Oriente.Saltillo, Coahuila, México. CP 25280
Tel: +52 844 4155752, ext. 5. Fax: + 52 844 4159234

ABSTRACT

To satisfy the world's growing appetite for energy and keep our planet healthy, at least 10 TW (or terawatt) of carbon-free power has to be produced by mid-century The process described in the present work is a CO_2-free biohydrogen production in an upflow anaerobic sludge blanket (UASB). The reactor was fed with 400 ml of a mixed microbial consortium, which received acid-thermal pretreatment. The reactor was used for developed biofilms in 44 spheres covered with ixtle (natural material) , and was tested at a hydraulic retention time (HRT) of 3 h using 4 L of mineral medium with glucose concentration of 20 g L^{-1}, at initial pH 5.0 and 18°C. The hydrogen produced was sent to a gas purification device in which H_2 is passed through a 2M NaOH solution, this is to obtain CO_2-free biohydrogen. The cumulative hydrogen production in the purification system was 52.30 mmoles/h*gSV at 230 h of fermentation. In this process was not detected carbon dioxide; and there was no methane generation due to the methanogenic pathway was inhibited, to produce hydrogen. The system had a efficiency of 81.2% in the consumption of the substrate, which for this fermentation was a synthetic medium with glucose.

Keywords: CO_2-free biohydrogen, Anaerobic sludge blanket reactor, Biofilms

1. Introduction

The current global energy demand is mostly dependent on reserves of fossil fuels, wich are depleting, and the world is facing severe pollution problems from the by-products of fossil fuels uses [1]. The scientific community has widely accepted the fact that the increasing CO_2 level due to the use of fossil resources is impacting the greenhouse gas effect and global warming. Therefore, different ways to harness the energy from clean

---

* Author for correspondence:
Leopoldo Javier Ríos González, Tel: +52 844 4155752, ext. 5. Fax: + 52 844 4159234
Email: leopoldo.rios@uadec.edu.mx

renewable sources are being developed, but the search for reliable energy sources is stillon [2].

Hydrogen gas is a clean energy carrier with a high energy content of 122 kJ g1 [3].Currently, hydrogen gas is expensive compared to other conventional energy sources because of the high-cost energy requirements for its widely used production methods.

Dark fermentation is the most studied and promising biological technology for biohydrogen production owing to its higher production rates and treatment capacity for organic wastes [4]. H_2 synthesizing bacteria exist commonly in environments such as soil, wastewater sludge and compost. All these materials can thus be used as an inoculum for fermentative H_2 production [5]. A large variety of materials, including glass beads, expanded clay, activated carbon, ceramic fittings and many types of synthetic polymeric materials, were tested as carrier materials for biomass growth. The bioreactor was filled with forty-four spheres wrapped with ixtle fiber, as natural support to the growth of H_2 producing microflora formation of biofilm.

This study presents biological production of CO_2-free hydrogen by anaerobic microbial mixed microflora in an upflow anaerobic sludge blanket (UASB) reactor, using a simple system of purification.

2. Materials and Methods

2.1. Construction details of the simple device for hydrogen collection

In the hydrogen purification and collection system (Fig. 1) for obtaining CO_2-free bio-H_2, the evolved H_2 gas from fermenter is collected and measured by displacement of 2 M NaOH in an inverted cylinder. NaOH solution was used to absorb $C0_2$ for purification [6].

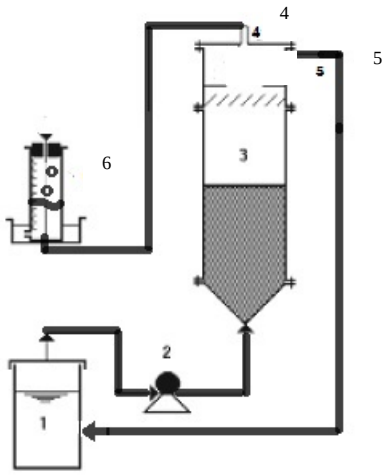

Fig.1. Diagrammatic representation of the simple gas purification and collection system for CO_2-free-H_2 production: 1) Influent tank; 2) Peristaltic Pump; 3)UASB Reactor; 4)Gas outlet; 5)Effluent outlet; 6)Gas collection system and measurement of the displaced liquid.

2.2. Type of inoculum and pretreatment.

Anaerobic microbial mixed culture (500 ml) was obtained from a upflow anaerobic sludge blanket (UASB) reactor that treated wastewater from brewery Modelo (Zacatecas, Mexico). Pretreatment was carried out as describe by Chen and Hu [7]. Sludge was macerated and was subject to heat pretreatment; it was heated in boiling water bath for a short period of time (30 min) first and then, cooled down. Heat pretreatment was followed by acidic pretreatment that involved decreasing the pH of the sludge or granule solution to 3.0 using 0.1 N HCl solution for 24 h and a readjustment of pH back to 7.0 by 0.1N NaOH solution.

2.3 Carrier material for biofilm growth

Two meters of ixtle fiber with an approximated diameter of 2.24 mm were used to wrap forty-four plastic balls of 25.54 mm of external diameter, and they were used for biofilm growth on the surface of the natural carrier material.

2.4.Dark fermentation and gas purification and collection.

Hydrogen gas production by anaerobic microbial mixed microflora from glucose at the concentration of 20 g L^{-1} was monitored. The continuous hydrogen production experiment were conducted an upflow anaerobic sludge blanket (UASB) reactor was conducted at 18°C in a 4 L fermenter. A 5 L (working volume 4 L) UASB reactor contained 400 mL of pretreated anaerobic sludge (0.2408 gL^{-1} VSS), sixty pretreated spheres. Reactor was fed by peristaltic pump (Manostat – division of Barnant Company, Simon varistaltic pump, USA. The composition of the medium (mg per liter) was as follows: glucose 20,000 (as the sole carbon source); NH_4Cl, 2,000; $NaHCO_3$, 6,720; K_2HPO_4, 125; $MgCl_2{\cdot}6H_2O$, 100; $MnSO_4{\cdot}6H_2O$, 15; $FeSO_4{\cdot}7H_2O$, 25; $CuSO_4{\cdot}5H_2O$, 5; $CoCl_2{\cdot}5H_2O$, 0.125 [5]. The pH was adjested to 5.0 using 3M HCl. The reactor was operated at a hydraulic retention time of 3 h. The reactor was used for developed biofilms in 44 spheres covered with ixtle (natural material.The evolved H_2 was collected from the reactor using a simple collection system for obtaining co2-free-bio-H_2 gas.

2.5 Analysis

2.5.1 Measuring of hydrogen and methane gas

Hydrogen and methane was measured by gas chromatography equipped with a thermal conductivity detector (VARIAN 3400) and a CP Molecular Sieve 5A Capillary Column (VARIAN). GC conditions were as followed: injector and detector temperatures 200ºC and column temperature 50°C, using Argon as carrier gas with flow rate 10 mL $min^{-1.}$

2.5.2 Analysis assessments

pH was determined by pH meter (HI 2550, HANNA instruments). Standards Methods [8] were used to determined biomass concentration (in terms of volatile suspended solid; VSS). Samples were first centrifuged at 10000 rpm for 10 min. Reducing sugar content was estimated using 3,5-dinitrosalicylic acid colorimetric method (DNS method) [9].

3. Results and Discussion

Major hydrogen producing microorganisms are in anaerobic sludges, however, sludge may contain consumers like methanogens, homo-acetogens, and non-hydrogen producers such lactic acid bacteria and Bacillus sp. reducing hydrogen production [10].Many pre-treatment methods were reported in the literature [11]. Kargi et al. [12] reported that heat pre-treatment may be effective in eliminating hydrogen consuming methanogens. In this study two pre-treatment methods were reported such as heat shock and acid-base treatment for elimination of hydrogen consumers, and analysis of biogas liberated of fermentation in this study was only composed of H_2 and carbon dioxide (CO_2) and no CH_4 was detected.

Table 1. Composition of liberated gases of Biological production of CO_2-free hydrogen by anaerobic microbial mixed microflora in an upflow anaerobic sludge blanket (UASB) reactor

Time (h)	H_2 Production Mmoles/h* g SV	CO_2 moles in reactor UASB	CO_2 moles in simple system of purification	CH_4 in reactor UASB	Reducing sugars (mg/L)	pH
0	0	0	0	0	21486.2	5
13	62.39	0.0017	0	0	18607.9	5.65
36.5	51.53	0.0020	0	0	14973.7	4.77
66.5	37.85	0.0021	0	0	11575.0	4.45
86.5	19.48	0.0022	0	0	10680.8	4.25
108.5	13.95	0.0022	0	0	9815.8	3.92
158.5	9.11	0.0027	0	0	10680.8	---
205.5	5.59	0.0027	0	0	---	3.55
229.5	4.49	0.0029	0	0	3908.8	3.46
				Efficiency	81.81%	

The maximum hydrogen production rate was reached after 13 h of fermentation [Fig.2], similar results were obtained by Morsy [6], where the maximum hydrogen production rate of *C. acetobutylicum* and in mixed cultures reached after 10 h of fermentation[6].
Several studies were performed using synthetic solutions prepared with tap water and simple sugars (glucose and sucrose) as the main carbon source, with the addition of nutrients (P and N) and micronutrients (Fe, Ca,Cu, Mg, Mn, Zn, and others) which are usually required for bacterial growth and activity (Hawkes et al., 2007); Substrate conversion ranged from 22% to 100% for APBRs, and from 7.2% to 99.9% for AFBRs [5]; in this study results of 88% of substrate conversion in UASB reactor were obtained for glucose [Fig. 3].

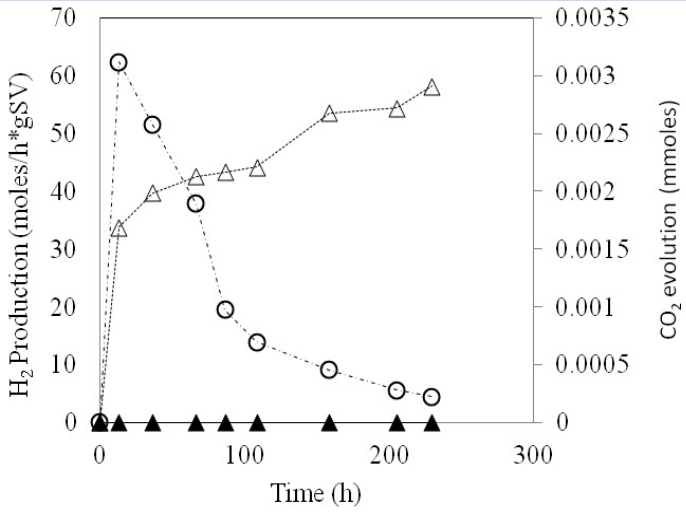

Fig.2. Hydrogen gas production (open circles) as well as CO_2 evolution among the UASB reactor (open triangles), and simple spurification system (closed triangles).

The pH is one of critical parameters affecting biological hydrogen production because pH affects the metabolic pathway of hydrogen-producing organisms. Most studies on the maximum hydrogen yield proposed a low pH between 5 and 6 [5], because the methanogenic activity is limited to a narrow pH between 6.5 and 7 . In terms of practical applications, it is important to determine on how the initial influent pH affects hydrogen production when there is no pH control during hydrogen fermentation. Optimum pH for CO_2-free bio-H_2 by anaerobic microbial mixed microflora was 5.65 [Fig.3],

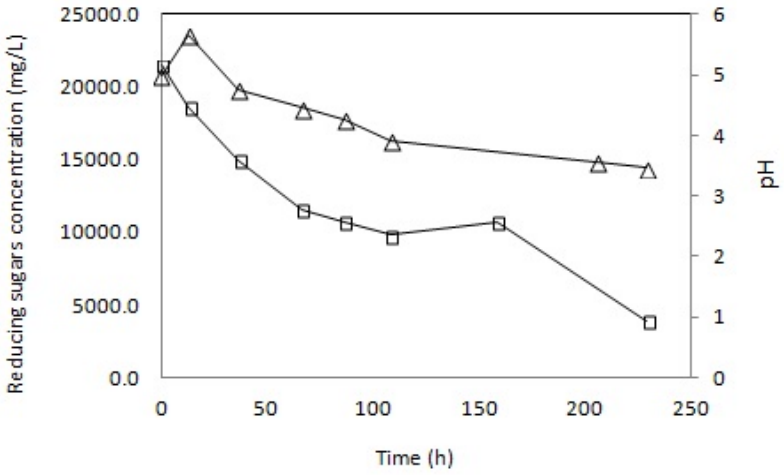

Fig.3. Change in pH (open triangles) and degradation of substrate (open squares) in UASB reactor for CO_2-free hydrogen production.

4. Conclusion

In this study production of CO_2-free hydrogen production was developed by anaerobic mixed cultures in an anaerobic upflow reactor using a simple H_2 gas collection and purification system. This suggests using mixed cultures in UASB reactor with two pre-treatment methods such as heat shock and acid-base treatment for elimination of hydrogen consumers, obtaining analysis of biogas liberated of fermentation composed only of H_2 and carbon dioxide (CO_2) and no CH_4 was detected. Analysis of biogas after purification system no CO_2 was detected. Furthermore, good efficiency degradation of the substrate was obtained .

Acknowledgements

The authors would like to thank the National Science Council of México, for financially supporting this research.

References

[1] Marbán G, Valdés-Solís T. Towards the hydrogen economy? Int J Hydrogen Energy 2007;32:1625–37.
[2] Ghimirea A., Frunzoc L., Pirozzi F., Trably E., Escudie R., Lens P., Espositoa G. A review on fark fermentative biohydrogen production from organic biomass:Process parameters and use of by-products.Applied Energy 2015; 144:73-95.
[3] Kapdan IK, Kargi F. Biohydrogen production from waste materials. Enzyme Microb Technol 2006;38:569–82.
[4] Das D, Veziroglu T. Advances in biological hydrogen production processes. Int J Hydrogen Energy 2008;33:6046–57.
[5] Barca C., Soric A., Ravana D., Giudici M., Ferrasse J. Anaerobic biofilm reactors for dark fermentative hydrogen production from wastewater: A review. Bioresource Technology 2015;185:386-98.
[6] Morsy F.CO_2-free biohydrogen production by mixed dark and photofermentation bacteria from sorghum starch using a modified simple purification and collection system.Energy 2015; 87:594-604.
[7] Chen S., Hu B. Pretreatment of methanogenic granules for immobilized hydrogen fermentation. Int J Hydrogen Energy 2007; 32 (15): 3266-3273.
[8] APHA, Standard Methods for the Examination of Water and Wastewater, American Public Health Association, New York, U.S.A. (1995).
[9] M. Dubois, K.A. Gillesa, J.K. Hamilton, P.A. Rebers, F. Smith, Anal Chem. 1956; **28,** 350-356.
[10]Heyndrix M, De Vos P, Hibau B, Stevens P, De Ley J. Effect of various external factors on the fermentative production of hydrogen gas from glucose by Clostridium butyricum strains in batch culture. Syst Appl Microbiol 1987;9:163e8.
[11]Zumar M., Mohee R., Hassan M. Effects of pre-treatment technologies on dark fermentative bio-hydrogen production: A review. Journal of Environmental Management 2015;157: 20-48.
[12] Kargi F., Argun H. Effects of sludge pre-treatment method on bio-hydrogen production by dark fermentation of waste ground wheat.Int. J Hydrogen Energy 2009; 34:8543–8548.
[13] Hawkes F., Hussy I., Kyazze G., Dinsdale R., Hawkes D. Continuous dark fermentative hydrogen production by mesophilic microflora: principles and progress. Int J Hydrogen Energ. 2007;32 (2): 172–184.

Chapter 5.11. Effect of the phenolic compounds in the sugar cane bagasse saccharification for the lignocellulosic ethanol production

E. González-Bautista[a]; J. C. Santana-Morales[a]; A. C. Ramos-Valdivia; H. M. Poggi-Varaldo[a]; T. Ponce-Noyola[a,*]

[a]Departamento de Biotecnología y Bioingeniería. Centro de Investigación y de Estudios Avanzados del Instituto Politécnico Nacional, México, D.F., C.P. 07360.

ABSTRACT

One of the most important steps for the production of second-generation ethanol from agro-industrial waste is the saccharification process. However during enzymatic hydrolysis, secondary metabolites of phenolic nature are released which are part of the lignin structure in the plant cell walls. This phenolic compounds work such as auxins compounds which are capable of inhibiting the growth of microorganisms when inhibit enzymes such as holocellulases. In this way a pretreatment should remove these inhibitory compounds. However even after pretreatment phenolic compounds still remain that may negatively affect the enzymatic activity. There are certain soluble polymers that can prevent such inhibition by their physicochemical properties and their ability to chemical-adsorb phenolic compounds in their structure. In this work we studied the capacity of polyethyleneglycol (PEG) and polyvinylpyrrolidone (PVP) to prevent enzyme inhibition of xylanases and CMCases of *Cellulomonas flavigena* strain PR-22 during saccharification of sugar cane bagasse pretreated with sodium hydroxide (NaOH). We evaluated the inhibition effect of phenolic compounds on the enzymatic activity of xylanases and CMCases. For this purpose a concentrated extract whit phenolic compounds was prepared from the hydrolysis of raw sugarcane bagasse. This extract was added to the reaction mixture at different concentrations and then we analyze the remaining activities of xylanases and CMCases after incubating at optimal conditions for each enzyme activity. We found 77% inhibition of xylanase activity with 100 µg of phenolic compounds and 66% in CMCase activity with 50 µg of phenolic compounds. PEG and PVP were added at 0.4% (p/v) to *C. flavigena* PR-22 cultures growning in sugarcane bagasse in order to avoid the effect of inhibition of the phenolic compounds. The addition of PEG avoid CMCase inhibition by phenolic compounds obtaining 92% of the original activity after the saccharification, while in the negative control this activity only reached 44%. On the other hand the PVP favor the xylanase activity in 62% and in the negative control only got 30% of the original activity. Cultures where PVP was added, accumulated 34% more reducing sugars than in control cultures, while cultures with PEG produced 30% more than its negative control.

Keywords: Ethanol production, Phenolic compounds, Saccharification, Holocellulases

---

* Author for correspondence:
Dra. Teresa Ponce Noyola, T.:5255 5747 3800 ext. 4317, E: tponce@cinvestav.mx

1. Introduction

Phenolic compounds are molecular structures containing at least one phenol group. These compounds are components of the lignin and are part of the plant cell wall. They possess the biological characteristic of being secondary products of the metabolism acting as phytoalexins, also contribute to pigmentation in some cases [1,2]. They are generally synthesized by one of two biosynthetic pathways: the shikimic acid pathway or route of malonic acid.

Phenolic compounds are associated with tannins and lignin particles and have the capability to absorb proteins and can deactivate cellulolytic enzymes [3]and β-glucosidases during the hydrolysis of microcrystalline cellulose [4]. Phenols including coumaric, galic and ferulic acids and tannins are released during pretreatments of lignocellulosic biomass [5]. Some polymers, as polyvinylpyrrolidone, have the capability to adsorb phenolic compounds in their structure; this polymer plus clay adsorves phenolic compounds from solution as high as 98.9% of the phenolic compounds [6].

In this work, we assayed the effect of the phenolic compounds released during the saccharification of sugarcane bagasse, over xylanase and CMCase activities of *C. flavigena* PR-22. Also we evaluated the effect of addition of PVP and PEG over the xylanase and CMCase activities and reducing sugars production before and after the saccharification process.

2. Materials and Methods

2.1. Enzyme inhibition by phenolic compounds

The inhibitory effect of phenolic compounds over holocelulase activity from *C. flavigena* PR-22 were evaluated. The enzymes were produced using a culture of *C. flavigena* PR-22 growing in mineral medium (MM) (Ponce-Noyola [7]) and Solka floc as a carbon source. To obtain the phenolic compunds, *C. flavigena* PR-22 on mineral medium supplemented with 3% of bagasse the conditions were: 37°C for 24h at 150 rpm after that the temperature was changed to 50°C for another 24 hours, the culture was centrifuged at 10,000 rpm for 10 minutes the supernatant was precipitated with trichloroacetic acid (TCA) 12% and neutralized with 1N KOH. Phenolic compounds were evaluated usign Folin-Ciocalteu´s phenol reagent 1N. Different concentrations of phenolic compounds (10, 20, 30, 40, 50, and 100 µg/mL were added to enzyme solution. We determinated the remaining activity of xylanases and CMCases after the interaction with the inhibitor.

2.2. Enzymatic protection of PVP and PEG

The enzymatic protection capacity of Polyvinylpyrrolidone (PVP 40) polyvinylpyrrolidone (PVP 360); insoluble polyvinylpyrrolidone (PVPP) and polyethylene glycol (PEG) was assayed. Polymers were added to *C. flavigena* PR-22 cultures. Xylanase and CMCase activities and total reducing sugars [8] (Miller, 1959) were evaluated after enzyme production process. For the saccharification process, teen stainless steel beads of 4 mm of diameter were added for the release of intracellular β-glucosidase and 3% of pretrated sugarcane bagasse. We determined the remaining enzyme activities (xylanases and CMCases), β-glucosidase activity [9], total phenolic compounds [10], and total reducing sugars produced.

2.3. Identification of phenolic compounds by thin layer chromatography

Phenolic compounds were extracted from crude sugarcane bagasse. Four g of ground substrate (mesh 60) was extracted with methanol:water (8: 2 v/v) ,then organic phase was recovered by centrifugation at 10,000 rpm for 5 minutes. One mL of the supernatant was concentrated in a speedvac Eppendorf 5301 for 1 h. The concentrated sample was resuspended in 50 mL of methanol and 50 mL of sample were placed on a plate of silica gel using chloroform:methanol:formic acid (85: 15: 1) as the mobile phase. The chamber was saturated with the mobile phase for 5 min and the silica plate is placed for 15 min. The plate was derivatized with (NP/PEG) 2-aminoethyl diphenilborinate 1% and 5% PEG 3350, (SIGMA). The phenolic compounds were revealed using a UV lamp at 365 nm.

2.4. Identification of the phenolic compounds by HPLC

Identification of the phenolic compounds was performed on a HPLC (Agilent Technologies). It was used 20 uL of sample that was previously filtered through to a 0.45 µm acrodisc (PALL). Separation was performed on a ZORBAX Eclipse XDB-C18 4.6 x 150 mm, 5 µm column using an isocratic method. The mobile phase consisted of methanol and water (50:50) with 200 mL of phosphoric acid with a flow rate of 0.8 mL/min for 20 min.

3. Results and Discussion

The inhibition of the enzymatic activity of xylanases and CMCases by phenolic compounds was evaluated at diferent concentrations of phenolic compounds. It was observed that 100 µg/ml of phenolic compounds inhibited 77% xylanase activity while 50 µg/ml inhibited 64% of CMCase activity (Fig. 1).

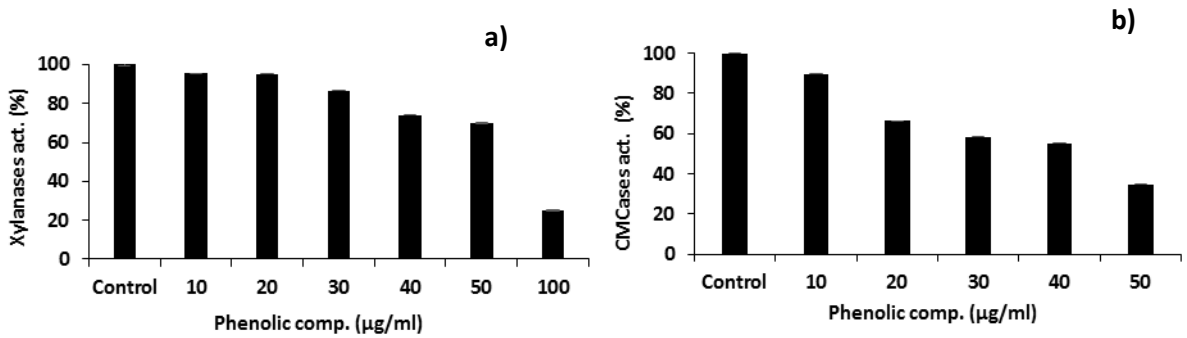

Fig 1. Inhibition tests: (a) inhibition of xylanases; and (b) CMCases by phenolic compounds.

We assayed diferent polymers to reduce the inhibitory effect of phenolic compounds over xylanase and CMCase activities in cultures of *C. flavigena* PR-22. The reducing

sugars and xilanases and CMCases activities at the begining and end of the saccharification process were evalued**.** When PVP 360 was added, the best production of reducing sugars was achieving reaching 45% more than the control. The xylanase activity increased 47% respecting to initial value, when PVP 40 was added, and 54% in the remaining activity using PVP 360 at the end of the saccharification. In the case of the CMCase activity, the addition of PEG in the culture practically protect 100% of the enzyme activity (Fig. 2).

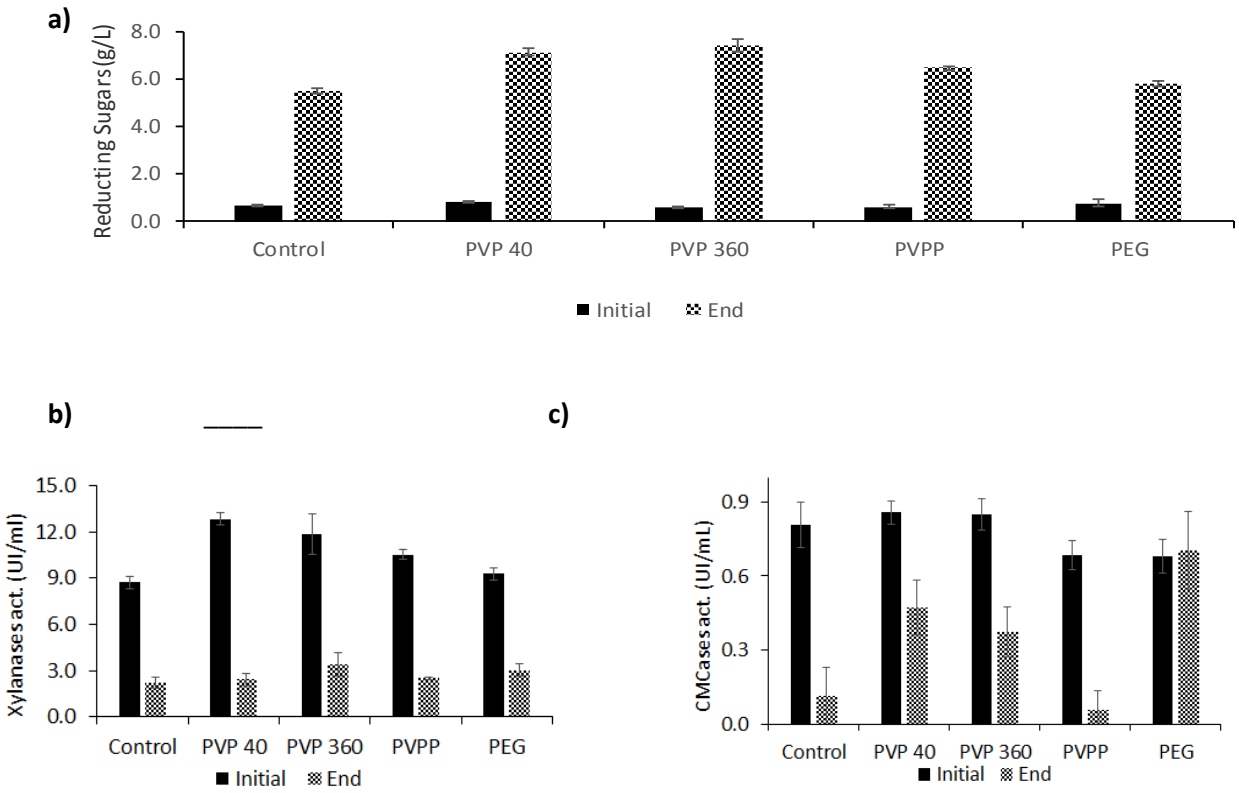

Fig. 2. Evaluation of the parameters before and after the saccharification adding PVP 40, PVP 360, PVPP and PEG on each cultures of *C. flavigena* PR-22: (a) Reducing sugars; (b) Xilanases; and (c) CMCases

The remaining β-glucosidase activity increased approximately 350% adding PVP 360 in the saccharification process (Fig. 3).

The main phenolic compounds identificated in the raw sugarcane bagasse by TLC were ferulic, cinamic, clorogenic and protocatequine (line C) (Fig. 4)

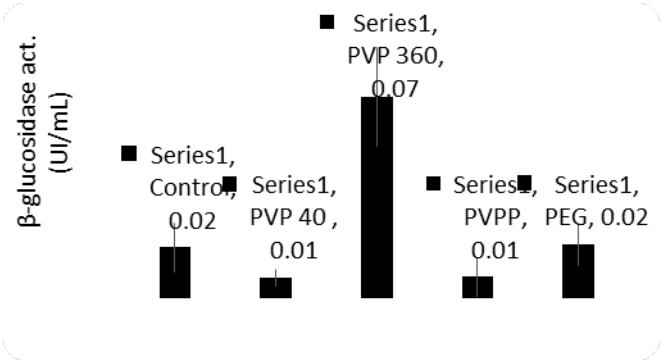

Fig. 3. β-glucosidase activity remaining in the saccharification adding different polymers

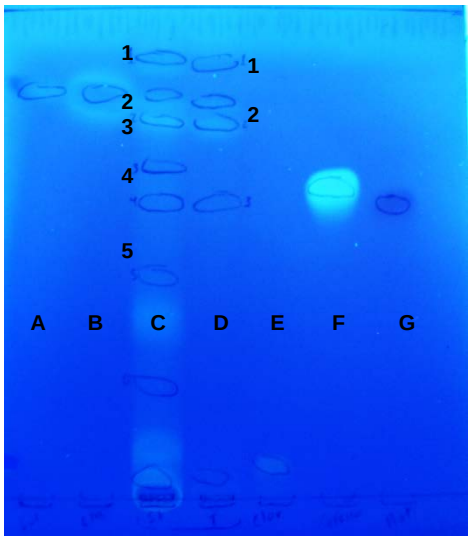

Fig. 4. Identification by TLC of phenolic compounds present in raw sugarcane bagasse

On the other hand the efficiency of the alkaline pre-treatment (1.5% NaOH) to remove lignin from the sugarcane bagasse was evaluated. It was observed that 70% of phenolic compounds were removed. Cinnamic acid is the only one compound that not decreased after the pretreatment (Fig. 5).

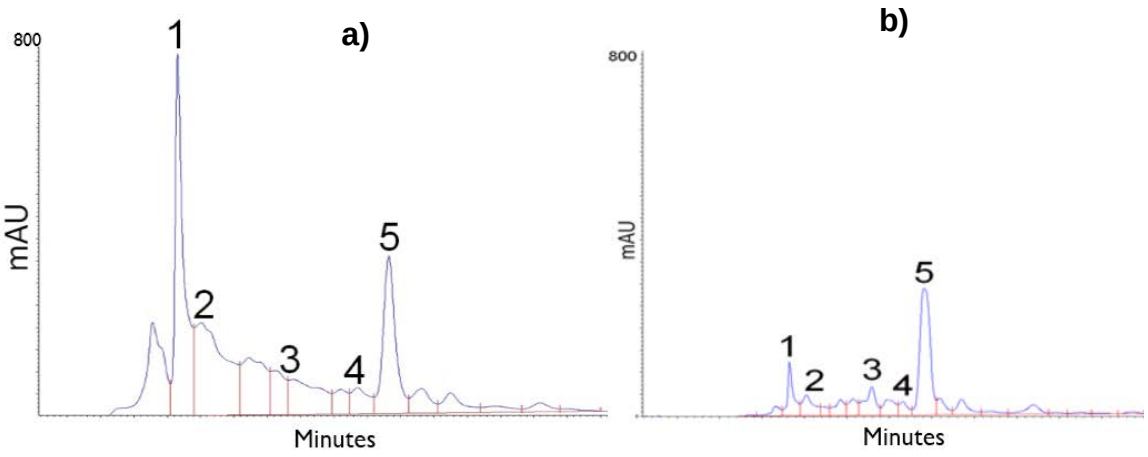

Fig.5. Phenolic compounds in (a) raw; and (b) pretreated sugar cane bagasse bagasse. Peaks (1) Gallic acid, (2) Chlorogenic acid, (3) Caffeic acid, (4) Coumaric acid, (5) Cinnamic acid.

4. Conclusion

Galic acid, chlorogenic acid, caffeic acid, coumaric acid and cinnamic acid were the main phenolic compounds identified in the sugarcane bagasse.

CMCase activity was 65% inhibited by 50 µg/ml of phenolic compounds while 100 µg/ml of these compounds inhibited 75% of xylanase activity but polymers like PVP 360 and PEG adsorbed the phenolic compounds protecting the enzymes activities. PVP 360 allowed to obtain 61% more reducing sugars in the saccharification compared with the control, since this polymer protect xylanase and CMCase activities from phenolic compounds inhibition.

Acknowledgements

This work was funded by CONACyT with the Project No. 236895. CONACYT also granted a graduate scholarship to EGB.

References

[1] Gimeno C. E. (2004). Compuestos fenólicos, un análisis de sus beneficios para la salud. OFFARM 23 (6):81.
[2] Pan X. (2008). J Biobased Mater Bioenergy. 1: 25–32.
[3] Palmqvist J, Meinander Q, Grage H., Hahn- Hagerdal B (1999) Biotechnol. Bioeng. 63, 46–55.
[4] Ximenes E, Youngmi K, Mosier N, Dien B, Ladisch M. (2011). Deactivation of cellulases by phenols. Enzyme and Microbial Technology 48: 54–60.
[5] Chen SF, Mowery RA, Scarlata SC, Chambliss CK (2007). Compositional analysis of water-soluble in corn stover. J Agric Food Chem. 55(15):5912-5918.

[6] Ahmet G, Turgay S, Yunus O, Galip M. (2000). Preparation and phenol captivating properties of polyvinylpyrrolidone-montmorillonite. Hybrid Materials 81(2):512 – 519.
[7] Ponce-Noyola, M.T. Obtención y caracterización de una mutante de *Cellulomonas flavigena* de alta velocidad específica de crecimiento en bagazo de caña. Sc D Thesis, 1992. Tesis doctorado ENCB-IPN, Mexico City, Mexico.
[8] Miller G. (1959) Use of dinitrosalicylic acid reagent for determination of reducding sugar. Anal Chem. 31:426-428.
[9] Kim H K, Pack M Y (1989) Cloning and expression of *Cellulomonas fimi* β-glucosidase genes in *Escherichia coli*. Enzyme Microb Technol. 11: 313-316.
[10] Singleton VL, Orhofer R, Lamuela-Raventos RM (1999). Analysis of total phenols and other oxidation substrates and antioxidants by means of Folin-Ciocalteau reagent. Methods Enzymol. 299:152–178.

Chapter 5.12. Microbial fuel cells equipped with low cost membranes for the treatment of leachates from biohydrogen production

G. Hernández-Flores[a]; H. M. Poggi-Varaldo[a,*]; O. Solorza-Feria[b]

[a]Environmental Biotechnology and Renewable Energies R&D Group, Dept. of Biotechnology and Bioengineering, Centro de Investigación y de Estudios Avanzados del Instituto Politécnico Nacional. Av. Instituto Politécnico Nacional 2508, Col. San Pedro Zacatenco, Delegación Gustavo A. Madero, México D.F., C. P. 07360 Apartado Postal: 14-740, 07000 México, D.F.
[b]Dept. of Chemistry, *ibídem.* Av. Instituto Politécnico Nacional 2508, Col. San Pedro Zacatenco, Delegación Gustavo A. Madero, México D.F., C. P. 07360 Apartado Postal: 14-740, 07000 México, D.F.

ABSTRACT

The aim of this work was to compare the performance of microbial fuel cell (*MFC*) fitted with alternative, low cost membranes (*AM*s). Lab scale single chamber *MFC*s were loaded with sulfate-reducing inocula as biocatalyst and leachate from dark fermentation of organic wastes as substrate. The *MFC*s were fitted with either an agar membranes *M2* (2% agar), *M6* (6% agar), a hybrid membrane made of agar and Nafion *MH*, or the control Nafion 117 membrane (*NF-117*).
We found that the internal resistances (R_{int}) were generally low for all the cells. The lowest R_{int} corresponded to alternative membranes *M6* and *MH* with a value *ca.* 90 Ω So, results of R_{int} tend to favour the *AM*s. The costs of these membranes were only 2.5 to 6% of the cost of the *NF-117* one. However, the powers delivered by *MFC* fitted with *AM*s were 4 to 40% (weighed average 28%) of the power of the cell fitted with the conventional *NF-117*. In spite of the reduced power, the *AM*s still exhibited a higher Power/Cost ratio (0.9 to 4.4. mW/US$) than that of the *NF* membrane (0.23 mW/US$.)
We should highlight that the *AM*s do not require the conditioning treatment with hazardous chemicals typical of *NF-117*. Therefore, there is another competitive edge of *AM*s in the form of avoided costs of chemicals and hazardous waste disposal.

Keywords: Leachate, Proton exchange membrane, Low cost membrane, Power/cost ratio, Microbial fuel cell, Internal resistance

1. Introduction

Microbial fuel cells (*MFC*s) are one type of the bioelectrochemical systems, and constitute a promising technology whereby is possible the energy generation from

---

* Author for correspondence:
Professor Dr. Héctor M. Poggi-Varaldo; T: 52 55 5747 3800 x 4324 ; E: r4cepe@yahoo.com

and bioremediation of effluents, as well as other applications through bio-electrochemical reactions using microorganisms as biocatalysts [1-4].

In the last years, renewable energy sources have attracted increasing attention due to current and future outlook by fossil fuels [5-7]. The *MFC*s represent an interesting alternative to produce electrical energy and provide wastewater treatment simultaneously. A wide range of soluble substrates (organics or inorganics) can be used as fuel to feed the *MFC*s. Furthermore, the fuel to *MFC*s in the form of effluents is typically a renewable source, cheaper or free and available around the world [8-12].

However, it has been reported that the scale up of *MFC*s is hindered by the typicall high costs of membrane or separator used in the design of *MFC*s, *inter alia* [2,13,14]. It has been shown that the membrane represents approximately 40% of the cost of *MFC*s [14-16] considering Nafion 117 membrane (*NF-117*) as proton exchange membrane (*PEM*). Rozendal et al. [14] predicted a fall in the separator cost till 20% of the total cost of the cell in the medium term. So far, Nafion is the material most often used for membranes in *MFC*s; it has become a non-official standard. Furthermore, the use of a separator such as membranes, may affect negatively the *MFC* performance increasing the internal resistance (R_{int}) of *MFC*s, the pH splitting, retard in the transfer of protons, among others issues [17-19]. Yet, a membrane is necessary as component in the *MFC*s to ensure a good performance and stability along the operation time due to other properties and features [17,20,21]. For instance, membranes act as separator between anodic and cathodic electrodes avoiding the electric short circuit, as a barrier to the transfer of other ions between the chambers, reducing the substrate flux from the anodic to cathodic chamber. Membranes also prevent the back-diffusion of the oxygen increasing the coulombic efficiency (*CE*), isolate the catalyst from the cathode in single-chamber *MFC*s and helps to ensure an efficient and sustainable operation along time [17,20,22].

In the open literature, it has been reported at least 20 different materials used as membrane o separator in *MFC*s e.g. ultrafiltration and microfiltration membranes, sulphonated polyether ether ketone membranes, anion and cation exchange membranes (e.g. AMI 7001, CMI-7000, Nafion 117), bipolar membranes, forward osmosis membranes, glass fiber mats, glass wool, cloth separators (J-Cloth and canvas), salt-agar slab and salt bridge, agar membrane, Zirfon membrane, ceramic membranes, nylon mesh, polyvinylidene fluoride (PVDF)/Nafion composite membranes, uncharged and sulfonated porous poly(vinylidene fluoride) membranes [6,13,16-20,23-32]. In general, the purpose of all of them is to reduce the cost of *MFC* by choosing more economic separators, to increase the *MFC* performance and decrease the overall R_{int} [17]. A survey of the costs of membranes/separators indicate the following ranges, depending on the type (in USD m^{-2}): anion exchange membranes AMI 7001, 80-83; cation exchange membranes such as CMI-7000 200, and Nafion 117, 1400-2200; plastic (polypropylene) mesh, 13-26; stainless steel mesh, 80-135; ultrafiltration membranes, 350, and J-cloth, 400 [17,31].

Interestingly, there are some works where *MFC*s have been tested without membranes (membraneless *MFC*s), however the *CE* has been low or falls down to unfeasible values [17,20,22,24,28]. For instance, Liu and Logan [22] worked with an air-cathode *MFC*, and using domestic wastewater as inocula and substrate evaluated the effect of presence and absence of a *PEM*. Although the *CE* was low (20%) using the membrane-less *MFC* the power density was higher than the *MFC* using *NF-117*, 146 mW m^{-2}. The *MFC* with *NF-117* displayed a power density of 28 mW m^{-2} and 28% of *CE*.

The aim of this work was to compare the performance of *MFC* fitted with alternative, low cost membranes (*AM*s) and compare their performance with the classical Nafion membrane using leachate from dark fermentation of organic wastes as substrate.

2. Materials and Methods

2.1. Experimental design

The experiment consisted of testing *MFC* performance equipped with several *AM*s as separators: *M2* (2% agar), *M6* (6% agar) and *MH* (hybrid membrane: 2% agar and 1% Nafion liquid); *NF-117* was used as reference membrane to compare the results. Graphite flakes (*GF*) with a surface area of 0.28 m^2 was used as anodic material [15,33,34].

The liquid fed to the *MFC*s was a mixture of sulphate-reducing inocula (*SR-In*) and leachate from dark fermentation of organic wastes as substrate. The experiments were carried out, without using any extra source of energy to mechanical mixing or heating. The cells were operated at room temperature (22 ± 1 °C).

The main response variables determined in the electrochemical characterizations were the maximum volumetric power ($P_{V,max}$) and the internal resistance (R_{int}), among others.

2.2. Microbial fuel cell

Single compartment, air-cathode *MFC*s were used to carry out all the experiments. The *MFC*s are horizontal cylinders built in Plexiglas 80 mm long and 57 mm internal diameter. The anodic chambers were packed with *GF* with a total surface area of 0.28 m^2. On the air side, the cathode was limited by a perforated plate of stainless steel 1 mm thickness. In the liquid side, the cathode was in contact with each of the *AM*s or *NF-117* tested as membranes. The cathode of the *MFC*s was a flexible carbon-cloth containing 0.5 mg cm^{-2} platinum catalyst (Pt 10 wt%/C-ETEK).

NF-117 was pretreated to activate and remove impurities using H_2O_2, deionized water and H_2SO_4 before to use in the *MFC* [35].

2.3. Preparation of membranes

2.3.1. M2 (2% agar)

Membranes of 2% agar (*M2*) were fabricated based on easily accessible, low cost agar. A solution of agar (agar/agar, from red algae *Gelidium* genus; purchased from Labcitec S.A. de C.V., Mexico City, Mexico) at 2% w v^{-1} was made by dissolving 0.64 g of agar in 32 mL of warm distilled water. Afterwards, while still warm, the solution was poured in a Petri dish of 8.37 cm diameter. The Petri dish was placed in an oven at 70 ºC for 9 h. With this treatment, the membrane achieved a dehydration extent of 98.08 ± 0.05% (Fig. 1). Typical thickness of the dry membrane was 274.17 ± 13 μm. Thickness was measured with an ultrasonic thickness gauge Minitest brand model 2100 from the company ElektroPhysik. Finally, before use in the cell, the dry membrane was painted with 0.5 mg cm^{-2} platinum catalyst (Pt 10 wt%/C-ETEK) [3,36].

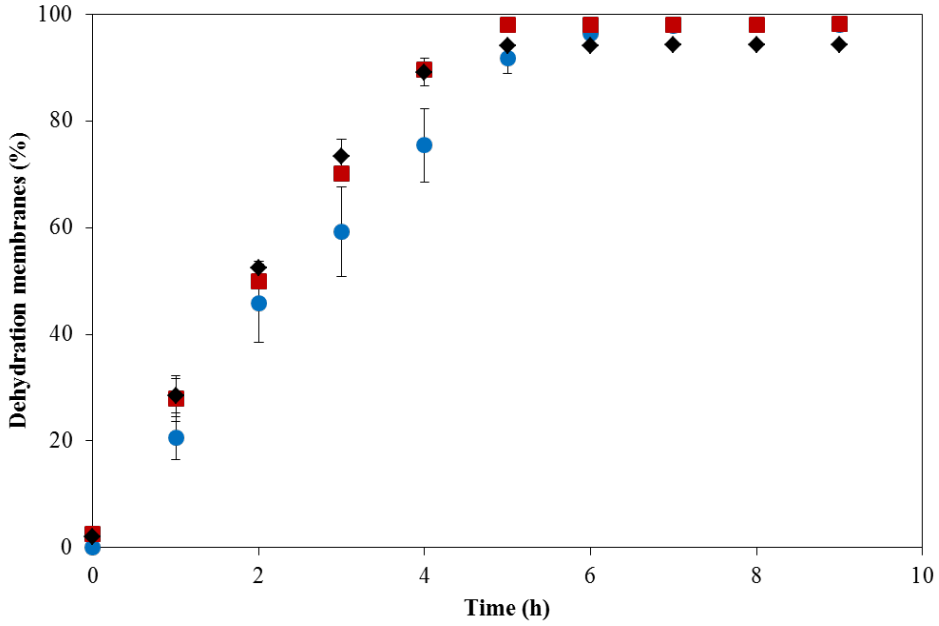

Fig. 1. Dehydration membranes at 70 ºC. Keys: Squares, agar 2%, *M2*; circles, agar 2%-Nafion 1%, *MH*; rhombus, agar 6%, *M6.*

2.3.2. M6 (6% agar)

These membranes were fabricated and conditioned in a similar way to *M2*, however the solution of agar was 6% w v^{-1}. The membrane achieved a dehydration extent of 94.27 ± 0.03% and the typical thickness of the dry membrane was 1010 ± 19 μm (Figure 1). Finally, before to use in the cell, the dry membrane was painted with platinum catalyst as we describe above.

2.3.3. MH (hybrid membrane: 2% agar and 1% Nafion liquid)

These membranes were made as following: a mixture of a solution 2% w/v of agar and 1% Nafion liquid (Nafion perfluorinated ion-exchange resin, 10 wt% dispersion in H_2O, Sigma Aldrich) was poured in a Petri dish of 8.37 cm diameter. Afterwards dehydration at 70 ºC for 9 h was carried out. The membrane achieved a dehydration extent of 97.92 ± 1.15% (Figure 1). The thickness of the dry membrane was 284 ± 15 μm. Finally, before to use in the cell, the dry membrane was coated with platinum catalyst as we describe above.

2.4 Sulphate-reducing inocula and leachate

The *MFC*s were loaded with a mix of a *SR-In* sampled from a sulphate-reducing complete mix reactor and fed with a semisynthetic leachate made with acetic, propionic and butyric acids as well as acetone and ethanol and mineral salts like $NaHCO_3$, Na_2CO_3, K_2HPO_4 and NH_4Cl [37-39].

The initial chemical oxygen demand (*COD*) and biomass concentration in the cell liquor were *ca.* 3524 ± 119 mg O_2 L^{-1} and 918 ± 3 VSS L^{-1}, respectively. The pH and the electrical conductivity were 7.54 ± 0.21 and 17.02 ± 0.42 mS cm^{-1}, respectively. *COD*,

volatile suspended solids *VSS*, pH and electrical conductivity were determined according to the Standard Methods [40].

2.5. Electrochemical characterization of the microbial fuel cells

The $P_{V,max}$, R_{int} and power density curve of the *MFC* were determined by duplicate, using the polarization curve method by varying the external resistance and recording both the voltage and the current intensity [2,20,34,36,41]. The voltage was measured and recorded with a Multimeter ESCORT 3146A.

The current was calculated by the Ohm's law and the R_{int} was calculated as the slope of the linear section of the curve voltage versus the current intensity [24,33,36]. The P_V and other characteristic variables were calculated as reported elsewhere [24,36].

The membrane performance was analyzed in terms of the corresponding Power/Cost ratio that was defined

$$\text{Power} - \text{to} - \text{Cost ratio} = \frac{P_s\ (\text{mW/m}^2)}{\text{Cost (US\$/m}^2)} \quad (1)$$

where P_s is the power density (surface) of the *MFC*, and Cost is the cost per unit area of the membrane

3. Results and discussion

Table 1 shows a detailed report all the values obtained from the electrochemical characterizations. In general, we found the R_{int} were low for all the cells. The *MFC*s performance values with the *AM*s were encouraging. The lowest R_{int} corresponded to alternative membranes *M6* and *MH* (Fig. 2a and b, respectively; Table 1). So, results of R_{int} tend to favour the alternative membranes. However, in terms of powers, the $P_{V,max}$ obtained by *MH* (3 400 mW m^{-3}) was higher than the power displayed by this set of alternative *AM*s tested.

Table 1. Electrochemical characterization of microbial fuel cells fitted with different membranes.

Parameter	Membranes			
	M2 [a]	***M6*** [b]	***MH*** [c]	***NF-117*** [d]
R_{int} (Ω)	112 ± 4	90 ± 5	88 ± 3	110 ± 1
$P_{v,max}$ (mW m^{-3})[e]	2146 ± 358	2374 ± 234	3383 ± 474	14246 ± 1450
I_{MFC} (mA)[f]	1.24 ± 0.10	1.44 ± 0.07	1.56 ± 0.11	3.20 ± 0.23
P_{cath} (mW m^{-2})[g]	61 ± 10	67 ± 6	96 ± 13	403 ± 41
$E_{MFC,OC}$ (mV)[h]	363 ± 26	339± 25	444 ± 15	724 ± 17

Notes: [a]membrane 2% agar; [b]membrane 6% agar; [c]membrane 2% agar + 1% Nafion; [d]Nafion 117 membrane; [e]Maximum volumetric power; [f]Current intensity value at the maximum power; [g]Maximum power density based on surface area of electrode (cathode); [h]Open circuit potential.

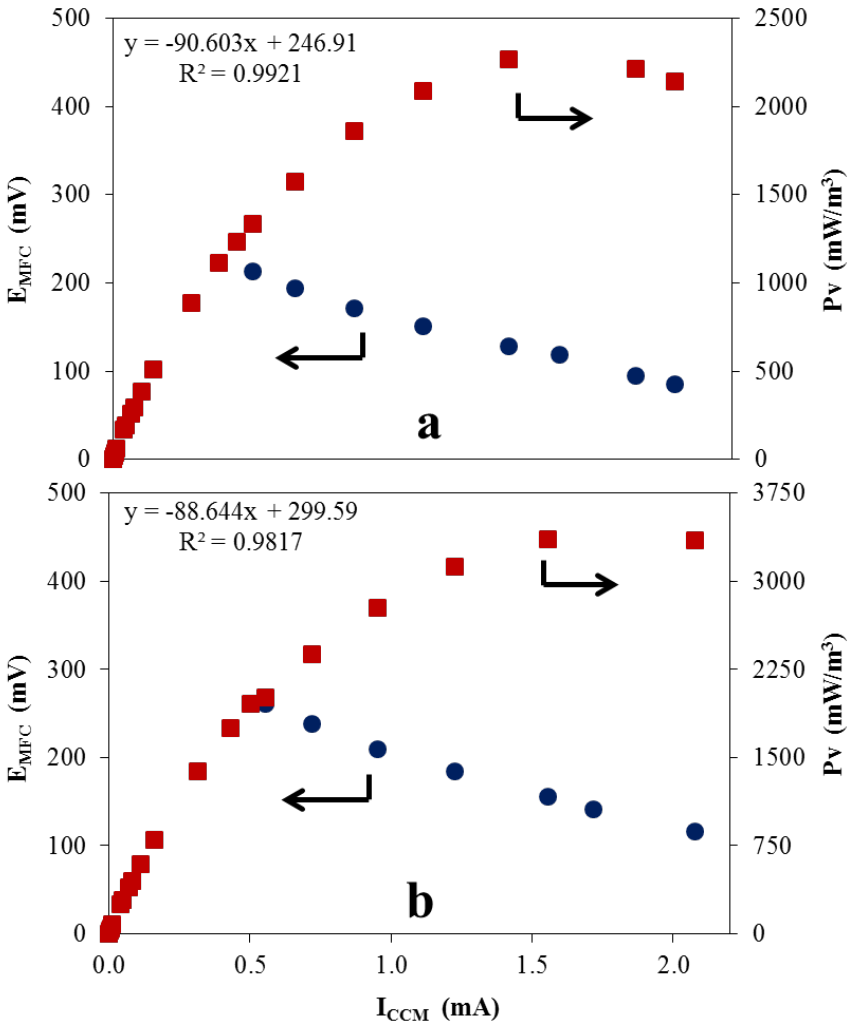

Fig. 2. Electrochemical characterization of the: (a) microbial fuel cell fitted with *M6* membrane; (b) microbial fuel cell fitted with *MH* membrane.

On the other hand, the performance values of the *MFC*s fitted with *M2*, the most economic membrane, were $P_{V,max}$ 2 150 mW m^{-3} whereas the R_{int} was 110 Ω(see figure 3). The *MFC*s fitted with *NF-117* used as reference showed a $P_{V,max}$ of 14 200 mW m^{-3}, however the value of the R_{int} was slightly higher than those displayed by *M6* and *MH* (Fig. 3, Table 1). So, powers delivered by *MFC*s fitted with *AM*s were 14 to 25% of the power of the cell fitted with the conventional *NF-117*.

In order to compare the cells in terms of power and costs, we developed an analysis in which the power and the cost of the membranes are involved, i.e., in terms of the Power-to-Cost ratio. Thus, in spite of the reduced power, the *AM*s still exhibited a higher Power/Cost ratio (0.9 to 4.4 mW $US\$^{-1}$) than *NF-117* (0.23 mW $US\$^{-1}$) Table 2. So, the variable Power-to-Cost ratio seems to favor the *AM*s developed for this work.

It worth mentioning that there are only a few works in which separators similar to our *AM*s were tested: salt bridge [23,42] and agar slab [25].

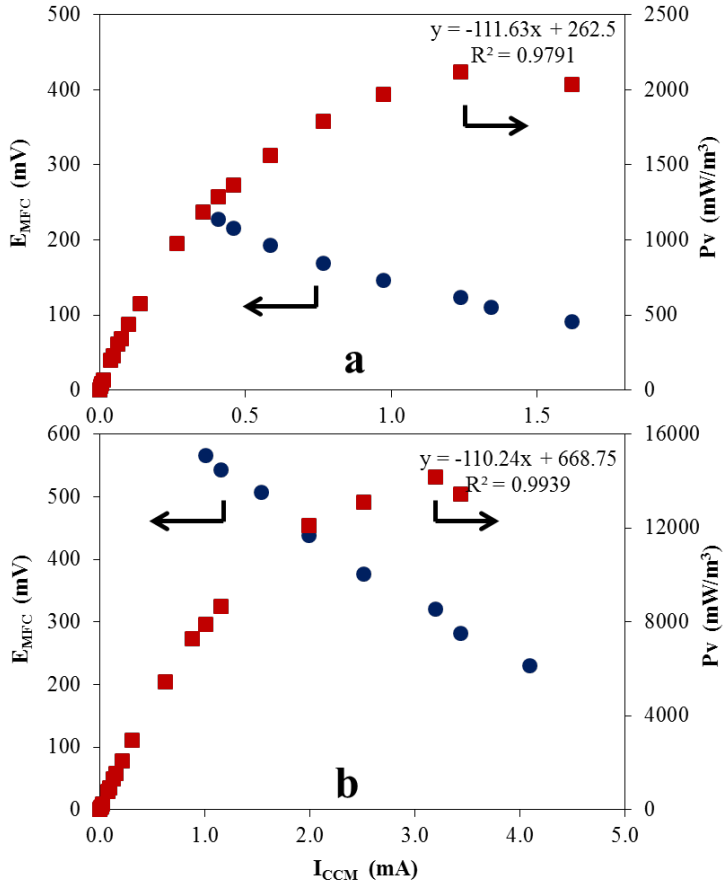

Fig. 3. Electrochemical characterization of the: (a) microbial fuel cell fitted with *M2* membrane; (b) microbial fuel cell fitted with *NF-117*.

Table 2. Summary of characterization results of the microbial fuel cells in our work.

Membrane types	P_s [a] (mW m^{-2})	Cost (US$ m^{-2})	Ratio Power-to-Cost (mW US$$^{-1}$)
NF-117	403 ± 41	1733	0.23
***M2* (2% agar)**	61 ±10	14	4.36
***M6* (6% agar)**	67 ± 6	41	1.63
MH	96 ± 13	107	0.89

[a]maximum surface area density power

Table 3 exhibits electrochemical parameters of several works with *MFC*s that used agar-like separators. Our value of power density was higher than those reported by Min et al. [23] and Kargi and Eker [25], and of the same order (although slightly lower) than

Table 3. Performance of microbial fuel cells fitted with agar-type separators and Nafion membranes.

Separator/membrane	Type of cell	Operation	Results (Average power density; internal resistance; potential)	Ref.
Salt bridge (agar)	Two-chamber	Batch; 4.22 g L^{-1} Sodium acetate; 30 °C; G. metallirreducens	2.2 mW m^{-2}; 19920 Ω < 20 mV	[23]
Nafion 117	Two-chamber	Batch; 4.22 g L^{-1} Sodium acetate; 30 °C; G. metallirreducens	4071 mW m^{-2}; 1286 Ω < 350 mV	[23]
Salt bridge (agar)	Two-chamber	Batch; 1.46 g COD L^{-1} chocolate industry; 28 ± 2 °C; activated sludge as microbial inoculum	145 mW m^{-2}; R_{int} NR; 190 mV (estimated from Fig. 1 article)	[42]
Nafion 117	Two-chamber	Batch; 1.46 g COD L^{-1} chocolate industry; 28 ± 2 °C; activated sludge as microbial inoculum	230 mW m^{-2}; R_{int} NR; 235 mV (estimated from Fig. 1 article)	[42]
Nafion 117	Two-chamber	Batch; 2.0 g COD L^{-1} 28 ± 2 °C; synthetic medium (glucose); activated sludge as microbial inoculum	245 mW m^{-2}; R_{int} NR; 242 mV (estimated from Fig. 1 article)	[42]
Salt-agar slab	Two-chamber	Batch; 6.0 g COD L^{-1} synthetic wastewater composed of diluted molasses; 26 ± 2 °C; Mixed culture sampled from the acidogenic unit of an anaerobic wastewater treatment plant	2.9 mW m^{-2}; R_{int} NR; Potential NR	[25]
Agar membrane	Single chamber	3.5 g COD L^{-1} semisynthetic leachate; 22 ± 1 °C; Sulphate-reducing inoculum	96 ± 13 mW m^{-2}; 88 ± 3 Ω 444 ± 15 mV	This work
Nafion 117	Single chamber	3.5 g COD L^{-1} semisynthetic leachate; 22 ± 1 °C; Sulphate-reducing inoculum	403 ± 41 mW m^{-2}; 110 ± 1 Ω 724 ± 17 mV	This work

NR: No reported

that observed by Patil et al. [49]. Unfortunately only Min et al. [23] reported the internal resistance of their *MFC* fitted with agar bridge; it had a high value of *ca*. 20 000 ohms. With caution due to limited comparison, our *MFC* equipped with agar membrane had a significantly lower internal resistance of 96 ohms than that of Min et al. [23]. Likely, the fact that our agar membranes had a lower thickness than the agar slab of Kargi and Eker [25] and the salt bridges used by Min et al. [23] and Patil et al. [42], could have contributed to our low R_{int} value.

In general, power density in our *MFC* fitted with agar membrane was between 4 to 40% (weighed average 28%) of the values obtained with control *MFC*s equipped with Nafion, both in the literature and our own work (Table 3). Despite this low value, the Power-to-Cost ratio of the agar membrane is very favourable and higher than the Power-to-Cost ratios of *MFC* fitted with Nafion membrane, as we have mentioned above. It is worth highlighting that the costs of our membranes were only 2.5 to 6% of the cost of the *NF-117* one.

Furthermore, the *AM*s in this work did not require the conditioning treatment with hazardous chemicals typical of *NF-117*. Therefore, there is another competitive edge of *AM*s in the form of avoided costs of chemicals and hazardous waste disposal.

4. Conclusion

Our research was focused on testing *AM*s in *MFC*s using leachate from dark fermentation of organic wastes. The *AM*s tested showed interesting results to use as *PEM* in *MFC*s. A higher Power/Cost ratio, 0.9 to 4.4. mW US^{-1} was obtained with the *AM*s whereas only a ratio of 0.23 mW US^{-1} was obtained for *NF-117*. Furthermore, the *AM*s do not need any pretreatment. In contrast, the *NF-117* membrane requires a pretreatment with hydrogen peroxide and sulfuric acid that in turn generates hazardous wastes, besides the increased costs of membrane fabrication and conditioning.

Finally, the development and application of *AM*s, showed promising results for *MFC* application to leachate treatment. It constitutes an attractive contribution to cost-effective and a more sustainable remediation of this leachates.

Acknowledgements

The authors wish to thank CINVESTAV and ICYTDF (now SECITI-GDF), Mexico, for financial support to this research (PICCO-10-28), and CONACYT for the Infrastructure Project 188281. Mr Giovanni Hernández-Flores, Sc D candidate, received a graduate scholarship from CONACYT, Mexico. The technical help of Mr. Rafael Hernández-Vera and technicians of the Environmental of Biotechnology and Renewable Energy R&D Group, CINVESTAV, is appreciated.

References

[1] Yang Y., Xu M., Guo J., Sun G. Bacterial extracellular electron transfer in bioelectrochemical systems. Process Biochemistry 2012; 47:1707-1714.

[2] Xia X., Tokash J.C., Zhang F., Liang P., Huang X., Logan B.E. Oxygen-reducing biocathodes operating

with passive oxygen transfer in microbial fuel cells. Environ. Sci. Technol. 2013 ; *47* (4):2085–2091.
[3] Vázquez-Larios A.L., Solorza-Feria O., Poggi-Varaldo H.M., González-Huerta R.G., Ponce-Noyola M.T., Ríos-Leal E., Rinderknecht-Seijas N. Bioelectricity production from municipal leachate in a microbial fuel cell: effect of two cathodic catalysts. Int. J. Hydrogen Energy 2014; 39:16667-16675.
[4] Hernández-Flores G., Poggi-Varaldo H.M., Solorza-Feria O., Ponce Noyola M.T., Romero-Castañón T., Rinderknecht-Seijas N. Tafel equation based model for the performance of a microbial fuel cell. Int. J. Hydrogen Energy 2015; In press DOI http://dx.doi.org/10.1016/j.ijhydene.2015.06.119.
[5] Cheng-Dar Y., Chung-Ming L., Liou E.M.L. A transition toward a sustainable energy future: feasibility assessment and development strategies of wind power in taiwan. Energy policy 2001; 29:951-963.
[6] Logan B.E., Regan J.M. Microbial challenges and harnessing the metabolic activity of bacteria can provide energy for a variety of applications, once technical and cost obstacles are overcome. Environ. Sci. Technol. 2006; 5172–5180.
[7] Das D., Veziroglu T.N. Hydrogen production by biological processes: a survey of literature. Int. J. Hydrogen Energy 2001; 26:13-28.
[8] Pant D., Bogaert G.V., Diels L., Vanbroekhoven K. A review of the substrates used in microbial fuel cells (*MFC*s) for sustainable energy production. Bioresour. Technol. 2010; 101:1533-1543.
[9] Logan B.E., Rabaey K. Conversion of wastes into bioelectricity and chemicals by using microbial electrochemical technologies. Science 2012; 337:686-690.
[10] Hou J., Liu Z., Yang S., Zhou Y. Three-dimensional macroporous anodes based on stainless steel fiber felt for high-performance microbial fuel cells. Journal of Power Sources 2014; 258:204-209.
[11] Modin O., Gustavsson D.J. Opportunities for microbial electrochemistry in municipal wastewater treatment–an overview. Water Sci. Technol. 2014; 69(7):1359-1372.
[12] Poggi-Varaldo H.M., Munoz-Paez K.M., Escamilla-Alvarado C., Robledo-Narváez P.N., Ponce-Noyola M.T., Calva-Calva G., Ríos-Leal E., Galíndez-Mayer J., Estrada-Vázquez C., Ortega-Clemente A., Rinderknecht-Seijas N. Biohydrogen, biomethane and bioelectricity as crucial components of biorefinery of organic wastes: a review. Waste Management Research 2014; 32:353-365, doi: 10.1177/0734242X14529178.
[13] Wei J., Liang P., Huang X. Recent progress in electrodes for microbial fuel cells. Bioresour. Technol. 2011; 102:9335-9344.
[14] Rozendal R.A., Hamelers H.V.M., Rabaey K., Keller J., Buisman C.J.N. Towards practical implementation of bioelectrochemical wastewater treatment. Trends in Biotechnology 2008; 26(8):450-459.
[15] Hernández-Flores G. Interim Report: Bioelectricity generation in microbial fuel cells that use enriched inocula and graphite flakes as anodic material. Sc D Thesis 2014, CINVESTAV-IPN, México, D.F.
[16] Shahgaldi S., Ghasemi M., Wan Daud W.R., Yaakob Z., Sedighi M., Alam J., Ismail A.F. Performance enhancement of microbial fuel cell by pvdf/nafion nanofibre composite proton exchange membrane. Fuel Processing Technology 2014; 124:290-295.
[17] Li W-W., Guo-Ping S., Xian-Wei L., Han-qing Y. Recent advances in the separators for microbial fuel cells. Bioresour Technol. 2011;102:244-252.
[18] Kim Y., Shin S.H., Chang I.S., Moon S.H. Characterization of uncharged and sulfonated porous poly(vinylidene fluoride) membranes and their performance in microbial fuel cells. Journal of Membrane Science 2014; 463:205-214.
[19] Kondaveeti S., Lee J., Kakarla R., Kim H.S., Min B. Low-cost separators for enhanced power production and field application of microbial fuel cells (*MFC*s). Electrochimica Acta 2014; 132:434-440.
[20] Logan B.E. Microbial Fuel Cells. John Wiley-Interscience. New Jersey, USA, 2007.
[21] Watson V.J., Saito T., Hickner M.A., Logan B.E. Polymer coatings as separator layers for microbial fuel cell cathodes. Journal of Power Sources 2011; 196(6):3009-3014.
[22] Liu H, Logan B.E. Electricity generation using an air-cathode single chamber microbial fuel cell in the presence and absence of a proton exchange membrane. Environ. Sci. Technol. 2004; 38:4040–4046.
[23] Min B., Cheng S., Logan B.E. Electricity generation using membranes and salt bridge microbial fuel cells. Water Research 2005; 39:1675-1686.
[24] Logan B.E., Hamelers B., Rozendal R., Schröder U., Keller J., Freguia S., Aelterman P., Verstraete W., Rabaey K. Microbial fuel cells: methodology and technology. Environ. Sci. Technol. 2006; 40:5181-5192.
[25] Kargi F., Eker S. Electricity generation with simultaneous wastewater treatment by a microbial fuel cell

(*MFC*) with Cu and Cu-Au electrodes. J. Chem. Technol. Biotechnol. 2007; 82:658-662.
[26] Ghangrekar M.M., Shinde V.B. Performance of membrane-less microbial fuel cell treating wastewater and effect of electrode distance and area on electricity production. Bioresour. Technol. 2007; 98:2879-2885.
[27] Mohan S.V., Raghavulu S.V., Sarma P.N. Biochemical evaluation of bioelectricity production process from anaerobic wastewater treatment in a single chambered. Biosens. Bioelectron. 2008; 23:1326-1332.
[28] Yang Y., Sun G., Xu M. Microbial fuel cells come of age. J. Chem. Technol. Biotechnol. 2010; 86:625-632.
[29] Sivasankaran A., Sangeetha D. Development of *MFC* using sulphonated polyether ether ketone (SPEEK) membrane for electricity generation from waste water. Bioresour. Technol. 2011; 102(24):11167-11171.
[30] Zhang X.Y., Cheng S., Wang X., Huang X., Logan B.E. Separator characteristics for increasing performance of microbial fuel cells. Environ. Sci. Technol. 2009; 43:8456-8461.
[31] Zhang X., Cheng S., Liang P., Huang X., Logan B.E. Scalable air cathode microbial fuel cells using glass fiber separators, plastic mesh supporters, and graphite fiber brush anodes. Bioresource Technology 2011; 102:372-375.
[32] Prabhu N.V., Sangeetha D. Characterization and performance study of sulfonated poly ether ether ketone/Fe_3O_4 nano composite membrane as electrolyte for microbial fuel cell. Chemical Engineering Journal 2014; 243:564-571.
[33] Hernández-Flores G., Poggi-Varaldo H.M., Solorza-Feria O., Romero-Castañón T., Ríos-Leal E., Galíndez-Mayer J., Esparza-García F. Batch operation of a microbial fuel cell equipped with alternative proton exchange membrane. Int. J. Hydrogen Energy 2015; In press DOI http://dx.doi.org/10.1016/j.ijhydene.2015.06.057.
[34] Hernández-Flores G., Poggi-Varaldo H.M., Solorza-Feria O., Ponce Noyola M.T., Romero-Castañón T., Rinderknecht-Seijas N. Improvement of microbial fuel cell performance by selection of anodic materials and enrichment of inoculum. J. New Mater. Electrochem. Syst. 2015; In press.
[35] Oh S.E., Logan B.E. Proton exchange membrane and electrode surface areas as factors that affect power generation in microbial fuel cells. Appl Microbiol Biotechnol. 2006; 70 :162–169.
[36] Vazquez-Larios A.L., Solorza-Feria O., Vazquez-Huerta G., Esparza-Garcia F.J., Rios-Leal E., Rinderknecht-Seijas N., Poggi-Varaldo H.M. A new design improves performance of a single chamber microbial fuel cell. J. New Mater. Electrochem. Syst. 2010; 13:219-226.
[37] Valdez-Vázquez I., Ríos-Leal E., Esparza-García F.J., Cecchi F., Poggi-Varaldo H.M. Semi-continuous solid substrate anaerobic digestors for H_2 production from organic waste: Mesophilic versus thermophilic regime. Int. J. Hydrogen Energy 2005; 30:1383-1391.
[38] Valdez-Vazquez I., Rios-Leal E., Carmona-Martinez A., Muñoz-Páez K., Poggi-Varaldo H.M. Improvement of biohydrogen production from solid wastes by intermittent venting and gas flushing of batch reactors headspace. Environ. Sci. Technol. 2006; 40:3409-3415.
[39] Poggi-Varaldo H.M., Carmona-Martínez A., Vázquez-Larios A.L., Solorza-Feria O. Effect of inoculum type on the performance of a microbial fuel cell fed with spent organic extracts from hydrogenogenic fermentation of organic solid wastes. J. New Mater. Electrochem. Syst. 2009; 12:49-54.
[40] APHA. Standard Methods for Examination of Water and Wastewater. 17th ed. APHA-AWWA-WEF, Washington DC, 1989.
[41] Damiano L., Jambeck J.R., Ringelberg D.B. Municipal solid waste landfill leachate treatment and electricity production using microbial fuel cells. Appl. Biochem. Biotechnol. 2014; 173:472–485.
[42] Patil S.A., Surakasi V.P., Koul S., Ijmulwar S., Vivek A., Shouche Y.S., Kapadnis B.P. Electricity generation using chocolate industry wastewater and its treatment in activated sludge based microbial fuel cell and analysis of developed microbial community in the anode chamber. Bioresource Technology 2009; 100:5132-5139.

Abbreviations and symbols

AM	alternative, low cost membrane
CE	coulombic efficiency
COD	chemical oxygen demand
$E_{MFC,OC}$	open circuit potential
I_{MFC}	current intensity

M2	agar membrane 2% agar
M6	agar membrane 6% agar
MFC	microbial fuel cell
MH	hybrid membrane: agar membrane 2% agar, Nafion liquid 1%
NF-117	Nafion 117 membrane
P_{cath}	maximum power density based on surface area of electrode (cathode)
PEM	protonic exchange membrane
P_s	power density based on surface area of electrode (cathode)
P_V	volumetric power
$P_{V,max}$	maximum volumetric power
R_{ext}	external resistance
R_{int}	internal resistance
VSS	volatile suspended solids

Chapter 5.13. Microbial fuel cells fed with municipal wastewater and leachates

G. Hernández-Flores[a]; H. M. Poggi-Varaldo[a,*]

[a]Environmental Biotechnology and Renewable Energies R&D Group, Dept. of Biotechnology and Bioengineering, Centro de Investigación y de Estudios Avanzados del Instituto Politécnico Nacional. Av. Instituto Politécnico Nacional 2508, Col. San Pedro Zacatenco, Delegación Gustavo A. Madero, México D.F., C. P. 07360 Apartado Postal: 14-740, 07000 México, D.F.

ABSTRACT

The goal of this work was to evaluate the extent of treatment and bioelectricity generation in microbial fuel cells (*MFC*) fed with municipal wastewater (*MWW*) and leachate from the Mexico City landfill "Bordo Poniente" section 1 and 4 (*L-1* and *L-4*). Leachates exhibited a medium organic strength and interestingly, their pH was alkaline.
An air-cathode, single chamber *MFC* was loaded first with *MWW* and sulfate-reducing consortium as inoculum (*SR-In*). During the batch operation with *MWW* an external resistance of 330 Ωwas used and an average removal of organic matter of 60% (η_{COD}) and 4% coulombic efficiency (*CE*) were achieved, along with average volumetric power (P_v) of 273 mW m^{-3}. Afterwards, two repeated more batches were carried out; where the *CE* significantly increased up to 48% whereas a η_{COD} slightly improved of 78% was reached in the last two periods. A 2nd experiment was carried out using a mixture of *MWW* and *L-4* aged leachate from the Mexico City landfill plus *SR-In*. Two more operation periods were carried out loading *L-4* y *L-1* as substrate into the *MFC*. When a mixture of *L-4* and *MWW* was loaded into the cell, the highest value of η_{COD} was observed in this wok, i.e., 86%. Afterwards, using 100% *L-4*, the η_{COD} and the *CE* achieved were 53% and 15%, respectively, whereas a P_v of 490 mW m^{-3} was observed. It seems that treatment of combined leachate and *MWW* had a beneficial effect on *MFC* performance. To the best of our knowledge this is the first report on the use of *MFC*s to the treatment of atypical leachates from Mexico City's landfill and its mixtures with *MWW*.

Keywords: Remediation, Municipal wastewater, Leachates, Microbial fuel cells, Coulombic efficiency, Organic matter removal

1. Introduction

Mexico discharges nearly 231 m^3 s^{-1} of municipal wastewater (*MWW*), *i.e.*, 7.1 Gm^3 yr^{-1}, and only 75% of the discharges are actually collected, whereas less than 30% receive

---

* Author for correspondence:
Professor Dr. Héctor M. Poggi-Varaldo; T: 52 55 5747 3800 x 4324 ; E: r4cepe@yahoo.com

some type of treatment [1,2]. Although *MWW* has a low concentration of organic matter (biochemical oxygen demand (*BOD*) typically < 300 mg L^{-1}) [2], and consequently, a low energy density generation could be expected in *MFC*s [3,4], its pollutant load still needs to be treated before disposal [5].

Landfills have been the main form of solid waste management worldwide, and in many countries, this is still the case. For instance, in the USA, nearly 54% of the solid waste produced in 2010 were disposed of in landfills, of a total 250 million tons per year [6]. Landfill leachates constitute aggressive effluents generated in the landfill system by a combination of biological, meteorological or weather, and geotechnical processes. In the modern practice, leachate must be collected and treated prior to its discharge to the environment [7].

According to Kjeldsen et al. [8] there are four primary types of pollutants in municipal solid waste (*MSW*) landfill leachate: dissolved organic matter, inorganic macrocomponents, trace metals, and xenobiotic compounds. Leachate management can be performed by recycling leachate back into the landfill, evaporation in ponds, treatment followed by disposal, or direct discharge to a municipal wastewater collection system although the latter is debatable according to current environmental standards. Typically, leachate exhibit low pH that adds to its aggressivity.

In Mexico, the metropolitan area of Mexico has a population of nearly 22 million inhabitants. The wastes of this population were collected in a sanitary landfill (*SL*) called "Bordo Poniente" (*BP*). *BP* has a surface area of 300 ha and received about 12, 600 ton per day; it has been in operation for 26 years. Approximately, 70 million tons of trashes are there. It becomes in the biggest environmental passive Mexico and the largest in Latin America. At the end of the 2011 the mega *SL BP* where the municipal solid waste was disposed of, was closed. After closure, the landfill still generates significant amounts of leachates with moderate-to-high organic matter concentration (http://www.excelsior.com.mx/comunidad/2013/03/05/887324).

Due to these characteristics, the *SL BP* has become an environmental liability because of the presence of leachates that infiltrate into the ground, contaminating both the surface water and the aquifer [9].

Interestingly, most of the organic pollutants in both the *MWW* and leachates, or the dissolved and colloidal organic matter, in principle can be used as fuel in *MFC*s. These devices can accomplish bioelectricity generation and wastewater depuration simultaneously [10-15]. *MFC*s are a relatively old concept. In 1911, Michael Potter, showed that microorganisms could create a voltage and convey an electrical current. Potter's research may be considered as the birth of *MFC*s; however, it was not until the 1960s that the concept and experimental work based on microbial electricity generation resumed again linked to the NASA space program, in the context of recycling human waste via conversion to electricity during space flights [3,16].

A *MFC* is an electro-biochemical reactor capable of directly converting organic matter into electricity. In the anodic chamber the microorganisms anaerobically oxidize the organic matter and release electrons and protons. The electrons are transported to the anode that acts as an intermediate, external electron acceptor. The electrons flow through an external circuit where there is a resistor or a device to be powered, producing electricity and finally react at the cathode with the protons and oxygen producing water [10,11,17-19].

Since the anodic process in the *MFC* is essentially anaerobic, effluent treatment in this device shows definite advantages over the conventional aerobic biological treatment of both *MWW* and leachates. Savings in aeration costs, both investment and operation costs, is the main advantage of *MFC*s [20]. Incidentally, aeration is a big consumer of electricity, whereas *MFC*s generate electricity.

There has been an intense research on substrates for *MFC* in the last years [21]. It has been shown that *MFC* can process a wide variety of influents, *inter alia* several industrial effluents. Also, a significant part of past research has been focused on the effect organic matter concentration of such influents on *MFC* performance [22]. It is apparent that *MWW* and leachates provide a practically zero cost source of organic matter for *MFC* operation and bioelectricity generation. On the other hand, the municipal authorities would consider the technology as long as the *MFC*s are able to provide some degree of treatment, that is, to remove the organic matter load of these municipal effluents. If the approach is feasible, it would be a win-win issue for both the City Authorities and the Energy Authorities.

Thus, the purpose of this work was to evaluate the extent of treatment and bioelectricity generation in microbial fuel cells (*MFC*) fed with municipal wastewater (*MWW*) and leachate from the Mexico City landfill "Bordo Poniente" section 1 and 4 (*L-1* and *L-4*).

2. Materials and Methods

2.1 Experimental design

The experiment consisted of the operation in a batch process of the *MFC*s divided in two phases (Table 1):

Table 1. Summary of the experimental design in this work.

Phase	Period	Feed type	Seeding	Initial *COD* [a] (mg mL^{-1})	pH	Initial Biomass in *MFC* *VSS* (mg L^{-1})
1	1	*MWW* [b]	*SR-In* [c]	208 ± 13	6.73 ± 0.04	205 ± 9
	2	*MWW*	*SR-In*	210 ± 11	6.41 ± 0.03	398 ± 23
	3	*MWW*	NI [d]	225 ± 12	7.11 ± 0.03	347 ± 16
2	4	*MWW* + *L-4* [e]	*SR-In*	1 950 ± 57	8.32 ± 0.05	197 ± 4
	5	*L-4* [f]	NI	11 620 ± 310	8.44 ± 0.03	183 ± 8
	6	*L-1* [g]	NI	4 050 ± 250	8.56 ± 0.05	162 ± 6

Notes: [a]chemical oxygen demand; [b]municipal wastewater; [c]sulphate-reducing inoculum; [d]no inoculation; [e]mixture of municipal wastewater and leachate from section 4 of the sanitary landfill; [f]leachate from section 4 of the sanitary landfill; [g]leachate from section 1 of the sanitary landfill

In phase 1, periods 1 and 2, the *MFC* was loaded with *MWW* and sulphate-reducing inoculum (*SR-In*) sampled from a seed, complete mix sulphate-reducing bioreactor. The internal resistance (R_{int}) and power density curve of the *MFC* were determined by duplicate by the polarization curve method [11,23-25]. The response variables studied of the characterization stage were the maximum volumetric power ($P_{v,max}$) delivered by the *MFC* as well as the R_{int} value.

Afterwards, the *MFC* was operated in repeated batch mode, by draw-and-fill of *MWW* in three periods (Table 1). The cell was connected to an external resistance (R_{ext}) similar in value to the R_{int} previously determined. In the first period of batch operation in Phase 1, biomass concentration was 205 mg *VSS* L^{-1} in the characterization. At the start of the 2nd period of the batch mode, the *MFC* was re-seeded and the biomass concentration reached a value of *ca.* 400 mg *VSS* L^{-1}. For the 3rd period of the batch operation, the biomass concentration in the *MFC* was *ca.* 350 mg *VSS* L^{-1}. No inoculation of biomass took place in this 3rd period.

In Phase 2, the *MFC* was loaded with a mixture of *MWW*, leachate from the Mexico City *BP* landfill, section 4 (*L-4*), and *SR-In*, and further characterized by the polarization curve method. Afterwards, the *MFC* was batch operated in 3 periods with different influents (Table 1). In Period 4, the influent was a mixture of *MWW* and leachate from *L-4* of the *SL* whereas in Periods 5 and 6 the influents were 100% *L-4* and *L-1*, respectively. The cell was connected to an R_{ext} similar in value to the R_{int} previously determined.

Biomass concentration was *ca.* 200 mg VSS L^{-1} in the characterization and first period of batch operation. No inoculation of biomass took place in the 5 and 6 periods and only the liquid phase was exchanged (spent liquor withdrawal followed by feeding of fresh influent).

The response variables studied in the batch operation were the average volumetric power (P_v) delivered by the cell, the organic matter removal efficiency (η_{COD}), and the Coulombic efficiency (*CE*) in each cycle.

2.2 Microbial fuel cell

The *MFC* consisted of a horizontal cylinder built in Plexiglas 80 mm long and 57 mm internal diameter. The anodic chamber was packed with graphite flakes. The cathode was a sandwich of circular layers (from inside to outside): proton exchange membrane (Nafion® 117), flexible carbon-cloth containing 0.5 mg cm^{-2} platinum catalyst (Pt 10 wt%/C-ETEK), and a perforated plate of stainless steel 1 mm thickness. The cathode was in direct contact with atmospheric air on the metallic plate side [11-13].

2.3 Sulphate-reducing inoculum

The *MFC* was seeded with a *SR-In* sampled from a complete mix reactor. The reactor was operated at 37 °C in a constant temperature room. An influent containing mainly sucrose as carbon source was fed at a flow rate of 120 mL d^{-1} to the complete mix sulphate-reducing bioreactor. Its composition was (in g L^{-1}): sucrose (5.0), glacial acetic acid (1.5), $NaHCO_3$ (3.0), K_2HPO_4 (0.6), Na_2CO_3 (3.0), NH_4Cl (0.6), Na_2SO_4 (11.0).

2.4 Municipal wastewater and leachates

The *MWW* was sampled from the influent channel of the Wastewater Treatment Plant "Cerro de la Estrella" of Mexico City. The *MWW* exhibited organic matter concentration of 220 ± 20 mg O_2 L^{-1} and pH of 6.7 ± 0.03 (Table 2).

Table 2. Characteristics of municipal wastewater and leachates.

Parameter	*MWW* [a]	*Leachates*	
		L-1 [b]	*L-4* [c]
BOD_5 (mg L^{-1}) [d]	145 ± 15	3 500 ± 100	10 600 ± 200
COD (mg O_2 L^{-1}) [e]	219 ± 20	4 300 ± 300	12 300 ± 500
BOD_5/COD [f]	0.65	0.81	0.86
TSS (mg L^{-1}) [g]	106 ± 11	250 ± 18	324 ± 27
VSS (mg L^{-1}) [h]	85 ± 7	200 ± 20	270 ± 30
Nitrogen Kjeldahl (mg L^{-1})	12.2 ± 2.0	300 ± 20	2 900 ± 30
Sulphates (mg S L^{-1})	0.41 ± 0.03	1 300 ± 10	280 ± 10
Alkalinity (g L^{-1})	0.2 ± 0.01	3.8 ± 0.08	16.2 ± 1
pH	6.7 ± 0.03	8.56 ± 0.05	8.26 ± 0.02
Electrical conductivity (mS cm^{-1})	0.31 ± 0.01	15.7 ± 0.2	36.7 ± 0.1

Notes: [a]municipal wastewater; [b]leachate from section 1 of the sanitary landfill; [c]leachate from section 4 of the sanitary landfill; [d]biological oxygen demand; [e]chemical oxygen demand; [f]biodegradability ratio; [g]total suspended solids; [h]volatile suspended solids.

The *COD* of domestic effluents tested in *MFC*s have been in the range 160 to 850 mg L^{-1} [4]. So, the *COD* concentration in our *MWW* fell in the low side of the range, and it can be considered a weak load *MWW*.

The leachates were sampled from Mexico City's *SL BP*. Two types of leachates were provided: samples from Section 1 (*L-1*) and samples from Section 4 (*L-4*), where the denomination 'section' is related to the chronological construction of the landfill cells. Organic matter contents of leachates were 4 300 and 12 300 mg *COD* L^{-1} for *L-1* and *L-4*, respectively (Table 2). Furthermore, a high value of the ratio BOD_5 COD^{-1} was observed that suggests that leachates are biodegradable [26,27]. Their pHs were alkaline, between 8 and 9.

Parameters of municipal wastewater and leachates were determined by Standard Methods [28].

2.5 Determination of internal resistance of the cells

The R_{int} of the cell was determined using the polarization curve method, by varying the R_{ext} and monitoring both the voltage and the current intensity [11,23-25]. Briefly, the *MFC* was operated at open circuit; then the R_{ext} was varied from 10 Ω to 10 MΩ and viceversa. The voltage was measured and recorded with a Multimeter ESCORT 3146A. The current was calculated by the Ohm's law and the R_{int} was calculated as the slope of the linear section of the curve voltage versus the current intensity [11,29].

3. Results and Discussion

3.1 Experiments of the 1st phase

In the cell characterization with *MWW*, the R_{int} of the cell and its $P_{v,max}$ were 350 Ω and 760 mW m^{-3}, respectively (Figure 1). Please note that the absolute value of the slope of the regression equation depicted in the inset represent the R_{int} of the *MFC*.

The next step was the batch operation with the cell connected to an R_{ext} of 330 Ω which was close to the R_{int} determined above (Figure 2a). In the first period the average P_V

(based on the steady values) was 273 mW m^{-3}, whereas the average η_{COD} and *CE* were 60% and 4%, respectively (Table 3). The organic matter removal was satisfactory, although *CE* was poor. They suggest that most of the removed organic matter is channeled to uses other than bioelectricity generation, for instance, biomass synthesis or by-products [23,30,31].

Afterwards, two more repeated batches were carried out (Periods 2 and 3), where the *CE* significantly increased up to 48% and the average η_{COD} also topped to 80% in Period 2. The P_V in the 2nd period improved by 17% and exhibited an average value of 315 mW m^{-3} (Table 3).

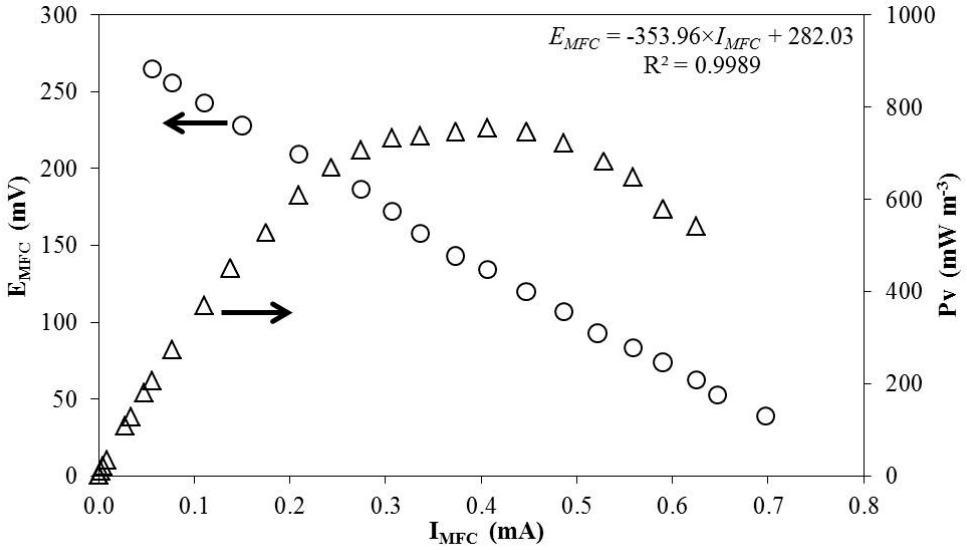

Fig. 1. Electrochemical characterization of the microbial fuel cell loaded with municipal wastewater. Keys: E_{MFC}, hollow circles; P_V, hollow triangles.

Table 3. Average performance of the microbial fuel cell operated in repeated batch mode.
Periods 1 - 3, R_{ext} = 330 Ω; Period 4 R_{ext} = 560 Ω; Periods 5 and 6, R_{ext} = 220 Ω.

Period	Influent	R_{ext} [a]	P_V [b] (mW m^{-3})	η_{COD} [c] (%)	*CE* [d] (%)
1	*MWW* [e]	330	273 ± 98	59	3.4
2	*MWW*	330	315 ± 63	80	47.5
3	*MWW*	330	51 ± 2	76	30
4	*MWW* + *L-4* [f]	560	82 ± 7	86	3.4
5	*L-4* [g]	220	489 ± 78	53	15
6	*L-1* [h]	220	378 ± 62	20	10

Notes: [a]external resitances used; [b]average volumetric power; [c]organic matter removal efficiency on *COD* basis; [d]coulombic efficiency; [e]municipal wastewater; [f]mixture of municipal wastewater and leachate from section 4 of the sanitary landfill; [g] leachate from section 4 of the sanitary landfill; [h]leachate from section 1 of the sanitary landfill.

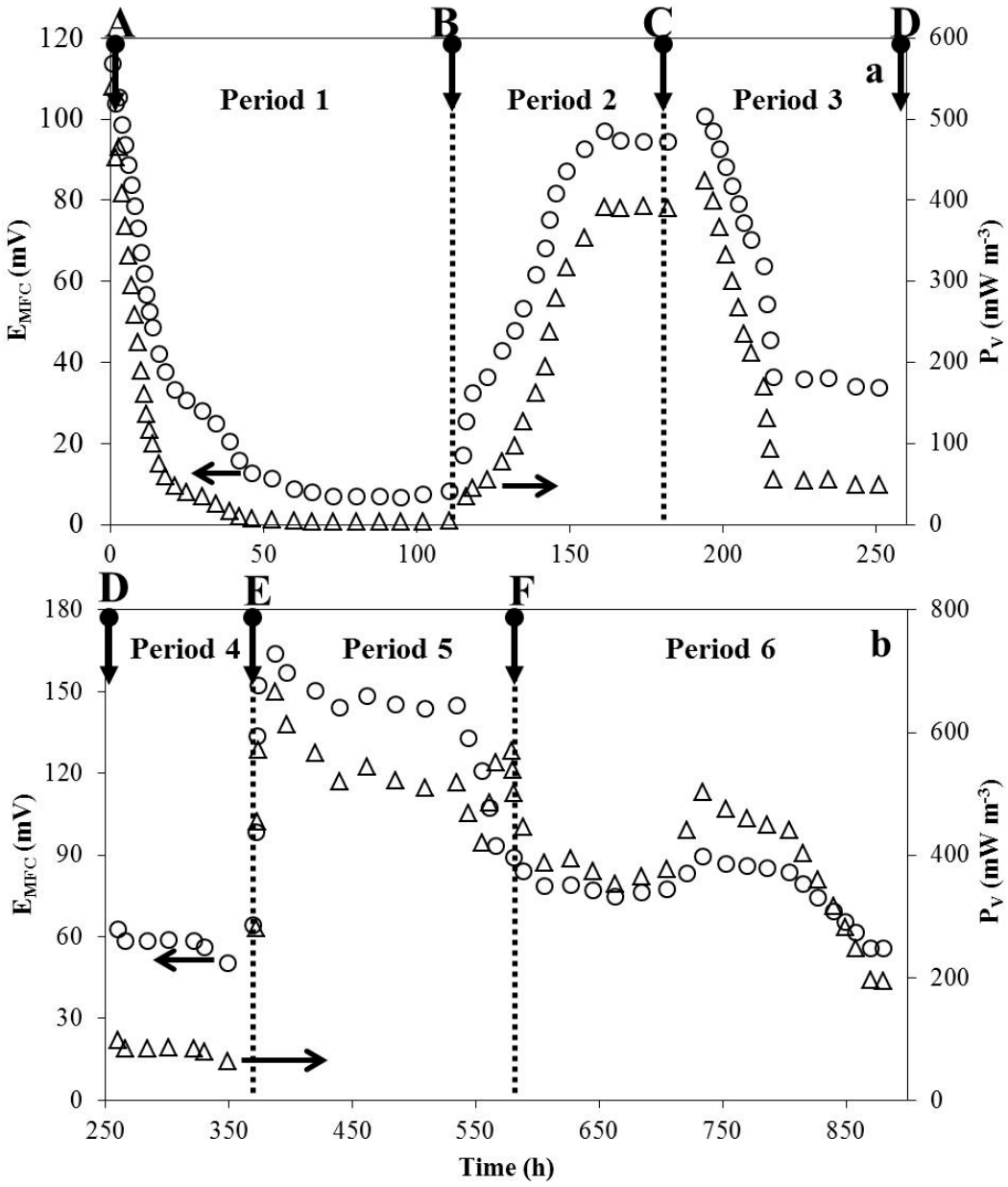

Fig. 2. Time course of **v**oltage and volumetric power of the microbial fuel cell in the six batch periods: (a) Periods 1 to 3; (b) Periods 4 to 6 (see Table 3).
Keys: E_{MFC}, hollow circles; P_V, hollow triangles; A, *MWW* plus seed; B, *MWW* plus seed; C, *MWW*; D, mixture *MWW* and *L-4* plus seed; E, *L-4*; F, *L-1*.

On the one hand, it could have been associated to the re-seeding the *MFC* with inoculum, on the other hand, a possible in-cell enrichment/acclimation could have occurred [32,33]. In Period 3, no re-seeding was performed, and this likely was associated to a decrease of P_V, although the values of η_{COD} and *CE* were still acceptable**.**

Ahn and Logan [4] carried out tests on treatment of a weak domestic wastewater (111 mg L^{-1} BOD) in a single-chamber *MFC* of 130 mL capacity equipped with multiple graphite fiber brush anodes and a single air cathode. In fed-batch operation, the maximum current density was 148 ± 8 mA m^{-2} using an R_{ext} of 1 000 Ω; the *CE* was 15%. The authors did not report power density values, but our calculations with their data indicate average P_V and P_{cath} *ca*. 2000 mW m^{-3} and 77 mW m^{-2}, respectively. Interestingly, when the cell was operated with a lower R_{ext} of 100 Ω, the performance of the device was significantly lower (130 mV, 1300 mW m^{-3}, and 48 mW m^{-2}) except for the *CE* that increased to 22%. High organic matter removals were reported (90% or higher). This difference was attributed to previous acclimation of the cells and former reports that high external resistances were associated to shorter lag phase for the development of an exoelectrogenic biofilm (electrochemically active bacteria or community) [4,34,35].

Anyway, power delivery in both tests by Ahn and Logan [4] were higher than those in our Periods of Phase 1 (Table 3), although our *CE* was higher (up to 47%) and η_{COD} were slightly lower (up to 80%). Differences on the cell operation mode could be related to differences in performance. As it is known, in fed-batch operation, the influent is continuously fed to the reactor without effluent extraction, until the end of the run is attained [36]. On the other hand, in batch mode, the cell is punctually loaded with influent, in one presentation, with no further addition of influent during the run. So, the supply of organic matter to the bioelectrochemical devices is much higher in the fed-batch (m_{BOD}= Q*[BOD]*t, Q is the flow rate of influent during the run, t is the time of the run) than in the batch operation ($m'_{BOD} = V_{net}$*[BOD], V_{net} is the net volume of the anodic chamber), which can explain the higher powers in spite of the lower *CE*.

Our values of P_V and *CE* were higher than those reported by Liu et al. [37], although the η_{COD} was similar. Indeed, Liu et al. [37] used domestic wastewater with a concentration similar to our work (220 mg L^{-1}) to produce electricity in a *MFC* and remove organic matter from the effluent. Their system was an air cathode single chamber *MFC* with eight graphite electrodes as anodes. The cell was operated in continuous flow with an effluent obtained from a local wastewater treatment plant. The maximum electrical power generated by their system was 26 mW m^{-2} (190 mW m^{-3}) and under these conditions the η_{COD} was up to 80% of the wastewater. In contrast, the *CE* was relatively low, less than 12%.

In another work using domestic wastewater as substrate, Liu and Logan [38] in an air-cathode *MFC* containing carbon electrodes examined the power generation. The microorganisms in domestic wastewaters were used as biocatalyst. Using the domestic wastewater the average power density was 28 ± 3 mW m^{-2} (with P_V of 700 ± 100 mW m^{-3}) and the *CE* was 28%. Furthermore, they showed the effect of the absence of proton exchange membrane (*PEM*) on *MFC* performance. When the *PEM* was removed the *CE* decreased (20%) and the power density increased 5-fold (146 ± 8 mW m^{-2}; P_V of 3 700 ± 200 mW m^{-3}). Thus, their results show that the *CE* not only depends of the substrate or biocatalyst, the *PEM* also plays an important role on the *CE*. Yet, not only presence/absence of *PEM* impacts *MFC*'s performance, also the type of membrane or separator can have a decisive influence [3].

In general, the relatively low performance of *MFC* treating *MWW* has been attributed first, to the fact that domestic wastewater is considered a dilute effluent (low concentrations of substrate as *COD* substrate) compared to other influents used in laboratory tests. It is

known that power production in *MFC*s commonly follows a hyperbolic relationship (Monod) with substrate concentration; therefore, it is expected a reduced power delivery at low *COD* [4,38-40]. Second, the organic matter of *MWW* is a complex mixture of carbohydrates, proteins, and lipids. According to Fornero et al. [3] and other works, collective experience with *MFC*s has shown that complex substrates such as *MWW* and leachates are associated to low *CE* and relatively lower removals of organic matter, whereas simple organic compounds, i.e., acetate, and simple effluents (one substrate or at most two combined substrates) are associated to high *CE* and higher removals of *COD* [3,39]. In the review by Fornero et al. [3] several issues related to the pattern described above are discussed. Indeed, they compiled several experimental works with *MFC*s and showed that a trend emerged with the subgroup that tested complex influents (municipal wastewater, slaughterhouse wastewater, piggery wastes, hospital effluents, and brewery wastewater) showing lower *CE* with a highest level of 36% compared to the subgroup of experiments that used synthetic wastewaters, with a highest level of 98% *CE*. Fornero et al. [3] discussed that one reason for this pattern of higher *CE*s for carboxylic acids compared to the lower values for complex wastewaters, could be the loss in efficiency of electron transfer in the anodic foodweb anchored in the *MFC*. In experiments by Rabaey et al. [41] with acetate and glucose as model substrates, the highest *CE* was achieved with acetate glucose likely because the exolectrogen species, i.e., *Geobacter sp*., can convert acetate to bicarbonate (CO_2), protons, and electrons directly without sustaining a fermentative population. On the other hand, the degradation of complex substrates requires a more complex consortium, where fermentative microbes can play a significant role. The latter likely will consume a fraction of the energy (electrons) for synthesis and maintenance and so the electron transfer would be less efficient [41,42]. Third, the low electrical conductivity of *MWW*, typically below 1 mS cm^{-1}, can result in lower power densities compared to those obtained with influents that possess high conductivity or are supplemented with buffer solutions to mitigate possible pH gradients in lab experiments [4].

3.2 Experiments of the 2nd Phase

In the characterization studies of the second phase, where the influent was a mixture of *MWW* and leachate, the R_{int} of the cell was 620 Ω and $P_{v,max}$ was 90 mW m^{-3} (Figure 3a). These values were poorer than those obtained with only *MWW*. In principle, the cell characteristics seemed to predict a cell performance lower than that recorded with only *MWW*.

One reason of this pattern could be related to a lack of acclimation to leachate. Another reason could be the alkaline pH of the mixture (8.3 or higher) as discussed below.

In the first period of phase 2 (period 4, Table 3) showed an attractive η_{COD} (86%) although the volumetric power was below 100 mW m^{-3} and the *CE* was very poor (Figure 2b, Table 3). Again lack of acclimation of biomass to leachate could have had a negative effect. Also, the Nafion membrane probably was not the best type of separator for handling alkaline leachates in *MFC*s. Indeed, it has been shown that highly-selective *PEM*s that are typical of hydrogen fuel cells (i.e., Nafion) are less than ideal for *MFC*s. Indeed, at neutral pHs typical of most wastewaters fed to *MFC*s, cations rather than protons are the chemical species moving from the anode to the cathode [3,43-45].

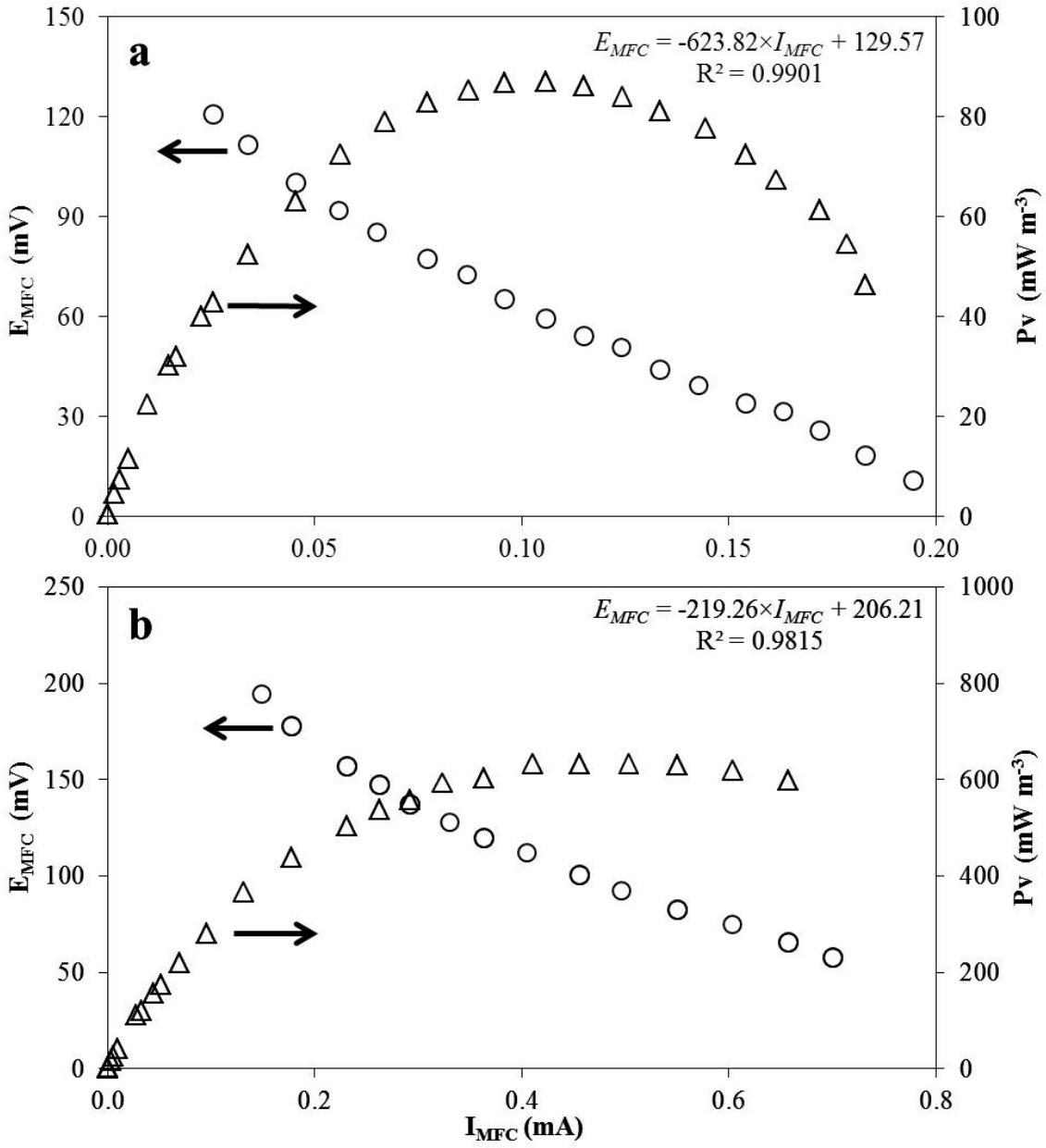

Fig. 3. Electrochemical characterization of the microbial fuel cells loaded with **a**) a mixture of municipal wastewater and leachate from section 4 of the sanitary landfill **b**) only leachate from section 4 of the sanitary landfill. Keys: E_{MFC}, hollow circles; P_V, hollow triangles.

Furthermore, Harnisch et al. [46] reported that using an anion exchange membrane in a *MFC* lead to better results than a cation exchange membrane. Recent results of our Group [47] showed that single chamber *MFC*s equipped with Zirfon membrane (an anion exchange separator) delivered a volumetric power 16.5-fold superior to that of a *MFC*s equipped with the conventional Nafion membrane, in the batch operation with alkaline

leachate. Therefore, selection of the separator depends to a great extent on the composition of anolytes (and catholytes in two-chamber cells).

In Period 4, we diluted the leachate with *MWW* in order to increase the *COD* concentration of the *MWW* and to reduce the pH in the mixture. We hypothesized that mixing both effluents could lead to better results. You et al. [48] also used this strategy of leachate dilution prior to its treatment in single chamber *MFC*. However, they used tap (drinking) water to reduce the *COD*, which is environmentally debatable. In our case, results show that mixing *MWW* and leachate did not necessarily improve *MFC* performance, except for high organic removal efficiency.

Before starting the 5th period, the *MFC* was characterized with 100% *L-4* as influent. We found a much lower R_{int} (220 Ω) and an attractive value of $P_{v,max}$ of 650 mW m^{-3} (Figure 3b) much higher than the value obtained in the characterization of the same *MFC* when loaded with 100% *MWW* (Figure 1).

Batch operation of the cell in the 2nd period of phase 2 (period 5, Table 3) resulted in significantly increased both *CE* and power whereas a moderate value of η_{COD} 53% was achieved, in spite that no new inoculum was seeded into the *MFC*. As we discussed above, a beneficial in-cell acclimation process could have been responsible of this improvement [32,33]. The trend of a relatively high average volumetric power was kept in Period 6 when the leachate fed was L-1. However, the average η_{COD} and *CE* were lower than those in Period 5.

Damiano et al. [6] also designed and operated *MFC*s to carry out the treatment of landfill leachate while electricity was simultaneously produced.

4. Conclusion

In the cell characterization with *MWW*, the R_{int} of the cell and its $P_{v,max}$ were 350 Ω and 760 mW m^{-3}, respectively.

Batch operation with *MWW* with the cell connected to an R_{ext} of 330 Ω, average overall removal of organic matter of 60% *COD* and 4% *CE* were achieved. Afterwards, two repeated more batches were carried out, where the *CE* significantly increased up to 78% whereas the η_{COD} slightly improved (48%).

On the other hand, in the experiments with *MWW* mixed with leachate, the *MFC* effected an attractive η_{COD} (86%) although the electrochemical performance of the cell was poorer than those with *MWW* alone and leachate alone. So, contrary to what was expected, there was no evidence of a better *MFC* performance when using a substrate that was a mixture of *MWW* and leachate.

Re-inoculation of the *MFC* seemed to have a positive effect on *CE* of the process. Also, there was preliminary evidence that indicated that in-cell inoculum enrichment or acclimation has occurred.

Thus, *MFC* application to municipal effluents (wastewater and leachates) holds promise for effluent depuration, and further investigation is warranted.

Acknowledgements

The authors thank Mr. Rafael Hernández-Vera, Ms Perla A. Bello-Mayén, and technicians of the Environmental of Biotechnology and Renewable Energy R&D Group, CINVESTAV-IPN for their excellent technical help.

References

[1] Ávila García P. Agua, cultura y sociedad en México. Co-edición El Colegio de Michoacán: Instituto Mexicano de Tecnología del Agua. 2002; ISBN 970-679-083-7.
[2] Tchobanoglous G., Burton F.L., Stensel H.D. Wastewater Engineering-Treatment and Reuse, McGraw-Hill's, 4th edition, 2003.
[3] Fornero J.J., Rosenbaum M., Angenent L.T. Electric power generation from municipal, food, and animal wastewaters using microbial fuel cells. Electroanalysis 2010; 22(7-8):832-843.
[4] Ahn Y., Logan B.E. Domestic wastewater treatment using multi-electrode continuous flow *MFC*s with a separator electrode assembly design. Applied Microbiology and Biotechnology 2013; 97:409-416.
[5] Secretaría de Medio Ambiente, Recursos Naturales y Pesca (1996) Norma Oficial Mexicana NOM-001-SEMARNAT-1996.
[6] Damiano L., Jambeck J.R., Ringelberg D.B. Municipal solid waste landfill leachate treatment and electricity production using microbial fuel cells. Applied Biochemistry and Biotechnology 2014;173:472-485.
[7] Tchobanoglous G., Kreith F. Handbook of solid waste management McGraw-Hill, 2nd edition, 2002.
[8] Kjeldsen P., Barlaz M.A., Rooker A.P., Baun A., Ledin A., Christensen T.H. Present and long-term composition of MSW landfill leachate: A review. Critical Reviews in Environmental Science and Technology 2002; 32(4):297-336.
[9] Belmonte-Jiménez S.I., Bortolotti-Villalobos A., Campos-Enríquez J.O., Pérez-Flores M.A., Delgado-Rodríguez O., Ladrón de Guevara-Torres M.A. Electromagnetic methods application for characterizing a site contaminated by leachates. Revista Internacional de Contaminación Ambiental 2014; 30(3):317-329.
[10] Poggi-Varaldo H.M., Carmona-Martínez A., Vázquez-Larios A.L., Solorza-Feria O. Effect of inoculum type on the performance of a microbial fuel cell fed with spent organic extracts from hydrogenogenic fermentation of organic solid wastes. J. New Mater. Electrochem. Syst. 2009; 12:49-54.
[11] Vazquez-Larios A.L., Solorza-Feria O., Vazquez-Huerta G., Esparza-Garcia F.J., Rios-Leal E., Rinderknecht-Seijas N., Poggi-Varaldo H.M. A new design improves performance of a single chamber microbial fuel cell. J. New Mater. Electrochem. Syst. 2010; 13:219-226.
[12] Hernández-Flores G., Poggi-Varaldo H.M., Solorza-Feria O., Ponce Noyola M.T., Romero-Castañón T. Rinderknecht-Seijas N. Tafel equation based model for the performance of a microbial fuel cell. Int. J. Hydrogen Energy 2015; In press. http://dx.doi.org/10.1016/j.ijhydene.2015.06.119
[13] Hernández-Flores G., Poggi-Varaldo H.M., Solorza-Feria O., Romero-Castañón T., Ríos-Leal E., Galíndez-Mayer J., Esparza-García F. Batch operation of a microbial fuel cell equipped with alternative proton exchange membrane. Int. J. Hydrogen Energy 2015; In press. http:// dx.doi.org/10.1016/j.ijhydene.2015.06.057.
[14] Poggi-Varaldo H.M., Munoz-Paez K.M., Escamilla-Alvarado C., Robledo-Narváez P.N., Ponce-Noyola M.T., Calva-Calva G., Ríos-Leal E., Galíndez-Mayer J., Estrada-Vázquez C., Ortega-Clemente A., Rinderknecht-Seijas N.F. Biohydrogen, biomethane and bioelectricity as crucial components of biorefinery of organic wastes: A review. Waste Management & Research 2014; 32:353-365. doi:10.1177/0734242X14529178.
[15] Hernández-Flores G., Poggi-Varaldo H.M., Solorza-Feria O., Ponce Noyola M.T., Romero-Castañón T., Rinderknecht-Seijas N. Improvement of microbial fuel cell performance by selection of anodic materials and enrichment of inoculum. J. New Mater. Electrochem. Syst. 2015; In press.
[16] Schröder U. Anodic electron transfer mechanisms in microbial fuel cells and their energy efficiency. Physical Chemistry Chemical Physics 2007; (9):2619-2629.
[17] Du Z., Li H., Gu T. A state of the art review on microbial fuel cells: A promising technology for

wastewater treatment and bioenergy. Biotechnology Advances 2007; 25:464-482.
[18] Lefebvre O., Al-Mamun A., Ooi W.K., Ng H.Y., Tang Z. Chua D.H.C. An insight into cathode options for microbial fuel cells. Water Science and Technology 2008; 57(12):2031-2037.
[19] Torres C.I., Marcus A.K., Lee H.S., Parameswaran P., Krajmalnik-Brown R. Rittmann B.E. A kinetic perspective on extracellular electron transfer by anode-respiring bacteria. FEMS Microbiology Reviews 2010; 34(2010):3-17.
[20] Rozendal R.A., Hamelers H.V.M., Rabaey K., Keller J., Buisman C.J.N. Towards practical implementation of bioelectrochemical wastewater treatment. Trends in Biotechnology 2008; 26(8):450-459.
[21] Pant D., Bogaert G.V., Diels L., Vanbroekhoven K. A review of the substrates used in microbial fuel cells (MFCs) for sustainable energy production. Bioresource Technology 2010; 101:1533-1543.
[22] Poggi-Varaldo H.M., Vazquez-Larios A., Solorza-Feria O. Microbial fuel cells. In: Rodríguez-Varela FJ, Solorza-Feria O, Hernández-Pacheco E, editors. Fuel cells. Montr_eal, Canada: Book Livres; 2010. p. 124-161.
[23] Logan B.E. Microbial fuel cells. John Wiley-Interscience. New Jersey, USA, 2007.
[24] Watson V.J., Logan B.E. Analysis of polarization methods for elimination of power overshoot in microbial fuel cells. Electrochemistry Communications 2011; 13:54-56.
[25] Xia X., Tokash J.C., Zhang F., Liang P., Huang X., Logan B.E. Oxygen-reducing biocathodes operating with passive oxygen transfer in microbial fuel cells. Environmental Science & Technology 2013; 47(4):2085-2091.
[26] Poggi-Varaldo H.M., Rinderknecht-Seijas N. A differential availability enhancement factor for the evaluation of pollutant availability in soil treatments. Acta Biotechnologica (Engineering in Life Sciences, Ed John Wiley) 2003; 23:271-280.
[27] Singh S.K., Tang W.Z. Statistical analysis of optimum Fenton oxidation conditions for landfill leachate treatment. Waste Management 2013; 33(1):81-88.
[28] APHA, AWWA and WPCF. Standard Methods for the Examination of water and Wastewater. 21st ed. American Public Health Association, American Water Works Assotiation and Water Environment Federation, Washington, 2005; 874 pp.
[29] Logan B.E., Hamelers B., Rozendal R., Schröder U., Keller J., Freguia S., Aelterman P., Verstraete W., Rabaey K. Microbial fuel cells: Methodology and technology. Environmental Science & Technology 2006; 40(17):5181-5192.
[30] Logan B.E., Rabaey K. Conversion of wastes into bioelectricity and chemicals by using microbial electrochemical technologies. Science 2012; 337:686-690.
[31] Hsu L., Chadwick B., Kagan J., Thacher R., Wotawa-Bergen A., Richter K. Scale up considerations for sediment microbial fuel Cells. RSC Advances 2013; 3:15947-15954.
[32] Ortega-Martínez A.C., Juárez-López K., Solorza-Feria O., Ponce-Noyola M.T., Galindez-Mayer J., Rinderknecht-Seijas N., Poggi-Varaldo H.M. Analysis of microbial diversity of inocula used in a five-face parallelepiped and standard microbial fuel cells. Int. J. Hydrogen Energy 2013; 38:12589-12599.
[33] Ortega-Martínez A., Juárez-López K., Solorza-Feria O., Ponce-Noyola M.T., Ríos-Leal E., Rinderknecht-Seijas N.F., Poggi-Varaldo H.M. Parallel Connection and Sandwich Electrodes Lower the Internal Resistance in a Microbial Fuel Cell. J. New Mater. Electrochem. Syst. 2012; 15(3):187-194.
[34] Hong Y., Call D.F., Werner C.M., Logan B.E. Adaptation to high current using low external resistances eliminates power overshoot in microbial fuel cells. Biosensors and Bioelectronics 2011; 28(1):71-76.
[35] Zhang L., Zhu X., Li J., Liao Q., Ye D. Biofilm formation and electricity generation of a microbial fuel cell started up under different external resistances. Journal of Power Sources 2011; 196(15):6029-6035.
[36] Bailey J.E., Ollis D.F. Biochemical Engineering Fundamentals. McGraw-Hill Education; 2nd edition. USA, 1986.
[37] Liu H., Ramnarayanan R., Logan B.E. Production of electricity during wastewater treatment using a single chamber microbial fuel cell. Environmental Science & Technology 2004; 38(7): 2281-2285.
[38] Liu H., Logan B.E. Electricity generation using an aircathode single chamber microbial fuel cell in the presence and absence of a proton exchange membrane. Environmental Science & Technology 2004; 38:4040-4046.
[39] Min B., Logan B.E. Continuous electricity generation from domestic wastewater and organic substrates in a flat plate microbial fuel cell. Environmental Science & Technology 2004; 38(21):5809-5814.
[40] Torres C.I., Kato M.A., Rittmann B.E. Kinetics of consumption of fermentation products by anode-

respiring bacteria. Applied Microbiology and Biotechnology 2007; 77(3):689-697.
[41] Rabaey K., Clauwaert P., Aelterman P., Verstraete W. Tubular microbial fuel cells for efficient electricity generation. Environmental Science & Technology 2005; 39:8077- 8082.
[42] Liu H., Cheng S., Logan B.E. Production of electricity from acetate or butyrate using a single-chamber microbial fuel cell. Environmental Science & Technology 2005; 39:658-662.
[43] Rozendal R.A., Hamelers H.V.M., Buisman C.J.N. Effects of membrane cation transport on pH and microbial fuel cell performance. Environmental Science & Technology 2006; 40:5206- 5211.
[44] Zhao F., Harnisch F., Schröder U., Scholz F., Bogdanoff P., Herrmann I. Environmental Science & Technology 2006; 40:5191- 5199.
[45] Fornero J.J., Rosenbaum M., Cotta M.A., Angenent L.T. Microbial fuel cell performance with a pressurized cathode chamber. Environmental Science & Technology 2008; 42:8578-8584.
[46] Harnisch F., Schröder U., Scholz F. The suitability of monopolar and bipolar ion exchange membranes as separators for biological fuel cells. Environmental Science & Technology 2008; 42:1740-1746.
[47] Hernández-Flores G., Poggi-Varaldo H.M., Romero-Castañón T., Solorza-Feria O. Harvesting energy from leachates in microbial fuel cells using an anion exchange membrane. XV International Congress of the Mexican Hydrogen Society 2015.
[48] You S.J., Zhao Q.L., Jiang J.Q., Zhang J.N., Zhao S.Q. Sustainable approach for leachate treatment: Electricity generation in microbial fuel cell. Journal of Environmental Science and Health, Part A 2006; 41:2721-2734.

Abbreviations and symbols

BP	bordo poniente
CE	coulombic efficiency
COD	chemical oxygen demand
$E_{MFC,max}$	maximum potential of the cell
$E_{MFC,OCP}$	open circuit potential of the cell
L-1	leachate from section 1 of the sanitary landfill
L-4	leachate from section 4 of the sanitary landfill
MFC	microbial fuel cell
MWW	municipal wastewater
P_{cath}	power density per unit area of electrode
P_v	average volumetric power
$P_{v,max}$	maximum volumetric power
R_{ext}	external resistance
R_{int}	internal resistance
SR-In	sulphate-reducing inoculum
SL	sanitary landfill

Greek characters

η_{COD}	organic matter removal efficiency on COD basis

Chapter 5.14. Optimal slow pyrolysis of pomace reaction conditions for the generation of a feedstock gas for hydrogen production

M. R. Baray Guerrero; J. M. Salinas Gutiérrez; M. J. Meléndez Zaragoza; A. López Ortiz; V. Collins-Martínez*

Departamento de Ingeniería y Química de Materiales, Centro de Investigación en Materiales Avanzados, S.C., Miguel de Cervantes 120, Chihuahua, Chih., México, 31136.

ABSTRACT

The present research is aimed to explore optimal reaction conditions for the generation of a gas product, through the slow pyrolysis of pomace, to be used as a feedstock for the production of H_2 by the absorption enhanced reforming of methane (AER) process scheme. Pyrolysis experiments were performed in a tubular reactor under conditions of rich syngas production (300–450 °C) and for specific solid heating rates (5-20 °C/min). Permanent gases (CO, CH_4 and CO_2), aromatic tars, and chars were quantified at different heating rates and isothermal conditions. Results indicate that at a temperature of 400 °C a maximum of 71.5% W of non-condensable volatile matter (NCVM) can be obtained along with 25.4% W of condensable volatile matter (CVM), while only 3% W of residual matter (RM) was produced. At this favorable conditions (NCVM) a gas composition of 41% CO, 38% CO_2 and 21% CH_4 was generated. A thermodynamic analysis of this product gas was performed under the steam reforming of methane (SMR) combined with CO_2 solid absorption by CaO for the production of high purity H_2. Thermodynamic calculations using a steam to methane ratio (S/C) of 4 and 1 mol of CaO/mol of CH_4 indicate that a maximum H_2 production is achieved at 690 °C along with a composition of 74.1 % H_2, 16.2% CO, 7.6% CO_2 and 2.1% CH_4 with no carbon formation.

Keywords: Pyrolysis of Pomace, Hydrogen production and CO_2 capture

1. Introduction

The use of biomass for the production of energy has become an important strategy aimed to reduce the harmful environmental impact of today's use of fossil fuels. Energy derived from biomass and solid wastes, has been the heart of many thermochemical and biochemical processes [1]. In thermochemical processes, gasification and pyrolysis has reached greater energy conversions than direct combustion. During gasification, fuel molecules (H_2, CH_4, CO and CO_2) are produced, while biomass is transformed into gaseous

---

* Author for correspondence: V. Collins Martinez, T: 526144391129; E: virginia.collins@cimav.edu.mx

products [2]. Furthermore, biofuels produced from various lignocellulosic materials such as wood, agricultural or forest residues, have the potential to be a valuable substitute (or supplement to gasoline biofuels) to liquid or gaseous fuels for the transport sector [3]. One specific example of a biomass waste is the apple pomace, which is the residue generated in the process of extraction of apple juice. This apple pomace, is formed by a complex mixture of shell, seed kernel, calyx, stem and soft tissue, which is representative of the pomace, and this contains mainly cellulose, hemicellulose, lignin and pectin.

Moreover, a great deal of research has been made focused on flash and vacuum pyrolysis, process conditions and its yield. However, slow pyrolysis has been overlooked, probably because in this kind of processes solid residues are the interested product and condensable and non-condensable products are burned or directly emitted to the atmosphere [4] and as a consequence, up to date there are no studies involving the slow pyrolysis of Mexico's apple pomace. This condensable and non-condensable matter that usually is called bio-oil and bio-gas, respectively; is suitable to be employed as feedstock for hydrogen production [5].

Two main technologies for hydrogen production that have been explored in recent years are biomass steam gasification and biomass slow pyrolysis [6]. It has been reported that fast pyrolysis followed by steam methane reforming of oil delivers less H_2 yield. The H_2 production cost from supercritical water gasification is too high. Compared with fast pyrolysis and supercritical water gasification, steam gasification performs better. However, the efficiency of the steam methane reforming of the products from the slow pyrolysis process can be enhanced towards the production of hydrogen from biomass (apple pomace) [7].

Furthermore, in biomass-derived carbohydrates steam reforming reactions, if CO_2 is removed immediately, according to Le Chatelier principle, its partial pressure decreases and the equilibrium shifts to the direction that favors hydrogen production [8-11]. This makes possible high fuel (i.e. CH_4) conversion at relatively low temperatures and production of high quality hydrogen (95%) with only traces of carbon oxides (in the order of 1 vol. %). This concept has been called absorption enhanced steam reforming (AESR) [12]. Recent experiments by Yi and Harrison [13] demonstrated that in the presence of an absorbent fairly good conversion and very low concentrations of CO can be achieved even at very low pressures (1 bar) and temperatures (460 °C). A potential absorbent material should have good CO_2 capacity at high temperatures, be easily regenerable and thermally stable to allow a cyclic absorption-desorption process. Experimental studies have demonstrated that in situ carbonation of CaO within the steam reformer is able to generate high H_2 concentrations [9-10]. Thus, this absorbent (CaO) have become highly attractive to be used under the AESR process. Therefore, a thermodynamic analysis can be of paramount importance to investigate fundamental reaction parameters influencing the output of H_2-rich gas from the AERS of non-condensable volatile matter (NCVM) produced from the slow pyrolysis of apple pomace. However, NCVM composition is of great importance, since from this depends the final hydrogen production purity and quantity.

Hence, the present research is aimed to explore optimal reaction conditions for the generation of a gas product (NCVM), through the slow pyrolysis of pomace, to be used as a feedstock for the production of H_2 by the absorption enhanced reforming of methane (AER)

process scheme. Furthermore, a thermodynamic analysis will be performed to explore the hydrogen production by the AER of the NCVM.

2. Experimental

2.1 Sample Characterization

Apple pomace samples were collected from the northern state of Chihuahua (Cuauhtémoc, Chihuahua) and subjected to a drying process, crushed, grounded and sieved to achieve a particle size of 150 mm. The elemental and proximal analyzes for the apple pomace sample were performed using a Carlo Erba EA-1110 elemental analyzer and an atomic emission spectrometer coupled with ICP (ICP Thermo Jarrell Ash IRIS/AP DUO). Lignin, cellulose, hemicellulose and pectin content from the pomace were determined using gravimetric techniques, described in ASTM (E 1756-95, D1106-95) and ASTM (D1103-60). Moisture, volatiles and ash content was determined according to the procedure described in ASTM E (871-82), ASTM (872-82) and ASTM (1755-1795), respectively. In order to determine the particle size (dp), samples were analyzed with dimensions: dp < 150 mm (150 mm), 150 < dp < 180 mm (180 mm), 180 < dp < 250 mm (250 mm), and 250 < dp < 450 mm (450 mm)

2.2. Determination of bagasse pyrolysis parameters

Operating parameters that directly influence biomass pyrolysis are: temperature, particle size (dp), heating rate and residence time [14]. The production of a greater amount of volatile matter was the criterion applied for determining the value of the operating parameters. For this purpose, Thermogravimetric Analysis (TGA) tests were performed in TA Instruments Q500. TGA conditions employed to find optimal values for temperature and particle size were; a N_2 flowrate of 150 cm^3/min and a heating rate of 10 °C/min. In order to verify the effect of the heating rate over the production of volatile matter, three samples of cane bagasse with the same particle size were exposed at different heating rates; 5, 10, 15 and 20 °C/min. Residence time, which was defined as the time required for a 90% volatilization of the sample, was determined by varying the residence time at different temperatures (pyrolysis in stages) [15]. This was achieved by the combination of the dynamic and isothermal TGA operating modes under the following conditions: particle size of 420 < dp < 840 µm, heating rate of 10 °C/min, N_2 flowrate of 100 cm^3/min, isotherms of 150, 200, 250, 300, 350, 400, 450, 500 and 550 °C and residence time of 60 min.

2.3. Quantification of the pyrolysis products

The carbon residue percentage (CR) was obtained from the fractioned pyrolysis performed in the TGA using a residence time of 60 min. The condensable matter was gravimetrically quantified during the fractioned pyrolysis and this was performed in a fixed-bed tubular reactor coupled to a condensing system as described in Figure 1.

The pyrolysis apparatus was composed of a stainless steel tubular reactor, heated by an electrical furnace to temperatures up to 600 °C in an inert N_2 atmosphere (see Fig. 1). The stainless steel tubular reactor had an internal diameter of 2 cm and a heated length of 27

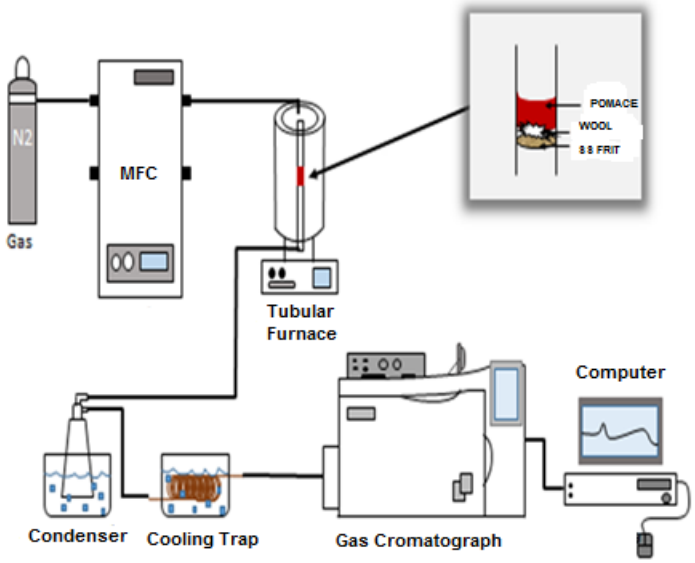

Fig. 1. Experimental reactor setup for the pyrolysis of pomace.

cm. Apple pomace samples were introduced into the center of the preheated reactor and held with a porous stainless steel frit and quartz wool. The carrier gas (N_2) was also used as a tracer. Its flow rate (100 cm^3/min) was controlled by a mass flow rate regulator (Brooks Instrument). Condensable volatiles are trapped in a copper coil condenser cooled to 2 °C. In order to determine the amount of mass of condensable volatiles, the weight change before and after each cycle of the pyrolysis was measured. The volatile compounds were separated and identified by gas chromatography using a Perkin Elmer Clarus 500. Detection of non-condensable gases ((N_2, H_2, CO, CO_2, CH_4, C_2H_4, and C_2H_6) was performed simultaneously with the devolatilization process. Condensable products were collected and stored for each isotherm to be analyzed later. In order to determine the amount of condensable volatile products, the heat exchanger was weighted before and after each pyrolysis stage using an analytic balance. The condensable volatile matter percentage (% CVM) for each isotherm was calculated according to the following expressions:

$$CVM = CVM/MB_1 \times 100 \quad (1)$$

where: MB1 is the initial pomace mass, the percentage of non-condensable volatile matter (%NCVM) was obtained from the pyrolysis material balance:

$$\%NCVM = 100\% - \%CVM - \%RC \quad (2)$$

where the % RC is the percentage of carbon residue.

2.4. Thermodynamic analysis

All calculations were performed through the use of the equilibrium module of the HSC chemistry software [16]. HSC calculates the equilibrium composition of all possible combination of reactions that are able to take place within the thermodynamic system. These equilibrium calculations make use of the equilibrium composition module of the HSC program that is based on the Gibbs free energy minimization technique. The GIBBS program of this module finds the most stable phase combination and seeks the phase compositions where the Gibbs free energy of the system reaches its minimum at a fixed mass balance, constant pressure and temperature.

3. Results and discussion

3.1 Physicochemical characterization of pomace

Table 1 presents results of the physicochemical characterization performed on the apple pomace. These results are comparable to the ones reported in the literature related to other typical bagasse biomass [17-26].

The thermal decomposition of the apple pomace reveals two main regions attributed to the decomposition of cellulose and hemicellulose. The first decomposition mass loss that occurs at low temperatures can be associated to the process of pyrolysis of hemicellulose and at higher temperatures the weight loss is associated with decomposition of cellulose. Moreover, mass losses for the decomposition of lignin are not observed in this temperature range. Understanding of the volatilization of apple pomace is important because pyrolysis is the first step in a process of gasification or combustion [27]. Furthermore, in this TGA plot it is observed that the greatest amount of volatile material is produced at a heating rate of 5 °C/min, which is the curve that ends its decomposition at a lower temperature (~540 °C). When heating rate increases, the required time to reach a certain temperature value increases, enabling dehydration, depolymerization, carbonylation, carboxylation and transglycosylation reactions. As a consequence, the amount of devolatilized matter is increased. The obtained curves at different heating rates, after a certain decomposition stage at high heating rate, reach a common value typical of the mass solid residue [28]. The largest sample weight loss is located from a temperature range of 200-450 °C, as can be observed in Fig. 1, and this can be attributed to the devolatilization process. Analyzing this behavior, according to the literature the weight loss that occurs at 200 °C is related to the beginning of the lignin and hemicellulose pyrolysis contained in the apple pomace [29]. From 250 and up to approximately 350 °C the high decomposition rate arises and in this region the maximum devolatilization of hemicellulose, cellulose and lignin is achieved. Remaining molecules of these compounds generate the next weight loss that corresponds to the temperature (up to 550 °C) in which the reaction ends.

Table 1. Apple pomace physicochemical data.

Parameter	Units	Magnitude
Elemental analysis [a]		
C	%	47.98
H	%	6.65
N	%	0.78
S	%	-----
O	%	37.5
Composition analysis [a,b]		
Cellulose	%	47.5
Hemicellulose	%	27.8
Lignin	%	22.4
Proximal analysis		
Humidity [c]	%	8.87
Volatile matter	%	81.32
Fixed carbon	%	6.41
Ash ($420 < d_p < 840$ μm)	%	5.10
Ash composition		
Al	%	0.51
B	%	11.43
Ba	%	37.75
Ca	%	2.01
Cr	%	0.80
Cu	%	8.50
Fe	%	0.35
K	%	7.73
Mg	%	1.54
Mn	%	10.24
Na	%	0.23
Ti	%	17.51
V	%	0.56
Extractable		
Ethanol	%	2.69
Physical properties		
Density	Kg/m^3	110.3
Calorific value	KJ/Kg	7639.18

a Dry bagasse basis **b** Extractable free **c** Wet basis

Experimental TGA curves obtained for the apple pomace under different heating rates are presented in Figure 2. Figure 3 presents a TGA plot of the apple pomace biomass (APB) subjected to different particle size fractions at a heating rate of 10 °C/min. In this Figure it can be observed that particle sizes smaller or equal than 150 μm are the ones that allow the generation of the greater amount of volatile matter. The difference in volatiles production with respect to the size of the particles is attributed to a main reason: particles greater than 425 μm, during the devolatilization process, some problems arise related to the heat and mass transfer [30], as reported by Lou and Stanmore [31].

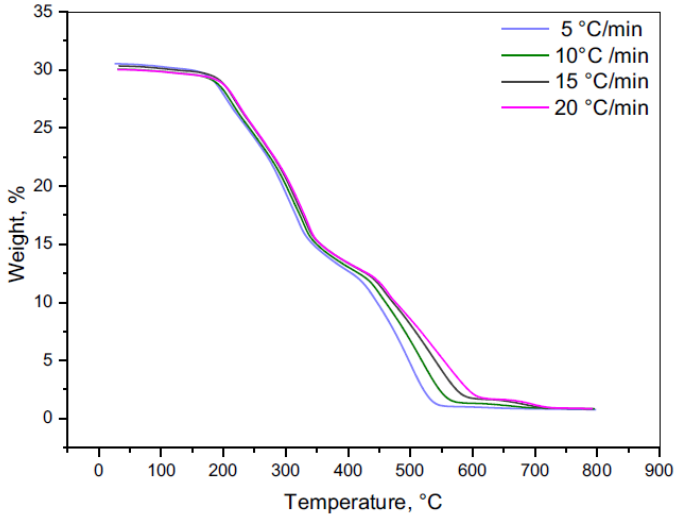

Fig. 2. TGA curves for the pyrolysis of apple pomace under N_2 at different heating rates.

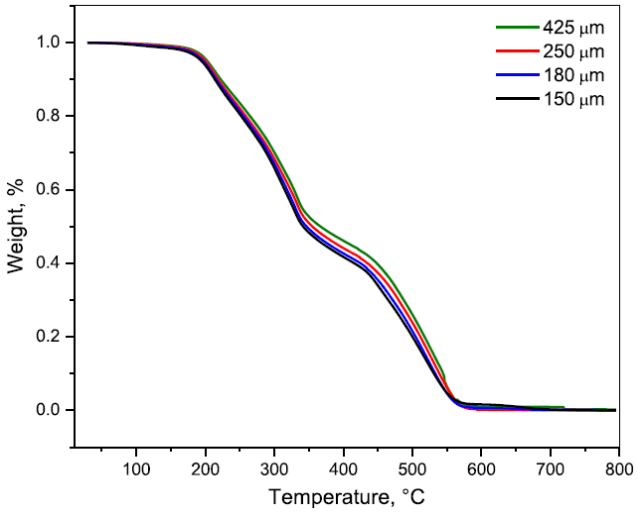

Fig. 3. TGA curves for the pyrolysis of the apple pomace under N_2 at a heating rate of 10 °C/min and different particle sizes.

3.2. Apple pomace pyrolysis fractions yield

Table 2 presents the percentage of each one of the product phases of the apple pomace pyrolysis obtained in each isotherm (condensable and non-condensable products and carbonaceous residue). In general, pomace pyrolysis studies that report the yield in each of its fractions were performed exclusively at the maximum working temperature (600 °C).

It can be observed (Table 2) that experimental values at a temperature of 550 °C are very close to the ones reported in other studies [17, 26]. Furthermore, it can be observed that at temperature of 400 °C the amount of the non-condensable volatile matter (NCVM)

is the greatest. Therefore, this is the temperature that will be selected for the further conversion to hydrogen through the absorption enhanced reforming of methane (AER) process scheme.

Table 2. Production of carbon, condensable and non-condensable matter for the pomace pyrolysis at several isotherms.

Temperature (° C)	CVM (%)	NCVM (%)	RC (%)
150	9.99	0.15	89.85
200	17.98	4.39	77.62
250	24.98	23.69	51.32
300	34.92	37.23	27.85
350	34.65	49.86	15.48
400	25.42	71.51	3.07
450	72.01	24.54	3.36
500	74.60	22.59	2.81
550	75.01	23.56	1.43
600	82.33	16.45	1.22

In this Table it can be observed that experimental values at a temperature of 550 °C are very close to the ones reported in other studies [17, 26].

Furthermore, it can be observed that at temperature of 400 °C the amount of the non-condensable volatile matter (NCVM) is the greatest. Therefore, this is the temperature that will be selected for the further conversion to hydrogen through the absorption enhanced reforming of methane (AER) process scheme.

Figure 5 presents the time response of the main gas composition from the pomace pyrolysis isotherm at 400 °C. Results indicate that at a temperature of 400 °C a maximum of 71.5% W of non-condensable volatile matter (NCVM) can be obtained along with 25.4% W of condensable volatile matter (CVM), while only 3% W of residual matter (RM) was produced. A Figure 3 shows that at this favorable conditions (NCVM) an average gas composition of 41% CO, 38% CO_2 and 21% CH_4 was generated.

3.3 Thermodynamic analysis

Considering the results obtained from the identification of most significant volatile compounds, in which an average gas composition of 41% CO, 38% CO_2 and 21% CH_4 was generated. This composition was used to perform a thermodynamic analysis under the AER process scheme and the high purity hydrogen can be produced through the combination of the following reactions:

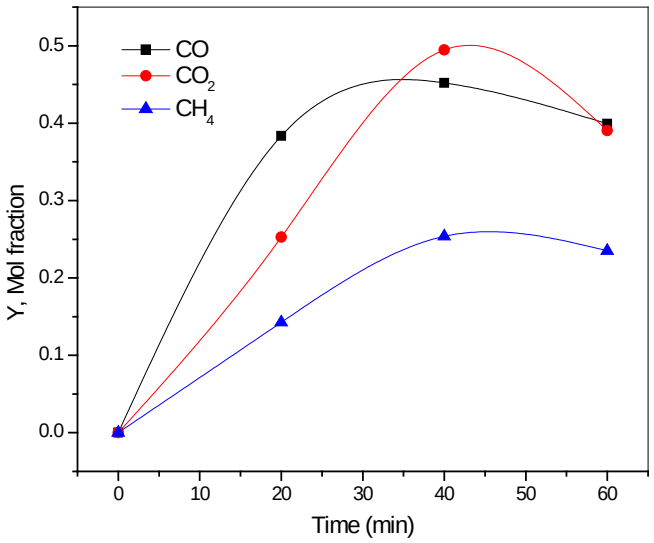

Figure 5. Reactor gas product composition at 400°C for the pomace pyrolysis

$$CH_4 + 2H_2O = CO_2 + 4H_2 \quad (3)$$

$$CO + H_2O = CO_2 + H_2 \quad (4)$$

$$CaO + CO_2 = CaCO_3 \quad (5)$$

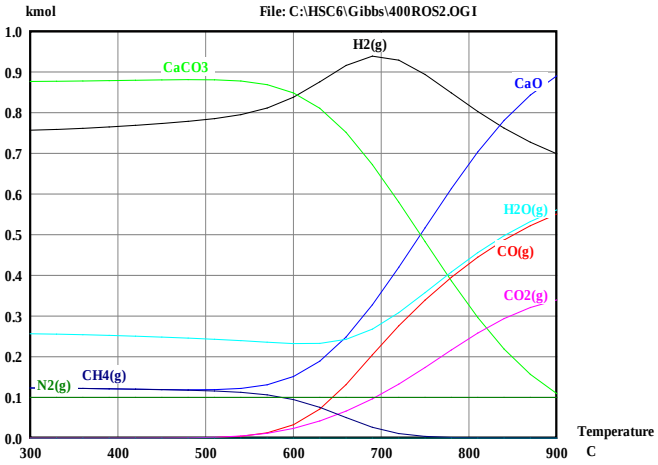

Figure 6. Thermodynamic analysis results for the gas product composition at 400°C for the pomace pyrolysis.

The AER is composed of reactions (3)-(5), which correspond to the steam reforming reactions in combination with the CO_2 absorption reaction by CaO (5) to produce high purity hydrogen. For thermodynamic modeling purposes the feed consisted of 1 kmol of the methane mixture with 4 moles o H_2O, which corresponds to a steam to carbon ratio of 4 (S/C) and 1 mol of CaO with results of this thermodynamic analysis presented in Figure 6.

According to results from Figure 6 the thermodynamic calculations using a steam to methane ratio (S/C) of 4 and 1 mol of CaO/mol of CH_4 indicate that a maximum H_2 production is achieved at 690 °C along with a composition of 74.1 % H_2, 16.2% CO, 7.6% CO_2 and 2.1% CH_4 with no carbon formation.

4.Conclusion and recommendation

The present research explored optimal reaction conditions for the generation of a gas product, through the slow pyrolysis of pomace, to be used as a feedstock for the production of H_2 by the absorption enhanced reforming of methane (AER) process scheme. Pyrolysis experiments were performed in a tubular reactor under conditions of rich syngas production (300–450 °C) and for specific solid heating rates (5-20 °C/min). Permanent gases (CO, CH_4 and CO_2), aromatic tars, and chars were quantified at different heating rates and isothermal conditions. Results indicate that at a temperature of 400 °C a maximum of 71.5% W of non-condensable volatile matter (NCVM) were obtained along with 25.4% W of condensable volatile matter (CVM), while only 3% W of residual matter (RM) was produced. At this favorable conditions (NCVM) a gas composition of 41% CO, 38% CO_2 and 21% CH_4 was generated. A thermodynamic analysis of this product gas was performed under the steam reforming of methane (SMR) combined with CO_2 solid absorption by CaO for the production of high purity H_2. Thermodynamic calculations using a steam to methane ratio (S/C) of 4 and 1 mol of CaO/mol of CH_4 indicate that a maximum H_2 production is achieved at 690 °C along with a composition of 74.1 % H_2, 16.2% CO, 7.6% CO_2 and 2.1% CH_4 with no carbon formation.

References

[1] Mueller-Langera F, Tzimasb E, Kaltschmitta M, Petevesb S. Techno-economic assessment of hydrogen production processes for the hydrogen economy for the short and medium term. Int J Hydrogen Energy 2007; 32:3797–810.

[2] Rapagna S, Jand N, Foscolo PU. Catalytic gasification of biomass to produce hydrogen rich gas. Int J Hydrogen Energy 1998; 23(7):551–7.

[3] I.D.A.E. Instituto para la Diversificación y el Ahorro de Energía. Biomasa. Available at: http://www.idae.es/index.php/idpag.233/relcategoria.1037/relmenu.48/mod.pags/mem.detalle

[4] Brossard LE, Cortez LAB, Penedo M, Bezzon G, Olivares E. Total condensable effluents yield in slow pyrolysis of bagasse briquettes. Energ Convers Manage 2000; 41:223-33.

[5] Seda A, Mustafa K, Ahmet K. Thermodynamic analysis of steam assisted conversions of bio-oil components to synthesis gas. Int J Hydrogen Energy 2009; 34:1752-9.

[6] Garcia L, French R, Czernik S, Chornet E. Catalytic steam reforming of bio-oils for the production of hydrogen: effects of catalyst composition. Appl. Catal. A: General 2000; 201:225-39.

[7] Parthasarathy P. and Sheeba K. N. Combined slow pyrolysis and steam gasification of biomass for hydrogen generation—a review. Int. J. Energy Res. 2015; 39:147–164.

[8] Brun-Tsekhovoi AR, Zadorin AN, Katsobashvili YR, Kourdyumov SS. The process of catalytic steam-reforming of hydrocarbons in the presence of carbon dioxide acceptor. In: Proceedings of the world hydrogen energy conference, Vol. 2. New York: Pergamon Press; 1986. p. 885-900.
[9] Hufton J R, Mayorga S, Sircar S. Sorption-enhanced reaction process for hydrogen production. AIChE J 1999; 45:248-56.
[10] Balasubramanian B, Lopez-Ortiz A, KaytakougluS, Harrison D P. Hydrogen from methane in a single step process. Chem Eng Sci 1999; 54:3543-52.
[11] Abandes J C. Novel combustion cycles incorporating capture of CO_2 with CaO. Chem Eng J 2002; 90:303-6.
[12] Davda RR, Shabaker JW, Huber GW, Dumesic JA. A review of catalytic issues and process conditions for renewable hydrogen and alkanes by aqueous-phase reforming of oxygenated hydrocarbons over supported metal catalysts. Appl Catal B Environ 2005; 56:171-86.
[13] Yi KB, Harrison D P. Low-pressure sorption- enhanced hydrogen production. Ind Eng Chem Res 2005; 44:1665-9.
[14] Raja A S, Kennedy R Z, Pillai BC, Lindon R. Lee C. Flash pyrolysis of jatropha oil cake in electrically heated fluidized bed reactor. Energy 2010; 35:2819-23.
[15] Uden PC. ChemInform abstract: nomenclature and therminology for analytical pyrolysis. ChemInform 1994; 25. http://dx.doi.org/10.1002/chin.199412307.
[16] Roine A. Chemical reaction and equilibrium software with extensive thermo-chemical database. Outokumpu HSC 6.0 chemistry for windows; 2010.
[17] Garcia-Perez M, Chaala A, Ror C. Vacuum pyrolysis of sugarcane bagasse. J Anal Appl Pyrol 2002; 65:111-36.
[18] Carrier Marion, Hugo Thomas, Gorgens Johann, Knoetze Hansie. Comparison of slow and vacuum pyrolysis of sugar cane bagasse. J Anal Appl Pyrolysis 2011; 90:18-26.
[19] Cohce MK, Dincer I, Rosen MA. Energy and exergy analyses of a biomass-based hydrogen production system. Bioresour Technol 2011; 102:8466-74.
[20] Akhtar Javaid, Amin NorAishah Saidina. A review on operating parameters for optimum liquid oil yield in biomass pyrolysis. Renew Sustain Energy Rev 2012; 16:5101-9.
[21] Ounas A, Aboulkas A, El harfi K, Bacaoui A, Yaacoubi A. Pyrolysis of olive residue and sugar cane bagasse: nonisothermal thermogravimetric kinetic analysis. Bioresour Technol 2011; 102:11234-8.
[22] Aboyade Akinwale O, Carrier Marion, Meyer Edson L, Knoetze Johannes H, Go¨ rgens Johann F. Model fitting kinetic analysis and characterisation of the devolatilization of coal blends with corn and sugarcane residues. Thermochim Acta 2012; 530:95-106.
[23] Lutza H, Romeirob GA, Damascenoc RN, Kutubuddina M, Bayer E. Low temperature conversion of some Brazilian municipal and industrial sludges. Bioresour Technol 2000; 74:103-7.
[24] Ramirez JR, Lagunas LM. Engineering properties of sugarcane bagasse. Int Sugar J 2010; 112:354-61.
[25] Luo M, Stanmore B. The combustion characteristics of char from pulverized bagasse. Fuel 1992; 71:1074-6.
[26] Zandersons J, Gravitis J, Kokorevics A, Zhurinsh A, Bikovens O, Tardenaka A, et al. Studies of the Brazilian sugarcane bagasse carbonisation process and products properties. Biomass Bioenergy 1999; 17:209-19.
[27] Min F, Zhang M, Chen Q. Non-isothermal kinetics of pyrolysis of three kinds of fresh biomass. J China Univ Min Technol 2007; 17(1):105-11.
[28] Zabaniotou AA, Kantarelis EK, Theodoropoulos DC. Sunflower shells utilization for energetic purposes in an integrated approach of energy crops: laboratory study pyrolysis and kinetics. Bioresour Technol 2008; 99:3174-81.
[29] Munir S, Daood SS, Nimmo W, Cunliffe AM, Gibbs BM. Thermal analysis and devolatilization kinetics of cotton stalk, sugar cane bagasse and shea meal under nitrogen and air atmospheres. Bioresour Technol 2009; 100:1413-8.
[30] Antony Raja S, Robert Kennedy Z, Pillai BC, Lindon Robert Lee C. Flash pyrolysis of jatropha oil cake in electrically heated fluidized bed reactor. Energy 2010; 35:2819-23.
[31] Luo M, Stanmore B. The combustion characteristics of char from pulverized bagasse. Fuel 1992; 71:1074-6.

Chapter 5.15. Potential of pretreated solids applied to an OFMSW biorefinery to improve the performance of hydrogen production: a review

L. Romero-Cedillo[a]; H. M. Poggi-Varaldo[a,*]; T. Ponce-Noyola[a,*]; E. Ríos-Leal[a]; A.C. Ramos-Valdivia[a;] C.M. Cerda-García Rojas[b]; J. Tapia-Ramírez[c]

[a]Departament of Biotechnology and Bioengineering, Environmental Biotechnology and Renewable Energy Group, Cinvestav-IPN, México, D.F.
[b]Departament of Chemistry, Cinvestav-IPN, México, D.F.
[c] Departament of Genetics and Molecular Biology, Cinvestav-IPN, México, D.F.

ABSTRACT

The organic fraction of municipal solid waste (*OFMSW*), mainly composed of lignocellulosic polymers, is extremely complex. Its composition limits the access and action of degrading enzymes. Therefore is necessary to apply a pretreatment to promote degradation of these polymers. In recent years, this option have been studied and the main objective of different pretreatment methods is to remove the lignin content and decrease the cellulose crystallinity.

In this work, we focus on describing the conventional pretreatments applied to *OFMSW*, with the goal to improve the hydrogen production as well as other gas biofuels. The most common pretreatments are mechanical, alkaline, acid diluted, thermochemical and enzymatic. One of the challenges in the use of pretreatments is the selection of appropiate pretreatment; for example, the alkaline pretreatment is known to be more effective to remove lignin and improve the porosity in lignocellulosic biomass (wood and agricultural wastes). In this context, has been successful the alkaline pretreatment of food wastes, showing an improve on biohydrogen generation (156 mLH_2/g VS using KOH 6N and 63 mL H_2/g VS on untrated food wastes). In the other side, some wastes with low content of lignin has increased up to 6 times the biohydrogen production, for instance through the application of mixed alkali and dilute acid pretreatment, from 1.41 mL H_2/g COD to 7.9 mL H_2/g COD, using sewage sludge. However, less is known on pretreatment of the *OFMSW*. Other studies have shown that pretreated biomass has been succesful employed to improve the performance of the processes, in specific to generate hydrogen or biomethane. In this context, recently studies on semi-continuous system, have been evaluated the hydrogen potential of fermented organic wastes (FOW), pretreated by cellulases and found a theoretical increase of 100% in terms of H_2 yields, raising the hydrogen production from 21 LH_2/Kg VS to 43 LH_2/Kg VS. We conclude that waste pretreatments constitute a family of process that undoubtedly will significantly contribute to increase yields of bioenergy in biohydrogen-based biorefineries.

Keywords: Biohydrogen; Biorefinery; Cellulose, Hydrogen; Lignin; Methane; *OFMSW*; Pretreatment

---

* Authors for correspondence:
T: 5255 5747-3800 x 4324 & 4317, E: r4cepe@yahoo.com

1. Introduction

Municipal solid waste (MSW), mainly composed of food waste and paper-cardboard wastes, typically have a large fraction of lignocellulose [1]. This polymer is composed of cellulose, hemicellulose, lignin, plus several inorganic compounds and (organic) extractives [2]. Cellulose, is a linear polysaccharide of glucose made of cellobiose units, these chains are packed by hydrogen bonds called microfibrils. The latter, in turn, are attached to each other by hemicellulose and amorphous polymers (main components are galactose, arabinose, rhamnose, glucuronic acid, galacturonic acid, mannose and xylose) [3]. Unlike cellulose, which is linear, strong and cristallyne, hemicellulose has an amorphous and branched structure with less resistance to hydrolysis making it more accesible to the enzymes and easier to hydrolyze [4].

Lignin is a phenyl propane polymer linked with ester bonds that cover stably and strongly the cellulose and hemicellulose [5]; the major components of this structure are *p*-coumaryl alcohol, coniferyl alcohol and sinapyl alcohol. Is also known that lignin contains phenolic, methoxyl, hydroxyl and terminal aldehyde groups, in the less soluble side chain [6]. The presence of lignin in biomass makes it difficult the attack of the cellulose by enzymes and bacteria, in order to generate fermentable sugars. Also, during the degradation or saccharification process, furan compounds can be derived from the lignin and could inhibit the fermentation [7].

The main goal of pretreatments is to enhanced the enzyme accessibility to substrate, allowing the release of fermentable sugars, most conventional pretreatments are classified in four categories, physical, chemical, biological and physico-chemical [8]. For example, when using pretreated feedstock through grinding of feedstock in an anaerobic digester, there is an increase in biogas, stabilization of temperature, moisture content and a more uniform mixing. In general, these effects can be identified as solubilization, particle size-reduction, biodegradability enhancement, and degradation of organic matter [9]. In order to increase the surface area and reduce the degree of polymerization, this characteristic can be obtained through the milling and grinding of the material, according to the final particle size; several studies have been demonstrated the improved in the degradability of food during anaerobic digestion [10].

When dilute acid pretreatment is used at moderate temperatures, in a range of 140 to 190 °C, it can effectively remove and recover most of hemicellulose as dissolved sugars, while solubilized lignin precipitates onto biomass. Some preteatments conditions promote the formation of soluble lignin compounds such as hydroxy methyl furfural (HMF), furfural and others. On the other hand, alkali pretreatments can solubilize both lignin and hemicellulose. Its effect depends on saponification of intermolecular ester bonds cross-linking xylan hemicelluloses and other components, such as lignin [11]. Even when a pretreatment do not necessary remove lignin, was hypothesized that high temperature have significant impact in the state of lignin (distribution, structure, etc.) that constituting biomass [12].

The purpose of this work is to review the main pretreatments applied to the *OFMSW*, which increase of cellulose accessibility and could significantly improve the

harvested hydrogen in biological hydrogen production processes such as dark fermentation of wastes.

2. Classification of pretreatments

Pretreatments are typically classified in these groups, *(i)* thermochemical; *(ii)* physichochemical; *(iii)* enzymatic or biological. In the following sections, we describe the main treatments, their scopes, advantages, and disadvantages.

2.1 Thermochemical pretreatments

Among the main characteristics on the physical and chemical properties of typical municipal wastes, that have been altered during pretreatment, are found the decreased viscosity and increase in solubilization of organic matter [13]. Previous research, evaluated the effect of thermal pretreatment in different residues such as kitchen waste, vegetable fruit/residue and waste activated sludge, they determined that thermophilic pretreatments cannot improve methane recovery but they can accelerate the hydrolysis of *OFMSW*, thus minimizing the hydraulic retention time for degradation and volume of the reactors [14]. In the following section, are presented the most conventionally thermochemical pretreatments. Table 1 shows results of improved biohydrogen and biomethane yields obtained in different studies using thermochemical pretreatments to a variety of organic substrates (wastes and wood).

2.1.1. Alkali pretreatment

Some pretreatments are relatively effective to accomplish solubilisation of sludge, with regard to their efficiency, the order corresponds as follows: NaOH, KOH, $Mg(OH)_2$ and $Ca(OH)_2$. However, high concentrations of sodium and potassium, can promote inhibition during anaerobic digestion. This treatment, is usually combined with thermal pretreatment. Have reported increases of considerable methane in anaerobic digestion batch, which were obtained up to 310 L/Kg SVin, 88% increase if compared with the control processs wich obtained 165 L/KgSV_{in} [15]. In other research, it was found that the alkaline pretreatment of waste activated sludge improved the solubilization and the biochemical methane potential for anaerobic digestion co-digestion of municipal organic waste; the addition of 45 meqNaOH/L at 55 °C, allowed an increase of 88% obtaining 310 mLCH_4/g VS_{added}, after 20 days [16].

On the other hand, one of advantages of alkali pretreatments is the removal of uronic acid, first responsible for inhibiting the cellulose accessibility in enzymatic saccharification. Moreover, alkali treatment increase the biodegradability of the cell walls due to the broken of the lignin bonds with hemicellulose and cellulose [17]. Despite being an economic treatment, alkaline methods present some disadvantages such as the difficult separation and removal of salts formed in the process, longer times of operation, and requirements of constant mixing; in some cases is necessary an additional step to neutralizing and remove lignin and inhibitors [18].

2.1.2. Dilute acid pretreatment

Although concentrated acid is highly effective on cellulose hydrolysis, it is extremely toxic, corrosive, dangerous and expensive. Also, after the biomass pretreatment, requires a

recover of acid whereby the process becomes expensive. Depending on the operational conditions, dilute acid pretreatment hydrolyzes up to 100% of the hemicellulose into sugars such as xylose, galactose and arabinose; however, although lignin can be disrupt in high degree, is not effective dissolving lignin in most cases [19].

Dilute acid is one of the mainly used methods of chemical pretreatments, which main objective is to solubilize the hemicellulose fraction in the biomass and make the cellulose more accessible for enzymatic hydrolysis. The sugar released from the hemicellulose, can be recovered in a range of 80-95%, depending on the substrate and the operational conditions applied [20].

However the increase of acid concentration or high temperature, leads to an increase of inhibitor compounds, for instance furan derivatives and phenolic compounds, which can cause damage on fermentative microorganisms [21]. Another disadvantage using this treatment is the formation of inhibitors, for instance acid pretreatment by using sulfuric acid or hydrochloric acid has been extensively studied due its high efficiency and catabolic activity. Despite the negative effects like the formation of toxic derivatives, it has been reported interesting results during dark fermentation on biohydrogen generation: food wastes treated with acid diluted at pH 1.0 lead to an increase of H_2 yields from 4.4 mL g^{-1} SV to 89.5 mL g^{-1} SV, representing *ca.* 1900 % gain with respect to the control [22].

On the other hand, using organic wastes as feed, and pretreated through acid diluted 1N HCl, also has been observed a significant improvement in the hydrogen yield (1130.3%), where the treatment has generated 86 mL g^{-1} SV, compared against 6.99 mL g^{-1} SV [23].

2.1.3. Organosolv

In this process, originally the organic solvents were used to dissolve and degrade the lignin from lignocellulosic biomass, also was designed as a pulping process for the production of paper pulp. More recently, it has drawn attention, mainly because the delignified pulp have a good response to enzymatic hydrolysis. There is a wide range of organic solvents that can be applied in organosolv treatment, including methanol, ethanol, acetic acid, formic acid, amines and ketones [24].

Due to the costs of solvents, ethanol and methanol are desirable over alcohols with higher boiling points such as ethylene glycol or tetrahydrofurfuryl alcohol. However, ethanol is an inhibitor for the hydrolytic process, so that is necessary remove the traces of alcohol **[25]**.

One of the advantages in this method is the easy recover of organic solvents by distillation and recycled for pretreatment. Another one interesting potential, is the recovered lignin after pretreatment, has desirable characteristics that can be used for several products or derivatives; in an organosolv pretreatment, the biomass is conditioned in an aqueous-organic solvent mixture with the addition of an acid catalysts, such as H_2SO_4 [26].

2.2. Physicochemical pretreatments

Among the conventional methods can be found, are mechanical and thermal, both have being implemented in industrial level, integrating on its pretreatment process technologies such as high pressuring machines, ultrasound and microwave. Table 2 compiles results on the influence on the anaerobic digestion and dark fermentation of physicochemical pretreatments. These treatments had positive effect on the production of

biomethane by increasing 40% of total biogas in continuous test using *OFMSW* as feed [33]. To enhance the effectiveness of these pretreatments, have been used simultaneously in

Table 1. Thermochemical pretreatments applied to different residues, and influence on the biohydrogen and biomethane production.

Pretreatment	Conditons	Substrate	Process	Product yield	Ref.
Alkaline	6N KOH, pH 11	Food waste	Batch, 300 ml, 37°C	156 mL H_2/g VS (63mL H_2/g VS)	**[27]**
Dilute acid mixed alkaline and heated	12N HCl and 5N KOH, pH 5.5, 150 °C, 30 min	Sewage sludge	Batch, 1.5 L, 30 °C	7.9 mL H_2/g COD (1.41 mL H_2/g COD)	**[28]**
Alkaline	8g NaOH/100g TS $_{sludge}$	Pulp and paper sludge	Batch , 37 °C, 700 ml and 42 d	0.32 m^3 CH_4/Kg VS $_{removal}$ (0.12 m^3 CH_4/Kg VS $_{removal}$)	**[29]**
Alkaline	1.25 M NaOH, 24 h	Corn stover	Batch, 2L, 37 °C, 40 d	372.4 L Biogas /Kg SV (275.9 L Biogas /Kg SV)	**[30]**
Dilute acid, mixed ammonia liquor and ultrasonic irradiaton	0.5% H_2SO_4, 6% ammonia liquor, 0.6% HCl, 20 min ultrasonic irradiation	Apple pomace	Batch, 37 °C, 150 ml	134.04 ml H_2/gTS (65.81 ml H_2/gTS)	**[31]**
NMMO[a]	15 h, 130 °C	Milled spruce	Batch, 55 °C, 40 ml, 11 d	395 NmLCH_4/g carbohydrate (106 NmLCH_4/g carbohydrate)	**[32]**
NMMO	15 h, 130 °C	Spruce chips	Batch, 55 °C, 40 ml, 7d	202 NmLCH_4/g carbohydrate (17 NmLCH_4/g carbohydrate)	**[32]**
NMMO	15 h, 130 °C	Rice Straw	Batch, 55 °C, 40 ml, 7d	328 NmLCH_4/g carbohydrate (45 NmLCH_4/g carbohydrate)	**[32]**
NMMO	15 h, 130 °C	Triticale straw	Batch, 55 °C, 40 ml, 7d	362 NmLCH_4/g carbohydrate (53 NmLCH_4/g carbohydrate)	**[32]**

[a] NMMO, N-methylmorpholine-N-oxide

the same processes by combining physical and chemical technologies; however the potential in each case varies depending on the type of substrate, thus the optimization in continuous system is still investigated.

2.2.1. Mechanical (Milling)

This pretreatment is used with the purpose of decreasing size particle of the biomass and cellulose crystallinity while enhancing the rate of hydrolysis **[34].** Is an attractive method because it requires less energy to start the process, unlike other pretreatments. In previous studies, have been obtained increase of biogas production (62%, respect to the control), by applying grinding treatment to anaerobic digested sludge. In this research, combined the effects of milling and temperature, using balls of 0.25 mm, at a rate of 10 m s^{-1} during 6 min at 60 °C of temperature; whereas the operational conditions for anaerobic digestion were at 37 °C and 21 days, in a batch system [35].

2.2.2. Ammonia fiber explosion

The AFEX (Ammonia Fiber Explosion) process produces only a pretreated solid biomass, while other pretreatments such a steam explosion produce a slurry that can be recovered in a solid and liquid fractions; the main parameters to control this treatment are ammonia and water loading, temperature, pressure and time [36]. In this process, the biomass is exposed at high temperatures, generally in a range of 90-100 °C, for a period of 30 min, followed by an immediate reduction of pressure; it should be noted that optimum conditions for AFEX depends on the composition of lignocellulosic biomass [37]. For instance, the best operational parameters in switchgrass pretreatment were reported to be 100 °C, ammonia loading of 1:1 (1 kg of ammonia per kg of dry matter), and 5 min of retention time. Contrary to other pretreatments, the main advantage of AFEX method is no formation of undesirable products such as furanes in dilute acid and steam explosion pretreatment, however is a more appropriate method to pretreat biomass with less content of lignin [38].

2.2.3. Steam explosion

Hydrothermal pretreatments promote the enzymatic hydrolysis in some agricultural residues and hardwood [39]. Unlike chemical pretreatments, this method doesn't require acid or alkali but is necessary a special operational unit, elevated temperature (range of 190-210 °C) and high pressure (4.12 MPa). High temperature increase the breakdown of the released sugars during the treatment, producing derivatives compounds, such as furanes and 5-HMF (Hydroxy-methylfurfural) from hexose sugars. As mentioned before, this toxic compounds may inhibit the enzymes in fermentation process [40]. In table 2, it summarized some physicochemical pretreatments implemented for conditioned the organic fraction.

2.3 Enzymatic or biological pretreatments

Biological pretreatment using microorganisms can also be used to treat lignocellulosic substrates and enhance anaerobic digestion process. In some cases the enzymes are applied into a single-stage anaerobic digester or be used to pretreat biomass material prior to anaerobic digestion. Table 3 displays concentrated information on results of enzymatic pretreatments, as well as and operational conditions used in different systems and substrates.

Sometimes the enzymatic hydrolysis of lignocellulose with no pretreatment, is not very effective because the high stability of the material to be degraded by the enzymes [41]. However, there some advantages: since no chemicals used in biological pretreatments, there is no need for recovery of chemicals and does not release toxic compounds to

environment. For instance, brown, white and soft fungi have been used for degradation of lignin and hemicelluloses from the lignocellulosic biomass.

Table 2. Some physicochemical pretreatments evaluated in various substrates, and influence on the anaerobic digestion and dark fermentation.

Pretreatment	Conditons	Substrate	Process	Product yield	Ref.
Sparging CO_2	Flow: 30 ml CO_2/min, 20 min	*OFMSW*	Batch, 35 °C, 3.5 L, pH 5.5	69.9 mLH_2/gVS (56.1 mLH_2/gVS)	**[46]**
Ozonation	1-5 mg O_3/mL $_{sludge}$	Palm oil mil effluent	Batch, 37 °C, 60 mL, pH 5.5	146 mL H_2/g COD (48.6 mL H_2/gCOD)	**[47]**
Steam explosion´+[a]HMF	200 °C, 1.5 MPa, 5 min+HMF 1000mg/L	Cornstalk	Batch, 37 °C, 100 rpm, 5 L, 100 h	0.58 mL H_2/L substrate (0.02 mLH_2/L susbtrate)	**[48]**
High temperature microwave	145 °C, 40 min	*OFMSW*	Batch, 33 °C, 8d	122 m^3 biogas/ton *OFMSW* (80 m^3 biogas/ton *OFMSW*)	**[49]**
Ultrasound	7500 KJ/Kg TS	Cattle manure and sewage sludge	CSTR, 36 °C	0.85 LCH_4/L substrate (0.65LCH4/L substrate)	**[50]**
Ultrasound	7500 KJ/Kg TS	Cattle manure and sewage sludge	CSTR, 55 °C	0.82 LCH_4 (0.49 LCH_4/L substrate)	**[50]**
Grinding and cavitation	Size particle <0.5mm, 20-10,000KHz	Tritical	Batch, 37 °C, 47 d	340 Nm^3CH_4/Ton VS (250 Nm^3CH_4/Ton VS)	**[51]**

[a]HMF: Hydroxy methyl furfural

Although it is noteworthy that efficient degradation of lignin, depends on the enzymes mainly produced by basidiomycete like lignin peroxidase, laccase and manganese peroxidase [42]. Some representative species of white rot fungi, such as *Pleurotus ostreatus*, have been successfully employed to pretreat rice straw and corn stover for improving the degradation of lignin and increase the accessibility of cellulolytic enzymes enhancing release of sugars [43]. Additionally, white rot fungi species can reduce the amount of phenolic compounds [44], this latter is interesting since has been observed that such inhibitors can decrease the biogas production up to 50% having a concentration in a range of 120 to 594 mg of phenolic compounds/g volatile suspended solids [45].

Other studies evaluated the potential of enzymatic pretreatment for enhanced biohydrogen production. For instance, cassava wastewater has been pretretated with, 0.05%, 0.1% and 0.2% of α- amylase and reported an increase in yield of H_2 from 2.08 mol g^{-1} COD to 5.02 mol g^{-1} COD [57].

Another interesting aspect in the use of biological treatments is the enzymatic abundance of microbial species, allowing them to be used in a wide range of industrial

processes. For instance, some bacteria and actinomycetes have been explored for cellulose production, including the genus *Clostridium*, *Cellulomonas*, *Bacillus*, *Ruminococcus*, *Erwinia*, *Acetovibrio* and *Streptomyces.*

Table 3. Enzymatic pretreatments studied in different organic wastes, and effect on the production of gas biofuels. (The values of yields between parentheses correspond to biofuel production without pretreatment.)

Pretreatment	Conditions	Substrate	Process	Product yield	Ref.
Cellulases	40 [a]FPU g/VS, 72 h, 50 °C	[b]FOW	Semi-continuous, 55 °C	43 LH_2/Kg $_{dry\ basis}$ (21 LH_2/Kg $_{dry\ basis}$)	**[52]**
Fungal mash (glucoamylase)	10U[c]/g dry FW[d], 60 °C, 100 rpm, 24 h	Food waste	Batch, 35 °C, 30 mL, 150 rpm, 30 d	468.2 mLCH_4/gVS (197.9 mLCH_4/gVS)	**[53]**
Lipase	Enzyme 0.08% (v/v)	Cottage cheese	Batch, 100 ml mesophilic, 60 d	450 mLCH_4/gVS (320 mLCH_4/gVS)	**[54]**
Protease	Enzyme 0.06% protease (v/v)	Cottage cheese	Batch, 100 ml mesophilic, 60 d	396 mLCH_4/gVS (328 mLCH_4/gVS)	**[54]**
Laccase	2U/g biomass, 30 °C, 24 h	Corn stover	Batch, 30 d, 30 °C	344 LCH_4/Kg VS (277 LCH_4/Kg VS)	**[55]**
MnP[e]+VP[f]	5U/g biomass 30 °C, 6 h	Corn stover	Batch, 30 d, 30 °C	309 LCH_4/Kg VS (263 LCH_4/Kg VS)	**[55]**
Laccase+VP	Laccase 2U/g +1.5U/g, 30 °C, 6 h	Corn stover	Batch, 30d, 250 ml, 30° C	238.4 NLCH_4/Kg VS (207 NLCH_4/Kg VS)	**[56]**
Laccase+VP	Lacase 2U/g +1.5U/g, 30 °C, 6 h	Wheat straw	Batch, 30d, 250 ml, 30° C	250.5 NLCH_4/Kg VS (248.2 NLCH_4/Kg VS)	**[56]**
Laccase+VP	Lacase 2U/g +1.5U/g, 30 °C, 24 h	Flax	Batch, 30d, 250 ml, 30° C	244.1 NLCH_4/Kg VS (214.9 NLCH_4/Kg VS)	**[56]**
Laccase+VP	Lacase 2U/g +1.5U/g, 30 °C, 6 h	Hemp	Batch, 30d, 250 ml, 30° C	241 NLCH_4/Kg VS (248 NLCH_4/Kg VS)	**[56]**
Laccase+VP	Lacase 2U/g +1.5U/g, 30 °C, 6 h	Ensilage maize	Batch, 30d, 250 ml, 30° C	354.8 NLCH_4/Kg VS (333.3 NLCH_4/Kg VS)	**[56]**

Notes: [a] FPU: Filter Paper Units [b]; FOW: Fermented organic waste; [c] U: enzyme units; [d] FW: Food waste; [e]MnP: manganese peroxidase; [f] VP: versatile peroxidase.

The bacteria *Ruminoccocus albus*, typically present in anaerobic rumen, can produce cellulolytic enzymes with a high activity, of which β-glucosidase catalyzes the hydrolysis of cellobiose and cello-oligosaccharides during the final degradation of cellulosic materials [58]. Its metabolic characteristics and the ability to degrade this dimer, is attractive to be evaluated in anaerobic processes such as dark fermentation.

4. Perspectives and conclusion

There is a wide variety of pretreatments that have been successfully used to increase the production of biohydrogen or biomethane. However, their effectiveness can be affected mainly depending on the type of feed or substrate. Due to the chemical nature of the biomass and the reactions that occur during the treatments, in most cases they form compounds that can inhibit biological processes that occur during the dark fermentation. An interesting option is the application of enzymatic pretreatments to eliminate HMF or toxic compounds or furanes, through microorganisms such as fungi, which can produce laccasses or MnP. This treatment, has allowed increase the biomethane from 277 LCH_4/Kg VS to 344 LCH_4/Kg VS; These compounds should be evaluated to determine the degree of inhibition during process operation and further limit their training to know their effect. The substrate complexity, and nature of feedstock, are related with the enzyme affinity, for instance the use of cellulases on fermented organic wastes, could improve the yileds on hydrogen production almost 2 times in semi-continuous reactor. We conclude that waste pretreatments constitute a family of processes that undoubtedly will significantly contribute to increased yields of bioenergy in biohydrogen-based biorefineries.

Acknowledgements

The authors want to express their gratitude to CONACYT for a graduate scholarsip #369317 and the SMH for Congress registration scholarship to LR-C.

References

[1] Sims, R. Biomass and resources bioenergy options for a cleaner environment in developed and developing countries. 2003, Elsevier Science: London, UK.

[2] Ha, M.A., Apperley, D.C., Evans, B.W., Huxham, I.M., Jardine, W.G., Vietor, R.J., Reis, D. Vian, B., Jarvis, M.C. Fine structure in cellulose microfibrils: NMR evidence from onion and quince. 1998. *Plant J.*, *16*: 183-190.

[3] Taherzadeh, M.J., Karimi, K. Pretreatment of Lignocellulosic Wastes to Improve Ethanol and Biogas Production: A Review. 2008, *Int. J. Mol. Sci*., 9: 1621-1651.

[4] Barakat, A., Monlau, F., Steyer, J.P., Carrere, H. Effect of lignin-derived and furan compounds found in lignocellulosic hydrolysates on biomethane production. *Bioresource Technology*. 2012, 104: 90-99.

[5] Ayyachamy, M., Cliffe, F.E., Coyne, J.M., Collier, J., Tuohy, M.G. Lignin: unatpped biopolymers in biomass conversion technologies. 2013, *Biomass Conv. Bioref*, 3: 255-269.

[6] Novaes E, Kirst M, Chiang V, Winter-Sederoff H, Sederoff R. Lignin and biomass: a negative correlation for wood formation and lignin content in trees. 2010, *Plant Physiol*, 154:555–561.

[7] Kumar, R., Hu, F., Sannigrahi, P., Jung, S., Ragauskas, A. J., Wyman, C.E. Carbohydrate Derived-Pseudo-Lignin Can Retard Cellulose Biological Conversion. 2013, *Biotechnology and Bioengineering*, 110:737-753.

[8] Mood, S.H., Golfhesan, A.H., Tabatabaei, M., Jouzani, G.S., Najafi, G.H., Gholami, M., Ardjmand, M. Lignocellulosic biomass to bioetanol, a comprehensive review with a focus on pretreatment. 2013, *Renewable and Sustainable Energy Reviews*, 27: 77-93.

[9] Antognoni1, S., Ragazzi1, M., Rada, E.C., Plank, R., Aichinger, P., Kuprian, M., Ebner, Ch. Potential Effects of Mechanical Pre-treatments on Methane Yield from Solid Waste Anaerobically Digested. 2013, *International Journal of Environmental Bioremediation & Biodegradation*, 1:20-25.

[10] Cesaro, A., Belgiorno, V. Pretreatment methods to improve anaerobic biodegradability of organic municipal solid waste fractions. 2014, *Chemical Engineering Journal*, 240: 24-37.

[11] Cuvilas, C.A., Yang W. Spruce Pretreatment for Thermal Application: Water, Alkaline, and Diluted Acid Hydrolysis. 2012, *Energy Fuels*, 26: 6426-6431.

[12] Selig, M.J., Viamajala, S., Decker, S.R.,Tucker, M.P., Himmel, M.E., Vinzant, T.B. Deposition of lignin droplets produced during dilute acid pretreatment of maize stems retards enzymatic hydrolisis of cellulose. 2007, *Biotechnol. Prog*, 23:1333-1339.

[13] Duff, S. J. B. and Murray, W. D. Bioconversion of forest products industry waste cellulosics to fuel etanol: A review. 1996, *Bioresour. Technol.* 55: 1–33.

[14] Liu, X., Wang, W., Gao, X., Zhou, Y., Shen, R. Effect of thermal pretreatment on the physical and chemical properties of municipal biomass waste. 2012, *Waste Manage.* 32: 249–255.

[15] Carrere, H., Dumas, C., Battimelli, A., Batstone, D.J., Delgenes, J.P., Steyer, J.P., Ferrer, I. Pretreatment methods to improve sludge anaerobic degradability: A review. 2010, *Journal of Hazardous Materials*, 183:1-15.

[16] Heo, N.H., Park, S.C., Lee, J.S., Kang, H. Solubilization of waste activated sludge by alkaline pretreatment and biochemical methane potential (BMP) tests for anaerobic co-digestion of municipal organic waste. 2003, *Water Science & Technology*, 48: 211-219.

[17] Gupta, R., Pal Khasa, Y., Chander Kuhad, R. Evaluation of pretreatments methods in improving the enzymatic saccharification of cellulosic materials. 2011, *Carbohydrate Polymers*, 84: 1103-1109.

[18] Menon, V., Rao. Trends in bioconversion of lignocellulose: Biofuels, platform chemicals & biorefinery concept. 2012, *Progress in Energy and Combustion Science*, 38: 522-550.

[19] Zheng, Y., Zhao, J., Xu, F., Li, Y. Pretreatment of lignocellulosic biomass for enhanced biogas production. 2014, *Progress in Energy and Combustion Science*, 42: 35-53.

[20] Vasconcelos, S.M., Pinheiro-Santos, A.M., Moraes-Rocha,G.J., Souto-Maior, A.M. Diluted phosphoric acid pretreatment for production of fermentable sugars in a sugarcane-based biorefinery. 2013, *Bioresource Technology*, 135:46-52.

[21] Lin, R., Cheng, J., Ding, L., Song, W., Zhou, J., Cen, K. Inhibitory effects of furan derivatives and phenolic compounds on dark hydrogen fermentation. 2015, *Bioresource Technology*, 196: 250-255.

[22] Kim, D.H., Kim, S.H., Shin, H.S. Hydrogen fermentation of food waste without inoculum addition. 2009, *Enzyme Microb. Technol.* 45: 181-187.

[23] Ruggeri, B., Tommasi, T. Efficiency and efficacy of pre-treatment and bioreaction for bio-H2 energy production from organic waste. 2012, *International. Journal of Hydrogen Energy*. 37: 6491-6502.

[24] Kautto, J., Realff, M.J., Ragauskas, A.J. Design and simulation of an organosolv process for bioethanol production. 2013, *Biomass. Conv. Bioref*. 3: 199-212.

[25] Chiaramonti, D., Prussi, M., Ferrero, S., Oriani, L., Ottonello, P., Torre, P., Cherchi, F. Review of pretreatment processes for lignocellulosic etanol production, and development of an innovative method. 2012, *Biomass and Bionergy*, 46: 25-35.

[26] Hallac, B, Sannigrahi, P., Pu, Y., Ray, M., Murphy, R.J., Ragauskas, A.J. Effect of Ethanol Organosolv Pretreatment on Enzymatic Hydrolysis of *Buddleja da*W*idii* Stem Biomass. 2010, *Ind. Eng. Chem. Res.* 2010, 49*:* 1467–1472.

[27] Jang, S., Kim, D.H., Yun, Y.M., Lee, M.K., Moon, C., Kang, W.S., Kwak, S.S., Kim, M.S. Hydrogen fermentation of food waste by alkali-shock pretreatment: Microbial community analysis and limitation of continuous operation. 2015, *Bioresource Technology*, 186: 215-222.

[28] Jung, H.K., Daekeun, K., Tae, J.L. Hydrogen production and microbial diversity in sewage sludge fermentation preceded by heat and alkaline treatment. 2012, *Bioresource Technology*, 109: 239-243.

[29] Lin, Y., Wang, D., Wu, S., Wang, Ch. Alkali pretreatment enhances biogas production in the anaerobic digestion of pulp and paper sludge. 2009, *Journal of Hazardous Materials*, 170: 366-373.

[30] Zhu, J., Wan, C., Li. Y. Enhanced solid-state anaerobic digestion of corn stover by alkaline pretreatment. 2010, *Bioresource Technology*, 101: 7523-7528.

[31] Wang, H., Wang, J., Fang, Z., Wang, X., Bu, H. Enhanced bio-hydrogen production by anaerobic fermentation of apple pomace with enzyme hydrolisis. 2010, *International Journal of Hydrogen Energy*, 35: 8303-8309.

[32] Teghammar, A., Karimi, K., Sárvári, I. H., Taherzadeh, M.J. Enhanced biogás production from rice straw, triticale straw and softwood spruce by NMMO pretreatment. 2012, *Biomass and Bioenergy*, 36: 116-120.

[33] Cesaro, A., Belgiorno, V. Pretreatment methods to improve anaerobic biodegradability of organic municipal solid waste fractions. 2014, *Chemical Engineering Journal*, 240: 24-37.

[34] Ntaikou, I., Antonopoulou, G., Lyberatos, G. Biohydrogen production from biomass and wastes via dark fermentation: a review. 2010, *Waste Biomass Valor*, 1: 21-39.

[35] Kopp, J., Müller, J., Dichtl, N., Schwedes, J. Anaerobic digestion and dewatering characteristics of mechanically disintegrated sludge. 1997, *Water Sci. Technol.* 36: 129–136.
[36] Carrasco, J.E.,Saiz, M.C.; Navarro, A.; Soriano, P.; Saez, F.; Martinez, J.M. Effects of dilute-acid and steam explosion pretreatments on the cellulose structure and kinetics of cellulosic fraction hydrolysis by dilute acids in lignocellulosic materials. *Appl. Biochem. Biotechnol.* 1994, 45: 23-34.
[37] Alizadeh, H.; Teymouri, F.; Gilbert, T.I.; Dale, B.E. Pretreatment of switchgrass by ammonia fiber explosion (AFEX). *Appl. Biochem. Biotechnol.* 2005, 124: 1133-1141.
[38] Taherzadeh, M.J., Karimi, K. Pretreatment of Lignocellulosic Wastes to Improve Ethanol and Biogas Production: A Review. 2008, *Int. J. Mol. Sci*., 9: 1621-1651.
[39] Heitz, M., Capek-Ménard, E., Koeberle, P.G., Gagné, J., and Chornet, E. Fractionation of *Populus tremuloides* at the pilot plant scale: Optimization of steam pretreatment conditions using the STAKE II technology 1991, *Bioresour. Technol.* 35: 23–32.
[40] Negro, M.J., Manzanares, P., Ballesteros, I., Oliva, J.M., Cabañas, A., Ballesteros, M. Hydrothermal Pretreatment Conditions to Enhance Ethanol Production from Poplar Biomass. 2003, *Applied Biochemistry and Biotechnology*, 105-108.
[41] Parawira, W. Enzyme research and applications in biotechnological intensification of biogas production. 2012, *Critical Reviews in Biotechnology*, 32: 172-186.
[42] Sindhu, R., Binod, P., Pandey. A. Biological pretreatment of lignocellulosic biomass–An overview. 2015, *Bioresource Technology*, http://dx.doi.org/10.1016/j.biortech.2015.08.030.
[43] Liu, J., Wang, M.L., Tonnis, B., Habteselassie, M., Liao, X., Huang. Fungal pretreatments of switchgrass for improved saccharification and simultaneous enzyme production. 2013, *Bioresource Technology*, 135: 39-45.
[44] Schroyen, M., Vervaeren, H., Vandepitte, H., Van Hulle, W.H., Raes, K. Effect of enzymatic pretreatment of various lignocellulosic substrates on production of phenolic compounds and biomethane potential. 2015, *Bioresource Technology*, 192: 696-702.
[45] Hernandez, J.E., Edyvean, R.G.J. Inhibition of biogas production and biodegradability by substituted phenolic compounds in anaerobic sludge. 2008, *Journal of Hazardous Materials*, 160: 20-28.
[46] Bru, K., Blazy, V., Joulian, C., Trably, E., Latrille, E., Quéméneur, M., Dictor, M.C. Innovative CO2 pretreatment for enhancing biohydrogen production from the organic fraction of municipal solid waste (*OFMSW*). 2012, *International Journal of Hydrogen Energy*, 37: 14062-14071.
[47] Wimonsong, P., Nitisoravut, S. Pretreatment Evaluation and its application on Palm oil mill effluent for Bio-Hydrogen Enhancement and methanogenic activity repression. 2009, *Pakistan Journal of Biological Sciences*, 12: 1127-1133.
[48] Liu, Z., Zhang, Ch., Wangb, L., He, J., Li, B., Zhang, Y., Xing, X. Effects of furan derivatives on biohydrogen fermentation from wet steam-exploded cornstalk and its microbial community. 2015, *Bioresource Technology*, 175: 152-159.
[49] Shahriari, h., Warith, m., Hamoda, m., Kennedy, K.J. Anaerobic digestion of organic fraction of municipal solid waste combining two pretreatment modalities, high temperature microwave and hydrogen peroxide. 2012, *Waste Management*, 32:41-52.
[50] Quiroga, G., Castrillón, L., Fernández-Nava, Y., Marañón, E., Negral, L., Rodríguez-Iglesias, J., Ormaechea, P. Effect of ultrasound pre-treatment in the anaerobic co-digestion of cattle manure with food waste and sludge. 2014, *Bioresource Technology*, 154: 74-79.
[51] Antognoni1, S., Ragazzi1, M., Rada, E.C., Plank, R., Aichinger, P., Kuprian, M., Ebner, Ch. Potential Effects of Mechanical Pre-treatments on Methane Yield from Solid Waste Anaerobically Digested. 2013, *International Journal of Environmental Bioremediation & Biodegradation*, 1:20-25.
[52] Escamilla-Alvarado, C., Poggi-Varaldo, H.M., Ponce-Noyola, T., Ríos-Leal, E., Robles-Gonzalez, I., Rinderknecht-Seijas, N. Saccharification of fermented residues as integral part in a conceptual hydrogen-producing biorefinery. *In Press*: 2015, *International. Journal of Hydrogen Energy*, doi.org/10.1016/j.ijhydene.2015.06.164.
[53] Kiran, E.U., Trzcinski, A.P., Liu, Y. Enhancing the hydrolysis and methane production potential of mixed food waste by an effective enzymatic pretreatment. 2015, *Bioresource Technology*, 183: 47-52.
[54] Prabhudessai, V., Salgaonkar, B., Braganca, J., Mutnuri, S. Pretreatment of Cottage Cheese to Enhance Biogas Production. 2014, *BioMed Research International*, doi/10.1155/2014/374562.
[55] Schroyen, M., Vervaeren, H., Van Hulle, W.H., Raes, K. Impact of enzymatic pretreatment on corn stover degradation and biogas production. 2014, *Bioresource Technology*, 173: 59-66.

[56] Schroyen, M., Vervaeren, H., Vandepitte, H., Van Hulle, W.H., Raes, K. Effect of enzymatic pretreatment of various lignocellulosic substrates on production of phenolic compounds and biomethane potential. 2015, *Bioresource Technology*, 192: 696-702.
[57] Leaño, E.P., Babel, S. Effects of pretreatent methods on cassava wastewater for biohydrogen production optimization. 2012, *Renewable Energy*, 39: 339-346.
[58] Nanda, S., Mohammad, J., Reddy, N.S., Kozinski, J.A., Dalai, A.K. Pathways of lignocellulosic biomass conversion to renewable fuels. 2014, *Biomass Conv. Bioref*., 4:157-191.

Notation

AFEX	ammonia fiber explosion
COD	chemical oxygen demand
FOW	fermented organic wastes
FW	food waste
FPU	filter paper units
HMF	hydroxy methyl furfural
MnP	manganese peroxidase
MSW	municipal solid waste
NMMO	N-methylmorpholine-N-oxide
OFMSW	organic fraction of municipal solid waste
U	enzyme units
VP	versatile peroxidase.

6
Control and power conditioning

Chapter 6.1. Energy management system for a hybrid hydrogen-solar sustainable house

O. Aguado-Sánchez[a*]; R. de G. González-Huerta [b,*]; D.J. Cortés-Rodríguez [a]

[a]Instituto Politécnico Nacional, ESIME Culhuacan, Av. Santa Ana No. 1000, 14430, Mexico City, Mexico
[b]Instituto Politécnico Nacional, ESIQUIE, Unidad Profesional Adolfo López Mateos Edificio No. 7, 07738 Mexico City, Mexico.

ABSTRACT

An energy management system for hydrogen-solar hybrid sustainable house is described in this paper. The house has three different power sources that consist of two proton exchange membrane fuel cells, a rigid photovoltaic panel grid and a flexible photovoltaic panel grid. These power sources have different characteristics that result in different power capabilities therefore a control system is necessary to interconnect these sources, be sure about the right energy distribution and take care of the function of each device on the system. In order to do this, measures are done and programmable logic controller is connected to display system state and energy requirements. Developed algorithm performs switch actions to split or join the different voltage buses from loads demand to feed a specific bus with more power. Algorithm includes a manual mode that allows the user to select different available buses in order to avoid energy blackouts because of the priority loads distributed in the house. Although, the energy management system developed in this paper has been designed for three sources, it can be extended to more different power sources and more output buses.

Keywords: Sustainable house, Power management, Hydrogen fuel cells, Solar cells

1. Introduction

Currently, the most common hybrid system used is a set of photovoltaic panels integrate a battery stack for energy store (mainly lead acid type), it offers the advantage of long lifetime with minimal maintenance [1]. Recently, energy storage like H2 has received significant attention because of benefits as longer lifetime of H2 tanks and lower price than batteries. Moreover, H2 must be produced by nonpolluting electrolysis of water; this reduce batteries dependence which are made of toxic materials.

Gobal warming has caused an intense renewable energies research . As a consequences important advances have been made to enable the use of photovoltaic (PV) energy, fuel cells and wind energy as sustainable process [2,3]. Particularly, sustainable house accept

---

* Author for correspondence:
Octavio Aguado Sánchez, Tel. +52-55.4524.4916, octavio.oas@gmail.com

any kind of renewable energy over the others. Several problems are involved when H2 is used like energy source, generation and storage process issues must be solved like: fuel cells interconnection with other energy sources. This paper shows the interconnection of two fuel cells (FC), two different photovoltaic panels (PV) and two batteries stacks. Interconnection system also allows different kind of AC and DC loads to be powered, for this purpose it requires a dedicated control algorithm to manage the frequent interaction and power flow among the sources (PV and FC), battery stacks and the loads.[4,5]

Researches show that a single dispatch strategy cannot yield best results under dynamic operating conditions and hence suggests a combined dispatch strategy [6]. In a separate research, the authors analyzed a PV–FC–Battery hybrid system using three control strategies, wherein they observed the second control strategy to provide best average hybrid system efficiency [7].

Interconnection system allows that sources that work as isolated way, only provide energy for their respective load, now it has the ability to be connected with other sources and other loads. The implementation of the power and control stages make a powerful system that can operate with one or more voltage sources simultaneously.

2. Materials and Methods

2.1 System harware description

Figure 1 shows power distribution system diagram, the main part is the control system at center, which manages all the connections between the power sources and the energy distribution to the loads. Some devices are shown but are not explained in this paper because they are only used to energize the main equipment described below.

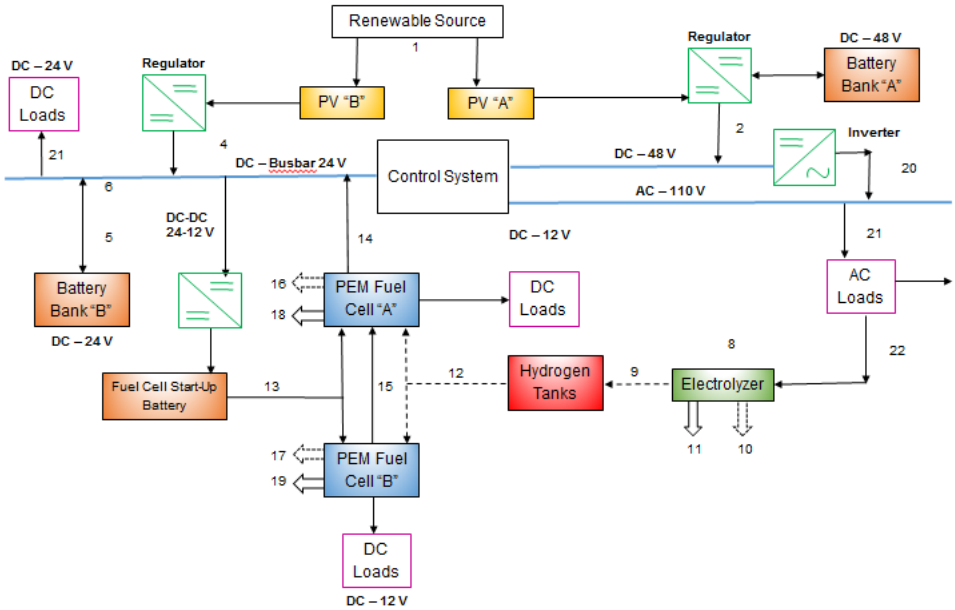

Fig. 1. Single diagram of the power distribution system

2.2 Main output voltage bus

The main output is a 120 VAC bus. Devices involved to generate the 120 VAC for distribution in the sustainable house are: rigid photovoltaic panels, 48VDC battery stack, charge controller and inverter, see figure 2. This part of the system generates most of the energy and it is the voltage bus with highest demand.

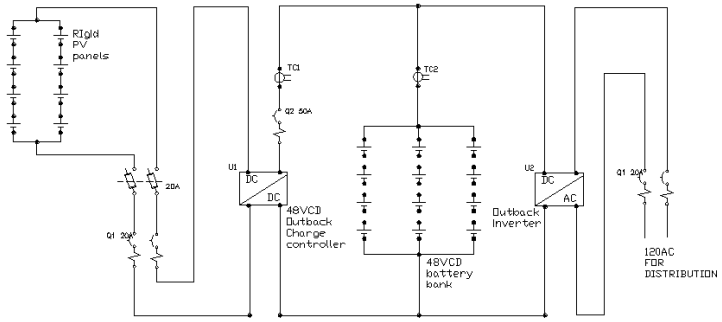

Fig. 2. Electric scheme of 48VDC and 120VAC voltage buses

2.2.1 Rigid photovoltaic panels

The rigid photovoltaic panels are connected as two parallel arrangements . Each one is built of four panels in series and delivers power of 135W each one, so the total maximum power generated is 1080W, which efficiency is reduced to about 850W at peak hours solar radiation. Each panel generates an open circuit voltage around 17.57V, so the whole arrangement generates 70.28V. A closed circuit falls around 54V.

2.2.2 Main battery stack

To store the energy generated by solar rigid panels, a batteries bank for solar deep cycle applications was assembled, such bank consists of three parallel arrays of four batteries in series each one. Because of each battery is 1200Wh / day, then the full bank capacity is 14.41Kw / day, this is considering the efficiency and download of this type of power that is multiplied by 0.5 factor , it is obtained 8.3Kw / day that allows about 50 hours of battery life without exceeding the daily demand which is calculated 3.2KW/day.

2.2.3 Charge controller and inverter

Charge controller is neccessary to protect the battery against overload and deep-discharge. This device regulates the voltage and constantly monitors the charge state of the batteries in order to extend its lifetime. The controller used is a FLEX MA 60 of the Outback brand, which for this case is set to the value of voltage is 48VDC battery bank.

Since most of the loads that are distributed in the house works in alternate current, such as computers, air conditioner, refrigerator and lighting, an inverter is necessary to convert the direct current from rigid photovoltaic panels and battery bank to supplay alternate current . The inverter was selected for an operating voltage of 48VDC given the above sources and its output voltage 120VAC 60Hz with a ± 10% variation in voltage and frequency ± 1%. Note that this voltage bus apart from feeding the distributed loads within the house serves to energize some of the devices within the cabinet operating at 120VAC.

2.3 The 24VDC voltage bus

This voltage bus is primarily intended for the control stage and for feeding other low consumption loads. Since the control device is effecting all actions of activating/deactivating relays, it requires to be energized all the time and independent of the other buses. This photovoltaic arrangement is composed of three parallel arrays of two panels in series each one. At open circuit each panel is about 27VCD and 100W because add result is 54V and 600W. Flexible photovoltaic panels have its own energy storage, it is composed by four batteries, two in serie and these in parallel. The energy supplied by the (PV) must pass through a stage of voltage regulation, this stage is performed by a Xantrex charge controller from Schneider Electric with current capacity up to 60 A and regulation option between 12V, 24V and 48V and serves as a controller to switch from photovolaic panels and batteries to power the load.

2.4 Fuel cells and its output buses

The sources used to generate these buses are called proton exchange membrane (PEM) or fuel cells, they are devices that generate electricity and heat from the chemical reaction between hydrogen and oxygen and whose by-product is water. For this application two fuel cells of HORIZON brand are used and are called PEM A and PEM B. Each of these cell generates an open circuit voltage arround 17V, and closed circuit voltage of 12VDC and 500W capacity each. These device generates two 12VDC buses, for this application they are called 12VDC main an 12VDC secondary

2.5 Design of the power distribution system

Regarding each source characteristics and their capabilities, the different ways of interconnection were evaluated. The choiced scheme is shown in figure 3 here, devices as well as relay contacts that allow connections are shown. From this scheme, different possible configurations can be obtained, such configurations are explained in the following subsections.

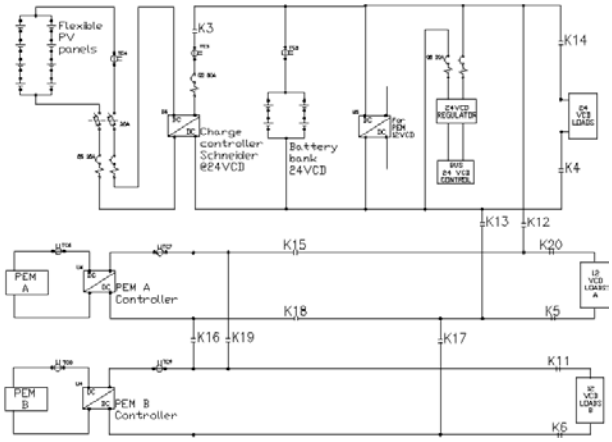

Fig. 3. DC voltage buses for control and other loads

2.5.1 Main 24VDC bus

The first voltage bus that is included in the controller program is the main 24VDC bus, whose sources are the flexible solar panels and the 24VCD battery bank. For this

configuration must be activated K14 and K4 relays and forcibly turned off the relays K13 and K12 to avoid connecting with other sources. While K14 and K4 remain activated a voltage is taken into contacts to energize the required loads.

This voltage bus, which was previously mentioned is specially designed for the control stage, and energize continuously the programmable logic controller PLC, the human machine interface HMI and relays so they always have independent function and are the main part of the system.

2.5.2 Main and secondary 12VDC buses

The main 12VDC bus, the fuel cell PEM A its used. In this configuration must be activated K15, K20, K18 and K5 relays, and disabled the K13, K12, K16 and K17 relays. Secondary bus of 12VDC, corresponds to the second fuel cell, PEM B. For this configuration it must be activated relays K6 and K11 and K16 off, K19 and K17.

2.6 Higher power buses

Now the configurations in which the sources are interconnected to generate greater capacity voltage buses are explained, for which the control algorithm performs a procedure to activate and deactivate some of the relays required for the connections

2.6.1 The 24VDC higher power bus

In this case the three sources of energy, flexible panels along with its battery bank, fuel cell PEM A and fuel cell PEM B are used. For the 24VDC higher power bus, first have to deactivate all the relays except K20 and K5 because they could be used at that time to energize the load in their contacts.

In the next stage of connection, the two fuel cells must be set in serie, so that the sum of the voltage is approximately 24VDC ± .5VCD, this is done through the relay K16 which connects the positive pole of the PEM B to the negative pole of the PEM A, in the next stage the K15 and K17 relays are activated and in the last stage K13 and K12 are activated so that you are connecting to the main bus of 24VDC to have more total power from the source and to supply surplus power, if the load demands it.

2.6.2 The 12VDC higher power bus

In the case that main voltage bus 12VDC being used, but is required to connect more load, the system can configure a 12VDC higher power bus, for this use, both fuel cells are connected in parallel, retaining the voltage but increasing the power. Their empowerment is done by disengaging all the relays except K14 and K4 that are not involved in this configuration and by the K19 and K17 relays, the fuel cells are paralleled. Finally the K20 and K5 relays which is where the load is connected are activated.

2.7. Design of the algorithm of power distribution system

To implement the control section, a programmable logic controller PLC SIEMENS S7-1500 was used, who through a programmed algorithm is responsible for activating the mechanical 24 VDC coil relays depending on carrier selection. The program control was based in the identifying the inputs, outputs and possible combinations that result in the logic circuit, then the inputs and outputs of the program are shown in table 1.

Table 1. Input and outputs for the control algorithm

Input Variables :	
A =	24VDC main button
B =	12VDC main button
C =	12VDC Secondary button
D =	24VDC higher power button
E =	12VDC higher power button
Output Variables :	
F1 =	24VDC main voltage bus
F2 =	12VDC main voltage bus
F3 =	12VDC Secondary voltage bus
F4 =	24VDC higher power bus
F5 =	12VDC higher power bus

A truth table was used to know the logic combinational logic with which the controller is programmed. In table 2 expressions obtained are shown.

Table 2. Activation expressions

F0 :	(~D*~E)+(~B*~C*~D)
F1 :	(~D*~E)
F2 :	(~D*~E)
F3 :	(~A*~B*~C*~E)
F4 :	(~B*~C*~D)

2.8. HMI interface for voltage buses selection

The HMI interface consists of a touch screen connected to the PLC that allows the operator to select the required buses and display system information . This screen is designed to allow the user review the different buses with their respective devices and their component contact. Each bus is selected by buttons as shown in figure 4.

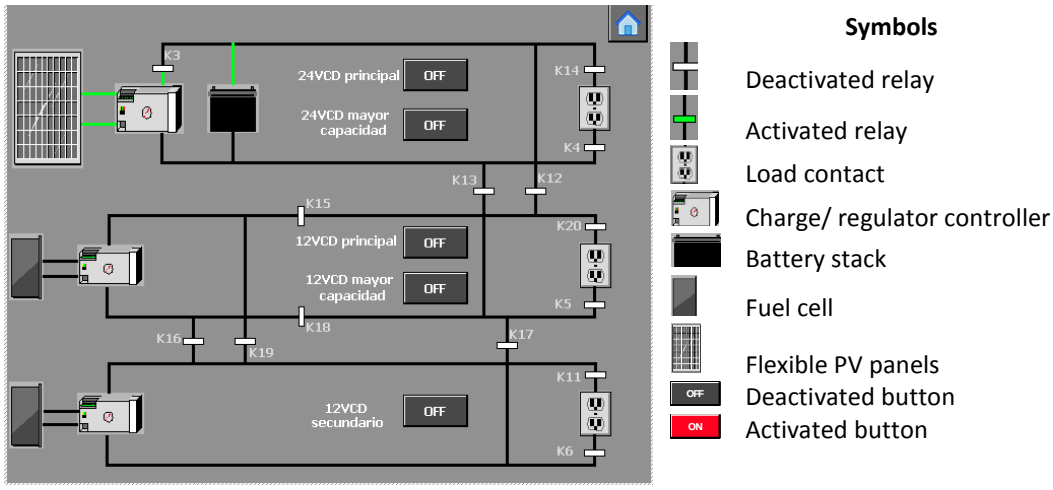

Fig. 4. HMI screen for voltage buses selection

Beside each circuit activation buttons are shown, with five configurations allowed. When a button is pressed, it changes from red to green, indicating that the bus is active. The relay contacts are blank initially and they will be set in green to indicate they are active.

To be clear with the operator and for safety reasons, the buttons were added with a display/undisplay option, this mean, under configuration selected conditions, the buttons which can interfere with other button settings will not be visible.

2.9. Protection

In order to avoid short circuit or bad connection, if only for a fraction of a time that could endanger any of the devices and provoke an incident, the control algorithm runs a series of delays between each stage of relays activation . For this purpose the relays depend of the configuration are activated like cascade and the time between the connections is 2 seconds.

3. Results and system evaluation

The system was evaluated to be sure that all planned functionality works. Every possible bus configurations was achieved. A user manual was written to sure that the HMI is friendly enough to person with basic knowledge in photovoltaic, fuel cells and electrical-electronic was asked to read the manual and to take two hours training.

Some issues are detected, for example it is neccessary be sure that the fuel cells work in a stable mode to provide to the system 12VDC each before interconnect, because a lower or higher voltage level may produce a desbalance and bring problems with the system.

4. Conclusion

The advantage of electronic controllers to manage systems that involve power distribution are essential since the operators do not require activate manually the switches and avoid shock electric risk and even the system damage. In this application the algorithm was successful, in fact it can be applied to other systems where more sources are implemented. Using the HMI interface allows easily system manipulate and know its condition. To enable the use of H2 as energy agent it will be necessary to interconnect energy sources and loads of diverse characteristics such as interconnection system that must be a combination of hardware and carefully crafted algorithms.

A second stage in this development includes an automatic mode that let the system automatically make the correct relays conmutations to distribute the energy to the respective loads. For this purpose it is neccessary to have all the sources turned on in case of higher demand and a series of current and voltage sensors to be sure the right voltages, to know the system status and the loads demand.

Acknowledgements

This work has been supported by multidisciplinary project IPN-SIP 1683 and Programa Redes Temáticas CONACYT/RTH2

References

[1] Singh GK.,. Solar power generation by PV (photovoltaic) technology: a review. Energy 2013;53(1):1–13.
[2] Zahedi A. Technical analysis of an electric power system consisting of solar PV energy, wind power, and hydrogen fuel cell, Universities Power Engineering Conference AUPEC;2007, pp. 1e5.
[3] Alam, MS, Gao, DW. Modeling and Analysis of a Wind/PV/Fuel Cell Hybrid Power System in HOMER. Industrial Electronics and Applications. 2nd IEEE Conference on ICIEA; 2007, pp. 1594e1599
[4] Li C-H, Zhu X-J, Cao G-Y, Sui S, Hu M-R. Dynamic modeling and sizing optimization of stand-alone photovoltaic power systems using hybrid energy storage technology. Renew Energy 2009;34(3):815–26.
[5] Becherif M, Ayad MY, Wack M. Control study of fuel cell, battery and solar hybridization power sources. In: IEEE Ind. Appl. Soc Annual Meet; 2010, 1–8.
[6] Ipsakis D, Voutetakis S, Seferlis P, Stergiopoulos F, Elmasides C. Power management strategies for a stand-alone power system using renewable energy sources and hydrogen storage. Int J Hydrogen Energy 2009;34(16):7081–95.
[7] Gupta A, Saini RP, Sharma MP. Modelling of hybrid energy system – Part II:Combined dispatch strategies and solution algorithm. Renew Energy 2011;36(2):466–73.

Chapter 6.2. Control implementation of a DC-DC energy router for renewable sources

D. Navarro Durán[a,*]; E. Perez Hernandez[a]; J. Resa Trejo[a]; D. Cortés Rodríguez[a]

[a]Instituto Politecnico Nacional Superior School of Electrical and Mechanical Engineering Av. Santa Ana No. 1000 Mexico City 04430, Mexico Teléfono 01 55 5624 2000. david.navarro.d@gmail.com

ABSTRACT

It is undeniable that renewable energies are the sources of the future. The energy demand will continue to grow and if it is supplied by fossil fuels a negative impact will cause complications as pollution and climatic change. On the other hand, the renewable energies has the disadvantage of being dependent on the environmental conditions. As a consequence a single renewable energy cannot supply the energy demanded all the time, hence a combination of the renewable sources is the best approach to this end. Many approaches have been developed to combine different power sources, but in some circumstances the energy requirements is not fully harnessed.

A better approach to improve the energy management is to develop a power electronic converter which allows sources from different characteristics to cooperate simultaneously to power a load. The device that achieves this goal has been called “energy router” by some researchers. Multi-input power electronic converters have been studied because with the proper control they can accomplish the energy router goal. There are many power electronic converters which can perform energy routing, but many of those topologies complicate the controller design.

In this paper a multi-input buck converter is implemented as an energy router. To achieve the energy transfer a sliding mode control is developed, considering α parameters to determine the energy provided by each source. To evaluate the controller performance a simulation is presented, and favorable results were obtained under load variations and different energy rating conditions. To go further a 50 W prototype was designed to implement the controller, the experimental results show a stable control with good voltage output regulation.

Keywords: Renewable sources, Power energy Router, Nonlinear control, Energy transfer

---

* Corresponding author:
D. Navarro Durán, Instituto Politecnico Nacional Superior School of Electrical and Mechanical Engineering Av. Sta. Ana No. 1000 Mexico City 04430, Mexico Teléfono 01 55 5624 2000, david.navarro.d@gmail.com

1. Introduction

It is expected that the electric energy demand will grow 85% between 2009 and 2035, to meet the CO_2 emission goals at least 44% of this energy will must to be generated from renewable sources. Renewable energies can be integrated in all kind of electric systems, from huge interconnected networks to small autonomous systems or buildings. According to an study realized by BP oil company on June 2012 [1], the world energy consumption mostly comes from fossil fuels and is about 87%, the nuclear energy is the 5%, hydroelectric is 6% and the 2% comes from other renewable sources (including eolian, solar, biodiesel among others).

A disadvantage from renewable sources is the fact that they depend on changing and uncertain environmental conditions, causing that this kind of sources can not supply a continuously the energy. Another problem to solve is the load variability and perturbations present in the distribution network when they are interconnected to it (see [12,28]). One solution to maintain a constant energy supply are the Hybrid Energy Systems, that can combine one or more renewable energy sources with traditional storing systems that can also be interconnected with the electric energy infrastructure.

The interconnection of different renewable energy sources in the Hybrid Energy Systems, it is a complex subject, since voltage levels can vary widely [15, 20, 22]. For example, the interconnection of an eolian generator and a photovoltaic one, taking into account multiple climatic conditions, such as a sunny day with no wind, or a cloudy day with a lot of wind and very little luminosity. So, to improve the usage of renewable energies, it is necessary to have a device capable of manipulating the power from every source, working cooperatively, and not one that just maintains a constant voltage or current. Such a device has been called energy router [13, 23 ,26].

In recent years derived from DC-DC converters, multi-input converters have been developed, allowing to feed a load by at least two different voltage DC sources [2, 7, 10, 27]. Multi-input converters have been used in different applications such as hybrid vehicles. For example in [25, 26] multi-input converters allow to interconnect different sources to achieve a desired voltage in a DC bus. On hybrid vehicles applications, a fuel cell, a battery and supercapacitors are connected to supply the required energy to the vehicle. Although the sources supply the needed energy to the vehicle, there is no policy to achieve an efficient energy usage.

Other examples to interconnect renewable energies by multi-input converters are presented in [3, 25, 32], in these schemes the main goal is also to regulate a DC bus. Even when these solutions allow the interconnection of two sources working cooperatively the energy is not used efficiently. Most cases the energy is stored in batteries or sent to the electrical network. From the previous references it can be observed that control of multi-input converters has focused in regulating the load voltage [7, 10, 25], regardless of the optimal way of using the energy.

The controller is the algorithm that allows the multi-input converters to perform the energy routing. Among the different control techniques nonlinear controllers can significantly improve the performance of power electronic converters see [4, 8, 9 ,19, 29, 30. If in addition the controller is digitally implemented some flexibility can be added to

applications like warnings and protection signals, autodiagnose, communication with other devices, etc. [11, 21, 24].

Although there has been efforts to obtain direct discrete models for power converters, they are small signal models, see [17]. As a matter of fact most of the digital control theory is for linear systems. The main cause of this situation is due to obtaining a discrete large signal models of nonlinear systems suitable for control design is very difficult and even impossible. Hence, the path that is usually employed for nonlinear digital control is to design an analog controller based on a continuous-time model, and then implement a digital approximation of such analog controller, hoping that the digital approximation performance to be similar to the analog one. Usually, the digital approximation performs well for small enough sampling time.

The kind of controllers used in this paper are Sliding-Mode Controllers (SMC). SMC are known to be robust and reliable. Furthermore, since SMC are discontinuous, they are particularly suitable for power converters (See [4, 19, 33] and the references therein). The idea behind the controllers employed in this paper, is the same that the long established current-mode control. That is, to make that the inductor(s) current(s) be a function of the output voltage(s). This idea can be used in several converter topologies. In addition the kind SMC used on this paper are simple and could be implemented digitally on a microcontroller.

The paper is organized as follows on section 2 the energy router topology is modeled by discontinuous differential equations, at the end a generalized nonlinear discontinuous state space model is presented. On section 3 a controller for the energy router is presented, initially on subsection 3.1 an analog controller is developed. The capabilities of recent microcontrolles allow to implement more complex controller, so on subsection 3.2 is presented a methodology to discretized the energy router controller. The controller is evaluated on section 4, presenting the simulation results on subsection 4.1, and on subsection 4.2 the experimental results obtained with a 50W prototype. At last on section 5 some conclusions are presented.

2. DC-DC energy router topology

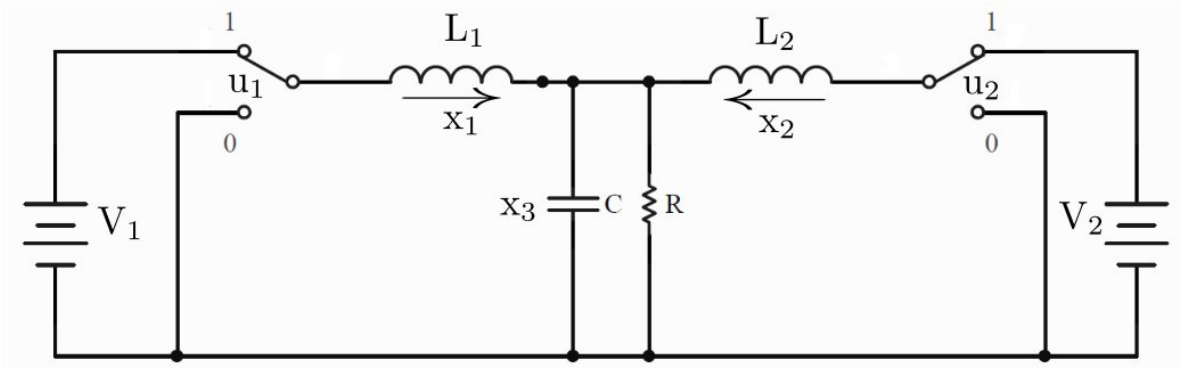

Fig. 1 Multi-input buck converter

In this section a multi-input buck converter is modeled. To keep the notation simple only two sources are considered, however, is not difficult to extend the analysis to more sources. Fig. 1 shows a simplified diagram of a multi-input buck converter for two sources.

As it is shown in the Figure V_1 and V_2 are the voltage of each power supply, L_1 and L_2 are the inductances, C is the capacitance and R is the load. The system state is composed of inductor currents x_1, x_2 and the output voltage x_3. A procedure to obtain a discontinuous model for this converter is to find out system equations for every possible configuration of the switches and then to combine all of them into a single model.

Considering $u_1 = 0$ and $u_2 = 0$ it is obtained

$$L_1\dot{x}_1 = -x_3 \quad (2a)$$

$$L_2\dot{x}_2 = -x_3 \quad (1b)$$

$$C\dot{x}_3 = x_1 + x_2 - \frac{x_3}{R} \quad (1c)$$

when $u_1 = 1$ and $u_2 = 1$, the model results

$$L_1\dot{x}_1 = V_1 - x_3 \quad (3a)$$

$$L_2\dot{x}_2 = V_2 - x_3 \quad (2b)$$

$$C\dot{x}_3 = x_1 + x_2 - \frac{x_3}{R} \quad (2c)$$

considering $u_1 = 0$ and $u_2 = 1$ it is obtained

$$L_1\dot{x}_1 = -x_3 \quad (4a)$$

$$L_2\dot{x}_2 = V_2 - x_3 \quad (3b)$$

$$C\dot{x}_3 = x_1 + x_2 - \frac{x_3}{R} \quad (3c)$$

finally considering $u_1 = 1$ and $u_2 = 0$ results

$$L_1\dot{x}_1 = V_1 - x_3 \quad (5a)$$

$$L_2\dot{x}_2 = -x_3 \quad (4b)$$

$$C\dot{x}_3 = x_1 + x_2 - \frac{x_3}{R} \quad (4c)$$

Combining models (1-4) into a single one, it is obtained

$$L_1\dot{x}_1 = u_1V_1 - x_3 \quad (6a)$$

$$L_2\dot{x}_2 = u_2V_2 - x_3 \quad (5b)$$

$$C\dot{x}_3 = x_1 + x_2 - \frac{x_3}{R} \quad (5c)$$

It is important to point out that the model (5) is a discontinuous model because $u_{1,2} \in \{0,1\}$.

An average model can be derived from this one substituting the instantaneous states x_1, x_2 and x_3 by its averages $\tilde{x}_1$, $\tilde{x}_2$ y $\tilde{x}_3$ and the instantaneous switch positions u_1 and u_2 by its averages $\tilde{u}_1$ and $\tilde{u}_2$ (see [5, 32] for example). Usually power electronics specialist call $\tilde{u}_1$ and $\tilde{u}_2$ duty cycles and denotes them as d_1 and d_2 respectively.

3. Energy router controller design

In most of the situations power electronic converters supply a regulated voltage to an unknown load, so a control algorithm should be developed to maintain the desired voltage at the output. In many applications an analog controller is developed and implemented, but the new technologies commonly are implemented on microcontrollers because some additional features can be added to improve the monitoring of the converter. In this section a analog controller for the energy router is developed, and in the next subsection a digital implementation of the same controller is digitalized.

3.1 Analog controller

An energy router is an electronic device which has to accomplish the requirements

1. The power from source V_1 will provide a ratio α_1 of the total power consumption, while source V_2 will provide a ratio α_2. That is

$$P_{V_1} = \alpha_1 P_R \quad (7a)$$
$$P_{V_2} = \alpha_2 P_R \quad (6b)$$

where P_{V_1} and P_{V_2} are the average power provided by the source 1 and the source 2 respectively. And should be considered $\alpha_{1,2} \in (0,1)$ with $\alpha_1 + \alpha_2 = 1$.

2. The load voltage is regulated to a desired value

$$x_3 \to V_{ref} \quad (8)$$

In [13] has been shown that the multi-input buck converter is able to function as an energy router in the sense that if the system starts with a particular initial conditions there exist an open-loop controller that accomplishes the energy router goals. Considering the energy router starts at the initial conditions

$$x_{1ss} = \alpha_1 \frac{V_{ref}}{R} \quad (9a)$$
$$x_{2ss} = \alpha_2 \frac{V_{ref}}{R} \quad (8b)$$
$$x_{3ss} = V_{ref} \quad (8c)$$
$$\tilde{x}_{1ss} + \tilde{x}_{2ss} = (\alpha_1 + \alpha_2)\frac{V_{ref}}{R} = \frac{V_{ref}}{R} \quad (8d)$$

However in practice we can not rely neither in special initial condition nor in open-loop controller. Hence a closed loop controller is necessary.

It has been shown from some decades now that in general, control of power converters is easier if the voltage is indirectly controlled through the current (see for example [16, 18]). Based on this observation the following switching laws are proposed

$$u_i = \begin{cases} 1 & si \quad \tilde{x}_i - x_{iref} < 0 \\ 0 & si \quad \tilde{x}_i - x_{iref} > 0 \end{cases}; \qquad i = \{1,2\} \quad (10)$$

where $\tilde{x}_{1_{ref}}$ and $\tilde{x}_{2_{ref}}$ are expressions that must depend on the output voltage in order to achieve a desired output voltage. In what follows these references are obtained.

To accomplish the goal given by (7) let suppose for a moment that

$$v = x_1 + x_2 \quad (11)$$

is a fictitious control in (5**c)**. In this way, (5**c)** becomes the first order linear system

$$\dot{x}_3 = ax_3 + bv \quad (12)$$

where $a = \frac{-1}{RC}$ and $b = \frac{1}{C}$. It is well known (see [14]) that system (11) can be compensated by

$$v = k_p(V_{ref} - x_3) + k_{int}\int_0^t (V_{ref} - x_3)d\tau \quad (13)$$

that is, a classic PI controller where the gains k_p and k_i are adjusted based on linear control techniques. From (10) and (12) the sum of the desirable current references can be obtained

$$x_{1ref} + x_{2ref} = k_p(V_{ref} - x_3) + k_{int}\int_0^t (V_{ref} - x_3)\,d\tau \quad (14)$$

From (10), (11) and (12) it can be concluded that if

$$x_1 + x_2 \to x_{1ref} + x_{2ref} \quad (15)$$

where $x_{1ref} + x_{2ref}$ is given by (13) then the goal given by **(7)** is achieved. Nevertheless, the goals given by **(6)** can not yet be guaranteed. However, note that for the goals **(6)** to be achieved then in steady state conditions **(8)** must hold. Hence in steady state equations

$$x_{1ss} = \alpha_1(x_{1ref} + x_{2ref}) \quad (16)$$

$$x_{2ss} = \alpha_2(x_{1ref} + x_{2ref}) \quad (15b)$$

must hold. From (13) and (15) it can be concluded that for the goals **(6)** to be achieved, conditions

$$x_1 \to x_{1ref} = \alpha_1\left[k_p(V_{ref} - x_3) + k_{int}\int_0^t (V_{ref} - x_3)\,d\tau\right] \quad (17a)$$

$$x_2 \to x_{2ref} = \alpha_2\left[k_p(V_{ref} - x_3) + k_{int}\int_0^t (V_{ref} - x_3)\,d\tau\right] \quad (16b)$$

must hold.

To conclude this subsection, it should be noted that control algorithm given by **(9)** and (16) can also be expressed using the standard notation for sliding mode controllers:

$$u_i = \begin{cases} 1 & si \quad \sigma_i(x) < 0 \\ 0 & si \quad \sigma_i(x) > 0 \end{cases} \quad (18)$$

with

$$\sigma_i(x) = x_i + \alpha_i\left(k_p(x_3 - V_{ref}) + k_{int}\int_0^t (x_3 - V_{ref})\,d\tau\right) \quad (19)$$

A continuous control law is a good approach, but considering flexibility is not a suitable solution since a minimum change on the controller will be a new design for the controller circuit. In the next section the controller is digitalized.

3.1 Digital controller

Till now, controller (17) and (18) has been implemented with analog components. A digital implementation would add some flexibility to the intended application, for example: a) warning and diagnose signals can be added. b) communication with other devices becomes possible, c) the

power converter could be embedded in a larger digital device and cooperate with the rest of the equipment. In what follows it will be shown that such controller can be digitally implemented and programed in a microcontroller (μC).

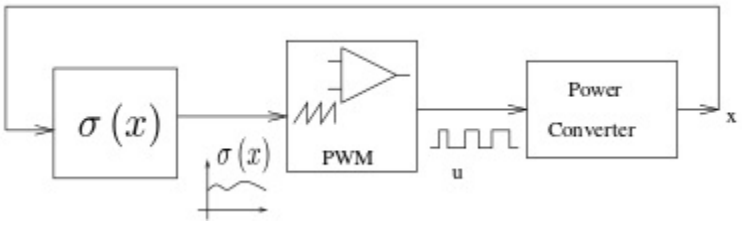

Fig. 2 PWM implementation of the SMC given by (17) and (18)

It is important to point out that in the controller depicted in Fig. 2, the construction of σ is separated from the PWM block. Hence, the program on the μC only have to approximate (18). Let call the time elapsed between two σ calculations the refreshing period of the controller. It is important to point out that this refreshing period does not have to be equal to the switching period.

In the ideal case the refreshing period of σ function (T_σ), should be faster than the switching period (T_s). However to achieve this ideal, a large computing power is needed. Since term $(x_3(t) - V_{ref})$ changes slowly, the integral can be approximated by the trapezoidal method as follows. Let us call

$$F(t) = \int_0^t f(s)ds \qquad (20)$$

then

$$F\big((k+1)T\big) = F(kT) + \frac{f\big((k+1)T\big) + f(kT)}{2}T \qquad (21)$$

In the previous discussion it has been shown that the terms in (18) could be calculated with low refreshing period without loosing valuable information. It is important to denote that the stability region from continuous and discrete systems is different, thats is the reason to obtain a discrete model. Since the control is implemented on a micro controller the PI tunning gains should be selected as a digital control system, so the assumption of the linear model (11) must expressed as

$$G(z) = \frac{b}{z - e^{-aT}} \qquad (22)$$

so the controller gains k_p and k_i should be selected to be on the stability region.

4. Energy router results

To study the controller response simulation and experimental results are presented. To compare the simulation results and the experimental results the system parameters tried to be almost the same.

4.1 Simulation results

An energy router is simulated under different circumstances to evaluate the controller performance, the router parameters are presented on the Table 1. To simulate different

power conditions the parameter α changes every $5ms$, considering that $\alpha_1 = 0.25$ y $\alpha_2 = 0.75$ and after $5ms$ their new values are $\alpha_1 = 0.75$ and $\alpha_2 = 0.25$.

Table 2 Energy router simulation parameters

V_o	$14V_{CD}$
L_1	$200\mu H$
L_2	$240\mu H$
C	$20\mu F$
R	10Ω
V_1	$25V_{CD}$
V_2	$20V_{CD}$
α_1	0.25
α_2	0.75

Another disturbance added to the simulation is a load change, considering that the load changes from 5Ω to 10Ω every $10ms$.

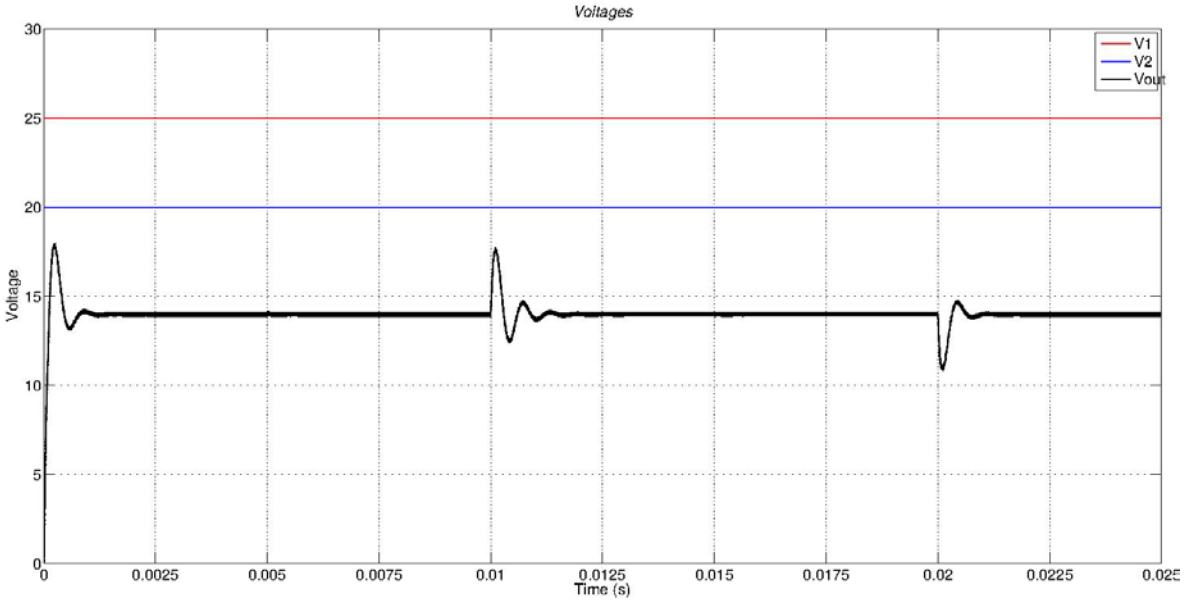

Fig. 3. Energy router voltages

In Fig. 3 the input voltages provided by the sources and the output voltage are presented, note that the changes on the power conditions determined by α are from mV and do not present a significant disturbance on the output voltage. On the other hand the load changes present a significant disturbance on the output voltage, but the control reestablishes the desired output voltage on a short time $1.5ms$.

In Fig. 4 the currents on both inductors and the load current could be appreciated, notice that on the currents the factor α changes the current supplied by each source but the

load current maintains its value. On the other hand when the load changes and there is a transient response on the inductor currents and the output current.

In Fig. 5 the source power and the output power could be appreciated. As it is shown on Fig. 5 the changes on the parameter α modify the power supplied by each source, but the power on the load remains constant. On the other hand, the load changes forces the output power to change and so the power supplied by each source is adjusted to the feed the new load with the proportion determined by α.

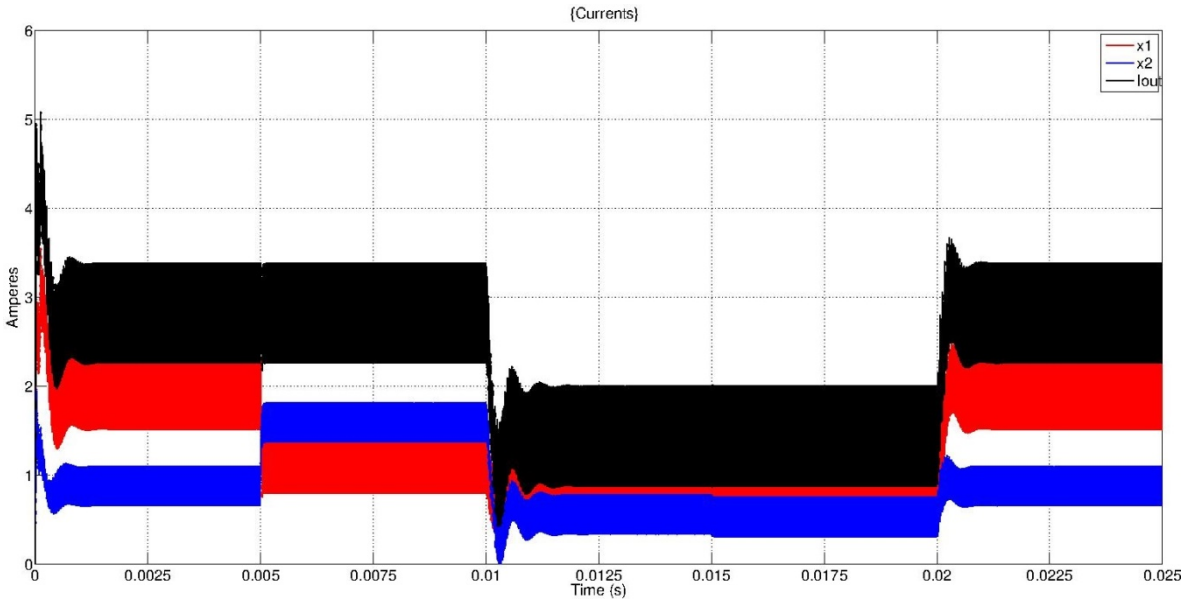

Fig. 4. Energy router currents

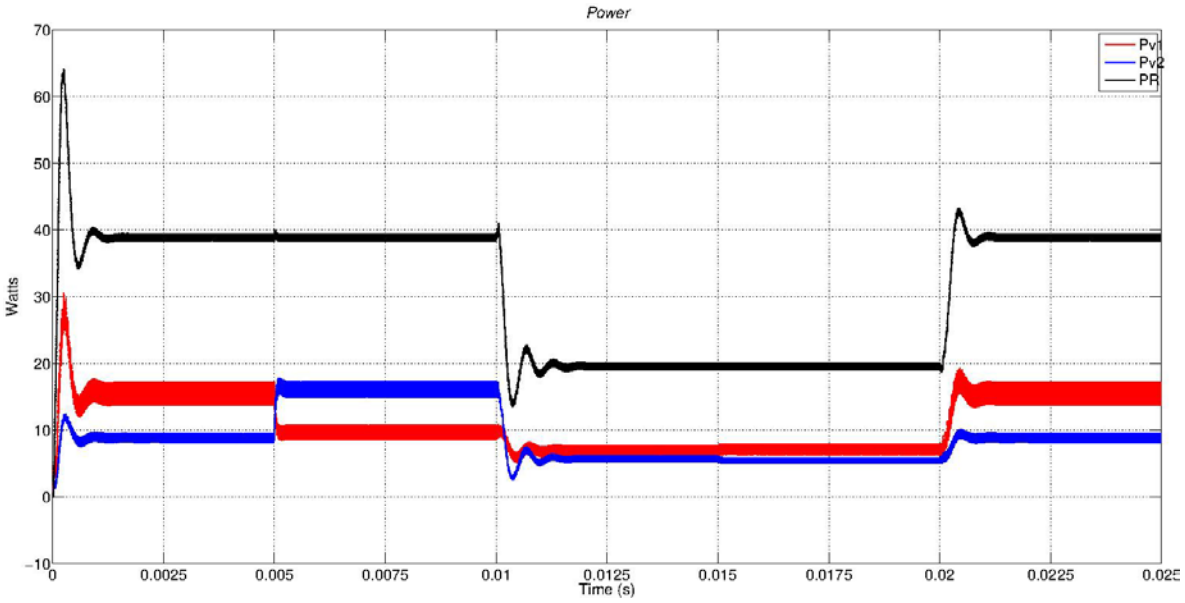

Fig. 5. Energy router power

4.2 Experimental results

An energy router prototype was developed to test the controller on a real application under variable circumstances to evaluate the controller performance, the router parameters are presented on the Table 2. Additionally the controller algorithm was programmed using a FRDM-K64F freesclae microcontroller.

Table 3 Energy router parameters.

V_o	$14V_{CD}$
L_1	$200\mu H$
L_2	$240\mu H$
C	$20\mu F$
R	33Ω
$V_{1,2}$	$24V_{CD}$
α_1	0.4
α_2	0.6
V_o	$14V_{CD}$

In Fig. 6 it is appreciated the results when the energy router has α variations. The α factor change from $\alpha_1 = 0.4$ and $\alpha_2 = 0.6$ to $\alpha_1 = 0.6$ and $\alpha_2 = 0.4$ every 2 seconds. Note that this variations are an extreme case, since the renewable sources have slow variations. The experimental results match with the simulation results, as it can be appreciated on Fig. 6 the voltage is almost constant, but the currents are set to new values when the parameter alpha changes.

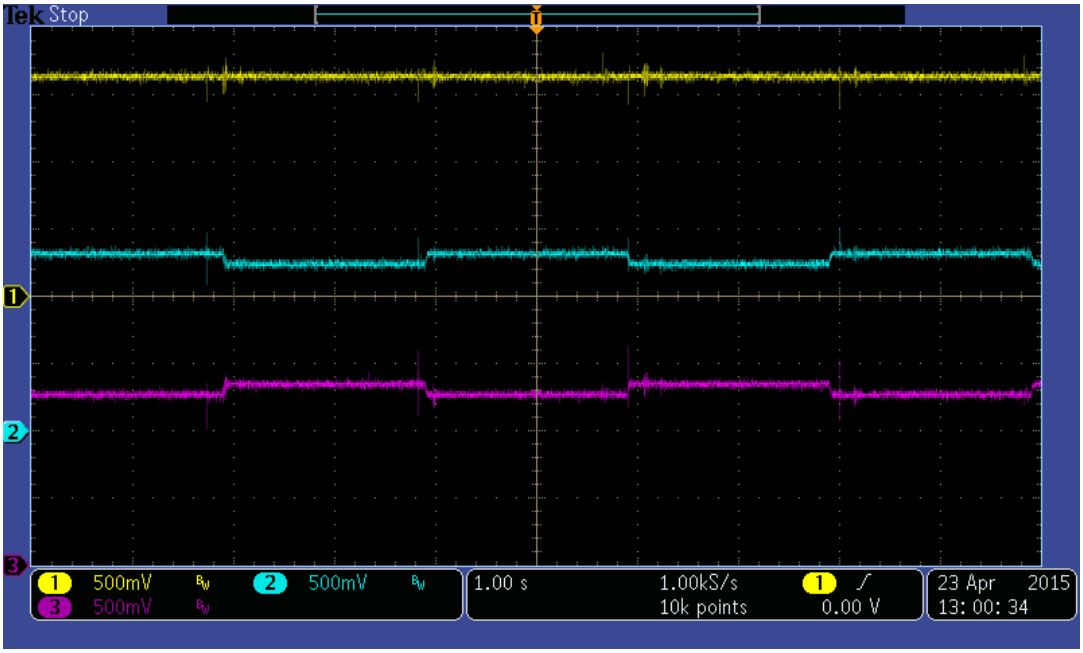

Fig. 6. Output voltage and inductor currents under α variations (Output voltage- yellow, current on inductor 1- blue, current on inductor 2-purple)

In Fig. 7 the experimental results only considered the load variations. A circuit that changes the load was developed to perform this test, such circuit change the load from 33Ω to 16.5Ω every $160ms$. Note from Fig. 7 that there is a slight perturbation on the voltage at the time the change is done, but the controller recovers rapidly to the desired voltage. In this result the currents just adapt to load requirements.

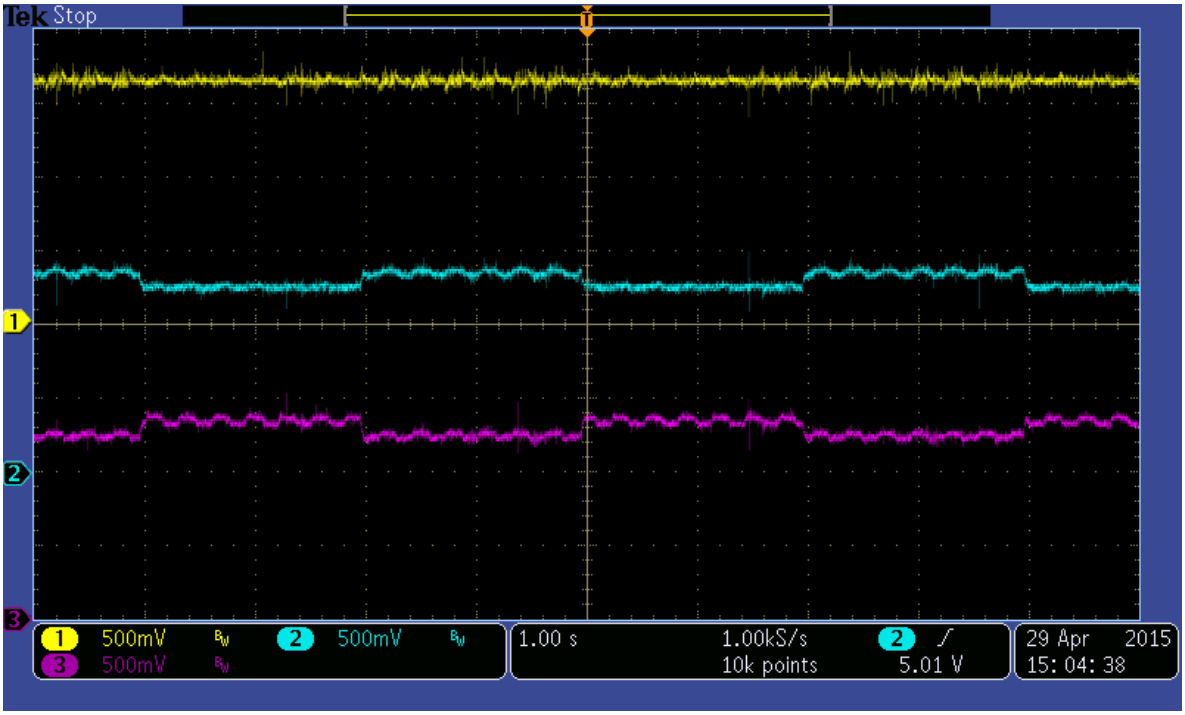

Fig. 7. Output voltage and inductor currents under load variations (Output voltage- yellow, current on inductor 1- blue, current on inductor 2-purpule)

The last test performed was to combine the two previous experiments load and alpha variations. On this test the energy router performance was evaluated considering the α factor change from $\alpha_1 = 0.4$ and $\alpha_2 = 0.6$ to $\alpha_1 = 0.6$ and $\alpha_2 = 0.4$ every 2 seconds and the load variation from 33Ω to 16.5Ω every $160ms$. It could be appreciated on Fig. 8 that the voltage is perturbation by the load variations, but the controller tries to set the output at the desired value, the α variations do not represent a major importance on the voltage perturbations.

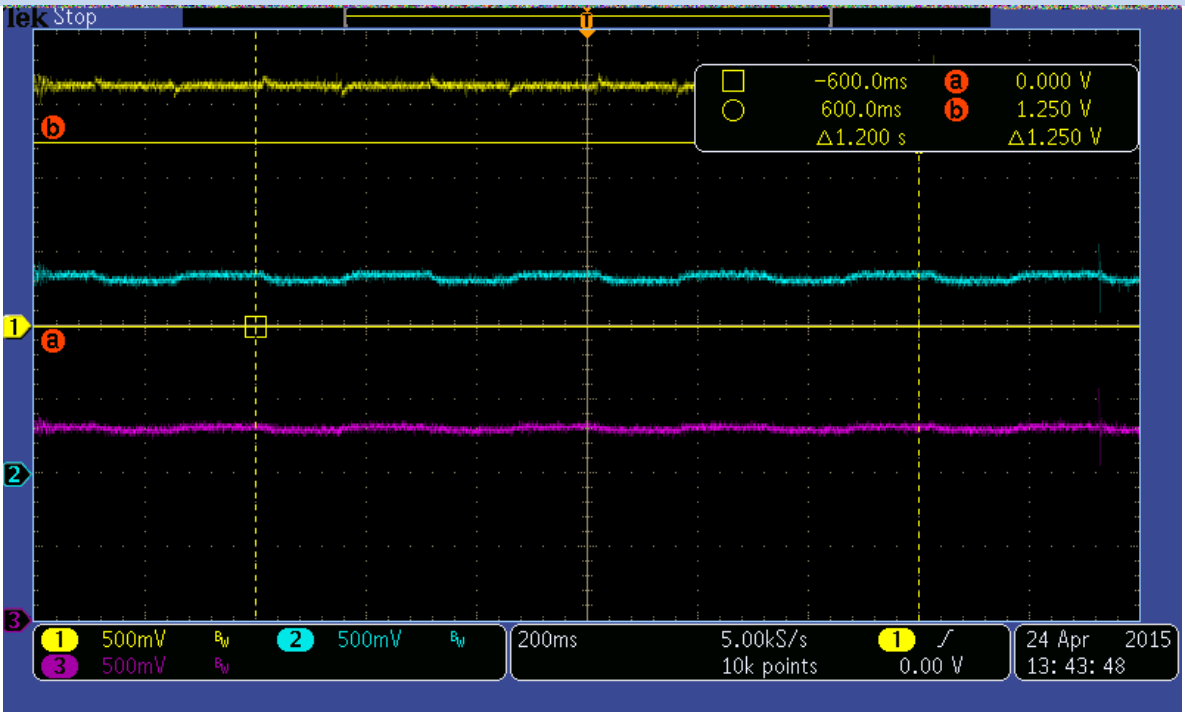

Fig. 8. Output voltage and inductor currents under α and load variations (Output voltage-yellow, current on inductor 1- blue, current on inductor 2-purple)

5. Conclusion

In this paper an approach to control digitally an energy router is presented. An algorithm to control the multi-input power electronic converter that allows to determine the energy provided by each source is developed. Digital implementations add some advantages and flexibilities, that is the reason the control algorithm is digitalized and programed on a microcontroller.

A methodology to perform a discretization of the proposed controller is presented. To evaluate the digital approximation is simulated and implemented on a microcontroller, in both cases with satisfactory results. The proper control of the energy router could help to improve the usage of renewable energies such as fuel cells, photovoltaic, eolian, among others.

Acknowledgements

This research has been partially supported by Mexico City Secretariat of Science, Technology and Innovation under grant ICYTDF-198-2012.

References

[1] BP Statistical Review of World Energy. June 2010.
[2] Bryan G. Dobbs and Patrick L. Chapman. A Multiple-Input DC-DC Converter Topology. Power Electronics Letters, IEEE (Volume:1 , Issue:1).

[3] Huang-Jen Chiu, Hsiu-Ming Huang, Li-Wei Lin, and Ming-Hsiang Tseng. A multiple-input dc/dc converter for renewable energy systems. In Industrial Technology, 2005. ICIT 2005. IEEE International Conference on, pages 1304–1308, Dec 2005.
[4] D. Cortes, N. Vázquez, and J. Alvarez. Dynamical sliding-mode control of the boost inverter. IEEE Transactions on Industrial Electronics, 56(9):3467–3476, September 2009.
[5] Cortes D. Generación de Voltajes de Corriente Alterna Mediante Convertidores de Alta Frecuencia de Conmutación. PhD thesis, Centro de Investigación Cientifica y Estudios Superiores de Ensenada, 2004.
[6] A. Di Napoli, F. Crescimbini, S. Rodo, and L. Solero. Multiple input dc-dc power converter for fuel-cell powered hybrid vehicles. In Power Electronics Specialists Conference, 2002. pesc 02. 2002 IEEE 33rd Annual, volume 4, pages 1685–1690, 2002.
[7] Alexis Ding, Guanyu Kwasinski. Digital constant on-time controlled Multiple-input buck and buck-boost converters. In Applied Power Electronics Conference and Exposition (APEC), 2013 Twenty-Eighth Annual IEEE , vol., no., pp.1376,1382. doi: 10.1109/APEC.2013.6520479, 17 March 2012.
[8] G. Escobar, P. Hernandez-Briones, P. Martinez, M A. Henandez-Gomez, and R. Torres-Olguin. A repetitive-based controller for the compensation of 6l _ 1 harmonic components. IEEE Transactions on Industrial Electronics, 55(8):3150–3158, August 2008.
[9] G. Escobar and H. Sira-Ramirez. A passivity based-sliding monde control approach for the regulation of power factor precompensators. In Proceedings of the 37th IEEE Conference on Decision and Control, pages 2423–2424, Tampa, FL, USA, December 1998.
[10] S. ; Ghanbari Farjah, E.; Rezaee. Sliding mode control of a novel multiinput split-inductor Buck-Boost converter. In Electrical & Computer Engineering (CCECE), 2012 25th IEEE Canadian Conference on, vol., no., pp.1,4 doi: 10.1109/CCECE.2012.6334820, 29 April 2012.
[11] R. Gopinath, S. Kim, H. Jae-Hong, N. Prasad, B. Mark, and Jo. W. Howze. Development of a low cost fuel cell inverter system with dsp control. IEEE Transactions on Power Electronics, 19(5):1256–1262, September 2004.
[12] Florin Hartescu Ion Miciu. Monitoring System for Co-generative Power Plants. Studies in Informatics and Control, ISSN 1220-1766, vol. 18 (4), pp. 379-388, 2009.
[13] Domingo CORTÉS. Israel MACIAS, David NAVARRO. Controlling Multi-input Converters to Act as Electric Energy Router. tudies in Informatics and Control, ISSN 1220-1766, 24(1):23–32, 2015.
[14] K. Ogata. Modern Control Engineering. Prentice Hall, USA, 3 edition, 1997.
[15] K. Sopian Khatib Tamer, A. Mohamed. Optimal sizing of building integrated hybrid PV/diesel generator system for zero load rejection for Malaysia. Energy and Buildings. ELSEVIER. Vol. 43, No. 12, Pag. 3430-3435.
[16] P.C. Liu Yan-Fei, Sen. A general unified large signal model for current programmed DC-to-DC converters. IEEE Transactions on Power Electronics, Volume:9 , Issue: 4.
[17] D. Maksimovic and R. Zane. Small-signal discrete-time modeling of digitally controlled pwm converters. Power Electronics, IEEE Transactions on, 22(6):2552 –2556, nov. 2007.
[18] Middlebrook R. D. Modeling current-programmed buck and boost regulators. IEEE transactions on Power Electronics.
[19] E. M. Navarro-López, D. Cortes, and C. Castro. Design of practical sliding-mode controllers with constant switching frequency for power converters. Electric Power Systems Research, 79:796–802, 2009.
[20] B. Escobar O. Beltrán, R. Barbosa. Análisis y propuesta de un protocolo para la gestión de la energía de un sistema híbrido Eólico-Solar-Hidrógeno. In Conr. int. ing. electrón. mem. Eléctro, vol. 33, pp. 222-227 Chihuahua, Chih. México., 2011.
[21] Li Peng, Yong Kang, Xuejun Pei, and Jian Chen. A novel pwm technique in digital control. IEEE Transactions on Industrial Electronics, 54(1):338–346, February 2007.
[22] F. Mendoza. R. Dufo Lopez, J.L. Bernal Agustín. Diseño y análisis económico de los sistemas PV-viento híbridos conectados a la red para la producción intermitente de hidrógeno. Energy policy, Vol. 37, No. 8, Pag. 3082, August 2009.
[23] V. Ramirez, R. Ortega, R. Grino, A. Sanchez-Squella, and O. Bethoux. Theory and experimental results of two dynamic energy routers. In American Control Conference (ACC), 2012, pages 2128–2133, June 2012.
[24] V.M. Rao, A.K. Jain, K.K. Reddy, and A. Behal. Experimental comparison of digital implementations of single-phase pfc controllers. IEEE Transactions on Industrial Electronics, 55(1):67–78, January 2008.

[25] D. Lefebvre S. zerkaoui, A. B. Mbooup. Sliding mode based control strategy for multisources renewable energy system. In Electric Power and Energy Conversion Systems, 2009. EPECS '09. International Conference on , vol., no., pp.1,6, 10 November 2009.
[26] R.; Griño Sánchez-Squella, A.; Ortega. Dynamic Energy Router. Control Systems, IEEE , vol.30, no.6, pp.72,80, doi: 10.1109/MCS.2010.938096, December 2010.
[27] Seung H. Choung and Alexis Kwasinski. Multiple-input DC-DC converter topologies comparison. In Industrial Electronics, 2008. IECON 2008. 34th Annual Conference of IEEE.
[28] Yang TIAN Shanzhi LI, Haoping WANG. NNPID-based Stator Voltage Oriented Vector Control for DFIG based Wind Turbine Systems. Studies in Informatics and Control, ISSN 1220-1766, vol. 23 (1), pp. 5-12, 2014.
[29] Tan Siew-Chong, Y. M. Lai, and C. K. Tse. General design issues of sliding-mode controllers in dc-dc converters. IEEE Transactions on Industrial Electronics, 55(3):1160–1174, March 2008.
[30] Tan Siew-Chong, Y. M. Lai, C. K. Tse, L. Martínez-Salamero, and Wu Chi-Kin. A fast-response sliding-mode controller for boost-type converters with a wide range of operating conditions. IEEE Transactions on Industrial Electronics, 54(6):3276–3286, December 2007.
[31] L. Solero, A. Lidozzi, and J.A. Pomilio. Design of multiple-input power converter for hybrid vehicles. Power Electronics, IEEE Transactions on, 20(5):1007–1016, Sept 2005.
[32] V. Utkin. Sliding Modes in Control and Optimization. Communications and Control Egineering. Springer Verlag. ISBN: 3540535160., 1991.
[33] R. Venkataramanan, A. Sabanovic, and S. Cuk. Sliding mode control of dc-to-dc converters. In IEEE Industrial Electronics Conference IECON, pages 251–258, San Francisco CA, USA, 1985. IEEE.

Chapter 6.3. Cascaded multilevel inverter for fuel cell applications

V. Sanchez[a,*]; J. Rosas-Caro[b]; A. Valderrabano[b]; F. Beltrán[c]; R. Barbosa[a]; B. Escobar[d]

[a]Universidad de Quintana Roo, Boulevard Bahía s/n, Chetumal, Q. Roo, México, CP 77019
[b]Universidad Panamericana UP campus Gudalajara, Circunvalación Poniente #49, Zapopan, Jalisco, México, CP 45010.
[c]Universidad Autónoma Metropolitana, Unidad Azcapotzalco, Av. San Pablo #180, México, D.F. CP 02200.
[d]Centro de Investigación Científica de Yucatán, Unidad de Energías Renovables, Carretera Sierra Papacal-Chuburna Puerto km 5, Yucatán, México.

ABSTRACT

Fuel cell generation systems are expected to see a significant increase in their practical usage due to several advantages they offer over conventional generation systems. However, fuel cells generate DC power so that a power conversion is required in order to be interconnected with AC power systems. Multilevel converters allow obtain a desired AC voltage by adding several DC voltages. This work presents a single-phase multilevel boost cascaded inverter which employs only one DC power source. The converter is ideal for Fuel Cell applications as inverter stage in energy generation or grid integration. Multilevel inverter proposed uses a floating capacitor in order to generate a DC voltage level which is added to the main DC source. Besides, proposed switching procedure for the multilevel inverter keeps the capacitor voltage equal to the DC source without a complex control task. Operating principle, analysis and simulation results of a 5-level cascaded multilevel inverter are shown.

Keywords: Multilevel inverter, Fuel cells, Power conditioning converters, Renewable systems

1. Introduction

Multilevel inverters technology has reached high performance in medium and high voltage systems [1],[2], as in AC drives, power quality and power conversion applications [3]-[5]. There are three basic multilevel inverter topologies [6]: neutral point clamped (NPC), flying capacitors (FC) and cascaded H-bridge (CHB), the main feature of this converters is the use of low voltage devices to obtain a higher AC voltage by connecting the load to different levels of DC voltage to synthesize a nearly sinusoidal wave.

---

* Corresponding author:
Víctor M. Sánchez Huerta. Tel: +52 9838350300, Fax: +529838329656. Email: vsanchez@uqroo.edu.mx

Cascaded multilevel inverters are composed by a series connection of H-bridge inverters or also called full bridge inverters [7], due to a similar structure in each module in a fault condition it is possible interchange a damaged module or bypass the fault without redesign the power stage and without disconnect the load [8].

The modularity and the possibility of use asymmetric topologies have made this converter more interesting to develop applications concerned in power conversion as well as in uninterruptible power systems [9] and regenerative drives [10]. However, the main drawback of cascade converters is the requirement of one separate DC source for each H-bridge module in applications that involve active power, some contributions for solve this disadvantage is the use of a multi-pulse transformer and rectifiers, but this implies increment of size and cost [11].

The use of capacitors as sources in multilevel cascade inverters was presented in [12] that consists of a single DC source and capacitors as sources for the remain modules; a similar approach, without inductors, was proposed in [13], in this converter's implementation the capacitor is charged by the load current and maintaining its voltage to a smaller value than the DC source using a control system to regulate it, however the controller response causes output voltage unbalance. Using this same principle a three leg inverter was implemented as boost stage for a three phase motor in electric vehicle applications [14]. On the other hand, the energy generation using DC renewable sources are based in a DC-DC converter with high boost ratio and one inverter [15].

In available configurations of single DC-source multilevel converters the flying H-bridge can not provide real power to the load and acts such a filter reducing the voltage distortion in the load, also the capacitor voltage are minor than the DC-source due to its operation principle, in this proposed topology the capacitor has the same voltage of the DC-source.

This paper presents a 5-level cascade converter with active power interchange between modules for boost voltage capability, without a complex control this converter needs only one DC-source make it ideal for renewable systems integration fed by DC-DC converters.

2. Materials and Methods

2.1. Basic circuit topology and operating principle

The proposed circuit architecture is shown in Fig. 1. Cascaded multilevel inverter is basically composed by two full bridge inverters, a DC voltage source and one capacitor.

The first full bridge inverter is comprised by the switches s_1, s_2, $\bar{s_1}$, $\bar{s_2}$ and the DC voltage source. Moreover, the second full bridge inverter is composed by the switches s_3, s_4, $\bar{s_3}$, $\bar{s_4}$ which are connected to one flying capacitor, similarly to [12-14]. With the eight switches of the two full bridge inverters, a total number of sixteen switching states can be configured as is described in [16]. On the other hand, s_{aux} and the diode d_{aux} are used to charge the flying capacitor to the DC source voltage ($+V_{DC}$). The multilevel cascaded inverter proposed in this work is a simplification of the topology presented in [16], where has reduced the number of the auxiliary switches as well as the number of the switching states.

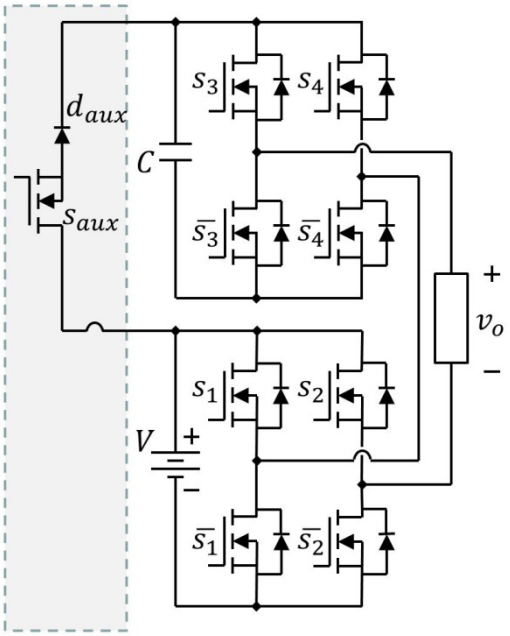

Fig. 1. Topology of the multilevel cascaded inverter proposed.

The switches are activated with a special switching sequence for maintain the capacitor charged as well as to supply energy to the load. The output voltage has five levels in similar way to a symmetric multilevel cascade inverter. The switching sequence for the inverter proposed is obtained of a sinusoidal pulse width modulation (SPWM). The SPWM utilized this work consists in to compare a sinusoidal signal (reference signal) with four triangle signals (carrier signals) in order to obtain the gate signals for the switches of the inverter proposed, as is shown in Fig. 2.

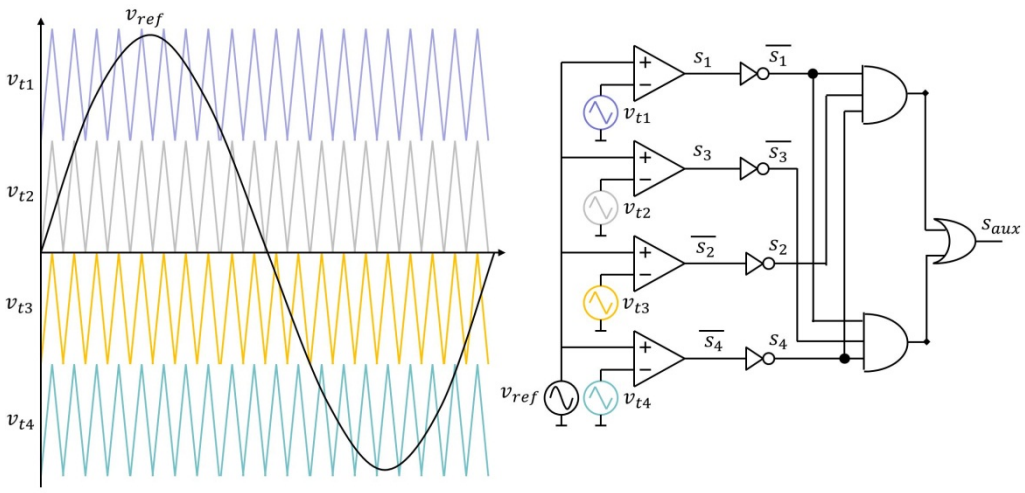

Fig. 2. SPWM and gate signals generating circuit.

In Fig.2, s_1, s_2, s_3, s_4 and s_{aux} are the gate signals for the switches named in Fig.1. The sinusoidal signal frequency determines the fundamental frequency of the AC output voltage. In this work a frequency of 50 Hz is selected as fundamental frequency for the AC

output voltage. Fig. 3 shows the AC output voltage obtained where it possible to observer the five levels of the output voltage as result of the summation of the voltage obtained of the two full bridge inverters.

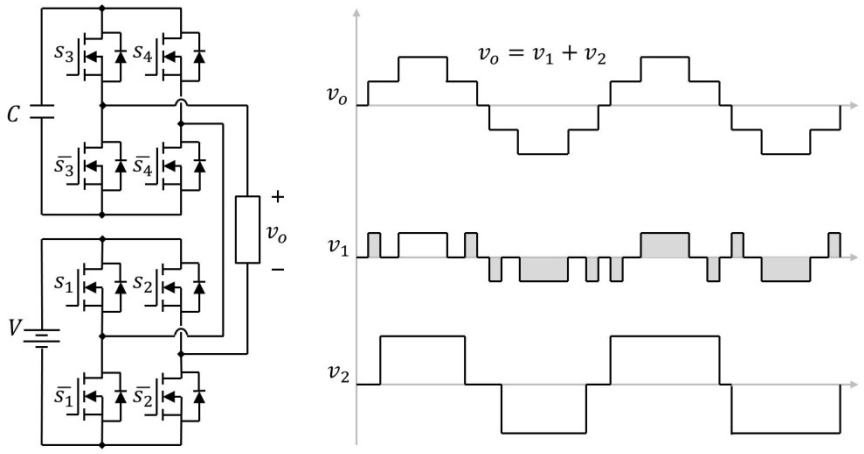

Fig. 3. Output voltage of the multilevel cascade inverter.

The SPWM used allows that the multilevel cascaded inverter operates with just five of the sixteen possible switching states. Table I shows this switching sequence related with the output voltages values.

Table 1. Switching sequence for the 5-level multilevel cascaded inverter.

S_1	S_2	S_3	S_4	S_{aux}	V_o
1	0	1	0	0	$+2V_{DC}$
0	1	0	0	1	$+V_{DC}$
0	0	0	0	1	*0*
0	1	0	0	1	$-V_{DC}$
0	1	0	1	0	$-2V_{DC}$

The equivalent circuits for each one of these switching states are shown in Fig. 4 that depicts the inverter operating principle at fundamental frequency. This principle is based in taking advantage of the redundant switching sequence to charge the capacitor by the DC source. It is noteworthy that the capacitor is charged during three states ($+V_{DC}$, 0V, and $-V_{DC}$) which corresponding the conducting state for S_{aux}. In the $+2V_{DC}$ and $-2V_{DC}$ the capacitor voltage is used in order to obtain these levels. This operating principle allows boosting with only one DC source voltage to twice the DC input voltage.

Although the capacitor is charged in 3 of 5 levels if a high modulation index is used the discharging time becomes bigger than the charging time, to avoid a big drop of output

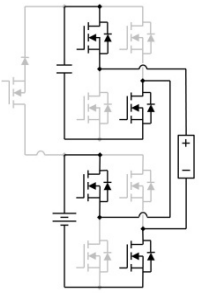

(a) Output voltage = $+2V_{DC}$

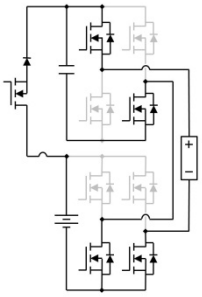

(b) Output voltage = $+V_{DC}$

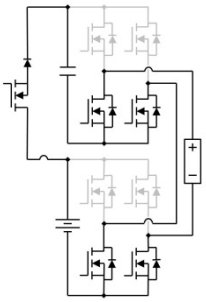

(c) Output voltage = 0V

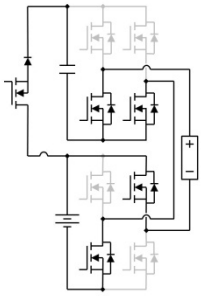

(d) Output voltage = $-V_{DC}$

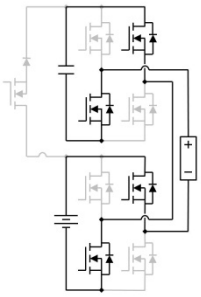

(e) Output voltage = $-2V_{DC}$

Fig. 4. Equivalent circuits for the cascaded multilevel inverter according with the five switching states allowed.

voltage an adequate capacitance value must be selected. This value is related to the load power demand and the output voltage ripple desired.

3. Results and Discussion

Simulation results of the multilevel cascaded inverter are presented in this section. The proposed converter was simulated in Simulink™ and the Piece-wise Linear Electrical Circuit Simulation (PLECS) software. Power converter parameters are shown in Table 2.
A PEMFC stack model is used in the simulation as the DC input voltage. PEMFC model simulates one stack of 24 V_{DC} volts and 1.2 kW. Fig. 5 shows the system simulated.

Fig. 6 depicts the output voltage of the multilevel cascaded inverter with a resistive load of 50 Ω.

Table 2. Simulation parameters for the multilevel inverter.

Parameter	Value
Input voltaje	24 V
Load	50 ohms
Fundamental frequency	50 Hz
Carrier frequency	2 kHz
Capacitor	440 μF, 1.32 mF

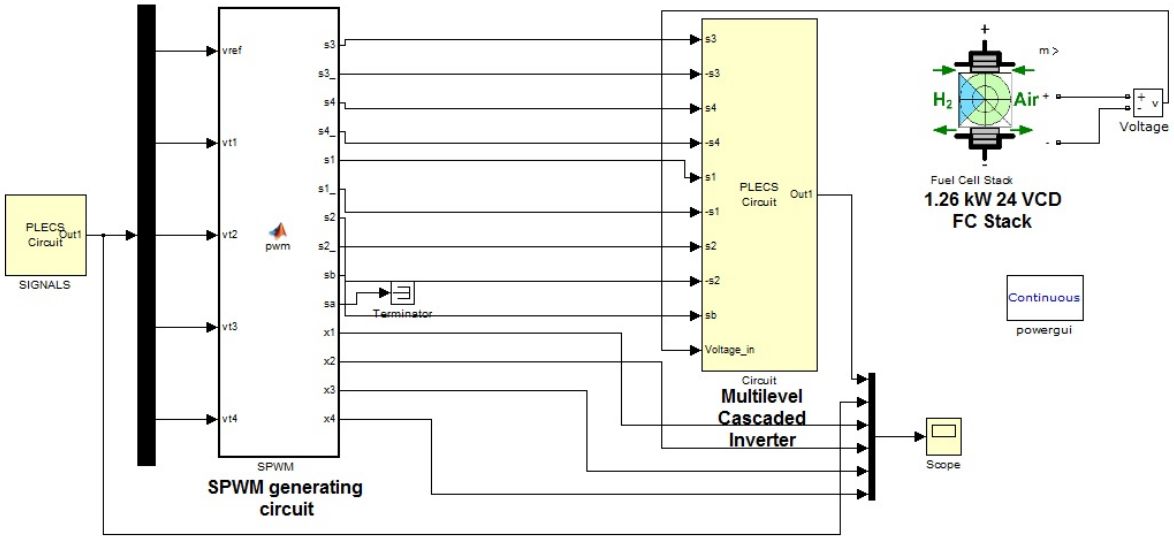

Fig. 5. System simulated of the PEMFC stack with the Multilevel cascaded inverter.

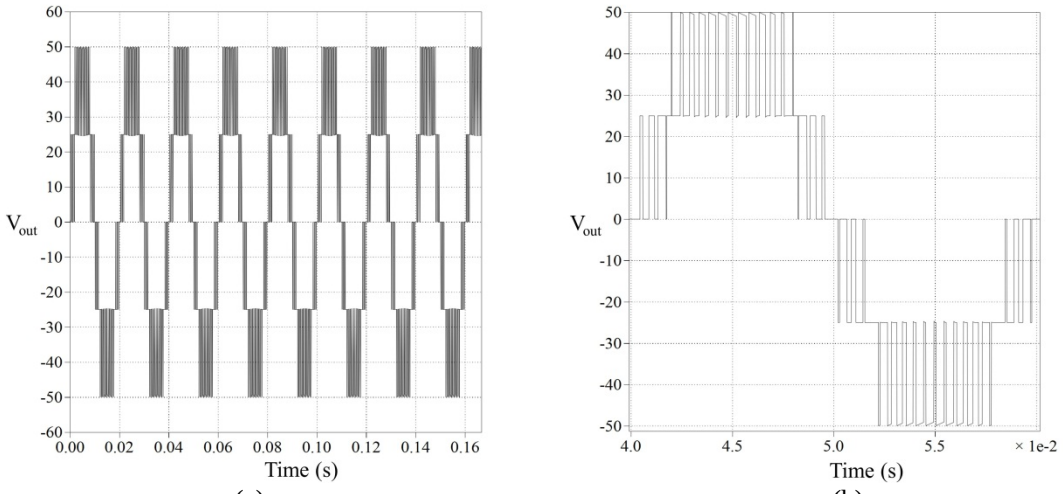

Fig. 6. AC output voltage of the Multilevel cascaded inverter. (a) Five-level output voltage. (b) Zoom of the output voltage

Simulation results displayed in Fig. 6 demonstrate that the multilevel cascaded inverter duplicates the PEMFC voltage due to that the flying-capacitor is charged to the PEMFC voltage during determined switching states. It is important to note that SPWM used for the multilevel cascaded inverter allows that the AC output voltage is symmetrical. In Fig.7 is shown the flying-capacitor voltage.

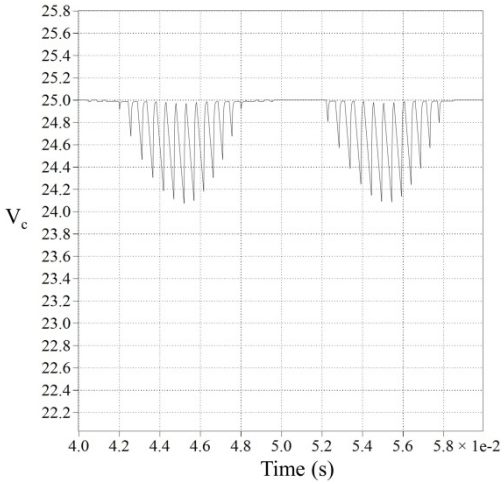

Fig. 7. Voltage on the flying-capacitor.

As shown in Fig.7, the voltage on the flying-capacitor has a ripple less to 1 Volt. This low ripple voltage on the flying capacitor allows a minimal change on the output voltage value of the multilevel cascaded inverter.

In Fig.8, the current supplied by the PEMFC is shown.

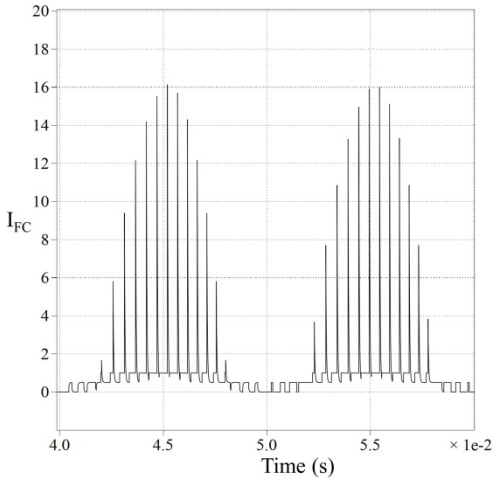

Fig. 8. Input current supplied by the PEMFC.

Although the current drawn to the PEMFC is pulsatile, the frequency of these pulses is low. This fact allows to consider no damage to the PEMFC. Finally, Fig. 9 displays the AC output current of the multilevel cascaded inverter.

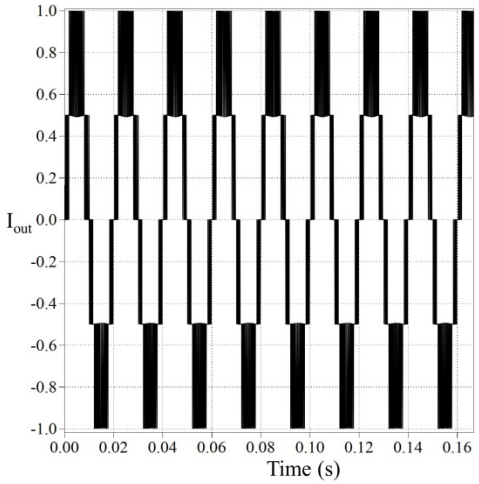

Fig. 9. AC output current.

Symmetrical AC output current is obtained of the multilevel cascaded inverter, as is shown in Fig. 9.

4. Conclusion

A Multilevel Cascaded Inverter has been presented in this work. The proposed Multilevel Cascade Inverter has three main advantages, (i) Employs only one DC source as input, (ii) it has a higher boosting ratio than available topologies with single DC source and (iii) the boost modules easily can be added or replaced. Also, the converter is proposed in order to be integrated as inverter and boost stage in conditioning systems fed by DC-DC converters in a fuel cell application. Simulation results shown the adequate performing of the multilevel cascaded inverter when is connected with a PEMFC.

The converter can be extended in a modular way, easily can multiply the input voltage around two or three times with logic control implementable in a low cost microcontroller, the use of PWM techniques allows to connect a relatively small LC filter at output to obtain a purely sinusoidal wave, experimental results demonstrated the converter's performance.

Acknowledgements

The authors are thankful to SEP-CONACYT for the support of this project under Grant CB-2013/221988 and project 252003 "Programa de Redes Temáticas (RTH2)". Also, V. Sanchez and R. Barbosa wish acknowledge to the "División de Ciencias e Ingenierías" of the Quintana Roo University for the support received to realize this work.

References

[1] Rodríguez J, Lai J. S., Peng F.Z. Multilevel Inverters: A survey of topologies, controls and applications. IEEE Transactions on Industrial Electronics 2002; 49: 724-738.

[2] Franquelo L.G., Rodríguez J., León J.I., Kouro S., Portillo R., Prats M.A.M. The age of multilevel converters arrives. IEEE Ind. Electron. Mag. 2008; 2: 28–39.

[3] Tolbert L.M., Peng F.Z., Hableter T.G. Multilevel converters for large electric drives. IEEE Transactions on Industry Applications 1999; 35: 36-44.
[4] Rodríguez J., Bernet S., Wu B., Pontt J., Kuoro S. Multilevel voltage source converter topologies for industrial medium voltage drives. IEEE Transactions on Industrial Electronics 2007; 54: 2930-2945.
[5] Flores P., Dixon J., Ortuzar M., Carmi R., Barriuso P., Moran L. Static Var compensator and active power filter with power injection capability, using 27-level inverters and photovoltaic cells. IEEE Trans. Ind. Electron. 2009; 56: 130–138.
[6] Lai J.S., Peng F.Z. Multilevel converters - A new breed of power converters. IEEE Transactions on Industry Applications 1995; 32: 509-517.
[7] Malinowski M., Gopakumar K., Rodríguez J., Pérez M.A. A survey on cascaded multilevel inverters. IEEE Transactions on Industrial Electronics 2010; 57: 2197-2206.
[8] Lezana P., Ortiz G. Extended operation of cascade multi-cell converters under fault condition. IEEE Transactions on Industrial Electronics 2009; 56: 2697–2703.
[9] Mori O., Yamada M., Iwata A., Maruyama S., Okada J., Hatakeyama Y. A single phase uninterruptible power system with gradationally controlled voltage inverter. Proc. IEEE Industrial Electronics Conf. 2006; 1956-1961.
[10] Lezana P., Rodriguez J, Oyarzun D.A. Cascaded multilevel inverter with regeneration capability and reduced number of switches. IEEE Trans. Ind. Electron. 2008, 55: 1059–1066.
[11] Baier C.R., Guzmán J.I, Espinoza J.R., Pérez M.A., Rodríguez J.R. Performance evaluation of a multicell topology implemented with single-phase nonregenerative cells under unbalanced supply voltages. IEEE Transactions on Industrial Electronics 2007; 54: 2969–2978.
[12] Corzine K.A., Hardrick F.A., Familiant Y.L. A cascaded multilevel H-bridge inverter utilizing capacitor voltages sources. IASTED Conf.-PES 2003, 290–295.
[13] Du Z., Tolbert L.M., Chiasson J.N. A cascade multilevel inverter using a single DC source. Conf. Rec. IEEE APEC 2006, 426–430.
[14] Du Z., Ozpineci B., Tolbert L.M., Chiasson J.N. DC-AC cascaded H-bridge multilevel boost inverter with no inductors for electric/hybrid electric vehicle applications. IEEE Transactions on Industry Applications 2009; 45: 963–970.
[15] Lai J.S. Power conditioning circuit topologies. IEEE Ind. Electron. Mag. 2009; 2: 24–34.
[16] Gonzalez-Hernandez J.G., Martinez-Bernal J.E., Valderrabano-Gonzalez A., Rosas-Caro J.C., Beltran-Carbajal F., Ramirez-Arredondo J.M., Gonzalez-Lopez J.M. Bootstrap cascaded multilevel inverter. IEICE Electronics Express 2014; 11:1-9.

7
Policies, economy and market strategies

Chapter 7.1. Infraestructure analysis of the hydrogen refueling station in Mexico

N. Nuñez García; D. Morales Herrera; A. Zaragoza González; M. Sanchez Vazquez; R. de G. González Huerta*

IPN-ESIQIE, Laboratorio de Electroquímica y Corrosión, UPALM, CP 7738, DF, México

ABSTRACT

Finding a new source of energy that is renewable and generates a technological impact is needed; one that will benefit the country in terms of growth and development of new technology and social structures. Hydrogen, as an alternative source of energy, is proposed to be used as an energy vector. Studies and articles worldwide claim that the use of hydrogen is not a luxury but an absolute need. The implementation of hydrogen is linked to the development of infrastructure for the production, storage and recharging, plus technical specifications that must be considered. Mexico is seen as a country 90% dependent on fossil fuels, it is currently in an initial phase for the implementation of alternative energy, to reduce the bad environmental impact.

To gain acceptance of the use of hydrogen, a study about comprising implementing of hydrogen stations is being conducted. The research is based on studies reported in the US, Germany, Spain, Japan and Brazil which show a line of investigation that began 10 years ago for the use of hydrogen as fuel in transport systems. The tested technology involves the development of three types of hydrogen refueling stations: 1) On-Site, 2) Pipeline delivery 3) Liquid or gaseous hydrogen delivery. The proposal presented in this research is based on the implementation of an On-Site station in Mexico, where technical, economic and geographic characteristics are necessary for the installation of a safe hydrogen refueling in cars and buses. With this investigation we pretend to impulse our country to a new route of clean tecnology.

Keywords: Refueling station, Infraestructure, Hydrogen, Safety, Implementation

1. Introduction

The implementation of hydrogen as an energy vector is now a necessity. A decade ago it began using hydrogen in cars, but now its implementation turns out to be an economic and social challenge.

On the social side, we can describe the following issues:

---

*Author for correspondence: Rosa de Guadalupe González Huerta, (+52) 55 57296000 x 54246, rosgonzalez_h@yahoo.com.mx

1. Studies on hydrogen as an energy vector focus on technical specifications but not in the social acceptance.
2. The feasibility of the project is both economically and social trust, for the replacement of fossil fuels by hydrogen.
3. Social acceptance should be the first factor to introduce hydrogen to the market.

Related to the economic aspects, they are affected by the following factors:

1. The technology based on hydrogen, proves to be expensive at the beginning and a capital investment high.
2. The technological packages to implement a hydrogen refueling station don't generate earnings nor are profitable if you do not have cars that consume it.
3. The implementation of a hydrogen refueling station does not guarantee the profitability of the project.
4. The fear of investing in this technology and the probabilities of failure limited to investors and countries to opt for the use of hydrogen.

The aspects to evaluate about the advantages and disadvantages of the use and implementation of hydrogen refueling stations turns out to be a complex issue for study. To gain acceptance of the use of hydrogen, a study about comprising implementation of hydrogen stations is being conducted in this work.

2. Refueling stations

This article is based on hydrogen refueling stations and studies in the United States for the implementation of hydrogen, specifically in California, Figure 1. In this state, the trial and error phase were successfully concluded and the results can be modified as it needed anywhere in the United States. The feasibility is determined based on the success of the method of implementation.

Below is show technical information and description of the processes developed and used by California. In the future this technology could be applied to Mexico. Nowadays and based on the needs of each country, there have been four different sizes of hydrogen service stations:

- Very small stations: The filling time of the vehicle is approximately 3 to 5 minutes, however you must wait 20 to 25 minutes to perform another recharge. This condition is a limiting because motorists would reject this technology because the waiting time between batteries recharges.
- Small and medium stations: Have a filling time of 3 minutes, a delivery time of 3 minutes a standby time of 5 minutes, compared with a very small station, is more feasible implementing this type of HRS. Under these conditions, they can be used for the industrial sector and for the daily life of people.
- Large stations: There are no limitations, as these HRS operate alternately between filling and recharging, are the most expensive and the idea of this HRS builds on gas stations that we know today.

Fig. 1. Refueling station

3. Description of storage systems

3.1 On site Hydrogen storage (storage system hydrogen gas)

Compressed hydrogen gas is stored in the ground or on the deck of cylinders, tubes or vessels. The level of pressure and the capacity of the storage system must be designed taking into account the supply pressure, frequency of delivery, the economy and the specification of process performance. The on-site gas storage system has to be designed so that it can handle a flow of hydrogen safely from a trailer within the pressure range 20 to 50 Mpa, Figure 2.

If the gas has to be delivered with a liquid system cryo compressor then the operating temperature of the components, which are part of this module, will have to be defined. The buried tanks will be equipped with corrosion protection.

The storage system is provided with pressure gauges, a ventilation system and isolation valves to allow the system to shut down for maintenance or inspection. An emergency valve shall interrupt the flow of hydrogen compressor in case of an event outside of specification. It will be located as close as possible to the storage system.

3.2 Liquid Hydrogen Storage.

It is it supplied by a trailer; it is stored in a storage container either above ground or underground. The buried tanks will be equipped with corrosion protection. An emergency valve shall interrupt the flow of hydrogen compressor in case of an event outside of specification. It will be located as close as possible to the storage system, Figure 3.

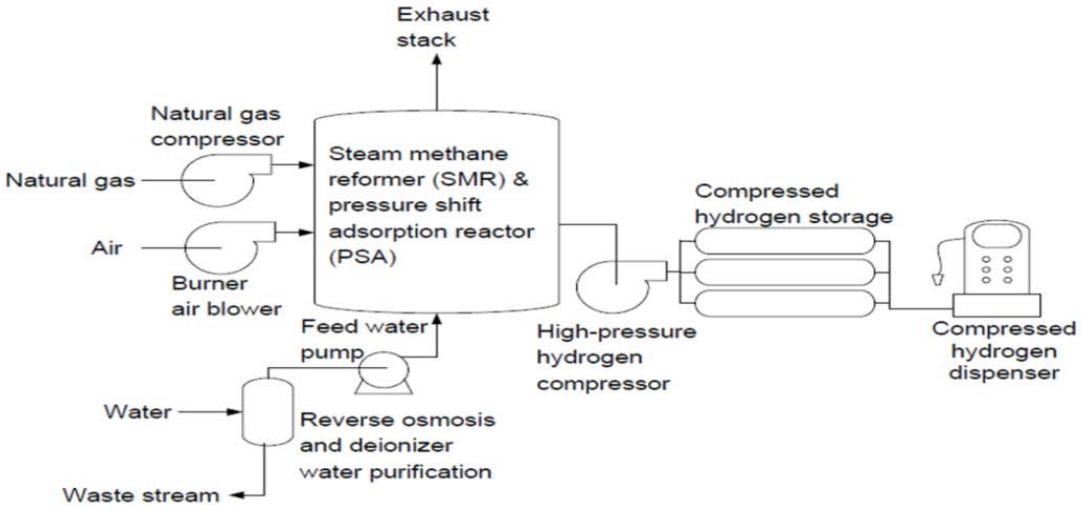

Fig. 2. A configuration of an onsite SMR station.

Based on the performance for stations of various sizes will be designed taking into account the level of pressure and the capacity of the storage system, which should be designed based on the ranges of supply pressure, frequency of delivery, the economy and specification process performance. The compression system performance will depend on the overall capacity HRS. The power required to drive the compressor depends on the size of the HRS and the inlet pressure is available.

According to the different sizes of stations, pressure and capacity of the hydrogen compression system shall be designed taking into account the economic implications. Refueling the vehicle can be achieved by direct filling from the compression system or through high pressure cascade, in both cases, the system should be designed according to size.

4. Codes and standards to use hydrogen

Interested in fuel cell vehicles parts, government agencies, standards development organizations and industries are responsible for leading the effort to develop standards and codes. The International Organization for Standardization (ISO) has established a purity of 99.97% H2 as a standard for PEMFC with a maximum subsidy of 0.2 ppm of carbon monoxide and 4 ppb for hydrogen sulfide (ISO 14687-2: 2012).

For all types of hydrogen station, compression, storage and distribution of hydrogen gas must follow certain codes and standards. Some pioneering hydrogen stations in the state of California were based on SAE Standard J2601 standard: "Fueling Protocols for Gaseous Hydrogen Surface Light Duty Vehicles" for their hydrogen fuel dispensers:

- SAE J2601 applies to light-duty vehicles with storage capacity of 1-10 kg of H2 to 70 MPa and 1 to 7.5 kg to 35 MPa. The criteria include the maximum temperature of fuel at the pump, the maximum fuel flow rate, the maximum rate of pressure rise

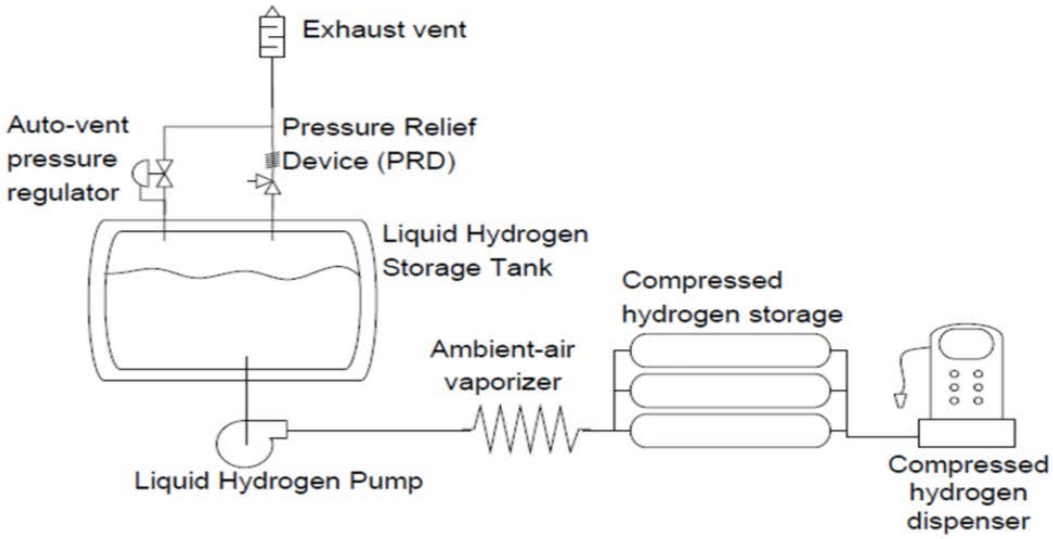

Fig. 3. A configuration of a hydrogen station with liquid hydrogen delivery.

and other performance criteria based on the cooling capacity of the dispenser station.

- NFPA 2. California became in the first jurisdiction in the nation to adopt and approve the 2011 edition of the National Fire Protection Association 2 (NFPA 2). The purpose of this code is to provide fundamental guarantees for the construction, installation, storage, piping, use and handling of hydrogen in the form of compressed gas (GH2) or cryogenic liquid form (LH2).

- NFPA 52 (Vehicular Gaseous Fuel Systems Code). This code safeguards people and installations with requirements that mitigate the fire and explosion hazards associated with compressed natural gas (CNG) and liquefied natural gas (LNG) engine fuel systems and fueling facilities. This Code applies to all facilities with LNG storage in containers of 70,000 gallons or less.

- NFPA 55 (Compressed Gases and Cryogenic Fluids Code). This code facilitates protection from physiological, over-pressurization, explosive, and flammability hazards associated with compressed gases and cryogenic fluids. This code to provide fundamental safeguards for the installation, storage, use, and handling of compressed gases and cryogenic fluids in portable and stationary cylinders, containers, and tanks in all occupancy types.**5.**

5. Contributions

We focus in scientific input which present the research undertaken for the implementation of the technology using hydrogen as an energy vector. We know the need in terms of technological advances that the country has, and the need to innovate and use new technologies. With this work we will present the features and specifications both technical and economic to generate audience interest and find support for the development of it.

6. Conclusion

The technology that uses hydrogen as fuel for vehicles today is a reality in developed countries; in this regard Mexico has a technological delay of 10 years. Therefore, the motivation to develop this article was to present this technology and seek support for introducing to the country, the sustainable development of a new energy source, taking as main idea the implement of hydrogen prototypes to show the feasibility, in this case the hydrogen refueling system.

Acknowledgements

This work has been supported by multidisciplinary project IPN-SIP 1683 and Programa Redes Temáticas CONACYT/RTH2.

References

[1] Nan Qin, Paul Brooker, “Hydrogen Fueling Stations Infraestructure”, University of Central Florida, 2014
[2] "Hydrogen Vehicle and Infrastructure Codes and Standards Citations," National Renewable Energy Laboratory.
[3] NFPA 52, Vehicular Gaseous Fuel Systems Code, 2010 edition.
[4] NFPA 55, Compressed Gases and Cryogenic Fluids Code, 2010 edition.
[5] NFPA 2, Hydrogen Technologies Code, 2011 edition

[6] California fuel cell partnership, Driving for the future [serial online] 2015, Available from: URL: http://www.fuelcellpartnership.org/
[7] “A California Road Map: The Comercialization of Hydrogen Fuel Cell Vehicles”, California Fuel Cell Partnership 2014.
[8] “Petroleum Dependence”, California Fuel Cell Partnership 2012.
[9] Gerhard Achtelik, California Hydrogen Activities [serial online] 2015, Available from: URL: http://www.arb.ca.gov/msprog/zevprog/hydrogen/hydrogen.htm
[10] http://www.fuelcellstandards.com/home.html

Chapter 7.2. Public policy performance for social development: solar energy approach to assess technological outcome in Mexico City Metropolitan Area

A. R. Arenas-Aquino[a,*]; Y. Matsumoto-Kuwabara[b]; M. Kleiche-Dray[c]; R. Baquero-Parra[d]; C. González-Brambila[e]; G. Isunza-Vizuet[f]; H. M. Poggi-Varaldo[g]

[a] Department of Science Methodology, Centro de Investigación y de Estudios Avanzados, 2508 Instituto Politécnico Nacional, San Pedro Zacatenco, Distrito Federal, 07360, Mexico.
[b] Department of Electrical Engineering, *ibid*.
[d] Department of Physics, *ibid*.
[g] Department of Biotechnology *ibid*.
[c] IRD - Ceped & IFRIS, 19 Rue Jacob, Paris, 75006, France.
[e] Academic Department of Administration, Instituto Tecnológico Autónomo de México, 1 Río Hondo, Progreso Tizapán, Distrito Federal, 01080, Mexico.
[f] Centro de Investigaciones Económicas, Administrativas y Sociales, 120 Lauro Aguirre, Agricultura, Distrito Federal, 11360, Mexico.

ABSTRACT

Mexico City, Metropolitan Area (MCMA) is the most populated urban area in the country. In 2010, MCMA required 14.8% of total energy domestic demand, but greenhouse gas emissions accounted for 7.7% of domestic emissions. Mexico has massive renewable energy potential that could be harnessed through solar photovoltaic (PV) technology. In that matter, marginalized population is severely affected by techno-environmental repercussions, therefore, there are several government policies within MCMA that focus on energy issues and social exclusion. The problem to explore is the relationship between local and federal public strategies in MCMA and their stance on energy transition concern, social empowerment, new technology appropriation and the will to boost social development and urban sustainability. A public policies typology was conducted through instruments of State intervention approach, based on political agenda articulation and environmental local interactions. In energy-environmental sector, six policies and seventeen instruments were identified and for social sector, three policies and ten instruments were detected. Social equality is encouraged by means of forthright funding and in-kind support and energy policies focus on non-renewable energy subsidies and electric transmission infrastructure investment. There is a lack of vision for using PV technology as guiding axis for marginalized population development. It is essential to promote economic and political rearrangement in order to level and structure environmental governance. Environmental networks consolidation must be achieved with participatory democracy and it is essential to understand people's representation about their own needs along with renewable energy.

Keywords: Photovoltaic technology, Social development, Environmental governance, Mexican policy

---

*Author for correspondence: Angel Raúl Arenas Aquino, +52 55 6131 0946, rarenas@cinvestav.mx

1. Introduction

Mexico City Metropolitan Area (MCMA) is the largest and most populated urban area in the country. It is delimited by 16 Federal District (FD) deputations with 8.851 million inhabitants and 59 municipalities in the State of Mexico (SM) with 11.168 million inhabitants [1]. In 2010, MCMA required 14.8% of total energy domestic demand, but greenhouse gas emissions accounted for 7.7% of domestic emissions [2] [3].

Mexican territory is within the so-called "sun belt", which is one of Earth's highest solar incidence areas; over 5 kilowatt-hour per square meter per day radiation [4]. This big renewable energy potential could be harnessed through solar photovoltaic (PV) technology. This technology is economically competitive to electrify vulnerable areas that do not require much power, often, this feature makes PV devices installation less expensive than extending traditional electric lines [5].

Although techno-environmental implications affect all socio-economic sectors, marginalized populations are severely affected because of their high dependence on resources around them and their limited ability to adapt to both present and future energy conditions [6]. In consequence, State intervention is essential, since it is the agency that should regulate production modes, promote economic activities, boost population welfare and incorporate population sectors that, because of their conditions and needs, do not share the economic dynamics benefits [7]. Therefore, there are several government policies within MCMA that focus on energy issues and social exclusion, most important policies belong to Federal government. Why local policies do not seem to achieve such importance?

Hence, the problem to explore is the relationship between local and federal public strategies in MCMA and their stance on energy transition concern, social empowerment and new technology appropriation. Moreover, public programs allegedly struggle to set strict rules in order to assist marginalized population; are this strategies, allowing boost social development and urban sustainability? Previous works regarding to these matters have not been made neither for MCMA nor for Mexico, despite the transdisciplinary approach and the importance for governance problems regarding social inclusion and urban technological adaptation.

The aims of this research are to assess MCMA's energy transition and social development government policies; analyze the social and environmental political agenda articulation; and discover local interactions between social interests, techno-environmental marginalization and PV technology-based energy transition.

2. Materials and Methods

The public policies typology was conducted through Theodore Lowi's instruments of State intervention approach, based on political agenda articulation and environmental local interactions. Public policies can be classified according to their effect on society and the relationships between those involved in their making [8]:

- Distributive: designed to distribute, set or assign privileges, powers or resources to citizens.
- Regulatory: aimed at regulating and controlling agents' activities of certain sector.

- Constitutive: modifies the State organization. Establishes rules of powers distribution in a social environment and creates decision-making procedures.
- Redistributive: policy that fundraises from some social groups or regions to give to others, particularly based on poverty or vulnerability.

When designing a public policy, the State decides on the use of one or other instrument for its implementation, these are known as "instruments of State intervention". Study based on legal and administrative instruments can give indications on how the State and institutions understand the problem to solve and reveals the conception of authority.

Policies and State instruments rating was defined around main ideas, some of these concepts may depend on the context and reality in which research takes place. Main ideas were:

- Energy transition and PV technology.
- Environmental impact and mitigation.
- Marginalization and multidimensional effects in social sector.

Also, policies had to meet certain criteria to be selected, but did not have to meet them all:

- To mention renewable energy and/or energy transition as a main development point.
- To locate their objectives within MCMA.
- To be supported by legislative framework.
- To be up to date in political agenda (regardless data is not updated, this depends on several factors).
- To consider (even in general terms) application of PV technology.
- To aim some of its goals for marginalized population development.

For policies and State instruments research, information from Federal, FD and SM governments was used as well as some private consultancy firms and non-governmental organizations (NGO). Internet search was the main tool to collect the information because official data is available either digitalized or printed, this helped to make a fast research. Search was made mainly within Social Development, Public Works, Housing, Natural Resources, Communications, Environment and Energy ministries (also known as secretariats) or administrative offices for each three governments. Policies were sub-divided in two sectors: energy-environmental and social sector policies.

3. Results and Discussion

For energy-environmental sector, six policies were identified:

1. Plan Nacional de Desarrollo (National Development Plan) [9].
2. Ley General de Cambio Climático (Climate Change General Law) [10].
3. Estrategia Nacional de Energía (National Energy Strategy) [11].
4. Programa de Acción Climática de la Ciudad de México (Mexico City Climate Action Program) [12].
5. Iniciativa Ante el Cambio Climático (Climate Change Initiative) [13].
6. Agenda de Sustentabilidad Ambiental para la ZMVM (Environmental Sustainability Agenda for MCMA) [14].

First three belong to Federal administration, fourth to FD government, fifth to SM government and sixth altogether between FD and SM governments. Also, seventeen State instruments were identified, as shown in table 1.

Table 1. Typological table of public policies in energy-environmental sector

POLICY	CLASS	MAIN INSTRUMENTS	MAIN AGENCY
National Development Plan	Distributive Regulatory Constitutive Redistributive	FIRCO (Shared Risk Trust) [15]	SAGARPA (Agriculture, Cattle, Rural Development, Fishing and Nutrition Ministry)
		PROSOLAR [16]	SENER (Energy Ministry)
		Programa Especial de Cambio Climático (Special Climate Change Program) [17]	Federal Government / SENER / SEMARNAT (Environment and Natural Resources Ministry)
		Programa Nacional de Infraestructura (National Infrastructure Program) [18]	Federal Government / SENER / SCT (Communications and Transport Ministry)
		Programa Especial Concurrente para el Desarrollo Rural Sustentable (Sustainable Rural Development Special Concurrent Program) [19]	Federal Government / SAGARPA
		Programa Nacional de Vivienda (National Housing Program) [20]	Federal Government / SEDATU (Agrarian, Land and Urban Development Ministry)
		Programa Especial de Producción y Consumo Sustentable (Sustainable Production and Consumption Special Program) [21]	Federal Government / SENER / SEMARNAT
		Programa Especial para el Aprovechamiento de Energías Renovables (Development of Renewable Energy Special Program) [22]	Federal Government / SENER
		Programa Sectorial de Energía (Energy Sector Program) [23]	Federal Government / SENER / CONUEE (National Commission for Efficient Use of Energy)
		Programa Nacional para el Aprovechamiento Sustentable de la Energía (National Program for Sustainable Energy Development) [24]	Federal Government / SENER / CONUEE
Climate Change General Law	Distributive Regulatory Constitutive Redistributive	Estrategia Nacional de Cambio Climático (National Climate Change Strategy) [25]	Federal Government / SENER
		Programa Especial de Cambio Climático (Special Climate Change Program) [26]	Federal Government / SENER / SEMARNAT

National Energy Strategy	Distributive Regulatory Constitutive Redistributive	Crecimiento Económico (Economic Growth)	CONUEE / SENER / CFE (Federal Electricity Commission) / CRE (Energy Regulation Commission)
		Inclusión Social (Social Inclusion)	
		Programa Sectorial de Energía (Energy Sector Program)	
Mexico City Climate Action Program	Distributive Regulatory Constitutive Redistributive	Plan Verde de la Ciudad de México (Mexico City Green Plan) [27]	SEDEMA GDF (FD Environment Ministry)
		Programa General de Desarrollo (General Development Program) [28]	SEDEMA GDF / SEDUVI (FD Housing and Urban Development Ministry) / INVI (FD Housing Institute)
Climate Change Initiative	Regulatory	Ley de Cambio Climático (Climate Change Law) [29]	GEDOMEX (SM Government) / SMA EDOMEX (SM Environment Ministry)
Environmental Sustainability Agenda for MCMA	Distributive Regulatory Constitutive Redistributive	Comisión Ambiental Metropolitana (Metropolitan Environmental Commission) [30] [31]	SEDEMA GDF / SMA GEDOMEX

For social sector, three policies were identified:

1. Plan Nacional de Desarrollo (National Development Plan).
2. Programa General de Desarrollo del Distrito Federal (FD General Development Program).
3. Reducción de la pobreza, marginación y vulnerabilidad (Poverty, marginalization and vulnerability reduction). [32]

The first belongs to Federal administration, the second to FD government, and third to SM government. Ten State instruments were identified as shown in Table 2.

In December 2013, a Congress-approved constitutional reform on energy was enacted. According to this federal government reform, geothermal and nuclear resources were classified as clean energy sources; from this conclusion, federal government plans to boost public and private investment in both fields [34]. Between 2008 and 2012, FD raised 26 actions aimed at mitigating 12% of annual greenhouse gas emissions in Mexico City. To carry out the implementation of all these actions, a budget of 56,152 million pesos was required [35]. In May 2014, 113 social projects were approved in FD, with a budget of million pesos [36]. Water pumping for agriculture is the most important topic in policies regarding PV technology and water solar heating is the main use for solar technology; but direct investment in PV is still far behind expectations within MCMA. Until 2014, 4,615 house solar collectors have been installed against 285 PV modules settled for street lighting [37].

Table 2. Typological table of public policies in social sector

POLICY	CLASS	MAIN INSTRUMENTS	MAIN AGENCY
National Development Plan	Distributive Regulatory Constitutive Redistributive	Zonas Prioritarias (Priority Areas)	SEDESOL (Social Development Ministry)
		Opciones Productivas (Productive Options)	
		Coinversión Social (Social joint investment)	
		Programa Nacional de Desarrollo Social (National Social Development Program) [33]	SEDESOL / SAGARPA / SEDATU
FD General Development Program	Distributive Regulatory Constitutive Redistributive	Programa Coinversión (Joint Investment Program)	SDS DF (FD Social Development Ministry)
		Atención social a familias que habitan en vecindades y viviendas precarias en el DF (Social services for families living in substandard housing and neighborhoods in Mexico City)	
		Atención preventiva y emergente a personas afectadas por contingencia o en vulnerabilidad social (Preventive and emergent services for people affected by contingency or social vulnerability)	
		Tu ciudad te re-quiere (Your city needs you)	
		Programa comunitario de mejoramiento barrial (Neighborhood improvement community program)	
Poverty, marginalization and vulnerability reduction	Distributive Redistributive	Por mi comunidad (For my community)	SEDESEM (SM Development Ministry)

On the other hand, social programs concentrate to solve marginalized population problems through building missing infrastructure and making goods donations such as food, clothes and beds. But public agencies do not guide their budgets to solve MCMA's vulnerable population root issues by means of education, cultural understanding and socioeconomic opportunities. In addition, an assessment made by Social Studies and Public Information Centre yields different results regarding housing building services; according to Consejo Nacional de Evaluación de la Política de Desarrollo Social (CONEVAL), Priority Areas Development Program benefited 29,710 households with electric service, but SEDESOL claims there were 30,268 households [38] [39]. Such discrepancies are repeated throughout all three government policies of both energy-environmental and social sectors. Despite some NGOs were consulted, the data source comes directly and exclusively from government measurements. Nevertheless, published results between different government's

agencies did not match despite they were supposed to use the same data. World Bank, German Society for International Cooperation (GIZ) and Global Environment Facility (GEF) are the most important NGOs funders for energy and social development.

According to overall results, energy policies focus on non-renewable energy subsidies and electric transmission infrastructure investment. On the other side, social equality is encouraged by means of forthright funding and in-kind support. However, typology points out a lack of vision for using both renewable and PV technology as guiding axis for MCMA's marginalized population development and energy transition. Besides, local and federal governments have drawn up plans for urban growth regardless the inhabitants' perspective. Moreover, no public policy addresses the energy transition problem and social exclusion from a transdisciplinary point of view. Finally, it should be noted that State of Mexico government has not published enough solid results of their programs and policies since 2010.

These results cast doubts on transparency and reliability of public information. Besides, government measurements, assessments and analysis of their own programs have political trend to enhance public opinion.

4. Conclusion

The solution to public information reliability problem should be discussed from the majority perspective, considering the vision of those who govern, too. It must be placed in non-government policies context, all kinds of environmental movements and social networking integration as key means to face urban environmental degradation and therefore to advance towards its reversal. Fighting against environmental degradation from eco-social perspective is a condition without which urban sustainability is not possible, this means energy revolution and to use new technologies.

Urban development and energy transition sustained by PV technology should emerge as alternative and solution to MCMA's social-environmental degradation. It is needed to maintain energy and materials continuity flow, contributing to renew natural cycles through urban and rural socioeconomic activities.

A forecast of social and environmental deterioration should not be given without indicating what would be an alternative model which environmental and economic policies could be articulated with. But economic and political rearrangement is most important; to level and structure environmental governance.

Urban approach is unable to modify design and implementation of public policies, since they come from power centers. Therefore, it should be considered a circumscribed way of social appropriation to MCMA's institutionally established geopolitical boundaries. Multi-sectorial approach brings the idea near to integrate existing economic activities inside and outside a specific territory.

Acknowledgements

The authors wish to thank CONACYT for a graduate scholarship #346887 to the first author. Work was done with support from Transdisciplinary PhD program in Scientific and

Technological Development for Society within "Centro de Investigación y de Estudios Avanzados" (CINVESTAV) facilities. Special thanks to SMH and XV International Congress of the Mexican Hydrogen Society for a student participant fellowship.

References

[1] Instituto Nacional de Estadística y Geografía. Delimitación de las Zonas Metropolitanas de México 2010. [Cited March 2014]. Available from URL: http://www3.inegi.org.mx/sistemas/productos/

[2] Secretaría de Medio Ambiente y de Recursos Naturales - Instituto Nacional de Ecología. Inventario Nacional de Emisiones de Gases de Efecto Invernadero 1990-2010. [Cited March 2014]. Available from URL: www2.inecc.gob.mx/publicaciones

[3] Secretaría del Medio Ambiente del Distrito Federal. Inventario de Emisiones de la Zona Metropolitana del Valle de México. [Cited February 2014]. Available from URL: www.sma.df.gob.mx/inventario_emisiones/

[4] Alemán-Nava G., Casiano-Flores V., Cárdenas-Chávez D., Díaz-Chávez R., Scarlat N., Mahlknecht J., Dallemand J.F., Parra R. Renewable energy research progress in Mexico: A review. Renewable and Sustainable Energy Reviews 2014; 32:140-153.

[5] Cassedy E.S. Prospects for Sustainable Energy: A Critical Assessment. UK: Cambridge University Press; 2000.

[6] Juárez Neri V.M. Condiciones de la vivienda en la zona metropolitana del Valle de México en el año 2000. Revista electrónica de geografía y ciencias sociales 2003; 146:40.

[7] Ezcurra E., Mazari M., Pisanty I., Aguilar A. La Cuenca de México: Aspectos ambientales críticos y sustentabilidad. Mexico: Fondo de Cultura Económica; 2006.

[8] Lowi T. American Business. Public Policy, Case-Studies, and Political Theory. World Politics 1964; 16:677-715.

[9] Gobierno de los Estados Unidos Mexicanos. Plan Nacional de Desarrollo 2013-2018. [Cited March 2014]. Available from URL: http://pnd.gob.mx

[10] Gobierno de los Estados Unidos Mexicanos. Ley General de Cambio Climático. [Cited February 2014]. Available from URL: www.diputados.gob.mx/LeyesBiblio

[11] Secretaría de Energía, Estrategia Nacional de Energía 2013-2027. [Cited March 2014]. Available from URL: www.sener.gob.mx/portal/Default.aspx?id=2613

[12] Secretaria del Medio Ambiente del Distrito Federal. Programa de Acción Climática de la Ciudad de México, Avances 2011. [Cited July 2014]. Available from URL: www.sma.df.gob.mx/sma/links/download

[13] Secretaria del Medio Ambiente del Estado de México. Iniciativa Ante el Cambio Climático 2009. [Cited July 2014]. Available from URL: http://portal2.edomex.gob.mx/sma/cuida_medioambiente/cambio_climatico/groups/public/documents/edomex_archivo

[14] Comisión Ambiental Metropolitana. Agenda de Sustentabilidad Ambiental para la Zona Metropolitana del Valle de México 2010. [Cited January 2014]. Available from URL: http://portal2.edomex.gob.mx/sma/cuida_medioambiente/publicaciones_sma

[15] Fideicomiso de Riesgo Compartido. Informe de rendición de cuentas 2006-2012. [Cited March 2014]. Available from URL: www.firco.gob.mx

[16] Secretaria de Energía - Deutsche Gesellschaft für Internationale Zusammenarbeit. Programa de Fomento de Sistemas Fotovoltaicos en México 2012. [Cited January 2014]. Available from URL: www.giz.de

[17] Secretaria de Medio Ambiente y de Recursos Naturales. Programa Especial de Cambio Climático 2014-2018. [Cited June 2014]. Available from URL: www.encc.gob.mx

[18] Secretaría de Hacienda y Crédito Público. Programa Nacional de Infraestructura. [Cited August 2014]. Available from URL: www.presidencia.gob.mx/pni

[19] Secretaría de Agricultura, Ganadería, Desarrollo Rural, Pesca y Alimentación. Programa Especial Concurrente para el Desarrollo Rural Sustentable 2014-2018. [Cited June 2014]. Available from URL: www.sagarpa.gob.mx/tramitesyServicios/Paginas/default.aspx

[20] Secretaría de Desarrollo Agrario, Territorial y Urbano. Programa Nacional de Vivienda 2014-2018. [Cited June 2014]. Available from URL: www.sedatu.gob.mx/sraweb/programas/
[21] Secretaria de Medio Ambiente y de Recursos Naturales. Programa Especial de Producción y Consumo Sustentable 2014-2018. [Cited June 2014]. Available from URL: www.semarnat.gob.mx
[22] Secretaria de Energía. Programa Especial para el Aprovechamiento de Energías Renovables 2014-2018. [Cited June 2014]. Available from URL: www.sener.gob.mx/portal/Default.aspx?id=2613
[23] Gobierno de los Estados Unidos Mexicanos. Programa Sectorial de Energía 2007-2012. [Cited July 2014]. Available from URL: www.sener.gob.mx/webSener/res/0/
[24] Secretaria de Energía. Programa Nacional para el Aprovechamiento Sustentable de la Energía 2014-2018. [Cited June 2014]. Available from URL: www.sener.gob.mx/portal/Default.aspx?id=2613
[25] Secretaria de Medio Ambiente y de Recursos Naturales. Estrategia Nacional de Cambio Climático 2013. [Cited January 2014]. Available from URL: www.encc.gob.mx
[26] Secretaria de Medio Ambiente y de Recursos Naturales. Programa Especial de Cambio Climático 2014-2018. [Cited June 2014]. Available from URL: www.encc.gob.mx
[27] Secretaria del Medio Ambiente del Distrito Federal. Plan Verde Ciudad de México 2010. [Cited February 2014]. Available from URL: www.planverde.df.gob.mx
[28] Sistema de Información del Desarrollo Social del Distrito Federal. Programa General de Desarrollo 2013-2018. [Cited June 2014]. Available from URL: www.sideso.df.gob.mx
[29] Gobierno del Estado de México. Ley de Cambio Climático del Estado de México 2013. [Cited March 2014]. Available from URL: www.edomex.gob.mx
[30] Roccatti M. La Comisión Ambiental Metropolitana: un nuevo esquema de coordinación. La Constitución y el Medio Ambiente. Mexico: Instituto de Investigaciones Jurídicas; 2007.
[31] Comisión Ambiental Metropolitana. Agenda de Sustentabilidad Ambiental para la Zona Metropolitana del Valle de México 2010. [Cited January 2014]. Available from URL: http://portal2.edomex.gob.mx/sma/cuida_medioambiente/publicaciones_sma
[32] Secretaria de Desarrollo Social del Estado de México. Programas Sociales 2014. [Cited July 2014]. Available from URL: http://portal2.edomex.gob.mx/sedesem/programas_sociales/index.htm
[33] Secretaría de Desarrollo Social. Programa Nacional de Desarrollo Social 2014-2018. [Cited July 2014]. Available from URL: www.sedesol.gob.mx/es/SEDESOL/Programas_Sociales
[34] Gobierno de los Estados Unidos Mexicanos. Plan Nacional de Desarrollo 2013-2018 Primer Informe. [Cited August 2014]. Available from URL: http://pnd.gob.mx
[35] Secretaria del Medio Ambiente del Distrito Federal. Programa de Acción Climática de la Ciudad de México 2008-2012. [Cited March 2014]. Available from URL: www.sedema.df.gob.mx/sedema/index.php/temas-ambientales/cambio-climatico
[36] Secretaría Particular del Jefe de Gobierno. Segundo Informe de Gobierno del Distrito Federal 2014. [Cited September 2014]. Available from URL: www.informedegobiernocdmx.com
[37] Secretaria del Medio Ambiente del Distrito Federal. Programa de Acción Climática de la Ciudad de México, avances 2011. [Cited July 2014]. Available from URL: www.sma.df.gob.mx/sma/links/download
[38] Centro de Estudios Sociales y de Opinión Pública de la Cámara de Diputados LX Legislatura. El programa para el desarrollo de zonas prioritarias: evolución y evaluación. Work Document #117. Mexico; 2011.
[39] Consejo Nacional de Evaluación de la Política de Desarrollo Social. Informe de Evaluación de la Política de Desarrollo Social en México 2012. [Cited February 2014]. Available from URL: www.coneval.gob.mx

Chapter 7.3. Technical analysis and environmental gains of including biohydrogen in a conventional oil refinery

E. Mar-Juárez[a]; F. J. Ortega-García[b]

[a] Mexican Petroleum Institute, Dept. of Biomass Transformation, Dirección de Investigación en Transformación de Hidrocarburos. Av. Eje Central Lázaro Cárdenas Norte 152, Col. San Bartolo Atepehuacan, Delegación Gustavo A. Madero, México D.F., C. P. 07730 México, D.F.
[b]Dept. of Chemical Services, *ibídem.* Av. Eje Central Lázaro Cárdenas Norte 152, Col. San Bartolo Atepehuacan, Delegación Gustavo A. Madero, México D.F., C. P. 07730 México, D.F

ABSTRACT

Hydrogen is fundamental for the modern oil refining industry, as it is vastly used in hydrogenation processes like hydrodesulfurization or catalytic hydrocracking. The goal is to remove sulfur and nitrogen from the feedstocks by forming hydrogen sulfide and ammonia, thus making “cleaner” fuels.
Hydrogen is mainly produced in oil refineries via the catalytic reforming of light hydrocarbons with steam, typically using natural gas as a feedstock. Other technological to produce Hydrogen are variations of the technology mentioned like partial oxidation of hydrocarbons and autothermal reforming.
In this paper, an alternative feedstock like biomass is technologically studied to produce part of the hydrogen needs of an oil refinery via its gasification and consequent reformation of this syngas. The biomass studied is wheat and sorghum husk which is cheaper than natural gas and has the clear advantage that its greenhouse gas emissions are practically zero. A life cycle evaluation is also carried out that clearly establishes that using biohydrogen in an oil refinery is feasible and very beneficial, because it reduces the huge ecological footprint, and is a concrete alternative in the short term because it uses infrastructure that is already there.

Keywords: Hydrogen production, Hydrogen economy, Biohydrogen, Biomass, Oil refining

1. Introduction

Fossil fuels (coal, oil and natural gas) have been instrumental to achieve an industrialized civilization since they are the energy source that has allowed the spectacular growth society has experienced over the last 3 centuries. The situation could be continued for at least another 300 years but the inter-related problems between the use of these energy sources and our environment have become among the biggest challenges world faces today; in particular, the balance between the energy sustainability needed to grow and the carbon

---

*Author for correspondence: Elizabeth Mar-Juárez, (5255) 9175 8377, emar@imp.mx

emissions from the fossil fuels. In this vision two main factors exist that promote the use of hydrogen, one economic and the other environmental. The economic factor has progressively gained importance and has led mankind to seek new sources to meet the ever increasing demand for energy as the known world petroleum reserves are limited and are to be depleted in the next 100 years at the present rate of consumption [1, 2]. Additional aspects of the economic factor are the raise in the extraction, production and processing costs of the available petroleum and alternate hydrocarbon reserves. The environmental factor focuses in the fact that the use of fossil fuels has contributed significantly to pollution and ecological deterioration. We need to think that in regards to our health and energy safety the world is forced to search for new energy sources and alternatives that are attractive in a closer future [2-4].

In recent years, biomass has attracted considerable attention as a renewable energy source because it is the only renewable source of fixed carbon. So, biomass has positioned itself in the energy sources spectrum for three reasons: first, it is a renewable resource that could be sustainable, if it is developed adequately and well planned for the future; second, it has a positive balance, closer to zero in emissions harmful to the environment [5-7]; third, it has a significant economic potential to be a future commodity because of its low market value. The energy potential of biomass can be easily used either by direct combustion or by systems that generate an energy vector such as hydrogen that in itself has a high commercial value in an oil refinery or in different industries.

Thus, the economic value of biomass may increase significantly if used as feedstock for pyrolysis, liquefaction or gasification. The pyrolysis of biomass is a known process that has been done for centuries, primarily for the production of charcoal. Still, only in the last century research has been done to determine and control the physical and chemical processes that occur [8].

The conversion of biomass into fuels that can be easily used with existing infrastructure is a major challenge nowadays. There are two basic approaches for the conversion of biomass: thermochemical and biochemical. The biochemical pathway is extremely selective with respect to the final product, for example for the production of ethanol it is a relatively slow process. In contrast, the thermochemical via has higher reaction rates but tend to be less selective, so a range of products are obtained that need to be purified.

Among the alternatives for thermochemical processes is gasification. This process consists of a partial combustion of the biomass which is mainly composed of carbon, hydrogen and oxygen so synthesis gas, CO and H2 are obtained. These products can be transformed into liquid fuels by Fischer-Tropsch synthesis. This work describes a process scheme to convert biomass (lignocellulose) into hydrogen and also some liquid fuels that can be integrated for consumption in the refinery or used to produce gasoline and diesel.

2. Process description

For converting lignocellulose (biomass) into liquid fuels, the scheme illustrated in FIG 1 is proposed. This process includes: a dryer and a crusher for biomass preparation, a gasification reactor, a permutable reactor, a Fischer-Tropsch reactor and a separator unit.

The system would operate as follows: the lignocellulose is fed to a dryer to remove moisture, the dryer is heated using the carbon dioxide (CO2) hot stream from the permutable reactor. The biomass is crushed and fed to the gasification reactor where the synthetic gas is produced (carbon monoxide (CO) and hydrogen (H2)). Part of the CO produced is fed to the permutable reactor where in the presence of steam, is converted into carbon dioxide and hydrogen. This stream is mixed with the stream from the gasification reactor and fed into the Fischer-Tropsch reactor, where they are transformed into gasoline and diesel. These products are separated from the gas and sent to storage.

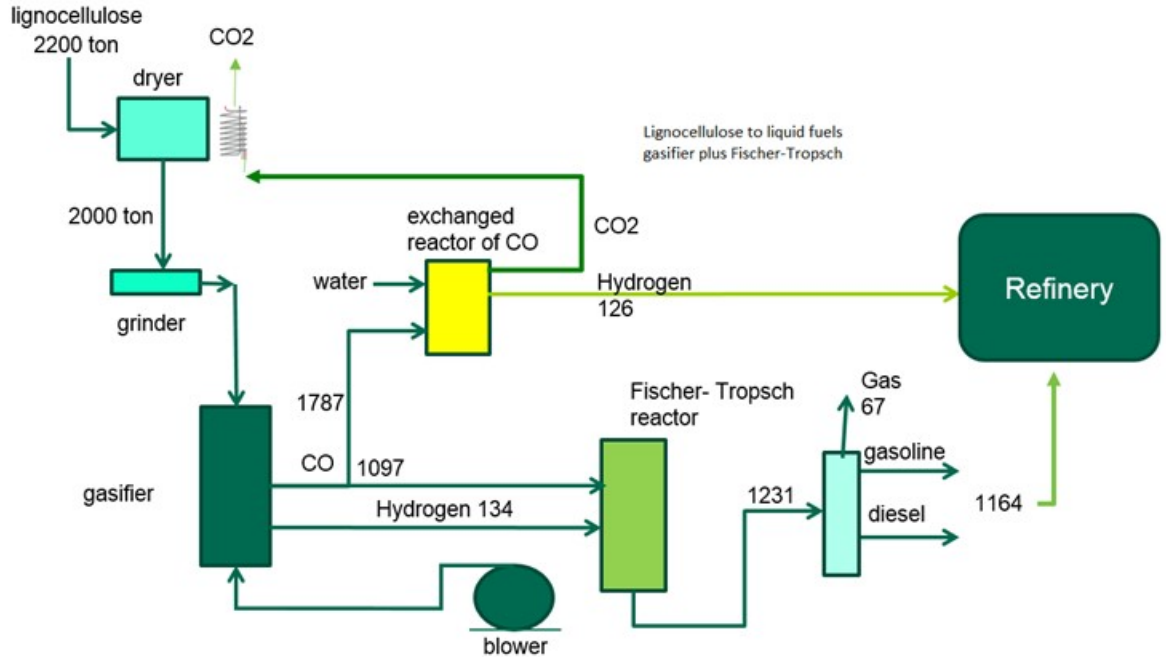

Fig. 1. Process flow chart for production of hydrogen, and liquid fuels.

3. Results and Discussion

Considering only the gasification and permutable reactors, the first business case studied was with a feed of 2200 metric tons of lignocellulose about 230 metric tons of hydrogen could be obtained which could replace 126 tons of the hydrogen produced by natural gas reforming. The idea was to produce hydrogen and high quality fuels that can be mixed with the process streams of the refinery so commercial gasoline and diesel are obtained, 1164 liters of fuels feedstock are produced.The net economic balance is very attractive considering a cost for the metric ton of biomass of 80 USD, where the profit is of 630 USD/ton. The hydrogen produced avoids the use of 252 metric tons of natural gas that costed at 2011 prices the equivalent of $17,156 USD.

Biomass is much cheaper than natural gas, and although it also produces large amounts of CO2, it is carbon fixed as a natural source and part of the carbon cycle, so environmentally neutral. This does not happen with natural gas where the carbon source is

fossil based and not part of the natural cycle. The processing scheme proposed in this work may be independent or integrated into a conventional oil refinery in which case it can leverage and use existing infrastructure.

The environmental impact of producing hydrogen with the process scheme proposed in this work would reduce emissions of greenhouse gases by 693 tons of fossil CO2 equivalent / day (CO2 eq), which is equal in value to stop emitting 2% of the total emissions of Pemex Refining [9]. Specifically if this scheme was operating in the Cadereyta Refinery, the emissions reduction would be around 15% of this facility. This could contribute to help meet the target set by the Mexican government to reduce emissions according to the National Emissions Inventory of Greenhouse Gases, presented in 2012 for the United Nations, which states that Mexico was responsible for 748.3 mega tonnes of CO2 eq, from which 16.6% originated in the oil and gas industry (Pemex) and that from the total of these emissions omitting the Cantarell facilities, 38% originate from the activities of Pemex Refining as shown in Figure 2. A reduction of 2% in the total system could be a very interesting option.

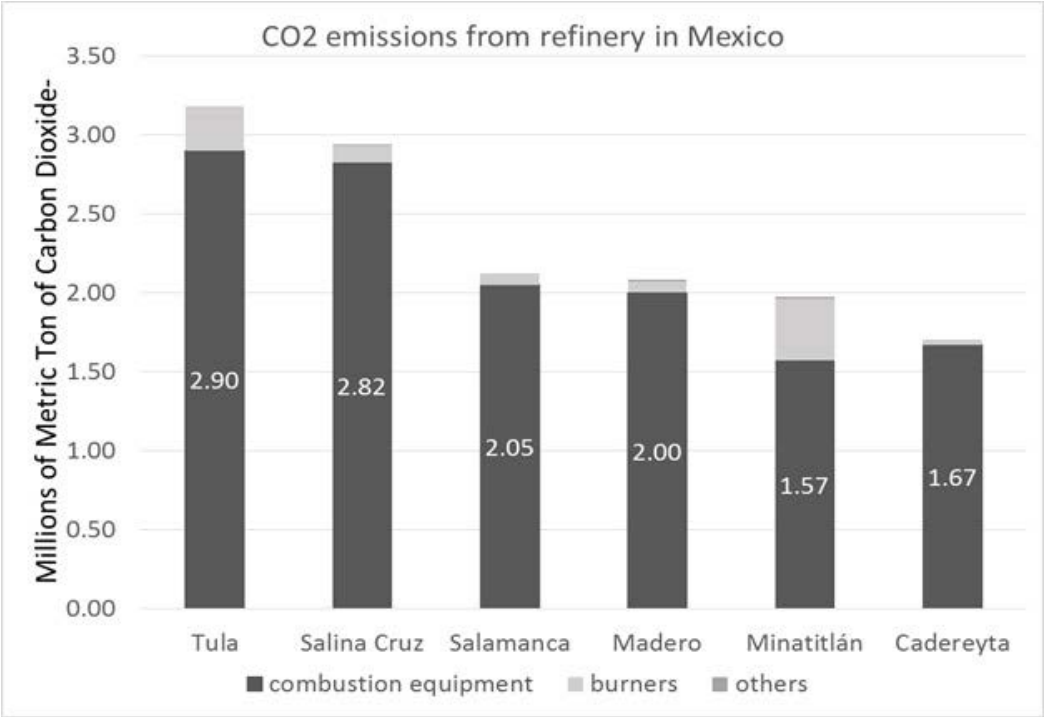

Fig. 2. Environmental impact of refining processes in Mexico

A second process scheme was considered as a business alternative. The aim was to use all the hydrogen produced (232 metric tons) in the Fischer-Tropsch reactor resulting in the production of 1630 liters of liquid fuel and 95 of gas as seen in Figure 3. This business model presents a profit of $ 580 USD/ton so it is more profitable to produce hydrogen to be used in the oil refinery processes.

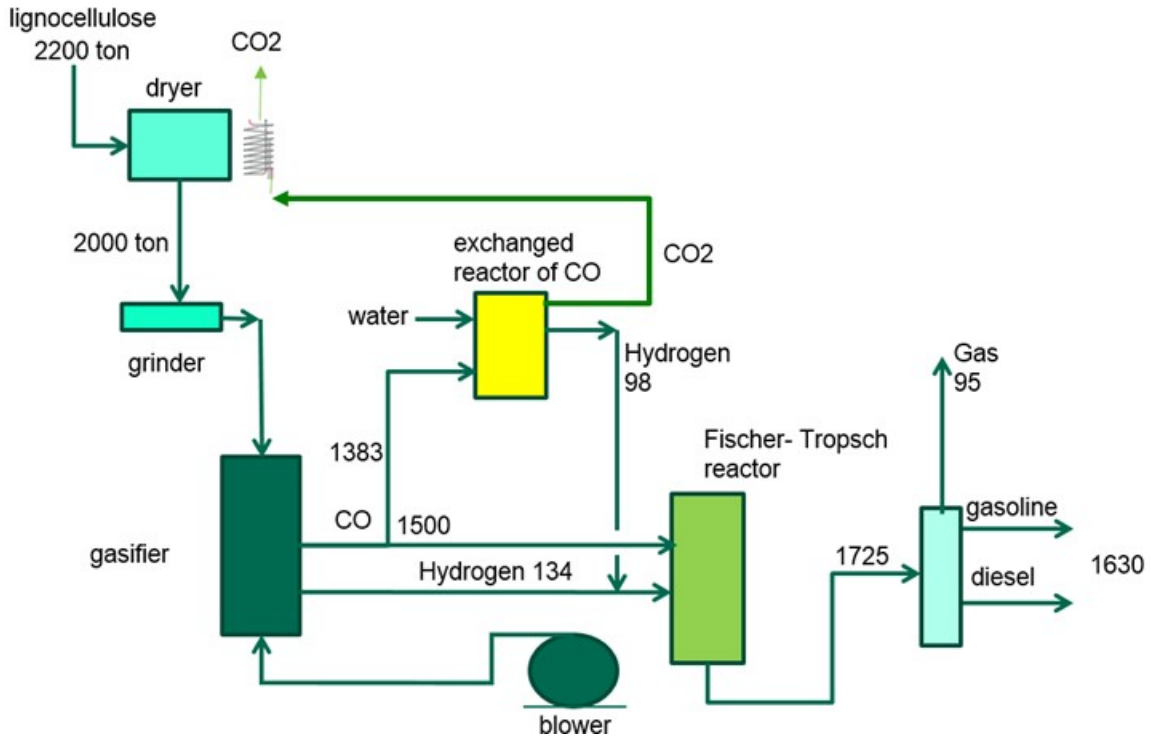

Fig. 3. Alternative process for the production of fuels "green"

4. Conclusion

Hydrogen is believed to be the fuel of the future, however as seen in the last 30 years, there are many challenges facing the transition from a hydrocarbon liquid fuels economy to a hydrogen one. The problem we see is that the first option mentioned always to produce hydrogen is always derived from a fossil fuel feedstock, thus it is always either carbon intensive or too expensive because of carbon sequestration costs.

Therefore, it would be a more viable alternative to produce hydrogen from resources which are carbon neutral and renewable for long term environmental sustainability. Biomass is one of the resources which can be readily used to produce hydrogen. Lignocellulosic based biomass is abundant and does not compete with the food resource availabilities; it is also considerably cheaper than crude oil on an energy basis.

In this work we show that it is possible to produce hydrogen and liquid fuels from biomass using mature technologies like biomass gasification, also that the process is economically viable and that the integration into a conventional oil refining system helps reduce emissions of fossil carbon dioxide.

Nonetheless, further research is needed to develop new technologies to convert lignocellulose into hydrogen since the ones available are still in the nascent stages and require further development to improve the efficiency and reduce the costs of production.

References

[1] Li Y., Xue B, He X. Catalytic synthesis of ethylbenzene by alkylation of benzene with diethyl carbonate over HZSM-5 Catalysis Commun, 10 (2009), p. 702.
[2] Sigar C.P., Soni S.L, Mathur J., Sharma D. Performance and emission characteristics of vegetable oil as diesel fuel extender. Energy Sources Part A, 31 (2009), p. 139.
[3] Dincer K. Lower emissions from biodiesel combustión. Energy Sources Part A, 30 (2008), p. 96.[4] Martínez J. Experimentos de gasificación con cascarilla de arroz colombiana en lecho fluidizado. Tesis de Ingeniería Mecánica, Universidad Pontificia Bolivariana, Medellín, Colombia, 2005.
[5] Encinar J.M., González J.F., González J. Steam gasification of Cynara cardunculus L.: influence of variables, Fuel Processing Technology, Vol. 75, 27-43, 2002.
[6] Gil J., Corella J., Aznar M., Caballero M. Biomass gasification in atmospheric and bubbling fluidized bed: effect of the type of gasifying agent on the product distribution, Biomass and Bioenergy, Vol. 17, 389-403, 1999.
[7] Werther J., Saenger M., Hartge E., Ogada T., Siagi Z., Combustion of agricultural residues. Progress in Energy and Combustion Science, Vol. 26, 1-27, 2000.
[8] Senneca O. Kinetics of pyrolysis, combustion and gasification of three biomass fuels, Fuel Processing Technology, Vol. 88, 87-97, 2007.
[9] Secretaria de Medio Ambiente y Recursos Naturales. Inventario Nacional de Emisiones de Gases de Efecto Invernadero 1990 – 2010. Consultado en línea noviembre del 2014. http://www.inecc.gob.mx/cpcc-lineas/597-cpcc-inventario.

Chapter 7.4. Market research in Mexico of Hydrogen technologies

A.A. Hernández Bautista[a,*], J.M. Pineda Sandoval[a], R. de G. González Huerta[b]

[a]IPN-ESIME-Azc, SEPI, Av. De las Granjas, N°.682, Azcapotzalco. CP. 02250. México DF.
[b]ESIQIE-IPN, Laboratorio de Electroquímica y Corrosión, UPLAM, CP 07738, México, D.F

ABSTRACT

Research into the use of hydrogen energy is extensive; however, your participation in the current energy system is still small compared to other similar sources of renewable energy. According to the information obtained about the hydrogen supply and demand, the significant presence of hydrogen is found in some countries of the European Union, USA and Japan. In addition, some consume projections in countries like Brazil, Argentina, Australia, and wide world were reviewed. Nevertheless, this information is insufficient to make a projection of the supply and demand of using hydrogen in our country. For this, the article highlights the importance of spreading the use of hydrogen in our society, and also the result of a market research developed to know the feasibility of commercialization of oxyhydrogen reactors.

Keywords: Market research, Supply and demand, Hydrogen Technologies

1. Introduction

The demand about fossil fuels every day increases around the world, and with this the depletion of these resources. For this reason, it is important the research and development of alternative energies which could act as a complement in the current energy system. Among a variety of sources, hydrogen had shown being one of the most promising options because of its physical and chemical properties [1].

Despite of its unique characteristics, hydrogen used as fuel had not been extensive promoted, especially in developing countries. In contrast, some European countries and United States have already developed a hydrogen infrastructure and projects about this technology [2]. In other countries like Brazil, Argentina and Australia [3], [4] simulation and projections about the economic benefits in a long term throughout the use of hydrogen as fuel had been published. According these projections, a fast introduction of hydrogen economy would be accelerated the creation of a strong hydrogen economy. For this reason, this paper has to highlight the strong necessity to implement and extend the use of H_2 in Mexico, in order to create economic progress from both, society and scientific community [5].

---

*Author for correspondence: Areli Anai Hernández Bautista; (55)49522435; E-mail: anaihb@hotmail.com

Exist different ways to promote the use of hydrogen, particularly through the mass media and the internet. First it is development functional prototypes necessaries, after it could be turned into functional products for the generation and use of H_2. These products must have an affordable price and long duration. Additionally, they have to be carefully tested to ensure that can work under safe conditions to be competitive and represent an actual alternative to reduce the use of gasoline and the CO_2 emissions [6]. The introduction of a quality product could be the key to open a new and unexplored market that would generate substantial profits.

For these reason, a multidisciplinary group conformed by students from manufacturing and automotive engineering of the IPN, with the collaboration of ESIQIE and ESIME are developing a system which through electrolysis generates a mixture of hydrogen and oxygen (named oxy-hydrogen gas) that is added in the air intake of internal combustion engine, with the intention of enrich the air-gasoline mixture until 10%. It's not the first attempt to achieve this goal [6], [7], [8]. However, we are trying to introduce in the market the product to analyze public acceptance.

The group collaborates to transfer this technology and develop a technological enterprise. The first step to create any business is the market research; for quantify the supply and demand of product that it want to be offered [9].

A preliminary research performed about the supply and demand of hydrogen and electrolyzer in Mexico, indicates that in this country exist a great opportunity to commercialize hydrogen energy because these devices have a low cost. Even is necessary the promotion of hydrogen energy as fuel, this work must be pushed by the scientific community involved on this topic.

The aim of this paper is show a general view of the participation of hydrogen in the current energy system, principally on the countries where their participation is significant and, otherwise, the preliminary result of the market research show us that is necessary analyze the level of acceptance of the oxyhydrogen reactor developed by the group.

2. Materials and Methods

According to Echarri [10] to achieve technology transfer is necessary to follow the next methodology

1. Identify the necessities of the potential costumers
2. Research your competition
3. Broadcast the innovation over diverse communication media
4. Evaluation and selection by costumer
5. The correct negotiation of technology
6. Exploitation of the technology by the finally user.

Figure 1 show the steps in the methodology suggested by Baca [9], which was followed, to elaborate a market research.

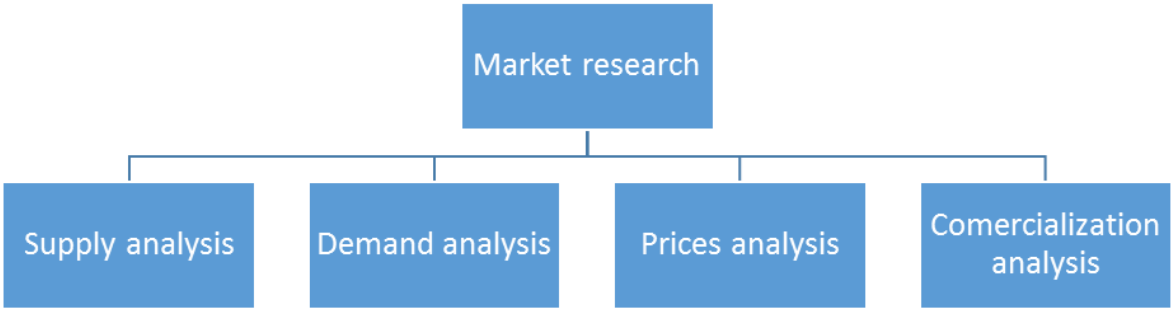

Fig. 1. Methodology for market research [9]

The present investigation began by looking for all the information available in secondary sources related to the historical data of hydrogen supply and demand in Mexico. Nevertheless there is no significant information about the topic in this country. As a consequence was necessary to design an inquiry to know the opinion of potential customers.

The non-probability sampling was used due to the nature of the product. The survey was applied to all that people who possess a car, and the economic possibility to acquire the product, it means, those who belongs, at least to the middle class.

The designed inquiry consists of nine questions that tried to give a general perspective of the level of acceptance from people with this uncommon product. Inquiries were applied through social networks and personally.

3. Results and Discussion

Until now, 95 people had been respondents. Of the total sample, 59% were men and 41% were women. The following question was asked about the gasoline spending that the potential costumer makes weekly. The intention of this question is to show the saving money if they use a hydrogen reactor. The amount of money that 64% respondents pay weekly for fuel is between $300 and $500. User can effortlessly deduce that an electrolysis system that generates more hydrogen is necessary to save more fuel and the return of investment occurs faster.

Third question was about the number of cylinders in the automobile engine to calculate the possible average size of the electrolysis system and also the average cost. The majority of respondents own a four-cylinder automobile.

The fourth question is from perception about hydrogen as fuel and it try to collect the impression of people by using hydrogen to save gasoline under safe and environmentally friendly conditions. Figure 2 shows that much people found the idea very interesting.

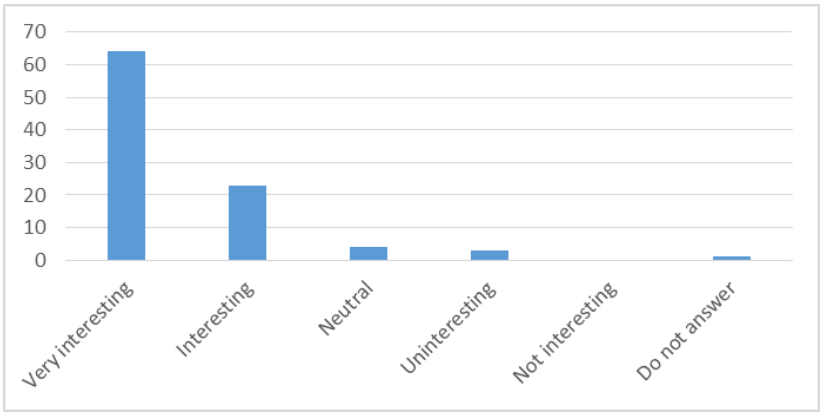

Fig. 2. Perception of using hydrogen mixed with fuel under safe and environmentally friendly conditions

The fifth yes-no question is one of the most important because allows to know whether people would invest on an electrolysis system. The answer to this question was very satisfactory founding that 85% of the people respondent would probably buy an electrolysis system if this would save at least a 15% of gasoline, (Figure 3).

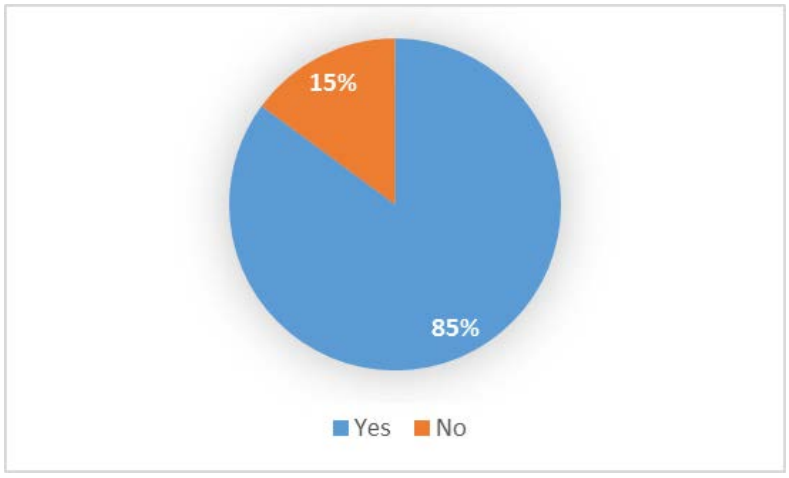

Fig. 3. Probability of investment in an electrolysis system

Question number six was designed to found out which aspects are the most important at the moment to acquire this kind of product, as is represented in Figure 4. Although most of one answer could have been chosen, the principal factor to buy an electrolysis system is the price and percentage of gasoline saved. Others factors that people consider important to acquire this devise is cost-benefit ratio.

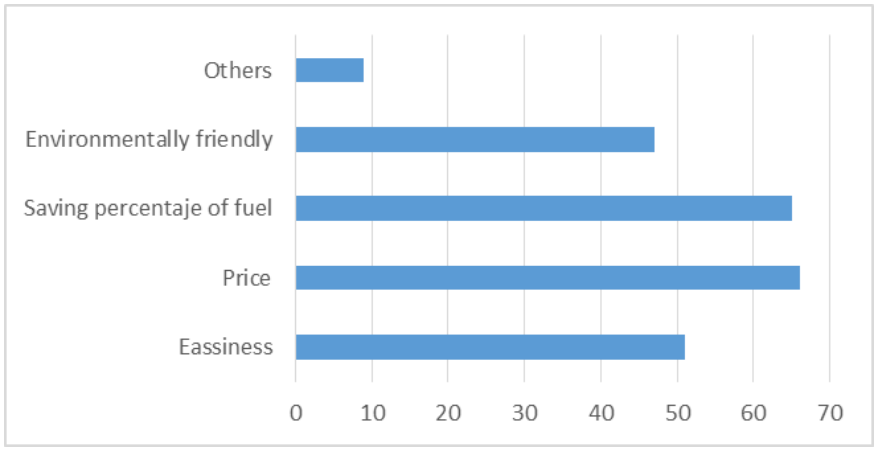

Fig. 4. Determinant factors in the acquisition of an electrolysis system.

The possibility of use hydrogen energy for economic and environmental benefits from the society must be widespread. In the seventh question of the quiz, people were asked to choose the way they would prefer to receive information about hydrogen and oxyhydrogen reactor. Answers are clearly represented in Figure 5, where is easy to appreciate that Internet is the preferred way to receive this kind of information. In this question the respondents also could chose more than one reference with the intention of know the best way of advertise the oxyhydrogen reactors.

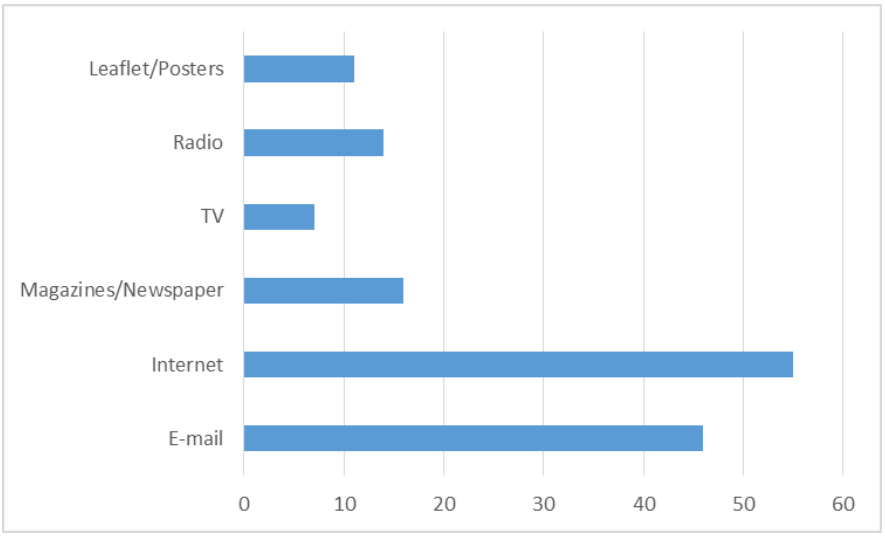

Fig. 5. Preferred media to receive information about hydrogen and electrolysis systems

The eighth question shown, as is possible to appreciate in Figure 6, the price people are willing to pay the product mentioned above. Most of them would pay in average $8,000 pesos for it, which exhibit the importance of optimize the model to low the price of the

electrolysis system without sacrifice the quality and the profits for the developers. The price ranges were calculated based on the functional prototype developed.

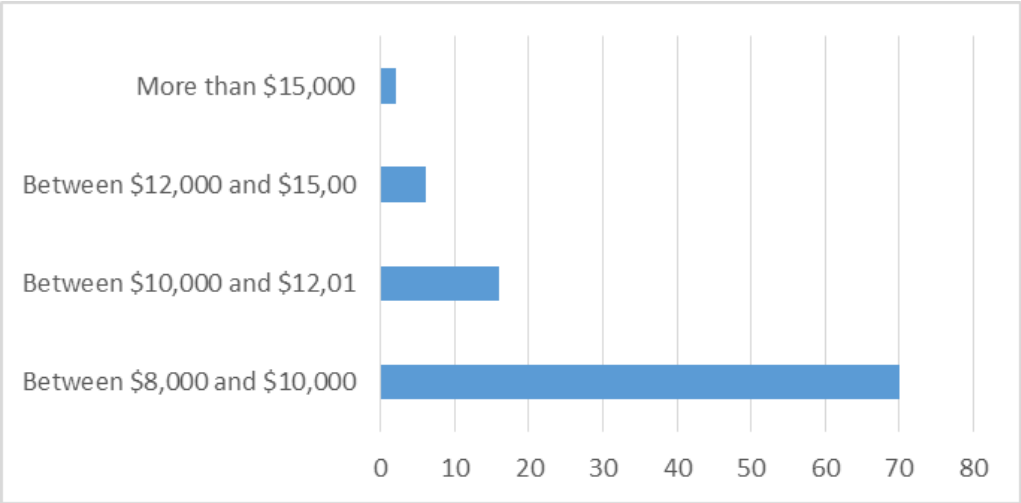

Fig. 6. Price people could afford for an oxyhydrogen reactor

Finally, question 9 was made so as to know directly if people would or would not buy the product. These questions have only 3 options: yes, immediately; yes after a while; and no, they would not buy it. Fortunately 93% of people answer that they would buy the product, but 73% would wait a while of after introduction in the market. As consequence, is essential to ensure the reliability of a product like this and, as was told, spread actively the large advantage of the use of hydrogen to provoke a faster introduction in the market.

4. Conclusion

The introduction of an electrolysis system in market would be well accepted by society. This is the reason for the strong necessity to extend the knowledge not only of hydrogen but also all technologies and projects that are being cultivating in national universities

This first approach to the preference of people allows to know the principal characteristics, that a product like this, have to possess in order to be successful in market; price and percentage of gasoline saved, but also that product would be environmentally friendly and easy to use.

This study also exhibit that the best current way of making publicity is by internet, in contrast with the preconceived idea that massive media, like TV. As is well-known, is much cheaper to start an advertising campaign by internet rather than on radio and television.

As inquiries show, the optimization of the oxyhydrogen system is crucial to lowering the sale price owing to the involved in the innovation process (researchers, state and society [5]) could obtain profits of hydrogen energy.

In summary, it exist a considerable potential market for an electrolysis system in Mexico, since the scientific community has to develop a product that have competitive price and works under high quality standards.

Acknowledgements

This work has been supported by multidisciplinary project IPN-SIP 1683 and Programa Redes Temáticas CONACYT/RTH2. The insightful comments from reviewers are gratefully acknowledged.

References

[1] Gutiérrez Jodra, L. El hidrógeno, combustible del futuro. Rev. R. Academia de Ciencias Exactas, Físicas y Naturales 2005; 99: 49-67.
[2] Bennaceur K., Clark B., M. Orr F., Ramakrishnan T.S.,.Roulet C., Stout E. El hidrógeno:¿Un futuro portador energético? Oilfield Review. Schlumberger 2005; 34-47.
[3] Do Sacramento, E.M., Carvalho, P. C. M., De Lima, L. C. & Veziroglu, T.N. Feasibility study for the transition towards a hydrogen economy: A case study in Brazil. Energy Policy 2013; 62: 3-9.
[4] K. biswas W., Thompson C. B., Islam N. M. enironmental life cycle feasibility assesment of hydrogen as an automotive fuel in Wenstern Australia. 2013; 38: 246-254.
[5] Bozeman B., Rimes H., Youtie J. The evolving state-of-the-art in technology transfer research: Revisting the contingent effectiveness model. Research Policy 2015; 44: 34-49.
[6] Ciniviz M., Köse H. Hydrogen use in internal combustion engine: a review. Academic Paper 2012; 1: 1-15.
[7] White C.M., Steeper R.R., Lutz A.E. The hydrogen- fueled internal combustion engine: a technical review. International Journal of Hydrogen Energy 2006; 31: 1292-1305.
[8] Das L.M. Near-term introduction of hydrogen engines for automotive and agricultural application. International Journal of Hydrogen Energy 2002; 27: 479-487.
[9] Baca U. G. Evaluación de Proyectos. Mexico City: Mc Graw Hill; 2009.
[10] Echarri, A., Pendás A. La transferencia de tecnología. Aplicación práctica y jurídica. Madrid: Fundación CONFEMETAL 1999.

8
Nanostructured materials

Chapter 8.1. Ionic and thermal conductivity of $Ln_2Hf_2O_7$ hafnates (Ln=lanthanides) prepared by mechanical milling

F. A. López-Cota[a]; J. A.Díaz-Guillén[b]; O. J. Durá[c]; M. A. López de la Torre[c]; A. F. Fuentes[a*]

[a]Cinvestav Unidad Saltillo, Apartado Postal 663, 25000-Saltillo, Coahuila, Mexico.
[b]División de Estudios de Posgrado e Investigación, Instituto Tecnológico de Saltillo, 25280-Saltillo, Coahuila Mexico.
[c]GFMA, Departamento de Física Aplicada, Escuela Técnica Superior de Ingenieros Industriales, Universidad de Castilla-La Mancha, 13071-Ciudad Real, Spain.

ABSTRACT

Lanthanide hafnates with the general formula $Ln_2Hf_2O_7$ (Ln = Sm^{3+}, Eu^{3+}, Gd^{3+}, Dy^{3+}, Y^{3+}, Ho^{3+}, Yb^{3+}), were prepared at room-temperature, via a mechanochemical reaction between the corresponding elemental oxides. Irrespective of the lanthanide ion involved, milling promotes the formation of highly disordered and *fluoritelike* materials. Post-milling thermal treatments decrease the stability of the fluorite phase, and facilitate the formation of its ordered derivative, the pyrochlore structure but only for Ln = Sm^{3+}, Eu^{3+}, Gd^{3+}. The electrical, and thermophysical characterization of the as-prepared powders, showed clear differences between phases adopting the pyrochlore or fluorite structures. Impedance spectroscopy measurements revealed that in general, these hafnates are good ionic conductors at high temperatures; however, those adopting the pyrochlore structure gave higher conductivity values (σ_{dc} at 750°C > 10^{-3} $S \cdot cm^{-1}$) than those crystallizing as fluorites (σ_{dc} at 750°C < $5 \cdot 10^{-4}$ $S \cdot cm^{-1}$). Lower thermal conductivities were found also for pyrochlore-type hafnates (e.g., $Eu_2Hf_2O_7$ κ ~1.3 $W \cdot m^{-1} \cdot K^{-1}$ at 800°C) than for fluorites.

Keywords: Mechanical milling, Pyrochlore, Conductivity, Fluorite

1. Introduction

Lanthanide oxides with the $Ln_2B_2O_7$ general stoichiometry (B^{4+} = Ti^{4+}, Zr^{4+}), have gained considerable attention in recent years because of their high thermochemical stability, and structural flexibility, susceptible to alteration via processing and/or doping. The series exhibit many chemical and physical properties of scientific, and technological interest such as high oxygen ion mobility at high temperatures or very low thermal conductivity, to mention some [1-5]. Moreover, they are attractive component materials for electrochemical

---

*Author for correspondence: A. F. Fuentes**;** +52 844 4389617; email: fuentesaf@live.com**;** Tel.: +52 844 4389617; email: fuentesaf@live.com

devices (e.g., solid oxide fuel cells), and thermal barrier coatings (TBCs). Some members of the series show also great potential to incorporate actinides in solid solution, and are under consideration as host phases for the immobilization of high level radioactive waste [6,7]. By contrast, little has been published about the physical, and chemical properties of lanthanide hafnates $Ln_2Hf_2O_7$. The present contribution analyzes the electrical, and thermal properties of mechanochemically prepared $Ln_2Hf_2O_7$ powders [8-10].

Depending on the Ln^{3+} to Hf^{4+} size ratio (r_{Ln}/r_{Hf}), $Ln_2Hf_2O_7$ oxides will adopt [11] either, the anion deficient fluorite structure ($r_{Ln}/r_{Hf} < 1.46$) or its ordered derivative, the pyrochlore structure ($r_{Ln}/r_{Hf} \geq 1.46$). Accordingly, $Ln_2Hf_2O_7$ are anion deficient fluorites when Ln = Dy^{3+}-Lu^{3+} and Y^{3+}, and pyrochlore-type oxides when Ln = La^{3+}-Tb^{3+}. Both structures are depicted in figure 1. The ideal fluorite structure can be described as a face-centered cubic array of cations (S.G. = Fm3m (225); Z = 4), with anions placed at all the available tetrahedral interstices; cations, and anions fully occupy the 4*a* (0,0,0), and 8*c* (¼,¼,¼) Wyckoff sites. The ideal pyrochlore structure is also isometric (S.G. = Fd3m (227); Z = 8), although cations are ordered on two nonequivalent sites. Selecting the origin choice 2 of the space group, the larger cation (*i.e.*, Ln^{3+}) is located at the 16*d* position (½,½,½) surrounded by 8 oxygen ions forming an axially compressed scalenohedron. The smaller cation (Hf^{4+}) is placed at the 16*c* site (0,0,0), within a trigonal antiprism with all 6 oxygen ions at equal distances from the metal atom.

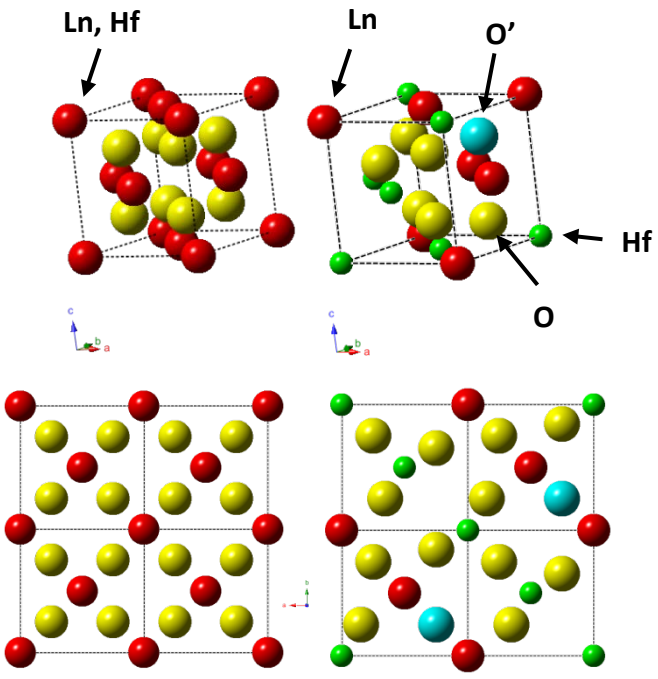

Fig. 1. Top: Idealized representations of a single fluorite type cell (right) and 1/8th of a $Ln_2Hf_2O_6O'$ pyrochlore unit cell (left). Bottom: plane projection of 8 fluorite type cells (right) and a single pyrochlore cell (left).

Furthermore, pyrochlore oxides contain two non-equivalent, and tetrahedrally coordinated oxygen ions. Therefore, they are better represented as $Ln_2B_2O_6O'$ with O located at the 48*f* (x,⅛,⅛) position, and O' at the 8*b* (⅜,⅜,⅜) site.

The 48*f*-site is surrounded by two Ln, and two Hf nearest neighbors; whereas, the 8*b*-site is coordinated by four Ln metal atoms. A distinctive peculiarity of the pyrochlore structure is the presence of an additional interstitial site in the unit cell, 8*a* (⅛,⅛,⅛), nominally empty in ideal (ordered) structures, but easily accessible for anions. Because of the refractory nature of both, HfO_2 and Ln_2O_3 oxides, preparing these materials by the traditional solid state reaction at high temperatures, requires long, and repeated firing cycles above 1500°C. All samples analyzed in this work were prepared at room-temperature by a mechanically induced chemical reaction.

Mechanical milling (MM) has recently become a very popular powder processing method because it is simple to implement, solvent-free, and capable of providing enough volume of the target material in an economically viable manner [12]. As a far-from-equilibrium method, MM frequently yields uncommon, and highly defective metastable phases. Moreover, conversion to the "true" equilibrium phases induced by additional processing (*e.g.*, post-milling annealing), offers the possibility of isolating fairly stable intermediate states, which are inaccessible for more conventional processing techniques [13]. The properties of many ceramics might be greatly affected by the presence of structural defects and disorder which occur easily in pyrochlore oxides; the density of defects in any particular sample is influenced by both, intrinsic (*e.g.*, chemical composition and cations size mismatch), and extrinsic factors (*e.g.*, thermal history and processing conditions). A high density of structural defects might have a beneficial effect on both, the ionic conductivity and the thermal resistivity of ceramic oxides.

2. Materials and Methods

Seven compositions of general formula $Ln_2Hf_2O_7$, were prepared by mechanically milling stoichiometric mixtures of the corresponding high purity elemental oxides, *i.e.*, Ln_2O_3 (Ln = Sm^{3+}, Eu^{3+}, Gd^{3+}, Dy^{3+}, Y^{3+}, Ho^{3+}, Yb^{3+}) and HfO_2. Milling was carried out in a Retsch PM400 planetary ball mill preparation procedure.

Figure 2a shows the evolution of the ($2HfO_2 + Sm_2O_3$) starting mixture selected as representative of the series, with milling time; as shown, milling even for a short time (1 h), produces considerable changes in the XRD pattern of the initial mixture: milling reduces the intensity, and increases the breadth of the characteristic reflections of both starting chemicals, monoclinic HfO_2 and B-Sm_2O_3. These changes which are easily observed by XRD at the initial stages of mechanochemical reactions, are basically due to: (i) a decreasing particle size, and (ii) the formation and accumulation of defects in the reactants crystal structure.

After milling for 6 hrs, a mechanically induced chemical reaction takes place, and new reflections emerge, the most evident between 29° and 30° (2 theta). The intensity of this new set reflections increases with increasing milling time, and they are the only ones present after processing the sample for 24 hrs; at this point, the XRD pattern obtained resembles that characteristic of a *fluoritelike* material. No evidence of the superlattice reflections characterizing the long-range ordering of cations, anions, and vacancies of the

ideal pyrochlore structure [14], is observed (*e.g.*, Miller indexes (111), (311) or (331) lines at ~15°, ~28° and ~38° (2 theta) respectively).

Irrespective of the lanthanide ion involved, similar XRD patterns were obtained for all the as-prepared samples (figure 2b). Therefore, milling promotes the formation of fully disordered and *fluoritelike* $Ln_2Hf_2O_7$ materials, instead of the ordered pyrochlore derivative predicted by the size mismatch criteria mentioned above. The small shift observed in the diffraction lines towards lower angles (2θ) with increasing Ln^{3+} size, proves the existence of a mechanically induced chemical reaction: $Ln_2Hf_2O_7$ lattice parameter increases from $Yb_2Hf_2O_7$ to $Sm_2Hf_2O_7$. Post-milling thermal treatments at high temperature, facilitate a phase transition to the pyrochlore structure when Ln = Sm^{3+}, Eu^{3+}, Gd^{3+}; as an example, figures 2c and 2d show the evolution of the $Sm_2Hf_2O_7$ phase with temperature. Some of the pyrochlore superstructure reflections emerge after firing at 1500°C (*e.g.*, Miller indexes (311) at ~28°, 2θ). Interestingly, *fluoritelike* $Sm_2Hf_2O_7$ powders are stable even after firing at 1200°C, underlying the possibilities of mechanical milling for generating metastable, but fairly stable phases. The remaining hafnates (Ln = Dy^{3+}, Y^{3+}, Ho^{3+}, Yb^{3+}) persist as fluorites even after firing at 1500°C. No additional reflections belonging to third phases or reactants are ever observed.

Fig. 3 shows some results of our samples electrical characterization. Figures 3a and 3b illustrate respectively, the frequency, and temperature dependence of the real parts of the *dc* conductivity, and permittivity (both as log-log representations) for the $Sm_2Hf_2O_7$ material, selected as representative of the series. Similar plots were obtained for the remaining samples analyzed in this work. The conductivity dependence with frequency observed at low temperatures in figure 3a, may be described by (i) a frequency-independent plateau at low frequencies associated to the *dc* conductivity regime, and (ii) a cross-over to a power-law type dependence at high frequencies. This behavior is the main signature of the so-called *"Universal Dielectric Response"* (UDR) proposed by A.K. Jonscher [15]; this response may be described by an empirical expression of the type, $\sigma'(\omega) \propto \omega^n$, and has been linked to the existence of cooperative effects in the dynamics of mobile ions.

The decrease in conductivity visible at low frequencies (*S*-shaped graphs), is caused by blocking effects at grain boundaries, which is a characteristic feature of materials where the conductivity is mostly ionic. Blocking effects are also evident in figure 3b, where the real part of this sample's permittivity, is plotted as a function of frequency, and temperature; blocking effects shift towards higher frequencies with increasing temperature.

The temperature dependence of each sample *dc* conductivity was analyzed by using an Arrhenius-type expression of the form $(\sigma_{dc}\cdot T) = \sigma_0 \cdot exp(-E_{dc}/k_B \cdot T)$, where σ_0 and E_{dc} are respectively, the pre-exponential factor (related to the effective number of mobile charge carriers), and the activation energy for long range ion migration. Figure 3c shows the plot of the product $(\sigma_{dc}\cdot T)$, against the reciprocal of T, for the $Sm_2Hf_2O_7$ sample; the solid line in the graph represents the least square best fit of the experimental data, to an Arrhenius law confirming that ionic diffusion in the sample is thermally activated.

Similar representations were obtained for all the samples analyzed in this work. E_{dc}, and σ_0 can be easily calculated from the slope, and intercept respectively, of such linear fits. Table 1 shows calculated activation energies for each sample, together with their σ_{dc} at 750°C; whereas, figure 3d represents the product $(\sigma_{dc}\cdot T)$ at the same temperature, *vs.* the size mismatch (r_{Ln}/r_{Hf}), for the series. Higher conductivity, and lower activation energies are obtained for pyrochlore-type $Ln_2Hf_2O_7$ than for their more disordered analogues

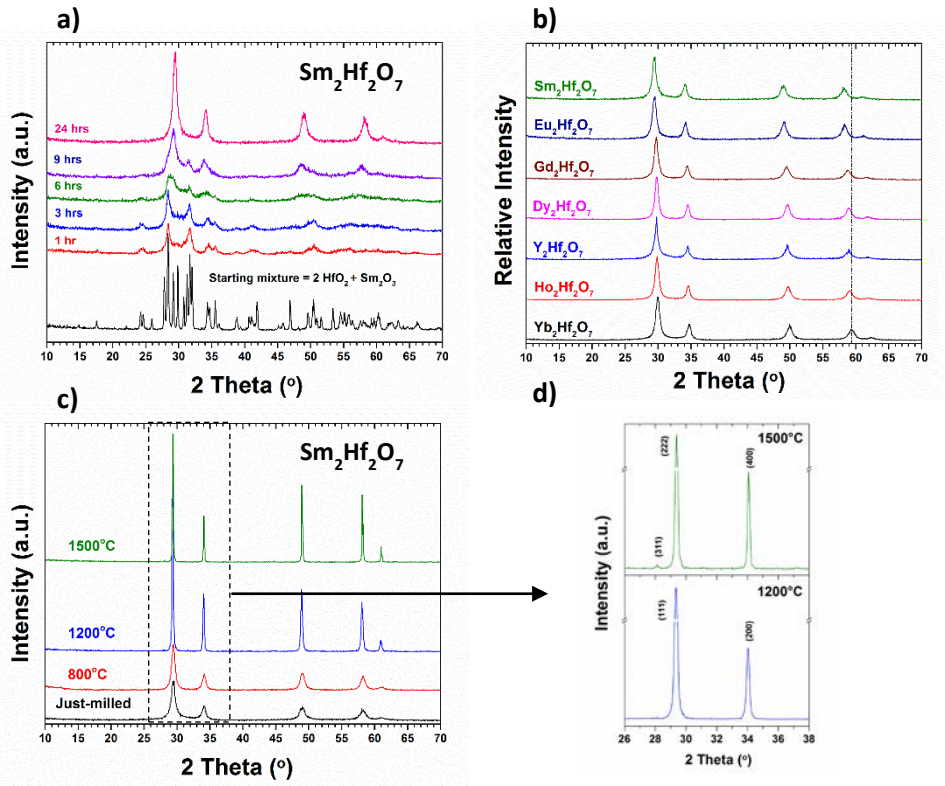

Fig. 2. (a) Evolution of the HfO_2:Sm_2O_3 reaction mixture (2:1 molar ratio) with milling time; (b) XRD patterns obtained for all the samples mechanochemically prepared in this work; (c) evolution of the $Sm_2Hf_2O_7$ sample, with post-milling thermal treatments; d) zoom of an area of the XRD pattern of the same compound, where the main reflections characterizing the pyrochlore superstructure can be found.

crystallizing with the fluorite structure: higher degree of structural disorder, leads to higher energy penalty for migration, and lower conductivity. These results are consistent with previous observations in similar lanthanide zirconate, and titanate systems [16,17]: more disorder does not necessarily imply higher ionic conductivity.

Although there are various thermal and mechanical requirements to be considered when evaluating a prospective material for thermally insulating coatings, the main metric would be probably, its thermal conductivity (κ) at operating temperatures. In this context, $Ln_2Zr_2O_7$ zirconates are receiving a great deal of attention because of their low κ, high melting points and rather sluggish sintering kinetics [4,5]. However, little information has been published about the thermal properties of $Ln_2Hf_2O_7$ hafnates. Figure 4 shows some representative data of our samples thermophysical characterization.

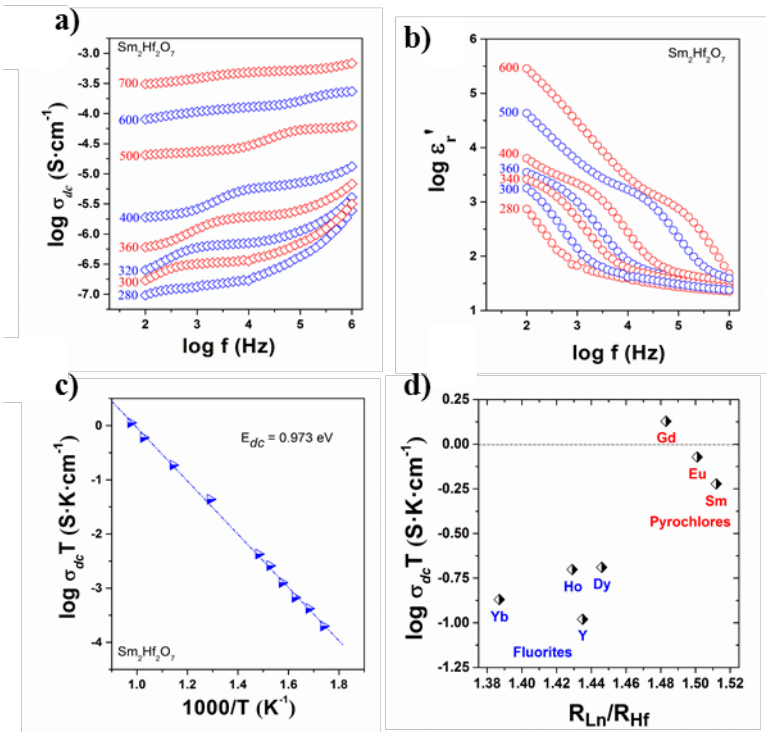

Fig. 3. Real parts of the *dc* conductivity, and permittivity of $Sm_2Hf_2O_7$, as a function of frequency, and temperature [(a) and (b)]; Arrhenius plot showing conductivity temperature dependence (c). (d) Conductivities obtained in this work at 700°C as a function of the R_{Ln}/R_{Hf} size ratio.

Bulk densities determined by the Archimedes' method proved that none of the pellets fabricated with the as-prepared hafnates, and sintered at 1500°C, were fully densified but showed considerable residual porosity. Experimental densities ranged from 75 to 90% of the theoretical density, as calculated from each sample's lattice parameter obtained from the XRD data. As shown in figure 4a, samples' thermal diffusivity (α) dependence with temperature, is similar to most polycrystalline materials: it decreases slightly with temperature to reach an almost temperature-independent value above 400°C; this behavior has been related with a dominant heat transfer mechanism via phonons. The range of values of thermal diffusivity obtained for these samples synthesized by mechanical milling, is between 0.6 and 0.36 mm^2/s Temperature dependence of the specific heat capacity (Cp) shown in figure 4b is consistent with the Dulong-Petit law which is an indicator that the measurements were made correctly, and that the theory and practice match. The thermal conductivity decreases initially between 100 to 400°C, and from this temperature a small increase can be related to the contribution of heat transfer by radiation is appreciated. The values of *k* for all samples tested at 800°C ranged from 1.3 to 2.5 W/mK; interestingly, all

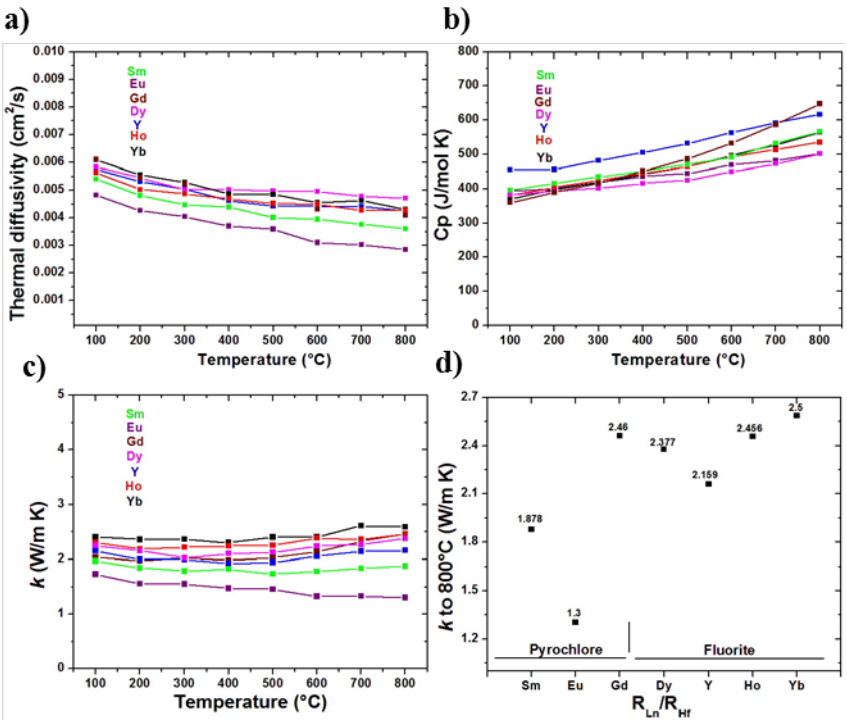

Fig. 4. Thermophysical properties of $Ln_2Hf_2O_7$ hafnates: thermal diffusivity (a), specific heat capacity (b), thermal conductivity (c), and thermal conductivity at 800°C plotted vs. the size mismatch

Table 1. σ_{dc} (750°C), and E_{dc} for pyrochlore- and fluorite-type $Ln_2Hf_2O_7$

Phase	σ_{dc} **(S·cm^{-1})**	E_{dc} **(eV)**
$Sm_2Hf_2O_7$	$1.09\cdot10^{-3}$	0.973
$Eu_2Hf_2O_7$	$1.32\cdot10^{-3}$	0.870
$Gd_2Hf_2O_7$	$1.90\cdot10^{-3}$	0.963
$Dy_2Hf_2O_7$	$4.00\cdot10^{-4}$	1.297
$Y_2Hf_2O_7$	$2.20\cdot10^{-4}$	1.326
$Ho_2Hf_2O_7$	$5.01\cdot10^{-4}$	1.395
$Yb_2Hf_2O_7$	$2.75\cdot10^{-4}$	1.124

the samples tested exhibit lower thermal conductivity values than YPSZ due to phonon dispersion by oxygen vacancies present in these materials and defects induced by mechanical grinding.

4. Conclusion

Mechanical milling is a suitable powder processing method to obtain $Ln_2Hf_2O_7$ powders at room temperature. As-prepared powders show XRD patterns similar to those characteristic of fluoritelike materials. Milling time needed to obtain single phase products increases with increasing lanthanide size. Post-milling thermal treatmetns at high temperature produce a phase transition to pyrochlore-type structures for Sm, Eu and Gd. The ionic conductivity showed better values on phases with pyrochlore structure than those with fluorite arrangement. Low thermal conductivity values are favored by structural defects in the crystal lattice introduced by mechanical grinding such as grain boundaries and high molecular weights. Lanthanide hafnates have better thermal properties than those currently used (YSZ) as thermal barrier coatings.

Acknowledgements

Authors would like to thank the financial support by CONACYT (Grants CB-2011-01-166995 and CB-2013-01-221701) and Tecnologico Nacional de Mexico.

References

[1] Díaz-Guillén J.A., Fuentes A.F., Díaz-Guillén M.R., Almanza J.M., Santamaría J., León C., The effect of homovalent A-site substitutions on the ionic conductivity of pyrochlore-type $Gd_2Zr_2O_7$, J. Power Sources 2009; 186: 349-352.

[2] Díaz-Guillén J.A., Díaz-Guillén M.R., Padmasree K.P., Fuentes A.F., Santamaría J., León C., High ionic conductivity in the pyrochlore-type $Gd_{2-y}La_yZr_2O_7$ solid solution ($0 \leq y \leq 1$), Solid State Ionics 2008; 179: 2160-2164.

[3] Hagiwara T., Yamamura H., Nishino H., Relationship between oxide-ion conductivity and ordering of oxygen vacancy in the $Ln_2Zr_2O_7$ (Ln = La, Nd and Eu) system using high temperature XRD, J. Fuel Cell Sci. Technol. 2011; 8: 051020.

[4] Vassen R., Cao X., Tietz F., Basu D., Stöver D., Zirconates as new materials for thermal barrier coatings, J. Am. Ceram. Soc. 2000; 83: 2023-2028.

[5] Wan C., Qu Z., Du A., Pan W., Order-disorder transition and unconventional thermal conductivities of the $(Sm_{1-x}Yb_x)_2Zr_2O_7$ series, J. Am. Ceram. Soc. 2011; 94: 592-596.

[6] Sickafus K.E., Minervini L., Grimes R.W., Valdez J.A., Ishimaru M., Li F., McClellan K.J., Hartmann T., Radiation tolerance of complex oxides, Science 2000; 289: 748-751.

[7] Ewing R.C., Weber W.J., Lian J., Nuclear waste disposal-pyrochlore ($A_2B_2O_7$): nuclear waste form for the immobilization of plutonium and minor actinides, J. Appl. Phys. 2004; 95: 5949-5971.

[8] Roy C.K., Noor-A-Alam M., Choudhuri A.R., Ramana C.V., Synthesis and microstructure of Gd_2O_3-doped HfO_2 ceramics, Ceram. Int. 2012; 38: 1801-1806.

[9] Shlyakhtina A.V., Shcherbakova L.G., Polymorphism and high-temperature conductivity of $Ln_2M_2O_7$ (Ln = Sm-Lu; M = Ti, Zr, Hf) pyrochlores, Solid State Ionics 2011; 192: 200-204.

[10] Shlyakhtina A.V., Belov D.A., Stefanovich Y.S., Kolbanev I.V., Karyagina O.K., Egorov A.V., Savilov S.V., Shcherbakova L.G., δ-Phase to defect fluorite (order–disorder) transition in the R_2O_3–MO_2 (R = Sc, Tm, Lu; M = Zr, Hf) systems, Mater. Res. Bull. 2011; 46:512-517.

[11] Subramanian M.A., Aravamudan G., Subba Rao G.V., Oxide pyrochlore-a review, Prog. Solid State. Chem. 1985; 15: 55-143.

[12] Fuentes A.F., Takacs L., Preparation of multicomponent oxides by mechanochemical methods, J. Mater. Sci. 2013; 48: 598-611.

[13] Sanjuán M.L., Guglieri C. Díaz-Moreno S., Aquilanti G., Fuentes A.F., Olivi L., Chaboy J, Raman and X-ray absorption spectroscopy study of the phase evolution induced by mechanical milling and thermal treatments in $R_2Ti_2O_7$, Phys. Rev. B 2011, 84: 104207.

[14] Heremans C., Wuensch B.J., Stalick J.K., Prince E., Fast-ion conducting $Y_2(Zr_yTi_{1-y})_2O_7$ pyrochlores: neutron Rietveld analysis of disorder induced by Zr substitution, J. Solid State Chem. 1995; 117: 108-121.

[15] Jonscher A.K., Dielectric relaxation in solids, Londres, Chelsea Dielectric Press, 1984.

[16] Díaz-Guillén M.R., Moreno K.J., Díaz-Guillén J.A., Fuentes A.F., Ngai K.L., García-Barriocanal J., Santamaría J., León C., Ction size effects in oxygen ion dynamics of highly disordered pyrochlore-type ionic conductors, Phys. Rev. B 2008; 78: 104304.

[17] Frechero M.A., Durá O.J., Díaz-Guillén M.R., Moreno K.J., Díaz-Guillén J.A., García-Barriocanal J., Rivera-Calzada A., Fuentes A.F., León C., Oxygen ion dynamics in pyrochlore-type ionic conductors: effects of structure and ion-ion cooperativity, J. Non-Cryst. Solids 2015; 407: 343-354.

Chapter 8.2. Electrical properties of $Gd_{1-x}Ca_xTi_2O_{7-\delta}$ ionic conductors obtained by a novel ultrasound-assisted wet-chemistry method

M. R. Valdés-Ibarra[a]; K. P. Padmasree[a]; S. M. Montemayor[b]; J. A. Díaz-Guillén[c]; A. F. Fuentes[a,*]

[a] Cinvestav Unidad Saltillo, Apartado Postal 663, 25000-Saltillo, Coahuila, Mexico.
[b] Centro de Investigación en Química Aplicada, Blvd. Enrique Reyna No. 140, 25294-Saltillo, Coahuila, Mexico.
[c] División de Estudios de Posgrado e Investigación, Instituto Tecnológico de Saltillo, 25280-Saltillo, Coahuila Mexico.

ABSTRACT

Different compositions of ceramics materials of general formula $Gd_{1-x}Ca_xTi_2O_7$ (x = 0, 0.05 and 0.1), interesting materials on views of their application as ionic conductors in Solid Oxide fuel Cells (SOFC), were prepared by a novel wet-chemistry method assisted by ultrasound. Appropriate amounts of titanium isopropoxide, and Gd^{3+} and Ca^{2+} nitrates were dissolved in a mixture of ethanol and ethylene glycol under a vigorous magnetic stirring; the solution was then, irradiated for 1 h, aged and dried at 95°C to yield a gel, which was further processed at various temperatures and characterized by using different analytical techniques. Electrical properties of the as-prepared powders were measured as a function of temperature and frequency by using impedance spectroscopy. Ca-doped $Gd_2Ti_2O_7$ samples show impedance spectra similar to those typical of most solid electrolyte materials; whereas, log-log representations of the frequency dependence of the real part of the electrical conductivity at different temperatures, are in agreement with the so-called "Universal Dielectric Response" (UDR) proposed by A.K. Jonscher. The complex impedance plots Arrhenius plots confirm that the *dc* conductivity is thermally activated with activation energies within the 0.77-0.89 eV range. An increasing of *dc* conductivity is promoted by substitution of Gd^{3+} by Ca^{2+} in these titanates. This behavior is related to the creation of vacancies in the structure, which facilitates the ion migration process.

Keywords: Gadolinium titanate, Ionic conductivity, Ultrasound, Impedance spectroscopy

1. Introduction

Lanthanide titanates $Ln_2Ti_2O_7$ belong to a family of ternary oxides which can show a pyrochlore-type cubic structure, exhibing a wide range of physical and chemical properties of interest in fundamental science and practical applications. The pyrochlore are materials of great interest because depending on their chemical composition, have a variety of physical and chemical properties that give rise to a significant number of potential applications in many areas of technological interest. The structure of pyrochlore can be considered derivative of fluorite, in particular those in which B is a

---

* Author for correspondence: tel.: +52 844 4389617; email: fuentesaf@live.com

tetravalent cation (Ti and/or Zr) and A as trivalent (Y and/or lanthanides) [1-4]. Pyrochlore investigations today are focused on applications such as solid electrolyte in fuel cells [5] as they are excellent ionic conductors, in thermal barriers as a coating for metal parts exposed to high temperatures [6] and as matrices for immobilization of highly active nuclear waste [1].

There are numerous groups of researchers that have focused on the study of $Gd_2Ti_2O_7$ and $Gd_2Zr_2O_7$ as ionic conductors. They also report to $Gd_2Ti_2O_7$ as an intrinsically poor ionic conductor and thereby suitable for study with a variety of aliovalent dopant substitutions. In particular they have analyzed the relative efficacy of Ca^{2+} substitution on the Gd^{3+} and Al^{3+} on the Ti^{4+} site on enhancing ionic conductivity, since in the titanates pyrochlores, the addition of acceptors such as calcium instead of gadolinium results in a charge compensation by oxygen vacancies [7-11]. Moreover, regarding to the energy that is required to contribute to conduction process, ionic conductors must oppose an energy barrier to jump from their position and contribute to the charge transport. This activation energy for the conduction process is denoted as E_{dc} [12-15]. The conductivity value is very sensitive to the values of Edc and of this condition depends on whether a material is suitable to be applied in different technology areas [16].

The ideal response of an ionic conductor in which the charge carrier ions do not interact with each other and move freely through the lattice is given by an electrical conductivity with a constant value for all frequencies, corresponding to the conductivity value reaching or σ_{dc}. However, when analyzing the electrical conductivity of the ceramic ion-conducting behavior of a remote ideal response it is commonly observed. This behavior is universal because it is showed by materials including the set of ionic conductors and cover from polymers to semiconductors. In all these compounds, conductivity is a function of frequency and is not constant as predicted by the ideal response. Such behavior is characterized by a potential dependence with temperature, with a fractional power between 0 and 1. This behavior was analyzed and revealed by A.K. Jonscher, who is considered responsible for the so-called "Universal Dynamic Response" commonly used to describe this behavior [17].

Conventionally, a multitude of synthesis methods have been used to obtain similar materials, such as mechanochemistry, sol-gel, solid-state reaction, co-precipitation, to mention some [18]. Sonochemical or ultrasound assisted synthesis is an alternative method to the above-mentioned techniques. The underlying principle for the reaction promoted by ultrasound in a liquid medium is due to the dynamics of the bubbles, i.e. formation, growth and implosive collapse [19]. In the present work attempts to obtain the aforementioned materials by the sonochemical technique; the basic principle of this technique is acoustic cavitation, consisting in the formation, growth and collapse (implosion) of microbubbles when a sound wave of sufficient intensity is propagated through a liquid [20-22].

2. Materials and Methods

Three compositions with general formula $Gd_{1-x}Ca_xTi_2O_7$ (x=0, 0.05 and 0.1 in atomic percent) were synthesized by a sonochemical reaction. As starting reagents were used gadolinium nitrate hexa-hydrate [$Gd(NO_3)_3 \cdot 6H_2O$] and calcium nitrate tetra-hydrate [$Ca(NO_3)_2 \cdot 4H_2O$], (*Sigma Aldrich, 99.9%*) using titanium tetra-isopropoxide {$Ti[OCH(CH_3)_2]_4$}, *(Sigma Aldrich, 97%)* as precursor, and performing calculations for

0.01mol, the solvents employed were Ethanol and Ethylene glycol. Solutions were mixed in the vessel of reaction and subjected to ultrasound for 1 hour at room temperature in a *Sonics Vibra-Cell VCX750* reactor. The product obtained of ultrasound cycle was dried at 95°C for 12 hours and calcined 2 hours at 800°C to remove organic compounds and analyze with the appropriate analysis the formation of the desired phases. After calcinations, samples were analyzed by X-ray powder diffraction (XRD) in a diffractometer *X'Pert Philips*, using the CuK_{α} (λ=1.541874 Å). From the obtained patterns, crystallite size was calculated by using the Scherrer equation. Finally to carry out electrical measurements and to determine the ionic conduction properties of these materials, synthesized powders were uniaxially pressed to obtain pellets (diameter of 1 cm and thickness of 0.1 cm) which were sinterized at two different temperatures, 1200 and 1500ºC (heating and cooling rate = 2°C/min).

Analysis of electrical properties was carried out in air by Impedance Spectroscopy using a Solartron 1260 Frequency Response Analyzer over the 100 Hz-1MHz frequency range. Electrodes were made by coating both sides of the pellets with conductive platinum paint and firing them at 600°C to eliminate organic components and harden the Pt coating. Conductivity *dc* values and the activation energy E_{dc} of all studied samples were compared to the $Gd_2Ti_2O_7$ (x = 0).

3. Results and discussion

3.1 Synthesis of $Gd_{1-x}Ca_xTi_2O_7$ and structural characterization

Fig. 1(a) shows the XRD patterns corresponding to the compositions $Gd_{1-x}Ca_xTi_2O_7$ (x=0, 0.05 and 0.1) synthesized by sonochemistry and after a thermal treatment at 800°C for 2 hours. The XRD pattern of gadolinium titanate ($Gd_2Ti_2O_7$) shows the main reflections corresponding of the pyrochlore-type superstructure, similar to the reported XRD pattern of the same pyrochlore by the International Centre for Diffraction Data (ICDD) (PDF 23-0259) and showed in Figure 1(b). This is corroborated mainly by the reflections corresponding to Miller indices (111) and (311) at 15.2 and 38.5° (2θ) respectively. Figure 1(a) also show the diffraction patterns of two compositions doped with calcium (x = 0.05 and 0.1).

In both samples, pyrochlore structure is present and there is no evidence of shift of reflections towards smaller angles by effect of doping and consequently, a change in the unit cell volume when Gd is replaced by Ca. Crystallite size was calculated by Scherrer equation, for the samples with x = 0.05 and 0.1, obtaining a values of 29 and 26 nm respectively.

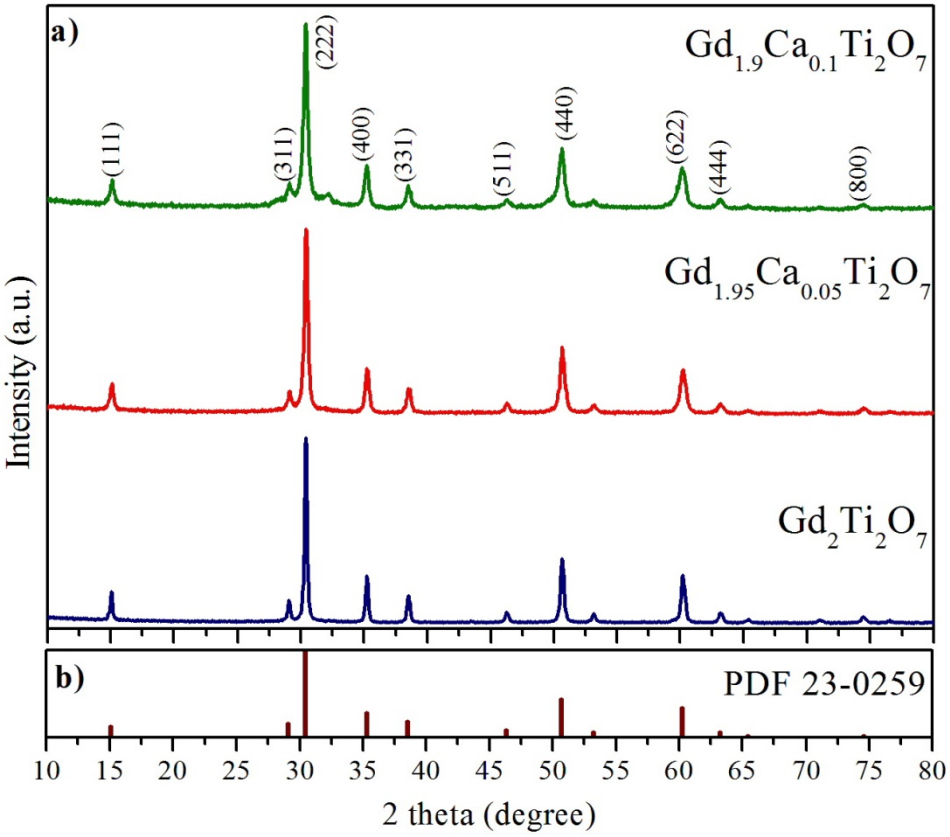

Fig. 1. X-ray diffraction patterns: a) $Gd_2Ti_2O_7$, $Gd_{1.95}Ca_{0.05}Ti_2O_7$ and $Gd_{1.9}Ca_{0.1}Ti_2O_7$, all obtained by synthesis induced by ultrasound and treated at 800°C for 2 hours, b) reported pattern for the $Gd_2Ti_2O_7$ (ICDD PDF 23-0259)

3.2 Electrical properties

3.2.1. Analysis of electrical conductivity

Figure 2 shows a typical representation in double-logarithmic scale of dependence the real part of the conductivity as a function of frequency (in a range from 100Hz to 1MHz) and measurement temperature (220-700°C) for the $Gd_{1.95}Ca_{0.05}Ti_2O_7$ composition (a) 1200°C and (b) 1500°C. As can be seen, there is a potential dependence of the conductivity with frequency at low temperatures and high frequencies, such behavior is consistent with the *Dinamic Universal Response*, established by A.K. Jonscher. In this type of representation the value of the conductivity *dc* (bulk) at each temperature is manifested as a plateau in which the value of the conductivity is independent of frequency. Also is clearly see that with increasing temperature the value of the conductivity *dc* (bulk) and both the dependence potential region as the crossover frequency shift to higher frequencies to be out of the experimental window increases.

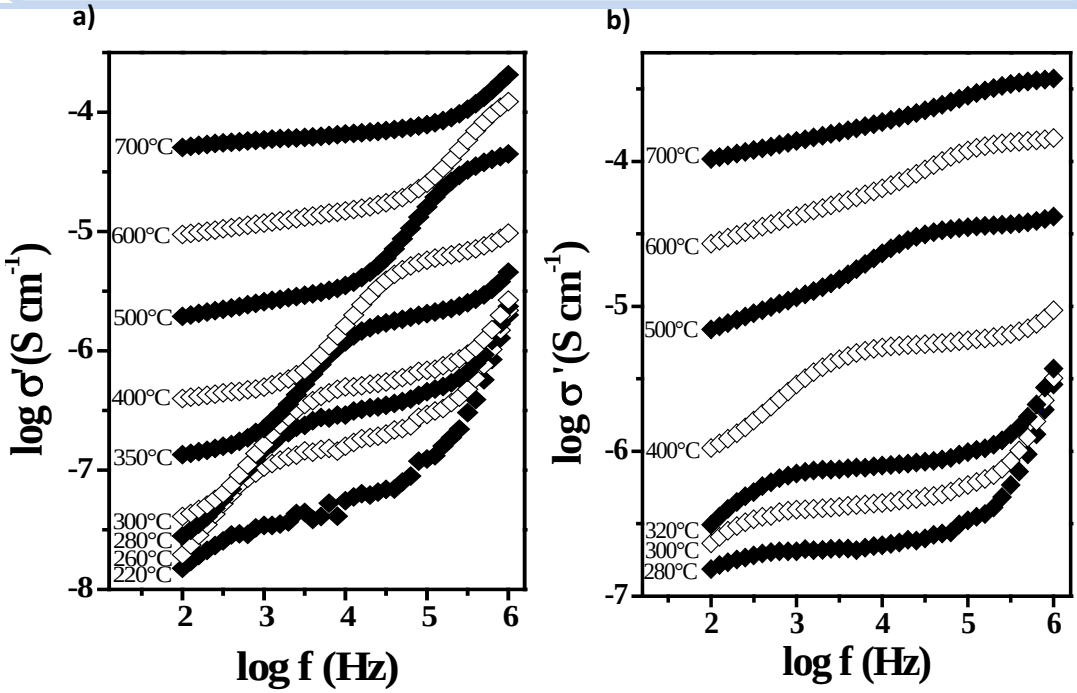

Fig. 2. (a) Real part of the conductivity as a function of frequency at several temperatures for $Gd_{1.95}Ca_{0.05}Ti_2O_7$ sinterized at 1200°C; and (b) at 1500°C.

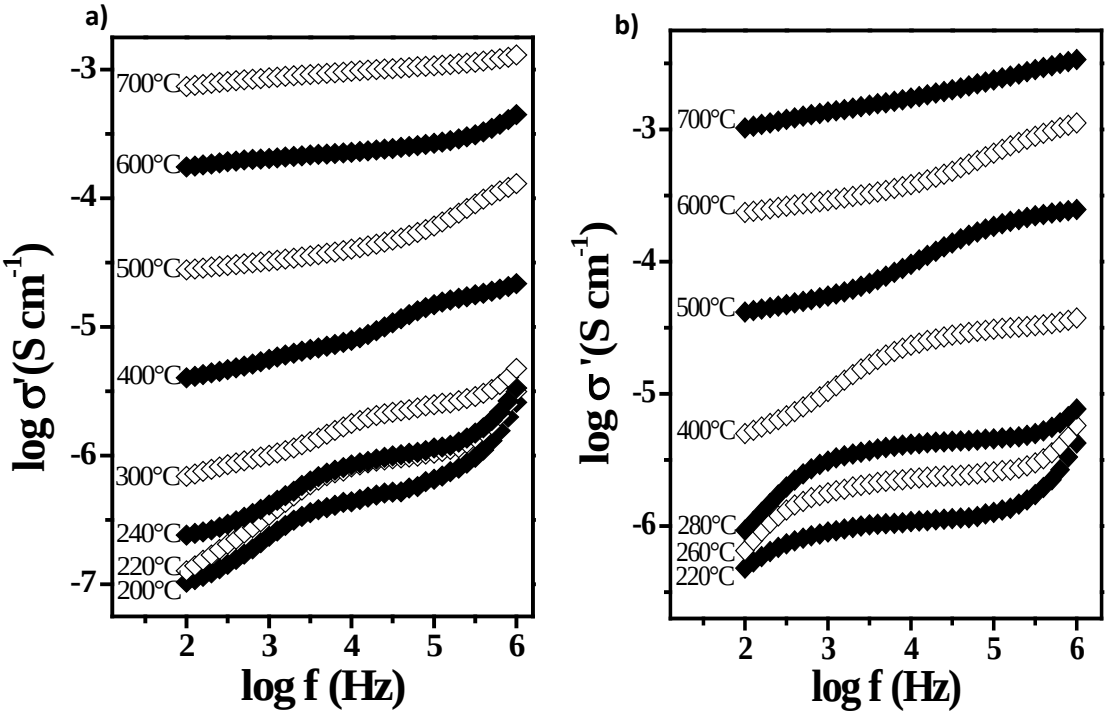

Fig. 3. (a) Real part of the conductivity as a function of frequency at several temperatures for $Gd_{1.9}Ca_{0.1}Ti_2O_7$ sinterized at 1200°C; and (b) at 1500°C.

From Figures 2 and 3, it is clear that *dc* conductivity is lightly higher for samples sintered at 1500ºC. Results also show that an increasing of the Ca content improves the *dc* conductivity, for both sintering temperatures. This behavior is related with an increasing of the number of vacancies, generated when Gd^{3+} is replaced by an element with different oxidation state (Ca^{2+}).

3.2.2. Analysis of the electrical permittivity

Figure 4(a) and (b) show the real part of the electrical permittivity as a function of frequency and temperature for the same composition in a log-log representation, for the composition for $Gd_{1.9}Ca_{0.1}Ti_2O_7$ sinterized at 1200 (a) and 1500ºC (b) . Blocking effects at grain boundaries and electrodes, which are characteristic of a charge transport dominated by the contribution of hopping ions, are evident in this graph and also points to the ionic nature of the electrical conductivity in these materials.

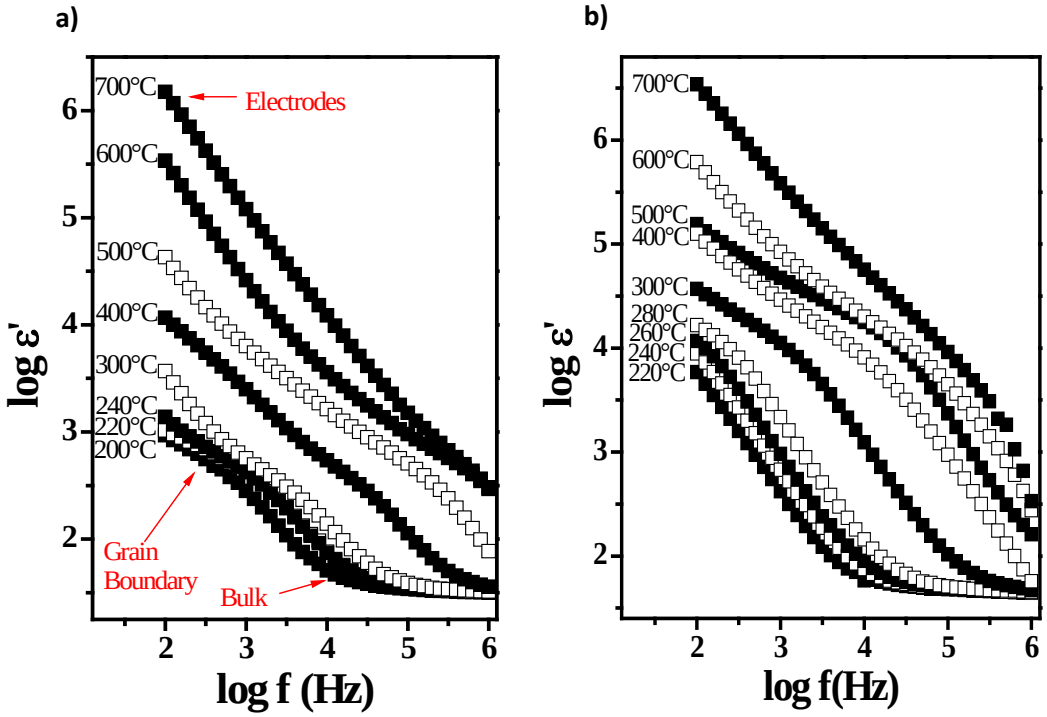

Fig. 4. (a) Frecuency dependence of the the real part of the permittivity as function of the frequency at several temperatures for $Gd_{1.9}Ca_{0.1}Ti_2O_7$ at 1200°C; and (b) at 1500°C.

Similarly, these same blocking effects can be observed in the representation of the imaginary impedance component (Z") vs. real component (Z') taken at different temperatures for Ca-doped compositions, in which there are at least two semicircles, at high and low frequencies respectively, showing capacitance values related to the grain (bulk) and grain boundary contribution, respectively. **Figures 5** and **6** show the above representations for the two compositions doped with calcium (x = 0.05 and 0.1), sintered at 1200 and 1500°C.

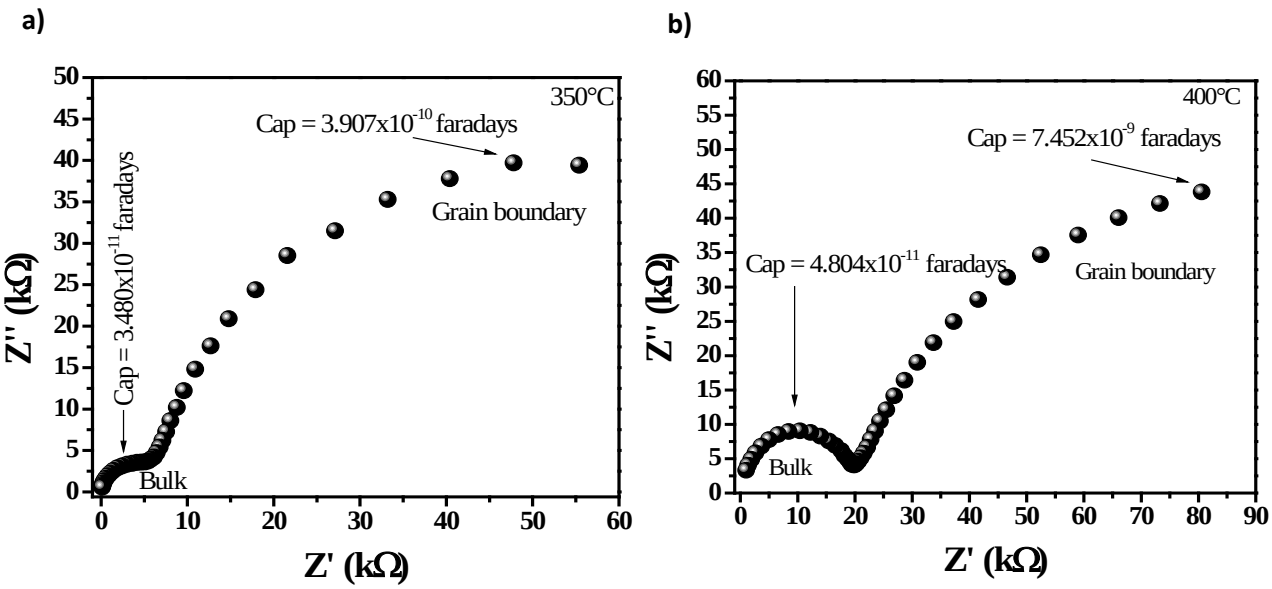

Fig. 5. Complex impedance plot obtained for $Gd_{1.95}Ca_{0.05}Ti_2O_7$ a) at 350°C for sample sintered at 1200°C and b) at 400°Ce sample sintered at 1500°C.

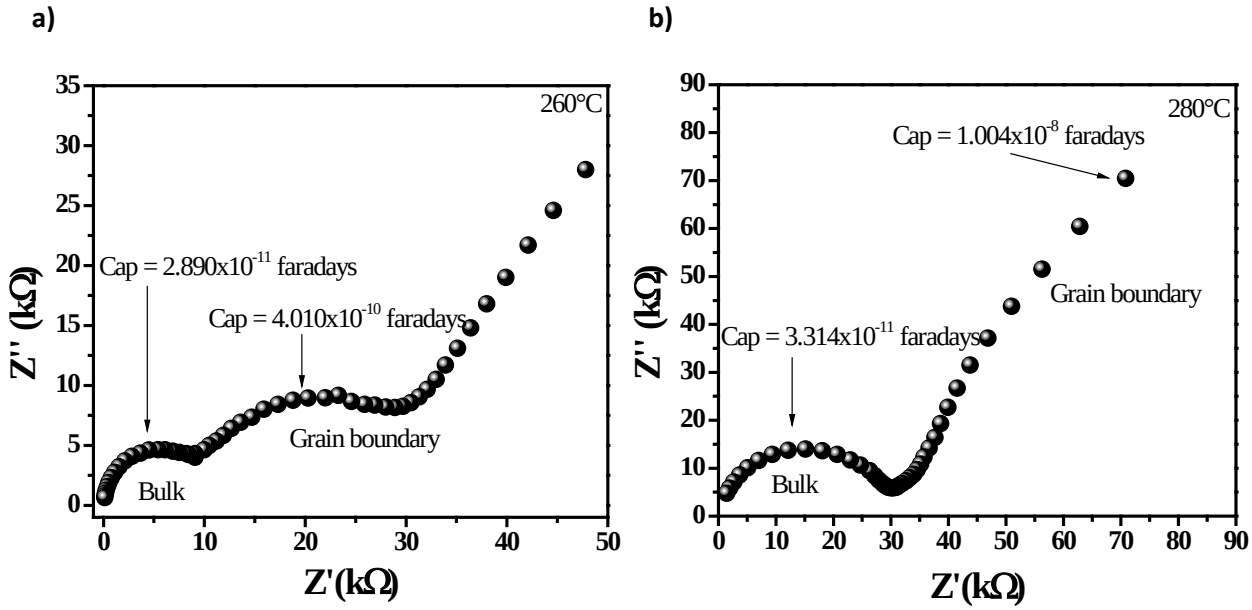

Fig. 6. Complex impedance plot obtained for $Gd_{1.9}Ca_{0.1}Ti_2O_7$: (a) at 260°C for sample sintered at 1200°C; and (b) at 280°C for the sample sintered at 1500°C.

3.2.3. Analysis of the dc conductivity

The dependence of the *dc* conductivity with temperature for all compositions was analyzed using an Arrhenius type representation of the form:

$$\sigma_{dc} T = (\sigma_0) \exp(-E_{dc}/k_B T) \quad (1)$$

where σ_0 is the pre-exponential factor which is related to the effective number of mobile oxygen ions and E_{dc} denotes the activation energy for the ion conduction process. The *dc* conductivity values used for this representation were obtained directly from the plots of conductivity versus frequency for each composition. The fit of the experimental data in thermally activated processes usually generate straight lines whose slope is proportional to the activation energy associated with long range conduction (E_{dc}) making it possible to determine the activation energy values for each composition. **Figure 7** shows such representations of calcium-doped compositions and undoped $Gd_2Ti_2O_7$ (GTO). An Increasing of *dc* conductivity is evident for doped samples, mainly for the composition $Gd_{1.9}Ca_{0.1}Ti_2O_7$. This behavior is an evidence of the positive effect of doping in pyrochlores, since improve notoriously the conductivity values, independently of sintering temperature.

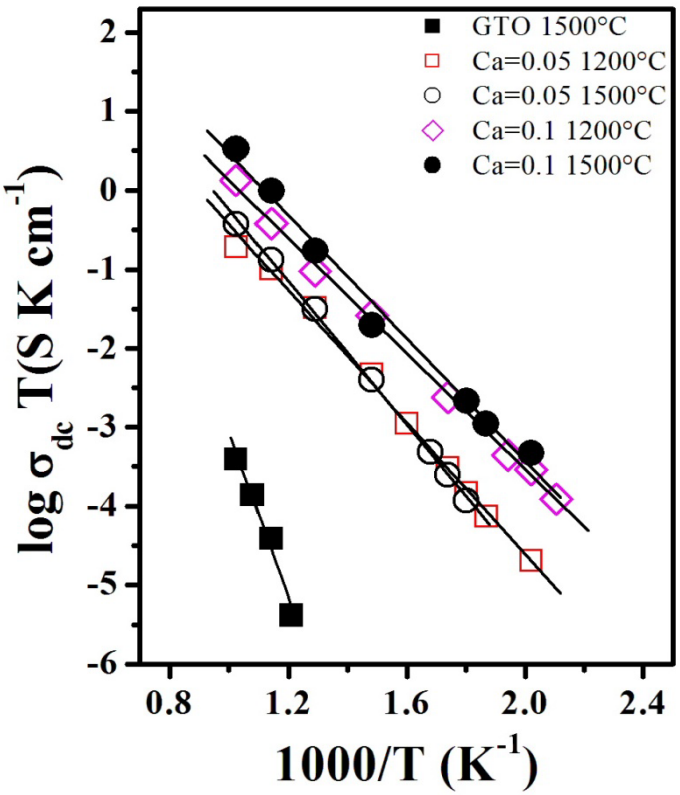

Fig. 7. Arrhenius plots of the *dc* conductivity for the all synthesized compositions studied in this work.

Table 1 shows the values of the activation energy E_{dc} and *dc* conductivity for Ca-doped compositions.

Table 1. Conductivity dc values and activation energies.

Temperature (°C)	Composition	σ_{dc} 700°C (S·cm^{-1})	E_{dc} (eV)
1200	$(Gd_{1.95}Ca_{0.05})Ti_2O_7$	$1.97x10^{-4}$	0.82
	$(Gd_{1.9}Ca_{0.1})Ti_2O_7$	$1.28x10^{-3}$	0.68
1500	$(Gd_{1.95}Ca_{0.05})Ti_2O_7$	$4.02x10^{-4}$	0.89
	$(Gd_{1.9}Ca_{0.1})Ti_2O_7$	$3.55x10^{-3}$	0.77

4. Conclusion

We have shown that different compositions of the system $Gd_{1-x}Ca_xTi_2O_7$ can be easily prepared at room-temperature, by synthesis induced by ultrasound, irradiating the solution for 1 hour and drying at 95°C. XRD results for the samples treated at 800°C revealed the presence of phases with a pyrochlore structure. Crystallite size obtained by Scherrer equation is nanometric for Ca-doped samples. Conductivity *dc* values are higher for Ca-doped samples, obtaining a maximum value of $3.55x10^{-3}$ S cm^{-1} for $(Gd_{1.9}Ca_{0.1})Ti_2O_7$ composition, sinterized at 1500ºC. Increasing of ionic conductivity is due to the creation of vacancies in the structure, which facilitates the ion migration process. E_{dc} values decrease as the percentage replacement of calcium is increased, which is logical since the barrier that must be overcome for ionic migration takes place is lower.

5. Acknowledgments

This work has been carried out with the financial support of CONACYT and Tecnológico Nacional de Mexico. The author M.R. Valdés-Ibarra thanks CONACYT for the scholarship for this work.

6. References

[1] M.A. Subramanian, G. Aravamudan, G. V. Subba Rao, *"Oxide Pyrochlores-A Review"*, Materials Science Research Center, Prog. Solid State Chemistry. 15 (1983) 55-143.

[2] A.F. Fuentes, K. Boulahya, M. Maczka, J. Hanuza, U. Amador, *"Synthesis of disordered pyrochlores, $A_2Ti_2O_7$ (A = Y, Gd and Dy), by mechanical milling of constituent oxides"*, Solid State Science, 7 (2005) 343-353.

[3] K.W. Eberman and J. Bernhardt, *"Order-Disorder Phenomena in $A_2B_2O_7$ Pyrochlore Oxides"*, JOM, Metals and Materials Society, 52, (2000) 19-21.

[4] N.J. Hess, B.D. Begg, S.D. Conradson, D.E. McCready, P.L. Gassman, W.J. Weber, *"Spectroscopic investigations of the structural phase transition in $Gd_2(Ti_{1-y})_2O_7$ Pyrochlores"*, Journal Physical Chemistry. 106 (2002) 4663-4667.

[5] V.V. Khartona, F.M.B. Marquesa, A. Atkinsonb, *"Transport properties of solid oxide electrolyte ceramics: a brief review"*, Solid State Ionics 174 (2004) 135– 149
[6] J. Feng, B. Xiao, R. Zhoua and W. Panb, *"Thermal conductivity of rare earth zirconate pyrochlore from first principles"*, Scripta Materialia, 68 (2013) 727–730.
[7] S.A. Kramer and H.L. Tuller, *"A novel titanate-based oxygen ion conductor: $Gd_2Ti_2O_7$"*, Solid State Ionics 82 (1995) 15-23.
[8] P.K. Moon, M.A. Spears and H.L. Tuller, "*Characterization of the Structure and Chemistry of Defects in Materials"*, eds. B.C. Larson, M. Ruhle and D.N. Seidman, Mater. Res. Soc. Proc., Pittsburgh, PA 138, (1989) 157-160.
[9] O. Porat, C. Heremans, and H.L. Tuller, *"Phase Stability and Electrical Conductivity in $Gd_2Ti_2O_7$–$Gd_2Mo_2O_7$ Solid Solutions"*, Journal of the American Ceramic Society, Vol.80 Issue 9 (1997) , 2278-2284.
[10] P.K. Moon and H.L. Tuller, *"Ionic Conduction in the Gd2Ti2O7-Gd2Ti2O7 system"*, Solid State lonic, Vol. 28-30 part 1 (1988), 470-474.
[11] S. Kramer, M. Spears and H.L. Tuller *"Conduction in titanate pyrochlores: role of dopants"*, Solid State Ionics, Vol. 72 part 2 (1994), 59-66.
[12] H. Iwahara, *"Conducting Materials; Solid-Ionic and Super-ionic"*, Encyclopedia of Materials: Science and Technology, (2008) 1-15.
[13] H. Iwahara, *"Solid-ionic and super-ionic"*, Encyclopedia of Materials: Science and Technology, (2001) 1-11.
[14] S.J. Skinner and J.A. Kilner, *"Oxygen ion conductors"*, Materials Today, Review Feature (2003), 30-37.
[15] L. Traquela, F. Marqués, V. Kharton, *"Oxygen Ion Conduction in Oxide Materials: Selected Examples and Basic Mechanisms"*, Bol. Soc. Esp. Ceram. V., 45 [3] (2006) 115-121.
[16] K. J. Moreno, G. Mendoza-Suárez, and A. F. Fuentes J. García-Barriocanal, C. León, and J. Santamaria, *"Cooperative oxygen ion dynamics in $Gd_2Ti_{2-y}Zr_yO_7$"*, Phys. Review B 71, 132301, 2005.
[17] A.K. Jonscher, *"Dielecric relaxation in solids"*, Chelsea Dielectric London, (1983).
[18] A.F. Fuentes and L. Takacs, *"Preparation of multicomponent oxides by mechanochemical Methods"*, Journal Mater Sci (2013) 48:598–611.
[19] Pankaj and M. Ashokkumar (eds.), *"Theoretical and Experimental Sonochemistry Involving Inorganic Systems"*, Springer Science, Chapter 8, 2011.
[20] A. Gedanken, *"Using Sonochemistry for the fabrication of nanomaterials"*, Ultrasonics Sonochemistry, 11 (2004) 47-55.
[21] L. H. Thompson and L. K. Doraiswamy, *"Sonochemistry: Science and Engineering"*, *Ind. Eng. Chem. Res.* 1999, *38*, 1215-1249.
[22] K.S. Suslick, *"Sonochemistry"*, Science, 247 (1990), 1439-1445.

Chapter 8.3. Electrocatalytic oxygen evolution reaction in alkaline media using a hydrotalcite-like material Ni/Co-Fe

J. Vazquez-Samperio[a,b]; M.A. Oliver-Tolentino[b]; A. Diaz-Romero[a]; A. Guzman-Vargas[b]; E. Reguera-Ruiz[a]

[a] Centro de Investigación en Ciencia Aplicada y Tecnología Avanzada del Instituto Politécnico Nacional, Legaria 694. Colonia Irrigación, 11500 México D. F.
[b] ESIQIE-IPN, Laboratorio de Investigación en Materiales Porosos Catálisis Ambiental y Química Fina, UPALM Edif. 7 P.B. Zacatenco México D.F. 07738, Mexico.

ABSTRACT

High activity, durable, and cost effective electrocatalyst for the oxygen evolution reaction (OER) plays an important role in electrochemical science and technology , for example, water- splitting by electrolysis for production of hydrogen. The first-row transition-metal-based OER catalysts, especially iron-, cobalt- and nickel-containing materials, are versatile candidates for replacement of precious catalysts due to their earth abundant nature, low cost, environmentally friendly, multiple valence state and high theoretical activity.In this study we reported the oxygen evolution reaction (OER) using a new and efficient hydrotalcite-like (LDH) material Ni/Co-Fe.

The LDH´s Ni/Co-Fe was synthesis by co-precipitation method at varied Ni/Co ratios (e.g. 1:1 (#1), 2:3 (#2), and 3:2 (#3)) keeping constant Ni/Co-Fe ratios (e.g. 2:1). The materials was characterized by X-Ray Diffraction, Infrared Spectroscopy, showed that the hydrotalcite structure was obtained. Then, Static magnetic measurements were performed in a superconducting quantum interference device (SQUID) with freshly prepared powdered samples. As previously reported for several magnetic LDHs, Ni/Co-Fe LDHs are ferrimagnets due to the coexistence of ferromagnetic Ni-OH-Ni, Ni-OH-Co or Co–OH–Co superexchange interactions and antiferromagnetic Co–OH–Fe, Fe–OH–Fe, Ni–OH–Fe or Ni-OH-Co interactions mediated by the –OH bridges. At room temperature, all samples are attracted by a conventional laboratory magnet. The behaviour in the Ni/Co-Fe–LDH´s is probably related to a superparamagnetic effect. The cyclic vltammetry experiments showed that OER start c.a. 0.43 V, where the LDH Ni/Co-Fe #2 presented a higher catalytic activity. This catalalityc activity is disscus due to effect of magnetic behavior in LDH's.

In summary, HDL's has been obtained by co-precipitation; HDL's have been structurally characterized by XRD, IR Spectroscopy , SQUID and their properties has been studied by voltammetric techniques. The HDL´s present superparamagnetic effect. The LDH Ni/Co-Fe (2:3 Ni:Co) exhibited the better catalytic activity.

Keywords: Water electrolysis, Hydrotalcite, Superparamagnetic, Ferrimagnetims

---

* Corresponding author:
M.A. Oliver-Tolentino, otma_iq@hotmail.com

1. Introduction

Layered double hydroxides (LDHs) are a class of ionic lamellar compounds made up of positively charged brucite-like layers with an interlayer region containing charge compensating anions and solvation molecules [1]. The general formula of LDHs can be represented as $[M^{II}_{1-x}M^{III}_{x}(OH)_2]_x^+(A^{n-}_{x/n})^{x-}\cdot mH_2O$, where M^{II} (M=Fe, Co, Ni, Cu, Zn,Mg, etc.) and M^{III} (M=Al, Cr, Ga, Mn, Fe, etc.) are divalent and trivalent metal cations, respectively; x is defined as the molar ratio of $M^{III}/ (M^{II}+M^{III})$ and generally has a value ranging from 0.2 to 0.33; A^{n-} are the interlayer anions [2, 3]. Based on the flexibility in elemental composition of LDH layers, metallic cations with electrocatalytic activity can be introduced into the LDH layer, and the metallic cations can reach highly uniform dispersion. Moreover, owing to their desirable properties including low cost, high catalytic activity, and high chemical stability, layered double hydroxides as electro-active materials in OERs have been attracting considerable attention. [4, 5].

Oxygen evolution reaction (OER) is an important half reaction involved in many energy conversion and storage processes such as water splitting [6]. However, the OER is kinetically sluggish in nature $4OH^- \rightarrow 2H_2O + O_2 + 4e^-$ in conditions alkaline because of its multistep proton-coupled electron transfer and typically requires a substantial driving overpotential of the thermodynamic potential (1.23 V) for water splitting ($H_2O \rightarrow H_2 +1/2O_2$) [6,7]. Therefore many efforts of the science community has devoted tremendous effort in exploring a robust, durable and cost-effective catalyst for the OER. Latest report demonstrates NiFe LDH has shown an activity than either of the parent metal catalyst, and comparable to the best noble catalysts (e.g. IrO_2 and RuO_2) for OER [8]. The magnetic behavior of NiFe LDHs, which can be adjusted by tuning the NiFe ratios in the NiFe LDHs, also has an important effect on the electrochemical process. LDHs with different types of chemical compositions have been largely investigated. Also, a few types of LDHs were prepared for electrocatalytic water oxidation mostly based on Co-, Ni- and Fe-associated active sites. [9,10,11].

In this study we reported the oxygen evolution reaction (OER) using a new and efficient hydrotalcite-like (LDH) material Ni/Co-Fe with different ratios and as its magnetic behavior affects to the oxygen evolution reaction.

2. Materials and Methods

The LDH´s Ni/Co-Fe was synthesis by co-precipitation method at varied Ni/Co ratios (e.g. 1:1 (#1), 2:3 (#2), and 3:2 (#3)) keeping constant Ni/Co-Fe ratios (e.g. 2:1). XRD patterns of the samples, as prepared were recorded on a D8 Advance Bruker instrument using Cu-Kα1 radiation (λ= 1.542Å). The spectroscopic analyze were recorded in a FT-IR spectrophotometer Perkin Elmer RX-1, with attenuated total reflectance accessory (ATR). Magnetic measurements were carried out with a Quantum Design superconducting quantum interference device (SQUID). Finally, the electrochemical experiences were

executed using an Autolab electrochemical workstation (PGSTAT320 potentiostat/ galvanostat).

The material LDH´s were disperse with ethanol and deposited on a FTO substrate (F : SnO_2, fluorine doped tin oxide over-layer) by spin coating method.

A typical three-electrode experimental cell equipped with a counter electrode of platinum and a reference electrode Ag/AgCl was used for the electrochemical characterization of the materials.

The electrochemical measurements were carried out in aqueous KOH solutions (1 M) and all potentials measured were converted to the reversible hydrogen electrode (RHE) scale according to the Nernst equation: $E_{RHE} = E_{Ag/AgCl} + 0.197 + 0.059pH$. The potential values were converted to over-potential values using the formula $\eta = E_{appl} - 0.401 + 0.197$.

3. Results and Discussion

The powder X-ray diffractogram of the samples Ni/Co-Fe #1, Ni/Co-Fe #2 and Ni/Co-Fe #3 are shown in Figure 1. The diffraction patterns for the as-synthesized LDH sample display the characteristic diffraction peaks of crystalline hydrotalcite-like LDHs, which are indexed in a hexagonal lattice with $R\bar{3}m$ rhombohedral symmetry (JCPDS: 220700). The values of the unit cell dimension (a,c) and chemical compositions are given in Table 1.

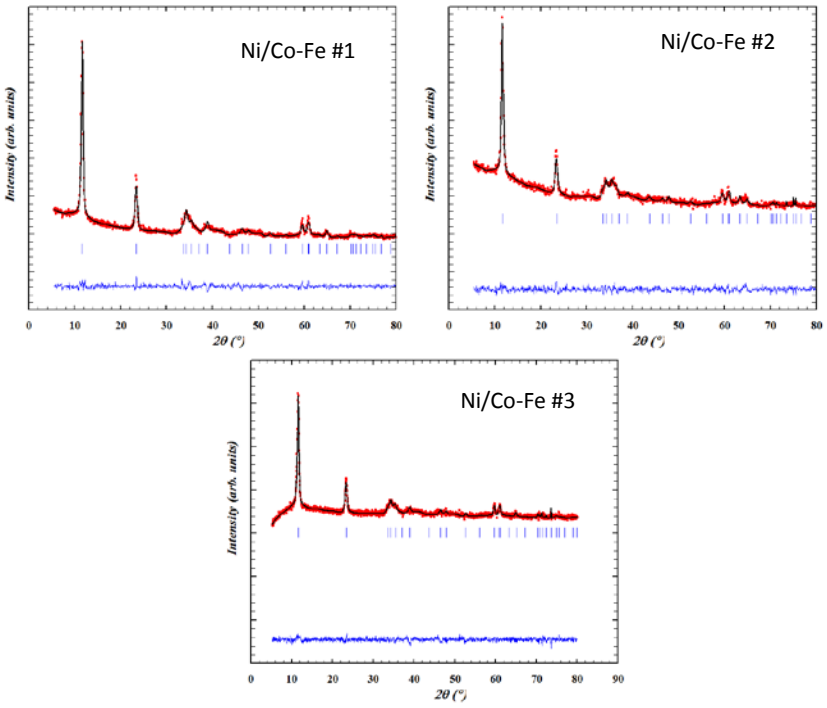

Fig. 1. A Le Bail fit of the observed XRD profile of LDH

Table 1. The unit cell dimension of HDL's

Sample	Composition	a (Å)	c (Å)
Ni/Co-Fe #1	$[Ni_{0.33}Co_{0.32}Fe_{0.34}(OH)_2](CO_3)_{0.17}$	3.0990	22.7956
Ni/Co-Fe #2	$[Ni_{0.27}Co_{0.39}Fe_{0.33}(OH)_2](CO_3)_{0.16}$	3.1017	22.7704
Ni/Co-Fe #3	$[Ni_{0.47}Co_{0.20}Fe_{0.32}(OH)_2](CO_3)_{0.16}$	3.0935	22.8010

FT-IR spectroscopies are specifically suited to identify the nature of the interlayer anion and investigate its interactions with the rest of the structure. The spectra of HDL's are presented in figure 2. The broad band between 4000 and 3000, and the band around 1630 cm^{-1} are attributed to the OH stretching mode of hydroxyl groups in the brucita-like layers and hydroxyl groups from interlayer water molecules. The broad shoulder around 3000 cm^{-1} has been ascribed to the OH stretching mode of hydroxyl groups hydrogen-bonded to interlayer carbonate anions. The ν_3 (CO_3^{2-}) vibration band around 1360 cm^{-1} is characteristic of carbonate anions in D_{3h} planar symmetry. The band close to 987 cm^{-1} can be attributed to the ν_1 (CO_3^{2-}) vibration band. Other absorptions below 1000 cm^{-1} are associated with M–O stretching and M–OH bending vibrations.

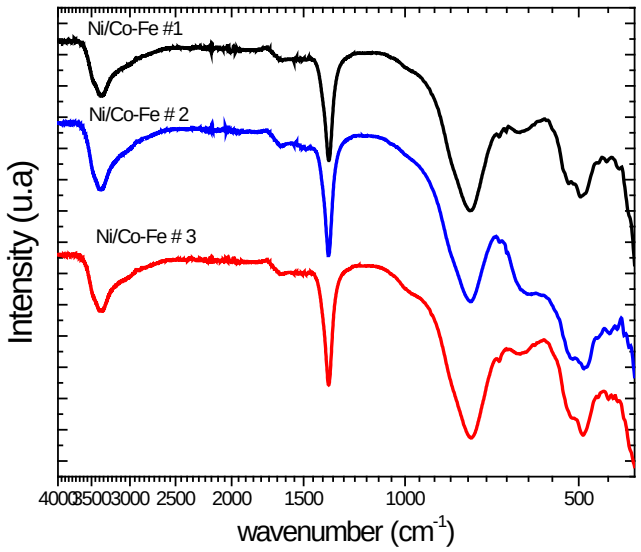

Fig. 2. FT-IR spectra of samples

Field cooled (FC) and zero-Field cooled (ZFC) experiments of the sample Ni/Co-Fe #1 (Fig.3.) indicated the presence of cooperative magnetism, presenting a broad maximum at ca. 3.28 K. As previously reported for several magnetic LDHs, the samples present a behavior Ni/Co-Fe LDHs ferromagnets due to the coexistence of ferromagnetic Ni-OH-Co or Co–OH–Co superexchange interactions and antiferromagnetic Ni-OH-Ni, Co–OH–Fe or Fe–OH–Fe interactions mediated by the –OH bridges.

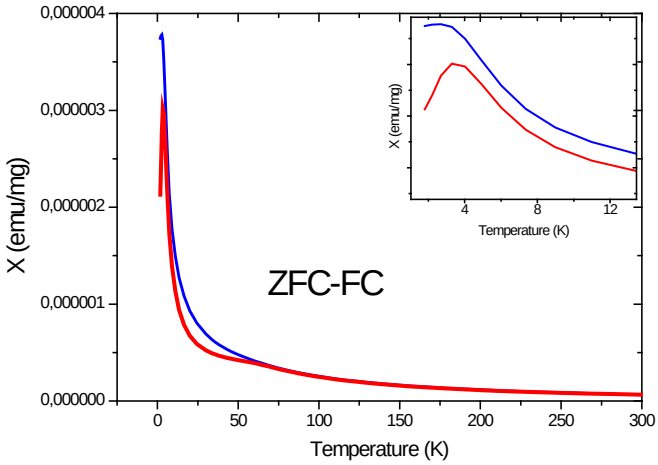

Fig. 3. ZFC-FC magnetization.

The current-potential characteristics obtained during linear sweep voltammetry (LVS), in 1 mol L^{-1} KOH solution, at 1 mV s^{-1} for LDH's, are displayed in Figure 4. The oxygen evolution reaction begins at 1.47V/RHE (η=250 mV), the Ni/Co-Fe#1 exhibited the best catalytic activity this behavior can be associated to presence of superexchange due to the Co-OH-Fe and Ni-OH-Fe interaction, before to OER the redox process of Ni^{III}/Ni^{II} and Co^{III}/Co^{II} are evident, however the shift in the potential can be associated to M-OH-M interaction.

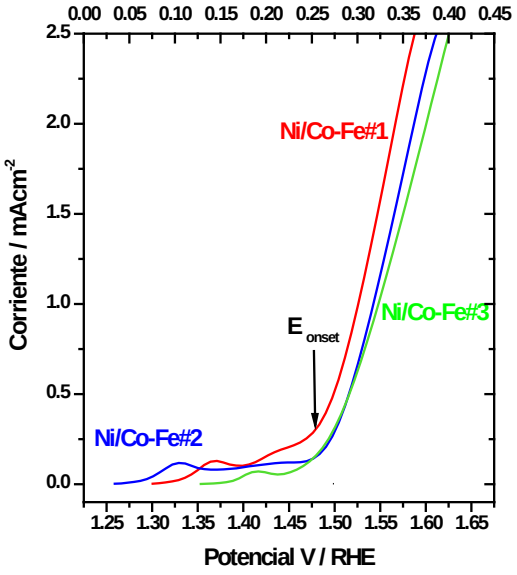

Fig. 4. LSV of LDH materials

4. Conclusion

In present work the electrocatalytic activity Layered Double Hydroxides Ni/Co-Fe materials towards Oxygen evolution reaction was evaluated, the results were explained by M-OH-M interaction which promotes the superexchange on the layer, increased the charge transfer during OER. The material labeled as Ni/Co-Fe#1 exhibited the best activity due to the Co-OH-Fe and Ni-OH-Fe interaction.

Acknowledgements

Projects SIP-IPN 20150898, CONACYT INFRA Projects 2014225161,

References

[1] Wang Q, O'Hare D (2012) Chem Rev 112:4124–4155
[2] Zhao MQ, Zhang Q, Huang JQ, Nie JQ, Wei F (2010) Carbon 48:3260–3270
[3] Garcia-Gallastegui A, Iruretagoyena D, Gouvea V, Mokhtar M, Asiri AM, Basahel SN, Al-Thabaiti SH, Alyoubi AO, Chadwick D, Shaffer MSP (2012) Chem Mater 24:4531–4539
[4] Z. Lu, W. Xu, W. Zhu, Q. Yang, X. Lei, J. Liu, Y. Li, X. Sun and X. Duan, Chem. Commun., 2014, 50, 6479–6482.
[5] Y. Zhang, B. Cui, C. Zhao, H. Lin and J. Li, Phys. Chem. Chem. Phys., 2013, 15, 7363–7369.
[6] Y. Liang, Y. Li, H. Wang, H. Dai, J. Am, Chem. Soc. 135 (2013) 2013e2036.
[7] F. Li, H. Gong, Y. Wang, H. Zhang, Y. Wang, S. Liu, S. Wang and C. Sun, J. Mater. Chem. A, 2014, 2, 20154-20163.
[8] Y. V. Geletii, Z. Huang, Y. Hou, D. G. Musaev, T. Lian and C. L. Hill, Journal of the American Chemical Society, 2009, 131, 7522-7523.
[9] M. W. Louie and A. T. Bell, J. Am. Chem. Soc., 2013, 135, 12329.
[10] G. Abellan, F. Busolo, E. Coronado, C. Martı -Gastaldo and A. Ribera, J. Phys. Chem. C, 2012, 116, 15756–15764.
[11] G. Abell´an, E. Coronado, C. J. G´omez-Garc´ıa, C. Mart´ı - Gastaldo and A. Ribera, Polyhedron, 2013, 52, 216–221.
[12] Y. Zhang, B. Cui, C. Zhao, H. Lin and J. Li, Phys. Chem. Chem. Phys., 2013, 15, 7363–7369.

Chapter 8.4. Insertion/Desertion of Na^{+} and Mg^{2+} in Cobalt Hexacyanoferrate towards electrochemical energy storage

Miguel A. Oliver Tolentino[a,b]; Dulce Rodríguez-Morán[c]; Berenice Tapia-Juarez[c]; Ariel Guzmán-Vargas[c]; Edilsor Reguera[a]

[a] Centro de Investigación en Ciencia Aplicada y Tecnología Avanzada, Legaria 694. Col. Irrigación, México D. F., C.P.: 11500.
[b] Departamento de Bioingeniería, UPIBI-IPN, Av. Acueducto de Guadalupe S/N, Gustavo A Madero, Barrio La Laguna Ticoman, 07340 Ciudad de México, D.F.
[c] Laboratorio de Investigación en Materiales Porosos, Catalisis Ambiental y Química Fina, ESIQIE-IPN, UPLM, Gustavo A. Madero, Ciudad de México, D.F.

ABSTRACT

Recently, battery research has focused on the high power and energy density needed for portable electronics. However, the requirements for grid-scale energy-storage are different, with emphasis on low-cost production. In this context the use of Mg^{2+} and Na^{+} in aqueous ion batteries has been an encouraging promise, due to the abundance of these alkaline ions in the planet. On the otherhand, open framework materials with the Prussian Blue crystal structure (PBAs) offer high power capabilities and low-cost synthesis. In this contribution the $KCo[Fe^{III}(CN)_6]$ was synthesized; the Co-HCF was mixed with amorphous carbon, polyvinylidenedifluoride, and graphite. The obtained suspension was deposited on a glassy carbon electrode; the experiments were carried out in a $NaNO_3$ and $MgNO_3$. The galvanostatic experiments shows a high stability for charge-discharge (>100 cylces) with a reversible capacity of 116.8 $mAhg^{-1}$ at 0.83C in presence of both Ion. This capacity is associated to redox process of Co^{III}/Co^{II} and Fe^{III}/Fe^{II} site, however the electrochemical mechanims during charge-discharge process is different provokes that the charge retention to different rate enhance in Mg^{+} ion batteries; this behavior is discussed based on the insertion and removal of ions and of their location within the cavities of the structure during the charge and discharge cycles.

Keywords: Insertion-Desertion, Open framework, Ion Batteries, Charge retention

1. Introduction

Recent studies has shown that Aqueous Rechargeable Alkali-Metal Ion Batteries (ARABs) are promising alternatives for large-scale applications which resolve several

---

* Author for correspondence:
Miguel Angel Oliver Tolentino, otma_iq@hotmail.com

challenges of conventional Lithium Ion Batteries (LIBs): (i) the safety issue of flammable organic electrolytes is fundamentally resolved, (ii) the rigorous manufacturing conditions are avoided, and the prices of the electrolyte solvent and salts are relatively low, and (iii) the ionic conductivity of the aqueous electrolyte is higher than those of organic electrolytes by 2 orders of magnitude, [1,2] resulting in high round-trip efficiency and energy density even with bulky and scalable electrodes.

Nevertheless, this technology has yet to be fully developed. Therefore, new materials systems are necessary for the inexpensive, efficient, durable, high-power batteries needed for use in connection with the grid. One alternative for ARABs is to use Prussian Blue Analogues (PBA) because these materials show in aqueous electrolytes an extremely long cycle life; fast kinetics and high efficiency during redox process [3,4]. This is because in aqueous media alkali ions can be inserted in the open framework structure in their hydrated (or partially hydrated) form, which suppressed activation energy for interfacial charge transfer and therefore improved kinetics [5].

In this context the ARABs have been studied using Li^+ as ion, however, Lithium is widely distributed in the Earth's crust but is not regarded as an abundant element. The relative abundance of lithium in the Earth's crust is limited to be only 20 ppm as shown in Figure 1 [6]. Indeed, the materials cost (the price of Li_2CO_3) was steeply increased during the first decade of this century [7].

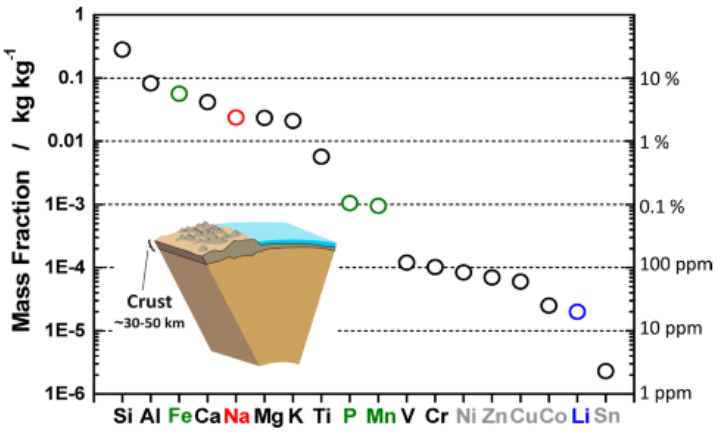

Fig. 1. Element abundance in the Earth's crust.

Moreover, lithium resources are unevenly distributed (mainly in South America); therefore, production of LIBs depends on the import of lithium from South America. In contrast to lithium, sodium resources are unlimited everywhere, and sodium and magnesium are the most abundant elements in the Earth's crust. The infinite sodium resources are also found in the ocean. Additionally, sodium and magnesium exhibited same physicochemical properties with respect to lithium, as shown in Table 1. In this work, the use of Cobalt hexacyanoferrate as host of Na^+ and Mg^{2+} is reported.

Table 1. Comparison of physical properties for lithium, sodium and magnesium

	Mg	Na	Li
Cation radius/pm	65	97	68
Atomic Weight/ g mol^{-1}	24.3	23	6.9
E°/ V vs NHE	-2.73	-2.7	-3.04
Melting point/ °C	650	97.7	180.5
Abundance/ mg kg^{-1}	23 x 10^3	23.6 x 10^3	20
Distribution	Everywhere	Everywhere	70% South America

2. Materials and Methods

The powder $KCo[Fe(CN)_6]$ labeled CoHCF, were preparing an aqueous solution of appropriate molar mixtures of $K_3[Fe(CN)_6]$ and $Co(SO_4)$ and it then added under stirring at room temperature. The formed precipitate was aged within the mother liquor for 24 h. The obtained solid is isolated by filtration, washed several times with distilled water and then air dried up to constant weight. XRD patterns of the samples, as prepared were recorded on a D8 Advance Bruker instrument using Cu-Kα1 radiation (λ= 1.542Å). The spectroscopic analyze were recorded in a FT-IR spectrophotometer Perkin Elmer RX-1, with attenuated total reflectance accessory (ATR). Raman spectra were recorded employed a spectrophotometer Labram HR800 with a laser operating at 530 nm.

Slurries containing the as-synthesized hexacyanoferrates, amorphous carbon (Timcal SuperP Li), polyvinylidenedifluoride (aldrich), and natural graphite (Alfaesar) in a ratio of 80:9:9:2 were prepared in Tetrahydrofuran. These slurries were deposited on carbon plate (Fuel Cell Grade), and dried at 80 °C.

Three electrode cell containing CoHCF working electrode, an Ag/AgCl reference electrode and carbon rod as counter electrode was used. Electrochemical analyses using Cyclic Voltammetry and Galvanostatic tests were carried out at room temperature in a potentiostat−galvanostat Versastat 3-400 (PAR).

3. Results and Discussion

The XRD powder patterns obtained for the CoHCF sample is shows in Figure 2A. Shown that materials crystallizes in a cubic cell (Fm-3m) with cell edge a=10.2666 Å. This is the

cell typical of Prussian blue analogs where the cell edge corresponds to the length of the Fe–C≡N–Co–N≡C–Fe chain. Its crystal structure can be considered as octahedral building units, $Fe(CN)_6$, assembled through Co atoms bonded at the N ends to form a 3D framework.

Since the Co atom also adopts an octahedral coordination, the 3:2 elemental ratio (Co:Fe) forces to 33.33% of vacancies of the whole building unit. For a compact structure within the unit cell 4 building blocks are accommodated but, considering 33.33% of $Fe(CN)_6$ vacant sites, the cell will be occupied by only 1.33 formula units of Co(2+) ferricyanide (see inset Fig 2A). This leads to an extended porous structure formed by pores of about 8.5 Å (diameter). Six Co atoms are found at the surface of these large pores, completing their coordination environment with water molecules, in average, $CoN_4(H_2O)_6$.

The pore filling is completed with zeolitic waters stabilized through hydrogen bonding interactions with the coordinated ones. This explains the relatively large hydration degree of the studied material, and also its easy dehydration on heating. These pores remain communicated by windows of about 4.5 Å.

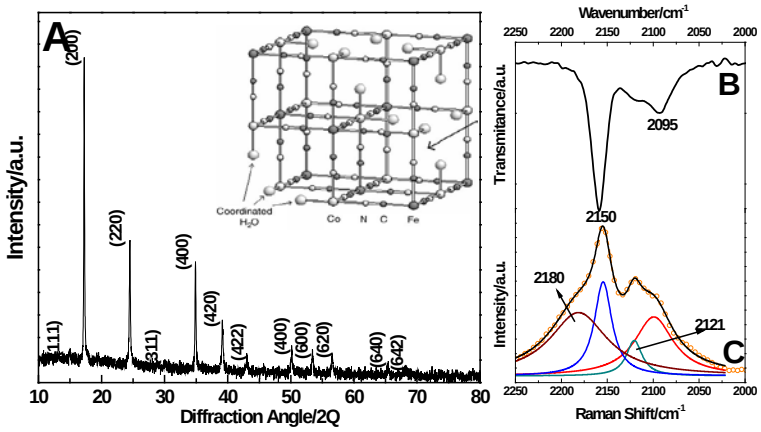

Fig. 2. (a) RDX, (b) FT-IR; and (c) Raman spectra

Due to the triple bond in C≡N is very sensitive to the oxidation state of the coordinating metals, the Raman and FT-IR technique were carried out, the Figure 2B and C exhibited the range corresponding to the cyanide stretching region (2000-2250 cm^{-1}). Lorentzian fitting were made to determine the position of the Raman signals.

The signal at 2160 cm^{-1}, corresponding to Fe(III)–C≡N–Co(II) chains. Whereas the bands at 2086 cm^{-1} and 2121 cm^{-1} are attributed to Fe(II)–C≡N–Co(II) chain, and to Fe(II)–C≡N–

Co(III) chain, respectively. The signal c.a. 2185 associated to Fe(III)–C≡N–Co(III) only is observed in Raman spectra.

Elemental analysis by ICP-OES found that CoHCF had a composition is $K_{0.75}Co_{1.13}[Fe(CN)_6]$. The cyclic voltammetry of CoHCF after 6 cycles in different electrolyte support (1 N of $NaNO_3$ and $Mg(NO_3)_2$) is presented in Figure 3. In presence of Na^+ showed a cathodic peak and anodic peak c.a. 0.65 and 0.55 V/NHE, associated to redox couple Fe^{III}/Fe^{II} during desertion/insertion of Sodium ion; whereas in presence of Mg^{2+} the i-E characteristic is different; during cathodic sweep exhibited two faradic process at 0.5 and 0.66 V/NHE and during anodic sweep the reduction peak c.a. to 0.64, 0.51 and 0.42 V/NHE are observed. This electrochemical behavior can be associated to redox couple Co^{III}/Co^{II} and Fe^{III}/Fe^{II}.

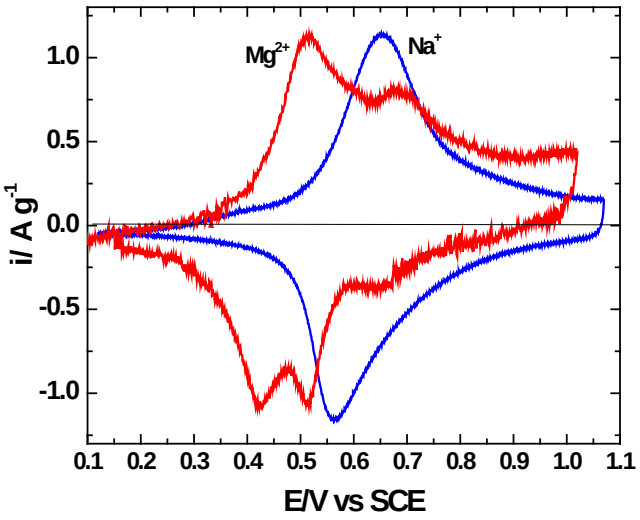

Fig. 3 Cyclic Voltammetry of CoHCF.

The charging/discharging cycling at 1C (For this study, 60 mA g^{-1} is defined as 1C) for CoHCF in $NaNO_3$ and $Mg(NO_3)_2$ is present in Figure 4; for electrode in $NaNO_3$ in the charging cycle is observed a flat plateau at the potential range 0.6-1 V/NHE. The maximum charging specific capacity is 55 mAh g^{-1}, this value is very similar compared with the theoretical capacity of CoHCF which is 64.8 mAh g^{-1}; whereas, during discharge the plateau is evident at potential range 0.5-0.8 V/NHE, with a theoretical capacity of 50 mAh g^{-1}.

On the other hand, the CoHCF in presences of magnesium showed during charge and discharge two plateaus due to the two redox couple involves during faradic process, the capacity increase; this can be attributed to position of cation inside to framework of CoHCF and to charge transfer between Co and Fe through C≡N chain.

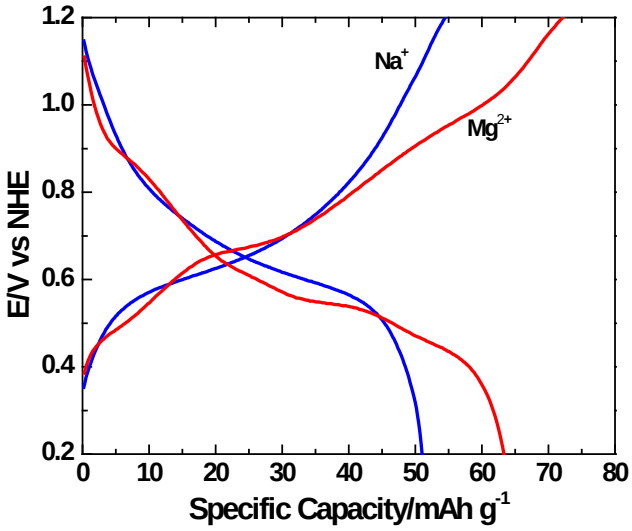

Fig. Galvanostatic behavior

4. Conclusion

In present work the insertion/desertion of sodium and magnesium in Cobalt hexacyanoferrate was presented, the electrochemical behavior depends to diffusion rate and to location of cation inside the Prussian blue framework.

Acknowledgements

Projects SIP-IPN 20150898, CONACYT INFRA Projects 2014225161,

References

[1] C.A. Powell, B.D. Morreale (2008) MRS Bull. 33: 309-315.
[2] V.S. Arunachalam, E.L. Fleischer (2008) MRS Bull. 33: 264-276.
[3] J.P. Holdren (2007) Science 315:737.
[4] J.M. Tarascon, M. (2011) Nature, 414:359-367.
[5] K. Kang, Y.S. Meng, J. Breger, C.P. Grey, G. Ceder (2006) Science 311:977-980.
[6] W. Tang, Y. Zhu, Y. Hou, L. Liu, Y. Wu, K.P. Loh, H. Zhang, K. Zhu (2013) Energy Enviorn. Sci. 6:2093-2104.
[7] W. Li, J.R. Dahn, D.S. Wainwright (1994) Science 26:1115-1118.

Chapter 8.5. Kinetic study of Ptx/Moy/CNT electrocatalyst in oxygen reduction reaction

S. Montoya Solís[a,b]; R. de G. González Huerta[a*]; M. Beltrán Villavicencio[b]; E. Torres Santillán[a]

[a]ESIQIE-IPN, Laboratorio de Electroquímica y Corrosión, UPALM, C.P. 07738, México D.F.
[b]UAM-Azc, CBI, Av. San Pablo, No.180, C.P. 02200, México D.F.

ABSTRACT

The kinetics of the oxygen reduction reaction (ORR) of Pt_x/Mo_y/CNT (x=10,8,5,2 and y=0,2,5,8) nanoparticles was studied in acid media. The carbon natotubes (CNT, Sigma-Aldrich 97%) were treated by an oxidation method in nitric acid aqueous solution (functionalization process). The electrocatalysts were synthesized by chemical reduction of the metal acetylacetonate (Pt and Mo) with $NaBH_4$ in methanol media. Materials were characterized structural and morphologically by X-ray diffraction, scanning electron microscopy and transmission electron microscopy. Electrochemical studies were performed by cyclic voltammetry and rotating disk electrode (RDE) techniques. Kinetic parameters exhibited Tafel slopes between 90 and 120 mV dec^{-1} and exchange current density of around 1×10^{-5} mA cm^{-2}. A four-electron reduction was found in all cases. The bests catalyst was 8% Pt 2% Mo/ NTC. The enhanced reactivity of the catalysts surfaces is attributed to their electronic and geometric structure associated to the bifunctional effects, in which the unique catalytic properties of each of the elements in the catalytic compound combine in a synergetic manner to yield a surface which results more active than each of the elements alone.

Keywords: Oxigen reduction reaction, Nanomaterials PtxMoy/CNT, Electrocatalyst

1. Introduction

The cathodic overpotential is strongly influenced by several physical parameters such as electrocatalysts intrinsic properties, active catalysts surface area, concentration and diffusion coefficient of the oxygen and so on. The novel electrocatalysts are specially aimed to promote the dissociation of the O–O bond during the oxygen reduction reaction (ORR) mechanism, and to maintain reactivity and selectivity on the electrode surface. Multimetallic and alloy catalysts have been particularly active area of research because it

---

* Corresponding author:
Rosa de Guadalupe González Huerta, (+52) 55 57296000 ext 54246, rosgonzalez_h@yahoo.com.mx

has been established that for the cathode reaction, multimetallic surfaces have superior activity to pure metal. Recently, carbon nanotubes (CNT) have received considerable attention as the supports of noble metal catalysts in heterogeneous catalysis, such as ORR. The interaction between metals nanoparticles and CNT in nanohybrid systems generates a peculiar microstructure or modification of the electron density of the metal clusters, and enhances the catalytic activity [1-6].

2. Materials and Methods

Platinum (Pt) and Molibdenum (Mo) nanoparticles were supported on multi-wall carbon nanotubes (CNTs Aldrich,12 nm in diameter and 10 μm in length) by impregnation method using platinum acetylacetonate [$(CH_3\text{-}COCHCO\text{-}CH_3)_2Pt$ Aldrich, 97%] and molybdenum acetylacetonate ($MoO_2(CH_3COCH_2COCH_2)_2$) Aldrich 98%] as precursors, Table 1 shows the nomenclature to describe synthesized materials. MWCNTs put in flask Erlenmeyer with metanol and mixed to 800 rpm, else were the precursor powders were properly mixed and dissolved in metanol to obtain a relation of Pt:Mo content of 0:10, 2:8, 5:5, 8:2 and 10:0 wt.% and this solution is placed dropwise into the flask Erlenmeyer to mixed with MWCNTs. $NaBH_4$ is used as reducing agent. CNTs impregnated were filtered and dried to 110 ºC during overnight and then put inside a horizontal quartz-tube reactor and heated at 300 ºC with hydrogen gas flow during 1 hrs.

Table 1. Synthesized catalysts PtxMoy/CNT.

Sample	Nomenclature
M1	Pt_{10}/NTC
M2	Pt_8Mo_2/NTC
M3	Pt_5Mo_5/NTC
M4	Pt_2Mo_8/NTC
M5	Mo_{10}/NTC

The crystal structure, particle size and morphology of the Pt_xMo_y/CNT electrocatalysts were analyzed by X-ray diffraction (XRD, Siemens D5000 using Cu-Kα radiation), scanning electron microscopy (SEM, JEOL 6300) and transmission electron microscopy (TEM, JEOL 2000FXII)

A conventional single three-electrode test electrochemical cell was used in the electrochemical experiments. All of the electrode potentials in this work are related to a normal hydrogen electrode (NHE) in a 0.5 M H_2SO_4 aqueous solution electrolyte. The electrochemical measurements were performed at room temperature using a Potentiostat AUTOLAB. The working electrode was a glassy carbon disk with a 5 mm diameter (0.19 cm^2). The counter electrode was a platinum mesh and the reference electrode was Hg/Hg_2SO_4/0.5 M H_2SO_4 (MSE = 0.680 V/NHE). The catalytic ink was prepared by dispersing 1 mg of catalyst in 8 μL of Nafion®, 15 μL of water and 75 μL of ethyl alcohol in an ultrasonic bath for 20 min. A drop containing 16 μL of catalyst ink was deposited onto the working electrode surface and dried at atmospheric conditions. After drying a thin

film of electrocatalyst was formed. The Pt loading on the glassy carbon was 80 μgPt cm-2 having concentrations of 10 wt% Pt on support. This condition was used in all samples so electrode thickness was the same for each catalyst. Lower Pt electrode loadings to permit achieve a thin-film, it results in decreased mass-transport resistance through the catalyst layer and giving complete access to the electrochemical area of the catalyst [21].

The electrodes were activated to electrochemical experiments in an oxygen free electrolyte, by scanning the potential in a region between 1.2 V/NHE to 0.0 V/NHE at 100 mV/s for 30 cycles, until a steady state voltamperogram was reached; finally, two cycles were performed at 50 mV s^{-1} in the same potential range to analyze the oxide-reducing signals on the catalyst surface. Thereafter, the electrolyte was saturated with pure oxygen for 30 min and maintained on the electrolyte surface during the rotating disk electrode (RDE) experiments. Hydrodynamic experiments were recorded in the range of rotation rate from 100 to 2500 rpm at 5 mV/s. Current density was normalized for a geometric area of 0.196 cm^2.

3. Results and Discussion

Figs. 1(a)-1(c) show the typical XRD patterns Pt_xMo_y/CNTs electrocatalysts with nominal Pt content relation of 0:10, 2:8, 5:5, 8:2 and 10:0 wt.% respectively. The broad reflections at 2θ= 39.7°, 46.2°, 67.6°, 81.4° and 85.8° suggest small Pt (PDF 04-0802) crystallites. The Pt crystallite size was estimated to be about 8-15 nm by using the Scherrer equation and the (111) reflections. The low intensity reflections at 2θ =26.2° well correspond to the (002) plane of the hexagonal graphite structure (PDF 04-1487), which has been previously assigned to CNTs [21]. The intensity of the CNTs reflection gradually decreases with increasing the Pt content implying a higher Pt coverage.

Fig. 2 shows the SEM micrographs of the samples M2 and M3. In M2 exists the characteristic tubular morphology, observing a no preferential orientation growth, it evident the presence of agglomerated CNT. CNT´s size is relatively long, because of their average length is on micrometers order. The M3 micrographs show a tubular structure with pronounced agglomeration of CNT, the oriented growth is random or unordered.

Figure 3 depicts the TEM micrographs of the samples M1 (a), M2 (b) y M3 (c). In all catalysts exist the characteristic tubular morphology of the CNT. In M1 the nanoparticles were well disperse on the CNT, with an average particles size from 3 nm to 8 nm. In M2 the nanoparticles were less disperse than M1 an average particles were bigger than M2, between 5 nm and 10 nm. In M3 the nanoparticles were bad disperse on the CNT, this is attributed to the low Pt load in the sample.

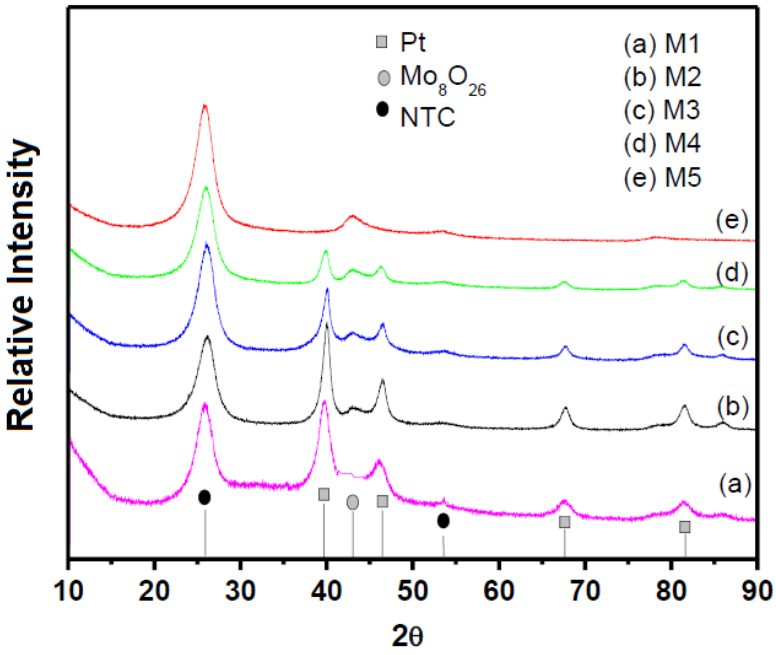

Fig. 1. Typical XRD patterns of PtyMox/CNT electro-catalysts with nominal Pt content of (a) 0:10, (b) 2:8, (c) 5:5, (d) 8:2 and € 10:0 wt.%

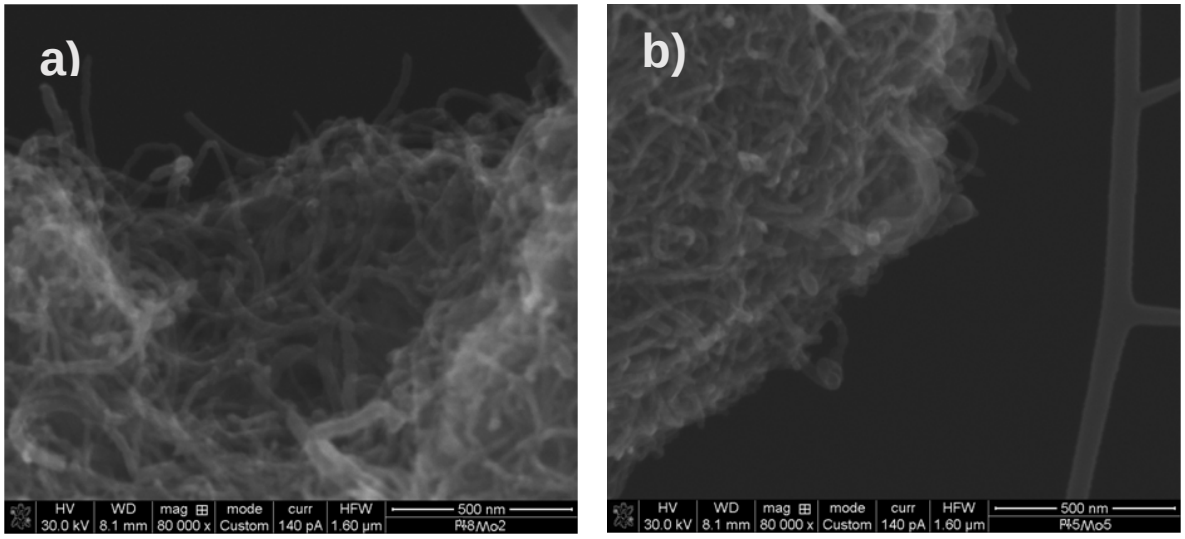

Fig. 2. SEM micrographs of the samples: (a) M2; and (b) M3

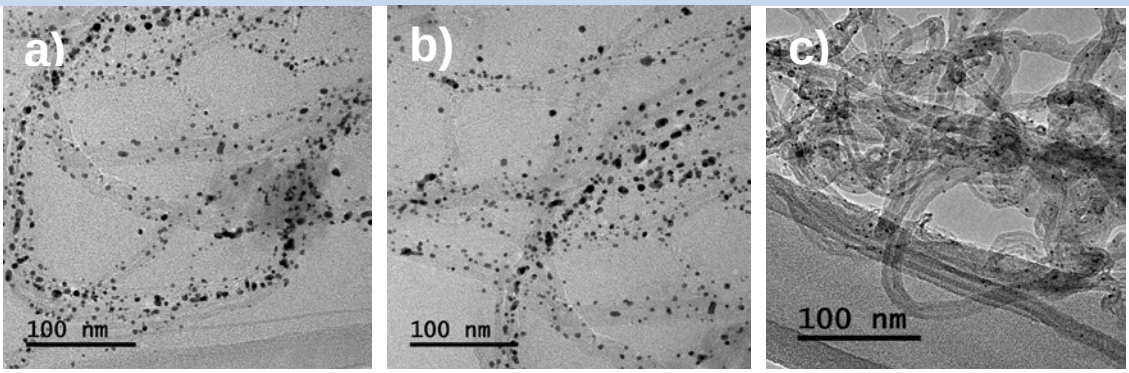

Fig. 3. TEM micrographs of the samples a) M1, b) M2 and c) M3

Figure 4 depicts the TEM image of the M2 electrocatalyst. This image reveals that Pt deposits consist of particles with a narrow size distribution uniformly distributed on the CNTs. The statistical analysis indicated that Pt nanoparticles have a size about 8 nm in diameter and M3 is about 10 nm.

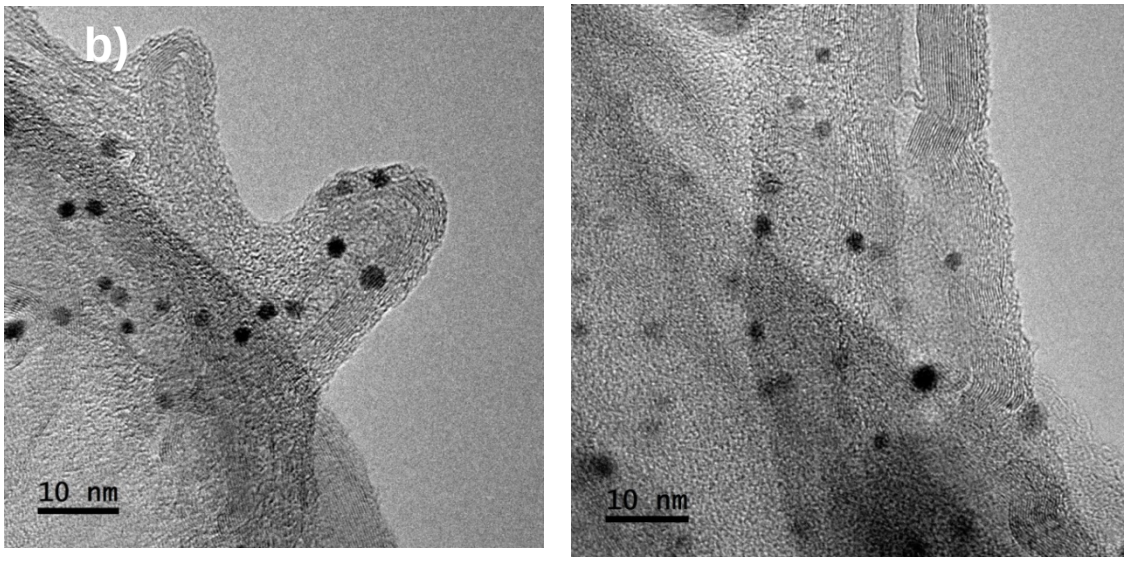

Fig. 4. TEM images of the M2 and M3 electro-catalysts.

Five PtyMox/CNT electro-catalysts were studied. The cyclic voltammetry characterization of electrodes prepared with these samples was performed in a nitrogen purged 0.5 M H_2SO_4 solution, at 50 mV s^{-1} scan rate. In this experiment, the electrodes were submitted to 2 cycles. Current density was normalized for a geometric area of 0.19 cm^2. Figure 5 (a) shows cyclic voltamograms of samples M1, M2, M3 and M4.

The M1, M2 and M3 electrodes present adsorption-desorption hydrogen region (Hupd) in a potential region of 0.0 V–0.3 V/NHE, which is characteristic in polycrystalline noble metals. The analysis at a more positive potential, corresponding to the anodic region, also shows a well-defined hydroxide-adsorbed peak. The cathodic scan shows the signal of reduction of the oxides formed during the anodic sweep. There is a slight difference in the current magnitude between M1 and M2, from TEM images, it was observed that M2 nanoparticles are more agglomerated than M1. On the other hand, M4 catalyst shows a striking difference in the current signal in all potential scan. This electrode presents a low electrocatalytic activity; we think it is due to the low load metal and distribution on the support decreases because platinum is coated with Mo compounds.

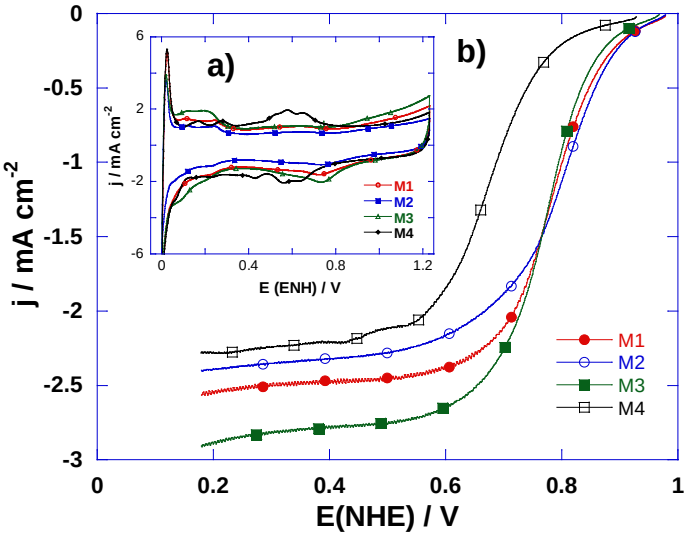

Fig. 5. (a) Cyclic voltammetry; and (b) lineal voltammetry of M1, M2, M3 and M4

Figure 5 (b) displays polarization curves of M1, M2, M3 and M4 samples at a rotating speed of 1600 rpm in 0.5 M H_2SO_4 at 298 in O_2-saturated electrolyte. Well-defined kinetic currents (0.85-0.95 V/NHE), mixed-diffusion limiting currents (0.85-0.70 V/NHE) and diffusion limiting currents (jL) (0.2-0.7 NHE) are observed in polarization curves M1, M2 and M3. There is a striking difference in M4 sample, all current profile is shifted to potential less positive which indicates low catalytic activity. It is considered to obtain the kinetic analysis, the overall measured current, j, can be expressed as being dependent on the kinetic current (j_K) , and the boundary-layer diffusion-limited current (j_L) which can be expressed in terms of the Koutecky-Levich equation (relationship between j-1 versus ω-1/2):

$$\frac{1}{j} = \frac{1}{j_K} + \frac{1}{j_L} = \frac{1}{j_K} + \frac{1}{B\omega^{1/2}} \qquad (1)$$

Where the diffusion-limited current can be expressed in terms of the Levich slope B, by:

$$j_L = 0.2nFD_{O_2}^{2/3}\nu^{-1/6}\omega^{1/2}C_{O_2} = B\omega^{1/2} \quad (2)$$

Where 0.2 is a constant term used when the rotation rate ω is expressed in revolutions per minute, Co is the oxygen solubility (Co =1.1 × 10^{-6} mol cm^{-3}), D is the oxygen diffusivity (Do=1.4 ×10-5 cm^2 s^{-1}), and ν is the kinetic viscosity of the electrolyte (ν = 1 × 10^{-2} cm^2 s^{-1}). In M1, M2 and M3 the oxygen reduction is fast enough that at high overpotentials a flat limiting plateau is observed. An explanation of the current plateau could be the distribution of the electrocatalytic sites on the electrode surfaces. It was considered that increases in the limiting current, M1 and M3, are associated with the increase of oxygen diffusion through the electrode surface when distribution of active sites is more uniform and the particles is smaller.

The inset in the Figure 6 show Cyclic voltammetry of M5, this profile indicate that exists an electrochemical stability but there is not catalytic activity and the whole signal possess an almost rectagular shape, as expected for a support electrode material.

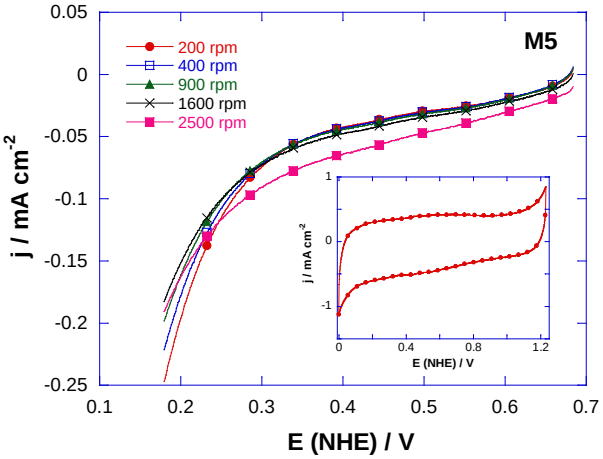

Fig. 6 a) Inset cyclic voltammetry and b) lineal voltammetry of M5

The mass transfer corrected Tafel plots deduced from the rotating disk electrode (RDE) measurements for the four catalysts are compared in Figure 7. Comparable Tafel-slope values between 90 and 120 mV dec^{-1} were obtained at low current density at 25 °C. These values indicated a mechanism where the first electron transfer rate Tafel is the determining step.

$$Pt\text{-}O2 + H+ + e- \rightarrow Pt\text{-}O2H \quad (3)$$

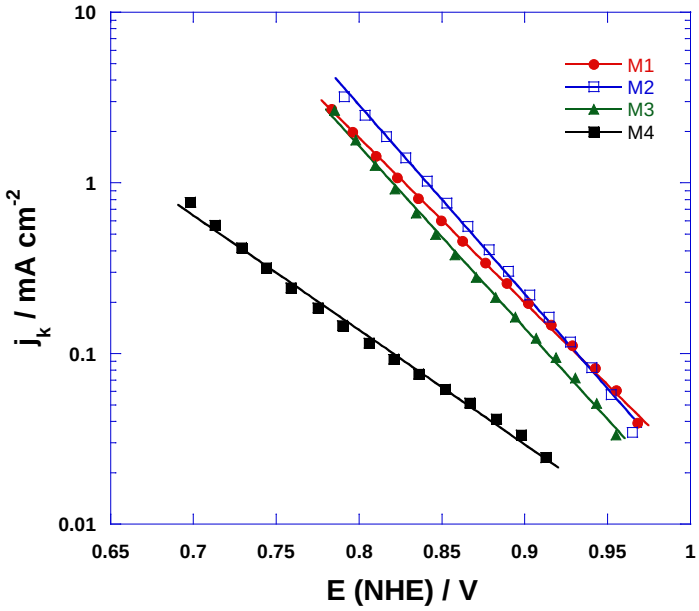

Fig. 7. Tafel slope of M1, M2, M3 and M4

If θ_i, the coverage with intermediates (Oads, O2ads, OHads), is ≈ 1, under Langmurian conditions (where coverage of oxide monolayer existed) the Tafel slope is measured as -60 mV dec^{-1}. If instead of $\theta_i \approx 1$ the other extreme is considered, $\theta i \approx 0$ (where electrode surface was oxide free) Tafel slope is -120 mV dec^{-1}. If θi is determined by a Temkin isotherm, in other words, for intermediate θ_i values, $0 < \theta_i < 1$ (where partial coverage of oxide species existed), Tafel slopes for the same mechanism are different. Under these conditions Tafel slopes can be between 60 and 120 mV dec^{-1}. For practical applications, it is preferable to work at a fixed current density (1 mA cm^{-2}) instead of using the value of the exchange current density due to the uncertainty of the real area of the ink type electrode but mainly in terms of the overpotential. Figure 5 (b) depicts also the corresponding potential attained at 0.1 mA cm-2, it is presented in Table 1.

Table 1. Electrochemical parameters of PtyMox/CNT electrocatalysts.

Catalizador	E_{ca} (V/ENH)	b (V dec^{-1})	α	j_0 (mAcm^{-2})	E V/NHE Current 1 mA cm^{-2}
M1	0.980	-0.102	0.57	$1.23x10^{-4}$	0.820
M2	0.983	-0.091	0.64	$5.58x10^{-5}$	0.840
M3	0.969	-0.097	0.60	$5.70x10^{-5}$	0.810
M4	0.930	-0.120	0.49	$6.87\ x10^{-5}$	0.670
M5	0.68	-	-	-	-

As it can be seen, M2 electrocatalysts have the higher potential at this current density and M4 catalyst had the less potential, so it would be considered as the worst from the four electrodes for the ORR in the acid electrolyte at 25°C. Thus, M2 sample (Pt_8Mo_2/NTC) exhibit higher catalytic activity for ORR in acidic medium. The enhanced reactivity of the catalysts surfaces is attributed to their electronic and geometric structure associated to the bifunctional effects, in which the unique catalytic properties of each of the elements in the catalytic compound combine in a synergetic manner to yield a surface which results more active than each of the elements alone. M2 contains lower Pt load, the Mo addition improves catalytic activity but in low percentages (2%) have to be integrated.

4. Conclusion

The electrocatalysts were synthesized by chemical reduction, SEM and TEM micrographs shows the characteristic tubular morphology of CNT, observing a no preferential orientation growth, with an average Pt particles size from 3 nm to 10 nm, M1 (Pt_{10}/NTC) showed the smaller particle size.

Electrochemical studies were performed by cyclic voltammetry and rotating disk electrode (RDE) techniques. Kinetic parameters exhibited Tafel slopes between 90 and 120 mV dec^{-1} and exchange current density of around 1×10^{-5} mA cm^{-2}. A four-electron reduction was found in all cases. The bests catalyst was M2 (Pt_8Mo_2/NTC).

The enhanced reactivity of the catalysts surfaces was attributed to their electronic and geometric structure associated to the bifunctional effects, in which the unique catalytic properties of each of the elements in the catalytic compound combine in a synergetic manner to yield a surface which results more active than each of the elements alone.

Acknowledgements

Authors thank CONACYT to the Programa de Redes Temáticas (RTH2) proyects 252003 and 249795; and IPN SIP multidisciplinary project 1683.

References

[1] Hassan A, Carreras A, Trincavelli J, and Ticianelli EA (2014) Effect of heat treatment on the activity and stability of carbon supported PtMo alloy electrocatalysts for hydrogen oxidation in proton exchange membrane fuel cells. J Power Sources. 247, 712–720.

[2] Higgins DC, Hoque MA, Hassan F, Choi J-Y, Kim B, and Chen Z (2014) Oxygen Reduction on Graphene–Carbon Nanotube Composites Doped Sequentially with Nitrogen and Sulfur. ACS Catal. 4, 2734–2740.

[3] Hu JE, Liu Z, Eichhorn BW, and Jackson GS (2012) CO tolerance of nano-architectured Pt-Mo anode electrocatalysts for PEM fuel cells. Int J Hydrogen Energy. 37, 11268–11275.

[4] Lebedeva NP and Janssen GJM (2005) On the preparation and stability of bimetallic PtMo/C anodes for proton-exchange membrane fuel cells. Electrochim Acta. 51, 29–40.

[5] Li DJ, Maiti UN, Lim J, Choi DS, Lee WJ, Oh Y, Lee GY, and Kim SO (2014a) Molybdenum Sulfide/N-Doped CNT Forest Hybrid Catalysts for High- Performance Hydrogen Evolution Reaction. Nano Lett. 14, 1228–1233.

[6] Li Q, Cao R, Cho J, and Wu G (2014b) Nanocarbon Electrocatalysts for Oxygen Reduction in Alkaline Media for Advanced Energy Conversion and Storage. Adv Energy Mater. 4, 1301415–1301434.

Chapter 8.6. Impedance study of the electrocatalytic reduction of oxygen on Pt/C and Pt-Ag/C

B. Ruiz Camacho[a,*]; E. Romero Mendoza[b]; J.C. Baltazar Vera[a]; R. Fuentes Ramírez[a]; O. Martínez Alvarez[b]

[a]Departamento de Ingeniería Química, Universidad de Guanajuato, División de Ciencias Naturales y Exactas, Noria Alta s/n, Col. Noria Alta, Guanajuato, Gto, 36050, México
[b]Ingeniería en Energía, Universidad Politécnica de Guanajuato, Av. Universidad Norte s/n, Juan Alonso Cortázar Guanajuato, 38483, México

ABSTRACT

Nanoparticles of Pt and Pt-Ag were synthesized using sonication at room temperature with no consecutive thermal treatment to catalyze the acid oxygen reduction reaction (ORR) at room temperature. The metal nanoparticles obtained were supported on carbon Vulcan substrate. The electrochemical impedance spectroscopy (EIS) at different potentials was used for study the mechanism reaction and the kinetic of ORR on Pt and Pt-Ag nanosized electrodes in acid electrolyte. The physical properties, morphology and crystallinity of the electrocatalysts synthesized were investigated by X-ray Diffraction (XRD) and Transmission Electron Microscopy (TEM) analysis. The kinetic of the silver and platinum nanoparticles in solution was followed using UV-vis spectroscopy. The ORR was analyzed in acid medium at room temperature. Both materials synthesized shows a nanoparticle size of < 10 nm, however the Pt/C monometallic sample exhibit more significative aggregation than Pt-Ag/C catalyst. Pt-Ag/C exhibit better electrochemical properties to catalyze the ORR compare to Pt/C. The analysis of the impedance diagrams of both materials tested revealed at least the presence of two-electron reaction process involved in the reduction reaction depending of the potential applied.

Keywords:EIS, Ultrasound, Oxygen reduction, Platinum, Silver

1. Introduction

The electrochemical impedance spectroscopy (EIS) technique has been extensively used to obtain information about oxygen reduction mechanisms. EIS has the advantage of making it possible to separate different rate process in the studied frequency domain, so it is an efficient tool to determine the main processes involved in the reaction [1-2]. It is know that oxygen reduction reaction (ORR) is the determining step in the global electrochemical

---

* Author for correspondence:
Beatriz Ruiz Camacho, +524737320006 ext. 8115, beatrizruizcamacho@gmail.com

process of the fuel cell.

According to Damjanovic, the model of ORR mechanism over Pt nanostructure in acid medium is a multi-electron reaction where the H_2O_2 formed during the ORR deteriorates the materials inside the PEMFC [3-5]. Therefore it is important to detect and evaluate the different mechanism and kinetic parameters of H_2O_2 formation, mainly in new materials proposed as electrocatalysts.

Recently a series of nanostructured Pt alloys with low Pt loadings have been investigated for ORR showing good catalytic properties, for example PtCuAg [6], PtPdAg [7] and PtAg [8]. Several investigations have been demonstrated that the use of silver (Ag) nanoparticles as electrode for ORR has shown similar mechanisms and kinetics for ORR catalysis than Ag showing an efficient four-electron reduction and higher tolerance toward methanol poisoning than Pt [9-10].

A variety of methodologies for synthesis nanoparticles of Pt and Ag have been reported as thermal process, photochemical, electrochemical, chemical reduction [11], etc. However, in most of them, thermal treatments, stabilizers or more than one reactive step is required [12]. In this sense sonochemical is proposed as an alternative method for synthesis of nanoparticles in aqueous solutions. In the present work the objective was to synthesize Pt-Ag nanoparticles using a simple methodology with no thermal treatment or stabilizing agent, and to investigate their catalytic activity and stability for the ORR. The mechanism of the ORR was investigated by EIS.

2. Materials and Methods

2.1 Electrocatalyst preparation

Pt and Pt-Ag nanoparticles were synthesized by ultrasound methodology. Carbon Vulcan XC72 was used as support of Pt and Pt-Ag. The hexachloroplatinic acid ($H_2PtCl_6.6H_2O$) and silver nitrate ($AgNO_3$) was the metal precursors. Ethanol was used as scavenger agent. All the sonication experiments were made in nitrogen atmosphere. For the synthesis of Pt/C, an alcohol solution of Pt precursor was sonicated for 5 h with an ultrasonic bath (42 kHz). After that, Pt supported on carbon was obtained by the addition of carbon Vulcan to the solution (10 wt. % Pt/C). This suspension was sonicated during 1 h. The solvent was removed by evaporation in an oven at 100°C for 2 h. In the case of the synthesis of Pt-Ag nanoparticles it was made with a sequential reduction methodology. First, an alcoholic solution of Ag precursor was sonicated for 3 h. Then, the Pt solution was mixing with the first solution and sonicating for 4 h. After that, carbon Vulcan was added to the solution and finally the solution was evaporated and dried (10 wt. % Pt-Ag/C).

2.2 Electrochemical characterization

The electrochemical characterization of the Pt/C and Pt-Ag/C was carried out by cyclic and EIS techniques using a potentiostat/galvanostat Gamry Instruments reference 3000 and a RDE710 rotation speed controller. A platinum mesh was used as the counter electrode, and a standard saturated calomel electrode (SCE=0.24V) as reference electrode. The potentials in this paper were related to the normal hydrogen electrode (NHE). Glassy carbon disk with a cross-sectional area of 0.196 cm^2 was used as a support for the thin films

and used as an ink-type working electrode. The catalytic ink was prepared with 1 mg of catalyst, 25 μL of 5 wt% solution Nafion® (Du Pont, 1100 EW) and 125 μL of ultrapure water. 10μL of this sonicated mixture were deposited on glassy carbon electrode. Cyclic voltammetry (CV) at 50 mV s^{-1} was performed in a nitrogen-saturated electrolyte to clean the electrode surface, from 0.05 to 1.2 V/NHE in acid medium (0.5 M H_2SO_4). The electrical impedance spectra results were obtained after the application of a potential step (E) of 180 s. During EIS experiments, the working electrode was rotated at 1000 rpm. The values of the E applied were 0.4-0.9 V/NHE. The amplitude of the ac signal perturbation was 10 mV. The frequency rang scanned was from 100 kHz to 10 mHz.

2.3 Physical characterization

The crystalline structure of the Pt/C and Pt-Ag/C catalysts was obtained by recording their X-ray diffraction (XRD) patterns on a Miniflex (Rigaku) equipment using a Cu anode (Kα, λ=1.5406 Å) and a Bragg-Brentano configuration. Particle size and morphology of samples were obtained with a high resolution transmission electron microscopy (TEM) using a TEM JEOL 1010 field emission operated at 80 kV.

3. Results and Discussion

Fig. 1 exhibits the CV curves of Pt/C and Pt-Ag/C catalysts in N_2 saturated 0.5 M H_2SO_4. CVs were performed to clean the electrode surface obtained after 20 cycles from 0.05 to 1.2 V/NHE in H_2SO_4 electrolyte at 50 mV s^{-1}. The curves of the bimetallic sample are compared at 1^{st}, 2^{nd} and 20^{th} cycles shown in the insets. Fig. 4(a) shows that after 20 cycles in acid medium, Pt-Ag exhibit similar electrochemical characteristics as Pt synthesized by ultrasound with different intensity of current density. Nevertheless, as can be seen in the inset of Fig. 4 the three initial CV cycles of Pt-Ag/C exhibit an anodic peak associated to the oxidative dissolution/leaching of Ag that decayed rapidly with increasing number CV.

In short a comparison of the ORR electrochemical activity of catalysts synthesized at 900 rpm obtained in acid electrolytes is presented in Fig. 5. In H_2SO_4 electrolyte, Pt-Ag/C sample exhibit an ORR half-wave potential of 80 mV higher compared to Pt/C Etek sample. It is worth to notice that Pt-Ag/C also shows the smallest over potential compared with Pt/C synthesized and commercial. Also, at the same rotation rate of 900 rpm, the limiting current density of Ag-Pt/C is lower that Pt/C samples (synthesized and commercial).

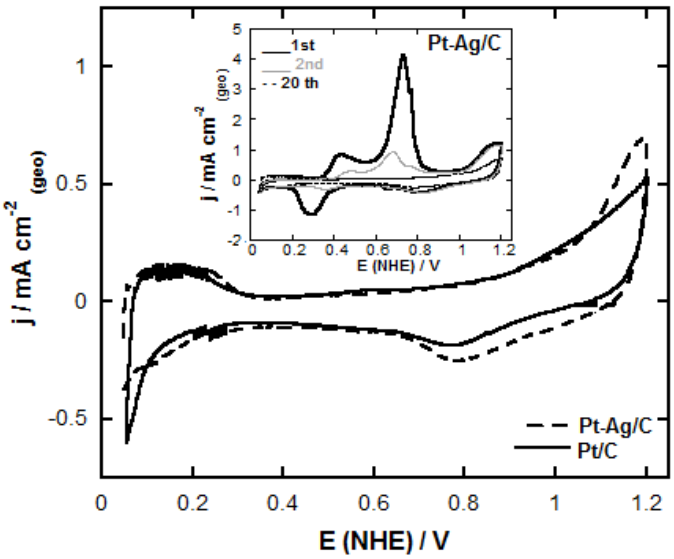

Fig. 1. Cyclic voltammograms of Pt/C and Pt-Ag/C samples synthesized by ultrasound in N_2 saturated 0.5 M H_2SO_4. The curves comparison of 1st , 2nd and 20th cycles of bimetallic sample is shown in the insets. Scan rate of 50 mV s^{-1} at 25°C.

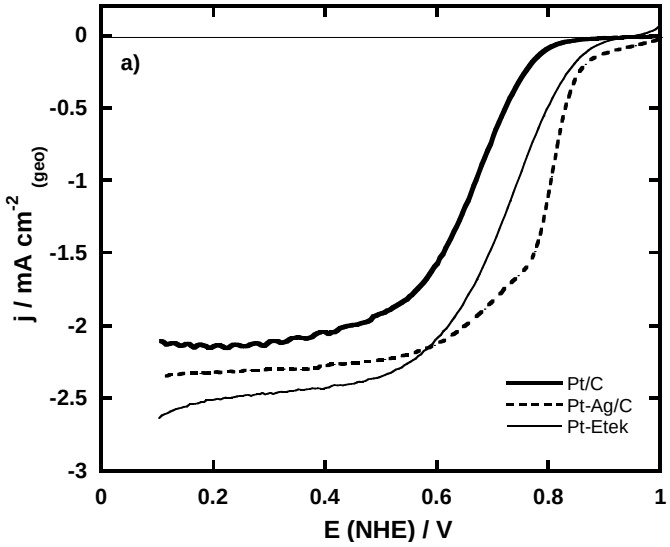

Fig. 2. Linear sweep voltammograms of Pt/C and Pt-Ag/C samples synthesized by ultrasound in O_2-saturated 0.5 M H_2SO_4 compared to Pt Etek sample. Scan rate at 5 mV s^{-1} at 25°C.

Fig. 3 represents typical Nyquist plots obtained at different potentials for ORR on a) Pt-Ag/C and b) Pt/C. The impedance diagrams show two behaviors depending on potential, associated with the directly and indirectly mechanism of the ORR. In this investigation, two catalyst synthesized (Pt-Ag/C and Pt/C) follows both ORR mechanisms. Nyquist diagrams

show only one loop at E>0.6 V / NHE related with a time constant of a single process of reduction of oxygen to water: $O_2+4H^++4e^-\leftrightarrow 2H_2O$. In contrast, Fig 3 shows that the Nyquist results exhibits two loops at E<0.6 V that corresponds to the two processes of the oxygen reduction, one first time constant can be related with the via 2-electrons to form H_2O_2; and the second time constant can be associated with a second process, presumably the reduction of H_2O_2 to H_2O formation [5].

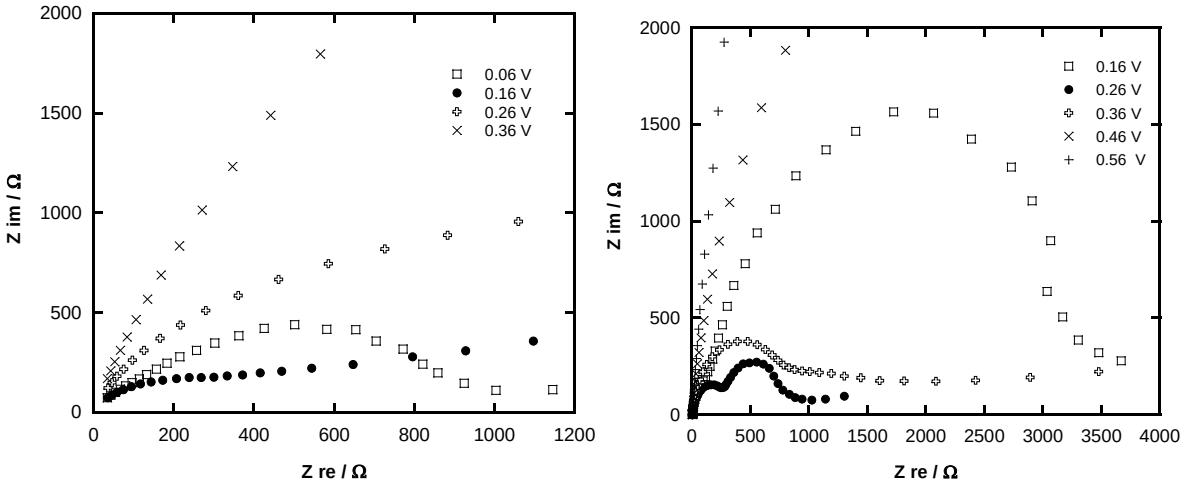

Fig. 3 Nyquist diagrams for ORR on Pt-Ag/C and Pt/C in oxygen saturated solution of 0.5 M H_2SO_4 using different potentials: 0.4, 0.5, 0.7 and 0.9 V/NHE. Frequency of 10 mHz-100 kHz. T= 25°C.

In order to obtain quantitative information from impedance spectra, one electric circuits was employed (Fig. 4) to fit the curves allowed for the resistance and the capacitance evaluation. The electrical circuit was use to simulate the impedance response at different potentials The R_s correspond to the solution resistance, R_{CT1} is the charge transfer resistance of the reduction process from O_2 to H_2O.. CPE_1 are the constant phase elements related with the capacitance of the double layer (C_{dl}) and the capacitance of all the adsorbed species, respectively.

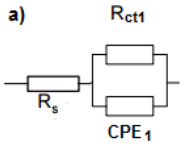

Fig. 4 Electric circuit employed to simulate the impedance response

The physical properties, morphology and crystalline of the electrocatalysts synthesized were investigated by X-ray Diffraction (XRD) and Transmission Electron Microscopy (TEM) analysis. Fig. 5 exhibit the XRD patters and TEM images of Pt/C and Pt-Ag/C catalyst. Both materials synthesized shows a nanoparticle size of < 10 nm, however the Pt/C monometallic sample exhibit less significant aggregation than Pt-Ag/C catalyst with

better dispersion onto the carbon. Both materials synthesized exhibit the faces crystallographic of platinum. Silver peaks in XRD results were not identified suggesting a low detection of the equipment due to the amorphous material obtained during the synthesis.

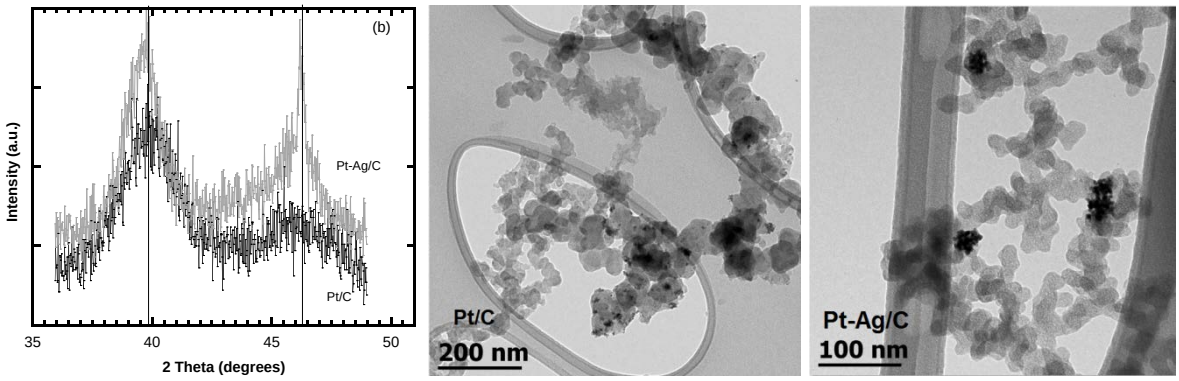

Fig. 5 XRD and TEM images of Pt/C and Pt-Ag/C catalysts synthesized by ultrasound.

4. Conclusion

Pt and Pt-Ag nanoparticles were synthesized following the sonication method. The kinetic parameters obtained show us that Pt-Ag/C has more electrochemical activity for the ORR compared to the Pt/C synthesized.

EIS results of materials synthesized exhibit one first time constant of impedance spectra associated to the reduction process from O_2 to H_2O. The values of charge transfer resistance obtained from the impedance study were used to determine the kinetic parameters of the ORR on Pt and Pt-Ag.

Acknowledgements

We thank to CONCYTEG project (119/2015) and Universidad de Guanajuato (001/2015) for its financial support of this work. Also thanks to the SMH and XV International Congress of the Mexican Hydrogen Society.

References

[1] F. Kuang, D. Zhang, Y. Li, Y. Wan, B. Hou, J. Solid State Electrochem. 13 (2009) 385.
[2] M.J. Escudero, A. Aguadero, J.A. Alonso, L. Daza, J. Electroanal. Chem. 611 (2007) 107.
[3] K. Kinoshita, Electrochemical Oxygen Technology, Wiley-InterScience Publication, New York, 1992.
[4] A. Damjanovic, M.A. Genshaw, J.O.M. Bockris, J. Chem. Phys. 45 (1966) 4057.
[5] G. Vázquez-Huerta, G. Ramos-Sánchez, A. Rodríguez-Castellanos, D. Meza-Calderón, R. Antaño-López, O. Solora-Feria, J. Electroanal. Chem. 645 (2010) 35.
[6] Y. Zhou, D. Zhang, J. Power Sources 278 (2015) 396.
[7] I.E. Pech-Pech, D.F. Gervasio DF, J.F. Pérez-Robles, J. Power Sources 276 (2015) 374.
[8] F. Yuan-Yuan, Z. Gui-Rong, M. Jun-Hong, L. Gang, X. Bo-Qing. Phys. Chem. Chem. Phys. 13 (2011) 3863.

[9] F.W. Campbell, S.R. Belding, R. Baron, L. Xiao, R.G. Compton, J. Phys. Chem. 113 (2009) 9053.
[10] Y. Lu, Y. Wang, W. Chen, J. Power Sources 196 (2011) 3033.
[11] H. Ma, B. Yin, S. Wang, Y. Jiao, W. Pan, S. Huang, S. Chen, F. Meng, Chem.Phys. Chem. 5 (2004) 68.
[12] C. He, L. Liu, Z. Fang, J. Li; J. Guo, Ultrason Sonochem. 21 (2014) 542-548.

Chapter 8.7. Selective heterogeneous nucleation of Platinum nanoparticles onto graphitic domains of multi-walled carbon nanotubes

C.A. Campos-Roldán[1,2,3], R.G. González-Huerta[1*]; J.R. Vargas-García[2], N. Alonso-Vante[3]

[1]ESIQIE-IPN Laboratorio de electroquímica y corrosión, UPALM 07738, México D.F., México
[2]Depto. Ing. Metalúrgia y Materiales, Instituto Politécnico Nacional, México 07300 D.F., México
[3]IC2MP, UMR-CNRS 7285, University of Poitiers, 4 rue Michel Brunet, 86022 Poitiers, France

ABSTRACT

The strong interaction between extended graphitic domains of multi-walled carbon nanotubes (MWCNTs) and platinum nanoparticles (Pt NP's) was investigated. Three different chemical treatments were performed on pristine home-made MWCNT to modify the graphitic domains, as revealed by Raman spectroscopy, whose analyses indicated the development of sp^2 character. The integrated G band intensity becomes higher and narrower than the integrated D band intensity.

Pt NP's were photo-deposited using UV-VIS light onto modified MWCNTs. The effect of the strong interaction on the electronic properties of Pt NP's was electrochemically probed by CO stripping. We can appreciate the CO oxidation multi-peak signals. A correlation between the in-plane crystallite size (L_a) of the carbon supports, and the oxidation charge of CO stripping experiments was made. Analyses of the CO oxidation revealed the presence of two peaks centered at 0.63V and 0.66V. We found that 80% of the electrochemical active surface area (*ECSA*) of the photo-deposited electrocatalyst correlates well with the highest L_a and belongs to the peak centered at 0.63V, whereas this parameter at the same electrode potential decreases as L_a decreases. Parallel with that observation, *ECSA* at 0.66V increases as the support possesses a high sp^3 character. This interaction results from the heterogeneous nucleation of Pt NP's onto the carbon support domains. It appears that π-system of graphitized carbon anchors Pt NP's in a way that strongly modifies the electronic properties of the Pt valence band.

Keywords: Carbon Nanotubes, Pt nanoparticles, CO oxidation, Oxygen Reduction Reaction

1. Introduction

Carbonaceous materials has been widely applied in electrochemical systems as support material for electrodes since their special properties, remarking their electrochemical active

---

* Author for correspondence:
Rosa de Guadalupe González Huerta, (+52) 55 57296000 ext 54246, rosgonzalez_h@yahoo.com.mx

surface, which make them a proper choice to many applications. On the other hand, since carbon nanotubes (CNT) were discovered, they have drawn attention intensively due to their excellent properties, such as high specific surface area, high electronic conductivity, outstanding chemical and electrochemical stability and so on [1-5]. Recently, CNT have received considerable attention as the supports of noble metal catalysts in heterogeneous catalysis, such as PEM fuel cells. The interaction between noble metal nanoparticles and CNT in nanohybrids induces a peculiar microstructure or modification of the electron density of the noble metal clusters, and enhances the catalytic activity [1].

The change of electronic properties of nanosized materials can be related to the degree of interaction with the substrate. Strong interactions between platinum clusters and highly oriented pyrolitic graphite (HOPG), CNT and XC-72 carbon black substrates have also been studied and recently explained by the possible formation of non-bonding π electronic states of graphite due to Pt-C hybridization [6]. This interaction seems responsible for lowering the adsorption energy of CO on Pt clusters and, therefore, leads to a weakening of the Pt-CO bond [6]. Metal/substrate interactions can be actually studied by examining the adsorption behavior of CO when it is used as a molecular probe.

2. Experimental

2.1. Chemicals

For this work, $Na_2PtCl_6{\cdot}6H_2O$ and $H_2PtCl_6{\cdot}6H_2O$ from Alfa-Aesar, CH_3COONa from Sigma-Aldrich, metanol and isopropanol from Sigma-Aldrich, Vulcan XC-72 from Cabot, and home-made Pristine multi-walled carbon nanotubes (CNT) were used. CNT were synthetized by conventional Chemical Vapor Deposition (CVD) technique. Then, CNT were functionalized with concentrated HNO_3 (f_N-CNT) as reported previously [7]. Finally, CNT were exfoliated (*e*-CNT) as reported previously [8].

2.2. Catalyst synthesis by Carbonyl Chemical Route

Pt-carbonyl complexs were synthesized by using metanol as a solvent through the reaction of Pt under CO atmosphere at 55ºC for 24 hwith constant stirring. After that, support material (Vulcan, CNT, f_N-CNT, f_{N+S}-CNT or *e*-CNT) were added to the carbonyl complex solution under N_2 atmosphere for 12 h in order to obtain a catalyst with 20 wt % loading onto the support. The solvent was evaporated and resulting powder was washed out with Milli-Q water and filtering in vacuum. The powder recovered was dried overnight. Finally, the resulting catalyst was heat-treated at 200ºC for 1 h under H_2.

2.3. Catalyst synthesis by Photodeposition

Support material (Vulcan, CNT, f_N-CNT, f_{N+S}-CNT or *e*-CNT) was mixed in N_2-saturated Milli-Q wáter in a photoreactor provided with an optical quartz window. A isopropanol solution containing $H_2PtCl_6{\cdot}6H_2O$ was added into the photoreactor and stirred for 3 h under UV light (Xe lamp, 159 W). Visible and infrared light was filtered out by a hot mirror UV, while a wáter filter (long-pass filter GG40) was used to prevent heating of

the samples. After the radiation time, the resulting powder was wash out with Milli-Q water, filtered in vacuum and dried overnight.

2.4. Characterization

2.4.1. Raman Spectroscopy. Raman spectra were obtained using a Horiba Jobin Yvon Spectrometer HR 800 with a laser of 532 nm in the range of 100-3100 cm^{-1}. Deconvolution analyses were done by using Fityk software.

2.4.2.Transmission Electron Microscopy. A High Resolution Transmission Electron Microscope (HRTEM) JEM 220FS was used to observe CNT morphology. Samples were prepared by suspending CNT into isopropyl alcohol, by using ultrasound during 15min. Then, an aliquot was impregnated on a copper grid. Finally, the samples were dried at room temperature.

2.4.3. Electrochemical Measurements. The catalytic ink was prepared as follows: a mixture containig 5 mg of catalyst (powder) and 3 mL of stock solution (20% isopropanol, 0.4% Nafion Sigma-Aldrich and 79.6% Mili-Q water) was dispersed for 30 min. Then, 3 μL of the mixture was dropped onto a glassy carbon electrode (geometric area of 0.0707 cm^2) and dried at room temperature. The electrochemical measurements were carried out at 25ºC by using a potentiostst (Autolab PGSTAT 30) in a typical three-electrode cell. The electrolyte was 0.1 M $HClO_4$. A Pt mesh and a reversible hydrogen electrode (RHE) were respectively used as counter and reference electrode. All the potentials in this work were reported respect RHE.

3. Results and Discussion

Raman spectra in the region of 800-2000 cm^{-1} of Carbon Vulcan, pristine multiwalled carbon nanotubes (CNT), nitric acid functionalized multi-walled carbon nanotubes (f_N-CNT) and exfoliated multi-walled carbon nanotubes (*e*-CNT) substrates are reported in Figure 1, and the inserts correspond a TEM image of every material.

It is possible to observe the typical features of carbonaceous materials, however, in this spectral region, there are overlapping bands. The typical *D* and *G* signals of MWCNT in the range for 800-2000 cm^{-1} are observed at *c.a.* 1350 cm^{-1} and *c.a.* 1580 cm^{-1} respectively [9-11].

Vulcan shows a high intensity and width of its *D* band, therefore this material posses a high degree of interstitial disorder along the *c*-axis between the crystallite planes [12]. Additionaly, it is well-known that the morphology of Vulcan is amorphous (see insert in Fig. 1). For CNT is posible to observe an amorphous carbon layer onto the surface of MWCNTs (see TEM image in Fig. 1). This amorphous carbon, added to disorder between crystalline planes, grants a considerable value of its *D* band intensity and width.

It is evident that crystalline quality of carbon sample after functionalization (f_N-CNT) becomes higher, due to both intensity and width of its *D* band are the smallest among

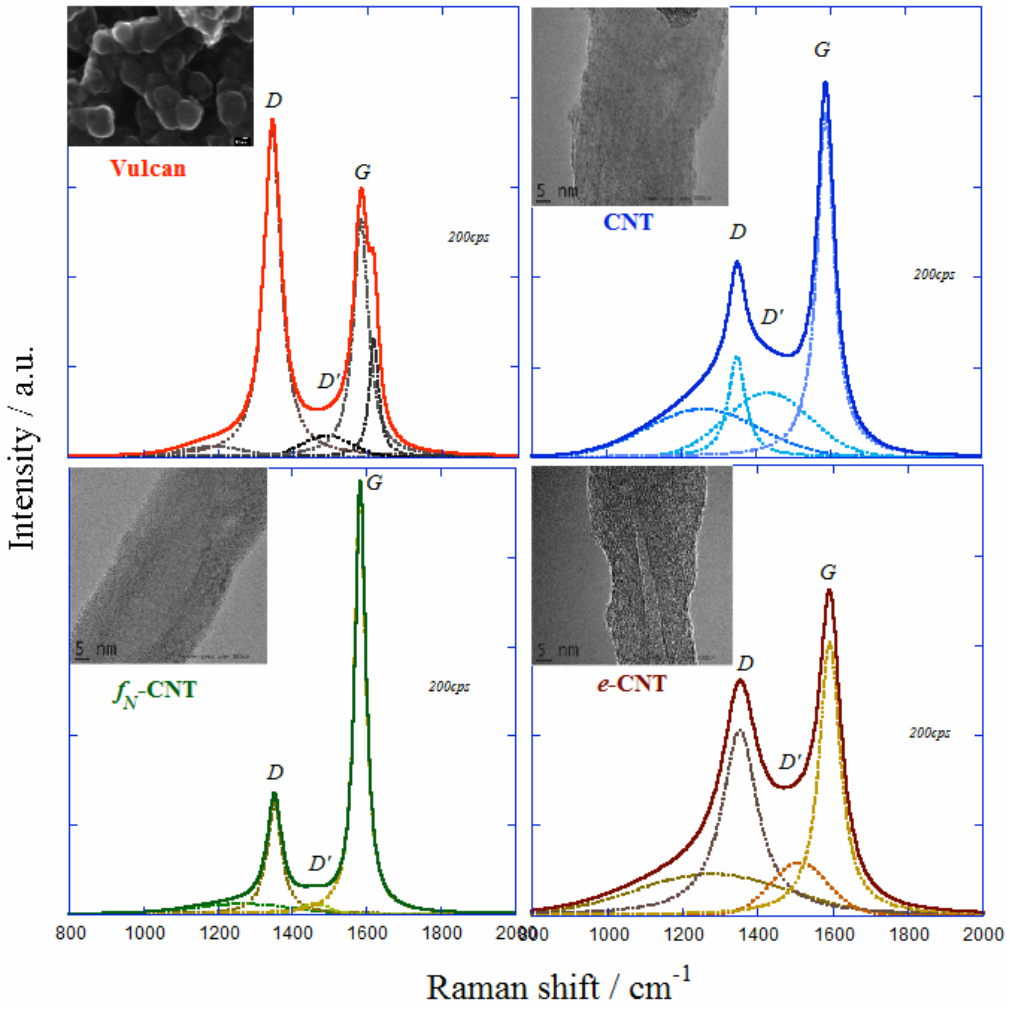

Fig. 1. Raman Spectra of Vulcan, CNT, f_N-CNT and e-CNT, recorded at λ_{laser}=532nm, from 800cm^{-1} to 2000cm^{-1}

materials under study. We can appresiate an ordered surface, without amorphous carbon (see TEM image in Fig. 1). Interestingly, *G* band becomes narrower and more intense after functionalization, suggesting an increment of sp^2 character of CNT. Finally, *e*-CNT granted a higher sp^3 character comparing to CNT. TEM image reveled a surface with a high defects density, which is the reason of the increment of intensity and width on its *D* band.

Deconvolution analysis was carried out by using Lorentzian line shapes for *D* and *G* bands, whereas Gaussian ones were used to fit the *D'* band as well as the band centered at *c.a.* 1200 cm^{-1} [6]. By deconvolution analysis (dotted lines), *D'* band (*c.a.* 1450 cm^{-1}) is well-defined from *D* band. Both signals are related to defects onto MWCNTs surface. For carbonaceous materials, it is possible to quantify the degree of graphitization by evaluating the *D* and *G* integrated intensity ratio ($I_{D/G}$). This ratio is commonly used to quantify the

amount of defects in the material as well as their in-plane crystallite size (L_a), which is a measure of the interdefect distance, using Equation 1 [6]:

$$L_a = 2.4x10^{-10}\ \lambda^4_{laser}\ \frac{I_G}{I_D} \qquad (1)$$

where λ_{laser} is the laser wavelength and I is the integrated intensity of the corresponding band. Table 1 summarizes the data for *D* and *G* bands from deconvolution analysis. From Table 1, f_N-CNT presents the highest value of L_a, therefore, the longest crystallite size. Whereas the graphitic structures of Vulcan, *e*-CNT and CNT, respectively, posses a high degree of interstitial disorder, that means, those materials do not possess extended graphitic domains.

Table 1. Raman Spectra analyses of Vulcan, CNT, f_N-CNT and e-CNT

	ω_D (cm^{-1})	ω_G (cm^{-1})	$I_{D/G}$	L_a (nm)
Vulcan	1350	1590	1.8027	10.66434
CNT	1349	1586	0.8923	21.54474
f_N-CNT	1353	1584	0.3663	52.47821
e-CNT	1353	1592	1.5051	12.77224

Figure 2 shows the CO-stripping voltammograms obtained from Pt photo and chemi-impragnated onto Vulcan, CNT, f_N-CNT and *e*-CNT.

We can appreciate the main CO oxidation potential region at *0.63V< E <0.80V*, leading to multi-peak perfil. Moreover, the shape of the CO stripping voltammograms is affected by the chemical nature of the carbon material used as support.

For all catalyst synthesized by Photodeposition (*PD*), it is observable three different signals: at *c.a.* 0.40V is visible a prepeak, and two peaks centered at *c.a.* 0.66V and 0.75V. The appearance of the prepeak suggest the oxidation of the CO molecules adsorbed on step sites, and of a small amount of CO molecules diffusing from the terraces to these sites, due to the different facets and defects of Pt nanoparticles [15-18].
Whereas the peak centered at *c.a.* 0.66V and *c.a.* 0.75V could be the result of two different interactions sites between Pt and carbon supports. Interestingly, the Electrochemical Active Surface (*EAS*), define as:

$$EAS = \frac{Q}{420\ \mu C\ cm_{Pt}^{-2}} \qquad (2)$$

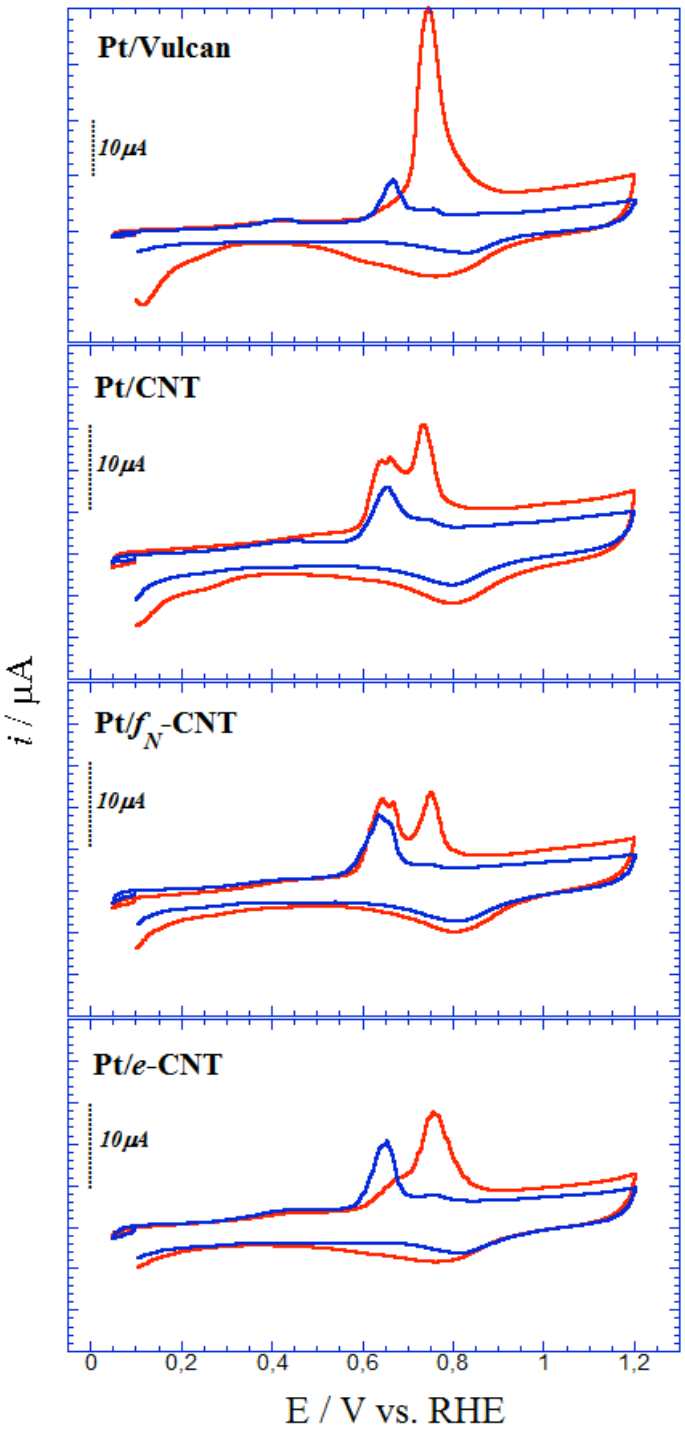

Fig. 2. CO stripping in 0.1M $HClO_4$, at 25ºC, at 5mV s^{-1}, for Pt/Vulcan, Pt/CNT, Pt/f_N-CNT and Pt/e-CNT, synthetized by Carbonyl Chemical Route (red line) and Photodeposition (blue line)

(where *Q* is the integrated intensity of the CO oxidation peaks) in all materials under study, the *EAS* of the peak centered at *c.a.* 0.66V is higher than the one centered at *c.a.* 0.75V, suggesting a selective nucleation of Pt nanoparticles onto a specific domain of carbon substrate [13-14].

Analyzing the catalyst Pt/Vulcan prepared by Carbonyl Chemical Route (*CCR*), is possible to observe the typical interaction between Pt and Vulcan, leads to a main peak centered at *c.a.* 0.75V, whereas catalyst supported on MWCNT prepared by *CCR* present two sucessive CO oxidation peaks, located at *c.a.* 0.66V and *c.a.* 0.75V. Interestingly, the *EAS* of both peaks depends on the crystalline degree of the carbon surface, determinated by their in-plane crystallite size (L_a). Figure 3 shows the dependence of the *EAS* in every peak of the voltammogram *vs.* L_a.

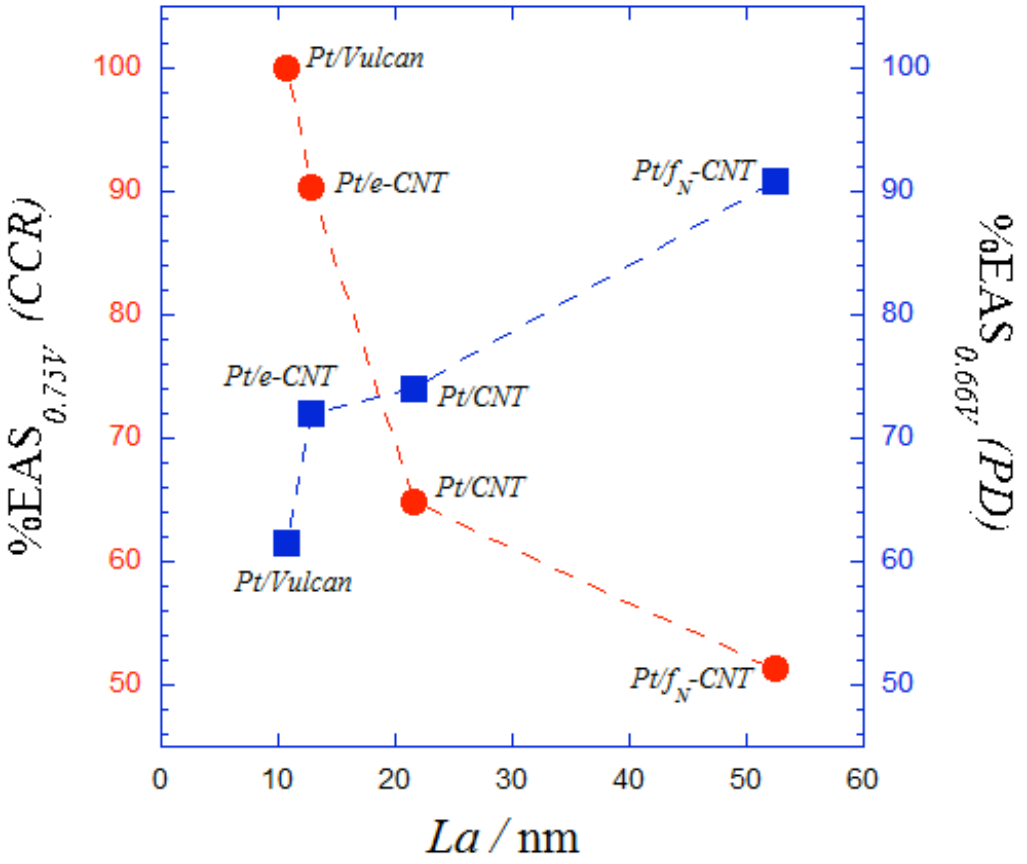

Fig. 3. %EAS at 0.75V of catalyst synthetized by Carbonyl Chemical Route (red line) and %EAS at 0.66V of catalyst synthetized by photodeposition (blue line) vs. in-plane crystallite size of support material

Table 2. Comparison between %EAS (at 0.66V and 0.75V) with the In-Plane Crystallite Size (La) for the catalyst prepared by Carbonil Chemical Route (CCR) and Photodeposition (PD)

	$\%EAS_{0.66V}$ (CCR)	$\%EAS_{0.75V}$ (CCR)	$\%EAS_{0.66V}$ (PD)	$\%EAS_{0.75V}$ (PD)	L_a (nm)
Pt/Vulcan	0	100	61.50	30.20	10.66434
Pt/CNT	32.60	64.79	74.04	20.95	21.54474
Pt/f_N-CNT	51.33	48.66	90.86	5.29	52.47821
Pt/*e*-CNT	7.74	90.39	72.05	18.95	12.77224

It is clear that the higher sp^3 character (defect density on the surface), the higher *EAS* at 0.75V; and the higher sp^2 character (ordered carbon domains), the higher *EAS* at 0.66V. Table 2 summarizes the ratio of *EAS* at 0.66V and the total *EAS* as a function of L_a. From the data shown in Table 2, it is evident that the *EAS* at 0.66V increase as L_a becomes higher, i.e., when the long-distance order increases in the graphitized structure. Therefore, the down-shift potential observed in the materials supported on MWCNT in CO stripping voltammograms could be related to the interaction of Pt nanoparticles with well-ordered graphitic domains. In adddition, *CCR* method allows a random nucleation on different domains, due to the peaks centered at *c.a.* 0.66V and *c.a.* 0.75V appears, whereas *PD* method exhibit a preferential nucleation of Pt onto sp^2 domains, thus UV light has an effect in the interaction Pt-graphitic domains, however, this interaction is not entirely understood.

Though this interaction is not well-understood, some explanations can be given. It is possible that, as a result of the Pt−C interaction, a strong decrease in Pt−Pt bond distance takes place. This can be favored during the heterogeneous nucleation and further growth of platinum particles onto the surface of the carbon support which may be responsible for the increase of the overlapping of *d*-orbitals by strongly increasing *d*−*d* interactions between Pt atoms as occurring in gold. As a result of the contraction phenomenon, a *d*-band movement, away from the Fermi level, is possible. Consequently, the interaction between the adsorbate states and metal valence band states can be strongly modified leading to changes in the interaction energy. Additionally, the adsorption phenomenon of CO at the Pt surface is accompanied by back-donation of Pt *d*-orbital into the unoccupied $2\pi^*$-orbital of CO. As a result of such interaction, between Pt and well-ordered graphitized domains, it is possible that the charge transfer occurs from Pt to C (according to the respective electronegativities of the elements) leading to a decrease in the *d*-orbital back-donation and consequently to a weakening of the Pt−CO bond [6].

4. Conclusion

After two different chemical treatments, CNT surface becomes more crystalline (functionalization) and less crystalline (exfoliation), obtaining opposite dominant carbon domains onto the surface.

By a chemical impregnation (CCR), CO stripping measurements reveled a randomly nucleation of Pt nanoparticles, however, by photodeposition method, we observed a preferential nucleation of Pt nanoparticles onto sp^2 domain of MWCNT, due to the higher

ECSA calculated from the main peak centerd at 0.68 V vs. RHE. This results strongly suggest a selective nucleation of nanoparticles onto sp^2 domains of carbon by the interaction with UV light.

5. Acknowledgememts

This work has been supported by multidisciplinary project IPN-SIP 1683 and Programa Redes Temáticas CONACYT/RTH2. C.A. Campos-Roldán acknowledges financial support from CONACYT-Mexico Nr.: MX-561206.

6. References

[1] Wu, B., Kuang, Y., Zhang, X., Chen, J. Noble metal nanoparticles/carbon nanotubes nanohybrids: Synthesis and applications. Nano Today 2011; 6: 75-90

[2] Hirsch, A., Vostrowsky, O. ., Functionalization of carbon nanotubes. Top Curr Chem 2005; 245:193-237

[3] Wang, S. Optimum degree of functionalization for carbon nanotubes. Current Applied Physics 2009; 9: 1146-1150

[4] Goo-Hwan, J. Surface functionalization of single-walled carbon nanotubes using metal nanoparticles. Trans. Nonferrous Met. Soc. China 2009; 9:1009-1012

[5] B. Rosario-Castro et. al., Combined electron microscopy and spectroscopy characterization of as-received, acid purified, and oxidized HiPCO single-wall carbon nanotubes, Materials Characterization 2009; 60: 1442-1453

[6] Ma, J., Habrioux, A., Guignard, N., Alonso-Vante, N. Functionalizing Effect of Increasingly Graphitic Carbon Supports on Carbon-Supported and TiO_2−Carbon Composite-Supported Pt Nanoparticles .J. Phys. Chem. C 2012; 116:21788-21394

[7] C. Mercado-Zúñiga et al. Synthesis of highly dispersed platinum particles on carbon nanotubes by an in situ vapor-phase method. Journal of Alloys and Compounds 2014; 615:S538–S541

[8]Wang, G., Ling, Y., Qian, F., Yang, X., Liu, X, Li, Y. Enhanced capacitance in partially exfoliated multiwalled carbon nanotubes. Journal of Power Sources 2011; 196: 5209-5214

[9] C. Domingo, G. Santoro, Raman spectroscopy of carbon nanotubes, Opt. Pura Apl. 2007; 40: 175-186

[10] R. Raffaelle et. al., Purity assessment of multiwalled CNT by Raman spectroscopy, Journal of Applied physics 2007; 101: 064307

[11] X. Zhao et al., Physica B 2002; 323: 265-266

[12] Jawhari, T.; Roid, A.; Casado, J., Carbon 1995; 33:1561−1565

[13] Ma, J., Habrioux, A., Morais, C., Lewera, A., Vogel, W., Verde, Y., Ramos, G., Balbuena, P., Alonso, N. Spectroelectrochemical Probing of the Strong Interaction between Platinum Nanoparticles and Graphitic Domains of Carbon. ACS Catal. 2013; 3:1940-1950

[14] Ma, J., et al. Induced electronic modification of Pt nanoparticles deposited onto graphitic domains of carbon materials by UV irradiation. Electrochemistry Communications 2013; 29:12–16

[15] Urchaga, P., et al. Electro-oxidation of COchem on Pt Nanosurfaces: Solution of the Peak Multiplicity Puzzle. Langmuir 2012; 28:3658-3663

[16] López-Cudero, A., et al. Potential dependence of the saturation CO coverage of Pt electrodes: The origin of the pre-peak in CO stripping voltammograms. Part 1. Journal of Electroanalytical Chemistry 2005; 579: 1-12

[17] López-Cudero, A., et al. Potential dependence of the saturation CO coverage of Pt electrodes: The origin of the pre-peak in CO stripping voltammograms. Part 2. Journal of Electroanalytical Chemistry 2006; 586:204-216

[18] Cuesta, A., et al. Potential dependence of the saturation CO coverage of Pt electrodes: The origin of the pre-peak in CO stripping voltammograms. Part 3. Journal of Electroanalytical Chemistry 2006; 586:184-195

Chapter 8.8. Synthesis and characterization of carbon nanofibers for fuel cell applications

R. Ojeda-López[a]; G. Ramos-Sánchez[a,b*]; J.G. Vazquez-Arenas[a]; J.M. Esparza-Schulz[a]; A. Dominguez-Ortíz[a]; I. González[a]

[a] Departamento de Química, Universidad Autónoma Metropolitana-Iztapalapa, Av. San Rafael Atlixco 186, Col. Vicentina, 09340 Mexico City, Mexico.
[b] Cátedras CONACYT comisionado a Universidad Autónoma Metropolitana.

ABSTRACT

Carbon nanofibers (CNFs) are materials with potential applications as electrode supports in fuel cells, mainly due to their interesting characteristics: i) high surface area, ii) controlled chemical properties, and iii) high electric conductivity. Enhanced interaction between the support and the active material is supposed to improve the catalyst dispersion and increase the resistance to agglomeration. CNFs can be prepared by nitrogen doping, this procedure allows the formation of specific sites on the nanofibers surface which lead to controlled size and dispersion of the active material.
In this work, polyacrylonitrile nanofibers (PAN) are synthesized by electrospinning, then CNFs are obtained by PAN carbonization. The properties of CNFs are controlled by the calcination conditions, two heat treatments make up the calcination process: i) stabilization under oxidizing atmosphere, and ii) carbonization under inert atmosphere. On the first process the fibers are treated at 543 K in order to promote cyclization and partial dehydrogenation, this process helps to keep the fibrous structure of system. On the second treatment CNFs are obtained by heating beyond 973 K, in this stage carbon content grows, and depending on the temperature varying ratios of amorphous and crystalline phases are formed. When the carbonization temperature increases, nitrogen and hydrogen concentrations decrease, but carbon array crystallinity rises. With the idea of prepare the best nanofibers to fuel cell operation, four different carbonization temperatures (973, 1073, 1173 and 1273 K) are explored. The electrochemical characterization indicates that all CNFs present a more positive oxidation potential in comparison to carbon Vulcan. This result is in agreement with thermogravimetric analysis in which CNF decomposition (CO_2 formation) is obtained at higher temperatures in comparison to commercial supports. Preliminary results indicate that the lower the calcination temperature the higher amount of N groups leading to improved interaction Pt nanoparticles – support.

Keywords: Fuel cell, CNF´s, PAN, Catalyst support

---

*Author for correspondence:
G. Ramos-Sánchez, +52 55 5804 4600 ext 4396, gramossa@conacyt.mx

1. Introduction

Carbon materials have generated a high impact in recent years due to their physical and chemical properties, notably high mechanical and thermal resistance as well as enhanced electric transport. Pristine carbon nanofibers have been developed for various applications for example: H_2 storage [1], electronics [2], as catalyst supports [3], and electrochemical fuel cell promoters [4]. Furthermore, these structures doped with nitrogen or boron, substantially modifies their electronic and surface properties [5], increasing efficiency in the mentioned applications.

Carbon nanofibers are filamentous materials mainly composed of hexagonal networks of carbon atoms on the sp^2 hybridization (structure similar to graphite), whose sheets of graphene form fibers of diameters varying between 3 to 100 nm and lengths of several hundred nanometers and even microns. The graphenes are disposed at an angle with respect to the axis of the fibers, which classifies them into three types, i) platelet, ii) fishbone and iii) parallel [6-7].

The method for producing nanofibers from polymeric solutions is electrospinning. The electrospinning equipment requires a power source that provides a high voltage difference, a syringe of metal with tip without beveled for the polymer solution and a metal collector (aluminum, copper, etc.) for depositing the nanofibres. This technique involves the application of a high voltage between the needle tip and the target. The polymer solution at the tip of the needle is subjected to electrostatic forces and capillaries. The equilibrium of capillary and electrostatic forces were called Taylor cone (deformed drop). When the electric field strength is higher than the surface tension, the polymer solution is ejected into the collector in the form of a very fine line [8-9]. On the way to the collector, the solvent evaporates and the polymer chains are intertwined to give rise to the formation of a nanofiber deposited on the collector, forming a nano-web [10].

Polyacrylonitrile (PAN) is one of the polymers usually used as precursors for CNFs fabrication and as solvent dimethylformamide (DMF) [11]. In particular, the PAN consists of large molecular chains of carbon, nitrogen and hydrogen in the form of stairs. When the PAN is heated at appropriate temperature conditions, the carbon chain molecules are joined while other elements are separated, the carbon atoms of the polymer distribution change and form a stable ring structure bearing tightly bound to each other. By reheating, increases the carbon content and an amorphous structure with partial crystallinity is maintained. The nitrogen and hydrogen atoms disappear and pure carbon hexagonal rings are oriented along of the chain, resulting in a significant upturn in material strength [12-13].

Fuel cells such as polymer electrolyte (PEMFCs) and direct methanol (DMFCs), utilize catalysts Pt/carbon as electrode materials for converting the chemical energy of a fuel into electricity through very sluggish electrocatalytic reactions, such as the oxidation reaction of methanol (MOR) in the DMFC anode and the oxygen reduction reaction (ORR) at the PEMFC cathode [14]. High conversion efficiency, low pollution and light weight make them attractive as energy conversion devices [15]. However, one of the main problems of fuel cells is the high production cost due to the use of noble metals such as Pt for electrode and durability issues mainly arising from carbon support instability. Therefore, the use of new porous carbon structures has been considered, those should present high surface area, nanoscale morphology, chemically active surface and good electrical conductivity [14,16]. CNF's used as support fuel cells might present advantages compared to conventional media

(activated carbon) because of the increased activity and selectivity of the catalysts in hydrogenation reactions, *e.g.* Ni supported on CNFs [17], also by its high mechanical strength, chemical inertness and potential use in both acidic or basic solutions [18]. In this work a systematic study of electrochemical and structural properties of CNFs is presented with the aim to be used as support for PEMFCs.

2. Materials and Methods

2.1 Materials

Polyacrylonitrile (PAN) was obtained from Aldrich and used without further purification. The 99.8 % N,N-dimethylformamide anhydrous (DMF) was purchased from Sigma-Aldrich. LIQUION solution LQ-1105 1100EW 5 wt. % was acquired from Ion Power, Inc.

2.2 CNF preparation

The concentration of 10 wt.% PAN/DMF solution was prepared by stirring at room temperature for 4 h. Electrospinning apparatus was set up horizontally and the applied voltages between the tip and collector were set at 20 kV. The tip-collector distance and flow rate were fixed at 10 cm and 0.02 mL min^{-1}, respectively. Subsequently, the PAN fibers were stabilized at 553 K in air atmosphere and carbonized at 1173 K under nitrogen atmosphere [13].

2.3 Characterization techniques

The textural properties of samples were determined by N_2 adsorption and the measurements were performed on a Micromeritics ASAP 2020 system at liquid nitrogen temperature (76 K, Mexico City), the samples were degassed at 423 K under vacuum. The specific surface area of the samples was calculated by using the multiple-point Brunauer-Emmett-Teller (BET) [19] method in the relative pressure range P/P^o=0.05-0.25. The pore size distribution curves were computed by using the non-local density functional theory (NLDFT) method [20]. SEM analysis was performed on a LEO VP (variable pressure) 1450 electron microscope, operated at an acceleration voltage of 15 kV and the sample preparation was for vaporization gold-palladium. Of the SEM analysis, some regions were selected for determine the nitrogen content through analysis EDS (energy dispersion spectroscopy). XRD analysis was obtained on a Bruker D8 Advance, using monochromatic CuKα radiation with a wavelength of 1.54 Å in the low angle region (10^o to 80^o in the 2θ scale). Raman spectra of the carbon fibers were taken with a Horiba Jobin Yvon T64000 microspectrometer, using 532.1 nm excitation, 20 mW power and 100x microscope objective, in the region of 50 and 1850 cm^{-1}.

2.4 Electrochemical characterization

Electrochemical measurements as cyclic voltammetry (CV) were performed on a potentiostat/galvanostat PARSTAT model 2273, in a 0.5 $mol \cdot L^{-1}$ $HClO_4$ solution. The working electrode was glassy carbon (7 mm in diameter) coated with as-prepared catalyst, mounted in an interchangeable holder (Pine Instruments). A saturated calomel reference electrode (SCE) was used for all electrochemical measurements [21-22].

The working electrode was prepared according to the following procedures. The CNFs was dispersed ultrasonically in a solution of LIQUION (Nafion 4.95-5.05 wt.%, water 20 wt.% and alcohol 75 wt.%) and isopropyl alcohol to obtain a homogenous black suspension. Then 20 μL of the mixture was pipetted onto the surface of glassy carbon (GC) electrode which was polished to a mirror finish with 0.05 μm of alumina pastes. Before testing, the electrolyte was bubbled with nitrogen for 15 min, and the current-potential curve was recorded in the presence of nitrogen. The scan rate was 0.005 $V \cdot s^{-1}$ with the scanning potential range of 0 to 1.43 V (vs ENH).

3. Results and Discussion

Fig. 1(a) shows SEM micrographs of polyacrylonitrile fibers with diameters between 500 and 600 nm, the diameter decreases about 50 % when the carbonization is performed (Figure 1(b) and 1(c)). EDS analysis showed that the carbonized nanofibers contained 82 % carbon, 10 % nitrogen and 8 % oxygen. The presence of nitrogen is apparently due to the C–N bonds which are typically found in PAN carbon fibers when the final temperature in the heat treatment is less than 2273 K [23].

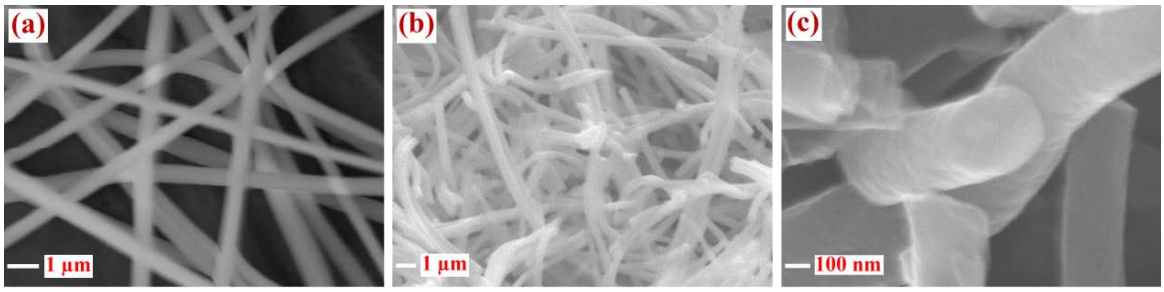

Fig. 1. SEM images of (a) polyacrylonitrile fibers, (b) and (c) carbon fibers.

Figure 2(a) presents the diffractogram obtained for carbonized fibers. The obtained diffraction peak at an angle of approximately 26° corresponds to the graphitic plane (002), where a greater amplitude thereof is diagnostic of a less structured material. D_{002} interlayer spacing obtained from the Bragg equation ($d_{002}=\lambda/2 \sin \theta$) is generally used as a quantitative parameter of the graphitic nature of these materials.

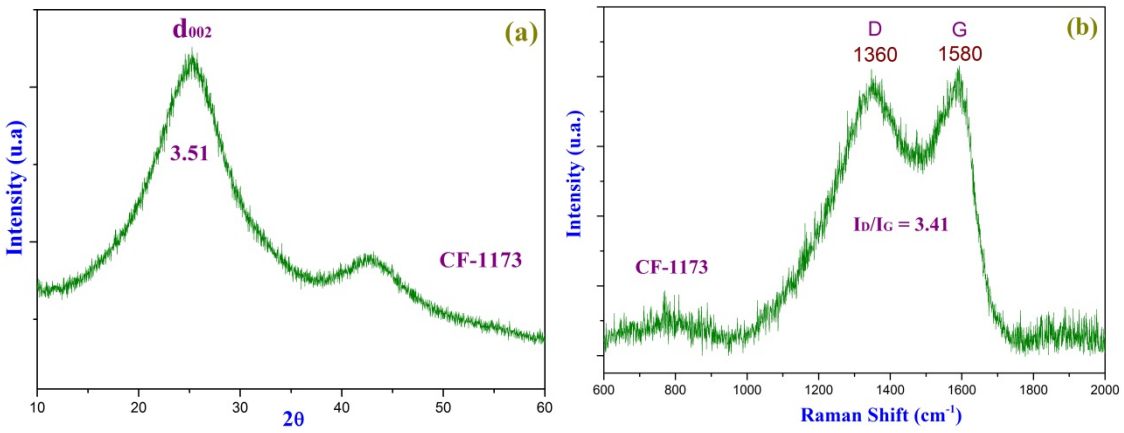

Fig. 2. (a) Difractogramm and (b) Raman spectra of carbon fibers.

Figure 2 (b) shows a Raman spectra of carbonized fibers, in which the observed G band at ~ 1580 cm^{-1}, is characteristic of all graphite materials and the D band at ~ 1360 cm^{-1}, is associated with presence of imperfections in the crystal structure. The D band intensity, associated with defects, decreases with increasing the temperature at which the thermal stabilization treatment is performed, which relates to an increase in the degree of ordering.

Nitrogen adsorption isotherm shown in Figure 3 is of type IV (IUPAC) with H4 hysteresis loop which is characteristic of carbon materials [24]. CF-1773 material has an area of 434 $m^2.g^{-1}$. The dominating pores are micrometer in size (<20 Å), with 55 % of the total volume of material. In these materials the pore size distribution is in the range of micropores and was calculated using the model NLDFT considering slit-pores, obtaining an average pore diameter of 13.26 Å.

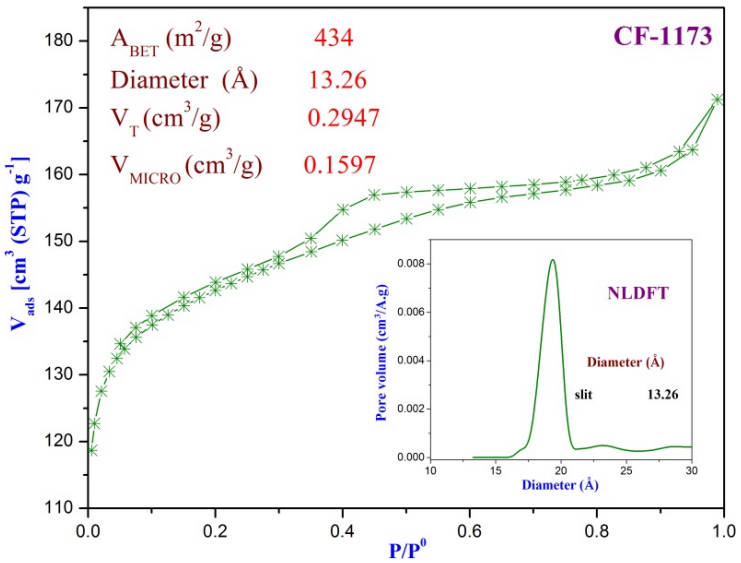

Fig. 3. Nitrogen sorption isotherm; distribution function of average pore size by the model NLDFT considering slit pores considering slit pores in the lower right box.

Preliminary electrochemical experiments were performed in order to determine the stability range of the as synthesized CNF. Fig. 4 shows the voltammetric response at the maximum applied potential. Several experiments were performed in cathodic and anodic directions changing the switching potential at several potentials from 0.9 to 1.4 V (SHE) on the cathodic swept and from 0.25 to 0 V (SHE) on the anodic one, for sake of simplicity in Fig. 4 only the last experiment is shown. Capacitive response is observed in most of the range of the experiments, except for a small increment in current on the cathodic swept indicative of either oxygen evolution or material oxidation. It is worth mentioning, that in commercial supports the oxidation of the support begin at potentials as low as 0.98 V (ENH), therefore CNFs present advantages as the oxidation occurs at much higher potentials.

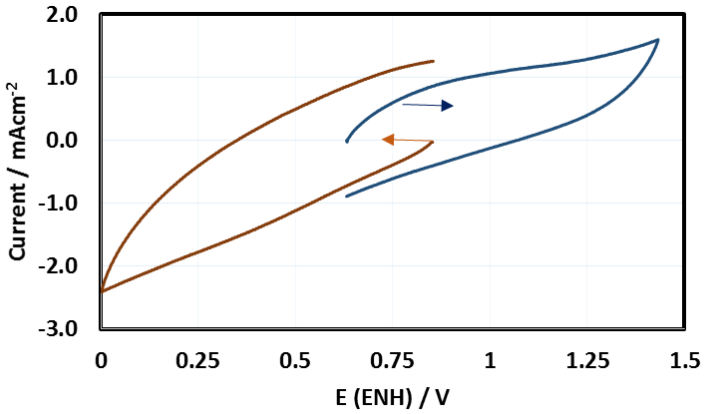

Fig. 4. Cyclic voltammetry analysis of CF-1773 in 0.5 mol·L^{-1} $HClO_4$ solution saturated by nitrogen at a scan rate of 0.005 V·s^{-1}

Further experiments are being carried out to determine the capacitance of the materials as well as experiments to determine the species formed during the electrochemical experiments. The CNFs synthesized here, present big advantages as the nitrogen amount is high and present nucleation sites for nanoparticle formation and growth.

4. Conclusion

In this work describes the fabrication of carbon fibers through electrospinning method. The results of XRD and Raman shown curves typical characteristics of carbon nanofibers. Through SEM micrographs was determined the diameter of the CNFs in the range from 200 to 300 nm.

The nitrogen adsorption characterization helped determine the BET surface area (434 $m^2.g^{-1}$) and average pore diameter (13.26 Å), as well as the total volume of pores, which 55 % corresponds to the presence of micropores. The nitrogen content was determined by EDS, for CF-1173 material was 10 wt.%

The CNFs present an extremely high oxidation potential which complemented with the presence of nitrogen as anchoring sites for Pt represent advantages for their use as support

for fuel cell applications. Further experiments are being conducted in order to confirm this hypothesis which will be reported elsewhere.

Acknowledgements

The authors acknowledge the financial support of the SMH (XV International Congress of the Mexican Hydrogen Society) and SEP-PROMEP Network "Diseño Nanoscópico y Textural de Materiales Avanzados", Project "Síntesis y Fisicoquímica de Materiales Mesoporosos" (UAM-I CA-31 Fisicoquímica de Superficies)".

References

[1] Blackman, J. M., Patrick, J. W., Arenillas, A., Shi, W. & Snape, C. E. Activation of carbon nanofibres for hydrogen storage. Carbon 2006; 44:1376–1385.
[2] Rao C.N.R. Novel materials, materials design and synthetic strategies: recent advances and new directions. J. Mater. Chem. 1999; 9:1–14.
[3] Keller N., Rebmann G., Barraud E., Zahraa O., Keller V. Macroscopic carbon nanofibers for use as photocatalyst support. Catal. Today 2005; 101:323–329.
[4] Wang C., Waje M., Wang X., Tang J.M., Haddon R.C., Yan Y.S. Proton exchange membrane fuel cells with carbon nanotube based electrodes. Nano Lett. 2004; 4:345–348.
[5] Stephan O., Ajayan P.M., Colliex C., Redlich P., Lambert J.M., Bernier P., Lefin P. Doping graphitic and carbon nanotube structures with boron and nitrogen. Science 1994; 266:1683–1685.
[6] Rodriguez N.M. A review of catalytically grown carbon nanofibers. J. Mater. Res. 1993; 8:3233–3250.
[7] Dresselhaus M. S., Dresselhaus G., Avouris P. Introduction to carbon materials research. Topics Appl. Phys. 2001; 80:1–9.
[8] Wang T., Kumar S. Electrospinning of polyacrylonitrile nanofibers. J. Appl. Polym. Sci. 1029; 102:1023–1029.
[9] Mottaghitalab V., Haghi A.K. A study on electrospinning of polyacrylonitrile nanofibers. Korean J. Chem. Eng. 2011; 28:114–118.
[10] Doshi J., Reneker D.H. Electrospinning process and applications of electrospun fibers. Journal of electrostatics 1993; 35:151–160.
[11] Gu S.Y., Ren J., Vancso G.J. Process optimization and empirical modeling for electrospun polyacrylonitrile (PAN) nanofiber precursor of carbon nanofibers. European Polymer Journal 2005; 41:2559–2568.
[12] Rahaman M.S.A, Ismail A.F., Mustafa A. A review of heat treatment on polyacrylonitrile fiber. Polymer Degradation and Stability 2007; 92:1421–1432.
[13] Dalton S., Heatley F., Budd P.M. Thermal stabilization of polyacrylonitrile fibres. Polymer 1999; 40:5531–5543.
[14] Su Fabing., Tian Zhiqun., Poh C.K., Wang Z., Lim S.H., Liu Z., Lin J. Pt nanoparticles supported on nitrogen-doped porous carbon nanospheres as an electrocatalyst for fuel cells. Chem. Mater. 2010; 22:832–839.
[15] Maiyalagan T., Silicotungstic acid stabilized Pt-Ru nanoparticles supported on carbon nanofibers electrodes for methanol oxidation. Int. J. Hydrogen Energy 2009; 34:2874–2879.
[16] Maass S., Finsterwalder F., Frank G., Hartmann R., Merten C. Carbon support oxidation in PEM fuel cell cathodes. J. Power Sources 2008; 176:444–451.
[17] Ismagilov Z.R., Kerzhentsev M.A., Shikina N.V., Lisitsyn A.S., Okhlopkova L.B., Barnakov Ch.N., Sakashita M., Iijima T., Tadokoro K. Development of active catalysts for low Pt loading cathodes of PEMFC by surface tailoring of nanocarbon materials. Catal. Today 2005; 102-103:58–66.
[18] Ochoa-Fernández E., Chen D., Yu Z., Tøtdal B., Rønning M., Holmen A. Carbon nanofiber supported Ni catalyst: Effects of nanostructure of supports and catalyst preparation. Catal. Today 2005; 102-103:45–49.
[19] Brunauer S., Emmet P.H., Teller E. Adsorption of Gases in Multimolecular Layers. J. Am. Chem. Soc., 1938; 60: 309-319.

[20] Ravikovitch P., Neimark A.V. Characterization of Micro- and Mesoporosity in SBA-15 Materials from Adsorption Data by the NLDFT Method. J. Phys. Chem. B., 2001; 105:6817-6823.
[21] Xi-Zhao W. Platinum Nanoparticles Supported on Carbon Nanofibers as Anode Electrocatalysts for Proton Exchange Membrane Fuel Cells. Acta Phys. Chim. Sin. 2011; 27:1–6.
[22] Ramos-Sánchez G., Bruno M.M., Thomas Y.R.J., Corti H.R., Solorza-Feria O. Mesoporous carbon supported nanoparticulated $PdNi_2$: A methanol tolerant oxygen reduction electrocatalyst. Int. J. Hydrogen Energy 2012; 37:31–40.
[23] Zhang W.X., Liu J., Wu G. Evolution of structure and properties of PAN precursors during their conversion to carbon fibers. Carbon 2003;41(14):2805–2812.
[24] Sing K.S.W. Reporting physisorption data for gas/solid systems with special reference to the determination of surface area and porosity (Recommendations 1984). Pure Appl. Chem., 1985; 57: 603-619.

Chapter 8.9. Bionano-bioparticles of magnetite from a microbial consortium with perchloroethylene treatment capabilities

L. Breton-Deval[a]; H. M. Poggi-Varaldo[a,*]; E. Ríos-Leal[a]; O. Solorza-Feria[b]

[a] Environmental Biotechnology and Renewable Energies R&D Group, Dept. of Biotechnology and Bioengineering, Centro de Investigación y de Estudios Avanzados del Instituto Politécnico Nacional. Av. Instituto Politécnico Nacional 2508, Col. San Pedro Zacatenco, Delegación Gustavo A. Madero, México D.F., C. P. 07360 Apartado Postal: 14-740, 07000 México D.F., México
[b] Dept of Chemistry, CINVESTAV, México D.F., México.

ABSTRACT

The purposes of this research were *(i)* to synthesize *NPs* using a biological-based method using bioparticles from anaerobic fluidized bed reactors, *(ii)* to evaluate the effect of the precursor salt used (either $Fe(NO_3)_3$ or $FeCl_3$) on *NP*s characteristics, and *(iii)* to evaluate the removal/degradation of *PCE* by these *NPs*. Bioparticles from anaerobic fluidized bed reactors were used as departing support for NP synthesis. The consortium could successfully synthese magnetite *NPs* without using expensive and hazardous chemical reducing agents. The diameter of *NPs* was 5 – 60 nm. Samples from the method that used the $Fe(NO_3)_3$ showed aggregates while the other *NP*s from the precursor iron chloride exhibited smaller size. The removal of *PCE* was more efficient for *NP*s formed from the chloride salt, after 4 days the removal was 99%. On the other hand, the *NPs* biosynthesized with Fe $(NO_3)_3$ removed 93% of *PCE*. Control units containing bioparticles with dehalogenating consortium but no *NPs* could just remove 38%. In general, the main *PCE* metabolite found was *TCE*, although at low concentrations. This suggested that *NP*s had a high dehalogenating efficiency. We conclude that the dehalogenating consortium is capable of synthesizing *NPs* that can effectively degrade *PCE*, second, the *NPs* obtained from $FeCl_3$ precursor exhibited smaller diameter and increased rates and extents of pollutant removal. Finally, our biosynthesis route for magnetite *NPs* implies significant savings in chemical reagents as well as energy in contrast to the typical chemical techniques for magnetite *NPs* fabrication

Keywords: biosynthesis, *PCE* treatment, water pollution, nanoparticles, bio-nano bio particles

* Author for correspondence:
Professor Dr. Héctor Mario Poggi-Varaldo
Environmental Biotechnology and Renewable Energies R&D Group,
Dept. Biotechnology & Bioengineering, CINVESTAV- I.P.N.
P.O. Box 14-740, 07000, México D.F., México
T: 5255 5747 3800 x 4324. F: 5255 5747 3313,
E: r4cepe@yahoo.com

1. Introduction

Perchloroethylene (*PCE*) is a chlorinated organic compound (*COC*) mainly used in dry cleaning industry, in metal cleaning operations. It has been widely used due to its no flammability, easiness to reuse and its strong solvent capacity [1]. However, it has been considered as a potentially toxic and carcinogen compound [2]. Moreover, daughter products of *PCE* reductive dechlorination, such as trichloroethylene (*TCE*), dichloroethylene (*DCE*) and vinyl chloride (*VC*) show higher toxicity than *PCE* itself [3].

In addition, *PCE* is the most reported organo-chlorinated contaminant in groundwater, where it forms a dense phase at the bottom of the aquifer. Due to its low solubility is difficult to remove, representing a sustained release source of the contaminant and a risk for the health and the environment [4]. Therefore the search of successful technologies that allow the efficient removal of these chlorinated compounds continues.

Several works have been carried out with the aim of removing *PCE* and their metabolites using iron nanoparticles (*NPs*) [5, 6, 7]. Iron is the material most used in the treatment of *COCs* compounds due to its low cost, abundance, ease, and reactivity [8]. The iron can serve as a fixed source of electrons for the reductive dehalogenation of *PCE* [9, 10,11]. The *NP* size have a high surface area to mass ratio, making them more reactive compared to the conventional iron. However the application of nano iron still faces challenges, such as the longevity, iron *NPs* could be very reactive; they quickly oxidize and lose their reductive power. Other challenge is the transport through aquifer. The *NPs* tend to agglomerate and form aggregates, resulting in a decrease in the activity and mobility of the particles [12].

There are different ways to synthesize *NPs*, namely, chemically, physical and biological methods. Regarding the latter some research has focused on the synthesis of *NPs* using specific microbes with promising results [13, 14].

The metals can act as nutrients for the microorganism or enzymatic cofactors; they are essential for some cellular process. However, high concentrations of some metals could be toxic [15, 16, 17]. The microorganisms have two different methods for capturing metal cations. One of them is inespecific whereas the second mechanism is very specific and uses the *ATP* hydrolysis as energy plus the chemiosmotic gradient [18]. Over the years microorganisms have developed strategies to tolerate the detrimental effects of high concentrations of metals such as synthesizing cellular components that capture ions by neutralizing its toxicity, using enzymes that are able to reduce metals, and with membrane transporters that expel harmful components out of the microbial cell. Synthesis of nanoparticles by microorganisms is based on the process that develop the metal resistant genes of the microorganism exposed to metals [19].

During this research the microbial consortium cellular machinery was used to reduce the metal cation and form *NP*s. We hypothesized that the *in situ* biosynthesis of *NPs* by the consortium would allow a prompt use of the *NPs* for effective dehalogenation of *PCE*. The microbial consortium, in turn, was grown on core activated carbon particles, that is, they originally formed bioparticles nearly 1.5 to 2 mm diameter. Therefore, the purposes of this research were *(i)* to synthesize active *NPs* using a biological-based method using bioparticles from anaerobic fluidized bed reactors as support and agent, *(ii)* to evaluate the

effect of the precursor salt used (either $Fe(NO_3)_3$ or $FeCl_3$) on *NP*s characteristics, and *(iii)* to evaluate the removal/degradation of *PCE* by these *NPs*.

2. Materials and Methods

2.1 Synthesis of bio nano bioparticles

The synthesis of *NP*s was carried out using the anaerobic consortium [20-22] grown on activated carbon particles, that is, bioparticles of ca. 1.5- 2mm diameter. Two different precursor salts of iron were tested $FeCl_3$ o $Fe(NO_3)_3$ at two different concentrations 0.15 and 0.25 M. That is, the experiment was a 2x2 factorial design. The media were prepared as follows: $((NH_4)_2HPO_4)$ (0.89 mg/L) plus MeOH (3mL/L) as electron donor solution was carefully added to a either $FeCl_3$ or $Fe(NO_3)_3$ salt (0.25 or 0.15 M final concentration in the medium) stirring few minutes ; pH was adjusted to a value of 5. This solution was added to serum bottles of 60 mL capacity that were previously loaded with 5 g of bioparticles sampled previously from an anaerobic fluidized bed bioreactor.

2.2. Batch PCE degradation

A batch experiment was implemented in order to test two different types of precursor salts, either $FeCl_3$ or $Fe(NO_3)_3$. Serum bottles of 60 mL capacity fitted with Teflon septa were used. The batch units were loaded with 5 g of dehalogenating bioparticles sampled from an anaerobic fluidized bed bioreactor, plus 5 mL/L methanol, and 0.15 or 0.25 M precursor salts, either $FeCl_3$ or $Fe(NO_3)_3$. For the degradation tests, *PCE* (80 mg/L) was added at the end of 3 days of incubation at 28°C. All experiments were performed by triplicate.

Control experiments were carried out to evaluate pollutant removal due to abiotic losses such as evaporation and adsorption. The controls were: *(i)* only bioparticles without metallic salt, *(ii)* the metallic salts without bioparticles, *(iii) PCE* without salts and without bioparticles.

2.3. Characterization of nanoparticles

The morphology of bio-nanoparticles was determined by scanning electron microscopy (*SEM*) using a microscope HRSEM-AURIGA 3916 and the chemical composition was measured by energy dispersive spectrum (*EDS*) detector coupled to *SEM*. X-ray diffraction (*XRD*) was performed in order to determine the crystal structure and crystallinity of the Fe/Pd *NPs*. The *XRD* patterns were measured in a Rigaku D/Max B system with a Cu Kα 1 ($\lambda = 1.541$ A) radiation source.

2.4. Analyses

PCE and chlorinated intermediates in the aqueous phase were analyzed by headspace chromatography in Perkin-Elmer chromatograph equipped with a flame ionization detector, a Perkin Elmer Elite-624 Series Capillary Columns. Injector and detector temperatures were 200°C and 250°C, respectively. The temperature program of the column was as follows: start at 40°C, followed by an increase of 6°C/min up to 119°C. Nitrogen was the carrier gas, at 18 psig.

3. Results and Discussion

The SEM images show spherical forms between 5 to 60 nm in the treatments with 0.25 M of $FeCl_3$ or $Fe(NO_3)_3$ (Fig. 1a and b). The images of the treatments with 0.15 M of of $FeCl_3$ or $Fe(NO_3)_3$ form irregular clusters (Fig. 1 c and d). The *EDS* spectrum contains peaks of C, O, and Fe. The C signals are attributed mainly to the carbon of the bioparticles. The atomic percentages as obtained by *EDS* quantification were 46.3% C, 24.5 % Fe, 12.5% O.

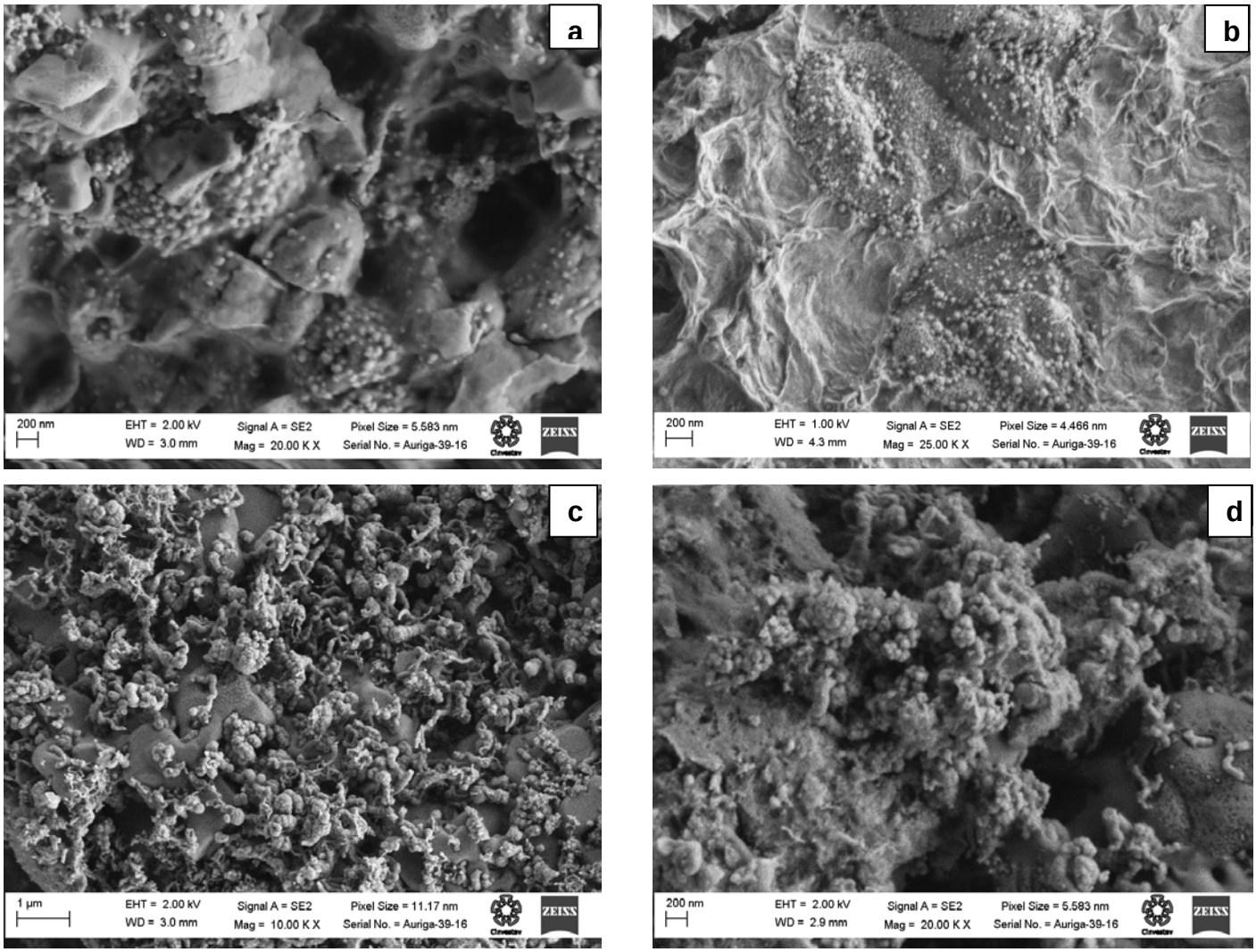

Fig. 1. Michrograph by scanning electron microscopy where (a) is the view of the surface of bioparticle that used 0.25 M of $FeCl_3$ as precursor salt, (b) used 0.25 M of $Fe(NO_3)_3$, (c) used 0.15 M of $FeCl_3$ and (d) used 0.15 M of $Fe(NO_3)_3$

The *XRD* study showed that reflections in the diagram were identified to belong to iron oxide Fe_3O_4 and iron. However the formation of iron in some samples was also noted. The analysis showed that *NPs* were of magnetite, however it is difficult to know if the fresh particle was different because fresh *NPs* could instantly start to reduce the *PCE*.

The removal of *PCE* was more efficient in the treatment that used $FeCl_3$ as precursor salt; after 4 days the removal was 99.12 ± 0.44 % (Fig. 2). The *NPs* biosynthesized with $Fe(NO_3)_3$ removed 93.01 ± 0.16 % of *PCE*. On the other hand, the control units containing bioparticles with the dehalogenating consortium but not *NPs* or precursors salts could remove 38% ± 1.5 and present metabolites as *TCE*, *DCE*, and *VC*. The control units with only precursor salts but no bioparticles removed just 4.58 ± 1.34 % with $Fe(NO_3)_3$ and 8.16 ± 1.84% with $FeCl_3$.

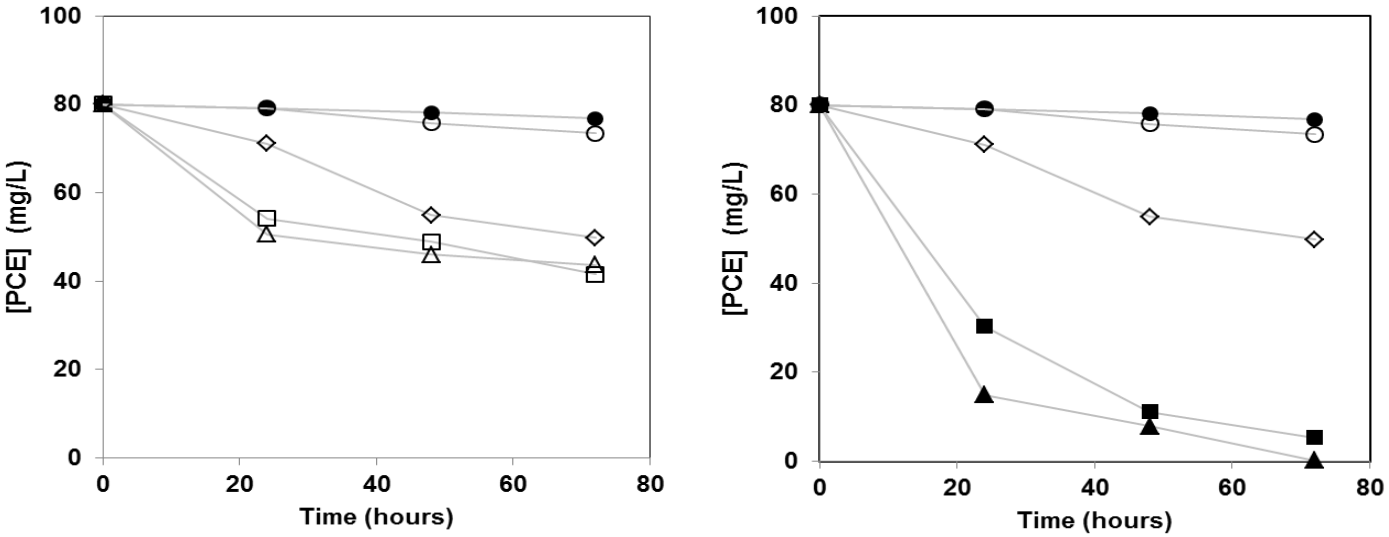

Fig. 2. Batch degradation of *PCE*. Keys: black circles, control with $FeCl_3$; white circles, control with $Fe(NO_3)_3$; white diamonds, is the treatment with the bioparticles; white squares, is the treatment with bionanobioparticles formed with 0.15 M $Fe(NO_3)_3$ as precursor; white triangles bionanobioparticles formed with 0.15 M $FeCl_3$; black squares is the treatment with bionanobioparticles formed with 0.25 M $Fe(NO_3)_3$ as precursor; white triangles, is the treatment with bionanobioparticles formed with 0.25 M $FeCl_3$ as precursor.

The treatments with a concentration of 0.15 M of precursor salts showed removals of 48 ± 1.8% using $Fe(NO_3)_3$ and 45 ± 0.78% using $FeCl_3$. It is likely that the *PCE* removal of the latter is the synergism of the consortium plus the salt.

4. Conclusion

First, we conclude that the biological synthesis of *NP*s on the surface of bioparticles sampled from anaerobic fluidized bed bioreactors lead to magnetite *NP*s with a high capability for degrading *PCE*.

Second, the bionanobioparticles formed in this way and obtained with the precursor salt $FeCl_3$ exhibited smaller diameter and increased rates and extents of pollutant removal. Abiotic removals were negligible, the high *PCE* removals were mainly effected by the bionanobioparticles. Biological removals (plain bioparticles) were moderate.

Finally, our biosynthesis route for obtaining magnetite *NPs* implies significant savings in chemical reagents (several of them expensive and hazardous) as well as energy compared to typical chemical techniques for *NPs* fabrication.

Acknowledgements

The authors wish to thank M. en I. Alvaro Ángeles Pascual, Dr. Daniel Bahena Uribe, and Dr. Jorge Roque De La Puente of LANE, CINVESTAV, for their excellent technical help and advice on the synthesis and characterization of *NPs*; Mr. Rafael Hernández-Vera for his help with batch tests of *PCE* degradation and lab management; Mr Gustavo Medina for his assistance with the technique of analysis of *PCE* and its metabolites. CONACYT granted a graduate fellowship to LMB-D and an Infrastructure Project 188281 to HMP-V.

References

[1] Albino J, Nambi I (2009) Effect of biosurfactants on the aqueous solubility of *PCE* and *TCE*. Journal of Environmental Science and Health. 44(14):1565-1573

[2] Aschengrau A, Rogers S, Ozonoff D (2003) Perchloroethylene contaminated drinking water and the risk of breast cancer : additional results from Cape Cod, Massachusetts, USA. Environmental Health Perspectives 111 (2): 167-175.

[3] EPA (2002) National Primary Drinking Water Standards. Office of Water (4606M); EPA 816-F-03-016; www.epa.gov/safewater.

[4] Shin M, Choi H, Kim D, Baek K. (2008). Effect of surfactant on reductive dechlorination of trichloroethylene by zero-valent iron. Desalination 223:299-307.

[5] Breton-Deval L. Solorza-Feria O., Rios-Leal E., Poggi-Varaldo H.M. (2013). Dechlorination of *PCE* with nanoscale particles of zero valent iron and palladium. In: R.R. Sirabian and R. Darlington. Bioremediation and Sustainable Environmental Technologies-2013. Battelle Press, Columbus, OH, USA. ISBN 978-0-9819730-7-4.

[6] Song H, Carraway E, Kim Y (2005) Synthesis of nano-sized iron for reductive dechlorination. Environ. Eng. Res. 10 (4): 174-180

[7] Wei J, Xu X, Liu Y (2004) Kinetics and mechanism of dechlorination of chlorophenol by nanoscale Pd/Fe. Chem. Res. Chinese U. 20 (1):71-76.

[8] Cross K.M., Lu Y., Zheng T., Zhan J., McPherson G.L., John V.T. (2014). Water decontamination using iron and iron oxide nanoparticles. In: Street, Sustich, Duncan and Savage. *Nanotechnology Applications for Clean Water*, 2nd Edition, Elsevier Inc., New York, USA.

[9] Xiu Z, Jin Z, Li T, Mahendra S, Lowry G, Alvarez P (2010) Effects of nano-scale zero valent iron particles on a mixed culture dechlorinating trichloroethylene. Bioresource Technology 101:1141-1146

[10] Zhou L, Thanh TL, Gong J, Kim JH, Kim EJ, Chang YS (2014). Carboxymethyl cellulose coating decreases toxicity and oxidizing capacity of nanoscale zerovalent iron. Chemosphere 104: 155-161.
[11] Wu L., Ritchie S.M.C. (2006). Removal of trichloroethylene from water by cellulose acetate supported bimetallic Ni/Fe nanoparticles. Chemosphere 63: 285-292.
[12] Phenrat, T., Saleh N., Sirk K., Tilton RD., Lowry GV. (2007). Aggregation and sedimentation of aqueous nanoscale zerovalent iron dispersions. Enviromental Science and Technology. 41: 284-290.
[13] Hulkoti N.I., Taranath T.C. (2014). Biosynthesis of nanoparticles using microbes – A review. Colloids and Surfaces B: Biointerfaces 121:474-483.
[14] Hennebel T. De Corte S., Verstraete W., Boon N. (2012). Microbial production and environmental applications of Pd nanoparticles for treatment of halogenated compounds. Current Opinion in Biotechnology 23:555-561.
[15] Suarez P., Reyes R. (2002). La incorporacon de metales pesados en las bacterias y su importancia para el ambiente. Interciencia 27(4):160-4
[16] Gonzales A.G., Pokrovsky O.S., Jimenez-Villacorta F., Shirokova L.S., Santana-Casiano J.M., Gonzalez-Davila M., Emnova E.E. (2014) Chemical Geology 372:32-45.
[17] Marrero-Coto J., Diaz-Valdivia A., Coto-Perez O. (2010). Mecanismos moleculares de resistencia a metales pesados en las bacterias y sus aplicaciones en la biorremediación. Revista CENICA Ciencias Biologicas 41(1):67-78.
[18] Eisele T.C. Gabby K.L (2014). Review of reductive leaching of iron by anaerobic bacteria. Mineral processing & extractive metal 35:75-104.
[19] Kaushik N., Thakkar M.S., Snehit S., Mhatre M.S. Rasesh Y., Parikh M.S. (2010) Biological synthesis of metallic nanoparticles. Nanomedicine: Nanotechnology, Biology and Medicine 6:257-262.
[20] Breton-Deval L, Poggi-Varaldo H.M., Rios-Leal E., Juarez K. (2013) Evaluation of bioreactors performance for pump and treat bioremediation of high concentrations of *PCE*. Chapter C-33 In: Darlington R, Sirabian M (Editors). *Bioremediation and Sustainable Environmental Technologies-2013*. Battelle Press, Columbus. Book in CD-ROM. ISBN 978-0-9819730-7-4
[21] Moreno-Medina C, Bretón-Deval L, Ríos-Leal E, Barrera-Cortés, Rinderknecht-Seijas N, Poggi-Varaldo HM. (2011). Incremento de la solubilización de percloroetileno con un tensoactivo no iónico. Interciencia 36:224-228.
[22] Herrera-Lopez D, García-Mena J, Poggi-Varaldo HM. (2007). The addition of zero-valent iron to batch bioreactors with simultaneous electron acceptors: influence on removal of high concentrations of perchloroethylene. In: Gavaskar AR, Silver CF (Editors). *In Situ and On-Site Bioremediation-2007,* Battelle Press, Columbus, OH, ISBN 978-1-57477-161-9

Notation

ATP	adenosine triphosphate
COC	chlorinated organic compound
DCE	dichloroethylene
EDS	energy dispersive spectrum
*NP*s	nanoparticles
PCE	perchloroethylene
SEM	scanning electron microscopy
TCE	trichloroethylene
VC	vinyl chloride
XRD	X-ray diffraction

Chapter 8.10. Comparative electrocatalytic study of Fe_3O_4@Pt/C and Fe_2O_3@Pt/C core-shell nanostructures for the ORR

N. M. Sánchez-Padilla[a]; S. M. Montemayor[b]; F.J. Rodríguez-Varela[a,c,*]

[a]Programa de Sustentabilidad en Recursos Naturales y Energía, Cinvestav Unidad Saltillo, Av. Industria Metalúrgica 1062, Parque Industrial Saltillo-Ramos Arizpe, Ramos Arizpe, C.P 25900, Coahuila, México.
[b]Centro de Investigación en Química Aplicada, Blvd. Enrique Reyna No. 140, Col. San José de los Cerritos, 25294 Saltillo, Coahuila, México.
[c]Programa de Nanociencias y Nanotecnología, Av. Industria Metalúrgica 1062, Parque Industrial Saltillo-Ramos Arizpe, Ramos Arizpe, C.P 25900, Coahuila, México.

ABSTRACT

In this work, a comparative study of the catalytic activity for the Oxygen Reduction Reaction (ORR) of the core-shell structures Fe_3O_4@Pt/C and Fe_2O_3@Pt/C is presented. The a two-step route was followed to obtain the materials. First, the cores were obtained via a modified co-precipitation method using etilenglicol (EG) as a surfactant. In a second step, the deposition of the Pt shell was made via impregnation-reduction, using $NaBH_4$ as reducing agent. The crystalline structure of the catalysts has been confirmed by XRD, showing the presence of the cubic inverse spinel phases of Fe_3O_4 or Fe_2O_3. The patterns showed also the reflectios of fcc Pt, having particle size below 5 nm. The electrochemical measurements were carried out in 0.5 M H_2SO_4 and 0.5 M KOH. The Fe_3O_4@Pt/C cathode delivered higher current density and showed higher degree of tolerance to ethanol than Fe_2O_3@Pt/C. On the other hand, both core-shell cathodes demonstrated enhanced tolerance properties related to a Pt/C cathode. Such characteristic has been attributed to the core-shell structure that modified the surface properties of Pt and also to the oxidation states of the iron oxide cores.

Keywords: Catalysts synthesis, Core-shell nanostructures, Oxygen reduction reaction

1. Introduction

Polymer Electrolyte Membrane Fuel Cells (PEMFC) are good choice to provide clean energy due to their high efficiency. However, the main fuel used in these cells is hydrogen, which has some important drawbacks: it needs to be produced from different sources, it is difficult to handle, and its storage is complex. Among the alternative technologies currently being developed, Direct Alcohol Fuel Cells (DAFC) fueled by organic liquids like ethanol

---

* Author for correspondence:
F.J. Rodríguez Varela, 52 +844 438-9600 (Ext. 8526), 25900, javier.varela@cinvestav.edu.mx

are being studied. However, Pt cathode catalysts are rapidly poisoned when crossover occurs. Because of this issue, and besides the extended use of platinum, the need to create new catalysts that increase the catalytic activity, reduce the Pt loading and improve tolerance towards ethanol crossover must be achieved.

Pt alloyed with magnetite (Fe_3O_4), or in a core-shell structure, proved to be suitable catalysts for the Oxygen Reduction Reaction (ORR) and the Ethanol Oxidation Reaction (EOR) [1-3]. Also, it has been reported that composite Pt-CeO_2 materials show enhanced the catalytic activity for the ORR and higher tolerance towards some organic fuels [4]. Maghemite (Fe_2O_3) is another iron oxide with similar crystalline structure than magnetite, but with different oxidation state. Magnetite has Fe^{3+} and Fe^{2+} states, while maghemite has only Fe^{3+} ions. There are several routes to obtain these iron oxides, one of them being coprecipitation, a quite straightforward method is very effectively obtain the oxides. Using different surfactants in the synthesis it is possible to obtain monodispersed particles with controlled size, which is a characteristic that helps in the formation of core-shell structures because high dispersity of the cores aids in the growing of a shell layer onto themselves [5, 6].

In this work, we synthesized core-shell cathodes using two iron oxides of similar crystalline structure but different oxidation state as the cores, along with Pt shells. In a modified coprecipitation method, ethylene glycol has been added as surfactant to improve the monodispersity in order to obtain such complicated architecture. The effect of the oxidation state of the cores on the catalytic activity for the ORR has been evaluated in acid and in alkaline media. The tolerance to ethanol has been evaluated as well.

2. Materials and Methods

The Fe_3O_4 particles were synthesized by coprecipitation method [7]. A solution with $FeCl_3*6H_2O$ and $FeCl_2*4H_2O$ (in a molar ratio of 1.5:2) were added to a concentrated NH_4OH (in a molar ratio of 14:1, respect to Fe_3O_4) under vigorous magnetic stirring. After 3 minutes of stirring, ethylene glycol was added into the solution and left in stirring for one hour. Then, the temperature was raised to 95 °C. Once the temperature was reached, the solution was removed from heat and let cool down to room temperature. In the whole procedure, pH was maintained 10 and finally was adjusted to 7 with HNO_3. In order to separate the powder the solution was rinsed thoroughly with water and acetone three times and dried at room temperature.

The Fe_2O_3 particles were obtained through the direct oxidation of the magnetite particles obtained in previous step. These particles were suspended in water with pH 3 (adjusted with HCl), the temperature was raised to 100 °C and stirred under aeration (with air) for one hour. The suspension color changed from black to reddish-brown. The particles were rinsed with water three times and dried at room temperature.

In a second step, the Fe_3O_4 or Fe_2O_3 particles used as seeds were suspended in a solution with $H_2PtCl_6*6H_2O$ (the atomic ratio used 1:1, core:Pt) in order to impregnate them. After 10 minutes of vigorous stirring, a solution with $NaBH_4$ was slowly added to reduce the Pt^{4+} to Pt^0 onto the surface of the iron oxides (the molar ratio was 2:1, $NaBH_4$:Pt^{4+}). Then, Vulcan XC-72 was added into the solution and after one hour of

vigorous stirring, the catalyst was rinsed with water three times and dried at room temperature.

To prepare the catalytic ink is as follows: separate mixture containing each catalysts, isopropanol and Nafion (5 μL) were prepared by ultrasound to form an ink with catalyst loading of 10 mg mL^{-1}. Then, an aliquot of 10 μL of the mix were deposited onto a 0.196 cm^2 geometrical area glassy carbon disc (mirror polished) fixed on a support. After drying, the working electrodes were obtained.

The catalytic activity was measured in a WaveDrive (Pine Inst.) bipotenciostat connected to a RDE (Pine Inst.). Both media, alkaline (0.5 M KOH) and acidic (0.5 M H_2SO_4), were tested. The counter electrode was a Pt coil and reference was Ag/AgCl. After 40 cycles at 50 mV s^{-1} cyclic voltammetry (CV) activation and CV profile at 20 mV s^{-1}, the ORR activity was measured at different rotation rates (400 until 2000 rpm) in a O_2-saturated electrolyte. CV was carried out to test the activity at 5 mV s^{-1}. Tolerance to ethanol in ORR was measured adding the alcohol in a 0.5 M concentration into the electrochemical cell and testing at 2000 rpm under oxygen bubbling.

3. Results and Discussion

The powders as obtained by a modified coprecipitation method (black) and after the oxidation step (reddish) were characterized by X-ray powder diffraction, Raman and infrared spectroscopies. Figures 1a) and 1b) show the experimental diffraction patterns from black and reddish powders, respectively. Both diffractograms show several peaks, wide and with a low intensity, due to a short-range atomic ordering or/and a very small particle size [8]. The position and intensities of all these peaks correspond to the main signals of those reported for iron oxides with a cubic crystal system and spinel structure in JCPDS 19-0629 (magnetite or Fe_3O_4) and JCPDS 39-1346 (maghemite or γ-Fe_2O_3). It is important to mention that there is only one significant difference between magnetite and maghemite structures; while in magnetite the 16 octahedral positions are occupied by both Fe^{2+} or Fe^{3+} ions, in maghemite these positions are occupied by 13 Fe^{3+} ions and 3 systematic vacancies. Additionally to this, a random distribution of vacancies, through octahedral positions (all of them equivalent), leads to the same symmetry of magnetite [9]. Therefore, XRD patterns of both Fe_3O_4 and γ-Fe_2O_3 can have the same diffraction peaks. The signals present at the experimental patterns of powders obtained in this work correspond to (220), (311), (400), (422), (511), (440) and (533) planes. In order to corroborate the presence of ethylene glycol on the samples, the FT-IR spectra were collected (see Figure 1c)). The stretching bands related to O-H, C-O and C-H bonds are more clearly present on magnetite than on maghemite sample. By Raman spectroscopy a broadening of some peaks allows to infer the structural change from magnetite to maghemite [10]. The Raman spectra obtained from black and reddish samples are shown at Figure 1d); as it is expected, both spectra are almost similar. However, for reddish powder the signal at 350 cm^{-1} shows a subtle broadening with respect to that from the black powder. This broadening lets to deduce that the experimental procedure used allows the obtaining of γ-Fe_2O_3 from Fe_3O_4.

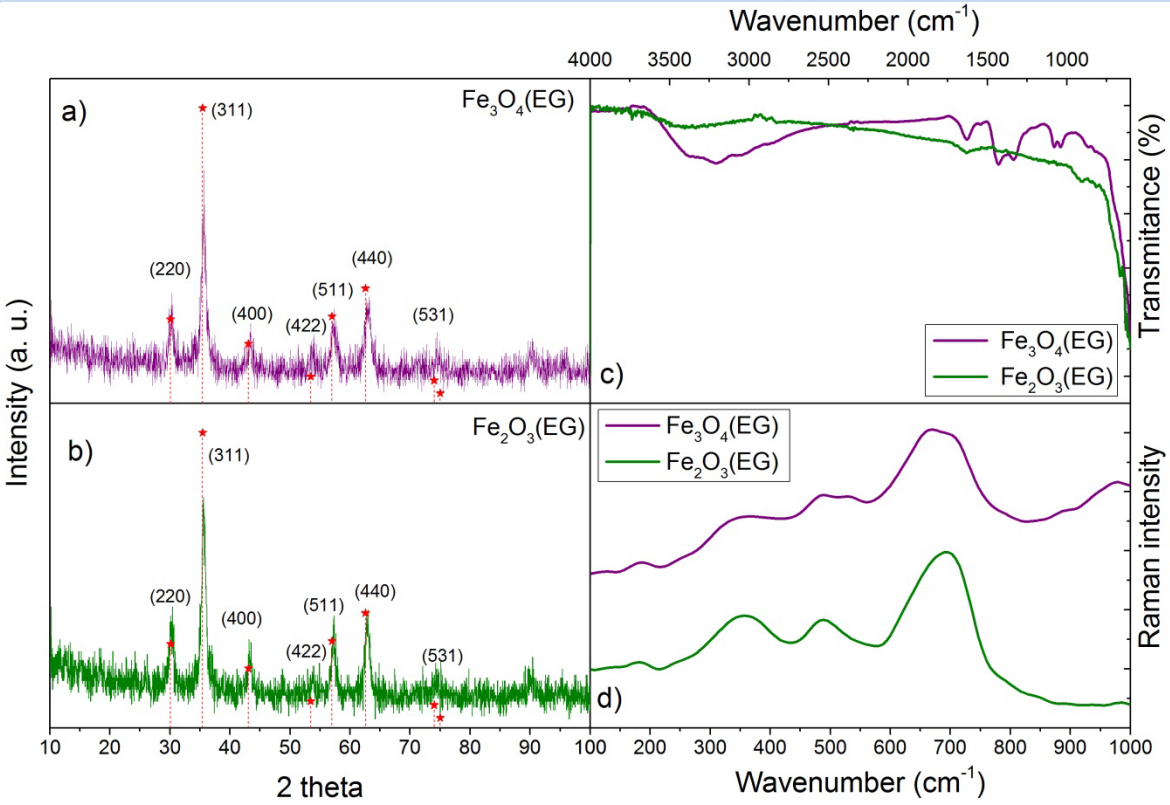

Fig. 4. Physicochemical characterization of Fe_3O_4 and Fe_2O_3 used as cores: a) Fe_3O_4 and b) Fe_2O_3 diffraction data; c) FT-IR spectra of Fe_3O_4 and $Fe2O_3$ with EG as surfactant and d) Raman spectra of both cores.

Figure 2 shows the diffraction patterns of the core-shell structures supported on Vulcan XC-72. Both materials present the fcc structure of Pt (Pt JCPDS 4-0802) with particle size of 4.7 and 6.3 Fe_3O_4@Pt/C and Fe_2O_3@Pt/C, respectively. The patterns also show the presence of Fe_3O_4 and Fe_2O_3 in each catalyst (a peak near to 35 ° 2θ).

Figure 3 depicts the catalytic activity for ORR on Fe_3O_4@Pt/C (Fig. 3a) and Fe_2O_3@Pt/C (Fig. 3b) in acidic media. The typical curves of platinoids materials are seeing, the three characteristic regions: i) kinetic region with a onset potential near to 0.8 V/RHE in each catalyst; ii) the mixed control region and iii) mass transfer region, where current density depends on the rotation rate. Note that Fe_3O_4@Pt/C current density is higher than Fe_2O_3@Pt/C. It is important to develop a highly selective catalyst that can be used in a DAFC, in order to prove the selectivity of these materials, the oxygen reduction on the catalysts were tested in presence of ethanol. High tolerance toward to a fuel oxidation is seeing in Fe_3O_4@Pt/C which means that this material can reduce oxygen selectively, while in Fe_2O_3@Pt/C is observed a mixed potential due to oxidation of ethanol and oxygen reduction which is reflected in an onset potential displacement to more negative potentials.

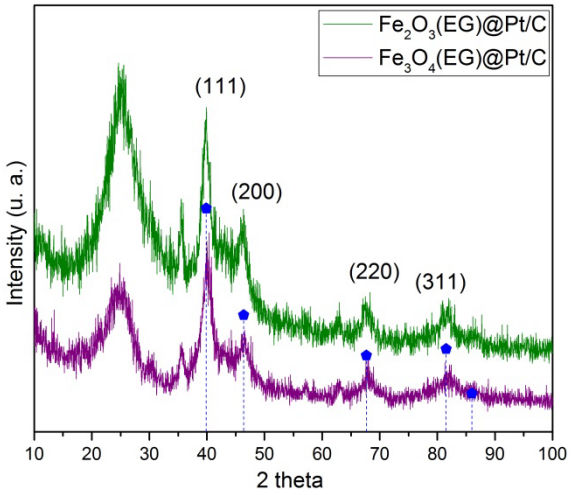

Fig. 5. XRD pattern for Fe_3O_4@Pt/C and Fe_2O_3@Pt/C.

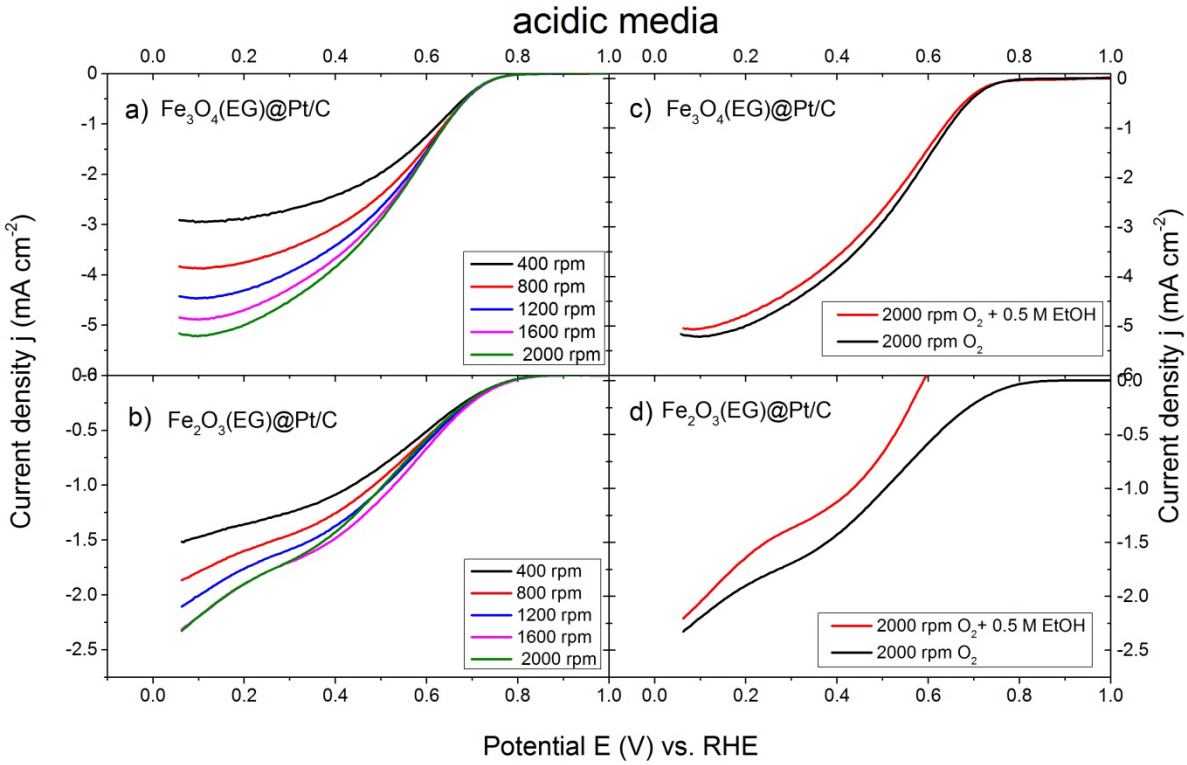

Fig. 6. Oxygen reduction reaction and tolerance toward ethanol oxidation of Fe_3O_4@Pt/C and Fe_2O_3@Pt/C in acidic media.

Figure 4 shows the ORR of both materials in alkaline media (a and b). The curves are reported against reversible hydrogen electrode through Nernst equation (Equation 1). Similar to acidic media, Fe_3O_4@Pt/C present a better performance in this reaction: its onset potential is near to 0.9 V/RHE and possess a better defined limiting current plateau with higher current densities (near to 6 mA cm^{-2} at 2000 rpm). Fe_2O_3@Pt/C have none well defined limiting current, but also presents onset potentials near to 0.9 V/RHE. Figure c and

d shows the tolerance towards ethanol. As it clearly sees and similar to results in acidic media, Fe3O4@Pt/C shows higher selectivity to ORR than Fe2O3@Pt/C due to its kinetic and mixed region remains intact without any displacement on the onset potential and any positive current.

$$E = E^0 + 0.059pH + E_{Ag/AgCl} \quad (1)$$

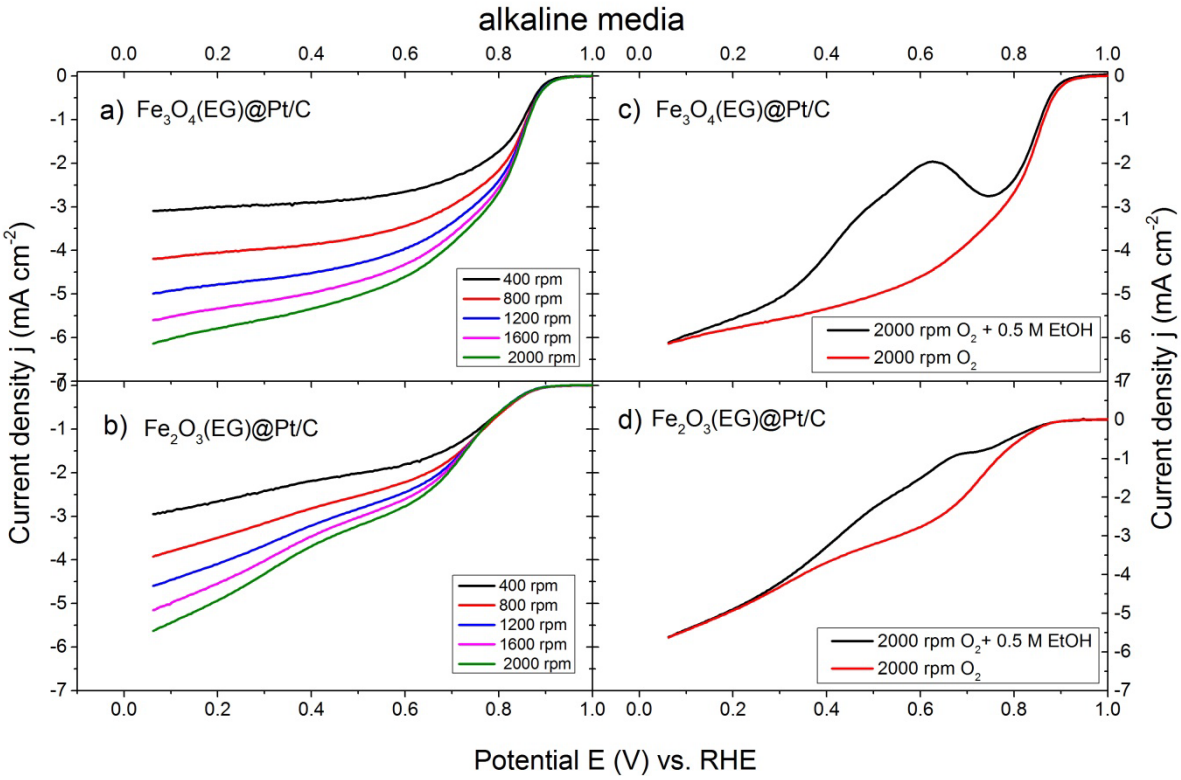

Fig. 7. Oxygen reduction reaction and tolerance toward ethanol oxidation of Fe_3O_4@Pt/C and Fe_2O_3@Pt/C in acidic media.

4. Conclusion

Both core-shell cathodes demonstrated high catalytic activity and enhanced tolerance properties related to a Pt/C cathode. Such characteristic has been attributed to the core-shell structure that modified the surface properties of Pt and also to the oxidation states of the iron oxide cores. Also, Fe_3O_4 seems to be a better core than Fe_2O_3 proving that iron oxide oxidation state affects the properties of Pt.

Acknowledgements

The authors are grateful to the National Council of Science and Technology (Conacyt) through the 252079, 241526 and 252003 projects. NMSP is thankful to Conacyt for the master's scholarship, to SMH and XV International Congress of the Mexican

Hydrogen Society for the fellowship to assistance to que congress. Authors also are grateful to Applied Chemistry Research Center (CIQA) to the facilities provided for the use of some of its installations.

References

[1] Sánchez-Padilla, N.M., Montemayor, S.M., Rodríguez-Varela, F.J. An Easy route to synthesize novel Fe3O4@Pt core-shell nanostructures with high electrocatalytic activity. J. New Mat Electrochem Systems 2012; 15:171-179.

[2] N. M. Sánchez-Padilla, D. Morales-Acosta, M. D. Morales-Acosta, S. M. Montemayor, F. J. Rodríguez-Varela. Catalytic activity and selectivity for the ORR of rapidly synthesized M@Pt (M = Pd, Fe3O4, Ru) core–shell nanostructures. Int. J. Hydrogen Energy 2014; 1–9.

[3] Meléndez-González, P.C., Montemayor, S.M., Morales-Acosta, D., Verde-Gómez, Y., Escobar, B., Rodríguez-Varela, F.J. Enhanced catalytic activity for ethanol oxidation reaction (EOR) using novel Pt-Fe3O4/MWCNT bimetallic electrocatalyst. J. New Mat Electrochem Systems 2014; 67-70.

[4] Altamirano-Gutiérrez, A., Fernández, A. M., Rodríguez Varela, F. J. Prepraration and characterization of Pt-CeO2 and Pt-Pd electrocatalysts for the oxygen reduction reaction in the absence and presence of methanol in alkaline medium. Int J. Hydrogen Energy 2013; 38:12657-12666.

[5] Shi Zhang Qiao, Jian Liu, Gao Qing (Max) Lu. In Xu, R., Pang, W., Huo, Q., editors. Modern Inorganic Synthetic Chemistry, Chapter 21. Amsterdam: Elsevier; 2011.

[6] Jana, N.R., Gearheart, L., Murphy, C.J. Seed-Mediated Growth Approach for ShapeControlled Synthesis of Spheroidal and Rod-like Gold Nanoparticles Using a Surfactant Template. Adv. Mater. 2001; 18:1389-1393.

[7] Gawande, M.B., Rathi, A.K., Tucek, J., Safarova, K., Bundaleski, N., Teodoro, O.M., Kvitek, L., Varma, R.S., Zboril, R. Magnetic gold nanocatalyst (nanocat-Fe–Au): catalytic applications for the oxidative esterification and hydrogen transfer reactions. Green Chem 2014; 16: 4019-4430

[8] Sun, Y.K., Ma, M., Zhang, Y., Gu, N. Synthesis of nanometer-size maghemite particles from magnetite. Colloids and Surfaces A: Physicochem. Eng. Aspects 2004; 245:15–19

[9] Shebanova, O.N., Lazor, P. Raman study of magnetite (Fe3O4): laser-induced thermal effects and oxidation. J. Raman Spectrosc. 2003; 34:845–852.

[10] Colomban, P., Cherifi, S., Despert, G. Raman identification of corrosion products on automotive galvanized steel sheets. J. Raman Spectrosc. 2008; 39: 881–886.

Chapter 8.11. Physicochemical and stability study of Ir-Sn-Sb-O materials as catalyst-supports for the oxygen evolution reaction

N. J. Pérez-Viramontes[a]; I. L. Escalante-García; C. Guzmán[a]; M. Galván-Valencia[a]; S. M. Durón-Torres[a*]

[a] Unidad Académica de Ciencias Químicas, Universidad Autónoma de Zacatecas, Campus Siglo XXI, Carretera Zacatecas-Guadalajara Km. 6.0, Ejido la Escondida, Zacatecas, Zacatecas, México, 98160.

ABSTRACT

A mixed oxide powder material, with general formula Ir-Sn-Sb-O, was prepared in one-step synthesis by the thermal decomposition of the chloride precursors H_2IrCl_6, $SnCl_4{\cdot}5H_2O$, and $SbCl_3$ in ethanol. This powder material is both an electrocatalyst and support for its possible use as anode in solid polymer electrolyte water electrolyzers (SPEWEs). Two theoretical atomic percentages of iridium (10 and 40 at. % Ir) in the reaction mixture were considered to investigate the electrocatalytic activity of the mixed oxides toward the oxygen evolution reaction (OER) in acidic media.

Preliminary results show that the mixed oxide material exhibited micrometric agglomerations of finer globular structures as observed from scanning electron micrographs (SEM). Addionally, the atomic composition of iridium was estimated to be near to the theoretical atomic percentages in the synthesis step for both mixed oxides materials, 10.7 at. % Ir for Ir-Sn-Sb-O (10) and, 45.0 at. % Ir for Ir-Sn-Sb-O (40) using energy dispersive X-ray analysis (EDAX) coupled to SEM. The present phases of the powder material and the particle size was analyzed by X-ray diffraction (XRD). The results indicated the presence of the iridium oxide, antimmony oxide and metallic iridium in both materials.

Overall, the particle size was estimated between 1 – 2 nm. The stability of the materials was evaluated by chronoamperometry (CA) at a potential of 1.55 V vs NHE during a period of 8 h, showing that the matetials are stable. The conductivity of the mixed oxides was measured by four-probe method, the conductivity of both materials are greater than SnO_2 and Sb-SnO_2. The results demonstrate a nanometric particle size with high stability for OER, thus the synthesized materials are suitable for their use as catalyst-support anode for PEM water electrolyzers.

Keywords: Iridium catalyst, Oxygen evolution reaction, Water electrolysis

1. Introduction

The so called Clean Energy Sources are suitable to reduce the environmental impact of fossil fuels, however they are intermittent, so that an energy storage step is necessary, this

---

*Author for correspondence:
Dr. Sergio M. Durón Torres, Tel: +524929256690 Ext. 4655; e-mail: duronsm@prodigy.net.mx

means the use devices such as batteries. Another alternative is the use of chemical energy storage, such is the case of hydrogen as an energy vector, which electrochemical reaction with oxygen produces a great amount of energy.[1–3]

Fuel cells are a viable alternative for electrochemeical energy production avoiding pollutants generation. In recent years, there have been an increased research in this type of devices, with the aim of maximizing their global efficiency. Related with the use of fuel cells, an increase in the research about the hydrogen production and storage has been observed.

There are different processes for H_2 production, such as hydrocarbon reforming, photocatalytic products, biodigesters, water thermolysis, electrolysis of water, etc. The water electrolysis is one of the most striking, because in the production of H_2, the secondary reaction product is O_2, unlike the others, which are obtained as byproducts pollutants such as CO, CO_2 and sulfur compounds. Polymer-electrolyte membrane water electrolyzer (PEMWE) it´s one of the most studied today.[4–6]

Water electrolysis is a process in which water molecule is separated into hydrogen molecules and oxygen through the use of electrical energy. In this process, a power source is connected to two electrodes which are in contact with water to react, in carrying out the reaction, hydrogen evolution occurs at the cathode, while the evolution of oxygen takes place in the anode side. Electrolysis of water requires excess energy in the form of overpotential to overcome activation barriers. No excess energy in water electrolysis, hydrogen and oxygen are produced slowly.[7]

The limiting reaction in the process of electrolysis is the oxygen evolution reaction (OER). To promote OER, have been used different types of catalysts, and has been found that precious metal oxides with rutile structure, such as ruthenium and iridium oxide have a higher electrocatalytic activity for this reaction. [8–10]. However, the materials used as catalysts for this reaction are of low abundance in the earth's crust, raising the price of such materials. For this reason, new materials are investigated on which disperse the active material to reduce the content of it, trying to get similar results to those that would be obtained if the pure material were used.[11]

Tin oxide doped with antimony (ATO) has been used in multiple applications, as in the case of fuel cells, batteries, gas sensors, solar cells. Recently has been invsestigated its use as a support for catalysts in water electrolyzers for OER due to its corrosion resistance in acidic media.[12,13] SnO_2-IrO_2 mixtures have been extensively studied for the oxygen evolution reaction in acidic environment. In recent years we have studied the synthesis methods for obtaining multimetal materials to reduce precious metals in the anode, waiting for the electrocatalytic activity is not affected.[14–18]

This study shows the synthesis of composite with general formula Ir-Sn-Sb-O by the thermal decomposition of the chloride precursors in ethanol. Also shown the physicochemical characterization and a stability study of the obtained materials for its application in PEMWE.

2. Materials and Methods

2.1 Synthesis of mixed oxide

Mixed oxides materials were prepared by a conventional thermal decomposition method as follows[19–22]. A 0.25 M solution of metal precursors based on H_2IrCl_6, $SnCl_4{\cdot}5H_2O$ and $SbCl_3$ (Aldrich) was prepared in pure ethanol. The metal precursor proportions in the solution were such that the calculated atomic percentages corresponded to (1) 10 at.% Ir, 85 at.% Sn, 5 at.% Sb or (2) 40 at.% Ir, 57 at.% Sn, 3 at.% Sb. The solution was then heated at 50 °C for 2 h in N_2 atmosphere. Afterwards, the mixed oxide precursor was calcined at 450 °C for 0.5 h. The synthesized powders were washed with deionized water and then dried. The materials synthetized by this procedure are denoted as Ir–Sn–Sb–O(*xx*) where *xx* represents the theoretical atomic % Ir (10 or 40 at.%) in the synthesis procedure with respect to the other metals, i.e. Ir–Sn–Sb–O (40) or Ir–Sn–Sb–O (10).

2.2 Physicochemical characterization

Scanning electron microscopy (SEM) was carried out on a field emission (JSM-7401F) microscope operated at 2 and 4 kV. Atomic composition of samples were evaluated by energy dispersive X-ray analysis (EDAX) coupled to SEM. The phase structure of powders and the crystal size of the materials were confirmed by X- ray diffraction (XRD) on a Bruker AXS (D8 Advance) diffractometer, using Cu Kα radiation and glancing-angle geometry at a step of 0.04° s^{-1} in the Bragg angle range of 0°–150°.

2.3 Stability probes

The stability of the catalytic materials were evaluated by chronoamperometry (CA) recording the oxygen evolution current at a constant potential of 1.55 V for 8 h. The measurements were conducted in a typical three-electrode cell, employing a potentiostat/galvanostat (EG&G, PAR Versastat 3). A sulfate electrode (0.63 V vs. NHE) was used as reference and a platinum mesh as counter electrode. A N_2-saturated aqueous solution of 0.5 M H_2SO_4 was employed as the electrolytic medium. The electrodes were prepared from a catalytic ink containing 3 mg of synthesized Ir–Sn–Sb–O, 10 μL of Nafion® (5 wt%, Adrich) and 60 μL of ethanol spectroscopic grade. The ink was then placed in an ultrasonic bath in order to get a homogeneous and well dispersed particles suspension. The ink was deposited on a glassy carbon electrode (GCE), 30 $\mu L cm^{-2}$, then the coated GCEs were dried at 50 °C. The electrode potentials in this work are referred to the normal hydrogen electrode (NHE) and the current density was normalized to the geometric area of the electrodes.

2.4. PEMWE single cell test

The electro catalytic activity if the Ir-Sn-Sb-O (40) material was evaluated in single cell PEMWE with an active area of 9 cm^2, Nafion® 117 membrane was employed as solid polymer electrolyte. As cathode was used a Pt/C mixture, and as anode the mixed oxide previously described, additionally assembly using commercial IrO_2 for comparison was prepared. The electrodes were prepared employing a methodology developed in the Instituto de Investigaciones Eléctricas, Cuernavaca, México. The polarization curves was

realized at four different temperatures (25 °C, 40 °C, 60 °C and 70°C) from 0 V to 2.5 V. So the volume of hydrogen could be obtained.

3. Results and Discussion

3.1 Physicochemical characterization

XDR patterns of the Ir-Sn-Sb-O materials are shown in Fig 1. The XDR results indicate that the two synthetized materials are a mixture of phases, exhibiting the presence of SnO_2 (2θ=26.6, 33.9, 37.9, 51.8, 65.9, 108.3 and 116) metallic Ir (2θ=40.7, 47.3, 69.1, 83.4, 88, 121.9 and 127.6) and IrO_2 (2θ= 28, 34.7, 40, 54, 57.9, 66 and 93.6) according to the JCPDS 41-1445, 46-10444 and 15-0870 files, respectively. According to the peak intensities, the IrO_2 and the SnO_2 are present in similar quantities in Ir-Sn-Sb-O (40) material, the superposition of diffraction signals of these two oxides produces the widening in some of the resulting peaks. The quantity of SnO_2 is higher than IrO_2 and metallic Ir in the sample of Ir-Sn-Sb-O (10) material, resulting in sharper signals. The presence of metallic iridium is observed in both samples, nevertheless is higher for Ir-Sn-Sb-O (40) than Ir-Sn-Sb-O (10), suggesting that the quantity of H_2IrCl_6 in the synthesis is the synthesis solution is a factor in the final phase distribution obtained in Ir-Sn-Sb-O materials.

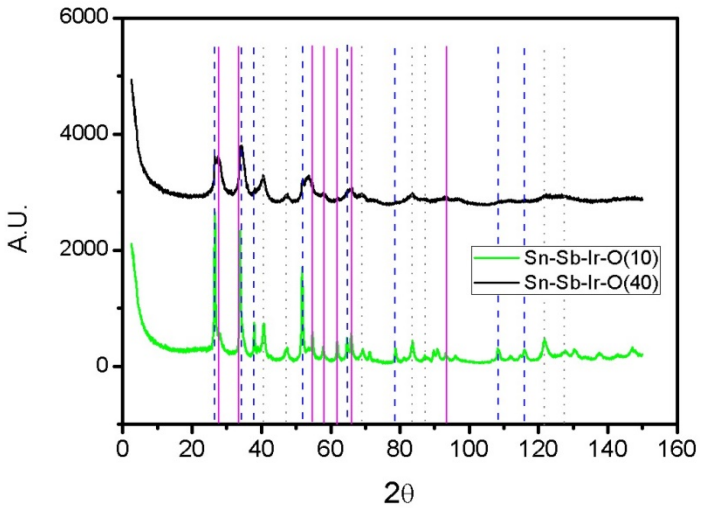

Fig. 1. X-ray diffraction patterns of synthesized materials, the horizontal lines correspond to the characteristic reflection peaks of (dashed line) SnO_2, (solid line) IrO_2 and (dotted line) Ir.

The SEM micrographs of the IR-Sn-Sb-O materials are shown in a Fig 2. The morphology of the Ir-Sn-b-O (40) material (Fig 2a) consist on micrometric agglomeration of globular structures of nanometric size, between 6 nm to 10 nm. The micrograph of Ir-Sn-Sb-O (10) (Fig 2b) shown a more dispersive particle that only could be resolved a more electron energies (4kV), the morphology of this material consist in quiasi-spherical particles of nanometric dimensions. The particles size were obtained form XDR patterns employing Scherrer equation.

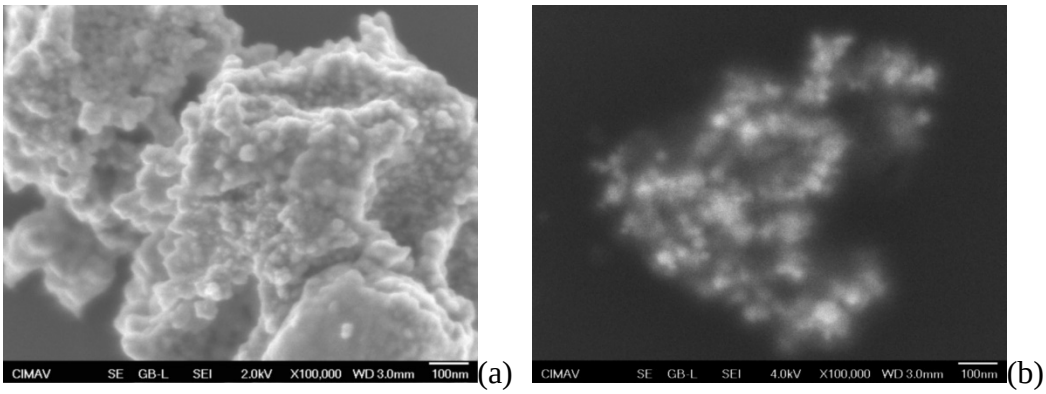

Fig 2. SEM images of the prepared materials a Ir–Sn–Sb–O (10) and b Ir–Sn–Sb–O (40)

The atomic and weight metal composition was obtained by EDAX, which are shown in Table 1. The atomic experimental percent obtained are near to the theoretical percentages used in the synthesis for materials, 10 at.% and 40 at.% Ir, nevertheless, in some regions of Ir-Sn-Sb-O (40) sample were found larger quantities (in some cases near to 87 at.% Ir). This heterogeneous composition is consistent whit XDR experimental phase distribution.

Table 1. EDAX composition of mixed oxides.

Element	Ir-Sn-Sb-O (10)		Ir-Sn-Sb-O (40)	
	% W	% A	% W	% A
Sn	79.9	85.3	38.6	49.4
Sb	3.9	4.1	4.5	5.6
Ir	16.2	10.7	56.9	45.0

3.2 Stability probes

The electro-catalytic activity and stability of Ir-Sn-Sb-O materials for oxygen evolution reaction were studied by chronoamperometric experiments. The current-time curves for Ir-Sn-Sb-O (10) and Ir-Sn-Sb-O (40) in 0.5 M H_2SO_4 at 1.55 V for 25000 s are shown in Fig 3. It can be seen that the current densities of the two mixed oxides drop quickly at the initial stage and then the electrode reaction of oxygen generation reaches a stationary state. The steady-state current density on Ir-Sn-Sb-O (40) electrode decrease to 50 mA cm^{-2} at final of the period, the current density for Ir-Sn-Sb-O (10) is 5 $mAcm^{-2}$, which is lowest value. The noise of the signal for the Ir-Sn-Sb-O (40) material is attributed at evolution of O_2, compared with the Ir-Sn-Sb-O (10) it does not generate large amounts of oxygen. Both materials exhibit stability in the period of probe.

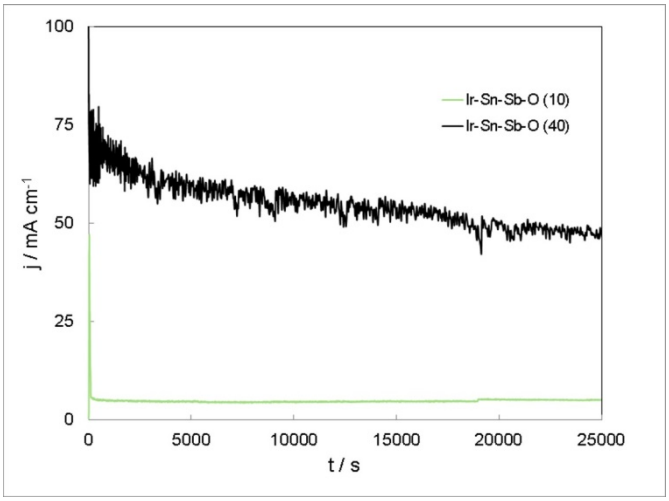

Fig 3. Chronoamperometric curves of Ir-Sn-Sb-O materials at 1.55 V in 0.5 M H_2SO_4.

3.3 PEMWE single cell test

Fig 4 gives the steady state polarization curves for PEMWE single cell, employing Nafion® 117 membrane as electrolyte, Pt/C as cathode and Ir-Sn-Sb-O as anode at different temperatures, 25 °C (Fig 4a), 40 °C (Fig 4b), 60 °C (Fig 4c) and 70 °C (Fig 4d). There is shown that the onset potential starts around 1.4 V for the IrO_2 electrode. In the case of the Ir-Sn-Sb-O (40) material, the onset potential starts around 1.5 V. Among in the Fig 4 is shown that in all the temperatures rang, the performance of the mixed oxide synthetized is poor compared with the anode comprised of IrO_2, at different potentials, however the amount of noble metal in the mixture is lower for the material Ir-Sn-Sb-O (40), since other metals are present. The performance of the mixed oxide is increasing with increasing temperature, which temperature being 70 ° C increases significantly compared to current lower temperatures, contrary to the performance observed with IrO_2 anode, which shows a similar performance for temperature of 60 ° C and 70 ° C. For mixed oxides of this type, where reported 1.6 V at 500 $mAcm^{-2}$ at 80 °C[18,14]. The volume of hydrogen produced was measured at 70 ° C to 2.5 V, resulting in a hydrogen flow of 50 $mLmin^{-1}$ for the assembly with Ir-Sn-Sb-O (40), and 68 $mLmin^{-1}$ for IrO_2.

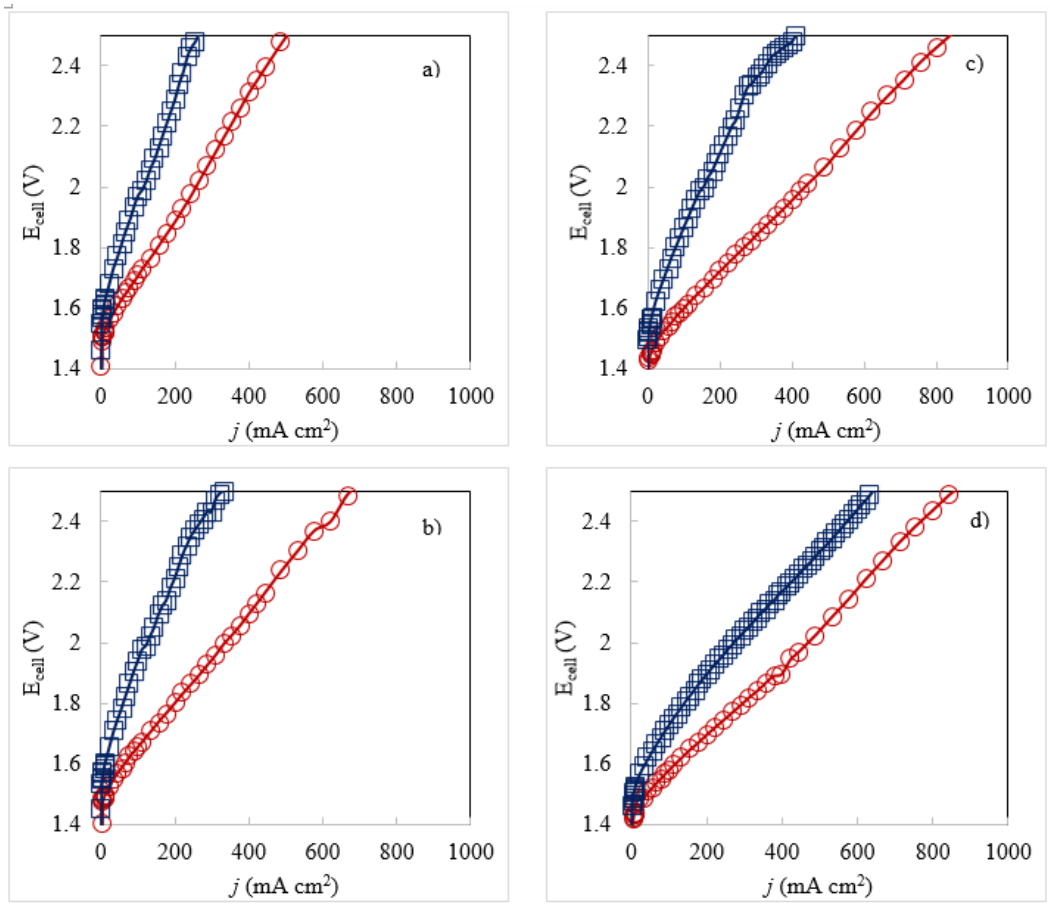

Fig 4. Steady state polarization curves of PEMWE cell, employing IrO2 anode (⊖) and Ir-Sn-Sb-O (40)(⊟) at different temperatures, a) 25 °C, b) 40 °C, c)60 °C and d) 70 °C.

4. Conclusion

The results of physicochemical analysis show the presence of Ir, IrO2, SnO2 and Sb, additionally a nanometric particle size is observed for both materials. This results could be confirmed whit additional physicochemical tests. The mixed oxide Ir-Sn-Sn-Sb-O are stable at a condition of low potential of 1.55 V, potential which the OER is present, however, as revelate PEMWE single cell test, the operating potential to obtain high current densities is close to 2.5 V, thus should perform stability tests close to these potential. The results suggest that the material should still be studied in order to optimize the synthetic methodology to obtain high current densities with a low iridium content.

Acknowledgements

The authors acknowledge financial support from the Mexican Council for Science and Technology (CONACyT, Project 167012). In addition, we would like to thank MSc. Carlos Ornelas for his help in the SEM/EDAX sample characterization at the Laboratorio Nacional de Nanotecnología, CIMAV. To Ph. D José Roberto Flores for his help in the realization in PEMWE single cell test at the Instituto de Investigaciones Eléctricas, IIE. SMH and XV International Congress of the Mexican Hydrogen Society for your attention for the participation in this congress.

References

[1] Dincer I, Acar C. Review and evaluation of hydrogen production methods for better sustainability. Int J Hydrog Energy n.d. doi:10.1016/j.ijhydene.2014.12.035.
[2] Kleijn R, van der Voet E. Resource constraints in a hydrogen economy based on renewable energy sources: An exploration. Renew Sustain Energy Rev 2010;14:2784–95. doi:10.1016/j.rser.2010.07.066.
[3] Ren J, Gao S, Tan S, Dong L, Scipioni A, Mazzi A. Role prioritization of hydrogen production technologies for promoting hydrogen economy in the current state of China. Renew Sustain Energy Rev 2015;41:1217–29. doi:10.1016/j.rser.2014.09.028.
[4] Millet P, Ngameni R, Grigoriev SA, Mbemba N, Brisset F, Ranjbari A, et al. PEM water electrolyzers: From electrocatalysis to stack development. Int J Hydrog Energy 2010;35:5043–52. doi:10.1016/j.ijhydene.2009.09.015.
[5] Grigoriev SA, Porembsky VI, Fateev VN. Pure hydrogen production by PEM electrolysis for hydrogen energy. Int J Hydrog Energy 2006;31:171–5. doi:10.1016/j.ijhydene.2005.04.038.
[6] Chaubey R, Sahu S, James OO, Maity S. A review on development of industrial processes and emerging techniques for production of hydrogen from renewable and sustainable sources. Renew Sustain Energy Rev 2013;23:443–62. doi:10.1016/j.rser.2013.02.019.
[7] Lee J, Jeong B, Ocon JD. Oxygen electrocatalysis in chemical energy conversion and storage technologies. Curr Appl Phys 2013;13:309–21. doi:10.1016/j.cap.2012.08.008.
[8] Audichon T, Mayousse E, Napporn TW, Morais C, Comminges C, Kokoh KB. Elaboration and characterization of ruthenium nano-oxides for the oxygen evolution reaction in a Proton Exchange Membrane Water Electrolyzer supplied by a solar profile. Electrochimica Acta 2014;132:284–91. doi:10.1016/j.electacta.2014.03.141.
[9] Audichon T, Mayousse E, Morisset S, Morais C, Comminges C, Napporn TW, et al. Electroactivity of RuO2–IrO2 mixed nanocatalysts toward the oxygen evolution reaction in a water electrolyzer supplied by a solar profile. Int J Hydrog Energy 2014;39:16785–96. doi:10.1016/j.ijhydene.2014.07.170.
[10] Ardizzone S, Bianchi CL, Cappelletti G, Ionita M, Minguzzi A, Rondinini S, et al. Composite ternary SnO2–IrO2–Ta2O5 oxide electrocatalysts. J Electroanal Chem 2006;589:160–6. doi:10.1016/j.jelechem.2006.02.004.
[11] Antolini E. Iridium as catalyst and cocatalyst for oxygen evolution/reduction in acidic polymer electrolyte membrane electrolyzers and fuel cells. ACS Catal 2014;4:1426–40. doi:10.1021/cs4011875.
[12] Xu J, Li Q, Hansen MK, Christensen E, Tomás García AL, Liu G, et al. Antimony doped tin oxides and their composites with tin pyrophosphates as catalyst supports for oxygen evolution reaction in proton exchange membrane water electrolysis. Int J Hydrog Energy 2012;37:18629–40. doi:10.1016/j.ijhydene.2012.09.156.
[13] Hu Y, Zhang H, Yang H. Synthesis and electrical property of antimony-doped tin oxide powders with barite matrix. J Alloys Compd 2008;453:292–7. doi:10.1016/j.jallcom.2006.11.062.
[14] Marshall A, Børresen B, Hagen G, Tsypkin M, Tunold R. Electrochemical characterisation of IrxSn1−xO2 powders as oxygen evolution electrocatalysts. Electrochimica Acta 2006;51:3161–7. doi:10.1016/j.electacta.2005.09.004.
[15] De Pauli CP, Trasatti S. Composite materials for electrocatalysis of O2 evolution: IrO2+SnO2 in acid solution. J Electroanal Chem 2002;538–539:145–51. doi:10.1016/S0022-0728(02)01055-0.

[16] De Pauli CP, Trasatti S. Electrochemical surface characterization of IrO2 + SnO2 mixed oxide electrocatalysts. J Electroanal Chem 1995;396:161–8. doi:10.1016/0022-0728(95)03950-L.
[17] Kadakia K, Datta MK, Velikokhatnyi OI, Jampani P, Park SK, Saha P, et al. Novel (Ir,Sn,Nb)O2 anode electrocatalysts with reduced noble metal content for PEM based water electrolysis. Int J Hydrog Energy 2012;37:3001–13. doi:10.1016/j.ijhydene.2011.11.055.
[18] Li G, Yu H, Wang X, Yang D, Li Y, Shao Z, et al. Triblock polymer mediated synthesis of Ir–Sn oxide electrocatalysts for oxygen evolution reaction. J Power Sources 2014;249:175–84. doi:10.1016/j.jpowsour.2013.10.088.
[19] Fierro S, Kapał ka A, Comninellis C. Electrochemical comparison between IrO2 prepared by thermal treatment of iridium metal and IrO2 prepared by thermal decomposition of H2IrCl6 solution. Electrochem Commun 2010;12:172–4. doi:10.1016/j.elecom.2009.11.018.
[20] Kadakia K, Datta MK, Velikokhatnyi OI, Jampani P, Park SK, Saha P, et al. Novel (Ir,Sn,Nb)O2 anode electrocatalysts with reduced noble metal content for PEM based water electrolysis. Int J Hydrog Energy 2012;37:3001–13. doi:10.1016/j.ijhydene.2011.11.055.
[21] Marshall A, Børresen B, Hagen G, Tsypkin M, Tunold R. Hydrogen production by advanced proton exchange membrane (PEM) water electrolysers—Reduced energy consumption by improved electrocatalysis. Energy 2007;32:431–6. doi:10.1016/j.energy.2006.07.014.
[22] Ouattara L, Fierro S, Frey O, Koudelka M, Comninellis C. Electrochemical comparison of IrO2 prepared by anodic oxidation of pure iridium and IrO2 prepared by thermal decomposition of H 2IrCl6 precursor solution. J Appl Electrochem 2009;39:1361–7. doi:10.1007/s10800-009-9809-2.

Chapter 8.12. Defects and disorder in the $Gd_2Hf_{2-x}Zr_xO_7$ solid solution: mechanochemical synthesis, characterization and electrical properties

N. M. Cepeda-Sánchez[a]; J. A. Díaz-Guillén[b]; U. Amador[c]; A. F. Fuentes[a*]

[a]Cinvestav Unidad Saltillo, Apartado Postal 663, 25000-Saltillo, Coahuila, Mexico.
[b]División de Estudios de Posgrado e Investigación, Instituto Tecnológico de Saltillo, 25280-Saltillo, Coahuila Mexico.
[c] Facultad de Farmacia, Departamento de Química y Bioquímica, Universidad San Pablo CEU, Urbanización Montepríncipe, 28668 Boadilla del Monte, Madrid, Spain.

ABSTRACT

This paper reports the mechanochemical synthesis and structural and microstructural characterization of different compositions in the $Gd_2Hf_2O_7$-$Gd_2Zr_2O_7$ system showing complete miscibility. Mixed oxides prepared by mechanical milling exhibit XRD patterns similar to those characteristic of fluoritelike materials despite of both end limits crystallizing with the pyrochlore structure. Post-milling thermal treatments at high temperatures favor the formation of ordered pyrochlore-type oxides. Electrical properties were measured by using impedance spectroscopy as a function of temperature, and frequency; conductivity (σ_{dc}), and activation energies (E_{dc}) for oxide ion migration in the system, were calculated as a function of the Hf/Zr ratio. As for the conductivity values of the system $Gd_2Hf_{2-x}Zr_xO_7$ indicate the activation energies for *dc* conductivity in the range 0.87-1.17 eV.

Keywords: Mechanical milling, Order-disorder transition, pyrochlore, Fluorite

1. Introduction

Ternary metal oxides with the general formula $A_2B_2O_7$ (wherein A and B are metals) are predominantly ionic, and crystallize with the pyrochlore structure. They have the ability to accept different lanthanide, and actinide elements in the A position; whereas, the B-site is occupied mostly for tetravalent elements such as Zr^{4+} and Ti^{4+}. This family of oxides exhibit a variety of physical, and chemical properties of interest depending on their chemical composition, the degree of order/disorder present, and the existence of defects (vacancies). Thus, the electrical nature of these materials can range from electrical insulators to semiconductors, ionic, electronic or mixed conductors, and superconductors.

---

* Author for correspondence:
Dr A. F. Fuentes, tel.: +52 844 4389617; email: fuentesaf@live.com

They also present very low thermal conductivity, and unusual low temperature physics leading to important technological applications. Therefore, pyrochlore oxides are promising candidate materials for fuel cells (SOFC, Solid Oxide Fuel Cells), thermal barrier coatings (TBCs) or inorganic matrices for the chemical immobilization of nuclear waste of high activity [1, 2]. Generally these oxides are synthesized by solid state reaction using high temperatures, and long periods of time. The synthesis by mechanical milling is a relatively inexpensive, and simple to carry out process; reagents are processed under far-from-equilibrium conditions yielding phases with a high concentration of structural defects which are difficult to obtain by conventional processing. This opens the possibility to manipulate the structure/microstructure of the target material by additional processing (e.g. heat treatment after milling), and optimize its properties.

The purpose of this research is to synthesize several compositions with the $Gd_2Hf_{2-x}Zr_xO_7$ general formula (x = 0, 0.4, 0.8, 1.2, 1.6 and 2), via a mechanochemical reaction, analyze its structure / microstructure, and study its thermal, and electrical properties. It is also intended to compare the results with those determined for materials with similar chemical composition but prepared by traditional ceramic method. The structural disorder in a pyrochlore type arrangement $A_2B_2O_7$ depends mainly of the size difference between the cations occupying two crystallographic available sites (the ratio R_A/R_B), and the bonding character. Therefore, by using appropriate chemical substitutions, it can be achieved phases similar chemical composition but different degree of order / structural disorder, and therefore properties. Furthermore, the degree of order / disorder that exists in these structures is strongly dependent on the processing method followed for the stages of interest.

2. Experimental

Six compositions of general formula $Gd_2(Hf_{2-x}Zr_x)O_7$ (x = 0, 0.4, 0.8, 1.2, 1.6 and 2) were prepared by mechanical dry milling, starting from mixtures of high purity cubic Gd_2O_3 (Aldrich Chem.Inc.,99.99%), monoclinic ZrO_2 (Aldrich Chem.Inc.,99.99%) and monoclinic HfO_2 (Aldrich Chem.Inc.,98%). Starting powders were weighed out in the appropriate stoichiometric ratio, and placed in 125mL zirconia containers with eight 20 mm diameter zirconia balls (mass ≈ 24 g) as to keep balls to powder mass ratio equal to 10:1. Mechanical milling was performed in air at room temperature, in a Retsch PM/400 planetary ball mill, using a rotating disc speed of 350 rpm, and reversed rotation every 20 min.

Phase evolution with milling time was followed by using X-ray powder diffraction in a Philips X'pert diffractometer using Ni-filtered CuKα radiation (λ = 1.5418 Å). Portions of these powder samples were subject to post-milling thermal treatment (12h) at temperatures of 1200 and 1500 ºC and analyzed by X-ray powder diffraction. The structural, and microstructural features of the materials were obtained from precise diffraction data obtained on a Bruker D8 high-resolution X-ray powder diffractometer, using monochromatic CuKα (λ = 1.5406 Å) radiation obtained with germanium primary monochromator, and equipped with a position sensitive detector (PSD) MBraun PSD-50M.

The measured angular range, the step size and counting times were selected to ensure enough resolution (the step size should be at least, 1/10 of the fwhms) and statics. The instrumental contribution to line broadening was evaluated using NIST LaB_6 standard

reference material (SRM 660a; μ= 1138 cm^{-1}, linear absorption coefficient for CuKα1 radiation). The structural refinements were carried out by the Rietveld method using the Fullprof program [3] and taking into account, simultaneously, the effects of the sample microstructure on the diffraction patterns according to a phenomenological approach described in detail elsewhere [4, 5].

Impedance studies were carried out on annealed pellets (10 mm diameter and ~1 mm thickness) by using a Solartron 1260 Frequency Response Analyzer to obtain electrical conductivity relaxation data. In order to analyze the relationship between electrical and structural (degree of ordering) properties in our powder samples, we study the temperature of 1500 ºC (for 12 h; heating and cooling rate 5 ºC/min). Electrodes were made by coating opposite faces of the pellets with SPI-Chem™ conductive platinum paint and firing them at 600 ºC to eliminate organic components and harden the Pt residue. Data were recorded in air for each sample from 280 to 750 ºC over the 100HZ-1 MHz frequency range. The evolution of the sintered pellets was analyzed by XRD.

3. Results and Discussion

3.1. Synthesis and characterization

Fig.1 shows and XRD study of the evolution of the Gd_2O_3:0.4HfO_2:1.6ZrO_2 reaction mixture selected as representative of the series, as a function of milling time. The remaining compositions showed a very similar behavior to that described here. Subsection 1(a) of the figure mentioned corresponds to the diffraction pattern obtained for the stoichiometric mixture of the starting reagents. As shown in Figure 1(b) after the first hour of milling, the characteristic reflections of the starting reagents suffer a considerable decrease in intensity (~ 89%), and increase in width compared to the diffractogram of the starting mixture 1(a); this effect is very common in mechanically milled powders as a result of decreasing particle size, and the accumulation of a significant number of structural defects. Cubic Gd_2O_3 (CG 2θ ~ 29º y 33º) undergoes a partial polymorphic transformation to the monoclinic B-Gd_2O_3 form. When thermally activated, this phase transition occurs at temperatures near 1200°C [6].

The identification of the chemical species within the first hour of grinding is difficult due to the superposition of reflections. However, the characteristic reflections of both ZrO_2 in, and HfO_2 of monoclinic symmetry (2θ ~ 24°, 32º, 51º, 52º), are also clearly observed.

The diffractograms obtained for 1, 3 and 6 hours of milling, exhibit reflections of lesser intensity compared to 9 hours, suggesting the amorphous phase content of the starting reactants. After nine hours of grinding, these reflections characteristics of fluorite type structure corresponding to the Miller indices (111), (200), (220) and (311) at 2θ ~ 29.5º, 34º, 49º and 58º are made respectively, highlighting that the chemical reaction between the starting reagents has been made. The diffractograms obtained are compared with the diffractogram reported in literature for $Gd_2Zr_2O_7$ fluorite phase (PDF 80-0471).

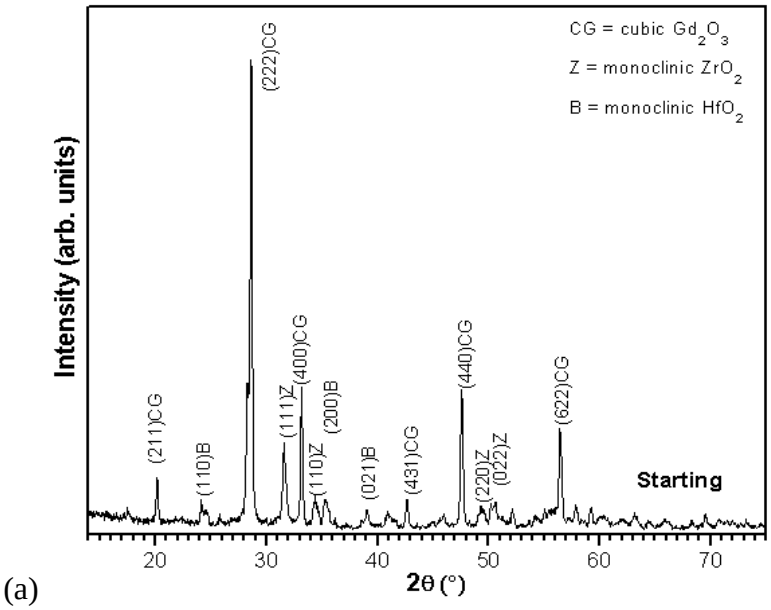

(a)

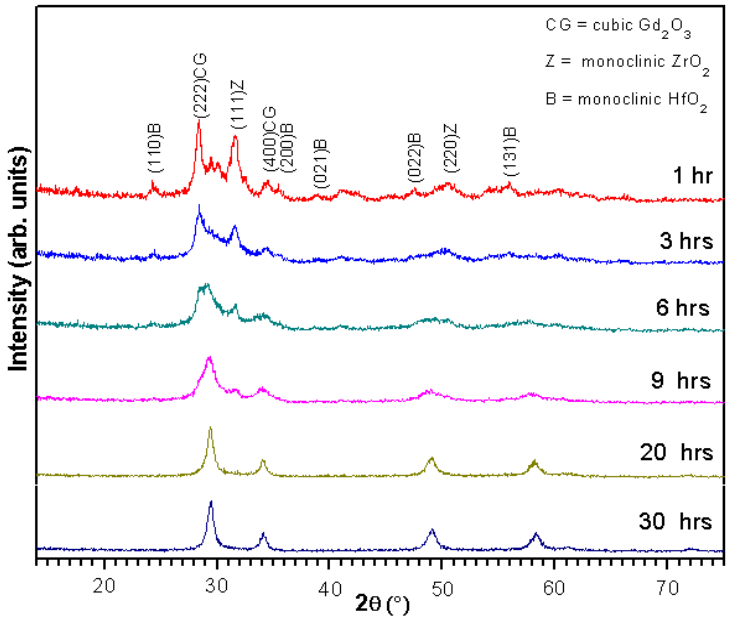

(b)

Fig. 1. (a) Diffractogram obtained for the stoichiometric mixture of the starting reagents (CG: Gd_2O_3 cubic, Z: ZrO_2 and B: HfO_2 are monoclinic). (b) diffractograms corresponding to the evolution of the mixtures (Gd_2O_3 +0.4HfO_2+1.6ZrO_2) with grinding time.

Fig. 2 shows a comparison of the diffractograms obtained after heat treatment at 1200 °C and 1500 °C for 12 hours for $Gd_2(Hf_{0.4}Zr_{1.6})O_7$ previously ground representative sample. As can be appreciated even by applying a heat treatment at 1200 °C continue the reflections characteristics of fluorite type structure. When heat treated at 1500 °C can be seen as reflections increase in number and size as corresponding to that reported in literature for the

pyrochlore phase Gd_2Zr_2O7 (PDF 79-1146), which match the Miller indices (111), (311) and (331) at 2θ ~ 15º, 28º and 37º respectively, confirming the origin to a more ordered structure of pyrochlore type.

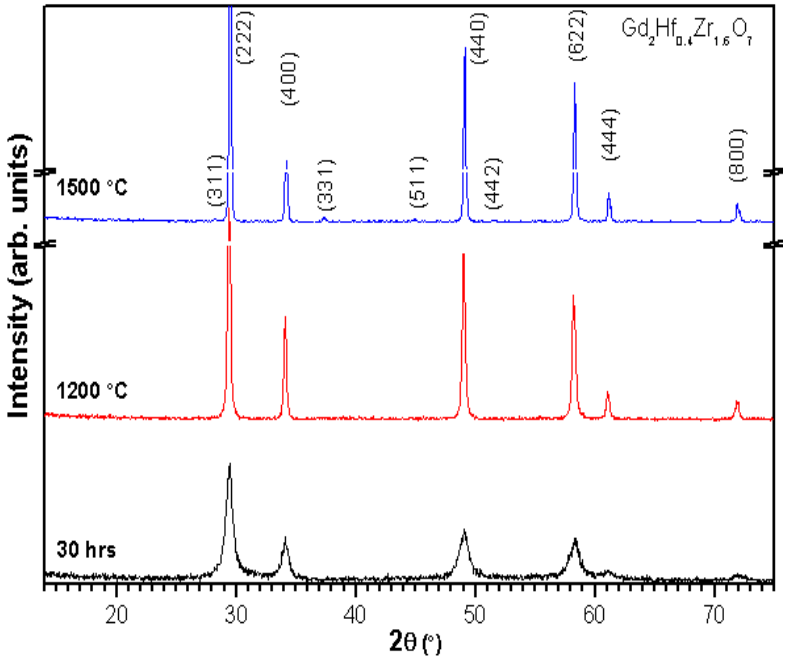

Fig. 2. For the selected samples $Gd_2(Hf_{0.4}Zr_{1.6})O_7$ ground for a period of 30 hours and heat treated at 1200 °C and 1500 °C diffractogram.

3.2. Structural evolution of powder samples with post-milling thermal treatments

The general formula of the oxides of pyrochlore structure can be written as $A_2B_2O_7$ or $A_2B_2O_6(1)O(2)$ with four types of non-crystallographically equivalent atoms. The ideal crystallizes in a cubic pyrochlore structure Fd3m (227) space group, considered as derived from a non-stoichiometric fluorite type. Depending on the R_{Ln}/R_B size ratio, $Ln_2B_2O_7$ oxides will adopt either the fully disordered anion deficient fluorite structure ($R_{Ln}/R_B < 1.46$) or its ordered derivative, the pyrochlore structure ($R_{Ln}/R_B \geq 1.46$); factors such as processing conditions or the nature of chemical bonding play also an important role in determining the specific degree of structural order/disorder of any particular composition [7].

One of the great peculiarities of the structure of pyrochlore type is its high flexibility and ability to accept structural defects [8]. The fundamental difference between non-stoichiometric fluorite and pyrochlore is that fluorite anionic vacancies are distributed randomly in the subnet anion, and the pyrochlore vacancies are ordered along a certain direction. The presence of such vacancies favors these materials exhibit excellent ionic conductivity.

The results of the final refined structural parameters obtained for the whole compositions of general formula $Gd_2(Hf_{2-x}Zr_x)O_7$ (x = 0, 0.4, 0.8, 1.2, 1.6 and 2) are collected in the Table 1. In Fig. 3. We show the graphic result of the fitting of the X-ray diffraction patterns corresponding to Gd_2O_3:0.4HfO_2:1.6ZrO_2 obtained by ball milling for 30 hours and this same sample after a thermal treatment at 1200 ºC for 12 hours. In this

figure of the powder $Gd_2(Hf_{0.4}Zr_{1.6})O_7$ does not show any superstructure reflections characterizing the pyrochlore long-range atomic ordering of cationas, anions, and vacancies (i.e. the Miller indices (111), (311) and (331) at 2θ ~ 15º, 28º and 37º respectively). This powders prepared by mechanical milling consist of a single phase anion-deficient fluorite-type of structure which remains stable up to, at least, the highest firing temperature used in this work at 1500 ºC. The Table 1 also present the cell parameters for these fluorites.

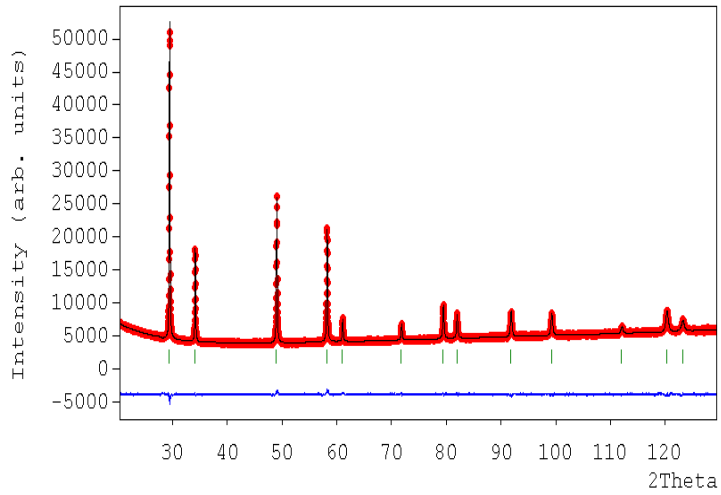

Fig. 3. Experimental (circles), calculated (solid line) and difference (bottom) X-ray diffraction patterns for the as-prepared $Gd_2(Hf_{0.4}Zr_{1.6})O_7$ powder sample after firing 12 h at 1200 ºC.

The powders fired at 1500 ºC show diffraction patterns with superstructure peaks, this reflections are evident in the Fig. 4. While the structural analysis we think that initially all the Gd ions to be constrained into the 16c sites and the presence of Hf and Zr ions occupy the positions 16d. But nevertheless, during the fitting process that much more scattering power should be located in the 16d sites which could only be accomplished by allowing Gd ions to move into the latter and consequently, removing Zr or Hf (these tetravalent ions have several similarities such as their ionic radii: Zr: 0.71 Å and Hf: 0.72 Å). Then we refined the occupation of both sites, when Hf and Zr ions moves to 16c sites and Gd ions occupy the site 16d.

The position of the oxygen in the structural refinement was assumed to be ordered as in the ideal pyrochlore structure whereas in fluorite 1/8 of the oxygen positions are empty random. The Table 2 present how the atomic arrangement is completely specified by giving the value of the cell parameter and the coordinate x position of the oxygen 48f [9, 10].

Table 1. Structural evolution of the $Gd_2(Hf_{2-x}Zr_x)O_7$ (x = 0, 0.4, 0.8, 1.2, 1.6 and 2) compositions with the temperature post-milling annealing treatment

Composition	$Gd_2Hf_2O_7$	$Gd_2Hf_{1.6}Zr_{0.4}O_7$	$Gd2Hf_{1.2}Zr_{0.8}O_7$	$Gd_2Hf_{0.8}Zr_{1.2}O_7$	$Gd_2Hf_{0.4}Zr_{1.6}O_7$	$Gd_2Zr_2O_7$
Treatment T (ºC)/time (h)	1200/12	1200/12	1200/12	1200/12	1200/12	1200/12
a (Å)	5.2451	5.244	5.254	5.254	5.2549	5.2601
R_B	2.09	1.89	2.13	1.78	1.86	4.18
R_{wp}	1.95	1.96	1.75	1.77	1.6	1.72
R_{exp}	1.48	1.53	1.24	1.39	1.35	1.34
X^2	1.73	1.65	1.97	1.61	1.39	1.63

All the samples have fluorite-like structure (S.G. Fm3m, n.225) with metals at 4a (0 0 0) and oxygen at 8c (0.25 0.25 0.25). The respective occupations being those given by the chemical formula; i.e. 0.5/0.5/0.45 for Gd/Hf/Zr and 7/8 for oxygen. Cell content is obtained as the site multiplicity times the occupancy; Z=1. $R_B = \Sigma|I_o - I_c|/\Sigma I_o$; $R_{wp} = [\Sigma w |y_o - y_c|^2 / \Sigma w |y_o|^2]^{1/2}$; $R_{exp} = [(N - P + C) / \Sigma(wy_0^2)]^{1/2}$; $x^2 = [R_{wp} / R_{exp}]^2$; N = number of data points; P = number of refined parameters; C = number of constrains; wi =1/variance(y_o) (weight for every data point).

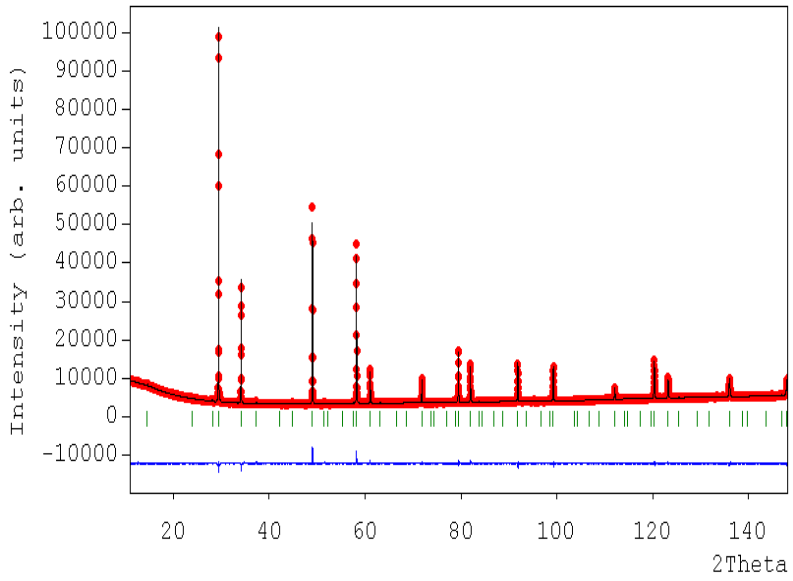

Fig. 4. Experimental (circles), calculated (solid line) and difference (bottom) X-ray diffraction patterns for the as-prepared $Gd_2(Hf_{0.4}Zr_{1.6})O_7$ powder sample after firing 12 h at 1500 ºC.

Table 2. Structural evolution of the $Gd_2(Hf_{2-x}Zr_x)O_7$ (x = 0, 0.4, 0.8, 1.2, 1.6 and 2) compositions with the temperature post-milling annealing treatment

Composition	$Gd_2Hf_2O_7$	$Gd_2Hf_{1.6}Zr_{0.4}O_7$	$Gd_2Hf_{1.2}Zr_{0.8}O_7$	$Gd_2Hf_{0.8}Zr_{1.2}O_7$	$Gd_2Hf_{0.4}Zr_{1.6}O_7$	$Gd_2Zr_2O_7$
Treatment T (ºC)/time (h)	1500/12	1500/12	1500/12	1500/12	1500/12	1500/12
a (Å)	10.494	10.5094	10.511	10.5074	10.4883	10.523
R_B	5.56	5.67	4.98	7.98	8.3	6.47
R_{wp}	2.5	2.05	2.01	2.54	3.31	2.17
R_{exp}	1.24	1.47	1.2	1.52	1.43	1.36
X^2	4.06	1.96	2.83	2.78	5.34	2.55
Gd/Hf/Zr in 16c, (0 0 0), Occ.	1.41/0.58	1.71/0.28	1.57/0.42	1.54/0.45	1.12/0.87	1.45/0.54
Gd/Hf/Zr in 16d, (1/2 1/2 1/2), Occ.	0.58/1.41	0.28/1.71	0.42/1.57	0.45/1.54	0.87/1.12	0.54/1.45
O (1) in 48f, (x 1/8 1/8), Occ.	1	1	1	1	1	1
x	0.403	0.398	0.401	0.404	0.401	0.393
O (2) in 8a, (1/8 1/8 1/8), Occ.	1	1	1	1	1	1

Samples treated at 1500 ºC have pyrochlore structure, (S.G. Fd3m, n.227). The occupations are given by the chemical formula; cell content is obtained as the site multiplicity times the occupancy; Z=8. $R_B = \Sigma|I_o - I_c|/\Sigma I_o$; $R_{wp} = [\Sigma w |y_o - y_c|^2 / \Sigma w |y_o|^2]^{1/2}$; $R_{exp} = [(N - P + C) / \Sigma (wy_0^2)]^{1/2}$; $x^2 = [R_{wp} / R_{exp}]^2$; N = number of data points; P = number of refined parameters; C = number of constrains; wi =1/variance(y_o) (weight for every data point).

3.3. Electrical measurements

The conductivity process is thermally activated, as a function of temperature, and is expressed by the empirical Arrhenius relationship:

$$\sigma = \frac{\sigma_0}{T}\exp -\left[\frac{E_a}{kT}\right] \quad (1)$$

where σ_0 is a pre-exponential factor among others depends on the charge carrier density, T is the absolute temperature, E_a is the activation energy of the process k is the Boltzmann constant ($1.3807\ 10^{-23}$ J·K^{-1}). The amount of energy needed for the mobile species can overcome the energy barrier (E_a) and the ion can access the vacancy is an important condition to determine if the material is feasible to apply or not. The conductivity values are very sensitive to the activation energy; an ion conductor E_a usually within a range of 0.6-0.8 eV [9]. To measure the electrical properties of the synthesized materials and proceeds to uniaxially pressing the powders in a hydraulic press, obtaining tablets which are sintered at different temperatures. Subsequently examining electrical properties depending on temperature and frequency by impedance spectroscopy technique on a Solartron 1260 analyzer is performed. Its measurement was performed in an oven which

allows studying the behavior from 280 to 750 ºC. Activation energies for $Gd_2(Hf_{1.2}Zr_{0.8})O_7$ sample is shown in Fig. 4. In the case of the activation energy E_{dc}, the value found was of 1.0369 eV, while the value of E_a was 0.549 eV. The energy associated with the process of conducting long-range E_{dc} always be greater than the energy required to move an ion to its potential well E_a, since the value E_{dc} also involves a penalty due to the interaction with other ions or your environment during movement of each of these; this interaction is known in the field of ionic conduction as correlation.

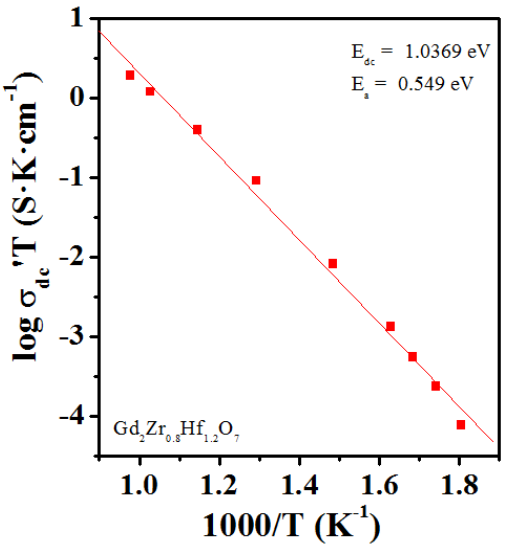

Fig. 5. Arrhenius representation for $Gd_2(Hf_{1.2}Zr_{0.8})O_7$ shows logarithm of the dc conductivity versus 1000 / T.

In Fig. 5, the conductivity values obtained for $Gd_2Hf_{2-x}Zr_xO_7$ composition are presented, depending on the degree of substitution, when x = 0, 0.4, 0.8, 1.2, 1.6 and 2, measured at a temperature of 750 °C. This graph clearly highlights that the higher conductivity zirconium content of the samples increases, particularly the sample with 1.6 atomic percent of zirconium (with the activation energy for dc of 1.16 eV), as it presents the highest value for that property. The conductivity values of the system $Gd_2Hf_{2-x}Zr_xO_7$ indicate the activation energies for dc conductivity in the range of 0.87-1.17 eV.

4. Conclusion

In this study, the $Gd_2(Hf_{2-x}Zr_x)O_7$ (x = 0, 0.4, 0.8, 1.2, 1.6) have been synthetized at room temperature just by mechanical milling of the constituent oxides in a planetary ball mill. Chemical changes in the compounds was followed by XRD diffraction, and showing after at 30 hours they appreciate reflections characteristics of a disorderly arrangement of fluorite-type. However, the pyrochlore-type structure appear in the XRD pattern of samples after annealing at temperatures as 1500 ºC, showing the superstructure peaks. The structural order in the samples depends of R_{Ln}/R_B ratio and of the heat treatment after milling. For the conductivity values of the system $Gd_2(Hf_{2-x}Zr_x)O_7$ indicate the activation energies for dc conductivity are in the range of 0.87-1.17 eV.

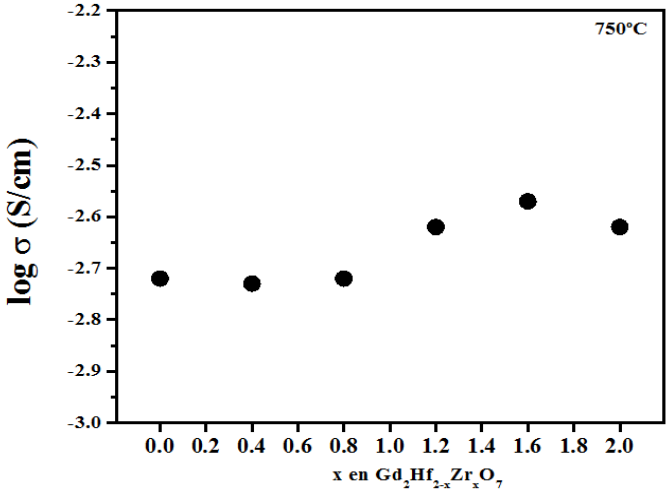

Fig. 6. Conductivity behavior for compound $Gd_2(Hf_{2-x}Zr_x)O_7$, when x = 0, 0.4, 0.8, 1.2, 1.6 and 2, prepared at a temperature of 750 °C.

Acknowledgements

This work has been carried out with the financial support of Mexican CONACYT. Helpful discussions with U. Amador are greatly appreciated.

References

[1] M.B. Jonson, D. James, A. Bourque, H. Dabkowska, B. Gaulin, M. White, Journal of Solid State Chemistry (2009) DOI:10.1016.
[2] B.P. Mandal, A.K. Tyagi, Journal of Alloys and Compounds 437 (2007) 260.
[3] J. Rodriguez Carvajal, Physica B 192 (1993) 55-69. The program and manual can be found at http://www.llb.cea.fr/fullweb/powder.htm).
[4] J. Lian, J. Chen, L. M. Wang,, R. C. Ewing,, J. M. Farmer, L. A. Boatner, K. B. Helean, Phys. Rev. B. 68(2003) 13107.
[5] K. J. Moreno, R. Silva-Rodrigo, A. F. Fuentes, J. Alloy Compd. 390 (2005) 230.
[6] P. K. Moon, H. L. Tuller, Solid State Ion, (1988) 470.
[7] M.A. Subramanian, G. Aravamudan, G.V. Subba Rao, Progress in Solid State Chemistry 15, (1985) 55-143.
[8] Lian, J., Chen, J., Wang, L., Ewing, R, Farmer, J., Boatner, L. and Helean, K., Physical review B 68 (2003) 134107.
[9] A. F. Fuentes, K. Boulahya, M. Maczka, J. Hanuza, U. Amador, Solid State Sci. 7 (2005) 343.
[10] K. J. Moreno, A. F. Fuentes, U. Amador, J. Santamaría, C. León, Journal of Solid State Chemistry 179 (2006) 3805.

Chapter 8.13. Synthesys of carbon nanomaterials doped with sulfur as electrocatalysts in fuel cells

E. Montiel-Macias[a,*]; P. B. Balbuena[b]; A. M. Valenzuela-Muñiz[a]; Y. Verde-Gómez[a]

[a]Instituto Tecnológico de Cancún, Av. Kabah Km. 3, Cancún, Q. Roo, México, 77515.
[b]Department of Chemical Engineering, Texas A&M University, TAMU 3122, College Station, TX, USA, 77843.

ABSTRACT

In recent years, many efforts have been made to develop new materials that could replace or reduce the use of Pt in fuel cells electrocatalysts. Under this consideration, differents materials based on carbon doped with heteroatoms applied as catalysts or catalyst supports in fuel cells have been investigated, e.g. N, B, P and S. In this work sulfur-doped carbon nanomaterials were synthesized by a chemical vapor deposition modified method, where toluene and thiophene were used as sources of carbon and sulfur, respectively. Ferrocene was used as a growing precursor. Different synthesis scenarios were evaluated to determine the optimal synthesis conditions. Physical and chemical characterization was performed by X-Ray Diffraction, Scanning and Transmission Electron Microscopy, in order to determinate structural and morphological properties. The chemical elemental analysis was done by energy dispersive spectroscopy.

Keywords: Sulfur doped carbon, Electrocatalysts, Fuel Cells

1. Introduction

The search for new energy alternatives that are friendly to the environment has gained importance on the last years. From this perspective, fuel cells have been recognized as a promising option for the clean energy production.

Two of the most important components on a fuel cell are the anode and cathode, where their electrocatalysts usually have been manufactured based on noble metals as platinum (Pt) or supported platinum on carbon materials (Pt/C), due to its stability and high electro catalytic activity. However, due to the scarcity of Pt and therefore its high cost, they have been sought alternatives to replace or reduce the amount of this metal. On the other hand one the biggest challenges on a fuel cell is improving performance on the cathode for the Oxygen Reduction Reaction (ORR). An alternative to meet these challenges is generating

---

* Corresponding author:
Elizabeth Montiel Macias, phone +529988807432, elizabethmontielmacias@hotmail.com

new materials that improve the performance of the cathode in ORR and reduce material costs.

It has been found that by doping carbon materials with heteroatoms (N, S, B, P, among others) from the synthesis, some of their properties such as electrical conductivity, basicity, oxidation stability, catalytic activity, and so on, are affected [1]. A review of recent literature it was found that further exploration made towards carbon doping is mostly using nitrogen heteroatom [2-6] and less research work has been done using heteroatoms such as boron [7, 8], phosphorus [9, 10] and sulfur [11-15].

For the reasons above mentioned, this paper presents the preliminary results on the synthesis by chemical vapor deposition modified method of carbon materials doped with sulfur. The analyzed synthesis parameters were the preheating temperature and gas carrier flow. Physical and chemical characterizations were performed by X-Ray Diffraction (XRD), scanning and high resolution scanning electron microscopy (SEM and HRSEM), in order to determine the structural and morphological properties. The chemical elemental analysis was done by X-ray energy dispersive spectroscopy (EDS).

2. Materials and Methods

Materials and reagents used in the synthesis of carbon nanomaterials were toluene anhydrous (99.8% Sigma), thiophene (99%, AlfaAesar), ferrocene (98%, Sigma Aldrich), argon (99.998%, Praxair) and quartz tube as substrate. Prior to use, quartz tube was washed with ethanol and acetone, reagent grade. The other materials were used as received from the supplier.

The synthesis of sulfur doped carbon nanomaterials (S-CNMs) was carried out by the chemical vapor deposition modified method (CVDMM). The CVDMM synthesis equipment was a tubular furnace in which a quartz tube was used as substrate to growth of the S-CNMs. A precursor solution of toluene-thiophene (4:1%vol.) was prepared as carbon and sulfur source, respectively. Additionally, ferrocene was added to the solution as organometallic precursor. Prior to introduce the synthesis solution into the tubular furnace (900°C) a preheating treatment was carried out. The solution was pumped through the substrate quartz tube using argon as carrier gas. After that all the precursor solution was pumped, the atmosphere in the tube was kept under an inert atmosphere until it cools to room temperature. The parameters effect such as the preheating temperature (180 and 200 °C) and carrier gas flow rate (0.5 and 1 L/min) were evaluated.

Subsequently to the synthesis process, the samples were treated to remove residual iron and amorphous carbon. The cleaning treatment was performed using a reflux system with concentrated nitric acid during 12 hours, the solution S-CNMs-acid was kept under stirring. After the cleaning treatment, the nanostructures were recovered by filtration, and washed with distilled water to remove the residual acid. Finally, the samples were dried overnight at 80^0C in air. Samples were labeled according to the following code: 180SNBY9, 200SNBY9, 180SNAY9 and 200SNAY9 where A and B correspond to carrier gas flow of 1.0L/min and 0.5L/min, respectively. 180 and 200 to the preheating temperature of 180^0C and 200^0C, respectively. The 180NAY9 and 200NAY9 labels are use to describe the samples without sulfur at 180 and 200°C, respectively.

The structural properties were analyzed by XRD analysis using a Bruker Difractometer, model D8 Advance. Bragg-Brentano mode was used, a step size of 0.02, from 10 to 90 2θ. The morphology and microstructure of the samples were characterized by SEM using a microscopes HITACHI model SU8000 and TESCAN model VEGA3. In order to determine the chemical composition, EDS signals were collected by a Bruker X-ray microanalysis detector.

3. Results and Discussion

The XRD patterns of the synthesized samples are presented in Figure 1. In all samples the diffraction patterns show the characteristic plane of graphite 2H in the plane (002) at 2θ=26.3. All samples synthesized with sulfur, show a peak intensity on 2θ=44.6918, a second peak at 2θ=65.0517 and third peak at 2θ=82.37 which correspond to the crystalline planes (110), (200) and (211) and (122) correspond to Fe_3C; these peaks could be attributed to metallic Fe [16], encapsulated in the carbon nanostructures due to growth mechanisms [17]. The peaks labeled at 37.57 and 53.13 2θ on planes (121) and (122) correspond to Fe_3C. Finally the carbon sulfur samples also shows peaks in 2θ=29.91, 33.66 and 43.14 in the crystalline planes of (110), (112) and (114), respectively, correspond to FeS.

The elemental atomic percentage in the samples is presented in Table 1. The sample with the highest sulfur atomic percentage is 180SNAY9, followed by 200SNBY9, 200SNAY9 and 180SNBY9 samples. The iron elemental analysis follows the same trend.

In SEM analysis, it was observed the formation of tubular shapes in the samples using Ar flow of 1L/min in both preheating temperatures (Figure 2a and 2c). However in samples with Ar flow of 0.5L/min, the tubular structures formation is not clear observed at 180°C (Figure 2b), meanwhile there is evidence of CNT growth for preheating temperature of 200 °C (Figure 2d).

In the sample 180NAY9, it was observed tubular shapes (Figure 3a) marked by the ellipse, on the same figure also concentric tubular structures was observed (marked with dashed circles in Figure 3a). The average diameters in sample 180SNAY9 were 237 nm. On the other hand, Figure 3b shows conical shapes (dashed triangle) from sample 200SNAY9. The shapes have a bigger diameter at the bottom than the top, where the average diameters sizes were 368 nm and 187 nm, for the bottom and the top, respectively.

The HRSEM micrographs showed the formation of larger length tubular shapes when carrier gas flow was 1L/min (Figure 4a and 4c) than the samples synthetized at 0.5L/min (Figure 4b and 4d).

Smooth concentric structures surrounded by a granular layer (4a and 4b) were observed, such textures were not observed in the sample synthesized without sulfur, for example in sample 180NAY9 where only smooth structures were observed (Figure 4e). The granular texture observed in the sulfured samples, it could be attributed to the defects formation due to the sulfur atoms are attached to the carbon in order to form pentagons and heptagons rings [16]. Although the amount of sulfur present in the samples according to the chemical analysis is small compared to other authors [15] it was sufficient to modify the surfaces of the samples.

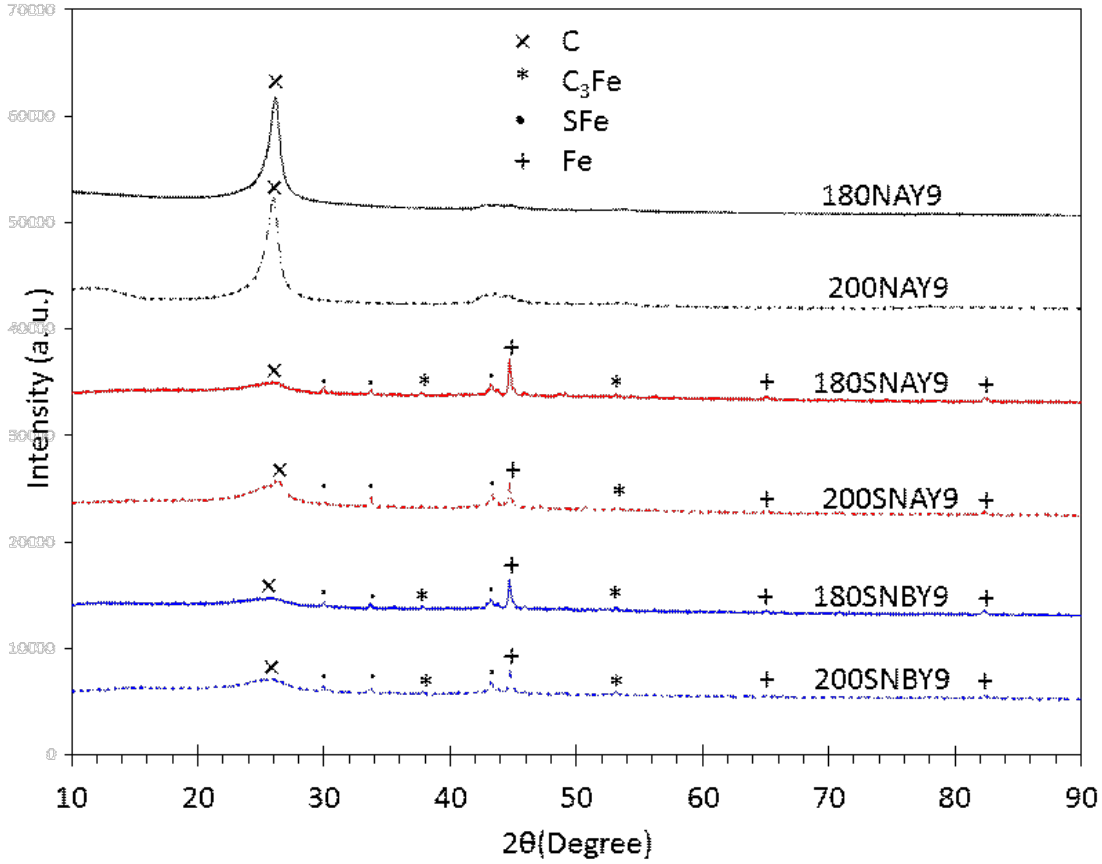

Figure 1. X-ray diffraction patterns.

Table 1. EDS elemental chemical analysis for the synthesized samples

Sample	at %			
	C	Fe	O	S
180NAY9	94.8	0.38	4.17	--
200NAY9	93.98	0.25	5.77	--
180SNAY9	94.12	1.77	3.42	0.69
180SNBY9	91.52	1.52	6.54	0.41
200SNAY9	95.79	1.34	2.28	0.59
200SNBY9	91.39	2.57	5.34	0.69

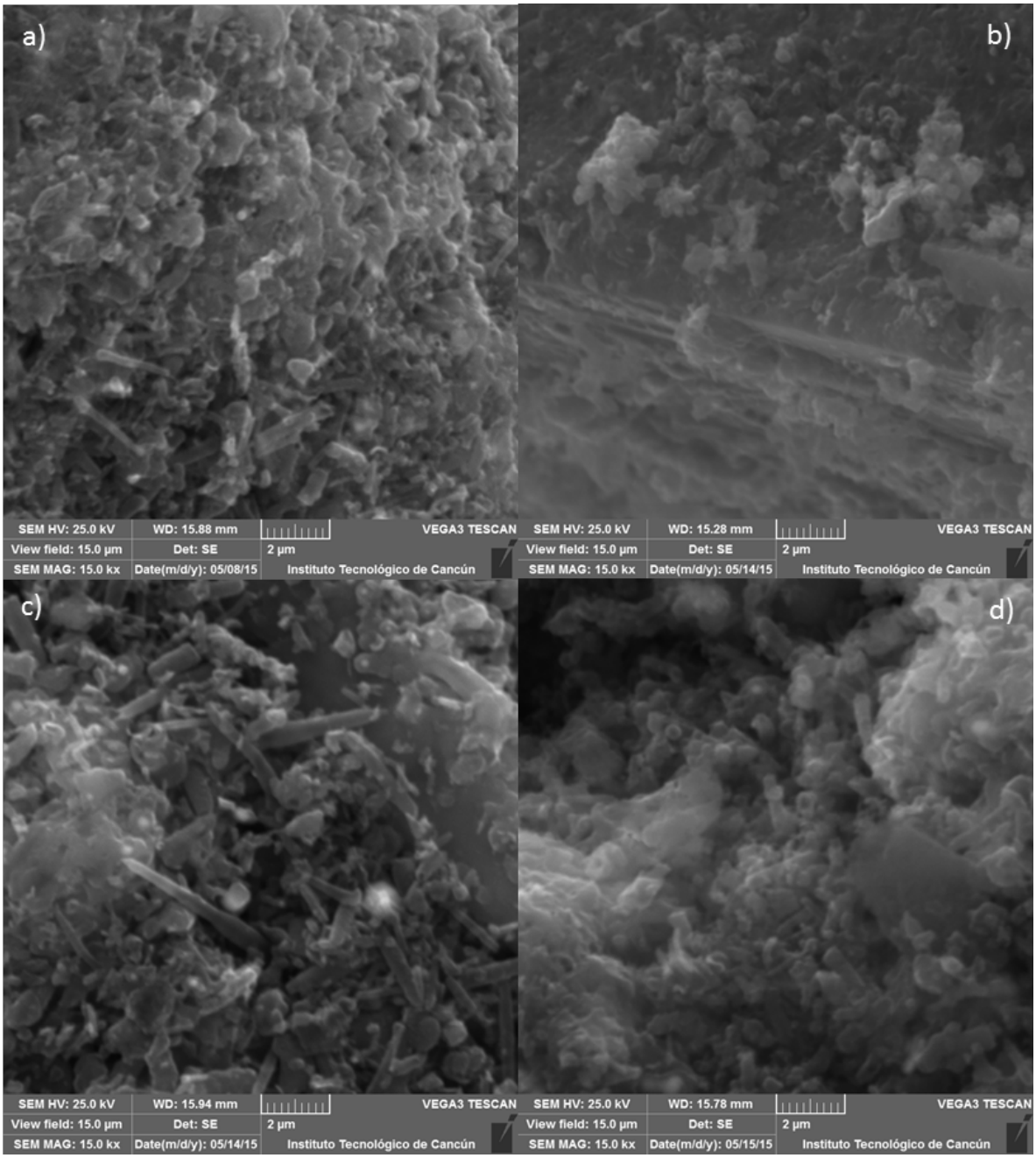

Fig. 2. SEM micrographs obtained. at 15 kX of samples:
(a) 180SNAY9, (b) 180SNBY9, (c) 200SNAY9, and (d) 200SNBY9.

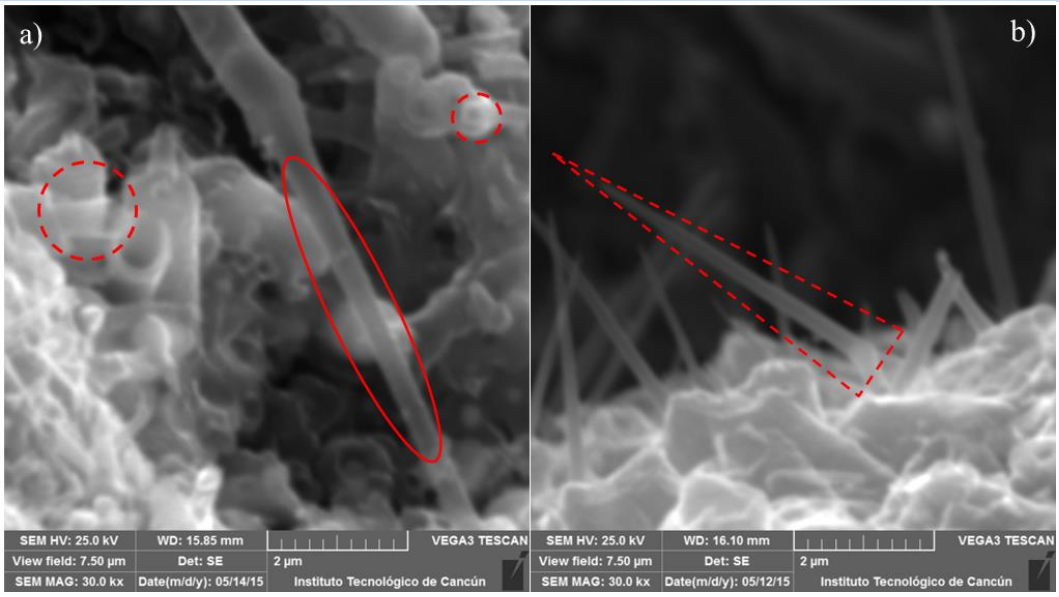

Fig. 3. SEM micrographs at 30 kX. Morphologies of samples (a) 180SNAY9; and (b) 200SNAY9.

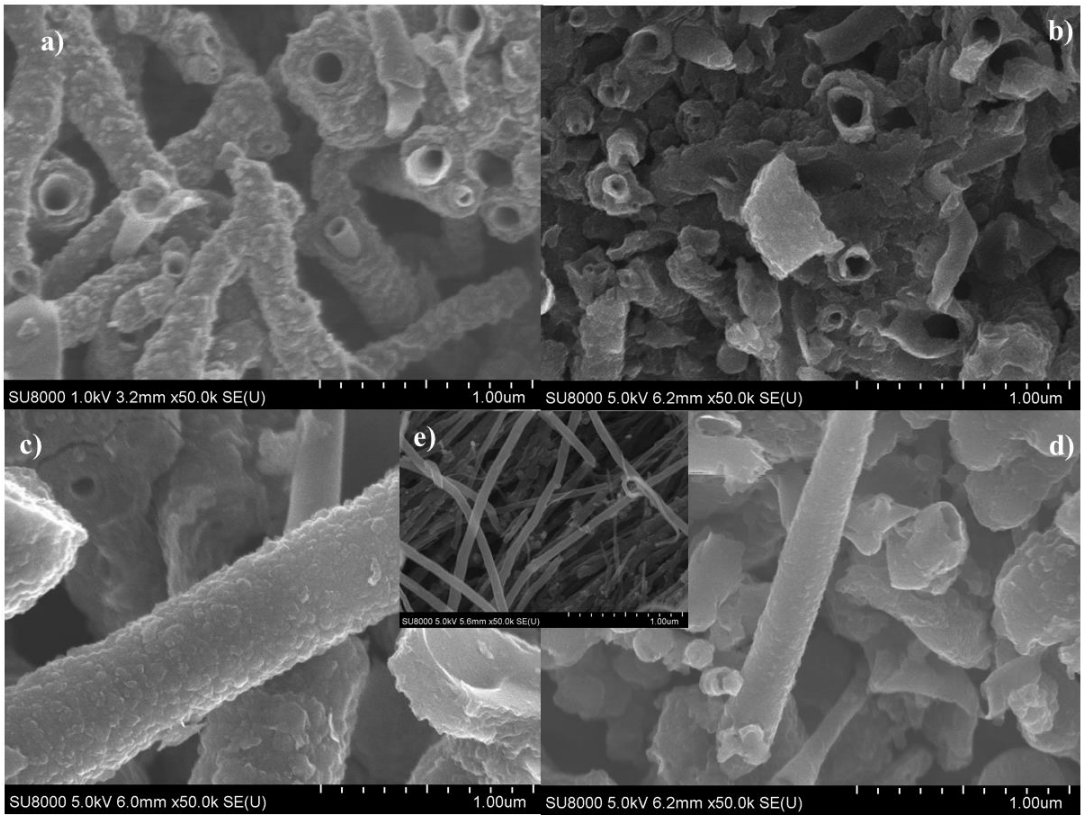

Fig. 4. HRSEM micrographs for samples 50kX magnification for (a) 180SNAY9, (b) 180SNBY9, (c) 200SNAY9, (d) 200SNBY9, and (e) 180NAY9.

4. Conclusion

Carbon nanomaterials doped with sulfur were synthesized. According to the characterizations, it was observed the formation of tubular structures with conical shape. The materials show surface irregularities, which could be attributed to defects caused by the inclusion of sulfur in the carbon surface lattice.

The influence of the variation in the synthesis parameters revealed that the highest Ar flow rate the diameter and length of materials are increased. As for the influence of the variation in the preheating temperature, a tendency was not observed to favor of the formation and growth of tubular structures.

It was expected that the formation of surface defects in the synthesized materials may promote the electrochemical activity, improving the general performance of the synthesized materials towards Oxygen Reduction Reaction.

Acknowledgements

The authors acknowledge the financial support provided by Tecnológico Nacional de México (TNM), under project 5528.15-P and RTH2 CONACYT network. The authors also thank to McGill University for the HRSEM analysis.

References

[1] Sun C-L., Chang C-T., Lee H-H, Zhou J., Wang J., Sham T. K., Pong W-F. Microwave-assisted synthesis of a core shell MWCNT/GONR heterostructure for the electrochemical detection of ascorbic acid, dopamine, and uric acid. ACS NANO 2011; 5:3, 7788-7795.

[2] Chetty R., Kundu S., Xia W., Bron M, Schuhmann W., Chirila V., Brandl W., Reinecke T., Muhler M. PtRu nanoparticles supported on nitrogen-doped multiwalled carbon nanotubes as catalyst for methanol electro oxidation. Electrochimica Acta, 2009; 54: 4208–4215.

[3] Wang C., Huang Z., Zhan L., Wang Y., Qiao W., Liang X., Ling L. Nitrogen-doped carbon nanotubes synthesized with carbon nanotubes as catalyst. Diamond & Related Materials 2011; 20: 1353–1356.

[4] Liu J., Zhang Y., Ionescu M.I., Li R., Sun X. Nitrogen-doped carbon nanotubes with tunable structure and high yield produced by ultrasonic spray pyrolysis. Appl. Surface Sci 2011; 257: 7837–7844.

[5] Bo X., Han C., Zhang Y., Guo L. Confined nanospace synthesis of less aggregated and porous nitrogen-doped graphene as metal-free electrocatalysts for oxygen reduction reaction in alkaline solution. ACS Appl. Mater. Interfaces, 2014; 6: 3023−3030.

[6] Liu M., Song Y., He S., Tjiu W.W., Pan J., Xia Y.Y., Liu T. Nitrogen-doped graphene nanoribbons as efficient metal-free electrocatalysts for oxygen reduction. ACS Appl. Mater. Interface 2014.

[7] Panchakarla L.S., Subrahmanyam K.S., Saha S.K., Govindaraj A., Krishnamurthy H.R., Waghmare U.V., Rao C.N.R. 2009. Synthesis, structure, and properties of boron- and nitrogen-doped graphene. Adv. Mater., 2009; 21: 4726–4730.

[8] Gao G., Vecitis C. D. Doped Carbon Nanotube Networks for Electrochemical Filtration of Aqueous Phenol: Electrolyte Precipitation and Phenol Polymerization. ACS Appl. Mater. Interfaces 2012; 4: 1478−1489.

[9] Cruz-Silva E., Cullen D.A., Gu L., Romo-Herrera J.M., Charlier J.C., Smith D., Terrones H., Terrones M. Heterodoped nanotubes: Theory, synthesis, and characterization of phosphorus-nitrogen doped multiwalled carbon nanotubes. ACS Nano. C 2008; 2: 3, 441–448.

[10] Yu D., Xue Y., Dai L. Vertically aligned carbon nanotube arrays co-doped with phosphorus and nitrogen as efficient metal-free electrocatalysts for oxygen reduction. J. Phys. Chem. Lett. 2012; 3: 2863−2870.

[11] Ren W., Li F., Bai S. Cheng H.M. The Effect of Sulfur on the Structure of Carbon Nanotubes Produced by a Floating Catalyst Method. J. Nanosci. Nanotechnol. 2006; 6: 5, 1339-1345.

[12] Yang Z., Yao Z., Li G., Fang G., Nie H., Liu Z., Zhou X., Chen X., Huang S. Sulfur-Doped Graphene as an Efficient Metal-free Cathode Catalyst for Oxygen Reduction. ACS NANO 2012; 6: 1, 205–211.
[13] Wang H.,Bo X., Zhang Y., Guo L. Sulfur-doped ordered mesoporous carbon with high electrocatalytic activity for oxygen reduction. Electrochimica Acta 2013; 108: 404–411.
[14] Shervedani R. K., Amini A. Carbon black/sulfur-doped graphene composite preparated by pyrolysis of graphene oxide with sodium polysulfide for oxygen reduction reaction. Electrochemica Acta 2014; 142: 51-60.
[15] Li W., Yang D., Chen H., Gao Y., Li H. Sulfur-doped carbon nanotubes as catalysts for the oxygen reduction reaction in alkaline medium. Electrochimica Acta 2015; 165: 191–197.
[16] Cui T., Li R., Huang Z., Kang F., Wan K.,Wu D. Effect of sulfur on enhancing nitrogen-doping and magnetic properties of carbon nanotubes. Nanoscale Research Letters 2011; 6: 77.
[17] Dresselhaus MS, Dresselhaus G, Avouris P. Carbon nanotubes. Springer, USA. 2000.

Chapter 8.14. Effect of the graphene and other supports for the oxygen reduction and evolution in alkaline media

M. A. Garcia-Contreras [a,b*]; P. Hosseini-Benhangi [a]; A. Taheri- Najafabadi[a]; E. Gyenge[a]

[a] Dept of Chem and Biolgical Engng & Clean Energy Res Center, The University of British Columbia, 2360 East Mall, Vancouver, BC, Canada V6T 1Z3
[b]Dept of Chemistry, ININ, Carr. México-Toluca s/n, La Marquesa Ocoyoacac, Edo. De Méx 52750

ABSTRACT

Graphene holds promise for many key areas of research including energy storage and conversion, biotechnology, novel electronic devices and so forth. Bifunctional O_2 cathodes which can catalyze both ORR (O_2 reduction reaction) and OER (O_2 evolution reaction) are the backbone of rechargeable metal-air batteries as well as regenerative fuel cells. Mn oxides have been vastly employed as a robust cost-effective multifunctional and environmental friendly electrode material in battery industry. The electrolytic γ-MnO_2 is known as the most electrochemically active crystallographic form of MnO_2 for ORR in alkaline media. However, poor OER electrocatalytic activity in alkaline media impairs its application for bi-functional catalysts. This could be overcome by adding another class of catalyst active for OER to the MnO_2. $LaCoO_3$, also known as a perovskite-type oxide, has been reported to display electrocatalytic activity for OER in alkaline electrolytes in comparison to Pt or MnO_x as well as durability. A literature search on other bifunctional electrodes shows that the MnO_2-perovskite catalytic system is very competitive with other catalysts presented in the literature, while having the advantage of cost efficiency and easy preparation methodology. Our research aimed at investigating the effect of the support on the performance of MnO_2-based catalysts for both ORR and OER with long cycle life. The mechanisms for OER and ORR of the mixed catalysts and the role of support were investigated by a combination of surface characterization methods and electrochemical techniques. $LaCoO_3$ was synthesized via co-precipitation methods. A novel approach toward electrochemical exfoliation of graphite assisted by ionic liquids (ILs) was used to synthesize both graphene and N-doped graphene. The catalyst layer consisted of MnO_2:$LaCoO_3$:Support:Nafion with a weight ratio of 1:1:1:0.67. The support varied from the electrochemically synthesized graphene and N-doped graphene to graphitized C. Cyclic voltammetry tests were performed in O_2 and N_2 saturated 6 M KOH at 293 K to investigate the electrocatalytic activity of the MnO_2-$LaCoO_3$ catalyst on different supports as well as its long-term durability. Raman and X-ray photoelectron spectroscopies as well as SEM analysis were employed to further characterize the catalyst layer.

Keywords: Manganese dioxide electrode, Bifunctional oxygen electrocatalyst, Oxygen reduction reaction

---

*Author for correspondence: Miguel García, Tel. 52553297200 Ext. 12281; miguel.garcia@inin.gob.mx

1. Introduction

Graphene, as the rising star in the world of advanced materials, offers game-changing prospects for many key areas of research including energy storage and conversion, biotechnology, novel electronic devices and so forth [1]. Bifunctional oxygen cathodes which can catalyze both ORR (oxygen reduction reaction) and OER (oxygen evolution reaction) are the backbone of rechargeable metal-air batteries as well as regenerative fuel cells [2-4].

Manganese oxides have been vastly employed as a robust cost-effective multifunctional and environmental friendly electrode material in battery industry, from primary to rechargeable metal-air batteries, as well as alkaline fuel cells and capacitors [4]. The electrolytic manganese dioxide (γ-MnO2) is known as the most electrochemically active crystallographic form of MnO2 for ORR in alkaline media with Tafel slope of 40 mV dec-1 and a low overpotential of -375 mV [2, 5]. However, poor OER electrocatalytic activity of MnOx in alkaline media diminish the hope of finding an exclusive bi-functional catalyst for both ORR and OER [2]. This could be avoided by adding another class of catalyst active for OER to the MnO2. LaCoO3 , also known as a perovskite-type oxide, has been reported to demonstrate distinguished electrocatalytic activity for OER in alkaline electrolytes in comparison to Pt or MnOx, i.e. up to 1 mA cm-2 at 1600 mV (vs. RHE) as well as a Tafel slope of 60 mV decade-1 with excellent durability over 100 cycles in 0.1 M KOH [2, 6]. A thorough comparison with literature regarding other bifunctional electrodes shows that the MnO2-perovskite catalytic system is very competitive with other catalysts presented in the literature, while having the advantage of cost efficiency and easy preparation methodology [2].

Our research is aimed at investigating the effect of support on the performance of MnO2-based catalysts for both ORR and OER with long cycle life. The mechanisms for OER and ORR of the mixed catalysts and the role of support are investigated by a combination of surface characterization methods and electrochemical techniques.

2. Materials and Methods

In the present work, $LaCoO_3$ was synthesized via co-precipitation methods. While different methods for graphene synthesis has been proposed in the literature, a novel approach toward electrochemical exfoliation of graphite assisted by ionic liquids (ILs) was used to synthesize both graphene and N-doped graphene. This approach provides three main features: cost efficiency due to low IL content, extended electrochemical stability in a non-aqueous electrolyte, and high exfoliation yield by effective anionic intercalation within the graphitic layers by IL/acetonitrile electrolyte with dramatically lower loads of ionic liquids (~1:50 IL/acetonitrile vol. ratio), Fig. 1.

The catalyst layer consisted of MnO_2:$LaCoO_3$:Support:Nafion with a weight ratio of 1:1:1:0.67. The support varies from the electrochemically synthesized graphene and N-doped graphene to graphitized carbon. Cyclic voltammetry tests were performed in O_2 and N_2 saturated 6 M KOH at 293 K to investigate the electrocatalytic activity of the MnO_2-$LaCoO_3$ catalyst for both OER and ORR on different supports. The longer-term durability of the electrodes was also investigated by performing 100 repeated OER-ORR

voltammetric cycles. Combination of Raman and X-ray photoelectron spectroscopy (XPS) as well as SEM analysis were employed to further characterize the catalyst layer.

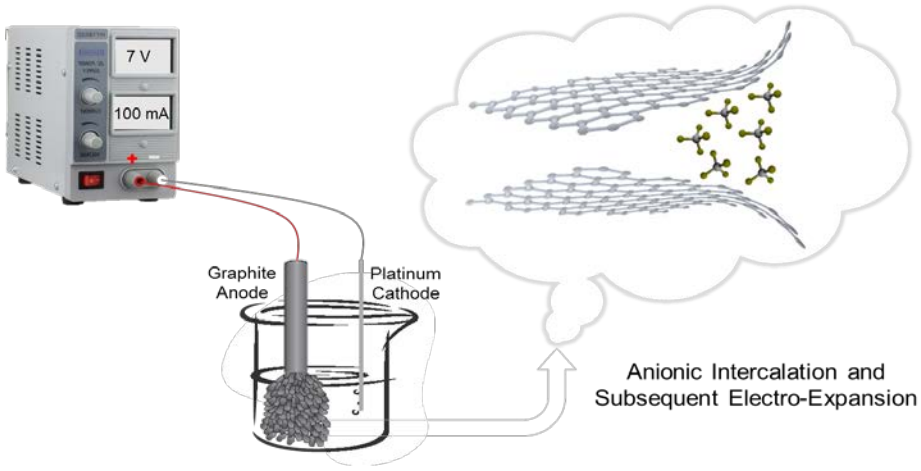

Fig. 1. Experimental setup used for graphite anodic exfoliation

3. Results and Discussion

3.1 Characterization

- Majority of products
- ✓ Ultrathin layers of folded/crumpled GN (AFM: < 5 layers)
- ✓ ~500 nm average length based on 250 sample images
- Minority
- ✓ Nanotubes: sheet folding due to intercalation
- ✓ Nanoparticles: breakage of sheets' vertices

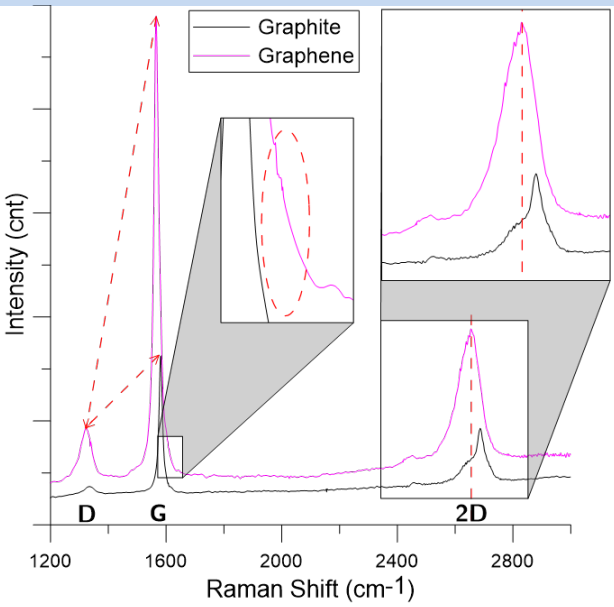

Fig. 2. Raman spectra of graphene

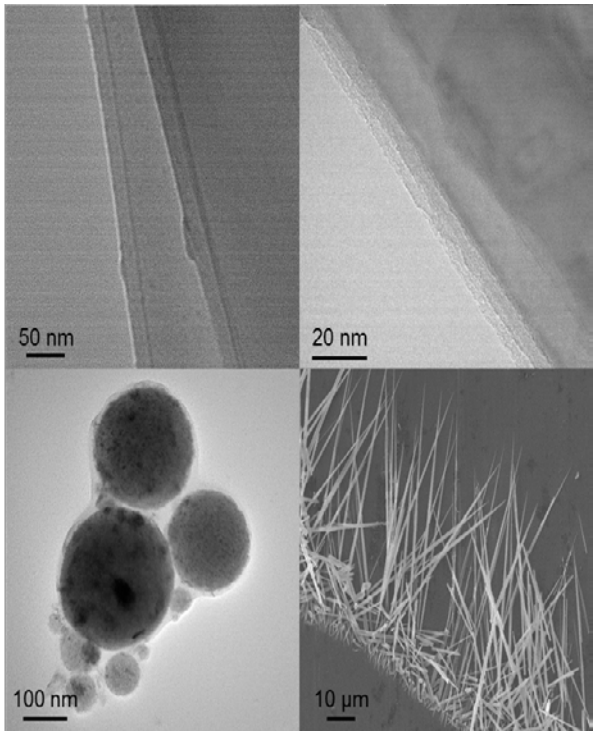

Fig. 3. SEM/TEM images for electro-exfoliation

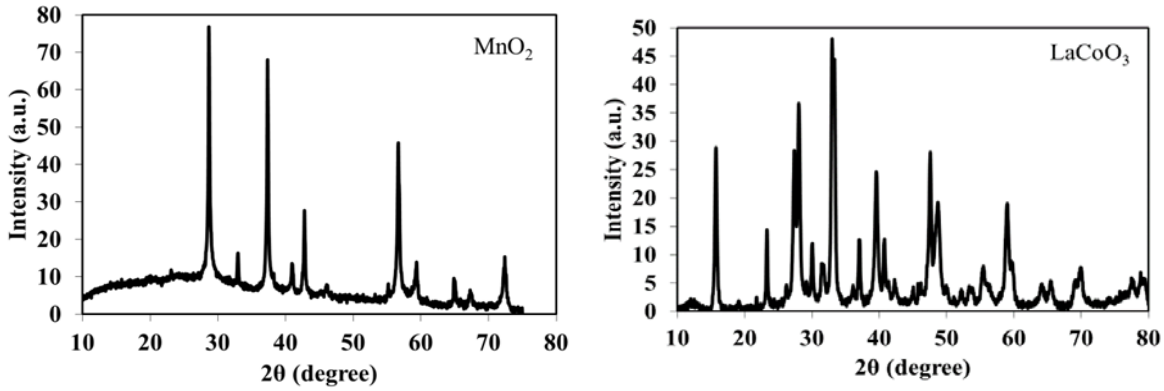

Fig 4. XRD spectra of: a) commercial Sigma-Aldrich MnO2powder, b) synthesized LaCoO3powder

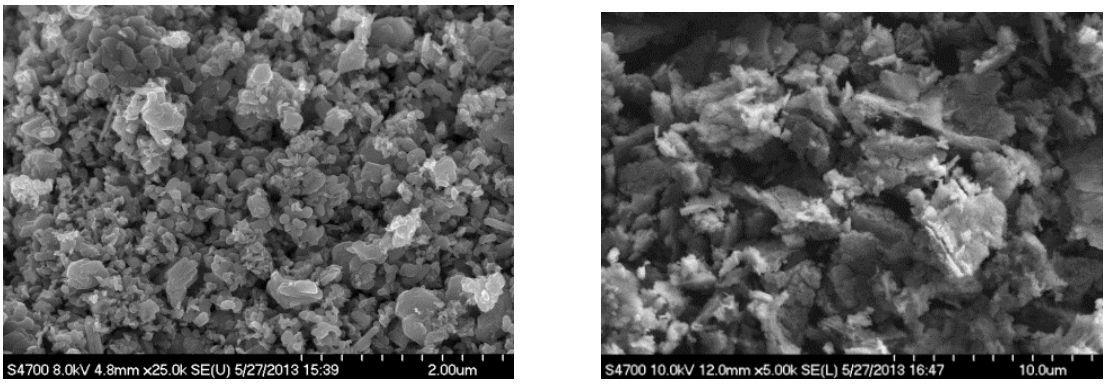

Fig. 5 SEM images of: (a) commercial Sigma-Aldrich MnO_2 powder, and (b) synthesized $LaCoO_3$ powder

3.2 Catalytic Performance

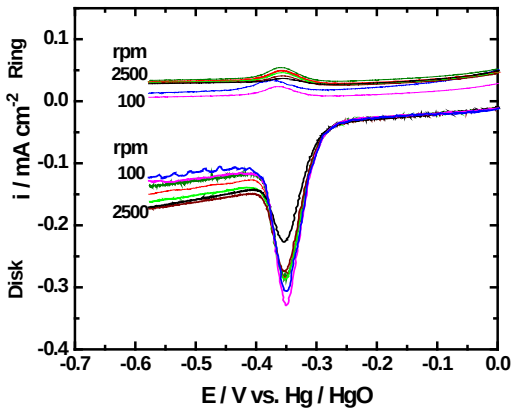

Fig 6. RRDE voltammograms of MWCNT+Graphene for ORR in 6M KOH

Table 1. Number of electrons ,% of H_2O_2 and onset Potential during ORR on supports @ 1600 rpm in 6M KOH at room temperature

Support	Number of electrons	Potential range / V vs Hg/HgO	% H_2O_2	Onset Potential for ORR @ 1600 rpm / V vs Hg/HgO
Graphene	2.3-2.0	-0.35-0.4	83-97	-0.031
N-Doped Graphene	2.8-2.2	-0.35-0.4	60-88	-0.043
MWCNT + Graphene	2.3-2.0	-0.35-0.4	80-99	-0.048
Vulcan	2.4-2.0	-0.35-0.4	78-100	-0.030

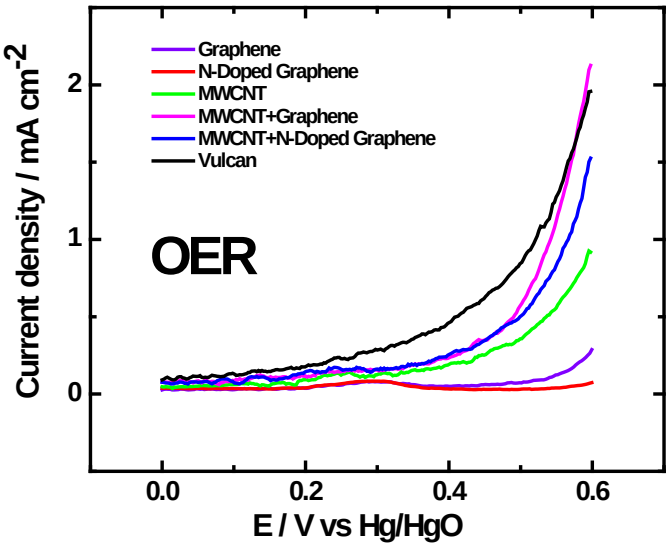

Fig. 7. OER on supports in 6M KOH @ 400 rpm , RT

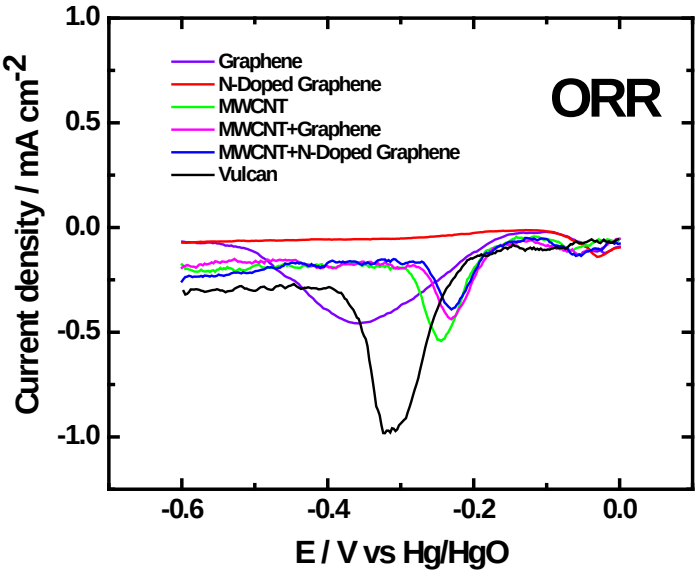

Fig. 8. ORR on supports in 6M KOH @ 400 rpm , RT

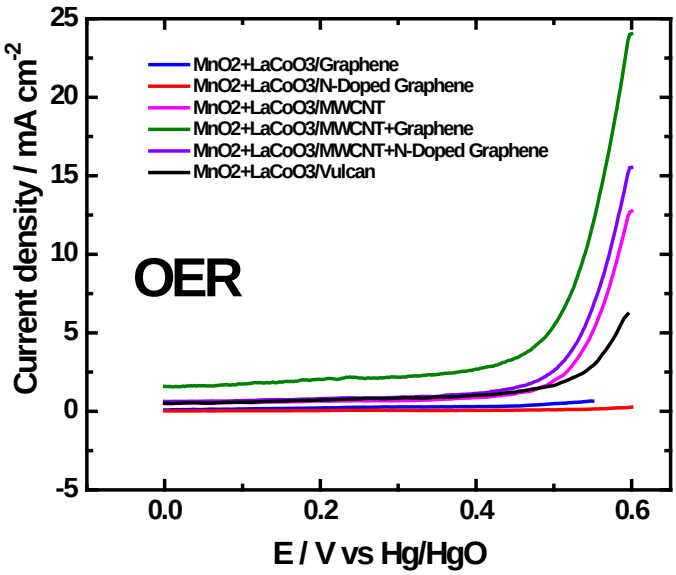

Fig 9. OER on MnO2+LaCoO3 / supports in 6M KOH @ 400 rpm, RT.

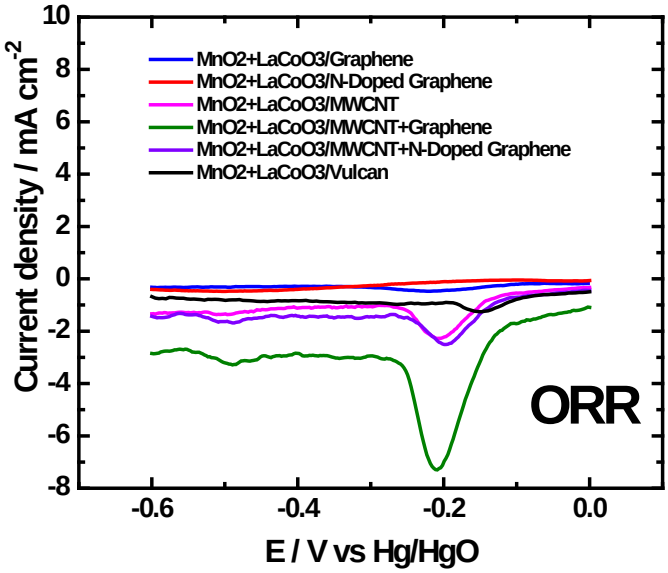

Fig 10. ORR on MnO2+LaCoO3 / supports in 6M KOH @ 400 rpm, RT.

4. Conclusion

GNs could be produced electrochemically (~500 nm long with < 5 layers); major products were crumpled and folded graphene sheets.

Graphene and Doped Graphene showed low activity for OER and ORR, whereas followed mainly a 2e path for ORR.

Graphene + MWCNT showed a synergistic effect as support of MnO_2-$LaCoO_3$ catalyst that induced a higher performance for OER and ORR.

Acknowledgments

The authors acknowledge the generous financial support of The University of British Columbia, and Natural Sciences and Engineering Research Council of Canada. M. A. García-Contreras is grateful to CONACYT and ININ, MEXICO for financial support to conduct a Research Stay at UBC

References

[1] A.T. Najafabadi, E. Gyenge, Carbon, 71 (2014) 58-69.
[2] P.H. Benhangi, A. Alfantazi, E. Gyenge, Electrochimica Acta, 123 (2014) 42-50.
[3] J. Ludwig, J. Power Sources, 155 (2006) 23-32.
[4] A. Serov, A. Aziznia, P.H. Benhangi, K. Artyushkova, P. Atanassov, E. Gyenge, Journal of Materials Chemistry A, (2013).

[5] E.L. Gyenge, J.-F. Drillet, J. Electrochem. Soc., 159 (2012) F23-F34.
[6] M. Risch, A. Grimaud, K.J. May, K.A. Stoerzinger, T.J. Chen, A.N. Mansour, Y. Shao-Horn, The Journal of Physical Chemistry C, 117 (2013) 8628-8635.

Chapter 8.15. Role of functionalized carbon support on the electroactivity of Platinum and Palladium

A. Godinez-Garcia[a]; Dominic F. Gervasio[b]

[a]Departamento de Ingenieria de Procesos e Hidraulica, Universidad Autonoma Metropolitana, Unidad Iztapalapa, Av. San Rafael Atlixco 186, 09340 Mexico City, Mexico.
[b]The University of Arizona, Department of Chemical and Environmental Engineering. Harshbarger 108, 1133 E. James Rogers Way, Tucson, Az 85721-0011, USA.

ABSTRACT

Platinum and Palladium nanoparticles were supported on carbon nanotubes and nanofibers using high-intensity sonication in order to study the support effect on the electroactivity of the palladium and platinum nanoparticles for the oxygen reduction reaction (ORR). Scanning electronic microscopy and electrochemical techniques were used for analyzing microstructure and morphology of the synthesized electrocatalysts. The results showed that acid functionalization of the used supports increased the electrochemical double layer, that it is a consequence of an increasing of the surface area. However, the electroactivity decreased because these functionalized supports also decrese the electrical conductance as the electrochemical characterization showed.

Keywords: Platinum and Palladium, Nanomaterials, Carbon nanotubes, Carbon nanofibers, Electrocatalysts

1. Introduction

Proton exchange membranes fuel cells (PEMFC's) are the best candidate to substitute internal combustion engines in automobiles. However, mass production of PEMFC's technologies has not been carried out because there are still some issues that do them not economically viable [1]. One of those issues is the expensive cost of the components of PEMFC's, meanly platinum that is the catalyst that is used in the cathode and anode of those devices. As far we know, platinum and platinum alloys have the best catalytic activity for the anodic hydrogen oxidation and cathodic oxygen reduction reaction. Research has carried out for substitution of Pt by other more affordable materials such as doped carbon nanotubes, porphirines, palladium alloys etc.. However, all the new materials

---

* Author for correspondence:
A. Godínez García, +52-55-58044600, ext. 1244, 09340, Mexico DF, Mexico, andgodinez@xanum.uam.mx

still have several difficulties in order to be used for practical application; due to their low catalytic activity, stability or time performance [2].

Since platinum as far the moment is the best catalyst for practical applications of PEMFC´s, it is still necessitated for the new automobile prototypes [3]. So that, it is important to find the way to decrease the amount of Pt used in the membrane electrode assemblies (MEA's) and also the way of improving the stability of the catalyst. Commonly, nanoparticles of platinum are supported in porous carbon such as carbon black vulcan XC-72. However after some time of working the carbon support is oxidized and the nanoparticles of catalyst start to agglomerate, so the performance of PEM fuel cells decrease slowly and eventually disappears. Therefore, research about using multiwall carbon nanotubes (MWCNT's) and carbon nanofibers (CNF's) as support of catalysts have been explored to develop more stable PEMFC electrodes [4].

It is well known that performance of a catalyst depends of the surface morphology of the support; because it determines the reactive area where the chemical reactions are carried out. Since, in this work Pt and Pd nanoparticles were supported on different carbon nanotubes and carbon nanofibers; and the electrochemical activity and the PEMFC performance before and after of functionalizing the supports were determined.

2. Materials and Methods

2.1 Synthesis

The catalyst samples were prepared by chemical reduction using $NaBH_4$ and high intensity ultrasound (3mm horn, operated at 20% intensity during 10 minutes) for dispersion of carbon and nanoparticles. A total amount of $3.07x10^{-5}$ mol $H_2Cl_2Pt*6H_2O$ was used as chemical precursor of the Pt nanoparticles; this amount was dissolved in 50ml deionized water. Eight carbon supports were used for depositing 10wt.% Pt and 10wt.% Pd nanoparticles: catalytic multi wall carbon nanotubes ($MWCNT_{Catal}$), nanocyl multiwall carbon nanotubes (CNT_{Nanoc}), carbon nanofibers 2-171 ($CNF_{2\text{-}171}$), carbon nanofibers 4-171 ($CNF_{4\text{-}171}$) were received from Materials and Electrochemical Research Corporation (MER Corp from Tucson, Arizona, US). The functionalization of those carbon supports was done using nitric acid (ACS reagent, HNO_3), concentrated, during 3 hours under ultrasonic bath. Of this way were obtained catalytic functionalized multi wall carbon nanotubes (F-$MWCNT_{Catal}$), nanocyl functionalized multi wall carbon nanotubes (F-$MWCNT_{Nanoc}$), functionalized carbon nanofibers 2-171 (F-$CNF_{2\text{-}171}$) and functionalized carbon nanofibers 4-171 (F-$CNF_{4\text{-}171}$).

To obtain the Pd metallic nanostructures, first, the ionic metal chloride species were dissolved in aqueous KCl solution, and then they were chemically reduced to metallic species. Palladium(II) chloride ($PdCl_2$) does not have good solubility in water, however it readily dissolves when a small amount of KCl is added to the solution, because a coordination complex, K_2PdCl_4, forms that is very soluble in water. This occurs according to the following chemical reaction [5].

$$PdCl_2 + 2\,KCl \rightarrow K_2PdCl_4 \qquad (1)$$

Accordingly, 50 ml of an aqueous solution at $9.4x10^{-4}$M $PdCl_2$ was prepared and mixed with $5.3x10^{-4}$ mol KCl. Then the chemicals were mixed using an ultrasonic bath at 65 °C during one hour, the color of the solution changed from opaque orange to transparent yellow. Next step was to add the carbon support in order to obtain 10 wt. % of nanoparticles and sonicated during 10 minutes before adding the $NaBH_4$. The samples were centrifuged, rinsed and dried.

2.2 Physical and electrochemical characterization

Catalyst morphology was determined in a field emission SEM Instrument (FE-SEM), Hitachi S-4800 Type II/ThermoNORAN NSS EDS, was operated at 15 kV.

Electrochemical experiments were evaluated in a double compartment three-electrode test cell at 298 K. The electrolyte was a 0.5 M H_2SO_4 solution prepared from deionized water which was degassed with N_2, during voltammetric activation of the working electrode, and saturated with O_2 for 20 min before each electrochemical measurement to determine the kinetics of the ORR by thin-film rotating disk electrode (TF-RDE) technique (ref). A spectroscopic graphite rod was used as the counter electrode and saturated calomel electrode (SCE made with Cl (4 M) $|Hg_2Cl_2(s)|Hg(l)|$ Pt and E^{SCE}= 0.241 V *versus* NHE) was the reference electrode.

2.4 MEA preparation

The membrane electrode assembly (MEA) was prepared using the catalytic nanoparticles dispersed on the carbon supports (10% wt. nanoparticles). The catalytic ink used for the preparation of the MEA‘s was obtained mixing (under ultrasonic agitation for 30 min) the catalytic nanoparticles with 456 ml of isopropyl alcohol and 25 ml of 5 wt.% Nafion solution (from Sigma-Aldrich). The catalyst loading was 0.1mg nanoparticles/cm^2 sprayed over a carbon cloth gas diffusion layer (GDL) with an area of 4 cm^2. After the catalyst layer was deposited on the GDL, a Nafion layer was over coated from 25 ml of Nafion solution plus 175 ml isopropyl alcohol. The prepared electrode was used as cathode; a commercial electrode as anode (0.5mgPt/cm^2). Those were hot pressed to a Nafion 115 membrane by pressing at a pressure of 0.625 ton/cm^2 and temperature of 135 °C in air for 2.5 min. For comparison, a MEA was made using two commercial gas diffusion electrodes (GDE’s, 0.5mgPt /cm^2 from Fuel Cells Etc) as anode and cathode. Fuel cells were tested at room temperature and pressure.

3. Results and Discussion

In order to know the morphology and size of the different supports a characterization was carried out using FE-SEM. In the figure 1a is shown the morphology of $MWCNT_{Catal}$ (Catalytic MWCNT produced by chemical vapor deposition 7 +/- 2 micron length, with purity of >90) and in the Figure 1b is shown the diameter size distribution for those nanotubes that it is in the range from 30 to 200nm. The Pt nanoparticles deposited onto the $MWCNT_{Catal}$ are shown in the figure 1c and the size particle distribution is shown in the figure 1d, the diameter is in the range from 3 to 9 nm (an average size of 6nm).

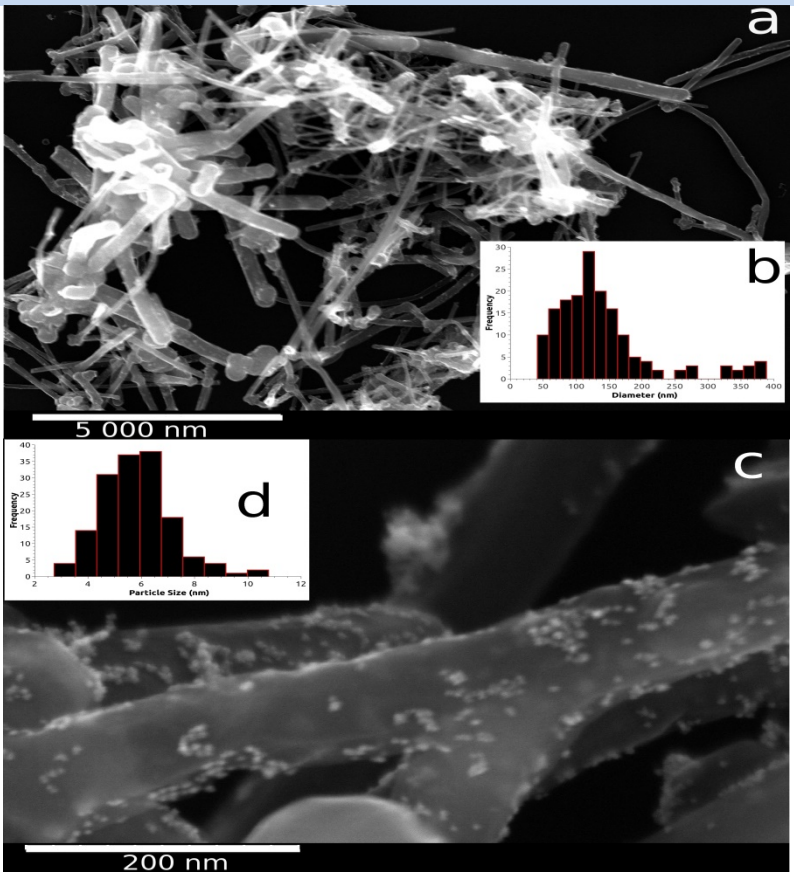

Fig. 1. (a) Catalytic multi wall carbon nanotubes ($MWCNT_{Catal}$); (b) Diameter size distribution; (c)Pt nanoparticles deposited onto $MWCNT_{Catal}$; (d) Size distribution of Pt nanoparticles.

Figure 2 shows the morphology of the carbon nanofibers 4-171 ($CNF_{4\text{-}171}$) (herringbone nanofiber, synthesis by CVD), for those nanofibers the range of diameter size distribution is from 50 to 150 nm. When the Pt nanoparticles were deposited onto the $CNF_{4\text{-}171}$ the range of size distribution is from 3 to 7nm (an average of 5nm). It can be observed that those particles have a small variation respect to the nanoparticles deposited onto the $MWCNT_{Catal}$. Of similar way, the Pt nanoparticles deposited onto another carbon supports were characterized; they showed only small variation on their particle size distribution. For the case of Pd nanoparticles the range of the size distribution diagram is from 6 to 16nm (an average size of 10nm), that means that Pd nanoparticles synthesized by this synthesis method are bigger than Pt particles.

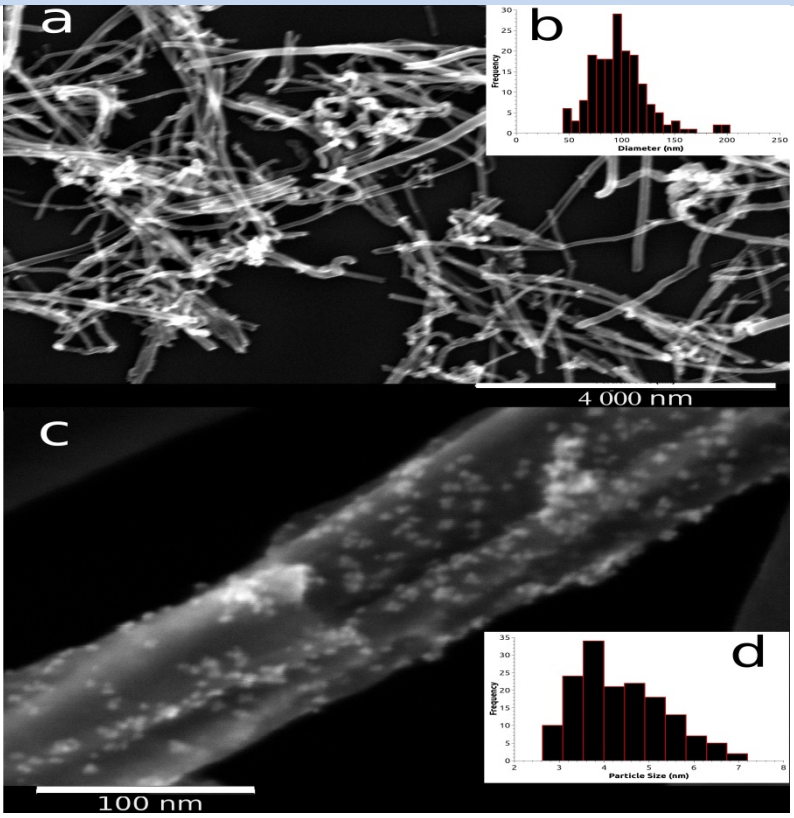

Fig. 2. (a) Carbon nanofibers 4-171 ($CNF_{4\text{-}171}$); (b) Diameter size distribution; (c) Pt nanoparticles deposited onto $CNF_{4\text{-}171}$; (d) Size distribution of Pt nanoparticles.

All the synthesized samples were characterized using cyclic voltammetry in order to determine their potential application as electrocatalysts. In the figure 3a, the cyclic voltammetry curves for Pt nanoparticles deposited onto different supports are shown. From comparison of the figure 3a and 3b, it is easy to observe qualitatively that if the carbon support is functionalized the double layer (DL) capacitance increase; the more stable carbon structure the double layer increasing is smaller. In this case the $MWCNT_{Catal}$ nanotube is the most stable carbon structure. Therefore, it can be noted that there is an inverse relation between the double layer increasing and the stability of the support.

Quantitative values for the double layer capacitance of all the synthesized catalysts were obtained using different sweep rates in the DL region; as it is depicted in figure 4. So that, the information to determine the double layer capacitance is provided by the slope of a linear fit [6]. The results are presented in the tables 1 and 2. From those tables, it can be observed that after functionalizing the supports almost all the materials increases the DL capacitance; with exception of the $MWCNT_{Catal}$ nanotubes. This was attributed to the $MWCNT_{Catal}$ stability under corrosive conditions.

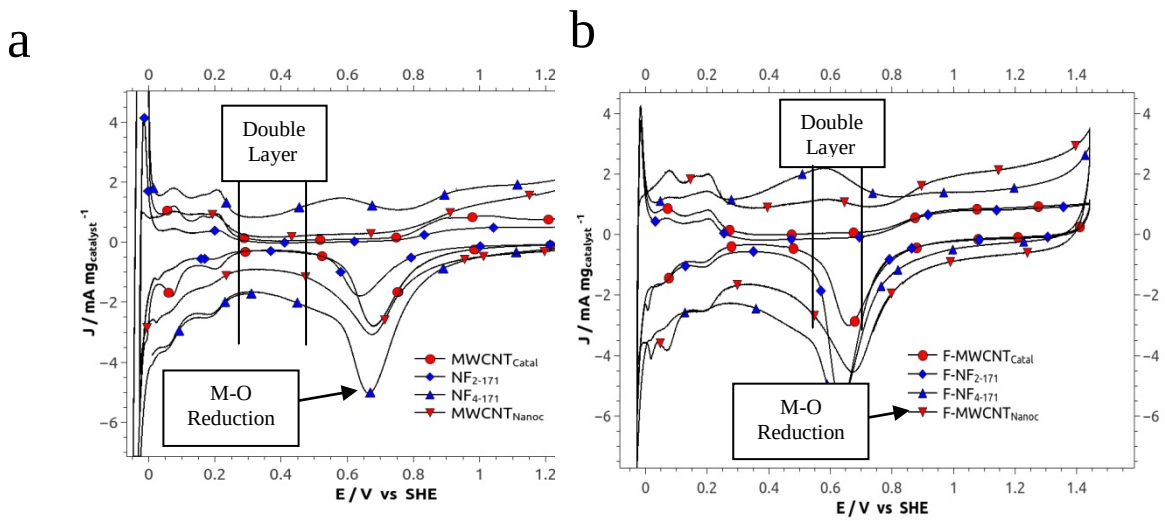

Fig. 3. Cyclic voltammetry for Pt nanoparticles deposited onto different supports. (a) Not functionalized carbon supports; (b) Functionalized carbon supports.

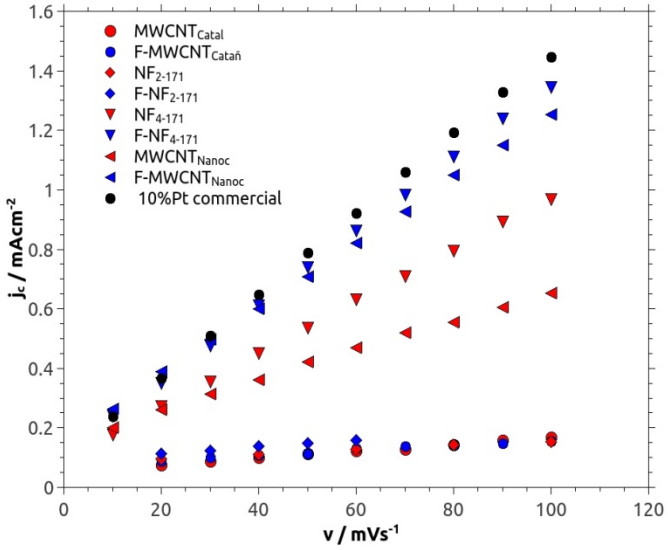

Fig. 4. Capacitive density *vs* sweep rate for the Pt nanoparticles onto different supports.

Table 1. Double layer capacitance for 10%wt. Pd Catalysts

10%wt. Pd Catalysts			
	C ($mFcm^{-2}$)		C ($mFcm^{-2}$)
Catalytic MWCNTs	1.2±0.07	Funct.	1.0±0.04
Creos 2-171 NF	1.4±0.02	Funct.	0.6±0.09
Creos 4-171 NF	6.9±0.04	Funct.	16.0±0.04
NC 7000 MWCNTs	6.3±0.06	Funct.	10.6±0.03

Table 2. Double layer capacitance for 10%wt. Pt Catalysts

10%wt. Pt Catalysts			
	C ($mFcm^{-2}$)		C ($mFcm^{-2}$)
Catalytic MWCNTs	1.10±0.04	Funct.	0.80±0.05
Creos 2-171 NF	0.70±0.05	Funct.	1.10±0.1
Creos 4-171 NF	8.80±0.01	Funct.	12.40±0.08
NC 7000 MWCNTs	4.90±0.08	Funct.	10.90±0.05
10% Pt commercial	13.50±0.09		

Beside of determining the DL capacitance, the Tafel kinetic parameters (charge transfer coefficient, α; Tafel slope, b; exchange current density, j_0) for the Tafel equation ($\eta = a + b \log |j_k|$) were obtained using the TF-RDE technique (ref). It is well known that the rate of the cathodic reaction is proportional to the exchange current density. So, j_0 provide information about the reaction rate for the ORR; with this is possible to compare the catalytic electroactivity of the different supported nanoparticles.

In the Figure 5a are shown the Tafel plots obtained after carrying out linear sweep voltammetry. From this figure, it is possible to observe that the best support is the not functionalized nanofiber 4-171 ($CNF_{4\text{-}171}$). After functionalization this nanofiber decreased the kinetic properties of the Pt nanoparticles. This decreasing is attributed to a low resistance to acid attack. A thermal treatment of this $CNF_{4\text{-}171}$ nanofiber (>2000 °C, now it is named nanofiber $CNF_{2\text{-}171}$) favors the stability but decrease a little the kinetic properties of the catalyst.

The Tafel parameters were calculated and written in the tables 3 and 4 for Pt and Pd catalyst respectively. In those tables can be observed that the exchange current density (j_0) for the catalyst supported on nanofiber 4-171 decreased almost 10 times after the acid treatment. j_0 for $MWCNT_{Catal}$ nanotubes and $CNF_{2\text{-}171}$ nanofibers, after acid treatment, did not change considerably. This behavior was attributed to the stability of $MWCNT_{Catal}$ nanotubes and $CNF_{2\text{-}171}$ nanofibers under corrosive media.

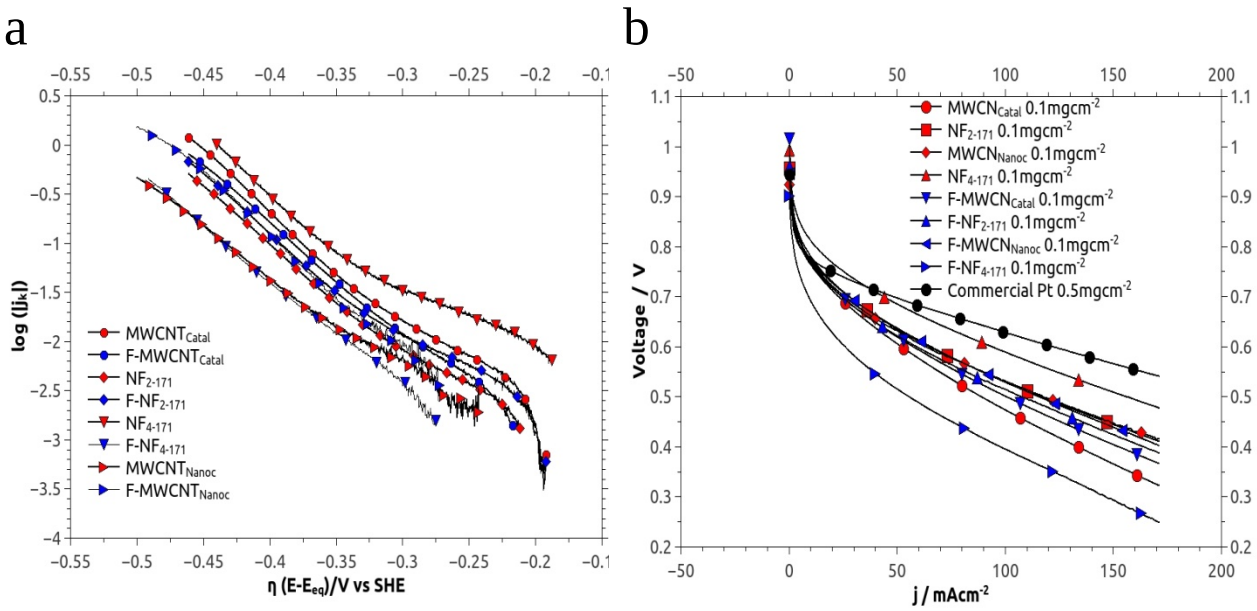

Fig. 5. (a) Linear sweep voltammetry used for obtaining the Tafel parameters of the Pt catalysts (b) MEA's performance for Pt nanoparticles onto different supports.

Table 3. Tafel parameters of the 10%wt. Pd Catalysts.

10%wt. Pd Catalysts							
	α	-b / Vdec^{-1}	j_0 / mAcm^{-2}		α	-b / Vdec^{-1}	j_0 /mAcm^{-2}
Catalytic	0.61	0.095	1.0 x10^{-6}	Funct.	0.61	0.096	2.4x10^{-6}
Creos 2-171	0.55	0.105	3.6x10^{-6}	Funct.	0.55	0.105	5.5x10^{-6}
Creos 4-171	0.48	0.121	1.25x10^{-5}	Funct.	0.57	0.102	3.8x10^{-6}
NC 7000	0.67	0.086	2.63x10^{-7}	Funct.	0.58	0.101	3.5x10^{-6}

Table 4. Tafel parameters of the 10%wt. Pt Catalysts.

10%wt. Pt Catalysts							
	α	-b / Vdec^{-1}	j_0 /mAcm^{-2}		α	-b/ Vdec^{-1}	j_0 / mAcm^{-2}
Catalytic	0.48	0.121	6.0x10^{-5}	Funct.	0.58	0.100	4.3x10^{-5}
Creos 2-171	0.48	0.122	3.1x10^{-5}	Funct.	0.49	0.120	3.9x10^{-5}
Creos 4-171	0.53	0.110	7.2x10^{-5}	Funct.	0.611	0.095	2.68x10^{-6}
NC 7000	0.54	0.109	4.9x10^{-6}	Funct.	0.68	0.085	1.24x10^{-6}
10% Pt	0.51	0.115	1.4x10^{-4}				

The MEA's performance was tested in a single PEMFC (see figure 5b). This test shows that the $CNF_{4\text{-}171}$ nanofiber is the best support for the Pt catalysts, as it was observed in the TF-RDE characterization. However, the stability of the support under PEMFC working conditions will be tested in a next work.

Also in the figure 5b is observed that despite of using only a loading of 0.1mg Pt/cm^2 the performance of the $CNF_{4\text{-}171}$ catalyst is close to the commercial GDE (0.5mg Pt/cm^2). Therefore, the structure of the herringbone carbon nanofibers helps to improve the dispersion of the catalyst particles onto the surface. However, it is probably that the same sites, where the particles are attached, be easily attacked by acids. A high temperature treatment improves stability of the nanofibers, but it decreases the number of useful sites for a favorable dispersion of the catalyst nanoparticles.

4. Conclusion

Pt and Pd nanoparticles were supported onto carbon nanotubes and nanofibers using high intensity ultra-sonication. Moreover, the carbon nanotubes and nanofibers were functionalized using nitric acid in order to compare the reaction rate of the ORR after functionalizing. The FE-SEM pictures showed that the particle size distribution did not change significantly from one support to another.

The double layer capacitance results showed that almost all the materials increased the DL capacitance; with exception of the $MWCNT_{Catal}$ nanotubes. This was attributed to the $MWCNT_{Catal}$ stability under corrosive conditions. The exchange current density (j_0) obtained by TF-RDE for the catalyst supported on nanofibers 4-171 (this support provided the best kinetic properties for Pd and Pt) decreased almost 10 times after the acid treatment. However, j_0 for $MWCNT_{Catal}$ nanotubes and $CNF_{2\text{-}171}$ nanofibers, after acid treatment, did not change considerably.

Also the functionalization of the 4-171 and 2-171 nanofibers decreased the performance of the single proton exchange membrane fuel cell (PEMFC) used for testing; showing that functionalization of the nanofibers not favors PEMFC performance. But functionalization of carbon nanotubes, that they were the most stable carbon structures under the corrosive environment, showed a small improvement in the PEMFC performance.

Acknowledgements

A.G.G. appreciates the funding provided by the national council of science and technology (CONACYT) for the postdoctoral stay in the University of Arizona (U of A) through the program of postdoctoral and sabbatical stays 2012–2014, also to Materials and Electrochemical Research Corporation (MER corporation) for providing the carbon nanotubes and nanofibers used in this research.

References

[1] Sharma S., Pollet B. G., Support materials for PEMFC and DMFC electrocatalysts—A review, J. of Power Sources 2012; 208: 96-119.

[2] Alexey S., Chan K., Review of non-platinum anode catalysts for DMFC and PEMFC application, Applied Catalysis B: Environmental, 2009; 90, 3–4: 313–320.

[3] Bliznakov S., Vukmirovic M., Yang L., Sutter E., Adzic R.R., Pt Monolayer on Electrodeposited Pd Nanostructures-Advanced Cathode Catalysts for PEM Fuel Cells, ECS Trans. 2011; 41,1: 1055-1066.

[4] Lee k., Zhang J., Wang H., Wilkinson D. P., Progress in the synthesis of carbon nanotube- and nanofiber-supported Pt electrocatalysts for PEM fuel cell catalysis, Journal of Applied Electrochemistry. 2006; 36, 5: 507-522.

[5] Gabriele B., Costa M., Salernoe G., Chiusoli G. P., An efficient and selective palladium-catalysed oxidative dicarbonylation of alkynes to alkyl- or aryl- maleic esters, J.Chem. Soc., Perkin Trans. 1, 1994: 83–87.

[6] Godínez-García A., Pérez-Robles J.F., Martínez-Tejada H. V., Solorza-Feria O. Characterization and electrocatalytic properties of sonochemical synthesized PdAg nanoparticles, Materials Chemistry and Physics , 2012; 134: 1013-1019.

Chapter 8.16. Synthesis of carbon nanotubes doped with nitrogen towards the electroreduction of oxygen in alkaline media

I. Zeferino González*; G. Rosado Ortíz; A.M. Valenzuela Muñiz; J.Y. Verde Gómez

Instituto Tecnológico de Cancún, Av. Kabah Km. 3, Cancún, Q.R., México, 77500.

ABSTRACT

The unique properties of carbon nanotubes, makes them ideal materials for many applications, however, for specific applications it is necessary to modify the properties of materials. Doping of carbon nanoestructure is one of the most effective ways to change their properties. Incorporating nitrogen atoms into the carbon structure can drastically change their properties. One of the most outstanding potential applications found for carbon doped is as a catalyst for oxygen reduction reaction (ORR) in fuel cells. So, in this wok nitrogen doped carbon nanotubes (N-CNTs) was synthesized simultaneously by the chemical vapor deposition modified method. Pyridine was used as carbon and nitrogen precursor and ferrocene as catalyst for the nanotubes growth. The composite material was investigated using scanning electron microscopy, transmission electron microscopy, X ray difraction and X-ray photoelectron spectroscopy. The electrocatalytic performance of the material was evaluated towards the oxygen reduction reaction by linear sweep voltammetry measurements. A catalyst-coated rotating disk electrode at different rotation rates in 0.1 M KOH solution was evaluated. The electrocatalyst N-CNTs improved the electrocatalytic activity for ORR which proceeds in a nearly four-electron pathway. The favorable result was due to the higher content of nitrogen that was incorporated into the structure of carbon. Moreover, according the characterization studies indicated that pyrrolic nitrogen may act as active sities of catalysts for ORR.

Keywords: Nitrogen doped carbon nanotubes, Chemical vapor deposition, Oxygen reduction reaction

1. Introduction

The decrement not only in the dependence on hydrocarbons but also and carbon dioxide emissions is becoming an urgent need. This requires significant changes in the global energy system, including the introduction of new technologies that are able to produce and use more efficient and clean energy. The fuel cells technology is currently an emerging

---

* Corresponding author:
Isaias Zeferino González, T: 52 (998) 8807432 ext: 1020, 1012, E: zeferino.isaias@yahoo.com.mx

field that has potential to make a significant impact on sustainable energy power sources [1,2].

One of the challenges in the commercialization of fuel cells is the high cost and scarcity of platinum based catalysts. Therefore, alternative electrocatalysts are needed. Systems based on doped carbon nanostructures (without the use of precious metals) have been proposed as a good option to solve both of the drawbacks before mentioned [3,4,5].

There have been several studies about the synthesis of carbon nanotubes doped with nitrogen atoms using different carbon-nitrogen precursors by the method chemical vapor deposition [6,5,7,3]. It has been shown that these materials have high electrocatalytic activity for oxygen reduction in alkaline electrolyte, which exhibits properties similar to platinum [8,9,10,11].

Wong et al. [12] synthesized N-CNTs via CVD with ethylenediamine and iron phthalocyanine. The material exhibited a significant onset potential (0.05 V vs. SCE) and low Tafel slope of 77 mV dec^{-1}. Moreover, the highest electron transfer number of 3.90 was obtained. This study demonstrated that the N-CNTs was able to show comparable ORR activity with Pt/C catalyst. Similar results were obtained by Borghei et al. [11], N-CNTs with very low nitrogen content (0.56 at%) by a process involving the coating of acid functionalized N-CNTs with polyaniline. The resulting N-CNTs exhibited a remarkable electrocatalytic activity for the ORR. The onset potential for ORR obtained was of 0-03 V vs. Ag/AgCl. The high activity of material was due to the exceptional accessibility for the catalytic sites located in the open and porous nitrogen-doped layer surrounding the N-CNTs core. On the other hand, Subramanian et al. [13] prepared nitrogen-doped vertically aligned carbon nanotube carpets. The material was obtained by nitrogen plasma treatment of the CNTs directly grown on stainless steel substrate by CVD. This material reduces oxygen in lower overpotential under basic condition, with onset potential at -0.12 V vs. Ag/AgCl. More recently, Ge et al. [8] synthesized a new electrocatalyst for ORR derived from in situ growth of metal-organic frameworks on carbon nanotubes. The material yielded comparable catalytic activity than commercial platinum-based catalysts and low Tafel slope of 49 mV dec^{-1}. The excellent performance of material was attributable to the formation of structured porous and nitrogen doped carbon nanotubular composites. These studies show that the N-CNTs possess good electrocatalytic property towards ORR in alkaline medium, they could serve as catalyst for application in cathodes of alkaline fuel cells [13].

Hence, this study presents the production and evaluation of nitrogen doped carbon nanotubes (N-CNTs) *in situ* that were synthesized by the modified method chemical vapor deposition. The N-CNTs have the advantage that they were synthesized from available and inexpensive materials. Moreover, the physical, chemical and electrochemical of materials were analyzed to elucidate their electrocatalytic performance for the kinetics of oxygen reduction reaction.

2. Materials and Methods

2.1. N-CNTs synthesis

N-CNTs synthesis was carried out by the method a modified chemical vapor deposition. Pyridine (99.5%, Merck) was used as a source of both carbon and nitrogen, and

ferrocene (98%, Aldrich) as a metal catalyst for the nanotubes growth. Small Vycor tubes (0.7 cm internal diameter and 50 cm length) were utilized as substrates which were placed in the centre of a tubular furnace (Lindberg/blue). Synthesis was carried out by heating the tube furnace and injecting the precursor solution under argon protection. At the end of the synthesis reaction, the tubular furnace was cooled down up to room temperature under argon gas flow. The final products were obtained from the inside of the Vycor tube. N-CNTs were washed with concentrated nitric acid (66.5%, J.T. Baker) for 12 h and dried in an oven for 12 h.

2.2. Physical and chemical characterization

The Scanning electron microscope (SEM) Hitachi SU8230 was used to the morphology and topology studies of the materials. The samples were placed on the copper grid, supported on the sample holder of the microscope. Images were acquired from different areas of the sample, in order to assess their average characteristics. Transmission electron microscopy (TEM) imaging carried out on JEOL JEM-2200FS to provide high resolution images of the samples. For TEM analysis, the samples were dispersed in ethanol by sonication and then placed on copper grid support. The diffraction pattern were obtained on a X Ray Diffractometer Bruker D8 Advanced, operated at 40kV and 40 mA. Cu-Kα radiation was used with a wave length λ =1.5418 Å.

2.3. ORR activity evaluation

The electrochemical evaluation was carried out in a rotating disk electrode (RDE) with BAS equipment at different rotation speeds, connected to an potentiostat / galvanostat Epsilon, whose response was analyzed by the Epsilon EC-200-XP software. A conventional three electrodes electrochemical cell was used and a solution of 0.1 M KOH as electrolyte. The electrodes that were used are: a working electrode of glassy carbon with a geometric area of 0.07 cm^2, a reference electrode of Ag/AgCl in saturated 3 mol L^{-1} KCl and a platinum wire as counter electrode. The catalyst ink that contained of 5 mg N-CNTs mixed with 0.5 mL of ethanol and 30 µL Nafion solution was prepared by sonication for 1 h. 20 µL of catalyst ink was deposited on the glassy carbon electrode surface and was subsequently slowly dried at room temperature. The working electrode potential was swept from -1 to 0 V vs Ag/AgCl at a scan rate of 10 mV s^{-1}. Before the electrochemical test, the electrolyte was saturated with argon gas and a potential sweep was performed in order to obtain a background reading. After the background scan, oxygen gas was introduced by 30 min. to saturate the solution. The experiments were performed at the same scan rate with different working electrode rotation speeds.

3. Results and Discussion

The morphology of the samples of N-CNTs was studied by SEM and TEM. The fig. 1a shows the micrograph of the N-CNTs, in which nanotubes outer diameter sizes are observed, furthermore clearly shows the morphology of tubular carbon. Fig. 1b shows the N-CNTs micrograph of high-resolution TEM. The nanotube show the characteristic tubular shape, various forms of roughness on the outer and several compartments inside, which evidences that are multi-walled carbon nanotubes. A feature commonly observed after

incorporation of nitrogen in the nanotube network structures are the bamboo like form which are observed in Fig. 1b, which indicates that the materials were doped with nitrogen [14]. According to the results of EDX by SEM, ~5 at. % nitrogen was incorporated into the structure of the nanotubes.

a) **b)**

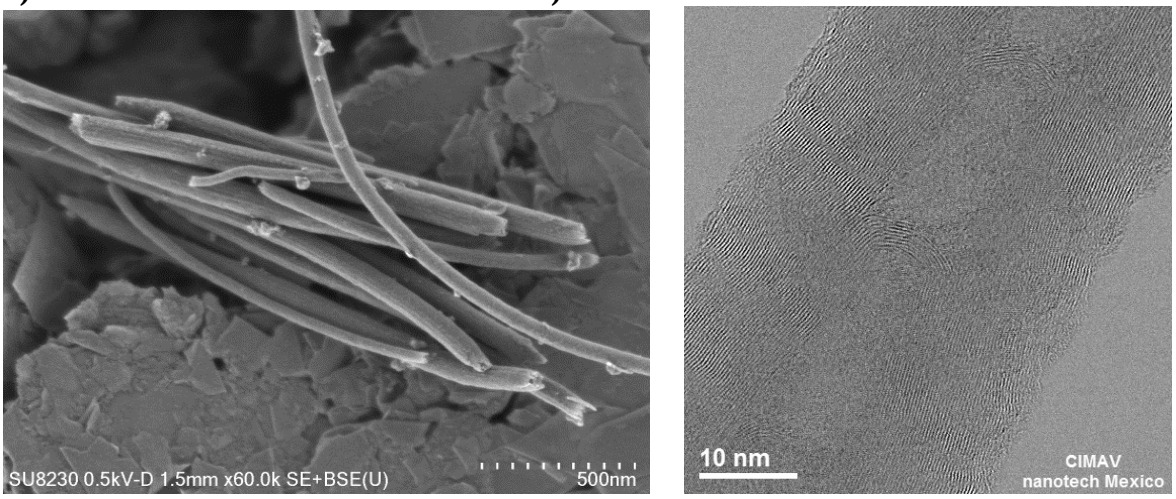

Fig. 1. Micrographs of the samples of N-CNTs obtained by a) HRSEM and b) HRTEM.

Fig. 2 shows the X-ray diffraction patterns obtained from the N-CNTs. It has also been included the pristine CNT for comparisons. Diffraction patterns exhibit intensity 2H graphite phase, which is associated with the formation of N-CNTs multiwall. The first peak located at 26° corresponds to the carbon (002) which forms the hexagonal shape of the graphite. Other peaks located at 42.5°, 44.5° and 53.9 are also corresponding to the graphite (100), (101) and (004) respectively [15,16]. The peaks located at 37.7°, 45.8°, 49.1° and 77.9° corresponding to the (210), (112), (221) and (401) respectively of the iron carbide (Fe_3C) [17]. The iron carbide particles created during the synthesis process and served as seeds for the growth of nanotubes [18], therefore most of Fe_3C are trapped within the structure of the N-CNTs. Fe_2O_3 was also found in the diffraction pattern associated to the peak located at 43.5° corresponding to the plane (202). The Fe_2O_3 could come from the catalytic agent (residual iron), unreacted and oxidized during sample handling [19,20].

On the other hand, linear sweep voltammetry was used to evaluate the electrochemical performance of the N-CNTs. Fig. 3a shows the polarization curves of the electrochemical reduction of molecular oxygen using N-CNTs and 20 wt. % Pt/C to compare. The onset potential of N-CNTs is about -0.18 V vs. Ag/AgCl. This favourable result of the N-CNTs can contribute in reducing overpotential for the activation energy, indicating that the materials possess good electrocatalytic activity for ORR with respect to the onset potential [21,22]. Moreover, the hydrodynamic behavior of the N-CNTs sample was studied by rotating disk electrode at different rotation speeds in oxygen saturated 0.1 M KOH solution.

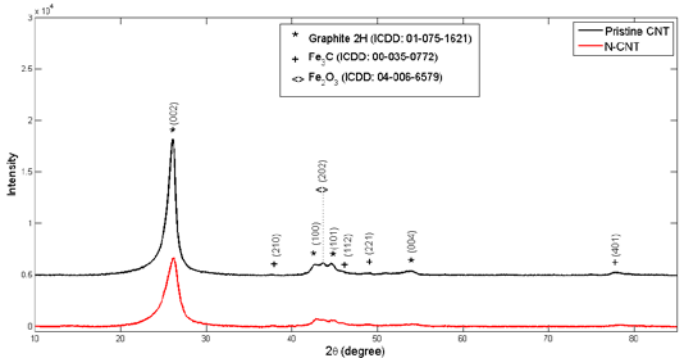

Fig. 2. XRD patterns of the N-CNTs synthesized.

As it is shown in Fig. 3b the current densities increase with increasing rotation speed; it reveals that the diffusion of oxygen which reaches the surface of N-CNTs performs the ORR. The kinetic parameters were analyzed using the Koutecky-Levich (K-L) equations:

$$1/j = 1/j_k + 1/j_k = 1/Bw^{1/2} \quad (1)$$

$$j_k = nFK_fC_O \quad (2)$$

$$j_d = 0.2nFD_O^{2/3}V^{-1/6}C_O \quad (3)$$

where j is the measured current density, jk and j_d are the kinetic and diffusion limited current density respectively, K_f is the electrochemical rate constant for O_2 reduction, D_O is the diffusion coefficient of oxygen ($1.9x10^{-5}$ cm^2 s^{-1}), C_O is its concentration in the bulk ($1.2x10^{-6}$ mol cm^3) and V is the kinematic viscosity of the solution (0.01 cm^2 s^{-1}). The data are given for 0.1 M KOH [7].

The K-L plots of oxygen reduction on the N-CNTs sample are presented in Fig. 3c. The K-L lines show the good linearity and parallelism, indicating that the ORR process over the N-CNTs electrocatalyst follows first-order kinetics in the selected potential range [23]. The number of electrons transferred per O_2 molecule (n) was calculated from the slope of the K-L lines. The before mentioned slopes are parallel to the theoretical line for 4 transferred electrons (e-). Therefore, is possible to imply that the ORR of the N-CNTs is performed by the process of 4 e-. The desirable route for successful ORR would reduce oxygen molecules directly to water, through the 4 e- path [24,25].

A more detailed comparison of the catalytic activity of the material can be obtained by the Tafel slope, which is obtained from the values of kinetic current density (j_k). In Fig. 3d the Tafel slope is plotted, which shows the exponential relationship between the potential and kinetic current density. The slope estimated for the N-CNTs sample, was 75.20 mV dec^{-1}, which it is a value close to the 20 wt. % Pt/C catalyst (70.68 mV dec^{-1}). A low value of Tafel slope is highly advantageous since it permits the attainment of a high catalytic current density at low applied potentials [8].

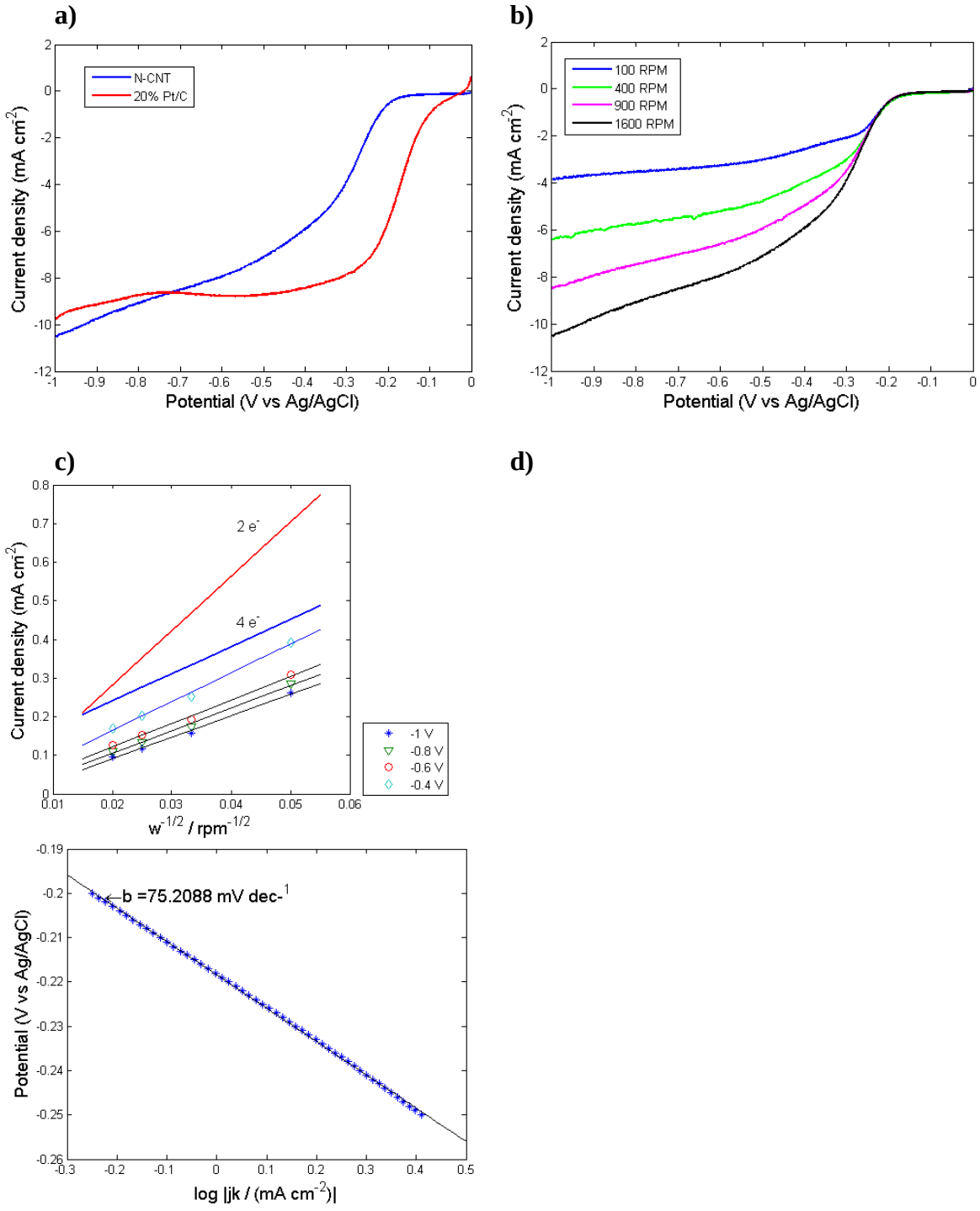

Fig. 3. a) Curves for ORR of the N-CNTs and 20% Pt/C in O_2-saturated 0.1 M KOH at 1600 rpm, scan rate to 10 mV s^{-1}, b) curves of oxygen reduction with different rotation speed, c) Koutecky-Levich plot for O_2 reduction at various potentials, d) Tafel plot of ORR on N-CNTs sample.

Based on the polarization curves results, the N-CNTs sample exhibited high activity towards the ORR; the most probable factor for the catalytic activity is related to the active sites, as well as the exposed edge plane defects, formed by nitrogen-doping in the CNTs. These results are in accordance to the SEM and TEM analysis.

4. Conclusion

The synthesized N-CNTs showed high electrocatalytic activity towards the oxygen reduction reaction with an onset potential of -0.18 V vs. Ag/AgCl. Practically, most of the process ORR of doped carbon nanotubes is carried out through a process of transferring four electrons efficiently. In addition, a low Tafel slope (75.20 mV dec^{-1}) was obtained which is advantageous for ORR kinetics. This favorable result was attributed to the 5 at. % nitrogen that was incorporated into the structure of the nanotubes. Therefore, N-CNTs can reduce oxygen without the use of precious metal electrocatalysts, which makes them suitabl

e candidates for reduction of oxygen at the cathode of the alkaline fuel cell.

Acknowledgements

The authors acknowledge the financial support provided by Tecnológico Nacional de México (TNM), under project 5201.14-P. Also thanks to NANOTECH – CIMAV for technical support in HRTEM and McGill University for HRSEM results.

References

[1]DOE (Department of Energy). Fuel cell handbook. seventh edition ed.: EG&G Technical Services Science applications International Corporation; 2004.

[2]IEA (International Energy Agency). Prospects for hydrogen and fuel cells: OECD/IEA; 2005

[3]Chen Z, Higgins D, Tao H, Hsu RS, Chen Z. Highly Active Nitrogen-Doped Carbon Nanotubes for Oxygen Reduction Reaction in Fuel Cell Applications. Journal Physical Chemistry C. 2009; 113: p. 21008-21013.

[4]Wong W, Daud WRW, Mohamad AB, Kadhum AAH. Influence of nitrogen doping on carbon nanotubes towards the structure, composition and oxygen reduction reaction. International Journal of Hydrogen Energy. 2013; 38: p. 9421-9430.

[5]Wang C, Huang Z, Zhan L, Wang Y, Qiao W, Liang X, et al. Nitrogen-doped carbon nanotubes synthesized with carbon nanotubes as catalyst. Diamond & Related Materials. 2011; 20: p. 1353-1356.

[6]Xiong C, Wei Z, Hu B, Chen S, Li L, Guo L, et al. Nitrogen-doped carbon nanotubes as catalysts for oxygen reduction reaction. Journal of Power Sources. 2012; 215: p. 216 - 220.

[7]Alexeyeva N, Shulga E, Kisand V, Kink I, Ta K. Electroreduction of oxygen on nitrogen-doped carbon nanotube modified glassy carbon electrodes in acid and alkaline solutions. Journal of Electroanalytical Chemistry. 2010; 648: p. 169–175.

[8] Ge L, Yang Y, Wang L, Zhou W, De Marco R, Chen Z, et al. High activity electrocatalysts from metal–organic framework-carbon nanotube templates for the oxygen reduction reaction. Carbon. 2015; 82: p. 417-424.

[9] Truong-Phuoc L, Duong-Viet C, Doh WH, Bonnefont A, Janowska I, Begin D, et al. Influence of the reaction temperature on the oxygen reduction reaction on nitrogen-doped carbon nanotube catalysts.

Catalysis Today. 2015; 249: p. 236-243.
[10] Domínguez C, Pérez-Alonso FJ, Salam MA, Al-Thabaiti SA, Obaid AY, Alshehri AA, et al. On the relationship between N content, textural properties and catalytic performance for the oxygen reduction reaction of N/CNT. Applied Catalysis B: Environmental. 2015; 162: p. 420-429.
[11] Borghei M, Kanninen P, Lundahl M, Susi T, Sainio J, Anoshkin I, et al. High oxygen reduction activity of few-walled carbon nanotubes with low nitrogen content. Applied Catalysis B: Environmental. 2014; 158-159: p. 233-241.
[12] Wong WY, Daud WRW, Mohamad AB, Kadhum AAH, Loh KS, Majlan EH, et al. The Impact of Loading and Temperature on the Oxygen Reduction Reaction at Nitrogen-doped Carbon Nanotubes in Alkaline Medium. Electrochimica Acta. 2014; 129: p. 47-54.
[13] Subramanian P, Cohen A, Teblum E, Nessim GD, Bormasheko E, Schechter A. Electrocatalytic activity of nitrogen plasma treated vertically aligned carbon nanotube carpets towards oxygen reduction reaction. Electrochemistry Communications. 2014; 49: p. 42-46.
[14] Maubane MS, Mamo MA, Nxumalo EN, Otterlo WAL, Coville NJ. Tubular shaped composites made from polythiophene covalently linked to Prato functionalized N-doped carbon nanotubes. Synthetic Metals. 2012; 162: p. 2307– 2315.
[15] Higgins DC, Wu J, Li W, Chen Z. Cyanamide derived thin film on carbon nanotubes as metal free oxygen reduction reaction electrocatalyst. Electrochimica Acta. 2012; 59: p. 8-13.
[16] Fu T, Liu R, Lv J, Li Z. Influence of acid treatment on N-doped multi-walled carbon nanotube supports for Fischer-Tropsch performance on cobalt catalyst. Fuel Processing Technology. 2014; 122: p. 49-57.
[17] Choi CH, Lee SY, Park SH, Woo SI. Choi Chang Hyuck, Seung Yong Lee, Sung Hyeon Park, Seong Ihl Woo. Highly active N-doped-CNTs grafted on Fe/C prepared by pyrolysis of dicyandiamide on Fe2O3/C for electrochemical oxygen reduction reaction. Applied Catalysis B: Environmental. 2011;(103): p. 362-368.
[18] Kaushik G, Kumar M, Maruyama T, Ando Y. Tailoring the field emission property of nitrogen-doped carbon nanotubes by controlling the graphitic/pyridinic substitution. Carbon. 2010; 48: p. 191-200.
[19] Multi-walled carbon nanotubes by spray-pyrolysis using a new iron organometallic complex as catalytic agent. Journal of nanoscience and nanotechnology. 2008; 8: p. 6456-6460.
[20]
[21] Alonso Nuñez G, Valenzuela Muñiz AM, Paraguay Delgado F, Verde Y. New organometallic precursor catalysts applied to MWCNT synthesis by spray-pirolysis. Optical materials. 2006; 29: p. 134-139.
[22] Rodriguez Varela FV, Solorza Feria O, Hernández Pacheco E. Celdas de combustible Canada; 2010.
[23] Zhu S, Zhu C, Li B, Higgins D, Wang H, Li H, et al. Nitrogen-doped carbon nanotubes as air cathode catalysts in zinc-air battery. Electrochimica acta. 2011; 56: p. 5080-5084.
[24] Zhang J. PEM fuel cell electrocatalysts and catalyst layer, fundamental and aplications Canada: Springer; 2008.
[25] Alonso-Vante N. Electroquímica y electrocatálisis. Materiales: aspectos fundamentales y aplicaciones Buenos aires: E-libro.net; 2003.

9
Environmental aspects

Chapter 9.1. Solar radiation measurements to optimize a PV system acording to local weather conditions

V. Juárez Casildo[a]; M. Tufiño Velázquez[b]; A. Yunez Cano[c]; R. de G. González Huerta[a]*

[a]ESIQIE-IPN, Lab. Electroquímica y Corrosión, UPALM, CP 07738, México, D.F.
[b]ESFM-IPN, Laboratorio de Física Avanzada, UPALM, CP 07738, México, D.F.
[c]CIITEC-IPN, Cda. Cecati s/n, Col. Sta. Catarina, CP 02250 Azc., México D.F.

ABSTRACT

PV panels have become in one the most promising technologies because the energy source used by them is free and environmental friendly. However, we should consider the variation of weather conditions, including daily and seasonal changes of solar irradiance. The interest in the use of solar energy has promoted the measure and recording of local weather in potential sites to combine its use with sustainable power sources. In this work, it was analyzed the solar radiation measurements from a meteorological monitoring station placed in the roof of a sustainable house located in the north side of Mexico City . In order to meet the continuous power delivery from a PV system, high capacity and deep discharge batteries are often used as the stored energy in them can be used during night. From this analysis the average monthly irradiance incident on the photovoltaic system to determine an appropriate charge and to achieve optimization of energy consumption obtained from solar panels was obtained. A PV-Hydrogen hybrid power system (PV-H2) could be used to supply energy to the mobile house without using batteries. The study of this approach is in progress.

Keywords: Solar radiation, PV system, Local weather, Hydrogen storage system

1. Introduction

The accelerated growth of population has brought an increase in the energy demand for the production of goods and services. This fact has involved at the same time high cost environmental damages and economic troubles such as global warming and increase in the electricity costs. In Mexico, greenhouse gas emissions are mainly due to the transport sector and electricity production. Regarding the last sector, electrical power consumption per household is around 33% of total energy production. Installing a photovoltaic (PV) system provides several benefits to a homeowner; as he is producing his own electricity, his utility bills will be lower.

---

*Author for correspondence:
Rosa de Guadalupe González Huerta, T: 5255 57296000 ext 54246, E: rosgonzalez_h@yahoo.com.mx

Nowadays, society is immersed in a world where technology has developed rapidly, so energy demand makes us depend largely on energy derived from fossil fuels that threaten our existence on the planet because of the pollution generated. It is known that 70% of greenhouse gases emitted into the atmosphere are mainly due to the production of electricity; besides this we have another very serious problem caused mainly by excessive population growth leading to an increasing demand of energy. The solution to these problems lies in the use of those natural resources that are freely available at no cost, as is the case of wind and solar energy. By installing photovoltaic systems we may sustainably generate electricity by using solar radiation throughout the day. It is worth to notice that PV systems can last up to 15 years or more, thus providing long-term protection against rising electricity rates due to the increased energy demand; installation of PV systems may also cause an increase in the value of a house.

All the above features makes a PV system a promising technology for a more stable and enduring future besides being friendly to the environment. For the best use of solar energy it is necessary to consider the weather conditions of the location based on daily, monthly and seasonal variations of incident solar radiation since it is a factor that directly affects the production of electricity. A study of the behavior of solar radiation in the location where to the PV system is installed is essential for knowing two very important things: how much electric energy is produced and how much is consumed. Another advantage of these sustainable technologies is that society can learn to be responsible with the amount of energy consumed daily. Monitoring of irradiation is performed by a weather station installed on the roof of the sustainable house located in the north of Mexico City and it is aimed to optimize the use of the installed PV system [1,2].

2. Materials and Methods

In a PV system, electricity production depends mainly on two factors: the size and efficiency of the PV array encompassed with the solar resource at the site of installation. Figure 1 shows a typical plot of irradiance (W/m^2) during one day. It can be seen that irradiance is zero during night due to the absence of sun. Irradiance starts increasing from zero after sunrise reaching its maximum at noon where it starts to decrease until the sunset when becomes zero again [3-5].

To quantify the amount of energy that provides the variable sun power over time, it is necessary to determine the area under the power curve by integration.

$$Energy = \int_{t1}^{t2} P(t) \cdot dt \tag{1}$$

where t is the time and P is sun power.
Dividing the energy by the area of solar panels, we obtain

$$\frac{Energy}{m^2} = \int_{t1}^{t2} \frac{P(t)}{m^2} \cdot dt \tag{2}$$

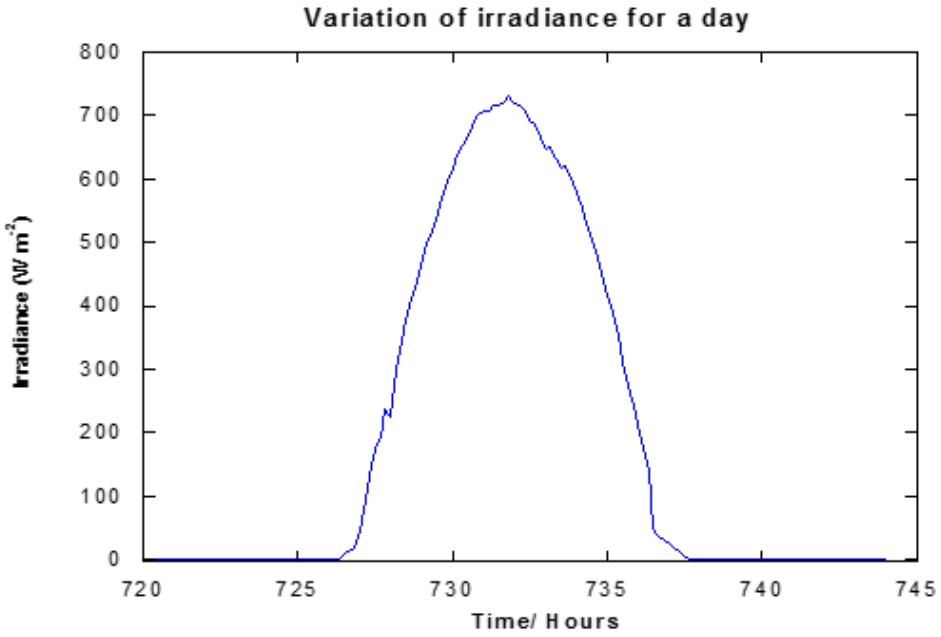

Fig. 8. Irradiance variation with time in the period of one day

$$Irradiation = \int_{t1}^{t2} I(t) \cdot dt \qquad (3)$$

The solar irradiance monitoring was conducted during the period of one year which comprised the second half of 2014 and the first half of 2015 by using a meteorological station with an integrated environmental monitoring subsystem that is normally used to determine the magnitude and direction wind speed, as well as temperature and relative humidity of the site, rainfall, solar radiation, UV radiation and pressure. This monitoring subsystem consists of three modules, the first module (a) includes a CR1000 data logger with a memory interface for an industrial type memory card, a 12V charger / controller, 10 thermocouple temperature sensors, an infrared radiometer with two solar radiation sensors, a multi-sensor, a program for network management and reporting.

The second module is a wireless Vantage Pro 2 Plus weather station (b) with a Mark Davis Weather-link software. Module three is the Winverter™ Monitor Standard Out-Back and Mac V3 Solar sensor (c) software; this software is a tool to monitor, through a workstation, the energy-production by PV panels and how different is the energy consumption by the house from graphical reporting, helping to make the system more efficient and thus adjusting the renewable systems [6], Figure 2 (a).

The measuring equipment of the weather station was installed on the roof of the sustainable house in a particular position so that measurements of wind speed and temperature irradiation were taken efficiently, Figure 2(b).

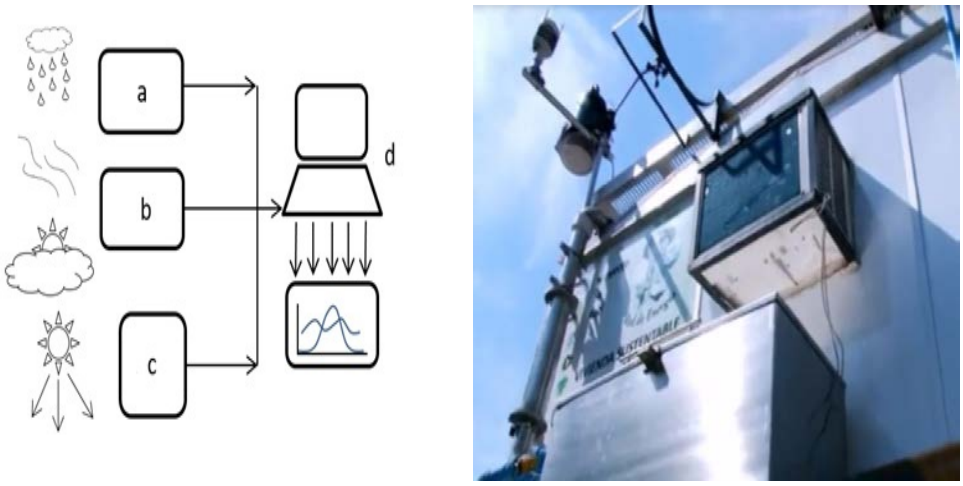

Fig. 2 (a) Subsystem modules of the weather station, and
(b) Weather station installed on the roof of a sustainable home

Experimental irradiance data were recorded daily in 10 minute intervals, obtaining around 562,500 irradiance values that were stored in the memory card, this data is handled in two software calculation with which average values were calculated and different graphs were made.

The Excel software served as a tool for organizing and managing data, while Kaleida Graph 4.0 provides through diagrams valuable information required in our study. In calculating the area under the curve of the tabulated data for a given month a daily average of irradiation incident on the photovoltaic panels could be made, thus establishing an optimal consumption of the produced electricity, Figure 3.

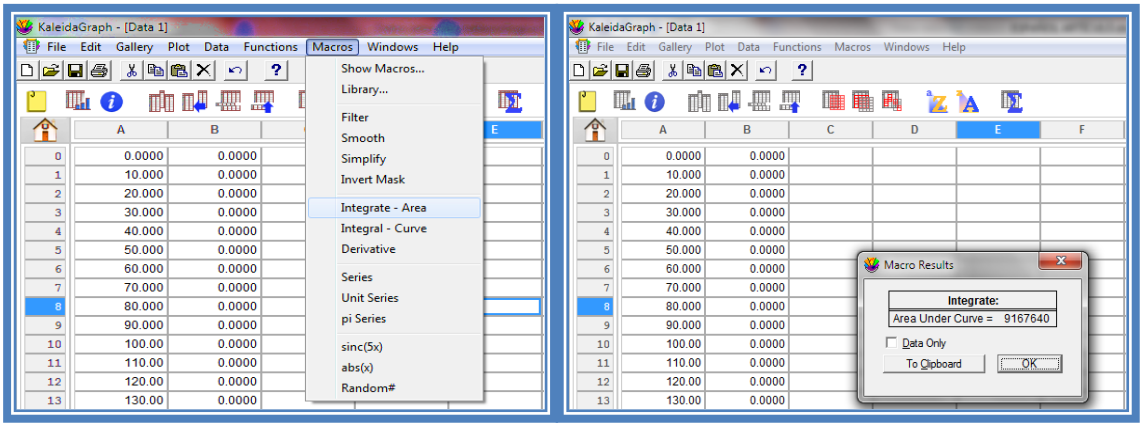

Fig 3. KaleidaGraph. Calculation of solar irradiation in August.

3. Results and Discussion

According to the information provided by the weather station and based on proper management of data Irradiance vs Time graph was done, we found that during the year, August showed the highest irradiance values, around 1000 (W/m^2). Figure 4 shows the behavior of solar irradiation in the north of Mexico City during all the year.

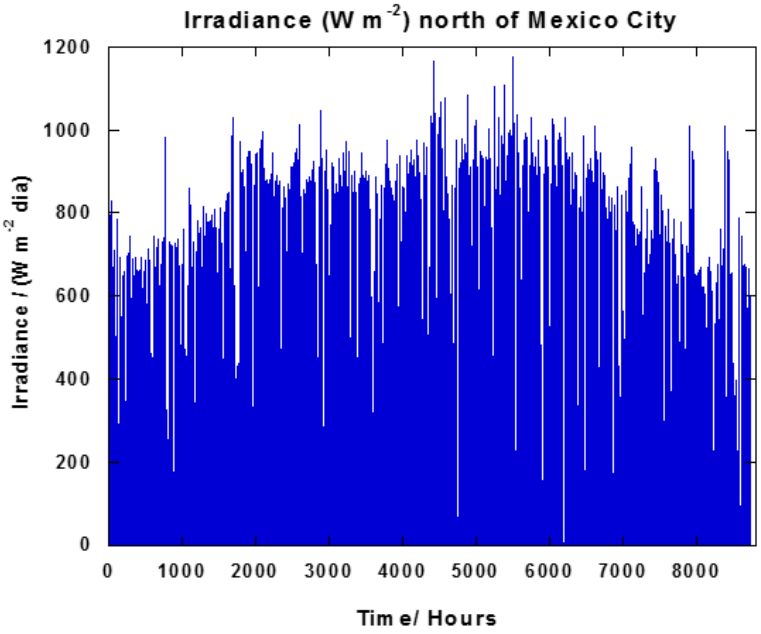

Fig. 4. Irradiance variation for a year in the north of Mexico City

From the calculation of the area under the curve applied to the values of average irradiance for each month, we could obtain the graph of the electricity production of the PV system versus time throughout the year, Figure 5.

Figure 6 shows a comparison of irradiance variation with time curves for different weather stations near Mexico City. We note that the values that we obtained are below those provided by different institutions, because of this big difference; we had to adjust the energy production by the PV system.

The solar performance is highly variable and it becomes necessary to know in which specific days we have good irradiance to observe that the energy production of the PV system meets the energy demand. Table 1 describes the best and worst days of the year of solar irradiance; moreover Figure 7 shows the behavior for days with high and low solar irradiance.

Finally, according to the energy output of the PV system it can be defined directly how much energy we should consume daily to be responsible. It is important to note that our consumption also changes according to the season and it may not have the same behavior of energy production. Figure 8 represents the annual energy production and consumption.

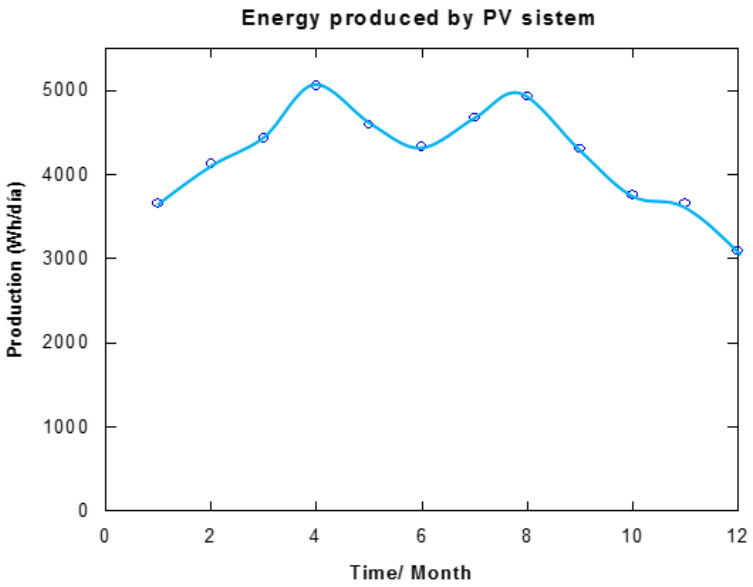

Fig. 5. Production of energy by the PV system for one year.

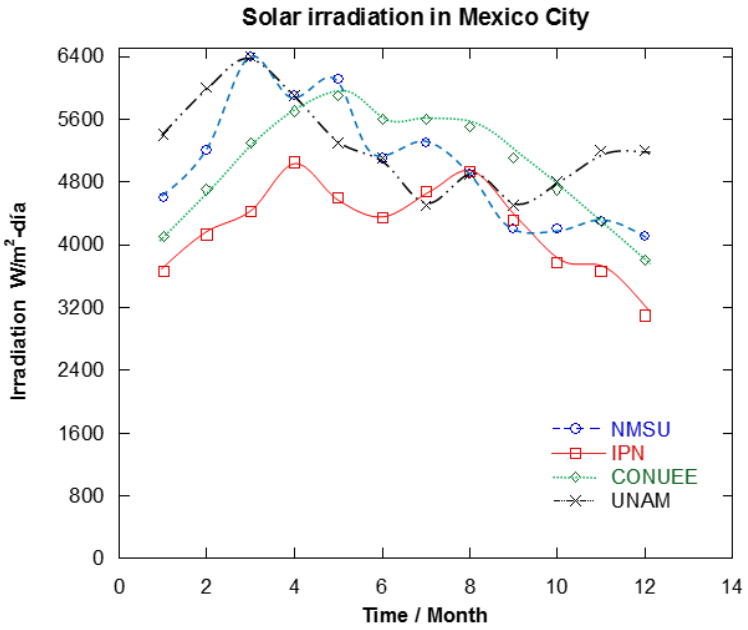

Fig. 6 Solar irradiance for different weather stations

Table 1. Days with highest and lowest solar irradiance.

Date	Ref	Irradiance W m^{-2}	Energy Wh/day
12/08/2014	1	1176	3289.8
24/12/2014	2	211	812.0
12/07/2014	3	1077	3080.3
22/08/2014	4	860	4601.0
31/01/2015	5	732	4699.5
26/03/2015	6	944	6688.8

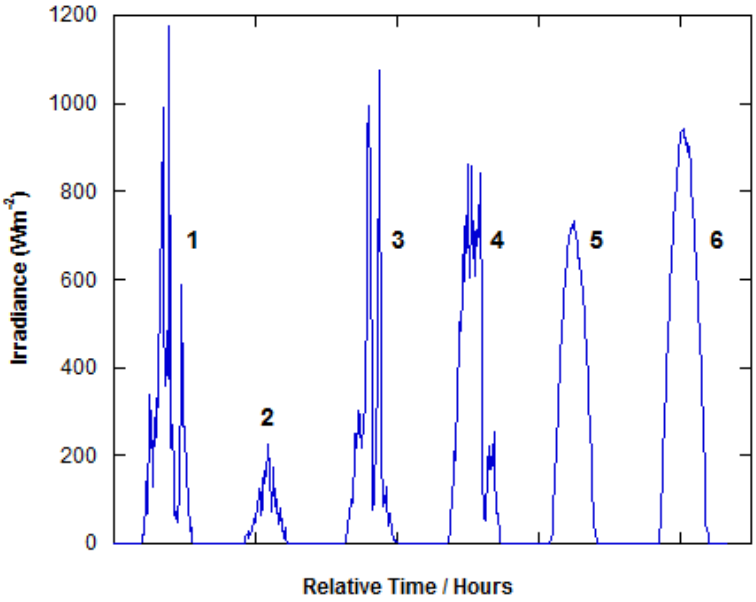

Fig. 7. Best and worst days during 2014-2015

We note that during May, June, July and August more energy is required to have a very hot weather, but it is worth to note that during that time a lower irradiance was recorded**.** Thus, from this analysis the average monthly irradiance incident on the PV system can be used to determine an appropriate charge and achieve optimization of the produced energy by the PV system.

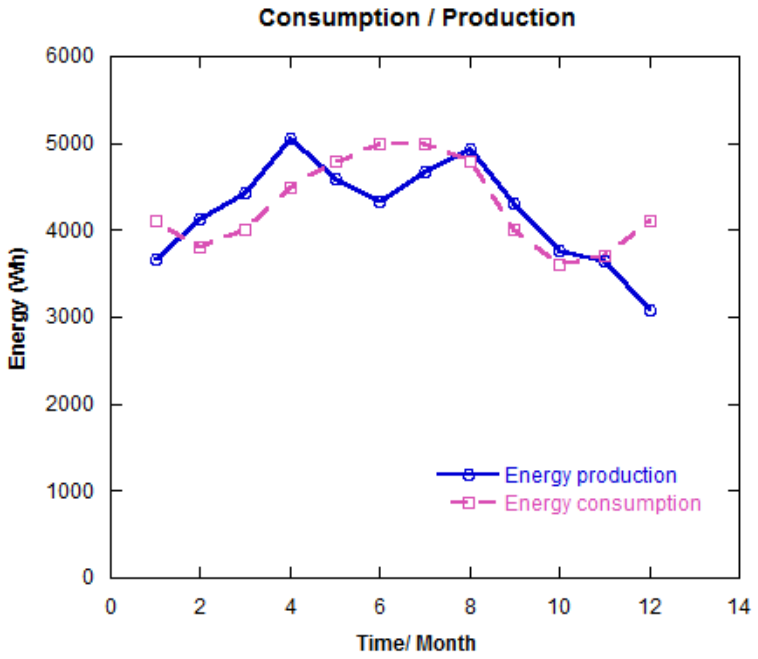

Fig. 8. Consumption and production of energy in 2014-2015

4. Conclusion

In this work, the behavior of solar radiation was recorded by a weather station installed on the roof of a sustainable house in the north of Mexico City; it was also compared with data obtained by other stations,. The aim was to monitor solar radiation throughout the year and to analyze its variable behavior in a particular place. It is very valuable to have a weather station in a sustainable house, so if we have the knowledge of local climate and how much energy is produced by the PV panels, we can have better control of energy consumption.

Renewable energy has received more attention recently. Solar radiation is considered the most preferred renewable energy source for its availability and inexhaustibility. However, due to the selective geographical availability and intermittency of solar radiation, it has been a challenge to generate a highly reliable power source with PV modules. To overcome this limitation, a PV-Hydrogen hybrid power system (PV-H2) could be used to supply electricity to a mobile house. The study of this approach is in progress and it will be discussed in a future paper.

Acknowledgements

This work has been supported by multidisciplinary project IPN-SIP 1683 and 1725; and Programa Redes Temáticas CONACYT/RTH2.

References

[1] A. Yunez Cano, “Modelado 3D e integración de una casa sustentable solar-hidrógeno”, Tesis de licenciatura ESIQIE-IPN, asesora Dra. Rosa de Guadalupe González Huerta, 2013.

[2] Ana Paulina González Arceo, “Empleo de paneles solares en vivienda sustentable para la mejora de la calidad del aire en la ciudad de México”, Tesis de licenciatura, asesor Dr. Miguel Tufiño Velázquez, 2014.

[3] Geophysics Institute, Radiación Solar Promedio Disponible en la Ciudad de México, UNAM., Mexico., 2005

[4] Vejar Ruiz S., “Desarrollo de un Sistema Fotovoltaico-Hidrógeno-Celda de combustible de 1Kw de potencia para la generación, almacenamiento y uso eficiente de energía”. ¿Tesis? 2010

[5] Mehmed E., Erkan D., Suat S., Junseok S., Suha Y., Osman K., “A mobile renewable house PV/wind/ fuel cell hybrid power system”, ¿datos revista? 2010.

[6] Patente, Solicitud en trámite ante el IMPI-México: “Sistema bioclimático ecológico para el abastecimiento de agua y energía en una vivienda”. Inventores Rosa de Guadalupe González Huerta, Miguel Tufiño Velázquez, Gerardo Contreras Puente, Claudia Alicia Cortes Escobedo, Domingo de Jesús Cortes Rodríguez, María Guadalupe Rodríguez Angeles, Armando Yunez Cano, Daniel Jiménez Olarte, Octavio Aguado Sánchez (2015).

Chapter 9.2. Conversion of cellulose, hemicellulose and lignin from urban waste to saccharides for biohydrogen production using hydrolysis

J. C. Gómora-Hernández[a,b]; M. C. Hernández-Berriel[b]; S. M. Fernández-Valverde[a,*]

[a]Depto. de Química, Instituto Nacional de Investigaciones Nucleares, A.P. 18-1027, Mexico D.F. C.P.11801, Mexico. Tel. 5553297200 ext 12277
[b]Instituto Tecnológico de Toluca, Avenida Tecnológico s/n, Fraccionamiento la Virgen, Metepec, Estado de México, México. C.P. 52149. Tel. 7222087200

ABSTRACT

The organic fraction of municipal solid waste in Mexico (>50%) is disposed in landfills or open dumps. Upon degradation they contribute to pollution primarily through the emission of CH_4 and CO_2, H_2S also is formed and the fatty acids produced are leachate producing soil erosion. The fruit and vegetable waste (FVW) part of urban waste has lignocellulosic materials (cellulose, hemicellulose and lignin) whose complex structures are difficult to break down to generate fermentable sugars. However, some treatments such as hydrolysis in acid media renders lignocellulosic materials available for biohydrogen production. In this work, FVW obtained from Santiago Tianguistengo Market, Mexico State, was investigated for hydrolysis in phosphoric acid to produce fermentable sugars. The volatile fraction and ashes were determined by gravimmetry and the composition by thermogravimetric analysis. For hydrolysis, one gram of dried waste was mixed with 10 mL of phosphoric acid and heated at 50 ^{O}C in sealed vials immersed in a thermostated shaking bath. Samples were taken every hour, filtered and the solid was washed and dried at 50°C until constant weight was reached, before analyzing by Infrared Spectroscopy (IR). The volatile fraction was 89.4 wt.%. and ashes 10.6 wt.%. The TGA analysis results in DTA values of 299.5 ^{O}C corresponding to 30.9 wt.%.of cellulose, hemicellulose (248.6 ^{O}C) 21.7 wt.%. and lignin (450 ^{O}C) 12.5 wt.% in dry basis. The IR spectra of the reference sample shows vibrations characteristic of cellulose, hemicellulose and lignin. The α-glucosidic (C-O-C) bond vibration of starch and saccharose disappears before 13h. reaction time and also lignin vibrations at 1510 and 1590 cm^{-1}. The β-glucosidic vibration bond at 889 cm^{-1} (C-O-C), related to cellulose and hemicellulose decreases but is still present after 25 h reaction time. The fermentable sugars were recoverdes by evaporation, with a dried base yield of 0.61 g/g FVW and 68.2 wt % related to total volatile solids.

Keywords: Organic waste, Hydrolysis, Fermentable sugars, Biohydrogen production

---

*Author for correspondence: Suilma M. Fernández-Valverde, +52 01 55 53 29 72 00 ext. 12277: suilma.fernandez@inin.gob.mx

1. Introduction

Organic waste (OW) is defined such as material that becomes of bioconversion process: agricultural, industrial and urban residues provide plenty of OW with useful composition that can be converted into valuable products [1]. With the rapid growth and development of population and industrialization, OW have taken up a large portion of all waste quantity reaching 46% approximately of the global solid wastes, which is one of the reasons to improve the utilization of these solid wastes [2]. On the other hand, in Mexico the organic fraction of urban solid wastes (USW) corresponding to food waste and garden residues has reached 52.4% in 2012, this percentage has decreasing in the last decades attributed to economy and consumption change patterns [3]. Fruits and vegetables waste (FVW) represents a potential energy resource if they can be properly and biologically converted into biohydrogen, biomethane or biodiesel, however the lignocellulosic fraction of OW is hardly used for biohydrogen production microorganisms due to heterogeneous structure, crystallinity index and degree of polymerization of cellulose, accessible surface area, and physical barrier of lignin[4].

Lignocellulosic wastes are composed of cellulose, hemicellulose and lignin, some others materials such as elements, proteins and proteins are also found in the OW residues in different proportion based on the sources where they were obtained [5]. According to Agbor et al. [6], cellulose is a major structural component of cell walls and it provides mechanical strength and chemical stability to plants. Cellulose is a homopolymer composed by β-D-glucopyranose linked via β(1-4) glycosidic bonds with amorphous and crystalline zones. The second most abundant polymer is hemicellulose, which is a heterogeneous biopolymer of pentoses, hexoses and acetylated sugars, the third main component of lignocellulosic materials is lignin, which confers rigidity, impermeability and resistance to microbial attacks to plant cell wall.

In order to partially remove of lignin and hemicellulose, reduce cellulose crystallinity, increase the porosity of biomass and improve the formation of sugars a treatment is necessary [5]. Usually treatment procedures should be economically feasible and could prevent the formation of byproducts inhibitory to subsequent hydrolysis and fermentation processes, also treatment outcomes must be balanced against their impact on the cost of downstream processing steps and operation costs [7]. In theory, the ideal treatment process produces a disrupted, hydrated substrate that is easily hydrolyzed but avoids the formation of sugar degradation products and fermentation inhibitors [5,6]. Various physical, chemical and biological treatment methods have been investigated by various researchers in the last three decades, however, chemical treatment has been proven to be a promising one when these were followed after anaerobic digestion [5,7]. Among all chemical treatments, acid method is considered a promising way for industry applicability. The acid pretreatment can operate either under a high temperature and low acid concentration or under low temperature and high acid concentration, the lower operating temperature in concentrated acid process presents advantage over dilute acid process, however, high acid concentration makes it extremely corrosive [4,8]. Some studies have been done using dilute acids such as

phosphoric[9,10], sulfuric [11] and even hydrochloric acid [12] at high temperatures, however, at these conditions the saccharides produced are not stable resulting in the further decomposition to form and levulinic acids via furan intermediates. In this type of processes phenolic compounds are also formed from the partial breakdown of lignin [13]. Both, phenolic compounds and sugar decomposition products are called “inhibitors”, which must be removed prior fermentation. Evaporation processes removes volatile compounds such as acetic acid, lactic acid and furfural increasing the sugar concentration present in hydrolyzate [5,9].

Advantages of concentrated acid hydrolysis over dilute acid hydrolysis process are higher conversion from polysaccharides to monosaccharides with minimum formation of by products with careful control of reaction conditions and no limitation of biomass resources [4,13]. The aim of the present work was to identify the effect of acid on FVW using FTIR spectrometry and to determine the sugar production which can be used for biohydrogen generation by phosphoric acid hydrolysis process.

2. Materials and Methods

2.1 Raw material

The FVWs were obtained from Santiago Tianguistenco market , Mexico State, stored in airtight bag and transfered into laboratory where FVW were separated in each kind of fruit and vegetable. In the previous work made by Ávila [14], a special FVW composition was used due to their high amount of starch (5.4% in dried base). The constituent of organic sample employed in this study is shown in **Table 1**. Each fruit and vegetable were mixed and previously dried at ambient temperature and milled.

Table 1. Composition of FVW used in this study.

Waste	%W	Waste	%W	Waste	%W
Lettuce	4.31	Cauliflower	4.31	Corn	8.32
Tomatoe	1.68	Stalks and leaves	21.8	Avocado	0.24
Mango	0.12	Pineapple	1.8	Pumpkin	1.92
Lemon	0.6	Chili	0.12	Squash	2.63
Coriander	1.5	Ejote	0.84	Carrot	0.96
Papaya	0.18	Watermelon	2.28	Orange	11.14
Grapefruit	13.11	Melon	20.12	Onion	1.44

Cellulose, hemicellulose and lignin composition in the FVW mixture was determined by thermogravimetric and differential thermogravimetric analysis (TGA-DTA) in a TA Instruments-Waters (DSC-TGA). The biomass was heated from ambient temperature to 700 °C with a heating rate of 10 °C/min in a nitrogen gas atmosphere at a flow rate of 20 mL/min. Furthermore, ashes and volatile total solids were quantified according to Standard Methods [15].

2.2 Hydrolysis of FVW with phosphoric acid

Hydrolysis of FVW was done following the conditions defined by Zhang *et al.* [16]. One gram of dried and milled FVW was soaked in deionized water in 50 mL vials, then 10 mL of phosphoric acid (83%) was added and the mixture was slowly homogeneized. The vials were immersed in a thermostated shaking bath at 50°C and two samples were taken every hour until 10 hours of reaction time, after this time the samples were taken every 2 hours until the end of experiment (25 hours). Each sample was filtered in order to separate the liquid and solid phases, then, the solid residue was washed with 50 mL of deionized water and ethanol (25 mL, twice). Finally, the samples were dried at 50°C overnight and ground into powder. The liquid phase was stored at 4°C.

2.3 Sugar recovery

The sugars obtained in the acid treatment were recovered in the liquid phase. The solution was neutralized with magnesium hydroxide in order to obtain magnesium phosphate (not soluble in water) libering the sugars. Then, they were separated by filtration, the supernatant liquid phase was evaporated in order to eliminate the inhibitors and crystalize the saccharides. The crystals were dried overnight and weighted. Finally, The FTIR analysis was carried out and the main characteristic vibrations of the saccharides were determined.

2.4 Fourier Transformed Infrared analysis

The samples were analyzed by Fourier transformed Infrared Spectra (FTIR) in an Infrared Nicolette Magna IR 550, using the potassium bromide technique in the range spectra of 400 to 4000 cm^{-1} with 4 cm^{-1} resolution. The final spectra were obtained with an average of 16 scans.

3. Results and Discussion

3.1 Raw material composition

The ashes and volatile total solids determined by gravimetric methods [15] were 10.6% and 89.4% respectively in agreement with the literature. Cellulose, hemicellulose and lignin content in biomass was determined by TGA-DTA techniques [17,18], the thermogravimetric curves are reported in **Figure 1**. In this figure the first and second weigth loses of FVW appears at 55.16°C and 152°C and correspond to moisture evaporation.

Degradation of hemicellulose and cellulose were observed at 248.6°C and 299.5°C respectively showing mass loses of 21.7% and 30.9% in dried base. Lignin, the most complex and stable carbohydrate has the highest degradation temperature of FVW [17], for this reason its degradation started at 450°C reaching 12.5 wt.% in dry basis.

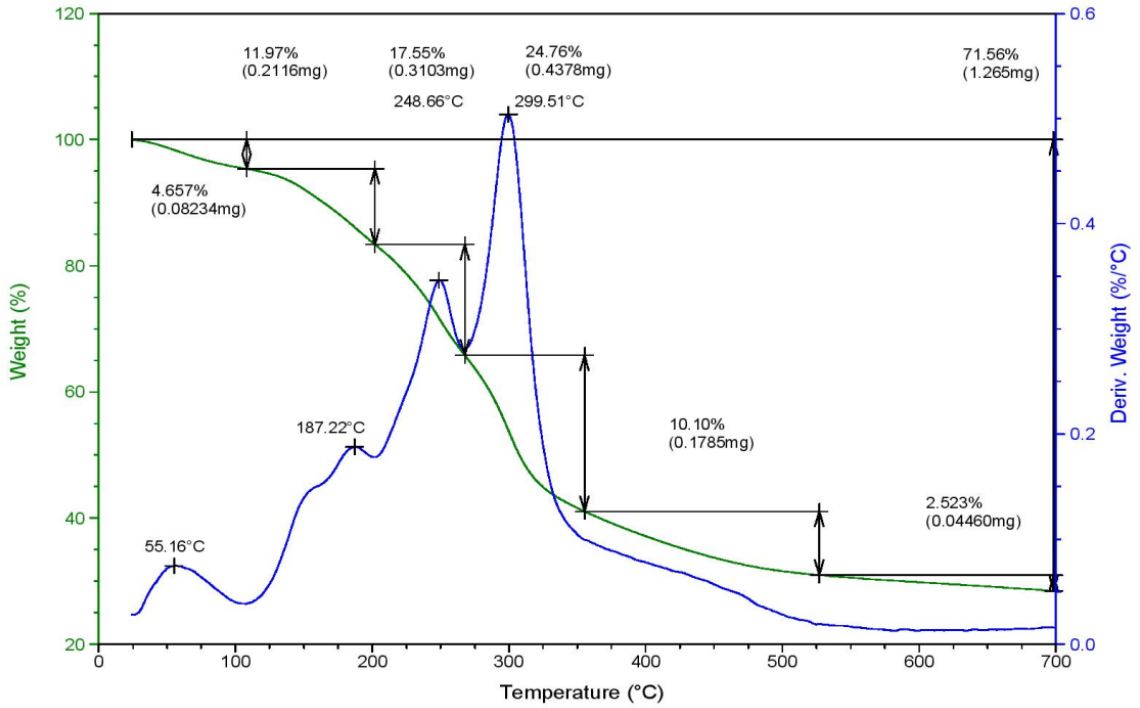

Fig. 1. Thermogravimetric and differential thermogravimetric analysis of FVW

The obtained results are in good agreement with Harun *et al*. [17] and Burhenne *et al*. [18], decomposition of hemicellulose and cellulose is the major stage in biomass pyrolysis initiating at 250°C and finishing at 350°C. Moreover, previous studies has shown lignin decomposition in the range of 400°C to 600°C, depending of the type and content of this carbohydrate in biomass[18].

3.2 FTIR analysis of hydrolyzed FVW

In all FTIR figures presented in this work, the acronyms C, H and L corresponds to cellulose, hemicellulose and lignin respectively, while α and β means alpha and beta glycosidic linkages. All the spectra were normalized and vibrations of different groups were identified in basis of previous researchers reported by Xu *et al.* [19], Ballesteros *et al.* [20] and Ibrahim *et al.* [21].

The FTIR analysis performed to FVW at 0 h (before treatement), 1 h and 3 h of reaction time are reported in **Figure 2**, before treatment the characteristic vibrations of cellulose, hemicellulose and lignin are observed, since 1h reaction time a peak appears at 829 cm^{-1} corresponding to P-O-C vibration of cellulose phosphate and at the same time the characteristic vibrations of cellulose, hemicellulose and lignin decresead, in the other side the peak at 1507 cm^{-1} increased, this can be attributed to interaction between acid and FVW causing a new polymerization of monolignols. Furthermore, β glycosidic bond attributed to cellulose, hemicellulose and cellobiose was found in all IR spectra from origin and all reactions times until the end of the experiment, last sample was taken at 25 h.

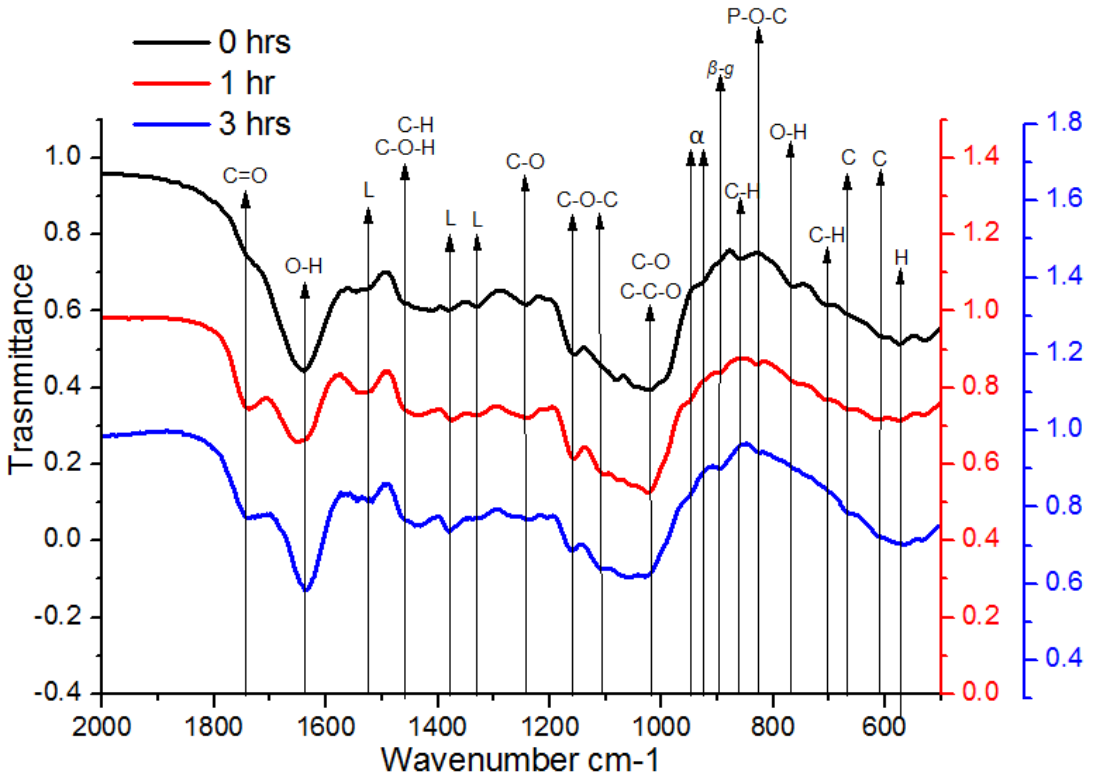

Fig. 2. FTIR spectra of FVW before treatment and after 1 and 3 hours of reaction time

The samples analyzed at 6 and 10 hours are reported in **Figure 3**. The α glycosidic linkage corresponding to starch and sucrose (956 cm^{-1}) is present at 6 h and dissapears after 10 hours reaction time. The bands at 1150, 1106 and 1056 cm^{-1} corresponding to cellulose make reference to ring skeletal and glycosidic bond [27,31], however, Ibrahim e*t al.* [30] located characteristic vibrations of residual glucose at 1460 and 1106 cm^{-1}

FTIR spectra of FVW pretreated with concentrated phosphoric acid for 13, 19 and 25 hours reaction time are reported in **Figure 4 (**the red scale is the same for the 25 reaction time), as can be seen all characteristic vibrations of lignin disappears before 13 hours. The hemicellulose vibration at 1731 cm^{-1} and cellulose vibration at 666 cm^{-1} are not observed after 19 hours reaction time.

The β-glycosidic bond found at 888 and 1156 cm^{-1} was observed until end of experiment (25 hours). Finally, the wavenumber at 1006 cm^{-1} corresponding to P-O-H appeared after 10 h, before this time this vibration cannot be observed due to excesive amount of peaks in the range of 829 to 1150 cm^{-1}.

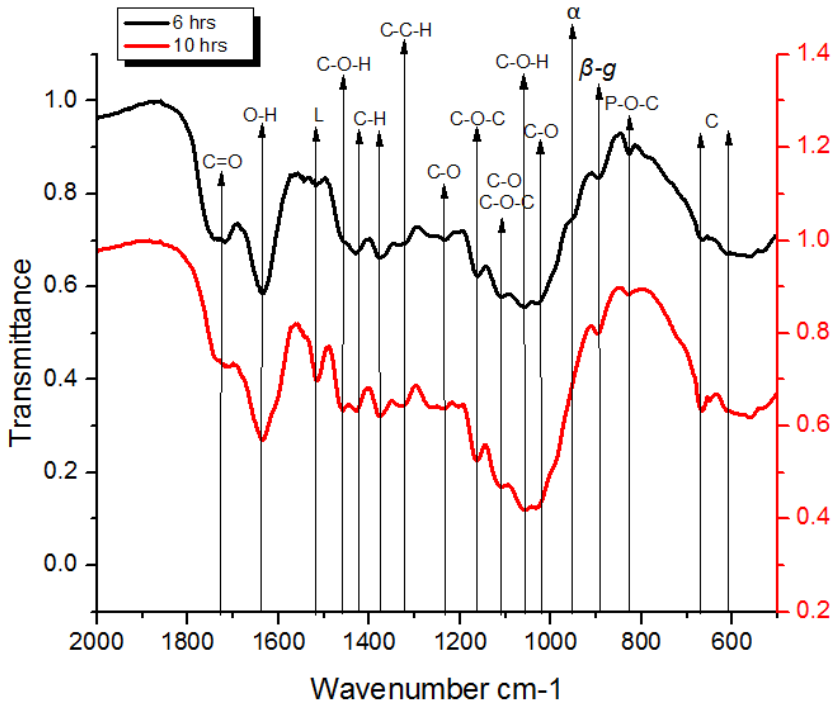

Fig. 3. FTIR spectra of FVW after 6 and 10 hours reaction time

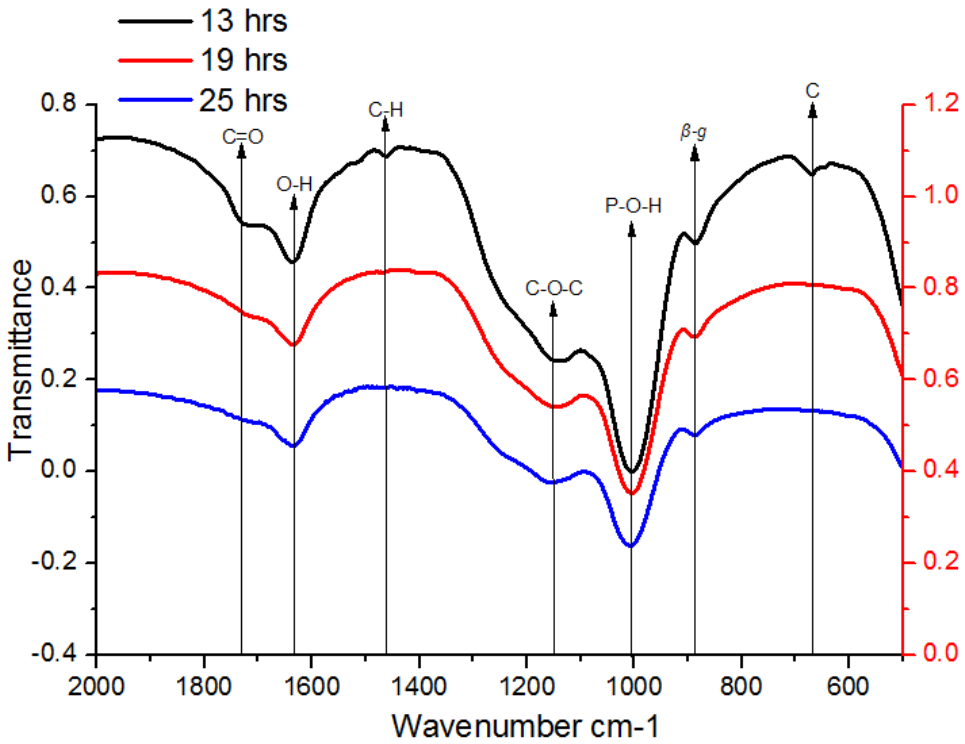

Fig. 4. FTIR spectra of FVW pretreated at 13, 19 and 25 hours reaction time

3.3 Sugar recovery and yields

To obtain fermentable sugars, that can be useful for biohydrogen production, the phosphated sugars presented in liquid phase resulting of hydrolysis at 25 hours was neutralized according to simplified following equation.

$$2H_3PO_4 + 3Mg(OH)_2 \rightarrow Mg_3(PO_4)_2 + 6H_2O \quad (1)$$

Once filtered, saccharides was concentrated by evaporation. The sugars were dried overnight at 50 °C and weighted. The fermentable sugar yield was 61 g sugars/100g of FVW and 68.2% related to volatile total solids. The sugar yield reached in this research is higher compared with that reported in phosphoric acid at different concentrations by Lenihan *et al.* [9] in Potatoe peel with 7% acid concentration and 135 °C [14], López-Linares *et al.* [10] hydrolysed rapeseed straw in 3% acid concentration and 200 °C and

Cao *et al.* [11] worked with corn stover in sulfuric acid at 2.13% and 121 °C. They reported yields of 55.2, 14.3 and 12.13 g / 100 g substrate respectively.

3.4 Sugars characterization by FTIR spectrometry

The Infrared spectra of dried sugars is given in **Figure 5** for comparison the xylose spectra is reported too, some xylose vibrations are observed however the intensities are not the same, showing the presence of other monosaccharides. The main vibrations are summarized in **Table 2.** They were identified according to Ibrahim *et al.* [21] and using monomeric sugar IR patterns.

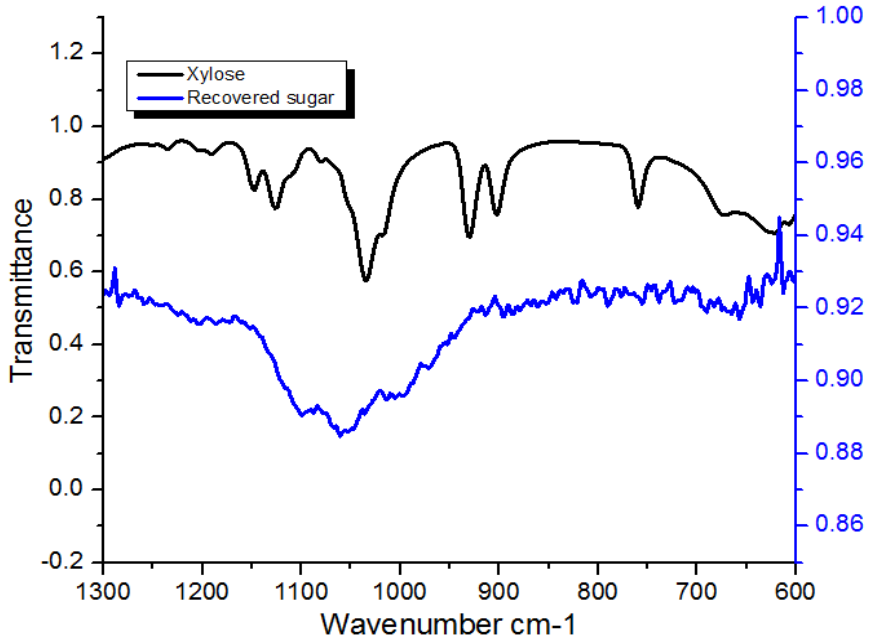

Fig. 5. FTIR spectra of soluble material and xylosa

Table 2. FTIR vibrations of sugar recovered after hydrolysis process

Chemical bonding	IR vibrations	Chemical bonding	IR vibrations
D-Glucose (C-O)	1150	D-Glucose (C-O and C-C)	1050
L-Xylose	1120	D-Glucose (C-O)	1022
D-Glucose (C-O)	1113	D-Glucose (C-O and C-C)	995
L-Xylose	1109	D-Fructose	949
L- Arabinose	1099	D-Fructose (C-H and C-C)	876
D-Glucose (C-O-H)	1098	D-Glucose (C-H)	858

From these results, soluble matter obtained in the hydrolysis process is a complex mixture of monosaccharides coming from the lignocellulosic fraction of OW. The majority vibrations correspond to D-glucose, however, characteristic vibrations of L-xylose, L-arabinose and D-fructose are present too. The high phosphoric acid concentration seems to be responsible of the formation of monomeric sugar in both configurations D and L.

4. Conclusion

A high production yield of soluble material was obtained composed by a mixture of sugars: arabinose, xylose, glucose and fructose were present in the mixture. The Recommended time to achieve the hydrolysis of lignocellulosic fraction of FVW with phosphoric acid is 25 h. Future studies will focus on characterizing the usefulness of lignocellulosic derived monosaccharides for biohydrogen production.

Acknowledgements

ITT and ININ sponsored this work. Julio César Gómora Hernández thanks CONACYT for his Master scholarship and SMH for scholarship grant. The authors thank also the technicians of the chemistry laboratory at ININ for their technical help.

References

[1] Liguori R., Amore A., Faraco V. Waste valorization by biotechnological conversion into added vlaue products. Appl Microbiol Biotechnol 2013;97:6129-6147.
[2] Xiaoguang Y., Han S. C., Chulhwan P., Seung W. K. Current states and prospects of organic waste utilization for biorefineries. Renew. Sustain. Energy Rev. 2015;49:335-349.
[3] Dirección General de Equipamiento e Infraestructura en Zonas Urbano-Marginadas, Sedesol, México. 2012.
[4] Zheng Y., Zhao J., Xu F., Li Y. Pretreatment of lignocellulosic biomass for enhanced biogas production. Prog Energy Combustion Sci 2014;42:35-53.
[5] Behera S., Arora R., Nandhagopal N., Kumar S. Importance of chemical pretreatment for bioconversion of lignocellulosic biomass. Renew. Sustain. Energy Rev. 2014;36:91-106.
[6] Agbor V. B., Cicek N., Sparling R., Berlin A., Levin D. B. Biomass pretreatment. Fundamentals toward application. Biotechnol. Adv. 2011;29:675- 685.

[7] Saratale G. D., Chen S. D., Lo Y. C., Saratale R. G., Chang J. S. Outlook of biohydrogen production from lignocellulosic feedstock using dark fermentation. A review. J Sci Ind Res. 2008;67:962-979.
[8] Taherzadeh M., Karimi K. Pretreatment of lignocellulosic wastes to improve ethanol and biogas production. A review. Int. J. Mol. Sci. 2008;9:1621-1651.
[9] Lenihan P., Orozco A., O´Neill E., Ahmad M. N. M., Rooney D. W., Walker G. M. Dilute acid hydrolysis of lignocellulosic biomass. Chem. Eng. J. 2010;156:395-403.
[10] López-Linares J. C., Cara C., Moya M., Ruiz E., Castro E., Romero I. Fermentable sugar production from rapeseed straw by dilute phosphoric acid pretreatment. Ind. Crops Prod. 2013;50:525-531.
[11] Cao G., Ren N., Wang A., Lee D. J., Guo W., Liu B., Feng Y., Zhao Q. Acid hydrolysis of corn stover for biohydrogen production using *Thermoanaerobacterium thermosaccharolyticum* W16. Int J Hydrogen Energy. 2009;34:7182-7188.
[12] Zu S., Li W., Zhang M., Li Z., Wang Z., Jameel H., Chang H. M. Pretreatment of corn stover for sugar production using dilute hydrochloric acid followed by lime. Bioresour Technol. 2014;152:364-370.
[13] Yoon S. Y., Han S. H., Shin S. J. The effect of hemicelluloses and lignin on acid hydrolysis of cellulose. Energy. 2014:1-6.
[14] Ávila V. E. Obtención de un energético limpio, hidrógeno, a partir de desechos orgánicos de frutas y verduras. Tesis Doctoral. Instituto Tecnológico de Toluca. México. 2010.
[15] APHA. Standard Methods for Water and Wastewater Examination, 21 st ed. American Public Health Association-American Water Works Association, Water Environment Federation Publication, Washington, DC. USA. 2005.
[16] Zhang J., Zhang J., Lin L., Chen T., Zhang J., Liu S., Li Z., Ouyang P. Dissolution of microcrystalline cellulose in phosphoric acid. Molecular changes and kinetics. Molecules. 2009;14:5027-5041.

[17] Harun M. Y., Radiah A. B. D., Abidin Z. Z., Yunus R. Effect of physical pretreatment on dilute acid hydrolysis of water hyacinth (*Eichhornia crassipes*). Bioresour Technol. 2011;102:5193-5199.
[18] Burhenne L., Messmer J., Aicher T., Laborie M. P. The effect of the biomass components lignin, cellulose and hemicellulose on TGA and fixed bed pyrolysis. Journal of Analytical and Applied Pyrolysis. 2013;101:177-184.
[19] Xu F., Yu J., Tesso T., Dowell F., Wang D. Qualitative and quantitative analysis of lignocellulosic biomass using infrared techniques. A mini-review. Appl Energy. 2012;94:99-107.
[20] Ballesteros L. F., Cerqueira M. A., Teixeira J. A., Mussatto S. I. Characterization of polysaccharides extracted from spent coffee grounds by alkali pretreatment. Carbohydrate Polymers. 2015;127:347-354.
[21] Ibrahim M., Alaam M., El-Haes H., Jalbout A. F., Leon A. Analysis of the structure and vibrational spectra of glucose and fructose. Ecl. Quim. 2006;31:15-21.

Chapter 9.3. Using hydrogen fuel and bio-ethanol in internal combustion engines to reduce emissions of greenhouse gases

J. D. Becerra-Ruiz[a]; R. G. Gonzalez-Huerta[b]; G. Macias-Bobadilla[c]*

[a.] División de Estudios de Posgrado, Facultad de Química, Universidad Autónoma de Querétaro. Cerro de las Campanas S/N col. Las Campanas. C.P. 76010, Querétaro, Qro. Mexico.
[b.] ESIQIE-IPN, Laboratorio de Electroquímica y Corrosión, C.P. 07738, D.F. México.
[c.] División de Estudios de Posgrado, Facultad de Ingeniería, Universidad Autónoma de Querétaro. Cerro de las Campanas S/N col. Las Campanas. C.P. 76010, Querétaro, Qro. Mexico.

ABSTRACT

This work investigates the effect of hydrogen-oxygen blends and bioethanol addition on the performance of a gasoline engine. Hydrogen-oxygen blend was added in the air intake system and bioethanol was mixed with gasoline into the vehicle tank. The tests were performed in both independent and additive combination cases, in a 1.6L (ZETEC ROCAM) gasoline engine corresponding to a vehicle FORD - Ka 2001, on which were made modifications for adding these mixtures, measured the engine´s operating temperature and exhaust fumes. The standard hydrogen-oxygen enrichment contributed to HC, CO_2 and CO emissions decrement. In addition to this was found in experiments that can be further improved if bioethanol is added, as indicated by some previously published studies, where the mixture of gasoline - bioethanol should not exceed 85-15% ratio respectively for engines they are not Flex-Fuel. Discussions were focused on the results obtained with the different proportions of bioethanol mixed with gasoline and hydrogen-oxygen blend, as well as measurements of the parameters of engine temperature, oxygen expelled by the engine which were compared with those measured by the Bosch - BEA gases v3.70-EURO-W (AMM-000-B6) automotive emissions analysis equipment. Because all of this is left to discussions that using blends of gasoline with bioethanol and hydrogen-oxygen enriched air reduces emissions of greenhouse effect gases from the engine and increase the performance of fossil fuel.

Keywords: Gasoline engines, Hydrogen enriched air, Enriched gasoline Bioethanol

1. Introduction

Because of the combustion of fossil fuels for power generation, transportation, industrial and domestic activities, air pollution worldwide increase is causing the phenomenon called global warming consisting of increased global temperatures [1]. Nationally in 2012, 14,734 premature deaths because of pollution were estimated. In Mexico, air pollution has represented the largest environmental cost, according to INEGI.

---

*Author for correspondence: Gonzalo Macías-Bobadilla, Universidad Autónoma de Querétaro, Querétaro, México, T: 442 252 2912, E: g.macias@uaq.mx

In the same year was 4.7% of PIB (Producto Interno Bruto) which is about sixteen thousand million pesos [2]. In addition to Mexico in 2012, Pemex announced that known oil reserves amounted to 32 years [3], in conjunction to the price fluctuations that last year came to cost over $ 100 dollars per barrel, which this year is less than $ 40 dollars [4]. For these reasons it is important to find alternative fuels to oil, which are renewable, polluting less, the production of these is technically and economically sustainable without affecting the land or see diminishing food supplies.

Hydrogen was first artificially produced and formally described by T. Von Hohenheim (also known as Paracelsus (1493-1541) who obtained artificially by mixing metals with strong acids. Paracelsus was unaware that the flammable gas generated in these chemical reactions consisted in a new chemical element [5].

The first time hydrogen was liquefy by James Dewar was in 1898 by using regenerative cooling on his invention [6]. Harold Urey discovered deuterium in December 1931 [7], and tritium was prepared in 1934 by Ernest Rutherford, Marcus Oliphant, and Paul Harteck [8]. Heavy water, which has deuterium instead of regular hydrogen in the water molecule was discovered by Urey's team in 1932 [9].

François Isaac de Rivaz built the first internal combustion vehicle that used a mixture of hydrogen and oxygen as fuel in 1806 [10]. Edward Daniel Clarke invented the hydrogen gas feedback (slipstream) in 1819 [11]. Döbereiner lamp and luminaire Drummond were invented in 1823 both using hydrogen gas to operate [9].

In case of Ethanol, this can be made from different cellulose materials and plants, also called biomass. U.S. Department of Energy reports than more of 95% of gasoline sold in USA in recent years uses ethanol as a mixed mode with gasoline to help oxygenate the combustion into the engine and reduce air pollution. The approved mixes for cars nonprofits ethanol is typically E10 (10% ethanol, 90% gasoline) [12].

From 1824 with Samuel Morey who created the world's first internal combustion engine that runs on ethanol and turpentine [13] to 1896 when Henry Ford built his first automobile called Quadricycle the history of ethanol use in combustion engines has been increasing its uses underneath the gasoline engines [14].

2. Materials and Methods

2.1. Materials

For the experiments an Electrolytic Cell was built at the Engineering Faculty from Universidad Autonoma de Queretaro to produce Oxy-Hydrogen which has the appropriated stoichiometric balance to be burned as it is produced, and is ideal to be used as a auxiliary fuel in the motor applied directly to the air admission multiple of the engine, this cell was composed by 41 stainless steel electrodes, 4 of them are positive and 5 are negative, the last 32 electrodes are neutral, the configuration used in the building of this cell was a serial-parallel, which allows to have and easy electrolytic recirculation and recuperation and is easy build, the diagram of the built cell is shown in Fig. 1 and the full diagram of the system, including the electrolytic recuperation, bubblers, dryers recipes, and pipes for the

interconnections between the recipes, the cell and the air admission multiple of the engine are shown in Fig. 2.

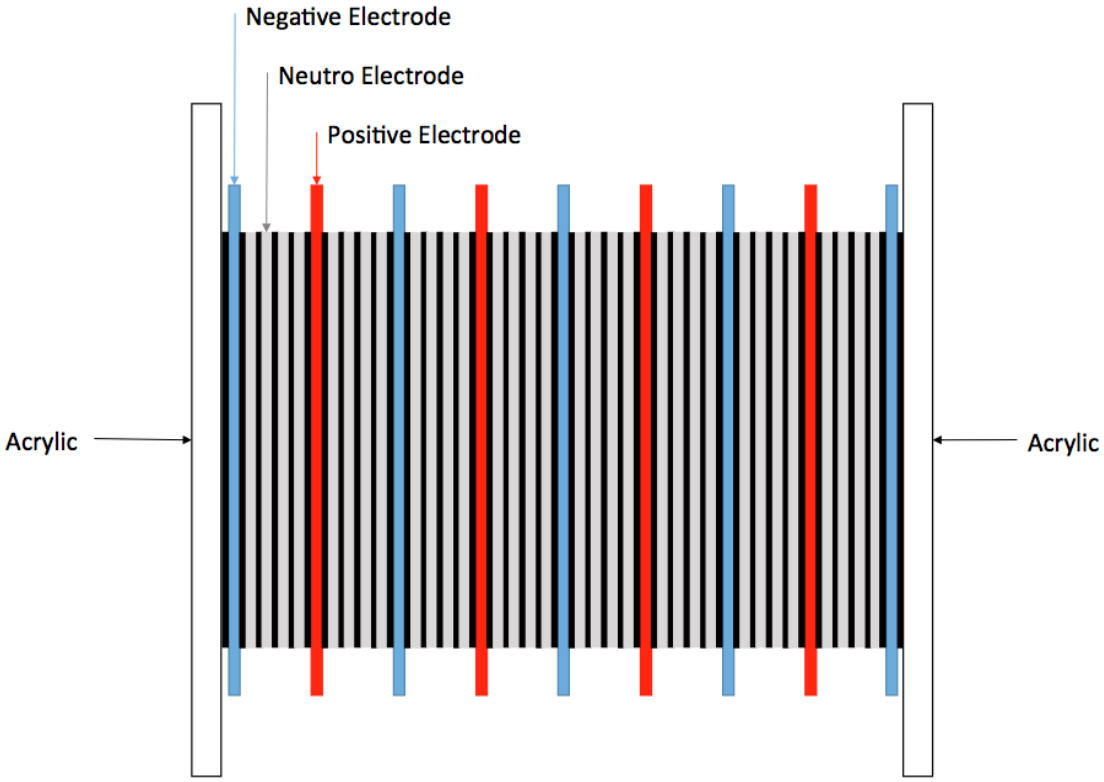

Fig. 1. Electrolytic cell assembly configuration

To energize the cell a deep cycle battery recharged by a solar panel has been used a special Max Power Point Tracker (MPPT) charger controller, to avoid using the same energy produced by the vehicle's engine throw alternator, on this way a positive balance in the system is obtained, also Fig. 2 shows how the recharged battery system has been mounted.

Additional to this, an electrical and security system has been installed in the vehicle to ensure the ignition of the cell only when the motor is turned on, to avoid accidents, this electrical security system reads the signals from the electrical ignition vehicle is to allow the cell working starts, otherwise without this security system the cell could be left ignited when the engine is not working and the Oxy-Hydrogen could be accumulated inside the engine hood an produce and accident.

The cell's electrical consumption was of 170W/h DC (12V @ 14.2A) and the cell's Oxy-Hydrogen production was approximately 1 Lt/min., all the experiments were been run with the full charged battery.

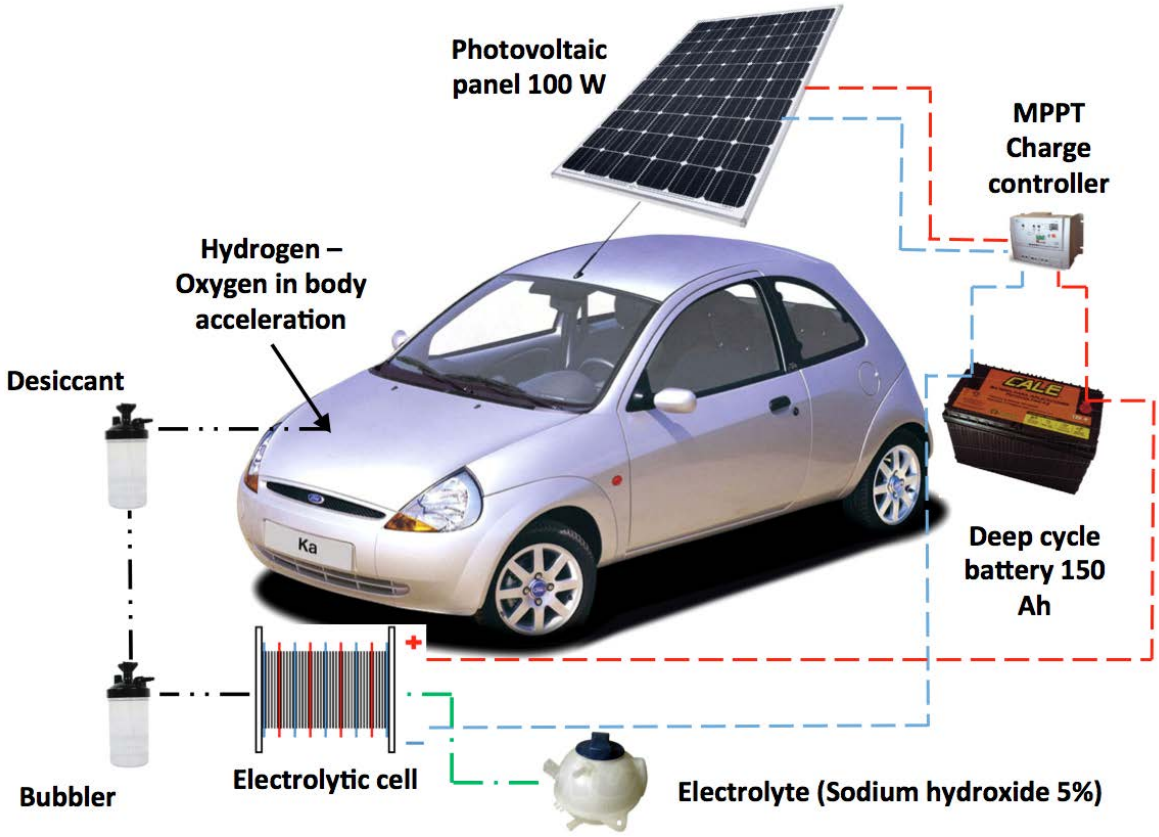

Fig. 2. Electric and electrolytic cell set ups in the experimental vehicle

In the case of Ethanol, this was produced at the Chemical Faculty of Universidad Autonoma de Queretaro by using candy waste fermentation and Bach cycle, to obtain a 99 % purified alcohol (Anhydrous Ethanol), also this is ideal to be mixed with gasoline in the ordinary gasoline tank of the vehicle as an auxiliary fuel for the engine that was used in the experimentations.

For the vehicle's exhaust fumes analysis, a Bosch - BEA gases v3.70-EURO-W (AMM-000-B6) automotive emissions analysis equipment was used, adding the respective fuels at different concentration in the case of the ethanol and running the respective test for gas emission detection recommended for Bosch. This equipment consists of a probe that measure exhaust gases and revolutions per minute (RPM) in the engine compare and determine gases concentration levels.

2.2. Methods

In order to obtain the effect of the different fuel added to the engine, different tests were been run according to the specification of the Bosch - BEA gases v3.70-EURO-W (AMM-000-B6) automotive emissions analysis equipment, at first only gasoline fuel test was made to obtain a reference of the natural gases expelled from the engine's exhaust fumes, after gasoline-hydrogen, gasoline-ethanol and finally gasoline-ethanol-hydrogen. In the case of

ethanol tests this were run at 5, 10, 15 and 20% concentration levels compared to gasoline [15].

Bosch - BEA gases v3.70 EURO-W (AMM-000-B6) automotive emissions analysis equipment procedure specifies that: a) RPM from the engine needs to be detected using the respective probe from the equipment to start the test and leave it connected during all the test, b) a zero calibration from the probe gases detection is needed to be done by putting the probe far away from the engines exhaust for at least 30 seconds, c) a low engine RPM (slow motion, typically 850RPM) gas detection needs to be done leaving the probe inside of the exhaust system for another 60 seconds, d) a incremented engine RPM (fast motion, typically 2500 RPM) gas detection needs to be done leaving the probe inside of the exhaust system for another 15 seconds, and finally again e) a low engine RPM (slow motion, typically 850 RPM) gas detection needs to be done leaving the probe inside of the exhaust system for the last 15 seconds.

Once the test has been completed following the appropriate steps the emission analysis equipment will print an inform referring to low and fast motion from the engine, and the average detected levels from RPM, Carbon Monoxide (CO), Carbon Dioxide (CO2), not burned Hydrocarbon (HC) and Oxygen (O2).

3. Results and Discussion

Figures 3 and 4 show CO%vol at Low Motion (850 RPM) and Fast Motion (2500 RPM) whit different kinds of fuel blends respectively. This is the result of average of 10 test done at each type of fuel blend.

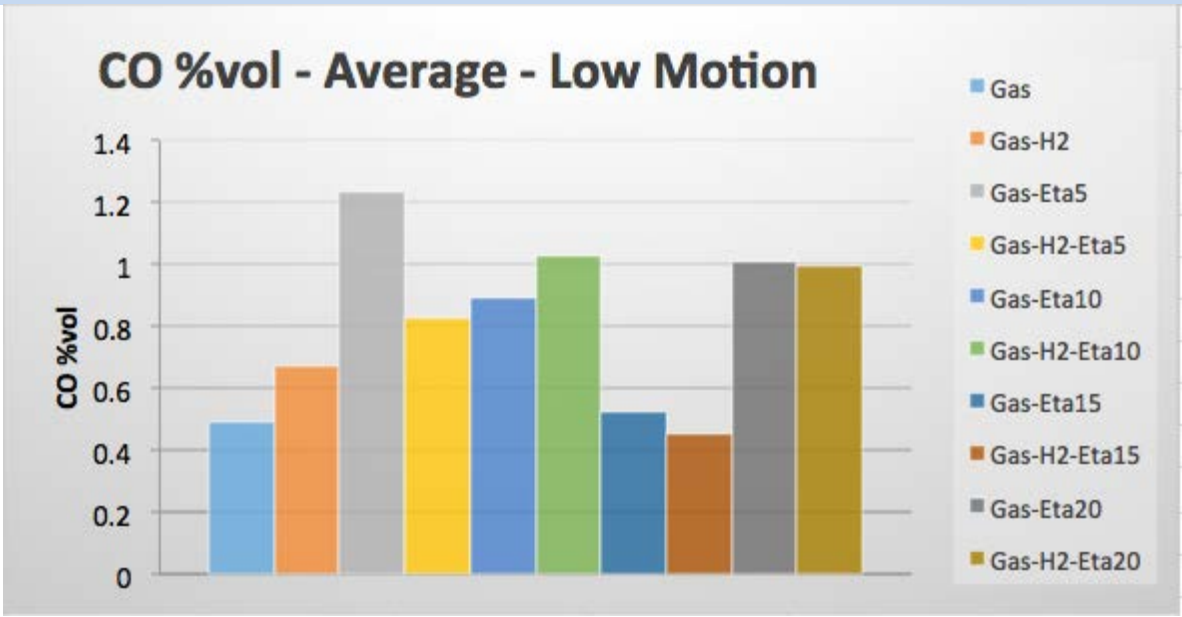

Figure 3 CO %vol – Average – Low Motion

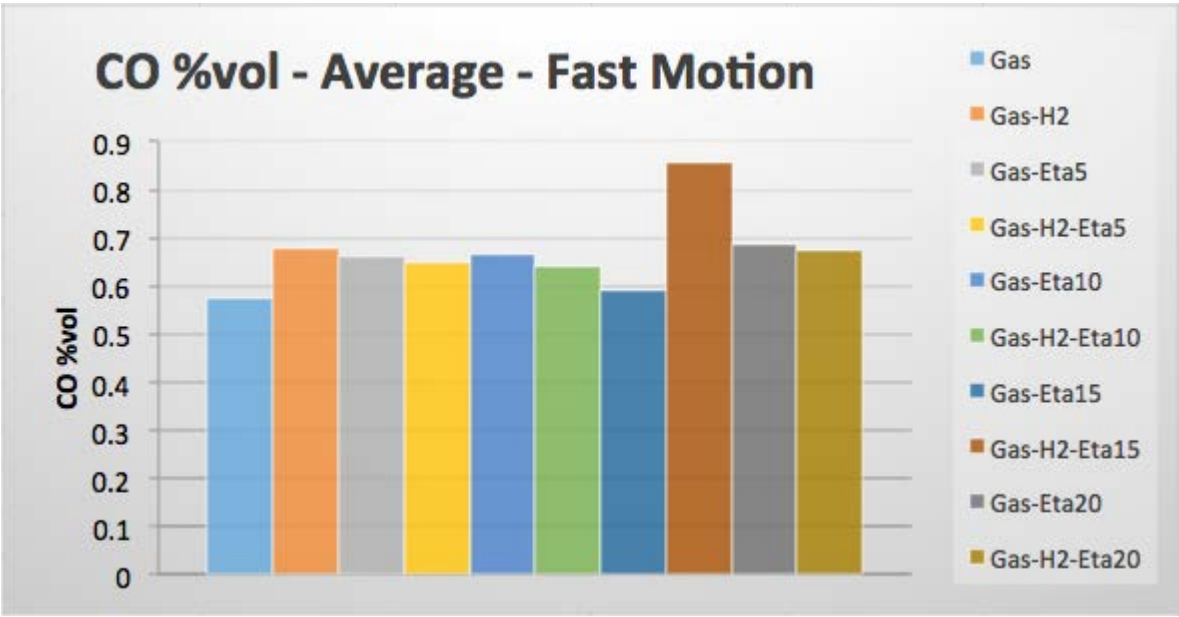

Figure 4. CO %vol – Average – Fast Motion

Figures 5 and 6 showCO2%vol at Low Motion (850 RPM) and Fast Motion (2500 RPM) whit different kinds of fuel blends respectively. This is the result of average of 10 test done at each type of fuel blend.

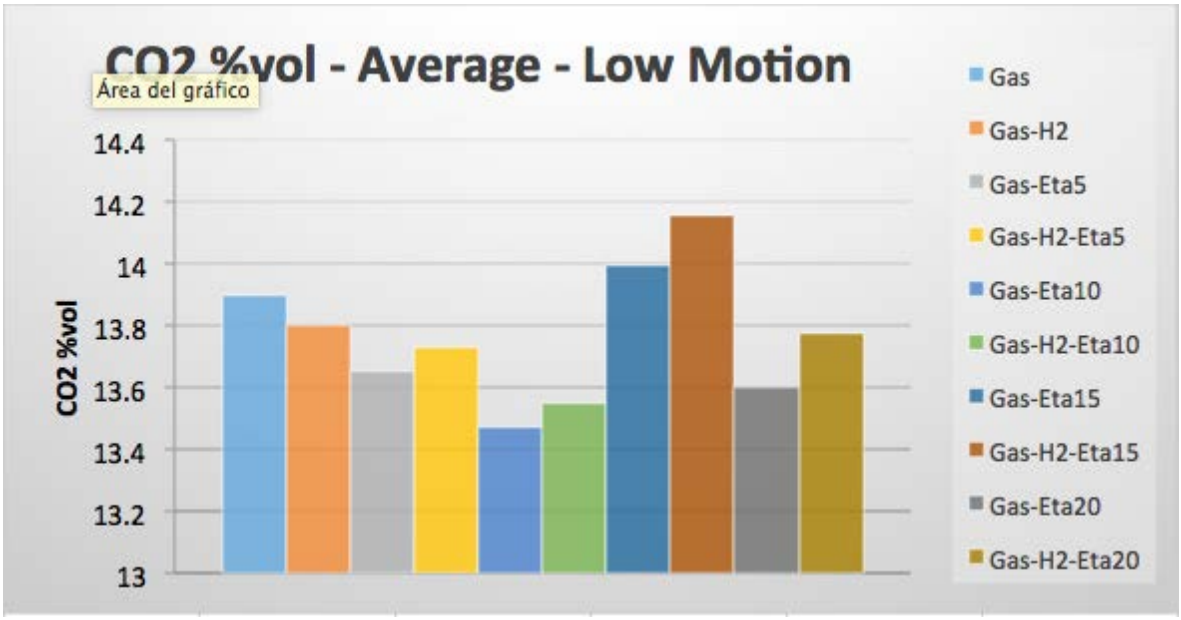

Figure 5. CO2 %vol – Average – Low Motion

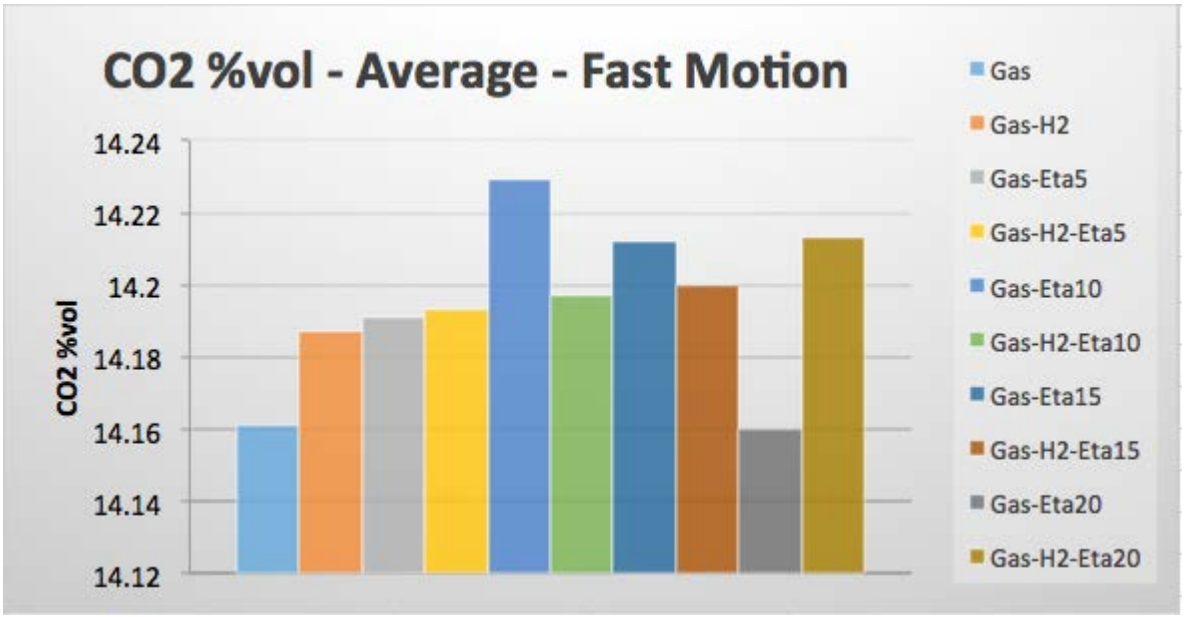

Figure 6. CO2 %vol – Average – Fast Motion

Figures 7 and 8 display the HC ppm at Low Motion (850 RPM) and Fast Motion (2500 RPM) whit different kinds of fuel blends respectively. This is the result of average of 10 test done at each type of fuel blend.

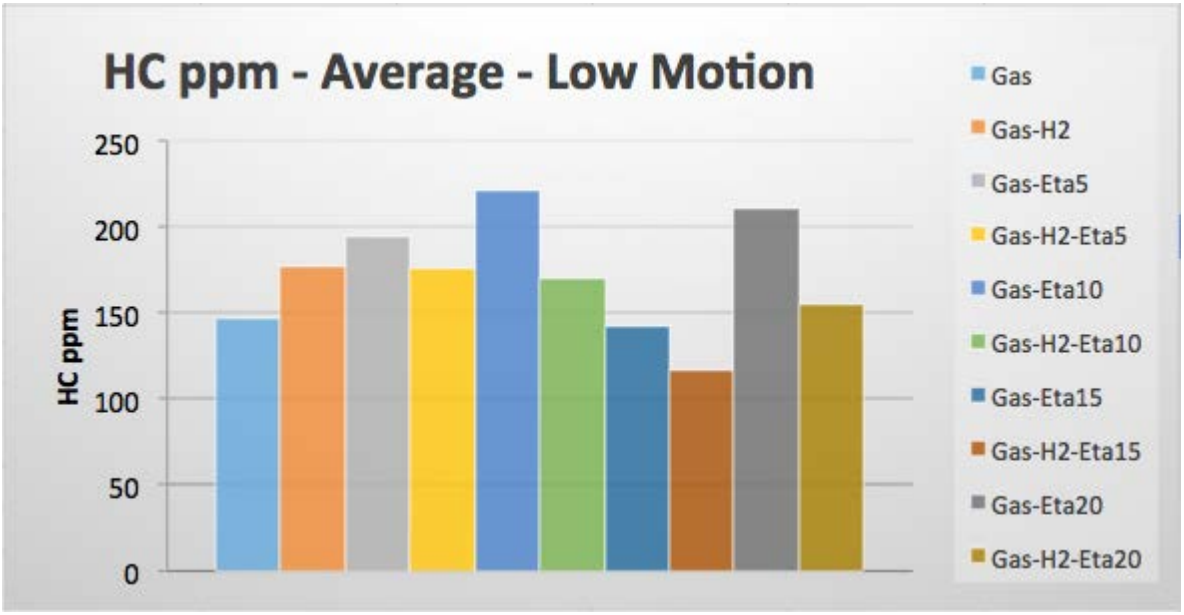

Figure 7. HC ppm – Average – Low Motion

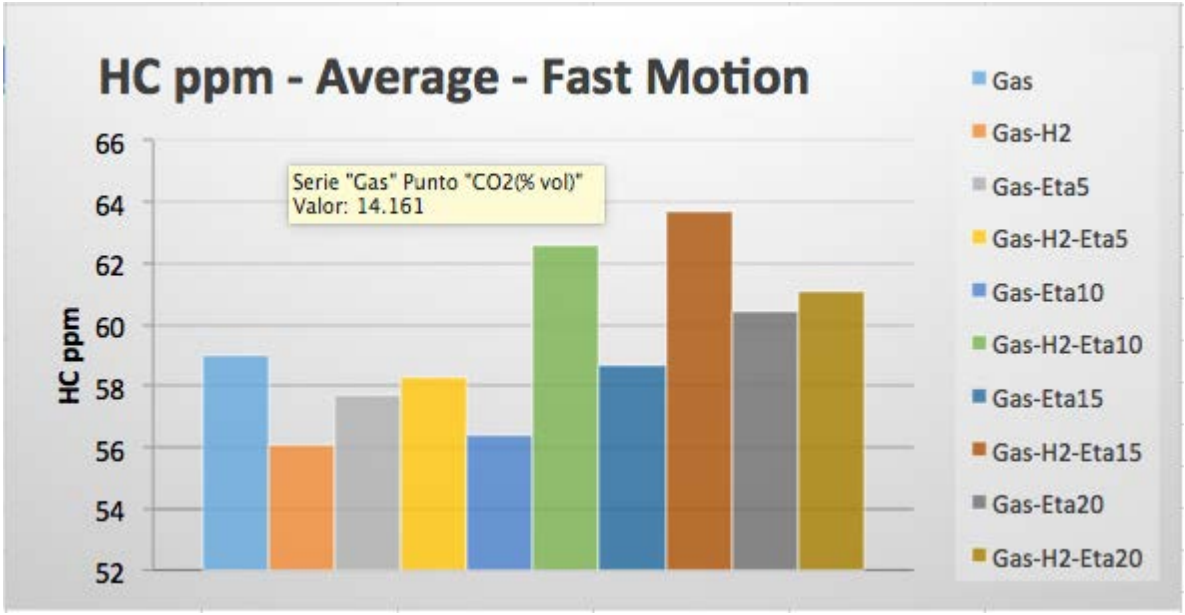

Figure 8. HC ppm – Average – Fast Motion

Figures 9 and 10 show O2%vol at Low Motion (850 RPM) and Fast Motion (2500 RPM) whit different kinds of fuel blends respectively. This is the result of average of 10 test done at each type of fuel blend.

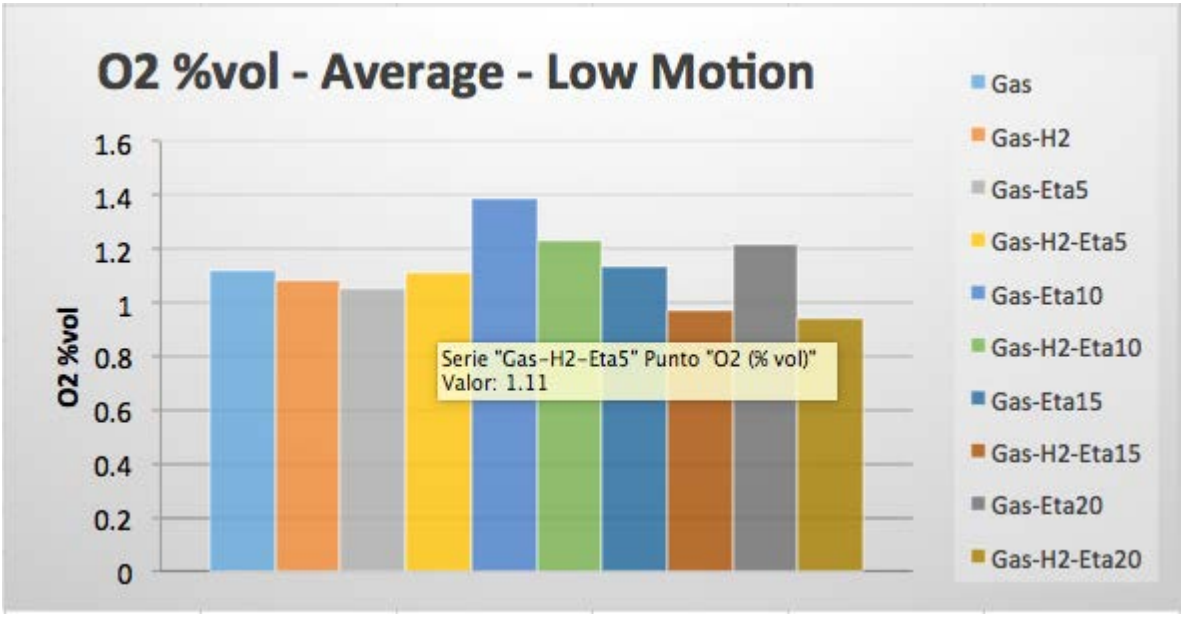

Figure 9. O2 %vol – Average – Low Motion

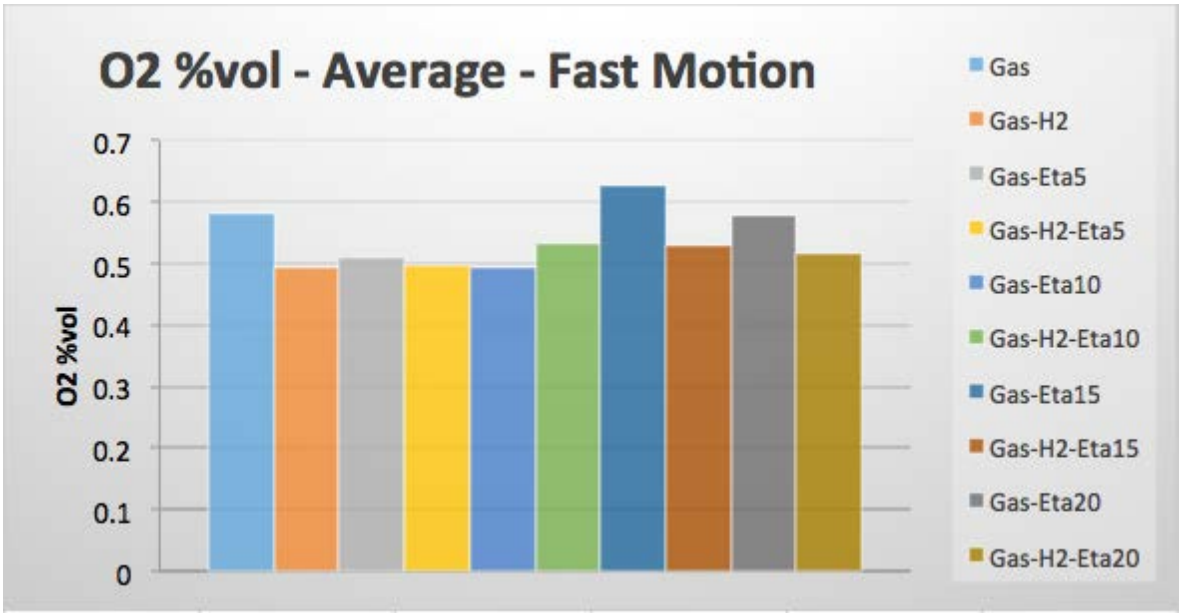

Figure 10. O2 %vol – Average – Low Motion

4. Conclusion

It was observed that Gasoline – Ethanol 15% and Gasoline – Oxy-Hydrogen – Ethanol 15% have the best performance, due at low motion (850 RPM) the CO it have the low presence, at same time that increase the CO2 emissions and not burned Hydrocarbons ppm (HC ppm) have the lower presence.

In case of Gasoline – Ethanol 15% and Gasoline – Oxy-Hydrogen – Ethanol 15%, also have the best behavior at Fast Motion (2500 RPM) because the CO2 and O2 have the higher presence, this according to the theoretical reference that explain that using ethanol as auxiliary fuel the most Oxygen in blend can be obtained.

But also it important to mention that Gasoline – Ethanol 15% and Gasoline – Oxy-Hydrogen – Ethanol 15% at Fast Motion (2500 RPM) have some undesired behavior due the higher CO and not burned Hydrocarbon ppm (HC ppm) detected.

Similarly in all cases of Gasoline – Ethanol 20% and Gasoline – Oxy-Hydrogen – Ethanol 20%, the worse behavior was detected.

Acknowledgements

Thanks to Universidad Autonoma de Queretaro presidency by providing financial support and to the Engineering Faculty - Campus San Juan del Rio for equipment support to develop this research.

Article review and edition by Languages Coordinator, Engineering Faculty, Universidad Autónoma de Querétaro, Carlos Villarreal S.

References

[1] Project BE. Examining the recent «pause» in global warming 2013.
[2] Económicas y Ecológicas INEGI s. f.
[3] Pemex. Reservas de hidrocarburos de Mexico al 1 de Enero de 2013. Mexico: Pemex Exploracion y Produccion; 2013 2013.
[4] Pemex. Seguimiento precio del Petróleo Mezcla Mexicana (MME) 2015. http://portalweb.sgm.gob.mx/economia/es/energeticos.html (accedido 10 de febrero de 2015).
[5] Científicos T. El hidrógenoTextos Científicos 2006. http://www.textoscientificos.com/quimica/hidrogeno (accedido 10 de febrero de 2015).
[6] Enciclopedia Britanica. Sir James Dewar. The Lancet 1923;201:708. doi:10.1016/S0140-6736(01)15299-2.
[7] Enciclopedia Britanica. Harold C s. f. http://global.britannica.com/biography/Harold-Urey.
[8] Enciclopedia Britanica. Tritium Chemical Isotope s. f. http://global.britannica.com/science/tritium (accedido 1 de agosto de 2015).
[9] Engel A. Nature's building blocks. An A-Z guide to the elements. Oxford: Oxford University Press; 2011. doi:10.1088/0957-4484/20/43/430202.
[10] Eckermann E. World History Of The Automobile. 371. Ilustrated, 2001, p. 1-72.
[11] Enciclopedia Britanica. Edward Daniel Clarke _ biography 2015. http://global.britannica.com/biography/Edward-Daniel-Clarke.
[12] Bayrakci AG, Koçar G. Second-generation bioethanol production from water hyacinth and duckweed in Izmir: A case study. Renewable and Sustainable Energy Reviews 2014;30:306-16. doi:10.1016/j.rser.2013.10.011.

[13] CC. The unsolved mystery of human ADP-dependent glucokinase 2015. https://www.physics.wisc.edu/~lmaurer/academic/morey/SamuelMorey.html#_edn43 (accedido 1 de agosto de 2015).

[14] Pahl G. The citizen-powered energy handbook : community solutions to a global crisis. 185-188, 2007, p. 347.

[15] Shahir S a., Masjuki HH, Kalam M a., Imran a., Ashraful a. M. Performance and emission assessment of diesel–biodiesel–ethanol/bioethanol blend as a fuel in diesel engines: A review. Renewable and Sustainable Energy Reviews 2015;48:62-78. doi:10.1016/j.rser.2015.03.049.

10
Miscellaneous

Chapter 10.1. Revising the molecular dynamics of hydrogen within the sulfur-ammonia fotothermochemical cycle through NMR spectroscopy

R. Orozco-Mena[a]; R. Marquez-Montes[a]; J. Mendoza-Chacón[a]; E. Herrera-Peraza[b]; H. Romero-Paredes[c]; D. Chavez-Flores[a]; V. H. Ramos-Sánchez[a,*]

[a]Facultad de Ciencias Químicas, Universidad Autónoma de Chihuahua, Nuevo Campus Universitario, Circuito Universitario, Chihuahua, Chih., México. C.P. 31125.
[b]Centro de Investigación en Materiales Avanzados, S.C., Miguel de Cervantes #120, Complejo Industrial Chihuahua, Chihuahua, Chih., México. C.P. 31109.
[c]Universidad Autónoma Metropolitana Iztapalapa, San Rafael Atlixco #186, Iztapalapa, México D.F., Mexico. C.P. 09340

ABSTRACT

Among thermochemical cycles, the sulfur family cycles have been shortlisted as the most promising routes to obtain hydrogen at large scale. A new foto thermochemical cycle within the same family has been developed in recent years: the sulfur-ammonia (S-NH_3) cycle. One of the major benefits of the S-NH_3 cycle is the production of H_2 at room temperature exploiting UV radiation by oxidation of aqueous $(NH_4)SO_3$.
We have already studied the photolytic oxidation of $(NH_4)SO_3 \cdot H_2O$ to produce H_2 under controlled and concentrated UV radiation using Raman microscopy to better understand the reaction dynamics and ultimately replicate such reaction within a solar reactor. It has been clearly revealed that water is required to promote photolytic oxidation of $(NH_4)SO_3$. Thus, at first sight, it seems rational to think that H_2 produced comes from water through direct splitting. However, the role of NH_4^+ ion in such reaction has been somehow neglected. Moreover the participation of the protons within NH_4^+ ion is yet unknown, in spite of the fact that they might be involved in the reaction mechanism that ultimately leads to hydrogen production.
Hence, this study aims to elucidate the reaction mechanisms involved in the oxidation of ammonium sulfite through an integral theoretical-experimental approach, consisting of isotopic substitution experiments carried out using NMR spectroscopy, which preliminarly have revealed the occurrence of two distinct proton entities in aqueous $(NH_4)SO_3$ and $(NH_4)SO_4$.

Keywords: Solar hydrogen, Photothermochemical cycles, NMR, Sulfur-ammonia

1. Introduction

According to estimations by the Energy Information Administration, by 2040 fossil fuels will supply 80% of the energy consumed worldwide [1]. The consumption of fossil fuels

---

*Author for correspondence: vramos@uach.mx, v.h.ramos.sanchez@gmail.com

represents several problems; one of the most important issues is generation of greenhouse gases, which contribute to climate change. For this and other reasons it is necessary to explore new alternatives to supply the energy that our society demands. Hydrogen is an energy carrier capable to replace fossil fuels and provide energy for transportation, industry, and households. Such model scenario is known as hydrogen economy. However, in order to really achieve a sustainable approach, it is mandatory to find new methods to produce hydrogen at large scale, maintaining the use of fossil fuels to a minimum. In order to replace steam reforming as the most widely used process to obtain hydrogen nowadays.

One of the viable options to achieve this goal is the Thermo Chemical Water Sulfur Cycles (TCWSCs). Among these, the sulfur family cycles have been shortlisted as the most promising routes to obtain hydrogen at large scale. European research projects such as HYTHEC and HYCYCLES have focused on studying the Sulfur-Iodine cycle and the Hybrid Sulfur cycle, respectively. [2,3] Recently, a new fotothermochemical cycle within the same family has been developed: the sulfur-ammonia (S-NH_3) cycle [4]. The S-NH_3 cycle is summarized in Figure 1. It is noteworthy to mention that as well as the other sulfur family cycles, already mentioned, at some point all of them exploit sulfate ions in aqueous solutions. It is well known the occurrence of different chemical species in aqueous $(NH_4)SO_3$, such as SO_3, SO_4 and S_2O_6 [5, 6]. Although spectroscopic studies have suggested other species: $S_2O_4^{-2}$, $S_2O_3^{-2}$, $S_2O_5^{-2}$, $S_2O_6^{-2}$, $S_4O_6^{-2}$, S_2^{-} and S_3^{+} [7]. Once oxidised, sulfate ions in aqueous solutions also exhibits a complex dynamics.

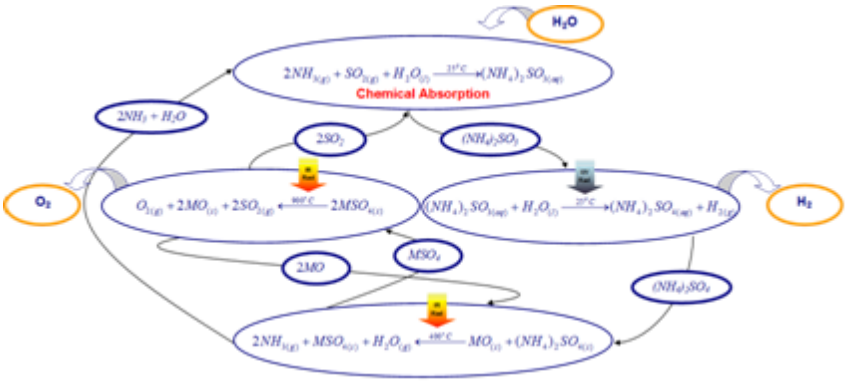

Fig. 1. The Sulfur-Amonnia fotothermochemical cycle.

We believe that water also plays an important role within the S-NH_3 cycle, particularly is of great relevance, since sulfite ions are directly involved in hydrogen production through photolytic oxidation. Moreover, the effect of the counterion, NH_4^+ in such aquocomplexes is also of great interest, based on the fact that it might be involved in the reaction mechanism that leads to hydrogen production.

Based on our previous experience with aqueous sulfate ions, we would expect to be able to elucidate the reaction mechanisms involved in the photolytic oxidation of ammonium sulfite. Particularly, it is of vital importance to understand how hydrogen is produced during this reaction…is it really that water molecules are splitting? Or are there any other intermediate mechanisms that lead to hydrogen formation in which NH_4^+ is

involved? The knowledge of these mechanisms is relevant to understand reaction kinetics and could lead to improvements in the process, in order to achieve higher levels of hydrogen production. Therefore, this study aims to elucidate the reaction mechanisms involved in the oxidation of ammonium sulfite through an experimental approach, consisting of isotopic substitution experiments carried out using NMR spectroscopy

2. Materials and Methods

2.1.Materials

All solutions were prepared in deionized water (RMP, MEX). Sodium sulfite 98% (Alfa Aesar, USA), Ammonium sulfite monohydrate 92%. In order to achieve the NMR experiments all the solution were prepared using D_2O 99.9% (Cambridge Isotope Laboratory) as solvent. The nuclear magnetic spectra were obtained on a 60 MHz Anasazi NMR spectrometer.

2.2. Set of experiments

The first set of experiment was carried out in order to know the NMR spectrum produced by the following solutions: $(NH_4)_2SO_3$ and Na_2SO_3; $(NH_4)_2SO_4$ and Na_2SO_4. methanol was used as reference in all the solutions. The measurement of $(NH_4)_2SO_3$ allowed to know if the proton exchange occurs and if it occurs immediately between the protons and the deuterium provided from the D_2O. The experiment with the Na_2SO_3 run as a control due to its lack of protons, thus was possible to compere booth spectrums. The $(NH_4)_2SO_4$ and Na_2SO_4 are the products from the oxidation of the ammonium and sodium sulfites. Therefore, the evaluation of these salts was also performed. Once obtained the spectra for all the solutions, additives volumes of peroxides were added hydrogen peroxide 30% was added gradually to the sulfites solution to promote the oxidation of sulfites. The concentration of sulfite solutions was 1M with 1% of methanol. In order to monitor the oxidation, 20 ul of H_2O_2 were added to the system and subsequently performing the analysis by NMR. This sequence was successively performed until a total of 300 uL of H_2O_2 were added to the system. Therefore 16 NMR spectra were obtained for each sulfite solution. The data analysis was performed using 9.1 software Origin and MesReNova for the proton integration.

3. Results and Discussion

According to the data obtained, in the sulfite ammonium experiment is clear that an exchange occurs inside the system. Before the reaction started (time 0) the magnetic resonance signal generated by the ammonium sulfite solution is located slightly below 5 ppm, being closer to the feature region of the spectrum to ammonium ion. However as the reaction proceed, the resonance signal moves to slightly below 4.7 ppm, in this part the system had 80 uL of H_2O_2. As it is added H_2O_2, the resonance signal begins to move until reaching the region of 5.2 ppm. The water resonance signal is at 4.8 ppm while the ammonium ion is around 5 ppm. It is suggested that the behavior generated during the

experiment could be due to the proton exchange between the ammonium ion and deuterium of heavy water. It is important to consider all the sources of protons in the system, there are traces of water contained in D_2O, the monohydrate ammonium salt, proton from the ion ammonium and the protons of H_2O_2 solution. It is therefore complex with a set of experiments to determine the mechanism of proton exchange in the present system (figure 2).

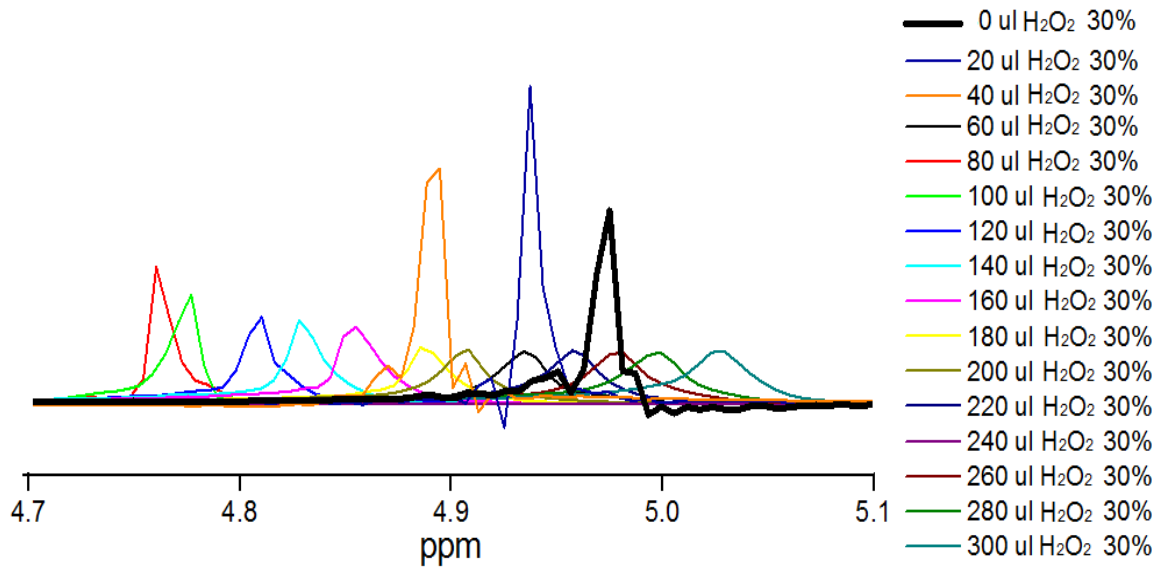

Fig. 2. 1H NMR spectra from the oxidation of ammonium sulfate by addition of H_2O_2

Therefore the experiment using the sodium sulfite solution was performed. In this case the behavior was different from the shown by the ammonium sulfite. Among the main differences is the location of the resonance signal at time 0. At this time the start signal is obtained in the signal corresponding to the water resonance region. In this situation the resonance signal also change as the experiment proceeds, however the displacement was 0.2 ppm and the signal remains near 4.8 ppm (figure 3).

When integrating the AUC it was found that for time 0 the ammonium sulfite solution showed a greater integration, which is reasonable because in this system two sources of protons were avoided; monohydrate salt and protons for the ammonium ion. The behavior of proton integration of both experiments are summarized in Figure 1.

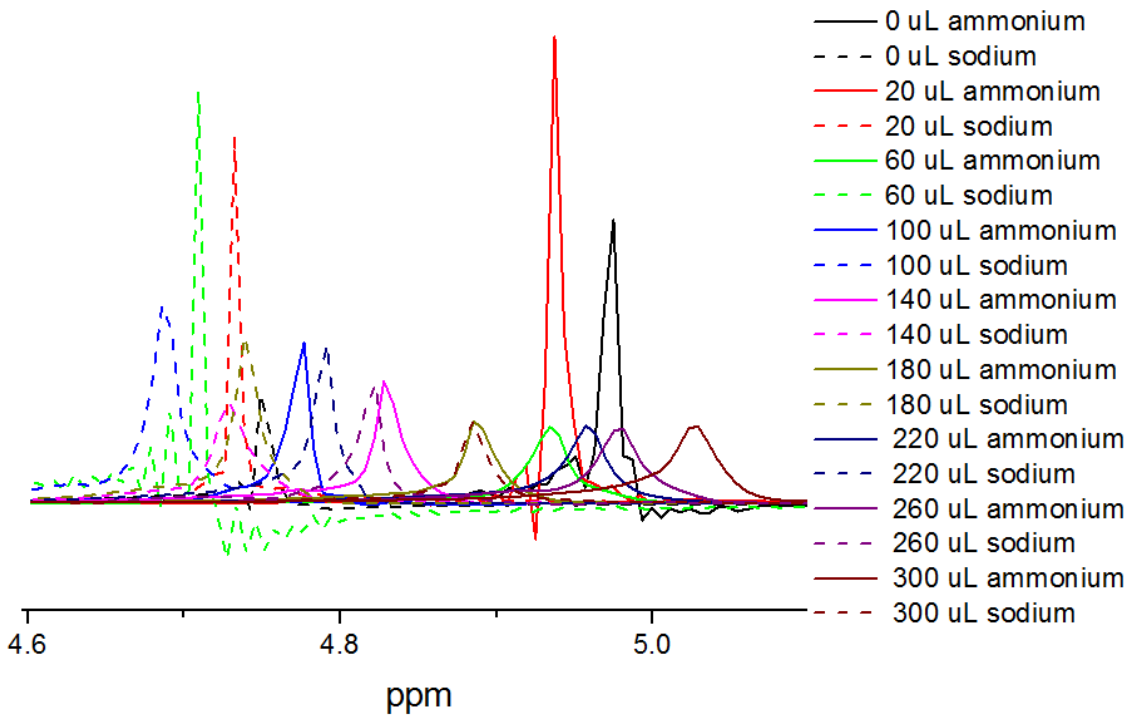

Fig, 3. 1H NMR spectra from the oxidation of ammonium sulfate (continued line) and sodium sulfite (dots) by addition of H_2O_2.

In which a more stable trend in the integration of sodium sulfite is shown. Whereas, the integrating behavior of the ammonium sulfite solution generates a less stable trend. It is important to remember that there is the generation of hydrogen, which as a gas produced during the oxidation reaction of aqueous solutions of sulfite. This may be the reason for the instability found in the ammonium sulfite solution and as i there is an exchange between protons and deuterons ammonia, at some point of the reaction is possible that they are releasing gaseous H_2 which generates light falls in integration values (figure 4).

Sanders *et. al*. [8] reported the behavior of isotope exchange of ammonium ion protons with deuterium presented in a H_2O / D_2O system. The authors argue that the pH of the system has a significant effect on the molecular dynamics solutions, due to importance of this parameter in the thermodynamic properties. On acid systems exist the NH_3D^+, $NH_2D_2^+$, NHD_2^+ and ND_4^+ ions. These species generate different spectra and multiplicities with slight variations in their location.

The isotopic exchange may also be determined by solvation shells and the intermolecular interaction. The intermolecular ammonium ion interaction is modified whenever occurs an isotopic substitution of any of its protons, this is due to the change in the distance between the cores and the collision partner.

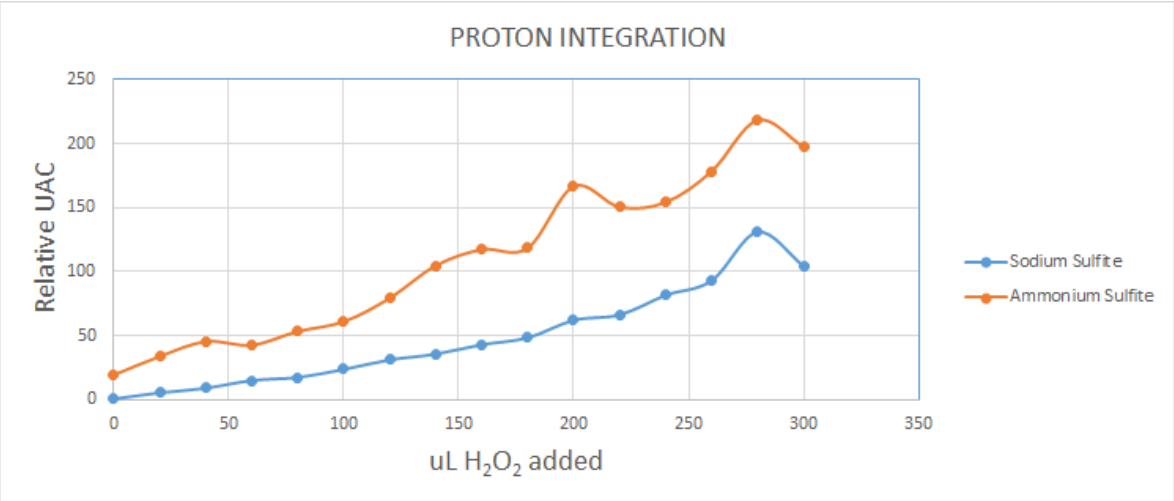

Figure 4. Proton integration for booth systems (ammonium and sodium sulfite) during the reaction. (The UAC values are represented in function of UAC generated by the methanol)

Another factor inherent in the system that have an effect on the isotopic substitution is the presence of the counter ion, which interacts directly with the solvation shells generating electrostatic changes and variation in the molecular distribution in this case SO_3^{2-}.

In the experiments presented, the pH values were 8.16 and 9.55 for sodium and ammonium solutions respectively. Under these conditions the isotopic exchange is faster generated [9] Therefore it is likely that the ammonium ion exchange their protons by deuterium, generating water molecules and partially deuterated ammonium ions. Because of this it is possible that in the early stages of the reaction resonance bands be flown to generate values close to 4.8 ppm. However when the oxidation occurs the pH of the reaction system decreases to a final value of 4.23, generating an acid medium. It is possible that the ammonium ion exchange their protons by deuterium present in the medium, which could be the reason why the resonance peaks slide to 5.2 ppm. It was not possible to analyze the multiplicity spectra signals because the capacity of the equipment was insufficient to obtain enough resolution. The results presented in this paper are not enough to derive conclusions about the dynamics of the isotope exchange in the system. However knowledge generated from this experiments and the information collected in the literature review shows the presence of a dynamic isotope exchange, which can be affected by different factors such as the pH, the concentration of the solutions, solvation shells and the presence of the counter ion.

It is necessary to generate the oxidation of sulfite solutions avoiding to add external protons, as consequence all the NMR signals would generate from the ammonium ion, allowing elucidate the dynamics of protons in the system. It is recommended the implementation of experimental methods to assess the formation of different species in the system during the reaction. It is not only important to assess the species generated directly

from the ammonium ion, also the molecular species formed from the sulfite/sulfate ions are important, since as reported in literature, these species would have an effect in isotopic exchange mechanism of the protons from the ammonium ion. Another technique that would generate important data is the computational chemistry. Through this theoretical tool it is possible to generate different data about the solvation shells and the intramolecular ammonium ion behavior during the reaction.

4. Conclusion

In this study we evaluated the reaction mechanisms involved in the oxidation of ammonium sulfite through NMR spectroscopy through the isotopic substitution experiments, which preliminarily have revealed the occurrence of two distinct proton entities in aqueous $(NH_4)SO_3$ and $(NH_4)SO_4$. However, it is required to keep investigating these phenomena using supplementary techniques, in order to obtain a holistic approach from the molecular dynamics.

Acknowledgements

The authors would like to thank the CONACYT, SENER and the CEMIE-Sol for providing the founding for this research through the Cosolπ project. The authors also would like to thank the SMH and XV International Congress of the Mexican Hydrogen Society for provide the founding to assist at the current meeting.

References

[1] Energy Information Administration, D.o.E. Official Energy Statistics from the U.S. Government. 2009 [cited 17-02-2009]; Available from: http://www.eia.doe.gov.

[2] Duigou, A.L., et al., *HYTHEC: An EC funded search for a long term massive hydrogen production route using solar and nuclear technologies.* International Journal of Hydrogen Energy, 2007. **32**(10–11): p. 1516-1529.

[3] Graf, D., et al., *Economic comparison of solar hydrogen generation by means of thermochemical cycles and electrolysis.* International Journal of Hydrogen Energy, 2008. **33**(17): p. 4511-4519.

[4] Cunping Huanga, et al., *Hydrogen production via photocatalytic oxidation of aqueous ammonium sulfite solutions* WHEC 16, 2006(Florida Solar Energy Center, University of Central Florida).

[5] Cunping Huanga, et al., *Hydrogen Production via UV Photolysis of Aqueous Ammonium Sulfite Solutions.* WHEC 16, 2006.

[6] Cunping, H., *Solar hydrogen production via pulse electrolysis of aqueous ammonium sulfite solution.* Solar Energy, 2013. **91**: p. 394.

[7] Tsujimura, T., et al., *Sulfur speciation and network structural changes in sodium silicate glasses: Constraints from NMR and Raman spectroscopy.* Geochimica et Cosmochimica Acta, 2004. **68**(24): p. 5081-5101.

[8] Sanders J,. Hunter B., Jameson s., Romeo G., Isotope effects on proton chemical shift and coupling constants in the ammonium ions $^{15,14}NH_{4-n}D_n^+$.Chemical Physics Letters. 1988; 145,5,471-476.

[9] Perryn Ch., Dwyer T., Baine P., Two-Dimensional NMR exchange study of proton exchange in aqueous ammonium ion: H/D primary Kinect isotope effect for direct Nitrogen-to-Nitrogen proton transfer.